Investigating structure-activity relationships and the mechanism of action of small-molecule ice recrystallization inhibitors

Leah Ellen McMunn

B.Sc. Honours Biomedical Sciences – University of Ottawa, 2018

A thesis submitted to the University of Ottawa in partial fulfillment of the requirements for the Doctorate in Philosophy degree in Chemistry

Department of Chemistry and Biomolecular Sciences
Faculty of Science
University of Ottawa

Candidate	Supervisor
_____	_____
Leah Ellen McMunn	Robert N. Ben

© Leah Ellen McMunn, Ottawa, Canada, 2025

Abstract

The cryopreservation of biological material is of critical importance to the success of numerous medical and industrial technologies, including supporting biobanks for immunotherapy cancer treatments and reproductive assistance, global food supply chains, as well as biodiversity and ecological preservation campaigns. However, current cryopreservation methods are complicated by the occurrence of ice recrystallization, a phenomenon of ice crystal growth, that has detrimental effects on the post-thaw recovery, viability, and functionality of cryopreserved materials. Over the last decade the Ben Laboratory has reported the discovery of several small-molecule ice recrystallization inhibitors (IRIs) that can be used during the cryopreservation of cells and tissues to control ice crystal growth and protect them against mechanical damage. While a vast library – consisting of thousands of IRIs – has been developed, only a handful have proven to be effective at improving cryopreservation outcomes in an *in vitro* or *in vivo* model. In part, this is due to a lack of knowledge on the mechanism by which these small-molecule IRIs work.

The research described throughout this thesis critically investigates the mechanism of action and structure activity relationships (SAR) of carbohydrate-based small-molecule IRIs as it relates to improving cryopreservation outcomes. Specifically, a study investigating mesenchymal stromal cell (MSC) cryopreservation was continued, where inhibition of ice recrystallization was reported to improve proliferation and immunotherapeutic potential (*chapter 2*). Then, nitrile- and amide-containing IRIs were investigated for the cryopreservation of red blood cells and the nitrile-containing IRIs were further studied as live-cell probes to monitor cellular uptake and internalization using novel Raman imaging techniques (*chapter 3*). Furthermore, several *O*-aryl-β-D-glucopyranoside compounds were rationally designed, synthesized, and tested for ice recrystallization inhibition activity by the 5-minute splat-cooling assay to aid future development and optimization of this class of compounds by correlating their activity with various structural features and parameters (*chapter 4*). In general, correlations are found with respect to a compound's polar surface area to molecular surface area ratio and predicted logP values; these correlations could be used to identify whether a compound would be active or inactive given a specific IC_{50} threshold but are unable to differentiate between compounds of similar structural features or activity. Given this limitation, a more traditional SAR approach was undertaken that investigated modifications to the hydroxyls of the carbohydrate core of the *O*-aryl-β-D-glucopyranoside 4-methoxyphenyl-β-D-glucopyranoside (PMP-Glc) resulted in the discovery of a library of novel C_4 *O*-methylated compounds with high nanomolar ice recrystallization inhibition activity (*chapter 5*). Finally, interactions between small-molecule IRIs and water molecules in both the liquid and solid states were investigated using proton

NMR relaxation time measurements that provided insight into the mechanism responsible for inhibiting ice recrystallization (*chapter 6*).

Collectively, this research provides detailed insight into the mechanism of action of small-molecule carbohydrate-based ice recrystallization inhibitors to inform downstream rational design campaigns. Furthermore, the addition of IRIs into standard cryopreservation protocols has the potential transform the landscape for translating clinical research into human health technology and ultimately improve the accessibility of cell-based therapeutics.

Notes on navigating this thesis

- *Underlined content can be ctrl+clicked (from the Word document) or clicked (from the PDF) to navigate to the respective section.*
- *All references can be found in one section at the end of the thesis in chapter 10.*
- *All experimental details and much of the numerical data for figures can be found in chapter 8.*

Acknowledgements

Throughout my graduate studies I am grateful to have received such tremendous support from family, friends, and colleagues (many of which have also become life-long friends). Without each and every one of you this journey *truly* would not have been possible and for that I am eternally thankful.

First and foremost, I would like to thank my supervisor, Dr. Robert Ben, for his unwavering support and guidance. Your dedication to interdisciplinary research and exploring new ideas provided me with the opportunity to work on such a variety of projects that I know I would not have been able to do elsewhere. Your mentorship has been foundational to my professional development as a scientist and has greatly influenced the success of my work.

To all past and present members of the Ben Lab, thank you for the camaraderie, collaboration, and many shared laughs. I am especially grateful to Marcus Diamante and Elly Walsh whose insights, encouragement, and pre-group meeting breakfasts at Father & Sons made this experience immeasurably more enjoyable – I could not have asked to work with a better team. I would also like to thank the undergraduate students Hannah Mayer, Stephanie Sibbald, Abigail Kos, and Sarah MacPhedran that I had the privilege of directly mentoring for their hard work, curiosity, and dedication to some challenging projects.

I am also thankful for having the opportunity to work with my many collaborative teams, whose expertise and generosity were able to enrich the research I was able to complete during my PhD. To Dr. Nicolas Bordenave and Dr. Adrian S. D'Costa, thank you for your support and efforts towards the relaxation time experiments. To Dr. Adrian Pegoraro and Dr. Albert Stolow, thank you for your guidance and time working on the Raman microscopy imaging experiments. I would also like to thank the entire team at the Ottawa Hospital Research Institute Cell Manufacturing Facility for their support on the MSC project, most especially Dr. Saad Khan for his organization and expertise. Finally, to the team at Canadian Blood Services Edmonton, including Dr. Jason Acker and Tracey Turner, for their integral support on the RBC cryopreservation work.

I wish to acknowledge the professors in the Department of Chemistry and Biomolecular Sciences who contributed formally, to my Thesis Advisory Committee and Defense Committee, as well as informally with respect to my professional development. Your feedback and support throughout this process have been invaluable. I would also like to thank the team at the science store for always making sure we had the supplies we needed (and for the friendship and support along the way!). Finally, I gratefully acknowledge the financial support I received from Canadian Blood Services through their Graduate Fellowship Program as well as the Society for Cryobiology for their travel awards that allowed me to share and grow my research through national and international collaboration.

To my close friends, thank you for keeping me grounded and reminding me there is life outside the lab. My liver may never completely recover from some of our taco nights and FnS patios, but the memories were overwhelmingly worth it, and I wouldn't change a thing.

To my family – thank you for your endless love and encouragement. Although this certainly isn't the doctor I planned on being (or that any of you may have thought I would become) when I first started my university journey, I could not be happier with where this journey has taken me. Most especially, thank you to my partner, Marcus, for being a constant source of support and inspiration through it all. I could not have done this without each and every one of you. Onto the next chapter!

- With love and endless gratitude

Table of Contents

Abstract ..... *ii*

Acknowledgements ..... *iv*

Table of Contents ..... *v*

List of Figures ..... *x*

List of Tables ..... *xxviii*

List of Schemes ..... *xxix*

List of Equations ..... *xxx*

List of Abbreviations ..... *xxxi*

List of Numbered Compounds ..... *xxxiv*

1. Introduction *1*

1.1. Cryopreservation **2**

1.1.1. Warming and cooling rates 2

1.1.2. Cryoprotective agents (CPAs) 4

1.2. Ice recrystallization **5**

1.2.1. The mechanism of ice recrystallization 5

1.2.2. Nature's strategies for controlling ice and mitigating cellular injury 7

1.2.2.1. Thermal hysteresis activity and ice binding of AF(G)Ps 8

1.3. Small-molecule ice recrystallization inhibitors **12**

1.3.1. Development of small-molecule ice recrystallization inhibitors 12

1.3.2. Assays for measuring ice recrystallization inhibition 18

1.3.3. Applications of small-molecule IRIs for cryopreservation 23

1.3.4. Avenues of continued research for small-molecule IRIs 27

2. Applying ice recrystallization inhibitors (IRIs) to the cryopreservation of mesenchymal stromal cells (MSCs) *31*

2.1. Ice recrystallization inhibition activity of *p*BrPh-Glc (25) and 2FA (27) **33**

2.2. Cryopreservation of bone-marrow derived mesenchymal stromal cells (BM-MSCs) with small-molecule ice recrystallization inhibitors *p*BrPh-Glc (25) and 2FA (27) **45**

2.3. Assessing donor-to-donor variation for the cryopreservation of bone-marrow derived mesenchymal stromal cells (BM-MSCs) **41**

2.3.1. Immediate post-thaw cryopreservation outcomes for BM-MSCs 42

2.3.1.1. Cell recovery 42

2.3.1.2. Cell viability assessed by Trypan Blue exclusion and AV/PI assay 43

2.3.1.3. Functionality: Proliferation as measured by EdU assay 46

2.3.2. Cryopreservation outcomes for BM-MSCs assessed following expansion post-thaw 48

2.3.2.1. Cell viability assessed by photomicrographs of cryopreserved BM-MSCs during the first four hours of expansion 52

2.3.2.2. Cell viability as assessed by Trypan Blue exclusion 54

2.3.2.3. Functionality: Proliferation as assessed by cell counts to assess the cell yield, number of population doublings, and doubling time 55

2.3.2.4. Cytotoxicity of *p*BrPh-Glc (**25**) and 2FA (**27**) *in vitro* 59

2.3.2.5. Functionality: Investigating the immunotherapeutic properties of cryopreserved BM-MSCs (IDO expression) 66

2.4. Cryopreservation of umbilical cord derived mesenchymal stromal cells (UC-MSCs) with small-molecule ice recrystallization inhibitor 2FA (27) 67

2.5. Summary of MSC cryopreservation with small-molecule IRIs..... 70

3. Investigating the permeation and internalization of small-molecule IRIs using Raman scattering techniques for the cryopreservation of red blood cells 74

3.1. Prior investigations with IRIs for to red blood cell cryopreservation 76

3.2. Cryopreservation of red blood cells (RBCs) using *nitrile*- and *amide*- containing ice recrystallization inhibitors..... 78

3.2.1. Synthesis of 4-azidophenyl-β-D-glucopyranoside (*p*N_3Ph-Glc, **29**), 4-cyanophenyl-β-D-glucopyranoside (*p*CNPh-Glc, **30**), and 4-carbamoylphenyl-β-D-glucopyranoside (*p*AmPh-Glc, **31**) 78

3.2.2. Ice recrystallization inhibition activity of *p*CNPh-Glc (**30**) and *p*AmPh-Glc (**31**) 80

3.2.3. Cryopreservation of red blood cells (RBCs) using *p*CNPh-Glc (**30**) and *p*AmPh-Glc (**31**) 80

3.2.4. Structure-activity relationship (SAR) studies for nitrile- and amide-containing ice recrystallization inhibitors 82

3.2.4.1. Structure and synthesis of nitrile- and amide- containing *O*-aryl-β-D-glucopyranosides and *N*-aryl-D-gluconamides.....83

3.2.4.2. Ice recrystallization inhibition activity of nitrile- and amide- containing *O*-aryl-β-D-glucopyranosides and *N*-aryl-D-gluconamides.....84

3.2.5. Summary of the cryopreservation of RBCs using nitrile- and amide- containing ice recrystallization inhibitors 87

3.3. Investigating the internalization of *O*-aryl-β-D-glucopyranosides IRIs..... 89

3.3.1. Techniques for imaging biological processes 91

3.3.1.1. Non-linear Raman scattering techniques and their use for investigating water molecules as they relate to cryopreservation 93

3.3.1.2. Live cell imaging using Raman spectroscopy 95

3.3.2. Raman-active small-molecule carbohydrates 97

3.3.2.1. Raman imaging methods development using small-molecule carbohydrates containing Raman tags……. 98

3.4. Screening of *nitrile*-containing ice recrystallization inhibitor candidates 100

3.4.1. Assessment of the cytotoxicity of nitrile- containing *O*-aryl-β-D-glucopyranosides. 101

3.4.1.1. Extended cytotoxicity studies of *m*CNPh-Glc (**37**) 103

3.5. Live-cell imaging of *nitrile*-containing IRI *m*CNPh-Glc (37)..... 106

3.5.1. Summary of Raman imaging studies using small-molecule carbohydrates.....114

4. Investigating structure-activity relationships for small-molecule ice recrystallization inhibitors (IRIs) 116

4.1. SAR campaigns that formed the foundation for understanding ice recrystallization inhibition activity as measured by the 30-minute SCA 119

4.1.1. Hydrophobicity and the effect of alkyl chain length on ice recrystallization inhibition activity 120

4.1.2. The effect of aryl-ring electronics on the ice recrystallization inhibition activity of *O*-aryl-pyranosides ……122

4.1.3. A multiparameter approach to predicting the ice recrystallization inhibition activity of *N*-aryl-D-gluconamides 123

4.1.4. Summarizing the SAR studies using activity as measured by the 30-minute SCA the potential implications of activity measured by the 5-minute SCA.....124

4.2. Comparing molecular descriptor relationships to ice recrystallization inhibition activity as measured by the 30-minute and 5-minute splat-cooling assays..... 124

4.2.1. Revisiting hydrophobicity as an important feature for ice recrystallization inhibition activity using the 5-minute SCA 128

4.3. A structure activity relationship (SAR) investigation of ice recrystallization inhibition activity of *O*-aryl-glucopyranosides are measured by the 5-minute splat-cooling assay (SCA)..130
4.3.1. A broad investigation of various molecular descriptors and parameters and their relationship to the ice recrystallization inhibition activity of *O*-aryl-β-D-glucopyranosides as measured by the 5-minute SCA 131

4.4. Limitations of molecular parameters to describe or predict ice recrystallization inhibition activity 140

4.5. Summarizing the structure-activity relationships of small-molecule IRIs 144

5. A comprehensive investigation of the ice recrystallization inhibition activity of PMP-Glc (26). 146

5.1. The effect of deuteration on the ice recrystallization inhibition activity of PMP-Glc (26) 149
5.1.1. Structure and synthesis of deuterated *O*-aryl-D-glucopyranosides 149

5.2. Probing the effect of hydroxyl methylation on the ice recrystallization inhibition activity of PMP-Glc (26) 153
5.2.1. Synthesis of *O*-methylated derivatives (**89**, **97**-**99**) of PMP-Glc (**26**) 154
5.2.2. Ice recrystallization inhibition activity of *O*-methylated derivatives (**89**, **97**-**99**) of PMP-Glc (**26**) ..156

5.3. Assessing the generalizability of alkylation substitutions to the carbohydrate core of PMP-Glc (26) 158
5.3.1. Synthesis and ice recrystallization inhibition activity of alkylated *O*-aryl-β-D-pyranosides 159
5.3.2. Cytotoxicity of PMP-Glc (**26**) and C_4 OMe PMP-Glc (**99**) 167

5.4. Understanding the positional impact of *O*-methylation on the ice recrystallization inhibition activity of PMP-Glc (26) 169
5.4.1. Assessing carbohydrate water interactions by ^{1}H and ^{13}C NMR 170
5.4.2. Assessing the interactions between a carbohydrate and a single water molecule using computational molecular dynamics simulations 174

5.5. Summary of PMP-Glc alkylation modifications and their impact on future small-molecule IRI development 180

6. Using ^{1}H NMR relaxation times to investigate the mechanism of action of small molecule ice recrystallization inhibitors (IRIs) 183

6.1. Nuclear magnetic resonance techniques for observing and measuring water molecule interactions 185
6.1.1. T_1 relaxation 186
6.1.2. T_2 relaxation 187
6.1.3. The relationship between water molecular motion and ^{1}H NMR relaxation times 188
6.1.4. General aim for NMR experiments using *N*-2-fluorophenyl-D-gluconamide (2FA, **27**) as the model IRI 190

6.2. Characterization of water molecules at below zero temperatures 191
6.2.1. Characterization of pure Milli-Q® water by spin-spin (T_2) relaxation time 191
6.2.2. Characterization of 2FA (**27**) in water solutions by spin-spin (T_2) relaxation time 193
6.2.3. Characterization by spin-lattice (T_1) relaxation time 196
6.2.4. Characterization of the ice lattice by measurement of dynamic ice shaping 199

6.3. Characterization of water molecules at above zero temperatures 200

6.4. Implications of relaxation times on understanding the mechanism of action of 2FA (27) 203

6.5. Screening additional IRIs for their impact on water molecule motion 205
6.5.1. Characterization of saline solutions by spin-spin (T_2) relaxation 211

6.6. Conclusion 213

7. Conclusion and future outlook 215

8. Supporting Information 218

8.1. General Methods and Procedures 218

8.1.1. Methods: Chapter 2 – Mesenchymal Stromal Cells (MSCs) 218
8.1.1.1. General culture of MSCs 218
8.1.1.2. Freezing and thawing of MSCs 218
8.1.1.3. Optimized step-down cooling procedure for MSC cryopreservation 218
8.1.1.4. MSC recovery and viability 219
8.1.1.5. EdU Cell Proliferation Assay 220
8.1.1.6. MSC Population doublings and doubling time 222
8.1.1.7. MSC IDO expression assay 222
8.1.2. Methods: Chapter 3 – Raman for Internalization 223
8.1.2.1. HepG2 cell culture 223
8.1.2.2. Measurement of internalization by SRS 224
8.1.3. Methods: Chapter 3 – Red Blood Cells 226
8.1.3.1. Blood collection and preparation 226
8.1.3.2. RBC freezing and thawing experiments 226
8.1.3.3. Post-thaw hemolysis measurement 227
8.1.4. Methods: Chapter 4 – Optimization of O-aryl-β-D-glucopyranoside structure by computation 227
8.1.5. Methods: Chapter 6 – NMR Characterization by T_1 and T_2 Relaxation 228
8.1.5.1. Sample preparation for NMR measurements 228
8.1.5.2. Stability of 2FA (**27**) 228
8.1.5.3. Temperature calibration and equilibration 229
8.1.5.4. NMR measurements 231
8.1.5.5. NMR data processing 231
8.1.5.6. Calculation of activation energy 232
8.1.5.7. Statistical analysis 233
8.1.6. Methods: General 233
8.1.6.1. Nanolitre osmometry assay for the determination of dynamic ice shaping (DIS) 233
8.1.6.2. Ice recrystallization inhibition 233
8.1.6.3. General cell culture: HepG2 234
8.1.6.4. HepG2 cytotoxicity assay: Resazurin 234
8.1.6.5. HepG2 cytotoxicity assay: Lactate dehydrogenase (LDH) assay 235
8.1.6.6. Graphical representations and statistics 236
8.1.7. General Experimental 236
8.1.8. General Procedures 238

8.2. Synthesis and Characterization 239

8.2.1. Properties and description of antifreeze protein AFP1 239
8.2.2. Synthetic Procedures and Compound Characterization 240
8.2.2.1. Previously established and widely applied ice recrystallization inhibitors 240
8.2.2.2. Common intermediates 253
8.2.2.3. Nitrile-containing compounds 255
8.2.2.4. Amide-containing compounds 269
8.2.2.5. *O*-aryl-β-D-glucopyranosides for structure activity relationship studies (chapter 4). 288
8.2.2.6. Deuterated derivatives 325
8.2.2.7. Methoxy- derivatives 351
8.2.2.8. Additional alkylation compounds (chapter 5) 381

8.3. Raw data for figures and additional plots 443

8.3.1. Ice recrystallization inhibition activity 443
8.3.2. Cytotoxicity Curves (LD_{50}) 486
8.3.3. MSC Cell Data 498
8.3.3.1. BM-MSC Donor Information 498

8.3.3.2. BM-MSC Donor 1 498
8.3.3.3. BM-MSC Donor 2 and 3 501
8.3.3.4. BM-MSC Pooled Data 502
8.3.3.5. IDO expression 503
8.3.3.6. UC-MSCs 504
8.3.4. RBC Cryopreservation Data 505
8.3.5. Raman internalization intensity 505
8.3.6. Chapter 4 506
8.3.7. Chapter 5 515
8.3.8. Chapter 6 517

9. Appendices 518

9.1. Appendix 1: Statement of Contributions 518

9.2. Appendix 2: Thesis Related Publications and Presentations 521
9.2.1. Publications 521
9.2.2. Presentations 521
9.2.2.1. Oral presentations 521
9.2.2.2. Poster presentations 522

9.3. Appendix 3: Non-Thesis Related Publications and Presentations 522
9.3.1. Publications 522
9.3.2. Presentations 524

9.4. Appendix 4: Community Work 524

9.5. Awards and Recognition 525

10. References 526

List of Figures

CHAPTER 1

Figure 1-1. A summary of low temperature biopreservation methods used to extend the shelf life of biologics.

Figure 1-2. (**A**) Comparison of cooling rate (°C/min) on the survival (%) of various cells cooled to -196 °C. *Reprinted with permission from Mazur (1980) as published by Springer.* (**B**) Effect of different cooling rates on cells during the freezing process. *Figure adapted from Mazur (1984) and created using Biorender.com.*

Figure 1-3. Cellular injuries associated with cryopreservation. *Reprinted with permission from Ma et. al. (2021) as published by Acta Biomaterialia.*

Figure 1-4. (**A**) Depiction of particle grain curvature for small grains versus large grains. (**B**) Representation of the grain boundary migration mechanism where molecules transfer from the smaller grains/crystals to larger/grains/crystals. (**C**) Visualization of water molecule organization in the bulk water phase, quasi-liquid layer (QLL), and ice crystal. (**D**) Depiction of the increase in oil droplet size representative of the Ostwald ripening mechanism. *Images adapted from Huang et. al. (2017) under CC 4.0 with video depiction found* here.

Figure 1-5. Structure of antifreeze-glycoprotein (AFGP) 8 (**1**) with n=4 tripeptide (Ala-Ala-Thr) repeats.

Figure 1-6. (**A**) Illustration of the phenomenon of thermal hysteresis. (**B**) Representation of ice crystal growth in the absence of dynamic ice shaping. Link to video format. (**C**) Representation of ice crystal growth with dynamic ice shaping. Link to video format.

Figure 1-7. (**A**) Schematic representation of the basal and prism faces of hexagonal ice (I_h) illustrating the a_1, a_2, a_3 and c axes. (**B**) Hydrogen bonding pattern and three-dimensional structure of water molecules in the ice lattice of I_h as depicted from the top and side view of the ice lattice. *Images adapted with permission from Springer nature and under CC BY-SA 4.0.*

Figure 1-8. Illustration of the binding of biological antifreeze (BA) molecules to the prism face (*a*-axes) of hexagonal ice (I_h) and the subsequent formation of bipyramidal ice crystals (dynamic ice shaping, DIS) due to forced ice crystal growth along the *c*-axis. *Images of both inhibition models adapted from Capicciotti et. al. (2013) under CC 3.0 from IntechOpen.*

Figure 1-9. Different types of biological antifreeze (BA) binding to ice planes. *Images adapted from Gharib et. al. (2022) under CC-BY from Frontiers.*

Figure 1-10. Structures and ice recrystallization inhibition activity of AFGP-8 (**1**), OGG-Gal (**2**), and *C*-Serine (**3**). Compounds prepared as a solution in phosphate-buffered saline and activity reported as a percent mean grain size (% MGS) measured from n=3 (mean ± standard deviation) ice wafers by splat-cooling assay using a 30-minute annealing time at -6.4 °C.

Figure 1-11. Ice recrystallization inhibition activity of *C*-linked AFGP analogues with different carbohydrate components (**2**, **4**-**6**) compared to AFGP-8 (**1**) and phosphate-buffered saline (PBS). Ice recrystallization inhibition activity presented as mean ± standard error of the mean (SEM) of the mean grain

size (MGS) and % MGS (normalized to PBS) of n=3 ice wafers assessed at 5.5 μM using a splat-cooling assay with a 30-minute annealing time at -6.4 °C. *Figure recreated from Czechura et. al. (2008)*.

Figure 1-12. Ice recrystallization inhibition activity of monosaccharides (**7**-**10**) and disaccharides (**11**-**15**) (assessed at 22 mM) compared to AFGP-8 (**1**) and OGG-Gal (**2**) (assessed at 5.5 μM). Ice recrystallization inhibition activity presented as mean ± standard deviation (SD) of the percent mean grain size (% MGS) normalized to phosphate-buffered saline (PBS) of n=3 ice wafers assessed using a splat-cooling assay with a 30-minute annealing time at -6.4 °C. *Figure recreated using data from Czechura et. al. (2008), Tam et. al. (2008) and Capicciotti (2014)*.

Figure 1-13. Plot of mean grain size (mm^2) and normalized MGS relative to the PBS control (% MGS) for various concentrations of D-galactose (**7**). Data reported from n=3 (mean ± standard deviation) ice wafers assessed by splat-cooling assay following a 30-minute annealing time at -6.4 °C. The 22 mM concentration is highlighted in red to indicate the concentration selected for screening of next-generation small-molecule IRIs. *Figure recreated using data from Czechura et. al. (2008)*.

Figure 1-14. Structures and ice recrystallization inhibition activity of β-octyl-Gal (**16**) and NOGlc (**17**). Compounds prepared as a solution in phosphate-buffered saline and activity reported as a percent mean grain size (% MGS) measured from n=3 (mean ± standard deviation) ice wafers by splat-cooling assay using a 30-minute annealing time at -6.4 °C. *Data obtained from Capicciotti et. al. (2012)*.

Figure 1-15. Structures and ice recrystallization inhibition activity of *N*-alkyl-2-(α-D-galactopyranosyl)-ethylamides (**19**-**21**), *N*-alkyl-erythronamides (**22**-**23**), and *N*-alkyl-D-gluconamides (**17** and **24**). Compounds prepared as a solution in phosphate-buffered saline and activity reported as a percent mean grain size (% MGS) measured from n=3 (mean ± standard deviation) ice wafers by splat-cooling assay using a 30-minute annealing time at -6.4 °C. *Data obtained from Ampaw et. al. (2019) and Trant et. al. (2013)*.

Figure 1-16. Structures and ice recrystallization inhibition activity of *O*-aryl-β-D-glucosides (**25**-**26**) and *N*-aryl-D-gluconamides (**27**-**28**). Compounds prepared as a solution in phosphate-buffered saline and activity reported as a percent mean grain size (% MGS) measured from n=3 (mean ± standard deviation) ice wafers by splat-cooling assay using a 30-minute annealing time at -6.4 °C. *Data obtained from Capicciotti et. al. (2016) and Briard et. al. (2016)*.

Figure 1-17. (**A**) Comparison of ice wafer images of a 10 μL droplet of phosphate-buffered saline using the splat-cooling assay (SCA) or a 1 μL droplet of a 40 % sucrose solution (w/v in water) using the sucrose-sandwich assay (SSA). Wafers were imaged after annealing for 40 minutes at -6.4 °C. *Images adapted and reprinted from Ampaw et. al. (2020) with permission from Springer.* (**B**) General schematic depicting the setup of the SCA. (**C**) Comparison of the early analysis methods for ice crystals imaged by the SCA (from left to right): without analysis, determining the mean largest linear grain size, the mean area by assumption of elliptical shape, or the area (mean grain size) of 12 crystals randomly selected by domain recognition software.

Figure 1-18. Change in ice crystal size (mean grain size in mm^2) over time (minutes) as a function of inhibitor concentration for (**A**) D-galactose (**7**) at concentrations of 22, 55, 110, and 220 mM as well as (**B**) PMP-Glc (**26**) at concentrations of 5.5, 11, and 22 mM compared to the negative control phosphate-buffered saline (PBS). Compounds prepared as a solution in phosphate-buffered saline and activity measured from n=3 (mean ± standard deviation) ice wafers by splat-cooling assay at -6.4 °C. *Figure recreated from Capicciotti (2014).*

Figure 1-19. Change in ice crystal size (mean grain size in mm^2) over time (minutes) as a function of inhibitor concentration for PMP-Glc (**26**) at various concentrations compared to the negative control phosphate-buffered saline (PBS). Ice wafers analyzed by the determination of the cross sectional area of (**A**) 12 randomly selected ice crystals on the image or (**B**) every crystal within a field of view. Compounds prepared as a solution in phosphate-buffered saline and activity measured from n=3 (mean ± standard deviation) ice wafers by splat-cooling assay at -6.4 °C. *Figure recreated from Capicciotti (2014) and Abraham (2015).*

Figure 1-20. Ice recrystallization inhibition activity of *p*BrPh-Glc (**25**) described by (**A**) the change in proportion of ice crystals residing in "bin 1" (mean grain size < 0.001 mm^2) over time (minutes) as a function of inhibitor concentration compared to the negative control phosphate-buffered saline (PBS) or (**B**) a plot of the normalized rate of ice crystal growth by multiple annealing times (full, k_{norm}) or a single annealing time (5-min or 10-min, v_{norm}). Compounds prepared as a solution in phosphate-buffered saline (PBS) and activity measured from n=3 (mean ± standard deviation) ice wafers by splat-cooling assay at -6.4 °C. *Figure recreated from Abraham (2015).*

Figure 1-21. Plot of normalized ice crystal growth rate (v_{norm}) in PBS against logarithm transformed compound concentration (in mM) for D-glucose (**8**), *p*BrPh-Glc (**25**), PMP-Glc (**26**), 2FA (**27**), and 2,6DFB (**28**). Determined by modified splat-cooling assay with a 5-minute annealing time at -6.4 °C. *Dose-response data collected by previous Ben Lab members (Dr. Anna Ampaw, Stephanie Abraham, and Dr. Madeleine Adam) and recreated for this figure.*

Figure 1-22. Ice recrystallization inhibition activity of D-glucose (**8**) from five different researchers to visualize person-to-person variation. Plot of normalized ice crystal growth rate (v_{norm}) in PBS against logarithm transformed compound concentration (in mM). Determined by modified splat-cooling assay with a 5-minute annealing time at -6.4 °C. Data reported as the mean ± standard deviation (SD). Reference data: A=Jatinder Singh, B=Leah McMunn (this thesis), C=Stephanie Abraham, D=Anna Ampaw, E=Sarah McPhedran (unpublished).

Figure 1-23. Comparison of cryopreservation outcomes in the presence of small-molecule IRIs compared to control cryopreservation solutions. (**A**) Mean post-thaw viability of red blood cells (RBCs) in the presence of *p*BrPh-Glc (**25**, 30 mM + 15 % glycerol) or PMP-Glc (**26**, 110 mM + 15 % glycerol) compared to the control solutions of 40 % (w/v) or 15 % (w/v) glycerol alone. (**B**) Mean post-thaw recovery of hematopoietic stem cells (HSPCs) and induced pluripotent stem cell derived neurons (iPSC-Ns) in the presence of different concentrations of 2FA (**27**) or 2,6DFB (**28**) compared to their control solutions of 10 % dimethyl sulfoxide (DMSO) or CS10 + 10 μM Rock Inhibitor respectively. (**C**) Mean post-thaw functionality (as measured by cell type specific assays) for mesenchymal stromal cells (MSCs), HSPCs, and iPSC-Ns compared to their respective control solutions. All data mean ± standard error of the mean (except MSCs panel C, mean ± standard deviation). Asterisks indicate statistical significance relative to the control determined by two-tailed unpaired student's t-test where $p \leq 0.05$ (*), 0.01 (**), 0.001 (***) or 0.0001 (****). *Figure adapted from McMunn et. al. (2024).*

CHAPTER 2

Figure 2-1. (**A**) Structures and current successful cryopreservation applications of small-molecule IRIs *p*BrPh-Glc (**25**) and 2FA (**27**). (**B**) Depiction of stem cell differentiation from pluripotent stem cells. Cryopreservation outcomes for cell types labelled in bold have been successfully improved by the incorporation of small-molecule ice recrystallization inhibitors (IRIs) as of 2024; Asterisk (*) indicates a cell type that has been explored but cryopreservation outcomes were not improved. *Figure created using Biorender.com.*

Figure 2-2. Ice recrystallization inhibition activity of compounds *p*BrPh-Glc (**25**) and 2FA (**27**). (**A**) Percent mean ice grain size (% MGS) normalized to phosphate-buffered saline (PBS) determined by modified splat-cooling assay (SCA) using a 30-minute annealing time at a 22 mM concentration at -6.4 °C. (**B**) Plot of normalized ice crystal growth rate (v_{norm}) in PBS against logarithm transformed compound concentration (in mM). Determined by modified SCA with a 5-minute annealing time at -6.4 °C.

Figure 2-3. Cell preparation protocol for assessment of cryopreservation outcomes for BM-MSCs isolated from a human donor from the ENACT-AMI clinical trial (NCT00936819) in the presence of small-molecule ice recrystallization inhibitors **25** and **27**. *Figure created using Biorender.com.*

Figure 2-4. Depiction of assays for quantifying cryopreservation outcomes of MSCs. (**A**) Trypan Blue exclusion viability assay. (**B**) Annexin V (AV)/Propidium Iodide (PI) viability assay. (**C**) EdU assay for cell proliferation. *Figure created using Biorender.com.*

Figure 2-5. Cryopreservation outcomes for BM-MSCs (donor 1) cryopreserved at 2.0 x 10^6 cells/mL in standard freezing medium (SFM) with and without IRIs **25** (30 mM) or **27** (15 mM). (**A**) Cell viability as measured by Trypan Blue exclusion assay immediately post-thaw. (**B**) Cell viability as measured by Annexin V (AV)/Propidium Iodide (PI) immediately post-thaw. Events were gated to include the cell region only with ≥ 10,000 cell region events analyzed per sample. (**C**) Cell recovery as measured by manual cell counts (hemocytometer) immediately post-thaw. Results mean ± standard error of the mean (SEM), n=1 SFM, n=3 + *p*BrPh-Glc (**25**) and + 2FA (**27**). Number of vials analyzed (sample size) indicated below each bar. Significance measured by Student's unpaired two-tailed t-test: ns = $p > 0.05$. *Data collected, analyzed and reported previously by Dr. Jessica Poisson.*

Figure 2-6. Cryopreservation outcomes for BM-MSCs (donor 1) cryopreserved at 2.0 x 10^6 cells/mL in standard freezing medium (SFM) with and without IRIs **25** (30 mM) or **27** (15 mM). Proliferation (cells in S-phase) measured after two days in culture by EdU assay. Events were gated to include the cell region only with ≥ 20,000 cell region events analyzed per sample. Results mean ± standard error of the mean (SEM), n=1 SFM, n=3 + *p*BrPh-Glc (**25**) and + 2FA (**27**). Number of vials analyzed (sample size) indicated below each bar. Significance measured by Student's unpaired two-tailed t-test: *** = $p \leq 0.001$. *Data collected, analyzed and reported previously by Dr. Jessica Poisson.*

Figure 2-7. Cryopreservation outcomes for BM-MSCs (donor 1) cryopreserved at 2.0 x 10^6 cells/mL in standard freezing medium (SFM) with and without IRIs **25** (30 mM) or **27** (15 mM). (**A**) Cell viability as measured by Trypan Blue exclusion assay immediately post-thaw and after a three-day culture. (**B**) Cell viability as measured by Annexin V (AV)/Propidium Iodide (PI) immediately post-thaw and after a three-day culture. (**C**) The number of population doublings and (**D**) the amount of time that was elapsed to achieve a single population doubling. Cells plated at 0.5 x 10^6 cells/mL. Results mean ± standard error of the mean (SEM), n=1 SFM, n=3 + *p*BrPh-Glc (**25**) and + 2FA (**27**). Number of vials analyzed (sample size) indicated below each bar. Significance measured by two-way ANOVA with Tukey's post-hoc analysis (**A** and **B**) or Student's unpaired two-tailed t-test (**C** and **D**): * = $p \leq 0.05$, ** = $p \leq 0.01$. *Data collected, analyzed and reported previously by Dr. Jessica Poisson.*

Figure 2-8. Photomicrographs of BM-MSCs cultured immediately post-thaw that were isolated from donor 1 and cryopreserved with either standard freezing medium (SFM) without or with the addition of IRIs **25** (30 mM) or **27** (15 mM). Images taken after three days in culture plated at a density of 0.50 x 10^6 cells/mL. Attached cells are visible as dark spots on the image. *Data collected, analyzed and reported previously by Dr. Jessica Poisson.*

Figure 2-9. Immediate post-thaw cell recovery for BM-MSCs cryopreserved at 2.0 x 10^6 cells/mL in standard freezing medium (SFM) with and without IRIs **25** (30 mM) or **27** (15 mM). Cell recovery as

measured by manual cell counts (hemocytometer). (**A**) Donor 1 (*results obtained by Dr. Jessica Poisson*). (**B**) Donor 2. (**C**) Donor 3. (**D**) Comparison of all three donors. Results mean ± standard deviation (SD). Number of vials analyzed (sample size) indicated below each bar. Significance measured by Student's unpaired two-tailed t-test for panel A, one-way ANOVA with Tukey's post-hoc analysis for panels B and C, and two-way ANOVA with Tukey's post-hoc analysis for panel D with only cross donor comparisons shown: ns = $p > 0.05$, * = $p \leq 0.05$, ** = $p \leq 0.01$.

Figure 2-10. Immediate post-thaw cell viability for BM-MSCs cryopreserved at 2.0 x 10^6 cells/mL in standard freezing medium (SFM) with and without IRIs **25** (30 mM) or **27** (15 mM). Cell viability as measured by Trypan Blue exclusion assay and Annexin V (AV)/Propidium Iodide (PI). Events for AV/PI were gated to include the cell region only with ≥ 10,000 cell region events analyzed per sample. (**A**) Donor 1 (*results obtained by Dr. Jessica Poisson*). (**B**) Donor 2. (**C**) Donor 3. (**D**) Comparison of all three donors where only significance across donors are shown. Results mean ± standard deviation (SD). Number of vials analyzed (sample size) indicated below each bar. Significance measured by two-way ANOVA with Tukey's post-hoc analysis: *** = $p \leq 0.001$, **** = $p \leq 0.0001$.

Figure 2-11. Flow cytometry dot plots for representative technical replicates of the Annexin V (AV)/Propidium Iodide (PI) assay for BM-MSCs cryopreserved from donors (**A**) 2 or (**B**) 3 in standard freezing medium (SFM) supplemented with or without IRIs **25** (30 mM) or **27** (15 mM). Events for AV/PI were gated to include the cell region only with ≥ 10,000 cell region events analyzed per sample.

Figure 2-12. Immediate post-thaw proliferation assessment of BM-MSCs cryopreserved at 2.0 x 10^6 cells/mL in standard freezing medium (SFM) with and without IRIs **25** (30 mM) or **27** (15 mM). Proliferation (cells in S-phase) measured after two days in culture by EdU assay with cells plated at 0.5 x 10^6 cells/mL. Events were gated to include the cell region only with ≥ 10,000 cell region events analyzed per sample. (**A**) Donor 1 (*results obtained by Dr. Jessica Poisson*). (**B**) Donor 2. (**C**) Comparison of all three donors where only significance across donors are shown. Results mean ± standard deviation (SD). Number of vials analyzed (sample size) indicated below each bar. Significance measured by Student's unpaired two-tailed t-test (**D**): * = $p \leq 0.05$, *** = $p \leq 0.001$.

Figure 2-13. Flow cytometry dot plots for representative technical replicates (**A-C**) of the 5-ethynyl-2′-deoxyuridine (EdU) assay for BM-MSCs cryopreserved from donor 2 in standard freezing medium (SFM) supplemented with or without ice recrystallization inhibitor **27** (15 mM). Events were gated to include the cell region only with ≥ 10,000 cell region events analyzed per sample.

Figure 2-14. Photomicrographs of BM-MSCs cultured immediately post-thaw that were isolated from donor 2 and cryopreserved with either standard freezing medium (SFM) without or with the addition of IRIs **25** (30 mM) or **27** (15 mM). Images taken three days after plating at a density of 0.05 x 10^6 cells/mL, 0.10 x 10^6 cells/mL, or 0.25 x 10^6 cells/mL. Attached cells are visible as dark spots on the image.

Figure 2-15. Post-thaw cryopreservation outcomes following a three-day culture of BM-MSCs (donor 2) cryopreserved at 2.0 x 10^6 cells/mL in standard freezing medium (SFM) with and without ice recrystallization inhibitor **27** (15 mM). Data for cells cryopreserved with **25** (30 mM) was omitted due to an insufficient quantity of viable cells. Cells were plated at 0.05 x 10^6 cells/mL, 0.10 x 10^6 cells/mL, or 0.25 x 10^6 cells/mL. (**A**) The cell viability as measured by Trypan Blue exclusion assay. (**B**) The quantity of cells obtained after the three-day culture relative to the initial plating density determined by manual cell count (hemocytometer). (**C**) The number of population doublings and (**D**) the amount of time that was elapsed to achieve a single population doubling. Results mean ± standard deviation (SD), n≥3 for all treatments, for samples that did not double in population a doubling time was not calculated and was omitted from (**D**). Number of vials analyzed (sample size) indicated below each bar. Significance measured by Student's unpaired two-tailed t-test: * = $p \leq 0.05$, ** = $p \leq 0.01$.

Figure 2-16. Photomicrographs of BM-MSCs cultured immediately post-thaw that were isolated from donor 2 and cryopreserved with either standard freezing medium (SFM) without or with the addition of IRIs **25** (30 mM) or **27** (15 mM). Images taken every hour up to four hours after plating at a density of 0.25 x 10^6 cells/mL. Attached cells are visible as dark spots on the image.

Figure 2-17. Photomicrographs of BM-MSCs cultured immediately post-thaw that were isolated from donor 3 and cryopreserved with either standard freezing medium (SFM) without or with the addition of IRIs **25** (30 mM) or **27** (15 mM). Images taken every hour up to four hours after plating at a density of 0.25 x 10^6 cells/mL. Attached cells are visible as dark spots on the image.

Figure 2-18. Photomicrographs of BM-MSCs cultured immediately post-thaw that were isolated from donor 1 (*results obtained by Dr. Jessica Poisson*) and 2 and cryopreserved with either standard freezing medium (SFM) without or with the addition of IRIs **25** (30 mM) or **27** (15 mM). Images taken after three days of expansion after plating at a density of 0.50 x 10^6 cells/mL for donor 1 or 0.25 x 10^6 cells/mL for donor 2. Attached cells are visible as dark spots on the image.

Figure 2-19. Cryopreservation outcomes following expansion of BM-MSCs cryopreserved at 2.0 x 10^6 cells/mL in standard freezing medium (SFM) with and without ice recrystallization inhibitors **25** (30 mM) or **27** (15 mM). Cell viability as measured by Trypan Blue exclusion assay (**A**) Donor 1 (*results obtained by Dr. Jessica Poisson*). (**B**) Donor 2. (**C**) Donor 3. (**D**) Comparison of all three donors where only significance across donors are shown. Results mean ± standard deviation (SD). Number of vials analyzed (sample size) indicated below each bar. Significance measured by Student's unpaired two-tailed t-test: * = $p \leq 0.05$.

Figure 2-20. Cryopreservation outcomes following expansion of BM-MSCs cryopreserved at 2.0 x 10^6 cells/mL in standard freezing medium (SFM) with and without IRIs **25** (30 mM) and **27** (15 mM). Cells were plated at 0.50 x 10^6 cells/mL for donor 1 and 0.25 x 10^6 cells/mL for donors 2 and 3. Cells counted after three days of expansion for donors 1 and 2 and two days of expansion for donor 3. Cell yield calculated as the percentage of cells counted following expansion relative to the quantity of cells initially plated (hemocytometer). (**A**) Donor 1 (*results obtained by Dr. Jessica Poisson*). (**B**) Donor 2. (**C**) Donor 3. (**D**) Comparison of all three donors where only significance across donors are shown. Results mean ± standard deviation (SD). Number of vials analyzed (sample size) indicated below each bar. Significance measured by Student's unpaired two-tailed t-test: * = $p \leq 0.05$, ** = $p \leq 0.01$.

Figure 2-21. Cryopreservation outcomes following expansion of BM-MSCs cryopreserved at 2.0 x 10^6 cells/mL in standard freezing medium (SFM) with and without IRIs **25** (30 mM) and **27** (15 mM). Cells were plated at 0.50 x 10^6 cells/mL for donor 1 and 0.25 x 10^6 cells/mL for donors 2 and 3. Cells counted after three days of expansion for donors 1 and 2 and two days of expansion for donor 3. A doubling time was not calculated if the sample did not achieve a single population doubling within the expansion time. (**A**) Donor 1 (*results obtained by Dr. Jessica Poisson*). (**B**) Donor 2. (**C**) Donor 3. (**D**) Comparison of all three donors where only significance across donors are shown. Results mean ± standard deviation (SD). Number of vials analyzed (sample size) indicated below each bar. Significance measured by Student's unpaired two-tailed t-test: * = $p \leq 0.05$, ** = $p \leq 0.01$.

Figure 2-22. General schematic for a resazurin-based cytotoxicity assay. *Figure created using Biorender.com.*

Figure 2-23. Plot of percent cell viability of HepG2 cells against logarithm transformed compound concentration (in mM) for *p*BrPh-Glc (**25**) and 2FA (**27**) with 1- and 24-hour incubations (**A**) without and (**B**) with the addition of 10 % dimethyl sulfoxide (DMSO). (**C**) Comparison of incubation time points for 10 % DMSO alone. Cells were plated in a 96-well plate at a density of 1.0 x 10^5 cells/mL and incubated at 37 °C in 5 % CO_2. Results determined by resazurin-based metabolic assay and reported as mean ± standard deviation (SD). Significance measured by Student's unpaired two-tailed t-test: **** = $p \leq 0.0001$.

Figure 2-24. Hydrolysis of *O*-aryl-glycosides by *in vitro* enzymes to release cytotoxic phenol metabolites.

Figure 2-25. Plot of percent cell viability of HepG2 cells against logarithm transformed compound concentration (in mM) for *p*BrPh-Glc (**25**) and 4-bromophenol with 1-hour and 24-hour incubations with the addition of 10 % dimethyl sulfoxide (DMSO). Cells were plated in a 96-well plate at a density of 1.0 x 10^5 cells/mL and incubated at 37 °C in 5 % CO_2. Results determined by resazurin-based metabolic assay and reported as mean ± standard deviation (SD).

Figure 2-26. General schematic for the assessment of IDO RNA expression for BM-MSCs isolated from a single donor (donor 2) from the ENACT-AMI clinical trial (NCT00936819) in the presence of small-molecule ice recrystallization inhibitor **27**. *Figure created using Biorender.com.*

Figure 2-27. Number of amplification cycles required to reach the desired fluorescence threshold for the detection of IDO RNA. Comparison of BM-MSCs isolated from a single donor (donor 2) from the ENACT-AMI clinical trial (NCT00936819) in the presence or absence of small-molecule IRI **27**. Results reported as mean ± standard deviation (SD), n=3. Number of vials analyzed (sample size) indicated below each bar. Significance measured by Student's unpaired two-tailed t-test: * = $p \leq 0.05$.

Figure 2-28. Post-thaw cryopreservation outcomes of UC-MSCs (donor 4) cryopreserved at 6.0 x 10^6 cells/mL in standard freezing medium (SFM, 10 % DMSO + 5 % HA in PLA) with and without IRI **27** (15 mM). Outcomes tested at multiple time intervals between 0 and 3 days. Cells were plated at (**A-C**) 1.0 x 10^4 cells/cm^2 or (**D-F**) 2.0 x 10^4 cells/cm^2. (**A,D**) Cell viability assessed by Trypan Blue exclusion assay, (**B,E**) Proliferation assessed by EdU assay. Results mean ± standard deviation (SD), n=3 for viability and yield, n=1 for proliferation. Number of vials analyzed (sample size) indicated within each bar. *These data were collected, analyzed, and reported by the team of researchers at the Ottawa Hospital Research Institute under the supervision of Dr. David Courtman.*

Figure 2-29. Comparison of post-thaw cryopreservation outcomes between UC-MSCs and BM-MSCs. UC-MSCs cryopreserved at 6.0 x 10^6 cells/mL, BM-MSCs cryopreserved at 2.0 x 10^6 cells/mL. (**A**) Cell viability measured by Trypan Blue exclusion assay. (**B,D**) Cell recovery and population doublings determined by manual cell count. Population doublings counted after 24 hours for UC-MSCs and 3 days for BM-MSCs. (**C**) Proliferation measured by EdU assay following 16 hours of culture for UC-MSCs and 2 days for BM-MSCs. UC-MSCs plated at 2.0 x 10^4 cells/cm^2 and 0.25 x 10^6 cells/mL for BM-MSCs. $n \geq 2$ from a single donor and results reported as mean ± standard deviation (SD). Number of vials analyzed (sample size) indicated below each bar. *The UC-MSC data were collected, analyzed, and reported by the team of researchers at the Ottawa Hospital Research Institute under the supervision of Dr. David Courtman.*

Figure 2-30. Immediate and post-expansion cryopreservation outcomes for BM-MSCs with data pooled from three different donors. Cells plated at a density of 0.50 x 10^6 cells/mL for donor 1 and 0.25 x 10^6 cells/mL for donors 2 and 3. Donors 1 and 2 cultured for three days prior to assessment of cryopreservation outcomes, donor 3 cultured for two days. Results mean ± standard deviation (SD). Number of donors analyzed (biological sample size) indicated below each bar. Significance measured by one-way ANOVA with Tukey's post-hoc analysis: * = $p \leq 0.05$.

CHAPTER 3

Figure 3-1. Methods of preservation for red blood cells, including both hypothermic storage and cryopreservation.

Figure 3-2. Effect of IRIs *p*BrPh-Glc (**25**) and PMP-Glc (**26**) at 30 mM and 110 mM respectively on the post-thaw integrity of RBCs (100 % - % hemolysis) at various concentrations of glycerol. RBCs were slow cooled (1 °C/min) to -40 °C and then rapidly cooled to the storage temperature of -80 °C prior to thawing (rapid) to 37 °C and measurement of hemolysis. Results reported as mean ± standard error of the mean (SEM). Significance measured by two-way ANOVA with Tukey's post-hoc test: ns = $p > 0.05$, * = $p \leq 0.05$, ** = $p \leq 0.01$, *** = $p \leq 0.001$, **** = $p \leq 0.0001$.

Figure 3-3. Structures of *O*-aryl-β-D-glucopyranoside compounds with *para*-azide (*p*N_3Ph-Glc, **29**), *para*-nitrile (*p*CNPh-Glc, **30**), and *para*-amide (*p*AmPh-Glc, **31**) functional groups.

Figure 3-4. Ice recrystallization inhibition activity of compounds **29**-**31**. Plot of normalized ice crystal growth (v_{norm}) in phosphate-buffered saline (PBS) against logarithm transformed compound concentration (in mM). Determined by modified splat-cooling assay with a 5-minute annealing time at -6.4 °C. Results reported as mean ± standard deviation (SD) for n=3 ice wafers. IC_{50} reported with error as the 95 % confidence interval range. *Data for the ice recrystallization inhibition activity of pN_3Ph-Glc (**29**) collected, analyzed, and reported by Dr. Jessica Poisson.*

Figure 3-5. Percentage of intact red blood cells (RBCs) post-thaw using 15 % glycerol in combination with compound **30** (12.5 mM, 25 mM, or 40 mM) or compound **31** (2.5 mM, 20 mM, or 50 mM). Samples were frozen either using a slow-cooling rate-controlled method (1 °/min to -40 °C) or fast-cooling dump freeze method (100 °C/min to -80 °C) followed by thawing in a 37 °C water bath. Hemolysis was measured by Drabkin's assay and presented as % intact RBCs = (100 % - % hemolysis). Data reported as mean ± standard error of the mean (SEM), n=2 cryovials frozen from units pooled from three blood-type and sex-matched donors provided by NetCAD.

Figure 3-6. Ice recrystallization inhibition activity of *O*-aryl-β-D-glucopyranosides (**26**, **33**-**36**). Ice recrystallization inhibition activity reported as mean ± standard deviation (SD) of the percent mean grain size (% MGS) normalized to phosphate-buffered saline (PBS) of n=3 ice wafers assessed at 22 mM using a splat-cooling assay with a 30-minute annealing time at -6.4 °C. *Figure recreated using data from Capicciotti (2014)*.

Figure 3-7. Ice recrystallization inhibition activity of (**A**) *O*-aryl-β-D-glucopyranoside compounds **30** and **37**-**38** and (**B**) *N*-aryl-D-gluconamides **39**-**41**. Plot of normalized ice crystal growth (v_{norm}) in phosphate-buffered saline (PBS) against logarithm transformed compound concentration (in mM). Determined by modified splat-cooling assay with a 5-minute annealing time at -6.4 °C. Results reported as mean ± standard deviation (SD) for n=3 ice wafers. IC_{50} reported with error as the 95 % confidence interval range.

Figure 3-8. Ice recrystallization inhibition activity of (**A**) *O*-aryl-β-D-glucopyranoside compounds **31** and **42**-**43** and (**B**) *N*-aryl-D-gluconamides **44**-**46**. Plot of normalized ice crystal growth (v_{norm}) in phosphate-buffered saline (PBS) against logarithm transformed compound concentration (in mM). Determined by modified splat-cooling assay. Results reported as mean ± standard deviation (SD) for n=3 ice wafers. IC_{50} reported with error as the 95 % confidence interval range.

Figure 3-9. Intracellular ice formation in HUVEC cells cooled to -40 °C at 90 °C/min in 0.9 % NaCl using SYTO13 staining (5 μM). Using warming rates of (**A**) 25 °C/min and (**B**) 2 °C/min. (**C**) The mean grain size of ice crystals (mm^2) is reported as a function of temperature (°C) for each warming rate. Data reported

as the mean ± standard error of the mean (SEM) and fit to a mono-exponential growth equation where $R^2 = 0.98$ (fast thaw) and 0.97 (slow thaw). *Reproduced from Poisson et. al. (2019) under CC-BY from ACS Publications*.

Figure 3-10. Intracellular ice formation in HUVEC cells cooled to -40 °C at 90 °C/min in 0.9 % NaCl with the addition of either (**AB**) 30 mM *p*BrPh-Glc (**25**) or (**CD**) PMP-Glc (**26**) using SYTO13 staining (5 μM). Warming rates of (**AC**) 25 °C/min and (**BD**) 2 °C/min. (**EF**) The mean grain size of ice crystals (mm^2) is reported as a function of temperature (°C) for each warming rate. Data reported as the mean ± standard error of the mean (SEM) and fit to a mono-exponential growth equation. *Reproduced from Poisson et. al. (2019) under CC-BY from ACS Publications*.

Figure 3-11. Energy diagrams representing (**A**) spontaneous Raman, (**B**) stimulated Raman scattering (SRS), and (**C**) coherent anti-stokes Raman scattering (CARS).

Figure 3-12. (**A**) Raman spectrum of a single cell of human primary glioblastoma (U87 cell line) with various band regions of interest highlighted, including the silent region (1800 cm^{-1} to 2800 cm^{-1}). *Reproduced from Xu et. al. (2021) under CC-BY from MDPI*. (**B**) Representation of the cell-silent region and the signal generated from biorthogonal Raman tags. *Reproduced from Vardaki et. al. (2024) under CC-BY from RSC*.

Figure 3-13. (**A**) Yamakoshi *et. al.*, visualization of HeLa cells cultured with EdU to generate merged images from 749 cm^{-1} (cytochrome C), 2123 cm^{-1} (alkyne – silent region - EdU), and 2849 cm^{-1} (lipids) wavenumbers (blue, red, and green channels respectively) over a course of 21 hours using spontaneous Raman. (**B**) Live cell images acquired at 2217 cm^{-1} to track the internalization of 7RH over a period of 45 minutes represented as blue in colour using stimulated Raman scattering (SRS) (scale bars 20 μm). *Figures reproduced with permission from their respective sources.*

Figure 3-14. Structures of established *O*-aryl-β-D-glucopyranoside IRIs *p*BrPh-Glc (**25**) and PMP-Glc (**26**) as well as their Raman reporter analogues with *para*-azide (*p*N_3Ph-Glc, **29**) or *para*-nitrile (*p*CNPh-Glc, **30**) functional groups.

Figure 3-15. Images of ice in the presence of *p*CNPh-Glc (**30**) measured using CARS microscopy using an off-resonance wavenumber of 2300 cm^{-1} or an on-resonance wavenumber of 2235 cm^{-1} with operating wavelengths of 844 nm and 1040 nm and 12 nm and 7 nm bandwidth respectively. (**A**) 50 mM *p*CNPh-Glc (**30**). Dark artifacts caused by condensation within the optical path. (**B**) Zoomed in region of panel A images highlighted in red. (**C**) 2.5 mM *p*CNPh-Glc (**30**) with optimized imaging set up. Cotton fibre present for focus in both sets of images. (**D**) Plot of Raman signal intensity with respect to a complete spectral scan of the zoomed in regions of the images in panel (**B**) for comparing off-resonance and on-resonance wavenumbers.

Figure 3-16. Structures, chemical synthesis yields, and ice recrystallization inhibition activity (IC_{50} as measured by the 5-minute splat-cooling assay) of *nitrile*-containing *O*-aryl-β-D-glucopyranosides **30** and **37-38** and *N*-aryl-D-gluconamides **39-41**.

Figure 3-17. 24-hour toxicity measurement of compounds **30**, **37-38**. Plot of percent cell viability of HepG2 cells against logarithm transformed compound concentration (in mM). Determined by resazurin-based metabolic assay following 24-hour incubation at 37 °C in 5 % CO_2. Results reported as mean ± standard deviation (SD), N=1 for compounds **30** and **38**, N=4 for compound **37**.

Figure 3-18. Plot of ice recrystallization inhibition activity of compounds **30**, **37-38** for visualization of efficacy index (EI). Red line denotes apparent maximum solubility in PBS. Blue line denotes IC_{50} of ice

recrystallization inhibition activity. Green line denotes LD_{50} of cell viability as determined from **Figure 3-17**. Results reported as mean ± standard deviation (SD).

Figure 3-19. Cytotoxicity measurement of *m*CNPh-Glc (**37**) after various incubation times (1-24 hours). Plot of percent cell viability of HepG2 cells against logarithm transformed compound concentration (in mM). Determined by resazurin-based metabolic assay following incubation at 37 °C in 5 % CO_2. Results reported as mean ± standard deviation (SD), N=4 for 24-hour incubation, N≥2 for 5.5-hour incubation, and N=1 for 1- and 3-hour incubations.

Figure 3-20. General schematic for the LDH cytotoxicity assay.

Figure 3-21. Cytotoxicity measurement of compound **37** after various incubation times (1-24 hours). Plot of percent cell viability of HepG2 cells against logarithm transformed compound concentration (in mM). Determined by LDH membrane integrity assay following incubation at 37 °C in 5 % CO_2. Results reported as mean ± standard deviation (SD), N≥1 for 24-hour incubation, N≥2 for 5.5-hour incubation, and N=1 for 3-hour incubation, and N=2 for 1-hour incubation.

Figure 3-22. Direct comparison of cytotoxicity as measured by resazurin-based assay or LDH release for (**A**) 5.5- and (**B**) 24-hour incubation time points with *m*CNPh-Glc (**37**). Results reported as mean ± standard deviation (SD).

Figure 3-23. (**A**) Stimulated Raman scattering (SRS) and (**B**) coherent anti-stokes Raman scattering (CARS) spectra of compound **37** (*m*CNPh-Glc) in standard cell culture medium in the absence of cells. Spectra obtained both with and without cross-phase modulation (XPM). Graphs plotted as a function of signal intensity against relative wavenumber (cm^{-1}); the x-axis was not fully calibrated such that accurate wavenumbers cannot be reported but the apparent wavenumber of the signals in all spectra was ~2200 cm^{-1}. *Spectral scan completed by Dr. Adrian Pegoraro at the National Research Council – Sussex Site (Ottawa, ON).*

Figure 3-24. Live HepG2 cells imaged in glass-bottom culture dishes using XPM-SRS following a 30-minute incubation with *m*CNPh-Glc (**37**, 30 mM). (**A**) Image taken at a 2850 cm^{-1} wavenumber to highlight the lipid (CH) cellular content. Three highlighted regions indicate the interstitial cell space (green), near the cell periphery (red), and far from the cell boundary (yellow). (**B**) Raman spectra graph plotted as a function of signal intensity against relative wavenumber (cm^{-1}); the x-axis was not fully calibrated such that accurate wavenumbers cannot be reported. Lipid (CH) peak region indicated is at an approximate wavenumber of 2850 cm^{-1} and the nitrile (CN) peak region is at an approximate wavenumber of 2200 cm^{-1}. *Spectral scan completed by Dr. Adrian Pegoraro at the National Research Council – Sussex Site (Ottawa, ON).*

Figure 3-25. Live HepG2 cells imaged in glass-bottom culture dishes using XPM-SRS following a 30-minute incubation with *m*CNPh-Glc (**37**, 30 mM). (**A**) Image taken at a 2850 cm^{-1} wavenumber to highlight the lipid (CH) cellular content. Three highlighted regions indicate different intracellular regions from a first cluster of cells (green = large region, blue = small, concentrated region) and a second cluster of cells (yellow). (**B**) Raman spectra graph plotted as a function of signal intensity against relative wavenumber (cm^{-1}); the x-axis was not fully calibrated such that accurate wavenumbers cannot be reported. Lipid (CH) peak region indicated is at an approximate wavenumber of 2850 cm^{-1} and the nitrile (CN) peak region is at an approximate wavenumber of 2200 cm^{-1}. *Spectral scan completed by Dr. Adrian Pegoraro at the National Research Council – Sussex Site (Ottawa, ON).*

Figure 3-26. Live HepG2 cells imaged in glass-bottom culture dishes using XPM-SRS a 4.5-hour incubation with *m*CNPh-Glc (**37**, 30 mM) followed by a saline wash and change to cell culture medium

containing no nitrile compounds (30-minute incubation, 37 °C, 5 % CO_2). HepG2 cells imaged off-resonance (lipid region, 2900 cm^{-1}) and on-resonance (silent region, for nitriles, 2230 cm^{-1}) in three different fields of view (**A-C**). *Spectral scan completed by Dr. Adrian Pegoraro at the National Research Council – Sussex Site (Ottawa, ON).*

Figure 3-27. Representative z-axis scan of HepG2 cells incubated (photos shown every two photos from a total of 18 from the entire scan or approximately every 2-4 µm) with *m*CNPh-Glc (**37**, 30 mM) for identification of cell aggregate centre of mass (intracellular space). Both scans were generated by imaging at a wavenumber of 2900 cm^{-1} using (**A**) XPM-SRS (link to view scan video) and (**B**) XPM-CARS (link to view scan video). *Spectral scan completed by Dr. Adrian Pegoraro at the National Research Council – Sussex Site (Ottawa, ON).*

Figure 3-28. Experimental design for the incubation of HepG2 cells in the presence of compound **37** (*m*CNPh-Glc, 30 mM) for monitoring time-dependent internalization using XPM-CARS.

Figure 3-29. (**A**) Plot of the signal intensity ratio calculated for HepG2 cells incubated with compound **37** (*m*CNPh-Glc, 30 mM, 37 °C and 5 % CO_2) over a period of 5.5 hours. Nitrile (CN) signal obtained at a wavelength of 2230 cm^{-1} and lipid (CH) signal obtained at a wavelength of 2900 cm^{-1}. Curve fit to an exponential growth equation where $(CN/CH) = {y_0}^{kt}$; where t = time in hours and y_0 is the initial ratio of CH/CN signal immediately after addition of compound. (**B**) Representative images of the HepG2 cell cluster depicting the signal at each of the two wavenumbers. Data reported as the mean and standard deviation of three different locations in the cell cluster at each time point. *Spectral scan completed by Dr. Adrian Pegoraro at the National Research Council – Sussex Site (Ottawa, ON).*

CHAPTER 4

Figure 4-1. Representation of ice recrystallization (in the absence of an IRI) and its proposed mechanism of inhibition by small molecules to disrupt the thermodynamic transfer of water molecules from one ice crystal to another.

Figure 4-2. Depiction of the relationship between ice recrystallization inhibition activity and hydration index (HI) for monosaccharide and disaccharides (**7**-**15**).

Figure 4-3. The development timeline for small-molecule ice recrystallization inhibitors (IRIs) starting in the 1950s with antifreeze (glyco)proteins and moving towards the libraries of *O*-aryl- and *O*-alkyl- β-D-glucopyranosides (such as **26** and **16**) and *N*-aryl and *N*-alkyl D-gluconamides (such as **27** and **17**) following the discovery of the importance of amphiphilicity to improve ice recrystallization inhibition activity of simple sugars (such as **7** and **8**). Ice recrystallization inhibition activity reported as the percent mean grain size (% MGS) of the compound as assessed by the 30-minute splat-cooling assay from n=3 ice wafers at a concentration of 22 mM (except **17**, which was assessed at 0.5 mM). [a] *Tam et. al. (2008)*, [b] *Capicciotti et. al. (2012 and 2016)*, *Briard et. al. (2016)*.

Figure 4-4. Structures of the (**A**) *p*-alkamidophenyl-β-D-glucopyranosides (**32**, **49**-**52**) and (**B**) *p*-alkoxyphenyl-β-D-glucopyranosides (**26**, **53**-**56**) assessed for the relationship between hydrophobicity and ice recrystallization inhibition activity by *Matt Alteen (Ben Lab, MSc 2013)*.

Figure 4-5. Structures of the (**A**) *N*-alkyl-D-aldonamides (**17**-**18**, **22**-**24**, **57**-**60**) and (**B**) *N*-cycloalkyl-D-aldonamides (**61**-**76**) assessed for the relationship between hydrophobicity and ice recrystallization inhibition activity by *Dr. Jennie Briard (Ben Lab, PhD 2016)*.

Figure 4-6. Hypothesized effect of altering the electron density at the anomeric oxygen (O_1) on intermolecular hydrogen bonding interactions and ice recrystallization inhibition activity for (**A**) electron donating group (EDG) and (**B**) electron withdrawing group (EWG) substitutions on *O*-aryl-pyranosides.

Figure 4-7. (**A**) Plot of normalized ice crystal growth rate (v_{norm}) in PBS against logarithm transformed compound concentration (in mM) for reducing sugars (**7-9**). Determined by modified splat-cooling assay with a 5-minute annealing time at -6.4 °C. (**B**) Plot of hydration index (HI) relative to ice recrystallization inhibition activity (IC_{50}) for reducing sugars (**7-9**) with 95 % confidence bands of the linear regression ($R^2 = 0.42$) shown.

Figure 4-8. Plot of the hydration index (HI) of reducing sugars (**7-9**) relative to their ice recrystallization inhibition activity presented as mean ± standard deviation (SD) of the percent mean grain size (% MGS) normalized to phosphate-buffered saline (PBS) of n=3 ice wafers assessed at 22 mM using a splat-cooling assay with a 30-minute annealing time at -6.4 °C. Data was analyzed by method (**1**) quantifying 12 random crystals from the wafer or method (**2**) quantifying the area of all crystals within the field of view. Data fit to a linear regression ($R^2 = 0.90$ and 0.37 with 95 % confidence bands of the linear regression shown). *% MGS activity data analyzed by method 1 from Capicciotti (2014).*

Figure 4-9. Plot of hydration index (HI) relative to ice recrystallization inhibition activity for reducing sugars (**7-9**) at (**A**) 22 mM or (**B**) 75 mM with respect to different annealing times. Data reported as mean ± standard deviation (SD) of the percent mean grain size (% MGS) normalized to phosphate-buffered saline (PBS) of n=3 ice wafers assessed using a splat-cooling assay at -6.4 °C. Data was analyzed by quantifying the area of all crystals within the field of view. Data fit to a linear regression with 95 % confidence bands of the linear regression shown.

Figure 4-10. Plot of hydration index (HI) relative to ice recrystallization inhibition activity for reducing sugars (**7-9**) at (**A**) 22 mM or (**B**) 75 mM with respect to different annealing times. Data reported as mean ± standard deviation (SD) of the normalized rate of ice recrystallization (v_{norm}) compared to phosphate-buffered saline (PBS) of n=3 ice wafers assessed using a splat-cooling assay at -6.4 °C. Data was analyzed by quantifying the area of all crystals within the field of view. Data fit to a linear regression with 95 % confidence bands of the linear regression shown.

Figure 4-11. Ice recrystallization inhibition activity of *p*-alkoxyphenyl-β-D-glucopyranosides **26**, **53**-**56**, **80**. Plot of normalized ice crystal growth rate (v_{norm}) in PBS against logarithm transformed compound concentration (in mM). Determined by modified splat-cooling assay with a 5-minute annealing time at -6.4 °C.

Figure 4-12. Ice recrystallization inhibition activity of *O*-aryl-β-D-glucopyranosides **25**-**26**, **29**-**32**, **53**-**56**, **80**-**86**. Plot of normalized ice crystal growth rate (v_{norm}) in PBS against logarithm transformed compound concentration (in mM). Determined by modified splat-cooling assay with a 5-minute annealing time at -6.4 °C.

Figure 4-13. Hammett plot of the relationship between IC_{50} and the electronic effect of the *para*- substituent for *O*-aryl-β-D-glucopyranosides that were newly tested for ice recrystallization inhibition activity using the 5-minute SCA. The $\log[(IC_{50\ R})/(IC_{50\ R=H})]$ for each derivative was plotted against the σ^{para} (σ_p) value for each substituent. *IC_{50} data for compounds* **29**, **32**, *and* **86** *tested and reported previously by Dr. Jessica Poisson (2019).*

Figure 4-14. Plot of the ratio of a compound's polar surface area (PSA) to its molecular surface area (MSA) as calculated by MarvinSketch® for various *O*-aryl-β-D-glucopyranosides relative to their ice recrystallization inhibition activity as measured by the 5-minute SCA. Data fit to a linear regression

($R^2 = 0.28$) with 95 % confidence bands of the linear regression shown. Ice recrystallization inhibition activity reported as the IC_{50} with 95 % confidence interval error of the dose-response curve for the representative compound as determined by splat-cooling assay with a 5-minute annealing time at -6.4 °C.

Figure 4-15. Plot of a compound's theoretical logP as calculated by (**A** and **B**) VCC ALOGPS 2.1 or (**C** and **D**) ACDLabs for various *O*-aryl-β-D-glucopyranosides relative to their ice recrystallization inhibition activity as measured by the 5-minute SCA. Data fit to a (**A** and **C**) linear regression ($R^2 = 0.49$ and 0.52) or (**B** and **D**) exponential curve fit ($R^2 = 0.49$ and 0.71) with 95 % confidence bands of the fit shown.

Figure 4-16. Plot of a compound's polar surface area (PSA) to its molecular surface area (MSA) as calculated by MarvinSketch® (top) or theoretical logP as calculated by VCC ALOGPS 2.1 (bottom) for various *O*-aryl-β-D-glucopyranosides relative to their ice recrystallization inhibition activity as measured by the 5-minute SCA (IC_{50}). Data fit to a linear regression with (**A**) the full data set ($R^2 = 0.28$ and 0.49), (**B**) compounds $IC_{50} \geq 45$ mM excluded ($R^2 = 0.68$ and 0.68) or (**C**) log-transformed ice recrystallization inhibition activity data ($R^2 = 0.47$ and 0.59) with 95 % confidence bands of trendline shown.

Figure 4-17. Plots of the log-transformed ice recrystallization inhibition activity relative to its (**A**) polar surface area (PSA) to molecular surface area (MSA) ratio as calculated by MarvinSketch® or (**B**) its theoretical logP value as calculated by VCC's ALOGPS 2.1 algorithm. Ice recrystallization inhibition activity as measured by the 5-minute SCA. Error bars for individual data points omitted.

Figure 4-18. Example of the conformation change of 4-methoxyphenyl-β-D-glucopyranoside (PMP-Glc, **26**) displayed using ChemCraft 1.8. Without pre-optimization the 3D structure interpretation was obtained from ChemDraw (with the carbohydrate chair in the $^4C_1$ conformation as the baseline). The optimized structure was obtained following a conformational search with CREST and geometry optimization using ORCA.

Figure 4-19. Plots of the log-transformed ice recrystallization inhibition activity relative to its polar surface area (PSA) to molecular surface area (MSA) ratio as calculated by MarvinSketch® or its theoretical logP value as calculated by VCC's ALOGPS algorithm. (**A**) All compound classes combined into a single plot; (**B**) *O*-aryl-β-D-glucopyranosides; (**C**) amino acid derivatives; (**D**) *O*-alkyl-β-D-glucopyranosides; (**E**) *N*-aryl-D-aldonamides; (**F**) *C*-alkyl-β-D-glucopyranosides; (**G**) naturally occurring mono and disaccharides. Ice recrystallization inhibition activity as measured by the 5-minute SCA; data for panels C-G collected in part by past members of the Ben Lab. Data fit to a linear regression with 95 % confidence bands of the linear regression shown. Error bars for individual data points omitted.

CHAPTER 5

Figure 5-1. Summary of the outcomes of past structure-activity relationship campaigns and their outcomes towards the optimization of ice recrystallization inhibition activity for aryl-pyranosides.

Figure 5-2. Structures and ice recrystallization inhibition activity of PMP-Glc (**26**) and derivatives with modifications at the O_6 position (**87**-**89**). Ice recrystallization inhibition activity reported as the percent mean grain size (% MGS) normalized to phosphate-buffered saline determined by modified splat-cooling assay at a concentration of 22 mM with a 30-minute annealing time at -6.4 °C. *Figure recreated from Capicciotti et. al. (2016)*.

Figure 5-3. Proposed deuterated analogues of PMP-Glc including deuteration at C_1, C_2, C_3, and C_6 (**90**-**93**).

Figure 5-4. Structures and ice recrystallization inhibition activity of deuterated PMP-Glc derivatives (**90**-**93**) compared to PMP-Glc (**26**). Plot of normalized ice crystal growth rate (v_{norm}) in PBS against

logarithm transformed compound concentration (in mM). Determined by modified splat-cooling assay with a 5-minute annealing time at -6.4 °C. A 95 % CI of "wide" indicates a greater than 500 mM span.

Figure 5-5. Structures and ice recrystallization inhibition activity of deuterated D-glucose derivatives (**94**-**96**). Plot of normalized ice crystal growth rate (v_{norm}) in PBS against logarithm transformed compound concentration (in mM). Determined by modified splat-cooling assay with a 5-minute annealing time at -6.4 °C.

Figure 5-6. Structures of *O*-methylated PMP-Glc (**26**) derivative targets (**89**, **97**-**99**).

Figure 5-7. Ice recrystallization inhibition activity of compounds **26**, **89**, **97**-**99**. Plot of normalized ice crystal growth (v_{norm}) in phosphate-buffered saline (PBS) against logarithm transformed compound concentration (in mM). Determined by modified splat-cooling assay with a 5-minute annealing time at -6.4 °C.

Figure 5-8. Ice recrystallization inhibition activity of alkylated derivatives of PMP-Glc (**26**) at the O_2 (**100**), O_3 (**101**-**102**), and O_4 (**103**-**104**) positions. Plot of normalized ice crystal growth (v_{norm}) in phosphate-buffered saline (PBS) against logarithm transformed compound concentration (in mM). Determined by modified splat-cooling assay with a 5-minute annealing time at -6.4 °C.

Figure 5-9. Ice recrystallization inhibition activity of compounds **26** & **99** compared to **107** & **108**, as well as **109**. Plot of normalized ice crystal growth (v_{norm}) in phosphate-buffered saline (PBS) against logarithm transformed compound concentration (in mM). Determined by modified splat-cooling assay with a 5-minute annealing time at -6.4 °C.

Figure 5-10. Ice recrystallization inhibition activity of compounds **26** & **99**, **82** & **110**, **37** & **111**. Plot of normalized ice crystal growth (v_{norm}) in phosphate-buffered saline (PBS) against logarithm transformed compound concentration (in mM). Determined by modified splat-cooling assay with a 5-minute annealing time at -6.4 °C.

Figure 5-11. Ice recrystallization inhibition activity of compounds **26** & **99** compared to **8** & **112**. Plot of normalized ice crystal growth (v_{norm}) in phosphate-buffered saline (PBS) against logarithm transformed compound concentration (in mM). Determined by modified splat-cooling assay with a 5-minute annealing time at -6.4 °C.

Figure 5-12. 24-hour toxicity measurement of compounds **26** and **99**. Plot of percent cell viability of HepG2 cells against logarithm transformed compound concentration (in mM). Determined by resazurin-based metabolic assay following 24-hour incubation at 37 °C in 5 % CO_2. Efficacy index (EI) calculated as each compound's LD_{50}/IC_{50}. Data presented as mean ± standard deviation (SD), N=1 for compounds **26**, N=2 for compound **99**.

Figure 5-13. Proton (^1H) and carbon (^{13}C) nuclear magnetic resonance (NMR) chemical shifts of ethanol and diethylether in deuterated DMSO (DMSO-d_6). The difference in chemical shift from ether to ethanol (upon alkylation of the hydroxyl) was calculated for each of the three (α, β, γ) positions.

Figure 5-14. Proton (^1H) NMR spectra of *O*-methylated derivatives (**89**, **97**-**99**) compared to PMP-Glc (**26**). All relevant protons on each spectra are labelled accordingly.

Figure 5-15. Carbon (^{13}C) NMR spectra of *O*-methylated derivatives (**89**, **97**-**99**) compared to PMP-Glc (**26**). All relevant protons on each spectra are labelled accordingly.

Figure 5-16. Proton (^{1}H) and carbon (^{13}C) chemical shifts for each *O*-methylated carbohydrate (**89**, **97**-**99**) relative to PMP-Glc (**26**). Blue colouring indicates an atom that was de-shielded compared to PMP-Glc (**26**) while red colouring indicates an atom that was shielded relative to PMP-Glc (**26**).

Figure 5-17. (**A**) Depiction of the CREST (2.11) conformational coordinate and the distinction between conformers and rotamers. (**B**) A single conformer of PMP-Glc (**26**). Structure representation created in *Chemcraft 1.8*. (**C**) The full plot of conformers of PMP-Glc (**26**) arranged from lowest to highest energy as calculated by CREST (2.11).

Figure 5-18. Depictions of PMP-Glc (**26**) in the twist-boat conformation (left) or the $^{4}C_{1}$ chair conformation (right) as determined by CREST (2.11). Energy calculations (free energy, ΔG) completed using ORCA (5.0.4) at the DEF2-TZVPP level of theory with the ωB97 hybrid functional using the CPCM implicit water solvation model and presented relative to the twist-boat conformation energy. Structure representations created in *Chemcraft 1.8*.

Figure 5-19. (**A**) Low energy conformation of PMP-Glc (**26**) as determined by CREST (2.11) then geometry optimized using ORCA (5.0.4) at the DEF2-TZVPP level of theory with the ωB97 hybrid functional using the CPCM implicit water solvation model. Structure representations created in *Chemcraft 1.8*. (**B**) Low energy conformation of Ph-Glc (**82**) as determined by *Çarçabal et. al. (2005)*. Green arrow indicates the direction of intramolecular hydrogen bonding. *Panel B recreated with permission from Çarçabal et. al. (2005) from ACS publications.*

Figure 5-20. PMP-Glc (**26**) forming a single hydrogen bond accepting interaction at O_2 (left) and a hydrogen bond donation interaction at OH-2 (right). Theoretical hydrogen bond shown as a blue dashed line. Structure representations created in *Chemcraft 1.8*.

Figure 5-21. Hydrogen bond accepting (HBA, top) and hydrogen bond donating (HBD, bottom) interactions of a single water molecule with PMP-Glc (**26**). Low energy conformations determined following conformational search by CREST (2.11) then geometry optimization and energy calculations (free energy, ΔG) completed using ORCA (5.0.4) at the DEF2-TZVPP level of theory with the ωB97 hybrid functional using the CPCM implicit water solvation model. Energy calculated relative to the lowest energy conformer in the set (where OH-6 was acting as a hydrogen bond acceptor). Structure representations created in *Chemcraft 1.8*.

Figure 5-22. Hydrogen bond accepting (HBA, top) and hydrogen bond donating (HBD, bottom) interactions of a single water molecule with C_4 OMe PMP-Glc (**99**). Low energy conformations determined following conformational search by CREST (2.11 or 2.12) then geometry optimization and energy calculations (free energy, ΔG) completed using ORCA (5.0.4) at the DEF2-TZVPP level of theory with the ωB97 hybrid functional using the CPCM implicit water solvation model. Energy calculated relative to the lowest energy conformer in the set (where OH-6 was acting as a hydrogen bond donor). Structure representations created in *Chemcraft 1.8*.

Figure 5-23. Lowest energy conformer of PMP-Gal (**107**) (left) and C_4 OMe PMP-Gal (**108**) (right) with a single water molecule. Determined following conformational search by CREST (2.11 or 2.12) then geometry optimization and energy calculations (free energy, ΔG) completed using ORCA (5.0.4) at the DEF2-TZVPP level of theory with the ωB97 hybrid functional using the CPCM implicit water solvation model. Structure representations created in *Chemcraft 1.8*.

CHAPTER 6

Figure 6-1. Plausible hypotheses for the mechanism of ice recrystallization inhibition by small molecule inhibitors (IRIs) as proposed by the Ben Lab. (**A**) Hypothesis 1. (**B**) Hypothesis 2. (**C**) Hypothesis 3.

Figure 6-2. Visual depiction of conversion from the time domain signal (FID in seconds) to the frequency domain spectra (in hertz) resulting from the processing of NMR spectrophotometer data by Fourier transformation (FT). *Reprinted from Hosur and Kakita (2022) with permission from Springer.*

Figure 6-3. Depiction of the nuclear vectors and their spin/motion associated with generating an NMR spectrum. *Figure adapted from Cao et. al. (2021) with permission from Elsevier.*

Figure 6-4. Magnetic vectors in response to an inversion recovery pulse sequence and the recording of magnetization as a function of time delay (τ). *Figure adapted from Louro (2013) with permission from Elsevier.*

Figure 6-5. Magnetic vectors in response to a standard (for FID) and Carr-Purcell Meiboom Gill (CPMG) pulse sequence and the recording of magnetization as a function of time delay (τ).

Figure 6-6. Plot of relaxation time as a function of molecular motion for T_1 (blue) and T_2 (red) relaxation. The Larmour frequency (B_0) is indicated at the T_1 relaxation time minima.

Figure 6-7. Exemplar of pure Milli-Q® water trial $T_{2\text{-FID}}$ and $T_{2\text{-CPMG}}$ relaxation between -15 °C and -1 °C. Data shown from one trial that is representative of the mean (from n=3 replicates). (**A**) From $T_{2\text{-CPMG}}$. (**B**) From $T_{2\text{-FID}}$. Grey = raw data, coloured = fitted model to **Equation 6-3** for the $T_{2\text{-CPMG}}$ data and **Equation 6-4** for the $T_{2\text{-FID}}$ data.

Figure 6-8. Natural logarithm transformed T_2 relaxation times of pure Milli-Q® water at temperatures between -15 °C and -1 °C. Calculated $E_{A_{H_2O}}$ (kJ•mol^{-1}) from the slope of the linear regression as $\ln(T_2) = \beta \times 1/T + \varepsilon$, with $E_{A_{H_2O}} = -R \times \beta$ where the universal gas constant $R = 0.008314$ kJ•K^{-1}•mol^{-1}, β = -8057 s•K, and ε = 19.2 s; $R^2 = 0.99$. All data points reported as mean ± SD (n=3).

Figure 6-9. Exemplar of 2FA (**27**)-supplemented water solution (concentrations of 1 mM to 10 mM) $T_{2\text{-FID}}$ relaxation between -15 °C and -3 °C. Data shown from one trial that is representative of the mean (from n=3 replicates). (**A**) 1 mM 2FA (**27**). (**B**) 3 mM 2FA (**27**). (**C**) 5 mM 2FA (**27**). (**D**) 10 mM 2FA (**27**). Grey = raw data, coloured = fitted model to **Equation 6-4**.

Figure 6-10. 2FA (**27**) $T_{2\text{-FID}}$ relaxation time comparison of water and 2FA (**27**)-supplemented water solutions (concentrations 1 mM to 10 mM) between -1 and -15 °C. Data reported as mean ± SD for n=3 replicates from **Table 6-2**.

Figure 6-11. Exemplar of pure Milli-Q® water and 2FA (**27**)-supplemented water solution (concentrations of 1 mM to 10 mM) $T_{1\text{-IR}}$ relaxation between -15 °C and -3 °C. Data shown from one trial that is representative of the mean (from n=3 replicates). (**A**) Pure Milli-Q® water. (**B**) 1 mM 2FA (**27**). (**C**) 3 mM 2FA (**27**). (**D**) 5 mM 2FA (**27**). (**E**) 10 mM 2FA (**27**). Grey = raw data, coloured = fitted model to Equation 6-5.

Figure 6-12. (**A**) Plot of ln(T_1) relaxation times (in s) against 1/T (in K^{-1}) for frozen pure water and 2FA (**27**) solutions (1 to 10 mM), below freezing temperature, with T ranging from -15 °C to -3 °C. (**B**) Calculated $E_{A_{H_2O}}$ (kJ•mol^{-1}) from the slope of the linear regression of the plot in left panel (**A**) as

$\ln(T_1) = \beta \times {}^{1}/_{T} + \varepsilon$, with $E_{A_{H_2O}} = -R \times \beta$ where the universal gas constant $R = 0.008314$ kJ•K^{-1}•mol^{-1}. All values and data points are reported as mean ± SD (n=3) from **Table 6-3**.

Figure 6-13. Nanoliter osmometry images to observe ice crystal behaviour for potential dynamic ice shaping (DIS) in the presence of: (**A**) Pure water (Milli-Q®), (**B**) 10 mM *N*-2-fluorophenyl-D-gluconamide (2FA, **27**) in water (Milli-Q®), or (**C**) 1 mg/mL AFP-1 in water (Milli-Q®).

Figure 6-14. Exemplar of pure Milli-Q® water and 2FA (**27**)-supplemented water solution (concentrations of 1 mM to 10 mM) trial $T_{2\text{-CPMG}}$ relaxation between +5 °C and +30 °C. Data shown from one trial that is representative of the mean (from n=3 replicates). (**A**) Pure Milli-Q® water. (**B**) 1 mM 2FA (**27**). (**C**) 3 mM 2FA (**27**). (**D**) 5 mM 2FA (**27**). (**E**) 10 mM 2FA (**27**). Grey = raw data, coloured = fitted model to **Equation 6-3**.

Figure 6-15. (**A**) Plot of $\ln(T_{2\text{-CPMG}})$ relaxation times (in s) against 1/T (in K^{-1}) for pure water and 2FA solutions (1 to 10 mM), above freezing temperature, with T ranging from +5 °C to +30 °C. (**B**) Calculated $E_{A_{H_2O}}$ (kJ•mol^{-1}) from the slope of the linear regression of the plot in left panel (**A**) as $\ln(T_{2-CPMG}) = \beta \times {}^{1}/_{T} + \varepsilon$, with $E_{A_{H_2O}} = -R \times \beta$ where the universal gas constant $R = 0.008314$ kJ•K^{-1}•mol^{-1}. All values are given as mean ± SD (n=3). Significant differences established by one-way ANOVA: ** = $p < 0.01$; *** = $p < 0.001$.

Figure 6-16. (**A**) Plot of $\ln(T_{2\text{-CPMG}})$ relaxation times (in s) against 1/T (in K^{-1}) for pure water and 2FA (**27**) solutions (0.1 to 10 mM), above freezing temperature, with T ranging from +5 °C to +30 °C. (**B**) Calculated $E_{A_{H_2O}}$ (kJ•mol^{-1}) from the slope of the linear regression of the plot in left panel (**A**) as $\ln(T_{2-CPMG}) = \beta \times {}^{1}/_{T} + \varepsilon$, with $E_{A_{H_2O}} = -R \times \beta$ where the universal gas constant $R = 0.008314$ kJ•K^{-1}•mol^{-1}. All values are reported as mean ± SD (n = 3 except 0.1 mM n = 2). Significant differences established by one-way ANOVA: ns = not significant; *** = $p < 0.001$.

Figure 6-17. Summary of small-molecule carbohydrate-based compounds and their ice recrystallization inhibition activity as measured by the 5-minute splat-cooling assay. PMP-Glc (**26**), PEP-Glc (**54**), *p*BrPh-Glc (**25**), *p*ClPh-Glc (**83**), 2FA (**27**), 3FA (**100**), 4ClA (**101**), *m*CNA (**40**), D-glucose (**8**), D-galactose (**7**), and G1CP-NH_4 (**102**).

Figure 6-18. (**A**) $T_{2\text{-CPMG}}$ relaxation times for various small-molecule ice recrystallization inhibitor candidates from **Table 6-6**. (**B**) All relaxation times from panel A normalized to the relaxation time of H_2O. Green indicates compounds that have a ν_{norm} of < 10 % at the tested concentration; orange a ν_{norm} of between 10-90 %; red a ν_{norm} of > 90 %.

Figure 6-19. $T_{2\text{-FID}}$ relaxation time comparison of water to 2FA (**27**, n=3), G1CP-NH_4 (**115**, n=2), NH_4Cl (n=1), *p*BrPh-Glc (**25**, 10 mM n=3. 40 mM n=2). (**A**) Represents the full comparison. (**B**) Represents a zoomed in (red) version of panel A. Data reported as the mean ± standard deviation.

Figure 6-20. Exemplar of (**A**) G1CP-NH_4 (**115**) solution (10 mM) and (**B**) NH_4Cl (10 mM) trial $T_{2\text{-CPMG}}$ relaxation between -15 °C and -3 °C. Data shown from one trial that is representative of the mean (from n=2 replicates for A and n=1 replicate for B). Grey = raw data, coloured = fitted model to **Equation 6-3**.

Figure 6-21. Natural logarithm transformed $T_{2\text{-FID}}$ relaxation times of pure Milli-Q® water and phosphate-buffered saline (PBS) at temperatures between -15 °C and -1 °C. Calculated $E_{A_{H_2O}}$ (kJ•mol^{-1}) from the slope of the linear regression as $\ln(T_2) = \beta \times 1/T + \varepsilon$, with $E_{A_{H_2O}} = -R \times \beta$ where the universal gas constant

$R = 0.008314$ kJ•K^{-1}•mol^{-1}, β = -8057 s•K, and ε = 19.2 s; R^2 = 0.99. All data points reported as mean ± SD.

Figure 6-22. Exemplar of phosphate-buffered saline (PBS) trial $T_{2\text{-CPMG}}$ relaxation between -15 °C and -5 °C. Data shown from one trial. Grey = raw data, coloured = fitted model to **Equation 6-3**.

Figure 6-23. Natural logarithm transformed $T_{2\text{-FID}}$ relaxation times of pure Milli-Q® water (n=3) and various dilutions of phosphate-buffered saline (PBS) at temperatures between -15 °C and -1 °C. Calculated $E_{A_{H_2O}}$ (kJ•mol^{-1}) from the slope of the linear regression as $\ln(T_2) = \beta \times 1/T + \varepsilon$, with $E_{A_{H_2O}} = -R \times \beta$ where the universal gas constant $R = 0.008314$ kJ•K^{-1}•mol^{-1}, β = -8057 s•K, and ε = 19.2 s; R^2 = 0.99. All data points reported as mean ± SD.

List of Tables

Table 4-1. Heat map of linear and exponential (exp) correlation coefficients R^2) from plots generated in Microsoft Excel® for comparison between a noted physicochemical parameter and ice recrystallization inhibition activity as measured by the 5-minute SCA (reported as an IC_{50}). All graphs can be found in the appendices (see *section 8.3.6*).

Table 6-1. Parameters of best fit for the $T_{2\text{-FID}}$ relaxation of pure Milli-Q® water at temperature intervals between -15 °C and -1 °C by **Equation 6-4**. Values represented as mean ± SD for n=3 replicates.

Table 6-2. Parameters of best fit for the $T_{2\text{-FID}}$ relaxation of 2FA (**27**)-supplemented water solutions (concentrations of 1 mM to 10 mM) at temperature intervals between -15 °C and -3 °C by **Equation 6-4**. Values reported as mean ± SD for n=3 replicates.

Table 6-3. Parameters of best fit for the $T_{1\text{-IR}}$ relaxation of pure Milli-Q® water and 2FA (**27**)-supplemented water solutions (concentrations of 1 mM to 10 mM) at temperature intervals between -15 °C and -3 °C by **Equation 6-5**. Values for the second component of relaxation were omitted from the table as they were all equal to zero. Values reported as mean ± SD for n=3 replicates.

Table 6-4. Parameters of best fit for the CPMG relaxation of pure Milli-Q® water and 2FA (**27**)-supplemented water solutions (concentrations of 1 mM to 10 mM) at temperature intervals between +5 °C and +30 °C by **Equation 6-3**. Values for the second component of relaxation were omitted from the table as they were all equal to zero. Values reported as mean ± SD for n=3 replicates.

Table 6-5. Categorization of ice recrystallization inhibition activity for various small-molecule carbohydrate-based IRIs. Full 5-minute SCA dose-response curves for the activity of these compounds can be found in *section 8.3.1*.

Table 6-6. Parameters of best fit for the $T_{2\text{-CPMG}}$ relaxation of pure Milli-Q® water and IRI-supplemented water solutions at +25 °C by **Equation 6-3** (n=1). The second component of the bi-exponential is not shown as $I_{CPMG\text{-}2}$ and $T_{2\text{-CPMG-}2}$ are both equal to zero for all samples tested. Values reported as mean ± SD for n=3 replicates.

List of Schemes

Scheme 3-1. Retrosynthesis of 4-azidophenyl-β-D-glucopyranoside (*p*N_3Ph-Glc, **29**) as prepared by Dr. Jessica Poisson (PhD 2019, Ben Lab).

Scheme 3-2. Synthesis of 4-cyanophenyl-β-D-glucopyranoside (*p*CNPh-Glc, **30**).

Scheme 3-3. Synthesis of 4-carbamoylphenyl-β-D-glucopyranoside (*p*AmPh-Glc, **31**).

Scheme 3-4. Synthesis of nitrile-containing *O*-aryl-β-D-glucopyranosides and *N*-aryl-D-gluconamides **30**, and **37**-**41**.

Scheme 3-5. Synthesis of amide-containing *O*-aryl-β-D-glucopyranosides and *N*-aryl-D-gluconamides **31**, and **42**-**46**.

Scheme 3-6. Synthesis of *meta*-hydroxybenzamide (**517**).

Scheme 4-1. Synthesis of *p*-alkoxyphenyl-β-D-glucopyranosides **26**, **53**-**56**, **80**-**81**.

Scheme 4-2. Synthesis of *O*-aryl-β-D-glucopyranosides **25**, and **82**-**84**.

Scheme 5-1. Synthesis of the C_1, C_2, and C_3 deuterated derivatives of PMP-Glc (**90**-**92**).

Scheme 5-2. Synthesis of the C_6 deuterated PMP-Glc derivative (4-methoxyphenyl)-6-deutero-β-D-glucopyranose (6D1 PMP-Glc, **93**).

Scheme 5-3. Synthesis of (4-methoxyphenyl)-2-*O*-methyl-β-D-glucopyranoside, C_2 OMe PMP-Glc (**97**).

Scheme 5-4. Synthesis of (4-methoxyphenyl)-3-*O*-methyl-β-D-glucopyranoside, C_3 OMe PMP-Glc (**98**).

Scheme 5-5. Synthesis of (4-methoxyphenyl)-4-*O*-methyl-β-D-glucopyranoside, C_4 OMe PMP-Glc (**99**).

SCHEME 5-6. Synthesis of (4-methoxyphenyl)-6-*O*-methyl-β-D-glucopyranoside, C_6 OMe PMP-Glc (**89**).

Scheme 5-7. Synthesis of O_2 (**100**), O_3 (**101**-**102**), and O_4 (**103**-**104**) alkylated derivatives of PMP-Glc (**26**).

Scheme 5-8. First attempted synthesis of (4-methoxyphenyl)-4-*O*-methyl-β-D-galactopyranoside (C_4 OMe PMP-Gal, **108**) *via* selective benzoylation of PMP-Gal (**107**).

Scheme 5-9. Finalized synthesis of (4-methoxyphenyl)-4-*O*-methyl-β-D-galactopyranoside (C_4 OMe PMP-Gal, **108**).

Scheme 5-10. Synthesis of (4-methoxyphenyl)-4-deoxy-β-D-glucoopyranoside (C_4 Deoxy PMP-Glc, **109**).

Scheme 5-11. Synthesis of phenyl-4-*O*-methyl-β-D-glucopyranoside, Ph-Glc (**82**) and phenyl-4-*O*-methyl-β-D-glucopyranoside, C_4 OMe Ph-Glc (**110**).

Scheme 5-12. Synthesis of 3-cyanophenyl-4-*O*-methyl-β-D-glucopyranoside, C_4 OMe *m*CNPh-Glc (**111**).

Scheme 6-1. Synthesis of *N*-2-fluorophenyl-D-gluconamide (2FA, **27**).

List of Equations

Equation 1-1: Monoexponential decay of ice crystals from bin 1 (as they increase in size beyond 0.001 mm^2).

Equation 1-2: Determination of the rate of ice recrystallization.

Equation 6-1: The rate of growth of magnetization in the z-axis over time following a T_1 inversion recovery pulse sequence.

Equation 6-2: The rate of decay of magnetization in the x-y plane over time following a T_2 FID or CPMG pulse sequence.

Equation 6-3: Bi-exponential function for determination of $T_{2\text{-CPMG}}$ relaxation time.

Equation 6-4: Bi-exponential function for determination of $T_{2\text{-FID}}$ relaxation time.

Equation 6-5: Bi-exponential function for determination of $T_{1\text{-IR}}$ relaxation time.

List of Abbreviations

#

E_{AH2O}: activation energy of water molecule motion

%

% MGS: percent mean grain size, percent mean ice grain size

1

^{13}C: carbon 13 isotope
^{1}H: hydrogen, proton

2

^{2}H: deuterium

3

3D: three-dimensional
3-OMG: 3-*O*-methyl-D-glucose (**548**)

A

Ac: acetyl
AF(G)P(s): antifreeze (glyco)protein(s)
AFP-1: type I antifreeze protein
AFP(s): antifreeze protein(s)
Ala: alanine
ALPB: analyical linearized Poisson-Boltzmann
ASA: solvent accessible surface area
ASA-: solvent accessible surface area for all atoms with a partial negative charge
ASA_H: solvent accessible surface area for all hydrophobic atoms
ASA_P: solvent accessible surface area for all polar atoms
ASA+: solvent accessible surface area for all atoms with a partial positive charge
ATP: adenosine triphosphate
AV: annexin V

B

B_0: external magnetic field strength
BAs: biological antifreezes
BM-MSCs: bone-marrow derived mesenchymal stromal cells
Bn: benzyl
BSA: bovine serum albumin

C

C_1: anomeric carbon
C-AF(G)P: carbon-linked antifreeze (glyco)protein
calcd.: calculated
CARS: coherent anti-Stokes Raman scattering
CAR-T: chimeric antigen receptor T
CBS: Canadian Blood Services
Cbz: benzyloxycarbonyl
cDNA: complementary deoxyribonucleic acid
CH_n/OH: number of carbons in an alkyl chain relative to the number of alcohols in the polyolchain
CI: confidence interval
C-linked: carbon-linked
COSY: correlation spectroscopy
CPA(s): cryoprotective agent(s)
CPMG: Carr-Purcell-Meiboom-Gill
CREST: Conformer-Rotamer Ensemble Sampling Tool
CRF: controlled-rate freezer
CS10: CryoStor®10

D

DAG: diacetone-D-glucose (**546**)
DCM: dichloromethane
DDR1: discoidin domain receptor 1
DEPT-135: distortionless enhancement by polarization transfer with 135 degree flip angle
dH_2O: distilled water
DIS: dynamic ice shaping
DMEM: Dulbecco's modified Eagle's medium
DMF: *N,N*-dimethylformamide
DMSO: dimethyl sulfoxide
DMSO-d_6: deuterated dimethyl sulfoxide
DPBS: Dulbecco's phosphate-buffered saline
DPG: 2,3-diphosphoglycerate
DRS: domain recognition software

E

E_A: activation energy
EDG: electron donating group
EdU: 5-ethynyl-2'-deoxyuridine
EI: electron impact, efficacy index
ESI: electrospray ionization
ESI+: positive electrospray ionization mode
Et: ethyl
EWG: electron withdrawing group

F

FBS: fetal bovine serum
FID: free induction decay, free-induction decay
FOV: field of view

G

GAPDH: glyceraldehyde-3-phosphate dehydrogenase
Glc: glucose
Gal: galactose

GLUTs: glucose transporters

H

HA: human albumin
HBA: hydrogen bond acceptor
HBD: hydrogen bond donation, hydrogen bond donor
hct: hematocrit
Hgb_s: supernatant hemoglobin
Hgb_T: total hemoglobin
HGM: high glycerol method
HI: hydration index
HLB: hydrophobic/lipophilic balance
HRMS: high resolution mass spectrometry
HSPCs: hematopoietic stem and progenitor cells
HSQC: heteronuclear single quantum coherence
HUVEC: human umbilical vein endothelial cells

I

*i*Bu: isobutyl
IC_{50}: half-maximal inhibitory concentration
IDO: indoleamine 2,3-dioxygenase
IFNγ: interferon gamma
I_h: hexagonal ice
IIF: intracellular ice formation
INT: iodonitrotetrazolium
*i*Pr: isopropyl
iPSC-Ns: induced pluripotent stem cell derived neurons
iPSCs: induced pluripotent stem cells
IR: infrared, inversion recovery
IRI(s): ice recrystallization inhibitor(s)

K

KIE: kinetic isotope effect
k_{norm}: normalized rate constant of ice crystal growth from analysis of multiple annealing times
k_{obs}: observed rate constant of ice crystal growth

L

LDH: lactate dehydrogenase
LGM: low glycerol method
logP: octanol-water coefficient
logS: aqueous solubility parameter
LRMS: low resolution mass spectrometry

M

Man: mannose
Max: maximum
MD: molecular dynamics
Me: methyl
MeCN: acetonitrile
MEM: minimum essential medium
MGS: mean grain size
Min: minimum
MOM: methoxy methyl
MRI: magnetic resonance imaging
MSA: molecular surface area
MSCs: mesenchymal stromal cells

N

NAD+: positively charged nicotinamide adenine dinucleotide in its oxidized state
NADH: nicotinamide adenine dinucleotide in its reduced state
NEAA: non-essential amino acids
NetCAD: Network Centre for Applied Development Services
n_h: hydration number
NMR: nuclear magnetic resonance
NOSEY: nuclear overhauser effect spectroscopy
NRC: National Research Council

O

O_1: anomeric oxygen
OHRI: Ottawa Hospital Research Institute
O-linked: oxygen-linked

P

PBS: phosphate-buffered saline
PCR: polymerase-chain reaction
Pd/C: palladium on carbon
Pen-Strep: penicillin/streptomycin
PI: propidium iodide
PLA: plasmalyte A
PMV: partial molar volume
Pr: propyl
Proj.: projection
PSA: polar surface area
PSA/MSA: polar surface area to molecular surface area ratio
pTSA•H_2O, *p*TsOH•H_2O: *p*-toluene sulfonic acid monohydrate
*p*TsOH: *p*-toluenesulfonic acid
PVA: polyvinyl alcohol

Q

QLL: quasi liquid layer, quasi-liquid layer
QSAR: quantitative structure activity relationship

R

RBC(s): red blood cell(s)
REDOX: reduction-oxidation
RF: radiofrequency
Rf: retention factor
ROS: reactive oxygen species
RT: reverse transcriptase
r.t.: room temperature
RT-PCR: reverse transcription polymerase chain reaction

S

SAGM: sodium chloride, adenine, glucose, and mannitol
SAR: structure activity relationship, structure-activity relationship
sat.: saturated
SCA: splat cooling assay, splat-cooling assay
SD: standard deviation
SEM: standard error of the mean
SFM: standard freezing medium
SRS: stimulated Raman scattering
SSA: sucrose sandwich assay

T

T_1: longitudinal, spin-lattice relaxation, spin-lattice
T_2: transverse, spin-spin relaxation, spin-spin
$T_{2\text{-CPMG}}$: T_2 relaxation times as calculated from a CPMG pulse sequence
$T_{2\text{-FID}}$: T_2 relaxation times calculated from the FID
Tal: talose
TBDMS: *tert*-butyldimethylsilyl
t-BuONO: *tert*-butyl
Temp: temperature
TES: triethylsilane
Tf: triflyl
TFA: trifluoroacetic acid
TH: thermal hysteresis
THF: tetrahydrofuran
Thr: threonine
TLC: thin layer chromatography
TMS-N_3: azidotrimethylsilane

U

UC-MSCs: umbilical cord derived mesenchymal stromal cells

V

v_{norm}: normalized rate constant of ice crystal growth from analysis of a single annealing time, normalized rate of ice crystal growth, normalized rate of ice recrystallization
vs.: versus

W

w/v: weight per volume

X

XPM: cross phase modulation

β

β-ME: β-mercaptoethanol

Σ

σ_p: Hammett *para* substituent constant

List of Numbered Compounds

1

1-D1 D-glucose: D-glucose-1-d1 (**94**)
1D1 PMP-Glc: (4-methoxyphenyl)-1-deutero-β-D-glucopyranose (**90**)

2

2,6DFB: *N*-(2,6-difluorobenzyl)-D-gluconamide (**28**)
2-D1 D-glucose: D-glucose-2-d1 (**95**)
2D1 PMP-Glc: (4-methoxyphenyl)-2-deutero-β-D-glucopyranose (**91**)
2FA: *N*-(2-fluorophenyl)-D-gluconamide (**27**)

3

3-D1 D-glucose: D-glucose-3-d1 (**96**)
3D1 PMP-Glc: (4-methoxyphenyl)-3-deutero-β-D-glucopyranose (**92**)
3FA: *N*-3-fluorophenyl-D-gluconamide (**113**)

4

4ClA: *N*-4-chlorophenyl-D-gluconamide (**114**)
4D1 PMP-Glc: (4-methoxyphenyl)-4-deutero-β-D-glucopyranose

6

6D1 PMP-Glc: (4-methoxyphenyl)-6-deutero-β-D-glucopyranose (**93**)

A

AFGP-8: antifreeze glycoprotein 8 (**1**)

C

C_2 OEt PMP-Glc: (4-methoxyphenyl)-2-*O*-ethyl-β-D-glucopyranoside (**100**)
C_2 OMe PMP-Glc: (4-methoxyphenyl)-2-*O*-methyl-β-D-glucopyranoside (**97**)
C_3 N_3 PMP-Glc: (4-methoxylphenyl)-3-*O*-azido-β-D-glucopyranoside
C_3 OEt PMP-Glc: (4-methoxyphenyl)-3-*O*-ethyl-β-D-glucopyranoside (**101**)
C_3 OMe PMP-Glc: (4-methoxyphenyl)-3-*O*-methyl-β-D-glucopyranoside (**98**)
C_3 OPr PMP-Glc: (4-methoxyphenyl)-3-*O*-propyl-β-D-glucopyranoside (**102**)
C_4 Deoxy PMP-Glc: (4-methoxyphenyl)-4-deoxy-β-D-glucopyranoside (**109**)
C_4 OEt PMP-Glc: (4-methoxyphenyl)-4-*O*-ethyl-β-D-glucopyranoside (**103**)
C_4 O*i*Bu PMP-Glc: (4-methoxyphenyl)-4-*O*-isobutyl-β-D-glucopyranoside (**106**)
C_4 O*i*Pr PMP-Glc: (4-methoxyphenyl)-4-*O*-isopropyl-β-D-glucopyranoside (**105**)
C_4 OMe Glc: 4-*O*-methyl-D-glucopyranoside (**112**)
C_4 OMe *m*CNPh-Glc: (3-cyanophenyl-4-*O*-methyl-β-D-glucopyranoside (**111**)
C_4 OMe Ph-Glc: phenyl-4-*O*-methyl-β-D-glucopyranoside (**110**)
C_4 OMe PMP-Gal: (4-methoxyphenyl)-β-D-galactopyranoside (**108**)
C_4 OMe PMP-Glc: (4-methoxyphenyl)-4-*O*-methyl-β-D-glucopyranoside (**99**)
C_4 OPr PMP-Glc: (4-methoxyphenyl)-4-*O*-propyl-β-D-glucopyranoside (**104**)
C_6 OMe PMP-Glc: (4-methoxyphenyl)-6-*O*-methyl-β-D-glucopyranoside (**89**)
C-serine: *C*-serine (**3**)

D

D-Gal: D-Galactose (**7**)
D-Glc: D-Glucose (**8**)
D-Lactose: D-Lactose (**12**)
D-Maltose: D-Maltose (**14**)
D-Man: D-Mannose (**9**)
D-Melibiose: D-Melibiose (**11**)
D-Sucrose: D-Sucrose (**15**)
D-Tal: D-Talose (**10**)
D-Trehalose: D-Trehalose (**13**)

G

G1CP-NH_4: Ammonium C-(1-deoxy-β-D-glucopyranosyl) methanephosphonate (**115**)

M

*m*AmA: *N*-3-carbamoylphenyl-D-gluconamide (**45**)
*m*AmPh-Glc: 3-carbamoylphenyl-β-D-glucopyranoside (**42**)
*m*CNA: *N*-3-cyanophenyl-D-gluconamide (**40**)
*m*CNPh-Glc: (3-cyanophenyl)-β-D-glucopyranoside (**37**)
*m*MePh-Glc: 3-methylphenyl-β-D-glucopyranoside (**36**)
MMP-Glc: 3-methoxyphenyl-β-D-glucopyranoside (**33**)

N

NHex Erythronamide: *N*-hexyl-erythronamide (**22**)
NHex Ethylamide: *N*-hexyl-2-(α-D-galactopyranosyl)-ethylamide (**20**)
NHexGlc: *N*-hexyl-D-gluconamide (**24**)
NOct Erythronamide: *N*-octyl-erythronamide (**23**)
NOct Ethylamide: *N*-octyl-2-(α-D-galactopyranosyl)-ethylamide (**21**)
NOGlc: *N*-octyl-D-gluconamide (**17**)
NPr Ethylamide: *N*-propyl-2-(α-D-galactopyranosyl)-ethylamide (**19**)

NPrGlc: *N*-propyl-D-gluconamide (**18**)

O

oAmA: *N*-2-carbamoylphenyl-D-gluconamide (**46**)
*o*AmPh-Glc: 2-carbamoylphenyl-β-D-glucopyranoside (**43**)
*o*CNA: *N*-2-cyanophenyl-D-gluconamide (**41**)
*o*CNPh-Glc: 2-cyanophenyl-β-D-glucopyranoside (**38**)
OGG-Gal: OGG-Galactose (**2**)
OGG-Glc: OGG-Glucose (**4**)
OGG-Man: OGG-Mannose (**5**)
OGG-Tal: OGG-Talose (**6**)
OMP-Glc: 2-methoxyphenyl-β-D-glucopyranoside (**34**)
OPr-Glc: *n*-propyl-β-D-glucopyranoside (**48**)

P

p-acetamidoPh-Glc: 4-acetamidophenyl-β-D-glucopyranoside (**49**)
*p*AmA: *N*-4-carbamoylphenyl-D-gluconamide (**44**)
*p*AmPh-Glc: 4-carbamoylphenyl-β-D-glucopyranoside (**31**)
PBP-Glc: 4-butoxyphenyl-β-D-glucopyranoside (**56**)
*p*BrPh-Glc: 4-bromophenyl-β-D-glucopyranoside (**25**)
p-butyramidoPh-Glc: 4-butyramidophenyl-β-D-glucopyranoside (**51**)
*p*ClPh-Glc: 4-chlorophenyl-β-D-glucopyranoside (**83**)
*p*CNA: *N*-4-cyanophenyl-D-gluconamide (**39**)
*p*CNPh-Glc: 4-cyanophenyl-β-D-glucopyranoside (**30**)
PEP-Glc: 4-ethoxyphenyl-β-D-glucopyranoside (**54**)
*p*FPh-Glc: 4-fluorophenyl-β-D-glucopyranoside (**86**)
Ph-Glc: phenyl-β-D-glucopyranoside (**82**)
PHP-Glc: 4-hexyloxyphenyl-β-D-glucopyranoside (**80**)
*p*IPh-Glc: 4-iodophenyl-β-D-glucopyranoside (**84**)
*p*MePh-Glc: 4-methylphenyl-β-D-glucopyranoside (**35**)
PMP-Gal: (4-methoxyphenyl)-β-D-galactopyranoside (**107**)
PMP-Glc: 4-methoxyphenyl-β-D-glucopyranoside (**26**)
pN_3Ph-Glc: 4-azidophenyl-β-D-glucopyranoside (**29**)
pNH_2Ph-Glc: 4-aminophenyl-β-D-glucopyranoside (**32**)
pNO_2Ph-Glc: 4-nitrophenyl-β-D-glucopyranoside (**85**)
*p*OHPh-Glc: 4-hydroxyphenyl-β-D-glucopyranoside (**53**)
POP-Glc: 4-octyloxyphenyl-β-D-glucopyranoside (**81**)
p-pentanamidoPh-Glc: 4-pentanamidophenyl-β-D-glucopyranoside (**52**)
PPP-Glc: 4-propoxyphenyl-β-D-glucopyranoside (**55**)
p-propionamidoPh-Glc: 4-propionamidophenyl-β-D-glucopyranoside (**50**)

β

β-octyl-gal: *n*-octyl-β-D-galactopyranoside (**16**)

1. Introduction

The preservation of biologics and their derivatives, as well as the development of related technologies, is of great importance to the future of clinical medicine and scientific research. Cellular therapies for blood-related diseases such as sickle cell anemia and myocardial infarctions, as well as various cancers and autoimmune diseases rely on biopreservation methods to maintain a constantly accessible supply of cell products.[1–3] To achieve successful biopreservation, one of three main methods can be used to slow biological processes (including cellular metabolism and proliferation) with the goal of extending the lifespan of the biologic; these methods include hypothermic storage, cryopreservation, or vitrification.[4]

Hypothermic storage is a simple, low cost preservation method that maintains biologics at temperatures between 4 and 10 °C using ice or conventional refrigerators.[5–7] At these temperatures many stress-induced pathways of cell death can still be activated, resulting in reduced cell quality and viability.[6,8–10] Therefore, hypothermic storage is typically only regularly used for cell transport or diagnostics, or when other preservation methods are not feasible (*i.e.,* for red blood cells[1] and whole organs intended for donation[11,12]), given it is only suitable for several days to a few weeks of preservation.[5–7] To extend the shelf-life of preserved biologics, extreme sub-zero temperatures (typically between -80 and -196 °C) must be used to effectively halt all biological processes.[5–7,13]

Cryopreservation and vitrification both use subzero temperatures (typically -196 °C) to allow biologics to be stored for upwards of 10-20 years depending on the type of biological material.[5–7,13–15] Both methods are extremely complex processes that require careful control of several key parameters (*i.e.*, sample volume, cooling rates, warming rates, cryoprotective additives and supplements, storage temperature, *etc.*) to ensure the biological material can be successfully returned to biologically relevant temperatures while minimizing cellular damage. Typically, cryopreservation involves the use of cryoprotective agents (CPAs) and slow cooling rates (~ 1 °C/min) to protect biologics from the inevitable formation of ice.[2,16,17] Currently, cryopreservation is used routinely during scientific research to preserve immortalized cell lines, and clinically to preserve sperm from various species in biobanks worldwide.[2] However, the cryopreservation of more complex cell types (*e.g.,* mesenchymal stromal cells) remains challenging due to the damage caused by the formation and uncontrolled growth of ice.[2] Vitrification avoids the formation of ice entirely and achieves a “glassy” ice-free state by rapidly cooling samples at rates of greater than 1000 °C/min.[15,18] However, the high concentrations of CPA that must be used to successfully achieve this ice-free state can result in significant toxicity and damage to the biologic.[13,19] In addition, improper devitrification (warming of samples that is too slow) can cause ice to form throughout the sample

that results in significant cellular damage. Therefore, the use of vitrification as a biopreservation method is currently only routinely used for the preservation of oocytes and embryos and is not widely used as a biopreservation method.[14,19,20] A summary of the three main low temperature biopreservation methods is shown in **Figure 1-1**.

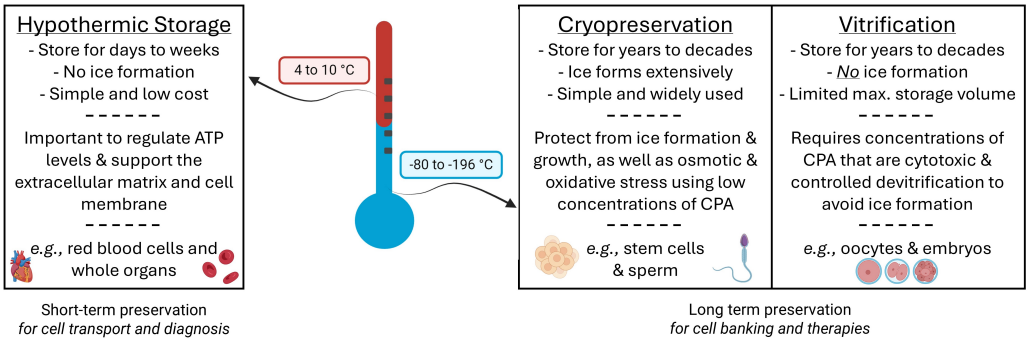


Figure 1-1. A summary of low temperature biopreservation methods used to extend the shelf life of biologics.[4,5,7]

1.1. Cryopreservation

Cryopreservation is currently the most widely used biopreservation method for the long-term storage of biological materials, including for cells that are critical for cellular therapy. However, the formation and subsequent growth of ice (both intra- and extra-cellular) during cryopreservation can cause significant losses to cellular recovery, viability, and functionality if not adequately controlled.[2,21–26] Current cryopreservation protocols rely primarily on the careful control of ice by manipulating cooling and warming rates as well as the addition of CPAs to mitigate the physicochemical stressors associated with the freezing and thawing processes of cryopreservation.[3,4,27,28]

1.1.1. Warming and cooling rates

The viability of a cryopreserved product post-thaw has been directly correlated to the rate at which it is cooled to extreme subzero temperatures as well as the rate at which it is warmed to return to biologically relevant temperatures. Optimal rates depend on the type of cell and are related to each cell type's relative membrane permeability to different substrates; this phenomenon is known as the two-factor hypothesis as described by Dr. Peter Mazur.[27,29] In the absence of other cryoprotective controls, red blood cells (RBCs) with highly permeable membranes are best cryopreserved using rapid cooling rates (> 1000 ºC/min) while more complex, less permeable cells such as embryos or marrow-derived stem cells (murine) are best cryopreserved using slower cooling rates (~ 1-10 ºC/min) (**Figure 1-2A**). The relationship between cell viability (%) and cooling rate (ºC/min) is an inverted U-shape, where both too slow and too rapid cooling rates are detrimental to cell survival (**Figure 1-2A**).[27,29]

Following an ice nucleation event as temperatures drop below 0 °C, ice initially forms in the extra-cellular space (**Figure 1-2B**). As the ice forms, solutes that are present in the extra-cellular space become excluded from the ice lattice, thus causing an efflux of water from the cell to balance the shifted osmotic pressure gradient.[18] If cells are cooled too quickly and cannot sufficiently dehydrate prior to freezing, the cell's membranes can be ruptured by the formation of ice in the intracellular space (**Figure 1-2B**).[18] The extent to which cells are affected by intracellular ice depends on their cell type, where those with cell-cell junctions have been found to be primarily unaffected by the formation of this ice, while cells without these junctions suffer can suffer from extensive mechanical damage to their membranes and internal organelles.[26,27,30–34] For most eukaryotic cells, a slow rate of cooling is used during freezing to allow the cells sufficient time to dehydrate and avoid the formation of intracellular ice. However, for cells that are highly permeable (*i.e.,* red blood cells) a rate of cooling that is too slow can result in excessive cell shrinkage due to the rapid efflux of water that exposes the cells to high intracellular solute concentrations that facilitate cell death (**Figure 1-2B**).[13,18,26,27]

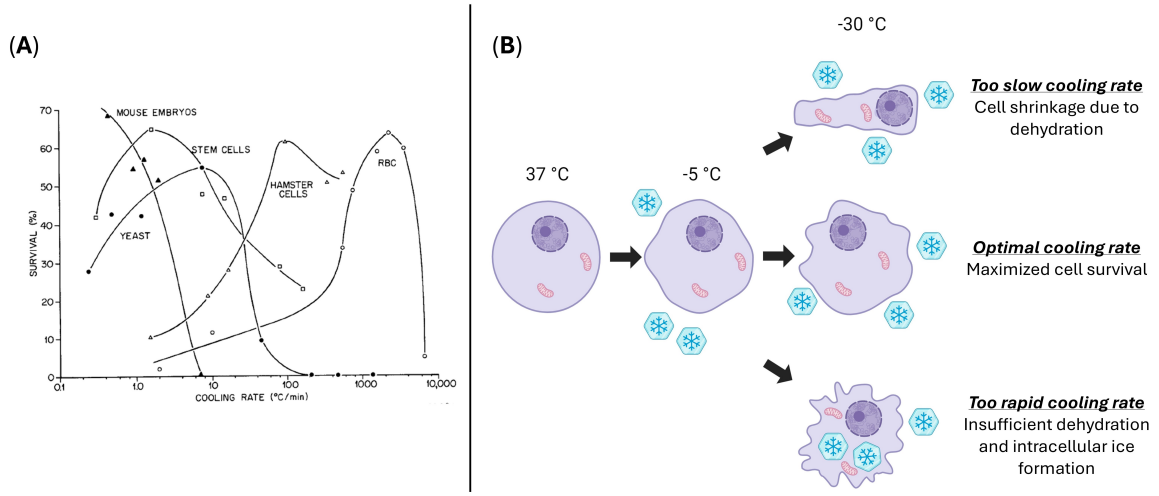


Figure 1-2. (**A**) Comparison of cooling rate (°C/min) on the survival (%) of various cells cooled to -196 °C. *Reprinted with permission from Mazur (1980) as published by Springer.*[29] (**B**) Effect of different cooling rates on cells during the freezing process. *Figure adapted from Mazur (1984)*[26] *and created using Biorender.com.*

Once a cell has been frozen it must eventually be able to be successfully returned to physiological temperatures. The optimal warming rate for cells that have been cryopreserved depends on the cooling rate that was used for freezing.[18] Cells that have been cooled too quickly, where intracellular ice has inevitably formed, will benefit from a fast rate of warming as this mitigates damage due to ice recrystallization (discussed in more detail in *section 1.2*).[18] Warming cells that have been slowly cooled, such as to avoid intracellular ice formation (IIF), is significantly more complex and the optimal warming rate is co-dependant on additional factors including cell type as well as CPA type and concentration.[18] Ultimately,

it is imperative that an individualized, cell-specific approach is taken when determining the cooling and warming rates for optimized cryopreservation protocols. In general, rapid warming rates (*i.e.,* plunge into a 37 °C water bath) are often employed in cryopreservation protocols where warming rate has not been thoroughly optimized for the given application to mitigate the risk of cellular damage due to ice recrystallization.

1.1.2. Cryoprotective agents (CPAs)

Cryoprotective agents (CPAs) are often added to cellular cryopreservation solutions to mitigate damage associated with ice formation (mechanical injuries), changes in osmotic pressures, and from reactive oxygen species (ROS) (**Figure 1-3**).[2,5,26,27] The two main types of CPAs, penetrating and non-penetrating, are classified based on their ability to cross cellular membranes.[35] Penetrating cryoprotectants such as glycerol or dimethyl sulfoxide (DMSO), which can cross a cell membrane, are generally employed in cryopreservation protocols utilizing slow cooling rates in order to prevent excessive cell shrinkage by replacing intracellular water and maintaining appropriate cell volumes.[35–38] On the other hand, non-penetrating cryoprotectants are generally higher molecular weight compounds such as trehalose or sucrose, that remain outside of the cell to support the integrity of the cellular membranes and facilitate dehydration by increasing the osmolality of the extracellular solution.[35,38–40] Therefore, non-penetrating cryoprotectants are typically employed in cryopreservation protocols that utilize rapid cooling rates to mitigate the risk of IIF.[26,35,38]

Despite their ability to protect cells from certain aspects of cryopreservation-related damage, many traditional CPAs (including glycerol and DMSO) have intrinsic toxicity that can cause injuries to cellular proteins and membranes (**Figure 1-3**).[41–43] To reduce the risk of cytotoxicity to cryopreserved cells, penetrating CPAs often need to be removed following thawing for their intended use case. In many circumstances however, removal of the CPA can be quite challenging (*e.g.,* the removal of glycerol from RBCs requires multiple washing phases),[44] and can lead to significant cellular damage. On the other hand, non-penetrating cryoprotectants tend to be less cytotoxic and their removal is not always necessary.[16,45,46] However, the post-thaw survival of cells cryopreserved using non-penetrating cryoprotectants is generally not as high compared to penetrating cryoprotectants and the exclusive use of non-penetrating cryoprotectants is not common in current cryopreservation applications.[3,35] Currently, the gold-standard CPA for cellular cryopreservation is DMSO, which was first reported as a CPA by Lovelock and Bishop in 1959.[47] While DMSO is the most ubiquitously used CPA, it has been reported to be cytotoxic if not adequately removed post-thaw, which can complicate the direct clinical use of cells that were cryopreserved with it.[41,48–51] In addition, it fails to address the damage that occurs to cells and tissues during

cryopreservation caused by ice recrystallization. As a result, novel compounds that are non-toxic (*i.e.,* biocompatible) and can address the mechanical damage caused by ice recrystallization represent a major avenue of on-going investigation for the large-scale optimization of cryopreservation for cells and tissues that are critical to several fields including scientific research, clinical medicine, and food science.

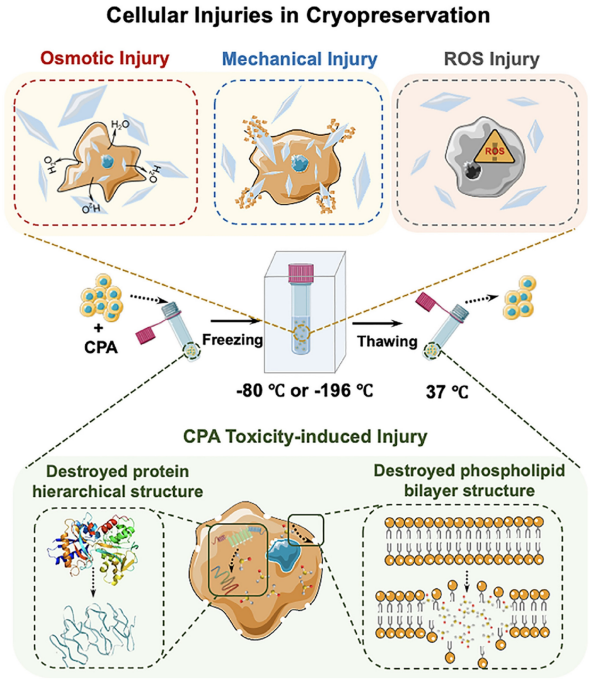


Figure 1-3. Cellular injuries associated with cryopreservation. *Reprinted with permission from Ma et. al. (2021) as published by Acta Biomaterialia.*[5]

1.2. Ice recrystallization

Ice recrystallization has been well established as detrimental to the cryopreservation of biological materials (cells, tissues, *etc.*) and the storage of frozen foods. For biological materials, ice recrystallization is the primary cause of cellular damage and death following cryopreservation.[18,24] Furthermore, for frozen foods, ice recrystallization has been reported to cause changes in texture and taste that are detrimental to the overall quality of the food product.[52] Therefore, a significant research effort has been made to understand the underlying mechanisms of ice recrystallization to ultimately mitigate the associated damage and improve the cryopreservation of biological materials and quality of frozen foods.

1.2.1. The mechanism of ice recrystallization

The process of recrystallization and its mechanism are extremely well documented in the geological and metallurgical sciences and can be described by the mechanisms of grain boundary migration[53–55] and Ostwald ripening[56–58].[59,60] The grain boundary migration mechanism relies on inherent energy differences between grains of material. At a microscopic level, the individual grains of a material tend to be slightly

curved, with the degree of curvature inversely proportional to the size of the grain; small grains have a higher degree of curvature (appear more convex and "bulging") while larger crystals have a smaller degree of curvature due to their increased overall surface area (appear more flat with increasing grain size) (**Figure 1-4A**). The larger the average degree of curvature of the system, the greater the overall free energy. Therefore, to reduce the system's overall free energy, molecules of smaller grains are migrated to larger grains to reduce the average degree of curvature and increase the average grain size, resulting in recrystallization (**Figure 1-4B**). However, the mechanism of recrystallization by grain boundary migration assumes that molecules are transferred directly from one grain to another, which neglects the presence of the interstitial bulk water phase that exists between ice crystals, and therefore is typically only used to describe the recrystallization of solid materials.[55,59,60] Furthermore, this mechanism also neglects to account for the transitionary, semi-ordered, layer known as the quasi-liquid layer (QLL) that exists between the organized ice lattice and disorganized bulk (unfrozen) water phases (**Figure 1-4C**).[61–67] The exact properties of the QLL have been debated extensively in literature, but it has been suggested that its features are dependent on several parameters including pressure, temperature, and solute concentration.[64,65,68–73] In addition, literature has suggested that the QLL properties may differ based on the face of ice from which they are calculated.[61,64] For example, the thickness of the QLL reduces from ~15 nm (40 monolayers of water) at temperatures near 0 °C to merely 0.3 nm thick (a single monolayer of water) at temperatures below -10 °C. While the exact role that the QLL plays in the mechanism of ice recrystallization is unknown, it is known to have a significant impact on the organization of water molecules as they transfer from one ice crystal to another.

Consequently, Ostwald ripening is the accepted mechanism used to describe the recrystallization process in aqueous solutions to ensure that the entire ice/bulk water/QLL system is accounted for.[53,56] Traditionally, the mechanism of Ostwald ripening has been used to describe the changing size of oil droplets in a liquid-oil emulsion, where the average size of each oil droplet increases over time while maintaining a constant oil volume (**Figure 1-4D**).[74,75] Recrystallization by this mechanism is driven thermodynamically, where larger particles are more energetically stable than smaller particles; molecules that reside at the surface of a particle are higher in energy than those in the interior as they cannot form the maximum number of bonding interactions and are consequently less ordered. Therefore, to reduce the overall energy of the system, water molecules are transferred from smaller ice crystals to larger ice crystals which results in an increase in the average ice crystal size and a decrease in the total number of ice crystals over time.[76,77] The QLL serves as a transitionary "semi-ordered" phase that supports the incorporation of water molecules in the disorganized bulk water layer into the growing, highly ordered, crystalline ice lattice. Ultimately, it is the net increase in ice crystal size over time that causes mechanical damage to cells and tissues during

cryopreservation; therefore, the inhibition of this process is critical to improving the viability, recovery, and functionality of biological materials post-thaw.

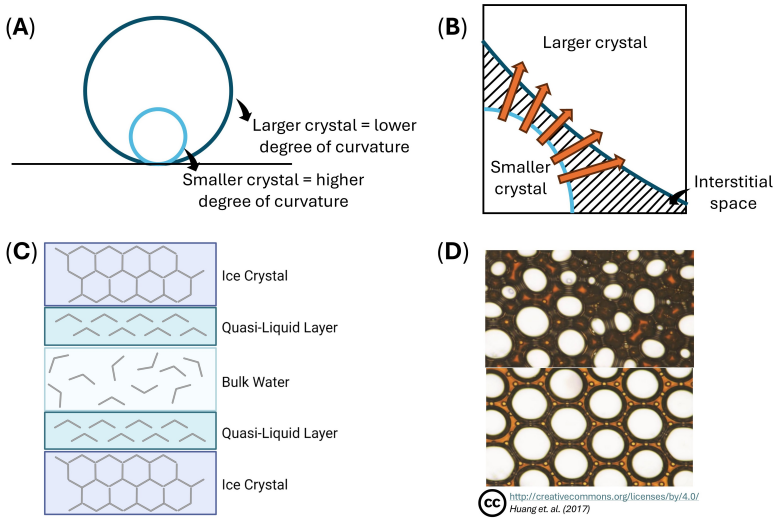


Figure 1-4. (**A**) Depiction of particle grain curvature for small grains versus large grains. (**B**) Representation of the grain boundary migration mechanism where molecules transfer from the smaller grains/crystals to larger/grains/crystals. (**C**) Visualization of water molecule organization in the bulk water phase, quasi-liquid layer (QLL), and ice crystal. (**D**) Depiction of the increase in oil droplet size representative of the Ostwald ripening mechanism. *Images adapted from Huang et. al. (2017) under CC 4.0 with video depiction found here.*[74]

1.2.2. Nature's strategies for controlling ice and mitigating cellular injury

The ability to inhibit ice recrystallization was first identified as a property of naturally occurring proteins and glycoproteins that would become known as biological antifreezes (BAs). These BAs, classified as either antifreeze proteins (AFPs) or antifreeze glycoproteins (AFGPs), were first observed in Antarctic fish in the 1950s (isolated in the 1960s)[78,79] and then later identified in several other animals, fish, and insects that live in environments that reach sub-zero temperatures.[78,80–83] AFPs are structurally diverse and vary in size, secondary structure, and globular structure depending on the species that they are isolated from.[84–86] However, AFGPs are more homologous, with eight subclasses (labelled AFGP 1 through 8) distinguished by molecular weight.[81,86,87] The smallest of the AFGPs, AFGP-8 (**1**), is 2.7 kDa in size containing four tripeptide repeats of alanine-alanine-threonine linked to a β-D-galactosyl-(1-3)-α-*N*-acetyl-D-galactosamine at the threonine residue followed by two *C*-terminal alanine residues (**Figure 1-5**). Ultimately, BAs, including AFGP-8 (**1**), have two primary modes of activity to control ice growth and protect the organisms from associated damage: (1) thermal hysteresis (TH) and (2) ice recrystallization inhibition.

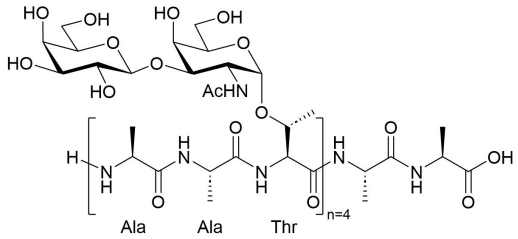


Figure 1-5. Structure of antifreeze-glycoprotein (AFGP) 8 (**1**) with n=4 tripeptide (Ala-Ala-Thr) repeats.

1.2.2.1. Thermal hysteresis activity and ice binding of AF(G)Ps

TH activity is defined as the ability of a compound to depress a solution's freezing point relative to its melting point (**Figure 1-6A**).[88–92,92–94] In nature, at temperatures only a few degrees below 0 °C, the presence of a BA keeps the fluids of an organism in a super-cooled state where stochastic nucleation of ice occurs but prevents ice growth (**Figure 1-6A**).[94] When temperatures drop below the depressed freezing point, rapid, "needle-shaped" ice growth occurs as a result of ice binding (known as dynamic ice shaping, DIS).[95,96] Both TH activity and DIS can be measured by nanolitre osmometry, where the growth and behaviour of a single ice crystal (suspended in oil) is monitored as a function of temperature change (**Figure 1-6B**).[96] While TH activity itself is not directly detrimental to cell survival, it is the associated DIS that is particularly lethal to cells given the cryopreservation of biological materials occurs at temperatures significantly colder than the typical freezing point depression that can be achieved by an AF(G)P (only 1-2 °C below freezing).[94,97–100]

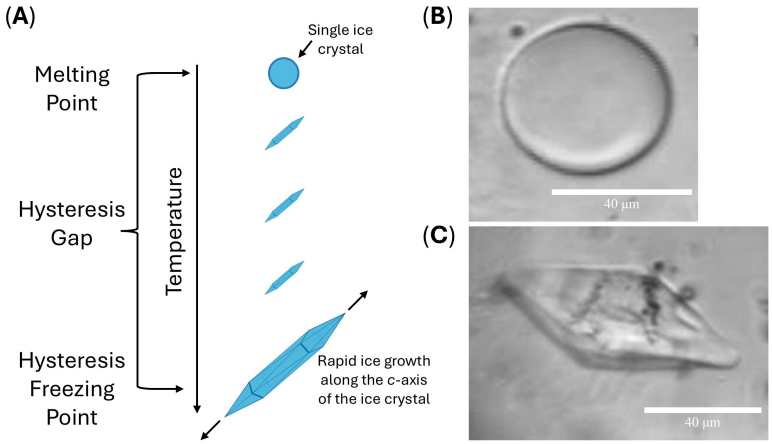


Figure 1-6. (**A**) Illustration of the phenomenon of thermal hysteresis. (**B**) Representation of ice crystal growth in the absence of dynamic ice shaping. Link to video format. (**C**) Representation of ice crystal growth with dynamic ice shaping. Link to video format.

The TH activity and corresponding DIS of BAs is a direct result of their ability to non-covalently "bind" to the surface of ice crystals and change the behaviour of ice crystal growth at a molecular level. In the absence of a BA that causes DIS, the structure of ice depends primarily on the pressure and temperature at which it forms; however, at temperatures below 0 °C and at atmospheric pressure the most common form

of ice is type one hexagonal ice (I_h, *aka* "ice one h").[101] In I_h, the ice lattice is characterized by four axes (a_1, a_2, a_3, and c), three planes (prism, pyramidal, and basal), and eight faces (**Figure 1-7A**).[62] The water molecules of I_h form a relatively open, low-density lattice in which each oxygen atom of a water molecule hydrogen bonds with two different hydrogen atoms on two different, adjacent, water molecules (**Figure 1-7B**).[61,62,102] While the exact properties of three-dimensional ice growth vary depending on the temperature and pressure at which it occurs, I_h at 0 °C and atmospheric pressure grows rapidly along the *a*-axes to form "sheets" of hexagonal-shaped crystals and this lattice appears chair-like in conformation along the *a*-axis and boat-like conformation along the *c*-axis (**Figure 1-7B**).[61,62,102]

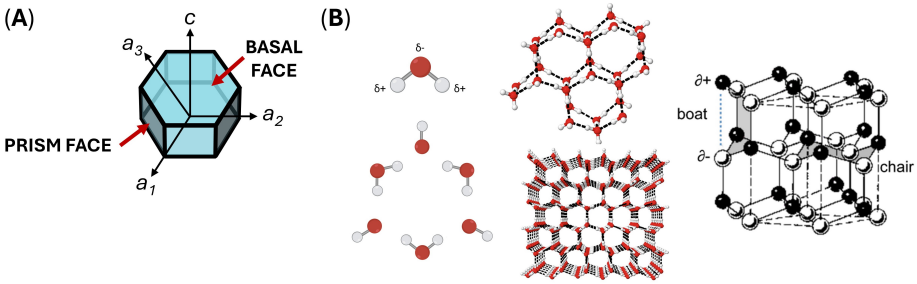


Figure 1-7. (**A**) Schematic representation of the basal and prism faces of hexagonal ice (I_h) illustrating the a_1, a_2, a_3 and c axes. (**B**) Hydrogen bonding pattern and three-dimensional structure of water molecules in the ice lattice of I_h as depicted from the top and side view of the ice lattice. *Images adapted with permission from Springer nature and under CC BY-SA 4.0.*[103]

In general, when AF(G)Ps are introduced into the aqueous system, they irreversibly absorb to the prism faces of the ice crystal, restricting ice crystal growth along the *a*-axis.[90,92] While binding to the basal plane (*c*-axis) has been reported (*i.e.*, type 1 AFP that was isolated from *Dendroides canadensis*)[104–107] as well as models that have proposed a mechanism of AF(G)P binding that is reversible in nature, the irreversible absorption-inhibition mechanism for binding along the *a*-axes is considered to be the most widely accepted and applied explanation for the binding of AF(G)Ps to the surface of ice crystals.[108–112] Under this mechanism, ice growth occurs only along the *c*-axis once temperatures drop below the lower limit of the TH gap (the hysteresis freezing point) which gives rise to the characteristic hexagonal bipyramidal crystal shape caused by DIS (**Figure 1-8**); Along the *a*-axes, ice growth cannot occur where the AF(G)P is absorbed but can occur on the ice surface between adjacent antifreeze molecules (**Figure 1-8**).[90,92]

Two models have been proposed that describe how BAs inhibit ice growth within the TH gap, known as the "step-pinning model" and the "mattress model".[90,93] Ultimately, ice growth by either model results in curved ice surfaces where the energetic cost of adding water molecules to the crystal surfaces where the BAs are bound becomes increasingly less favourable and thus a localized depression of freezing

point is observed [known as the Gibbs-Thomson (Kelvin) effect].[88] Importantly, the energetics of melting are not affected by this process which results in the formation of the hysteretic gap in temperatures between the freezing and melting points.[88,91,113]

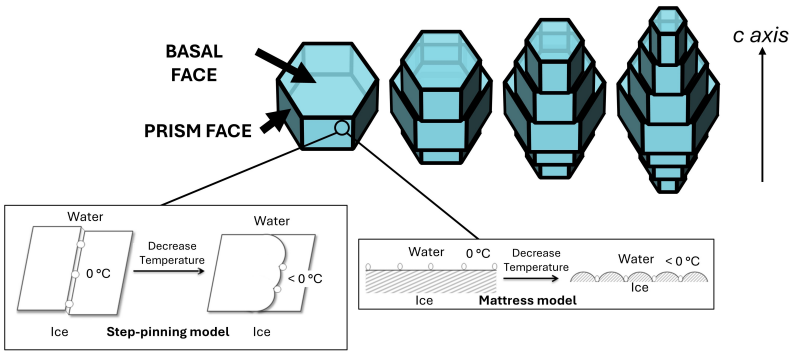


Figure 1-8. Illustration of the binding of biological antifreeze (BA) molecules to the prism face (*a*-axes) of hexagonal ice (I_h) and the subsequent formation of bipyramidal ice crystals (dynamic ice shaping, DIS) due to forced ice crystal growth along the *c*-axis. *Images of both inhibition models adapted from Capicciotti et. al. (2013) under CC 3.0 from IntechOpen.*[82]

At a more molecular level, the exact bonding interactions between an AF(G)P and the ice lattice differ based on the type of AF(G)P.[114] For example, while both type 3 AFP (isolated from *Zoarces americanus*) and $AFGP_{1\text{-}5}$ (isolated from various species of Antarctic fishes) bind to the *a*-axes, they form their binding interactions with different prism planes of the ice crystal (the pyramidal plane and primary prism plane respectively) (**Figure 1-9**).[114] In addition, while it is generally thought that hydrogen bonding interactions between the hydrophilic components (the carbohydrate or amino acid residues) of both AFPs and AFGPs with the ice lattice are responsible for their irreversible absorption, several key studies have found that the hydrophobic residues of AFPs can also have important entropic and enthalpic contributions to ice binding.[115–119]

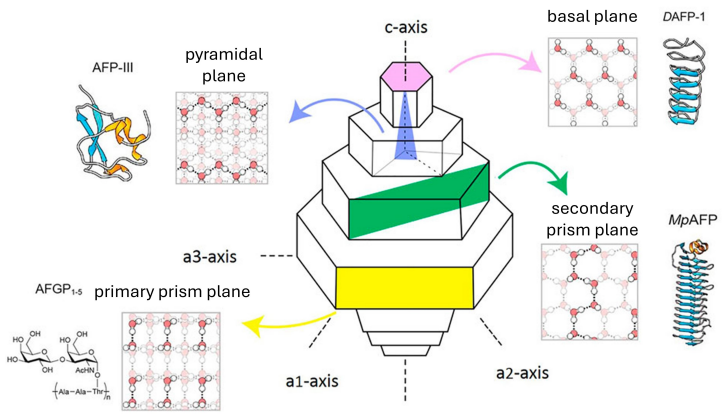


Figure 1-9. Different types of biological antifreeze (BA) binding to ice planes. *Images adapted from Gharib et. al. (2022) under CC-BY from Frontiers.*[114]

Early studies on the ice binding of AF(G)Ps proposed that their amino acid residues formed direct hydrogen bonding interactions at the prism face, where the distance between each residue exactly matched the spacing of oxygen atoms within the ice lattice.[91] It was later suggested that in addition to forming hydrogen bonds with the surface of the ice lattice, these amino acid residues also interacted with water molecules deeper within the ice lattice which effectively "anchored" the AF(G)P to the ice crystal.[92] This initial hypothesis was later supported by several studies accounting for the extensive hydrogen bonding of naturally isolated AFPs to the ice crystal surface.[120–125] However, the hypothesis was challenged once synthetic AFPs were tested that replaced the regularly spaced threonine amino acid residues with valine or serine; despite the ability for serine to form hydrogen bonds with the ice lattice, its presence caused a complete loss of TH activity, while valine caused little loss of activity and suggested that hydrophobic interactions may be important for conferring ice binding.[116,117,126]

It is important to note that ice binding, although not common to many compounds, is not a feature unique solely to AF(G)Ps. Other polymers, such as polyvinyl alcohol (PVA) also have the ability to bind to ice and exhibit TH activity and it is believed that this property is due to the spacing of PVA hydroxyl groups being closely matched to that of the prism plane of ice.[95,127,128] Furthermore, PVA has also been reported to inhibit ice recrystallization, where its activity increases with increasing molecular weight (*i.e.,* length) of the polymer.[129–132] However, given the DIS often observed with these polymeric compounds, they cannot be directly applied for the cryopreservation of cells and tissues at extreme sub-zero temperatures that fall outside of their respective TH gap.[94,97] Furthermore, despite the extensive studies that have been published investigating the key structural features that are required for the TH activity of AF(G)Ps and other polymeric compounds, few have directly investigated the impact of these modifications on ice recrystallization inhibition activity.[102,113,115,118,119,133–136]

1.3. Small-molecule ice recrystallization inhibitors

As previously described, ice recrystallization is one of the largest causes of cellular damage during cryopreservation. Therefore, inhibiting ice recrystallization is critical to improving cryopreservation outcomes (including the recovery, viability, and functionality of biological materials). While AF(G)Ps have been shown to exhibit ice recrystallization inhibition activity, their large-scale production and commercial manufacture through *de novo* synthesis or natural product isolation remain infeasible due to economic and sustainability barriers.[119,137] Modern molecular biology techniques have improved the production yield of natural AF(G)Ps (*e.g.*, by using heterologous protein expression), which most notably has permitted the use of fish AF(G)Ps by Unilever© to improve the quality and texture of their ice cream products.[138] Yet the resulting cost per milligram of isolated or synthesized AF(G)P remains very high and restricts large-scale adoption of these methods for cryopreservation.[85,139,140] More importantly, there are mixed reports on the efficacy of AF(G)Ps for use in the cryopreservation of biological materials, where both improvements and reductions in cryopreservation success have been observed, due to the associated TH activity and DIS of these peptides.[141–146] As a result, investigation into the important structural features of AF(G)Ps, specifically with respect to their ice recrystallization inhibition activity was required to facilitate the development of small-molecule ice recrystallization inhibitors (IRIs) for cryopreservation applications that could be rapidly deployed on large-scale.

1.3.1. Development of small-molecule ice recrystallization inhibitors

The vast majority of early studies on AFPs and AFGPs focused on how structural modifications affected TH activity, with very few directly investigating their impact on ice recrystallization inhibition activity.[102,113,115,118,119,133–136] As lengthy *de novo* synthesis of AF(G)Ps was the only method that permitted the direct chemical modifications (on an atom-by-atom basis) that was necessary for rational and targeted molecular design, these early studies focused on investigating TH activity as this was the property of AF(G)Ps that was best understood. In addition, direct investigations of ice recrystallization inhibition activity had not yet been observed in the absence of TH activity thus complicating any potential conclusions. However, in the early 2000's a serendipitous discovery by Dr. Adewale Eniade (Ben Lab, PhD 2001) and Dr. Suhuai Liu (Ben Lab, PhD 2006) showed that it was possible to decouple the ice recrystallization inhibition and TH activity of AFGPs, opening the door for direct investigation of ice recrystallization inhibition activity.[147,148]

Originally aiming to improve the metabolic stability of the naturally occurring oxygen-linked (*O*-linked) AFGPs, these studies synthesized several carbon-linked (*C*-linked) derivatives and found two compounds, OGG-Gal (**2**) and *C*-serine (**3**), that became the first reported examples of synthetic AFGP

analogues that possessed only ice recrystallization inhibition activity and little to no TH activity and/or DIS (**Figure 1-10**).[147,148]

In the early stages of small-molecule IRI development, ice recrystallization inhibition activity was measured by an acellular splat-cooling assay (SCA) that quantified the mean grain size (MGS) of ice crystals relative to a phosphate-buffered saline (PBS) control (measured as a normalized % MGS) (additional details on the assays used for quantifying ice recrystallization inhibition activity can be found in *section 1.3.2*).[149–151] Using this assay OGG-Gal (**2**) and *C*-serine (**3**) were found to have activity that was comparable to that of natural AFGP-8 (**1**) (% MGS at 5.5 μM: 27.4 ± 0.3 %, 19.6 ± 1.4 %, and 11.9 ± 0.2 % respectively) (**Figure 1-10**).[147,148] Additionally, OGG-Gal (**2**) (1.0-1.5 mg/mL) was found to result in comparable post-thaw viability to 2.5 % DMSO for the cryopreservation of human embryonic liver cells (~70 % cell viability) – highlighting that the inhibition of ice recrystallization in the absence of TH activity could prevent cellular damage during cryopreservation.[152]

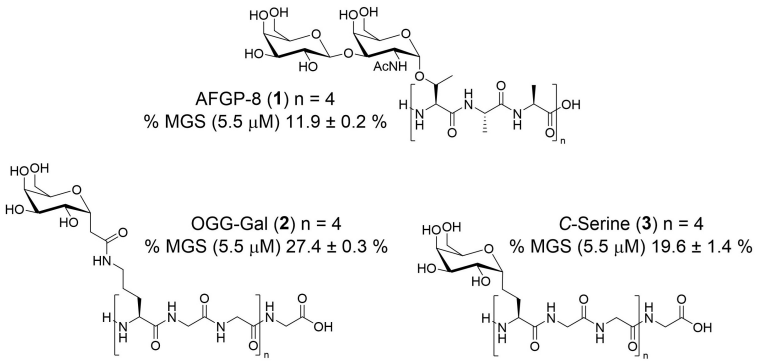


Figure 1-10. Structures and ice recrystallization inhibition activity of AFGP-8 (**1**), OGG-Gal (**2**), and *C*-Serine (**3**).[147,148] Compounds prepared as a solution in phosphate-buffered saline and activity reported as a percent mean grain size (% MGS) measured from n=3 (mean ± standard deviation) ice wafers by splat-cooling assay using a 30-minute annealing time at -6.4 °C.

More recently, other compounds with ice recrystallization inhibition activity have been reported that do not display TH activity (including biomass nanocelluloses[153] and synthetic polymers[95,154]) however the practical adoption of these large polymeric compounds for cryopreservation has been limited.[135,155] As previously mentioned, the development of small-molecule IRIs is highly desirable for cryopreservation applications due to their promising potential for facile large-scale preparation. Towards this objective, further investigation of the *C*-linked AFGPs found that modulation of the carbohydrate unit [replacing the terminal D-galactose unit with either D-glucose (OGG-Glc: **4**), D-mannose (OGG-Man: **5**), or D-talose (OGG-Tal: **6**)] directly impacted ice recrystallization inhibition activity.[156] OGG-Gal (**2**) was found to have the greatest activity, with a percent mean grain size (% MGS) normalized to PBS of 28.1 % (a mean grain size of 0.00354 ± 0.00013 mm^2) when assessed at 5.5 μM, with decreasing activity observed for OGG-Glc

(**4**, 75.4 %), OGG-Man (**5**, 94.7 %), and OGG-Tal (**6**, 89.5 %); the ice recrystallization inhibition activity of OGG-Man (**5**) and OGG-Tal (**6**) at 5.5 μM was comparable to that of the negative control solution (PBS) (**Figure 1-11**).[156]

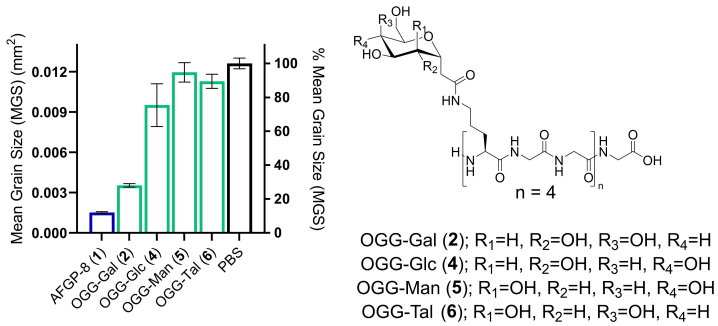


Figure 1-11. Ice recrystallization inhibition activity of *C*-linked AFGP analogues with different carbohydrate components (**2**, **4**-**6**) compared to AFGP-8 (**1**) and phosphate-buffered saline (PBS).[156] Ice recrystallization inhibition activity reported as mean ± standard error of the mean (SEM) of the mean grain size (MGS) and % MGS (normalized to PBS) of n=3 ice wafers assessed at 5.5 μM using a splat-cooling assay with a 30-minute annealing time at -6.4 °C. *Figure recreated from Czechura et. al. (2008)*.[156]

These results showed that the configuration of the carbohydrate could modulate ice recrystallization inhibition activity and suggested that the carbohydrate was essential for the activity of these molecules. However, the *C*-linked AFGP analogues still required lengthy several step syntheses for each building block and would be challenging to implement into large scale cryopreservation applications.[147] Therefore, the ice recrystallization inhibition activity of naturally occurring sugar monosaccharides (**7**-**10**) and disaccharides (**11**-**15**) was explored as a simplified model in order to gain further insight into the carbohydrate's role in inhibiting ice recrystallization. Interestingly, while the activity of the natural sugars was significantly reduced compared to 5.5 μM solutions of AFGP-8 (**1**) or OGG-Gal (**2**), they were able to inhibit ice recrystallization compared to the PBS control with % MGS values between 63.6 ± 3.3 % and 88.0 ± 2.9 % (22 mM) (**Figure 1-12**).[156,157] Furthermore, ice recrystallization inhibition activity was found to be significantly impacted by the nature of the carbohydrate sugar, which was consistent with previous investigations of the AFGP analogues. Most importantly, these simple carbohydrates alone were able to inhibit ice recrystallization without possessing TH activity or causing DIS.[157]

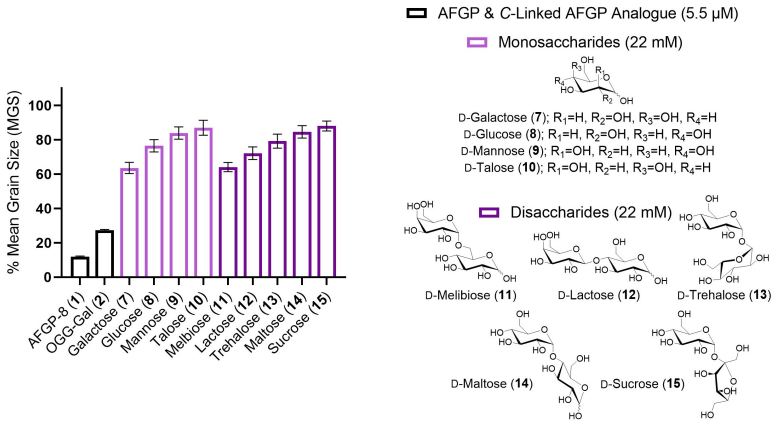


Figure 1-12. Ice recrystallization inhibition activity of monosaccharides (**7**-**10**) and disaccharides (**11**-**15**) (assessed at 22 mM) compared to AFGP-8 (**1**) and OGG-Gal (**2**) (assessed at 5.5 µM).[156–158] Ice recrystallization inhibition activity reported as mean ± standard deviation (SD) of the percent mean grain size (% MGS) normalized to phosphate-buffered saline (PBS) of n=3 ice wafers assessed using a splat-cooling assay with a 30-minute annealing time at -6.4 °C. *Figure recreated using data from Czechura et. al. (2008), Tam et. al. (2008) and Capicciotti (2014)*.[156–158]

These studies also noted that the ice recrystallization inhibition activity of the carbohydrates was concentration dependent. For example, concentrations of D-galactose (**7**) lower than 11 mM resulted in relative MGS percentages comparable to the PBS control, but activity improved as the concentration increased up to 220 mM (**Figure 1-13**).[157] The minimum concentration of D-galactose (**7**) that showed a measurable difference from the PBS control was 22 mM, therefore this concentration was used to screen the next generations of small-molecule IRIs and make direct comparisons between their activity.

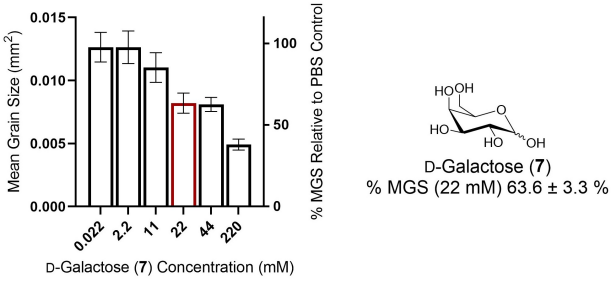


Figure 1-13. Plot of mean grain size (mm^2) and normalized MGS relative to the PBS control (% MGS) for various concentrations of D-galactose (**7**).[157] Data reported from n=3 (mean ± standard deviation) ice wafers assessed by splat-cooling assay following a 30-minute annealing time at -6.4 °C. The 22 mM concentration is highlighted in red to indicate the concentration selected for screening of next-generation small-molecule IRIs. *Figure recreated using data from Czechura et. al. (2008)*.[156]

Given the simplicity and accessibility of the carbohydrates, these findings formed the foundation for the future development of novel small-molecule ice recrystallization inhibitors. However, further improvement and optimization of ice recrystallization inhibition activity required investigation into the mechanism of action of these compounds. As these carbohydrates were not found to bind to ice, the Ben Lab hypothesized that their mechanism of action must be distinct from naturally occurring AF(G)Ps. The

hypothesis was that a small-molecule IRI must disrupt the thermodynamically-driven transition of water molecules from one ice crystal to another during recrystallization by altering the *inter*- and *intra*- molecular hydrogen bonding network of bulk water molecules.[156,157,159]

To test this hypothesis, small molecules that could sequester water and/or dramatically alter the structure of the bulk water network were considered as potential IRI candidates by the Ben Laboratory. These studies resulted in the investigation of two classes of carbohydrate-based non-ionic surfactant and hydrogelator compounds: the *O*-alkyl-β-D-galactosides and the *N*-alkyl-D-gluconamides.[160,161] In particular, the surfactant *n*-octyl-β-D-galactopyranoside (β-octyl-gal, **16**, % MGS = 20.8 ± 1.3 % at 22 mM) and the hydrogelator *N*-octyl-D-gluconamide (NOGlc, **17**, % MGS = 11.9 ± 0.8 % at 0.5 mM) were found to have ice recrystallization inhibition activity comparable to that of synthetic AFGP analogue OGG-Gal (**2**) and still did not display TH activity or cause DIS (**Figure 1-14**).[161] Unlike the AF(G)Ps and their analogues, these small-molecule compounds could be easily synthesized in two or less steps from commercially available reagents.[161] However, their use in biological systems as CPAs has been limited as their highly hydrophobic alkyl chain causes disruption of cell membranes which results in significant cytotoxicity;[162–164] for example, the addition of NOGlc (**17**) as an IRI additive for the cryopreservation of red blood cells (RBCs) resulted in significant post-thaw hemolysis (34 ± 1 % RBC integrity compared to 80 ± 5 % for the 20 % glycerol control).[162] In addition, compounds with a greater proportion of hydrophobicity often suffer from dramatic reductions in aqueous solubility, further limiting their use in biological applications as CPAs.

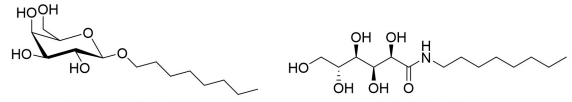
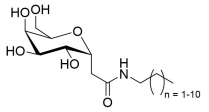


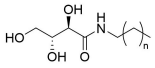
Figure 1-14. Structures and ice recrystallization inhibition activity of β-octyl-Gal (**16**) and NOGlc (**17**).[161] Compounds prepared as a solution in phosphate-buffered saline and activity reported as a percent mean grain size (% MGS) measured from n=3 (mean ± standard deviation) ice wafers by splat-cooling assay using a 30-minute annealing time at -6.4 °C. *Data obtained from Capicciotti et. al. (2012)*.[161]

As a result, shorter alkyl chains within the *N*-alkyl-D-gluconamide class of compounds were explored that ultimately suggested a minimum threshold of hydrophobicity was required for strong inhibition of ice recrystallization (*i.e.*, *N*-propyl-D-gluconamide, NPrGlc, **18**, has little to no measurable ice recrystallization inhibition activity at 22 mM, % MGS = 81.8 ± 3.4 %).[160,161] Two other classes of alkyl carbohydrates, the *N*-alkyl-2-(α-D-galactopyranosyl)-ethylamides (*e.g.,* **19**-**21**) and the *N*-alkyl-erythronamides (*e.g.,* **22**-**23**), were then developed to further investigate the impact of alkyl chain length on ice recrystallization inhibition activity.[160,165] Within the *N*-alkyl-2-(α-D-galactopyranosyl)-ethylamide class, ice recrystallization inhibition activity increased with hydrophobic chain lengths from 5 to 14 carbons

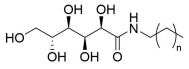
(**Figure 1-15**).[165] In addition, *N*-alkyl-erythronamides (**22**-**23**) with a smaller hydrophilic component were found to be less active IRIs than their corresponding *N*-alkyl-D-gluconamide with the same alkyl chain length (**17** and **24**) (**Figure 1-15**).[160] These findings suggested that establishing a balance between a molecule's hydrophobic and hydrophilic components was critical to the optimization process of small-molecule IRIs. However as previously stated, the alkyl hydrophobic motif of these classes of molecules limited their use in cell preservation applications.



***N*-alkyl-2-(α-D-galactopyranosyl)-ethylamides**
(**19**) n = 1; % MGS (22 mM) 67.7 ± 2.8 %
(**20**) n = 4; % MGS (22 mM) 55.9 ± 3.5 %
(**21**) n = 6; % MGS (22 mM) 9.03 ± 0.35 %



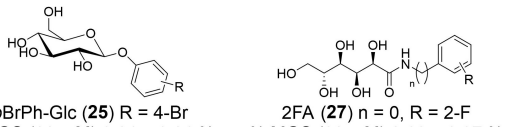
***N*-alkyl-erythronamides**
(**22**) n = 4; % MGS (22 mM) 67.6 ± 4.6 %
(**23**) n = 6; % MGS (22 mM) 56.4 ± 2.7 %



***N*-alkyl-D-gluconamides**
(**24**) n = 4; % MGS (22 mM) 3.38 ± 1.95 %
(**17**) n = 6; % MGS (0.5 mM) 11.9 ± 0.8 %

Figure 1-15. Structures and ice recrystallization inhibition activity of *N*-alkyl-2-(α-D-galactopyranosyl)-ethylamides (**19**-**21**), *N*-alkyl-erythronamides (**22**-**23**), and *N*-alkyl-D-gluconamides (**17** and **24**).[160,165] Compounds prepared as a solution in phosphate-buffered saline and activity reported as a percent mean grain size (% MGS) measured from n=3 (mean ± standard deviation) ice wafers by splat-cooling assay using a 30-minute annealing time at -6.4 °C. *Data obtained from Ampaw et. al. (2019) and Trant et. al. (2013)*.[160,165]

To maintain the amphiphilic nature of the alkylated compounds but attempt to overcome the cytotoxicity concerns arising from their physiochemical properties, *O*-aryl-β-D-glucoside and *N*-aryl-D-gluconamide targets were extensively investigated by the Ben Laboratory. By replacing the alkyl motif with an aryl functional group, the facile synthesis (in two or less steps) of the compounds was maintained as was their ice recrystallization inhibition activity. Several different compounds were identified as effective inhibitors of ice recrystallization following thorough structure activity relationship (SAR) studies including: 4-bromophenyl-β-D-glucopyranoside (*p*BrPh-Glc, **25**), 4-methoxyphenyl-β-D-glucopyranoside (PMP-Glc, **26**), *N*-(2-fluorophenyl)-D-gluconamide (2FA, **27**), and *N*-(2,6-difluorobenzyl)-D-gluconamide (2,6DFB, **28**) (**Figure 1-16**).[166,167] Importantly, 2FA (**27**) exhibited greater ice recrystallization inhibition activity than any other small-molecule IRI reported at that time (% MGS at 22 mM = 2.60 ± 0.37 %).[166] Furthermore, *p*BrPh-Glc (**25**) and PMP-Glc (**26**) were not reported to display TH activity or cause DIS (**27** and **28** had not yet been explicitly tested for DIS or TH).[158] These studies ultimately confirmed that the ice recrystallization inhibition activity of small-molecules could be optimized, modulated, and custom-tailored for their intended application.



*p*BrPh-Glc (**25**) R = 4-Br
% MGS (22 mM) 9.81 ± 0.81 %

2FA (**27**) n = 0, R = 2-F
% MGS (22 mM) 2.60 ± 0.37 %

PMP-Glc (**26**) R = 4-OMe
% MGS (22 mM) 22.9 ± 1.0 %

2,6DFB (**28**) n = 1, R = 2,6-F
% MGS (22 mM) 12.3 ± 0.7 %

Figure 1-16. Structures and ice recrystallization inhibition activity of *O*-aryl-β-D-glucosides (**25**-**26**) and *N*-aryl-D-gluconamides (**27**-**28**).[158,166–168] Compounds prepared as a solution in phosphate-buffered saline and activity reported as a percent mean grain size (% MGS) measured from n=3 (mean ± standard deviation) ice wafers by splat-cooling assay using a 30-minute annealing time at -6.4 °C. *Data obtained from Capicciotti et. al. (2016) and Briard et. al. (2016)*.[166,167]

Overall, the extensive SAR studies completed over the last two decades by researchers in the Ben Lab have shown that small-molecule compounds can inhibit ice recrystallization. However, during the early periods of small-molecule ice recrystallization inhibitor development, the general assay method that was used to quantify ice recrystallization failed to address the concentration- and time-dependence of the ice recrystallization process.[169,170] As a result, a modified version of the assay was developed to address these points of bias and provide more detailed, dose-dependent information about the ice recrystallization inhibition activity of small-molecules.

1.3.2. Assays for measuring ice recrystallization inhibition

Several assays have been reported since the late 1980's for both qualifying and quantifying the process of ice recrystallization and its inhibition.[149–151,169,171–174] Of these assays, the sucrose sandwich assay (SSA)[172] and the splat-cooling assay (SCA)[149–151,169] are most commonly used for their reliable quantification of ice recrystallization. Initially reported in 1988 by Knight *et. al*.[151], the SCA is generally used to quantify ice recrystallization within the context of cryopreservation due to its more accurate representation of the low percent unfrozen fraction (high ice:water ratio) of cryopreserved samples compared to the SSA (**Figure 1-17A**).[175] For the classic SCA, a 10 μL droplet of a salt-buffer solution was dropped onto a pre-cooled aluminum plate surface (-78 °C) where it froze into an ice wafer (~5 mm in radius and < 50 μm thick) that could be transferred to a cooling unit held below 0 °C for a predetermined annealing time (**Figure 1-17B**).[151] Images of the ice wafer then afforded semi-quantitative data of ice recrystallization as the mean largest linear dimension of the ice grain as a function of annealing time (**Figure 1-17C**).[151] Modifications were later made to the data analysis protocol for the classic SCA to improve its accuracy and reliability for data quantification, where domain recognition software (DRS) was used to randomly select 12 ice crystals from the wafer image for which each crystal's complex cross-sectional area could be calculated (**Figure 1-17C**).[150] This method of analysis no longer made assumptions about the shape of the ice crystal as the previous classic iterations had (either by linear dimension[151] or elliptical shape[149]) and therefore more accurately calculated ice recrystallization as a normalized mean ice grain size

(MGS) compared to a phosphate-buffered saline (PBS) control (**Figure 1-17C**).[150] As a result, direct comparisons could accurately be made between MGS values when observing the process of ice recrystallization under different experimental conditions which made it possible to detect and quantify compounds and conditions that were capable of inhibiting the process of ice recrystallization.

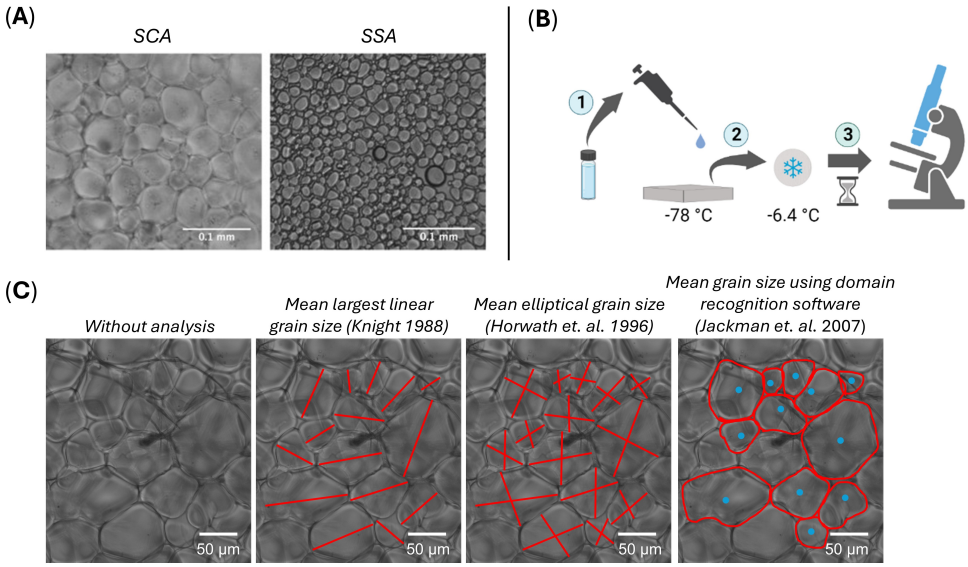


Figure 1-17. (**A**) Comparison of ice wafer images of a 10 µL droplet of phosphate-buffered saline using the splat-cooling assay (SCA) or a 1 µL droplet of a 40 % sucrose solution (w/v in water) using the sucrose-sandwich assay (SSA). Wafers were imaged after annealing for 40-minutes at -6.4 °C. *Images adapted and reprinted from Ampaw et. al. (2020) with permission from Springer.*[175] (**B**) General schematic depicting the setup of the SCA.[150,151] (**C**) Comparison of the early analysis methods for ice crystals imaged by the SCA (from left to right): without analysis, determining the mean largest linear grain size[151], the mean area by assumption of elliptical shape,[149] or the area (mean grain size) of 12 crystals randomly selected by domain recognition software[150].

To address the time- and concentration-dependence of ice recrystallization (and its inhibition using small molecules) at a constant temperature (-6.4 °C), the Ben Lab proposed a kinetic model for ice recrystallization in a system with a small total liquid volume (as is the case in an ice wafer created by the SCA).[158] As part of this model, the growth of ice crystals over time could be described in a monoexponential manner from which first-order rate constants could be derived to describe the increase in mean ice crystal area over time (**Figure 1-18**).[158,169] From these growth curves it was observed that both the initial rate of ice recrystallization, as well as the "end-point" plateau of ice crystal growth, could be affected by the addition of an ice recrystallization inhibitor such as D-galactose (**7**) or PMP-Glc (**26**) (**Figure 1-18**).[158]

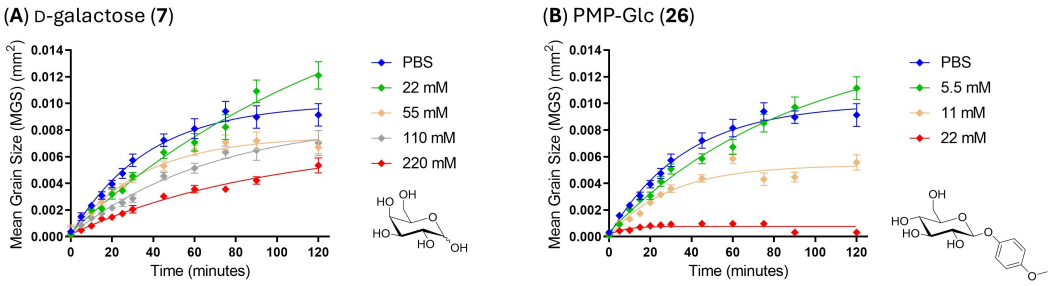


Figure 1-18. Change in ice crystal size (mean grain size in mm^2) over time (minutes) as a function of inhibitor concentration for (**A**) D-galactose (**7**) at concentrations of 22, 55, 110, and 220 mM as well as (**B**) PMP-Glc (**26**) at concentrations of 5.5, 11, and 22 mM compared to the negative control phosphate-buffered saline (PBS).[158] Compounds prepared as a solution in phosphate-buffered saline and activity measured from n=3 (mean ± standard deviation) ice wafers by splat-cooling assay at -6.4 °C. *Figure recreated from Capicciotti (2014).*[158]

From this information, it was hypothesized by the Ben Lab that the inhibition of ice recrystallization may be reversible (where the compound may initially inhibit ice recrystallization but its relative activity reduces over time) when the concentration of inhibitor was too low or the compound was insufficiently active [*e.g.*, 22 to 110 mM D-galactose (**7**) or 5.5 mM PMP-Glc (**26**)].[158] However, with sufficient concentration (*i.e.*, sufficient inhibition activity) the growth of ice crystals could be completely halted in an irreversible manner [*e.g.*, 11 or 22 mM PMP-Glc (**26**)].[158] It was also noted that the equilibrium or steady state area of ice crystals, as well as the time point at which this state was achieved, depended on the compound that was present as well as its concentration; For example, 22 mM PMP-Glc (**26**) achieved a steady state size of ~0.001 mm^2 after only 20 minutes whereas PBS alone did not achieve its steady state of ~0.009 mm^2 until ~90 minutes and 22 mM D-galactose (**7**) did not achieve a steady state within the 120 minute monitoring period (**Figure 1-18**).[158] Overall, these results highlighted that when ice recrystallization is observed at a constant temperature, the inhibition of ice recrystallization may occur *via* different methods depending on the type of inhibitor used and the chosen annealing time before quantifying activity.

Continued investigations into ice crystal behaviour over time by Stephanie Abraham (Ben Lab, MSc 2015) found that the heterogeneity of the ice crystal areas increased with longer annealing times.[170] This meant that following a 30-minute annealing time, the random selection of 12 crystals for determination of their cross-sectional area during ice recrystallization inhibition analysis was not representative of the mean grain size of the entire wafer as a whole.[170] For example, after 30 minutes of annealing, the average area of ice crystals in a wafer of PBS when circling only 12 random crystals was found to be $5.73 \pm 0.28 \times 10^{-3}$ mm^2 but when circling all crystals on the same image the average crystal size was almost half the size at only $2.83 \pm 0.35 \times 10^{-3}$ mm^2 (**Figure 1-19**).[158,170] However, the % MGS of the inhibitor (once

the MGS was normalized to the PBS control) appeared to be consistent between the two analysis methods; for example, the % MGS of a 22 mM solution of PMP-Glc (**26**) assessed at 22-23 % after random selection of 12 crystals and at 24 % after circling of every crystal.[170]

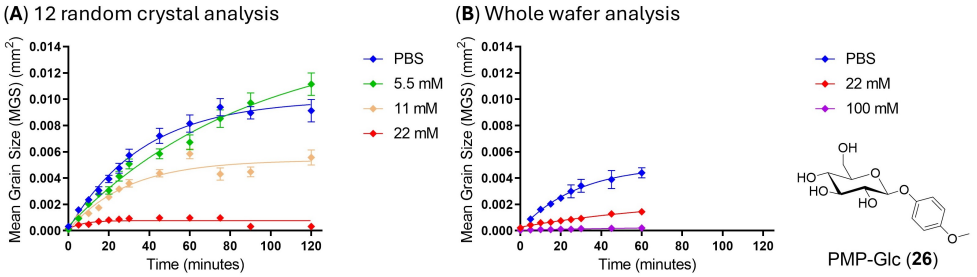


Figure 1-19. Change in ice crystal size (mean grain size in mm^2) over time (minutes) as a function of inhibitor concentration for PMP-Glc (**26**) at various concentrations compared to the negative control phosphate-buffered saline (PBS).[158,170] Ice wafers analyzed by the determination of the cross sectional area of (**A**) 12 randomly selected ice crystals on the image[158] or (**B**) every crystal within a field of view[170]. Compounds prepared as a solution in phosphate-buffered saline and activity measured from n=3 (mean ± standard deviation) ice wafers by splat-cooling assay at -6.4 °C. *Figure recreated from Capicciotti (2014) and Abraham (2015).*[158,170]

Following these key discoveries by the Ben Lab, modifications were made to the SCA that would address the potential avenues for bias inherent to the calculation of ice crystal mean grain size using the 30-minute annealing time with random assessment of only 12 total crystals. The new analysis method proposed by Abraham *et. al.,* involved testing compounds at multiple concentrations and accounted for the heterogeneity of crystals within the ice wafer by determining the area of all crystals within the given field of view (on average a minimum of approximately 100 ice crystals) assisted by image processing software such as ImageJ.[169,170] To quantify the activity of each compound, the change in area of ice crystals over time was monitored by incrementally measuring the proportion of crystal areas that were smaller than 0.001 mm^2 (**Figure 1-20A**).[169,170] The decay of crystals from this 0.001 mm^2 "bin" as they increase in area by recrystallization could then be described by a monoexponential decay constant according to **Equation 1-1**:

Equation 1-1. $A_t^{rel} = A_0^{rel}\left(e^{-k_{obs}t}\right) + A_\infty^{rel}$

where A_t^{rel} is the relative proportionate area of crystals under 0.001 mm^2 (within bin 1) at time t, A_0^{rel} is the fitted relative area at t = 0, k_{obs} is the fitted rate constant, and A_∞^{rel} is the final end point of the fitted data.[169,170] At t = 0, A_0^{rel} will be equal to 1.0, as the 0.001 mm^2 threshold was set such that all crystals within the given field of view at t = 0 would be smaller than 0.001 mm^2.[169,170] Additionally, the final end point A_∞^{rel} should eventually reach zero for given sufficient annealing time where insufficient inhibition of ice recrystallization occurs.[169,170] Thus a sample that retains 80 % of its crystals of mean area less than

0.001 mm^2 (in bin 1, p_1) after a period of 5 minutes of annealing (t) would have a rate of ice crystal growth (v) of 0.04 according to **Equation 1-2**.

Equation 1-2. $v = (1 - p_1)/t$

The slower the process of recrystallization, the slower the transition of crystals out of bin 1, the smaller the value of v, and ultimately the greater the inhibition of ice recrystallization. Of particular note, the practical implications of ice crystal area on cryopreservation outcomes (*i.e.*, how much cellular damage is caused by a given ice crystal size) have yet to be thoroughly investigated. Should a quantitative link be made between ice crystal size and cellular damage (or cryopreservation outcomes) as part of ongoing work in the Ben Lab, the threshold area of bin 1 could be adjusted to account for this information towards the optimization of ice recrystallization inhibition activity for cellular applications.

Nonetheless, fitting of the monoexponential decay given any threshold ice crystal area determines the initial rate of ice crystal growth for each given concentration of a compound and annealing time. The rate constants (k_{obs}) for this growth at each compound concentration could then be normalized to PBS (k_{norm}) and fit to a four-parameter dose-response model in order to calculate an IC_{50} (half-maximal inhibitory concentration) to describe each compound's ice recrystallization inhibition activity (**Figure 1-20B**).[170] Despite providing more detailed information about each compound's activity compared to the single concentration as assessed by the previous 30-minute assay, this method proved rather time consuming for the end user to run and analyze due to the multiple annealing times and concentrations required for complete kinetic analysis of each compound. However, further investigations found that the initial rate of ice recrystallization inhibition using only a five-minute annealing time was in good statistical agreement with the dose response that resulted from the full kinetic profile which drastically reduced the amount of time required for data collection (**Figure 1-20B**).[170] The normalized rate of ice crystal growth at a single annealing time (v_{norm}) could be plotted in a similar manner as k_{norm} to determine the IC_{50} values that describe each compound's relative activity.

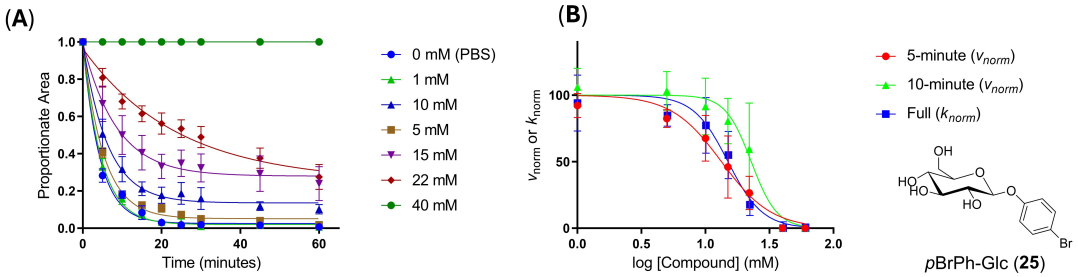


Figure 1-20. Ice recrystallization inhibition activity of *p*BrPh-Glc (**25**) described by (**A**) the change in proportion of ice crystals residing in "bin 1" (mean grain size < 0.001 mm^2) over time (minutes) as a function of inhibitor concentration compared to the negative control phosphate-buffered saline (PBS) or (**B**) a plot of the normalized rate of ice crystal growth by multiple annealing times (full, k_{norm}) or a single annealing time (5-min or 10-min, v_{norm}).[170] Compounds prepared as a solution in phosphate-buffered saline (PBS) and activity measured from n=3 (mean ± standard deviation) ice wafers by splat-cooling assay at -6.4 °C. *Figure recreated from Abraham (2015).*[170]

The five-minute annealing time point now captured ice recrystallization during the period with the highest rate of growth and thus provided a different view-point for the activity of ice recrystallization inhibitors compared to the "end-point" activity analysis of the 30-minute annealing time.[150,169,170] As a result, many compounds that had been previously assessed using the 30-minute SCA[150] began to be re-assessed using the updated 5-minute SCA[169,170] to gain more detailed dose-dependent information about their inhibition activity and improve the reliability of the data that may have been affected by ice wafer heterogeneity. For example, using the updated 5-minute, dose-dependent SCA, previous members of the Ben Lab determined the IC_{50} values of the *O*-aryl-β-D-glucoside and *N*-aryl-D-gluconamide IRIs *p*BrPh-Glc (**25**), PMP-Glc (**26**), 2FA (**27**), and 2,6DFB (**28**) to be 13.4 mM (95 % CI [10.8-16.0]),[170] 19.0 mM (95 % CI [17.0-21.4]),[170] 3.07 mM (95 % CI [3.00-3.14]),[176] and 10.5 mM (95 % CI [7.7-12.7])[176] respectively (**Figure 1-21**). In general, compounds that were reported as active inhibitors of ice recrystallization by the 30-minute SCA were also found to be active when measured by the 5-minute SCA; for example, the IC_{50} of D-glucose (**8**) was found to be 115.5 mM (95 % CI [101.4-136.2]), with more than 10-fold lower activity than the other four compounds (**Figure 1-21**).[177]

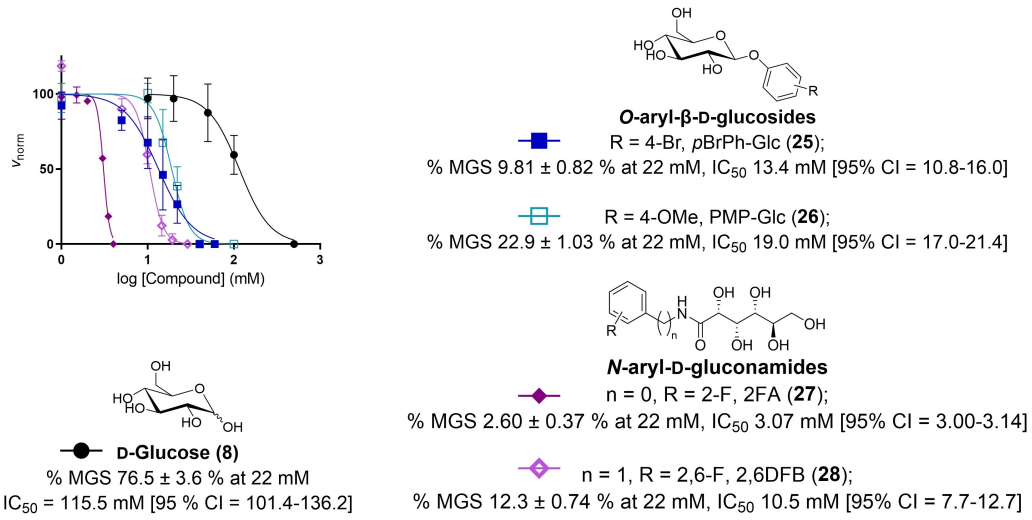
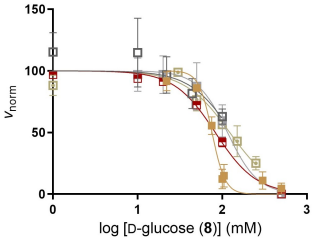


Figure 1-21. Plot of normalized ice crystal growth rate (v_{norm}) in PBS against logarithm transformed compound concentration (in mM) for D-glucose (**8**),[177] *p*BrPh-Glc (**25**),[170] PMP-Glc (**26**),[170] 2FA (**27**),[176] and 2,6DFB (**28**)[176]. Determined by modified splat-cooling assay with a 5-minute annealing time at -6.4 °C.[169] Data reported as the mean ± standard deviation (SD) of n=3 ice wafers. *Dose-response data collected by previous Ben Lab members (Dr. Anna Ampaw[177], Stephanie Abraham[170], and Dr. Madeleine Adam[176]) and recreated for this figure.*

Importantly, as part of the creation of large-scale libraries of candidate compounds, the reported IC_{50} values were found to vary depending on the individual researcher that completed the analysis. For example, the dose-response curve for D-glucose (**8**) has been generated by several different members of the Ben Lab over the last several years with IC_{50} values ranging between 75.7 mM (95 % CI [65.9-84.2] and ~130.4 mM (95 % CI [59.2-∞]) (**Figure 1-22**). IC_{50} values are reported as "approximate" values in cases where the maximum tested concentration (typically due to reaching the compound's aqueous solubility limit) does not achieve a v_{norm} of ≤ 50 %.



Researcher	IC_{50} (mM)	95 % Confidence Interval (CI) (mM)	R^2
A	82.8	70.8-98.4	0.99
B	75.7	65.9-84.2	0.97
C	~130.4	59.2-∞	0.74
D	115.5	101.4-136.2	0.99
E	122.6	90.3-173.2	0.94

Figure 1-22. Ice recrystallization inhibition activity of D-glucose (**8**) from five different researchers to visualize person-to-person variation. Plot of normalized ice crystal growth rate (v_{norm}) in PBS against logarithm transformed compound concentration (in mM). Determined by modified splat-cooling assay with a 5-minute annealing time at -6.4 °C.[169] Data reported as the mean ± standard deviation (SD) of n=3 ice wafers. Reference data: A=Jatinder Singh[178], B=Leah McMunn (this thesis), C=Stephanie Abraham[170], D=Anna Ampaw[177], E=Sarah McPhedran (unpublished).

In addition to person-to-person variation, the accuracy of an IC_{50} value depends directly on the data points that have been collected, with a greater number of data points on the slope of the curve leading to

greater confidence in the true IC_{50} value of a compound. With few data points on the slope of the curve, the error (generally described by a 95 % confidence interval) of the IC_{50} value could be wide; this error is especially exaggerated for compounds with shallow Hill slopes (generally between approximately -1 and +1). Collecting as many data points as possible on the slope of the curve would lead to more accurate determinations of a compound's true IC_{50} value under the given SCA conditions. However, as with any assay, the collection of each concentration data point requires additional time, and this cost must be weighed critically with the benefits of potentially greater accuracy of the IC_{50} value. Given that it is currently not yet understood how the ice recrystallization inhibition activity of a compound as measured by the acellular SCA translates to improved cryopreservation outcomes, the IC_{50} values serve only to provide relative ranking of compound activity for SAR studies as well as to guide the concentrations at which a compound could be used to inhibit ice recrystallization *in vitro*.

Furthermore, the role of these compounds during cryopreservation in any given cellular application is extremely complex as they may impart other cryoprotective effects in addition to their ice recrystallization inhibition activity; for example, the compounds may aid in balancing osmotic pressures *via* cell permeation (*i.e.*, penetrating cryoprotectants such as D-glucose) or stabilizing the cellular membranes (*e.g.*, non-penetrating cryoprotectants such as trehalose).[35] Therefore, as the exact concentrations used for each cellular application depend on multiple factors – including balancing cryoprotection with the compound's potential cytotoxicity and solubility limitations – a "rough" determination of the IC_{50} value often provides sufficient detail for the compound's working concentration to be more thoroughly optimized within the context of each individual cryopreservation application.

1.3.3. Applications of small-molecule IRIs for cryopreservation

The cryopreservation of cells and tissues is an extremely complex process that requires the careful control of several individual parameters to ensure cells can be successfully recovered post-thaw (see *section 1.1*). More importantly, each individual cell type requires an individualized approach for cryopreservation as their sensitivity to the effects of cryopreservation can be directly correlated to cellular structure and complexity. For example, the cryopreservation of red blood cells (RBCs) has been possible since the 1950s,[179] but non-terminally differentiated cell types such as mesenchymal stromal cells (MSCs) remain a significant challenge.[180–184] While initial cryopreservation success may be observed immediately post-thaw using general cryopreservation protocols, significant cell death and functionality loss is often observed 24-48 hours post-thaw due to stress-induced biomolecular pathways that are triggered.[24,185,186] Even established cryopreservation protocols, such as for RBCs, can be improved; the cryopreservation of RBCs only occurs routinely for the banking of rare blood phenotypes, despite the constant blood shortages

that would be mitigated by more routine banking, due to the time-consuming procedures required for the removal of the cryoprotective agent (CPA) glycerol.[1,44,179,187] In addition, ice recrystallization is often not addressed by current cryopreservation strategies, which as discussed previously, can have a significant impact on all outcomes of cryopreservation (including cell viability, recovery, and functionality). As a result, small-molecule IRIs have been at the forefront of investigation by the Ben Laboratory in a variety of different cryopreservation applications over the last two decades.[159,160,188] Of note, significant improvements to the cryopreservation outcomes of RBCs, hematopoietic stem and progenitor cells (HSPCs, isolated from umbilical cord blood), MSCs, and induced pluripotent stem cells (iPSCs) have been observed when small-molecule IRIs are introduced into the cryopreservation formulations.

The standard cryopreservation protocol in North America for RBCs requires the cells to be suspended in of a CPA solution containing 40 % (w/v) glycerol that can take upwards of an hour to remove prior to transfusion of a unit of RBCs.[1,44,179,187] Past experiments by the Ben Lab using this standard protocol found that RBCs post-thaw were comparable to fresh/unfrozen cells, with 98.3 % (± 0.3, n=2) RBCs intact.[162] However, reducing the glycerol concentration to only 15 % (w/v) resulted in a significant reduction in RBC viability to only 27.2 % (± 1.5, n=22).[162] Upon the addition of small-molecule IRIs *p*BrPh-Glc (**25**, 30 mM) and PMP-Glc (**26**, 110 mM) to the 15 % (w/v) glycerol solution, the percentage of intact RBCs post-thaw increased significantly with 47.8 % (± 2.4, n=18) and 68.9 % (± 1.8, n=10) viable respectively (**Figure 1-23A**).[162] These results highlighted the potential for small-molecule IRIs to be used in the cryopreservation of RBCs using reduced glycerol concentrations that could have a significant impact on improving the red cell unit supply chain.

Stem cells have recently emerged as a life-saving therapy for several disorders.[189–198] Cryopreservation of these cells is critical to the wide-scale deployment of these therapies, from clinical use in regenerative medicine, the creation of biobanks, as well as scientific research that enables disease modelling and drug discovery efforts.[199,200] Current cryopreservation strategies for HSPCs and MSCs utilize low concentrations of DMSO as the CPA that maintains the viability of these cells post-thaw;[180–184,201,202] however, similar conditions for iPSCs result in very low post-thaw viability compared to fresh/unfrozen controls.[203,204] Importantly, all three of these stem cell derivatives often suffer from reduced recovery or functionality post-thaw due to delayed onset cell death and poor post-thaw cell quality caused by damage during the freezing and thawing processes; HSPCs suffer from reduced engraftment,[166,205–211] MSCs suffer from impaired immunomodulatory properties,[180–184] and all three cell types suffer from delayed or impaired differentiation and proliferation.[166,180–184,203–211] Through several different projects over the last two decades, researchers in the Ben Lab have found that the introduction of small-molecule IRIs into the cryopreservation

formulations for these stem cell derivatives dramatically improves their outcomes following cryopreservation.

(1) For HSPCs:

No significant improvement in post-thaw viability was observed in the presence of IRIs 2FA (**27**) or 2,6-DFB (**28**) compared to the 10 % DMSO control.[166] However, the net post-thaw recovery of the cells was 1.6-fold greater (**, $p \leq 0.01$) with the addition of 2FA (**27**, 25 mM) and 1.4-fold greater (**, $p \leq 0.01$) with the addition of 2,6-DFB (**28**, 18 mM) compared to DMSO alone (**Figure 1-23B**).[166] Furthermore, the addition of 2FA (**27**, 25 mM) was found to improve the self-renewal capacity of leukocyte concentrates by 2-fold (**, $p \leq 0.01$) and had no significant cytotoxic effects following cryopreservation (**Figure 1-23C**).[166,212] The addition of small-molecule IRIs for the cryopreservation of HSPCs could reduce the risk of engraftment failure and permit widespread use of these cells for cellular therapy.

(2) For MSCs:

No significant improvement in post-thaw viability or recovery was observed in the presence of small molecule IRIs *p*BrPh-Glc (**25**, 30 mM) or 2FA (**27**, 15 mM) compared to the standard freezing media (SFM, 10 % DMSO + 5 % human serum albumin in plasmalyte A).[213,214] However, following a three-day culture the MSCs (isolated from a single donor) that had been cryopreserved with the addition of 2FA (**27**, 15 mM) had significantly greater proliferation rates, with lower doubling times and more population doublings (23.6 ± 1.6 % n=3, 27.4 ± 3.6 h n=3, 2.71 ± 0.32 n=3, respectively), compared to the control cryopreservation media of SFM alone (6.88 % n=1, 59.7 ± 5.3 h n=3, 1.22 ± 0.10 n=3, respectively) (**Figure 1-23C**).[213] Typically, MSCs require several days of culture following thawing from a bio-bank before they can be successfully administered to a patient to ensure sufficient clinical efficacy; therefore, the increased proliferation of MSCs following cryopreservation in the presence of small-molecule IRIs could ultimately improve the efficiency and cost of MSC-based therapies.

(3) For iPSCs:

The addition of 2FA (**27**, 10 mM) to the cryopreservation media (mFresR®) for iPSCs significantly improved both post-thaw viability and recovery (71.5 %, 65.0 %) compared to the control media alone (46.0 %, 47.6 %) and was also able to reduce the occurrence of delayed-onset cell death (*, $p \leq 0.05$).[215] Furthermore, 2FA (**27**) was also found to improve the cryopreservation outcomes of terminally differentiated, post-mitotic iPSC derived neurons (iPSC-Ns) where the

post-thaw recovery of cells cryopreserved with 5 mM or 10 mM 2FA (**27**) improved 1.5-fold compared to the control media (CS10) (****, $p \leq 0.0001$, **Figure 1-23B**).[215] Electrophysiological assessments of the iPSC-Ns found that the cells cryopreserved with 5 mM 2FA (**27**) began to establish synaptic function and neuronal network activity 21 days sooner than CS10 alone (27 days vs. 48 days) and had a significantly greater number of actively firing electrodes after 236 days in culture (****, $p \leq 0.0001$, **Figure 1-23C**).[215] The improved cryopreservation outcomes for iPSCs and iPSC-Ns represent a significant advancement for the long-term storage of these complex cell types and could improve the accessibility, feasibility, and timeliness of cell-based therapies for a variety of diseases.

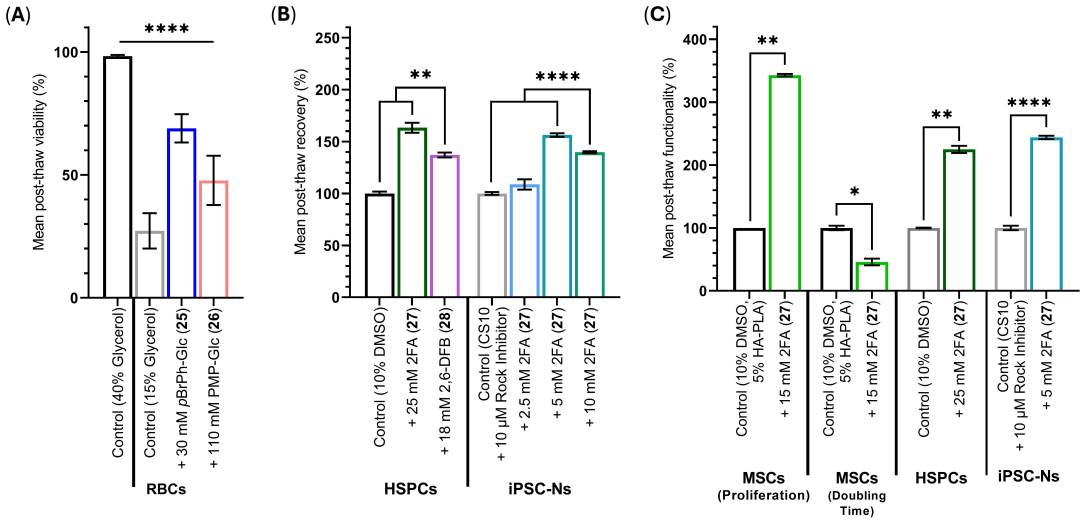


Figure 1-23. Comparison of cryopreservation outcomes in the presence of small-molecule IRIs compared to control cryopreservation solutions. (**A**) Mean post-thaw viability of red blood cells (RBCs) in the presence of *p*BrPh-Glc (**25**, 30 mM + 15 % glycerol) or PMP-Glc (**26**, 110 mM + 15 % glycerol) compared to the control solutions of 40 % (w/v) or 15 % (w/v) glycerol alone.[162] (**B**) Mean post-thaw recovery of hematopoietic stem cells (HSPCs) and induced pluripotent stem cell derived neurons (iPSC-Ns) in the presence of different concentrations of 2FA (**27**) or 2,6DFB (**28**) compared to their control solutions of 10 % dimethyl sulfoxide (DMSO) or CS10 + 10 µM Rock Inhibitor respectively.[166,212,215] (**C**) Mean post-thaw functionality (as measured by cell type specific assays) for mesenchymal stromal cells (MSCs), HSPCs, and iPSC-Ns compared to their respective control solutions.[166,212,213,215] All data mean ± standard error of the mean (except MSCs panel C, mean ± standard deviation). Asterisks indicate statistical significance relative to the control determined by two-tailed unpaired student's T-test where $p \leq 0.05$ (*), 0.01 (**), 0.001 (***) or 0.0001 (****). *Figure recreated with permission from McMunn et. al. (2024).*[188]

Collectively these results highlighted that small-molecule IRIs could be used to improve the post-thaw cryopreservation outcomes for several different cellular applications. However, it is important to note that no single uniform approach for the incorporation of small-molecule IRIs can be applied to the cryopreservation of all cell types. For example, RBCs showed improved cryopreservation outcomes using the *O*-aryl-β-D-glucopyranoside IRIs *p*BrPh-Glc (**25**) and PMP-Glc (**26**), yet *p*BrPh-Glc (**25**) did not

improve the cryopreservation outcomes for cryopreserved MSCs. Furthermore, while the *N*-aryl-D-gluconamides 2FA (**27**) and/or 2,6-DFB (**28**) improved the post-thaw functionality of stem cell products (HSPCs, MSCs, iPSCs, and iPSC-Ns) compared to their respective controls, detrimental effects have been observed when used for the cryopreservation of RBCs (Ben Lab, unpublished work). As a result, it is critical that an individualized approach be taken for the application of small-molecule IRIs to cryopreservation of cell products, taking into consideration any potential cytotoxicity and long-term biological effects, in order for these compounds to be successfully deployed into routine use.

1.3.4. Avenues of continued research for small-molecule IRIs

From the extensive compound library that has been generated by the Ben Lab, incorporating several different classes of small-molecule ice recrystallization inhibitors (IRIs), only a small percentage have been found to warrant further investigation *in vitro*.[188] More importantly, even fewer of these applied compounds have been found to successfully improve cryopreservation outcomes.[188] In part, the successful translation of compounds from the lab to clinical use in cryopreservation applications requires a thorough understanding of its mechanism of action and its potential interactions in the cellular environment. Extensive structure activity relationship (SAR) studies involving multiple classes of compounds have revealed the importance of amphiphilicity as a property of these IRIs;[156,157,160,161,165–167] however, investigation of several parameters that could be used to describe the interactions of these compounds with water molecules, such as octanol-water coefficients (logP) or polar surface area (PSA) to molecular surface area (MSA) ratios, have not shown clear trends that could be used to accurately predict compound activity.[160,168,178,216,217] Furthermore, QSAR-assisted modelling of IRI-candidate compounds could accurately predict whether a compound would be active (% MGS < 70 %) or inactive (% MGS > 70 %) (success rate of 82 %) but failed to discriminate more finely between active IRIs based on structural features alone.[217] Therefore, while parameter assisted predictions of ice recrystallization inhibition activity would greatly improve the rational design process, concrete conclusions are complicated by the multiple, dynamic non-covalent interactions formed by these molecules (in both the solid and liquid state of water).

Beyond understanding structure activity relationships, it is also important to consider the interactions of these compounds within a biological context. Currently, CPAs that can penetrate the cell membrane are widely used (*e.g.*, DMSO and glycerol) for cryopreservation applications to maintain osmotic pressure gradients during warming and thawing.[35] It has been reported by the Ben Lab that small-molecule IRIs are likely to be internalized into the cellular space as their cryoprotective effects are consistent with the profiles of other penetrating CPAs and ice recrystallization inhibition could be visually observed within the nucleus of HUVEC cells.[162,218] Therefore, internalization of these compounds is likely

generalizable to a variety of cell types; direct visualization of this process without disrupting the natural cell environment during cryopreservation could provide key insights into the impact of these compounds on the cell. Finally, consideration of the potential variability in cryopreservation outcomes for applications involving primary cells derived directly from donors is a key point of investigation for the large-scale deployment of IRI technology.

Considering these critical research questions that remain unanswered, this thesis will focus primarily on understanding the structure-activity relationships and underlying mechanism of action for small-molecule carbohydrate-based ice recrystallization inhibitors. Assessment of donor-to-donor variability in the post-thaw outcomes of MSCs cryopreserved with and without small-molecule IRIs will first be discussed, extending on a project started by Dr. Jessica Poisson (Ben Lab, PhD 2019) (**Chapter 2**). Investigation of RBC cryopreservation and the internalization of small-molecule IRIs using label-free Raman imaging techniques will then be explored in collaboration with Canadian Blood Services (CBS) and the National Research Council (NRC) (**Chapter 3**). The final three chapters will focus on a variety of methods that probe the interactions between small-molecule IRIs and water molecules. First, the key structural features of *O*-aryl-β-D-glucopyranosides will be discussed by evaluating correlational studies for the prediction of ice recrystallization inhibition activity (**Chapter 4**). Then, an iterative investigation of the interactions between PMP-Glc (**26**) and water molecules through a traditional structure-activity relationship study assisted by computational calculations and physical property measurements will be discussed (**Chapter 5**). Finally, relaxation times from proton nuclear magnetic resonance will be used to investigate the impact of small molecule IRIs on bulk water molecule organization in both unfrozen and frozen states to gain further insight into the mechanism of action of these compounds (**Chapter 6**).

2. Applying ice recrystallization inhibitors (IRIs) to the cryopreservation of mesenchymal stromal cells (MSCs)

Cellular therapies are a life-saving technology that often rely on cryopreservation to enable long-term storage to maintain a consistent and adequate supply of primary tissues and cell preparations. However, cryopreservation of these cells often results in diminished cell yield (reduced recovery and/or viability) and/or functionality losses that reduce their clinical efficacy.[2] Small-molecule ice recrystallization inhibitors (IRIs) have successfully improved cryopreservation outcomes for a variety of therapeutic cell types, including hematopoietic stem and progenitor cells (HSPCs),[166,168,176] induced pluripotent stem cells (iPSCs) and iPSC derived neurons (iPSC-Ns),[215,216,219,220] and chimeric antigen receptor T (CAR-T) cells.[215,220] Another type of stem cell, mesenchymal stromal cells (MSCs), are extremely attractive for cell-based therapies due to their immunomodulatory and tissue repair properties.[192–198] MSCs, like HSPCs, are multipotent stem cells that are typically isolated from bone marrow.[192,221] However, MSCs are clinically more versatile and accessible than HSPCs as they can also be isolated from other sources,[192,222] including adipose tissue,[223–225] amniotic fluid,[226,227] umbilical cord tissue,[223,228] the endometrium,[229,230] as well as dental tissue[231,232]. MSCs isolated from various different sources are currently involved in numerous clinical trials for the treatment of musculoskeletal, nervous, cardiovascular, and autoimmune diseases.[233]

A typical MSC-based therapy dose requires approximately between 10^6 and 10^8 cells/kilogram of a patient's body weight.[234–236] Due to the insufficient quantity of cells recovered from a single patient donation, the cells for an MSC-based therapy dose are typically isolated and pooled from multiple donors (*i.e.,* an allogenic transplant) to ensure that a sufficient quantity of cells is available for treatment and to improve their immunosuppressive efficacy.[237,238] To further increase the quantity of donated cells prior to therapeutic use the cells are then often expanded *in vitro*, but this has been reported to cause phenotypic changes and losses in therapeutic potency.[192,239–242] To mitigate these issues, MSCs can be stored and banked using cryopreservation to ensure continued and reliable access to MSC-based therapies.[180,182,243] Current clinical cryopreservation conditions for MSCs most commonly use an electrolyte-balanced solution supplemented with serum (typically PlasmaLyte A and human serum albumin)[244] with 10 % dimethyl sulfoxide (DMSO) as the cryoprotectant.[182,245] The cells are then cooled in a controlled rate freezer using an optimized "step-down" procedure and then stored in liquid nitrogen (-196 °C) until needed.[182,245] These conditions generally result in post-thaw recovery and viability of the frozen cells that are comparable to unfrozen cell product; however, their functionality, particularly their immunomodulatory properties and multilineage differentiation ability, can be significantly impaired post-cryopreservation.[180,182–184,246]

Currently, cryopreserved MSCs that are intended for use in clinical therapies are cultured for several days following thawing to ensure therapeutic efficacy.[182,245] However, as extended *in vitro* culture has been linked to phenotypic drift and reduced therapeutic potency,[192,239–242,247] and the treatment efficacy of MSC-based cell-therapies relies directly on the quality of the MSCs, it is imperative that the impact of cryopreservation on the functionality of MSCs be improved.

The Ben Lab has previously reported success improving the functionality of cryopreserved HSPCs using small-molecule IRIs,[166,168,176] and it was hypothesized that a similar approach with MSCs could ultimately improve the efficacy of MSC-based cellular treatments. Dr. Jessica Poisson (Ben Lab, PhD 2019),[214] in collaboration with a team of researchers under the supervision of Dr. David Courtman at the Ottawa Hospital Research Institute (OHRI), began initial investigations cryopreserving MSCs using the small-molecule IRIs 4-bromophenyl-β-D-glucopyranoside (*p*BrPh-Glc, **25**) and *N*-(2-fluorophenyl)-D-gluconamide (2FA, **27**) (**Figure 2-1A**). These IRIs were among the most active small-molecule carbohydrate-based IRIs that had been reported at the time by the Ben Lab and had proven to be successful in several other cellular cryopreservation applications; the IRI *p*BrPh-Glc (**25**) had been used to cryopreserve red blood cells (RBCs) at reduced glycerol concentrations,[158,162,168,248] while 2FA (**27**) had been used to improve the cryopreservation outcomes of multipotent HSPCs and pluripotent iPSCs (**Figure 2-1B**).[166,168,176,215,216,219,220] While the previous success of 2FA (**27**) in a stem cell derivative directly warranted its investigation as an ice recrystallization inhibitor for use in the cryopreservation of MSCs, it had been found to cause complete cell lysis when used as an additive for the cryopreservation of red blood cells (unpublished work by the Ben Lab). These results suggested that different IRIs, or different classes of IRIs, may be more suitable for the cryopreservation of certain cell types over others. Initial studies using *p*BrPh-Glc (**25**) for the cryopreservation of immortalized cell lines (HepG2 and TF-1α) had found that the IRI was detrimental to cell viability for these cell types.[158,168] However, it had not yet been tested in a non-terminally differentiated cell and therefore it was of interest to see if it could be successfully applied to cells at a different stage of differentiation. In addition, as the mechanism of action for these compounds remained unknown, the investigation of IRIs from both classes of molecules could provide insight into the structural features of small-molecule IRIs that are important for the cryopreservation of different cell types.

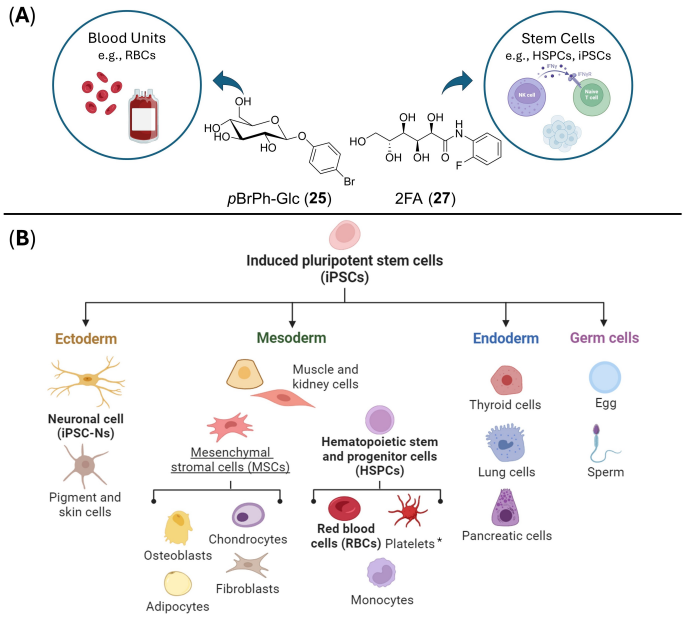


Figure 2-1. (**A**) Structures and current successful cryopreservation applications of small-molecule IRIs *p*BrPh-Glc (**25**) and 2FA (**27**). (**B**) Depiction of stem cell differentiation from pluripotent stem cells. Cryopreservation outcomes for cell types labelled in bold have been successfully improved by the incorporation of small-molecule ice recrystallization inhibitors (IRIs) as of 2024; Asterisk (*) indicates a cell type that has been explored but cryopreservation outcomes were not improved.[162,166,215,216,249] *Figure created using Biorender.com.*

2.1. Ice recrystallization inhibition activity of *p*BrPh-Glc (**25**) and 2FA (**27**)

The ice recrystallization inhibition activity of *p*BrPh-Glc (**25**) and 2FA (**27**) had been previously assessed by the Ben Lab using the 30-minute, single concentration splat-cooling assay (SCA, previously described in *section 1.3.2*). Using this assay, each compound's ice recrystallization inhibition activity was assessed at a 22 mM concentration and described as a percent mean ice grain size (% MGS) relative to the phosphate-buffered saline (PBS) control, where *p*BrPh-Glc (**25**) and 2FA (**27**) were reported to have a % MGS of 9.81 ± 0.82 % and 2.60 ± 0.37 % respectively (n=3, **Figure 2-2A**).[158,166–168] While this 30-minute assay data could be used as a useful screening tool to differentiate between compounds that are "active" or "inactive" at a 22 mM threshold, the single concentration testing failed to provide critical dose-dependent information on each compound's activity. The dose-dependent information is required to translate compounds from the acellular SCA into biological applications, where it is important to consider both cytotoxicity and pharmacokinetic parameters such as solubility and permeability.

Since the ice recrystallization inhibition activity of these two compounds was initially reported, the development of the updated 5-minute SCA (previously described in *section 1.3.2*)[169,170] has allowed for the determination of dose-dependent information on the activity of each compound. Using this assay, Stephanie Abraham (Ben Lab, MSc 2015) and Dr. Madeleine Adam (Ben Lab, PhD 2020) generated a dose-response

curve for each compound's activity in PBS; the half-maximal inhibitory concentration (IC_{50}) of *p*BrPh-Glc (**25**) was reported to be 13.4 mM (95 % CI [10.8-16.0])[170] and the IC_{50} of 2FA (**27**) was reported to be 3.07 mM (95 % CI [3.00-3.14])[176] (described previously in *section 1.3.2*, **Figure 1-21**). As the ice recrystallization inhibition activity of these compounds was assessed by two different graduate students and inter-person variation has been observed for the SCA, these compounds were re-tested to be able to make direct comparisons between their dose-response curves. The ice recrystallization inhibition activity of *p*BrPh-Glc (**25**) and 2FA (**27**) was found to be described by IC_{50} values of 6.75 mM (95 % CI [6.27-7.28]) and 3.47 mM (95 % CI [3.41-3.52]) respectively (**Figure 2-2B**).

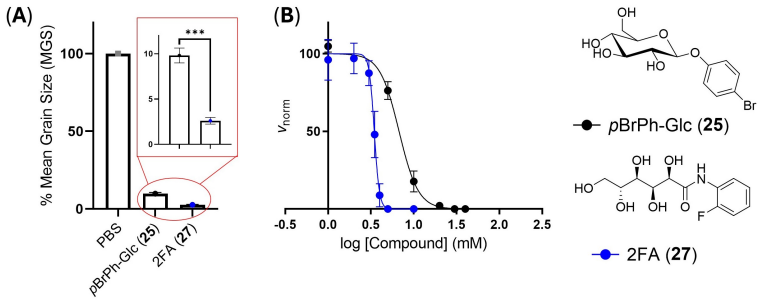


Figure 2-2. Ice recrystallization inhibition activity of compounds *p*BrPh-Glc (**25**) and 2FA (**27**). (**A**) Percent mean ice grain size (% MGS) normalized to phosphate-buffered saline (PBS) determined by modified splat-cooling assay (SCA) using a 30-minute annealing time at a 22 mM concentration at -6.4 °C.[149,150,166,167] (**B**) Plot of normalized ice crystal growth rate (v_{norm}) in PBS against logarithm transformed compound concentration (in mM). Determined by modified SCA with a 5-minute annealing time at -6.4 °C.[169] Data reported as the mean ± standard deviation (SD) of n=3 ice wafers.

While the ice recrystallization inhibition activity curve for 2FA (**27**) was found to be nearly identical to the previously reported value, a 2-fold difference was observed between the two IC_{50} values reported for *p*BrPh-Glc (**25**). As discussed previously (*section 1.3.2*), the acellular SCA dose-response curves act primarily as a guide for determining the approximate concentration range where each compound could be effectively used to inhibit ice recrystallization in cryopreservation applications. To be able to accurately and reliably compare between the IC_{50} values of different compounds while reducing the impact of inter-person, as many data points as possible should be collected at concentrations directly surrounding the inflection point of the dose-response curve. However, as the exact concentrations used for each cellular application depend on multiple factors (including balancing cryoprotection with the compound's cytotoxicity and solubility limitations), a rough IC_{50} value provides sufficient detail for the compound's concentration to be later optimized within the specific context of each individual application.

For the cryopreservation of MSCs, the concentration of each compound to be used was selected based on what was successful in their previous applications respectively; the IRI *p*BrPh-Glc (**25**) was applied to RBC cryopreservation at a 30 mM concentration, and 2FA (**27**) was used for HSPC

cryopreservation at concentrations of 12.5 mM and 25 mM.[162,166,248] Therefore, concentrations of 30 mM for *p*BrPh-Glc (**25**) and 15 mM for 2FA (**27**) (an intermediate of the concentrations used for HSPC cryopreservation) were selected for the cryopreservation of MSCs. Based on the generated dose-response curves for each compound, ice recrystallization was completely inhibited at concentrations of *p*BrPh-Glc (**25**) greater than 30 mM and 2FA (**27**) greater than 5 mM given a 5-minute annealing time (**Figure 2-2B**); therefore, both compounds were expected to be able to completely inhibit ice recrystallization at the selected concentration as indicated by the acellular splat-cooling assay results.

2.2. Cryopreservation of bone-marrow derived mesenchymal stromal cells (BM-MSCs) with small-molecule ice recrystallization inhibitors *p*BrPh-Glc (**25**) and 2FA (**27**)

The initial studies undertaken by Dr. Jessica Poisson (Ben Lab, PhD 2019)[213,214] and our collaborators at OHRI investigated the cryopreservation of MSCs that had been previously isolated from the bone marrow (BM-MSCs) of a single male donor (donor 1). These MSCs were obtained from the ENACT-AMI clinical trial (NCT00936819)[250,251] cryobank, thawed, passaged, and re-cryopreserved in cryovials at a density of 2.0 x 10^6 cells/mL in the standard freezing medium (herein referred to as SFM) for MSCs [containing 5 % human albumin (HA) and 10 % DMSO in PlasmaLyte A (PLA)] or in SFM that had been supplemented with either *p*BrPh-Glc (**25**, 30 mM) or 2FA (**27**, 15 mM). These new cell suspensions were then frozen using a controlled-rate freezer (CRF) programmed with a step-down temperature protocol that had been previously optimized for MSC cryopreservation by our collaborators at OHRI:[214]

(1) Cells were placed into the CRF in appropriate cryosolution and held at 18 ºC
(2) 5 ºC/min cooling until the chamber reached 4 ºC
(3) 1 ºC/min cooling until the sample reached -6 ºC
(4) 30 ºC/min cooling until the chamber reached -40 ºC
(5) 10 ºC/min warming until the chamber reached -18 ºC
(6) 1 ºC/min cooling until the chamber reached -40 ºC
(7) 5 ºC/min cooling until the chamber reached -80 ºC
(8) 10 ºC/min cooling until the chamber reached -180 ºC
(9) Wait at -180 ºC and then transfer to liquid nitrogen storage at -196 ºC

The cooling of the chamber in step four and subsequent warming during step five are commonly programmed steps for rate-controlled freezers to control the ice nucleation event and maintain a consistent sample cooling rate (~1 °C/min) despite the latent heat release that occurs during nucleation.[185,214,252] This

cooling procedure was evaluated during Dr. Poisson's (Ben Lab, PhD 2019) initial investigations, where uniform cooling profiles with minimal latent heat evolution during the ice nucleation event could be achieved for cell samples being cryopreserved in SFM-alone, or SFM supplemented with either *p*BrPh-Glc (**25**, 30 mM) or 2FA (**27**, 15 mM).[214]

With respect to storage time, the MSCs were held at -196 ºC in liquid nitrogen for as short as 24-hours but up to as long as 2-months. Theoretically, a sample held consistently below its critical storage temperature would not incur cellular damage.[13,185] However in reality, consistent maintenance of this ultra-low temperature is challenging and sudden, short-term warming of the samples can occur. These events, known as transient warming events (TWEs), can occur because of equipment failure or improper handling, but also inadvertently during routine cell inventory management. While the extent of damage associated with TWEs is dependent on a number of different factors, they are known to cause significant damage to cells/tissues as they can exacerbate the process of ice recrystallization.[26,248,253–255] Therefore, it has been suggested that the overall biobanking process, including storage and handling conditions, may be responsible for the issues related to MSC cryopreservation rather than simply the exposure to extreme sub-zero temperatures.[254] While the IRI *p*BrPh-Glc (**25**) has been reported by the Ben Lab to mitigate cryopreservation damage to RBCs caused by TWEs,[248] it is important to note that this was not explicitly tested by the experiments discussed in this thesis. Future studies should thoroughly investigate the impact of storage time and the related conditions on the cryopreservation outcomes of MSCs both with and without the addition of IRIs.

After storage, and once the cells were ready to be analyzed, they were thawed at room temperature until no ice was observed. As previously discussed in *section 1.1.1*, the general guidelines for cell cryopreservation often involve using slow cooling rates (~1 °C/min) and fast warming rates (by submersion in a 37 °C water bath) to ensure cells remain viable post-thaw;[18,252] however, the exact rates depend on several factors, including cell type and CPA concentration.[18,27,29,252] Our collaborators at OHRI previously determined that thawing the BM-MSCs at room temperature, with a slower rate of warming, ultimately led to the greatest cell viability given the freezing and storage conditions for their cells. Therefore, all cell handling for the experiments with IRI supplemented SFM, from cell donation to cell thawing from cryopreservation, exactly matched the OHRI cell manufacturing facility's approved protocols to maintain consistency with the ENACT-AMI clinical trial (NCT00936819).[250,251] After thawing, cryopreservation outcomes (including cell viability, recovery, and functionality) were assessed both immediately post-thaw and following three days in culture to evaluate the effect of small-molecule IRIs on the proliferative capacity of MSCs (**Figure 2-3**).

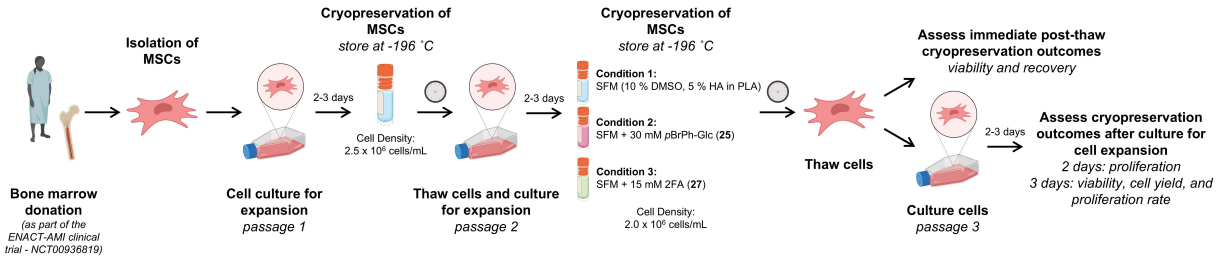


Figure 2-3. Cell preparation protocol for assessment of cryopreservation outcomes for BM-MSCs isolated from a human donor from the ENACT-AMI clinical trial (NCT00936819) in the presence of small-molecule ice recrystallization inhibitors **25** and **27**. *Figure created using Biorender.com.*

Cell recovery was assessed by manual cell counts using a hemocytometer and calculated as a percentage of cells relative to the quantity that were initially cryopreserved. The percent viability of the recovered cells was then assessed by Trypan Blue exclusion assay as well as by Annexin V (AV)/Propidium Iodide (PI) staining. The Trypan Blue exclusion assay was used to visually identify cells that had compromised membranes (late apoptotic or necrotic cells) as stained blue in colour on a hemocytometer (**Figure 2-4A**).[256] The AV/PI assay provided more precise information about cell viability using flow cytometry for fluorometric detection of early apoptotic cells that were stained by AV only, while late apoptotic cells stained by both AV and PI (necrotic cells could also be identified as those that were stained only by PI) (**Figure 2-4B**).[257] An initial assessment of MSC functionality was then measured as a function of cellular proliferation two days post-thaw by EdU (5-ethynyl-2'-deoxyuridine) assay.[258,259] In this assay, the alkyne containing nucleoside base analogue EdU becomes incorporated into the newly synthesized DNA of proliferating cells. Following addition of a fluorescently labelled azide, a copper (I) catalyzed cycloaddition ("click") reaction allows for fluorometric detection of cells that were in the S-phase of the cell cycle (those that were actively synthesizing DNA) by flow cytometry (**Figure 2-4C**).[258,259]

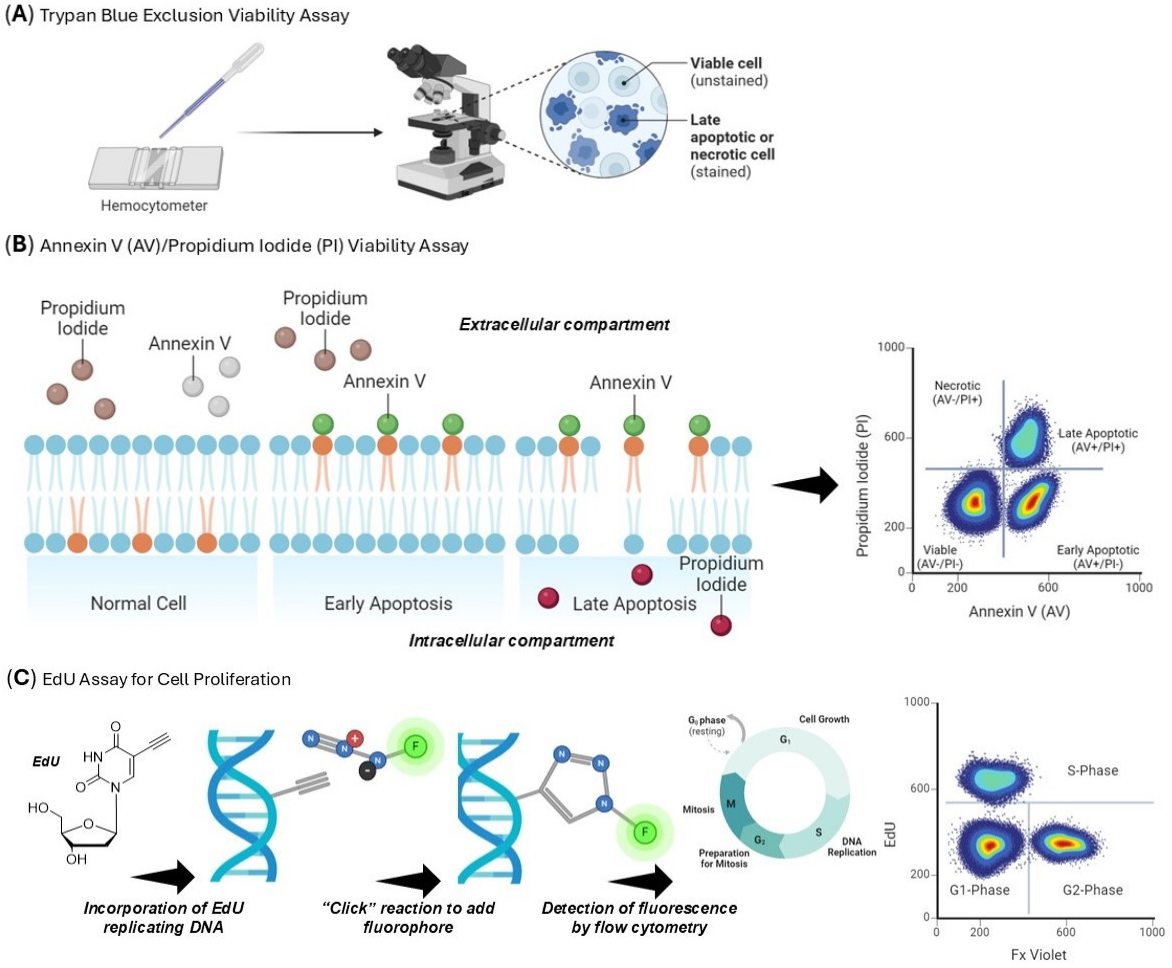


Figure 2-4. Depiction of assays for quantifying cryopreservation outcomes of MSCs. (**A**) Trypan Blue exclusion viability assay.[256] (**B**) Annexin V (AV)/Propidium Iodide (PI) viability assay.[257] (**C**) EdU assay for cell proliferation.[258,259] *Figure created using Biorender.com.*

For these initial studies by Dr. Poisson (Ben Lab, PhD 2019), the immediate post-thaw cell viability and recovery for all treatments was not significantly different, with all cell viability measured greater than 82.0 % (for both Trypan Blue and AV/PI measurements, **Figure 2-5A** and **B**) (n=3, $p > 0.05$, ns, **25** compared to **27**) and all recovery greater than 73.3 % (**Figure 2-5C**) (n=3, $p > 0.05$, ns, **25** compared to **27**). Only one replicate of the SFM-alone condition for this donor was analyzed due to a limited availability of cells that could be provided from the clinical trial therefore statistical comparisons with the control group could not be made.

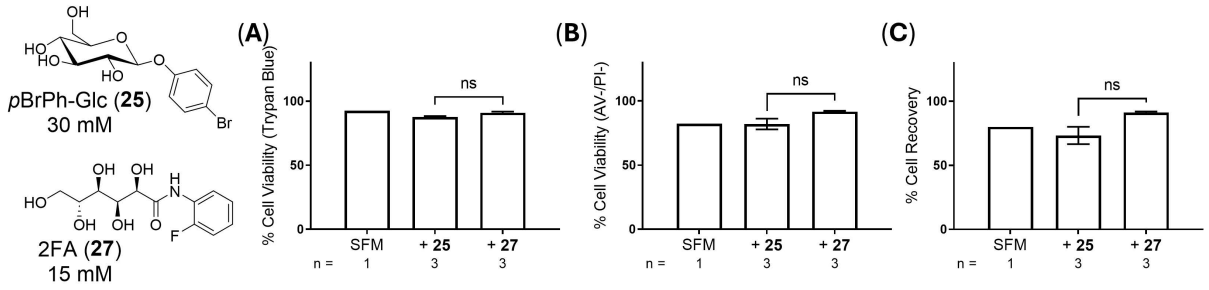


Figure 2-5. Cryopreservation outcomes for BM-MSCs (donor 1) cryopreserved at 2.0 x 10^6 cells/mL in standard freezing medium (SFM) with and without IRIs **25** (30 mM) or **27** (15 mM). (**A**) Cell viability as measured by Trypan Blue exclusion assay immediately post-thaw. (**B**) Cell viability as measured by Annexin V (AV)/Propidium Iodide (PI) immediately post-thaw. Events were gated to include the cell region only with ≥ 10,000 cell region events analyzed per sample. (**C**) Cell recovery as measured by manual cell counts (hemocytometer) immediately post-thaw. Results mean ± standard error of the mean (SEM), n=1 SFM, n=3 + *p*BrPh-Glc (**25**) and + 2FA (**27**). Number of vials analyzed (sample size) indicated below each bar. Significance measured by Student's unpaired two-tailed t-test: ns = $p > 0.05$. *Data collected, analyzed and reported previously by Dr. Jessica Poisson.*[213,214]

With respect to proliferation (measured two days post-thaw), the cells cryopreserved with *p*BrPh-Glc (**25**, 30 mM) were comparable to those cryopreserved in SFM alone, however those cryopreserved with 2FA (**27**, 15 mM) had a 4-fold increase (n=3, $p \leq 0.001$, ***) in the percentage of cells in the S-phase (6.9 %, 5.6 ± 0.5 %, and 23.6 ± 1.9 % for SFM-alone, SFM + **25**, and SFM + **27** respectively, ≥ 10,000 recorded cell events) (**Figure 2-6**). These results indicated that *de novo* DNA synthesis was occurring at a much higher rate for the cells cryopreserved with 2FA (**27**, 15 mM) suggesting a greater degree of functionality post-cryopreservation.

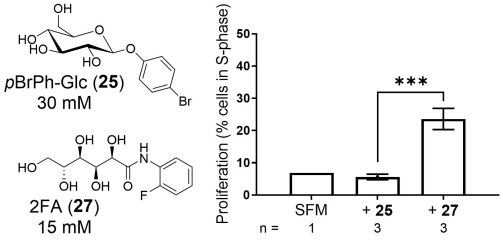


Figure 2-6. Cryopreservation outcomes for BM-MSCs (donor 1) cryopreserved at 2.0 x 10^6 cells/mL in standard freezing medium (SFM) with and without IRIs **25** (30 mM) or **27** (15 mM). Proliferation (cells in S-phase) measured after two days in culture by EdU assay. Events were gated to include the cell region only with ≥ 20,000 cell region events analyzed per sample. Results mean ± standard error of the mean (SEM), n=1 SFM, n=3 + *p*BrPh-Glc (**25**) and + 2FA (**27**). Number of vials analyzed (sample size) indicated below each bar. Significance measured by Student's unpaired two-tailed t-test: *** = $p \leq 0.001$. *Data collected, analyzed and reported previously by Dr. Jessica Poisson.*[213,214]

After three days of culture no abnormal morphological changes to the MSCs were observed (**Figure 2-8**) and manual counts of the cells further confirmed increased proliferation of the cells that were cryopreserved in SFM supplemented with 15 mM 2FA (**27**); the 2FA (**27**) cryopreserved cells had an increased number of population doublings and a shorter doubling time than those cryopreserved with either

SFM-alone or SFM supplemented with 30 mM *p*BrPh-Glc (**25**) (**25** compared to **27**, n=3, $p \leq 0.01$, **, **Figure 2-7C** and **D**). The viability of the cells after three days in culture was comparable to the viability as measured immediately post-thaw, with a lowest recorded viability of 89.1 % (**Figure 2-7A** and **B**). A significant increase in cell viability from the immediate post-thaw measurement to after three days in culture was observed for the cells cryopreserved in SFM + *p*BrPh-Glc (**27**, $p \leq 0.05$, *) suggesting that the cells may be recovering from some of the initial damage over the course of time in culture (**Figure 2-7B**). Furthermore, the cell viability after three days was significantly higher for the cells cryopreserved with 15 mM 2FA (**27**) than 30 mM *p*BrPh-Glc (**25**) when measured by the Trypan Blue exclusion assay (n=3, $p \leq 0.05$, *) (**Figure 2-7A**); however, no significant difference was observed between these conditions by the AV/PI assay (n=3, ≥ 10,000 recorded cell events, $p > 0.05$, ns) (**Figure 2-7B**).

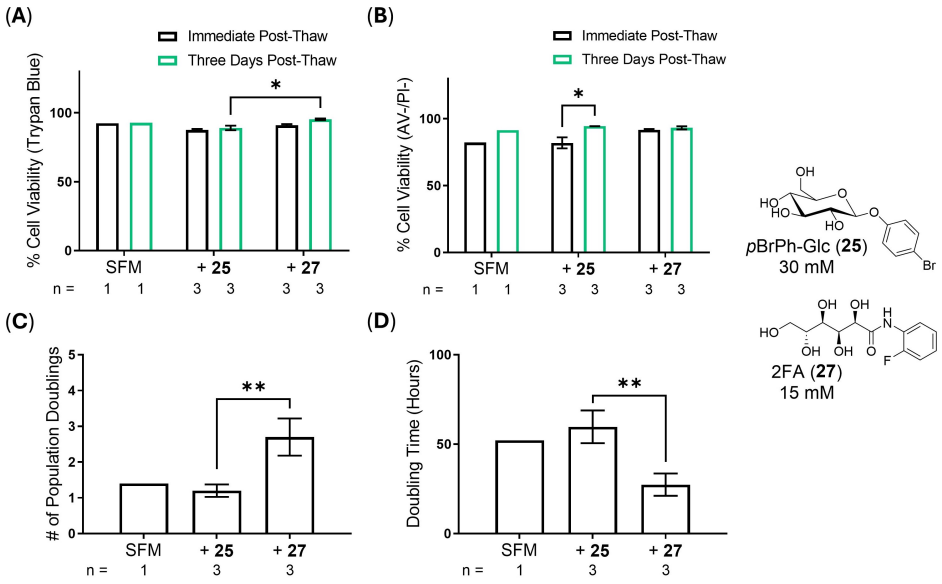


Figure 2-7. Cryopreservation outcomes for BM-MSCs (donor 1) cryopreserved at 2.0 x 10^6 cells/mL in standard freezing medium (SFM) with and without IRIs **25** (30 mM) or **27** (15 mM). (**A**) Cell viability as measured by Trypan Blue exclusion assay immediately post-thaw and after a three-day culture. (**B**) Cell viability as measured by Annexin V (AV)/Propidium Iodide (PI) immediately post-thaw and after a three-day culture. (**C**) The number of population doublings and (**D**) the amount of time that was elapsed to achieve a single population doubling. Cells plated at 0.5 x 10^6 cells/mL. Results mean ± standard error of the mean (SEM), n=1 SFM, n=3 + *p*BrPh-Glc (**25**) and + 2FA (**27**). Number of vials analyzed (sample size) indicated below each bar. Significance measured by two-way ANOVA with Tukey's post-hoc analysis (**A** and **B**) or Student's unpaired two-tailed t-test (**C** and **D**): * = $p \leq 0.05$, ** = $p \leq 0.01$. *Data collected, analyzed and reported previously by Dr. Jessica Poisson.*[213,214]

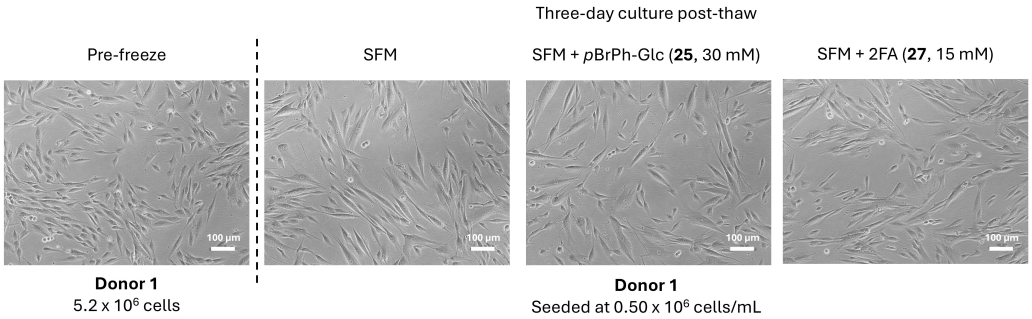


Figure 2-8. Photomicrographs of BM-MSCs cultured immediately post-thaw that were isolated from donor 1 and cryopreserved with either standard freezing medium (SFM) without or with the addition of IRIs **25** (30 mM) or **27** (15 mM). Images taken after three days in culture plated at a density of 0.50 x 10^6 cells/mL. Attached cells are visible as dark spots on the image. *Data collected, analyzed and reported previously by Dr. Jessica Poisson.*[213,214]

While both *p*BrPh-Glc (**25**) and 2FA (**27**) have proven to be successful additives for the cryopreservation of other cell types at these concentrations,[158,162,166,168,176,215,216,248] only 2FA (**27**, 15 mM) was beneficial for the cryopreservation of MSCs with improved proliferation rates post-thaw compared to SFM-alone; *p*BrPh-Glc (**25**, 30 mM) did not improve any of the measured cryopreservation outcomes compared to SFM-alone. However, as the addition of *p*BrPh-Glc (**25**, 30 mM) did not cause any detected deleterious effects during BM-MSC cryopreservation, additional testing to increase biological replicates and elucidate donor-dependent effects was warranted. Ultimately, an improved proliferation rate due to the addition of IRIs during cryopreservation could translate to shorter culture times and larger cell expansion to improve the availability of MSCs for use as clinical therapeutics.

2.3. Assessing donor-to-donor variation for the cryopreservation of bone-marrow derived mesenchymal stromal cells (BM-MSCs)

Given the increased proliferation of BM-MSCs cryopreserved with 2FA (**27**) that was observed during the preliminary experiments by Dr. Jessica Poisson (Ben Lab, PhD 2019),[213,214] we were interested in exploring the cryopreservation outcomes of cells isolated from two additional bone-marrow donors. Response to immunotherapy treatments and the overall therapeutic efficacy of cells isolated from a single donor are known to be variable, which is why MSCs are often pooled from multiple donors prior to administration of a cellular therapy.[237,238] Therefore, in a similar manner to the preliminary experiments by Dr. Jessica Poisson and our collaborators at OHRI (see *section 2.2*), BM-MSCs from two additional male donors (donor 2 and 3) were obtained from the ENACT-AMI clinical trial (NCT00936819)[250,251] cryobank. All three donors were between the ages of 23 and 27, Caucasian, healthy, and tested negative on an infectious disease panel (**Table 8-82**). All cell handling protocols (from cell donation to cell thawing from cryopreservation) were consistent with the previous experiments, and exactly matched the OHRI cell

manufacturing facility's approved protocols for the ENACT-AMI clinical trial (NCT00936819).[250,251] After thawing, cryopreservation outcomes (cell viability, recovery, and functionality) were assessed using the same measures as described previously, both immediately post-thaw and following cell expansion *via* culture.

2.3.1. Immediate post-thaw cryopreservation outcomes for BM-MSCs

2.3.1.1. Cell recovery

Following cryopreservation, cell recovery is calculated as a percentage of cells post-thaw relative to the number of cells that were initially frozen. This outcome does not necessarily consider the viability state of the cells (*e.g.,* whether the cells membranes are intact) but simply provides a visual count of cell quantity. Therefore, this outcome provides information about the quantity of cells that remained undestroyed (*i.e.,* did not become cell debris) because of the cryopreservation process.

Immediately post-thaw, the cryopreserved BM-MSCs from donor 2 had high cell recovery percentages across all tested conditions, with the mean cell recoveries all greater than 80.1 ± 10.3 % (n=7, **Figure 2-9B**). The cryopreserved BM-MSCs from donor 3 had more variable recovery percentages than donor 2, but all mean recovery percentages remained greater than 76.0 ± 16.9 % (n=4, **Figure 2-9C**). Overall, these results were consistent with the recovery percentages observed for donor 1 (73.3 ± 6.7 %, n=3, **Figure 2-9A**). Of note, the significantly greater recovery of donor 3 BM-MSCs cryopreserved with *p*BrPh-Glc (**25**, 30 mM) compared to donor 1 or 2 ($p \leq 0.01$, **, **Figure 2-9D**) was not considered practically meaningful when considering the poor cell viability results for these conditions that will be discussed in the subsequent section. Overall, cell recovery immediately post-thaw was found to not vary significantly by donor and was not significantly impacted (positively or negatively) by the presence of IRIs *p*BrPh-Glc (**25**) or 2FA (**27**, 15 mM) (**Figure 2-9**).

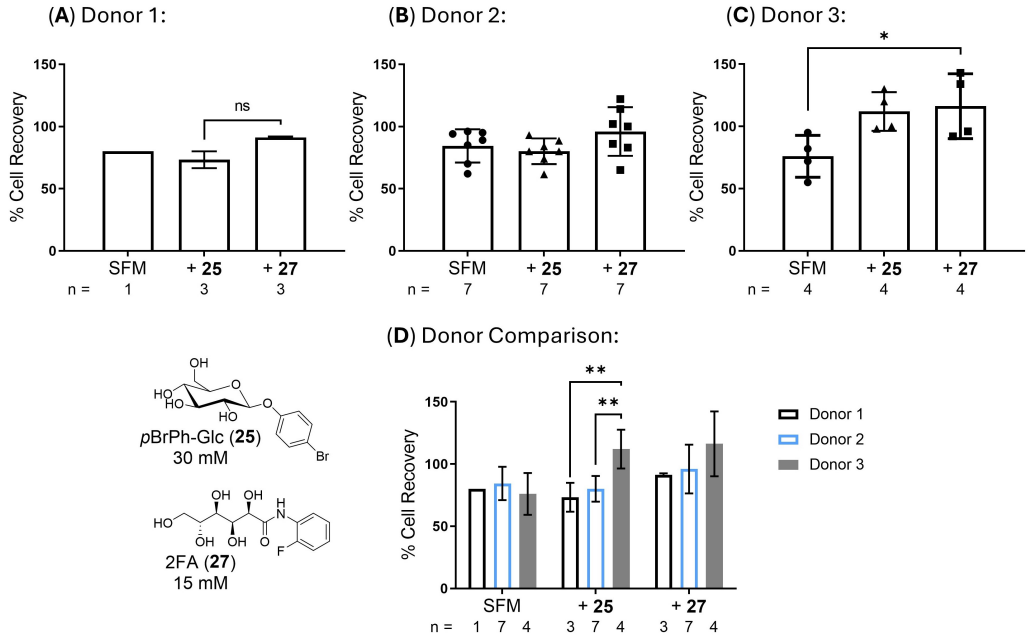


Figure 2-9. Immediate post-thaw cell recovery for BM-MSCs cryopreserved at 2.0 x 10^6 cells/mL in standard freezing medium (SFM) with and without IRIs **25** (30 mM) or **27** (15 mM). Cell recovery as measured by manual cell counts (hemocytometer). (**A**) Donor 1 (*results obtained by Dr. Jessica Poisson*).[213,214] (**B**) Donor 2. (**C**) Donor 3. (**D**) Comparison of all three donors. Results mean ± standard deviation (SD). Number of vials analyzed (sample size) indicated below each bar. Significance measured by Student's unpaired two-tailed t-test for panel A, one-way ANOVA with Tukey's post-hoc analysis for panels B and C, and two-way ANOVA with Tukey's post-hoc analysis for panel D with only cross donor comparisons shown: ns = $p > 0.05$, * = $p \leq 0.05$, ** = $p \leq 0.01$.

2.3.1.2. Cell viability assessed by Trypan Blue exclusion and AV/PI assay

Measurement of cell viability post-thaw provides more detailed context as to whether the recovered cells incurred damage or have had biomolecular stress-response pathways triggered during the cryopreservation process. The viability of BM-MSCs isolated from donor 2 and cryopreserved in SFM alone or SFM supplemented with 15 mM 2FA (**27**) were as expected, with both Trypan Blue and AV/PI assays resulting in mean cell viabilities greater than 86.0 % (**Figure 2-10B**). No significant difference in the cell viability was observed between the SFM-alone and 2FA-supplemented SFM freezing conditions for either assay ($n \geq 3$, $p > 0.05$, ns) (**Figure 2-10B**). However, the cells cryopreserved in SFM supplemented with 30 mM *p*BrPh-Glc (**25**) had significantly reduced cell viability, with only 77.7 ± 10.7 % viable as measured by the Trypan Blue exclusion assay ($n=7$, $p \leq 0.001$, ***) and only 7.9 ± 7.2 % viable as measured by the AV/PI assay ($n=3$, $p \leq 0.0001$, ****) (**Figure 2-10B**). The cell viability results for BM-MSCs isolated from donor 3 were consistent with donor 2, where all conditions had greater than 79.5 % viable as measured by the Trypan Blue exclusion assay and the viability of the cells cryopreserved with *p*BrPh-Glc

(**25**, 30 mM) as measured by the AV/PI assay was very low (2.8 %) compared to those cryopreserved with SFM supplemented with 2FA (**27**, 15 mM, 81.1 %) or SFM-alone (79.7 %) (**Figure 2-10C**).

When comparing between the three donors, no significant or meaningful difference ($n \geq 3$, $p > 0.05$, ns) was observed for the cell viability as measured by the Trypan Blue exclusion assay or by the AV/PI assay when comparing between the SFM or 2FA (**27**, 15 mM) supplemented SFM conditions (**Figure 2-10D**). However, a significant reduction in cell viability as measured by the AV/PI assay was observed for cells cryopreserved in SFM supplemented with *p*BrPh-Glc (**25**, 30 mM) for donor 2 compared to donor 1 ($n \geq 3$, $p \leq 0.0001$, ****), which was also observed for donor 3 when compared to donor 1 (**Figure 2-10D**). Only a single replicate for the AV/PI assay with donor 3 was recorded due to laboratory shutdowns caused by COVID-19.

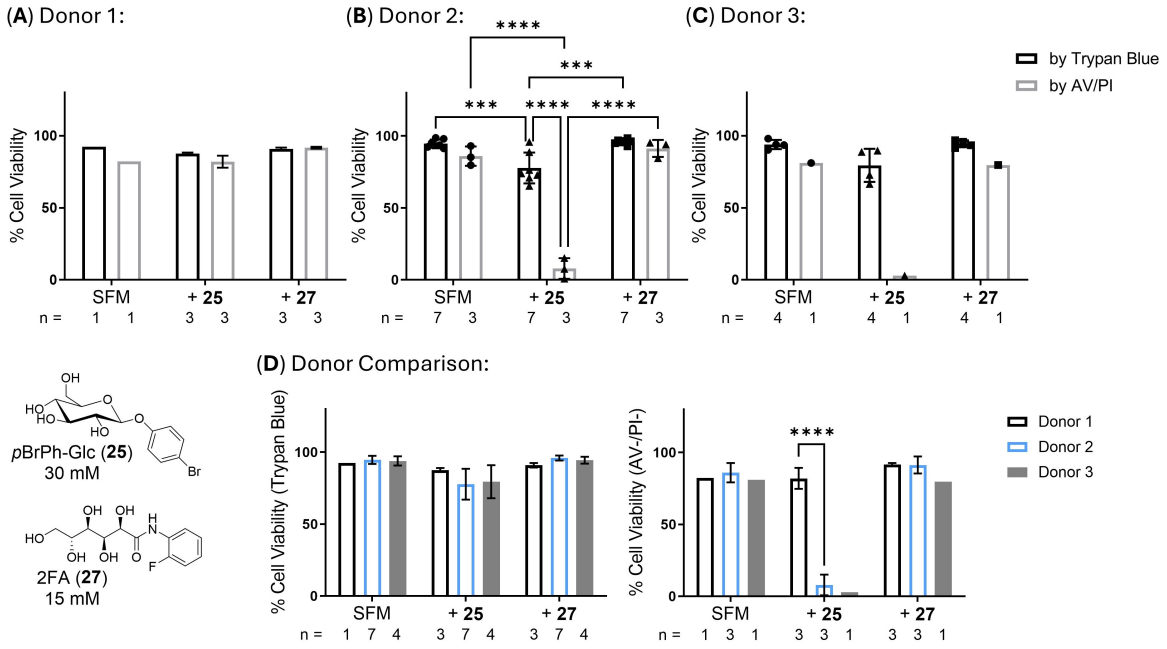


Figure 2-10. Immediate post-thaw cell viability for BM-MSCs cryopreserved at 2.0 x 10^6 cells/mL in standard freezing medium (SFM) with and without IRIs **25** (30 mM) or **27** (15 mM). Cell viability as measured by Trypan Blue exclusion assay and Annexin V (AV)/Propidium Iodide (PI). Events for AV/PI were gated to include the cell region only with ≥ 10,000 cell region events analyzed per sample. (**A**) Donor 1 (*results obtained by Dr. Jessica Poisson*).[213,214] (**B**) Donor 2. (**C**) Donor 3. (**D**) Comparison of all three donors where only significance across donors are shown. Results mean ± standard deviation (SD). Number of vials analyzed (sample size) indicated below each bar. Significance measured by two-way ANOVA with Tukey's post-hoc analysis: *** = $p \leq 0.001$, **** = $p \leq 0.0001$.

As previously discussed, the AV/PI assay provides more detailed information about cellular death than the Trypan Blue exclusion assay as it is able to specifically differentiate between cells that are necrotic, or in the early or late stages of apoptosis based on their staining profiles (**Figure 2-4B**).[256,257] The staining

of cells by AV and PI is monitored by flow cytometry, where cells are classified as viable (not stained by either AV or PI, AV-/PI-), in early apoptosis (stained by AV but not by PI, AV+/PI-), in late apoptosis (stained by AV and PI, AV+/PI+), or necrotic (stained by PI but not by AV, AV-/PI+). Both AV and PI are non-permeable cell stains that cannot bind/penetrate a healthy viable cell. However, in the early stages of apoptosis, phosphatidyl serine residues normally found only on the inner leaflet of the cell membrane flip to the outer leaflet and are accessible for binding by AV; in the later stages of apoptosis PI binds DNA that is no longer contained within the cytoplasm due to further compromise of the cell's membranes.

Given the Trypan Blue exclusion assay cannot identify early apoptotic cells and the AV/PI assay results showed significantly greater cell death in the presence of *p*BrPh-Glc (**25**), it was thought that this discrepancy could have been caused by a large population of early apoptotic cells (AV+/PI-, the lower right quadrant of each dot plot) that did not have sufficiently compromised cell membranes to be stained by Trypan Blue but would be counted as non-viable by the AV/PI assay. However, when comparing the representative dot plots for the flow cytometry results for each condition from donors 2 and 3 it was clear that only a small proportion of cells were early apoptotic (AV+/PI-), with the majority of cells in the late apoptotic population (AV+/PI+, the upper right quadrant of each dot plot) for both donors (**Figure 2-11**). In addition, a very small proportion of cells were stained as necrotic (AV-/PI+, the upper left quadrant of each dot plot) from either donor or for any condition (**Figure 2-11**).

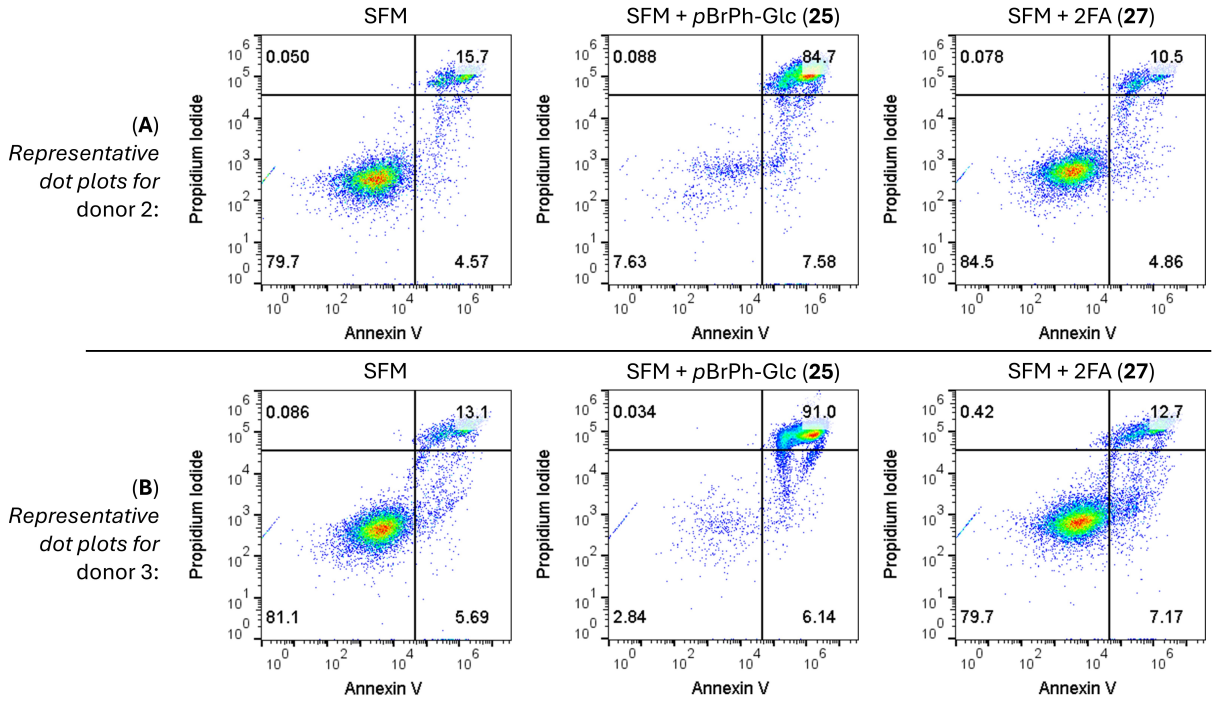


Figure 2-11. Flow cytometry dot plots for representative technical replicates of the Annexin V (AV)/Propidium Iodide (PI) assay for BM-MSCs cryopreserved from donors (**A**) 2 or (**B**) 3 in standard freezing medium (SFM) supplemented with or without IRIs **25** (30 mM) or **27** (15 mM). Events for AV/PI were gated to include the cell region only with ≥ 10,000 cell region events analyzed per sample.

While the Trypan Blue exclusion assay could be run immediately after cell thawing (within 5-10 minutes) and requires minimal cell manipulation, a multi-step staining protocol (30-40 minutes) must be completed for data to be collected by the AV/PI assay. It was hypothesized that the significant decrease in percent viable cells for *p*BrPh-Glc (**25**, 30 mM) treated cells across the two assays (n≥3, 77.7 ± 10.7 % *via* Trypan Blue compared to 7.9 ± 7.2 % *via* AV/PI, p ≤ 0.0001, ****, **Figure 2-10B**) could have been attributed to a delayed cell death response shortly after thawing the cells that was exacerbated by the staining protocol of the AV/PI assay; this apparent cytotoxicity response will be explored in greater detail in *section 2.3.2.4*.

2.3.1.3. Functionality: Proliferation as measured by EdU assay

To assess functionality, the proliferative capacity of cryopreserved BM-MSCs was evaluated by EdU assay. The EdU assay can differentiate between cells in different stages of the cell cycle by detecting the incorporation of a fluorescent nucleoside analogue into the actively synthesizing DNA of cells that are in the S-phase. It was found that the cells isolated from donor 2 that were cryopreserved in SFM supplemented with 2FA (**27**, 15 mM) had a 3-fold increase in the average percentage of cells that could be found in the S-phase of the cell cycle (n=3, ≥ 10,000 recorded cell events, p ≤ 0.05, *) and were actively proliferating at a higher rate than the cells cryopreserved in SFM-alone (**Figure 2-12B**, **Figure 2-13**). There

was an insufficient quantity viable cells in the plates from the *p*BrPh-Glc (**25**) frozen cells, further suggesting the possibility of delayed-onset cell death for the cells cryopreserved with this treatment, therefore proliferation could not be measured for these samples. These results were consistent with the EdU assay results for the cells isolated from donor 1, where a 4-fold increase in the percentage of S-phase cells was observed for the BM-MSCs cryopreserved with 2FA (**27**, 15 mM) compared to *p*BrPh-Glc (**25**, 30 mM, n=3, ≥ 10,000 recorded cell events, $p \leq 0.001$, ***) and SFM-alone (**Figure 2-12A**). Unfortunately, no proliferation data was collected by EdU assay for the cells cryopreserved from donor 3 due to laboratory shutdowns as a result of COVID-19.

When comparing between donors, the cells isolated from donor 2 had a significantly greater proportion in the S-phase after two days of culture following cryopreservation in SFM supplemented with 2FA (**27**, 15 mM) than donor 1 (n=3, $p \leq 0.05$, *) (**Figure 2-12C**). These results may represent donor-to-donor variation with respect to proliferation rates, however proliferation data from a third donor would be necessary to further elucidate this effect. Despite the difference between donors, the cells cryopreserved with 2FA (**27**, 15 mM) from both donors clearly showed improved proliferation rates compared to the cells cryopreserved with SFM-alone.

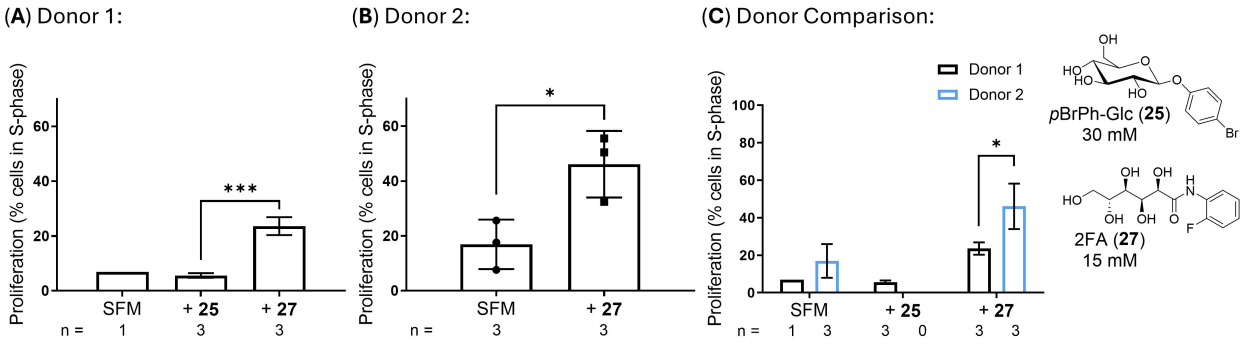


Figure 2-12. Immediate post-thaw proliferation assessment of BM-MSCs cryopreserved at 2.0 x 10^6 cells/mL in standard freezing medium (SFM) with and without IRIs **25** (30 mM) or **27** (15 mM). Proliferation (cells in S-phase) measured after two days in culture by EdU assay with cells plated at 0.5 x 10^6 cells/mL. Events were gated to include the cell region only with ≥ 10,000 cell region events analyzed per sample. (**A**) Donor 1 (*results obtained by Dr. Jessica Poisson*).[214] (**B**) Donor 2. (**C**) Comparison of all three donors where only significance across donors are shown. Results mean ± standard deviation (SD). Number of vials analyzed (sample size) indicated below each bar. Significance measured by Student's unpaired two-tailed t-test (**D**): * = $p \leq 0.05$, *** = $p \leq 0.001$.

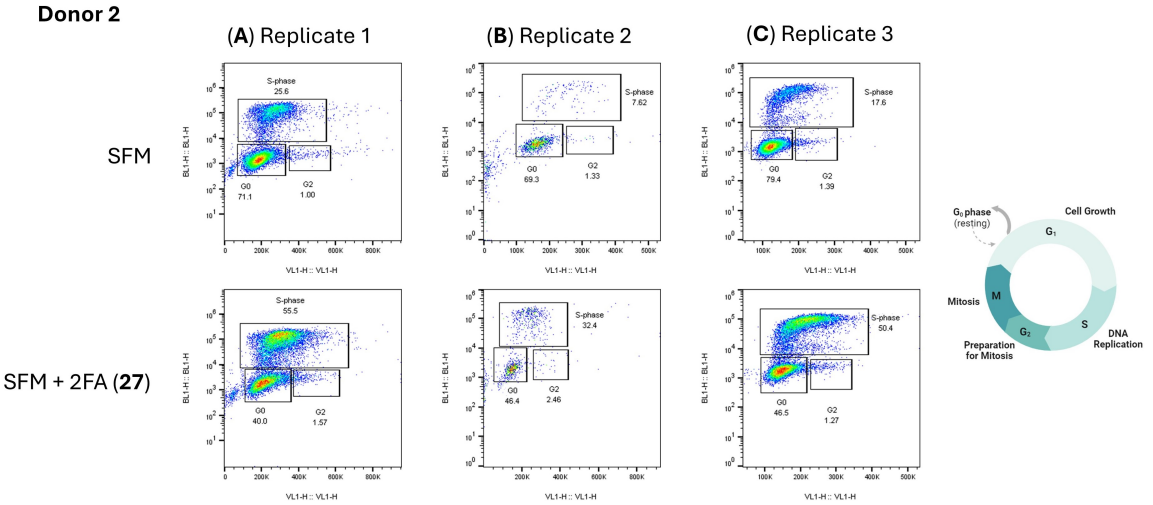


Figure 2-13. Flow cytometry dot plots for representative technical replicates (**A-C**) of the 5-ethynyl-2′-deoxyuridine (EdU) assay for BM-MSCs cryopreserved from donor 2 in standard freezing medium (SFM) supplemented with or without ice recrystallization inhibitor **27** (15 mM). Events were gated to include the cell region only with ≥ 10,000 cell region events analyzed per sample.

2.3.2. Cryopreservation outcomes for BM-MSCs assessed following expansion post-thaw

Following assessment of the recovery, viability, and functionality of the BM-MSCs immediately post-thaw, the cells that had been thawed were plated into culture flasks and expanded. After expansion, the cell yield, viability, and functionality were again assessed to determine the impact of cryopreserving BM-MSCs with small-molecule IRIs **25** (30 mM) or **27** (15 mM) compared to the standard freezing medium (SFM) alone. During the experiments with cells isolated from donor 1, it was noted that the cells (especially those that had been cryopreserved with 2FA, **27**) began to approach confluency by the end of the three-day culture.[214] Cell density is known to affect the growth rate of cells, where too high of a density can inhibit

cell growth due to reduced nutrients or contact inhibition while lower densities have been linked to faster proliferation rates due to improved access to nutrients and longer exponential growth periods.[247,260,261] Therefore, to ensure the cells did not near confluency by the end of the three-day culture and that their growth was not affected by too high of a cell density, the plating density for BM-MSCs isolated from donor 2 was reduced from 0.50 x 10^6 cells/mL (donor 1) to 0.25 x 10^6 cells/mL. Plating densities of 0.10 x 10^6 cells/mL and 0.05 x 10^6 cells/mL were also simultaneously examined. The cells from donor 3 were then plated at the most suitable density as determined from the plating density experiments with donor 2.

After three days in culture the cells from donor 2 were photographed, then immediately counted and assessed for viability using the Trypan Blue exclusion assay. The cells cryopreserved with *p*BrPh-Glc (**25**, 30 mM) supplemented SFM did not show any visible attachment to the plate (no black spots were visible representing attached cells, with only white spots visible that were attributed to bubbles and debris in the culture media) (**Figure 2-14**). Photomicrographs were not taken for the 0.10 x 10^6 cells/mL and 0.05 x 10^6 cells/mL density plates cryopreserved with *p*BrPh-Glc (**25**, 30 mM), however the cells appeared visibly similar to that of the 0.25 x 10^6 cells/mL plate. This result was consistent with the extremely low viability of these cells immediately post-thaw, confirming that *p*BrPh-Glc (**25**, 30 mM) was not suitable for the cryopreservation of BM-MSCs. For the cells cryopreserved in SFM supplemented with 2FA (**27**, 15 mM) an increase in the number of cells attached to the plate was visible compared to the cells cryopreserved with SFM-alone (**Figure 2-14**), which was consistent with the increased proliferation that was observed post-thaw using the EdU assay (**Figure 2-12D**).

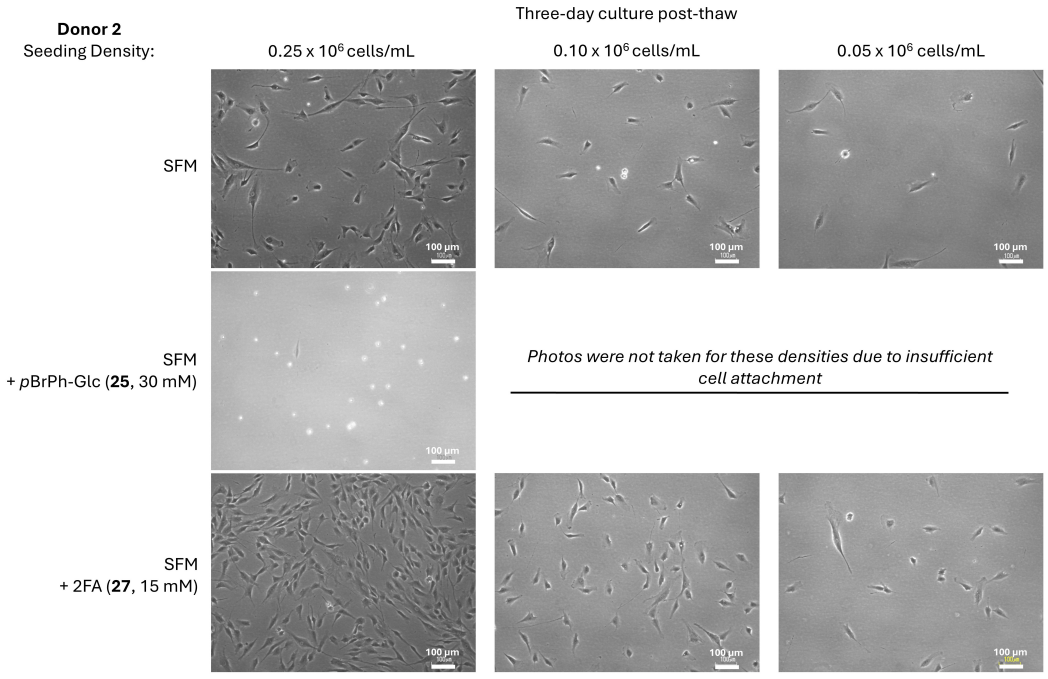


Figure 2-14. Photomicrographs of BM-MSCs cultured immediately post-thaw that were isolated from donor 2 and cryopreserved with either standard freezing medium (SFM) without or with the addition of IRIs **25** (30 mM) or **27** (15 mM). Images taken three days after plating at a density of 0.05 x 10^6 cells/mL, 0.10 x 10^6 cells/mL, or 0.25 x 10^6 cells/mL. Attached cells are visible as dark spots on the image.

Furthermore, no significant difference was observed in the cell viability as assessed by Trypan Blue exclusion assay across any condition (n=3, $p > 0.05$, ns) (**Figure 2-15A**); therefore, plating at any of these densities did not appear to affect cell viability. However, cell yield (the percentage of cells recovered after three days of culture relative to the number of cells that were originally plated) was significantly greater for the cells that had been cryopreserved with 2FA (**27**, 15 mM) at the highest two plating densities (0.25 x 10^6 cells/mL and 0.10 x 10^6 cells/mL) (n=3, $p \leq 0.01$, *) but not at the lowest cell density (0.05 x 10^6 cells/mL, n=3, $p > 0.05$, ns) (**Figure 2-15B**).

The cells plated at 0.25 x 10^6 cells/mL and 0.10 x 10^6 cells/mL and cryopreserved with 2FA (**27**, 15 mM) had significantly greater population doublings within the three-day culture period (0.25 x 10^6 cells/mL: n=3, $p \leq 0.05$, *; 0.10 x 10^6 cells/mL: n=3, $p \leq 0.01$, **) (**Figure 2-15C**). A population doubling count of less than zero, indicating a cell count at the end of culture that was lower than the initial plating density, could be attributed to delayed onset cell death whereby some cells were unable to attach to the plate at the beginning of culture or died and detached from the plate over time in culture and were washed out during medium changes. It was the cells cryopreserved in SFM-alone that did not successfully achieve a population doubling within three days for any of the plating densities, while the cells cryopreserved with 2FA (**27**, 15 mM) were able to reliably double in population when plated at a density

of 0.25 x 10^6 cells/mL (**Figure 2-15C**). The cells cryopreserved with 2FA (**27**, 15 mM) and plated at a density of 0.25 x 10^6 cells/mL also had the shortest overall doubling time (48.0 ± 9.5 hours) (**Figure 2-15D**). If a cell population did not achieve a single population doubling (a population doubling count of less than 1) within the three-day culture period then a doubling time was not calculated for that sample.

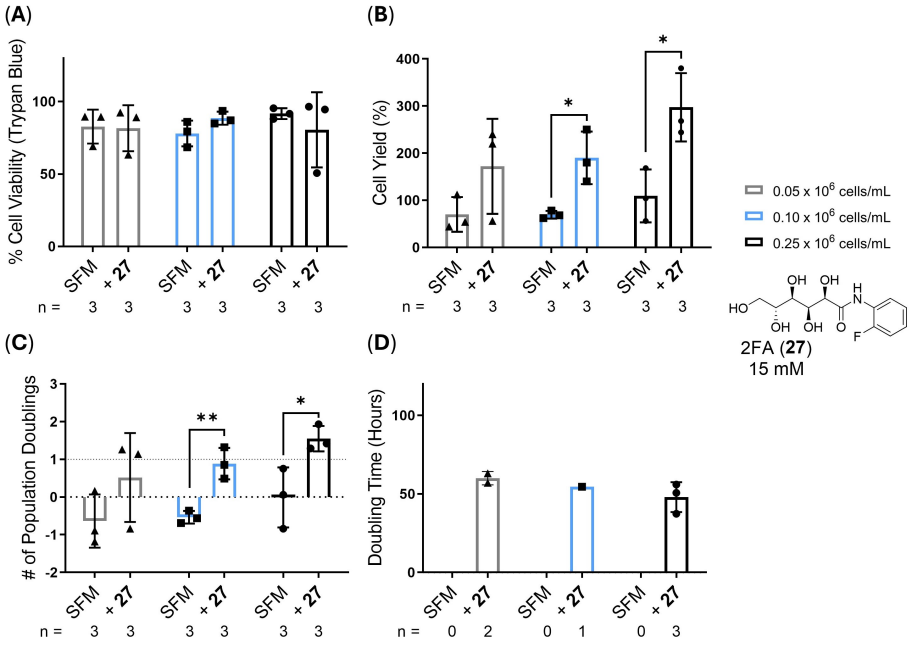


Figure 2-15. Post-thaw cryopreservation outcomes following a three-day culture of BM-MSCs (donor 2) cryopreserved at 2.0 x 10^6 cells/mL in standard freezing medium (SFM) with and without ice recrystallization inhibitor **27** (15 mM). Data for cells cryopreserved with **25** (30 mM) was omitted due to an insufficient quantity of viable cells. Cells were plated at 0.05 x 10^6 cells/mL, 0.10 x 10^6 cells/mL, or 0.25 x 10^6 cells/mL. (**A**) The cell viability as measured by Trypan Blue exclusion assay. (**B**) The quantity of cells obtained after the three-day culture relative to the initial plating density determined by manual cell count (hemocytometer). (**C**) The number of population doublings and (**D**) the amount of time that was elapsed to achieve a single population doubling. Results mean ± standard deviation (SD), n≥3 for all treatments, for samples that did not double in population a doubling time was not calculated and was omitted from (**D**). Number of vials analyzed (sample size) indicated below each bar. Significance measured by Student's unpaired two-tailed t-test: * = $p \leq 0.05$, ** = $p \leq 0.01$.

These results indicated that the plating density at which the improved proliferation of 2FA (**27**) frozen cells could be reliably observed after three days of culture without reaching cell confluency was 0.25 x 10^6 cells/mL. Therefore, to avoid nearing confluency as was observed during the experiments with donor 1 (plated at 0.50 x 10^6 cells/mL), the cells isolated from donor 3 were to be plated at the reduced density of 0.25 x 10^6 cells/mL. As previously discussed, cells reaching greater than 80 % confluency in culture has been linked to reduced cell viability and inhibited cell growth,[262] therefore plating at lower cell densities helped ensure the culture remained below this limit throughout the culture period. In the literature, lower cell densities have been linked to increased cell proliferation,[260,262,263] however the 0.25 x 10^6 cells/mL seeding density is already 10-fold lower than the recommended cell culture density for BM-MSCs

(Sigma-Millipore, 2.5 x 10^6 cells/mL)[264], therefore the 0.05 and 0.10 x 10^5 cell/mL densities may have been too low to reliably evaluate proliferation by manual cell counts for both the SFM-alone and SFM supplemented with 2FA (**27**, 15 mM) cryopreservation conditions.

2.3.2.1. Cell viability assessed by photomicrographs of cryopreserved BM-MSCs during the first four hours of expansion

During the investigations of plating density it was noted that the cells that had been cryopreserved with *p*BrPh-Glc (**25**, 30 mM) did not remain attached to the culture plate after three days of expansion (**Figure 2-14**). To investigate whether the detachment of these cells had occurred over time in culture or whether the cells did not initially attach to the cell culture plate at all, photomicrographs of the cells plated at 0.25 x 10^6 cells/mL were also taken each hour over the first four hours of expansion (**Figure 2-16**). Cells cryopreserved in SFM or 2FA (**27**) supplemented SFM (15 mM) began to attach after 1 hour and were almost completely attached within 4 hours (the cells were beginning to elongate in shape) (**Figure 2-16**). However, cells cryopreserved in *p*BrPh-Glc (**25**, 30 mM) supplemented SFM did not show any visible attachment to the plate within 4 hours of plating (**Figure 2-16**) and were consistent with the photomicrographs taken after three days in culture (**Figure 2-14**). These results were also consistent with photomicrographs of the cells isolated from donor 3 that were taken at each hour over the first four hours of culture (**Figure 2-17**).

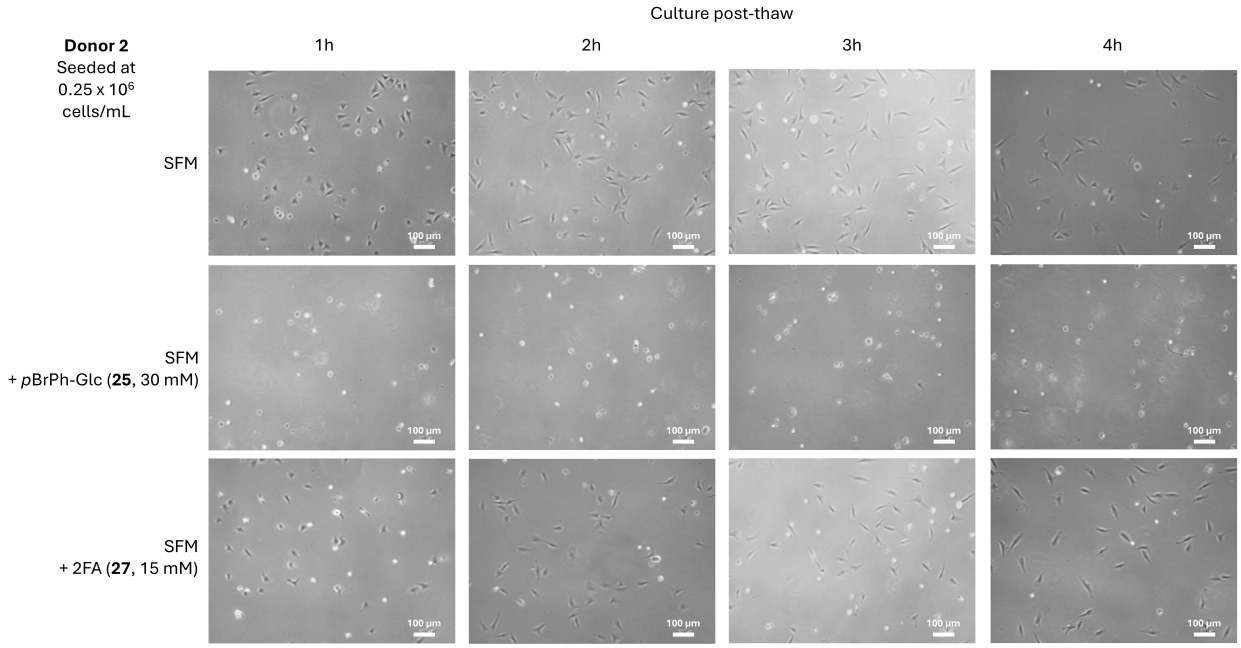


Figure 2-16. Photomicrographs of BM-MSCs cultured immediately post-thaw that were isolated from donor 2 and cryopreserved with either standard freezing medium (SFM) without or with the addition of IRIs **25** (30 mM) or **27** (15 mM). Images taken every hour up to four hours after plating at a density of 0.25 x 10^6 cells/mL. Attached cells are visible as dark spots on the image.

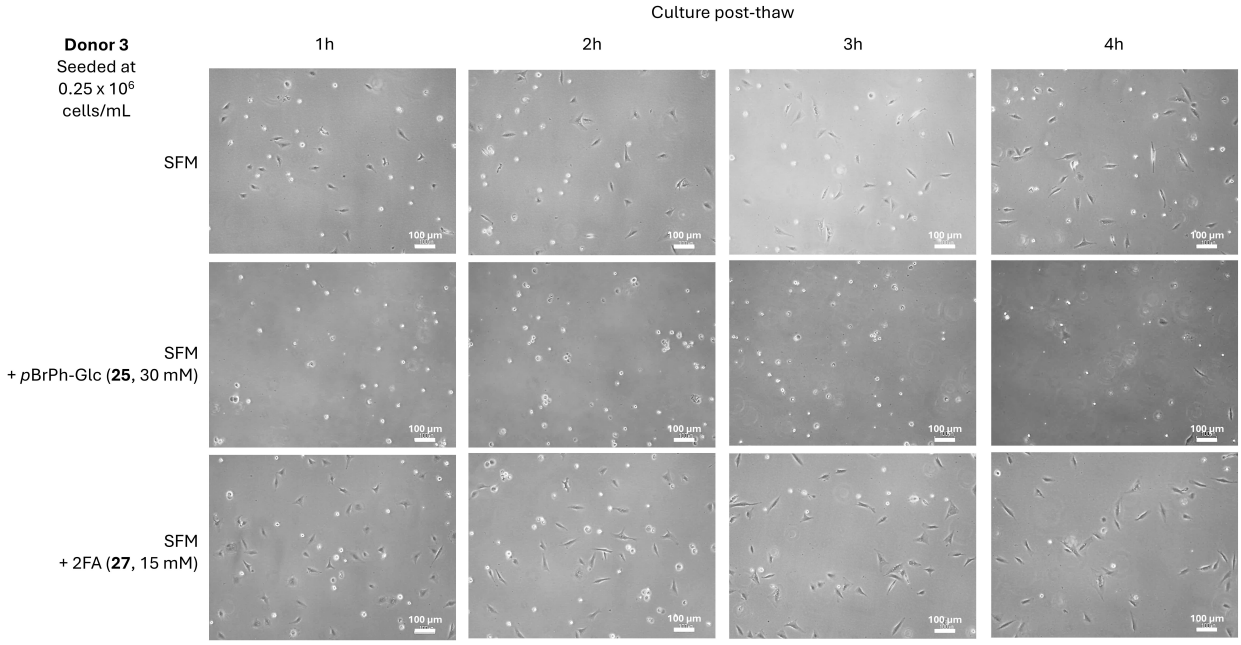


Figure 2-17. Photomicrographs of BM-MSCs cultured immediately post-thaw that were isolated from donor 3 and cryopreserved with either standard freezing medium (SFM) without or with the addition of IRIs **25** (30 mM) or **27** (15 mM). Images taken every hour up to four hours after plating at a density of 0.25 x 10^6 cells/mL. Attached cells are visible as dark spots on the image.

Combined with the poor immediate post-thaw viability data (**Figure 2-10B** and **C**), it was clear that the addition of *p*BrPh-Glc (**25**, 30 mM) during the cryopreservation of cells isolated from donor 2 or 3 was

deleterious and it was hypothesized that the addition of *p*BrPh-Glc (**25**) was cytotoxic to BM-MSCs during cryopreservation. Interestingly, this effect was not observed after three days of culture for the cells isolated from donor 1 in the presence of *p*BrPh-Glc (**25**, 30 mM), where the BM-MSCs appeared clearly attached to the culture flask (**Figure 2-18**).

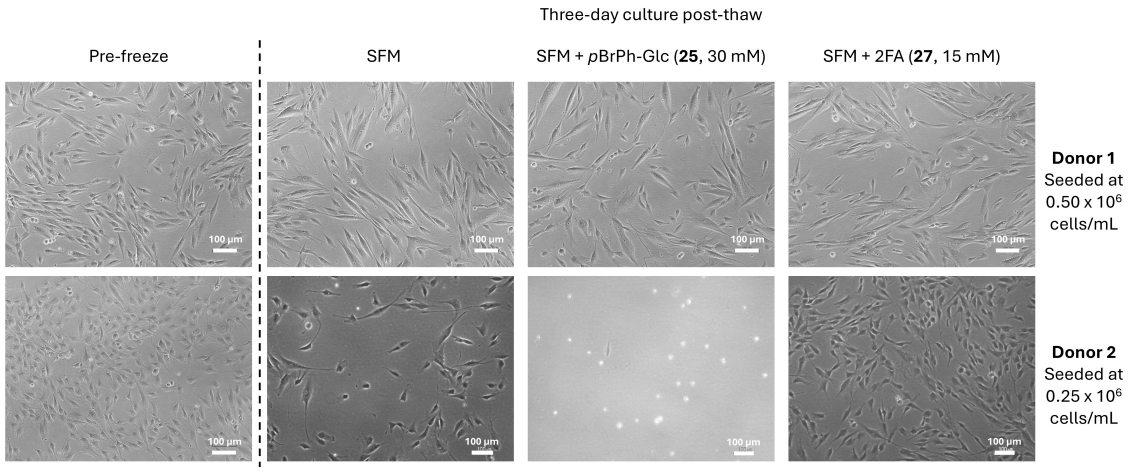


Figure 2-18. Photomicrographs of BM-MSCs cultured immediately post-thaw that were isolated from donor 1 (*results obtained by Dr. Jessica Poisson*)[214] and 2 and cryopreserved with either standard freezing medium (SFM) without or with the addition of IRIs **25** (30 mM) or **27** (15 mM). Images taken after three days of expansion after plating at a density of 0.50 x 10^6 cells/mL for donor 1 or 0.25 x 10^6 cells/mL for donor 2. Attached cells are visible as dark spots on the image.

These visual results clearly showed that there was a difference in the response of the cells isolated from donor 1 to *p*BrPh-Glc **25** (30 mM) compared to the cells isolated from donors 2 or 3. These differences could have been caused by the variation in technical factors including seeding density and/or the amount of time that the cells were stored in liquid nitrogen (-196 °C); however, further investigation will be required to elucidate the nature of this effect as part of future studies. Ultimately, due to detachment of the cells that had been cryopreserved with *p*BrPh-Glc (**25**, 30 mM) for donors 2 and 3, the extended culture cryopreservation outcomes could not be assessed for these cells and only comparison between the SFM-alone and SFM-supplemented with 2FA (**27**, 15 mM) conditions are presented below.

2.3.2.2. Cell viability as assessed by Trypan Blue exclusion

After expansion, the viability of the BM-MSCs from each donor was assessed by Trypan Blue exclusion assay. The viability of the cells was comparable between the two freezing conditions, with mean viability ranging from 80.5 ± 25.9 % (n=3) to 97.8 % (n=1) (**Figure 2-19D**). As previously discussed (see **Figure 2-7**), the viability of cells isolated from donor 1 and cryopreserved with *p*BrPh-Glc (**25**, 30 mM) was significantly lower than the cells cryopreserved with 2FA (**27**, 15 mM) (n=3, $p \leq 0.05$, *, **Figure 2-19A**) which may be the result of delayed onset cell death. When comparing between donors for the SFM-alone

and 2FA (**27**, 15 mM) supplemented SFM, there was no observed significant or meaningful difference in cell viability, which suggested that there was no impact of donor-to-donor variability on cell viability for any of the cryopreservation conditions ($p > 0.05$, ns) (**Figure 2-19D**).

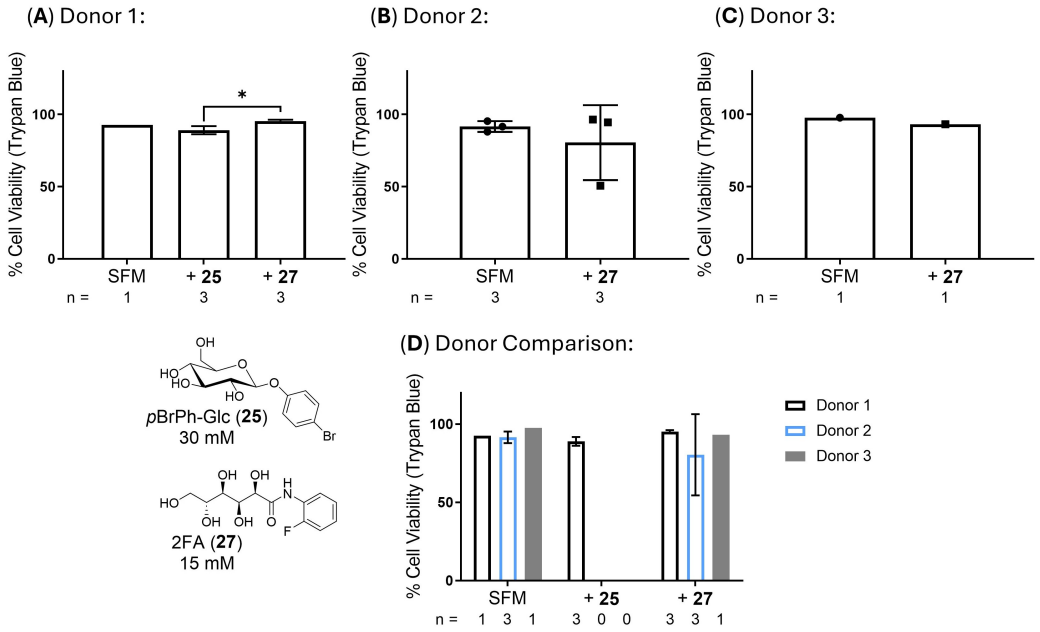


Figure 2-19. Cryopreservation outcomes following expansion of BM-MSCs cryopreserved at 2.0 x 10^6 cells/mL in standard freezing medium (SFM) with and without ice recrystallization inhibitors **25** (30 mM) or **27** (15 mM). Cell viability as measured by Trypan Blue exclusion assay (**A**) Donor 1 (*results obtained by Dr. Jessica Poisson*).[214] (**B**) Donor 2. (**C**) Donor 3. (**D**) Comparison of all three donors where only significance across donors are shown. Results mean ± standard deviation (SD). Number of vials analyzed (sample size) indicated below each bar. Significance measured by Student's unpaired two-tailed t-test: * = $p \leq 0.05$.

The viability of cells isolated from donor 1 was also assessed by AV/PI assay (see **Figure 2-7**) following expansion of the cells; however, AV/PI assay data were not collected for donors 2 and 3. Future experiments should investigate the viability of BM-MSCs cryopreserved with small-molecule IRIs using the AV/PI assay which would provide valuable insight into how the apoptotic population (early vs. late) may change over time in order to elucidate more precise information about the mechanism of cell death caused by *p*BrPh-Glc (**25**).

2.3.2.3. Functionality: Proliferation as assessed by cell counts to assess the cell yield, number of population doublings, and doubling time

Following expansion of the cells, the functionality of the BM-MSCs was assessed by manual cell counts to evaluate the proliferative capacity of the cells during culture. The cells cryopreserved from donors 2 and 3 were plated at 0.25 x 10^6 cells/mL, while the cells cryopreserved from donor 1 were plated at a density of 0.50 x 10^6 cells/mL. Due to laboratory shutdowns caused by COVID-19, only a two-day

expansion was completed for donor 3 with only one technical replicate (n=1), compared to the full three-day culture for donors 1 and 2 with three technical replicates (n=3). Despite the shorter culture time, the BM-MSCs from donor 3 that were cryopreserved with 2FA (**27**, 15 mM) had an increased cell yield and increased number of population doublings when compared to the cells frozen with SFM-alone (**Figure 2-20C** and **Figure 2-21C**). While neither cryopreservation condition was able to achieve a full population doubling within the two-day culture period, the BM-MSCs cryopreserved with 2FA (**27**, 15 mM) were proliferating at a faster rate than the cells cryopreserved with SFM-alone, with 0.60 population doublings for a total cell yield of 152 % compared to only 0.16 population doublings for a total cell yield of 112 % respectively (**Figure 2-20C** and **Figure 2-21C**).

These results were consistent with the findings for donors 1 and 2, where cell yield, doubling time, and number of population doublings all followed the same trends and indicated increased proliferation for the cells that had been cryopreserved with 2FA (15 mM, **27**) compared to *p*BrPh-Glc (**25**, 30 mM) or SFM-alone (**Figure 2-20D** and **Figure 2-21D**). The yield and number of population doublings for the cells isolated from donor 1 were significantly greater than donor 2 (n=3, $p \leq 0.05$, *), which was consistent with the results for donor 3 (**Figure 2-20D** and **Figure 2-21D**). Finally, the doubling time of BM-MSCs cryopreserved with 2FA (**27**, 15 mM) and isolated from donor 1 was significantly shorter than the doubling time for the cells isolated from donor 2 (n=3, $p \leq 0.05$, *) (**Figure 2-21D**).

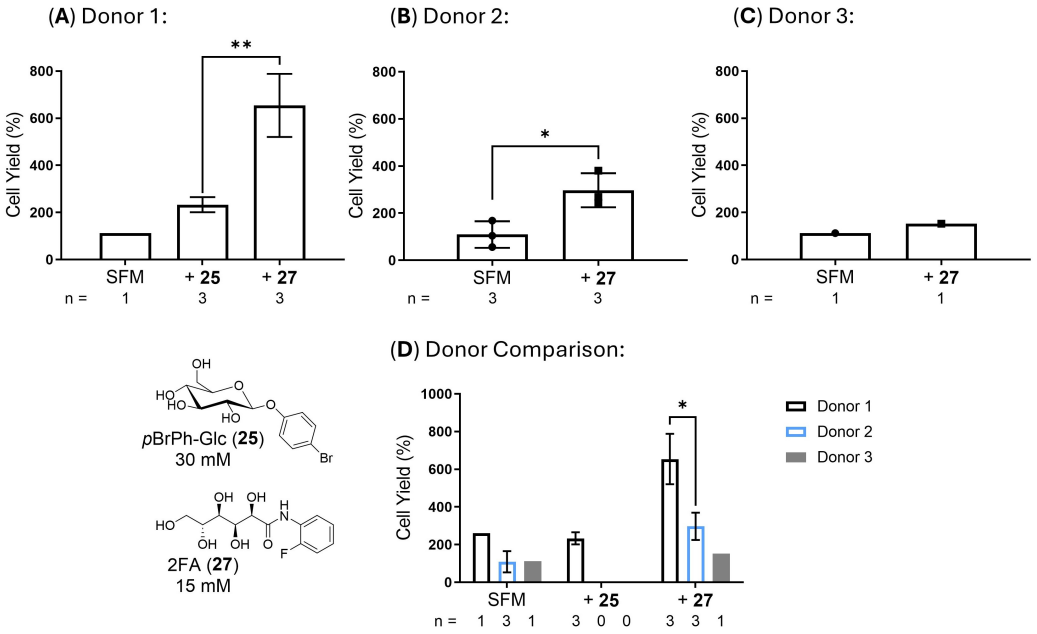


Figure 2-20. Cryopreservation outcomes following expansion of BM-MSCs cryopreserved at 2.0 x 10^6 cells/mL in standard freezing medium (SFM) with and without IRIs **25** (30 mM) and **27** (15 mM). Cells were plated at 0.50 x 10^6 cells/mL for donor 1 and 0.25 x 10^6 cells/mL for donors 2 and 3. Cells counted after three days of expansion for donors 1 and 2 and two days of expansion for donor 3. Cell yield calculated as the percentage of cells counted following expansion relative to the quantity of cells initially plated (hemocytometer). (**A**) Donor 1 (*results obtained by Dr. Jessica Poisson*).[214] (**B**) Donor 2. (**C**) Donor 3. (**D**) Comparison of all three donors where only significance across donors are shown. Results mean ± standard deviation (SD). Number of vials analyzed (sample size) indicated below each bar. Significance measured by Student's unpaired two-tailed t-test: * = $p \leq 0.05$, ** = $p \leq 0.01$.

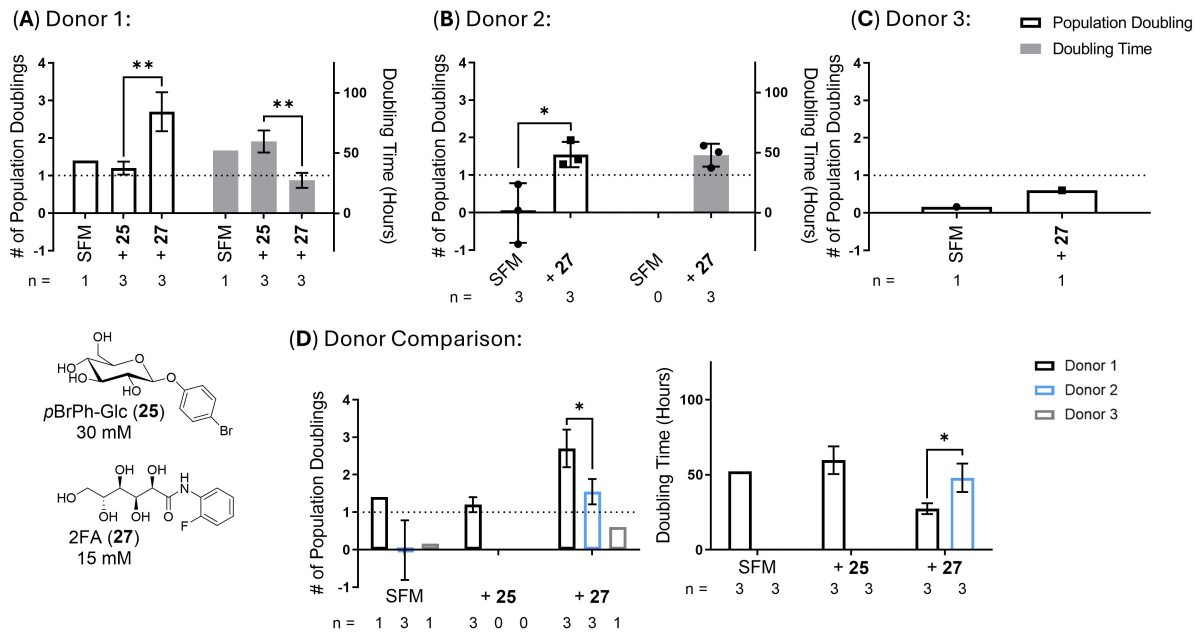


Figure 2-21. Cryopreservation outcomes following expansion of BM-MSCs cryopreserved at 2.0 x 10^6 cells/mL in standard freezing medium (SFM) with and without IRIs **25** (30 mM) and **27** (15 mM). Cells were plated at 0.50 x 10^6 cells/mL for donor 1 and 0.25 x 10^6 cells/mL for donors 2 and 3. Cells counted after three days of expansion for donors 1 and 2 and two days of expansion for donor 3. A doubling time was not calculated if the sample did not achieve a single population doubling within the expansion time. (**A**) Donor 1 (*results obtained by Dr. Jessica Poisson*).[214] (**B**) Donor 2. (**C**) Donor 3. (**D**) Comparison of all three donors where only significance across donors are shown. Results mean ± standard deviation (SD). Number of vials analyzed (sample size) indicated below each bar. Significance measured by Student's unpaired two-tailed t-test: * = $p \leq 0.05$, ** = $p \leq 0.01$.

Taken together, the immediate and post-culture cryopreservation outcomes shown above illustrate a clear donor-dependent difference in the results for cells treated with the different IRIs. With respect to proliferation, the data for the cells treated with 2FA (15 mM, **27**) during cryopreservation suggested an increased proliferation rate compared to those that were cryopreserved in SFM-alone (**Figure 2-12**, **Figure 2-20**, and **Figure 2-21**). The cells cryopreserved from donor 1 had a greater cell yield and greater number of population doublings compared to either of the other two donors, with donor 3 recording the lowest cell yield and number of population doublings of the three (**Figure 2-20**, and **Figure 2-21**). It has been reported that MSCs isolated from male sex donors have greater rates of proliferation and metabolic activity than MSCs isolated from female sex donors;[265] however, all three donors for this study were male (with similar age and matching ethnicity – see **Table 8-82**), thus the observed variation in proliferation cannot be attributed to sex-based differences alone. Furthermore, the cells did not undergo more than 20 population doublings throughout the study, minimizing the risk of cellular senescence (*i.e.,* cellular aging) on the study results. While other donor genetic factors are known to affect the proliferation of MSCs, these correlations are significantly less understood and often cannot be directly correlated to differences in proliferation potential.[237,266–268] In addition, while it is generally understood that these factors play a critical role in the

success of cellular therapeutics and their cryopreservation due to their underlying effect on critical cellular processes (*e.g.,* sex-dependent differences related to the immune and stress response pathways)[269–271], the exact relationships and correlations have yet be studied in detail. In part, this donor-to-donor variation is currently mitigated during on-going clinical trials and with on-the-market products by the creating large single donor cell banks or pooling material from multiple donors. However, further investigation of the donor-related differences as they relate to cryopreservation of cellular therapies are required in order to truly minimize the potential variation in treatment response rates arising from these products when generated from different donors. Finally, while the seeding density of the cells from donor 2 and 3 were reduced to prevent confluency at the end of expansion, a direct comparison between different seeding densities for all donors would be necessary to elucidate the impact these differences may have on cell yield, population doublings, and doubling time.

In addition to proliferation, a donor-dependent difference was also observed with respect to cell viability for the cells treated with *p*BrPh-Glc (**25**, 30 mM). The cells that were isolated from donor 1 remained viable and comparable to SFM-alone after testing by the AV/PI assay, but cells isolated from donors 2 and 3 were almost completely non-viable under the same conditions (both < 7.8 %) (**Figure 2-10**). As shown previously, the viability of BM-MSCs from donor 2 and 3 in the presence of *p*BrPh-Glc (**25**, 30 mM) by AV/PI assay was also significantly lower than the cells cryopreserved with SFM-alone or SFM supplemented with 2FA (**27**, 15 mM) (**Figure 2-10**), and was lower than the viability as measured by Trypan Blue exclusion assay (**Figure 2-10**), suggesting that the addition of *p*BrPh-Glc (**25**) at a 30 mM concentration during cryopreservation may be triggering molecular pathways leading to cell death shortly after thawing. To ascertain whether the apparent cytotoxic effect of *p*BrPh-Glc (**25**) was due to the compound itself or whether its toxicity was induced or exaggerated by the stressors of cryopreservation, and to provide commentary on the nature of the observed donor-dependent cell death, evaluation of the compound's *in vitro* cytotoxicity in the absence of freezing was investigated.

*2.3.2.4. Cytotoxicity of pBrPh-Glc (**25**) and 2FA (**27**) in vitro*

The cytotoxicity of both *p*BrPh-Glc (**25**) and 2FA (**27**) has been previously assessed in the absence of freezing/cryopreservation by several different graduate students in the Ben Lab.[158,168,176,214] However, these assessments did not make direct comparisons between the two compounds and often used different cytotoxicity assays, cell types, incubation times, and treatment conditions that made it challenging to make conclusions with respect to their relative cytotoxicity. In general, these previous studies exposed the cells to the compound of interest for a minimum 18 hour incubation and found that 2FA (**27**) did not lead to significant cell death,[168,176] while *p*BrPh-Glc (**25**) could lead to complete cell death at concentrations greater

than 20 mM.[158,214] These long incubation studies exposed the cells to the compound of interest for significantly longer than the expected exposure time that occurs during the cryopreservation process – where the cells are exposed for at maximum 1-2 hours prior to reaching sub-zero temperatures where molecular mechanisms of cell death would be paused. The longer incubation times were intended to provide an idea of the broader, long-term toxicity profile of these compounds and it was thought that although *p*BrPh-Glc (**25**) showed significant cytotoxicity at concentrations greater than 20 mM with long incubation times, it may be less toxic at the time points relevant to cryopreservation. As shorter incubation cytotoxicity studies had not been completed for *p*BrPh-Glc (**25**) or 2FA (**27**) prior to beginning the cryopreservation experiments with BM-MSCs, the compound concentrations used for the cryopreservation of BM-MSCs were selected solely based on what was previously successful for the cryopreservation of other cell types.[158,162,166,168,176,215,216,219,220,248] However, it was clear from the experiments presented in this chapter that even at the shorter exposure times that occur during cryopreservation, the 30 mM concentration of *p*BrPh-Glc (**25**) caused cell death when introduced to BM-MSCs.

To be able to directly compare the cytotoxicity of *p*BrPh-Glc (**25**) and 2FA (**27**) under matching conditions that were relevant to cryopreservation, the cytotoxicity of both compounds was reassessed using a resazurin-based colorimetric assay that measured cellular metabolic activity with incubation times of 1 hour and 24 hours. Resazurin is a cell-permeable REDOX indicator that is naturally low in fluorescence and creates a deep purple-blue colour when in solution (**Figure 2-22**).[272] Once added to cells in culture, viable cells with active metabolism use a molecule of NADH to reduce resazurin to resorufin, which is a highly fluorescent compound that changes the visible colour of the solution to pink (**Figure 2-22**).[272] Cells that have been damaged or are no longer able to undergo active metabolism will be unable to reduce the dye and will remain deep purple-blue in colour (**Figure 2-22**).[272] Cell viability can then be calculated by comparing the fluorescence output of each well to positive and negative controls (cell culture medium alone and Triton X-100 respectively). Using this assay, the cytotoxicity of *p*BrPh-Glc (**25**) and 2FA (**27**) was assessed in HepG2 cells; HepG2 cells are a eukaryotic immortalized liver cell line often used as a model system for the study of human hepatocyte metabolism and are frequently used as a cellular model for liver cytotoxicity.[273] The 1-hour time point was selected to more closely represent the exposure time to each compound that may occur during cryopreservation while the 24-hour time point was selected to as a comparison point to the previous cytotoxicity studies.

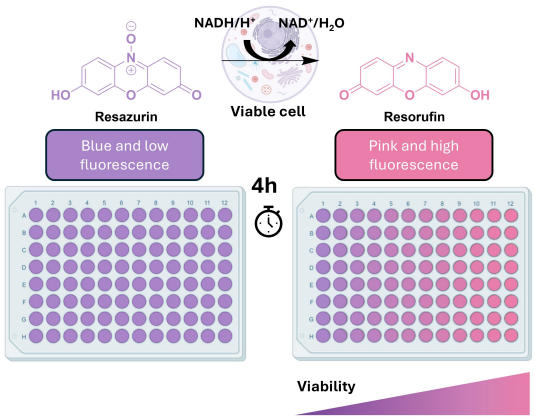


Figure 2-22. General schematic for a resazurin-based cytotoxicity assay.[272] *Figure created using Biorender.com.*

For these experiments, HepG2 cells were plated into a 96-well plate at a density of 1.0 x 10^5 cells/mL. The cells were then incubated with several different concentrations of each compound (**25** and **27**) in cell culture medium for 1 or 24 hours at 37 °C in 5 % CO_2 either with or without the addition of 10 % DMSO; as the BM-MSCs in this study were cryopreserved in a combination IRI + DMSO formulation, we were interested in assessing whether the presence of DMSO influenced the inherent cytotoxicity of either IRI. After the desired incubation time for each condition, resazurin was added to each well and then incubated for an additional 4 hours at 37 °C in 5 % CO_2 to allow for the dye to be reduced by viable cells.

The presence of DMSO in cell culture can be cytotoxic and has been reported to cause decreased cell proliferation,[274] initiate oxidative stress pathways,[275] or alter natural cellular processes,[276] and ultimately can result in complete cell death.[277] However, the cytotoxicity of DMSO is dependent on several factors, including its concentration, but also on the time and temperature of incubation.[274,277] Therefore, to control for the inherent cytotoxicity of DMSO, the viability of cells in the absence of IRIs was first assessed at each incubation time point. After a 1-hour incubation of HepG2 cells with 10 % DMSO, the average cell viability was 93.4 ± 9.2 % (N=8), which decreased significantly to only 38.3 ± 15.9 % (N=7, ****, $p < 0.0001$) after 24-hours (**Figure 2-23C**). Based on these results, no significant cytotoxicity was expected as a direct result of DMSO within the 1-hour incubation time point. Therefore, any increases in cytotoxicity that would be observed after incubation with the IRI were to be associated with the IRI itself or a combined effect caused by an interaction between DMSO and the IRI.

Irrespective of the addition of DMSO, both IRIs showed similar cytotoxicity profiles (dose-response curves) up to a concentration of 15 mM after a 1-hour incubation, with cell viability

remaining greater than 68.8 % (N≥2) (**Figure 2-23A-B**). In the absence of DMSO, *p*BrPh-Glc (**25**) resulted in significant cell death at concentrations greater than 15 mM following a 1-hour incubation, with only 19.2 ± 10.9 % (N=3) cell viability observed at 22 mM, and complete cell death observed at all concentrations greater than or equal to 30 mM (N≥2) (**Figure 2-23A**); 2FA (**27**) reached its maximum solubility in the cell culture medium used for HepG2 cells (in the absence of any DMSO) at 15 mM and therefore could not be tested at higher concentrations. Interestingly, the addition of 10 % DMSO appeared to temper the cytotoxicity of *p*BrPh-Glc (**25**) at concentrations greater than 15 mM following a 1-hour incubation, where complete cell death was not observed until a concentration of 45 mM (N=1, 50.6 ± 10.6 %) (**Figure 2-23B**). It was thought that the reduced cytotoxicity of *p*BrPh-Glc (**25**) may have been caused by improved aqueous solubility with the addition of DMSO which could mitigate potentially harmful imbalances in osmotic pressures, or by reducing its interactions with key cellular machinery enzymes through the formation of strong intermolecular hydrogen bond networks. Additional experiments with different concentrations of DMSO, different cell types, or different measures of cytotoxicity would be required to further elucidate the origin of this effect.

When the incubation time was extended to 24 hours, 2FA (**27**) did not show any further reductions in viability with all cells remaining greater than 72.5 % (N≥2) viable in the absence of DMSO (**Figure 2-23A**); however, exaggerated cell death was observed for *p*BrPh-Glc (**25**), where all concentrations greater than or equal to 12 mM resulted in nearly complete cell death (with a maximum cell viability of 4.90 ± 7.39 % at 12 mM) (**Figure 2-23A**). With the addition of 10 % DMSO, neither IRI showed significantly exaggerated cytotoxicity compared to the data observed in the absence of DMSO (**Figure 2-23A-B**); no reductions in cell viability beyond the inherent cytotoxicity of DMSO were observed for 2FA (**27**, with a minimum cell viability of 26.2 %, N=2) and all concentrations greater than or equal to 10 mM *p*BrPh-Glc (**25**) resulted in complete cell death (**Figure 2-23B**). Furthermore, the 24-hour results in the absence of DMSO were consistent with what has been previously reported by the Ben Lab for the cytotoxicity of each IRI with incubations of ≥ 18 hours.[158,168,176,214]

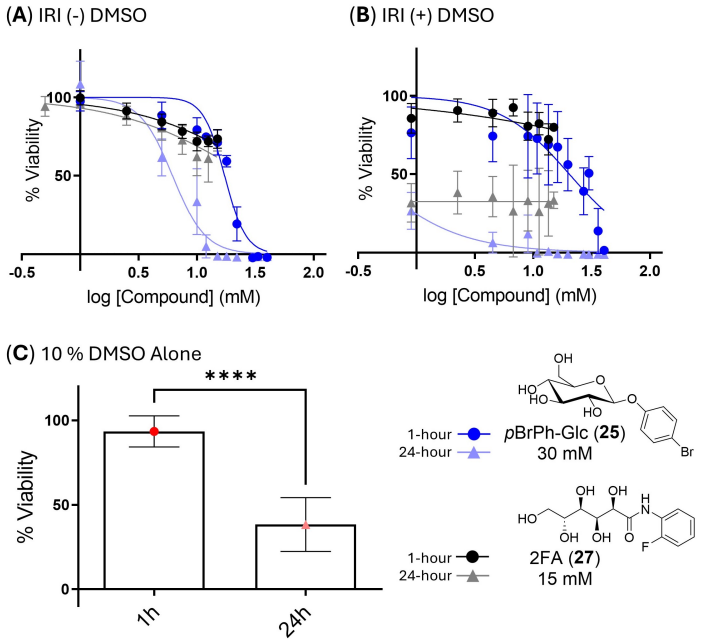


Figure 2-23. Plot of percent cell viability of HepG2 cells against logarithm transformed compound concentration (in mM) for *p*BrPh-Glc (**25**) and 2FA (**27**) with 1- and 24-hour incubations (**A**) without and (**B**) with the addition of 10 % dimethyl sulfoxide (DMSO). (**C**) Comparison of incubation time points for 10 % DMSO alone. Cells were plated in a 96-well plate at a density of 1.0 x 10^5 cells/mL and incubated at 37 °C in 5 % CO_2. Results determined by resazurin-based metabolic assay and reported as mean ± standard deviation (SD). Significance measured by Student's unpaired two-tailed t-test: **** = $p \leq 0.0001$.

These results clearly showed that while a 1-hour incubation resulted in less cell death than a 24-hour incubation with *p*BrPh-Glc (**25**) (LD_{50} = 17.3 mM 95 % CI = [15.8-18.6] and 6.17 mM 95 % CI = [5.12-7.32] respectively), the 30 mM concentration used in this study for the cryopreservation of BM-MSCs resulted in complete cell death of the HepG2 cells within a 1-hour incubation period (**Figure 2-23A**). This is consistent with the post-thaw results observed during the cryopreservation of BM-MSCs, where those frozen in the presence of 30 mM *p*BrPh-Glc (**25**) did not attach to the cell culture plates and showed near complete cell death as measured by AV/PI assay (**Figure 2-10**, **Figure 2-16**, and **Figure 2-17**). Therefore, it can be concluded that the toxicity of *p*BrPh-Glc (**25**) at 30 mM was not due solely to cryopreservation related damage but by inherent cytotoxicity of the compound itself.

The greater cytotoxicity of *p*BrPh-Glc (**25**) compared to 2FA (**27**) is hypothesized to be caused by differences in their chemical structures; *p*BrPh-Glc (**25**) is an *O*-aryl-β-D-glucopyranoside IRI comprised of a phenol moiety substituted at the C_1 carbohydrate position, while 2FA (**27**) is an *N*-aryl-D-gluconamide IRI where the hydrophobic aryl substituent is linked to an open-chain carbohydrate at the C_1 position *via* an amide bond (**Figure 1-16** or **Figure 2-1**). When compounds are exposed to different pH levels and endogenous cellular machinery (enzymes and proteins) *in vitro* or *in vivo*, they are susceptible to chemical

modification. For example, cleavage of the C_1 glycosidic bond of *O*-aryl-β-D-glucopyranosides occurs readily by enzymes such as glycosyl hydrolases, which results in the release of D-glucose and the corresponding phenol into the cytoplasmic space (**Figure 2-24**).[278] More importantly, cleavage of the C_1 glycosidic bond could also happen readily in the absence of enzymatic assistance simply under acidic or basic aqueous conditions. The amide bond of the *N*-aryl-D-gluconamide IRIs is significantly more stable than the *O*-glycosidic ether linkage and is therefore unlikely to be cleaved *in vitro* to release the corresponding aniline and open chain carbohydrate. As a result, it was hypothesized that the greater susceptibility for the *O*-aryl-β-D-glucopyranosides to undergo hydrolysis, resulting in the release of cytotoxic phenols,[279–282] was directly related to the increased cytotoxicity of this class of molecules over the *N*-aryl-D-gluconamides.

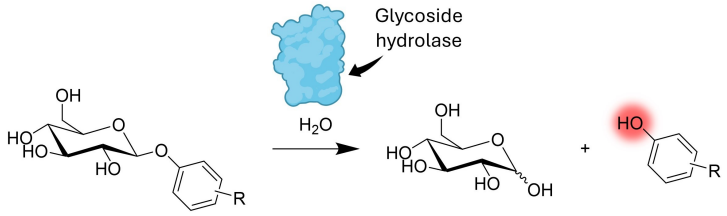


Figure 2-24. Hydrolysis of *O*-aryl-glycosides by *in vitro* enzymes to release cytotoxic phenol metabolites.

As it was hypothesized that the inherent cytotoxicity of *p*BrPh-Glc (**25**) was the direct result of C_1 glycosidic bond hydrolysis and the release of 4-bromophenol, we also assessed the inherent cytotoxicity of 4-bromophenol under the same conditions as *p*BrPh-Glc (**25**). Given 4-bromophenol was not soluble in the cell culture medium alone, it was only tested with the addition of 10 % DMSO. After a 1-hour incubation, 4-bromophenol resulted in complete cell death of the HepG2 cells at all concentrations greater than or equal to 7 mM, which was reduced to only 4 mM after a 24-hour incubation (**Figure 2-25**). After a 1-hour incubation, 4-bromophenol alone was significantly more cytotoxic than *p*BrPh-Glc (**25**), as expected, with LD_{50} values of 4.84 mM (95 % CI [4.68-5.02]) and 20.4 mM (95 % CI [14.1-29.9]) respectively (**Figure 2-25**).

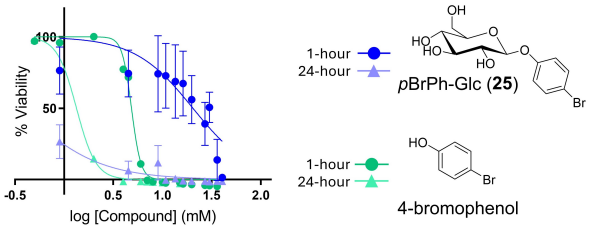


Figure 2-25. Plot of percent cell viability of HepG2 cells against logarithm transformed compound concentration (in mM) for *p*BrPh-Glc (**25**) and 4-bromophenol with 1-hour and 24-hour incubations with the addition of 10 % dimethyl sulfoxide (DMSO). Cells were plated in a 96-well plate at a density of 1.0 x 10^5 cells/mL and incubated at 37 °C in 5 % CO_2. Results determined by resazurin-based metabolic assay and reported as mean ± standard deviation (SD).

From these results, any concentration of 4-bromophenol greater than or equal to 7 mM was completely deleterious to HepG2 viability after a 1-hour incubation; however, complete cell death was only observed within 1 hour at concentrations of *p*BrPh-Glc (**25**) greater than 40 mM. The other byproduct from the hydrolysis of *p*BrPh-Glc (**25**), D-glucose, is not toxic at such low concentrations and is often used in cell culture media formulations at concentrations as high as 55 mM.[283] Therefore, the cytotoxicity of *p*BrPh-Glc (**25**) could be assumed to be caused entirely by the hydrolytic release of 4-bromophenol into the cytoplasm. Given these assumptions, within 1 hour of incubation *p*BrPh-Glc (**25**) is suggested to be at minimum 17.5 % hydrolyzed [7 mM 4-bromophenol from 40 mM *p*BrPh-Glc (**25**)] to result in complete death of the HepG2 cells. Furthermore, after a 24-hour incubation, the 10 mM concentration of *p*BrPh-Glc (**25**) resulted in complete cell death, suggesting that at this time point the *p*BrPh-Glc (**25**) had been at least 70 % hydrolyzed into the corresponding 4-bromophenol and D-glucose reducing sugar. Importantly, this analysis does not consider the inherent cytotoxicity of *p*BrPh-Glc (**25**) prior to hydrolysis, which may also affect cell integrity or processes. However, the cytotoxicity profile of 4-bromophenol provides critical insight into the cause of increased cell death that was observed for the BM-MSCs that were incubated with the *O*-aryl-β-D-glucopyranoside *p*BrPh-Glc (**25**) compared to the *N*-aryl-D-gluconamide 2FA (**27**).

In light of these results, the success of *p*BrPh-Glc (**25**) in red blood cells (RBCs) and not for the cryopreservation of BM-MSCs could be attributed to differences in the two cell types. RBCs are anucleate, with no intracellular organelles, and are highly specialized to deliver oxygen throughout an organism.[284] While RBCs contain a number of enzymes critical to their function (*e.g.*, ATPases, protein kinases, dehydrogenases, etc.), they have not been reported to contain glycoside hydrolases. On the other hand, MSCs are a multipotent, nucleated cell that are significantly more complex than RBCs as they must be able to differentiate into several other cell types depending on the organism's needs.[192] Therefore, is likely that the hydrolysis of *p*BrPh-Glc (**25**) was exacerbated in MSCs the due to the presence of glycoside hydrolases (found in the endoplasmic reticulum, Golgi apparatus, and lysosomes)[285] and thus may preclude its

continued investigation in cell models outside of RBCs. Lower concentrations of *p*BrPh-Glc (**25**) could be tested for the cryopreservation of MSCs or other stem cell derivatives given the IRI achieves complete inhibition of ice recrystallization at concentrations as low as 20 mM, however the risk of its cytotoxicity would likely hinder its adoption into standard cryopreservation protocols for human health therapeutics. Furthermore, while it is possible that the greater risk of cytotoxicity extends to the entire *O*-aryl-β-D-glucopyranoside family of ice recrystallization inhibitors, it is imperative that individualized studies be carried out for each IRI of interest given the highly complex nature of cryopreservation for non-terminally differentiated cell types.

2.3.2.5. Functionality: Investigating the immunotherapeutic properties of cryopreserved BM-MSCs (IDO expression)

In current clinical practice MSCs must be expanded *in vitro* prior to being administered to patients for immunotherapy as cryopreserved MSCs immediately post-thaw have reduced immunomodulatory properties compared to freshly isolated MSCs.[180,182–184,246] While improved proliferation post-thaw is indicative of cells that are more rapidly able to return to a state that is equivalent to pre-freeze, it does not provide direct information about their therapeutic potential and their ability to modulate an immune response. Human MSCs are known to modulate immune suppression through the expression of indoleamine 2,3-dioxygenase (IDO).[286] The expression of IDO occurs following stimulation by inflammatory cytokines such as interferon gamma (IFNγ).[287–289] Therefore, the immunomodulatory properties of the BM-MSCs that had been cryopreserved with and without 2FA (**27**, 15 mM), were assessed in a preliminary experiment with a single BM-MSC donor (N=1) by measuring the cellular expression of IDO. *p*BrPh-Glc (**25**, 30 mM) was excluded from these experiments due to the cytotoxicity that had been observed in previous experiments. For the IDO assay, BM-MSCs were cultured for 24 hours and then exposed to the inflammatory cytokine IFNγ (**Figure 2-26**). After a 24-hour incubation, the cellular RNA was isolated, the IDO RNA was amplified *via* reverse-transcription polymerase chain reaction (RT-PCR), and the production of IDO RNA was monitored by increasing fluorescence as a function of replication cycles (**Figure 2-26**). The number of amplification cycles required to achieve a set fluorescence threshold was recorded for each sample and was indicative of the quantity of desired IDO RNA detected in the sample, where a lower number of required cycles was the result of a greater quantity of cellular IDO RNA.

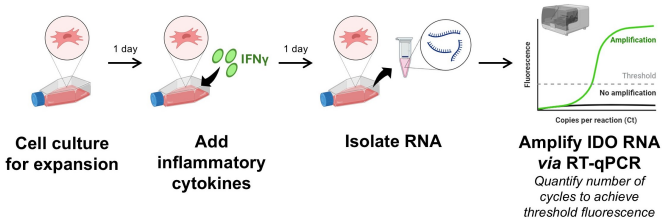


Figure 2-26. General schematic for the assessment of IDO RNA expression for BM-MSCs isolated from a single donor (donor 2) from the ENACT-AMI clinical trial (NCT00936819) in the presence of small-molecule ice recrystallization inhibitor **27**. *Figure created using Biorender.com.*

After treatment of the cells with IFNγ for 2 days, each sample's RNA was isolated and amplified by RT-PCR. The number of amplification cycles required to reach the desired fluorescence threshold for the cells cryopreserved in SFM alone was then directly compared to those cryopreserved with the addition of 2FA (**27**, 15 mM); the cells cryopreserved with 2FA (**27**, 15 mM) required significantly fewer cycles of RNA amplification to reach the fluorescence threshold than those cryopreserved in SFM alone (20.7 ± 0.2 cycles compared to 22.0 ± 0.5 cycles respectively, $p \leq 0.05$, *) (**Figure 2-27**).

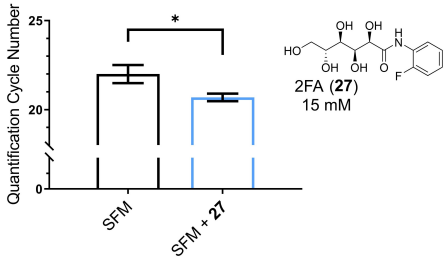


Figure 2-27. Number of amplification cycles required to reach the desired fluorescence threshold for the detection of IDO RNA. Comparison of BM-MSCs isolated from a single donor (donor 2) from the ENACT-AMI clinical trial (NCT00936819) in the presence or absence of small-molecule IRI **27**. Results reported as mean ± standard deviation (SD), n=3. Number of vials analyzed (sample size) indicated below each bar. Significance measured by Student's unpaired two-tailed t-test: * = $p \leq 0.05$.

This result confirmed that the addition of 2FA (**27**, 15 mM) to the cryopreservation of BM-MSCs has the potential to dramatically improve the therapeutic efficacy of cryopreserved MSCs which, in turn, will improve the accessibility of stem cell therapies by increasing cell yields and lowering production costs.

2.4. Cryopreservation of umbilical cord derived mesenchymal stromal cells (UC-MSCs) with small-molecule ice recrystallization inhibitor 2FA (**27**)

While BM-MSCs were the first reported source for MSCs and are therefore considered to be the most common source, the isolation of BM-MCSs requires a surgical biopsy procedure that is often painful for the donor.[192,290] As a result, studies have found that MSCs can be isolated from several different sources that are more readily accessible than BM-MSCs.[192,222–230,232,290,291] In addition, MSCs that have been isolated from umbilical cord blood and tissue (UC-MSCs) have been reported as a more a reliable source of MSCs

with greater proliferation and self-renewal capacity.[292,293] Therefore, we sought to explore whether UC-MSCs could also benefit from the addition of an IRI during cryopreservation in the same manner as BM-MSCs. The UC-MSCs were isolated from a single donor umbilical cord (donor 4, obtained as part of the ENACT-AMI clinical trial – NCT00936819),[250,251] seeded, expanded, and then cryopreserved at a density of 6.0 x 10^6 cells/mL with and without 2FA (**27**, 15 mM) in the standard freezing medium for MSCs [SFM, 10 % DMSO and 5 % human albumin (HA) in Plasmalyte A (PLA)]. The IRI *p*BrPh-Glc (**25**, 30 mM) was excluded from the cryopreservation studies for UC-MSCs because of the toxicity concerns that were observed with the BM-MSCs (see *section 2.3.2.4*). The same general cryopreservation protocol was followed for the UC-MSCs as the BM-MSCs (see *section 2.2*). After the cells were thawed following the OHRI cell manufacturing facility's approved protocols for the ENACT-AMI clinical trial (NCT00936819),[250,251] cryopreservation outcomes (cell viability, recovery, and functionality) of the cells were assessed.

For the BM-MSCs, measurements of the cryopreservation outcomes were taken immediately post-thaw and three days post-thaw for cell viability, two days post-thaw for cell proliferation by EdU-assay, and three days post-thaw for population doubling. These time points had been previously assessed as standard timepoints for the assessment of BM-MSCs following cryopreservation. However, as UC-MSCs have been reported to have greater proliferation potential than BM-MSCs,[292,293] we were interested in confirming whether these time points could also be applied to UC-MSCs; in addition, the plating density for these cells was investigated. The UC-MSCs were thawed and plated at either 1.0 x 10^5 cells/cm^2 or 2.0 x 10^5 cells/cm^2, with viability and proliferation assessed at time points ranging from 0 hours (immediately post-thaw) to three days post-thaw. With respect to cell viability (as assessed by Trypan Blue exclusion assay) no losses were observed, with all cell viability remaining greater than 95.5 % for all time points and both cell densities measured (**Figure 2-28A** and **D**). No significant differences were found in the overall cell yields for either cell density and any measured time point (**Figure 2-28C** and **F**), however at the 16-hour time point the cells cryopreserved with 2FA (**27**, 15 mM) had a greater proportion of cells in the S-phase than those cryopreserved with only the SFM (1.0 x 10^4 cells/cm^2: 30.5 compared to 18.1 respectively; 2.0 x 10^4 cells/cm^2: 45.6 compared to 33.3 respectively) (**Figure 2-28B** and **E**).

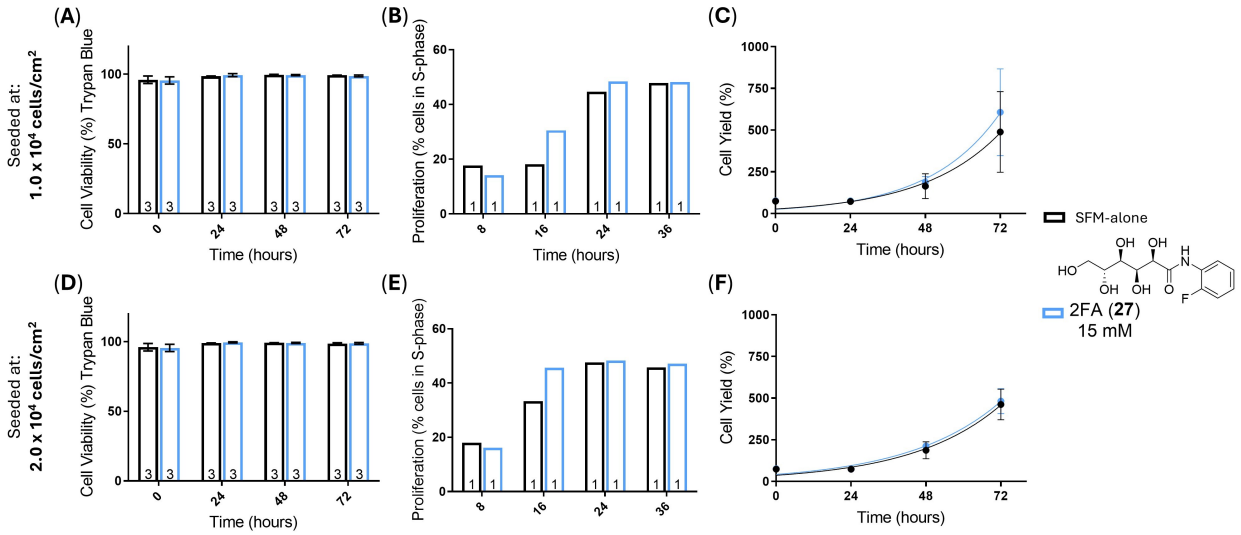


Figure 2-28. Post-thaw cryopreservation outcomes of UC-MSCs (donor 4) cryopreserved at 6.0 x 10^6 cells/mL in standard freezing medium (SFM, 10 % DMSO + 5 % HA in PLA) with and without IRI **27** (15 mM). Outcomes tested at multiple time intervals between 0 and 3 days. Cells were plated at (**A-C**) 1.0 x 10^4 cells/cm^2 or (**D-F**) 2.0 x 10^4 cells/cm^2. (**A,D**) Cell viability assessed by Trypan Blue exclusion assay, (**B,E**) Proliferation assessed by EdU assay. Results mean ± standard deviation (SD), n=3 for viability and yield, n=1 for proliferation. Number of vials analyzed (sample size) indicated within each bar. *These data were collected, analyzed, and reported by the team of researchers at the Ottawa Hospital Research Institute under the supervision of Dr. David Courtman.*

From these data, a 16-hour time point was selected for the assessment of proliferation by EdU assay as well as a plating density of 2.0 x 10^4 cells/cm^2 to complete additional technical replicates for the impact of 2FA (**27**, 15 mM) on the cryopreservation of UC-MSCs. Immediately post-thaw, recovery and cell viability (as measured by the Trypan Blue exclusion assay) were as expected, with 98.2 ± 7.8 % and 98.0 ± 2.3 % of the UC-MSCs recovered with 96.1 ± 3.4 % and 95.5 ± 3.4 % viability for the SFM and SFM supplemented 2FA (**27**, 15 mM) samples respectively (**Figure 2-29A** and **B**). Post-thaw functionality was then measured by EdU assay following seeding of the thawed UC-MSCs (at 20,000 cells/cm^2 – a total of 1.5 x 10^6 cells per T75 culture flask) after 16 hours in culture. Although not statistically significant ($p > 0.05$, ns), the UC-MSCs cryopreserved with 2FA (**27**, 15 mM) had a greater proportion of cells in the S-phase than the cells cryopreserved with SFM-alone (35.0 ± 8.1 % compared to 21.1 ± 7.9 % respectively) (**Figure 2-29C**). Furthermore, the cells cryopreserved with 2FA (**27**, 15 mM) had a significantly greater number of population doublings than the cells frozen with SFM-alone ($p \leq 0.01$, **, 1.40 ± 0.06 doublings compared to 0.79 ± 0.22 doublings respectively) (**Figure 2-29D**).

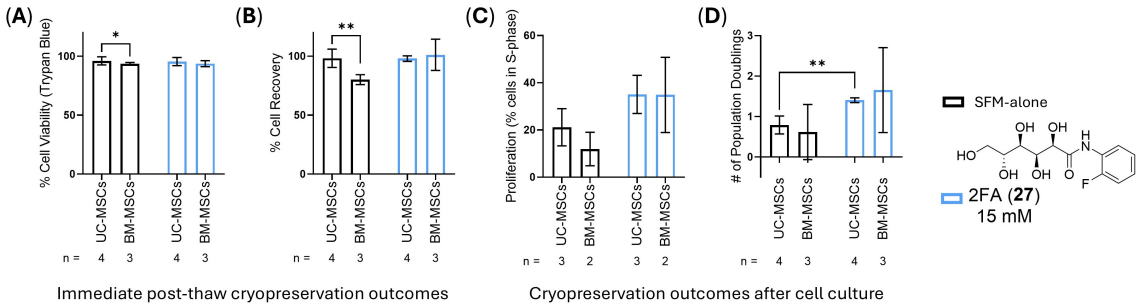


Figure 2-29. Comparison of post-thaw cryopreservation outcomes between UC-MSCs and BM-MSCs. UC-MSCs cryopreserved at 6.0 x 10^6 cells/mL, BM-MSCs cryopreserved at 2.0 x 10^6 cells/mL. (**A**) Cell viability measured by Trypan Blue exclusion assay. (**B,D**) Cell recovery and population doublings determined by manual cell count. Population doublings counted after 24 hours for UC-MSCs and 3 days for BM-MSCs. (**C**) Proliferation measured by EdU assay following 16 hours of culture for UC-MSCs and 2 days for BM-MSCs. UC-MSCs plated at 2.0 x 10^4 cells/cm^2 and 0.25 x 10^6 cells/mL for BM-MSCs. n≥2 from a single donor and results reported as mean ± standard deviation (SD). Number of vials analyzed (sample size) indicated below each bar. *The UC-MSC data were collected, analyzed, and reported by the team of researchers at the Ottawa Hospital Research Institute under the supervision of Dr. David Courtman.*

The results observed for the cryopreservation of UC-MSCs with the addition of small-molecule IRI 2FA (**27**, 15 mM) were consistent with what was observed and reported for BM-MSCs. While a significant difference could be observed in the number of population doublings between the UC-MSCs cryopreserved with and without 2FA (**27**, 15 mM), no significant difference was observed under the same conditions for BM-MSCs (**Figure 2-29D**). The UC-MSC data was representative of only a single biological replicate (a single donor, N=1) and additional biological replicates would be required to confirm the true generalizability of this finding. Given these results, it can be concluded that despite a need for further testing on the effect of donor-to-donor variation with respect to cryopreservation, 2FA (**27**, 15 mM) can successfully be used to improve the cryopreservation of MSCs isolated from different sources.

2.5. Summary of MSC cryopreservation with small-molecule IRIs

It had been previously demonstrated that the small-molecule carbohydrate-based ice recrystallization inhibitors (IRIs) *p*BrPh-Glc (**25**) and 2FA (**27**) could be successfully used as additives to improve the cryopreservation outcomes for red blood cells (RBCs) and hematopoietic stem and progenitor cells (HSPCs) respectively.[162,166] Given this success, a preliminary study by previous Ben Lab graduate student Dr. Jessica Poisson (PhD 2019) and a team of researchers at the Ottawa Hospital Research Institute (OHRI) investigated the potential for these IRIs to improve the post-thaw functionality of bone-marrow derived mesenchymal stromal cells (BM-MSCs).[213,214] This study found that while both IRIs could inhibit ice recrystallization and maintain high post-thaw cell viability and recovery, only 2FA (**27**, 15 mM) was able to improve the post-thaw functionality of cryopreserved BM-MSCs with a greater proportion of cells in the S-phase of the cell cycle, a greater number of population doublings, a shorter doubling time, and an

overall increased cell yield following cell expansion compared to the standard freezing medium alone (SFM, 10 % dimethyl sulfoxide and 5 % human albumin in PlasmaLyte A).[213,214] While these results were significant, as improved proliferation of cells post-thaw could ultimately lead to a greater quantity of MSCs available for therapeutic use, this study only evaluated the effect of small-molecule IRIs on the cryopreservation of cells isolated from a single BM-MSC donor. As donor-to-donor variation is known to affect the efficacy of immunotherapy treatments,[237,265,266,268] further testing with additional biological replicates was necessary.

As a result, this study sought to investigate the effect of small-molecule IRIs *p*BrPh-Glc (**25**) and 2FA (**27**) on the cryopreservation of BM-MSCs isolated from two additional sex-, ethnicity- and age-matched donors. Consistent with the findings of the first donor, high viability and recovery were observed for the cells cryopreserved in the SFM or SFM supplemented with 2FA (**27**, 15 mM). However, for the cells cryopreserved with *p*BrPh-Glc (**25**, 30 mM), a significant decrease in cell viability was observed by AV/PI flow cytometry. When the cryopreserved cells were plated and cultured for expansion, the cells that had been cryopreserved with *p*BrPh-Glc (**25**, 30 mM) were unable to attach to the culture plates while the cells cryopreserved with SFM alone or supplemented with 2FA (**27**, 15 mM) showed normal plate attachment and cell growth. Investigation into the cytotoxicity of *p*BrPh-Glc (**25**) in the absence of freezing found that a 1-hour incubation of HepG2 cells with a 30-mM concentration of *p*BrPh-Glc (**25**) resulted in complete cell death; these results suggested that hydrolysis of the *O*-aryl-β-D-glucopyranoside IRIs and subsequent release of phenols into the cytoplasmic space may preclude their continued investigation in more complex cell models.

While improved proliferation and therapeutic potential was reported for BM-MSCs cryopreserved with 2FA (**27**, 15 mM), there was significant donor-to-donor variation observed in the overall cellular response; the cells isolated from donor 1 had significantly greater post-thaw outcomes than donor 2 or donor 3. However, once the data from all three biological replicates were pooled together, no significant differences were observed for the proliferation of BM-MSCs post-thaw (**Figure 2-30D**, **F-H**); a significant difference was observed for the cell viability as measured by the Trypan Blue exclusion assay where the cells cryopreserved with *p*BrPh-Glc (**25**, 30 mM) were less viable than the cells cryopreserved with SFM alone or SFM supplemented with 2FA (**27**, 15 mM) ($p \leq 0.05$, *, **Figure 2-30A**).

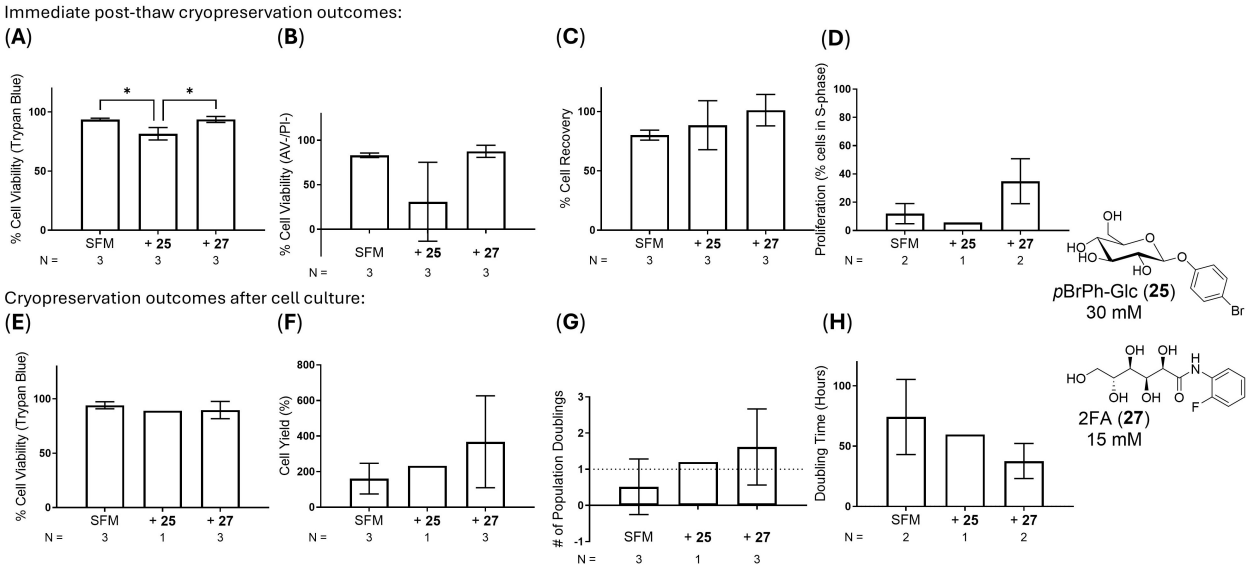


Figure 2-30. Immediate and post-expansion cryopreservation outcomes for BM-MSCs with data pooled from three different donors. Cells plated at a density of 0.50 x 10^6 cells/mL for donor 1 and 0.25 x 10^6 cells/mL for donors 2 and 3. Donors 1 and 2 cultured for three days prior to assessment of cryopreservation outcomes, donor 3 cultured for two days. Results mean ± standard deviation (SD). Number of donors analyzed (biological sample size) indicated below each bar. Significance measured by one-way ANOVA with Tukey's post-hoc analysis: * = $p \leq 0.05$.

As previously discussed, donor-dependent variation in the therapeutic potential of MSCs can be caused by differences in donor sex, age, health status, or genetic makeup.[237,265–268] However, the role of these factors as they relate to cryopreservation is significantly less well understood. Despite all three BM-MSC donors being matched, there is a large variation in their response to cryopreservation both in the absence or presence of small-molecule IRIs. While these donor-related differences are often mitigated during clinical studies by creating large single donor cell banks or pooling product from multiple donors, they present an avenue for improvement in the manufacturing of these cell therapy products. Further investigation of donor-factor related differences as they relate to cryopreservation are required to be able to generally apply small-molecule IRI technology to the cryopreservation of complex donated cells intended for use as human health therapeutics. In addition, the variation in cryopreservation outcomes post cell expansion could be caused by variation in culture conditions; therefore, rigorous optimization of storage times in liquid nitrogen, plating densities, and expansion periods, would be required.

Finally, consistent with the findings for the cells isolated from donor 1, the cells cryopreserved with 2FA (**27**, 15 mM) from donors 2 and 3 also showed improved proliferation post-thaw compared to the cells cryopreserved with SFM-alone; this finding was also replicated in MSCs that had been isolated from umbilical cord (UC-MSCs) highlighting that IRI technology can be applied to MSCs isolated from different sources. Finally, the addition of 2FA (**27**, 15 mM) was found to increase the production of indoleamine

2,3-dioxygenase (IDO) in cryopreserved BM-MSCs, which is used by human-MSCs to modulate the immune response. Taken together, these results further support the potential for 2FA (**27**) to be used as an additive for the cryopreservation of MSCs by improving the accessibility of MSC-based immunotherapies. However, given the high donor variability observed with respect to the immunotherapeutic properties of MSCs, additional biological replicates will be required in future to better understand the impact of donor-to-donor variation at a cellular level on the cryopreservation of MSCs in the presence of small-molecule ice recrystallization inhibitors.

3. Investigating the permeation and internalization of small-molecule IRIs using Raman scattering techniques for the cryopreservation of red blood cells

Red blood cells (RBCs) are routinely used in transfusion medicine for the treatment of several key diseases.[1] Once a unit of blood is donated and the RBCs are isolated, the unit can be stored for up to 42 days at 4 ºC (the North American hypothermic storage standard).[1,294] Beyond this time point, the quality of the stored RBCs dramatically deteriorates due to the formation of "lesions" that affect both the function and *in vivo* survival of the transfused RBCs.[295,296] Furthermore, this cellular damage has been directly related to adverse clinical outcomes for transfusion patients and have resulted in cases of increased post-operative infections, pneumonia, renal failure, and death.[297–300] As a result of their short shelf-life under hypothermic storage conditions, hundreds of RBC units are discarded each year, and the entire blood supply chain is prone to local shortages that put the health of patients as risk.[301,302] To mitigate these challenges, the shelf-life of RBCs can be extended if the units are cryopreserved; the United States Food and Drug Administration sets the shelf-life of cryopreserved RBC units to 10 years, but studies have shown that longer storage times are possible without significant detriment to the cells.[303–306] To ensure cryopreservation success and mitigate ice-related damage during the cryopreservation process, the addition of cryoprotective agents (CPAs) prior to freezing and careful control of cooling and warming rates throughout the entire cryopreservation process, is required (previously discussed in *section 1.1.1*).

There are currently two clinically approved methods for the cryopreservation of RBCs. In Europe, RBCs are cryopreserved using a low glycerol method (LGM) (typically 15-20 % w/v) and are rapidly cooled (> 100 ºC/min) prior to storage in liquid nitrogen (196 ºC) (**Figure 3-1**).[307–309] In North America, RBC units are suspended in a 40 % w/v solution of glycerol (the high glycerol method, HGM) and slowly cooled (1-3 ºC/min) to a final storage temperature below -65 ºC (in a mechanical freezer) (**Figure 3-1**).[44,308,309] As previously discussed in *section 1.1.2*, glycerol is a penetrating CPA that replaces intracellular water during freezing to protect RBCs from extreme dehydration leading to cell death.[35] However, prior to transfusion of a unit in a clinical setting the glycerol must be removed to concentrations of less than 1 % in order to avoid intravascular hemolysis and other clinical complications.[1,44,310,311]

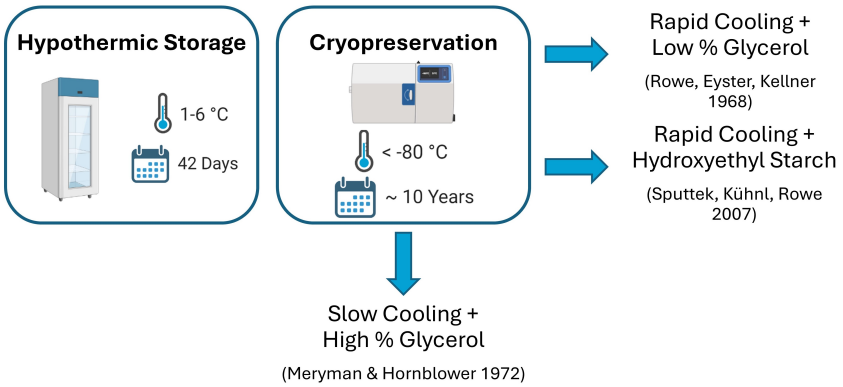


Figure 3-1. Methods of preservation for red blood cells, including both hypothermic storage and cryopreservation.[1,44,307,312]

It is the time-consuming glycerol removal process, requiring several washing steps to return the RBC unit to isotonic over a period of 50 minutes,[313] that presents a significant impediment to the regular use of cryopreserved RBC units in a clinical setting. Currently, military storage represents the majority of cryopreserved RBC units, and only rare blood phenotypes are routinely cryopreserved and transfused in standard clinical medicine.[187,309,314–316] In an attempt to eliminate the use of glycerol during RBC cryopreservation while maintaining high cell recovery and viability post-thaw to improve the feasibility of using cryopreserved RBC units, non-permeating additives such has hydroxyethyl starch (HES) have been explored as it was proposed that they would not need to be removed prior to transfusion;[308,312] however, non-permeating additives have not been approved for use as CPAs in the clinical setting to date.[1,3,187] In addition, while the LGM requires approximately half the amount of time for deglycerolization compared to the HGM, RBCs cryopreserved using the LGM method can only be stored for 24 hours due to the risk of bacterial contamination arising from the "open-bag" glycerolizing and deglycerolizing process.[309,313] To contrast, the automated closed-loop system used for the addition and removal of glycerol (the Haemonetics ACP-215 device) for RBCs cryopreserved using the HGM permits a shelf-life of up to 21 days post-thaw (depending on the components of the resuspension solution).[313,317–320] The automated equipment cannot withstand the liquid nitrogen temperatures required for the LGM,[309,313] and thus cannot be used for RBCs cryopreserved using this method. Furthermore, the storage and transportation of RBCs frozen using the HGM at temperatures of -80 °C is significantly more user and environmentally friendly than maintaining temperatures of -196 °C in liquid nitrogen. As a result, the HGM is the most broadly applied method for RBC cryopreservation and significant interest has arisen in the development of methods that can reduce the concentration of glycerol required for the cryopreservation of RBCs without drastically altering the already clinically approved HGM cryopreservation protocols.

3.1. Prior investigations with IRIs for to red blood cell cryopreservation

As has been previously discussed (*section 1.3.1*), the addition of ice recrystallization inhibitors (IRIs) to cryopreservation protocols has been found to dramatically improve cryopreservation outcomes of a number of different cell types.[158,162,166,168,213,215,216,321] For the cryopreservation of RBCs in particular, our laboratory has extensively reported on the success of the IRIs 4-bromophenyl-β-D-glucopyranoside (*p*BrPh-Glc, **25**) and 4-methoxyphenyl-β-D-glucopyranoside (PMP-Glc, **26**) (**Figure 3-2**).[162,167,248] Both compounds **25** and **26**, at concentrations of 30 mM and 110 mM respectively, were found to improve the cryopreservation outcomes of RBCs using the approved North American cryopreservation protocol (slow cooling rates and storage in a mechanical freezer at temperatures ≤ -65 ºC) with only 15 % (w/v) glycerol instead of the clinically approved 40 % (w/v) (**Figure 3-2**).[162] Critically, requiring 25 % less glycerol (w/v) enables significantly decreased post-thaw processing times and improves the accessibility and feasibility of use for cryopreserved RBC units.

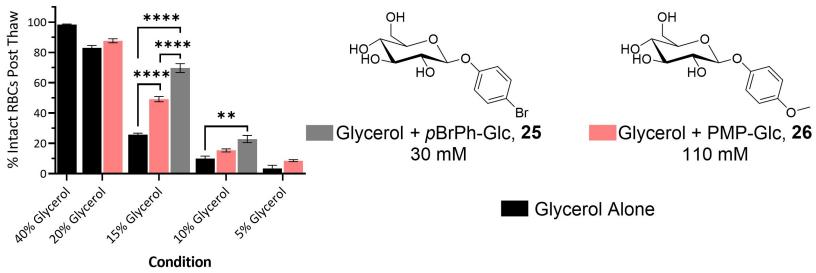


Figure 3-2. Effect of IRIs *p*BrPh-Glc (**25**) and PMP-Glc (**26**) at 30 mM and 110 mM respectively on the post-thaw integrity of RBCs (100 % - % hemolysis) at various concentrations of glycerol.[158,162] RBCs were slow cooled (1 °C/min) to -40 °C and then rapidly cooled to the storage temperature of -80 °C prior to thawing (rapid) to 37 °C and measurement of hemolysis. Results reported as mean ± standard error of the mean (SEM). Significance measured by two-way ANOVA with Tukey's post-hoc test: ** = $p \leq 0.01$, **** = $p \leq 0.0001$.

While these studies were extremely promising, the results clearly showed that glycerol could not be entirely removed from these cryopreservation solutions, even with the IRIs, without dramatically increasing RBC hemolysis (**Figure 3-2**). Therefore, it was critical to investigate the deglycerolization process for RBC units that had been cryopreserved with 15 % (w/v) glycerol and small-molecule IRIs *p*BrPh-Glc (**25,** 30 mM) or PMP-Glc (**26**, 110 mM).

RBCs are very sensitive to changes in osmotic pressure caused by both the addition and removal of glycerol that can ultimately lead to hemolysis if the cells swell beyond a maximum size or are returned to isotonic after shrinking below a certain size.[44,187,322] For RBC units cryopreserved with 40 % (w/v) glycerol, the glycerol is normally removed in three subsequent wash phases by the Haemonetics ACP-215 system: an initial 12 % saline wash, a 1.6 % saline wash, then finally a 0.9 % saline wash (isotonic).[313,323]

However, it was found that the standard deglycerolization procedures could not be directly applied to RBCs that had been cryopreserved with IRIs as a significant amount of hemolysis was observed.[158,214] Attempts to remove excess cryosolution before freezing or optimize the saline washing steps did not lead to improved deglycerolization success,[214] and thus the Ben Lab hypothesized that interactions between the IRI and the cell membrane were increasing the cell's susceptibility to osmotic stress during the deglycerolization process.[158] Dr. Poisson (Ben Lab, PhD 2019) later investigated a number of azide-containing *O*-aryl-β-D-glucopyranoside IRIs as cryopreservation additives for RBCs that were found to both improve the cryopreservation of RBCs at reduced glycerol concentrations and allowed deglycerolization of the units without significant hemolysis.[214] It was hypothesized at the time that the reduced hydrophobicity of these IRIs compared to *p*BrPh-Glc (**25**) or PMP-Glc (**26**) made the azide-containing IRIs less likely to negatively interact with the cell membrane during the deglycerolization washes.

More detailed investigations of the azide-containing IRIs found that 4-azidophenyl-β-D-glucopyranoside (*p*N_3Ph-Glc, **29**, 20 mM) could be used to cryopreserve RBCs at reduced glycerol concentrations (15 % w/v) using the standard slow cooling protocol and could be successfully deglycerolized using a two-phase washing protocol: an initial 4.5 % saline wash followed by a 0.9 % saline wash.[214] This procedure could be successfully applied to the cryopreservation of RBCs on both small (1 mL cryovial) and large scale (250 mL bagged unit) and maintained functionality of the RBCs as measured by mean cell volume, adenosine triphosphate (ATP) and 2,3-diphosphoglycerate (DPG) levels, methemoglobin concentration, oxygen affinity, membrane deformability, as well as extracellular potassium and sodium levels.[214] These results confirmed that RBCs cryopreserved with 15 % (w/v) glycerol and 20 mM *p*N_3Ph-Glc (**29**) were comparable in quality and function to those cryopreserved with 40 % (w/v) glycerol.

Unfortunately, one of the major limitations for the use of *p*N_3Ph-Glc (**29**) as an additive for the large-scale cryopreservation of RBCs was its chemical stability. The azide functional group is known to be photolabile and readily decompose,[324,325] which would be problematic for the safe storage of RBCs over long periods of time. Therefore, we were interested in exploring other, similar, functional groups and whether they could impart the same quality and functionality improvements for RBC cryopreservation as *p*N_3Ph-Glc (**29**) but with improved chemical stability.

3.2. Cryopreservation of red blood cells (RBCs) using *nitrile*- and *amide*-containing ice recrystallization inhibitors

It was previously hypothesized that the increased polarity of compound **29** (*p*N_3Ph-Glc) compared to *p*BrPh-Glc (**25**) or PMP-Glc (**26**) made it less likely to interact with the RBC membrane during the deglycerolization process.[158,214] Therefore, to maintain close structural similarity to *p*N_3Ph-Glc (**29**) but with improved chemical stability, *O*-aryl-β-D-glucopyranoside structures with *para*-nitrile (*p*CNPh-Glc, **30**) and *para*-amide (*p*AmPh-Glc, **31**) functionality were envisioned (**Figure 3-3**). In addition, compounds **29** and **30** were of interest as the *azide* and *nitrile* functional groups could be probed by label-free Raman imaging techniques which will be further discussed in <u>*section 3.3*</u>. Once synthesized, each of these compounds would be screened for ice recrystallization inhibition activity and then assessed for use as cryopreservation additives with RBCs using reduced glycerol concentrations in collaboration with a team of researchers at the Canadian Blood Services (CBS) research facility in Edmonton, Alberta under the supervision of Dr. Jason Acker.

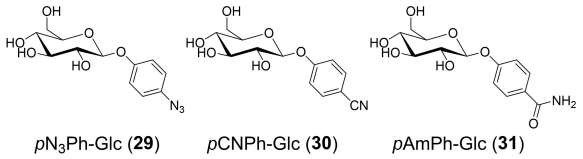
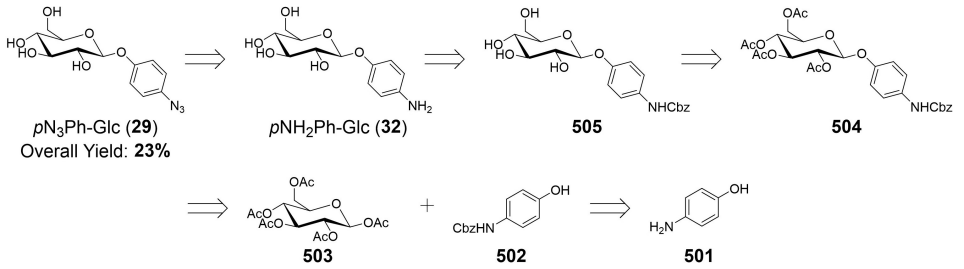


Figure 3-3. Structures of *O*-aryl-β-D-glucopyranoside compounds with *para*-azide (*p*N_3Ph-Glc, **29**), *para*-nitrile (*p*CNPh-Glc, **30**), and *para*-amide (*p*AmPh-Glc, **31**) functional groups.

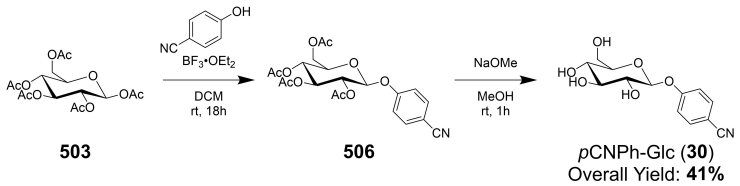
*3.2.1. Synthesis of 4-azidophenyl-β-D-glucopyranoside (pN_3Ph-Glc, **29**), 4-cyanophenyl-β-D-glucopyranoside (pCNPh-Glc, **30**), and 4-carbamoylphenyl-β-D-glucopyranoside (pAmPh-Glc, **31**)*

The structure and retrosynthesis for 4-azidophenyl-β-D-glucopyranoside (*p*N_3Ph-Glc, **29**) as reported by Dr. Jessica Poisson (Ben Lab, PhD 2019) is shown in **Scheme 3-1**.[214] After protection of 4-aminophenol (**501**) with benzyl chloroformate (CbzCl) to form **502**, it was reacted with β-D-glucose pentaacetate (**503**) using a traditional Lewis-acid assisted glycosidation procedure[214] to generate the protected intermediate **504**. Removal of the acetates using Zemplén[326] conditions (**505**), then reduction of the Cbz protecting group afforded 4-aminophenyl-β-D-glucopyranoside (*p*NH_2Ph-Glc, **32**) in four steps. The synthesis of **29** was then achieved in 5 total steps with a 23 % overall yield from *p*NH_2Ph-Glc (**32**) using *tert*-butyl nitrite (*t*-BuONO) and azidotrimethylsilane (TMS-N_3) (**Scheme 3-1**).



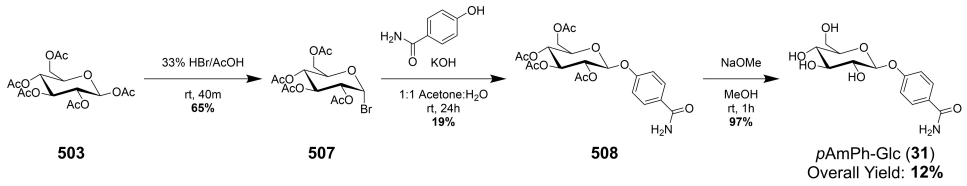
Scheme 3-1. Retrosynthesis of 4-azidophenyl-β-D-glucopyranoside (*p*N_3Ph-Glc, **29**) as prepared by Dr. Jessica Poisson (PhD 2019, Ben Lab).[214]

The structure and synthesis for 4-cyanophenyl-β-D-glucopyranoside (*p*CNPh-Glc, **30**) is shown in **Scheme 3-2**. The synthesis of **30** was be achieved following a standard two-step Lewis-acid assisted glycosidation procedure for the synthesis of *O*-aryl-β-D-glucopyranosides.[167] Starting from β-D-glucose pentaacetate (**503**), Lewis-acid activation of the anomeric acetate using $BF_3{\cdot}OEt_2$ selectively afforded the acetate-protected, β-linked product **506**. Deacetylation using Zemplén conditions[326] afforded the final product **30** (*p*CNPh-Glc) in a 41 % yield over two steps.



Scheme 3-2. Synthesis of 4-cyanophenyl-β-D-glucopyranoside (*p*CNPh-Glc, **30**).

The structure and synthesis of 4-carbamoylphenyl-β-D-glucopyranoside (*p*AmPh-Glc, **31**) is shown in **Scheme 3-3**. Unfortunately, **31** could not be synthesized using the Lewis-acid assisted glycosidation procedure that was described previously for the synthesis of compound **30** (**Scheme 3-2**). Instead, *p*AmPh-Glc (**31**) was prepared *via* a substitution reaction between acetobromo-α-D-glucose (**507**) and 4-hydroxybenzamide to generate the acetate protected intermediate **508**. The synthesis of acetobromo-α-D-glucose (**507**) was achieved by reaction of β-D-glucose pentaacetate (**503**) and a solution of hydrobromic acid in acetic acid. Deacetylation of **508** using Zemplén conditions[326] then afforded the final product **31** in three steps with a 12 % overall yield.



Scheme 3-3. Synthesis of 4-carbamoylphenyl-β-D-glucopyranoside (*p*AmPh-Glc, **31**).

*3.2.2. Ice recrystallization inhibition activity of pCNPh-Glc (**30**) and pAmPh-Glc (**31**)*

The ice recrystallization inhibition activity of *p*CNPh-Glc (**30**) and *p*AmPh-Glc (**31**) was determined by the 5-minute splat-cooling assay (previously described in <u>*section 1.3.2*</u>)[169,170]. The compounds were prepared in phosphate-buffered saline (PBS) and a dose-response curve of their activity was generated for each compound (**Figure 3-4**). The ice recrystallization inhibition activity of compound **29** (*p*N_3Ph-Glc) was previously reported by Dr. Jessica Poisson with an IC_{50} of 25.4 mM (95 % CI [18.1-35.6]).[214] For the newly synthesized compounds **30** (*p*CNPh-Glc) and **31** (*p*AmPh-Glc), an approximately 2-fold reduction in ice recrystallization inhibition activity was observed with IC_{50} values of 53.1 mM (95 % CI [42.1-66.9]) and 40.8 mM (95 % CI [34.1-48.9]) respectively (**Figure 3-4**).

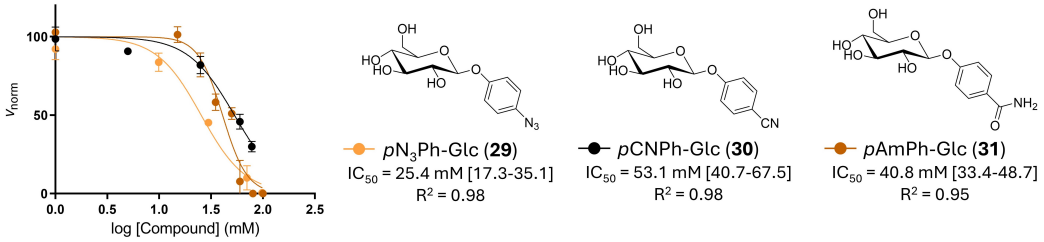


Figure 3-4. Ice recrystallization inhibition activity of compounds **29**-**31**. Plot of normalized ice crystal growth (v_{norm}) in phosphate-buffered saline (PBS) against logarithm transformed compound concentration (in mM). Determined by modified splat-cooling assay with a 5-minute annealing time at -6.4 °C.[169] Results reported as mean ± standard deviation (SD) for n=3 ice wafers. IC_{50} reported with error as the 95 % confidence interval range. *Data for the ice recrystallization inhibition activity of pN_3Ph-Glc (**29**) collected, analyzed, and reported by Dr. Jessica Poisson.*[214]

*3.2.3. Cryopreservation of red blood cells (RBCs) using pCNPh-Glc (**30**) and pAmPh-Glc (**31**)*

As the ice recrystallization inhibition activity of compounds **30** (*p*CNPh-Glc) and **31** (*p*AmPh-Glc), remained similar to that of compound **29** (*p*N_3Ph-Glc) with only a two-fold reduction in IC_{50}, we were interested in exploring their potential as additives for the cryopreservation of RBCs at reduced glycerol concentrations. For these studies, Canadian Blood Services' Network Centre for Applied Development Services (NetCAD) provided human red cell concentrate (a donated blood unit that has been depleted of the buffy coat and greater than 90 % of the plasma) suspended in a solution of sodium chloride, adenine, glucose, and mannitol (SAGM). The units were from three blood-type and sex-matched donors; transfusion of sex- or blood-type- mismatched donors has been linked to an increased risk of mortality often caused by

activation of the immune system in response to the foreign cells.[327,328] The three matched units were then pooled together to reduce the impact of donor-to-donor variability on the results and then suspended in cryosolution containing either 15 % (w/v) glycerol alone, or 15 % (w/v) glycerol containing compound **30** (*p*CNPh-Glc) or **31** (*p*AmPh-Glc). The compounds were then tested at three concentrations each such that the final cryopreservation solution contained either 12.5 mM, 25 mM, or 40 mM compound **30** (*p*CNPh-Glc) or 2.5 mM, 20 mM, or 50 mM compound **31** (*p*AmPh-Glc). The maximum concentration for each compound was selected based on its respective apparent maximum aqueous solubility in PBS.

Once cryosolution was added, the RBC concentrate solutions (300 µL of red cell concentrate in SAGM) were incubated for 10 minutes at room temperature prior to cooling to -5 °C in a cool methanol bath. To ensure each vial nucleated at the same temperature, the solutions were mechanically nucleated at -5 °C using metal forceps cooled in dry ice. Each vial was then cooled to -40 °C (cooling rate of 1 °C/min in a cool methanol bath) or -78 °C (cooling rate of > 100 °C/min by placing the vials directly into dry ice). After freezing, the samples were held at their final temperature for 1-2 minutes and then rapidly thawed by placing the vials into a 37 °C water bath. RBC hemolysis was then measured by Drabkin's assay[329] and reported as the percentage of intact RBCs post-thaw (100 % - % hemolysis).[329,330] No significant difference ($p > 0.05$, ns) was observed in the integrity of RBCs post-thaw with the addition of compound **30** (*p*CNPh-Glc) or **31** (*p*AmPh-Glc) compared to 15 % (w/v) glycerol alone (**Figure 3-5**).

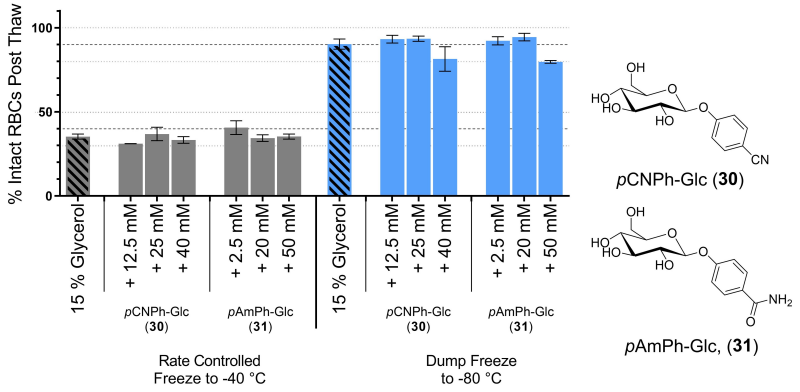


Figure 3-5. Percentage of intact red blood cells (RBCs) post-thaw using 15 % glycerol plus compound **30** (12.5, 25, or 40 mM) or **31** (2.5, 20, or 50 mM). Samples were frozen using a slow-cooling rate-controlled method (1 °/min to -40 °C) or fast-cooling dump freeze method (100 °C/min to -80 °C) followed by thawing in a 37 °C water bath. Hemolysis measured by Drabkin's assay and presented as % intact RBCs = (100 % - % hemolysis).[329] Data reported as mean ± standard error of the mean (SEM), n=2 cryovials frozen from units pooled from three blood-type and sex-matched donors provided by NetCAD. *Data collected in collaboration with Dr. Jason Acker's laboratory (University of Alberta) and Canadian Blood Services.*

While no significant improvement in the % intact RBCs post-thaw was observed for either compound, there was also no significant reduction indicating that the addition of *p*CNPh-Glc (**30**) and

*p*AmPh-Glc (**31**) did not exacerbate cryopreservation damage at reduced glycerol concentrations. As increased hemolysis was not observed, we sought to determine whether the presence of these compounds would permit deglycerolization using the two-step washing conditions that were used by Dr. Poisson for RBCs cryopreserved with *p*N_3Ph-Glc (**29**). However, immediately following collection of this data, COVID-19 forced the shutdown of all laboratory spaces and reduced capacity facilities as part of safe return-to-work protocols and travel restrictions between provinces prevented continued testing of these compounds in RBCs with our collaborators at Canadian Blood Services in Edmonton, AB. Therefore, future studies could investigate the deglycerolization of RBC units cryopreserved with *p*CNPh-Glc (**30**) or *p*AmPh-Glc (**31**).

3.2.4. Structure-activity relationship (SAR) studies for nitrile- and amide-containing ice recrystallization inhibitors

With the ultimate goal of improving the recovery of viable RBCs post-thaw with reduced glycerol concentrations, and to support future studies with *O*-aryl-β-D-glucopyranoside IRIs, regio-isomers of compounds **30** and **31**, with nitrile and amide substitutions in the *meta*- and *ortho*- positions were envisioned. Previous work by Dr. Chantelle Capicciotti (Ben Lab, PhD 2014) found that ice recrystallization inhibition activity was affected by both the nature of the substituent (*i.e., methoxy*- or *methyl*-) as well as regiochemistry of the substituent on the aryl ring (*ortho*-, *meta*-, *para*-).[167] For example, the *para-methoxy*- substituted *O*-aryl-β-D-glucopyranoside (PMP-Glc, **26**) had greater ice recrystallization inhibition activity than the *meta*- (MMP-Glc, **33**) and *ortho*- (OMP-Glc, **34**) position substitutions; however, there was no difference in activity for methyl-substituted derivatives in the *para*- (*p*MePh-Glc, **35**) or *meta*- (*m*MePh-Glc, **36**) positions (**Figure 3-6**).[167] Based on these results, it was of interest to explore the *meta*- or *ortho*- nitrile and amide derivatives and compare their ice recrystallization inhibition activity to **30** and **31**. Nitrile and amide *N*-aryl-D-gluconamides were also of interest to be investigated as this class of IRIs had been shown to improve the cryopreservation outcomes of various stem cell derivatives.[166,213,215,216,321]

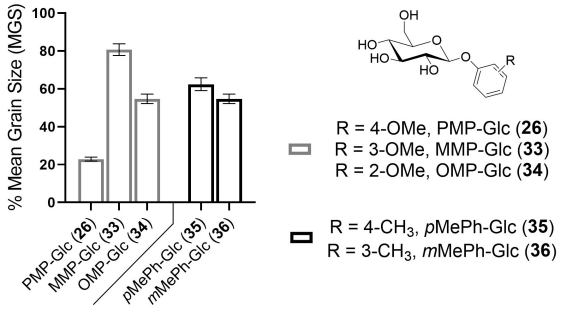
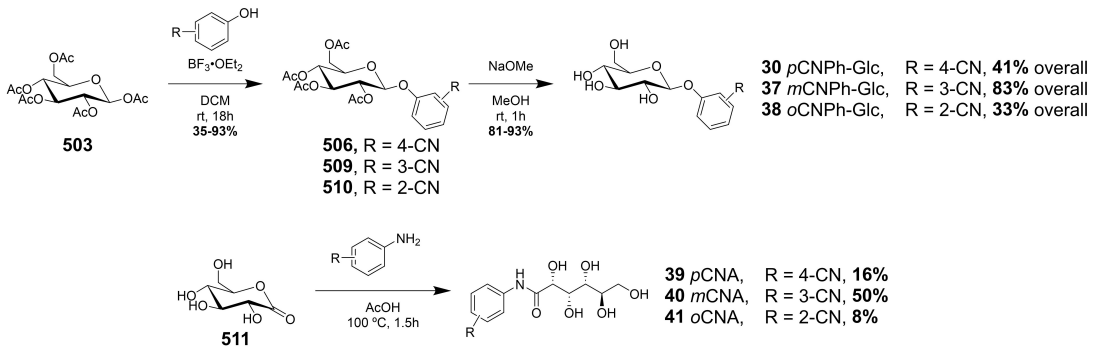


Figure 3-6. Ice recrystallization inhibition activity of *O*-aryl-β-D-glucopyranosides (**26**, **33**-**36**).[158,167] Ice recrystallization inhibition activity reported as mean ± standard deviation (SD) of the percent mean grain size (% MGS) normalized to phosphate-buffered saline (PBS) of n=3 ice wafers assessed at 22 mM using a splat-cooling assay with a 30-minute annealing time at -6.4 °C. *Figure recreated using data from Capicciotti (2014)*.[158,167]

3.2.4.1. Structure and synthesis of nitrile- and amide- containing O-aryl-β-D-glucopyranosides and N-aryl-D-gluconamides

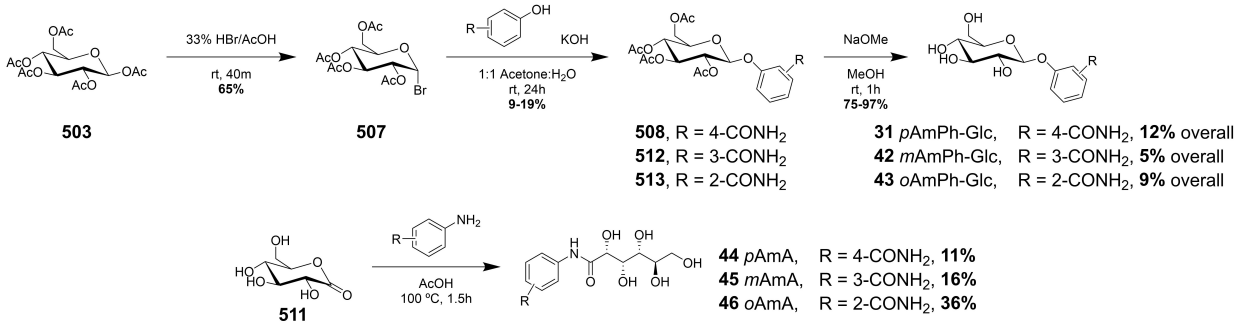
The structure and synthesis for all *nitrile*-containing molecules are shown in **Scheme 3-4**. The synthesis of **30** (*p*CNPh-Glc) was previously described in **Scheme 3-2**. The *meta*- and *ortho*- derivatives 3-cyanophenyl-β-D-glucopyranoside (*m*CNPh-Glc, **37**) and 2-cyanophenyl-β-D-glucopyranoside (*o*CNPh-Glc, **38**) were synthesized following the same general procedure as **30** (*p*CNPh-Glc) with 83 % and 33 % overall yields respectively (*via* the protected intermediates **506**, **509**, **510**). The *para*-, *meta*-, and *ortho*- derivatives of *N*-cyanophenyl-D-gluconamide (*p*CNA, **39**; *m*CNA, **40**; *o*CNA, **41** respectively) could be synthesized in one step from δ-D-gluconolactone (**511**) with 8-50 % yields. The lower observed yields for the synthesis of the *para*- and *ortho*- derivatives (**30**, **38**, and **39**, **41** respectively) was likely the result of reduced nucleophilicity of the respective hydroxybenzonitrile and aminobenzonitrile starting materials compared to the *meta*- derivatives (**37** and **40**).



Scheme 3-4. Synthesis of nitrile-containing *O*-aryl-β-D-glucopyranosides and *N*-aryl-D-gluconamides **30**, and **37**-**41**.

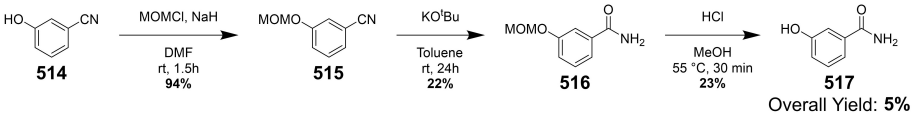
The structure and synthesis for all amide-containing molecules are shown in **Scheme 3-5**. The synthesis of **31** (*p*AmPh-Glc) was previously described in **Scheme 3-3**. The *meta*- and *ortho*- derivatives

3-carbamoylphenyl-β-D-glucopyranoside (*m*AmPh-Glc, **42**) and 2-carbamoylphenyl-β-D-glucopyranoside (*o*AmPh-Glc, **43**) were synthesized following the same general procedure as **31** (*p*AmPh-Glc) with 5 % and 9 % overall yields respectively (*via* the acetate protected intermediates **508**, **512**, and **513**). The *para*-, *meta*-, and *ortho*- derivatives of *N*-carbamoylphenyl-D-gluconamide (*p*AmA, **44**; *m*AmA, **45**; *o*AmA, **46** respectively) could be synthesized in the same manner as the nitrile derivatives (**39**-**41**) in one step from δ-D-gluconolactone (**511**) with 11-36 % yield.



Scheme 3-5. Synthesis of amide-containing *O*-aryl-β-D-glucopyranosides and *N*-aryl-D-gluconamides **31**, and **42**-**46**.

While the *para*- and *ortho*-hydroxybenzamides were commercially available, the *meta*-hydroxybenzamide (**517**) needed to be synthesized. Starting from *meta*-hydroxybenzonitrile (**514**), the hydroxyl was first protected using chloromethyl methyl ether (MOMCl) to generate the MOM-protected benzonitrile intermediate **515**. The nitrile was then oxidized to an amide using potassium *tert*-butoxide (KO^{t}Bu) to generate the MOM-protected benzamide **516**. Finally, a 1 M solution of hydrochloric acid (HCl) in methanol (MeOH) was used to remove the MOM protecting group and generate the final *meta*-hydroxybenzamide (**517**) in three steps with a 5 % overall yield (**Scheme 3-6**).



Scheme 3-6. Synthesis of *meta*-hydroxybenzamide (**517**).

3.2.4.2. Ice recrystallization inhibition activity of nitrile- and amide- containing O-aryl-β-D-glucopyranosides and N-aryl-D-gluconamides

The ice recrystallization inhibition activity of compounds **37**-**46** was then assessed by a modified splat-cooling assay (previously described in *section 1.3.2*)[169,170]. The compounds were prepared in phosphate-buffered saline (PBS) and a dose-response curve of their activity was generated for each compound (**Figure 3-7**). For the nitrile-containing compounds, **37** (*m*CNPh-Glc) was the most active with an IC_{50} of 26.8 mM (95 % CI [24.5-29.3]) (**Figure 3-7A**). The two other pyranosides were found to have

IC_{50} values of 53.1 mM (95 % CI [42.1-66.9]) (*p*CNPh-Glc, **30**, previously described in *section 3.2.2*) and 50.7 mM (95 % CI [33.0-77.8]) (*o*CNPh-Glc, **38**) (**Figure 3-7A**). Of the aldonamides, an IC_{50} was only reported for the *ortho*- substituted derivative **41** [*o*CNA, IC_{50} = 79.0 mM (95 % CI [53.9-158.2])] as compounds **39** (*p*CNA) and **40** (*m*CNA) only reached a normalized rate of ice recrystallization inhibition (v_{norm}) of 72.8 ± 1.7 % (80 mM) and 82.6 ± 6.8 % (45 mM) respectively at their apparent maximum solubility in PBS (**Figure 3-7B**).

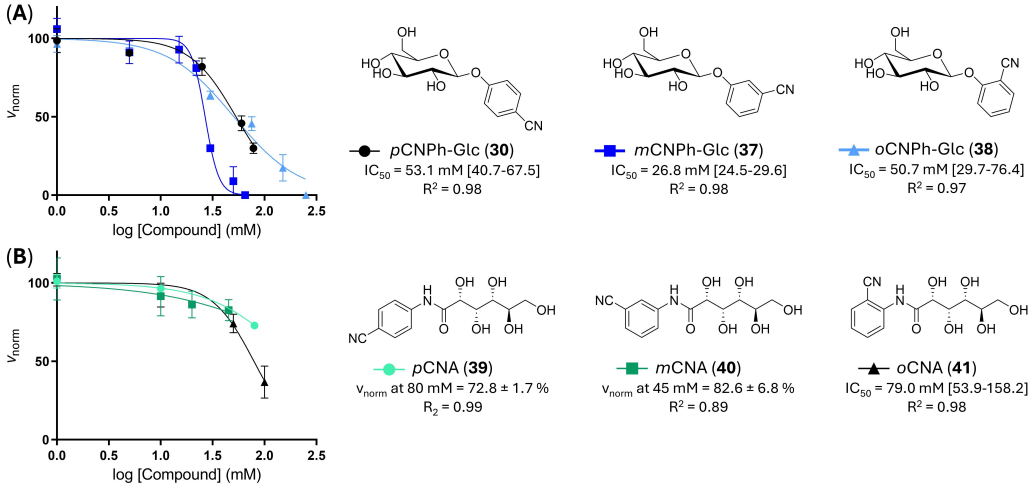


Figure 3-7. Ice recrystallization inhibition activity of (**A**) *O*-aryl-β-D-glucopyranoside compounds **30** and **37-38** and (**B**) *N*-aryl-D-gluconamides **39-41**. Plot of normalized ice crystal growth (v_{norm}) in phosphate-buffered saline (PBS) against logarithm transformed compound concentration (in mM). Determined by modified splat-cooling assay with a 5-minute annealing time at -6.4 °C.[169] Results reported as mean ± standard deviation (SD) for n=3 ice wafers. IC_{50} reported with error as the 95 % confidence interval range.

For the amide-containing compounds, the *ortho*- substituted gluconamide derivative **46** (*o*AmA) was found to be most active with an IC_{50} of 35.9 mM (95 % CI [33.7-38.1]) (**Figure 3-8B**). Of the pyranosides, compound **43** (*o*AmPh-Glc) had similar activity to compound **31** (*p*AmPh-Glc) with an IC_{50} value of 53.5 mM (95 % CI [42.2-67.8]) (compared to 40.8 mM (95 % CI [34.1-48.9]), previously reported in *section 3.2.2*) (**Figure 3-8A**). Compound **42** (*m*AmPh-Glc) was ~2-fold less active than **31** with an IC_{50} of 95.9 mM (95 % CI [76.3-113.3]) (**Figure 3-8B**). A full dose-response curve could not be generated for compounds **44** (*p*AmA) and **45** (*m*AmA) which only reached a minimum normalized rate of ice recrystallization inhibition (v_{norm}) of 56.1 ± 9.1 % (50 mM) and 96.9 ± 10.7 % (10 mM) respectively at their apparent maximum solubility in PBS (**Figure 3-8A**).

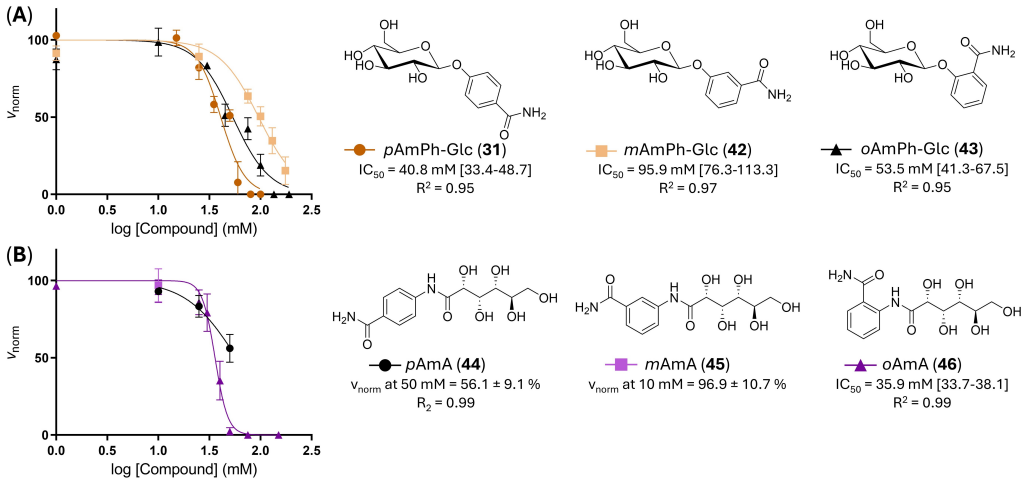


Figure 3-8. Ice recrystallization inhibition activity of (**A**) *O*-aryl-β-D-glucopyranoside compounds **31** and **42-43** and (**B**) *N*-aryl-D-gluconamides **44-46**. Plot of normalized ice crystal growth (v_{norm}) in phosphate-buffered saline (PBS) against logarithm transformed compound concentration (in mM). Determined by modified splat-cooling assay.[169] Results reported as mean ± standard deviation (SD) for n=3 ice wafers. IC_{50} reported with error as the 95 % confidence interval range.

The dose-response curves for the ice recrystallization inhibition activity of the three *N*-cyanophenyl-D-gluconamide derivatives **39-41** were comparable, indicating that the positioning of the nitrile functional group on the aromatic ring did not significantly impact ice recrystallization inhibition activity; the same was true for the *N*-carbamoylphenyl-D-gluconamide derivatives **44-46**. However, previous work by Dr. Madeline Adam (Ben Lab, PhD 2020) found reduced activity for *ortho*- and *meta*-*N*-aminophenyl-D-gluconamides compared to the *para*- derivative,[176] while Dr. Jennie Briard (Ben Lab, PhD 2016) and Marcus Diamante (Ben Lab, PhD candidate) found that the *para*-*N*-fluorophenyl-D-gluconamide was significantly less active than the *ortho*- or *meta*- derivatives.[168,331] Therefore, a substituent's regiochemistry may have an impact on ice recrystallization inhibition activity, but no clear trends could be elucidated as to which regioisomers may be more active than others.

Similarly, the position of the substituent on the aryl ring had a clear impact on the apparent solubility of the compounds in PBS, where the *ortho*- substituted compounds **41** (*o*CNA) and **46** (*o*AmA) were more soluble than the corresponding *para*- or *meta*- substituted derivatives. However, this finding has also been found to depend on the nature of the substituent, where Marcus Diamante (Ben Lab, PhD candidate) found that the *para*-*N*-fluorophenyl-D-gluconamide was more soluble than the *ortho*- or *meta*-derivatives in PBS.[331] In general, the ice recrystallization inhibition activity of compounds **39-41** and **44-46** was found to be lower than had been previously reported for *N*-aryl-D-gluconamides that were proven to improve cryopreservation outcomes, which had IC_{50} values in the range of 3-20 mM.[168,176,331] Therefore, it

was concluded that ice recrystallization inhibition activity was intolerant to a nitrile or amide functional group substitution on the aryl ring of *N*-aryl-D-gluconamides.

With respect to the ice recrystallization inhibition activity of the *O*-cyanophenyl-β-D-glucopyranosides and *O*-carbamoylphenyl-β-D-glucopyranosides, the *meta*-nitrile derivative **37** (*m*CNPh-Glc) was found to be significantly more active than the corresponding *para*- or *ortho*- derivatives (**30**, *p*CNPh-Glc or **38**, *o*CNPh-Glc) and all three of the amide-derivatives (**31**, **42-43**). However, the *para*- and *ortho*- substituted amide derivatives **31** (*p*AmPh-Glc) and **43** (*o*AmPh-Glc) were found to be significantly more active than the *meta*-amide derivative **42** (*m*AmPh-Glc). As previously discussed (**Figure 3-6**), Dr. Chantelle Capicciotti (Ben Lab, PhD 2014) found that for the *methoxy*- substituted derivative PMP-Glc (**26**), a *para*- substitution was essential to ice recrystallization inhibition activity as compounds **33-34** with *meta*- and *ortho*- substitutions resulted in dramatically decreased activity, but no difference in activity was observed upon shifting a the methyl substitution from the *para*- position to the *meta*- position for compounds **35-36**.[167] Therefore, consistent with the findings for the *N*-aryl-D-gluconamides, the impact of substitution positioning on ice recrystallization inhibition activity was functional group dependent and no clear trend as to which regiochemistry would be most active was observed.

It had been previously hypothesized by the Ben Lab that the electronic properties of the substituent may have an impact on ice recrystallization inhibition activity.[158] However, during an extensive structure-activity relationship (SAR) study of the *O*-aryl-β-D-glucopyranoside class of compounds by Dr. Capicciotti (Ben Lab, PhD 2014), no correlation between the electronic effects of a variety of *para*-substituents and ice recrystallization inhibition activity was observed;[158,167] this correlation study will be discussed in greater detail in *chapter 4*. Consequently, the impact of functional group substitution location on ice recrystallization inhibition activity was not caused solely by electronic effects and has been hypothesized to be confounded by several different factors.

3.2.5. Summary of the cryopreservation of RBCs using nitrile- and amide- containing ice recrystallization inhibitors

Cryopreservation can be used to extend the shelf-life of RBCs. However, to maintain RBC quality and functionality they must be cryopreserved in a solution of 40 % (w/v) glycerol as per the North American clinical standard.[1,44] The required deglycerolization of units prior to transfusion is a lengthy procedure (approximately 50 minutes) consisting of multiple washing steps that precludes the use of cryopreservation as a storage method for the vast majority of RBCs that are used clinically. Recently, the Ben Lab reported

that small-molecule carbohydrate-based ice recrystallization inhibitors (IRIs) could be used to reduce the required concentration of glycerol during cryopreservation to only 15 % (w/v) using IRIs *p*BrPh-Glc (**25**, 30 mM) or PMP-Glc (**26**, 110 mM).[162] These findings were significant as the processing times for deglycerolization would be significantly reduced and could ultimately improve the feasibility of routinely using cryopreserved RBCs in the clinical setting. However, it was noted that deglycerolization in the presence of these IRIs could not be achieved, and ultimately resulted in significant hemolysis of the RBCs.[158,214] Later studies by Dr. Poisson (Ben Lab, PhD 2019) investigating azide-containing IRIs found that cryopreservation in 15 % glycerol and subsequent deglycerolization could be achieved in two washing steps for *p*N_3Ph-Glc (**29**).[214] However, despite its success on both small and large scale, the azide functional group of **29** was photolabile and could readily decompose thus limiting its ability to be used in clinical cryopreservation applications for the long-term storage of RBCs.

It was hypothesized that deglycerolization in the presence of *p*N_3Ph-Glc (**29**) was achievable due to its lower hydrophobicity compared to *p*BrPh-Glc (**25**) or PMP-Glc (**26**). As a result, we sought to explore small-molecule IRIs that contained similar structural features to *p*N_3Ph-Glc (**29**) but with improved chemical stability. It was hypothesized that by incorporating a *para*-nitrile or *para*-amide functional group to the *O*-aryl-β-D-glucopyranoside scaffold in place of the *para*-azide functional group, we would be able to maintain the improved cryopreservation outcomes and successful deglycerolization that was achieved with *p*N_3Ph-Glc (**29**). Compounds *p*CNPh-Glc (**30**) and *p*AmPh-Glc (**31**) were synthesized in 41 % and 12 % overall yields respectively and were found to have IC_{50} values of 53.1 mM (95 % CI [42.1-66.9]) and 40.8 mM (95 % CI [34.1-48.9]) respectively. As the ice recrystallization inhibition activity of **30** and **31** was only reduced 2-fold compared to **29**, we sought to explore their potential as additives for the cryopreservation of RBCs using reduced concentrations of glycerol due to their improved chemical stability. Unfortunately, no significant improvement in the percentage of intact RBCs was observed post-thaw with the addition of *p*CNPh-Glc (**30**, 12.5-40 mM) or *p*AmPh-Glc (**31**, 2.5-50 mM). Exploration into whether these cells could be successfully deglycerolized was warranted, but due to laboratory shutdowns caused by the COVID-19 pandemic these experiments could not be completed but would be of interest for future studies.

In an effort to improve the ice recrystallization inhibition activity of compounds **30** and **31**, regio-isomers were synthesized that placed the nitrile and amide functional groups into the *meta*- and *ortho*-positions, as well as the corresponding open-chain *N*-aryl-D-gluconamide derivatives. The compounds *m*CNPh-Glc (**37**) and *o*AmA (**46**) were discovered to have comparable ice recrystallization inhibition activity to *p*N_3Ph-Glc (**29**) with IC_{50} values of 26.8 mM (95 % CI [24.5-29.3]) and 35.9 mM (95 % CI

[33.7-38.1]) respectively. Future work should focus on the testing of the more active nitrile-IRI *m*CNPh-Glc (**37**) and amide-IRI *o*AmA (**46**) in cellular applications. Overall, these results highlighted that nitrile- and amide- containing IRIs may be suitable analogues for the cryopreservation of RBCs at reduced glycerol concentrations.

3.3. Investigating the internalization of *O*-aryl-β-D-glucopyranosides IRIs

While small-molecule carbohydrate-based IRIs had been explicitly reported to improve the cryopreservation outcomes of RBCs by controlling extracellular ice growth during freezing,[162,166,248] it had also been noted that these IRIs (including *p*BrPh-Glc, **25** and PMP-Glc, **26**) could be cell-penetrating and inhibit intracellular ice recrystallization.[162,214,218] The exact mechanism by which intracellular ice formation occurs remains debated in literature,[27,34,332–335] however it is generally considered to be lethal to cells due to the resultant ice recrystallization and mechanical damage that can occur.[26,27,30–32] It is important to note that the location, size, and amount of intracellular ice is related to how much damage to cells is observed; where for some cell types, such as those with a high number of gap junctions, intracellular ice formation can be innocuous.[33,336] However, for most cell types the inhibition of intracellular ice recrystallization is considered to be an important factor for improving cryopreservation outcomes.

Early studies by Dr. Capicciotti (Ben Lab, PhD 2014) and Dr. Poisson (Ben Lab, PhD 2019) using an interrupted graded freezing protocol[33,35,337,338] concluded that the cryopreservation outcomes of RBCs in the presence of both *p*BrPh-Glc (**25**, 30 mM) and PMP-Glc (**26**, 110 mM) were consistent with that of a cell-permeating cryoprotectant.[162,218] Dr. Poisson (Ben Lab, PhD 2019) later visualized the effect of these IRIs on intracellular ice growth in HUVEC cells;[218] while HUVEC cells had been previously used in literature to investigate intracellular ice formation,[291,339,340] this was the first reported approach to observe subsequent intracellular ice growth (*i.e.,* recrystallization) and its inhibition using small-molecule IRIs.[218] To visualize intracellular ice growth, the HUVEC cells were stained with SYTO 13 (a fluorescent nucleic acid stain) to provide visualization of the cell nuclei and suspended first in solutions of 0.9 % NaCl with and without compound **25** (*p*BrPh-Glc, 30 mM) or compound **26** (PMP-Glc, 110 mM).[218]

First, the cell suspensions without IRI (in 0.9 % NaCl alone) were rapidly cooled (90 °C/min) to -40 °C to permit the formation of intracellular ice. The cells were then visualized and monitored by fluorescence microscopy using a technique developed by Acker and Croteau;[341] ice crystals presented as dark black spots within the nucleus as the large molecular weight fluorescent dye was excluded from the ice lattice (**Figure 3-9**). As the temperature was raised and the cells began to warm, ice recrystallization occurred resulting in the formation of fewer, larger ice crystals (**Figure 3-9**).[218] Decreasing the rate of

warming (from 25 °C/min to 2 °C/min) exacerbated the rate of ice recrystallization and as expected, where larger mean ice grain sizes were observed at the final temperature of -10 °C for the slower (2 °C/min) warming rate (**Figure 3-9C**).[218]

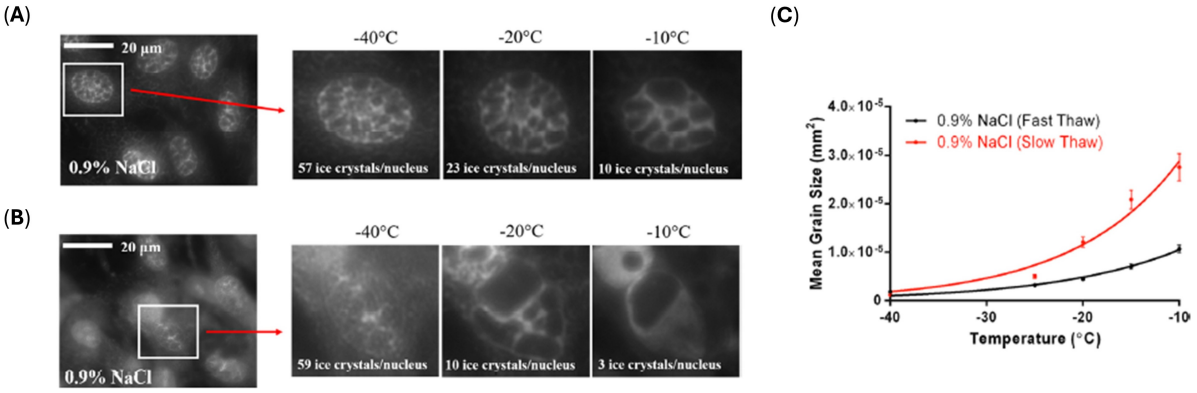


Figure 3-9. Intracellular ice formation in HUVEC cells cooled to -40 °C at 90 °C/min in 0.9 % NaCl using SYTO 13 staining (5 µM). Using warming rates of (**A**) 25 °C/min and (**B**) 2 °C/min. (**C**) The mean grain size of ice crystals (mm^2) is reported as a function of temperature (°C) for each warming rate. Data reported as the mean ± standard error of the mean (SEM) and fit to a mono-exponential growth equation where $R^2 = 0.98$ (fast thaw) and 0.97 (slow thaw). *Reproduced from Poisson et. al. (2019) under CC-BY from ACS Publications*.[218]

These experiments were then repeated in the presence of IRIs **25** (*p*BrPh-Glc, 30 mM) and **26** (PMP-Glc, 110 mM) to determine if a reduction in ice recrystallization could be observed.[218] The addition of either IRI resulted in significantly smaller ice crystals than 0.9 % NaCl alone as temperatures were warmed to -20 °C with either warming rate (**Figure 3-10**).[218] As temperatures were warmed to -10 °C, ice crystals in the presence of *p*BrPh-Glc (**25**) remained significantly smaller than those in 0.9 % NaCl alone (**Figure 3-10**).[218] However, rapid ice crystal growth was observed when the cells were slowly warmed (2 °C/min) to -10 °C in the presence of PMP-Glc (**26**), indicating that *p*BrPh-Glc (**25**) was more effective than PMP-Glc (**26**) at inhibiting ice recrystallization in this experiment (**Figure 3-10**).[218]

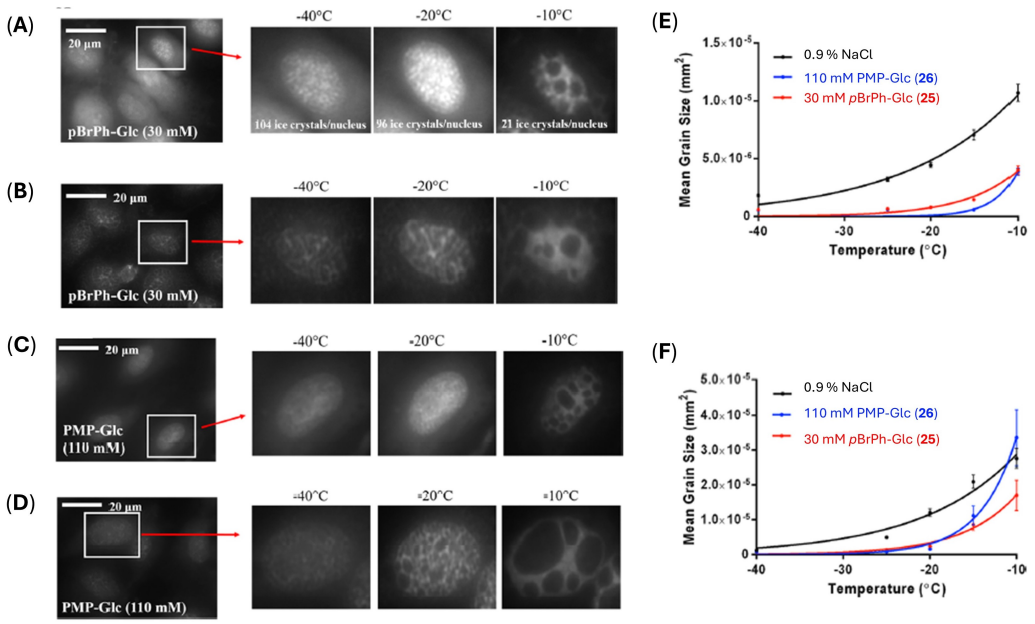


Figure 3-10. Intracellular ice formation in HUVEC cells cooled to -40 °C at 90 °C/min in 0.9 % NaCl with the addition of either (**AB**) 30 mM *p*BrPh-Glc (**25**) or (**CD**) PMP-Glc (**26**) using SYTO 13 staining (5 µM). Warming rates of (**AC**) 25 °C/min and (**BD**) 2 °C/min. (**EF**) The mean grain size of ice crystals (mm^2) is reported as a function of temperature (°C) for each warming rate. Data reported as the mean ± standard error of the mean (SEM) and fit to a mono-exponential growth equation. *Reproduced from Poisson et. al. (2019) under CC-BY from ACS Publications*.[218]

This study highlighted that small-molecule IRIs **25** (*p*BrPh-Glc, 30 mM) and **26** (PMP-Glc, 110 mM) were inhibitors of intracellular ice recrystallization, capable of controlling the rate and extent of recrystallization.[218] In addition to the hemolysis profiles of **25** (*p*BrPh-Glc) and **26** (PMP-Glc), these results implied that these IRIs were capable of permeating cellular membranes in order for this inhibition to occur.[162,218] However, given these were only indirect measurements of internalization we sought to explore more direct visualization measures of cellular uptake/internalization that could be achieved using optical and/or light microscopy techniques.

3.3.1. Techniques for imaging biological processes

Visual microscopy methods have revolutionized our understanding of biological processes, permitting a more detailed understanding of cellular processes and behaviour that have led to critical innovations in areas such as drug discovery and clinical medicine.[342–344] The earliest discovered technique, optical microscopy, utilizes visible light that is passed through multiple lenses to quickly generate a magnified view of a sample in a non-invasive manner;[345,346] however, as cells are clear and colourless these imaging techniques lack sufficient contrast to study internal cellular structures in detail.[346] Cell structures and components can be stained using different organic dyes such as Coomassie blue (for non-specific staining of proteins) or ethidium bromide (for staining of DNA by intercalation) to enhance contrast during

microscopy imaging.[347] However, these staining procedures often require "mounting" or "fixing" of the cells to a microscope slide which does not permit imaging of a live cell in its natural physiological state.[347] Alternatively, the discovery of phase contract microscopy made it possible for researchers to study the process of cell division in living cells by taking advantage of how light is differentially scattered by distinct cellular components and translating that to varying brightness levels on an image; this technique is one of the few methods able to quantify cellular structure without the use of fluorescent molecules.[346,348,349]

The addition of fluorescence to microscopy achieved significant improvements in the specificity and contrast of optical microscopy and permitted the direct observation of specific proteins or organic chemical compounds of interest within a cell with down to resolution of 10 nm.[345,350–352] Fluorescent labels, which absorb and emit light at different wavelengths depending on the molecule's properties,[345,352] have been instrumental in the visualization of numerous biomolecules that are critical to advancing scientific research. However, while these labels can provide high sensitivity images of a molecule that it is chemically bound to, they are often large and bulky molecules (*e.g.,* green fluorescent protein has a molecular weight of ~27 kilodalton) that can alter biological activity when used to tag and visualize small molecules.[345,352–354] Another significant drawback of fluorescent labelling is that the fluorophores undergo quenching and photobleaching after a limited period of time under excitation conditions, which ultimately leads to fluorophore destruction and can cause undesired physiological effects to the biological material of interest and lead to cell death.[345,352]

An alternative to brightfield and fluorescence microscopy that can provide both contrast and chemical selectivity is vibrational spectroscopy, including infrared (IR) and Raman scattering techniques.[354,355] These methods can be non-invasive, non-destructive, and can identify structural features of a molecule without requiring labels using the intrinsic vibration of different chemical bonds.[354–356] As a result, vibrational spectroscopy techniques can be used to visualize small molecules in a biological system without altering native activity. However, IR microscopy requires long excitation wavelengths that can result in low spatial resolution and more importantly the broad absorption of water makes imaging of aqueous systems extremely challenging.[355] To contrast, Raman scattering microscopy makes use of a shorter wavelength and operates within the visible spectral range, but requires high power, high excitation intensities, and long integration times that are often not well tolerated by the biological sample being imaged.[353,355] There are also complications with overlapping fluorescence excitation that limit the use of spontaneous Raman scattering microscopy for imaging biological systems.[355–358] Ultimately, these spontaneous vibrational methods are often limited to conclusions based solely on the structural fingerprints

of molecules that can be determined from the unique vibrational modes of their chemical bond.[353,355,356,359–363]

3.3.1.1. Non-linear Raman scattering techniques and their use for investigating water molecules as they relate to cryopreservation

Over the last several decades Raman spectroscopy methods have been developed that improve the sensitivity, spatial resolution, and/or specificity of spontaneous Raman microscopy.[364] Live cell imaging using Raman techniques has been made possible by use of wavelengths just outside the visible range (785 nm) to avoid degradation and photodamage from visible wavelengths and the coupling of Raman microscopes to cell incubators to provide 'true' live-cell study conditions.[365] While these improvements have enabled Raman imaging techniques to observe slower dynamic processes such as cell division or the distribution of biomolecules,[366,367] these spontaneous methods are limited by slow acquisition times and low efficiency signals. To overcome these challenges in sensitivity, non-linear scattering techniques including coherent anti-Stokes Raman scattering (CARS) and stimulated Raman scattering (SRS) have been developed.[364]

To understand the differences in these techniques, it is critical to understand the origins of a Raman signal. When a photon of light (often referred to as the pump photon) from a laser in the visible (or very near infrared or ultraviolet) range is directed onto a sample it becomes "scattered". Raman-type scattering occurs when the resultant scattered photon's energy is different from the pump photon's; if the energy of the scattered photon is equal to the pump photon, the process is known as Rayleigh scattering (**Figure 3-11A**).[364] Raman scattering can be further distinguished based on whether the resultant photon gains or loses energy with respect to the pump photon, referred to as Stokes scattering (red-shifted light) and anti-Stokes scattering (blue-shifted light) respectively (**Figure 3-11A**).[364] The difference in energy between the pump and scattered photon corresponds to the amount of energy that is required to excite a particular molecular vibration, and ultimately corresponds to the Raman signal that is observed for unique chemical bonds.[364]

Spontaneous Raman is known as an incoherent process, where once the pump photon is excited its relaxation from the virtual state to the final state can happen at any point in time, and to any possible final state.[364] Typically, only 1 in 10^8 photons undergo spontaneous Raman scattering which in part causes the relatively weak signals inherent to this technique.[364] On the other hand, SRS and CARS remove this randomness (and are therefore referred to as coherent processes) by introducing a second photon that stimulates the relaxation of the excited photon (**Figure 3-11B** and **C**).[364] While both SRS and CARS are

non-linear, optical forms of Raman spectroscopy, CARS uses two lasers to generate an anti-stokes signal (**Figure 3-11C**) that results in a lower required input power for the same signal output compared to SRS and with signals ~10^6 times stronger than spontaneous Raman.[356,358,364]

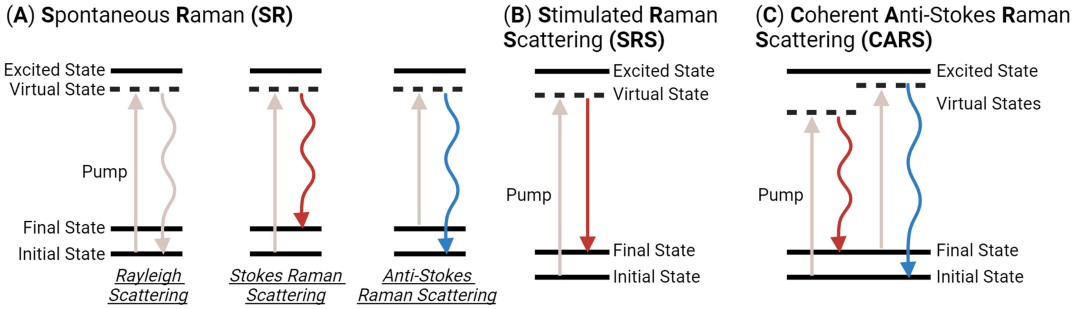


Figure 3-11. Energy diagrams representing (**A**) spontaneous Raman, (**B**) stimulated Raman scattering (SRS), and (**C**) coherent anti-stokes Raman scattering (CARS).

Outside of a live cell environment, spontaneous Raman spectroscopic methods have been used extensively to study the molecular structure of liquid water,[368–372] supercooled water,[370,373–375] ice,[376–378] and the ice-water interface[66,379]. Importantly, Raman spectra of the ice-water interface (known as the quasi-liquid layer; QLL) of a growing ice crystal found it to be primarily "water-like", with no observed peaks that corresponded to water in the solid "ice" state; slight differences from the spectra of bulk water were observed that were hypothesized to be the result of increased hydrogen bonding in the interstitial space.[379] Raman spectroscopy was also used to show that ionic molecules (*i.e.,* NaCl, HCl, HNO_3) change the hydrogen bonding network of the QLL.[66]

Solutions of antifreeze glycoproteins (AFGPs), both liquid and frozen, have also been investigated by Raman spectroscopy by comparing the spectra of bulk water and ice in the absence and presence of compound.[380] The Raman spectra of 5 % (w/v) solutions of AFGP-4 and AFGP-8 (**1**) at -0.3 °C and -5.0 °C showed distinct differences from pure water and bulk ice that were attributed to changes in hydrogen bonding caused by the presence of the antifreeze molecules; this effect was not observed at a 1 % (w/v) concentration of either AFGP.[380] The authors of this study also observed differences in the affinities of each AFGP to ice, where AFGP-4 was found evenly distributed throughout the ice lattice while AFGP-8 (**1**) was completely excluded from the ice phase.[380] Ultimately, these investigations have facilitated a greater understanding of the dynamics of water molecules at different temperatures and pressures that have been critical for advancing cryopreservation techniques and protocols.

Given its advantages for live-cell imaging over spontaneous Raman, the Ben Lab, in collaboration with researchers at the National Research Council (NRC; Ottawa, ON), has used CARS microscopy

techniques to investigate the nature of ice-water structure.[381] The obtained results using CARS microscopy techniques were consistent with those in the literature using other Raman spectroscopy methods and formed the foundation for the direct visualization of small-molecule IRIs in the intracellular space of live cells that will be discussed in this chapter.

3.3.1.2. Live cell imaging using Raman spectroscopy

Over the last several years, Raman spectroscopy methods have been used to visualize the internalization and permeation of small-molecule drugs and ligands within the intracellular space.[353,354,356,382,383] It is important to note that many of the Raman signals for these small molecules overlap with the chemical bonds of endogenous structures, including lipids and proteins.[353] Therefore, to provide high contrast from the background cellular environment and improve signal-to-noise ratios, it is critical that the compound of interest has a chemical bond that is not naturally found in the cellular space and does not overlap with endogenous Raman signals.[353,354] For the Raman spectroscopy of biologics, the spectral region below 1800 cm^{-1} is where most heteroatom-based functional groups appear (including alcohols, amines, amides, carbonyls, and phosphates) while the region above 2800 cm^{-1} represents the signals for most aliphatic bonds; therefore, the region between 1800 cm^{-1} and 2800 cm^{-1} is known as the "silent region" where most biological molecules do not produce a Raman signal (**Figure 3-12**).[353,354] Functional groups including $-N_3$ (azide), -C≡N (nitrile), -CD (deuterium-labelled carbon), and -C≡C (alkyne) functionality are found within this region and are therefore useful as tags for observing small molecules with Raman scattering techniques (**Figure 3-12**).

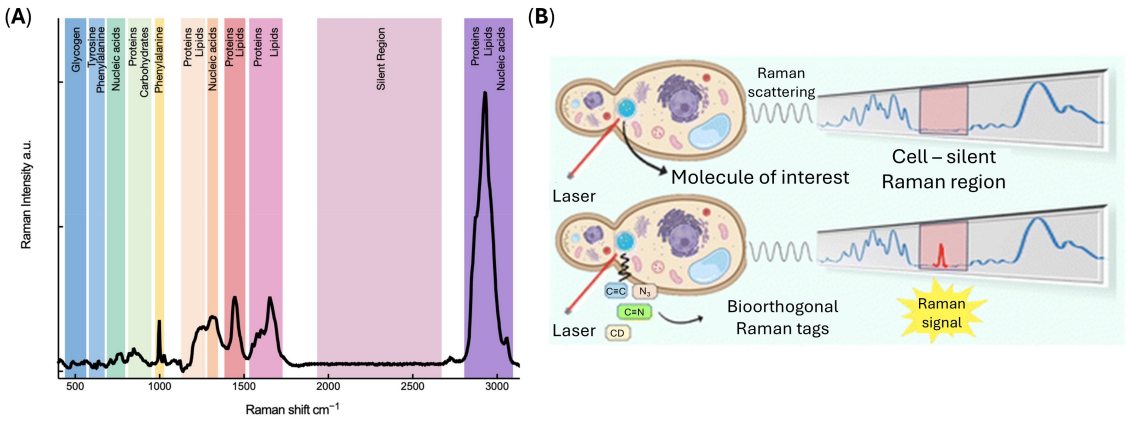


Figure 3-12. (**A**) Raman spectrum of a single cell of human primary glioblastoma (U87 cell line) with various band regions of interest highlighted, including the silent region (1800 cm^{-1} to 2800 cm^{-1}). *Reproduced from Xu et. al. (2021) under CC-BY from MDPI.*[384] (**B**) Representation of the cell-silent region and the signal generated from biorthogonal Raman tags. *Reproduced from Vardaki et. al. (2024) under CC-BY from RSC.*[385]

Raman reporter molecules have been used to study a variety of different cellular processes, including DNA synthesis using alkyne-tagged deoxyuridine (EdU: 5-ethynyl-2'-deoxyuridine) (**Figure 3-13A**).[383] In addition, Raman spectroscopy techniques have been used to monitor drug dynamics in live-cell systems. For example, Tipping *et. al.* investigated their drug candidate, an inhibitor of discoidin domain receptor 1 (DDR1) for the treatment of various cancers and inflammatory diseases, using SRS.[382] Their inhibitor, 7RH, contained an internal alkyne (-C≡C) functional group that permitted the simultaneous measurement of cell viability and drug localization over a period of 8 hours using SRS, without the need for the addition of dyes or sensors that would have altered the cell's natural physiological state (**Figure 3-13B**).[382]

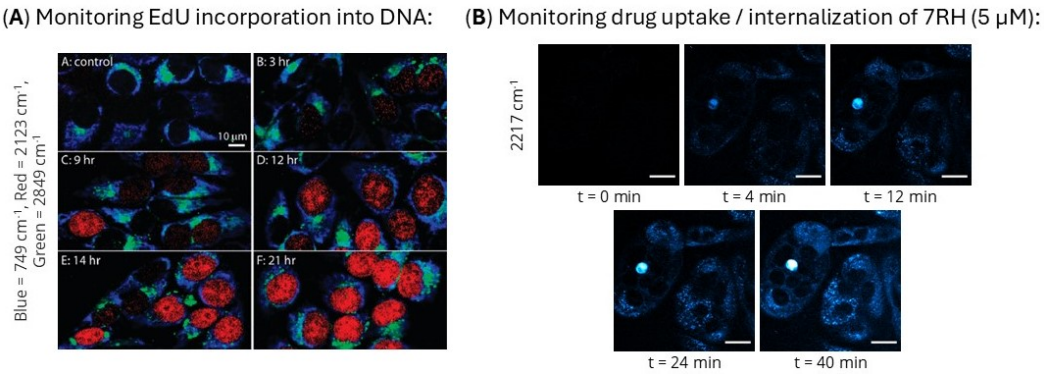
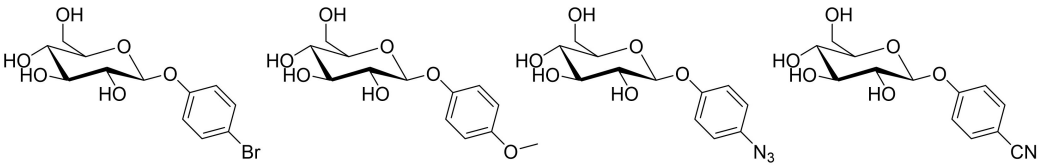


Figure 3-13. (**A**) Yamakoshi *et. al.*, visualization of HeLa cells cultured with EdU to generate merged images from 749-cm^{-1} (cytochrome C), 2123-cm^{-1} (alkyne, silent region, EdU), and 2849-cm^{-1} (lipids) wavenumbers (blue, red, and green channels respectively) over a course of 21 hours using spontaneous Raman.[383] (**B**) Live cell images acquired at 2217 cm^{-1} to track the internalization of 7RH over a period of 45 minutes represented as blue in colour using stimulated Raman scattering (SRS) (scale bars 20 μm).[382] *Figures reproduced with permission from their respective sources.*[382,383]

Considering the broad scope of Raman reporter small-molecules that have been successfully used for live-cell imaging with high sensitivity and specificity, it was of interest to the Ben Lab to investigate small-molecule IRIs using Raman imaging. More specifically, we hypothesized that Raman microscopy techniques would facilitate observation of the internalization and localization of these IRIs to gain insight into their mechanism of action within the cellular environment.

3.3.2. Raman-active small-molecule carbohydrates

The *O*-aryl-β-D-glucopyranoside IRIs *p*BrPh-Glc (**25**) and PMP-Glc (**26**) that were used for the previous internalization studies in RBCs and HUVEC cells, with *p*-bromo- and *p*-methoxy- aryl substitution respectively, do not show strong Raman signal in the silent region. As a result, these compounds were not directly suitable for investigation using Raman scattering techniques as their vibrational signals would not be able to be distinguished from the background cellular environment. Therefore, we investigated novel small-molecule candidates that maintained the *para*-substituted *O*-aryl-β-D-glucopyranoside IRI scaffold but were substituted with Raman reporters, including *para*-azide (*p*N_3Ph-Glc, **29**) or *para*-nitrile (*p*CNPh-Glc, **30**) functional groups to generate high resolution images that could provide context regarding the internalization and localization of IRIs in a cellular environment (**Figure 3-14**).



*p*BrPh-Glc (**25**) PMP-Glc (**26**) *p*N_3Ph-Glc (**29**) *p*CNPh-Glc (**30**)

Figure 3-14. Structures of established *O*-aryl-β-D-glucopyranoside IRIs *p*BrPh-Glc (**25**) and PMP-Glc (**26**) as well as their Raman reporter analogues with *para*-azide (*p*N_3Ph-Glc, **29**) or *para*-nitrile (*p*CNPh-Glc, **30**) functional groups.

While the alkyne functional group is frequently used for Raman microscopy methods and has been reported to have a sharper and stronger signal compared to the nitrile or azide substituents,[353,386] it was not investigated during the initial imaging experiments due to concerns with poor aqueous solubility of the final target. Future Raman imaging experiments with small-molecule carbohydrate ice recrystallization inhibitors could explore this functional group in greater detail. Furthermore, despite poor chemical stability of the azide functional group that would affect its adoption for large scale cryopreservation applications,[324,325] we were interested in exploring its potential as a Raman reporter for comparative purposes and research-oriented applications. The synthesis of *p*N_3Ph-Glc (**29**) and *p*CNPh-Glc (**30**) was previously described in *section 3.2.1*.

3.3.2.1. Raman imaging methods development using small-molecule carbohydrates containing Raman tags

To determine whether a Raman signal could be detected for compound **29** prior to chemical decomposition, it was prepared as a 20 mM solution in distilled water and a spontaneous Raman spectral scan was initiated for a 20 µL droplet of the solution. Unfortunately, the spectrum of the *p*-azide compound (*p*N_3Ph-Glc, **29**) following excitation with a 514-nm laser returned a broad, featureless signal typically associated with interference by fluorescence.[387] The fluorescence interference was further confirmed with adjustment of the laser to 785 nm, where the energy level was no longer sufficient to excite fluorescent molecules and the signal was no longer observed;[387] however, inconsistencies in the equipment prevented proper acquisition of the entire spectra at this wavelength. While Raman systems can be optimized to reduce the effects of fluorescence,[388] a specific vibrational band of interest must be known; as the azide functional group has a wide range of reference excitation wavelengths, optimization for this functional group could not be achieved. Furthermore, the azide functional group is photolabile and can readily decompose,[324,325] which likely contributed to the poor signal acquisition with samples of *p*N_3Ph-Glc (**29**). As a result, further studies developing the Raman imaging system for small-molecule carbohydrate-based IRIs focused solely on the nitrile-containing derivatives.

For the spontaneous Raman spectra of compound **30** (*p*CNPh-Glc), a 20 µL droplet (50 mM in distilled water) was placed onto a glass coverslip. From this sample, a very weak spontaneous Raman signal at 2235 cm^{-1} (using a 514 nm laser) could be observed throughout the droplet, as was expected for the uniform distribution of compound in solution at low millimolar concentrations. This result was promising, as no fluorescence interference was observed which had been problematic for *p*N_3Ph-Glc (**29**). As we were also interested in observing these compounds in a frozen state, the glass coverslip with sample (50 mM) was then placed into a cold stage cooled to -10 ºC, followed by manual ice nucleation using metal forceps cooled in dry ice. When imaging using the on-resonance wavenumber for the nitrile bond (2235 cm^{-1}) with CARS microscopy, bright intensity lines could be observed within the interstitial space between ice crystals that could not be observed when the wavenumber was shifted off resonance (into the lipid range of the spectrum, 2300 cm^{-1}) (**Figure 3-15A**). A spectral scan of the images in **Figure 3-15A** showed maximum peak intensity at the on-resonant wavenumber of 2235 cm^{-1} that was detectable at ~2.6x the background signal (noise) intensity for the bright areas in between ice crystals (**Figure 3-15D**). Unfortunately, further optimization of the system was required as condensation was found throughout the optical path that resulted in complicated dark artifacts covering both images (**Figure 3-15A**). After optimization, the experiments were repeated with various dilutions of the *p*CNPh-Glc (**30**) which resulted in clearer images with a signal that was distinguishable from background noise up to a 20x dilution, or approximately 2.5 mM in concentration (**Figure 3-15C**), confirming that low millimolar detection of *p*CNPh-Glc (**30**) was possible using this protocol.

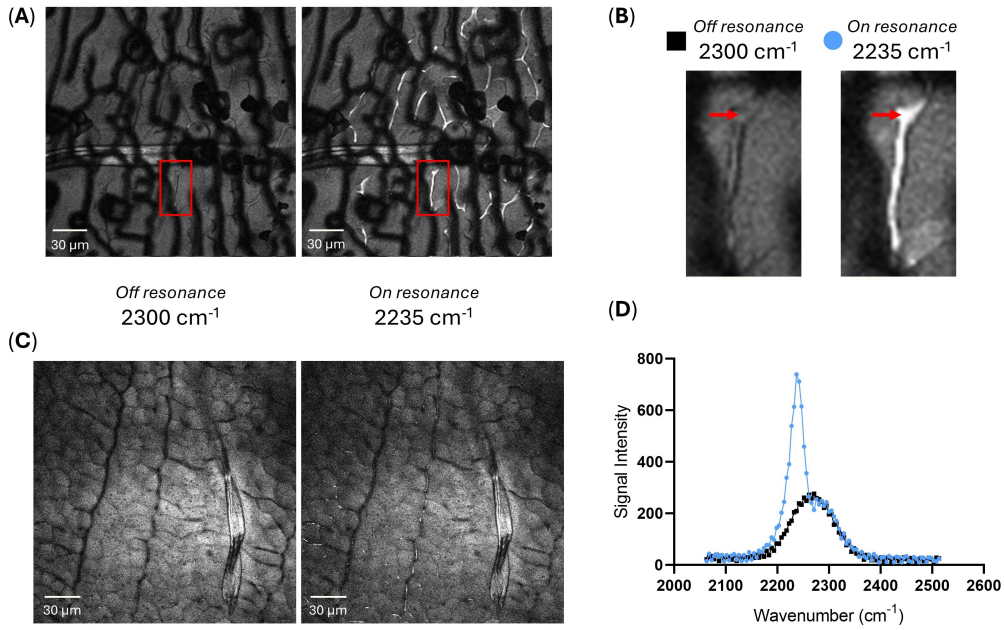


Figure 3-15. Images of ice in the presence of *p*CNPh-Glc (**30**) measured using CARS microscopy using an off-resonance wavenumber of 2300 cm^{-1} or an on-resonance wavenumber of 2235 cm^{-1} with operating wavelengths of 844 nm and 1040 nm as well as 12 nm and 7 nm bandwidth respectively. (**A**) 50 mM *p*CNPh-Glc (**30**). Dark artifacts caused by condensation within the optical path. (**B**) Zoomed in region of panel A images highlighted in red. (**C**) 2.5 mM *p*CNPh-Glc (**30**) with optimized imaging set up. Cotton fibre present for focus in both sets of images. (**D**) Plot of Raman signal intensity with respect to a complete spectral scan of the zoomed in regions of the images in panel (**B**) for comparing off-resonance and on-resonance wavenumbers.

Encouraged by the ability to reliably detect the Raman signal and obtain images in both a frozen and unfrozen state, we sought to determine the optimum conditions and parameters for live-cell imaging experiments. Unfortunately, immediately following collection of this data, COVID-19 forced the shutdown of all laboratory spaces. Reduced capacity facilities as part of safe return-to-work protocols made direct collaborations to continue Raman imaging experiments with the NRC challenging. However, these preliminary studies validated that it was possible to visualize nitrile-containing ice recrystallization inhibitors using Raman imaging techniques such as CARS.

3.4. Screening of *nitrile*-containing ice recrystallization inhibitor candidates

As the nitrile-containing Raman reporter compounds were intended for use in the cryopreservation of biological systems, steps towards optimizing ice recrystallization inhibition activity and cytotoxicity were a critical part of the development process. Therefore, while collaborative imaging experiments were on hold due to the COVID-19 pandemic, it was of interest to investigate the regio-isomers of *p*CNPh-Glc (**30**) with the nitrile functional group in the *meta*- (**37**) or *ortho*- (**38**) positions as well as the aryl nitrile-containing *N*-aryl-D-gluconamide derivatives (**39-41**) that had already been synthesized and tested for ice recrystallization inhibition activity as part of RBC cryopreservation experiments (*see section 3.2.4*).

Of the six compounds, *m*CNPh-Glc was the most active ice recrystallization inhibitor with an IC_{50} of 26.8 mM (95 % CI [24.5-29.3]) (**Figure 3-16**). As the ice recrystallization inhibition activity of compounds **39-41** was found to be significantly lower than had been previously reported for *N*-aryl-D-gluconamides,[168,176,331] these compounds were not investigated for live-cell imaging experiments.

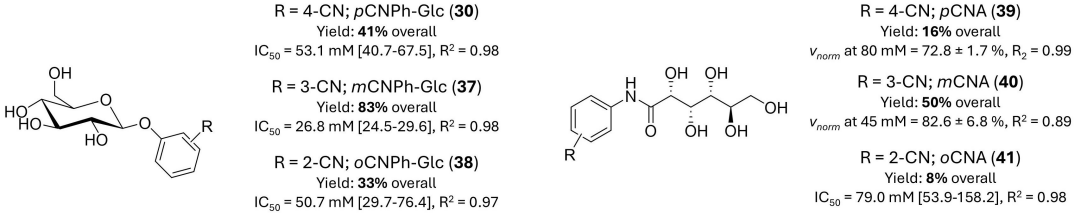


Figure 3-16. Structures, chemical synthesis yields, and ice recrystallization inhibition activity (IC_{50} as measured by the 5-minute splat-cooling assay) of nitrile-containing *O*-aryl-β-D-glucopyranosides **30** and **37-38** and *N*-aryl-D-gluconamides **39-41**.

3.4.1. Assessment of the cytotoxicity of nitrile- containing O-aryl-β-D-glucopyranosides

As the *nitrile*-containing *O*-aryl-β-D-glucopyranosides were intended for use in a live-cell environment, it was critical that the compounds be screened for their *in vitro* cytotoxicity prior to any cryopreservation or live-cell imaging studies. The cytotoxicity of compounds **30** and **37-38** was assessed using a resazurin-based colorimetric assay that measured cellular metabolic activity. As previously discussed in <u>*section 2.3.2.4*</u>, resazurin is a cell-permeable REDOX indicator that is naturally low in fluorescence (deep purple-blue colour) but viable cells with active metabolism can use a molecule of NADH to reduce resazurin to resorufin (pink in colour), which is highly fluorescent.[272] Cell viability can then be calculated by comparing the fluorescence output of each well to positive and negative controls. The cytotoxicity of each compound was assessed in HepG2 cells and a dose-response curve with respect to cell viability was generated following a 24-hour (37 ºC, 5 % CO_2) incubation with various compound concentrations.

After the incubation, all three compounds were found to be cytotoxic at similar concentrations, with LD_{50} values between 26.8 mM and 33.4 mM (**Figure 3-17**); compound **30** (*p*CNPh-Glc) was found to have an LD_{50} of 26.8 mM (95 % CI [26.2-27.5]), compound **37** (*m*CNPh-Glc) had an LD_{50} of 33.4 mM (95 % CI [29.5-37.8]), and compound **38** (*o*CNPh-Glc) had an LD_{50} of 31.4 mM (95 % CI [30.6-32.3]). As was discussed with the cytotoxicity assessment of *p*BrPh-Glc (**25**) and 2FA (**27**) in <u>*section 2.3.2.4*</u>, the 24-hour incubation is significantly longer than the cells would be exposed to a compound during cryopreservation; however, it provides a point of reference that is often used as an initial toxicity screening checkpoint for small-molecule IRI candidates that have been synthesized in the Ben Lab and further cytotoxicity experiments are completed as indicated by these initial screens.

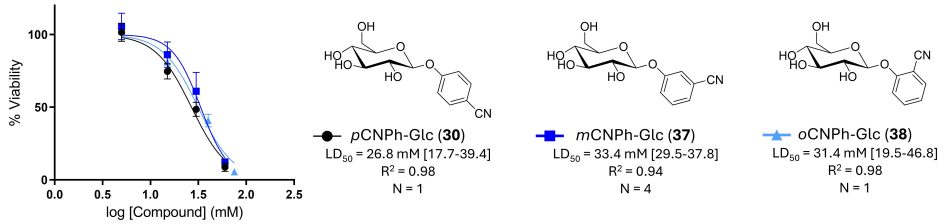


Figure 3-17. 24-hour toxicity measurement of compounds **30**, **37**-**38**. Plot of percent cell viability of HepG2 cells against logarithm transformed compound concentration (in mM). Determined by resazurin-based metabolic assay following 24-hour incubation at 37 °C in 5 % CO_2. Results reported as mean ± standard deviation (SD), N=1 for compounds **30** and **38**, N=4 for compound **37**.

While the three compounds had very similar cytotoxicity curves and relative LD_{50} values, it was most important to understand whether the compounds were toxic at concentrations where ice recrystallization was inhibited. For this comparison we determined each compound's efficacy index (EI), which was calculated as a ratio of LD_{50}/IC_{50}. For compounds **30**, **37**-**38**, only compound **37** (*m*CNPh-Glc) was calculated to have a EI > 1 (EI = 1.25) (**Figure 3-18**). Compounds **30** (*p*CNPh-Glc) and **38** (*o*CNPh-Glc) were found to have EI values between zero and one (0.50 and 0.62 respectively), meaning that at concentrations that were considered active for ice recrystallization inhibition activity there was also significant toxicity risk to the cells.

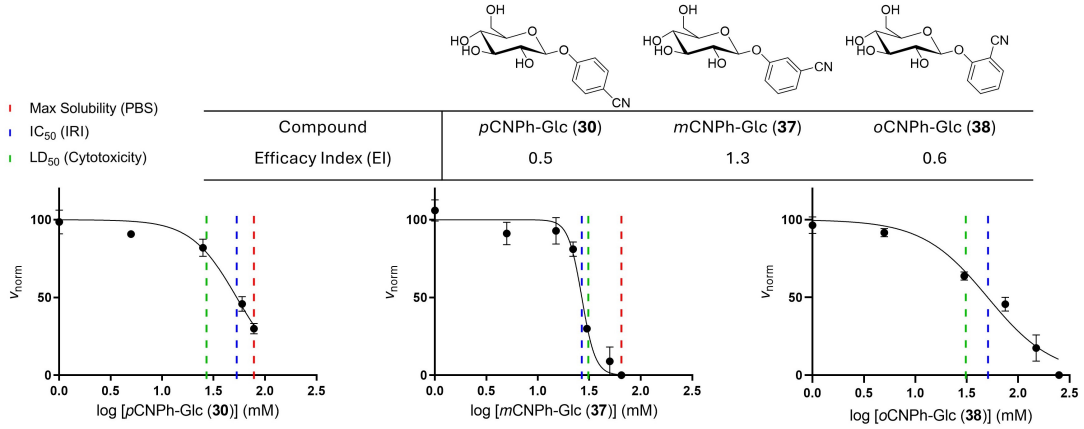


Figure 3-18. Plot of ice recrystallization inhibition activity of compounds **30**, **37**-**38** for visualization of efficacy index (EI). Red line denotes apparent maximum solubility in PBS. Blue line denotes IC_{50} of ice recrystallization inhibition activity. Green line denotes LD_{50} of cell viability as determined from **Figure 3-17**. Results reported as mean ± standard deviation (SD).

Although the EI for *m*CNPh-Glc (**37**) was greater than 1, its therapeutic window was quite small at only 6.6 mM. While the IC_{50} concentration for a small-molecule IRI provides information about its dose-dependent activity, these compounds are often used at concentrations above their IC_{50} in cryopreservation applications in order to achieve their maximum efficacy. For example, *p*BrPh-Glc (**25**) and 2FA (**27**) are used in their respective cryopreservation applications at concentrations of 30 mM and

15 mM despite their IC_{50} values of 6.75 mM (95 % CI [6.27-7.28]) and 3.47 mM (95 % CI [3.41-3.52]) respectively (**Figure 2-2**). Furthermore, even though the amount of time that the cells would be exposed to the compound during an imaging experiment would be significantly shorter (a maximum of 8 hours) than the 24-hour incubation time of the cytotoxicity experiment, the cytotoxicity results with *p*BrPh-Glc (**25**) showed that shorter incubation times do not necessarily translate to reduced cytotoxicity (see *section 2.3.2.4*). As a result, extended cytotoxicity experiments with shorter incubation times were required in order to better understand the concentrations at which *m*CNPh-Glc (**37**) could be used during live-cell imaging experiments while minimizing the risk of significant damage to cellular structures.

3.4.1.1. Extended cytotoxicity studies of mCNPh-Glc (37)

Previous cytotoxicity measurements (*via* resazurin-based assay in *section 3.4.1*) of *m*CNPh-Glc (**37**) were assessed following a 24-hour incubation (37 °C, 5 % CO_2) with HepG2 cells (**Figure 3-17**). From this assay, the cells were found to be 60.9 ± 13.1 % viable when incubated with a 30 mM concentration (just above the compound's IC_{50}) of **37** (N=4, **Figure 3-17**). To assess the cytotoxicity of *m*CNPh-Glc (**37**) at time points more relevant to our intended internalization studies, shorter incubation times of 1, 3, and 5.5 hours were assessed using the resazurin-based cytotoxicity assay to monitor for deficiencies in active cellular metabolism. From this assay, a slight reduction in the cytotoxicity of *m*CNPh-Glc (**37**) was observed at higher concentrations with shortened incubation times compared to the 24-hour incubation (**Figure 3-19**); the LD_{50} for incubation of compound **37** after 24-hour incubation was found to be 33.4 mM (95 % CI [29.5-37.8], N=4) and after a 5.5-hour incubation it was found to be 55.3 mM (95 % CI [35.2-309.5], N=2) (**Figure 3-19**). When comparing the cytotoxicity of *m*CNPh-Glc (**37**) at the 30 mM concentration, incubation times did not appear to affect its cytotoxicity, where a 1-hour incubation resulted in cell viability of 59.3 ± 2.9 % (N=1) and a 24-hour incubation resulted in a cell viability of 60.9 ± 13.1 % (N=4) (**Figure 3-19**).

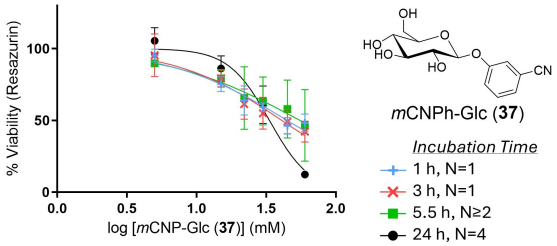


Figure 3-19. Cytotoxicity measurement of *m*CNPh-Glc (**37**) after various incubation times (1-24 hours). Plot of percent cell viability of HepG2 cells against logarithm-transformed compound concentration (in mM). Determined by resazurin-based metabolic assay following incubation at 37 °C in 5 % CO_2. Results reported as mean ± standard deviation (SD), N=4 for 24-hour incubation, N≥2 for 5.5-hour incubation, and N=1 for 1- and 3-hour incubations.

The inherent cytotoxicity of *m*CNPh-Glc (**37**) at concentrations near its IC_{50}, even at shorter incubations times, meant that any visualization of internalization may be confounded by a compromised cell membrane. However, the resazurin-based cytotoxicity assay measures the integrity of the cells from the perspective of metabolism which does not directly measure the integrity of the cellular membrane. Instead, membrane integrity can be directly assessed by measuring the activity of cytoplasmic enzymes, such as lactate dehydrogenase (LDH), that would be released into the cell culture medium upon damage to the cell membrane. For this assay, the quantity of LDH in the supernatant of cells was measured by monitoring the conversion of lactate into pyruvate that occurs *via* the concurrent reduction of positively charged nicotinamide adenine dinucleotide (NAD+) to uncharged nicotinamide adenine dinucleotide in its reduced state (NADH) by LDH (**Figure 3-20**). The NAD+ can then be regenerated by the conversion of the tetrazolium salt iodonitrotetrazolium (INT) to formazan by the co-enzyme diaphorase (**Figure 3-20**). The production of formazan is directly proportional to the amount of LDH released by a cell and therefore the absorbance of its red colour can be measured at 490 nm to quantify membrane integrity when compared to positive and negative controls.

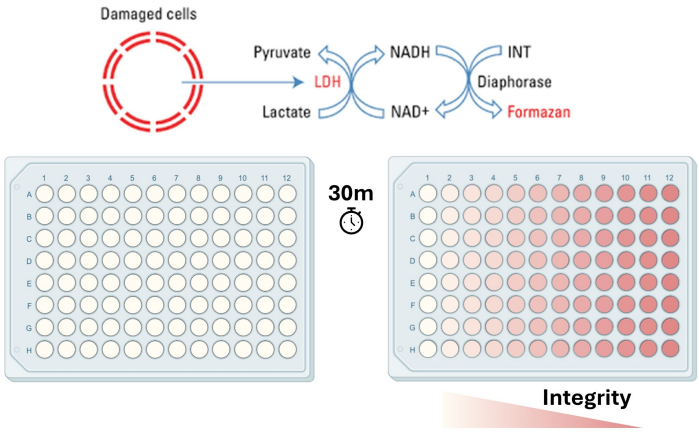


Figure 3-20. General schematic for the LDH cytotoxicity assay.[389]

The membrane integrity of HepG2 cells was therefore assessed following the incubation of HepG2 cells at 37 °C (5 % CO_2) for 1-24 hours with compound **37** (*m*CNPh-Glc) at several concentrations. When compared to the negative control (cell medium only), no meaningful membrane integrity loss was observed at any compound concentration with up to 5.5 hours of incubation (**Figure 3-21**). However, the 60 mM concentration showed a decrease in membrane integrity after a 24-hour incubation compared to a 5.5-hour incubation (**Figure 3-21**). Most importantly, no significant membrane integrity loss was observed at the 30 mM concentration for any incubation time point.

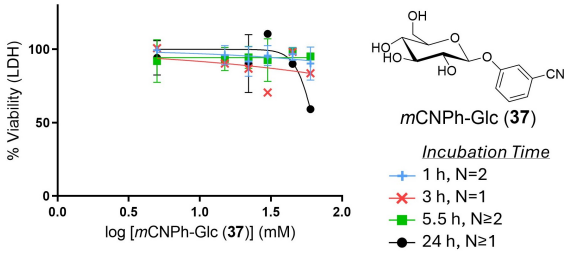


Figure 3-21. Cytotoxicity measurement of compound **37** after various incubation times (1-24 hour). Plot of percent cell viability of HepG2 cells against logarithm transformed compound concentration (in mM). Determined by LDH membrane integrity assay following incubation at 37 °C in 5 % CO_2. Results reported as mean ± standard deviation (SD), N≥1 for 24-hour incubation, N≥2 for 5.5-hour incubation, N=1 for 3-hour incubation, and N=2 for 1-hour incubation.

A number of different mechanisms can be responsible for cytotoxicity related cell death, including apoptosis, necrosis, autophagy, ferroptosis, and pyroptosis.[390,391] However, only certain modes of cell death, such as necrosis, involve early rupture of the cell membrane that would be detected by the LDH assay.[390,391] As minimal membrane integrity loss was observed within a 5.5-hour incubation (**Figure 3-22**), it was not likely that the necrotic pathway was triggered by incubation with *m*CNPh-Glc (**37**). Instead, cell death may have been caused by the triggering of other pathways (such as *via* apoptosis)[390–392] where cellular

metabolism had begun shutting down and the cascade(s) resulting in cell death had been initiated but the membranes had not yet been fully compromised.

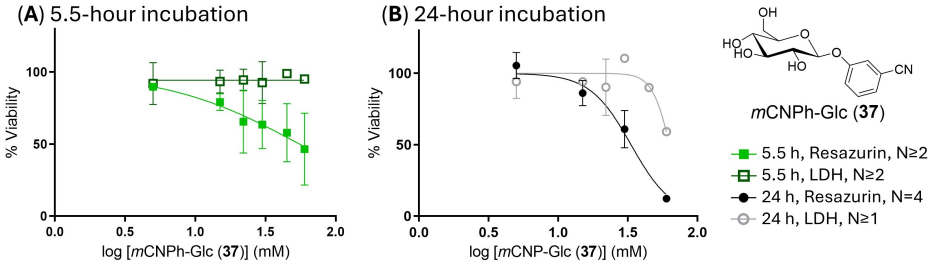


Figure 3-22. Direct comparison of cytotoxicity as measured by resazurin-based assay or LDH release for (**A**) 5.5- and (**B**) 24-hour incubation time points with *m*CNPh-Glc (**37**). Results reported as mean ± standard deviation (SD).

Interestingly, previous experiments by Dr. Jessica Poisson (Ben Lab, PhD 2019) noted that apoptosis was not triggered by azide-containing small-molecule IRIs when compared to staurosporine (a known activator of apoptosis) using a caspase3/7 assay.[214,393,394] Given the LDH assay results presented above rule out necrosis as a potential mechanism of cell death in the presence of *m*CNPh-Glc (**37**) and Dr. Poisson's results rule out apoptosis in the presence of compounds such as *p*N_3Ph-Glc (**29**) it is suggested that different mechanisms of cell death may be triggered by different compounds. Alternatively, a different mechanism entirely might be responsible for cellular death in the presence of small-molecule IRIs that does not present with a necrotic morphotype (rapid membrane integrity loss). It is also a possibility that apoptosis may be triggered through means other than caspase 3/7 which would be undetectable through the assay completed by Dr. Poisson. Future studies should investigate the addition of other inhibitors of cell death pathways to further probe the mechanisms of cell death that could be triggered by small-molecule ice recrystallization inhibitors and the cryopreservation process in general. Ultimately, these results provided confidence that any observed internalization that may be observed during live-cell imaging studies with *m*CNPh-Glc (**37**) was not due to toxicity related weakening of the cell's membrane structures.

3.5. Live-cell imaging of *nitrile*-containing IRI *m*CNPh-Glc (**37**)

While initial proof-of-concept studies for live-cell Raman imaging using nitrile-containing IRIs were completed with compound **30** (*p*CNPh-Glc) due to its structural similarity to established IRIs **25** (*p*BrPh-Glc) and **26** (PMP-Glc), compound **37** (*m*CNPh-Glc) had the best efficacy index and did not significantly weaken the cell's membranes following exposure of the compound for up to 5.5 hours. Therefore, continued experiments on the nitrile-containing IRIs as they move into a live-cell environment focused exclusively on using compound **37** (*m*CNPh-Glc).

Initially, Raman spectra of compound **37** (30 mM) in cell culture medium (Dulbecco's minimum essential medium supplemented with 10 % fetal bovine serum, 1 % penicillin/streptomycin, 1 % non-essential amino acids, and 0.1 % sodium pyruvate) were generated to confirm the appropriate wavelength that could be used obtain maximum signal intensity of the nitrile. The 30 mM concentration was selected based on the dose-response results for both ice recrystallization inhibition activity and cytotoxicity for *m*CNPh-Glc (**37**) where it lay directly in the centre of the compound's therapeutic window (**Figure 3-18**). Both SRS and CARS spectroscopy spectra were generated, with and without cross-phase modulation (XPM). The x-axes of these spectra were not fully calibrated during testing, therefore accurate wavenumbers cannot be reported; however, the observed signals appeared at a wavelength of ~2200 cm^{-1} as expected for the aryl nitrile based on literature values and previous testing results with compound **30** (*p*CNPh-Glc) (**Figure 3-23**). As the XPM-SRS setup provided the sharpest signal with the narrowest half-maximum line width (**Figure 3-23A**), this technique was used for further live-cell imaging experiments.

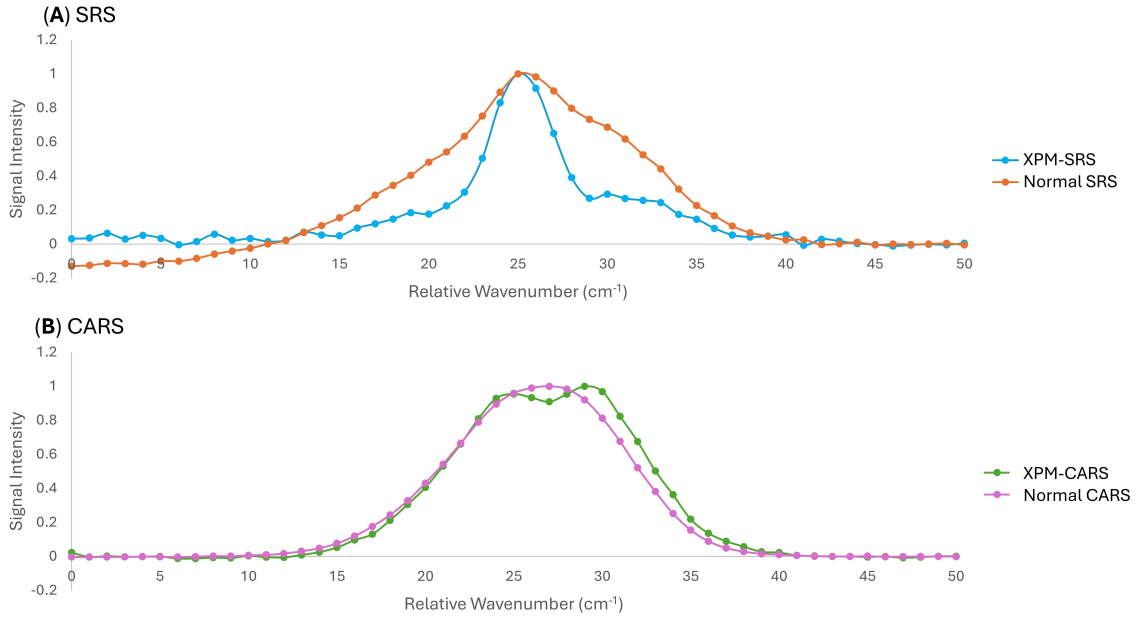


Figure 3-23. (**A**) Stimulated Raman scattering (SRS) and (**B**) coherent anti-stokes Raman scattering (CARS) spectra of compound **37** (*m*CNPh-Glc) in standard cell culture medium in the absence of cells. Spectra obtained both with and without cross-phase modulation (XPM). Graphs plotted as a function of signal intensity against relative wavenumber (cm^{-1}); the x-axes were not fully calibrated such that accurate wavenumbers cannot be reported, but the apparent wavenumber of the signals was ~2200 cm^{-1}. *Spectral scan completed by Dr. Adrian Pegoraro at the National Research Council – Sussex Site (Ottawa, ON).*

Given the successful detection of nitrile signal using CARS microscopy from the proof-of-concept work discussed in *section 3.3.2.1* and the ability to detect compound **37** (*m*CNPh-Glc) in the cell culture medium using XPM-SRS, we sought to establish whether compound **37** (*m*CNPh-Glc) could be detected

in the presence of live cells. After an incubation period of 24 hours (5 % CO_2, 37 °C) to allow the cells to adhere to the dish surface, the cells were transferred to the lab facilities at the National Research Council (NRC, Sussex site) for imaging. The cell culture medium in which the cells were grown and transported was removed 30 minutes prior to imaging, followed by washing of the cells with phosphate-buffered saline (PBS), and the addition of cell culture medium that had been supplemented with compound **37** (*m*CNPh-Glc, 30 mM) to the culture dish.

After 30 minutes of incubation with compound **37** (*m*CNPh-Glc, 30 mM), images of the cells were immediately obtained using the XPM-SRS setup with a wavenumber of 2850 cm^{-1} (to be able to clearly locate the cells by highlighting lipid content) including Raman spectra from three different regions of the image space: where no cells were present (yellow), the edges of a cell aggregate (red), and the interstitial cell space (green) (**Figure 3-24A**). Two distinct sets of peaks were observed on the Raman spectra that corresponded to lipids (CH) in the ~2850 cm^{-1} region and the nitrile peaks (CN) in the ~2200 cm^{-1} region (**Figure 3-24B**); exact wavenumbers for each peak could not be reported due to incomplete calibration of the x-axis. The peaks in the lipid region appeared as expected, where the highest intensity signal at ~2850 cm^{-1} was observed in the interstitial cellular space (green, **Figure 3-24B**). Interestingly, the peaks corresponding to the nitrile signal (in the ~2200 cm^{-1} region) also had the greatest signal intensity in the interstitial cell space (green) (**Figure 3-24B**); as no washout was performed for these experiments and the nitrile signal was significantly lower in the regions corresponding to only cell culture medium (yellow) (*m*CNPh-Glc, **37**, remained present throughout the cell culture medium while these spectra were obtained) the greater intensity of the nitrile signal in the interstitial space suggested that compound **37** (*m*CNPh-Glc) may be internalizing or concentrating near the HepG2 cells (**Figure 3-24B**).

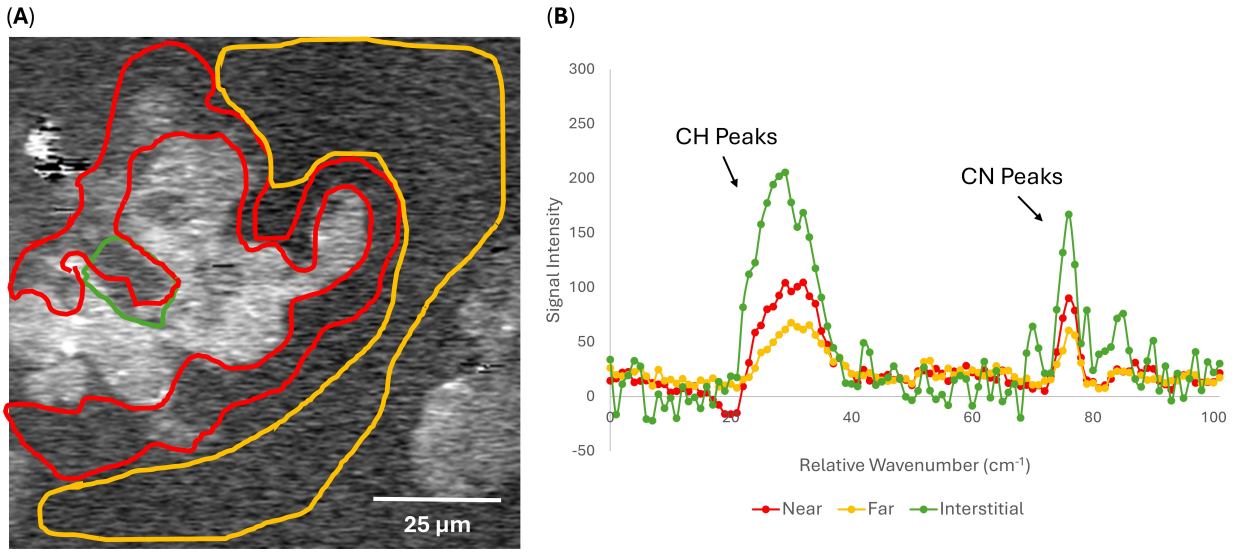


Figure 3-24. Live HepG2 cells imaged in glass-bottom culture dishes using XPM-SRS following a 30-minute incubation with *m*CNPh-Glc (**37**, 30 mM). (**A**) Image taken using a 2850 cm^{-1} wavenumber to highlight the lipid (CH) cellular content. Three highlighted regions indicate the interstitial cell space (green), near the cell periphery (red), and far from the cell boundary (yellow). (**B**) Raman spectra graph plotted as a function of signal intensity against relative wavenumber (cm^{-1}); the x-axis was not fully calibrated such that accurate wavenumbers cannot be reported. Lipid (CH) peak region indicated is at an approximate wavenumber of 2850 cm^{-1} and the nitrile (CN) peak region is at an approximate wavenumber of 2200 cm^{-1}. *Imaging completed by Dr. Adrian Pegoraro at the National Research Council – Sussex Site (Ottawa, ON).*

Three additional regions of the cells were then selected to further investigate the signal intensity patterns in the intracellular space of a HepG2 cell aggregate: high signal intensity (blue), a large area of the cell aggregate (green), and a second cell aggregate (yellow) (**Figure 3-25A**). These regions were selected to distinctly avoid the cell periphery (the boundary between the intracellular and extracellular space) such that it would be possible to gain greater insight into whether compound **37** (*m*CNPh-Glc) was being internalized or simply aggregating at the cell boundaries. From the Raman spectra, a distinct signal was again observed in the 2850 cm^{-1} range indicative of lipids (CH) as expected in all selected regions, however no distinct peak was observed in the 2200 cm^{-1} range in any of the selected regions that would have been indicative of the presence of the aryl-nitrile of *m*CNPh-Glc (**37**) (**Figure 3-25B**). Therefore, given a 30-minute incubation period (37 °C, 5 % CO_2), compound **37** (*m*CNPh-Glc, 30 mM) was not significantly internalized but instead appeared to be aggregating at the cell periphery.

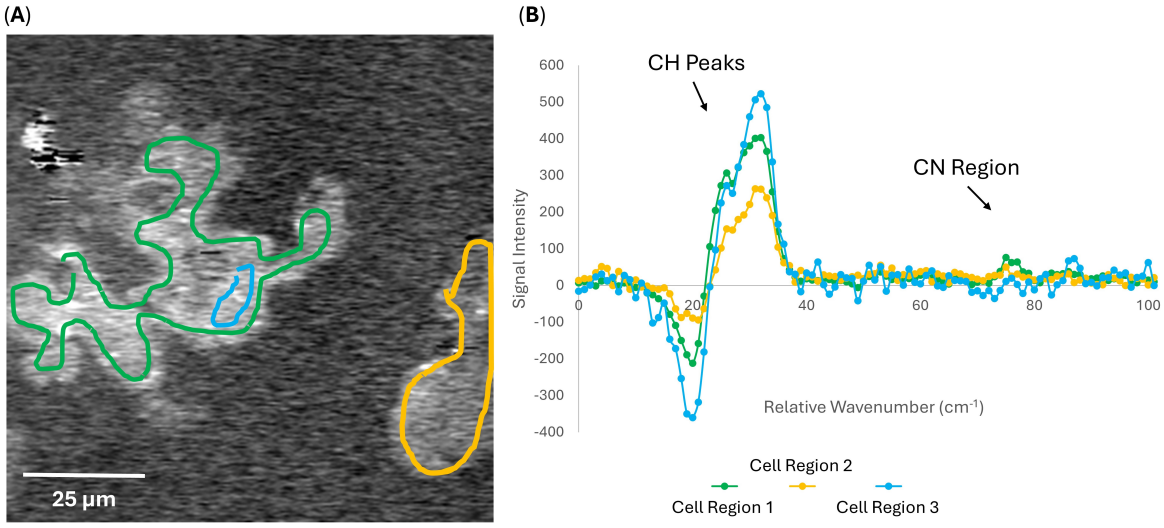


Figure 3-25. Live HepG2 cells imaged in glass-bottom culture dishes using XPM-SRS following a 30-minute incubation with *m*CNPh-Glc (**37**, 30 mM). (**A**) Image taken using a 2850 cm^{-1} wavenumber to highlight the lipid (CH) cellular content. Three highlighted regions indicate different intracellular regions from a first cluster of cells (green = large region, blue = small, concentrated region) and a second cluster of cells (yellow). (**B**) Raman spectra graph plotted as a function of signal intensity against relative wavenumber (cm^{-1}); the x-axis was not fully calibrated such that accurate wavenumbers cannot be reported. Lipid (CH) peak region indicated is at an approximate wavenumber of 2850 cm^{-1} and the nitrile (CN) peak region is at an approximate wavenumber of 2200 cm^{-1}. *Imaging completed by Dr. Adrian Pegoraro at the National Research Council – Sussex Site (Ottawa, ON).*

We therefore sought to explore longer incubation times with compound **37** (*m*CNPh-Glc, 30 mM) with the intention of elucidating whether the compound simply aggregated at the cell periphery or whether it eventually became internalized. For these experiments, the cells were prepared as previously described for the 30-minute experiments but were now incubated with compound **37** (*m*CNPh-Glc, 30 mM) in cell culture medium for 4.5 hours. After incubation, the cell medium containing compound **37** was removed, washed with PBS, replaced with standard cell culture medium (no nitrile-containing compound), and then incubated for an additional 30 minutes (37 °C, 5 % CO_2) prior to imaging to allow the cells to equilibrate to the changed cell medium. Images of three different fields of view were obtained both off-resonance (2900 cm^{-1}), to visualize lipid content, and on-resonance (2300 cm^{-1}) to visualize the nitrile of compound **37** (*m*CNPh-Glc, **Figure 3-26**). Bright signal could be observed in the images of the HepG2 cell aggregates when measured on-resonance that matched the location of the cell cluster that was observed in the off-resonance images (**Figure 3-26**), indicating that compound **37** (*m*CNPh-Glc, 30 mM) was able to be detected after 4.5 hours of incubation and remained concentrated at the HepG2 cell clusters following a saline wash and change to cell culture medium that contained no molecules with nitrile functional groups.

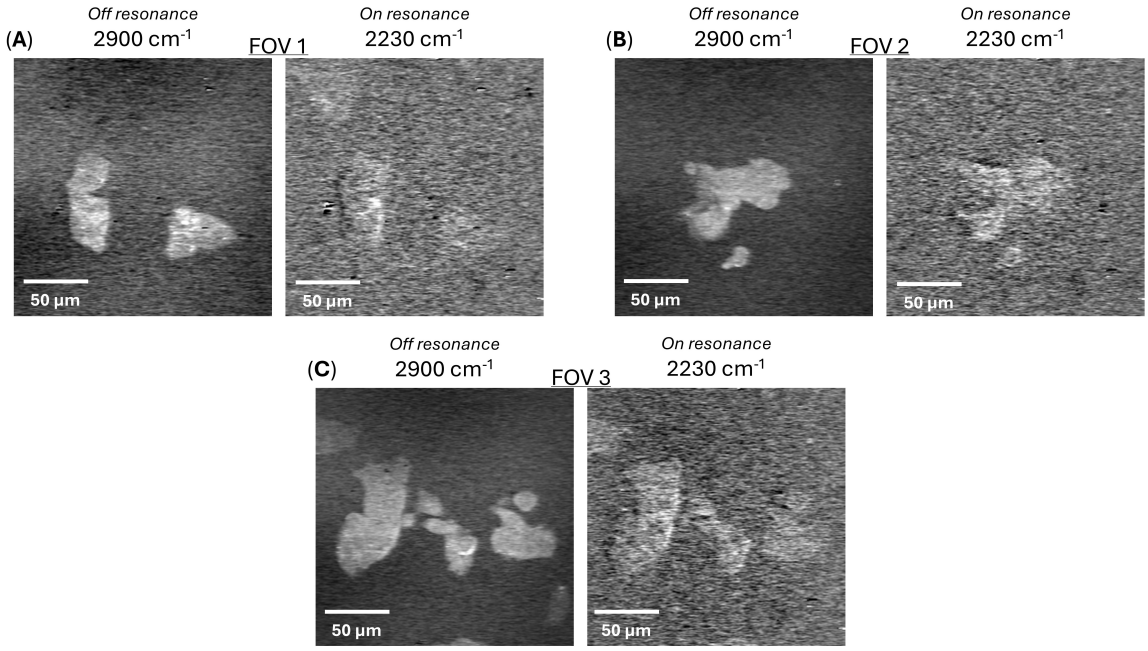


Figure 3-26. Live HepG2 cells imaged in glass-bottom culture dishes using XPM-SRS a 4.5-hour incubation with *m*CNPh-Glc (**37**, 30 mM) followed by a saline wash and change to cell culture medium containing no nitrile compounds (30-minute incubation, 37 °C, 5 % CO_2). HepG2 cells imaged off resonance (lipid region, 2900 cm^{-1}) and on resonance (silent region, for nitriles, 2230 cm^{-1}) in three different fields of view (**A-C**). *Imaging completed by Dr. Adrian Pegoraro at the National Research Council – Sussex Site (Ottawa, ON).*

While these results were promising as compound **37** (*m*CNPh-Glc) remained present even after a washout and medium change, the possibility remained that the compound may have been aggregating at the membrane rather than truly internalizing into the intracellular space. The Ben Laboratory has previously encountered potential interactions between small-molecule carbohydrate-based IRIs and cell membranes that were hypothesized to be the cause for the unsuccessful deglycerolization of cryopreserved red blood cells in the presence of *p*BrPh-Glc (**25**, 30 mM) or PMP-Glc (**26**, 110 mM).[158,162,214] Therefore, to further investigate the location of compound **37** (*m*CNPh-Glc), it was necessary to take advantage of the high resolution of Raman microscopy imaging to directly probe the intracellular space of the HepG2 cells. To locate the cell's intracellular space, a z-axis scan of the intended field of view was completed using XPM-SRS and XPM-CARS at 2900 cm^{-1} prior to addition of cell culture medium containing compound **37** (*m*CNPh-Glc, 30 mM) (**Figure 3-27**). Using this scan, the upper and lower edges of the cell periphery could be used to find the z-coordinate at the centre of mass for the cell aggregate.

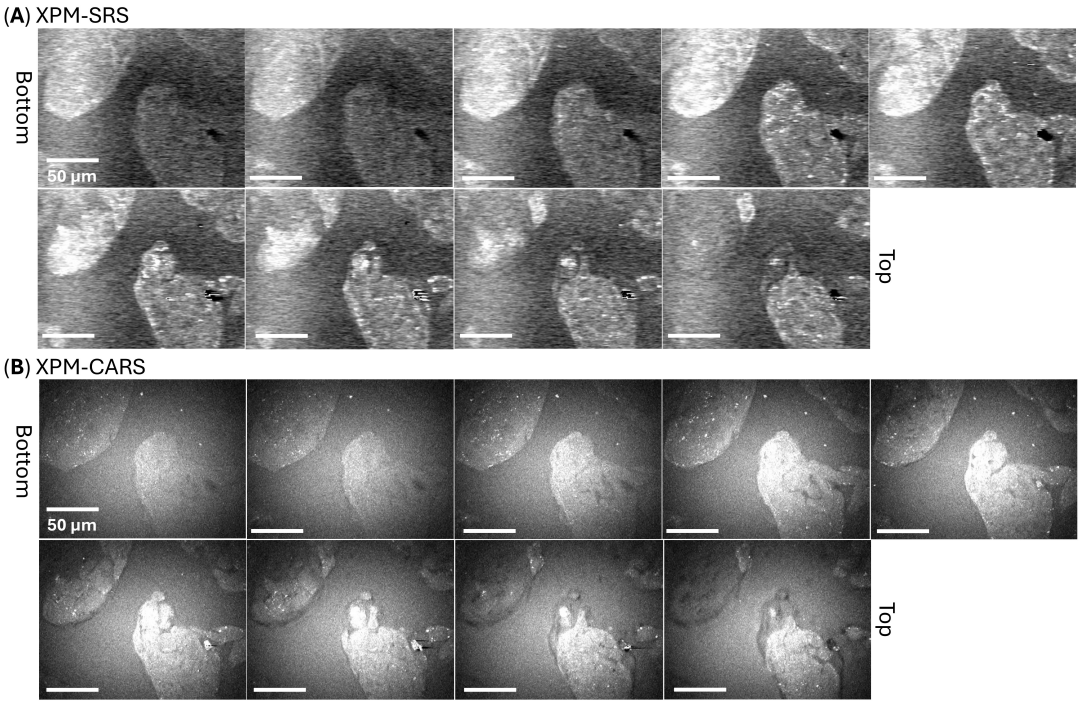


Figure 3-27. Representative z-axis scan of HepG2 cells incubated (photos shown every two photos from a total of 18 from the entire scan or approximately every 2-4 µm) with *m*CNPh-Glc (**37**, 30 mM) for identification of cell aggregate centre of mass (intracellular space). Both scans were generated by imaging at a wavenumber of 2900 cm^{-1} using (**A**) XPM-SRS (link to view scan video) and (**B**) XPM-CARS (link to view scan video). *Imaging completed by Dr. Adrian Pegoraro at the National Research Council – Sussex Site (Ottawa, ON).*

Compound **37** (*m*CNPh-Glc, 30 mM) was then added to each of the cell culture dishes and incubated in 5 % CO_2 at 37 ºC. For imaging at each desired time point, a single culture dish was removed from incubation, the cell culture medium containing compound was removed, the cells were washed with PBS, the cell culture medium was replaced with standard medium that did not contain any nitrile compounds, and then the cells were imaged at its centre of mass (based on the corresponding z-axis coordinate that had been previously determined) (**Figure 3-28**). Given the greater clarity of the XPM-CARS images from the z-stack scan (**Figure 3-27**), the XPM-CARS setup was used to obtain microscopy images for these experiments over a total time period of 5.5 hours.

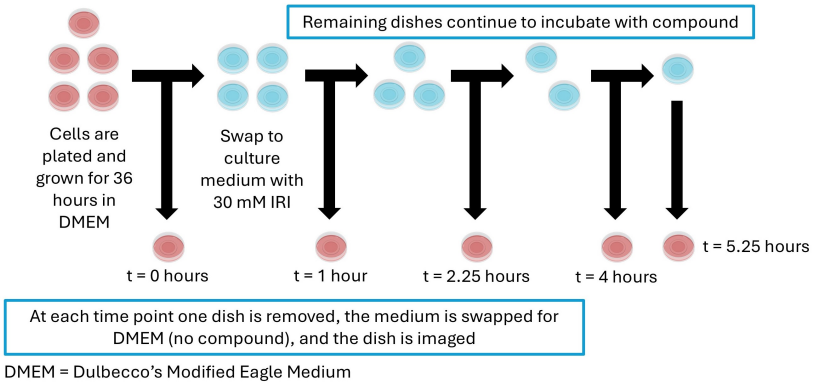


Figure 3-28. Experimental design for the incubation of HepG2 cells in the presence of compound **37** (*m*CNPh-Glc, 30 mM) for monitoring time-dependent internalization using XPM-CARS.

The relative ratio of CN (2230 cm^{-1}) to CH (2900 cm^{-1}) signal intensity could then be calculated from images taken at each incubation time point and plotted as a function of time to monitor the uptake of compound **37** (*m*CNPh-Glc) into the intracellular space (**Figure 3-29**). From the imaging results, a distinct increase in signal intensity was observed over time, indicating that compound **37** (*m*CNPh-Glc) was being internalized into cells and did not only reside at the cell periphery (**Figure 3-29B**). As the signal began to plateau after 5.5 hours (**Figure 3-29B**), it appeared as though the concentration of *m*CNPh-Glc (**37**) reached an equilibrium between the intracellular and extracellular space. In addition, the nitrile signal of *m*CNPh-Glc (**37**) was detectable within the intracellular space as early as one hour after initial addition of compound (**Figure 3-29B**).

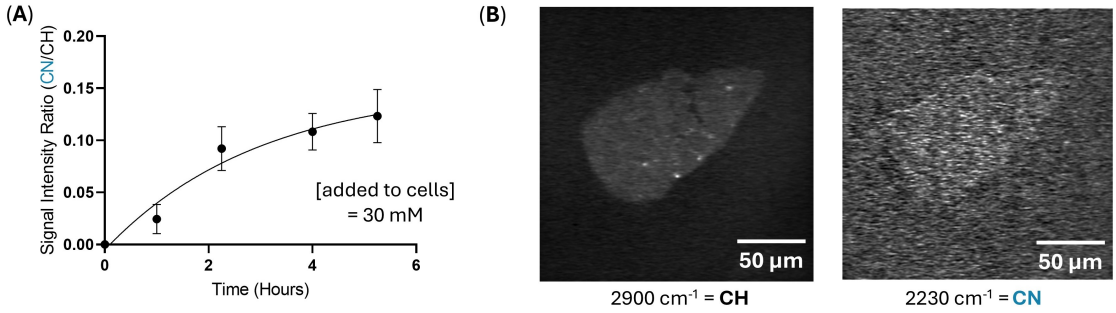


Figure 3-29. (**A**) Plot of the signal intensity ratio calculated for HepG2 cells incubated with compound **37** (*m*CNPh-Glc, 30 mM, 37 °C and 5 % CO_2) over a period of 5.5 hours. Nitrile (CN) signal obtained at a wavenumber of 2230 cm^{-1} and lipid (CH) signal obtained at a wavenumber of 2900 cm^{-1}. Curve fit to an exponential growth equation where $(CN/CH) = {y_0}^{kt}$; where t = time in hours and y_0 is the initial ratio of CH/CN signal immediately after addition of compound. (**B**) Representative images of the HepG2 cell cluster depicting the signal at each of the two wavelengths. Data reported as the mean and standard deviation of three different locations in the cell cluster at each time point. *Imaging completed by Dr. Adrian Pegoraro at the National Research Council – Sussex Site (Ottawa, ON).*

These imaging results provided critical evidence that *m*CNPh-Glc (**37**) was likely internalized into HepG2 cells as it could be found in the central intracellular space (the centre of mass for the cell cluster)

following a washout and change to cell culture medium that did not contain any nitrile-substituted compounds. Furthermore, these results were consistent with previous findings that indirectly investigated the internalization of *O*-aryl-β-D-glucopyranoside IRIs by Dr. Poisson and Dr. Capicciotti (Ben Lab, PhD 2019 and 2014 respectively).[162,214,218] As part of these studies, Dr. Poisson found that the internalization of IRIs *p*BrPh-Glc (**25**) and *p*N_3Ph-Glc (**29**) was not likely to be dependent on facilitated diffusion mediated by membrane expressed glucose transporters (GLUTs).[214] In many different cell types, including RBCs and HepG2 cells, GLUTs are responsible for the transport of D-glucose (**8**) and related analogues across the cell membrane.[395,396] However, these transporters are highly substrate specific, and can only transport certain isomers or configurations of carbohydrates across the cell membrane.[395–398] For example, the GLUT1 isoform is the most ubiquitously expressed and most well studied transporter of the family and does not tolerate the transport of D-glucose molecules with substitutions at C_1.[396,397] Dr. Poisson's studies inhibited the GLUT1 transporter in RBCs and observed that internalization of IRIs *p*BrPh-Glc (**25**) and *p*N_3Ph-Glc (**29**) still occurred, suggesting that their permeation was not dependent on facilitated diffusion mediated by GLUT1.[214] Instead, it was suggested that their internalization may be the result of passive diffusion through the cell membrane; this mechanism of internalization for substituted carbohydrates has been previously proposed by Barnett *et. al.* for phenyl-β-D-glucopyranoside (Ph-Glc, **82**) and *n*-propyl-β-D-glucopyranoside (OPr-Glc, **48**) as based on their lipophilic oil/water partition coefficients.[397] Therefore, the internalization of *m*CNPh-Glc (**37**) and other *O*-aryl-β-D-glucopyranoside IRIs is likely to be mediated by passive diffusion across the cell membrane based on the results discussed in this chapter.

3.5.1. Summary of Raman imaging studies using small-molecule carbohydrates

The ability for small-molecule ice recrystallization inhibitors *p*BrPh-Glc (**25**) and PMP-Glc (**26**) to permeate the cell membrane was previously investigated indirectly by Dr. Chantelle Capicciotti (Ben Lab, PhD 2014) and Dr. Jessica Poisson (Ben Lab, PhD 2019).[158,162,214,218] These initial studies used an interrupted graded freezing protocol to evaluate the hemolysis profiles of red blood cells (RBCs) in the presence of each compound and determined that they were consistent with that of a penetrating cryoprotective agent (CPA).[158,162,214] Later studies used fluorescent microscopy during the cryopreservation of HUVEC cells to visualize the process of ice recrystallization (and its inhibition) within the cell nucleus that provided visual evidence for the inhibition of intracellular ice recrystallization by *p*BrPh-Glc (**25**) and PMP-Glc (**26**).[218] To obtain more details on the permeation of small-molecule carbohydrate-based IRIs, we sought to use Raman microscopy techniques with high resolution and chemical specificity to directly visualize these compounds in the live-cell environment without the need for fluorescent tags.

As the IRIs *p*BrPh-Glc (**25**) and PMP-Glc (**26**) do not contain Raman reporter functional groups that would allow direct visualization within the cellular space over background cell signals, *O*-aryl-β-D-glucopyranoside compounds with *para*-azide (*p*N_3Ph-Glc, **29**) and *para*-nitrile (*p*CNPh-Glc, **30**) Raman reporter functional groups were envisioned. The Raman signal of *p*N_3Ph-Glc (**29**) proved to be too weak and inconsistent to observe at low millimolar concentrations and its low stability in aqueous solutions prevented its continued investigation in live-cell studies. However, initial investigations of the Raman signal of *p*CNPh-Glc (**30**) were promising, where the signal was detectable at ~2.6x the background signal (noise) intensity and remained distinguishable up to a 20x dilution, or approximately 2.5 mM in concentration. Due to the COVID-19 pandemic, continued Raman studies with these compounds were not immediately possible. However, as these compounds were intended for use as active ice recrystallization inhibitors in a live cell environment, we sought to explore the optimization of the ice recrystallization inhibition activity and cytotoxicity profiles of nitrile-containing IRIs in greater detail by developing the regioisomers with *meta*- or *ortho*- nitrile substitution.

From these optimization studies it was found that the *meta*- derivative *m*CNPh-Glc (**37**) had the greatest ice recrystallization inhibition activity with an IC_{50} of 26.8 mM (95 % CI [24.5-29.3]). In addition, its efficacy index of 1.3 (following a 24-hour incubation in HepG2 cells at 37 °C with 5 % CO_2) and that it was not found to damage the cell's membranes by LDH assay, situated it as the best candidate to carry forward into live-cell imaging experiments investigating permeation and localization. Following optimization of the imaging methodology, the time-dependent internalization of *m*CNPh-Glc (**37**) was successfully observed *via* coherent anti-stokes Raman scattering (CARS) microscopy with cross-phase modulation (XPM). Over a period of 5.5 hours the signal intensity corresponding to the nitrile of the IRI increased in an exponential fashion within the intracellular space of the HepG2 cell cluster. Ultimately, these studies created a methodology for the imaging of live-cells using XPM-CARS and provided critical context to the internalization of small-molecule IRIs. Future Raman imaging studies could utilize these methods to investigate more specific localization of the IRIs to gain insight into their mechanism of action, including experiments that involve cryopreservation with the addition of a cold stage.

4. Investigating structure-activity relationships for small-molecule ice recrystallization inhibitors (IRIs)

The development of small-molecule inhibitors during drug research campaigns often takes advantage of a known molecular mechanism or target to guide the development process. These campaigns also investigate the relationships between the structural features of various compounds of interest and their intended activity (*i.e.,* structure-activity relationship – SAR) to inform downstream development. The development process includes identifying sites of modification that could be used to optimize a compound's activity or improve physiochemical properties such as its solubility, permeability, or cytotoxicity.[399,400] While the phenomenon of ice recrystallization is generally well understood (see *section 1.2*), there is no molecular target (such as an enzyme or protein) that can be directly probed to gain insight into the binding interactions of the inhibitor. Despite being inspired by naturally-occurring antifreeze (glyco)proteins that bind to the surface of ice crystals in order to inhibit ice recrystallization, several examples of the carbohydrate-based small molecules have been found to be unable to bind to ice.[157,158] Therefore, it has been hypothesized by the Ben Lab that these compounds have a unique mechanism of action in which they form both *inter*- and *intra*-molecular hydrogen bonds to reduce the thermodynamically-driven transfer of water molecules from one ice crystal to another (see *section 1.3.1*) (**Figure 4-1**).[156,157,159,161]

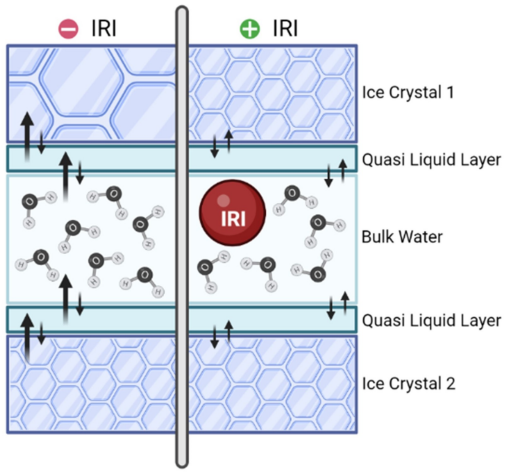


Figure 4-1. Representation of ice recrystallization (in the absence of an IRI) and its proposed mechanism of inhibition by small molecules to disrupt the thermodynamic transfer of water molecules from one ice crystal to another.

The proposed mechanism of action for small-molecule IRIs was established following key a SAR campaign by the Ben Laboratory that investigated the relationship between ice recrystallization inhibition activity and a compound's hydration number (n_h).[156,157] A molecule's n_h is defined as the number of water

molecules that are directly bound to the solute (*i.e.,* those that form the inner solvation/hydration shell of the compound).[401] In literature, values of hydration have been used to describe the effect of solutes on the three-dimensional structure of bulk water where molecules with a greater n_h have been said to poorly "fit" within the three-dimensional structure of bulk water while molecules with a lower n_h have a "fit" that better maintains the natural hydrogen bonding network of bulk water molecules.[401] A variety of molecular dynamics simulations, kinetic experiments, and physical measurement techniques have been used to determine the n_h for various common carbohydrates including monosaccharide (D-galactose, D-glucose, D-mannose, and D-talose **7**-**10**) and disaccharide (D-melibiose, D-lactose, D-trehalose, D-maltose, and D-sucrose **11**-**15**) sugars.[401–405]

When investigating the ice recrystallization inhibition activity of these carbohydrates (**7**-**15**), the Ben Lab observed that an increased n_h, and therefore a greater number of water molecules directly interacting with the carbohydrate, correlated with increased activity (as measured by the 30-minute SCA) ($R^2 = 0.89$ and 0.76 for monosaccharides and disaccharides respectively, **SI Figure 8-79A**).[157] Interestingly, despite the disaccharides having nearly double the n_h of the monosaccharides, they were not significantly more active and this discrepancy was attributed to differences in the relative three-dimensional "size" (*i.e.,* volume) of the carbohydrates.[157] When the partial molar volume (PMV) of each carbohydrate was accounted for by calculating its hydration index (HI) (n_h/PMV),[402,406,407] the correlation could be clearly attributed to both sets of sugars simultaneously with increasing ice recrystallization inhibition activity observed with increasing HI (*i.e.*, the number of water molecules tightly bound per unit volume of the carbohydrate) ($R^2 = 0.77$) (**Figure 4-2**, **SI Figure 8-79B**).[157]

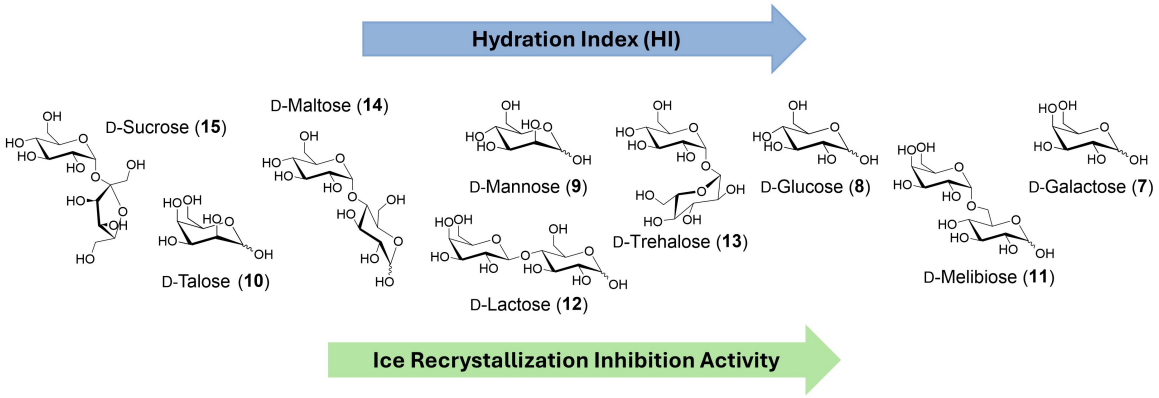


Figure 4-2. Depiction of the relationship between ice recrystallization inhibition activity and hydration index (HI) for monosaccharide and disaccharides (**7**-**15**).[157]

In other words, solutes with larger hydration indices, such as D-galactose (**7**) or D-melibiose (**11**), cause a greater disruption of the natural state of bulk water molecules than those with lower hydration

indices, such as D-talose (**10**) or D-sucrose (**15**). Therefore, in the context of ice recrystallization, the Ben Lab proposed that it was this disruption that would lead to an increased energy associated with the transfer of water molecules from one ice crystal to another, thereby reducing the thermodynamic drive of ice recrystallization.[157]

Since this early investigation on simple, naturally occurring carbohydrates, several studies by the Ben Lab have found the incorporation of hydrophobicity at the anomeric position (C_1) with alkyl or aryl substitutions to the anomeric oxygen (O_1) to be an effective strategy for improving ice recrystallization inhibition activity (**Figure 4-3**).[159,161,167] For example, the surfactant *n*-octyl-β-D-galactopyranoside (β-octyl-gal, **16**, % MGS = 20.8 ± 1.3 % at 22 mM) and the *O*-aryl-β-D-glucopyranoside PMP-Glc (**26**, % MGS = 22.9 ± 1.0 % at 22 mM) were found to have significantly greater ice recrystallization inhibition activity than D-galactose (**7**, % MGS = 63.6 ± 3.3 % at 22 mM) or D-glucose (**8**, % MGS = 76.5 ± 3.6 % at 22 mM) alone (**SI Figure 8-80**).[157,158,161,167]

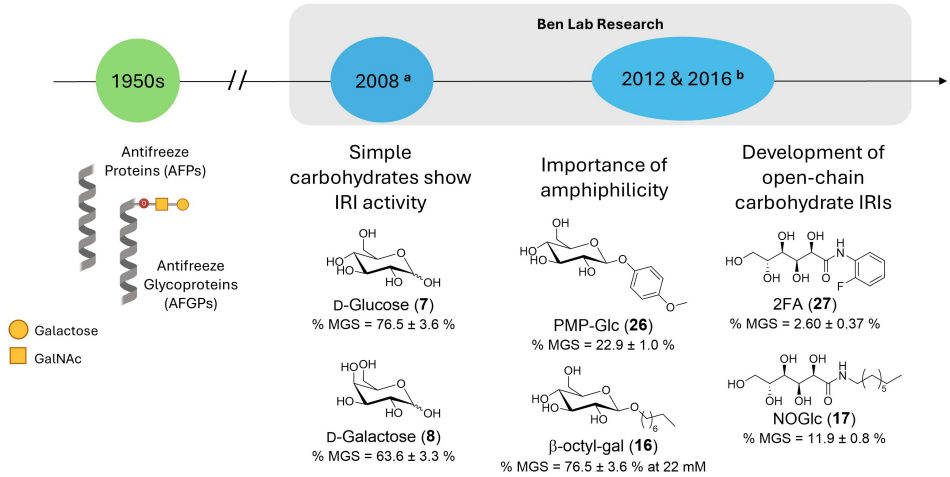


Figure 4-3. The development timeline for small-molecule ice recrystallization inhibitors (IRIs) starting in the 1950s with antifreeze (glyco)proteins and moving towards the libraries of *O*-aryl- and *O*-alkyl- β-D-glucopyranosides (such as **26** and **16**) and *N*-aryl and *N*-alkyl D-gluconamides (such as **27** and **17**) following the discovery of the importance of amphiphilicity to improve ice recrystallization inhibition activity of simple sugars (such as **7** and **8**). Ice recrystallization inhibition activity reported as the percent mean grain size (% MGS) of the compound as assessed by the 30-minute splat-cooling assay from n=3 ice wafers at a concentration of 22 mM (except **17**, which was assessed at 0.5 mM). [a] *Tam et. al. (2008)*[157], [b] *Capicciotti et. al. (2012 and 2016)*[161,167], *Briard et. al. (2016)*[166].

As with changes in the stereochemical configuration of carbons bearing hydroxyl groups, substitutions to the carbohydrate core (such as alkylation) have been found to impact a compound's n_h or PMV, and ultimately its HI.[158] For example, methylation of the anomeric oxygen (O_1) of different monosaccharides increased both their n_h and PMV compared to the corresponding unmethylated (reducing sugar) parent compounds (**7-9**) but an overall decrease in HI;[401,406] therefore, as expected, the decrease in

HI for these compounds was correlated with a decrease in ice recrystallization inhibition activity ($R^2 = 0.69$) (**SI Figure 8-81**).[158] Based on these findings, it has been hypothesized that the HI of substituted IRIs such as compounds **16** and **26** would be significantly greater than their reducing sugar counterparts. However, the determination of a compound's n_h and PMV to directly calculate its HI requires specialized equipment to obtain measurements of an aqueous solution's density *via* ultrasound.[401] As a result, these values have not yet been calculated or reported for many substituted carbohydrate derivatives or other small molecules and direct comparisons cannot be made between the library of IRIs that has been developed to date and their corresponding HI. Furthermore, with the aim of developing new and more effective IRIs for cryopreservation applications, a predictive measure for a compound's activity that did not require that the compound of interest be synthesized was desirable.

4.1. SAR campaigns that formed the foundation for understanding ice recrystallization inhibition activity as measured by the 30-minute SCA

Molecular descriptors and parameters that are computationally calculated based on a molecule's structure and chemical information have been used reliably and accurately to determine key structural features and provide direction during drug development campaigns. For example, molecular descriptors such as molecular weight, logP, and the number of hydrogen bond donors/acceptors (known as Lipinski's Rule of Five), have been used extensively to predict the solubility, permeability, and overall drug-like properties of molecules for decades.[408,409] These parameters could then be related to a measure of the drug's activity as determined by a high throughput assay, and correlations could be made that provide information about which types of structural features may be beneficial for activity and which may be detrimental.

With respect to ice recrystallization inhibition activity, the Ben Lab has undertaken several SAR campaigns to facilitate the development of new IRIs by relating various structural and physiochemical parameters to activity as measured by the 30-minute splat-cooling assay (SCA, described previously in *section 1.3.2*).[158,167,168,217,248,410] The investigated correlation studies have included individual parameters such as alkyl chain length, ratios of polar surface area to molecular surface area (PSA/MSA), and electronic effects of the aryl ring, as well as a multiparameter quantitative structure activity relationship (QSAR) within two of the largest classes of IRIs developed to date (the *O*-aryl-pyranosides and the *N*-alkyl-aldonamides).

4.1.1. Hydrophobicity and the effect of alkyl chain length on ice recrystallization inhibition activity

In general, the Ben Lab has found that the incorporation of hydrophobicity to small-molecule carbohydrates by alkylation has improved their ice recrystallization inhibition activity compared to reducing sugars alone as measured by the 30-minute SCA.[161] However, it has been noted that the relative degree of hydrophobicity that results in the greatest ice recrystallization inhibition activity varies between compound classes, and ultimately a specific conclusion cannot be broadly applied to all molecules.[168,411] For example, a study by Matt Alteen (Ben Lab, MSc 2013) noted that the ice recrystallization inhibition activity of the *p*-alkamidophenyl-β-D-glucopyranosides improved linearly with increasing alkyl chain length ($R^2 = 0.97$, **SI Figure 8-82**); hydrophobicity increased after acetylation of the free amine of 4-aminophenyl-β-D-glucopyranoside (*p*NH_2Ph-Glc, **32**) to generate compound **49**, followed by increased alkyl chain length with the propanamide (**50**), butanamide (**51**), and pentanamide (**52**) (**Figure 4-4A**).[411] However for the *p*-alkoxyphenyl-β-D-glucopyranosides, it was the ethyl alkyl chain length (PEP-Glc, **54**, % MGS = 5.77 ± 0.15 % at 22 mM) that was found to have the greatest ice recrystallization inhibition activity where both shorter and longer alkyl chains had reduced activity (**Figure 4-4B**, **SI Figure 8-82**). From the parent 4-hydroxyphenyl-β-D-glucopyranoside (*p*OHPh-Glc, **53**) activity initially increased with alkyl chain length upon methylation (PMP-Glc, **26**) and ethylation (PEP-Glc, **54**), but then decreased upon extension to the propyl (PPP-Glc, **55**, % MGS = 31.7 ± 2.1 % at 22 mM) and butyl (PBP-Glc, **56**) substitutions (% MGS = 39.5 ± 9.6 % at 22 mM) (**SI Figure 8-82**).[411]

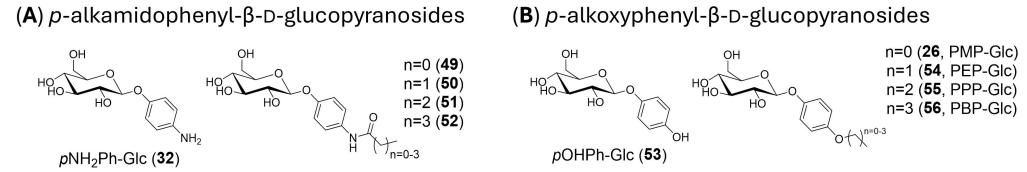


Figure 4-4. Structures of the (**A**) *p*-alkamidophenyl-β-D-glucopyranosides (**32**, **49**-**52**) and (**B**) *p*-alkoxyphenyl-β-D-glucopyranosides (**26**, **53**-**56**) assessed for the relationship between hydrophobicity and ice recrystallization inhibition activity by *Matt Alteen (Ben Lab, MSc 2013)*.[411]

A later study by Dr. Jennie Briard (Ben Lab, PhD 2016) came to a similar conclusion when investigating a series of *N*-alkyl- (**17**-**18**, **22**-**24**, **57**-**60**) and *N*-cycloalkyl-aldonamides (**61**-**76**) (open chain carbohydrates, **Figure 4-5A** and **B** respectively).[168] For each molecule, the ratio of its polar surface area (PSA) to its total molecular surface area (MSA) and a simplified ratio of the number of carbons in the alkyl chain (CH_n) relative to the number of hydroxyls in the polyol chain (OH) were used for comparison to ice recrystallization inhibition activity (measured by the 30-minute SCA). These two ratios (PSA/MSA and CH_n/OH) were used as analogous parameters to describe a molecule's amphiphilicity, where greater

hydrophobicity would result in lower PSA/MSA ratios, greater CH_n/OH ratios, and ultimately greater ice recrystallization inhibition activity.

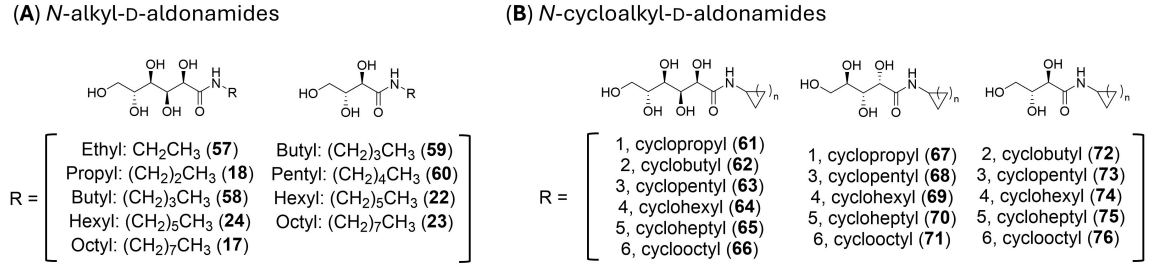


Figure 4-5. Structures of the (**A**) *N*-alkyl-D-aldonamides (**17**-**18**, **22**-**24**, **57**-**60**) and (**B**) *N*-cycloalkyl-D-aldonamides (**61**-**76**) assessed for the relationship between hydrophobicity and ice recrystallization inhibition activity by *Dr. Jennie Briard (Ben Lab, PhD 2016)*.[168]

As expected, a correlation was observed between decreasing PSA/MSA or increasing CH_n/OH ratio and increasing ice recrystallization inhibition activity of the *N*-alkyl-D-aldonamides; however, the variables were not well correlated with R^2 values of 0.23 and 0.12 respectively (**SI Figure 8-83A** and **C**).[168] The compounds *N*-octyl-D-gluconamide (**17**) and *N*-hexyl-D-gluconamide (**59**) were found to be the most active, with a % MGS of 8.14 ± 0.74 % (at 5.5 mM) and 3.38 ± 1.95 % (at 22 mM) respectively but were significant outliers with respect to the activity of the remaining molecules (all with % MGS greater than 45 %) that affected the strength of the correlation.[168] It is also important to note that the solubility of *N*-octyl-D-gluconamide (**17**) at 5.5 mM has not been reliably reproducible, which has been a confounding factor for these results and this SAR study overall.

With respect to the *N*-cycloalkyl-D-gluconamides, a strong linear correlation was observed between increasing CH_n/OH ratio and increasing ice recrystallization inhibition activity (R^2 = 0.81) (**SI Figure 8-84**).[168] However, when all cycloalkyl-aldonamides were incorporated into a single trend (including arabonamides and erythronamides), only a weak linear correlation was observed (R^2 = 0.31); furthermore, the observed trend was between increasing CH_n/OH ratio and decreasing ice recrystallization inhibition activity, which was the opposite of what was expected based on the proposed mechanism of action for these compounds (**SI Figure 8-84**).[168] Therefore, while increasing the hydrophobicity of carbohydrate-based compounds relative to their hydrophilicity was able to improve ice recrystallization inhibition activity in select scenarios with certain compounds, no clear correlation between alkyl chain length, PSA/MSA ratio, or CH_n/OH ratio and ice recrystallization inhibition activity as measured by the 30-minute SCA could be broadly applied towards the development of novel IRIs.

4.1.2. The effect of aryl-ring electronics on the ice recrystallization inhibition activity of O-aryl-pyranosides

Within the library of *O*-aryl-pyranosides that had been generated by the Ben Lab in the early 2010's it was discovered that different substituents on the aryl ring often had a significant impact on ice recrystallization inhibition activity. Initially, it was hypothesized that this effect may be caused by differences in electron density at the anomeric oxygen (O_1) and the impact of these electronic effects on the compound's interactions with bulk water molecules.[158,167] More specifically, substitution on the aryl ring with an electron donating group (EDG) was thought to increase the strength of hydrogen bonding interactions between O_1 and surrounding water molecules, ultimately resulting in improved ice recrystallization inhibition activity (**Figure 4-6A**); the opposite effect would be observed for an electron withdrawing group (EWG), where O_1 and water molecule hydrogen bonding interactions would be weakened resulting in reduced ice recrystallization inhibition activity (**Figure 4-6B**).

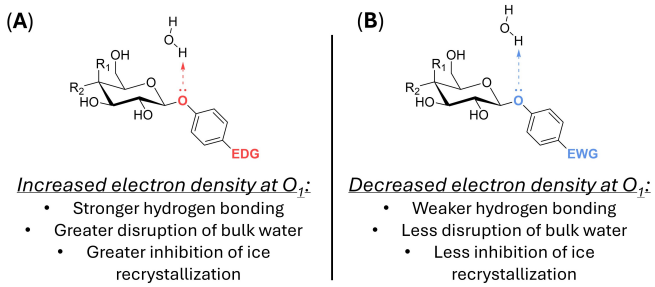


Figure 4-6. Hypothesized effect of altering the electron density at the anomeric oxygen (O_1) on intermolecular hydrogen bonding interactions and ice recrystallization inhibition activity for (**A**) electron donating group (EDG) and (**B**) electron withdrawing group (EWG) substitutions on *O*-aryl-pyranosides.

To test this hypothesis, previous work by Dr. John Trant (Ben Lab, PhD 2012) and Dr. Chantelle Capicciotti (Ben Lab, PhD 2014) assessed the ice recrystallization inhibition activity of various *para*-substituted *O*-aryl-β-D-galactopyranosides and *O*-aryl-β-D-glucopyranosides using the 30-minute SCA.[158,412] The activity of each derivative was then visualized as a Hammett plot, which described the relationship between the electronic effect of a *para* substituent, described by a constant (σ_p), and its ice recrystallization inhibition activity.

With the small subset of *O*-aryl-β-D-galactopyranosides tested by Dr. Trant, a strong linear correlation coefficient ($R^2 = 0.96$) was calculated for a linear regression with a very shallow negative slope ($\rho = -0.27$) indicating improved ice recrystallization inhibition activity with increasing electron withdrawal from O_1 (**SI Figure 8-85A**).[412] However, these results were inconsistent with the hypothesis that EDGs would improve ice recrystallization inhibition activity by increasing the electron density at the anomeric oxygen (O_1).[412] Therefore, the study was expanded to include a larger compound data set by Dr. Capicciotti

which ultimately found that the linear regressions had very poor linear correlation coefficients (R^2 = 0.03 and 0.11) and that there was no clear correlation with EDGs or EWGs (**SI Figure 8-85B**).[158] As a result, these studies concluded that the *para*- substituents of the aryl ring were not stabilizing a build up of positive or negative charge at O_1 by inductive, resonance, or electrostatic effects during the ice recrystallization process and that this parameter did not impact ice recrystallization inhibition activity. These studies also highlighted the importance of ensuring that the library of ice recrystallization inhibitor candidates includes sufficient diversity with respect to the parameter of interest.

4.1.3. A multiparameter approach to predicting the ice recrystallization inhibition activity of N-aryl-D-gluconamides

Given the difficulty in elucidating individual structural features important to ice recrystallization inhibition activity, it was thought that a multiparameter approach may be able to more accurately describe the complex interactions that occur during ice recrystallization and its inhibition. Therefore, a previous study by the Ben Lab investigated a more global approach to modelling and predicting the ice recrystallization inhibition activity of small-molecule carbohydrates in collaboration with researchers in Dr. Tom Woo's (University of Ottawa) laboratory. This project built a quantitative structure activity relationship (QSAR) model using the geometrical molecular descriptors of a compounds within the Ben Lab's library that was able to predict whether a novel proposed compound would be active (a % MGS of < 70 %) with a success rate of 82 % (**SI Figure 8-86**).[217] Unfortunately, the model failed to discriminate more finely between "active" compounds and also falsely identified compounds as inactive (false negatives) at a rate of 50 % (**SI Figure 8-86**),[217] which limited its routine use during small-molecule IRI development campaigns.

Recently, Warren *et. al.* (2024)[413] published a similar machine learning approach with the aim of predicting ice recrystallization inhibition activity for small-molecule carbohydrates (using the data set generated by Briard *et. al.*, 2016)[217] and their own library of amino acid derivatives.[413] Using their model, the authors were also able to predict whether compounds (both carbohydrate and amino acid derivatives) would be active or inactive (given a 70 % MGS threshold) at a rate similar to the model generated by Briard *et. al.*, but remained unable to more accurately predict the absolute ice recrystallization inhibition activity of small-molecule carbohydrates.[413] Consequently, the application of complex modelling as a tool to support the rational design of small-molecule IRIs requires significant further development prior to its routine adoption.

4.1.4. Summarizing the SAR studies using activity as measured by the 30-minute SCA the potential implications of activity measured by the 5-minute SCA

In general, the past SAR studies on small-molecule carbohydrates by the Ben Lab have failed to define the exact structural features or motifs that are important for ice recrystallization inhibition activity. While increasing the hydrophobicity of a compound relative to its hydrophilicity was found to improve ice recrystallization inhibition activity, the optimum degree of hydrophobicity varied from molecule to molecule and any broad correlations were inconclusive.[168,411] As a result, the vast majority of small-molecule IRI development to date in the Ben Lab has relied on iterative synthesis and activity testing of countless proposed analogues that is both time and cost inefficient. Therefore, it has remained a primary goal of the Ben Lab to understand the structural features that are important for ice recrystallization inhibition activity, to help predict whether a compound will be active or inactive and narrow the scope of potential IRI candidates to be screened.

As previously discussed (see *section 1.3.2*), depending on the assay that is used to quantify ice recrystallization inhibition different information about a compound's relative activity can be obtained. For example, the 30-minute SCA allowed for the direct comparison of compounds at the same concentration within a library but failed to address the time- and concentration- dependence of ice crystal growth and did not capture the heterogeneous nature of ice crystals[150,169] On the other hand, the 5-minute SCA was developed to address many of these points of concern where, most importantly, it quantified the concentration dependent ice recrystallization inhibition activity of a compound of interest.[169,170] As all past SAR campaigns focused on relationships to ice recrystallization inhibition activity as measured by the 30-minute SCA, this chapter aimed to use the 5-minute SCA to re-investigate key structural features from past SAR studies as well as with new molecular parameters that could be used to predict a candidate compound's interactions with bulk water molecules, and ultimately its ice recrystallization inhibition activity.

4.2. Comparing molecular descriptor relationships to ice recrystallization inhibition activity as measured by the 30-minute and 5-minute splat-cooling assays

Given that hydration values have not been determined for many substituted derivatives, its usefulness for the prediction of ice recrystallization inhibition activity for the small-molecule compounds of interest to the Ben Lab was extremely limited. However, with the goal of comparing the measurements of ice recrystallization inhibition activity between the 5- and 30-minute SCAs, it was pertinent to re-examine the relationship between hydration index (HI) and ice recrystallization inhibition activity. To

this end, the monosaccharide reducing sugars D-galactose (**7**), D-glucose (**8**), and D-mannose (**9**) were assessed for their ice recrystallization inhibition activity using the 5-minute SCA and were found to have IC_{50} values of 79.6 mM (95 % CI [62.7-95.4]), 75.7 mM (95 % CI [65.9-84.2]), and 83.4 mM (95 % CI [68.0-94.1]) respectively (**Figure 4-7A**). In contrast to the % MGS ice recrystallization inhibition activity as measured by the 30-minute SCA, no significant difference was observed between the IC_{50} values (determined from a minimum of six different concentrations) for any of the three monosaccharides. As a result, the expected correlation between HI and the ice recrystallization inhibition activity of each compound as quantified by an IC_{50} value was not observed (**Figure 4-7B**). The lack of correlation using the 5-minute SCA suggested that different parameters or structural features may be responsible for governing ice recrystallization inhibition as measured by this assay than the 30-minute SCA.

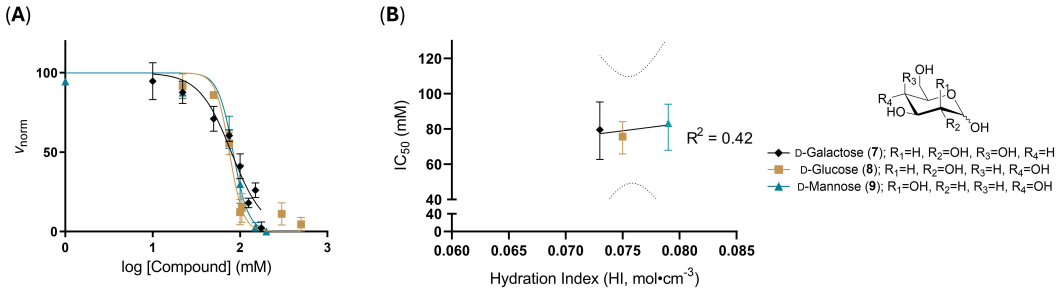


Figure 4-7. (**A**) Plot of normalized ice crystal growth rate (v_{norm}) in PBS against logarithm transformed compound concentration (in mM) for reducing sugars (**7-9**). Determined by modified splat-cooling assay with a 5-minute annealing time at -6.4 °C.[169] (**B**) Plot of hydration index (HI) relative to ice recrystallization inhibition activity (IC_{50}) for reducing sugars (**7-9**) with 95 % confidence bands of the linear regression (R^2 = 0.42) shown.

Between the two methods of SCA, several features including analysis method, annealing time, and concentrations tested differ in order to improve the quantification of ice recrystallization inhibition activity; however, the impact of these modifications on the relationship to HI was unclear. With respect to the analysis methods, the 30-minute assay only quantified a random subset of 12 ice crystals within an image, while the 5-minute SCA quantified the entire field of view (FOV). This change better addressed the heterogeneity of ice crystal size within each ice wafer but ultimately did not impact the observed % MGS (the mean grain size of ice crystals in the presence of an analyte compared to PBS alone) for a compound.[170] Therefore, it was not expected that the change in analysis method alone would be the underlying cause for the lack of correlation to HI.

To confirm this hypothesis, ice recrystallization inhibition was assessed after an annealing period of 30 minutes at -6.4 °C by quantifying every crystal within a FOV and directly comparing the correlation to the previous analysis (completed by Dr. Chantelle Capicciotti) of only 12 random crystals. As expected,

the % MGS of each compound was comparable as was the correlation to HI, where an increase in HI corresponded to an increase in % MGS. Of note however, the linear correlation coefficient decreased from 0.90 to 0.37 due to an increase in the standard deviation of the % MGS for each compound (n=3 wafers) (**Figure 4-8**). This increase confirmed that analysis of only 12 crystals on the wafer did not accurately capture the heterogeneity of ice crystal area across each wafer but ultimately did not directly impact the overall correlation to HI. Therefore, all future comparisons were made using analysis method 2 as per the current 5-minute SCA which quantified every ice crystal within each FOV.

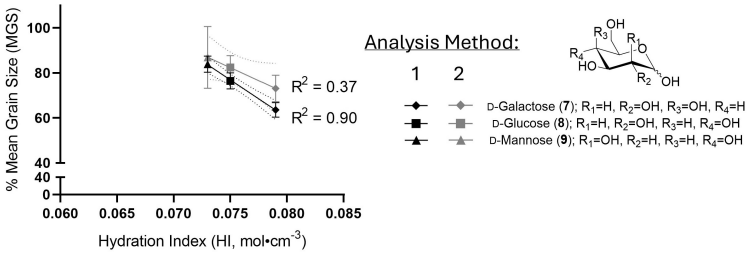


Figure 4-8. Plot of the hydration index (HI) of reducing sugars (**7-9**) relative to their ice recrystallization inhibition activity presented as mean ± standard deviation (SD) of the percent mean grain size (% MGS) normalized to phosphate-buffered saline (PBS) of n=3 ice wafers assessed at 22 mM using a splat-cooling assay with a 30-minute annealing time at -6.4 °C. Data was analyzed by method (**1**) quantifying 12-random crystals from the wafer[158] or method (**2**) quantifying the area of all crystals within the field of view. Data fit to a linear regression (R^2 = 0.90 and 0.37 with 95 % confidence bands of the linear regression shown).[157,158] *% MGS activity data analyzed by method 1 from Capicciotti (2014).*[158]

The relationship between HI and ice recrystallization inhibition activity was then assessed at different concentrations of compound (either 22 mM or 75 mM) and at different annealing times (between 5 minutes and 30 minutes). The 22 mM concentration captured the ice recrystallization inhibition activity of each compound where it was not found to be significantly active (no change from PBS was observed by the 5-minute SCA); on the other hand, the 75 mM concentration captured each molecule near its IC_{50} and was therefore indicative of a point where ice recrystallization inhibition activity was expected to be observed. The different annealing times would provide insight into whether the relationship between HI and ice recrystallization inhibition activity changed over time.

With respect to the two different concentrations, the % MGS of ice wafers in the presence of each compound at 22 mM was larger than the % MGS at the 75 mM concentration (at each annealing time point) as was expected. However, it was no longer possible to correlate the ice recrystallization inhibition activity of the reducing sugars (**7-9**) at the 75 mM concentration after a 30-minute annealing time (R^2 = 0.00) (**Figure 4-9B**). In fact, the only annealing time and concentration at which any correlation could be observed between the HI of the monosaccharides reducing sugars (**7-9**) and their ice recrystallization inhibition activity was at a concentration of 22 mM after a period of 30 minutes (R^2 = 0.37) (**Figure 4-9**).

Therefore, using the % MGS quantification of ice recrystallization inhibition activity, the correlation to HI may only be relevant at concentrations that minimally inhibit ice recrystallization and at annealing time points that represent a constant rate of ice crystal growth over time.

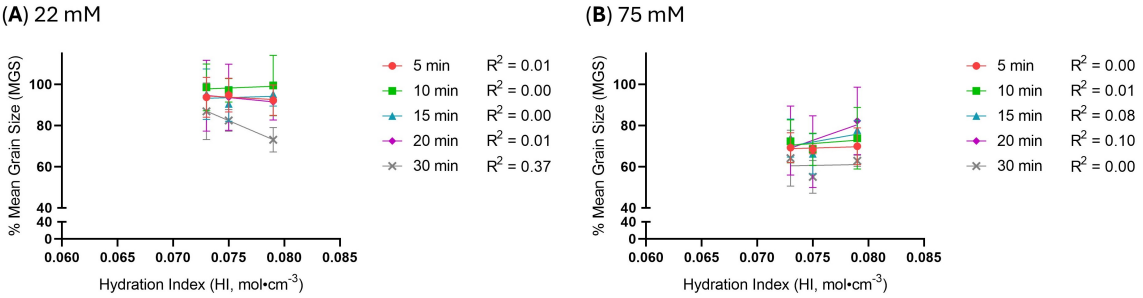


Figure 4-9. Plot of hydration index (HI) relative to ice recrystallization inhibition activity for reducing sugars (**7-9**) at (**A**) 22 mM or (**B**) 75 mM with respect to different annealing times. Data reported as mean ± standard deviation (SD) of the percent mean grain size (% MGS) normalized to phosphate-buffered saline (PBS) of n=3 ice wafers assessed using a splat-cooling assay at -6.4 °C. Data was analyzed by quantifying the area of all crystals within the field of view. Data fit to a linear regression with 95 % confidence bands of the linear regression shown.

Further investigation found that quantification of ice recrystallization inhibition activity by measure of the normalized rates of ice crystal growth (v_{norm}) after different periods of annealing did correlate with HI at either concentration (22 or 75 mM) or any annealing time (**Figure 4-10**). Of note, the only concentration at which the normalized rate of ice crystal growth was measurably reduced compared to PBS, indicative of a compound that was inhibiting ice recrystallization, was after a 5-minute annealing time (**Figure 4-10B**).

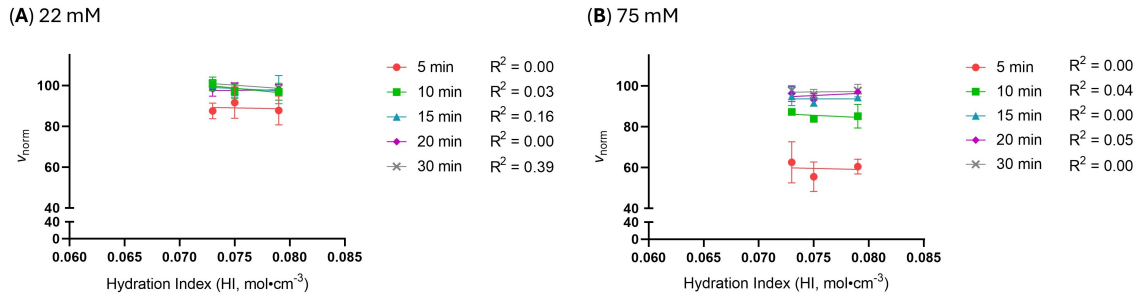


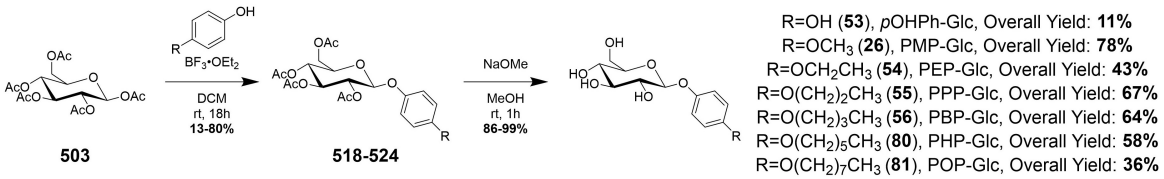
Figure 4-10. Plot of hydration index (HI) relative to ice recrystallization inhibition activity for reducing sugars (**7-9**) at (**A**) 22 mM or (**B**) 75 mM with respect to different annealing times. Data reported as mean ± standard deviation (SD) of the normalized rate of ice recrystallization (v_{norm}) compared to phosphate-buffered saline (PBS) of n=3 ice wafers assessed using a splat-cooling assay at -6.4 °C. Data was analyzed by quantifying the area of all crystals within the field of view. Data fit to a linear regression with 95 % confidence bands of the linear regression shown.

These results suggested that while the monosaccharide reducing sugars (**7-9**) could initially inhibit ice recrystallization and reduce the rate of ice crystal growth, they were unable to maintain the reduced rate

compared to PBS over longer annealing times. Furthermore, while this reduced initial rate translated to a reduced average crystal size (% MGS) compared to PBS, the inhibition was relatively weak and would not have been expected to significantly improve cryopreservation outcomes compared to the more active IRIs that have been reported in the last several years with examples of successful application to cellular cryopreservation (*e.g.*, *p*BrPh-Glc, **25** or 2FA, **27**). Therefore, while HI as a parameter provided us with insight into a plausible mechanism of action that required interactions with bulk water molecules (which was consistent with mechanistic studies that were undertaken as part of this thesis and will be explored further in *chapter 6*), the phenomenon of ice recrystallization inhibition by small molecules as a whole cannot be explained by HI alone.

4.2.1. Revisiting hydrophobicity as an important feature for ice recrystallization inhibition activity using the 5-minute SCA

Given the change in SCA (from 30- to 5-minute) caused an observed change in the relationship between ice recrystallization inhibition activity and HI, we were interested in re-exploring the relationship between hydrophobicity and hydrophilicity that was identified by several past studies using the 30-minute SCA. To this end, various *p*-alkoxyphenyl-β-D-glucopyranosides with increasing alkyl chain length were synthesized using the traditional Lewis-acid assisted glycosidation procedure that was described previously for 4-cyanophenyl-β-D-glucopyranoside (*p*CNPh-Glc, **30**, see *section 3.2.1*).[214] The corresponding phenol was reacted with β-D-glucose pentaacetate (**503**) using boron trifluoride diethyl etherate ($BF_3{\cdot}OEt_2$) to generate the protected intermediates **518-524** (**Scheme 4-1**). Removal of the acetates using Zemplén[326] conditions afforded the desired products with iteratively increasing alkyl chain length from 4-hydroxyphenyl-β-D-glucopyranoside (*p*OHPh-Glc, **53**) to 4-butxyphenyl-β-D-glucopyranoside (PBP-Glc, **56**), as well as the hexyl (**80**, PHP-Glc) and octyl derivatives (**81**, POP-Glc), in two steps with 11-78 % overall yield (**Scheme 4-1**).



Scheme 4-1. Synthesis of *p*-alkoxyphenyl-β-D-glucopyranosides **26**, **53**-**56**, **80**-**81**.

With respect to the ice recrystallization inhibition activity of these compounds as measured by the 5-minute SCA, the IC_{50} was found to improve ~10-fold upon methylation of the hydroxyl [from *p*OHPh-Glc (**53**) to PMP-Glc (**26**)] and then another ~10-fold upon extension by one CH_2 to PEP-Glc (**54**); the IC_{50} values were 133.3 mM (95 % CI [117.9-152.7]), 28.8 mM (95 % CI [26.6-31.2]), and 4.45 mM (95 % CI [4.29-4.62]) respectively (**Figure 4-11**). The ice recrystallization inhibition activity of the propyl derivative

(PPP-Glc, **55**, IC_{50} = 19.9 mM, 95 % CI [16.4-24.4]) decreased ~6-fold but then increased again (~3-fold) with the butyl substitution (PBP-Glc, **56**, IC_{50} = 6.25 mM, 95 % CI [4.08-8.93]) (**Figure 4-11**). The hexyl and octyl substituted derivatives (PHP-Glc and POP-Glc, **80**-**81**) had very low aqueous solubility in PBS. As a result, the hexyl substituted compound (PHP-Glc, **80**) could only achieve a maximum v_{norm} of 69.7 ± 6.2 % at its maximum solubility (4 mM) indicating that its activity may be similar to that of the butyl derivative (**56**) with a predicted IC_{50} of ~6.37 mM (**Figure 4-11**); the octyl substituted compound (POP-Glc, **81**) could not be solubilized in PBS at a concentration of 0.1 mM and as no small-molecule carbohydrate IRIs reported at the time of testing had shown meaningful activity below a 1 mM threshold the solubility and ice recrystallization inhibition activity of this compound was not assessed further.

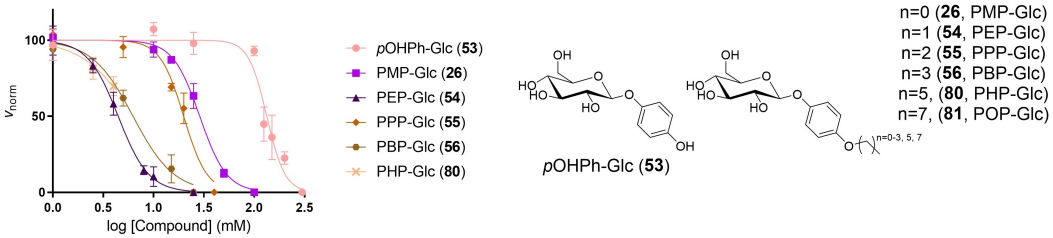


Figure 4-11. Ice recrystallization inhibition activity of *p*-alkoxyphenyl-β-D-glucopyranosides **26**, **53**-**56**, **80**. Plot of normalized ice crystal growth rate (v_{norm}) in PBS against logarithm transformed compound concentration (in mM). Determined by modified splat-cooling assay with a 5-minute annealing time at -6.4 °C.[169]

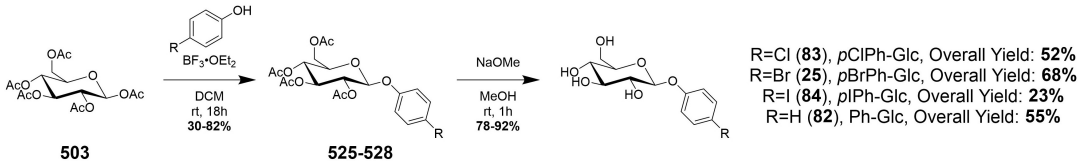
The ice recrystallization inhibition activity of the *p*-alkoxyphenyl-β-D-glucopyranosides confirmed that the incorporation of hydrophobicity to a compound could improve ice recrystallization inhibition activity as all alkylated derivatives were at least 10-fold more active than the parent *p*OHPh-Glc (**53**). However, conclusions regarding the optimum alkyl chain length remained inconclusive considering both the ethyl (PEP-Glc, **54**) and butyl (PBP-Glc, **56**) lengths were found to have nearly the same IC_{50} value. These results were inconsistent with the previous results from the 30-minute SCA obtained by Matt Alteen (Ben Lab, MSc 2013), where the ethyl substitution of PEP-Glc (**54**) was found to be optimal (see *section 4.1.1*).[411]

Importantly, PBP-Glc (**56**) was disregarded as a potential candidate for cellular cryopreservation applications due to its relatively weak ice recrystallization inhibition activity as measured by the 30-minute SCA. However, its activity was found to be comparable to one of the most active small-molecule IRIs at the time (2FA, **27**, *chapter 2*) using the 5-minute SCA. Importantly, these "false negative" results may have contributed to the inability to formulate direct conclusions during previous SAR campaigns. As a result, the remainder of this chapter will focus on a comprehensive structure-activity examination based on

different molecular and physiochemical properties across a diverse library of compounds and their activity as measured by the 5-minute SCA.

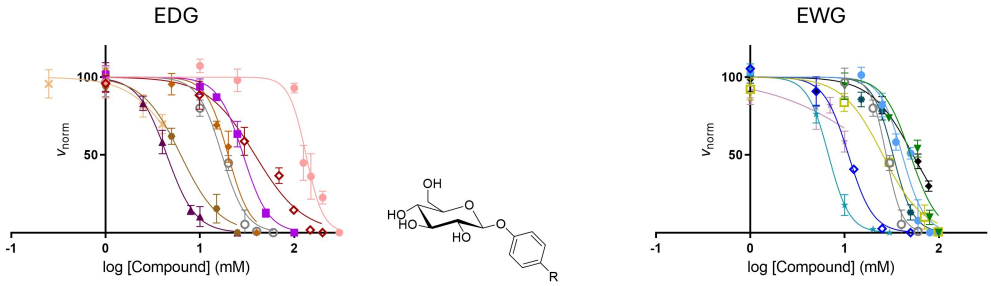
4.3. A structure activity relationship (SAR) investigation of ice recrystallization inhibition activity of *O*-aryl-glucopyranosides as measured by the 5-minute splat-cooling assay (SCA)

For this investigation we sought to generate a library of *O*-aryl-glucopyranosides, which have been extensively studied by the Ben Lab for their success as cryoprotectants for red blood cells[162,218] and as part of SAR campaigns for trends to hydrophobicity as well as electronic effects using the previous 30-minute SCA.[158,411,412] The library already included the *p*-alkoxyphenyl-β-D-glucopyranosides (**53**-**56**, **80**) discussed in *section 4.2.1* as well as the *O*-aryl-β-D-glucopyranosides with nitrile- (**30**), and amide- (**31**) functional groups as discussed in *chapters 2 and 3*; therefore, to fill out the library with diverse compounds the derivatives with an unsubstituted phenyl motif (**82**, Ph-Glc) as well as chloro- (**83**, pClPh-Glc), bromo- (**25**, pBrPh-Glc), and iodo- (**84**, pIPh-Glc) substitutions were synthesized using the traditional Lewis-acid assisted glycosidation procedure *via* the protected intermediates **525-528** (**Scheme 4-2**). Removal of the acetates using Zemplén[326] conditions afforded the desired products in two steps with 23-68 % overall yield (**Scheme 4-2**). In addition to these compounds, the *nitro*- substituted derivative 4-nitrophenyl-β-D-glucopyranoside (*p*NO_2Ph-Glc, **85**) was commercially available could therefore be used directly for testing.



Scheme 4-2. Synthesis of *O*-aryl-β-D-glucopyranosides **25**, and **82**-**84**.

The ice recrystallization inhibition activity of these compounds was then assessed by the 5-minute SCA and an IC_{50} value was determined for each compound (**Figure 4-12**). Other *para*-*O*-aryl glucopyranoside compounds that had been tested by previous Ben Lab student Dr. Jessica Poisson (PhD 2019) were also added to the comparison, including fluoro- (*p*FPh-Glc, **86**), azido- (*p*N_3Ph-Glc, **29**), and amino- (*p*NH_2Ph-Glc, **32**) substituted derivatives.[214] This library of compounds was selected to provide a wide range of substituents that varied in size, their electronic impact on the aromatic ring (electron donating versus electron withdrawing groups), and hydrogen bonding properties (donors and acceptors). Hydrocarbon substituents such as a methyl- (-CH_3) or ethyl- (-CH_2CH_3) were avoided due to potential solubility limitations of the substrates in PBS.



R=	NH_2	OH	OHex	OBu	OMe	OPr	OEt	H	F	N_3	I	Cl	Br	$CONH_2$	CN	NO_2
Symbol	◇	●	✕	●	■	◆	▲	○	▼	□	★	◇	★	●	◆	●
Cmpd #	**32**	**53**	**80**	**56**	**26**	**55**	**54**	**82**	**86**	**29**	**84**	**83**	**25**	**31**	**30**	**85**
IC_{50}	38.4	133.3	N/A	6.25	28.8	19.9	4.45	17.1	49.9	25.4	N/A	11.0	6.75	40.8	53.1	32.6
95 % CI	27.7-50.8	117.9-152.7	N/A	4.08-8.93	26.6-31.2	16.4-24.4	4.29-4.62	23.8-31.2	22.5-75.1	17.3-35.1	N/A	9.11-12.8	6.12-7.46	33.4-48.7	40.7-67.5	26.6-40.6
R^2	0.98	0.96	N/A	0.99	0.99	0.98	0.99	0.99	0.91	0.98	N/A	0.99	0.99	0.95	0.98	0.99

Figure 4-12. Ice recrystallization inhibition activity of *O*-aryl-β-D-glucopyranosides **25**-**26**, **29**-**32**, **53**-**56**, **80**-**86**. Plot of normalized ice crystal growth rate (v_{norm}) in PBS against logarithm transformed compound concentration (in mM). Determined by modified splat-cooling assay with a 5-minute annealing time at -6.4 °C.[169]

The majority of compounds that were found to strongly inhibit ice recrystallization by the 30-minute SCA when tested at a concentration of 22 mM (% MGS < 30 %)[167] were also found to have the lowest IC_{50} values as determined by the 5-minute SCA (*e.g.*, compounds **25**-**26**, and **83**). However, for the compounds that were previously found to be more poorly active (% MGS > 30 %), the IC_{50} values varied significantly; where for example Ph-Glc (**82**) and *p*OHPh-Glc (**53**) were found to have two of the highest % MGS values (64.4 ± 2.8 % and 61.8 ± 2.6 % respectively) but Ph-Glc (**82**) was found to have one of the lowest IC_{50} values (17.1 mM, 95 % CI [23.8-31.2]) while *p*OHPh-Glc (**53**) was found to have one of the highest (133.3 mM, 95 % CI [117.9-152.7]) (**Figure 4-12**). These results confirmed that the 30-minute SCA and its analysis method may have unintentionally biased the reporting of ice recrystallization inhibition activity with the incorporation of false negatives into the overall library. These false negatives would certainly have prevented active compounds from being considered for translation to cellular cryopreservation applications and may have impacted the conclusions made from previous SAR studies. As a result, it was pertinent to re-explore the relationship between ice recrystallization inhibition activity using the 5-minute SCA method that is currently used exclusively for small-molecule IRI development by the Ben Lab.

4.3.1. A broad investigation of various molecular descriptors and parameters and their relationship to the ice recrystallization inhibition activity of O-aryl-β-D-glucopyranosides as measured by the 5-minute SCA

Understanding the ice recrystallization inhibition activity of a compound at different concentrations is critical for guiding the translation of these compounds into cellular applications where activity, solubility, permeability, and cytotoxicity must all be carefully balanced. However, to narrow the field of potential

small-molecule compounds that could be investigated as IRIs it was of interest to explore computationally derived parameters that may be able to predict the ice recrystallization inhibition activity of compounds as measured by the 5-minute SCA. As part of this study, multiple molecular descriptors were investigated with a focus on parameters that could be used to describe the hydrophobicity of a molecule or its interactions with water molecules. These features were selected based on their importance to previous correlation studies that had been undertaken in the Ben Lab, as well as the hypothesized mechanism of action involving the disruption of water molecule transfer between ice crystals during recrystallization. Where possible, the parameters were calculated from multiple different sources – including ChemDraw;[414] MarvinSketch;[415] VCC ALOGPS;[416,417] and ACDLabs[418] – to compare between the results of each algorithm. The parameters that were investigated included:

- Polar surface area (PSA): Estimates total 3D van der Waals surface area of polar atoms using a 2D fragment-based approach
- Molecular surface area (MSA): Total 3D surface area based on van der Waals radii
- Solvent accessible surface area (ASA): Calculated using a 1.4 Å radius for one water molecule
    - ASA- & ASA+: Solvent accessible surface area of all atoms with a partial negative or positive charge respectively
    - ASA_H & ASA_P: Solvent accessible surface area of all hydrophobic or polar atoms respectively
- Hydrophobic/lipophilic balance (HLB): Ratio of hydrophobic to lipophilic regions in the molecule
- Dipole moment: Measure of the net polarity of a molecule to describe charge separation
- Polarizability: Calculated from the molar refractivity of a compound
- Molar refractivity: A measure of the total polarizability of one mole of a substance
- logP: the partition coefficient of a molecule between octanol and water
- logS: aqueous solubility (mol/L)
- Hammett (σ_p):[419–421] A linear free energy relationship parameter/substituent constant that describes how the field, inductive, and resonance electronics of a kinetic process are affected by different *para*-aryl substituents
- TAFT (σ_i):[419,422,423] A parameter that is an extension of the Hammett linear free energy relationship that describes the steric effects of a *para*-aryl substituent on a kinetic process in addition to the effect of field, inductive, and resonance electronics
- Other physiochemical properties including surface tension, boiling point & freezing point, critical temperature, volume, and pressure, heat of formation, enthalpy, Gibbs free energy, Dreiding

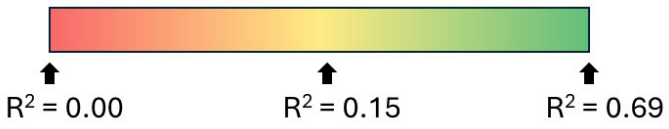
energy, MMFF94 energy, minimal & maximal projection area, minimal & maximal projection radius, length perpendicular to the minimum & maximum area, and van der Waals volume.

All parameters were calculated computationally and were plotted with respect to ice recrystallization inhibition activity data as measured by the 5-minute SCA and reported as an IC_{50} value for each compound. The graphical plots were then fit to either a linear [$y = (m * x) + b$] or exponential model [$y = (a * e^{(b*x)}$] using Microsoft Excel® for initial assessment of potential relationships between structure and activity. Previous work by Dr. Capicciotti (Ben Lab, PhD 2014) found that the inhibition of ice recrystallization may occur *via* different mechanisms depending on the inhibitor and the chosen annealing time before quantifying ice recrystallization inhibition activity (see *section 1.3.2*).[158] Therefore, the exponential fit was included to account for potential changes in the relative impact of different parameters at different levels of ice recrystallization inhibition activity. Furthermore, all correlations were made using the library of *O*-aryl-β-D-glucopyranosides shown in **Figure 4-12** (except where specifically indicated) with the exclusion of PHP-Glc (**80**) and *p*IPh-Glc (**84**); these two compounds did not achieve sufficient activity to generate data points at a v_{norm} below 50 % within their apparent solubility limits in PBS which could significantly reduce the accuracy of the IC_{50} value. A summary of all parameters, including the linear and exponential correlation coefficients for each plot, can be found in **Table 4-1**; each individual plot can be found in the supporting information for reference (see *section 8.3.6*).

Table 4-1. Heat map of linear and exponential (exp) correlation coefficients R^2 from plots generated in Microsoft Excel® for comparison between a noted physicochemical parameter and ice recrystallization inhibition activity as measured by the 5-minute SCA (reported as an IC_{50}). All graphs can be found in the appendices (see *section 8.3.6*).

Type	Calculated by	Linear R^2	Exp R^2
PSA	MarvinSketch	0.11	0.08
	ChemDraw	0.08	0.04
	ACDLabs [b]	0.11	0.07
MSA	MarvinSketch	0.18	0.19
ASA	MarvinSketch	0.20	0.20
ASA-		0.16	0.16
ASA+		0.04	0.02
ASA_H		0.22	0.19
ASA_P		0.05	0.02
PSA/MSA	MarvinSketch	0.28	0.21
PSA/ASA	MarvinSketch	0.31	0.24
PSA/ASA-		0.28	0.24
PSA/ASA+		0.15	0.08
PSA/ASA_H		0.18	0.09
PSA/ASA_P		0.00	0.00
ASA/MSA	MarvinSketch	0.14	0.17
ASA-/MSA		0.07	0.07
ASA+/MSA		0.04	0.03
ASA_H/MSA		0.17	0.09
ASA_P/MSA		0.13	0.06
HLB	MarvinSketch	0.13	0.06
Polarizability	ACDLabs [b]	0.24	0.30
Molar Refractivity	ChemDraw (Crippen) [a]	0.23	0.23
	ChemDraw (Viswanadhan) [a]	0.26	0.28
	ACDLabs [b]	0.26	0.28
logP	VCC	0.49	0.49
	ChemDraw (Crippen) [a]	0.29	0.17
	ChemDraw (Viswanadhan) [a]	0.23	0.12
	ACDLabs [b]	0.52	0.69
logS	VCC	0.31	0.25
	MarvinSketch at pH 7.4	0.14	0.04
	ChemDraw	0.38	0.39
Surface Tension	ACDLabs [b]	0.33	0.37

Type	Calculated by	Linear R^2	Exp R^2
Dipole Moment	MarvinSketch	0.01	0.01
Boiling Point	ChemDraw	0.01	0.01
Freezing Point		0.11	0.10
Critical Temp	ChemDraw	0.00	0.00
Critical Volume		0.20	0.21
Critical Pressure		0.34	0.48
Heat of Formation	ChemDraw	0.00	0.00
Enthalpy	ORCA	0.14	0.15
Gibbs Free Energy	ORCA	0.14	0.15
	ChemDraw	0.01	0.01
Electronic Energy	ORCA	0.10	0.06
Dreiding Energy	MarvinSketch	0.05	0.04
MMFF94 Energy	MarvinSketch	0.01	0.01
Min Proj. Area	MarvinSketch	0.15	0.13
Max Proj. Area		0.16	0.18
Min Proj. Radius	MarvinSketch	0.25	0.23
Max Proj. Radius		0.15	0.12
Length Perpendicular to Min Area	MarvinSketch	0.15	0.12
Length Perpendicular to Max Area		0.07	0.04
van der Waals Volume	MarvinSketch	0.19	0.18
Molar Volume	ACDLabs [b]	0.27	0.40
σ_p (Hammett)	Hansch *et. al.* (1991) [419]	0.01	0.00
σ_p (TAFT)		0.27	0.00



[a] Due to algorithm limitations, calculations with Crippen or Viswanadhan methods from ChemDraw were not possible for *p*N_3Ph-Glc (**29**) therefore this compound was not included in the corresponding regressions
[b] Due to database limitations, calculations with ACDLabs were not possible for *p*CNPh-Glc (**30**), *p*AmPh-Glc (**31**), or PPP-Glc (**55**) therefore these compounds were not included in the corresponding regressions

Of all parameters investigated in this study, 98 % of the correlation coefficients were < 0.50 and 66 % were < 0.20 indicating that there were not any very strong linear or exponential correlations with ice recrystallization inhibition activity as measured by the 5-minute SCA (**Table 4-1**). Physiochemical, geometrical, and energy related parameters such as boiling and freezing points, Gibbs free energy, and projection areas were generally very poorly correlated to ice recrystallization inhibition activity. However, given these parameters alone do not directly measure interactions with water molecules, it was not expected that they would be strongly correlated to ice recrystallization inhibition activity. Furthermore, the Hammett parameter (σ_p) was not found to be correlated with the log-transformed IC_{50} values of the compounds with a linear correlation coefficient of 0.01 (**Figure 4-13**); a correlation to this parameter was not expected based on the previous results from the SAR study by Dr. Trant[412] and Dr. Capicciotti[158] using the 30-minute SCA (see *section 4.1.2*). Slight variation in IC_{50} values was expected given the inclusion of data from different users that could be affecting the reliability of the relationship to σ_p; however, the correlation did not meaningfully improve if the data points collected by other students were removed from the plot ($R^2 = 0.05$, **SI Figure 8-88**).

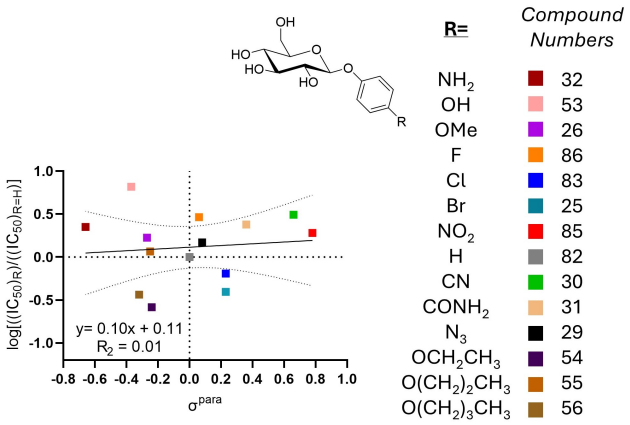


Figure 4-13. Hammett plot of the relationship between IC_{50} and the electronic effect of the *para*- substituent for *O*-aryl-β-D-glucopyranosides that were newly tested for ice recrystallization inhibition activity using the 5-minute SCA. The $\log[(IC_{50\ R})/(IC_{50\ R=H})]$ for each derivative was plotted against the σ^{para} (σ_p) value for each substituent.[419] *IC_{50} data for compounds* **29**, **32**, *and* **86** *tested and reported previously by Dr. Jessica Poisson (2019).*[214]

While the Hammett plot was originally created to describe the effect of changing electronic properties on the equilibrium constant for the ionization of benzoic acids, it has also been used to more generally describe the kinetic processes of a variety of chemical reactions.[420,421] Ice recrystallization, and thus its inhibition, is ultimately a time-dependent (*i.e.,* kinetic) process, where the size of ice crystals is described as a function of annealing time. Therefore, the Hammett substituent constants were thought to be an appropriate method for describing the effect of varying aryl ring electronics on ice recrystallization inhibition activity. If the electronic properties of the aryl ring were to have an impact on ice recrystallization

inhibition activity as expected, where greater inhibition (a smaller IC_{50}) would be observed with increasing electron donation (and described in **Figure 4-6**), the linear free energy relationship would have a positive value slope (ρ). The absolute value of the slope would then indicate the sensitivity of ice recrystallization to the electronics of the substituent compared to benzoic acid ionization (a $\rho > 1$ would indicate increased sensitivity and $0 < \rho < 1$ would indicate decreased sensitivity). As the slope (ρ) of the plot did not significantly differ from zero, it was confirmed that there was no significant correlation between the electronics of the *para*- position substituent and ice recrystallization inhibition activity. Instead, as the *para*-substituent had a dramatic impact on the compound's activity as a whole, it was thought that it may either directly form interactions with water molecules (*i.e.*, through hydrogen bonding interactions such as for compounds **32** or **53**) or indirectly affect the overall hydrogen bonding network of entire molecule (*i.e.*, for compounds that cannot directly hydrogen bond such as **82** or **83**), but cannot be explained solely by the effect of the substituent's electronics on the anomeric oxygen.

Instead, the parameters that were most strongly correlated to ice recrystallization inhibition activity were generally those that were related to the molecule's amphiphilicity and/or intermolecular interactions with water molecules. These included parameters such as ratios of PSA to a measure of molecular volume (either MSA or ASA), polarizability, molar refractivity, logP, logS, surface tension, and critical pressure (**Table 4-1**). In all cases, greater ice recrystallization inhibition activity was observed when each parameter represented increased interactions with water molecules or increased hydrophobicity. In general, these correlations were in line with the previous hypotheses and correlations related to hydration index and hydrophobicity. For example, when considered on its own, the polar surface area (PSA) of the molecule was very weakly correlated with ice recrystallization inhibition activity as measured by the 5-minute SCA (R^2 values of ≤ 0.11, **SI Figure 8-87**). However, when considering the ratio of polar surface area (PSA) to the molecule's molecular surface area (MSA) (calculated using MarvinSketch®), a weak linear correlation with R^2 value of 0.28 was found (**Figure 4-14**). Although the correlation between PSA/MSA and ice recrystallization inhibition activity for the *O*-aryl-β-D-glucopyranosides was weak, the general trend showed that compounds which had smaller ratios of PSA compared to their entire MSA could reasonably be predicted to be more active IRIs relative to compounds with a much greater PSA to MSA ratio.

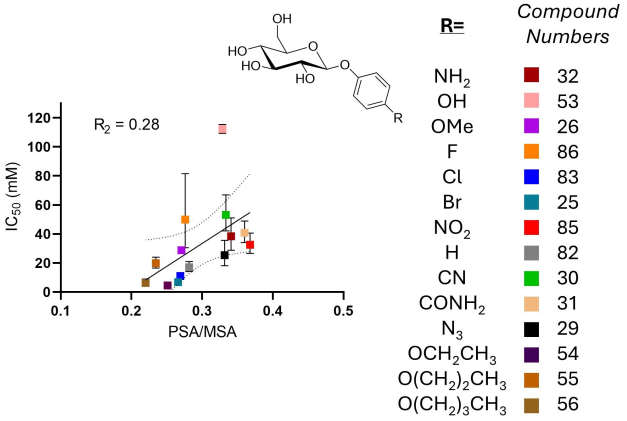


Figure 4-14. Plot of the ratio of a compound's polar surface area (PSA) to its molecular surface area (MSA) as calculated by MarvinSketch® for various *O*-aryl-β-D-glucopyranosides relative to their ice recrystallization inhibition activity as measured by the 5-minute SCA. Data fit to a linear regression ($R^2 = 0.28$) with 95 % confidence bands of the linear regression shown. Ice recrystallization inhibition activity reported as the IC_{50} with 95 % confidence interval error of the dose-response curve for the representative compound as determined by splat-cooling assay with a 5-minute annealing time at -6.4 °C.

While these updated correlations to ice recrystallization inhibition activity as measured by the 5-minute SCA were able to provide insight into the features that differentiated "active" compounds from "inactive" compounds, none of the investigated parameters were able to accurately predict the ice recrystallization inhibition activity of compounds within similar activity ranges nor between compounds of similarly related structural features. For example, within closely related PSA/MSA ratios the compounds which had a smaller PSA/MSA ratio such as PBP-Glc (**56**) with a ratio of 0.22, were not necessarily more active than those with a larger PSA/MSA ratio such as PEP-Glc (**54**) with a ratio of 0.26 (**Figure 4-14**).

Similarly, despite having the highest correlation by linear or exponential fit overall, the theoretical octanol/water partition coefficient (logP) also could not be used to accurately predict absolute ice recrystallization inhibition activity of compounds (**Figure 4-15**). However, the correlation was consistent with the finding that compounds which cause greater disruption to water molecules and have greater hydrophobicity were generally more active as ice recrystallization inhibitors. It is important to note that the R^2 values as calculated by Microsoft Excel® (in **SI Figure 8-87**) and GraphPad Prism (**Figure 4-15**) vary slightly due to differences in the formulas for the calculation of the correlation efficient between the two programs. Additionally, the logP calculation completed by the algorithm of ACDLabs resulted in a higher R^2 value ($R^2 = 0.71$) than VCC ALOGPS 2.1 ($R^2 = 0.49$) (**Figure 4-15B** and **D**) but ACDLabs was unable to calculate the theoretical logP value for compounds **30-31**, and **55** and therefore the included library contained only 11 compounds compared to the 14 in the correlation as calculated by VCC ALOGPS 2.1; when these three compounds were removed from the correlation with logP as calculated by VCC ALOGPS 2.1 the exponential correlation coefficient improved to 0.73, suggesting that the difference in R^2 values

between the two algorithms was not caused by differences in their accuracy for predicting ice recrystallization inhibition activity but instead due to a difference in the compounds included within the dataset.

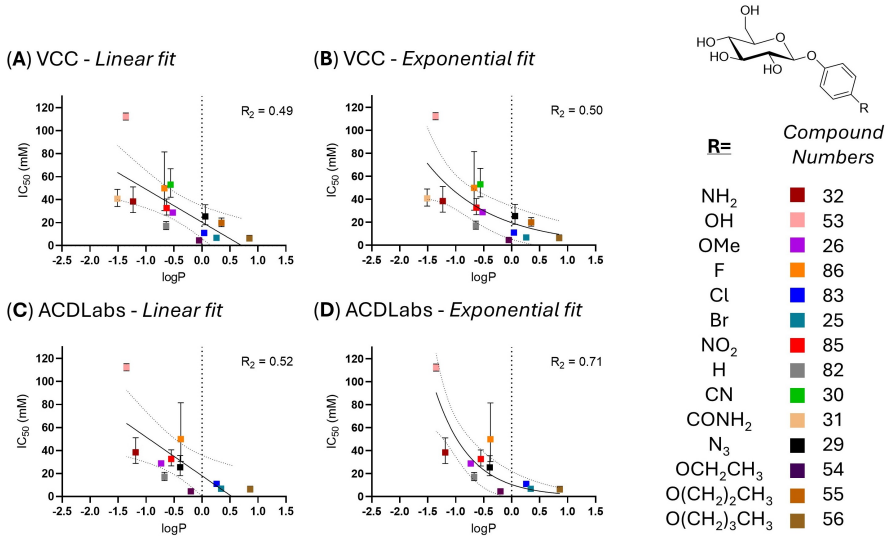


Figure 4-15. Plot of a compound's theoretical logP as calculated by (**A** and **B**) VCC ALOGPS 2.1 or (**C** and **D**) ACDLabs for various *O*-aryl-β-D-glucopyranosides relative to their ice recrystallization inhibition activity as measured by the 5-minute SCA. Data fit to a (**A** and **C**) linear regression (R^2 = 0.49 and 0.52) or (**B** and **D**) exponential curve fit (R^2 = 0.49 and 0.71) with 95 % confidence bands of the fit shown.

Despite the relatively small difference between the numerical values for the correlation coefficients (linear and exponential) between the more strongly correlated parameters and ice recrystallization inhibition activity, visual inspection of the plots suggested that compounds with very weak ice recrystallization inhibition activity as measured by the 5-minute SCA may not "fit" or "rely" on the parameters in the same manner as those that were moderately to highly active. For example, two different pharmaceutical drugs (*i.e.,* β_2 agonists and muscarinic antagonists) may cause the same therapeutic effect (*i.e.,* elevating cyclic adenosine monophosphate levels to cause bronchodilation) but target two different receptors (*i.e.,* G_s and G_i G-protein subunits respectively).[424] Therefore, it was thought that the exclusion of "inactive" compounds (which may not have the same mechanism of action as "active" compounds) from the data set or the logarithm transformation of the activity data could improve the accuracy of the linear correlation and provide more meaningful information about the relationship between the given parameter. The most inactive compounds were selected based on a threshold that excluded the highest 20 % of the total dataset, or IC_{50} values of greater than 45 mM.

Both exclusion of compounds with IC_{50} values greater than 45 mM and the logarithm transformation of IC_{50} values for the entire data set resulted in improved linear correlation coefficients of compared to the original correlation with the full data set (**Figure 4-16B** and **C** compared to **A**).

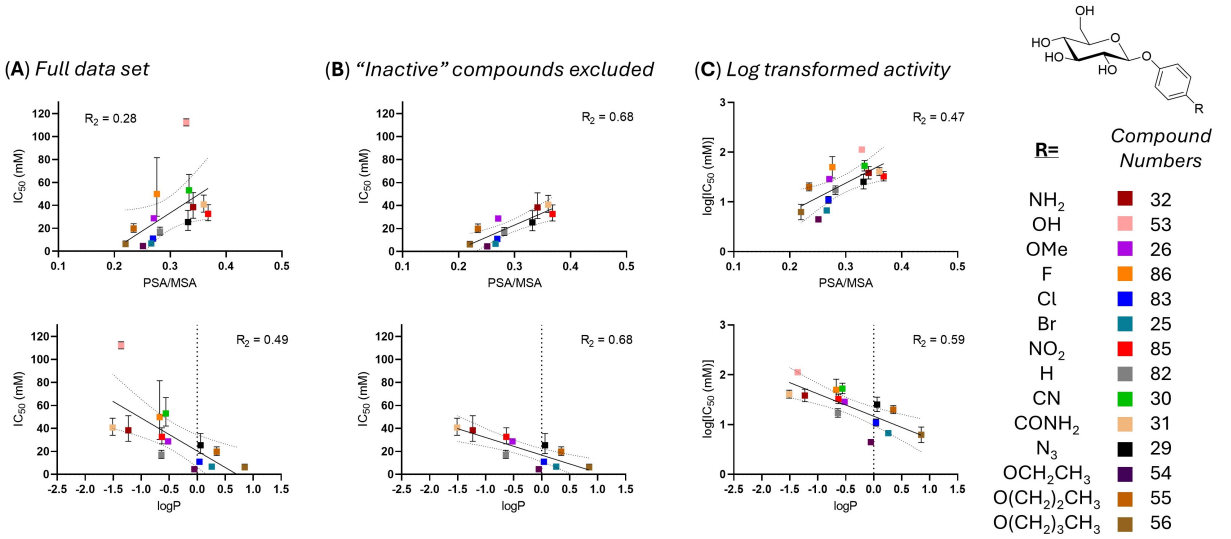


Figure 4-16. Plot of a compound's polar surface area (PSA) to its molecular surface area (MSA) as calculated by MarvinSketch® (top) or theoretical logP as calculated by VCC ALOGPS 2.1 (bottom) for various *O*-aryl-β-D-glucopyranosides relative to their ice recrystallization inhibition activity as measured by the 5-minute SCA (IC_{50}). Data fit to a linear regression with (**A**) the full data set (R^2 = 0.28 and 0.49), (**B**) compounds $IC_{50} \geq 45$ mM excluded (R^2 = 0.68 and 0.68) or (**C**) log-transformed ice recrystallization inhibition activity data (R^2 = 0.47 and 0.59) with 95 % confidence bands of trendline shown.

With the improved linear correlation coefficients, there was confidence in the importance of increasing a molecule's hydrophobicity relative to its hydrophilicity with respect to improving ice recrystallization inhibition activity. When using the log-transformed ice recrystallization inhibition activity, 5 in 6 compounds (or a proportion of 83 %) with a logP of greater than -0.5 had an IC_{50} value of less than 20 mM (compared to only 1 in 8 compounds, or a proportion of 12.5 %, with a logP less than -0.5) (**Figure 4-16C**). A similar finding was true for the correlation with PSA/MSA, where 6 in 8 compounds (or a proportion of 75 %) with a PSA/MSA ratio of less than 0.3 had an IC_{50} value of less than 20 mM (compared to none of the compounds with a PSA/MSA ratio greater than 0.3) (**Figure 4-16C**). Across both correlations only a single false negative was reported (Ph-Glc, **82**, with a logP < -0.5 despite a reported IC_{50} of < 20 mM) at a proportion of 7 %. On the other hand, there were three total occurrences of false positives at an occurrence of 21 %: *p*N_3Ph-Glc (**29**) with a logP of > -0.5, as well as PMP-Glc (**26**) and *p*FPh-Glc (**86**) with PSA/MSA ratios of < 0.3 despite IC_{50} values of > 20 mM (**Figure 4-16**). However, the false positives could be excluded from analysis if a requirement was set that "active" compounds (with IC_{50} < 20 mM) must meet both logP and PSA/MSA thresholds with values of > 0.5 and < 0.3 respectively. These findings may significantly improve the development of small-molecule ice recrystallization inhibitors, both from a time and cost perspective, by screening out derivatives from testing that do not meet specific criteria for

hydrophobic/hydrophilic balance. Furthermore, the incorporation of thresholds from other parameters that had relatively stronger linear or exponential correlation coefficients such as PSA/ASA ratio and logS could further improve the accuracy of potential development screens which should be explored further in future.

4.4. Limitations of molecular parameters to describe or predict ice recrystallization inhibition activity

While the correlations between ice recrystallization inhibition activity and the investigated parameters (such as PSA/MSA ratio and logP) supported the hypothesis that increasing the hydrophobicity of a small-molecule *O*-aryl-β-D-glucopyranoside would lead to improved ice recrystallization inhibition activity as measured by the 5-minute SCA, they ultimately failed to be able to account for the differences in ice recrystallization inhibition activity for compounds with very close measured activity (**Figure 4-16**). Despite having a near 2-fold difference in their IC_{50} values, the *ortho*-, *meta*-, or *para*- regioisomers of nitrile and amide substitutions on the aryl ring (**30-31**, **37-38**, and **42-43**) were calculated as having nearly identical physiochemical parameters with PSA/MSA ratios ranging between 0.326-0.334 and 0.356-0.360 as well as logP values that ranged between -0.56 to -0.58 and -1.50 to -1.51 respectively (**Figure 4-17**). In addition, the monosaccharide reducing sugars (**7-9**) were calculated as having identical PSA and logP values as the fragment-based approaches that were used for these calculations did not consider differences in stereochemistry (**Figure 4-17**).

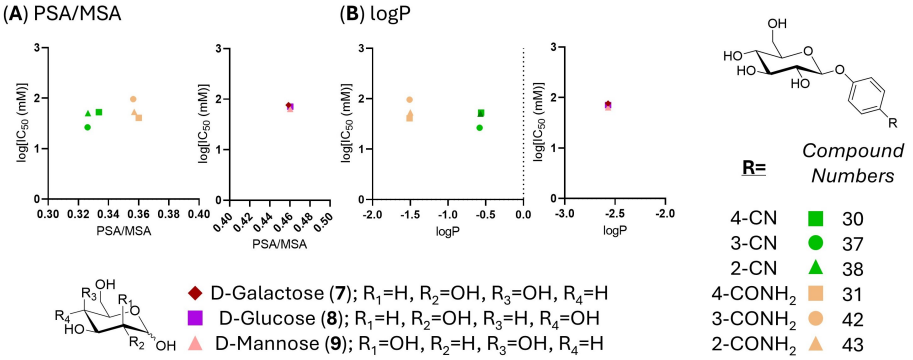


Figure 4-17. Plots of the log-transformed ice recrystallization inhibition activity relative to its (**A**) polar surface area (PSA) to molecular surface area (MSA) ratio as calculated by MarvinSketch® or (**B**) its theoretical logP value as calculated by VCC's ALOGPS 2.1 algorithm. Ice recrystallization inhibition activity as measured by the 5-minute SCA. Error bars for individual data points omitted.

These findings were consistent with a previous investigation into the relationship between logP and the ice recrystallization inhibition activity of various monosaccharides and disaccharides (measured by the 5-minute SCA) by Jatinder Singh (Ben Lab, MSc 2022). Importantly, it was found that the computational algorithms used to calculate logP often overestimated the lipophilicity of the carbohydrates.[178,425] Unfortunately, the fragment-based approaches often used by the currently accepted algorithms cannot

accurately capture the complex intramolecular hydrogen bonding networks inherent to polyol carbohydrates that are known to dramatically affect their solubility in aqueous media.[402,426] A similar issue was noted regarding the PSA/MSA calculations, where the compound sets that the computational algorithms were trained upon did not contain sufficient regio- or stereochemical diversity which may have limited the accuracy of such calculations.[427,428]

In addition, it was initially thought that the linear correlation coefficients for the plots with respect to PSA/MSA ratio could have been affected by poor calculations of each compound's three-dimensional MSA. In MarvinSketch®, the calculation of MSA is based directly on the calculated van der Waals surface of the molecule and thus depends on the conformation of the molecule during calculation. Calculation of the molecule's conformation is done using a single molecule in the gas phase, which neglects the effect that interactions between numerous molecules and the impact of an aqueous environment may have on their conformation. On the other hand, PSA is calculated using a fragment-based approach described by Ertl *et. al.* that used a database of van der Waals surface areas without requiring information about the 3D molecule structure and would not be impacted by inaccurate calculations of conformation.[429] Therefore, to minimize potential errors arising from calculations in the gas phase, the geometry of each compound was pre-optimized in an implicit water model with a higher level of theory prior to the calculation of MSA in MarvinSketch® with the aim of improving the accuracy of the molecule's conformation in aqueous solution.

Each compound underwent a conformational search using the Conformer-Rotamer Ensemble Sampling Tool (CREST)[430] and the geometry of the lowest energy conformer from this search was then optimized using ORCA (using the ωb97 functional and DEF2-TZVPP basis set with CPCM implicit water solvation)[431–433] (exact methods can be found in *section 8.1.4*). In general, the geometry optimization in ORCA resulted in a change in the orientation of the aryl ring which rotated about the anomeric oxygen (O_1); for example, the aryl ring of PMP-Glc (**26**) as drawn into ChemDraw with the carbohydrate in a $^4C_1$ chair conformation is oriented vertically in the XZ plane but with optimization through CREST and ORCA the aryl ring flattens into the XY plane (**Figure 4-18**).

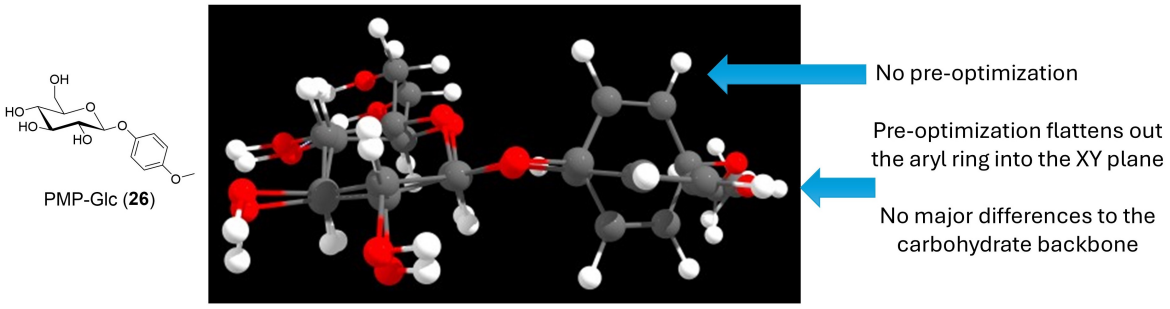


Figure 4-18. Example of the conformation change of 4-methoxyphenyl-β-D-glucopyranoside (PMP-Glc, **26**) displayed using ChemCraft 1.8. Without pre-optimization the 3D structure interpretation was obtained from ChemDraw (with the carbohydrate chair in the $^4C_1$ conformation as the baseline). The optimized structure was obtained following a conformational search with CREST and geometry optimization using ORCA.

An energy calculation of the original three-dimensional structures compared to the updated conformations confirmed in each case that the geometry had indeed been optimized using this method. As such, the geometry optimized structures were then inputted into MarvinSketch® and their MSA was re-calculated to be plotted again as a ratio of PSA/MSA to their ice recrystallization inhibition activity. However, despite the geometry optimization of each compound's 3D structure using CREST and ORCA, very little difference was found in the MSA values as calculated by MarvinSketch® (a maximum change in the PSA/MSA between the two data sets of 1.5 %) and thus no meaningful difference was observed in the linear correlation coefficients (R^2 = 0.53 and 0.54, **SI Figure 8-89**). Therefore, it was confirmed that the algorithms used by MarvinSketch® cannot accurately interpret small differences in geometry that distinguish the carbohydrates in this library which may have limited the accuracy of MSA calculations and the corresponding correlations to ice recrystallization inhibition activity. It is important to note that these calculations also did not take into account changes in geometry that occur with explicit solvation which may also have a significant impact on the interactions these molecules have with water and ultimately their ice recrystallization inhibition activity; this will be discussed in greater detail in *chapter 5*.

Finally, the ice recrystallization inhibition activity of other compound classes had been assessed by past members of the Ben Lab, including: *O*-linked and *C*-linked alkyl-β-D-glucopyranosides,[216] amino acid derivatives,[434] *N*-aryl-D-aldonamides,[176] and naturally occurring mono and disaccharides.[178] Therefore, it was of interest to assess whether the findings from *section 4.3* could be more broadly applied to ice recrystallization inhibition activity. When the log-transformed ice recrystallization inhibition activity (IC_{50}) of all compounds (including the *O*-aryl-β-D-glucopyranosides from *section 4.3.1*) were plotted with respect to their calculated PSA/MSA ratio or theoretical logP, a very weak linear correlation was observed for both parameters with R^2 values of 0.19 and 0.25 for PSA/MSA ratio and logP respectively (**Figure 4-19A**). In part, these weak correlations were caused by very weak fitting of the β-*C*-alkyl-glucopyranoside and amino

acid derivatives with R^2 values ≤ 0.17 (**Figure 4-19C** and **F**). However, the β-*O*-alkyl-glucopyranoside and *N*-aryl-D-aldonamide derivatives were both similar in correlation to the *O*-aryl-β-D-glucopyranoside derivatives that were previously plotted with R^2 values of 0.54 and 0.47 for PSA/MSA ratio and 0.51 and 0.35 for logP (**Figure 4-19**). The activity of the naturally occurring carbohydrates was more strongly correlated with logP than PSA/MSA ratio (R^2 = 0.19 and 0.50, **Figure 4-19G**) however this may have been affected by inaccuracies in the calculation of these parameters by the respective algorithms as previously discussed.

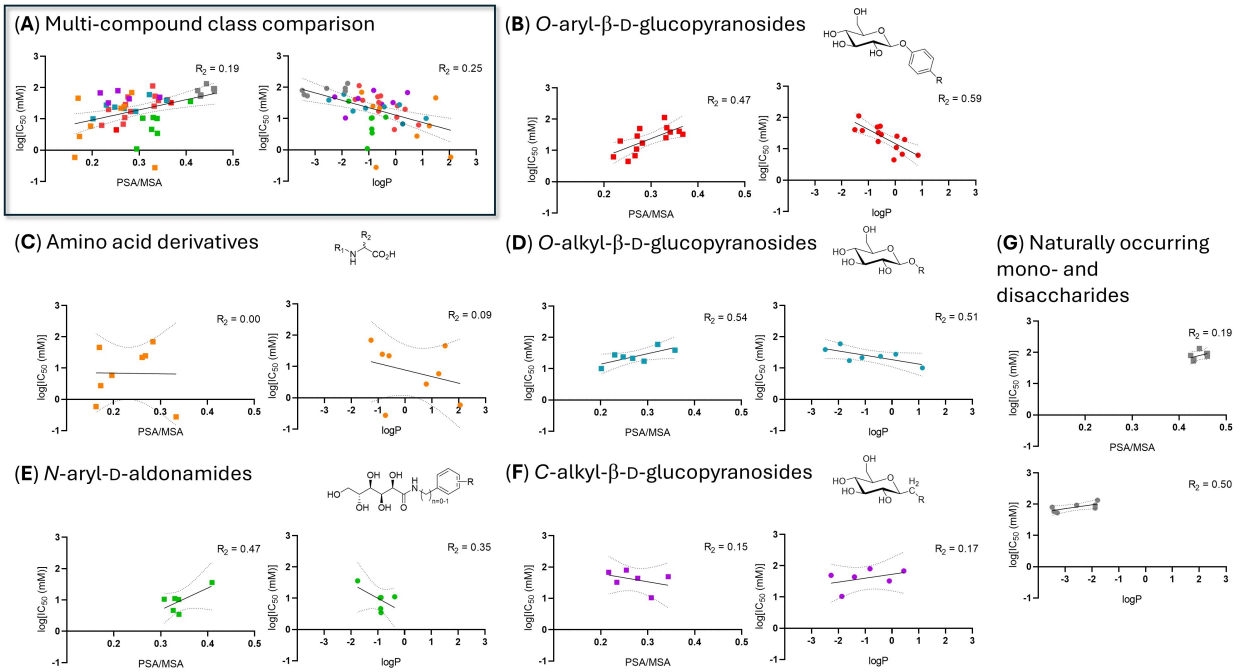


Figure 4-19. Plots of the log-transformed ice recrystallization inhibition activity relative to its polar surface area (PSA) to molecular surface area (MSA) ratio as calculated by MarvinSketch® or its theoretical logP value as calculated by VCC's ALOGPS algorithm. (**A**) All compound classes combined into a single plot; (**B**) *O*-aryl-β-D-glucopyranosides; (**C**) amino acid derivatives;[434] (**D**) *O*-alkyl-β-D-glucopyranosides;[216] (**E**) *N*-aryl-D-aldonamides;[176] (**F**) *C*-alkyl-β-D-glucopyranosides;[216] (**G**) naturally occurring mono and disaccharides[178]. Ice recrystallization inhibition activity as measured by the 5-minute SCA; data for panels C-G collected in part by past members of the Ben Lab.[176,178,216,434] Data fit to a linear regression with 95 % confidence bands of the linear regression shown. Error bars for individual data points omitted.

Considering these limitations, current predictive measures for ice recrystallization inhibition activity as measured by the 5-minute SCA remain primarily hindered by the accuracy of the calculations used to determine the quantifiable value for each parameter/structural feature. These inaccuracies may be exaggerated for classes of molecules which inherently have similar structural features that cannot be easily distinguished by fragment-based calculation approaches such as regio- and stereoisomers. While the accuracy of the IC_{50} values may also be a limiting factor to the accuracy of the correlations, the time associated with additional data collection and the overall complexity of translating these compounds into

cellular applications minimizes the importance of increasing the accuracy of each IC_{50} value. Furthermore, as the mechanism of action of these compounds is hypothesized to impact hydration and the interactions of multiple water molecules, pinpointing a single feature/atom/interaction and its direct impact on ice recrystallization may be futile until improved metrics are able to be considered.

Importantly, the relationships throughout this chapter only describe activity as measured by the acellular splat cooling assay; in other words, they do not provide direct insight into the importance of these parameters or trends on cryopreservation outcomes in the cellular environment. For example, using the thresholds for PSA/MSA and logP the IRI PMP-Glc (**26**) may have been excluded from further development despite its proven success as an additive for improving the cryopreservation of RBCs at reduced glycerol concentrations. Unfortunately, as only a handful of compounds have been translated to cellular applications thus far, it has not yet been possible to complete comprehensive studies relating structural features to cryopreservation outcomes. The Ben Lab currently has on-going investigations into the relationship between the acellular ice recrystallization inhibition activity as measured by the SCA and specific cryopreservation outcomes *in vitro* beginning with quantifying what "size" of ice crystal (or IC_{50} value) translates to what level of damage to a cell or tissue that has been cryopreserved. With the ability to better quantify the relationship between ice recrystallization inhibition and cryopreservation outcomes, future studies would be able to include other metrics such as a compound's cytotoxicity, solubility, and permeability, as well as key cryopreservation outcomes such as cell viability, recovery, and functionality in the development of new and improved ice recrystallization inhibitors.

4.5. Summarizing the structure-activity relationships of small-molecule IRIs

This chapter has explored the relationship between various physiochemical parameters and ice recrystallization inhibition activity. Previous members of the Ben Lab had investigated parameters such as hydration index (HI) and polar surface area (PSA) to molecular surface area (MSA) ratios and their potential correlation to ice recrystallization inhibition activity. However, updates to the SCA that were developed by Abraham *et. al.* to reduce inherent bias in the analysis of data produced by the 30-minute assay revealed several differences in ice recrystallization activity, including compounds that had been inaccurately reported as inactive (false negatives) and disregarded from further development. Using updated dose-response curves produced using the 5-minute SCA, it was possible to re-examine these correlations with ice recrystallization inhibition activity reported as an IC_{50} value.

While it was confirmed that ice recrystallization inhibition activity was not directly impacted by the electronics of the anomeric oxygen, an aryl-ring substituent could have a profound impact on ice

recrystallization inhibition activity. It was hypothesized that this impact was the result of the substituent directly interacting with water molecules or indirectly affecting the molecule's overall hydration network that was responsible for its ice recrystallization inhibition activity. Investigation of various other parameters found those that could be used to indirectly describe a molecule's interactions with water molecules were most strongly correlated to ice recrystallization inhibition activity including PSA to a measure of molecular volume (either MSA or ASA), polarizability, molar refractivity, logP, logS, surface tension, and critical pressure (**Table 4-1**). The linear correlation coefficients, and thus confidence in the relationship between these parameters and ice recrystallization inhibition activity, could be improved upon log-transformation of the IC_{50} values suggesting that molecules with very weak activity acted *via* a mechanism of action that did not rely on hydrophobicity in the same manner as compounds that were moderately to strongly active. Ultimately, while these correlations could not be used to accurately predict the activity of an unknown compound due to the complex nature of ice recrystallization inhibition, it was confirmed that increasing the hydrophobicity of a molecule led to improved ice recrystallization inhibition activity. Therefore, compounds that do not incorporate hydrophobicity whatsoever should be avoided during future development campaigns.

Therefore, these studies have shown that the calculation of parameters may be useful in providing general information about the important structural features for inhibiting ice recrystallization (they can reliably distinguish between compounds that may be "active" or "inactive" based upon a given activity threshold). However, future compound development must continue to rely on traditional design methods in which each compound is individually synthesized and screened for acellular ice recrystallization inhibition activity as these models are unable to predict the structural features that will be most active with high precision. While the development of multiparameter models may aid inhibitor development, they are presently limited by the accuracy of the computational calculations for small molecule carbohydrates and similar amphiphilic molecules. Furthermore, many parameters, including aqueous solubility or cytotoxicity, as well as cryopreservation outcomes such as viability, recovery, and functionality are critical to the successful application of these compounds in a cellular system. Therefore, it would be of interest for future studies to investigate multiple outcome metrics to accurately capture the complexity of ice recrystallization by small molecules in the cellular environment.

5. A comprehensive investigation of the ice recrystallization inhibition activity of PMP-Glc (26)

Over the last several decades of small-molecule ice recrystallization inhibitor (IRI) development by the Ben Lab, an extensive amount of research has been dedicated to investigating carbohydrate derivatives including *O*-aryl-pyranosides. From this class of compounds, (4-methoxyphenyl)-β-D-glucopyranoside (PMP-Glc, **26**) was found to be one of the most active using the 30-minute SCA and has been used to improve the cryopreservation outcomes of red blood cells (RBCs) at reduced glycerol concentrations (see *chapter 3*).[162,167] Further testing of PMP-Glc (**26**) and other derivatives of the *O*-aryl-β-D-glucopyranoside family of compounds using the updated 5-minute SCA has provided more detailed dose-dependent information about their activity that could be used to optimize translation of these compounds into cryopreservation applications (see *chapter 4*). However, while the vast majority of structure-activity relationship (SAR) studies to date have concluded that the hydrophobic/hydrophilic balance of small-molecule IRI candidates must be optimized, the specifics of which substitutions and in which locations these substitutions could be made in order to improve ice recrystallization inhibition activity remain unclear.[156–158,168,178,216]

Early investigations of the aryl-pyranoside class of compounds by the Ben Lab iteratively synthesized and tested different carbohydrate cores (*e.g.*, D-galactose, D-glucose, D-mannose), a variety of aryl motifs with different functional groups (*e.g.*, *methoxy*-, *bromo*-), different regiochemistry of the functional groups (*e.g.*, *ortho, meta, para*), and different linkages of the aryl motif to the C_1 carbon (*e.g.*, *O*-, *S*-, or *N*-linked including both α and β stereochemistry).[158,411] Using the 30-minute SCA to quantify ice recrystallization inhibition activity these studies generally found that modifications to the aryl ring of the glucopyranoside scaffold were not well tolerated, nor were changes to other carbohydrate epimers (*e.g.,* D-galactose or D-mannose). Ultimately, these studies were unable to establish clear directions for further development and optimization within this class of compounds as both the glucose core and the *p*-methoxyphenyl motif appeared to be necessary for strong activity (**Figure 5-1**). However, modifications to the hydroxyl positions of the carbohydrate scaffold had yet to be extensively explored and therefore presented a potential avenue for novel compound development (**Figure 5-1**).

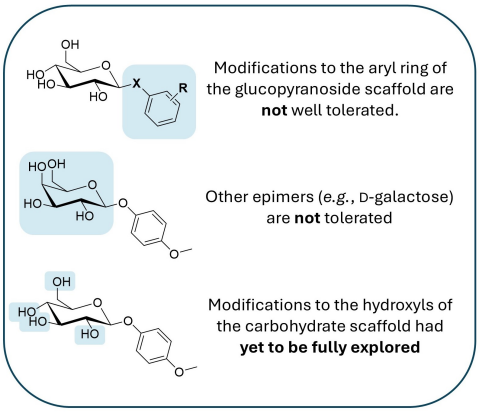


Figure 5-1. Summary of the outcomes of past structure-activity relationship campaigns and their outcomes towards the optimization of ice recrystallization inhibition activity for aryl-pyranosides.

Given that relying on parameter-based prediction of the structural features important for ice recrystallization inhibition activity has been largely unsuccessful, particularly when it comes to small structural changes (see *chapter 4*), the determination of structure-activity relationships for these compounds continues to directly rely on synthesis and experimental testing. Some initial investigations in this direction by Dr. Capicciotti (Ben Lab, PhD 2014) modified the C_6 position, including extension by one CH_2 unit (**87**), moving the methoxyphenyl substitution from the C_1 position onto C_6 (**88**), as well as *O*-methylation [(4-methoxyphenyl)-6-*O*-methyl-β-D-glucopyranoside, C_6 OMe PMP-Glc, **89**)]. In all three cases ice recrystallization inhibition activity as measured by the 30-minute SCA was reduced compared to the parent PMP-Glc (**26**) (**Figure 5-2**). Ultimately, these results suggested that modifications to the C_6 position should be avoided during future SAR campaigns however the impact of modifications to C_2, C_3, and C_4 had yet to be explored in detail.

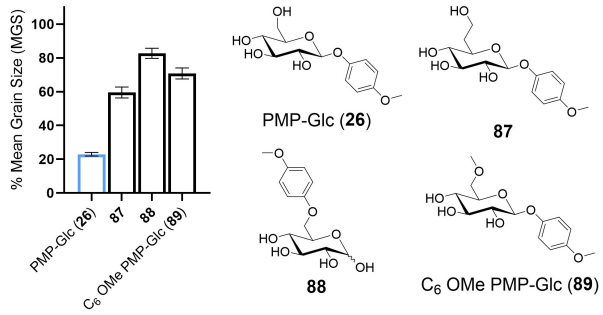


Figure 5-2. Structures and ice recrystallization inhibition activity of PMP-Glc (**26**) and derivatives with modifications at the O_6 position (**87**-**89**). Ice recrystallization inhibition activity reported as the percent mean grain size (% MGS) normalized to phosphate-buffered saline determined by modified splat-cooling assay at a concentration of 22 mM with a 30-minute annealing time at -6.4 °C.[158,167] *Figure recreated from Capicciotti et. al. (2016)*.[167]

Previous work in the Ben Lab has hypothesized that the hydroxyls of the core carbohydrate are responsible for interactions with water molecules that are critical for their ice recrystallization inhibition activity;[156,157] however, the specifics of these interactions (*e.g.*, which hydroxyls may act as hydrogen bond donors and which act as acceptors) are not well understood. The longstanding hypothesis for the mechanism of action of small-molecule carbohydrate-based IRIs has proposed disruption of the thermodynamically-driven transfer of water molecules from one ice crystal to another through the formation of stable intermolecular hydrogen bonds with bulk water molecules.[156,157] As previously discussed, the ability for a compound to interact with water molecules *via* hydrogen bonding depends on its three-dimensional space (including both regiochemistry and stereochemistry).[156,157,401,402] For example, when OH-2 and OH-4 of a $^4C_1$ carbohydrate are both axial (as in D-talose, **10**), intramolecular hydrogen bonding between the two hydroxyls reduces their ability to act as intermolecular hydrogen bonding partners with water.[402,435,436] However, if OH-2 and/or OH-4 are equatorial (as in D-galactose, **7**, or D-glucose, **8**), these hydroxyls are able to engage in more intermolecular hydrogen bonding with water molecules due to the lost intramolecular interaction.[401,402,437] It is the increased intermolecular interactions between the carbohydrate and water molecules that have been proposed to result in increased ice recrystallization inhibition activity by the Ben Lab.[156,157] As a result, this chapter aimed to explore various modifications to the carbohydrate core of PMP-Glc (**26**), beginning with deuteration and *O*-methylation, to evaluate the impact of altering each position's potential intermolecular interactions with bulk water molecules on ice recrystallization inhibition activity as measured by the 5-minute SCA.

5.1. The effect of deuteration on the ice recrystallization inhibition activity of PMP-Glc (**26**)

The substitution of a hydrogen (^{1}H) for deuterium (^{2}H) is generally known to impact the rates of chemical reactions *via* kinetic isotope effects (KIE). Generally, a reaction requiring the cleavage of a carbon-deuterium bond (C-D) will be several fold slower than the cleavage of the same bond replaced with hydrogen (known as a primary KIE); deuteration can also impact the cleavage of bonds at adjacent positions (known as a secondary KIE).[438,439] While, ice recrystallization inhibition does not involve the cleavage of bonds, deuteration could impact the non-covalent interactions formed between PMP-Glc (**26**) and surrounding bulk water molecules. For example, a study investigating the deuteration of caffeine found position specific effects with respect to changes in the lipophilicity of each isotopomer.[440,441] Ultimately, it has been proposed that the origin of the effect of deuteration on non-covalent interactions may be due to changes in the polarizability, polarity, and/or molecular volume of a molecule caused by the increased length of the C-D bond compared to a C-H bond.[441,442]

To investigate the impact of carbohydrate deuteration on ice recrystallization inhibition activity, four deuterated analogues of PMP-Glc (**26**) were envisioned with deuterium replacing the hydrogen at C_1, C_2, C_3, and C_6 respectively (**90-93**). The C_4 deuterated analogue (4-methoxyphenyl)-4-deutero-β-D-glucopyranose (4D1 PMP-Glc) was not synthesized as the deuterated reducing sugar starting material was not commercially available but may be of interest for future studies.

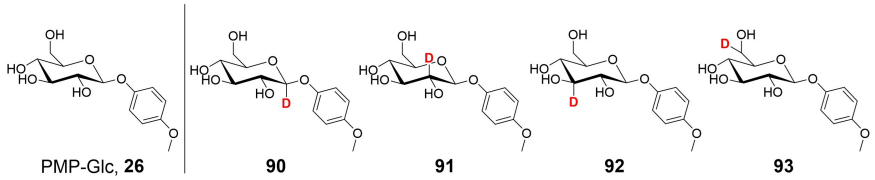
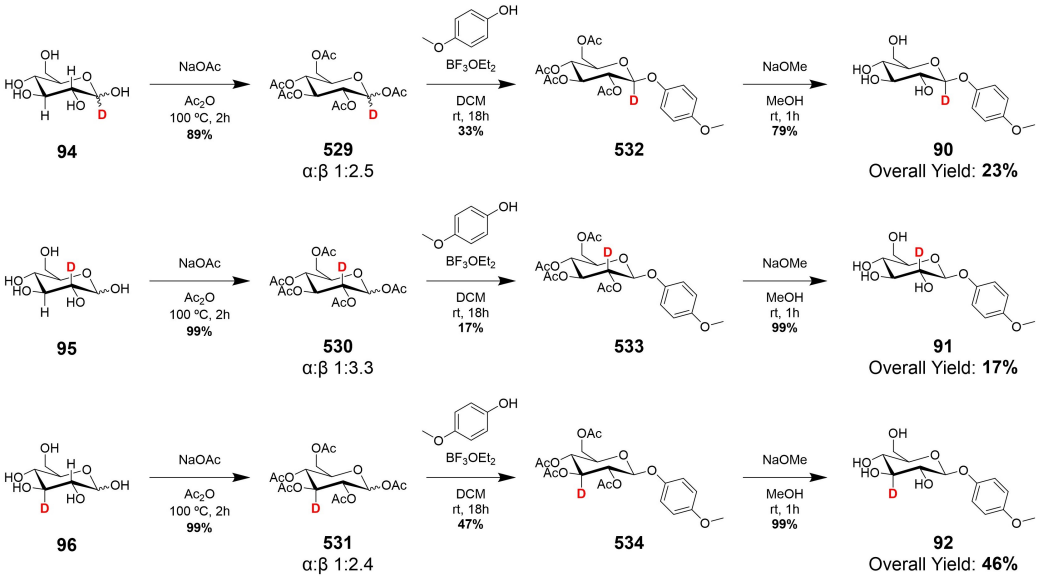


Figure 5-3. Proposed deuterated analogues of PMP-Glc including deuteration at C_1, C_2, C_3, and C_6 (**90-93**).

5.1.1. Structure and synthesis of deuterated O-aryl-D-glucopyranosides

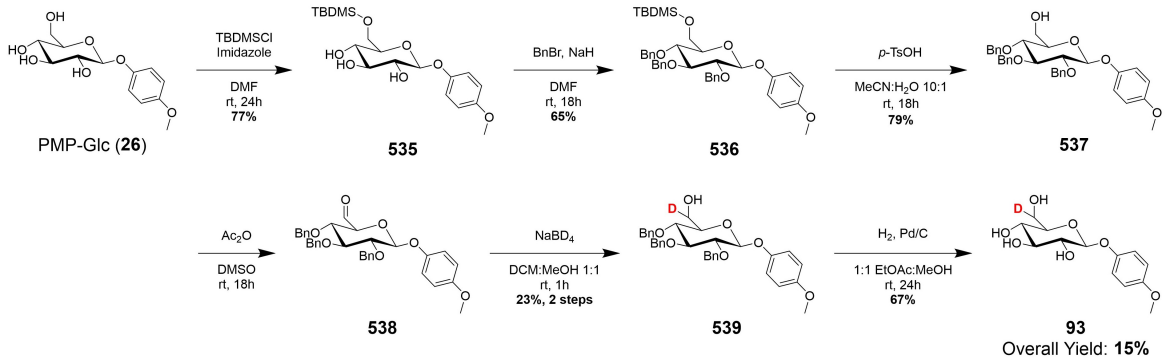
The mono-deuterated PMP-Glc derivatives at the C_1, C_2, and C_3 positions (**90-92**) were synthesized in 17-46 % overall yield starting from the corresponding commercially available reducing sugar derivative (**94-96**). Acetylation using sodium acetate (NaOAc) and acetic anhydride (Ac_2O) (**529-531**), followed by a traditional Lewis-acid assisted glycosidation using $BF_3{\cdot}OEt_2$[167] afforded the protected intermediates **532-534**. Deacetylation using standard Zemplén conditions[326] then afforded the final desired products (4-methoxyphenyl)-1-deutero-β-D-glucopyranose (1D1 PMP-Glc, **90**), (4-methoxyphenyl)-2-deutero-β-D-

glucopyranose (2D1 PMP-Glc, **91**), and (4-methoxyphenyl)-3-deutero-β-D-glucopyranose (3D1 PMP-Glc, **92**) (**Scheme 5-1**).



Scheme 5-1. Synthesis of the C_1, C_2, and C_3 deuterated derivatives of PMP-Glc (**90**-**92**).

The C_6 deuterated derivative (**93**) was synthesized starting from PMP-Glc (**26**), where the selective silylation of O_6 using *tert*-butyldimethylsilyl chloride (TBDMSCl) (**535**) and then benzyl protection of the remaining free hydroxyls afforded the protected intermediate **536**. Removal of the silyl protecting group using *p*-toluene sulfonic acid (*p*TsOH) afforded the intermediate with a free hydroxyl at C_6 (**537**). Oxidation of the free hydroxyl (**538**) followed by reduction using sodium borodeuteride ($NaBD_4$) achieved formation of the monodeuterated protected intermediate **539**. Finally, deprotection by hydrogenation with palladium on carbon (Pd/C) afforded the final product (4-methoxyphenyl)-6-deutero-β-D-glucopyranose (6D1 PMP-Glc, **93**) in 15% overall yield (**Scheme 5-2**).



Scheme 5-2. Synthesis of the C_6 deuterated PMP-Glc derivative (4-methoxyphenyl)-6-deutero-β-D-glucopyranose (6D1 PMP-Glc, **93**).

Once synthesized, the ice recrystallization inhibition activity of each derivative was to be assessed by the 5-minute modified splat-cooling assay (SCA). However, the ice recrystallization inhibition activity of the C_6 deuterated derivative (**93**) was not assessed as it was not soluble in PBS at concentrations above 0.1 mM. As previously discussed in *chapter 4*, no small-molecule carbohydrate IRIs reported at the time of testing had shown meaningful activity below a 1 mM threshold. In addition, the previous results of very poor ice recrystallization inhibition activity following modification of C_6 did not support further testing of 6D1 PMP-Glc (**93**) at lower concentrations.

The ice recrystallization inhibition activity of the three remaining deuterated derivatives (**90**-**92**) as assessed by the 5-minute SCA was found to result in a minimum four-fold loss in activity compared to the parent compound PMP-Glc (**26**) (**Figure 5-4**); the ice recrystallization inhibition activity of 1D1 PMP-Glc (**90**) and 3D1 PMP-Glc (**92**) were nearly two-fold different with IC_{50} values of 87.3 mM and 137.9 mM respectively. It is important to note that all three derivatives were unable to achieve a zero percent normalized rate of ice recrystallization (v_{norm}) at their maximum apparent solubility in phosphate-buffered saline (PBS) which could impact the accuracy of each individual IC_{50} value and cause wide confidence interval ranges.

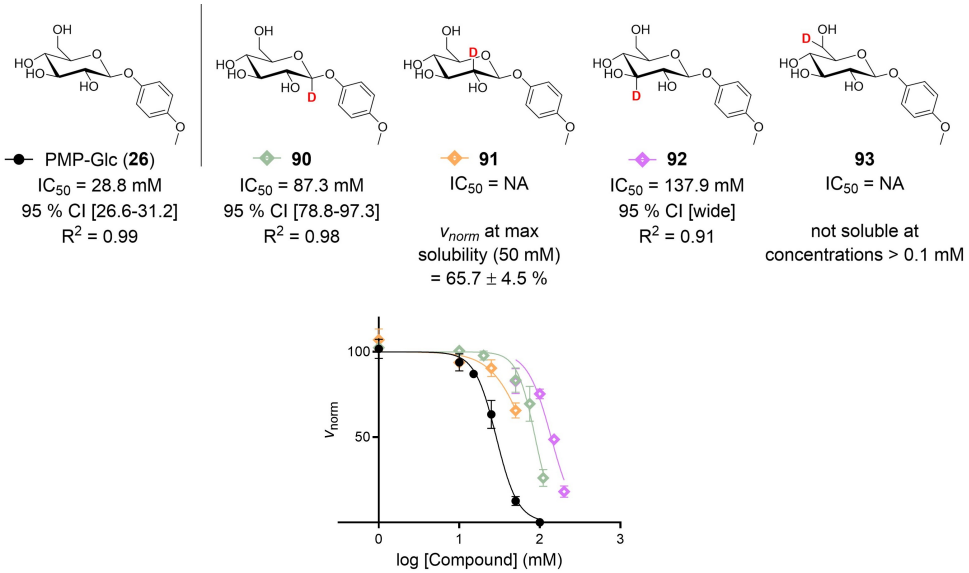


Figure 5-4. Structures and ice recrystallization inhibition activity of deuterated PMP-Glc derivatives (**90-93**) compared to PMP-Glc (**26**). Plot of normalized ice crystal growth rate (v_{norm}) in PBS against logarithm transformed compound concentration (in mM). Determined by modified splat-cooling assay with a 5-minute annealing time at -6.4 °C.[169] A 95 % CI of "wide" indicates a greater than 500 mM span.

The ice recrystallization inhibition activity of the three D-glucose derivatives with mono-deuteration at the C_1 (1-D1 D-glucose, **94**), C_2 (2-D1 D-glucose, **95**), and C_3 (3-D1 D-glucose, **97**) positions prior to substitution with the *para*-methoxyphenyl motif was also assessed as a base-line comparison using the 5-minute SCA. Compared to the parent compound D-glucose (**8**, IC_{50} = 75.7 mM, 95 % CI [65.9-84.2]), the three deuterated derivatives (**94-96**) were found to have similar, but slightly reduced ice recrystallization inhibition activity with IC_{50} values between 116.6 mM (95 % CI [95.0-140.8]) (**94**) and 126.0 mM (95 % CI [81.4-181.8] (**95**) (**Figure 5-5**).

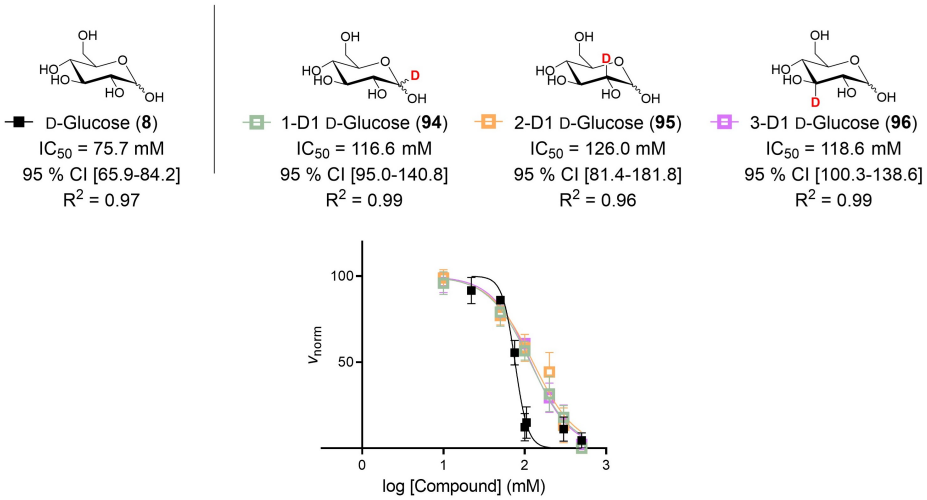


Figure 5-5. Structures and ice recrystallization inhibition activity of deuterated D-glucose derivatives (**94-96**). Plot of normalized ice crystal growth rate (v_{norm}) in PBS against logarithm transformed compound concentration (in mM). Determined by modified splat-cooling assay with a 5-minute annealing time at -6.4 °C.[169]

While no clear position-dependent effects could be observed due to the similarity between the activity of **90-93** and **94-96**, deuteration in general was detrimental to ice recrystallization inhibition activity. The impact of deuteration was less pronounced with the reducing sugars (**94-96** compared to the parent D-glucose, **8**), which supported previous SAR investigations that suggested the impact of a modification on ice recrystallization inhibition activity may differ by molecule class.

5.2. Probing the effect of hydroxyl methylation on the ice recrystallization inhibition activity of PMP-Glc (**26**)

While deuteration resulted in decreased ice recrystallization inhibition activity compared to PMP-Glc (**26**), the specific interactions with bulk water molecules that were critical for inhibiting ice recrystallization remained unclear. As a result, it was thought that the selective *O*-methylation, which would eliminate each hydroxyl group's capacity to act as a hydrogen bond donor, could be used to directly probe hydrogen bonding interactions between PMP-Glc (**26**) and bulk water molecules. In other words, if a decrease in the ice recrystallization inhibition activity was observed for an *O*-methylated derivative, then it would suggest that the hydroxyl at that position formed an important hydrogen bond donation interaction in PMP-Glc (**26**). To test this hypothesis, derivatives of PMP-Glc (**26**) that had been methylated at O_2 (**97**), O_3 (**98**), O_4 (**99**), and O_6 (**89**) were envisioned (**Figure 5-6**).

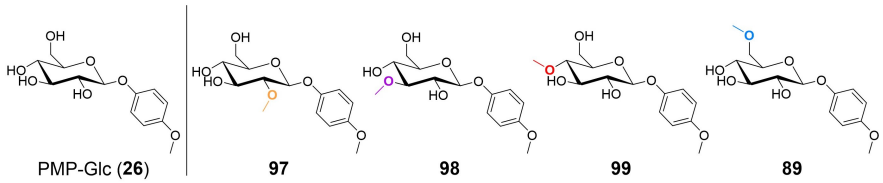
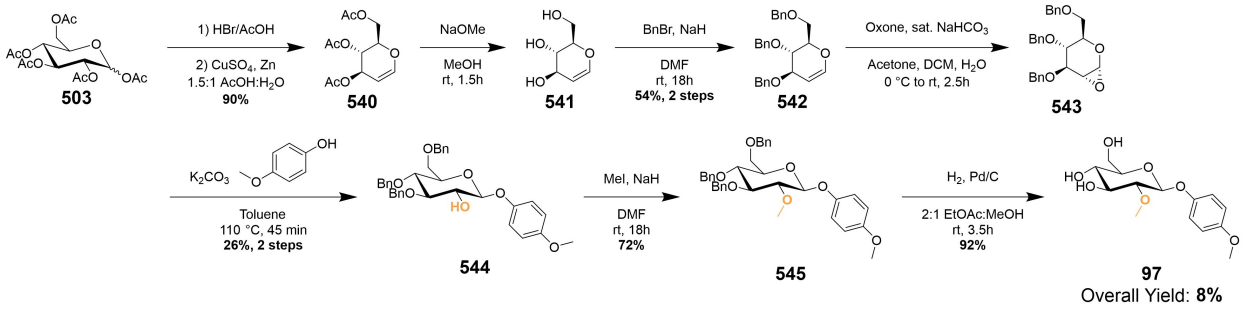


Figure 5-6. Structures of *O*-methylated PMP-Glc (**26**) derivative targets (**89**, **97**-**99**).

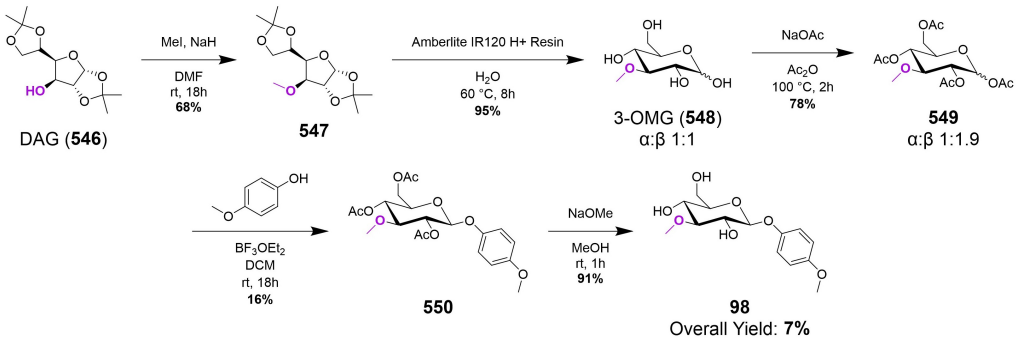
*5.2.1. Synthesis of O-methylated derivatives (**89**, **97**-**99**) of PMP-Glc (**26**)*

The synthesis of each derivative required a targeted synthetic approach to selectively methylate each position. Introduction of the methyl at O_2 involved first the formation of tri-*O*-acetyl-D-glucal (**540**) from β-D-glucose pentaacetate (**503**) *via in situ* formation of acetobromo-α-D-glucose (**507**) and subsequent copper-catalyzed oxidation with zinc. Following deprotection of **540** using standard Zemplén conditions[326], the π-bond between C_1 and C_2 of D-glucal (**541**) was then converted into an epoxide (**543**) and reacted immediately with 4-methoxyphenol to selectively generate the *trans*, β-*O*-aryl-linked glucose intermediate **544**. Methylation of the free hydroxyl at C_2 of **544** generated the protected intermediate **545**. Subsequent removal of the benzyl protecting groups using palladium on carbon under a hydrogen gas atmosphere resulted in formation of the desired product (4-methoxyphenyl)-2-*O*-methyl-β-D-glucopyranoside (C_2 OMe PMP-Glc, **97**) in seven total steps with an 8 % overall yield (**Scheme 5-3**).



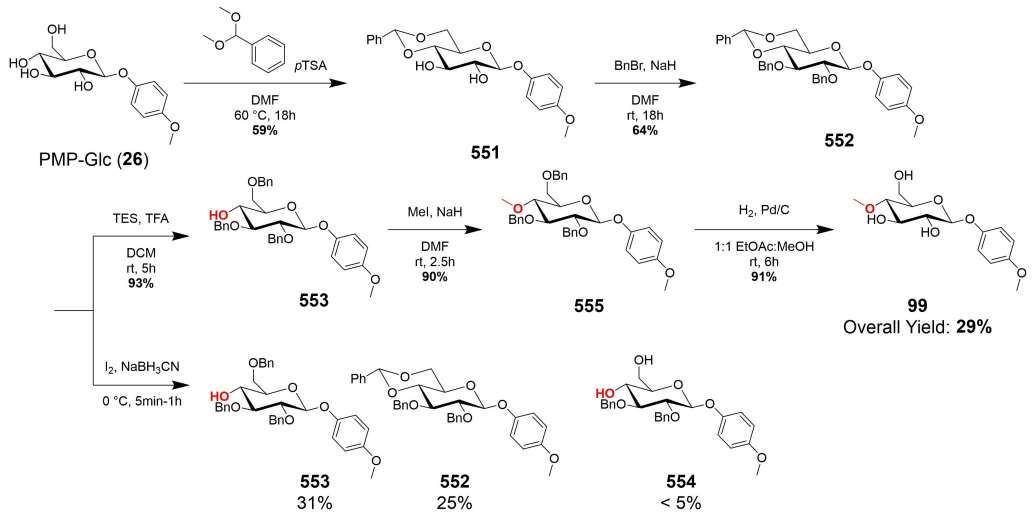
Scheme 5-3. Synthesis of (4-methoxyphenyl)-2-*O*-methyl-β-D-glucopyranoside, C_2 OMe PMP-Glc (**97**).

Selective *O*-methylation of O_3 was achieved starting from commercially available diacetone-D-glucose (DAG, **546**). Methylation of DAG (**547**) followed by subsequent removal of the acetonide protecting groups afforded the O_3 methylated intermediate 3-*O*-methyl-D-glucose (3-OMG, **548**). Acetylation of 3-OMG (**548** to **549**), followed by traditional Lewis-acid assisted glycosidation using $BF_3{\cdot}OEt_2$ (**550**),[167] and then deacetylation using standard Zemplén conditions[326] afforded the final product (4-methoxyphenyl)-3-*O*-methyl-β-D-glucopyranoside (C_3 OMe PMP-Glc, **98**) in five steps with a 7 % overall yield (**Scheme 5-4**).



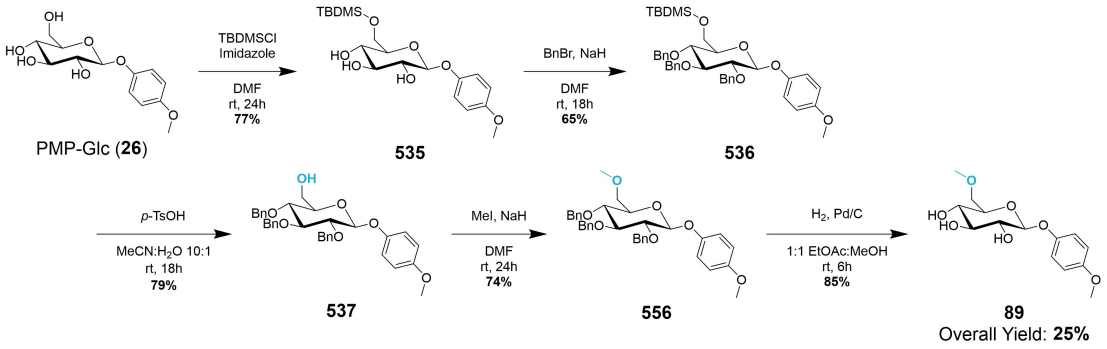
Scheme 5-4. Synthesis of (4-methoxyphenyl)-3-*O*-methyl-β-D-glucopyranoside, C_3 OMe PMP-Glc (**98**).

The selective *O*-methylation of O_4 and O_6 was achieved starting from a large-scale batch preparation of PMP-Glc (**26**) that was previously described in *section 4.2.1* in 78 % yield over two steps. From PMP-Glc (**26**), protection of O_4 and O_6 with a benzylidene acetal (**551**) followed by the benzyl protection of O_2 and O_3 afforded the protected intermediate (4-methoxyphenyl)-2,3-di-*O*-benzyl-4,6-*O*-benzylidene-β-D-glucopyranoside (**552**). To favour the regioselective ring opening of the benzylidene acetal with O_4 deprotected, traditional synthetic methods use $NaCNBH_3$ and HCl;[443] on the other hand, the use of $LiAlH_4$ and $AlCl_3$ favours the regioselective deprotection of O_6.[444–446] In recent years these methods have been an area of research, resulting in the publication of several procedures that make use of less water/air sensitive reagents.[447] For this thesis, initial attempts at the selective opening to favour deprotection of O_4 (**553**) used catalytic iodine and sodium cyanoborohydride ($NaCNBH_3$).[448] The reaction under these conditions was extremely time-sensitive and highly dependent on reaction scale, which resulted in inconsistent yields and high quantities of recovered starting material (**552**) or the double-deprotected (4-methoxyphenyl)-2,3-di-*O*-benzyl-β-D-glucopyranoside (**554**) product recovered from the reaction. As a result, alternative reaction conditions for the regioselective deprotection of O_4 were attempted that readily achieved the desired product (4-methoxyphenyl)-2,3,6-tri-*O*-benzyl-β-D-glucopyranoside (**553**) using triethylsilane (TES) and trifluoroacetic acid (TFA) in a 93 % isolated yield. Subsequent methylation (**555**) and deprotection of **553** then afforded the final product (4-methoxyphenyl)-4-*O*-methyl-β-D-glucopyranoside (C_4 OMe PMP-Glc, **99**) in five steps with a 29 % overall yield using the TES/TFA regioselective opening conditions for the benzylidene acetal (**Scheme 5-5**).



Scheme 5-5. Synthesis of (4-methoxyphenyl)-4-*O*-methyl-β-D-glucopyranoside, C_4 OMe PMP-Glc (**99**).

Finally, the selective *O*-methylation of O_6 from PMP-Glc (**26**) was achieved following the regioselective protection of O_6 with the bulky *tert*-butyldimethylsilyl (TBDMS) protecting group (**535**) and subsequent benzyl protection of the remaining free hydroxyls using benzyl bromide to form the protected intermediate (4-methoxyphenyl)-2,3,4-tri-*O*-benzyl-6-*O*-*tert*-butyldimethylsilyl-β-D-glucopyranoside (**536**). Acid-catalyzed deprotection of O_6 (**537**), followed by *O*-methylation (**556**) and hydrogenation of the benzyl protecting groups using catalytic palladium on carbon (Pd/C) afforded the desired product (4-methoxyphenyl)-6-*O*-methyl-β-D-glucopyranoside (C_6 OMe PMP-Glc, **89**) in five steps with a 26 % overall yield (**Scheme 5-6**).



Scheme 5-6. Synthesis of (4-methoxyphenyl)-6-*O*-methyl-β-D-glucopyranoside, C_6 OMe PMP-Glc (**89**).

*5.2.2. Ice recrystallization inhibition activity of O-methylated derivatives (**89**, **97-99**) of PMP-Glc (**26**)*

Following synthesis of each of the four *O*-methylated derivatives of PMP-Glc (**26**), their ice recrystallization inhibition activity was assessed by the 5-minute modified SCA. The compounds (**89**, **97-99**) were prepared in PBS and a dose-response curve of their activity was generated for each compound

(**Figure 5-7**). Before any methylation substitutions, the IC_{50} PMP-Glc (**26**) was determined to be 28.8 mM (95 % CI [26.6-31.2]) (**Figure 5-7**). It was found that the methylation of O_6 (**89**) resulted in a reduction in the maximum aqueous solubility of the compound to only 30 mM compared to the greater than 110 mM solubility that was observed for PMP-Glc (**26**). When tested for ice recrystallization inhibition activity at the 30 mM maximum solubility, C_6 OMe PMP-Glc (**89**) did not achieve a full dose-response curve and only reached a minimum normalized rate of ice recrystallization (v_{norm}) of 90.7 ± 5.9 % and was therefore considered to be inactive (**Figure 5-7**). Methylation of O_3 (**98**) resulted in a two-fold reduction in ice recrystallization inhibition activity compared to PMP-Glc (**26**) with an IC_{50} value of 60.7 mM (95 % CI [51.3-72.0]), while methylation of O_2 (**97**) did not change the IC_{50} compared to PMP-Glc (**26**) with a value of 24.8 mM (95 % CI [17.7-33.4]) (**Figure 5-7**). Of particular note, methylation of O_4 (**99**) resulted in a 10-fold increase in ice recrystallization inhibition activity compared to PMP-Glc (**26**) with an IC_{50} of 3.19 mM (95 % CI [3.04-3.37]) (**Figure 5-7**).

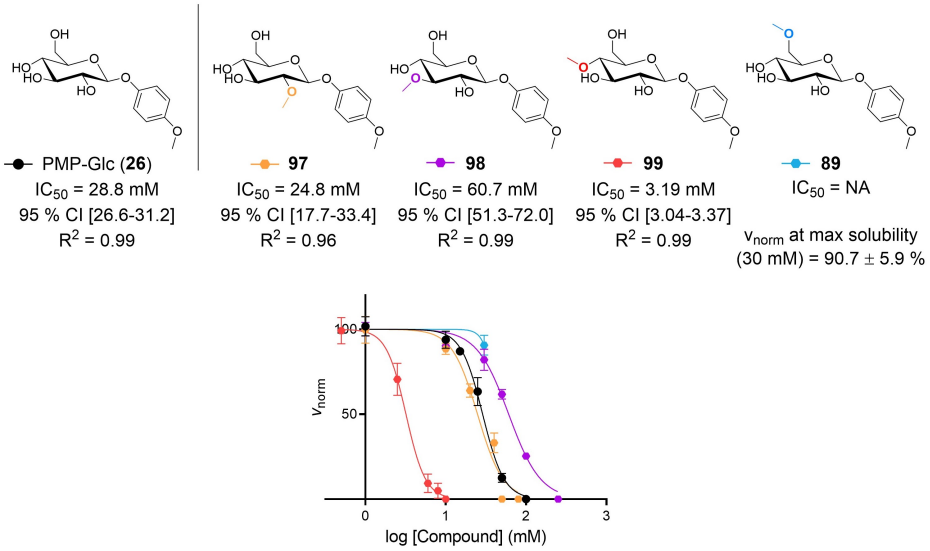


Figure 5-7. Ice recrystallization inhibition activity of compounds **26**, **89**, **97-99**. Plot of normalized ice crystal growth (v_{norm}) in phosphate-buffered saline (PBS) against logarithm transformed compound concentration (in mM). Determined by modified splat-cooling assay with a 5-minute annealing time at -6.4 °C.[169]

As previously discussed (**Figure 5-2**), the loss in aqueous solubility (and thus apparent reduction in ice recrystallization inhibition activity) upon *O_6* methylation (**89**) was consistent with previous results by Dr. Capicciotti (Ben Lab, PhD 2014).[158] Therefore, these results confirmed that hydrogen bond donation from the hydroxyl at C_6 was an important interaction for the inhibition of ice recrystallization. Literature studies have shown that due to the flexibility and accessibility of the C_6 position, it is strongly involved in hydrogen bonding with bulk water molecules;[436,449] removing or modifying C_6 position generally reduces

hydrogen bonding capacity which can also result in aqueous solubility reductions. As a result, future campaigns developing *O*-aryl-pyranoside IRIs should avoid modifications to C_6 position.

With respect to the remaining hydroxyls, a clear, position-dependent effect could be observed when comparing O_2, O_3, and O_4. *O*-methylation of O_2 (**97**) was tolerated as no change in activity was observed; these results suggested that the hydrogen bonding interactions of this position were not critical to ice recrystallization inhibition activity. On the other hand, the reduction in activity following methylation at O_3 (**98**) suggested that hydrogen bond donation of the hydroxyl at this position was important for ice recrystallization inhibition activity. This result was similar to O_6, however as the aqueous solubility of **98** was improved compared to PMP-Glc (**26**) the hydrogen bonding interactions that are important for aqueous solubility may differ from the interactions that are important for ice recrystallization inhibition activity. Finally, the significant increase in ice recrystallization inhibition activity upon *O*-methylation at position 4 (**99**) suggested that hydrogen bond donation at this position was not required and may in fact be detrimental to ice recrystallization inhibition. This result was of great interest as part of the SAR campaign as it was one of the first reported examples of an improvement in ice recrystallization inhibition activity upon the addition of a hydrophobic substitution to the carbohydrate core; it also presented a unique opportunity to explore the tolerance of the O_4 position to other modifications.

It is important to note that the observed position-dependent effects may vary based on the type of substitution and the molecule class being investigated. A previous study investigating modifications to the hydroxyls of PMP-Glc (**26**) found that activity could be improved by azide substitution at the C_3 position [(4-methoxylphenyl)-3-*O*-azido-β-D-glucopyranoside, C_3 N_3 PMP-Glc], where activity improved 5-fold compared to PMP-Glc (**26**) despite also lacking the ability to act as a hydrogen bond donor, but activity decreased significantly from PMP-Glc (**26**) to [(4-methoxylphenyl)-4-*O*-azido-β-D-glucopyranoside, C_4 N_3 PMP-Glc].[214] Another study by Dr. Jennifer Chaytor (Ben Lab, PhD 2009) found minimal change in ice recrystallization inhibition activity with respect to changing the position of an *O*-methoxy for *C*-allylated glucose derivatives when measured by the 30-minute SCA.[381]

5.3. Assessing the generalizability of alkylation substitutions to the carbohydrate core of PMP-Glc (**26**)

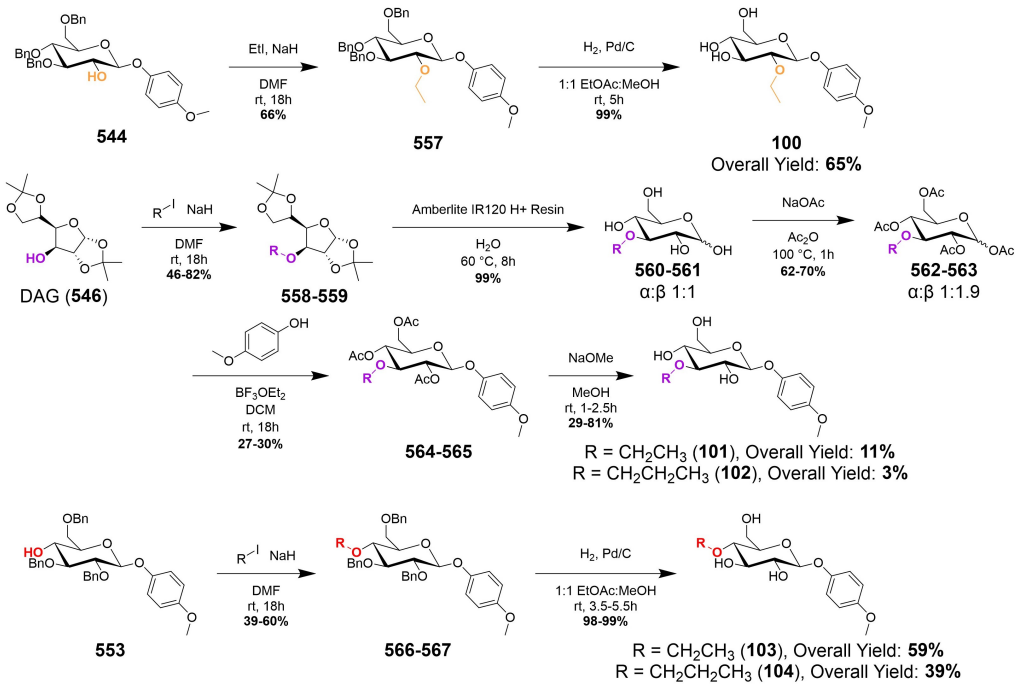
To date, the primary focus of the Ben Lab's investigations into substitutions on the carbohydrate core of IRI candidates have focused on polar functional groups with the aim of improving overall aqueous solubility. While these studies have generally been successful at improving solubility, their impact on ice recrystallization inhibition activity was variable, and often caused dramatic reductions in activity.[177,214,450]

Given the 10-fold improvement in ice recrystallization inhibition activity observed by the methylation of O_4 on the PMP-Glc scaffold (**99**), it was suggested that while polar modifications may not be tolerated, hydrophobic/non-polar modifications should be investigated in greater detail. To this end, additional hydrophobic modifications were made to the O_2, O_3, and O_4 positions of PMP-Glc (**26**) to further probe the effect of hydrophobicity at each of these positions on ice recrystallization inhibition activity. The effect of substitutions at C_6 was not further investigated due to the dramatic decrease in aqueous solubility that was observed upon methylation that was consistent with previous findings by graduate students in the Ben Lab as previously discussed.

5.3.1. Synthesis and ice recrystallization inhibition activity of alkylated O-aryl-β-D-pyranosides

Additional alkyl substitutions were investigated for the O_2, O_3, and O_4 positions that were synthesized from their respective intermediates with the desired free hydroxyl (previously shown in **Scheme 5-3** for the O_2 derivative, **Scheme 5-4** for the O_3 derivative, and **Scheme 5-5** for the O_4 derivative). Alkylation of the free hydroxyl at C_2 of **544** with ethyl iodide (EtI) generated the protected intermediate **557**. Subsequent removal of the benzyl protecting groups using palladium on carbon under a hydrogen gas atmosphere resulted in formation of the desired product (4-methoxyphenyl)-2-*O*-ethyl-β-D-glucopyranoside (C_2 OEt PMP-Glc, **100**) in seven steps with an 8 % overall yield (**Scheme 5-7**). Selective *O*-ethylation and *O*-propylation of O_3 was achieved in the same manner as *O*-methylation (see **Figure 5-4**) from diacetone-D-glucose (DAG, **546**) using EtI or propyl iodide (PrI). The final products (4-methoxyphenyl)-3-*O*-ethyl-β-D-glucopyranoside (C_3 OEt PMP-Glc, **101**) and (4-methoxyphenyl)-3-*O*-propyl-β-D-glucopyranoside (C_3 OPr PMP-Glc, **102**) were achieved in five steps with an 11 % and 3 % overall yield respectively (**Scheme 5-7**).

For the O_4 position, alkylation using EtI or PrI (**566** to **567**) and deprotection of **553** afforded the final products (4-methoxyphenyl)-4-*O*-ethyl-β-D-glucopyranoside (C_4 OEt PMP-Glc, **103**) and (4-methoxyphenyl)-4-*O*-propyl-β-D-glucopyranoside (C_4 OPr PMP-Glc, **104**) in five steps with a 59 % and 39 % overall yield respectively (**Scheme 5-7**). Alkylation of **553** with isopropyl iodide (*i*PrI) or isobutyl iodide (*i*BuI) did not afford the alkylated intermediates **568** and **569** therefore the final products (4-methoxyphenyl)-4-*O*-isopropyl-β-D-glucopyranoside (C_4 O*i*Pr PMP-Glc, **105**) and (4-methoxyphenyl)-4-*O*-isobutyl-β-D-glucopyranoside (C_4 O*i*Bu PMP-Glc, **106**) could not be synthesized (**Scheme 5-7**). The lack of reaction with the branched isopropyl and isobutyl functional groups was attributed to their increased steric bulk compared to the linear ethyl and propyl substitutions of **103** and **104**.



Scheme 5-7. Synthesis of O_2 (**100**), O_3 (**101-102**), and O_4 (**103-104**) alkylated derivatives of PMP-Glc (**26**).

With the substituted derivatives synthesized, the dose-response curves were generated by modified 5-minute SCA. Ethylation at the O_2 position (**100**) resulted in an IC_{50} of 6.31 mM (95 % CI [5.51-7.06]), a four-fold increase in ice recrystallization inhibition activity compared to the parent and the *O*-methylated derivatives (**26** and **97**) (**Figure 5-8A**). While ice recrystallization inhibition activity improved slightly upon ethylation of O_3 (**101**) with an IC_{50} of 40.5 mM (95 % CI [29.8-55.1]), extension to the propyl (**102**) resulted in a loss in aqueous solubility and a maximum v_{norm} of 63.2 ± 7.0 % (at 40 mM) (**Figure 5-8B**). Finally, no significant change in IC_{50} was observed upon ethylation (**103**) or propylation (**104**) of O_4 compared to methylation with values of 2.88 mM (95 % CI [2.01-3.96]) and 2.77 mM (95 % CI [2.08-3.60]) respectively (**Figure 5-8C**); the ice recrystallization inhibition activity of these compounds was comparable to that of the O_4 methyl derivative **99**, and remained 10-fold more active than PMP-Glc (**26**) (**Figure 5-8C**).

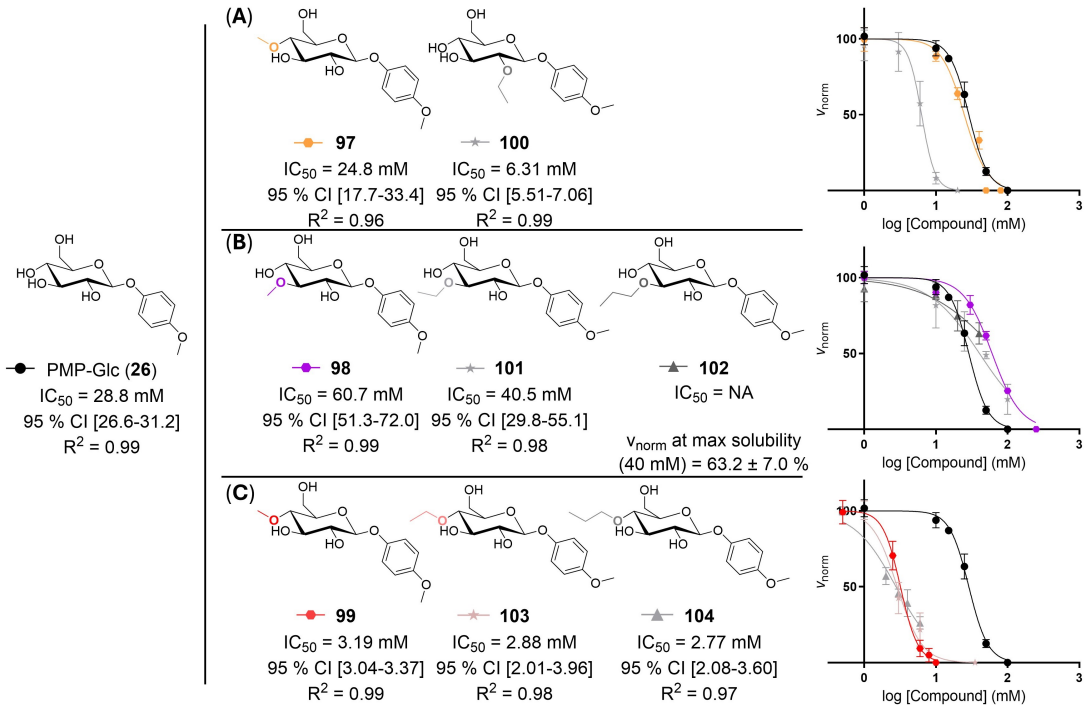


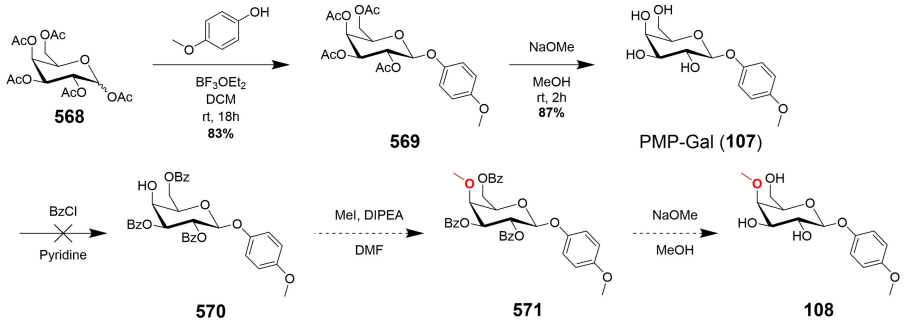
Figure 5-8. Ice recrystallization inhibition activity of alkylated derivatives of PMP-Glc (**26**) at the O_2 (**100**), O_3 (**101-102**), and O_4 (**103-104**) positions. Plot of normalized ice crystal growth (v_{norm}) in phosphate-buffered saline (PBS) against logarithm transformed compound concentration (in mM). Determined by modified splat-cooling assay with a 5-minute annealing time at -6.4 °C.[169]

The improvement in activity upon ethylation of O_2 (**100**) suggested that the addition of hydrophobic substituents to this position may generally improve ice recrystallization inhibition activity similar to O_4. Additional substitutions at the O_2 position, such as propylation or butylation, would need to be tested in future to confirm the tolerance and generalizability of this finding; however, due to the relatively longer synthetic route compared to O_3 or O_4, these molecules would be limited in their use for large scale cryopreservation applications. On the other hand, while both the O_3 and O_4 positions were tolerant to increasing alkyl chain length (at the cost of reduced aqueous solubility), the significant improvement in activity at the O_4 position was of interest for further investigation.

Based on the alkylation results, it was suggested that hydrogen bond donation from the -OH at the C_4 position was not important for activity but that a hydrogen bond accepting interaction at O_4 was critical. To further probe this hypothesis, O_4 methylation of (4-methoxyphenyl)-β-D-galactopyranoside (PMP-Gal, **107**) to synthesize (4-methoxyphenyl)-4-*O*-methyl-β-D-galactopyranoside (C_4 OMe PMP-Gal, **108**) as well as removal of the hydroxyl at C_4 entirely with (4-methoxyphenyl)-4-deoxy-β-D-glucopyranoside (C_4 Deoxy PMP-Glc, **109**) were explored. Given the established importance of stereochemical configuration on ice recrystallization inhibition activity, the galactose derivative **108** and the deoxygenated derivative **109**

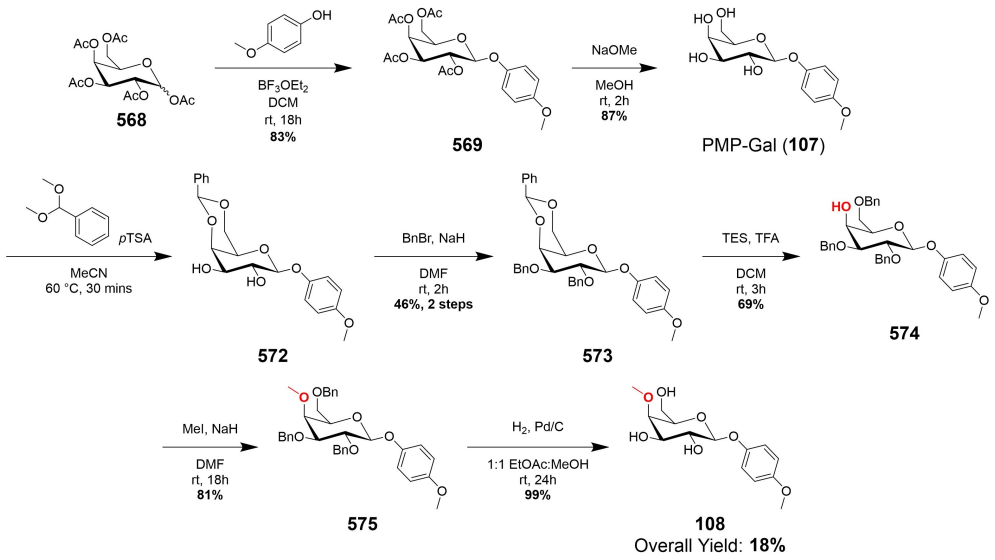
would provide insight into the importance of the oxygen in the equatorial position compared to the axial position.

Initial attempts to synthesize compound **108** utilized a benzoyl protecting group strategy from PMP-Gal (**107**) that was intended to produce intermediate **570** with the C_4 hydroxyl deprotected (**Scheme 5-8**).[451] However, a mixture of protected products was consistently obtained that resulted in di-benzoylated and tetra-benzoylated products that significantly reduced the yield of **570** upon purification. The regioselective benzoylation procedure has been frequently applied to alpha substituted galactosides such as methyl-α-D-galactopyranoside;[452,453] however, the reactivity of O_4 when the anomeric configuration is β has been reported to be higher than that with the α-anomer.[454] The increased reactivity of O_4 with a β-anomeric configuration may have reduced the selectivity of the benzoylation reaction and resulted in the observed mixture of products.



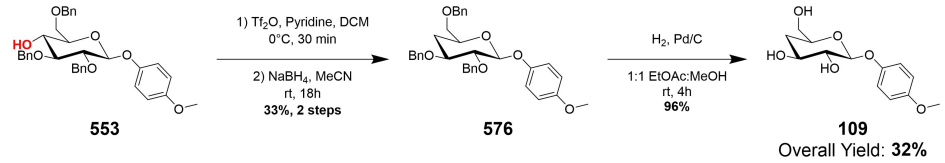
Scheme 5-8. First attempted synthesis of (4-methoxyphenyl)-4-*O*-methyl-β-D-galactopyranoside (C_4 OMe PMP-Gal, **108**) *via* selective benzoylation of PMP-Gal (**107**).

While this benzoylation pathway would have saved two synthetic steps compared to the synthetic strategy used for compound **99**, it was abandoned due to the unreliable and low yields. As a result, the final synthesis of (4-methoxyphenyl)-4-*O*-β-D-galactopyranoside (C_4 OMe PMP-Gal, **108**) followed the exact same synthetic pathway as **99** and led to the final product in seven total steps with an 18 % overall yield (**Scheme 5-9**).



Scheme 5-9. Finalized synthesis of (4-methoxyphenyl)-4-*O*-methyl-β-D-galactopyranoside (C_4 OMe PMP-Gal, **108**).

The C_4 deoxygenated derivative (4-methoxyphenyl)-4-deoxy-β-D-glucopyranoside (C_4 Deoxy PMP-Glc, **109**) was synthesized from the O_4 deprotected intermediate (**553**). The free hydroxyl was reacted with triflic anhydride (Tf_2O) and then reduced using sodium borohydride ($NaBH_4$) to produce the protected, deoxygenated intermediate **576**. Deprotection of the benzyls then afforded the desired product (**109**) in two steps in a 32 % overall yield (**Scheme 5-10**).



Scheme 5-10. Synthesis of (4-methoxyphenyl)-4-deoxy-β-D-glucopyranoside (C_4 Deoxy PMP-Glc, **109**).

As expected, removal of the oxygen at C_4 proved detrimental to ice recrystallization inhibition activity as measured by the 5-minute SCA where a 3-fold reduction in IC_{50} value was observed for the deoxygenated derivative **109** (73.8 mM, 95 % CI [53.0-160.3]) (**Figure 5-9**). This result confirmed that the presence of O_4 was required and that increasing the likelihood or strength of a hydrogen bond accepting interaction at this position may increase ice recrystallization inhibition activity. Interestingly, methylation of O_4 of PMP-Gal (**108**) also led to a near 10-fold improvement in activity compared to PMP-Gal (**107**) with IC_{50} values of 4.65 mM (95 % CI [3.60-5.63]) and 55.2 mM (95 % CI [42.2-70.2]) respectively (**Figure 5-9**). Despite the near two-fold difference in activity between PMP-Glc (**26**) and PMP-Gal (**107**), the activity of the O_4-methylated derivatives (**99** and **108**) was nearly the same. These results suggested that the stereochemistry of carbon 4 may not have an impact on ice recrystallization inhibition activity upon

O-methylation; however, the exact meaning of this modification would require further investigation into the specific interactions between these carbohydrates and bulk water molecules.

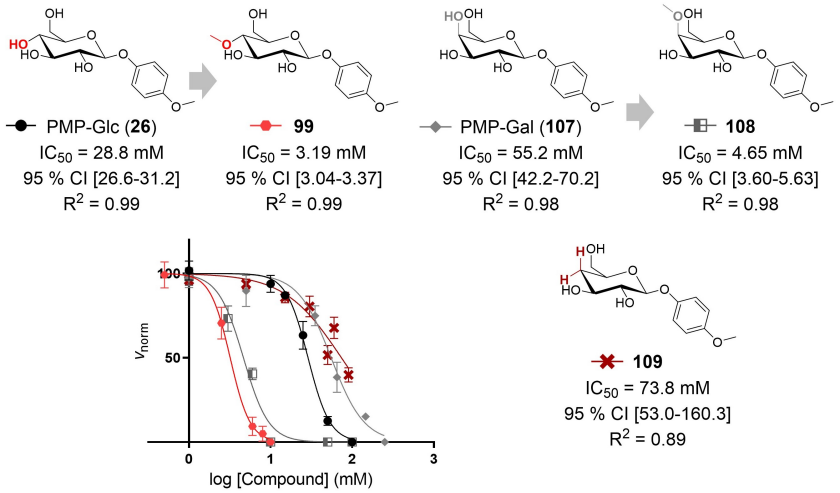
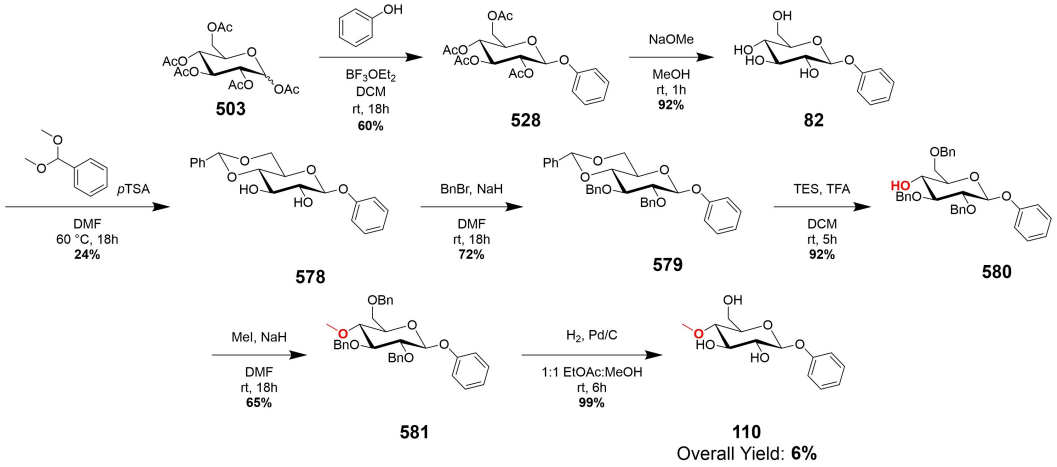


Figure 5-9. Ice recrystallization inhibition activity of compounds **26** & **99** compared to **107** & **108**, as well as **109**. Plot of normalized ice crystal growth (v_{norm}) in phosphate-buffered saline (PBS) against logarithm transformed compound concentration (in mM). Determined by modified splat-cooling assay with a 5-minute annealing time at -6.4 °C.[169]

Next, O_4 methylated derivatives of phenyl-β-D-glucopyranoside (Ph-Glc, **82**) and phenyl-β-D-glucopyranoside (*m*CNPh-Glc, **37**), phenyl-4-*O*-methyl-β-D-glucopyranoside (C_4 OMe Ph-Glc, **110**) and (3-cyanophenyl)-4-*O*-methyl-β-D-glucopyranoside (C_4 OMe *m*CNPh-Glc, **111**), were synthesized and tested by the 5-minute SCA to assess whether methylation of O_4 could be generally applied to other glucopyranosides to improve ice recrystallization inhibition activity. The phenyl substituted glucopyranoside (**82**) was of interest as it served as an unsubstituted control for which any future studies that compared the effect of alkylation and aryl ring substitution. On the other hand, the nitrile- substituted glucopyranoside (**37**) was important as it could be used to improve non-invasive live-cell imaging Raman microscopy techniques as well as the cryopreservation of red blood cells (RBCs) as discussed in *chapter 3* should improved ice recrystallization inhibition activity be observed.

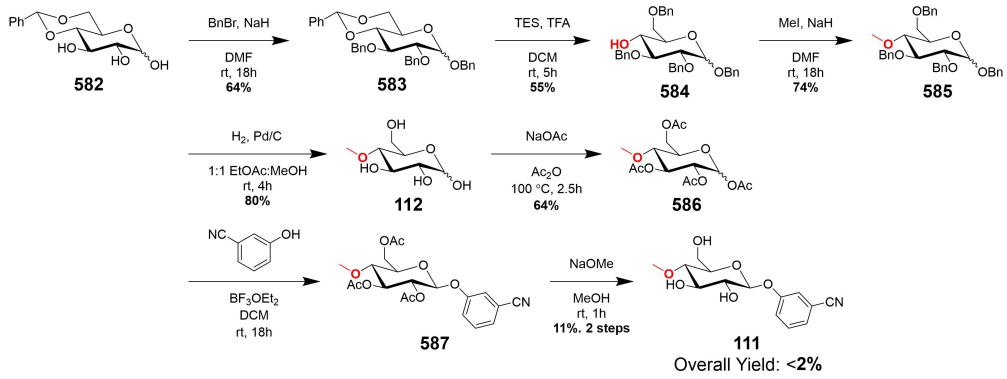
The synthesis of **110** followed the same synthetic pathway as **99**, where a traditional Lewis-acid assisted glycosidation from β-D-glucose pentaacetate (**503**) using $BF_3{\cdot}OEt_2$ (**528**),[167] followed by deacetylation using standard Zemplén conditions[326] afforded phenyl-β-D-glucopyranoside (Ph-Glc, **82**) in two steps with a 55 % overall yield (**Scheme 5-11**). From Ph-Glc (**82**), protection of O_4 and O_6 with a benzylidene acetal (**578**) followed by the benzyl protection of O_2 and O_3 afforded the protected intermediate phenyl-2,3-di-*O*-benzyl-4,6-*O*-benzylidene-β-D-glucopyranoside (**579**) (**Scheme 5-11**). Regioselective deprotection of O_4 readily achieved the desired intermediate phenyl-2,3,6-tri-*O*-benzyl-β-D-

glucopyranoside (**580**) using TES and TFA (**Scheme 5-11**). Subsequent methylation (**581**) and deprotection of **580** afforded the final product phenyl-2,3,6-tri-*O*-benzyl-β-D-glucopyranoside (C_4 OMe Ph-Glc, **110**) in five steps with a 29 % overall yield (**Scheme 5-11**).



Scheme 5-11. Synthesis of phenyl-4-*O*-methyl-β-D-glucopyranoside, Ph-Glc (**82**) and phenyl-4-*O*-methyl-β-D-glucopyranoside, C_4 OMe Ph-Glc (**110**).

The synthesis of **111** could not use the same synthetic methods as **99** and **110** as the aryl-nitrile functional group was not stable to the Pd/C reducing conditions used for removal of the benzyl protecting groups in the final step of the synthesis. Instead, synthesis of C_4 OMe *m*CNPh-Glc (**111**) began from commercially available 4,6-*O*-benzylidene-D-glucose (**582**) followed by benzylation of the remaining hydroxyls (**583**) and regioselective ring opening of the acetal to provide 1,2,3,6-tetra-*O*-benzyl-D-glucopyranoside with a free hydroxyl at C_4 using TES and TFA (**584**). Subsequent methylation (**585**) and deprotection afforded 4-*O*-methyl-D-glucopyranoside (C_4 OMe Glc, **112**). Finally, acetylation using sodium acetate (NaOAc) and acetic anhydride (Ac_2O) (**586**) followed by Lewis-acid assisted glycosidation using $BF_3{\cdot}OEt_2$ with 3-cyanophenol (**587**),[167] and deacetylation using standard Zemplén conditions[326] afforded the final product (C_4 OMe *m*CNPh-Glc, **111**) in seven steps with < 2 % overall yield (**Scheme 5-12**).



Scheme 5-12. Synthesis of 3-cyanophenyl-4-*O*-methyl-β-D-glucopyranoside, C_4 OMe *m*CNPh-Glc (**111**).

The ice recrystallization inhibition activity of C_4 OMe Ph-Glc (**110**) as determined by the 5-minute SCA was described by an IC_{50} of 1.99 mM (95 % CI [1.40-2.56]) (**Figure 5-10**). As the parent compound Ph-Glc (**82**), was found to have an IC_{50} of 17.1 mM (95 % CI [14.0-21.0]), O_4 methylation again caused a 10-fold improvement in ice recrystallization inhibition activity (**Figure 5-10**). The same was true for O_4 methylation of *m*CNPh-Glc (**37** to **111**), where the IC_{50} value improved from 26.8 mM (95 % CI [24.5-29.6]) to 0.81 mM (95 % CI [0.78-0.84]) (**Figure 5-10**).

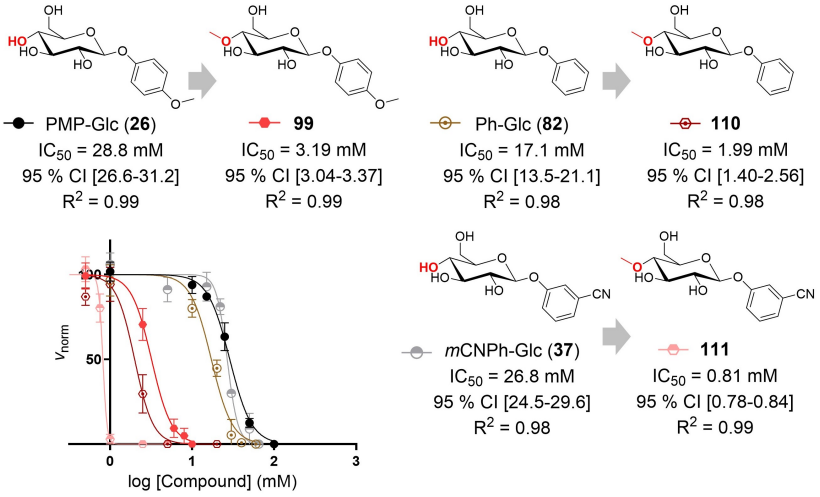


Figure 5-10. Ice recrystallization inhibition activity of compounds **26** & **99**, **82** & **110**, **37** & **111**. Plot of normalized ice crystal growth (v_{norm}) in phosphate-buffered saline (PBS) against logarithm transformed compound concentration (in mM). Determined by modified splat-cooling assay with a 5-minute annealing time at -6.4 °C.[169]

Not only did the ice recrystallization inhibition activity of the O_4 methylated compounds improve at least 10-fold compared to their parent compounds, but they were also among the most active *O*-aryl-β-D-glucopyranoside IRIs that had been reported to date. As discussed in *chapter 4*, the majority of active *O*-aryl-β-D-glucopyranoside IRIs have been reported with IC_{50} values that reside in the 25-75 mM range. Two of the most active compounds, *p*BrPh-Glc (**25**) and PEP-Glc (**54**), were reported with IC_{50} values of

6.75 mM (95 % CI [6.12-7.46]) and 4.45 mM (95 % CI [4.29-4.62]) respectively. Recent unpublished data by Marcus Diamante (Ben Lab, PhD Candidate) has found *N*-alkyl-D-gluconamide compounds with IC_{50} values in the 50-100 μM range,[331] however until now, this level of activity had not been observed for the *O*-aryl-β-D-glucopyranosides.

Interestingly, methylation of the O_4 position of D-glucose to 4-*O*-methyl-D-glucopyranoside (**112**), did not result in the same 10-fold improvement in ice recrystallization inhibition activity as with the derivatives where O_1 was arylated. The IC_{50} of C_4 OMe Glc (**112**) was found to be 76.2 mM (95 % CI [72.9-79.7]) which was comparable to the IC_{50} of the D-glucose (**8**) reducing sugar prior to methylation. Therefore, the improvement in ice recrystallization inhibition activity upon alkylation at O_4 could only be generalized to compounds that were substituted at C_1. To further test this hypothesis experimentally, a greater library of substitutions at C_1 could be tested including different C_1 linkers such as *N*- or *S*- as well as alkyl hydrocarbons.

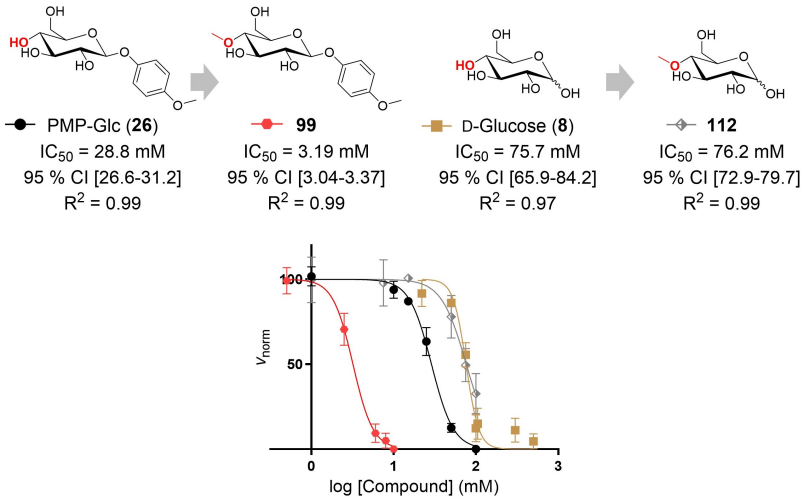


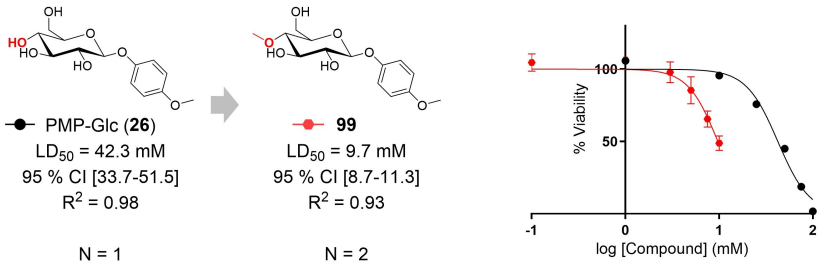
Figure 5-11. Ice recrystallization inhibition activity of compounds **26** & **99** compared to **8** & **112**. Plot of normalized ice crystal growth (v_{norm}) in phosphate-buffered saline (PBS) against logarithm transformed compound concentration (in mM). Determined by modified splat-cooling assay with a 5-minute annealing time at -6.4 °C.[169]

*5.3.2. Cytotoxicity of PMP-Glc (**26**) and C_4 OMe PMP-Glc (**99**)*

The significant improvement in ice recrystallization inhibition activity upon *O*-methylation at the C_4 position was an extremely important finding in the development of novel small-molecule IRIs. Improving ice recrystallization inhibition activity would ultimately reduce the concentration of an IRI required for a given cryopreservation application and could reduce the risk of cellular cytotoxicity. With respect to the *O*-aryl-β-D-glucopyranoside IRIs, cytotoxicity was previously suggested to be the result of the corresponding phenol that was released during metabolism by glycosidase enzymes (see

section 2.3.2.4). For example, mesenchymal stromal cells (MSCs) that had been cryopreserved with the *O*-aryl-β-D-glucopyranoside *p*BrPh-Glc (**25**) at a concentration of 30 mM were found to be completely non-viable as measured by two different cell viability assays post-thaw (see *chapter 2*); this concentration was approximately where the normalized rate of ice recrystallization reached 0 %, indicating that no ice crystal growth was observed beyond the 0.001 mm^2 threshold within the 5-minute annealing period. However, *p*BrPh-Glc (**25**) was found to result in complete cell death observed at all concentrations greater than or equal to 30 mM (N≥2) as measured by resazurin assay in HepG2 cells after a 1-hour incubation (**Figure 2-23A**). If the activity of *p*BrPh-Glc (**25**) was greater, such as could reasonably be achieved by O_4 methylation based on the previous generalization results, lower concentrations may be able to inhibit ice recrystallization and improve cryopreservation outcomes without as great of a cytotoxicity risk. However, this hypothesis assumes that the cytotoxicity of the newly *O*-methylated compound was not also increased to the same degree as ice recrystallization inhibition activity [*i.e.,* the efficacy index (EI), the ratio of a compound's LD_{50} to IC_{50}, must not decrease].

To assess and compare the cytotoxicity of PMP-Glc (**26**) to its O_4 methylated derivative (**99**), the resazurin cytotoxicity assay was used to determine each compound's LD_{50} after a 24-hour incubation. The LD_{50} of PMP-Glc (**26**, N=1 biological replicate) was found to be 42.3 mM (95 % CI [33.7-51.5]) (**Figure 5-12**); this result was consistent with the toxicity reported by Dr. Capicciotti (Ben Lab, PhD 2014) that found 50-60 % viability of HepG2 cells in the presence of 44 mM PMP-Glc (**26**) after an 18-hour incubation.[158] On the other hand, the LD_{50} of C_4 OMe PMP-Glc (**99**, N=2 biological replicates) dropped significantly compared to PMP-Glc at 9.7 mM (95 % CI [8.7-11.3]) (**Figure 5-12**). Therefore, C_4 OMe PMP-Glc (**99**) was significantly more toxic, approximately 4.5-fold, than PMP-Glc (**26**) with the addition of the C4 methoxy group. Most importantly however, given the ice recrystallization inhibition activity of the *O*-methylated derivative improved nearly 10-fold, the overall EI was increased from 1.5 to 3.0.



Compound	PMP-Glc (**26**)	C_4 OMe PMP-Glc (**99**)
Efficacy Index (EI)	1.5	3.0

Figure 5-12. 24-hour toxicity measurement of compounds **26** and **99**. Plot of percent cell viability of HepG2 cells against logarithm transformed compound concentration (in mM). Determined by resazurin-based metabolic assay following 24-hour incubation at 37 °C in 5 % CO_2. Efficacy index (EI) calculated as each compound's LD_{50}/IC_{50}. Data presented as mean ± standard deviation (SD), N=1 for compounds **26**, N=2 for compound **99**.

Based on these results, O_4-methylation should be considered as a general strategy for improving ice recrystallization inhibition activity of *O*-aryl-β-D-pyranosides to reduce the concentrations required for cryopreservation and reduce overall risk of cytotoxicity in cellular applications. From a mechanistic point of view however, we remained interested in exploring the impact that *O*-methylation in a positionally dependent manner may have on the overall interactions between these molecules with bulk water in order to inhibit ice recrystallization.

5.4. Understanding the positional impact of *O*-methylation on the ice recrystallization inhibition activity of PMP-Glc (**26**)

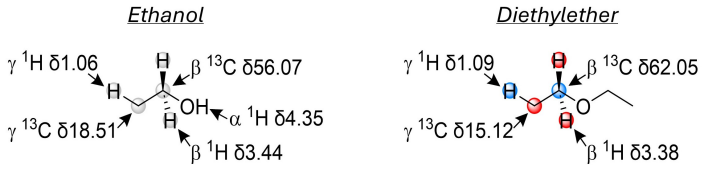
Based on the hypothesized mechanism of action of these compounds, it was thought that methylation at the O_4 position favoured the formation of hydrogen bonding interactions with bulk water molecules that were important for inhibiting ice recrystallization. While the exact interactions between a carbohydrate and bulk water molecules are complex due to the numerous *inter*- and *intra*- molecular interactions that can form, there have been a handful of studies that have reported position specific hydrogen bonding patterns. For example, OH-4 of β-phenyl-D-glucose (**82**) has been reported to form a key hydrogen bond donation (HBD) interaction with bulk water molecules as confirmed by gas phase computation calculations and infrared (IR) spectroscopy experiments.[455,456] A similar molecular dynamics study by Dashnau *et. al.* found that OH-4 played a pivotal role in the hydration of a carbohydrates depending on its interactions with OH-2 and OH-6.[436]

Upon *O*-methylation, the *inter*- and *intra*- molecular interactions would be disrupted; for example, HBD by OH_4 is no longer possible and therefore different hydrogen bonding interactions must be favoured.

It was hypothesized that the newly formed hydrogen bonding interaction(s) may be important for ice recrystallization inhibition activity given the near 10-fold improvement that was observed from PMP-Glc (**26**) to C_4 OMe PMP-Glc (**99**). As a result it was of interest to use both nuclear magnetic resonance (NMR) and computational methods in the presence of a single water molecule to investigate the hydrogen bonding interactions and how they change from PMP-Glc (**26**) to the *O*-methylated derivatives (**89**, **97**-**99**).

5.4.1. Assessing carbohydrate water interactions by ^{1}H and ^{13}C NMR

In NMR, ^{1}H chemical shift is primarily sensitive to neighbouring functional groups, where an increase in surrounding electron density leads to shielding (upfield, decreased chemical shift) of the proton of interest and a decrease leads to de-shielding (downfield, increased chemical shift).[457] Based on this principle, alkylation of a given hydroxyl (the α-position) of PMP-Glc (**26**) would change the surrounding chemical environment such that a directly attached carbon (β) would be de-shielded while its protons would be shielded, and adjacent carbons (γ) would be shielded while their protons would be de-shielded (*e.g.*, the chemical shifts of ethanol vs. diethyl ether, **Figure 5-13**) relative to the molecule before alkylation.[458–461]



Position	Δ(δ_{ether}-$\delta_{ethanol}$) ^{1}H	^{13}C
α	N/A	N/A
β	-0.06	+5.98
γ	+0.03	-3.39

Measured in DMSO-*d6*

⊕ Positive value = de-shielded
up in chemical shift upon alkylation

⊖ Negative value = shielded
down in chemical shift upon alkylation

Figure 5-13. Proton (^{1}H) and carbon (^{13}C) nuclear magnetic resonance (NMR) chemical shifts of ethanol and diethylether in deuterated DMSO (DMSO-d_6). The difference in chemical shift from ether to ethanol (upon alkylation of the hydroxyl) was calculated for each of the three (α, β, γ) positions.

In addition to direct changes in chemical shift caused by a substitution or modification, changes in hydrogen bonding could also be investigated using ^{1}H and ^{13}C NMR chemical shifts, coupling constants, as well as solvent and deuterium isotope effects of chemical shifts.[457,462–467] With respect to the ^{1}H chemical shift of a hydroxyl involved in hydrogen bonding, it would be de-shielded relative to a hydroxyl in the same chemical environment that was not involved in hydrogen bonding (*e.g.*, the ^{1}H chemical shift of the hydroxyl of ethanol would be de-shielded by 2.93 ppm from $CDCl_3$ to DMSO-d_6).[458–461] The effect of hydrogen bonding on the ^{1}H and ^{13}C chemical shift of β and γ positions depended on whether the α position was a hydrogen bond donor (HBD) or HBA (*e.g.*, the chemical shifts of ethanol in $CDCl_3$ vs. DMSO-d_6 and of acetone in $CDCl_3$ vs. CD_3OD-d_4).[458–461] Due to this variability, ^{13}C NMR has been more frequently

used to investigate the hydrogen bonding interactions of compounds than ^{1}H NMR. For example, protein folding interactions can be elucidated by monitoring ^{13}C chemical shift changes of amide carbonyl carbons where a carbonyl accepting a hydrogen bond would be de-shielded at the carbon compared to when it was not a HBA.[468] However, it is important to note that a given chemical shift value is the result of a summation of all potential factors that could affect a nuclei's chemical shift (*e.g.*, carbohydrates that have extensive intra- and inter-molecular hydrogen bond networks are globally shifted further downfield than aliphatic alcohols despite the local chemical environment being structurally similar[469]) which can complicate analyses.[457–459]

To determine the change in ^{1}H and ^{13}C chemical shifts caused by the methylation of each hydroxyl position of PMP-Glc and gain insight into their hydrogen bonding patterns, the *O*-methylated derivatives (**89**, **97-99**) were prepared in DMSO-d_6 and spectra were calibrated to the solvent peak (δ2.50 ppm) in order to assign each proton and carbon's chemical shift (**Figure 5-14** and **Figure 5-15**, see *section 8.3.7* for zoomed in spectra). Due to the speed of proton exchange rates, polar aprotic solvents such as DMSO-d_6 or reduced temperatures must be used to slow down proton exchange and permit investigation of carbohydrate conformation and their hydrogen bonding interactions.[470,471] All chemical shifts were then normalized to the chemical shift of the respective proton or carbon of PMP-Glc (**26**) to provide the relative chemical shift change at each position that results from the methylation of each oxygen.

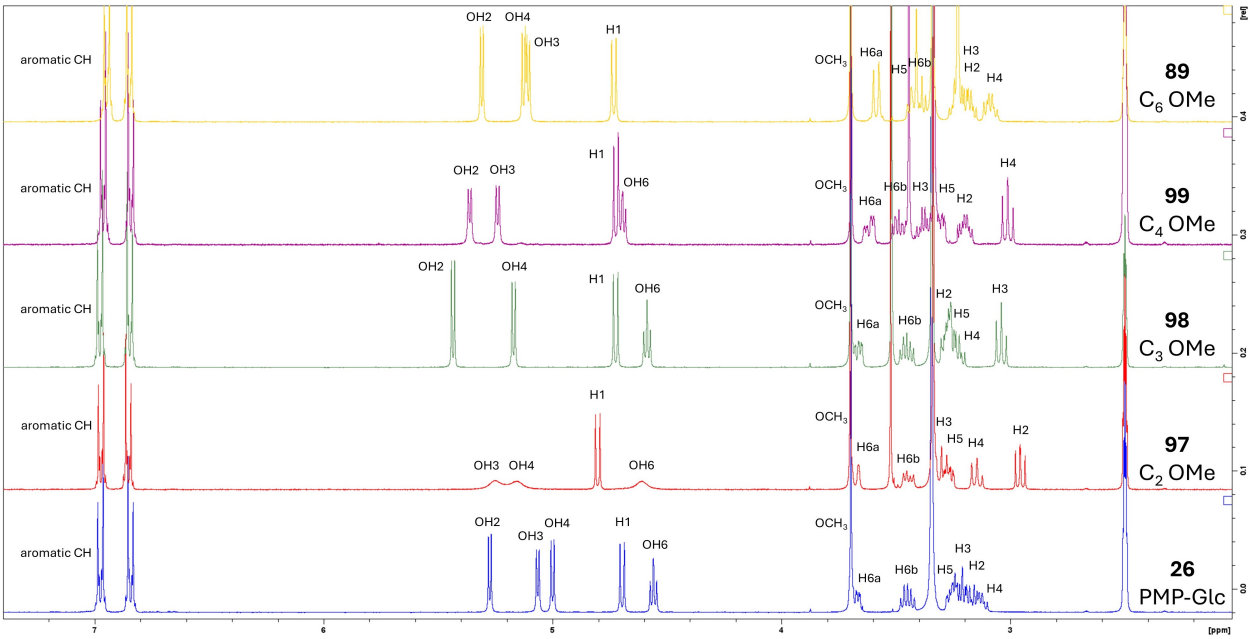


Figure 5-14. Proton (^{1}H) NMR spectra of *O*-methylated derivatives (**89**, **97-99**) compared to PMP-Glc (**26**). All relevant protons on each spectra are labelled accordingly.

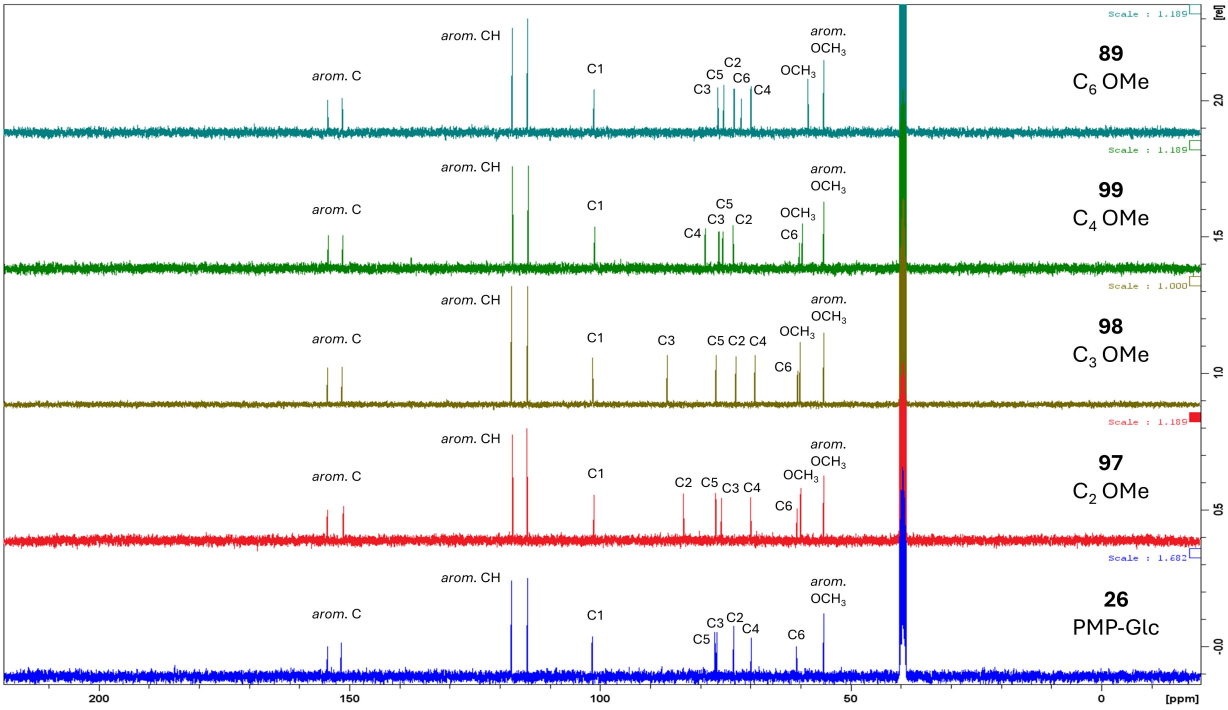
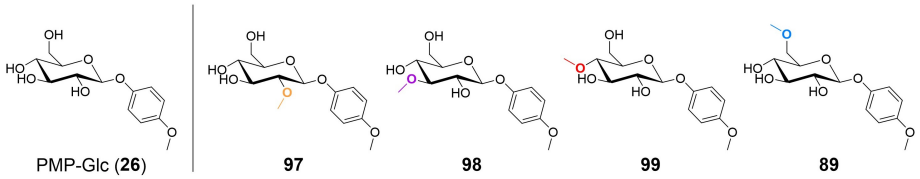


Figure 5-15. Carbon (^{13}C) NMR spectra of *O*-methylated derivatives (**89**, **97-99**) compared to PMP-Glc (**26**). All relevant protons on each spectra are labelled accordingly.

From the normalization of chemical shifts, a negative relative value indicated that the signal of interest was shielded (red) compared to PMP-Glc (**26**) and a positive relative value indicated that the signal of interest was de-shielded (blue) upon *O*-methylation (**Figure 5-16**). From the change in the chemical

environment alone, the methylation of each oxygen of PMP-Glc (**26**) was expected to result in an overall de-shielding of the respective β carbon and shielding of its protons. In general, the β carbon after each methylation was de-shielded as expected by 9.2-11.0 ppm, with C_6 experiencing the greatest de-shielding and C_4 experiencing the least (**Figure 5-16**); the protons at the β position also shielded as expected by -0.06 to -0.26 ppm (**Figure 5-16**). With respect to the adjacent positions (γ), methylation in general resulted in shielding of the carbons (by as little as -0.1 to as much as -1.7 ppm) and de-shielding of the protons (by 0.03 to 0.18 ppm) as was expected (**Figure 5-16**). In addition, methylation of any position resulted in de-shielding of the remaining un-methylated hydroxyl protons by as much as 0.19 ppm (**Figure 5-16**).



	^{1}H Chemical Shift													^{13}C Chemical Shift						
Compound	H_1	H_2	H_3	H_4	H_5	H_{6a}	H_{6b}	OCH_3 arom	H_2O	OH_2	OH_3	OH_4	OH_6	C_1	C_2	C_3	C_4	C_5	C_6	OCH_3 arom
26	0.00	0.00	0.00	0.00	0.00	0.00	0.00	0.00	0.00	0.00	0.00	0.00	0.00	0.0	0.0	0.0	0.0	0.0	0.0	0.0
97	0.10	-0.26	0.05	0.01	0.03	0.00	0.00	0.00	0.00	NA	0.19	0.16	0.05	-0.4	10.0	-0.9	0.1	-0.1	-0.1	0.0
98	0.03	0.06	-0.20	0.08	0.01	-0.01	0.00	0.00	0.00	0.16	NA	0.17	0.03	-0.1	-0.4	9.9	-0.7	-0.2	-0.3	-0.1
99	0.02	-0.01	0.14	-0.13	0.07	-0.06	0.03	0.00	-0.01	0.08	0.18	NA	0.14	-0.4	0.2	-0.3	9.2	-1.5	-0.5	-0.1
89	0.03	-0.04	-0.02	-0.05	0.18	-0.09	-0.06	0.00	0.00	0.03	0.05	0.13	NA	-0.3	-0.1	-0.1	0.0	-1.7	11.0	-0.1

Figure 5-16. Proton (^{1}H) and carbon (^{13}C) chemical shifts for each *O*-methylated carbohydrate (**89**, **97-99**) relative to PMP-Glc (**26**). Blue colouring indicates an atom that was de-shielded compared to PMP-Glc (**26**) while red colouring indicates an atom that was shielded relative to PMP-Glc (**26**).

It must be noted that the use of DMSO-d_6 as the solvent for these experiments overestimates the proportion of HBAs in solution compared to the aqueous environment (where H_2O can be a HBD or HBA) in which cryopreservation, and thus ice recrystallization, occurs. This meant that the corresponding de-shielding chemical shift changes that may have been observed by the formation of additional HBA interactions with the solvent at a given position would not have been observed. In addition, the impact of other *inter*-molecular ionic interactions between the carbohydrate and DMSO or carbohydrate-carbohydrate interactions may be confounding the changes in chemical shift that were observed in this study.

Ultimately, the magnitude of ^{13}C chemical shift change that was observed for each position upon *O*-methylation was greater than expected and varied by carbohydrate position; for example, only a 5.98 ppm downfield shift was observed for the β carbon upon alkylation of ethanol to diethylether (**Figure 5-13**)[458,459] which was nearly doubled for the carbohydrates (9.2-11.0 ppm, **Figure 5-16**). It was hypothesized that the difference in chemical shift could be caused by differences in hydrogen bonding (both *inter*- and *intra*-

molecular) at each position due to *O*-methylation. From the ^{13}C NMR of PMP-Glc (**26**), the C_6 carbon was most shielded and experienced the greatest de-shielding compared to the other three carbons containing hydroxyls. This suggests that the C_6 hydroxyl was most impacted by the HBD interactions that were lost upon *O*-methylation; this was consistent with previously discussed literature where the C_6 hydroxyl is critical for hydrogen bonding interactions with bulk water molecules.[436,449] On the other hand, the C_4 carbon experienced the least de-shielding upon *O*-methylation which would suggest that it was least impacted by the substitution and the loss of HBD interactions.

5.4.2. Assessing the interactions between a carbohydrate and a single water molecule using computational molecular dynamics simulations

Given the complexity associated with deconvoluting the interactions between multiple water molecules and a polyol carbohydrate by NMR, we sought to simplify the model and use computational methods to investigate interactions with only a single water molecule. From this model we investigated the free energy of a single hydrogen bond donation and accepting interaction at each of the four carbohydrate oxygens (at C_2, C_3, C_4, and C_6).

First, a conformational search of PMP-Glc (**26**) in the absence of a water molecule was completed to assess the *intra*-molecular hydrogen bonding interactions between the carbohydrate hydroxyls. The conformational search of PMP-Glc (**26**) was performed in an implicit water solvent model (CPCM) using CREST[430] (2.11 or 2.12) and produced a set of > 1500 distinct conformers within a 12 kcal/mol window (**Figure 5-17**); the algorithm was developed to exclude rotamers, however many rotamers were maintained within the output library which resulted in the large number of potential conformations to be analyzed.

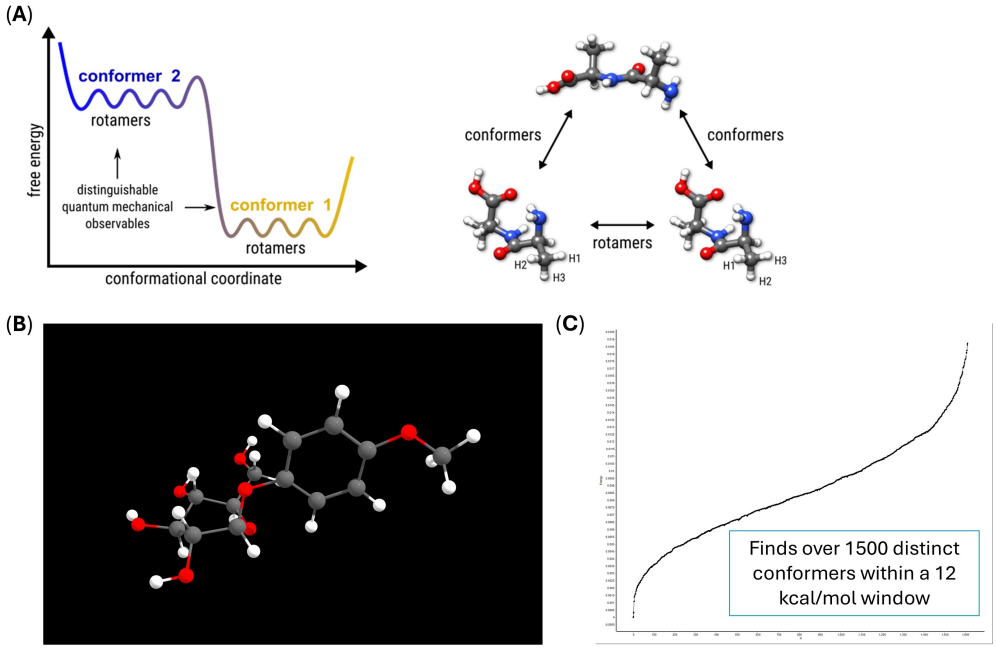
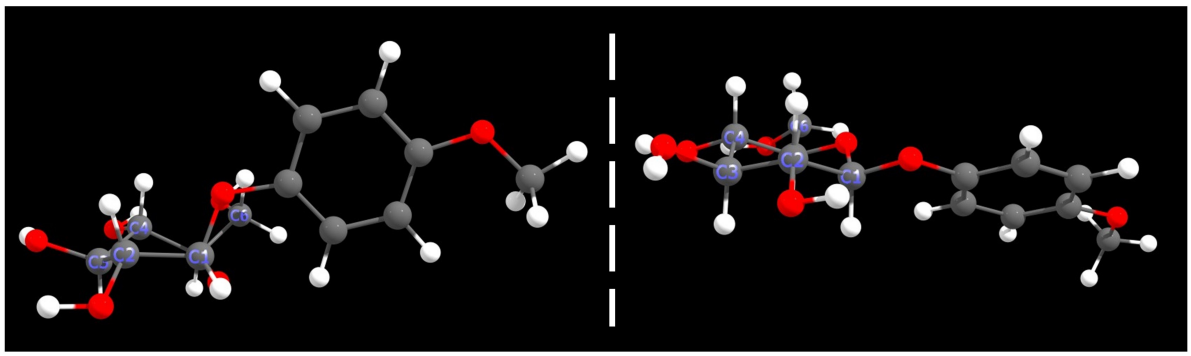


Figure 5-17. (**A**) Depiction of the CREST (2.11) conformational coordinate and the distinction between conformers and rotamers. (**B**) A single conformer of PMP-Glc (**26**). Structure representation created in *Chemcraft 1.8*.[472] (**C**) The full plot of conformers of PMP-Glc (**26**) arranged from lowest to highest energy as calculated by CREST (2.11)[430].

From the CREST algorithm, the lowest energy carbohydrate structure returned by the search was in a twist-boat conformation; however, based on known hexose and cyclohexane conformations the expected lowest energy conformation for the carbohydrate, a $^4C_1$ chair, was not observed until the 12th lowest conformer in the search. Given the unexpected energy ranking of the conformers, the full library was narrowed using chemical intuition to select distinct conformations that were each individually geometry optimized using ORCA (5.0.4)[473,474] at the DEF2-TZVPP[475] level of theory with the ωB97[431] hybrid functional using the CPCM implicit water solvation model[433] (the CREST conformational search was completed at the GFN2-xTB/ALPB(H_2O) level). Following geometry optimization by ORCA (5.0.4)[473,474], the $^4C_1$ chair conformation was found to be the lowest in energy as expected at a ΔΔG of 4.99 kcal/mol lower than the twist-boat conformation (**Figure 5-18**); the energy difference between these two conformations was consistent with the energy difference between the same two conformations for cyclohexane (5.5 kcal/mol).[476]

PMP-Glc (**26**)



CREST: Lowest energy conformer – twist-boat

Following geometry optimization with ORCA:
ΔΔG = 0.00 kcal/mol

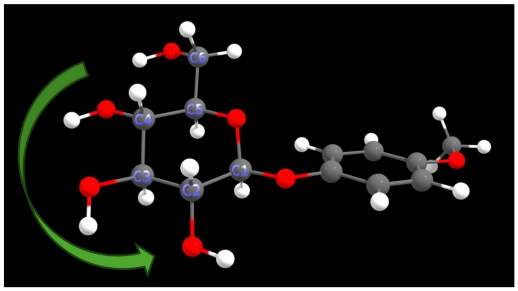
CREST: 12th lowest energy conformer – $^4C_1$ chair

Following geometry optimization with ORCA:
ΔΔG = -4.99 kcal/mol

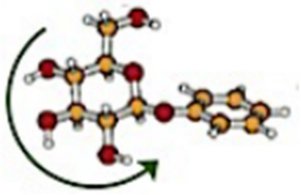
Figure 5-18. Depictions of PMP-Glc (**26**) in the twist-boat conformation (left) or the $^4C_1$ chair conformation (right) as determined by CREST (2.11)[430]. Energy calculations (free energy, ΔG) completed using ORCA (5.0.4)[473,474] at the DEF2-TZVPP[475] level of theory with the ωB97[431] hybrid functional using the CPCM implicit water solvation model[433] and presented relative to the twist-boat conformation energy. Structure representations created in *Chemcraft 1.8*.[472]

The $^4C_1$ conformation was also consistent with what was previously reported by Çarçabal *et. al.* (2005) where the hydroxyls form intramolecular hydrogen bonds in a counterclockwise orientation beginning with OH-6 and terminating at OH-2 (**Figure 5-19**).

(**A**) PMP-Glc (**26**) low energy conformation as determined by CREST (2.11) conformational search and ORCA geometry optimization



(**B**) Low energy conformation as determined by *Çarçabal et. al. (2005)*



β-Ph-D-Glucopyranose
(**82**)

Figure 5-19. (**A**) Low energy conformation of PMP-Glc (**26**) as determined by CREST (2.11)[430] then geometry optimized using ORCA (5.0.4)[473,474] at the DEF2-TZVPP[475] level of theory with the ωB97[431] hybrid functional using the CPCM implicit water solvation model[433]. Structure representations created in *Chemcraft 1.8*.[472] (**B**) Low energy conformation of Ph-Glc (**82**) as determined by *Çarçabal et. al. (2005)*.[455] Green arrow indicates the direction of intramolecular hydrogen bonding. *Panel B recreated with permission from Çarçabal et. al. (2005) from ACS publications.*[455]

We then sought to explore the hydrogen bonding interactions that each hydroxyl could make with a single water molecule. For this assessment the $^4C_1$ chair conformation of each derivative was constrained such that partial or full ring flips to other conformations were not possible. Then, the single water molecule

was constrained to the hydroxyl of interest (with a force constant of 0.25 and at a distance of 1.8 Å) such that it formed either a hydrogen bond donation or a hydrogen bond accepting interaction with the carbohydrate position. For example, the hydroxyl at C_2 of PMP-Glc (**26**) can be a hydrogen bond donor or acceptor with a single bulk water molecule (**Figure 5-20**).

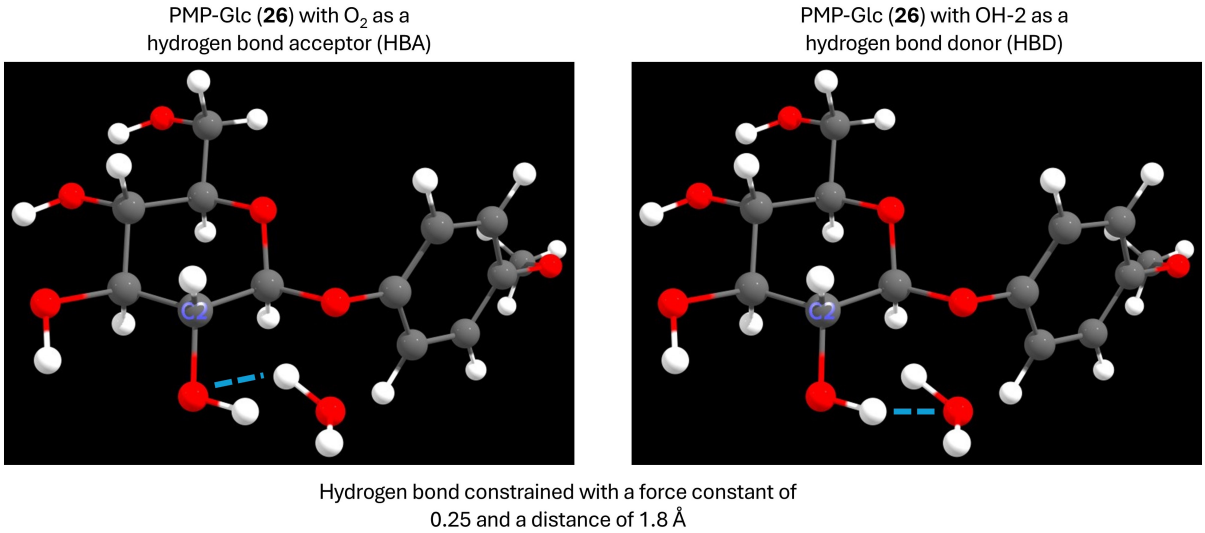
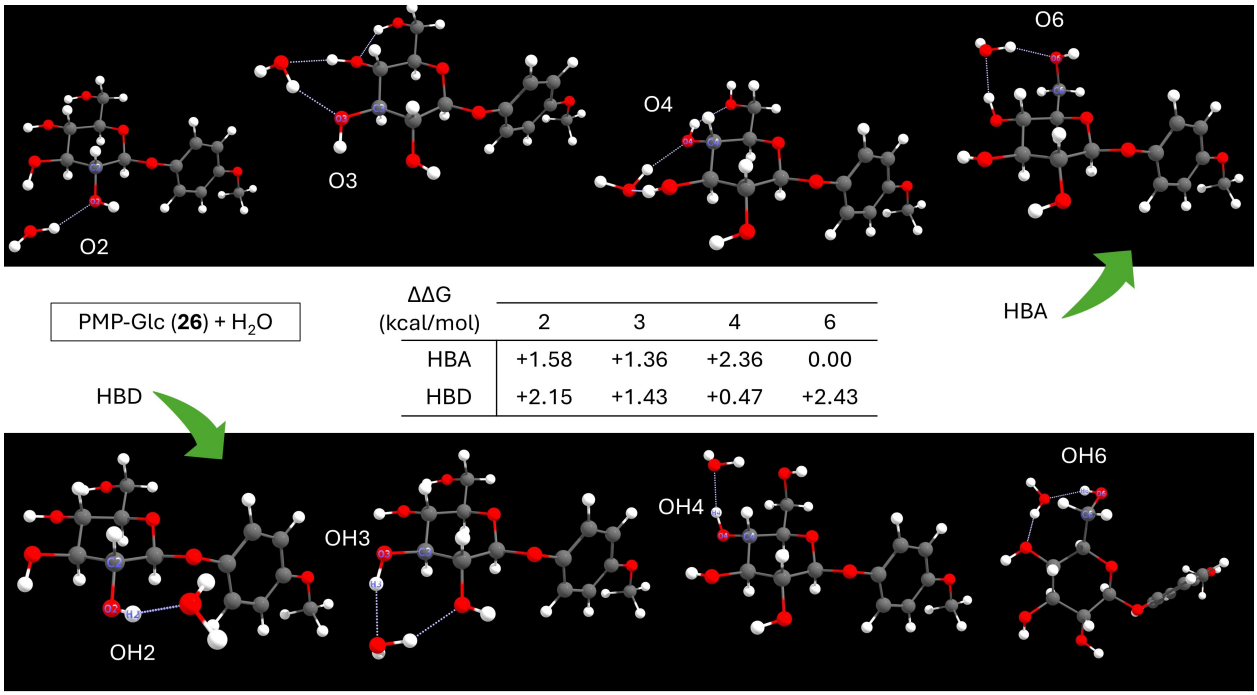


Figure 5-20. PMP-Glc (**26**) forming a single hydrogen bond accepting interaction at O_2 (left) and a hydrogen bond donation interaction at OH-2 (right). Theoretical hydrogen bond shown as a blue dashed line. Structure representations created in *Chemcraft 1.8*.[472]

A conformation search was then initiated using CREST (2.11 or 2.12)[430] which identified unique conformers within a 12 kcal/mol window of the lowest energy conformer. Once again, CREST failed to adequately narrow the library of conformers that were included and as a result chemical intuition was required to identify distinct/unique conformers. From the narrowed library of conformers, the lowest energy conformers from CREST were then geometry optimized in ORCA using the same procedures as previously described. The relative free energy and a depiction of the low energy conformation for each configuration (hydrogen bond donor or acceptor at each carbon position) can be found in **Figure 5-21**.



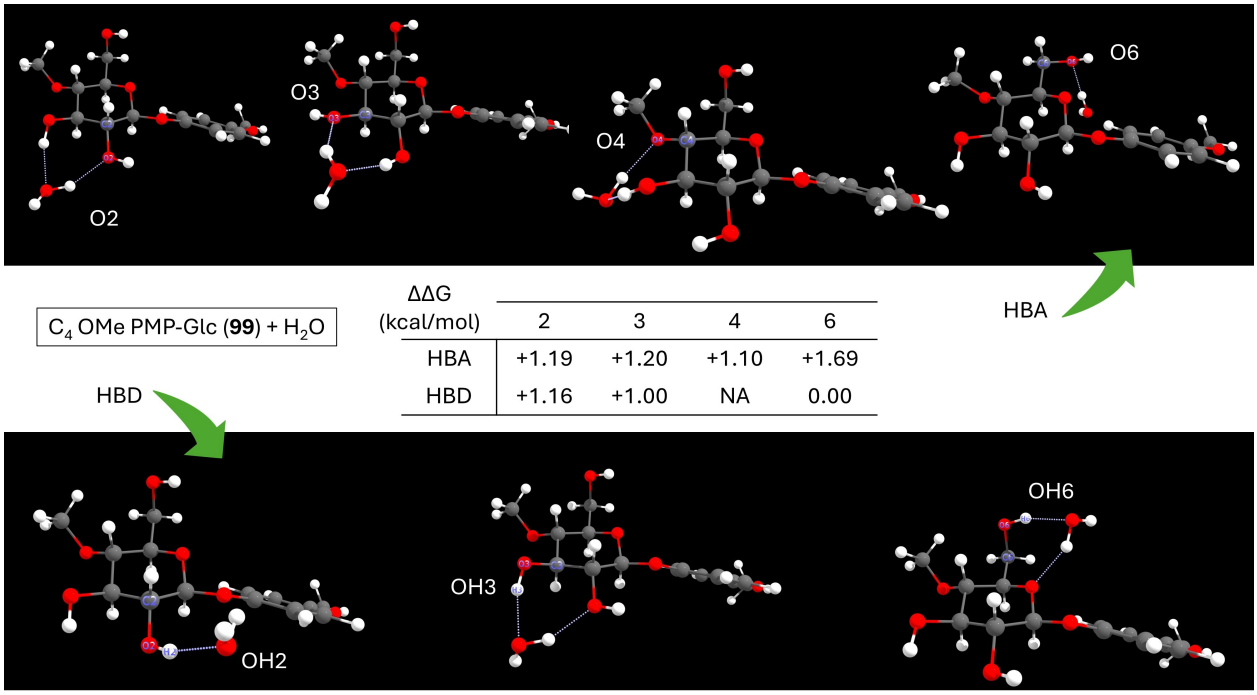
ΔΔG (kcal/mol)	2	3	4	6
HBA	+1.58	+1.36	+2.36	0.00
HBD	+2.15	+1.43	+0.47	+2.43

Figure 5-21. Hydrogen bond accepting (HBA, top) and hydrogen bond donating (HBD, bottom) interactions of a single water molecule with PMP-Glc (**26**). Low energy conformations determined following conformational search by CREST (2.11)[430] then geometry optimization and energy calculations (free energy, ΔG) completed using ORCA (5.0.4)[473,474] at the DEF2-TZVPP[475] level of theory with the ωB97[431] hybrid functional using the CPCM implicit water solvation model[433]. Energy calculated relative to the lowest energy conformer in the set (where OH-6 was acting as a hydrogen bond acceptor). Structure representations created in *Chemcraft 1.8*.[472]

From all configurations, the lowest energy was found when OH-6 was acting as a hydrogen bond acceptor; this interaction also formed a simultaneous hydrogen bond where O_4 was acting as a hydrogen bond donor. This result was again consistent with results found by Çarçabal *et. al.* (2005) where the weakest intramolecular hydrogen bond was found between OH-4 and OH-6 and therefore was the first site of insertion for a water molecule during hydration; also consistent was that the shift in hydrogen bonds to a clockwise orientation once the single water molecule was inserted.

From these results we were also able to observe that with a single water molecule present, OH-2, OH-3, and OH-6 were most stable as hydrogen bond acceptors (**Figure 5-21**); interestingly, OH-4 was most stable as a hydrogen bond donor (ΔΔG HBA = 1.89 kcal/mol greater than HBD, **Figure 5-21**). Considering the methylation of O_4 resulted in a near 10-fold improvement in ice recrystallization inhibition activity and a hydrogen bond donation interaction at this position was no longer possible, we were interested in repeating the previous conformational search with C_4 OMe PMP-Glc (**99**) to explore the changes in hydrogen bonding interactions that may be responsible for the improvement in activity. Following the conformational search

by CREST, conformer selection, and geometry optimization by ORCA, the low energy conformers for each hydrogen bonding interaction can be found in **Figure 5-22**.



ΔΔG (kcal/mol)	2	3	4	6
HBA	+1.19	+1.20	+1.10	+1.69
HBD	+1.16	+1.00	NA	0.00

Figure 5-22. Hydrogen bond accepting (HBA, top) and hydrogen bond donating (HBD, bottom) interactions of a single water molecule with C_4 OMe PMP-Glc (**99**). Low energy conformations determined following conformational search by CREST (2.11 or 2.12)[430] then geometry optimization and energy calculations (free energy, ΔG) completed using ORCA (5.0.4)[473,474] at the DEF2-TZVPP[475] level of theory with the ωB97[431] hybrid functional using the CPCM implicit water solvation model[433]. Energy calculated relative to the lowest energy conformer in the set (where OH-6 was acting as a hydrogen bond donor). Structure representations created in *Chemcraft 1.8*.[472]

Considering the lowest energy structures for each hydrogen bonding interaction of a single water molecule with C_4 OMe PMP-Glc (**99**), hydrogen bond donation was now preferred at all three possible sites (OH-2, OH-3, and OH-6). Most interestingly, the lowest energy conformation of C_4 OMe PMP-Glc (**99**) with a single water molecule was HBD from OH-6 with a simultaneous hydrogen bond accepting interaction at the ring oxygen (O_5). Based on the 10-fold improvement in ice recrystallization inhibition activity observed for C_4 OMe PMP-Glc (**99**) and the hypothesized mechanism of action of these compounds, it was thought that this hydrogen bonding interaction (with OH-6 as a HBD and O_5 as a HBA) may be critical for inhibition ice recrystallization.

Interestingly, when the same search and optimization were performed for PMP-Gal (**107**) and C_4 OMe PMP-Gal (**108**), the lowest energy hydrogen bonding interaction again shifted from between OH-4 and OH-6 to between OH-6 and O_5 following *O*-methylation (**Figure 5-23**). While the conformation with

a single water molecule for PMP-Glc (**26**) and PMP-Gal (**107**) were in the same area, the hydrogen bonding interactions shifted from OH-4 as a HBD and O_6 as a HBA (**Figure 5-21**) to O_4 as the HBA and OH-6 as the HBD (**Figure 5-23**). The difference in these two conformations may also account for the difference in ice recrystallization inhibition activity observed between the two molecules. More importantly however, the hydrogen bonding interactions of C_4 OMe PMP-Glc (**99**) and C_4 OMe PMP-Gal (**108**) were nearly identical with OH-6 acting as a HBD and O_5 acting as a HBA (**Figure 5-21** and **Figure 5-23**).

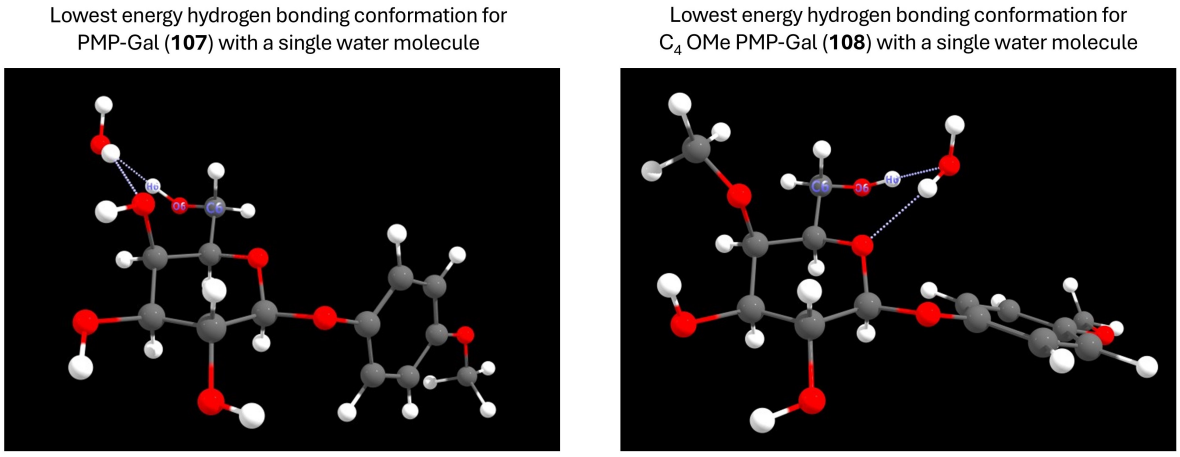


Figure 5-23. Lowest energy conformer of PMP-Gal (**107**) (left) and C_4 OMe PMP-Gal (**108**) (right) with a single water molecule. Determined following conformational search by CREST (2.11 or 2.12)[430] then geometry optimization and energy calculations (free energy, ΔG) completed using ORCA (5.0.4)[473,474] at the DEF2-TZVPP[475] level of theory with the ωB97[431] hybrid functional using the CPCM implicit water solvation model[433]. Structure representations created in *Chemcraft 1.8*.[472]

Based on these results, carbohydrates that form the OH-6 HBD to O_5 HBA interaction should be prioritized during future development campaigns. In addition, we have shown that the computation of low energy conformers and single water molecule interactions may be able to aid in the development of new and improved small-molecule IRIs.

5.5. Summary of PMP-Glc alkylation modifications and their impact on future small-molecule IRI development

The small molecule ice recrystallization inhibitor (IRI) PMP-Glc (**26**) has been successfully used to cryopreserve RBCs, however attempts to further optimize its ice recrystallization inhibition activity have been generally unsuccessful.[158,167,177,214] The past campaigns focused primarily on different carbohydrates, modifications to the aryl substituent and the nature of the linkage, as well as modifications to the C_6 position, but very little emphasis had been placed on investigating whether modifications or substitutions could be made to the carbohydrate hydroxyls directly. As a result, we were interested in investigating an iterative

structure-activity relationship approach that would simultaneously probe the importance of hydrogen bonding at each of the four carbohydrate hydroxyls through deuteration and methylation.

Mono-deuteration of C_1 (**90**), C_2 (**91**), and C_3 (**92**) to replace each position's hydrogen resulted in a minimum of four-fold decrease in ice recrystallization inhibition activity compared to the parent PMP-Glc (**26**); however, no clear position-dependent relationships were observed. A similar observation was made when the mono-deuterated glucose derivatives (**94**-**96**) were tested for ice recrystallization inhibition activity compared to the parent D-glucose (**8**). Therefore, it was determined that deuteration in general was detrimental to ice recrystallization inhibition activity, but the compounds were unable to provide further insight into the hydrogen bonding interactions that may be critical for this activity.

We then investigated derivatives of PMP-Glc (**26**) that had been methylated at each of the carbohydrate hydroxyls (**89**, **97**-**99**) to remove the ability for each position to donate a hydrogen bond to bulk water molecules. Upon testing each derivative for ice recrystallization inhibition activity, it was found that *O*-methylation at the C_6 position (**89**) resulted in a dramatic decrease in aqueous solubility that was consistent with previous findings using the 30-minute SCA as well as reports on the importance of OH-6 to the overall solvation and hydration of carbohydrate-based compounds. Furthermore, *O*-methylation at C_3 (**98**) resulted in a 2-fold loss in ice recrystallization inhibition activity while at the C_2 position (**97**) no significant change in activity was observed. However, *O*-methylation at the C_4 position (**99**) resulted in a 10-fold improvement in ice recrystallization inhibition activity as measured by the 5-minute SCA (from an IC_{50} of 28.8 mM to an IC_{50} of 3.19 mM). Compared to other *O*-aryl-β-D-glucopyranoside IRIs, this was among the most active derivatives from this class that had been reported to date.

Further investigation of alkylation at the O_4 position found that it was tolerant to ethyl and propyl substitutions (**103**-**104**), meaning that the IC_{50} values remained in the 1-5 mM range. Ice recrystallization inhibition activity was also maintained if the *O*-aryl functional group was changed to a phenyl or 3-cyanophenyl (**110**-**111**), suggesting that *O*-alkylation may be an effective strategy in general for improving the ice recrystallization activity of *O*-aryl-β-D-glucopyranosides. Interestingly, the activity improvement was not observed upon *O*-methylation of D-glucose (**8** to **112**), suggesting that there may be an interaction between the hydrophobic methyl at C_4 and the aryl at C_1 that contributes to the improved ice recrystallization inhibition activity.

Most importantly, cytotoxicity screening of PMP-Glc (**26**) and its O_4 methylated derivative (**99**) found a two-fold improvement in efficacy index upon *O*-methylation as the LD_{50} was only decreased by

4.5-fold relative to the 10-fold improvement in ice recrystallization inhibition activity. As a result, *O*-methylation may be a particularly effective strategy for reducing cytotoxicity risk of this class of compounds in cellular applications. For example, the *m*-nitrile derivative *m*CNPh-Glc (**37**) used for Raman imaging experiments suffered from a very small efficacy index, only 1.3, which limited the concentrations at which it could be used which could be mitigated by alkylating the O_4 position such as with compound **111**.

With respect to hydrogen bonding interactions, it was thought that the improved activity may be caused by the lost hydrogen bond donation interaction at OH-4 but that hydrogen bond accepting interactions may be critical. This hypothesis was supported by the significant loss in ice recrystallization inhibition activity that was observed upon deoxygenation at the C_4 position (**109**, IC_{50} = 73.8 mM) of PMP-Glc; however, the activity of PMP-Gal (**107**) was also improved 10-fold upon *O*-methylation at C_4 (**108**). These results suggested that the stereochemistry at C_4 was not important for the *O*-methylated derivatives (**99** and **108**) which was in contrast to the findings of the parent compounds (**26** and **107**).

Further investigation of hydrogen bonding patterns by NMR and computational studies with a single water molecule found that upon *O*-methylation at C_4, for both compounds **99** and **108**, the lowest energy placement of a single water molecule formed accepted a hydrogen bond from OH-6 and donated a hydrogen bond to O_5. These results suggested that future studies may be able to use computational assessments to guide IRI development and that this hydrogen bonding interaction should be investigated in greater detail.

6. Using ^{1}H NMR relaxation times to investigate the mechanism of action of small molecule ice recrystallization inhibitors (IRIs)

Several different classes of molecules have been reported to inhibit ice recrystallization, including antifreeze (glyco)proteins (AF(G)Ps),[98,141,477] polymers such as polyvinyl alcohol (PVA),[154,478] as well as carbohydrate-based small-molecule ice recrystallization inhibitors (IRIs)[159,160,188]. The ice recrystallization inhibition activity of AF(G)Ps and PVA as caused by ice binding has been well established and was previously described in detail in *section 1.2.2*. While the mechanism by which small-molecule carbohydrate-based compounds inhibit ice recrystallization is significantly less understood, the Ben Lab has proposed three different hypotheses that could explain their activity (**Figure 6-1**):

1) The IRI binds directly to the surface of an ice crystal. This binding causes both dynamic ice shaping (DIS) and thermal hysteresis (TH).
2) The IRI gets incorporated into the ice lattice and creates defects in the ice lattice structure. The water molecules that are part of the ice lattice are therefore able to move more freely.
3) The IRI interacts exclusively with water molecules in the liquid water phase and limits their ability to migrate through the bulk liquid water during the ice recrystallization process.

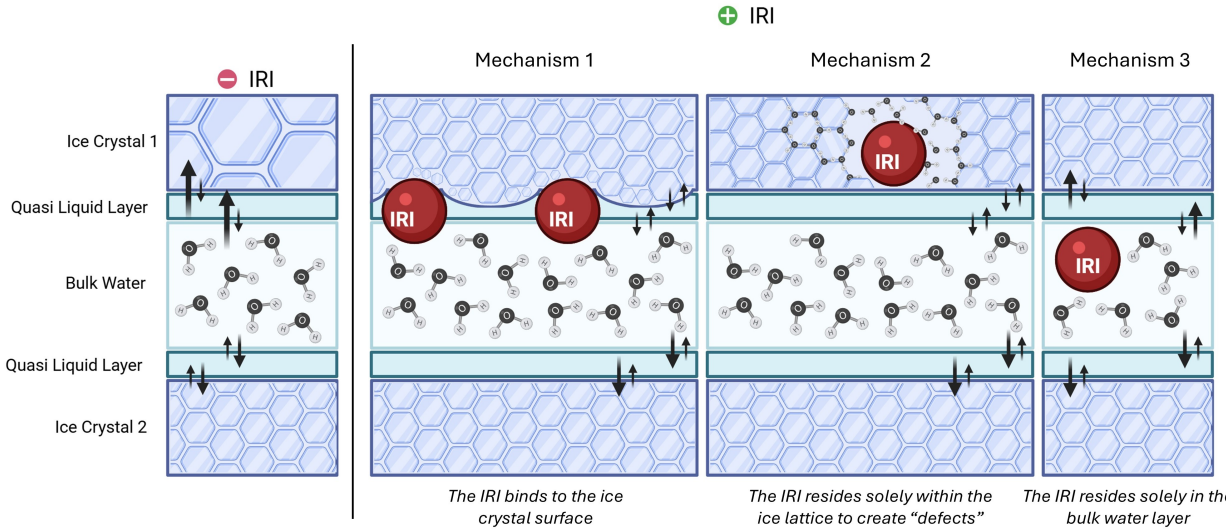


Figure 6-1. Plausible hypotheses for the mechanism of ice recrystallization inhibition by small molecule inhibitors (IRIs) as proposed by the Ben Lab. (**A**) Hypothesis 1. (**B**) Hypothesis 2. (**C**) Hypothesis 3.

The first proposed hypothesis is consistent with the mechanism of ice recrystallization inhibition that has been observed with polymeric molecules including AF(G)Ps and PVA. The ice binding of these compounds results in a localized freezing point depression (TH activity), due to the Gibbs Thomson

(Kelvin) effect, and causes DIS.[88–97,128] Inhibition of ice recrystallization in the presence of these compounds also occurs due to ice binding as it becomes increasingly difficult for water molecules to add to the spaces between absorbed IRIs as the degree of curvature increases.[88,90,91,93,113] It has been previously suggested that small-molecule carbohydrate-based molecules do not inhibit ice recrystallization by this mechanism as TH activity and DIS were not observed by nanolitre osmometry for several key established IRIs (see *section 1.3.1*).

Incorporation of solutes into the ice lattice *via* the second mechanism is hypothesized to inhibit ice recrystallization by breaking apart and disrupting the hydrogen bond network of the ice lattice. This concept is best exemplified with ice that is formed in the presence of ionic salts. During the freezing of water in the presence of ionic salts, most ions are excluded from the ice lattice; however, a small portion of ions can become trapped in the lattice in a process known as "ice doping" that can affect the physicochemical properties of ice.[479–481] A similar phenomenon is possible for larger solutes such as short chain PVA molecules with a growing ice front or with the formation of clathrate hydrates.[128,482] Relative to an "undoped" ice lattice, the average water molecule in a "doped" lattice could move more freely due to the created defects and weakened overall hydrogen bond network. This would result in the ice lattice having an increased overall free energy (due to increased entropy), reducing the energetic gap between the ice lattice and bulk water, and ultimately reducing the drive for water molecules to add to a growing ice surface from bulk water.

The third hypothesis has been previously proposed by the Ben Lab for carbon-linked AF(G)P [*C*-AF(G)P] analogues and other small-molecule carbohydrate-based IRIs that do not display TH activity or cause DIS.[156,157,159,161] This hypothesis was first suggested when a correlation was observed between the ice recrystallization inhibition activity of a carbohydrate and its hydration index (see *section 4.2*); the more hydrated the carbohydrate was by water molecules relative to its molecular volume (hydration index), the more active it was as an ice recrystallization inhibitor.[156,157] Based on this correlation it was argued that compounds with greater hydration, and therefore a worse "fit" into the three-dimensional (3D) hydrogen-bonded network of bulk water molecules,[401] increased the disorder of the bulk water phase and made it less energetically favourable for water molecules to move from the highly ordered ice lattice into the more disorganized bulk water phase during ice recrystallization. Importantly, this correlation provided an initial explanation for the mechanism of ice recrystallization inhibition activity in the absence of ice binding and highlighted the importance of being able to observe/measure the interactions between a small-molecule IRI and water molecules in the pursuit of a mechanism of action. However, as previously discussed, the measurement of hydration values requires specialized equipment that is often not readily

accessible. More importantly, hydration index alone cannot be used to accurately describe the relationship between structure and ice recrystallization inhibition activity as measured by the 5-minute splat-cooling assay (SCA) for substituted carbohydrates derivates (see *section 4.2*). Therefore, it was of interest to explore more widely available methods and techniques that could be used to measure an IRI's interactions with water molecules in order to better understand their mechanism of action and relating it to activity as measured by the 5-minute SCA.

6.1. Nuclear magnetic resonance techniques for observing and measuring water molecule interactions

In addition to ultrasound measurements of water density to determine hydration values, carbohydrate interactions with water molecules have been previously characterized by terahertz spectroscopy,[403,483] molecular dynamics (MD) simulations,[455,456,484,485] spin-probe electron spin resonance,[486] and most notably by nuclear magnetic resonance (NMR). One of the most common uses of ^{1}H NMR in the chemical sciences is to investigate the structure of a compound of interest.[460,461] For this use, an NMR spectrophotometer induces and then records an electromagnetic signal as a function of time from the sample of interest, called a free-induction decay (FID). This signal is then mathematically transformed (*via* Fourier transformation) to generate an NMR spectrum that is reported as a function of frequency (**Figure 6-2**).[487] However, for applications investigating more dynamic properties such as molecular motion, it is the raw FID prior to Fourier-transformation that provides the most useful information. In the food sciences, the FID generated by NMR has been used to characterize water content, sample homogeneity, as well as changes in properties following freeze storage.[488–491] Clinically, NMR is also known as magnetic resonance imaging (MRI) where tissues in the body can be mapped and imaged from the FID based on differences in the motion of localized water and fat molecules.[460]

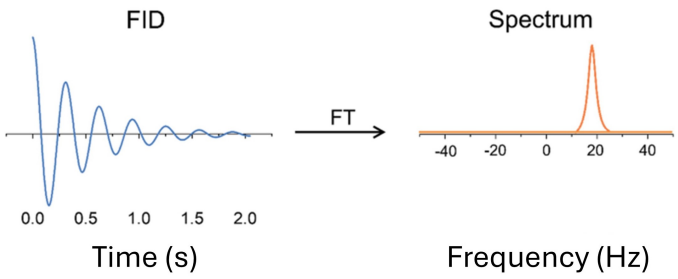


Figure 6-2. Visual depiction of conversion from the time domain signal (FID in seconds) to the frequency domain spectra (in hertz) resulting from the processing of NMR spectrophotometer data by Fourier transformation (FT). *Reprinted from Hosur and Kakita (2022) with permission from Springer.*[487]

To generate a raw FID, the electromagnetic signal generated by individual nuclei in the sample of interest is recorded in response to an applied electromagnetic pulse. The nuclei of interest for NMR have

spin (or angular momentum) resulting in a magnetic moment that can be represented by a single directional vector (**Figure 6-3A**). The frequency at which each nucleus spins is known as the Larmor frequency, calculated as the sum of the magnitude of an applied external field (B_0) and the gyromagnetic ratio of the nucleus. In an undisturbed sample at thermal equilibrium, the orientation of each of these vectors is random. However, when the sample is exposed to the external magnetic field from an NMR spectrophotometer, the vectors exist in either a low or high energy state; the low energy state places vectors in direct alignment with the external magnetic field while in the high energy state the vectors are oriented 180° to the external magnetic field (**Figure 6-3B**). At thermal equilibrium, the vectors flip infrequently between the low and high energy states but when a radiofrequency (RF) pulse with an appropriate energy level is applied the nuclear vectors are induced to flip from the low energy state to the high energy state, increasing the proportion of vectors residing in the high energy state (**Figure 6-3C**). Following the RF pulse, the nuclear vectors undergo relaxation and release energy to return the sample to thermal equilibrium and the NMR spectrophotometer measures this release of energy over time to generate the FID (**Figure 6-3D**). Different types of relaxation [including longitudinal (T_1, or spin-lattice) and transverse (T_2, or spin-spin) relaxation phenomena] as well as changes in the amount of time a relaxation process takes can provide direct insight into the molecular motion of nuclei and ultimately of entire molecules.

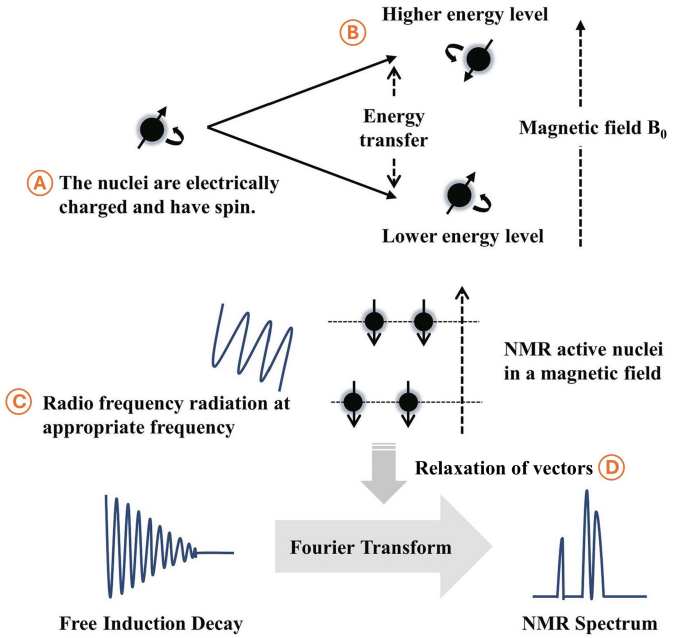


Figure 6-3. Depiction of the nuclear vectors and their spin/motion associated with generating an NMR spectrum. *Figure adapted from Cao et. al. (2021) with permission from Elsevier.*[492]

6.1.1. T_1 relaxation

T_1 relaxation occurs when a nucleus releases its energy to the surrounding environment, including to other molecules in the sample and the remainder of the molecule containing the nucleus of interest, and

is measured in the z-axis by an inversion recovery pulse sequence.[460] For an inversion recovery experiment, an initial 180° RF pulse is applied that inverts the spin population across the z-axis (**Figure 6-4A**). The nuclei begin relaxing back to thermal equilibrium and after a designated period of time (τ), a 90° pulse is applied followed by immediate acquisition of the FID (**Figure 6-4B**). This pulse sequence is repeated with increasing τ, such that the intensity of the vector in the z-axis is measured and plotted as a function of τ (**Figure 6-4C**). The rate of growth of magnetization in the z-axis over time following these pulses can be expressed by **Equation 6-1**.

Equation 6-1. $I(\tau) = I_{\infty}\left(2e^{(-\tau/T_1)}\right)$

From the plot of magnetization signal over time, the T_1 relaxation time is derived as the time required for the signal to grow from 0 to (1 - 1/e), or approximately 63 % of its final maximum value.[460]

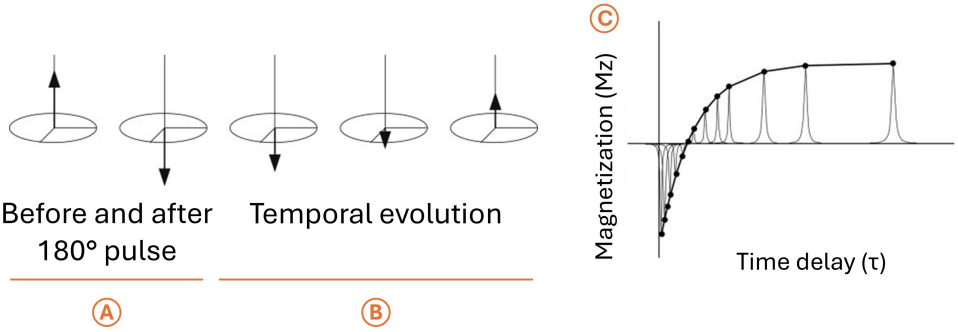


Figure 6-4. Magnetic vectors in response to an inversion recovery pulse sequence and the recording of magnetization as a function of time delay (τ). *Figure adapted from Louro (2013) with permission from Elsevier.*[493]

6.1.2. T_2 relaxation

T_2 relaxation is an adiabatic redistribution of energy among the nuclei without the whole spin system losing energy (the lifetime of any individual nucleus in the high energy state may be reduced, but the total number of nuclei in this state remains unchanged). T_2 relaxation times of nuclear vectors are measured in the xy-axes directly from a ^{1}H NMR FID as well as the FID following a Carr-Purcell-Meiboom-Gill (CPMG) pulse sequence. For both the direct FID and the CPMG pulse sequence, the first RF pulse is 90° to the bulk magnetic field and rotates magnetization of the vectors into the y-direction (**Figure 6-5A**). The individual spins then fan out in the xy-plane due to a loss of phase coherence (caused by heterogeneity of the individual magnetic spin frequencies) (**Figure 6-5B**). The direct FID is collected after this point and measured as the decay of magnetization in the xy-plane (**Figure 6-5C**). For the CPMG pulse sequence, a series of 180° pulses is applied (called a spin-echo experiment) after a period of time (τ) following the initial 90° pulse and the resultant magnetization is then detected (**Figure 6-5D**). This process

is repeated with increasing τ and the decay of magnetization in the xy-plane is monitored over time (**Figure 6-5E**) and can be expressed by **Equation 6-2**.

Equation 6-2. $I(2\tau) = I_0\left(2e^{(-2\tau/T_2)}\right)$

From the plot of magnetization signal over time (both raw FID and the FID resulting from the CPMG pulse sequence), the T_2 relaxation time is derived as the time required for the signal to decay to 1/e, or approximately 37 % of its initial maximum value.

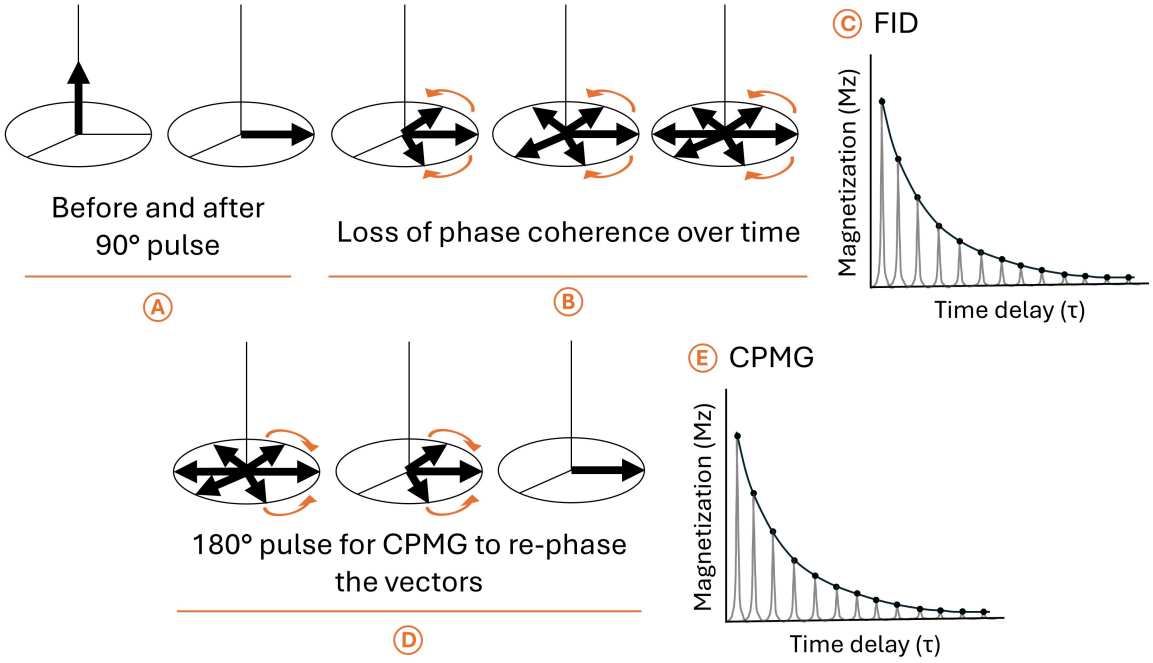


Figure 6-5. Magnetic vectors in response to a standard (for FID) and Carr-Purcell Meiboom Gill (CPMG) pulse sequence and the recording of magnetization as a function of time delay (τ).

6.1.3. The relationship between water molecular motion and ^{1}H NMR relaxation times

Importantly, both T_1 and T_2 relaxation are particularly sensitive to molecular motion. T_1 relaxation is most efficient, and therefore produces the shortest relaxation times, when the rate of molecular motion (also known as molecular tumbling rate) is approximately equal to the Larmor frequency. Molecules with motion that is faster or slower than the Larmor frequency are less efficient at energy exchange with the environment and will have longer T_1 relaxation times (**Figure 6-6**). For example, liquid water has a wide range of tumbling rates (as it is relatively fluid in its 3D structure) so most molecules in the system are not moving at a rate equal to the Larmor frequency at a given moment in time; therefore, liquid water molecules are primarily inefficient at T_1 relaxation and have a long T_1 relaxation time. As molecular motion is restricted (*e.g.*, such as partially restricted water molecules of hydration layers or completely restricted

when frozen in ice) the proportion of molecules moving at the Larmor frequency will increase (given the significantly narrower possible range of molecular motion) and thus these slower moving molecules will be proportionately more efficient at T_1 relaxation and have a shorter T_1 relaxation time.

When T_1 relaxation occurs, it is always accompanied by a corresponding T_2 relaxation process (note that T_2 relaxation can occur independent of T_1 relaxation). In liquid water where molecular motion is fast, the time for T_1 relaxation is approximately equal to the time for T_2 relaxation. As molecular motion decreases, T_2 relaxation times also decrease, whereby very slowly moving molecules (*e.g.*, macromolecules and water bound to proteins or at very low temperatures) have very short T_2 values (**Figure 6-6**). Therefore, it is the differences that can be observed in T_1 and T_2 relaxation times as a function of temperature that can provide detailed information on molecular motion in the presence of different compounds, including small-molecule IRIs.

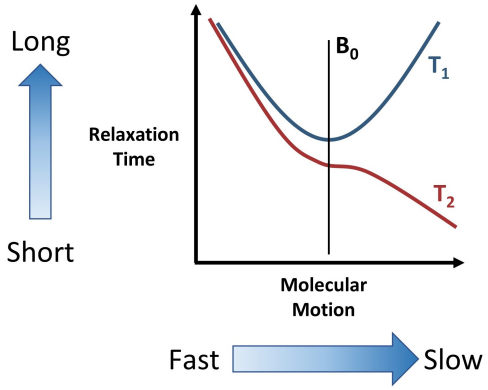


Figure 6-6. Plot of relaxation time as a function of molecular motion for T_1 (blue) and T_2 (red) relaxation. The Larmour frequency (B_0) is indicated at the T_1 relaxation time minima.[494]

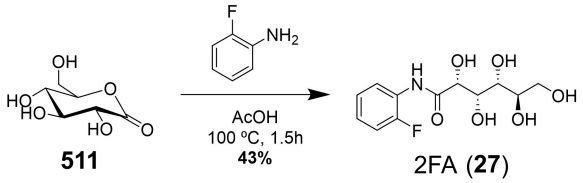
The temperature dependence of ^{1}H relaxation times can then be used to derive the activation energy of water molecule motion ($E_{A_{H_2O}}$) through both T_1 and T_2 relaxation modes.[494] Decreased $E_{A_{H_2O}}$ from T_1 relaxation has been reported to be caused by small amounts of solute impurities (*e.g.*, NaCl) that create defects in the ice lattice structure and allow water molecules to move more freely in the ice lattice.[479] In the liquid state, the molecular motion of water has been studied in the presence of dispersed polymers, where an increased $E_{A_{H_2O}}$ was associated with a lower crystallization energy of amorphous solid pharmaceuticals and decreased motion of water molecules.[495–499] In the context of ice recrystallization, ^{1}H NMR has been successfully utilized to study the liquid and solid states of water in ice cream.[499,500] Thus, using $E_{A_{H_2O}}$ obtained from ^{1}H NMR T_1 and T_2 characteristic relaxation times of water molecules in both the liquid and solid states respectively, it was hypothesized that the effect of small-molecule carbohydrate-based IRIs on

the molecular motion of water could be used to elucidate a formal mechanism of action based upon the three previously described hypotheses.

*6.1.4. General aim for NMR experiments using N-2-fluorophenyl-D-gluconamide (2FA, **27**) as the model IRI*

Over the past several decades the Ben Lab has developed a large scope of non-polymeric, small-molecule, carbohydrate-based ice recrystallization inhibitors (IRIs). From this library, *N*-2-fluorophenyl-D-gluconamide (2FA, **27**) has proven to be highly effective for the cryopreservation of numerous cell types including: cord-blood units,[212] hematopoietic stem and progenitor cells,[166] mesenchymal stromal cells (MSCs),[213] and induced-pluripotent stem cells (iPSCs)[215].

In addition to its successful improvement of cryopreservation outcomes, 2FA (**27**) can be readily synthesized from commercially available, low-cost reagents, and is rapidly purified by recrystallization (**Scheme 6-1**);[166] it also remains one of the most active carbohydrate-based small-molecule IRIs that has been reported to date with an IC_{50} of 3.47 mM (95 % CI [3.41-3.52]) (see <u>*section 2.1*</u>).[166,188] Therefore, 2FA (**27**) is a highly relevant model for investigating the mechanism of action of these IRIs.



Scheme 6-1. Synthesis of *N*-2-fluorophenyl-D-gluconamide (2FA, **27**).

Therefore, the aim of this study was to characterize the effect of the IRI 2FA (**27**) on the following:

(1) DIS during the recrystallization process to identify whether 2FA (**27**) was binding to the ice crystal surface and changing the shape/habit of the ice crystal.
(2) The molecular motion of water molecules in the solid state, through the $E_{A_{H_2O}}$ obtained from ^{1}H NMR relaxation times to identify whether 2FA (**27**) impacted the molecular motion of water molecules in the ice lattice.
(3) The molecular motion of water molecules in the liquid state, through the $E_{A_{H_2O}}$ obtained from ^{1}H NMR relaxation times to identify whether 2FA (**27**) impacted the molecular motion of water molecules in the bulk water layer.

Should 2FA (**27**) inhibit ice recrystallization in accordance with hypothesis 1, we would expect to observe DIS as part of experimental aim 1. We would also expect to observe a change in the relaxation

times (due to a change in molecular motion) associated with both the ice lattice and bulk water molecules. Inhibition of ice recrystallization by hypothesis 2 would result in an increase in molecular motion (and a decrease in $E_{A_{H_2O}}$) within the ice lattice due to the formation of defects that break apart the organized hexagonal network of ice. Finally, inhibition by hypothesis 3 would result only in a change in molecular motion of bulk water molecules (leaving the ice lattice unaffected); it was thought that a net decrease in molecular motion (and an increase in $E_{A_{H_2O}}$) would be observed due to the formation of organized hydration shells surrounding 2FA (**27**) in the bulk water layer that disrupt the natural state of bulk water molecule interactions.

6.2. Characterization of water molecules at below zero temperatures

At below zero temperatures, the samples of pure water and 2FA (**27**)-supplemented water were frozen but would be comprised of both solid and liquid components (due to an unfrozen bulk water fraction that is present between ice crystals at high sub zero temperatures – the structure of ice has been previously described in <u>*section 1.2.1*</u>). T_2 relaxation times were used to characterize each of these components, where the raw FID was used to detect very short relaxation times typical of solids (due to their much slower molecular motion) and the CPMG pulse sequence was used to detect the relatively longer relaxation times typical of the liquid component.[500] T_1 relaxation times were then used to characterize the overall structure of the ice lattice due to its sensitivity to defects in the hydrogen-bonded structure.[479,480] Previous work has used these methods to characterize the components of water, ice, and sucrose mixtures, as well as for mixtures of ice creams.[499,500]

6.2.1. Characterization of pure Milli-Q® water by spin-spin (T_2) relaxation time

T_2 relaxation was first measured on pure water between -15 °C and -1 °C (**Figure 6-7**). Raw relaxation curves obtained from the CPMG pulse sequence and the raw FID were then processed with MS Excel Solver (Microsoft, Redmond, WA) to determine the parameters of best fit. The CPMG curves were fit with a bi-exponential function (**Equation 6-3**) where $S_{CPMG}(t)$ was the intensity of the CPMG signal measured over time t, $T_{2-CPMG-1}$ and $T_{2-CPMG-2}$ were the characteristic spin-spin relaxation times of the signal, and I_{CPMG-1} and I_{CPMG-2} were the characteristic intensities of the components of the CPMG relaxation signal.

Equation 6-3: $$S_{CPMG}(t) = I_{CPMG-1} \times e^{\left(-\left(\frac{t}{T_{2-CPMG-1}}\right)\right)} + I_{\mathrm{CPMG-2}} \times e^{\left(-\left(\frac{t}{T_{2-CPMG-2}}\right)\right)} + (cst)$$

The FID curves were fit with a bi-gaussian function (**Equation 6-4**) where $S_{FID}(t)$ was the intensity of the FID signal measured over time t, $T_{2-FID-1}$ and $T_{2-FID-2}$ were the characteristic spin-spin relaxation times

of the signal, and I_{FID-1} and I_{FID-2} were the characteristic intensities of the components of the FID relaxation signal.

Equation 6-4: $$S_{FID}(t) = I_{FID-1} \times e^{(-(\frac{t}{T_{2-FID-1}})^2)} + I_{FID-2} \times e^{(-(\frac{t}{T_{2-FID-2}})^2)} + (cst)$$

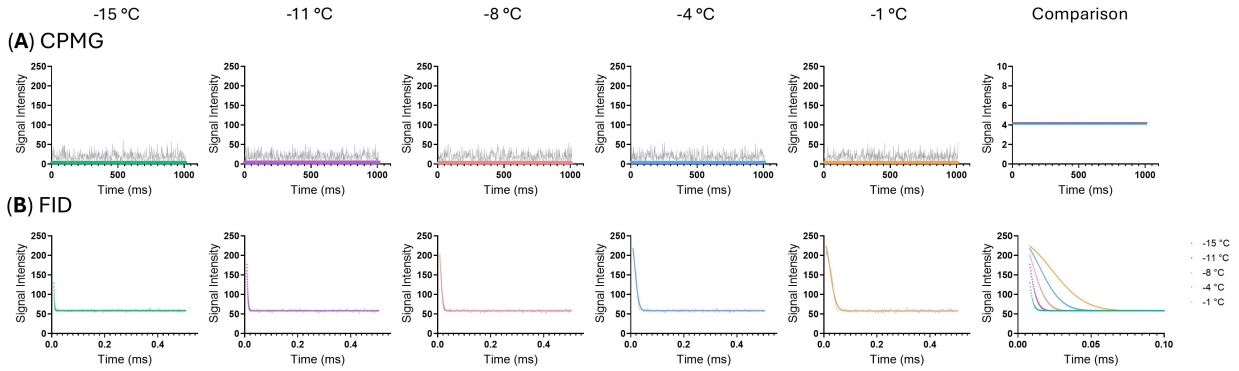


Figure 6-7. Exemplar of pure Milli-Q® water trial $T_{2\text{-FID}}$ and $T_{2\text{-CPMG}}$ relaxation between -15 °C and -1 °C. Data shown from one trial that is representative of the mean (from n=3 replicates). (**A**) From $T_{2\text{-CPMG}}$. (**B**) From $T_{2\text{-FID}}$. Grey = raw data, coloured = fitted model to **Equation 6-3** for the $T_{2\text{-CPMG}}$ data and **Equation 6-4** for the $T_{2\text{-FID}}$ data.

From the fitted curves, T_2 relaxation times were derived at each temperature as the time required for the signal to decay to 1/e, or approximately 37 % of its initial maximum value (**Table 6-1**). Fitting of the FID relaxation curves (by **Equation 6-4**) provided a single, short (less than 30 µs), T_2 relaxation (**Table 6-1**). Interestingly, no molecular relaxation was detected by the CPMG pulse sequence ($T_{2\text{-CPMG}}$) where the signal intensity did not surpass background (**Figure 6-7**). As the $T_{2\text{-CPMG}}$ times would be representative of the liquid bulk water molecules found between solid ice crystals in a frozen sample, these results suggested that either an unfrozen fraction (bulk water molecules) did not exist or contained too few water molecules and thus the nuclear relaxation was below the limit of detection for these methods. Ultimately, $T_{2\text{-CPMG}}$ relaxation times would therefore be unable to provide insight into the molecular motion of bulk water molecules in a sample of pure frozen water under these conditions.

Table 6-1. Parameters of best fit for the $T_{2\text{-FID}}$ relaxation of pure Milli-Q® water at temperature intervals between -15 °C and -1 °C by **Equation 6-4**. Values represented as mean ± SD for n=3 replicates.

T (°C)	-15	-11	-8	-4	-1
$I_{FID\text{-}1}$	0	0	0	0	0
$T_{2\text{-FID-}1}$ (ms)	0	0	0	0	0
$I_{FID\text{-}2}$	374.8 ± 75.0	255.3 ± 36.3	200.1 ± 2.3	183.5 ± 0.9	181.5 ± 5.9
$T_{2\text{-FID-}2}$ (μs)	6.19 ± 0.4	8.83 ± 0.5	13.4 ± 1	20.6 ± 1	30.7 ± 2
cst	61.59 ± 5.46	61.46 ± 5.44	61.52 ± 5.49	61.38 ± 5.32	60.96 ± 5.34

All T_2 relaxation times that were calculated from the FID ($T_{2\text{-FID}}$) under these conditions were shorter than 40 μs which was consistent with previously reported values characteristic of frozen water protons (11 to 40 μs)[499]. Furthermore, a linear relationship between the natural logarithm of the $T_{2\text{-FID}}$ relaxation times and reciprocal temperature was observed with a calculated $E_{A_{H_2O}}$ of 67.0 ± 3.2 kJ/mol (**Figure 6-8**); this value agreed with some previously reported values (55 – 66 kJ/mol)[501] but not with others (15 – 16 kJ/mol)[499,502]. However, small changes in experimental conditions (*i.e.* NMR magnet frequency, trace level impurities, *etc.*) and differences in ice polymorphism,[501] could lead to large changes in the $E_{A_{H_2O}}$ calculated from T_2 relaxation. Therefore, direct comparisons between the $E_{A_{H_2O}}$ as calculated from spin-spin relaxation measurements are not meaningful to understanding the molecular motion of water molecules, and the relative $T_{2\text{-FID}}$ and $T_{2\text{-CPMG}}$ relaxation times were used only to confirm our methods and aid in the identification and characterization of the solid and liquid phases of the frozen solutions in future experiments.[494]

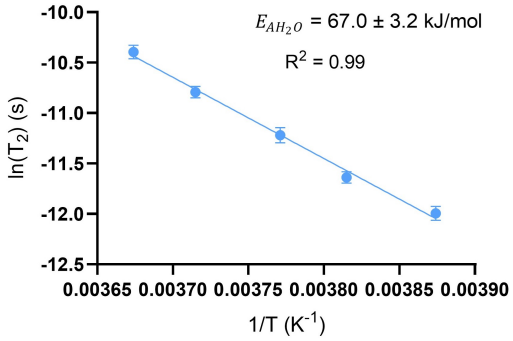


Figure 6-8. Natural logarithm transformed T_2 relaxation times of pure Milli-Q® water at temperatures between -15 °C and -1 °C. Calculated $E_{A_{H_2O}}$ (kJ•mol^{-1}) from the slope of the linear regression as $\ln(T_2) = \beta \times 1/T + \varepsilon$, with $E_{A_{H_2O}} = -R \times \beta$ where the universal gas constant $R = 0.008314$ kJ•K^{-1}•mol^{-1}, β = -8057 s•K, and ε = 19.2 s; R^2 = 0.99. All data points reported as mean ± SD (n=3).

*6.2.2. Characterization of 2FA (**27**) in water solutions by spin-spin (T_2) relaxation time*

T_2 relaxation of samples supplemented with 2FA (**27**) was measured at concentrations of 1 mM to 10 mM in water and at temperatures between -15 °C and -3 °C (**Figure 6-9**). 2FA (**27**) does not inhibit ice

recrystallization at concentrations below 2 mM, but completely inhibits ice recrystallization at concentrations greater than 5 mM (**Figure 2-2**). As a result, concentrations of 1, 3, 5, and 10 mM were selected for determination of ^{1}H NMR relaxation times and $E_{A_{H_2O}}$ to cover the entire range of 2FA's (**27**) ice recrystallization inhibition activity. The maximum temperature was lowered to -3 °C (from -1 °C for pure water) to ensure that no sample melting occurred during relaxation time measurement as the presence of solutes in water solutions can lower melting temperatures. In the same manner as the pure water samples (see *section 6.2.1*), the raw relaxation curves from both the raw FID and CPMG pulse sequence were processed using MS Excel Solver (Microsoft, Redmond, WA) to determine the parameters of best fit using **Equation 6-3** and **Equation 6-4**.

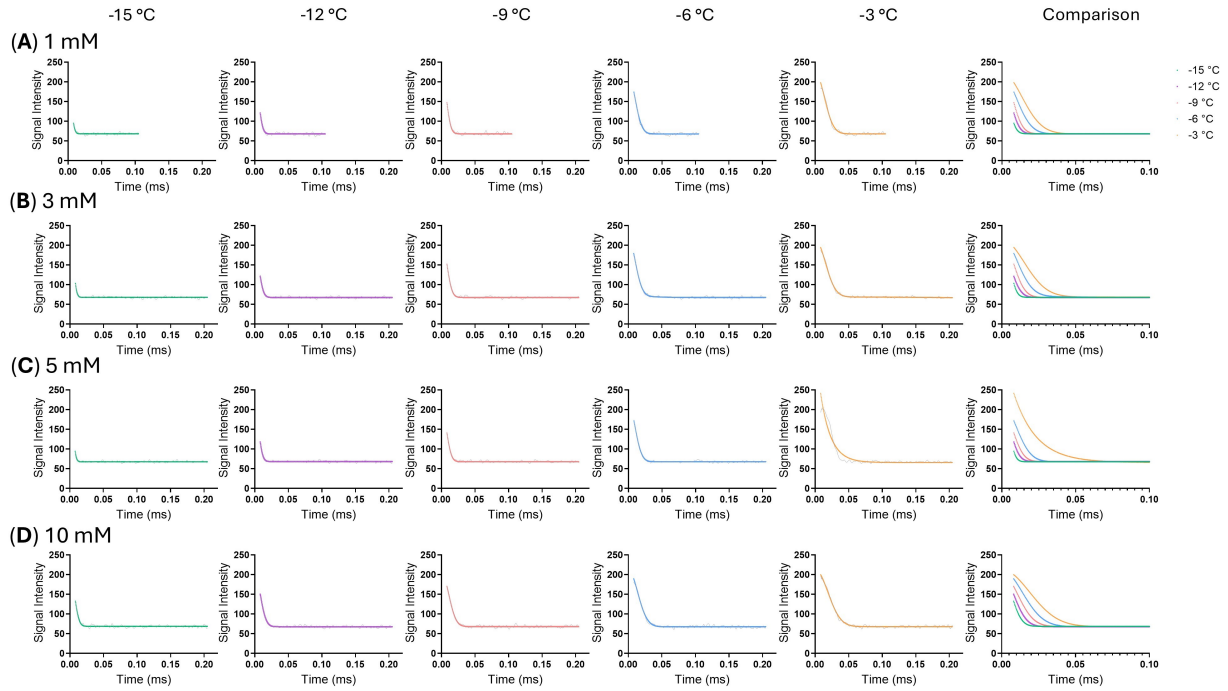


Figure 6-9. Exemplar of 2FA (**27**)-supplemented water solution (concentrations of 1 mM to 10 mM) $T_{2\text{-FID}}$ relaxation between -15 °C and -3 °C. Data shown from one trial that is representative of the mean (from n=3 replicates). (**A**) 1 mM 2FA (**27**). (**B**) 3 mM 2FA (**27**). (**C**) 5 mM 2FA (**27**). (**D**) 10 mM 2FA (**27**). Grey = raw data, coloured = fitted model to **Equation 6-4**.

T_2 relaxation times were again derived from the fitted curves at each temperature as the time required for the signal to decay to 1/e, or approximately 37 % of its initial maximum value (**Table 6-2**). Consistent with the measurements of pure Milli-Q® water, the samples supplemented with 2FA (**27**) had only a single $T_{2\text{-FID}}$ relaxation component at each temperature, all shorter than < 30 µs (**Figure 6-10**), that corresponded to the T_2 relaxation of the protons of water molecules in the solid (ice) phase. Also consistent with the pure water measurements, no relaxation was detected by the CPMG pulse sequence (see **SI Figure 8-93**).

Table 6-2. Parameters of best fit for the $T_{2\text{-FID}}$ relaxation of 2FA (**27**)-supplemented water solutions (concentrations of 1 mM to 10 mM) at temperature intervals between -15 °C and -3 °C by **Equation 6-4**. Values reported as mean ± SD for n=3 replicates.

	T (°C)	-15	-12	-9	-6	-3
1 mM	I_{FID-1}	0	0	0	0	0
	$T_{2\text{-FID-1}}$ (ms)	0	0	0	0	0
	I_{FID-2}	129.8 ± 38.2	127.3 ± 17.6	139.7 ± 17.5	151.5 ± 3.6	153.8 ± 2.5
	$T_{2\text{-FID-2}}$ (µs)	6.56 ± 0.9	8.02 ± 0.2	10.2 ± 0.5	13.6 ± 0.8	18.8 ± 0.7
	cst	67.79 ± 0.48	67.87 ± 0.17	67.92 ± 0.30	67.77 ± 0.11	67.77 ± 0.14
3 mM	I_{FID-1}	0	0	0	1.4 ± 2.5	15.3 ± 26.5
	$T_{2\text{-FID-1}}$ (ms)	0	0	0	0.6 ± 0.4	0.9 ± 0.1
	I_{FID-2}	134.7 ± 38.2	124.5 ± 13.1	142.9 ± 4.9	148.8 ± 3.0	148.2 ± 3.1
	$T_{2\text{-FID-2}}$ (µs)	7.77 ± 1	9.86 ± 0.7	12.1 ± 1	15.7 ± 1	22.1 ± 1
	cst	67.89 ± 0.44	67.53 ± 0.32	67.91 ± 0.21	67.82 ± 0.48	52.68 ± 25.86
5 mM	I_{FID-1}	0	0	0	2.17 ± 3.8	0
	$T_{2\text{-FID-1}}$ (ms)	0	0	0	0.55 ± 0.4	1.43 ± 0.5
	I_{FID-2}	140.6 ± 42.8	120.6 ± 11.8	136.9 ± 2.2	145.8 ± 0.6	225.7 ± 75.2
	$T_{2\text{-FID-2}}$ (µs)	6.89 ± 1	9.35 ± 1	11.4 ± 0.9	15.0 ± 1	18.8 ± 3
	cst	67.84 ± 0.16	68.08 ± 0.37	67.99 ± 0.09	67.43 ± 0.22	67.05 ± 1.20
10 mM	I_{FID-1}	0	0	0	0	0
	$T_{2\text{-FID-1}}$ (ms)	0	0	0	0	0
	I_{FID-2}	113.8 ± 28.1	127.5 ± 3.1	141.3 ± 8.2	142.9 ± 2.4	146.9 ± 1.8
	$T_{2\text{-FID-2}}$ (µs)	9.50 ± 0.6	11.5 ± 2	14.1 ± 2	18.7 ± 2	25.1 ± 2
	cst	68.17 ± 0.36	67.75 ± 0.22	67.86 ± 0.31	67.95 ± 0.55	67.88 ± 0.16

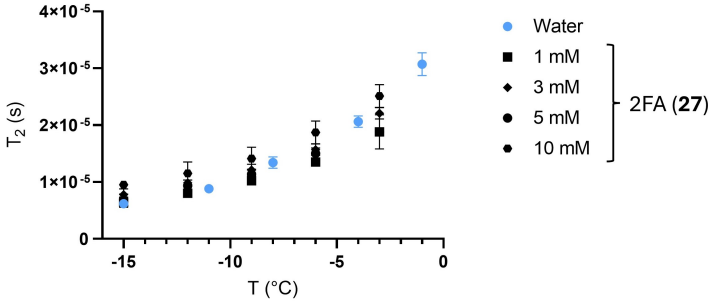


Figure 6-10. 2FA (**27**) $T_{2\text{-FID}}$ relaxation time comparison of water and 2FA (**27**)-supplemented water solutions (concentrations 1 mM to 10 mM) between -1 and -15 °C. Data reported as mean ± SD for n=3 replicates from **Table 6-2**.

The results for the protons in the ice lattice in the presence of 2FA (**27**) were consistent with that of pure water. Similar measurements of T_2 relaxation in literature by *Lucas et. al.* on concentrated sucrose-water and casein-water solutions (< 61.3 % w/w in water) found that in addition to the single $T_{2\text{-FID}}$ relaxation representative of the protons of water molecules in the ice lattice, two relaxation times resulting from the from the CPMG pulse sequence were also observed.[500] These two relaxations that were not

detected in the presence of 2FA (**27**) were attributed to relaxation of water molecules in an unfrozen liquid fraction and the labile protons of sucrose and casein.[500] As higher concentrations of solute would be expected to produce greater proportions of unfrozen (liquid) fraction,[500,503] the results from the spin-spin relaxation at temperatures between -15 °C and -3 °C showed that 2FA (**27**)-supplemented samples with a maximum of only 0.3 % (w/w) in water were comprised of an essentially solid ice-lattice with the possibility of a very small unfrozen (liquid) fraction that was too small to be detected by these methods.

6.2.3. Characterization by spin-lattice (T_1) relaxation time

Spin-lattice (T_1) relaxation of water and 2FA (**27**)-supplemented water samples was characterized by an inversion recovery (IR) pulse sequence between -15 °C and -3 °C (**Figure 6-11**). Raw relaxation curves obtained from the IR pulse sequence were then processed with MS Excel Solver (Microsoft, Redmond, WA), in a similar manner to the processing of T_2 relaxation data, to determine the parameters of best fit. The IR curves were fit with a bi-exponential function (**Equation 6-5**) where $S_{IR}(t)$ was the intensity of the IR signal measured over time t, T_{1-IR-1} and T_{1-IR-2} were the characteristic spin-lattice relaxation times of the signal, and I_{IR-1} and I_{IR-2} were the characteristic intensities of the of the components of the IR relaxation signal.

Equation 6-5: $$S_{IR}(t) = I_{IR-1} \times \left(1 - e^{\left(-\left(\frac{t}{T_{1-IR-1}}\right)\right)}\right) + I_{\mathrm{IR}-2} \times \left(1 - e^{\left(-\left(\frac{t}{T_{1-IR-2}}\right)\right)}\right) + (cst)$$

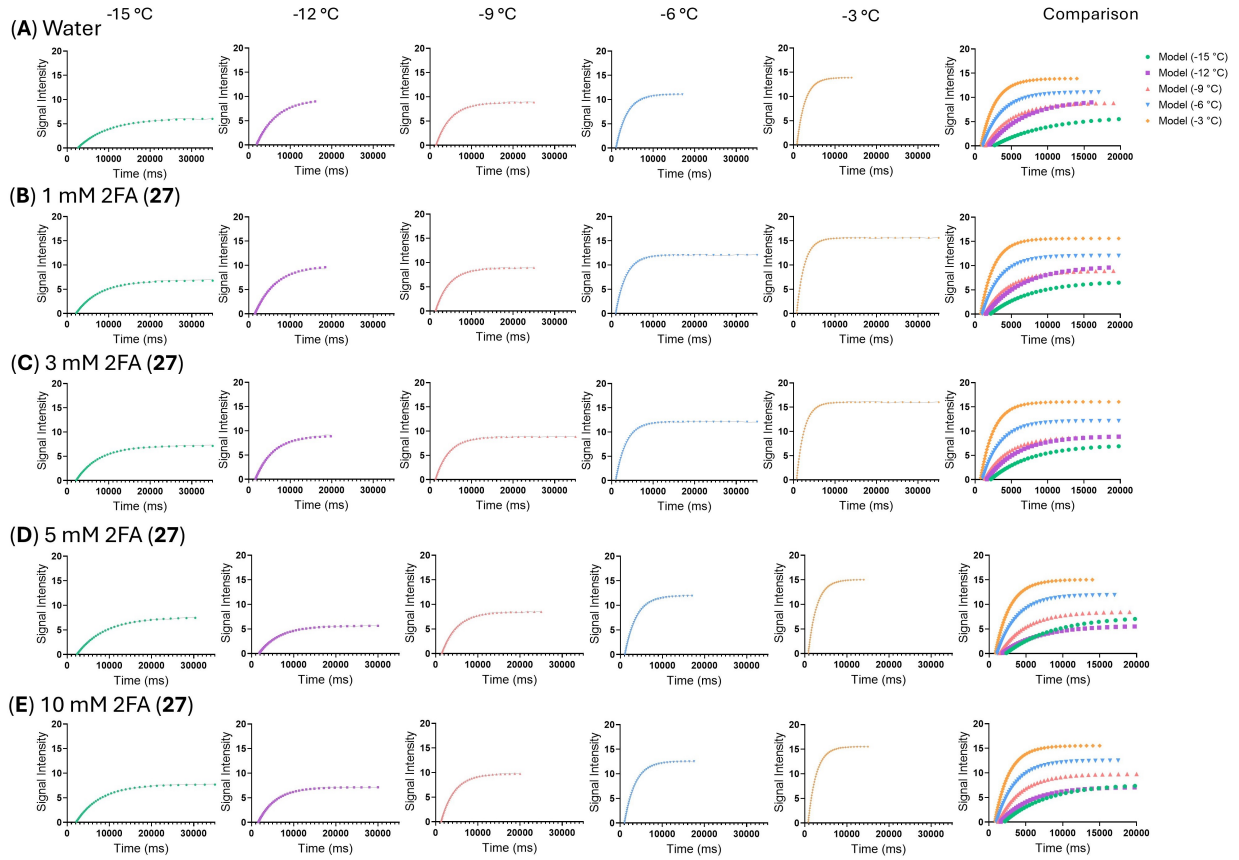


Figure 6-11. Exemplar of pure Milli-Q® water and 2FA (**27**)-supplemented water solution (concentrations of 1 mM to 10 mM) $T_{1\text{-IR}}$ relaxation between -15 °C and -3 °C. Data shown from one trial that is representative of the mean (from n=3 replicates). (**A**) Pure Milli-Q® water. (**B**) 1 mM 2FA (**27**). (**C**) 3 mM 2FA (**27**). (**D**) 5 mM 2FA (**27**). (**E**) 10 mM 2FA (**27**). Grey = raw data, coloured = fitted model to **Equation 6-5**.

T_1 relaxation times were derived from the fitted curves at each temperature as the time required for the signal to grow from 0 to (1 - 1/e), or approximately 63 % of its final maximum value (**Table 6-3**). All relaxation was characterized by a single T_1 relaxation time, between -15 °C and -3 °C, indicating that a single population of water molecules (a single mode of molecular motion) was present in the sample. Considering that the T_2 relaxation times of these samples indicated that there was an insignificant unfrozen fraction, the population of water molecules observed by this experiment were determined to also be only those that made up the solid ice lattice.

No significant difference ($p > 0.05$) was observed between the T_1 relaxation times of each sample at each temperature, or across the temperature range, except for pure water and the 3 mM 2FA (**27**)-supplemented water sample which were significantly different at -15 °C ($p = 0.022$). The T_1 relaxation time of the 3 mM 2FA (**27**)-supplemented sample was lower than that of pure water by 9.8 %, however, given this difference was only observed at one temperature point for one sample, this result was not likely

to be experimentally meaningful. Therefore, the consistent T_1 relaxation times suggested that 2FA (**27**) did not impact the molecular motion of the water molecules in the frozen ice lattice and as a result, hypothesis 3 (in which the IRI resides solely within the bulk water layer) was most likely with respect to mechanism of action.

Table 6-3. Parameters of best fit for the $T_{1\text{-}IR}$ relaxation of pure Milli-Q® water and 2FA (**27**)-supplemented water solutions (concentrations of 1 mM to 10 mM) at temperature intervals between -15 °C and -3 °C by **Equation 6-5**. Values for the second component of relaxation were omitted from the table as they were all equal to zero. Values reported as mean ± SD for n=3 replicates.

	T (°C)	-15	-12	-9	-6	-3
Water	$I_{IR\text{-}1}$	72.9 ± 113.4	8.9 ± 2.3	11.2 ± 3.0	13.9 ± 4.3	16.5 ± 4.4
	$T_{1\text{-}IR\text{-}1}$ (s)	6.90 ± 0.41	5.03 ± 0.30	3.63 ± 0.28	2.66 ± 0.18	1.96 ± 0.09
	cst	65.5 ± 113.2	0.09 ± 0.16	0.27 ± 2E-3	0.99 ± 1.72	8E-8 ± 8E-8
1 mM	$I_{IR\text{-}1}$	219.16 ± 183.5	10.11 ± 4.78	10.63 ± 2.63	14.53 ± 3.44	19.23 ± 5.54
	$T_{1\text{-}IR\text{-}1}$ (s)	6.00 ± 0.48	4.85 ± 0.39	3.43 ± 0.14	2.50 ± 0.11	1.85 ± 0.08
	cst	0.50 ± 0.82	1.26 ± 0.32	1.44 ± 0.04	1.49 ± 0.03	1.54 ± 6E-3
3 mM	$I_{IR\text{-}1}$	15.14 ± 13.56	7.66 ± 1.32	9.52 ± 0.63	12.52 ± 0.51	15.94 ± 0.59
	$T_{1\text{-}IR\text{-}1}$ (s)	5.71 ± 0.19	4.31 ± 0.03	3.27 ± 0.10	2.49 ± 0.08	1.85 ± 0.08
	cst	7.8 ± 13.2	0.14 ± 0.14	0.27 ± 4E-4	0.18 ± 0.15	0.09 ± 0.15
5 mM	$I_{IR\text{-}1}$	7.57 ± 0.51	7.25 ± 2.21	8.77 ± 0.15	12.28 ± 0.44	15.13 ± 0.70
	$T_{1\text{-}IR\text{-}1}$ (s)	6.59 ± 0.19	4.90 ± 0.09	3.58 ± 0.16	2.66 ± 0.12	1.97 ± 0.13
	cst	0.27 ± 1E-3	0.27 ± 2E-3	0.27 ± 1E-3	0.27 ± 2E-3	0.18 ± 0.15
10 mM	$I_{IR\text{-}1}$	7.93 ± 1.05	7.73 ± 0.41	10.45 ± 2.51	12.81 ± 2.25	15.69 ± 2.46
	$T_{1\text{-}IR\text{-}1}$ (s)	6.16 ± 0.52	4.54 ± 0.51	3.55 ± 0.33	2.60 ± 0.16	1.96 ± 0.17
	cst	0.27 ± 2E-3	0.27 ± 3E-3	1.15 ± 1.46	1.09 ± 1.43	1.06 ± 1.37

The $E_{A_{H_2O}}$ for the water molecules in the ice lattice for each condition was then determined by plotting the natural logarithm of the T_1 relaxation times against the respective reciprocal temperature (K^{-1}) (**Figure 6-12A**). The $E_{A_{H_2O}}$ of pure frozen water was found to be -60.9 ± 2.8 kJ/mol (**Figure 6-12B**), which was consistent with previous findings in literature for pure water as derived from T_1 relaxation (-14.1 ± 0.1 kcal/mol = -59.0 ± 0.4 kJ/mol).[500,504] Furthermore, no significant difference was found ($p > 0.05$) between the $E_{A_{H_2O}}$ of pure water compared to the 2FA (**27**)-supplemented samples, with $E_{A_{H_2O}}$ values between -58.4 ± 4.9 kJ/mol (5 mM 2FA, **27**) and -54.2 ± 1.7 kJ/mol (3 mM 2FA, **27**) (**Figure 6-12B**).

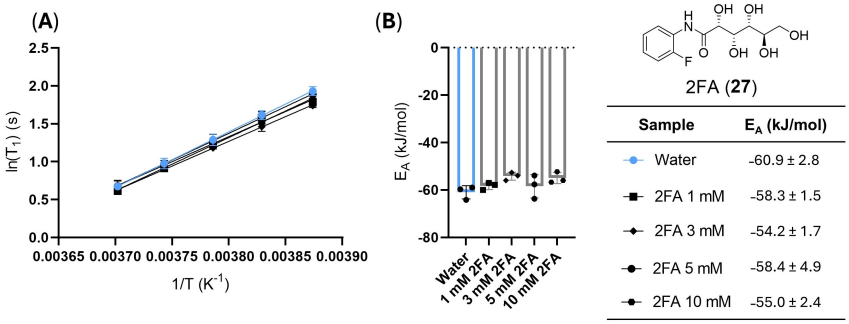


Figure 6-12. (**A**) Plot of ln(T_1) relaxation times (in s) against 1/T (in K^{-1}) for frozen pure water and 2FA (**27**) solutions (1 to 10 mM), below freezing temperature, with T ranging from -15 °C to -3 °C. (**B**) Calculated $E_{A_{H_2O}}$ (kJ•mol^{-1}) from the slope of the linear regression of the plot in left panel (**A**) as $\ln(T_1) = \beta \times {}^{1}/_{T} + \varepsilon$, with $E_{A_{H_2O}} = -R \times \beta$ where the universal gas constant $R = 0.008314$ kJ•K^{-1}•mol^{-1}. All values and data points are reported as mean ± SD (n=3) from **Table 6-3**.

T_1 values have been reported to be sensitive to changes in ice-lattice structure (defects) caused by small quantities of impurities. For example, ionic compounds (*i.e.* HCl, HBr, HI, NaCl, and $NaNO_3$) create ice-lattice defects at concentrations as low as 1 ppm that were detected by significant decreases in the $E_{A_{H_2O}}$ derived from T_1 relaxation compared to the ice lattice of pure water.[479] As no difference was observed in the $E_{A_{H_2O}}$ of 2FA (**27**)-supplemented samples compared to pure water, it was confirmed 2FA (**27**) had no effect on the structure of the ice lattice. This lack of effect was observed regardless of the concentration of 2FA (**27**) in the sample, and even at concentrations that were shown to experimentally inhibit ice recrystallization (*e.g.* 10 mM). Therefore, it could be stated that 2FA (**27**) would not be incorporated within the ice-lattice during freezing, eliminating hypothesis 2 and discrediting hypothesis 1 as the potential mechanism of action for 2FA (**27**).

6.2.4. Characterization of the ice lattice by measurement of dynamic ice shaping

To complement the findings in the previous section and further disprove hypothesis 1 as a potential mechanism of action, nanolitre osmometry measurements were used to measure dynamic ice shaping (DIS).[96,161] Without the introduction of a compound that binds to ice, a single frozen crystal of pure water appears round and circular (**Figure 6-13A**). In the presence of an ice binding protein such as AFP-1, a characteristic bipyramidal shaping of the ice crystal was observed as expected (**Figure 6-13C**). When a solution of 10 mM 2FA (**27**) in Milli-Q® water was assessed, no DIS was observed as the ice crystal appeared rounded and comparable to the sample containing only pure water (**Figure 6-13B**).

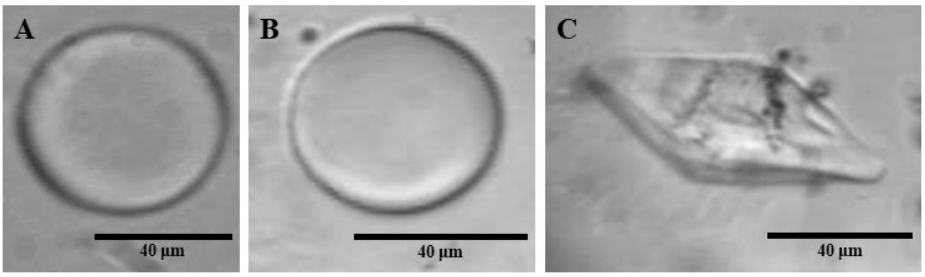


Figure 6-13. Representative nanolitre osmometry images to observe ice crystal behaviour for potential dynamic ice shaping (DIS) in the presence of: (**A**) Pure water (Milli-Q®), (**B**) 10 mM *N*-2-fluorophenyl-D-gluconamide (2FA, **27**) in water (Milli-Q®), or (**C**) 1 mg/mL AFP-1 in water (Milli-Q®).

While these were the first reported results noting the absence of DIS for the small-molecule IRI 2FA (**27**), they were consistent with measurements reported for other small-molecule IRIs [including *n*-octyl-β-D-galactopyranoside (β-octyl-Gal, **16**), *N*-octyl-D-gluconamide (NOGlc, **17**), (4-bromophenyl)-β-D-glucopyranoside (pBrPh-Glc, **25**), and (4-methoxyphenyl)-β-D-glucopyranoside (PMP-Glc, **26**)].[158,161] In addition to the results obtained from the T_1 relaxation times of the frozen samples in *section 6.2.3*, these results further confirmed that 2FA (**27**) did not bind to the ice lattice during freezing. Therefore, the ice recrystallization inhibition activity of 2FA (**27**), was not the result of defects created at the surface of, or within, the ice lattice due to compound binding leaving hypothesis 3 as most likely with respect to mechanism of action.

6.3. Characterization of water molecules at above zero temperatures

Following the results comparing frozen samples of pure water to those supplemented with 2FA (**27**), the only remaining hypothesis for its mechanism of action was that it must be interacting exclusively with water molecules in the liquid water phase (hypothesis 3). These interactions must, in some way, limit the ability for water molecules to migrate through the bulk liquid water phase during the ice recrystallization process to ultimately inhibit ice recrystallization. Therefore, to determine the effect that 2FA (**27**) had on the molecular motion of water molecules in the bulk water phase, the T_2 relaxation times of pure water and solutions of 2FA (**27**) between +5 °C and +30 °C were measured following a CPMG pulse sequence (**Figure 6-14**). The CPMG pulse sequence is most commonly used to monitor molecular motion at above zero temperatures as it was designed "focus" the magnetization of vectors which can be used to get more detailed information about T_2 relaxation (compared to the raw FID which measures the overall decay of magnetization).[460,491,494] The CPMG relaxation curves were processed using MS Excel Solver (Microsoft, Redmond, WA) to determine the parameters of best fit using **Equation 6-3** as previously described in *section 6.2.1*.

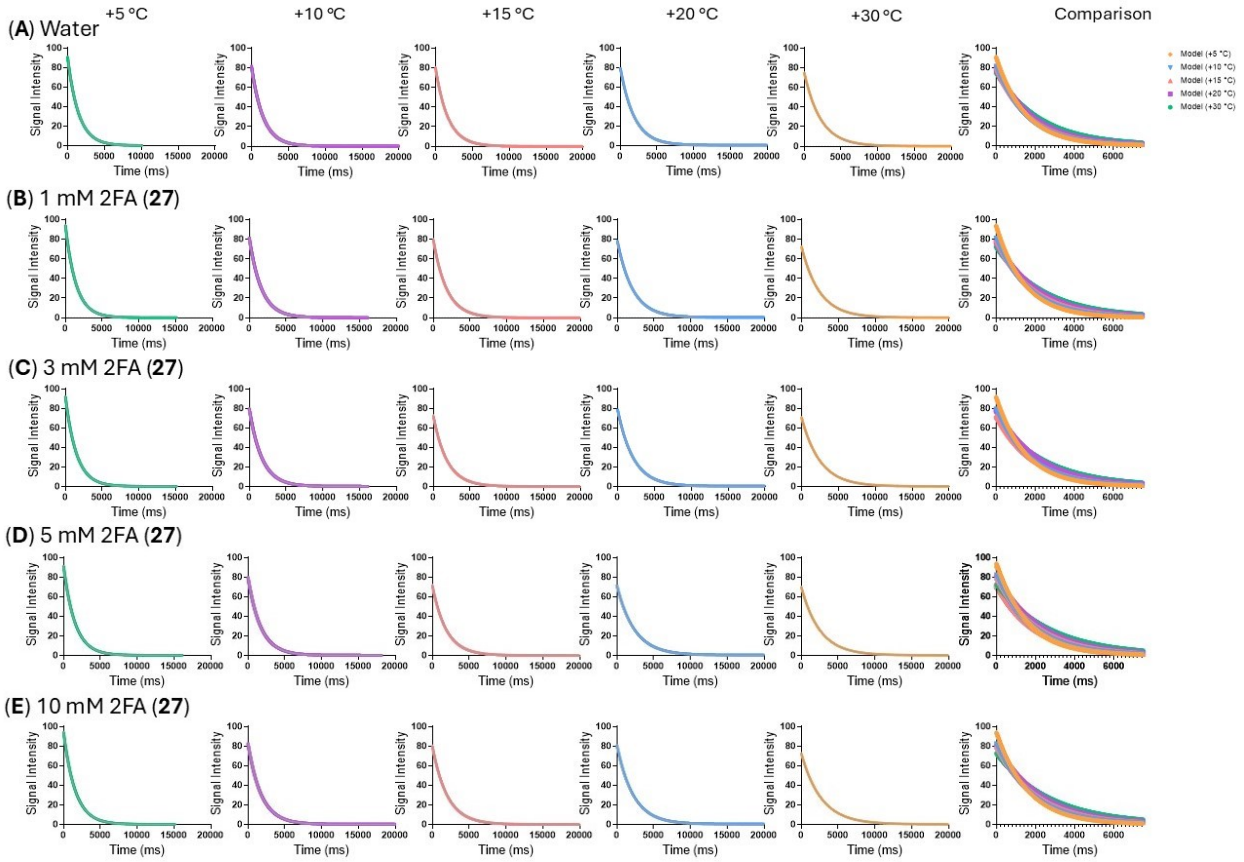


Figure 6-14. Exemplar of pure Milli-Q® water and 2FA (**27**)-supplemented water solution (concentrations of 1 mM to 10 mM) trial $T_{2\text{-CPMG}}$ relaxation between +5 °C and +30 °C. Data shown from one trial that is representative of the mean (from n=3 replicates). (**A**) Pure Milli-Q® water. (**B**) 1 mM 2FA (**27**). (**C**) 3 mM 2FA (**27**). (**D**) 5 mM 2FA (**27**). (**E**) 10 mM 2FA (**27**). Grey = raw data, coloured = fitted model to **Equation 6-3**.

The $T_{2\text{-CPMG}}$ relaxation times were derived from the relaxation curves in the same manner as the $T_{2\text{-FID}}$ relaxation times previously described (see *section 6.2.1*). Consistent with the relaxation times of the ice lattice, only a single relaxation time was observed for all samples at temperatures between +5 °C and +30 °C (**Table 6-4**) indicating that only a single population of water molecules was observed. Due to the low concentration of 2FA (**27**) in solution, this result was expected as the relaxation of the protons from the water molecules would overwhelm the relaxation from the significantly lower number of protons from 2FA (**27**).

Table 6-4. Parameters of best fit for the CPMG relaxation of pure Milli-Q® water and 2FA (**27**)-supplemented water solutions (concentrations of 1 mM to 10 mM) at temperature intervals between +5 °C and +30 °C by **Equation 6-3**. Values for the second component of relaxation were omitted from the table as they were all equal to zero. Values reported as mean ± SD for n=3 replicates.

	T (°C)	5	10	15	20	30
Water	I_{CPMG-1}	91.6 ± 1.4	80.2 ± 2.2	78.3 ± 3.5	78.9 ± 0.8	75.2 ± 4.4
	$T_{2-CPMG-1}$ (s)	1.49 ± 0.01	1.56 ± 9E-3	1.76 ± 0.07	1.93 ± 0.08	2.23 ± 0.01
	cst	0.04 ± 0.05	0.11 ± 0.01	0.10 ± 0.03	0.12 ± 0.06	0.13 ± 0.04
1 mM	I_{CPMG-1}	91.8 ± 1.9	79.7 ± 1.7	78.1 ± 1.7	76.3 ± 6.1	70.4 ± 2.4
	$T_{2-CPMG-1}$ (s)	1.50 ± 0.07	1.70 ± 0.06	1.91 ± 0.07	2.10 ± 0.03	2.50 ± 0.07
	cst	0.09 ± 5E-3	0.09 ± 0.02	0.09 ± 0.01	0.10 ± 0.01	0.12 ± 5E-3
3 mM	I_{CPMG-1}	91.9 ± 1.3	76.9 ± 2.5	78.5 ± 5.3	78.9 ± 0.6	75.8 ± 4.7
	$T_{2-CPMG-1}$ (s)	1.50 ± 0.02	1.65 ± 0.05	1.85 ± 0.04	2.06 ± 0.05	2.44 ± 0.06
	cst	0.09 ± 0.01	0.09 ± 0.01	0.10 ± 4E-3	0.10 ± 0.01	0.13 ± 0.02
5 mM	I_{CPMG-1}	91.6 ± 1.2	80.1 ± 1.2	73.8 ± 2.2	77.4 ± 6.1	69.8 ± 1.8
	$T_{2-CPMG-1}$ (s)	1.59 ± 0.07	1.80 ± 0.09	2.00 ± 0.11	2.32 ± 0.09	2.69 ± 0.17
	cst	0.08 ± 0.01	0.08 ± 0.01	0.08 ± 0.01	0.09 ± 0.01	0.11 ± 3E-3
10 mM	I_{CPMG-1}	93.9 ± 1.0	80.3 ± 4.1	79.1 ± 2.8	74.8 ± 4.7	73.0 ± 0.6
	$T_{2-CPMG-1}$ (s)	1.60 ± 0.01	1.82 ± 0.01	2.06 ± 0.02	2.26 ± 0.04	2.77 ± 0.06
	cst	0.08 ± 0.02	0.09 ± 0.02	0.07 ± 0.01	0.09 ± 0.03	0.09 ± 0.04

A plot of the natural logarithm transformed T_{2-CPMG} relaxation times against the respective reciprocal temperature (K^{-1}) allowed for determination of $E_{A_{H_2O}}$ for water molecules in the bulk water (liquid) phase (**Figure 6-15A**). In the absence of solutes, pure water has been reported to have an activation energy (E_A) for self-diffusion of between 4-5 kcal/mol (16.7-21.0 kJ/mol) at temperatures between 1 and 45 °C;[505–507] this value corresponds to the approximate amount of energy of required to break a hydrogen bond between water molecules. While the $E_{A_{H_2O}}$ of pure water as calculated by our T_{2-CPMG} relaxation times differs from these reported values, calculated at 11.7 ± 0.5 kJ/mol (or 2.8 ± 0.1 kcal/mol), the individual T_2 relaxation times were consistent with those found in literature (1.98 s at 20 °C and 2.36 s at 50 °C)[508]. This suggested that a differences in methodology for the determination of activation energies may be responsible for the variation in E_A values. Ultimately, a direct comparison of the $E_{A_{H_2O}}$ for all samples with 2FA (**27**) to that of pure water as measured by T_{2-CPMG} relaxation (11.7 ± 0.5 kJ/mol or 2.8 ± 0.1 kcal/mol) found a significant increase in activation energy with values that ranged from 13.8 ± 0.6 kJ/mol to 15.2 ± 0.5 kJ/mol (3 mM and 5 mM, $p < 0.01$; 1 mM and 10 mM $p < 0.001$) (**Figure 6-15B**). These results confirmed that 2FA (**27**) at concentrations as low as 1 mM slowed the molecular motion of water molecules and increased the activation energy for water molecule motion which would ultimately lead to the inhibition of ice recrystallization.

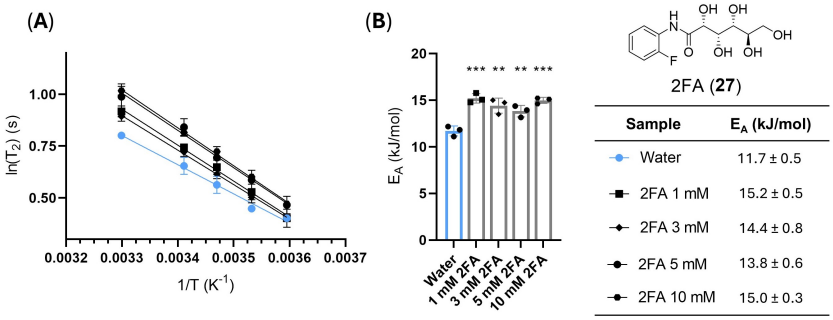


Figure 6-15. (**A**) Plot of ln($T_{2\text{-CPMG}}$) relaxation times (in s) against 1/T (in K^{-1}) for pure water and 2FA solutions (1 to 10 mM), above freezing temperature, with T ranging from +5 °C to +30 °C. (**B**) Calculated $E_{A_{H_2O}}$ (kJ•mol^{-1}) from the slope of the linear regression of the plot in left panel (**A**) as $\ln(T_{2-CPMG}) = \beta \times {}^{1}/_{T} + \varepsilon$, with $E_{A_{H_2O}} = -R \times \beta$ where the universal gas constant $R = 0.008314$ kJ•K^{-1}•mol^{-1}. All values are reported as mean ± SD (n=3). Significant differences established by one-way ANOVA: ** = $p < 0.01$; *** = $p < 0.001$.

Further dilution of 2FA (**27**) to a 0.1 mM concentration resulted in relaxation times that were similar to that of pure Milli-Q® water (**Figure 6-16A**). Additionally, the $E_{A_{H_2O}}$ of the 0.1 mM solution was no longer significantly different from pure water (**Figure 6-16B**). These results confirmed that the effect of 2FA (**27**) on the molecular motion of water, and thus the inhibition of ice recrystallization, was concentration dependent.

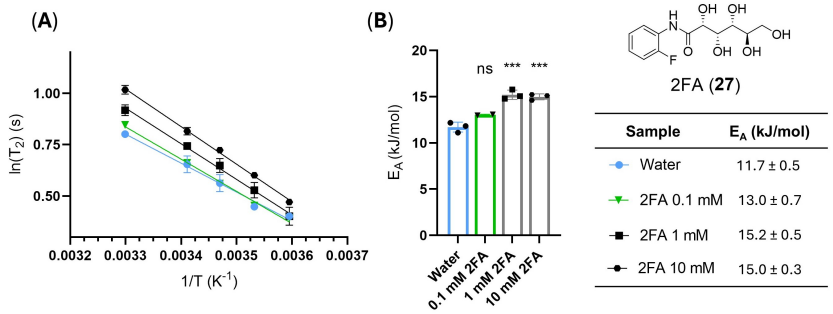


Figure 6-16. (**A**) Plot of ln($T_{2\text{-CPMG}}$) relaxation times (in s) against 1/T (in K^{-1}) for pure water and 2FA (**27**) solutions (0.1 to 10 mM), above freezing temperature, with T ranging from +5 °C to +30 °C. (**B**) Calculated $E_{A_{H_2O}}$ (kJ•mol^{-1}) from the slope of the linear regression of the plot in left panel (**A**) as $\ln(T_{2-CPMG}) = \beta \times {}^{1}/_{T} + \varepsilon$, with $E_{A_{H_2O}} = -R \times \beta$ where the universal gas constant $R = 0.008314$ kJ•K^{-1}•mol^{-1}. All values are reported as mean ± SD (n = 3 except 0.1 mM n = 2). Significant differences established by one-way ANOVA: ns = not significant; *** = $p < 0.001$.

6.4. Implications of relaxation times on understanding the mechanism of action of 2FA (**27**)

The ice recrystallization inhibition activity of carbohydrate-based small-molecule IRI 2FA (**27**) was hypothesized to be the result of: (1) direct binding to the surface of the ice crystals, (2) the creation of defects within the ice lattice, or (3) interactions with water molecules in the liquid phase between ice crystals

without direct interaction with the ice lattice. Measurements of frozen solutions of 2FA (**27**) in water from this study suggested that binding of 2FA (**27**) to the surface of ice crystals and any subsequent changes to the structure of the ice lattice were not plausible mechanisms for its ice recrystallization inhibition activity; 2FA (**27**) did not affect the $E_{A_{H_2O}}$ within the ice lattice (**Figure 6-12**) and did not result in DIS (**Figure 6-13**). Additionally, T_2 relaxation measurements of solutions of 2FA (**27**) in water at above zero temperatures increased $E_{A_{H_2O}}$, particularly at concentrations where 2FA (**27**) showed IRI activity (**Figure 6-15**). As water molecules must be sufficiently mobile to migrate from crystal to crystal *via* the interstitial liquid phase during ice recrystallization, the results presented herein showed that 2FA (**27**) decreased the mobility of water molecules in the liquid phase which ultimately resulted in the inhibition of ice recrystallization.

As discussed previously in *section 1.3.1* and *chapters 4-5*, amphiphilic molecules such as 2FA (**27**) with delicately balanced hydrophobic and hydrophilic motifs have been found to be the most effective IRIs.[156,157,167,410] Based upon these findings, and in light of these relaxation time studies, the hydrophilic component (polyol) of 2FA (**27**) must contribute to the inhibition of ice recrystallization by sequestering tightly bound water molecules within hydration shells (as commonly observed with proteins[403,509] and polysaccharides[495,510,511]) and disrupting the natural network of bulk water molecules. Additionally, this hydrophilic component must ensure that 2FA (**27**) can be incorporated into the liquid phase (*i.e.*, that the IRI has sufficient aqueous solubility). Furthermore, the hydrophobic structural features (aryl ring) of 2FA (**27**) must play a critical role in its ice recrystallization inhibition activity by preventing its inclusion within the lattice of ice crystals and further disrupting the structure of bulk water molecules in the liquid phase. The network of water molecules surrounding the hydrophobic moieties of the small-molecule may be disrupted (as has been shown with perfluoromethyl compounds)[512] or with C_4 *O*-alkylated derivatives from *chapter 5*, in turn enhancing the cohesiveness of the hydration layers around the hydrophilic moieties of 2FA (**27**).

Finally, it is important to note that cryo-concentration[513] may play a role in the IRI activity of 2FA (**27**) and similar small molecules. During freezing, 2FA (**27**) was found to be excluded from the ice lattice and would become concentrated within the interstitial liquid phase between ice crystals. However, while all four tested concentrations of 2FA (**27**) were found to impact the molecular motion of water molecules, the 1 and 3 mM concentrations were unable to sufficiently inhibit ice recrystallization as measured by the 5-minute SCA (**Figure 2-2** and **Figure 6-15**). Two possibilities are proposed that may explain this phenomenon:

(1) Upon freezing, cryo-concentration of the IRI within the liquid phase may result in inhibition of ice recrystallization only after reaching an effective concentration threshold. This threshold would directly depend on the concentration of the starting solution. Despite initially residing within the bulk water layer, an ineffective concentration of IRI would result in the molecules of IRI eventually becoming overgrown by an ice front and trapped within the ice lattice over time. This phenomenon has been observed as ice grows in a solution of brine or in the presence of short-chain polymers (*e.g.* PVA_5 and PVA_{10}) that are not active ice recrystallization inhibitors.[131,480,514]

(2) There are differences in the overall interactions between water molecules in the absence and presence of a solute at different temperatures, especially for water molecules that exist in a super-cooled state.[515–517] Therefore, while the above zero measurements confirmed that 2FA (**27**) was able to significantly impact water molecule motion, the 1 and 3 mM solutions must not reach a required concentration threshold to significantly affect molecular motion, which would depend on the nature of the interactions between the IRI and water molecules, at cryo-relevant temperatures following cryo-concentration.

To test these hypotheses, the observation of proton spin relaxation and activation energy of the molecular motion of water after increasing the proportion of unfrozen fraction in samples below freezing temperature and under conditions that promote ice recrystallization over time are required in future studies.

6.5. Screening additional IRIs for their impact on water molecule motion

With a mechanism of action for the ice recrystallization inhibition of 2FA (**27**) confirmed whereby the transition of water molecules through the bulk water phase was disrupted by the presence of the IRI, we sought to determine whether these findings could be applied to other established small-molecule carbohydrate-based compounds that have been previously investigated as IRIs (**Figure 6-17**).

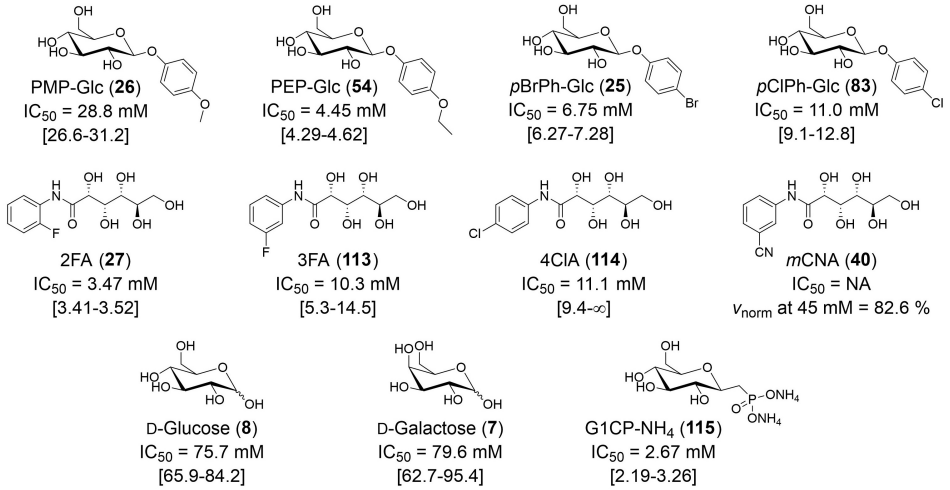


Figure 6-17. Summary of small-molecule carbohydrate-based compounds and their ice recrystallization inhibition activity as measured by the 5-minute splat-cooling assay. PMP-Glc (**26**), PEP-Glc (**54**), *p*BrPh-Glc (**25**), *p*ClPh-Glc (**83**), 2FA (**27**), 3FA (**113**), 4ClA (**114**), *m*CNA (**40**), D-glucose (**8**), D-galactose (**7**), and G1CP-NH_4 (**115**)[177].

Each of the compounds described above were prepared at a concentration of 20 mM in PBS and a 10 mM sample was made by serial dilution; if the compound was not soluble at 20 mM, it was diluted to 10 mM and thus only tested at this concentration. These concentrations were selected to provide a data set comprised of compounds with a wide range of ice recrystallization inhibition activity across a structurally diverse set of molecules (see *section 8.3.1* for full 5-minute SCA dose response curves for each compound). For the purposes of this study, three categories of ice recrystallization inhibition activity were established based on the activity of each compound at the indicated concentration as determined from their dose-response curves: highly active = ν_{norm} less than 10 %, moderately active = ν_{norm} between 10 and 90 %, and inactive = ν_{norm} greater than 90 % (**Table 6-5**).

Table 6-5. Categorization of ice recrystallization inhibition activity for various small-molecule carbohydrate-based IRIs. Full 5-minute SCA dose-response curves for the activity of these compounds can be found in *section 8.3.1*.

Highly Active	Moderately Active	Inactive
ν_{norm} < 10 %	ν_{norm} between 10 and 90 %	ν_{norm} > 90 %
2FA (**27**) (10 mM)	4ClA (**114**) (10 mM)	*m*CNA (**40**) (10 and 20 mM)
3FA (**113**) (20 mM)	3FA (**113**) (10 mM)	PMP-Glc (**26**) (10 and 20 mM)
PEP-Glc (**54**) (10 and 20 mM)	*p*ClPh-Glc (**83**) (10 mM)	D-Glucose (**8**) (10 and 20 mM)
*p*BrPh-Glc (**25**) (10 and 20 mM)		D-Galactose (**7**) (10 and 20 mM)
*p*ClPh-Glc (**83**) (20 mM)		
G1CP-NH_4 (**115**) (10 mM)		

A difference in relaxation time was observed for the different concentrations of 2FA (**27**) in liquid water at above zero temperatures, most notably at temperatures warmer than 15 °C (**Figure 6-15A**). This increase in relaxation time was attributed to the ability for 2FA (**27**) to slow down liquid water molecule motion (ultimately increasing the activation energy of water molecule motion) and thus inhibit ice recrystallization. Therefore, to efficiently screen whether the other IRI candidates had a similar effect on liquid water molecule motion, the $T_{2\text{-CPMG}}$ relaxation time of each preparation of small-molecule carbohydrate-based compound was measured at 25 °C (**SI Figure 8-94**). The raw relaxation curves were then processed using MS Excel Solver (Microsoft, Redmond, WA) to determine the parameters of best fit using **Equation 6-3** in the same manner as previously described in *section 6.2.1*. The $T_{2\text{-CPMG}}$ relaxation times were derived in the same manner as previously described (see *section 6.2.1*). Consistent with the relaxation times of 2FA at above zero temperatures (**Figure 6-14**, **Table 6-4**), only a single $T_{2\text{-CPMG}}$ relaxation time was observed for all samples (**Table 6-6**).

Table 6-6. Parameters of best fit for the $T_{2\text{-CPMG}}$ relaxation of pure Milli-Q® water and IRI-supplemented water solutions at +25 °C by **Equation 6-3** (n=1). The second component of the bi-exponential is not shown as $I_{CPMG\text{-}2}$ and $T_{2\text{-CPMG-}2}$ are both equal to zero for all samples tested. Values reported as mean ± SD for n=3 replicates.

Compound	Water	2FA (**27**)	3FA (**113**)		4ClA (**114**)
Concentration	---	10 mM	10 mM	20 mM	10 mM
$I_{CPMG\text{-}1}$	77.5	82.0	77.0	76.8	76.9
$T_{2\text{-CPMG-}1}$ (s)	2.04	2.52	2.02	1.97	2.05
cst	0.11	0.11	0.11	0.11	0.11
Compound	D-Glucose (**8**)		*m*CNA (**40**)		G1CP-NH_4 (**115**)
Concentration	10 mM	20 mM	10 mM	20 mM	10 mM
$I_{CPMG\text{-}1}$	78.3	78.3	78.3	78.9	78.8
$T_{2\text{-CPMG-}1}$ (s)	2.06	2.06	2.08	2.18	1.43
cst	0.11	0.11	0.11	0.10	0.15
Compound	D-Galactose (**7**)		PEP-Glc (**54**)		PMP-Glc (**26**)
Concentration	10 mM	20 mM	10 mM	20 mM	10 mM
$I_{CPMG\text{-}1}$	77.9	77.7	77.5	77.9	77.7
$T_{2\text{-CPMG-}1}$ (s)	2.03	1.99	2.01	2.10	2.22
cst	0.11	0.11	0.12	0.12	0.11
Compound	*p*BrPh-Glc (**25**)		*p*ClPh-Glc (**83**)		PMP-Glc (**26**)
Concentration	10 mM	20 mM	10 mM	20 mM	20 mM
$I_{CPMG\text{-}1}$	77.2	78.0	78.7	78.9	77.4
$T_{2\text{-CPMG-}1}$ (s)	2.12	2.02	2.03	2.14	2.38
cst	0.11	0.11	0.11	0.11	0.10

While 2FA (**27**) caused an increase in $T_{2\text{-CPMG}}$ relaxation time at room temperature (25 °C), as expected, there was no overall trend between the relaxation times and ice recrystallization inhibition activity of the other compounds tested (**Figure 6-18**). Compounds that were similarly active to 2FA (**27**) did not show the same increase in $T_{2\text{-CPMG}}$ relaxation time, and in fact showed no difference in the relaxation time compared to pure water at all (*e.g.*, 20 mM **54** and 20 mM **25**) (**Figure 6-18**). As these tests were carried out at above zero temperatures, it was hypothesized that the cryo-concentration that occurs during freezing must play a critical role in the observed ice recrystallization inhibition activity of compounds that are active at these concentrations when frozen and analyzed by the SCA.

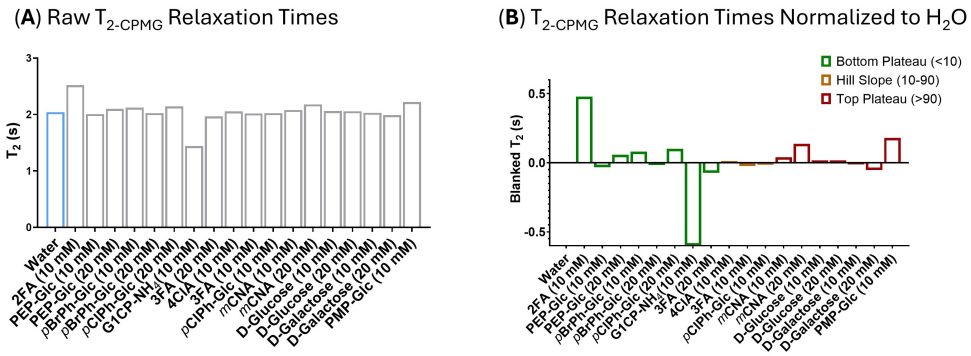


Figure 6-18. (**A**) $T_{2\text{-CPMG}}$ relaxation times for various small-molecule ice recrystallization inhibitor candidates from **Table 6-6**. (**B**) All relaxation times from panel A normalized to the relaxation time of H_2O. Green indicates compounds that have a ν_{norm} of < 10 % at the tested concentration; orange a ν_{norm} of between 10-90 %; red a ν_{norm} of > 90 %.

Of note, the presence of G1CP-NH_4 (**115**) dramatically reduced the $T_{2\text{-CPMG}}$ relaxation times of water molecules in the liquid phase. Despite being similarly active to 2FA (**27**) (with similar IC_{50} values and ν_{norm} at the tested concentration), G1CP-NH_4 (**115**) had a directly opposite effect on the molecular motion of water molecules at 25 °C. By reducing the relaxation time, water molecules were slower moving in the presence of G1CP-NH_4 (**115**) which suggested an increase in the organization of water molecules in solution.[518]

As previously discussed, salt-based compounds would be expected to affect the overall structure of the ice lattice which can be directly investigated by measuring $T_{2\text{-FID}}$ relaxation times. Measurements of T_1 relaxation would be more sensitive to the impact of incorporating ionic salts, however these measurements are significantly more time-consuming than $T_{2\text{-FID}}$ measurements (on the scale of hours compared to minutes). Therefore, the $T_{2\text{-FID}}$ measurements can serve as a preliminary indicator of the salt's effect on the ice lattice; however, it is important to note that the absence of a change in relaxation by $T_{2\text{-FID}}$ does not necessarily indicate a lack of impact on ice lattice structure.

In the presence of G1CP-NH_4 (**115**) the relaxation time of water molecules in the ice lattice dramatically increased compared to pure water and 2FA (**27**) solutions (**Figure 6-19**). This suggested that the structure of the ice lattice was disrupted by the presence of compound **115** (10 mM). As the core structure of G1CP-NH_4 (**115**) is a pyranoside rather than an aldonamide (2FA, **27**), the $T_{2\text{-FID}}$ relaxation of another pyranoside IRI *p*BrPh-Glc (**25**) was also measured to determine the change in relaxation time could be attributed to structural differences. However, *p*BrPh-Glc (**25**) also did not significantly change the $T_{2\text{-FID}}$ relaxation times of water molecules compared to pure water or 2FA (**27**) (**Figure 6-19**) even at concentrations where ice recrystallization was completely inhibited (40 mM). Finally, the $T_{2\text{-FID}}$ relaxation

time of ammonium chloride (NH_4Cl) (10 mM) was also measured to isolate the impact of the salt ion itself on the molecular motion of water molecules in the ice lattice. From this experiment, the $T_{2\text{-FID}}$ relaxation time of NH_4Cl was found to be comparable to G1CP-NH_4 (**115**, 10 mM), indicating that the decrease in relaxation time of liquid water molecules could be attributed directly to the NH_4^+ ion of the salt-based compound **115**.

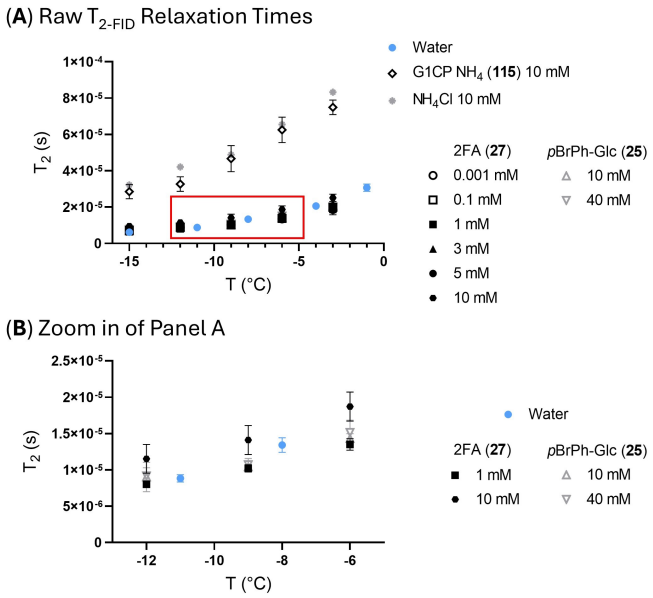


Figure 6-19. $T_{2\text{-FID}}$ relaxation time comparison of water to 2FA (**27**, n=3), G1CP-NH_4 (**115**, n=2), NH_4Cl (n=1), *p*BrPh-Glc (**25**, 10 mM n=3. 40 mM n=2). (**A**) Represents the full comparison. (**B**) Represents a expanded (red) version of panel A. Data reported as the mean ± standard deviation.

In addition to reduced relaxation times of the ice lattice, G1CP-NH_4 (**115**) also showed relaxation as detected by the CPMG pulse sequence, indicating that a sufficient liquid phase was present in these samples which could be detected by the NMR spectrophotometer even at temperatures as cold as -15 °C (**Figure 6-20A**). Interestingly, NH_4Cl at the same concentration (10 mM) did not show relaxation from the CPMG pulse sequence (**Figure 6-20B**) and appeared to have an insignificant liquid/unfrozen fraction at all temperatures which was consistent with that of pure water. The results suggested that the carbohydrate portion of the G1CP-NH_4 (**115**) salt was also important for increasing the quantity of unfrozen fraction in the tested sample and that the addition of salts alone at a 10 mM concentration is not sufficient. Ultimately, this information could be useful for increasing the percent unfrozen fraction of samples to monitor the impact of small-molecule compounds on the bulk water phase of a frozen sample.

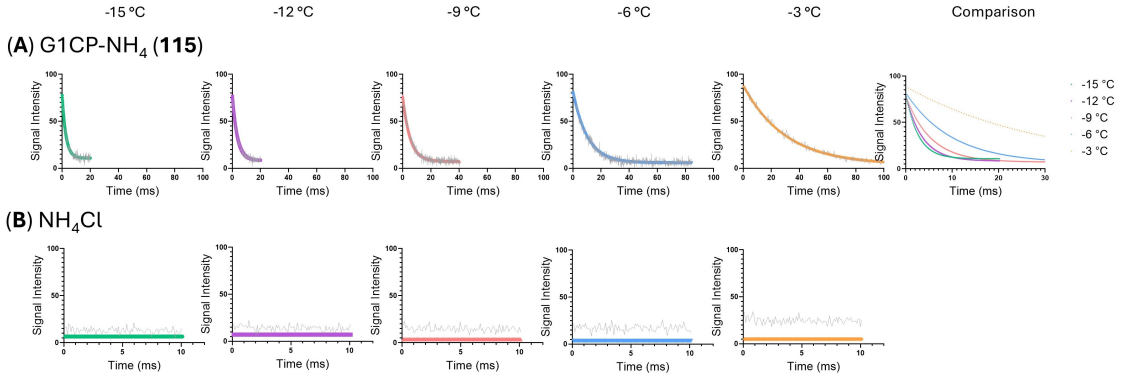


Figure 6-20. Exemplar of (**A**) G1CP-NH_4 (**115**) solution (10 mM) and (**B**) NH_4Cl (10 mM) trial $T_{2\text{-CPMG}}$ relaxation between -15 °C and -3 °C. Data shown from one trial that is representative of the mean (from n=2 replicates for A and n=1 replicate for B). Grey = raw data, coloured = fitted model to **Equation 6-3**.

6.5.1. Characterization of saline solutions by spin-spin (T_2) relaxation

As the splat-cooling assay for determining ice recrystallization inhibition activity utilizes phosphate-buffered saline (PBS) as the solvent, we sought to investigate the impact of using PBS instead of water on relaxation times. The goal of these studies was ultimately to increase the proportion of unfrozen fraction to a sufficient, detectable, quantity and then measure the impact of small-molecule carbohydrates on water molecules in the liquid phase of a frozen, aqueous, solution.

The T_2 relaxation time of PBS was first measured directly from the FID (in the same manner as *section 6.2.1*) at temperatures between -15 °C and -5 °C. From these measurements, the activation energy of water molecule motion in the ice lattice of a frozen PBS solution was found to be 26.7 ± 1.8 kJ/mol (**Figure 6-21**). While the exact values for activation energy derived from T_2 relaxation are extremely sensitive to small changes in experimental conditions as previously discussed, the reduction in total activation energy was consistent with what was expected upon the introduction of salts whereby salts disrupt the hydrogen bond network of the ice lattice. Therefore, the water molecules of the ice lattice can move more freely and thus have greater molecular motion resulting in shorter T_2 relaxation times.

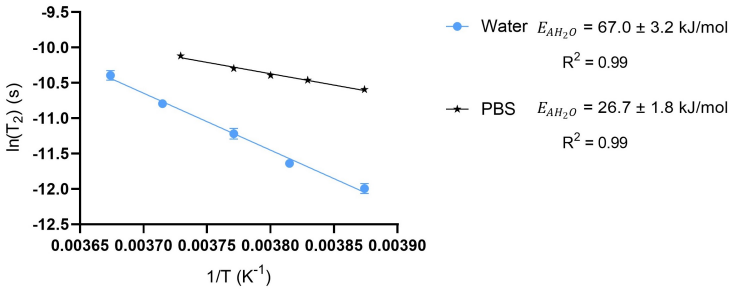


Figure 6-21. Natural logarithm transformed $T_{2\text{-FID}}$ relaxation times of pure Milli-Q® water (n=3) and phosphate-buffered saline (PBS) (n=1) at temperatures between -15 °C and -1 °C. Calculated $E_{A_{H_2O}}$ (kJ•mol^{-1}) from the slope of the linear regression as $\ln(T_2) = \beta \times 1/T + \varepsilon$, with $E_{A_{H_2O}} = -R \times \beta$ where the universal gas constant $R = 0.008314$ kJ•K^{-1}•mol^{-1}, β = -8057 s•K, and ε = 19.2 s; R^2 = 0.99. All data points reported as mean ± SD.

More importantly, measurement of $T_{2\text{-CPMG}}$ relaxation was detectable even at -15 °C, indicating the presence of a significant, detectable, unfrozen fraction for PBS (**Figure 6-22**). As the total concentration of salts in PBS is 10-fold greater than the concentration of IRIs tested in this study (PBS is an aqueous solution comprised of four salts at a total concentration of 149.3 mM: 8.1 mM Na_2HPO_4, 1.5 mM KH_2PO_4, 137 mM NaCl, and 2.7 mM KCl), we sought to examine whether there was a minimum concentration of PBS that could be used while still being able to detect an unfrozen fraction at -15 °C. Three dilutions of PBS were prepared and the T_2 relaxation of these samples was determined from a CPMG pulse sequence (in the same manner as *section 6.2.2*) at temperatures between -15 °C and -5 °C.

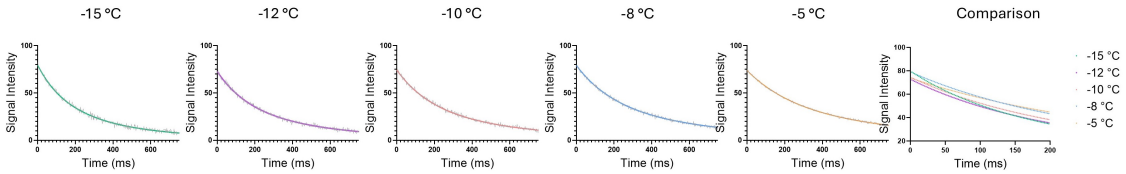


Figure 6-22. Exemplar of phosphate-buffered saline (PBS) trial $T_{2\text{-CPMG}}$ relaxation between -15 °C and -5 °C. Data shown from one trial. Grey = raw data, coloured = fitted model to **Equation 6-3**.

The three dilutions of PBS tested were 2-fold, 8-fold, and 10-fold, resulting in total salt concentrations of 74.7 mM, 18.7 mM, and 14.9 mM respectively. The results showed that even at a 10-fold dilution of PBS, a significant unfrozen fraction was present for which its relaxation could be detected by a CPMG pulse sequence, even at the coldest temperature of -15 °C (**Figure 6-23**).

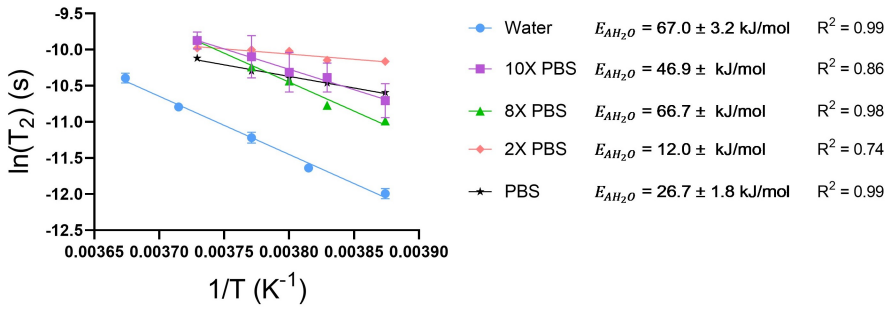


Figure 6-23. Natural logarithm transformed $T_{2\text{-FID}}$ relaxation times of pure Milli-Q® water (n=3) and various dilutions of phosphate-buffered saline (PBS) at temperatures between -15 °C and -1 °C. Calculated $E_{A_{H_2O}}$ (kJ•mol^{-1}) from the slope of the linear regression as $\ln(T_2) = \beta \times 1/T + \varepsilon$, with $E_{A_{H_2O}} = -R \times \beta$ where the universal gas constant $R = 0.008314$ kJ•K^{-1}•mol^{-1}, β = -8057 s•K, and ε = 19.2 s; $R^2 = 0.99$. All data points reported as mean ± SD.

These results suggested that it may be possible to incorporate a small-molecule carbohydrate-based IRI into a saline solution in order to measure the effect that the IRI has on water molecules in the liquid (unfrozen) fraction at below zero temperatures. These experiments may allow for investigation into the effect of cryo-concentration and provide further insight into the mechanism of action of these IRIs.

6.6. Conclusion

While the mechanism of ice recrystallization and its inhibition by antifreeze (glyco)proteins (AF(G)Ps has been well established, inhibition by small molecules that have been developed by the Ben Lab over the last several decades has remained unclear. Throughout the development of these compounds, the Ben Lab has proposed three key hypotheses for their mechanism of action which include binding to the ice crystal surface akin to the mechanism for AF(G)Ps, incorporation into the hydrogen bonding lattice of an ice crystal, and/or interactions exclusively with the bulk water phase that exists between ice crystals. Each of these mechanisms are based upon the concept that in order to inhibit ice recrystallization, the thermodynamically-driven process of transferring water molecules from one ice crystal to another must be disrupted.

This chapter investigated the interactions between the small-molecule IRI 2FA (**27**) and water molecules by determining ^{1}H NMR relaxation times of water-based solutions with different concentrations of 2FA (**27**) at various temperatures both below and above 0 °C. Using both spin-lattice (T_1) and spin-spin (T_2) relaxation time experiments, these studies were able to determine that 2FA (**27**) had no impact on the water molecules of the ice lattice in frozen samples. This finding was further supported by dynamic ice shaping (DIS) measurements that ruled out ice binding as a potential mechanism of action for 2FA (**27**). Using T_2 relaxation times of bulk water molecules at above zero temperatures, a significant reduction in the

molecular motion of water molecules was observed in the presence of 2FA (**27**). These results were concentration dependent, where at concentrations of 0.1 mM the molecular motion of the water molecules was comparable to that of pure water. More importantly, the activation energy of water molecule motion ($E_{A_{H_2O}}$) in the presence of 2FA (**27**) was significantly greater (15.0 kJ/mol) compared to pure water (11.7 kJ/mol). Taken together, these results confirmed that the small-molecule IRI 2FA (**27**) acts by a mechanism that affects the molecular motion of bulk water molecules, without disturbing the ice lattice, in order to inhibit ice recrystallization.

While investigation of different small-molecule carbohydrates by time-domain NMR was inconclusive with respect to ice recrystallization inhibition activity, it was proposed that cryo-concentration may play a significant role in the mechanism of action of these compounds. As a result, future studies should investigate the effect of small molecules on the relaxation times of bulk water molecules at below zero temperatures. Saline solutions (such as phosphate-buffered saline) should be used to increase the unfrozen fraction of samples and permit direct investigation of the bulk water phase.

This study represented the first of its find to utilize time-domain NMR in the context of cryopreservation and, more specifically, ice recrystallization. The results presented herein could be leveraged to aid the design and screening of next generation ice recrystallization inhibitors; where it would be critical to maximize the energetic barrier of water molecule motion and minimize the effective concentration of ice recrystallization inhibitor required for cryopreservation applications.

7. Conclusion and future outlook

This thesis explored the development and evaluation of small-molecule ice recrystallization inhibitors (IRIs) with a focus on exploring their mechanism of action. Despite decades of research generating novel, successful IRIs for various cryopreservation applications, our understanding of the important structural features of these compounds and how they work in both acellular and cellular applications has remained limited. However, gaining insight into the mechanism of action of small-molecule IRIs is critical to their application in biological systems to ultimately improve cryopreservation outcomes. Therefore, this thesis focused on exploring various IRIs from an interdisciplinary perspective, involving biological cryopreservation studies with mesenchymal stromal cells (MSCs) and red blood cells (RBCs), microscopy imaging experiments with novel Raman scattering techniques for monitoring cellular uptake and internalization, computational prediction and parameterization and fundamental synthetic design to assess structure activity relationships, as well as the implementation of nuclear magnetic resonance techniques to determine relaxation times that could be used probe IRI-water molecule interactions.

Chapter 2 applied small-molecule IRIs *p*BrPh-Glc (**25**) and 2FA (**27**) for the cryopreservation of bone marrow-derived mesenchymal stromal cells (BM-MSCs). Importantly, 2FA (**27**) significantly improved post-thaw cell proliferation and population doublings without compromising cell viability or recovery. These findings were extended to umbilical cord-derived MSCs (UC-MSCs), supporting the generalizability of these finding to different donors and different stem cell sources. Future studies should address the donor-to-donor variability that was observed and investigate the impact of transient warming events (TWEs), including storage time and temperature, on cryopreservation outcomes in this specific context. Moreover, mechanistic investigations into how the addition of 2FA (**27**) influences cell cycle progression post-thaw could inform targeted cryoprotectant design.

Chapter 3 explored the internalization and permeation of nitrile- and amide- substituted IRIs using Raman microscopy for live-cell imaging. *m*CNPh-Glc (**37**) was found to passively diffuse into cells, a finding supported by earlier work in the Ben Lab that suggested IRI uptake was independent of glucose transporters such as GLUT1. These findings laid the groundwork for understanding intracellular IRI behavior, which is critical for their inhibition of intracellular ice recrystallization. Future work should investigate internalization under cryopreservation conditions (*i.e.,* at reduced temperatures) and utilize the

sensitivity of Raman-based imaging to investigate localization and distribution of the small-molecule IRIs within the intracellular space.

Chapter 4 presented a systematic structure-activity relationship (SAR) investigation of O-aryl-β-D-glucopyranosides, leveraging the 5-minute splat cooling assay (SCA) to quantify ice recrystallization inhibition activity and its relationship to various structural and physicochemical parameters. Measures of hydrophobicity, including logP and polar surface area/molecular surface area (PSA/MSA) ratios, and electronic effects were assessed as part of the investigation, although predictive power remained limited due to the structural similarity of candidate molecules and limitations of existing computational models to differentiate between the compounds. Future efforts towards SAR campaigns of a similar nature should focus on developing more nuanced descriptors that incorporate 3D conformational features, hydrogen-bonding capacity, and interaction with water molecules. Additionally, integrating correlation outcomes that consider post-cryopreservation cell viability (to assess toxicity risk), recovery, and functionality into the SAR models could facilitate multiparameter optimization and improve the accuracy and applicability of any findings.

Chapter 5 focused on traditional SAR study of the IRI PMP-Glc (**26**), investigating modifications at each of the hydroxyl positions through deuteration and *O*-alkylation. Deuteration at C_1, C_2, and C_3 diminished activity, suggesting a global requirement for hydrogen bonding, although no specific site emerged as essential. In contrast, *O*-methylation at C_4 dramatically enhanced activity (IC_{50} from 28.8 mM to 3.19 mM), making it one of the most potent IRIs from this class of compounds that had been evaluated to date. Investigation of specific hydrogen bonding interactions by NMR and computational calculations found that the formation of a donation interaction by OH-6 and an accepting interaction at the anomeric oxygen may be an important interaction for the inhibition of ice recrystallization. Future research should explore the generalizability of C_4 modification and investigate how this modification impacts hydrogen bonding with bulk water and ice surfaces. These findings also prompt deeper investigation into carbohydrate-water interactions at specific positions and their role in inhibiting ice crystal growth. Due to the low mM activity of C_4 OMe PMP-Glc (**99**), testing of this IRI in various cryopreservation applications is also warranted.

Chapter 6 advanced the mechanistic understanding of small-molecule IRIs by using ^{1}H NMR relaxation measurements to study water mobility in the presence of 2FA (**27**) and related compounds. T_1 and T_2 relaxation times revealed that 2FA (**27**) slowed the motion of bulk water molecules and increased the activation energy of water molecule motion, supporting the hypothesis that these IRIs disrupt the

thermodynamically driven transfer of water molecules between ice crystals by residing within the unfrozen bulk water layer. Interestingly, when other small-molecule compounds with ice recrystallization inhibition activity were assessed, not all had a measurable effect on the relaxation times. This result suggested that different mechanisms of action may occur for different IRIs, or that cryo-concentration may play a significant role in ice recrystallization inhibition. Future work should involve real-time observation of ice recrystallization dynamics in IRI-treated solutions of phosphate-buffered saline (PBS) to increase the quantity of unfrozen fraction and permit relaxation measurements at sub-zero conditions more representative of cryopreservation.

To summarize, this thesis has demonstrated that small-molecule IRIs represent a promising class of cryoprotectants with broad utility across cell types. Understanding of their mechanism of action will greatly support future development and applications to novel biological systems. Further research campaigns will be complicated by a lack of understanding of the interactions between these compounds and ice/water, which should ultimately lead to prioritized research in this area. By integrating molecular design, biophysical characterization, and functional testing, this work has laid the foundation for rational IRI development and more effective cryopreservation strategies.

8. Supporting Information

8.1. General Methods and Procedures

8.1.1. Methods: Chapter 2 – Mesenchymal Stromal Cells (MSCs)

8.1.1.1. General culture of MSCs

Donor MSCs that had been previously collected and cryopreserved at passage 1 in Master cell banks maintained by Dr. David Courtman's research team at the Ottawa Hospital Research Institute (OHRI) were thawed and cultured in NutriStem XF medium [Biological Industries 05-200-1A, supplemented with 0.6 % NutriStem SF supplement mix (Biological Industries 05-201-1U) and 10 µg/mL gentamycin (Gibco 15710-064)] in 175 cm^2 flasks (Corning®). Cells were incubated at 37 ºC in 5 % CO_2 and maintained with medium changes every two to three days. After a maximum of one week in culture, cells were lifted from the flasks using TrypLE Select (Gibco 12563-029) for use in experiments.

8.1.1.2. Freezing and thawing of MSCs

MSCs from culture were aliquoted into 15 mL conical tubes to a concentration of 2 x 10^6 cells/mL in cell culture medium. The cells were pelleted by centrifugation at 400 g for 5-15 minutes at room temperature. The supernatant was then removed, and the cells were resuspended in 1 mL standard freezing medium [SFM, 10 % DMSO (WakChemie, WAK-DMSO-10) and 5 % human albumin (CSL Behring, 02274663) in PlasmaLyte-A (Baxter, JB2544)] with or without ice recrystallization inhibitor (IRI). For cells to be cryopreserved with the addition of an IRI, the compound was prepared to its desired final concentration in SFM. The cell suspensions were then transferred to 2 mL cryogenic vials (Corning, 430488) and frozen in a controlled rate freezer (ThermoScientific, CryoMed Model 7452) using an optimized step-down program (*section 8.1.1.3*) followed by storage in liquid nitrogen vapour (-196 ºC). Following storage, cells were slowly thawed by the addition of 1 mL of pre-warmed cell culture medium (37 ºC) to each vial in accordance with standard operating procedures at OHRI's cell manufacturing facility.

8.1.1.3. Optimized step-down cooling procedure for MSC cryopreservation

Cells were placed into controlled-rate freezer in appropriate cryosolution and held at 18 ºC with temperature changes as follows:

(1) 5 ºC/min cooling until the chamber reaches 4 ºC
(2) 1 ºC/min cooling until the sample reaches -6 ºC
(3) 30 ºC/min cooling until the chamber reaches -40 ºC

(4) 10 ºC/min warming until the chamber reaches -18 ºC
(5) 1 ºC/min cooling until the chamber reaches -40 ºC
(6) 5 ºC/min cooling until the chamber reaches -80 ºC
(7) 10 ºC/min cooling until the chamber reaches -180 ºC
(8) Wait at -180 ºC and then transfer to liquid nitrogen storage at -196 ºC

The amount of storage time at -196 ºC in liquid nitrogen following freezing of the cells with the different cryosolutions varied from as short as 24-hours to up to 2-months at maximum.

8.1.1.4. MSC recovery and viability

Cell counts to determine MSC recovery were obtained using a hemocytometer. Percent cell recovery was calculated by dividing the total cell count by the initial cell count (*e.g.,* the number of cells after culture divided by the number of cells initially seeded onto a culture plate). Cell viability was assessed by the Trypan Blue exclusion method and by flow cytometry with annexin V/propidium iodide staining.[256,257]

For the Trypan Blue exclusion assay, an aliquot of the cell suspension to be assessed was diluted 1:1 in Trypan Blue and loaded onto a hemocytometer. The total number of viable (unstained) and non-viable (blue stained) cells were counted, and the percentage of viable cells was calculated using **Equation 8-1**.

Equation 8-1. $\%\ viability = \frac{(total\ \#\ of\ viable\ cells)}{[(total\ \#\ of\ viable\ cells)+(total\ \#\ of\ non-viable\ cells)]}(100\%)$

For flow cytometry assessment using annexin V (AV)/propidium iodide (PI), an aliquot of cells (0.5 x 10^6 to 2.0 x 10^6 cells) was transferred to a 15 mL conical tube and centrifuged at 400 g for 5 minutes at room temperature. The cell pellet was resuspended in 1X Annexin-binding buffer (Life Technologies, V13246) to a concentration of 1 x 10^6 cells/mL and 100 µL was added to each of four 5 mL flow cytometry tubes representing an unstained control, an annexin V (Alexa Fluor ® 488, Life Technologies, A13201) only sample, a PI (Life Technologies, V13242) only sample, and an AV/PI double stain sample. To the AV only sample, 5 µL Alexa Fluor ® 488 was added. To the PI only sample, 50 µL 0.1 % Triton X-100 (Sigma Aldrich, X100-500 mL) and 1 µL 1X PI (in 1X Annexin-binding buffer) were added. To the AV/PI double stain sample 5 µL Alexa Fluor ® 488 and 1 µL 1X PI was added. 400 µL 1X Annexin-binding buffer was added to each tube to a minimum total tube volume of 500 µL. A minimum of 10,000 events were recorded for each sample on the flow cytometer (ThermoFisher, Attune® Acoustic Focusing Cytometer, 4453328). Viable cells were identified as both AV and PI negative.

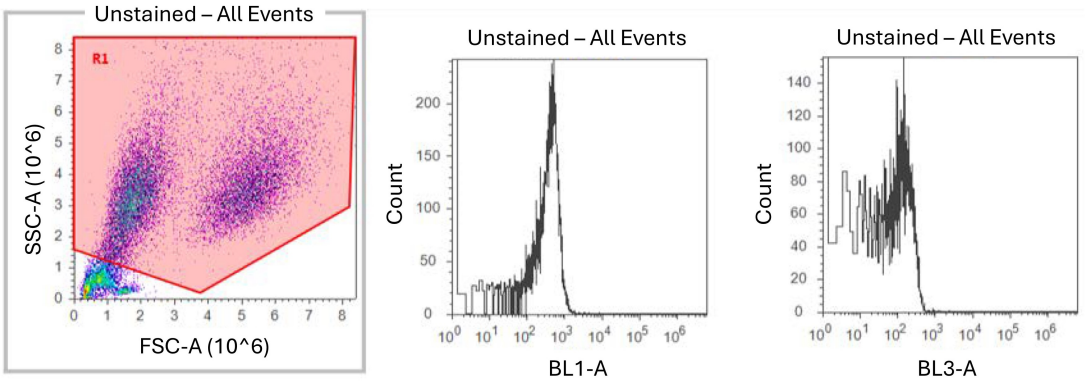


Figure 8-1. Density plot and histograms showing the appropriate position of an unstained cell population with a polygonal gate (R1) excluding debris. *Figure included from the standard operating procedures of the cell-manufacturing facility at OHRI.*

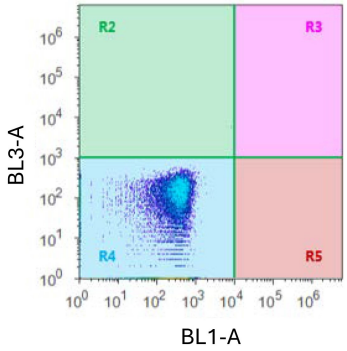


Figure 8-2. Density plot with quadrant gate demonstrating appropriate positioning of the cell population after voltage adjustments on the unstained cells. *Figure included from the standard operating procedures of the cell-manufacturing facility at OHRI.*

8.1.1.5. EdU Cell Proliferation Assay

Cells were thawed from cryopreservation storage (see *section 8.1.1.2*), seeded in 75 cm^2 flasks (Corning®) at a density of 2 x 10^5 cells/flask, and cultured for two days at 37 °C in 5 % CO_2 (see *section 8.1.1.1* for general MSC culture conditions). After two days, EdU (prepared as a 10 mM stock solution in DMSO from the Click-iT® EdU Flow Cytometry Assay Kit, Molecular Probes, C10420) was added to the flask to a final concentration of 10 µM and incubated at 37 °C in 5 % CO_2 for two hours. The cells were then detached from the flask using TrypLE Select (Gibco 12563-029), added to a conical tube, and centrifuged at 400 g for 5 minutes at room temperature. The supernatant was removed and the pellet was washed once with 1 % bovine serum albumin (BSA) in phosphate-buffered saline (PBS), re-pelleted, and then resuspended in 1 % BSA in PBS. Following the Click-iT® EdU Flow Cytometry Assay Kit (Molecular Probes, C10420) protocol, 100 µL of cell suspension and 100 µL of click-iT® fixative were added to a 5 mL polystyrene flow cytometry tube and incubated for 15 minutes at room temperature protected from light. The cells were then washed with 1 % BSA in PBS and pelleted by centrifugation at

400 g for 5 minutes at room temperature. The supernatant was discarded, and the pellet was resuspended in 100 µL of 1X Click-iT® saponin-based permeabilization and wash reagent. After a 15-minute incubation at room temperature protected from light, 0.5 mL of Click-iT® reaction cocktail (for one tube: 2 % 100 mM aqueous solution of $CuSO_4$, 0.5 % Alexa Fluor® 488 working solution in DMSO, and 10 % 1X Click-iT® EdU buffer solution in PBS to a total volume of 500 µL) was added. The tubes were incubated for 30 minutes at room temperature protected from light, then washed with 1X Click-iT® saponin-based permeabilization and wash reagent, pelleted by centrifugation at 400 g for 5 minutes at room temperature, and the pellet was resuspended in 100 µL of 1X Click-iT® saponin-based permeabilization and wash reagent. The samples were then analyzed by flow cytometry using 488 nm excitation with a green emission filter. A minimum of 10,000 events were recorded for each sample on the flow cytometer (ThermoFisher, Attune® Acoustic Focusing Cytometer, 4453328).

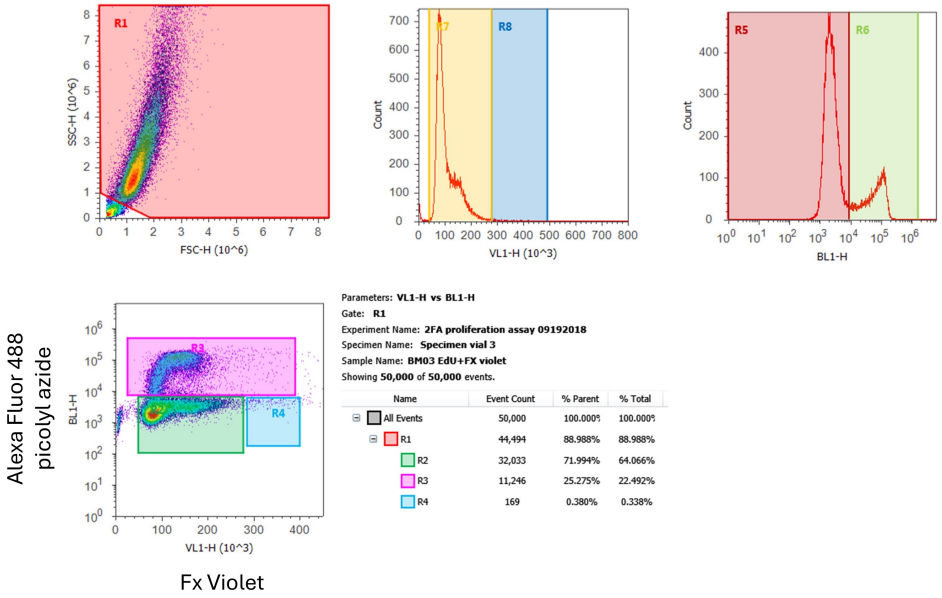


Figure 8-3. Density plot and histograms showing the appropriate position of an unstained cell population with a polygonal gate (R1) excluding debris as well as quadrant gates demonstrating appropriate positioning of the cell population after voltage adjustments on the unstained cells for S-phase, G_1, and G_2 phase cell populations. *Figure included from the standard operating procedures of the cell-manufacturing facility at OHRI.*

8.1.1.6. MSC Population doublings and doubling time

Population doubling time was calculated using **Equation 8-2**:

Equation 8-2: $N(t) = N(0)[2^{t/d}]$

where N(t) = the number of cells harvested after (t) hours in culture, N(0) = the number of cells initially seeded, t = the number of hours in culture, and d = the doubling time of the cells. From this equation, the number of population doublings is equal to t/d.

8.1.1.7. MSC IDO expression assay

Cells from each treatment of interest were cultured until 60 % confluent in 75 cm^2 flasks (Corning®) at a density of 2 x 10^5 cells/flask at 37 °C in 5 % CO_2 (see *section 8.1.1.1* for general MSC culture conditions). At 60 % confluency, 10 ng/mL of Interferon gamma (IFNγ, recombinant human, R&D Systems, 285-IF-100/CF) was added to the cell culture flask. One matching flask was kept as the negative control treatment. The flasks were incubated for 48 hours at 37 °C in 5 % CO_2, after which the cell culture medium was decanted, and the cells were washed once with PBS. The cells were then removed from the flask by scraping into PBS and pelleted by centrifugation at 1,000 g for 1 min. If necessary, the cells could be frozen at -80 °C (see *section 8.1.1.2*) until ready to isolate the RNA. RNA was isolated from the MSC pellet using the RNeasy Mini Kit (Qiagen, 74104).

Briefly, each MSC pellet was thawed slightly to loosen it from the cryotube. 600 µL of Buffer RLT containing β-mercaptoethanol (β-ME, Sigma-Aldrich, M6250, 10 µL of per 1 mL of Buffer RLT) was added to dissolve each pellet and to inhibit RNases. The lysate was transferred to a QIAshredder spin column (Qiagen, 79654) in a 2 mL collection tube and centrifuged for 2 min at full speed. After centrifugation, 1 volume (600 µL) of 70 % ethanol was added and mixed by pipetting. Up to 700 µL of the sample (including precipitate) was transferred to an RNeasy spin column (Qiagen, 74104) in a 2 mL collection tube and was then centrifuged for 15 seconds at > 8,000 g. If the original sample (after addition of ethanol) exceeded 700 µL, successive aliquots were centrifuged in the same RNeasy spin column with the flow-through discarded after each centrifugation. After the final successive centrifugation, 700 µL of Buffer RW1 was added to the RNeasy spin column and was centrifuged for 15 seconds at > 8,000 g. The flow-through was discarded and then two subsequent washes with Buffer RPE (500 µL) were completed: the first was followed by a 15 second centrifugation at > 8,000 g, the second was centrifuged for 2 min at > 8,000 g. The spin column was then placed in a new 1.5 mL collection tube and 30-50 µL of RNase-free water was added, followed by centrifugation for 1 min at > 8,000 g. RNA concentration was then measured using a Nanodrop2000 (ThermoScientific) for both the treated and control samples.

After RNA isolation, a reverse transcriptase (RT) reaction was set up to amplify the RNA content by polymerase-chain reaction (PCR) using the Gene Amp RNA PCR Core kit (Life Technologies, N808-0143). All samples plus a no RNA negative control and a no RT negative control were loaded onto a BioRad T100 Thermal Cycler (BioRad, 186-1096). The program was set to denature at 95 °C for 5 minutes, anneal/extend at 42 °C for 15 minutes, and hold at 4 °C for 5 minutes. Following completion of the program all cDNA samples were diluted 5x in dH_2O. The cDNA was then amplified using SYBR Green Universal Master mix (Life Technologies, 4344463) for both IDO and GAPDH (control) expression Each sample was prepared to a total volume of 20 µL in 96-well multiplate PCR plate (BioRad, MLL9601) sealed with a plate sealer (microseal B, BioRad, MSB1001). The qPCR (BioRad, CFX96) program was set to denature at 95 °C for 10 minutes, then amplify (*via* denature at 95 °C for 15 seconds then anneal/extend at 60 °C for 1 minute, repeat 40x).

The fold change of IDO RNA was then calculated using **Equation 8-3**:

Equation 8-3: $2^{((C_{q+IDO}-C_{q+GAPDH})-(C_{q-IDO}-C_{q-GAPDH}))}$

where Cq was the quantification cycle threshold for each of the four treatment conditions: +IDO = amplification with IDO primers from the +IFNγ treatment, -IDO = amplification with IDO primers from the -IFNγ (control) treatment, +GAPDH = amplification with GAPDH primers from the +IFNγ treatment, and -GAPDH = amplification with GAPDH primers from the -IFNγ (control) treatment.

8.1.2. Methods: Chapter 3 – Raman for Internalization

8.1.2.1. HepG2 cell culture

Cells were cultured as described in *section 8.1.6.3*. For imaging experiments, cells were detached from the T-75 culture flasks (CLS-3275, Corning®) following a wash with Dulbecco's phosphate-buffered saline (DPBS, without calcium or magnesium, Gibco, 14190144) and then incubation with Accutase (Sigma, A6964) for 15 minutes. A hemocytometer was used to obtain a live cell count by Trypan Blue (Sigma, T8154) exclusion assay. Cells were replated into 35 mm glass-bottom microscope culture dishes (P35G-1.5-10-C) at a density of 3.0 x 10^4 cells/mL in minimum essential medium (MEM, M4655, Sigma) supplemented with 10 % fetal bovine serum (FBS, heat-inactivated, 10082147, Gibco), 1 % penicillin/streptomycin (Pen-Strep, Hyclone, 100X solution, SV30010), 1 % non-essential amino acids (NEAA, M7145, Sigma), and 0.1 % of a 1 M solution of sodium pyruvate. Cells were incubated overnight (12-18 h) in 5 % CO_2 at 37 °C.

8.1.2.2. Measurement of internalization by SRS

For imaging experiments, the 35-mm glass-bottom microscope dishes containing HepG2 cells in supplemented MEM were transferred to the facilities at the National Research Council (NRC) Sussex. The cells were maintained at room temperature during transfer and then placed into a stage-top incubator (37 °C, 5 % CO_2) upon arrival at the NRC laboratories. A minimum of 5 dishes were transferred for measurement at each given time point. Once ready for imaging, the standard supplemented MEM was removed from each dish and was replaced with supplemented MEM containing 30 mM *m*CNPh-Glc (**37**). Four of the dishes were returned to the stage-top incubator (37 °C, 5 % CO_2), one dish was placed immediately onto the SRS microscope setup for imaging at time=0 h. At each desired time point, a dish was removed from incubation, placed onto the SRS microscope setup, a scanning z-stack was performed to identify a centre of mass of a cell, and then imaging was completed at both 2900 cm^{-1} and 2230 cm^{-1} to obtain signal intensity measurements at the lipid and nitrile wavenumbers respectively.

The methods below for Raman imaging for internalization were reprinted from the open access article published by Adrian F. Pegoraro and Albert Stolow in Optica Express (2024) 10.1364/OE.531274.[519]

"CM-SRS is based upon modification of a spectral focusing AM-SRS setup described previously (…).[520] The current setup is shown in (…) [(**Figure 8-4**)]. Briefly, a dual output Insight DS + laser (Spectra-Physics, USA) produced two synchronized outputs at 80 MHz repetition rate. One (here the SRS Pump beam, blue) is tunable from 680-1300 nm, with a transform-limited pulse duration of approximately 120 fs across this tuning range. The second output (the SRS Stokes beam, red) was centred at a fixed wavelength of 1040 nm and has a transform-limited pulse duration of 220 fs. The Stokes beam was used to generate the requisite co-chirped and contra-chirped configurations, described below. The tunable Pump output was passed through a half-wave plate (λ/2) and polarizing beam splitter (PBS) to control the average power, before being sent to a variable delay stage (DS, for scanning of the Raman spectrum in spectral focusing) and then to a dichroic mirror (DM) recombiner (Pump + Stokes). The fixed 1040 nm Stokes output was sent through a Pockels cell (350-160, Conoptics, USA) modulated at 1 MHz, the driving waveform for which was provided by a function generator (DS345, Stanford Research Systems, USA). For AM-SRS implementations, following a PBS, the rejected output (vertical dashed red line) was blocked and the transmitted output (horizontal dashed red line) was sent to the DM recombiner. The combined Pump and Stokes beams were sent through 60 cm of SF11 glass, thus providing the co-chirped configuration. To ensure that the magnitudes of the linear chirps of the three input beams (pump, co-chirped Stokes, contra-chirped Stokes) are well matched, we utilized the internal, tunable dispersion compensation provided by

the Insight laser to achieve chirp matching at the focus of the microscope. For CM-SRS implementations, the rejected output, used to generate the contra-chirped beam, was sent through a λ/2 plate to rotate the beam to the same polarization state as the co-chirped output, and then to a grating compressor, followed by a delay stage to accurately synchronize the two 1040 nm beams. The co- and contra-chirped Stokes beams were recombined using a 50:50 beam splitter (BS) before being sent to the DM recombiner and the 60 cm SF11 glass. Note that the grating compressor was adjusted so that despite the 60 cm of glass the correct contra-chirped configuration (…) was achieved at the microscope focus. Therefore, by blocking or unblocking the CM-SRS contra-chirped arm, one can seamlessly switch between AM- and CM-SRS. Importantly: for CM-SRS measurements, the modulation between the co- and contra-chirped beams is set by the Pockels cell at 1 MHz rate in the current implementation. The home-built microscope used galvo mirrors (GVSM002-US, Thorlabs, USA) connected to a microscope frame (Olympus IX-71). Measurements of (…) HepG2 cells used a 60x, 1.2 NA water objective (UPlanSapo, 60x, 1.2 NA, Olympus, Japan) (…). In all cases, forward propagating light was collected using an objective lens (LUMPlanFI/IR, 40x, NA 0.8 water immersion, Olympus, Japan). Collected light was filtered (BrightLine 850/310, Semrock, USA and 1064-71 NF, Iridian, Canada) to remove the Stokes light before being sent to a photodiode (PD, FDS10X10, Thorlabs, USA) operating under reverse bias. The photodiode signal was filtered using 1 MHz bandpass RF filter (#3128, KR Electronics, USA) before being amplified by a transimpedance amplifier (DHCPA-100 Femto Messtechnik, GmbH, Germany). The output of the amplifier was sent to a lock-in amplifier (UHFLI, Zurich Instruments) which was referenced to the Pockels cell drive signal. Typically, a 20 μs time constant was used. All data collection and drive of the galvanometer mirrors were synchronized using ScanImage. For all measurements, the power in each 1040 nm arm of the AM and CM-SRS was 50 mW before the microscope. (…) For measurements of HepG2 cells, the tunable beam was set to a central wavelength of 800 nm with average power of 50 mW for measurements around a Raman shift of 2850 cm^{-1}, whereas a central wavelength of 844 nm with an average power of 100 mW was used for measurements around a Raman shift of 2230 cm^{-1}. To acquire Raman spectra, the time delay between the pump and Stokes beams was scanned so as to vary the instantaneous frequency difference between the lasers."

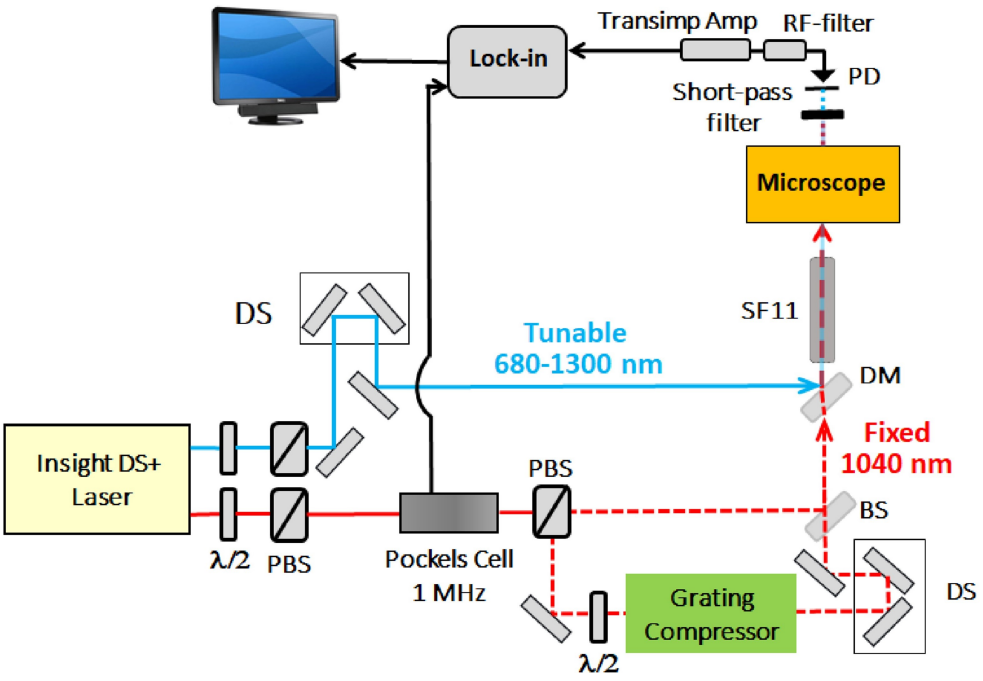


Figure 8-4. Schematic for the CM-SRS microscopy setup for measuring the internalization of *m*CNPh-Glc (**37**) in HepG2 cells.

8.1.3. Methods: Chapter 3 – Red Blood Cells

8.1.3.1. Blood collection and preparation

All red blood cells (RBCs) were obtained from Canadian Blood Services' Network Centre for Applied Development (NetCAD). All experimental protocols were approved by NetCAD and CBS. Ethics approvals were obtained from the research ethics board at CBS and the University of Alberta (the site where experiments were completed). The provided units of whole blood were collected from healthy donors with informed consent using standardized phlebotomy guidelines approved by Canadian Blood Services (CBS). The units were then processed by NetCAD using the buffy coat method to produce leukocyte reduced SAGM RBC units.[330] The red cell concentrate units were sex and blood type ABO Rh matched, pooled, and then re-split into individual units to reduce the impact of donor-to-donor variability on results.

8.1.3.2. RBC freezing and thawing experiments

Compounds to be tested were prepared in duplicate at 2X the desired concentration in a 30 % glycerol solution (57 Glycerolyte, Baxter diluted in 0.9 % saline/0.2 % dextrose). For each desired ice recrystallization inhibitor compound and concentration to be tested, an equal volume of the corresponding freezing solution was added to 150 µL of SAGM RBCs to a total volume of 300 µL (final glycerol concentration 15 %). Three control solutions of 15 % glycerol alone (without any ice recrystallization

inhibitors) were also prepared. RBC suspensions in the desired cryosolutions were transferred to cryotubes and incubated at room temperature for 10 minutes. After incubation the cryotubes were immersed in a methanol bath cooled to -5 °C. A thermocouple was inserted into one of the 15 % glycerol + RBC control cryotubes to monitor the temperature decrease in 1 second increments. When the internal temperature of the cryotube reached -5 °C, ice nucleation of each cryotube was induced mechanically using metal forceps cooled in liquid nitrogen. The cryotubes were then returned to the methanol bath and held at -5 °C for 5 minutes. After the incubation, one cryotube from each duplicate remained in the methanol bath and was cooled at a rate of 1 °C/min to a final internal temperature of -40 °C (the slow-cooling method); the second cryotube from each duplicate was removed from the methanol bath and placed directly into dry ice (-78 °C) (the rapid cooling method). Each cryotube was then thawed in a 37 °C water bath.

8.1.3.3. Post-thaw hemolysis measurement

Post-thaw hematocrit (hct), supernatant hemoglobin, and total hemoglobin levels were used to calculate percent hemolysis were determined following all freezing experiments by comparing the concentration of supernatant hemoglobin (Hgb_s) to the total hemoglobin (Hgb_T) using Drabkin's method.[329,330] Percent hemolysis was calculated using **Equation 8-4**:

Equation 8-4. $\%\ hemolysis = ((100 - hct) \times Hgb_s)/Hgb_T$

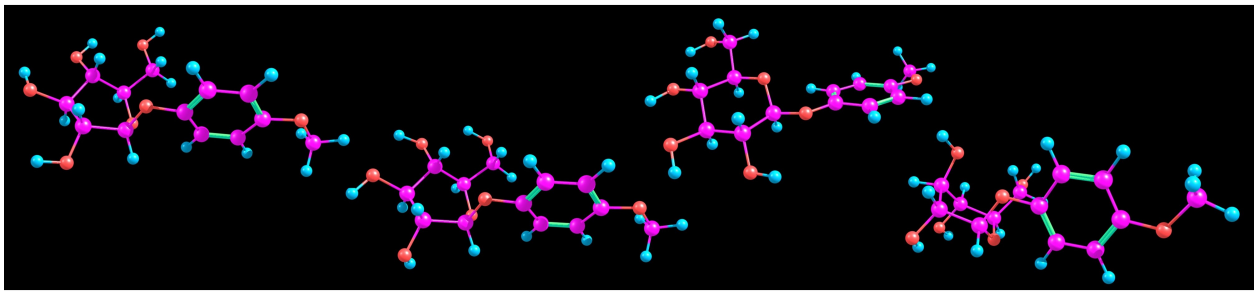
RBC freezing results were reported as the % integrity of the RBCs (calculated as 100 % - % hemolysis).

8.1.4. Methods: Chapter 4 – Optimization of O-aryl-β-D-glucopyranoside structure by computation

The Conformer Rotamer Ensemble Sampling Tool (CREST)[430] was used to perform a conformational search of each given carbohydrate. The structure of the compound was first generated in ChemDraw (23.1.2, Revvity)[414] in three dimensions and saved as a .xyz coordinate file. This file was then used as the baseline "pre-optimization" structure for the compound. The conformational search using CREST (2.11)[430] was run at the GFN2 level of theory[521] with implicit water solvation by the ALPB (analytical linearized Poisson-Boltzmann) model. From the conformational search, several structures were returned as lowest in energy that were not in the $^4C_1$ chair conformation. Therefore, chemical intuition was used to select a sampling of the low energy conformers to be optimized at a higher level of theory with vibrational frequency calculations to select the true lowest energy conformer of the compound of interest. These calculations were completed by ORCA (5.0)[473,474] using the ωb97 functional and DEF2-TZVPP basis set with CPCM implicit water solvation.[431–433] The final optimized structure from ORCA was used to input

into correlation studies to compare the effect of geometry optimization on potential structure-activity relationships to ice recrystallization inhibition activity.

For example, within ~1 kcal/mol of the low energy conformer as calculated by the CREST conformational search for PMP-Glc (**26**), four distinct conformers were obtained and only one of which was in the $^4C_1$ chair conformation. However, once the Gibbs free energy was calculated by ORCA, the conformer in the $^4C_1$ conformation was correctly identified as the low energy structure that was used for correlation studies.



Relative Energy (kcal/mol) *CREST*	0.00	0.68	0.99	1.09
Relative Gibbs Free Energy (kcal/mol) *ORCA*	4.99	5.90	0.00	6.26

Figure 8-5. Comparison of PMP-Glc (**26**) conformers following search by CREST[430] including energy calculations (in kcal/mol) and optimization by ORCA[473,474] with vibrational frequency calculation for energy (in kcal/mol).

8.1.5. Methods: Chapter 6 – NMR Characterization by T_1 and T_2 Relaxation

8.1.5.1. Sample preparation for NMR measurements

For each solute, dilutions were prepared with Milli-Q® water (> 18.2 MΩ·cm) at the highest desired concentration – lower concentration solutions were prepared by serial dilution. 10 mm-diameter TD-NMR tubes (Bruker, Billerica, MA) were filled with 2 mL of each sample solution and sealed with parafilm. Tubes were frozen with -20 °C (-1.7 °C/min) in a commercial freezer overnight and analyzed within 28 days of preparation.

*8.1.5.2. Stability of 2FA (**27**)*

Over the course of the experiments to determine $E_{A_{H_2O}}$, 2FA (**27**) was stored frozen as a solution (maximum concentration 10 mM) in H_2O at -20 °C. To determine the storage shelf-life of 2FA (**27**) under

these conditions, ^{1}H NMR was used to monitor for chemical decomposition over time. 10 mM 2FA (**27**) was prepared in a solution of 10 % D_2O, 90 % H_2O and placed in a -20 °C freezer. Prior to measurement (30-60 minutes), the sample was removed from the freezer to thaw. The sample was mixed immediately prior to measurement. ^{1}H NMR spectra (16 scans, 300 MHz, Bruker) were taken at regular intervals from day 0 up to day 56 with suppression of the water peak at 4.69 ppm. Spectra were calibrated to the residual water peak. No discernible change was observed in the ^{1}H NMR spectra over the course of 56 days, therefore under the specified storage conditions no significant decomposition of 2FA (**27**) was expected over this duration (**Figure 8-6**).

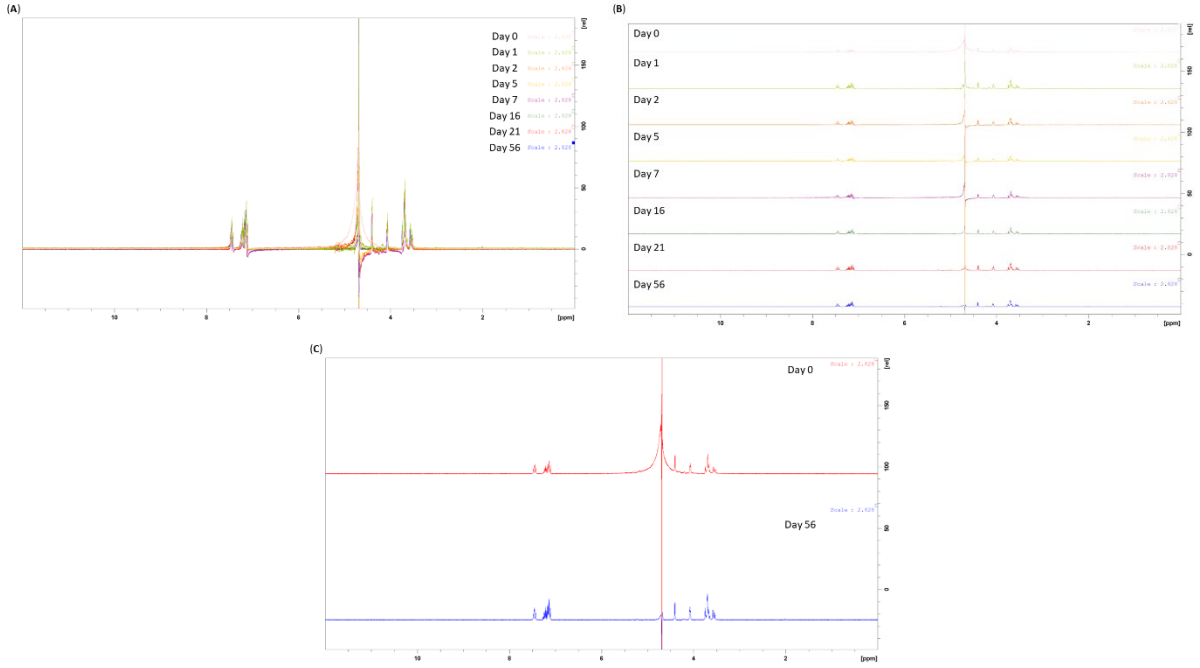
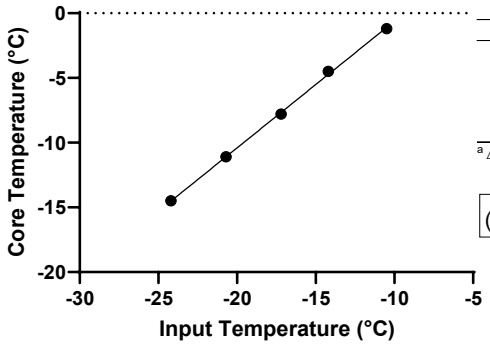


Figure 8-6. ^{1}H NMR for determining the stability of *N*-2-fluorophenyl-D-gluconamide (2FA, **27**, 10 mM) under experimental storage conditions (-20 ˚C in 90 % H_2O, 10 % D_2O) over the course of 56 days. All spectra are scaled to 2.828 intensity for comparison. Water peak is suppressed (4.69 ppm) and spectra are calibrated to the residual water peak (4.69 ppm). (**A**) Overlay of spectra from each day. (**B**) Stack of spectra from each day. (**C**) Direct comparison of day 0 (red) to day 56 (blue).

8.1.5.3. Temperature calibration and equilibration

Due to an observed temperature difference between the input temperature at the instrument controller and the temperature at the core of the sample, a temperature calibration regression was generated to ensure that measurements were taken at the desired sample core temperature (**Figure 8-7**). A K-type thermocouple (Omega Instruments, 5SRTC-TT-K-40-72-ROHS) was inserted and frozen into the centre of the sample to allow for real-time measurement of the sample's core temperature every second (using a temperature logger, Omega Instruments, RDXL6SD-USB). For temperature measurement, the sample with

an inserted thermocouple was removed from the -20 °C freezer and directly inserted into the pre-cooled NMR (249 K or -24.2 °C). Following stabilization of the sample's core temperature (observed in real-time), the set temperature of the controller was increased in regular intervals from 249 K (-24.2 °C) to 262.7 K (-10.5 °C). These temperatures were selected based on the coldest temperature that the controller and instrument components could consistently reach and such that the sample remained frozen throughout the entire measurement period.



Time (hh:mm:ss)	T_I (K)	T_C (°C)	T_A (°C)	Δ (°C) [a]
00:10:19	249	-24.2	-14.5	9.7
00:15:19	252.5	-20.7	-11.1	9.6
00:22:34	256	-17.2	-7.8	9.4
00:27:46	259	-14.2	-4.5	9.7
00:32:48	262.7	-10.5	-1.2	9.3

[a] $\Delta = T_A$ (°C) – T_C (°C)

$(T_C) = 0.9786*(T_I) + 9.169$, $R^2 = 0.99$

Figure 8-7. Temperature calibration fit to a linear regression. The required input temperature (T_I) was calculated for any given desired core temperature (T_C) given $T_C = 0.9786(T_I) + 9.169$, $R^2 = 0.99$.

A linear regression fit of the temperature data could then be used to derive the required input temperature (T_I) for each desired core temperature (T_C) of the sample (**Equation 8-5**):

Equation 8-5: $T_C = 0.9786(T_I) + 9.169$

Equilibration of sample's core to the set temperature of the controller was achieved after 5 minutes (**Figure 8-8**). Therefore, for ^{1}H NMR relaxation time measurement tubes were given 5 minutes to stabilize at the set temperature prior to measurement. All temperatures presented throughout *chapter 6* were reported as sample core temperatures after equilibration to the set temperature.

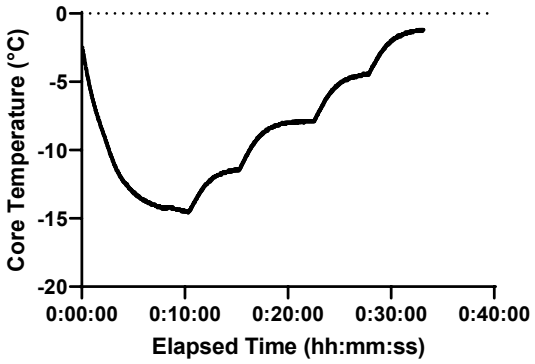


Figure 8-8. Equilibration of pure Milli-Q® water sample core temperature (°C) to set input temperature. Temperature recorded every second using a K-type thermocouple (5SRTC-TT-K-40-72-ROHS) on an Omega temperature data-logger (RDXL6SD-USB) for a total duration of 35 minutes.

8.1.5.4. NMR measurements

^{1}H relaxation experiments were carried out with a Bruker Minispec mq20 TD-NMR spectrometer (Bruker, Billerica, MA) operating at 0.47 T and 20 MHz and equipped with a temperature control unit. Calibration of the temperature control unit and evaluation of time to temperature equilibration of the samples were performed with a thermocouple inserted in an NMR tube filled with 2 mL of water and positioned in the spectrometer's probe. Each sample was equilibrated at the set temperature for 5 minutes prior to measurement. ^{1}H relaxation was measured at sample temperatures ranging from 258.2 K (-15 °C) to 303.2 K (+30 °C).

Spin-spin (T_2) relaxation was characterized from Free Induction Decay (FID, sampling rate of 1 μs^{-1}) and from the Carr-Purcell-Meiboom-Gill (CPMG) sequence (pulse interval τ between 0.04 and 3 ms). Spin-lattice (T_1) relaxation was characterized from an inversion-recovery (IR) sequence. 90 to 100 data points were acquired between 30 ms and the recovery delay after the beginning of the sequence. Recovery delay times ranged between 35 s at 258.2 K and 10 s at 270.2 K. Each experiment (sample x temperature) was measured in triplicate with data reported as the mean ± standard deviation of the mean.

8.1.5.5. NMR data processing

Relaxation curves obtained from FID, CPMG, and IR sequences were processed with MS Excel Solver (Microsoft, Redmond, WA). The FID curves were fitted with a bi-gaussian function (**Equation 8-6**):

Equation 8-6: $$S_{FID}(t) = I_{FID-1} \times e^{(-(\frac{t}{T_{2-FID-1}})^2)} + I_{FID-2} \times e^{(-(\frac{t}{T_{2-FID-2}})^2)} + (cst)$$

where $S_{FID}(t)$ was the intensity of the FID signal measured over time t, $T_{2-FID-1}$, and $T_{2-FID-2}$ were the characteristic spin-spin relaxation times of the signal, and I_{FID-1} and I_{FID-2} were the characteristic intensities of the components of the FID relaxation signal.

The CPMG curves were fitted with a bi-exponential function (**Equation 8-7**):

Equation 8-7: $$\boldsymbol{S_{CPMG}(t) = I_{CPMG-1} \times e^{\left(-\left(\frac{t}{T_{2-CPMG-1}}\right)\right)} + I_{\mathbf{CPMG-2}} \times e^{\left(-\left(\frac{t}{T_{2-CPMG-2}}\right)\right)} + (cst)}$$

where $S_{CPMG}(t)$ was the intensity of the CPMG signal measured over time t, $T_{2-CPMG-1}$, and $T_{2-CPMG-2}$ were the characteristic spin-spin relaxation times of the signal, and I_{CPMG-1} and I_{CPMG-2} were the characteristic intensities of the components of the CPMG relaxation signal.

The inversion recovery (IR) curves were fitted with a bi-exponential function (**Equation 8-8**):

Equation 8-8: $$\boldsymbol{S_{IR}(t) = I_{IR-1} \times \left(1 - e^{\left(-\left(\frac{t}{T_{1-IR-1}}\right)\right)}\right) + I_{\mathbf{IR-2}} \times \left(1 - e^{\left(-\left(\frac{t}{T_{1-IR-2}}\right)\right)}\right) + (cst)}$$

where $S_{IR}(t)$ was the intensity of the IR signal measured over time t, T_{1-IR-1}, and T_{1-IR-2} were the characteristic spin-lattice relaxation times of the signal, and I_{IR-1} and I_{IR-2} were the characteristic intensities of the of the components of the IR relaxation signal.

FID, CPMG and IR curves were fitted with bi-gaussian and bi-exponential functions in search of multiple relaxation components. However, only negligible or artefactual secondary relaxation components were observed. Therefore, only results of mono-gaussian and mono-exponential fits are presented in the results of this study.

8.1.5.6. Calculation of activation energy

The natural logarithms of T_{2-FID}, T_{2-CPMG}, and T_{1-IR} were plotted against reciprocal temperature ($1/T$ in K^{-1}). The plots were fitted with a linear function (**Equation 8-9**):

Equation 8-9: $$\boldsymbol{lnT_i = \beta \times {}^{1}/_{T} + \varepsilon}$$

where T_i was a relaxation time in seconds (either T_{2-FID}, T_{2-CPMG}, or T_{1-IR}) and T is the temperature in Kelvin (K). Activation energy of molecular motion ($E_{A_{H_2O}}$ in $kJ \cdot mol^{-1}$) was calculated from the slope of the linear correlations (β) with **Equation 8-10** where the universal gas constant $R = 0.008314\ kJ \cdot K^{-1} \cdot mol^{-1}$.

Equation 8-10: $E_{A_{H_2O}} = -R \times \beta$

8.1.5.7. Statistical analysis

Values were reported as mean ± standard deviation (SD) of three measurements unless otherwise specified. Significant differences were established with one-way ANOVA. GraphPad Prism 9 software (GraphPad Software Inc., San Diego CA) was used to perform statistical analysis, to make graph plots, and to model the IRI activity plots.

8.1.6. Methods: General

8.1.6.1. Nanolitre osmometry assay for the determination of dynamic ice shaping (DIS)

Nanolitre osmometry was performed using a Clifton nanolitre osmometer (Clifton Technical Physics, Hartford, NY), as previously described by Chakrabartty and Hew.[96] All measurements were performed with the sample of interest prepared in MilliQ® water. Temperature was controlled by a programmable Peltier unit (S3 Series 800, Alpha Omega Instruments) connected to an 99 % ethanol:ethylene glycol (50:50) chilling bath (NESLAB RTE7, ThermoScientific). A 1 µL droplet of the sample of interest was placed into an oil-filled well of the osmometer. The sample was frozen and slowly thawed until a single ice crystal remained suspended in oil. Ice crystal morphology (both still images and video recordings) was observed through a Leitz compound microscope equipped with an Olympus 20× (infinity-corrected) objective and a Leitz Periplan 32X photo eyepiece using a Hitachi KPM2U CCD camera connected to a Toshiba MV13K1 TV/VCR system as previously described.[161]

8.1.6.2. Ice recrystallization inhibition

Ice recrystallization inhibition activity was determined using a modified splat cooling assay.[169,170] The candidate compound of interest was dissolved in phosphate-buffered saline (PBS) and serially diluted to the desired concentrations for testing. To test each compound concentration, a 10 µL droplet of solution was dropped from a height of two metres onto a polished aluminum block cooled to -78 °C using dry ice. The wafer was then transferred from the aluminum block onto a glass coverslip and placed into a cryostage held at -6.4 °C by a programmable Peltier temperature control unit (S3 Series 800, Alpha Omega Instruments) connected to an 99 % ethanol:ethylene glycol (50:50) chilling bath (NESLAB RTE7, ThermoScientific) where it was left to anneal for five minutes. The wafer was then imaged using a digital camera (Nikon OEM) fitted to a microscope and the ice crystal area was analyzed from each image (containing a minimum of 30 ice crystals) using ImageJ[522]. Ice crystal areas were sorted into bins (in increasing increments of 0.001 mm^2) using Microsoft Excel and the proportionate area of each bin was calculated by summing the area of each crystal within said bin and dividing by the sum of the area of all

crystals in the image. For each IRI concentration, three ice wafers were analyzed, and the average rate of ice crystal growth over the 5-minute annealing period was determined and normalized to the positive control (PBS). A plot of the normalized rate constants (v_{norm}) against log-transformed concentrations were fitted with a two-parameter sigmoidal curve (where the top and bottom plateaus are set to 100 and 0 respectively) to enable determination of the IC_{50} according to **Equation 8-11**:

Equation 8-11. $$v_{norm} = \frac{100}{1+10^{[(HillSlope)(logIC_{50}-log[Compound])]}}$$

8.1.6.3. General cell culture: HepG2

HepG2 (human liver hepatocellular carcinoma cells, ATCC, HB-8065) were thawed from stock (stored in liquid nitrogen vapour in cell culture media + 10 % dimethyl sulfoxide) and cultured in T-75 flasks (CLS-3275, Corning®) at a density of 1.0 x 10^6 cells/flask in minimum essential medium (MEM, M4655, Sigma) supplemented with 10 % fetal bovine serum (FBS, heat-inactivated, 10082147, Gibco), 1 % penicillin/streptomycin (Pen-Strep, Hyclone, 100X solution, SV30010), 1 % non-essential amino acids (NEAA, M7145, Sigma), and 0.1 % of a 1 M solution of sodium pyruvate. The plated cells were incubated at 37 °C in 5 % CO_2 and the cell culture medium was changed every 48-72 hours. Once cells reached 80-85 % confluency (approximately one week after plating) they were washed with Dulbecco's phosphate-buffered saline (DPBS, without calcium or magnesium, Gibco, 14190144) and then incubated with Accutase (Sigma, A6964) for 15 minutes to detach the cells from the flask. A hemocytometer was used to obtain a live cell count by Trypan Blue (Sigma, T8154) exclusion assay. Cells were replated into 75 cm^2 flasks to be passaged for continued cell culture or were used in the appropriate cytotoxicity assays.

8.1.6.4. HepG2 cytotoxicity assay: Resazurin

To the wells of a 96-well plate (3370, Corning ®, clear & flat-bottomed, uncoated) was added 10,000 cultured HepG2 cells (passage 8-19) in 100 µL supplemented MEM (components described above in *section 8.1.6.3*) per well. The plate was then incubated at 37 °C in 5 % CO_2 for 12 to 24 hours to ensure cell attachment. The cell culture medium was then aspirated and replaced with 100 µL supplemented MEM containing the compound of interest at different concentrations prepared by serial dilution (n≥3 wells per concentration). A set of wells was reserved as a fluorescence blank that did not contain cells and were filled with 100 µL supplemented MEM without compound. A second set of wells was reserved as the positive control, where the cells were exposed to 100 µL supplemented MEM without compound. A third set of wells was reserved as the negative control, where the cells were exposed to 100 µL supplemented MEM containing 1 % Triton-X-100 (Sigma, X100). The plate was then incubated for the desired period of exposure time (1-24 hours) at 37 °C in 5 % CO_2. Following incubation, 10 µL of 498 µM resazurin (CAS 62758-13-8) prepared in sterile DPBS was added to each well in the dark. The plate was then incubated in

the dark for 4 hours at 37 °C in 5 % CO_2 after which the fluorescence of each well was recorded by a SpectraMax Absorbance microplate reader using a 530 nm excitation wavelength and a 590 nm emission wavelength. The average fluorescence reading from the blank wells was subtracted from all other well readings. The % viability of cells in each well was then calculated according to **Equation 8-12**:

Equation 8-12. $\%\ \boldsymbol{viability} = \left(\frac{\boldsymbol{F_{sample} - F_{neg}}}{\boldsymbol{F_{pos} - F_{neg}}}\right)(\mathbf{100}\ \%)$

where F_{sample} is the fluorescence reading of a cell containing the concentration or compound of interest, F_{neg} is the average fluorescence reading of all cells plated as the negative control, and F_{pos} is the average fluorescence reading of all cells plated as the positive control.

For each compound tested at multiple concentrations, a plot of the % viability against log-transformed concentrations was fit with a two-parameter sigmoidal curve (where the top and bottom plateaus are set to 100 and 0 respectively) to enable determination of the LD_{50} according to **Equation 8-13**:

Equation 8-13. $v_{norm} = \frac{100}{1+10^{[(HillSlope)(logIC_{50} - log[Compound])]}}$

8.1.6.5. HepG2 cytotoxicity assay: Lactate dehydrogenase (LDH) assay

Cytotoxicity by the lactate dehydrogenase (LDH) assay was assessed using the Pierce LDH Cytotoxicity Assay kit by ThermoFisher Scientific (#88954). To a 96-well plate (3370, Corning®, clear & flat bottomed, uncoated) was added 7,500 cultured HepG2 cells (passage 8 to 19) in 100 µL supplemented MEM (components described above in *section 8.1.6.3*) per well. The plate was then incubated at 37 °C and 5% CO_2 for 12 to 24 hours to cell attachment. The cell medium was then aspirated and replaced with 100 µL supplemented MEM with the target compound added at the desired concentrations for testing (n≥3 wells per concentration). A set of wells were reserved as blanks with no cells, containing only 100 µL supplemented MEM. A set of wells were reserved as the positive control (spontaneous LDH release), where the cells were exposed to only 100 µL supplemented MEM (no compound). A set of wells was reserved as the negative control (maximum LDH release), where the cells were exposed to 100 µL supplemented MEM and 10 uL of lysis buffer (from the LDH kit). The plate was then incubated with the compound containing supplemented MEM for the desired period of time (1-24 hours) at 37 °C at 5 % CO_2. Following incubation, the cell culture plate was agitated gently and 50 µL of the supernatant from each well was transferred to a new 96-well plate (3370, Corning®, clear & flat bottomed, uncoated). To the new 96-well plate, 50 µL of the reaction mixture (made from 600 µL of assay buffer + 11.4 mL of substrate stock solution from the LDH kit) was added to each well. The plate was gently mixed and then incubated protected from light for

30 minutes at room temperature. After incubation, 50 µL of stop solution (from the LDH kit) was added to each sample well. The plate was gently mixed followed be reading of the absorbance of each well (within 1-2 hours of the addition of stop solution) by a SpectraMax Absorbance microplate reader at both 490 nm and 680 nm wavelengths. The absorbance reading from each well at 680 nm was subtracted from the corresponding well's absorbance reading at 490 nm; the average absorbance reading from the blank wells was subtracted from all other wells. The absorbance reading of given test condition was presented as % viability calculated using **Equation 8-14**:

Equation 8-14. $\%\ \boldsymbol{Cytotoxicity} = \frac{\boldsymbol{compound\ treated\ LDH\ activity - spontaneous\ LDH\ activity}}{\boldsymbol{maximum\ LDH\ activity - spontaneous\ LDH\ activity}}(\mathbf{100}\%)$

For each compound tested at multiple concentrations, a plot of the viability (1-cytotoxicity) against log-transformed concentrations was fitted to two-parameter sigmoidal curve (where the top and bottom plateaus are set to 100 and 0 respectively) to enable determination of the LD_{50} according to **Equation 8-13**.

8.1.6.6. Graphical representations and statistics

All graphical representations and statistical analyses were completed using GraphPad Prism 9 Software (Boston, MA, USA, www.graphpad.com).[523]

8.1.7. General Experimental

D-galactose (**7**, CAS # 59-23-4), D-glucose (**8**, CAS # 50-99-7), and D-mannose (**9**, CAS # 3458-28-4) were used directly from commercially available sources. Mono-deuterated glucose derivatives were purchased from Cambridge Isotope Laboratories and tested for IRI activity directly upon receiving.

- **94**: D-glucose (1-D1, 98%), DLM-1150-0.25, CAS# 106032-61-5, Lot# I-17852
- **95**: D-glucose (2-D1, 98%), DLM-1271-0.25, CAS# 106032-60-4, Lot# I-15143
- **96**: D-glucose (3-D1, 97-98%), DLM-3557-0.1, CAS# 51517-59-0, Lot# I-23680

Other commercially available and tested materials included *p*-nitrophenyl-β-D-glucopyranoside (*p*NO_2Ph-Glc, **85**, CAS # 2492-87-7), D-galactose (**7**, CAS # 59-23-4), D-glucose (**8**, CAS # 50-99-7), and D-mannose (**9**, CAS # 3458-28-4).

All chemical reagents were purchased from commercial sources and used without further purification unless otherwise indicated. Reactions were monitored by thin layer chromatography (TLC) on 0.2 mm pre-coated silica gel on aluminum (60 F_{254}, E. Merck) visualized using ultra-violet light (254 nm). Where appropriate, TLC plates were stained for visualization using orcinol (0.2 w/v % orcinol and 11.4 v/v

% H_2SO_4 in water), permanganate (1 w/v % $KMnO_4$, 3.33 w/v % K_2CO_3 in water), *p*-anisaldehyde (2.67 v/v % *p*-anisaldehyde, 3.33 v/v % H_2SO_4, and 1.33 v/v % acetic acid in ethanol), or ninhydrin (0.2 w/v % ninhydrin in ethanol). Flash chromatography was performed using SiliCycle silica gel (R12030B, 230-400 mesh, 40-63 μm, 60 Å) or using the SepaBean Machine T (SPBT02000200-1, Santai Science) with SepaFlash standard series cartridges (40-63 μm, 60 Å, S-5101, Santai Science). pH testing was completed using wide-range pH paper (Hydrion, pH 10.0 to 13.0) or a digital pH meter. Where required, reactions completed under anhydrous conditions were run under argon atmosphere and the transfer of air/water sensitive reagents was completed using oven-dried needles and disposable sterile Luer-lock syringes (76837, VWR). Anhydrous toluene, dichloromethane (DCM), and acetonitrile (MeCN) were dispensed from a benchtop solvent purifier (SPBT-1, LC Technology Solutions Inc) using the recommended purification columns; anhydrous dimethyl sulfoxide (DMSO), *N,N*-dimethylformamide (DMF), or tetrahydrofuran (THF) were dried and stored over activated 4 Å beaded molecular sieves (208604, Sigma).[524]

All nuclear magnetic resonance (NMR) spectroscopy for compound characterization was performed using a Bruker Avance 300, 400, 500, or 600 MHz instrument (Bruker, Madison, WI) at ambient temperature and pressure and NMR solvents were used as indicated for each characterization; the NMR solvents included deuterated water (D_2O), deuterated chloroform ($CDCl_3$), deuterated methanol (MeOD-d_4), deuterated DMSO (DMSO-d_6), or deuterated acetone ($CO(CD_3)_2$-d_6). All spectral data were reported as the chemical shift (in ppm) referenced using the corresponding residual solvent peaks. Splitting patterns were reported as: singlet (s), doublet (d), triplet (t), quartet (q), quintet (qu), sextet (sxt), septet (sept), multiplet (m), broad (br), doublet of doublets (dd), doublet of doublet of doublets (ddd), or doublet of triplets (dt). For characterization and identification of novel synthesized compounds, both ^1H (proton) and ^{13}C (carbon) NMR were reported using DEPT-135, ^1H-^1H COSY, ^1H-^1H NOSEY, and ^1H-^{13}C HSQC spectra where appropriate to assign all molecular signals. High resolution mass spectrometry (HRMS) or low resolution mass spectrometry (LRMS) was performed on novel compounds by the John L. Holmes Mass Spectrometry Facility (University of Ottawa, Ottawa, ON) using a Micromass Q-TOF mass spectrometer (Waters Corporation, Milford, MA) in positive electrospray ionization mode (ESI+).

In general, if a material was tested for ice recrystallization inhibition activity or used in a cellular application it was lyophilized prior to use. Where lyophilization was required to isolate the final product it was explicitly stated within the synthetic procedure for that derivative.

8.1.8. General Procedures

General Procedure 8-1: Lactone opening with anilines to produce an *N*-aryl-aldonamide

The following general procedure was adapted from literature.[166] δ-Gluconolactone (**511**, 1.0 eq) was dissolved in acetic acid (0.2 M) and the desired aniline (1.5 eq) was added. The solution was stirred at 100 °C for 1.5 hours and then concentrated. Once dry, the crude was purified by recrystallization or by hot solvent washes to yield the corresponding *N*-aryl-D-gluconamide.

General Procedure 8-2: Lewis-acid assisted glycosidation with phenols to produce an *O*-aryl-β-glucopyranoside

The following general procedure was adapted from literature.[167,525] β-D-glucose pentaacetate (**503**, 1.0 eq) and the desired phenol (1.1-1.2 eq) were dissolved in dry DCM (0.25 M) in a flame dried flask under argon at 0 °C with 4 Å molecular sieves (powdered). Boron trifluoride diethyl etherate (2.5 eq) was added to the solution slowly. The solution was stirred overnight (~18 h) at room temperature. The reaction solution was then diluted with DCM and quenched with the slow addition of a saturated solution of $NaHCO_3$. The solution was filtered through Celite® and the organic layer (DCM) was washed using sat. $NaHCO_3$, H_2O, and brine. The organic layer was dried using Na_2SO_4, filtered, and concentrated *in vacuo*. The crude was purified by column chromatography or recrystallization to provide the corresponding acetate-protected *O*-aryl-β-glucopyranoside.

General Procedure 8-3: Zemplén deacetylation

The following general procedure was adapted from literature.[167,326] The desired acetate-protected *O*-aryl-β-glucopyranoside (1.0 eq) was dissolved in MeOH (0.1-0.2 M). NaOMe (1 M solution in MeOH) (0.1 to 1.0 eq) was added to the solution and it was stirred at room temperature until reaction completion (monitored by TLC, ~1-2 hours). Upon reaction completion, Amberlite® IR-120 (H+) ion-exchange resin (pre-washed with MeOH) was added to a solution pH < 4 (monitored by indicating pH paper, Hydrion wide range). The solution was filtered through cotton, and the filtrate was concentrated *in vacuo*. If necessary, the product was purified by recrystallization to yield the corresponding deprotected *O*-aryl-β-pyranoside.

General Procedure 8-4: Acetylation using NaOAc and Ac_2O

The following general procedure was adapted from literature.[214] The desired carbohydrate (1.0 eq) was dissolved in acetic anhydride (7.0 eq) in a flame-dried flask under argon. NaOAc (3.0 eq) was added to the reaction mixture and it was stirred at 100 °C for two hours. Reaction progress was monitored *via* TLC, and upon completion the reaction was cooled, diluted with DCM, and washed with water. The organic phase was dried with Na_2SO_4, filtered, and concentrated *in vacuo*. The

desired product can generally be used in the next step without further purification as a mixture of alpha and beta products or can be purified by column chromatography if necessary.

General Procedure 8-5: Methylation of a free hydroxyl

The desired compound with a free hydroxyl (1.0 eq) was dissolved in DMF (0.1 M) in a flame-dried flask under argon at 0 °C. NaH (60 % dispersion in mineral oil) (2.0 eq) was added and the solution was stirred for 5 minutes. MeI (5.0 eq) was added dropwise and the reaction was stirred at room temperature for 24 hours. The reaction was then diluted with DCM and washed with dH_2O and brine. The organic phase was dried using Na_2SO_4, filtered, and concentrated *in vacuo*. The crude was purified by column chromatography if necessary to provide the corresponding pure methylated compound.

General Procedure 8-6: Benzylation of a free hydroxyl

The desired compound (1.0 eq) was dissolved in DMF (0.1 M) in a flame-fried flask under argon at 0 °C. NaH (60 % dispersion in mineral oil) (1.5 eq per hydroxyl to be protected) was added and the solution was stirred for 5 minutes. BnBr (1.2 eq per hydroxyl to be protected) was added dropwise and the reaction was stirred at room temperature for 24 hours. The reaction was diluted in DCM and washed with dH_2O and brine. The organic phase was dried using Na_2SO_4, filtered, and concentrated *in vacuo*. The crude was purified by column chromatography if necessary to provide the corresponding pure benzylated compound.

General Procedure 8-7: Removal of benzyl protecting groups by hydrogenation

The desired benzyl protected compound (1.0 eq) was dissolved in a 2:1 or 1:1 mixture of EtOAc and MeOH (0.06 M), Pd/C (10 mol %) (0.1 eq-1.0 eq) was added and the reaction mixture was purged several times with H_2. The mixture was stirred under H_2 atmosphere until complete by TLC, filtered over Celite® and the volatiles were evaporated to afford the desired deprotected pyranoside product. If necessary, the product was purified by recrystallization.

8.2. Synthesis and Characterization

8.2.1. Properties and description of antifreeze protein AFP1

Prof. Sakae Tsuda from the National Institute of Advanced Industrial Science and Technology (AIST) in Sapporo, Japan provided the sample and all descriptive data for AFP1.

Source: Barfin plaice, *Pleuronectes pinnifasciatus*

Components: Mixture of 7 isoforms

Amino Acid Sequence: DTASDAAAAAAATAAAAAAAAAATAKAAAEAAAATAAAAR

Molecular Weight: 3285.53 Da (40 residues)

Calculated pI: 4.56

Maximum Thermal Hysteresis: 3.2 ˚C @ 500 mg/mL

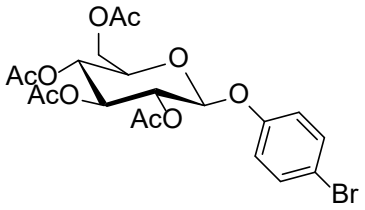
Heat Stability: 70% recovered after heating to 95 ˚C

Tolerable pH: 3 – 11

Target Ice Plane: 2˚ prism plane (whole planes if concentrated)

8.2.2. Synthetic Procedures and Compound Characterization

8.2.2.1. Previously established and widely applied ice recrystallization inhibitors

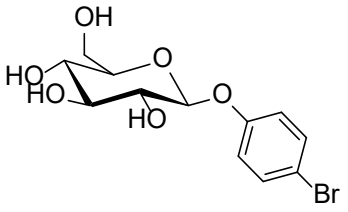


(4-bromophenyl)-2,3,4,6-tetra-*O*-acetyl-β-D-glucopyranoside (526): The title compound was synthesized according to a modified **General Procedure 8-2**.[167,525] β-D-glucose pentaacetate (**503**, 25.7 mmol, 1.0 eq) and 4-bromophenyl (31.3 mmol, 1.2 eq) were dissolved in dry DCM (0.25 M) in a flame dried flask under argon at 0 ºC with 4 Å molecular sieves (powdered). Boron trifluoride diethyl etherate (48 % solution) (64.2 mmol, 2.5 eq) was added to the solution slowly. The solution was stirred overnight (18h) and then quenched with sat. $NaHCO_3$ upon reaction completion. The solution was diluted in DCM, filtered through a Celite® pad, and then washed using sat. $NaHCO_3$, H_2O, and brine. The organic layer was dried using Na_2SO_4, filtered, and concentrated *in vacuo*. If necessary, the crude white powder was purified by recrystallization from EtOAc/Hexanes to yield the final product as a white powder (**82 %**).

Characterization was consistent with that found in literature.[162]

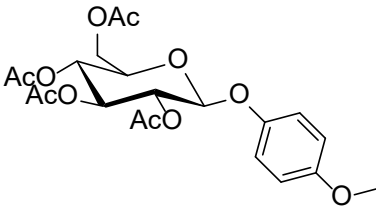
^{1}H NMR: (400 MHz, $CDCl_3$) *∂*7.41-7.38(m, 2H, *arom.*), 6.89-6.86(m, 2H, *arom.*), 5.31-5.22(m, 2H, H-2 and H-3), 5.15(t, *J* = 9.8 Hz, 1H, H-4), 5.03(d, *J* = 7.5 Hz, 1H, H-1). 4.28(dd, *J* = 12.3, 5.4 Hz, 1H, H-6a), 4.16(dd, *J* = 12.3, 2.4 Hz, 1H, H-6b), 3.84(ddd, *J* = 10.0, 5.3, 2.4 Hz, 1H, H-5), 2.07(s, 3H, OAc *CH_3*), 2.06(s, 3H, OAc CH_3), 2.04(s, 3H, OAc CH_3), 2.03(s, 3H, OAc CH_3). **^{13}C NMR:** (101 MHz, $CDCl_3$) *∂* = 170.7 (OAc C), 170.4 (OAc C), 169.5 (OAc C), 169.4 (OAc C), 156.0 (C *arom.*), 132.6 (2xCH), 119.0 (2xCH), 116.1 (C *arom.*), 99.3 (C-1), 72.8 (C-3/C-2), 72.3 (C-5), 71.3 (C-3/C-2), 68.3 (C-4), 62.0 (C-6 CH_2), 20.81 (OAc CH_3), 20.76 (OAc CH_3), 20.74 (OAc CH_3), 20.72 (OAc CH_3).

(4-bromophenyl)-β-D-glucopyranoside (*p*BrPh-Glc, 25): The title compound was synthesized according to **General Procedure 8-3**.[167,326] (4-bromophenyl)-2,3,4,6-tetra-*O*-acetyl-β-D-glucopyranoside (**526**, 21.2 mmol, 1.0 eq) was dissolved in MeOH (0.07 M) and a 1 M solution of NaOMe in MeOH (3.0 mmol, 0.15 eq) was added to the solution to stir for 1 hour. Upon reaction completion, Amberlite IR120 H+ resin (washed in MeOH) was added to a pH < 4. The solution was filtered, and the filtrate was concentrated *in vacuo*. The product was recrystallized from MeOH to yield the final product as a white powder (**83 %**).



^{1}H NMR: (400 MHz, DMSO-d_6) ∂7.47-7.43(m, 2H, *arom.*), 7.01-6.97(m, 2H, *arom.*), 5.33(d, *J* = 4.8 Hz, 1H, O*H*-2), 5.10(d, *J* = 4.5 Hz, 1H, O*H*-3), 5.03(d, *J* = 5.3 Hz, 1H, O*H*-4), 4.85(d, *J* = 7.4 Hz, 1H, H-1), 4.56(t, *J* = 5.7 Hz, 1H, O*H*-6), 3.68(ddd, *J* = 11.7, 5.2, 1.8 Hz, 1H, H-6a), 3.48-3.42(m, 1H, H-6b), 3.32-3.12(m, 4H, H-2 and H-3 and H-4 and H-5). **^{13}C NMR:** (101 MHz, DMSO-d_6) ∂ = 156.7 (C *arom.*), 132.1 (2xCH), 118.5 (2xCH), 113.3 (C *arom.*), 100.4 (C-1), 77.1 (C-2/C-3/C-4/C-5), 76.5 (C-2/C-3/C-4/C-5), 73.2 (C-2/C-3/C-4/C-5), 69.7 (C-2/C-3/C-4/C-5), 60.7 (C-6 CH_2). **LRMS (ESI):** m/z calcd for $C_{12}H_{15}BrO_6Na$ $[M+Na]^+$ 357.0 and 359.0, found 357.0 and 359.0.

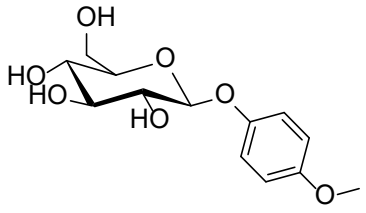
(4-methoxyphenyl)-2,3,4,6-tetra-*O*-acetyl-β-D-glucopyranoside (519): The title compound was synthesized according to a modified **General Procedure 8-2**.[167,525] β-D-glucose pentaacetate (**503**, 13.1 mmol, 1.0 eq) and 4-methoxyphenol (18.6 mmol, 1.5 eq) were dissolved in dry DCM (0.6 M) in a flame dried flask under argon at 0 ºC with 4 Å molecular sieves (powdered). Boron trifluoride diethyl etherate (48 % solution) (28.8 mmol, 2.5 eq) was added to the solution slowly. The solution was stirred overnight (18 h) and then quenched with sat. $NaHCO_3$ upon reaction completion. The solution was diluted in DCM, filtered through a Celite® pad, and then washed using sat. $NaHCO_3$, H_2O, and brine. The organic layers were dried using Na_2SO_4, filtered, and concentrated *in vacuo*. If necessary, the crude white powder was purified by recrystallization from EtOAc/Heptanes or EtOAc/Hexanes to yield the final product as a white powder (**80 %**).



Characterization was consistent with that found in literature.[167]

^{1}H NMR: (400 MHz, $CDCl_3$) ∂6.97-6.92(m, 2H, *arom.*), 6.84-6.78(m, 2H, *arom.*), 5.31-5.20(m, 2H), 5.16(t, *J* = 9.8 Hz, 1H), 4.95(d, *J* = 7.7 Hz, 1H, H-1), 4.29(dd, *J* = 12.4, 5.3 Hz, 1H, H-6a), 4.16(dd, *J* = 12.2, 2.5 Hz, 1H, H-6b), 3.80(ddd, *J* = 10.0, 5.2, 2.5 Hz, 1H, H-5), 3.77(s, 3H, OCH_3), 2.08(s, 3H, OAc CH_3), 2.07(s, 3H, OAc CH_3), 2.04(s, 3H, OAc CH_3), 2.03(s, 3H, OAc CH_3).

(4-methoxyphenyl)-β-D-glucopyranoside (PMP-Glc, 26): The title compound was synthesized according to **General Procedure 8-3**.[167,326] (4-methoxyphenyl)-2,3,4,6-tetra-*O*-acetyl-β-D-glucopyranoside (**519**, 10.5 mmol, 1.0 eq) was dissolved in MeOH (0.2 M) and a 1 M solution of NaOMe in MeOH (1.0 mmol, 0.1 eq) was added to the solution to stir for 1 hour. Upon reaction completion, Amberlite IR120 H+ resin (washed in MeOH) was added to a pH < 4. The solution was filtered, and the filtrate was concentrated *in vacuo*. The product was recrystallized from 99 % EtOH to yield the final product as a white powder (**98 %**).

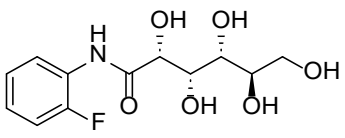


Characterization was consistent with that found in literature.[167]

^{1}H NMR: (400 MHz, D_2O) ∂7.10-7.06(m, 2H, *arom.*), 6.97-6.92(m, 2H, *arom.*), 4.97(d, *J* = 7.6 Hz, 1H, H-1), 3.89(dd, *J* = 12.4, 2.1 Hz, 1H, H-6a), 3.77(s, 3H, OCH_3), 3.71(dd, *J* = 12.5, 5.7 Hz, 1H, H-6b), 3.58-3.42(m, 4H, H-2 and H-3 and H-4 and H-5). **^{13}C NMR:** (101 MHz, D_2O) ∂ = 154.7 (*arom.* C), 150.8 (*arom.* C), 118.1 (2xCH *arom.*), 115.0 (2xCH *arom.*), 101.1 (C-1), 76.0 (C-2/C-3/C-4/C-5), 75.5 (C-2/C-3/C-4/C-5), 72.9 (C-2/C-3/C-4/C-5), 69.4 (C-2/C-3/C-4/C-5), 60.5 (C-6 CH_2), 55.7 (OCH_3).

^{1}H NMR: (400 MHz, DMSO-d_6) ∂7.00-6.95(m, 2H, *arom.*), 6.86-6.82(m, 2H, *arom.*), 5.28(d, *J* = 4.9 Hz, 1H, OH-2), 5.06(d, *J* = 4.7 Hz, 1H, OH-3), 5.00(d, *J* = 5.2 Hz, 1H, OH-4), 4.70(d, *J* = 7.5 Hz, 1H, H-1), 4.56(t, *J* = 5.8 Hz, 1H, OH-6), 3.70(s, 3H, OCH_3), 3.70-3.66(m, 1H, H-6a), 3.48-3.42(m, 1H, H-6b), 3.28-3.10(m, 4H, H-5 and H-3 and H-2 and H-4). **^{13}C NMR:** (101 MHz, DMSO-d_6) ∂ = 154.3 (C *arom.*), 151.5 (C *arom.*), 117.6 (2xCH *arom.*), 114.4 (2xCH *arom.*), 101.5 (C-1), 77.0 (C-5), 76.6 (C-3), 73.3 (C-2), 69.8 (C-4), 60.8 (C-6 CH_2), 55.4 (OCH_3).

***N*-2-fluorophenyl-D-gluconamide (2FA, 27):** The title compound was synthesized according to a modified literature procedure[166,212] which was summarized in **General Procedure 8-1**. Gluconolactone (**511**, 28.1 mmol, 1.0 eq) was dissolved in acetic acid (0.5 M) and

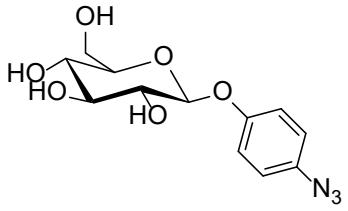


2-fluoroaniline (35.2 mmol, 1.2 eq) was added. The solution was stirred at 100 °C for 1.5 hours and then concentrated. The crude brown sludge was recrystallized three times from 99 % EtOH to yield the pure product as a white powder (**43 %**).

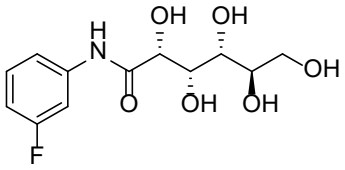
Characterization was consistent with that found in literature.[166,212]

^{1}H NMR: (400 MHz, DMSO-d_6): ∂9.20(s, 1H, NH), 8.13(dt, J = 7.9, 1.8 Hz, 1H*, arom.*), 7.28(ddd, J = 11.1, 7.8, 1.6 Hz, 1H*, arom.*), 7.20-7.10(m, 2H*, arom.*), 5.95(d, J = 3.3 Hz, 1H, OH-2), 4.67(d, J = 7.0 Hz, 1H, OH-3), 4.62-4.60(m, 2H, OH-4 and OH-5), 4.38(t, J = 5.3 Hz, 1H, OH-6), 4.26-4.23(m, 1H, H-2), 4.05-4.00(m, 1H, H-3), 3.61-3.47(m, 3H, H-4 and H-5 and H-6a), 3.42-3.37(m, 1H, H-6b). **^{13}C NMR:** (101 MHz, DMSO-d_6): ∂ = 171.5 (C *amide*), 152.7 (d, $J_{C\text{-}F}$ = 243.3 Hz, *arom.* C), 125.9 (d, $J_{C\text{-}F}$ = 10.6 Hz, *arom.* C), 124.7 (d, $J_{C\text{-}F}$ = 7.8 Hz, *arom.* CH), 124.5 (d, $J_{C\text{-}F}$ = 3.3 Hz, *arom.* CH), 122.0 (*arom.* CH), 115.2 (d, $J_{C\text{-}F}$ = 19.2 Hz, *arom.* CH), 73.9 (C-2), 72.2 (C-4/C-5), 71.6 (C-4/C-5), 70.3 (C-3), 63.3 (C-6 CH_2).

(4-azidophenyl)-β-D-glucopyranoside (*p*N_3Ph-Glc, 29): The title compound was synthesized and provided by Dr. Jessica Poisson for all experiments discussed in this thesis.[214]



***N*-3-fluorophenyl-D-gluconamide (3FA, 113):** The title compound was synthesized according to a modified literature procedure[166,212] which was summarized in **General Procedure 8-1** with the assistance of undergraduate student Abigail Kos. Gluconolactone (**511**, 11.3 mmol, 1.0 eq) was dissolved in acetic acid (0.2 M) and 3-fluoroaniline (17.1 mmol, 1.5 eq) was added. The solution was stirred at 100 °C for 1.5 hours and then concentrated. The crude brown sludge was recrystallized several times from 95 % EtOH to yield the pure product as a white powder (**38 %**).

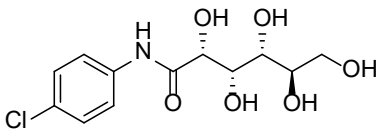


Characterization was consistent with that found in literature.[168]

^{1}H NMR: (400 MHz, DMSO-d_6): ∂9.77(s, 1H, NH), 7.72(dt, J = 11.9, 2.2 Hz, 1H*, arom.*), 7.51(ddd, J = 8.1, 1.9, 0.8 Hz, 1H*, arom.*), 7.35-7.30(m, 1H*, arom.*), 6.90-6.85(m, 1H, *arom.*), 5.75(d, J = 5.2 Hz, 1H,

OH-2), 4.61-4.55(m, 3H, OH-3 and OH-4 and OH-5), 4.37(t, *J* = 5.7 Hz, 1H, OH-6), 4.18(dd, *J* = 5.1, 3.8 Hz, 1H, H-2), 4.02-3.99(m, 1H, H-3), 3.59(ddd, *J* = 10.9, 5.6, 2.5 Hz, 1H, H-6a), 3.54-3.47(m, 2H, H-4 and H-5), 3.42-3.36(m, 1H, H-6b). **^{13}C NMR:** (101 MHz, DMSO-d_6): ∂ = 172.1 (C *amide*), 162.1 (d, J_{C-F} = 240.7 Hz, *arom.* C), 140.4 (d, J_{C-F} = 11.2 Hz, *arom.* C), 130.2 (d, J_{C-F} = 9.5 Hz, *arom.* CH), 115.4 (d, J_{C-F} = 2.6 Hz, *arom.* CH), 109.8 (d, J_{C-F} = 20.9 Hz, *arom.* CH), 106.3 (d, J_{C-F} = 26.3 Hz, *arom.* CH), 74.2 (C-2), 72.2 (C-4/C-5), 71.5 (C-4/C-5), 70.4 (C-3), 63.3 (C-6 CH_2).

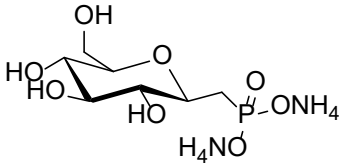
***N*-4-chlorophenyl-D-gluconamide (4ClA, 114):** The title compound was synthesized according to a modified literature procedure[166,212] which was summarized in **General Procedure 8-1** with the assistance of undergraduate student Abigail Kos. Gluconolactone (**511**, 5.9 mmol, 1.0 eq) was dissolved in acetic acid (0.2 M) and 4-chloroaniline (6.0 mmol, 1.0 eq) was added. The solution was stirred at 100 °C for 1 hour and then concentrated. The crude brown sludge was recrystallized from 95 % EtOH to yield the pure product as a white powder (**46 %**).



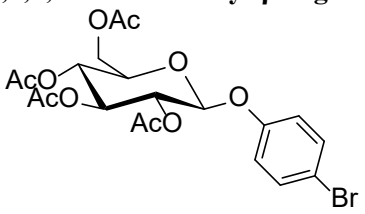
Characterization was consistent with that found in literature.[166]

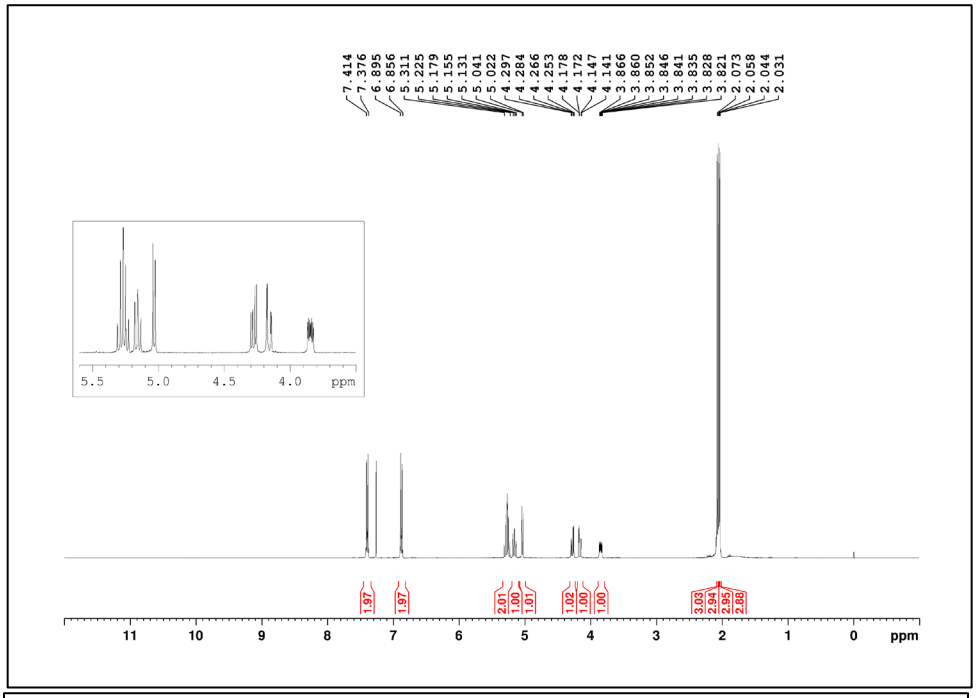
^{1}H NMR: (400 MHz, DMSO-d_6): ∂9.70(s, 1H, NH), 7.78-7.75(m, 2H*, arom.*), 7.36-7.34(m, 2H*, arom.*), 5.71(d, *J* = 5.2 Hz, 1H, OH-2), 4.59-4.53(m, 3H, OH-3 and OH-4 and OH-5), 4.36(t, *J* = 3.8 Hz, 1H, OH-6), 4.18(dd, *J* = 4.9, 3.8 Hz, 1H, H-2), 4.03-3.98(m, 1H, H-3), 3.59(ddd, *J* = 10.8, 5.5, 2.5 Hz, 1H, H-6a), 3.54-3.47(m, 2H, H-4 and H-5), 3.42-3.36(m, 1H, H-6b). **^{13}C NMR:** (101 MHz, DMSO-d_6): ∂ = 171.8 (C *amide*), 137.6 (*arom.* C), 128.4 (*arom.* 2xCH), 126.9 (*arom.* C), 121.2 (*arom.* 2xCH), 74.2 (C-2), 72.2 (C-4/C-5), 71.5 (C-4/C-5), 70.3 (C-3), 63.3 (C-6 CH_2).

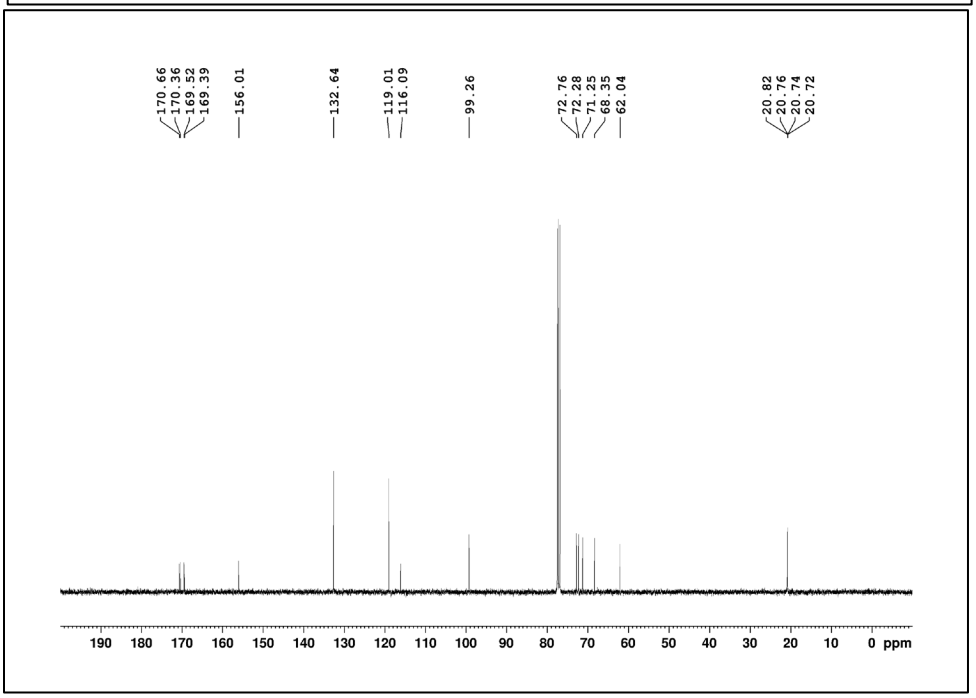
Ammonium *C*-(1-deoxy-β-D-glucopyranosyl) methanephosphonate (G1CP-NH_4, 115): The title compound was synthesized and provided by Dr. Anna Ampaw for all experiments discussed in this thesis.[177]



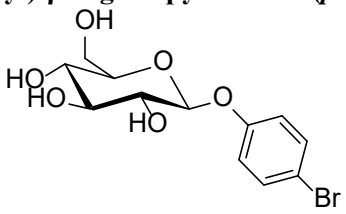
(4-bromophenyl)-2,3,4,6-tetra-*O*-acetyl-β-D-glucopyranoside (526):

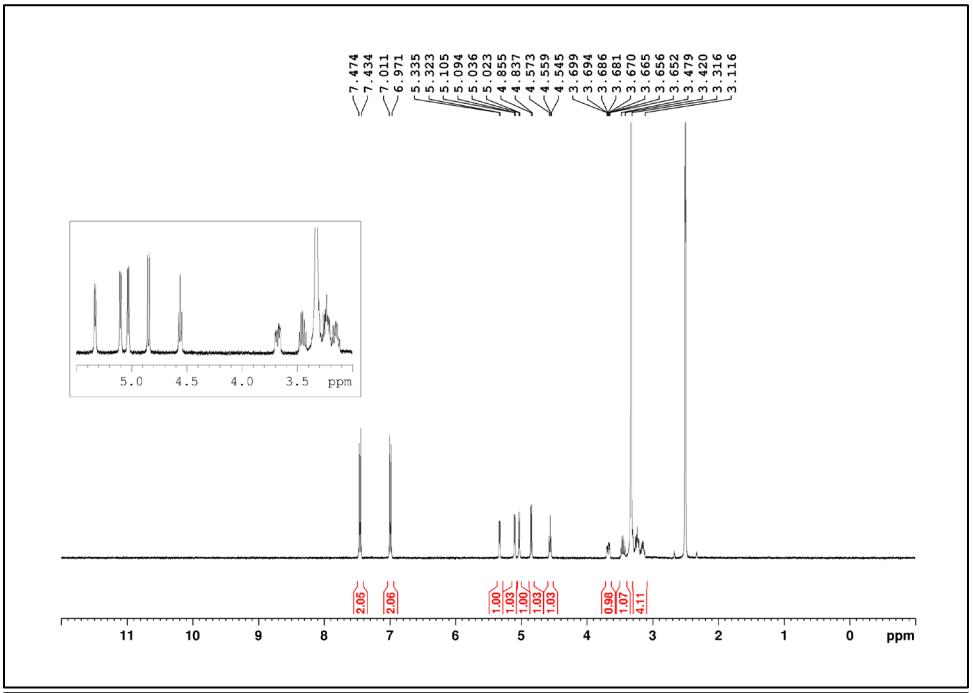


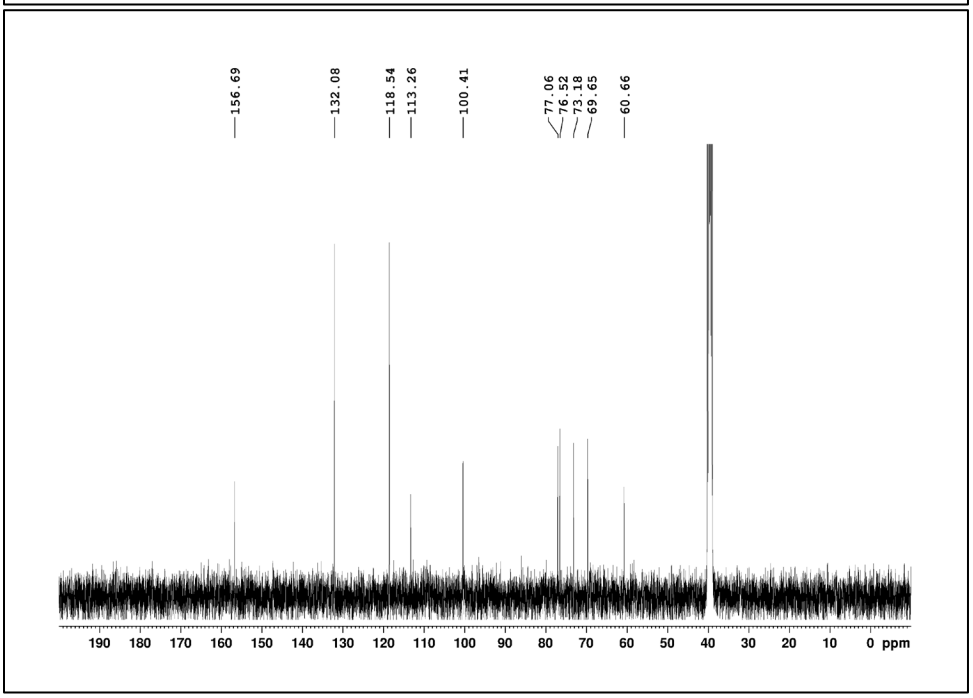




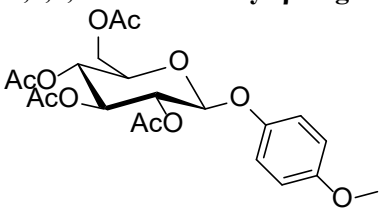
(4-bromophenyl)-β-D-glucopyranoside (*p*BrPh-Glc, 25):

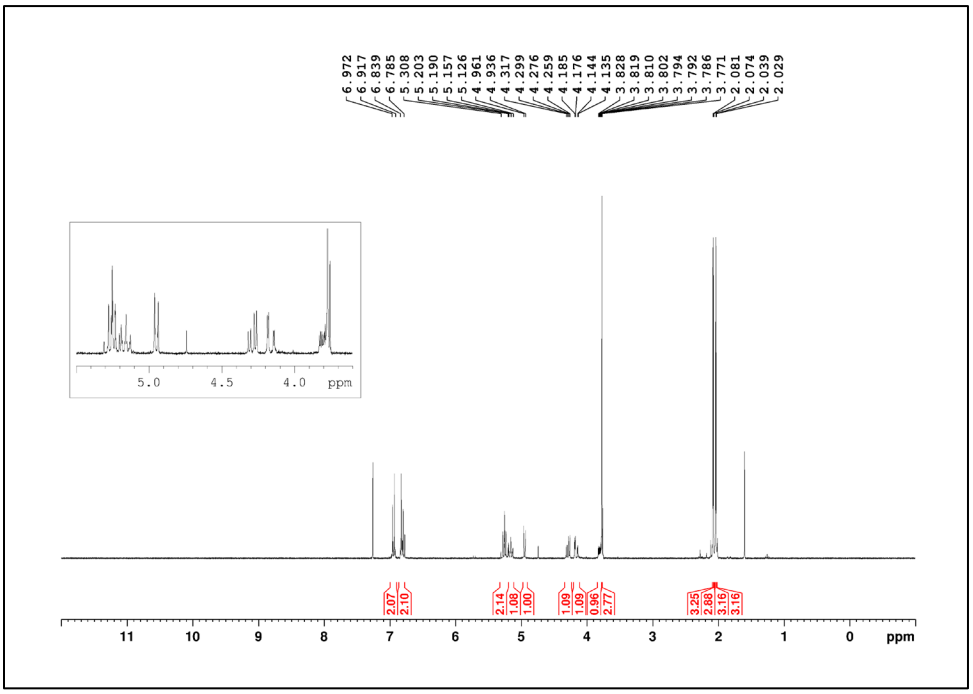




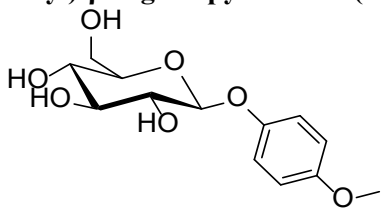


(4-methoxyphenyl)-2,3,4,6-tetra-*O*-acetyl-β-D-glucopyranoside (519):

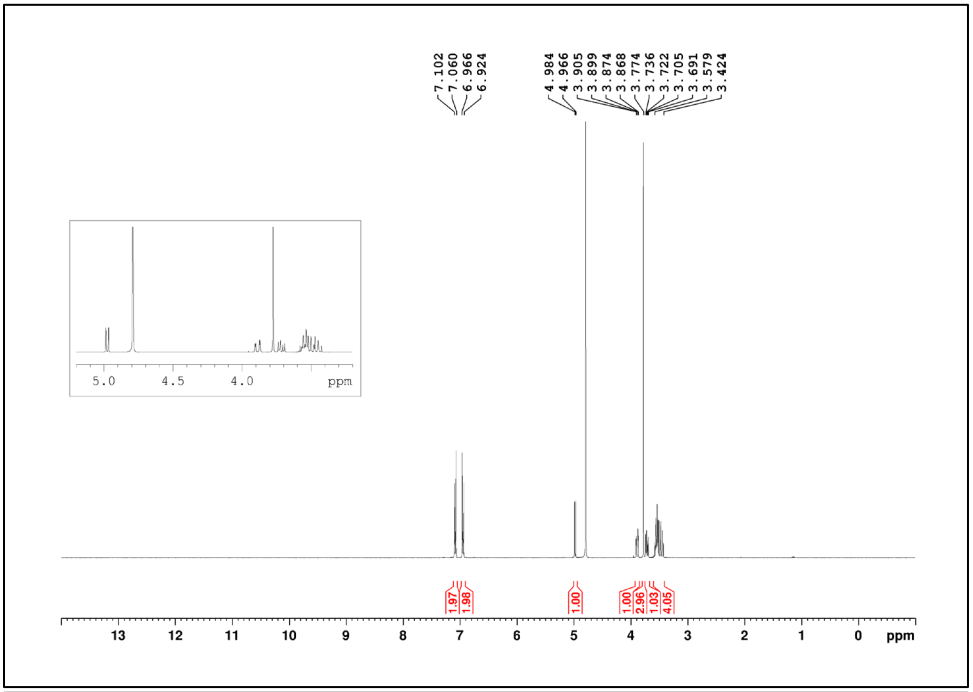


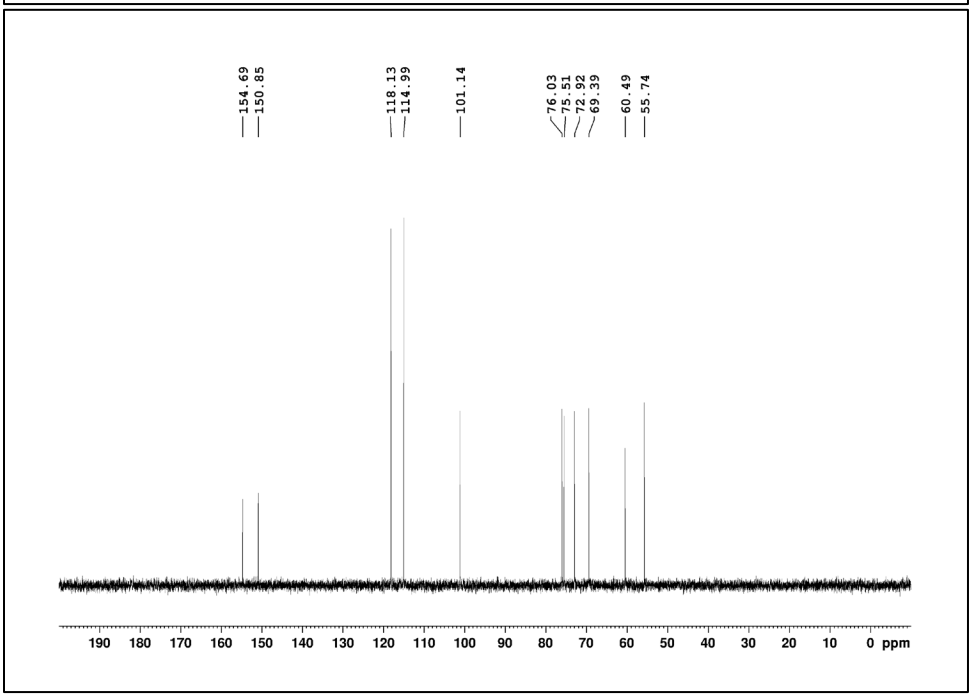


(4-methoxyphenyl)-β-D-glucopyranoside (PMP-Glc, 26):

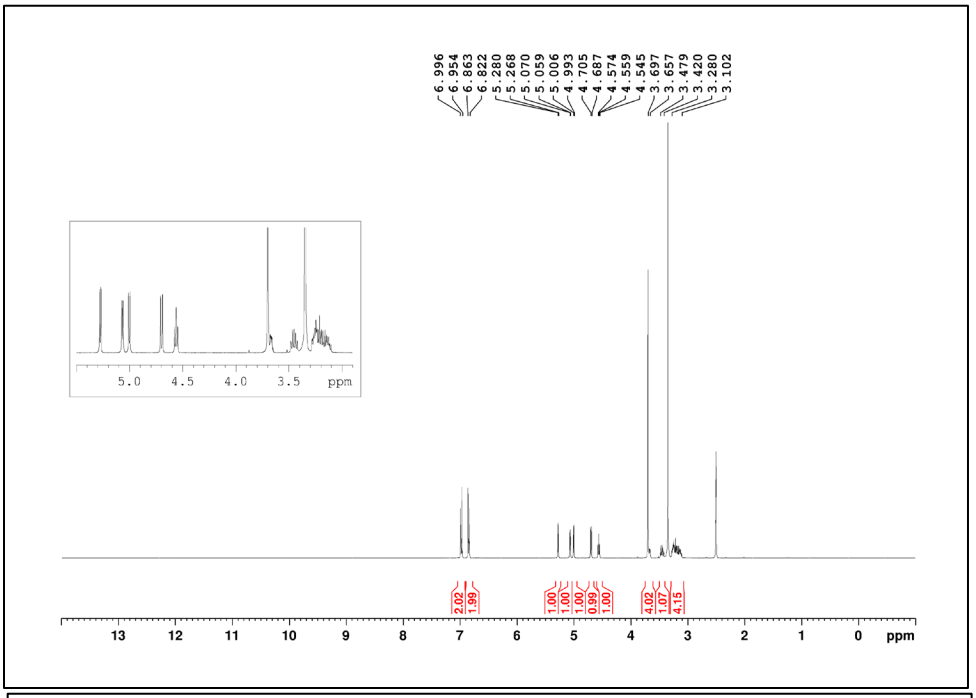


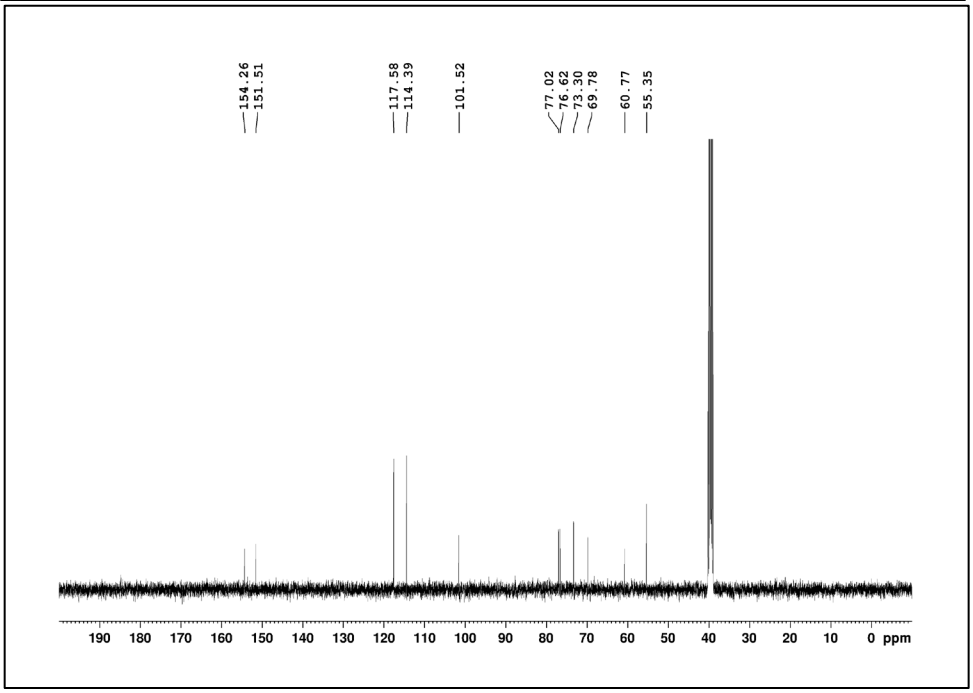
in D_2O



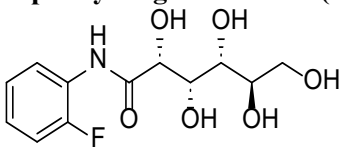


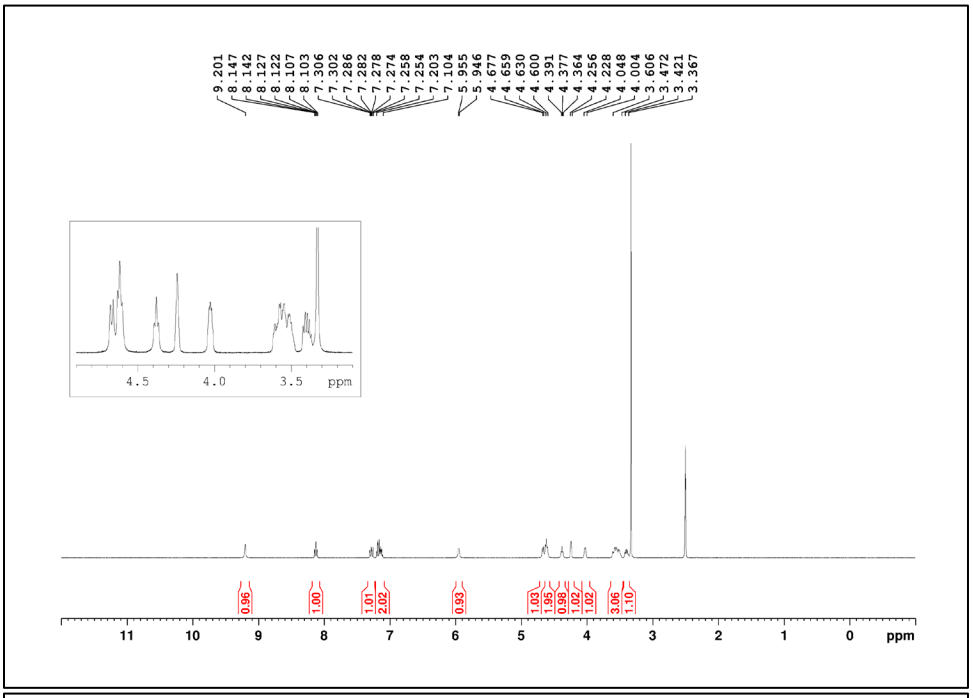
in DMSO-d_6:

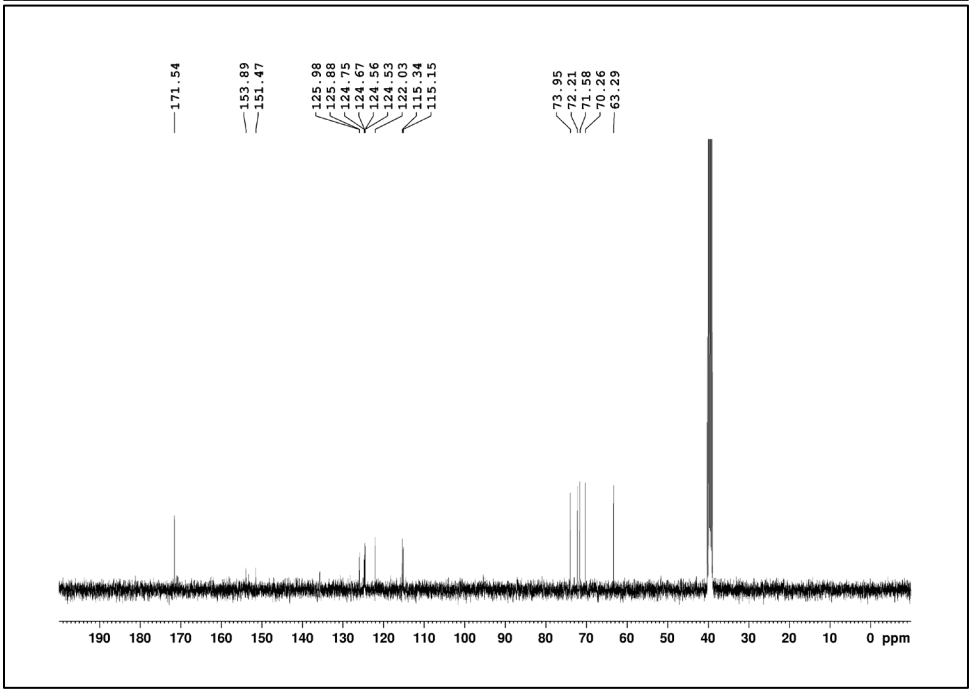

6.996
6.954
6.863
6.822
5.280
5.268
5.070
5.059
5.006
4.993
4.705
4.687
4.574
4.559
4.545
3.697
3.657
3.479
3.420
3.280
3.102
5.0
4.5
4.0
3.5
ppm
2.02
1.99
1.00
1.00
1.00
0.99
1.00
4.02
1.07
4.15
13
12
11
10
9
8
7
6
5
4
3
2
1
0
ppm


154.26
151.51
117.58
114.39
101.52
77.02
76.62
73.30
69.78
60.77
55.35
190
180
170
160
150
140
130
120
110
100
90
80
70
60
50
40
30
20
10
0 ppm

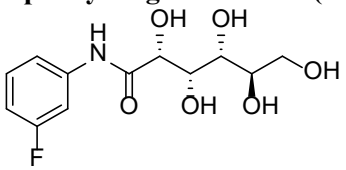
_N_-2-fluorophenyl-D-gluconamide (2FA, 27):

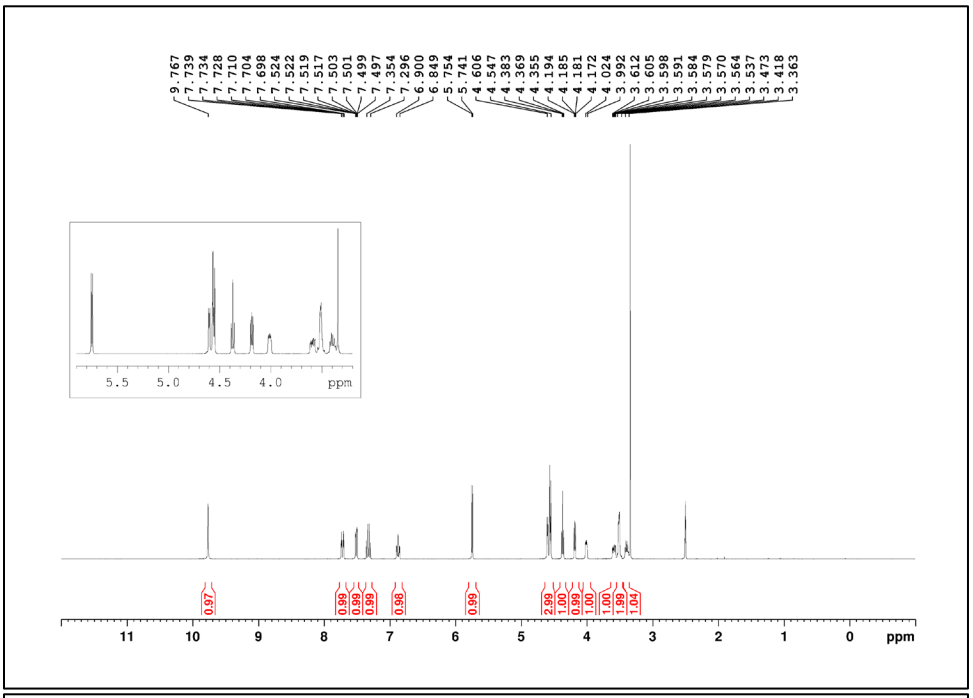


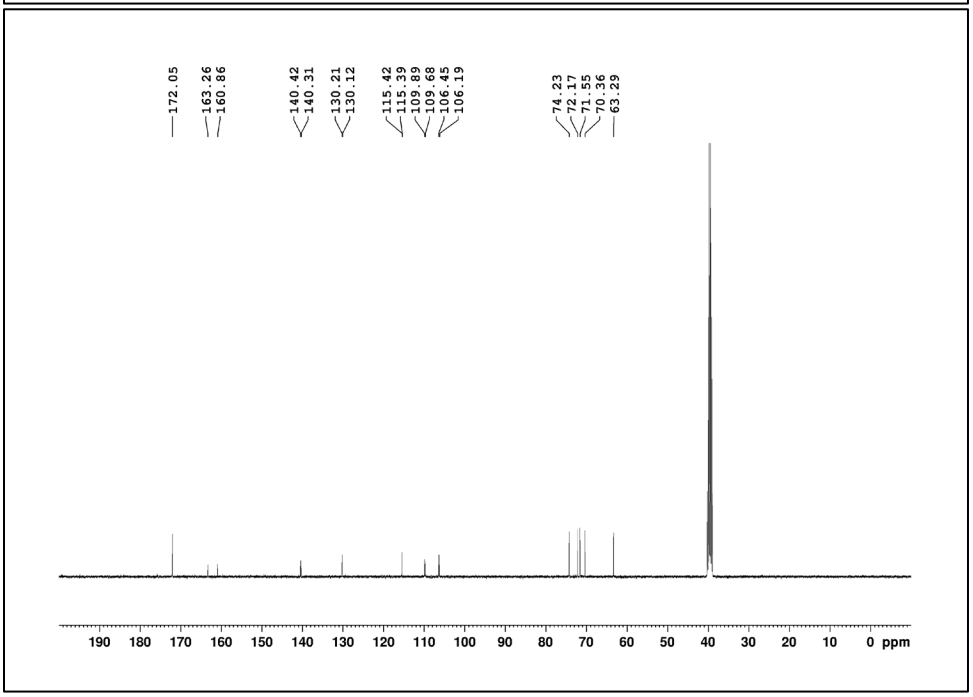




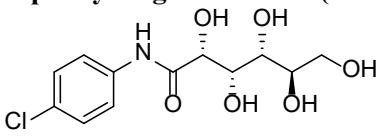
_N_-3-fluorophenyl-D-gluconamide (3FA, 113):

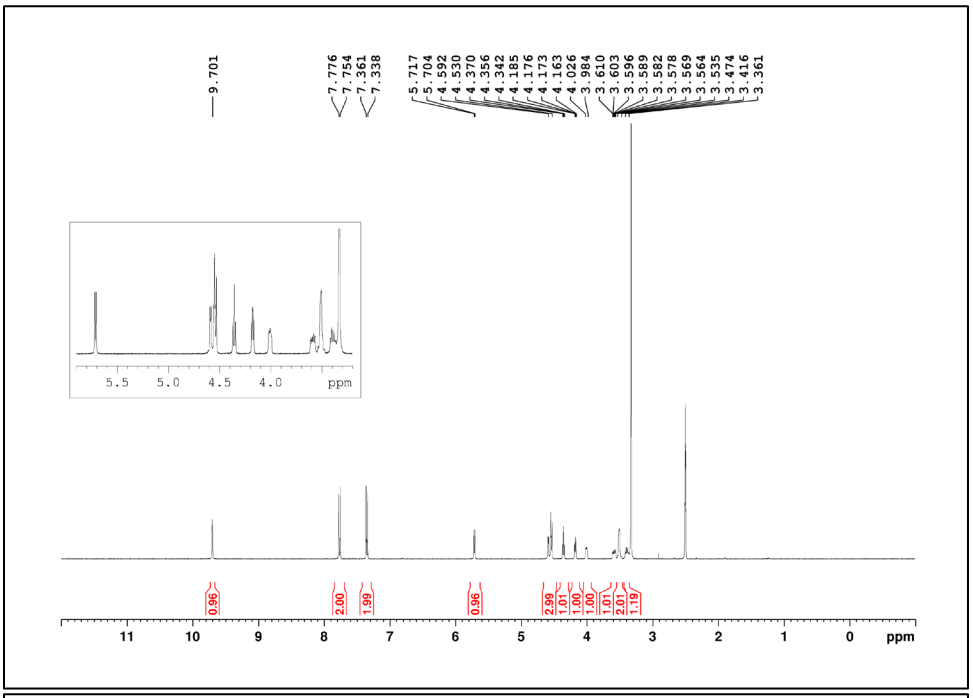


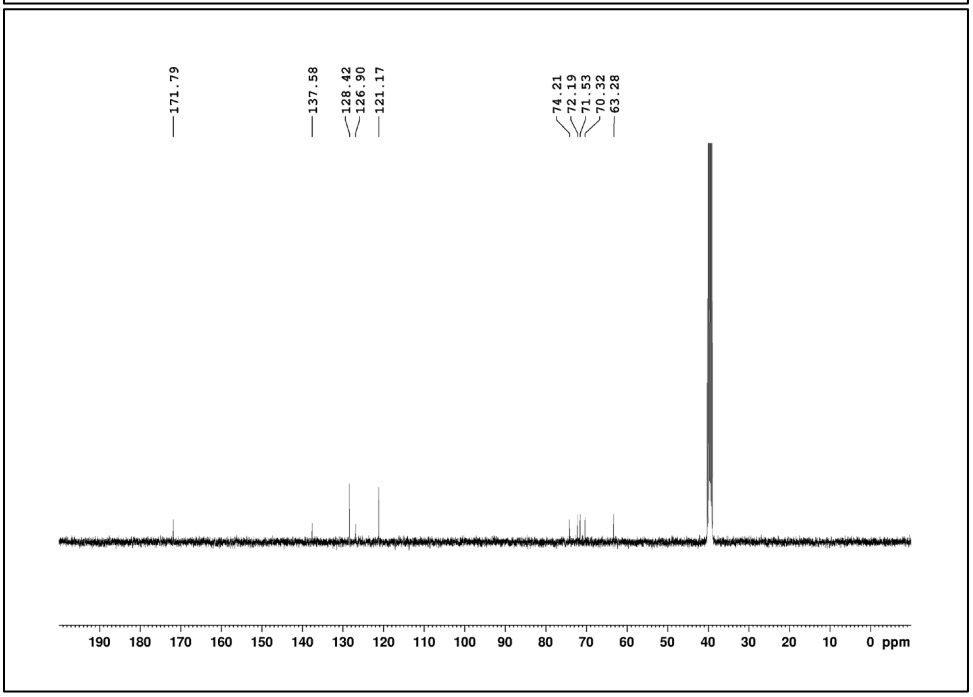




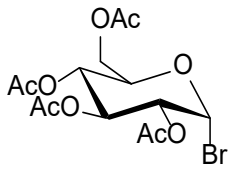
_N_-4-chlorphenyl-D-gluconamide (4ClA, 114):







8.2.2.2. Common intermediates

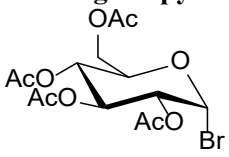


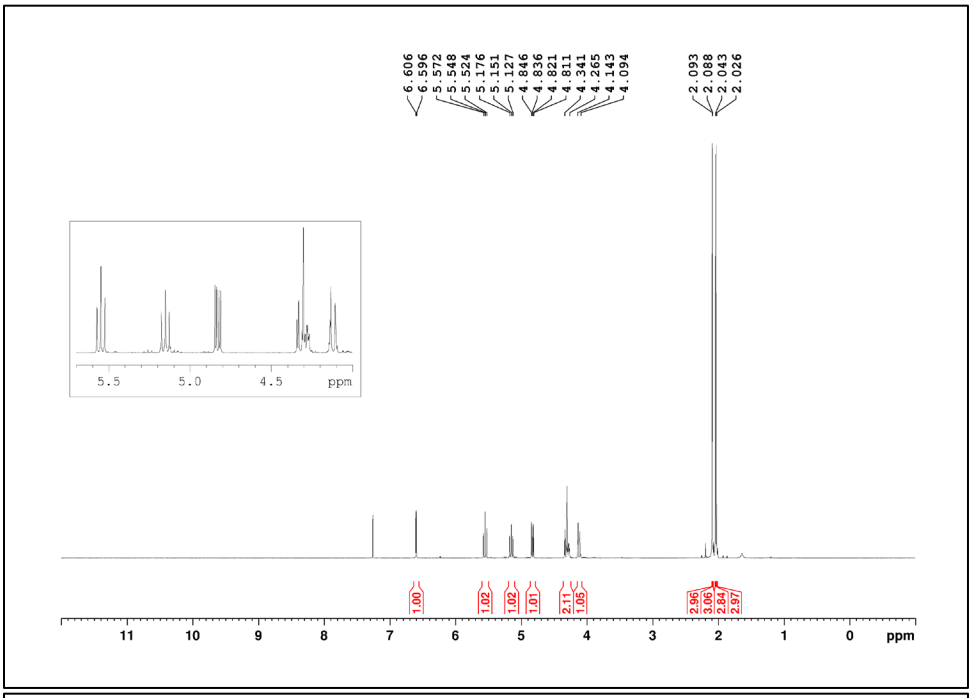
Acetobromo-α-D-glucopyranose (507): The title compound was synthesized according to a modified literature procedure.[526] β-D-glucose pentaacetate (**503**, 12.8 mmol, 1.0 eq) was dissolved in 33 % HBr in AcOH (128.5 mmol, 10.0 eq). The solution was stirred at room temperature for 40 minutes and was then poured over ice-water. The solution was then diluted with DCM and washed with water until the aqueous phase ran neutral in pH (monitored by pH paper, Hydrion wide range). The organic phase was dried using Na_2SO_4, filtered, and concentrated *in vacuo*. The crude oil was recrystallized from ether to form the desired product as white crystals (**65 %**). The product could be stored under argon at 0 °C if necessary but was best when used immediately in subsequent reactions.

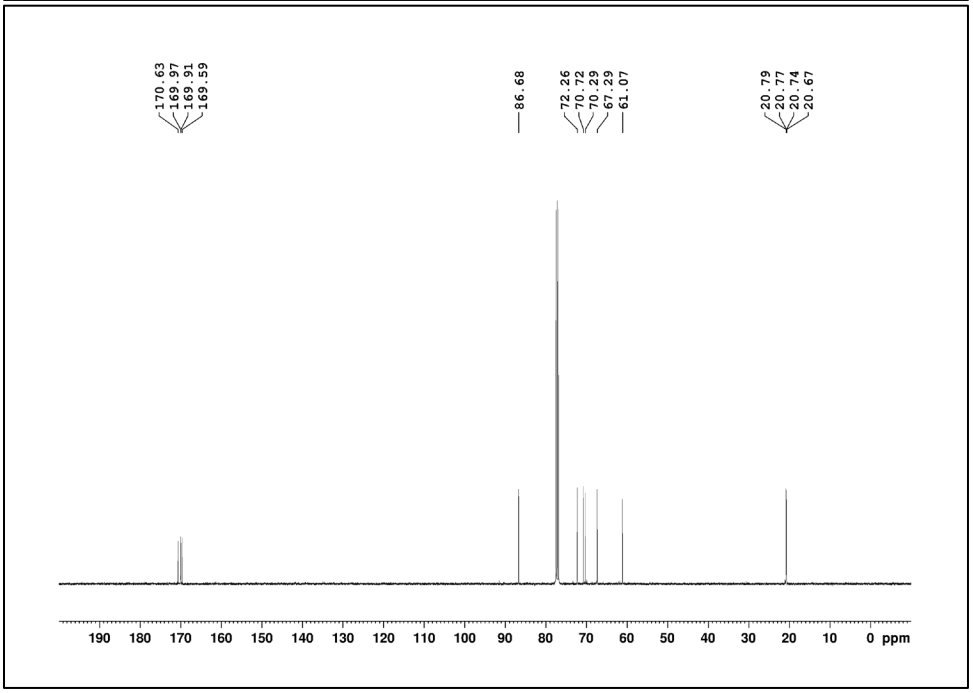
Characterization was consistent with that found in literature.[527]

^{1}H NMR: (400 MHz, $CDCl_3$) ∂6.60(d, J = 4.0 Hz, 1H, H-1), 5.55(t, J = 9.7 Hz, 1H, H-3), 5.15(t, J = 9.8 Hz, 1H, H-4), 4.82(dd, J = 10.0, 4.1 Hz, 1H, H-2), 4.34-4.27(m, 2H, H-5 and H-6a), 4.14-4.09(m, 1H, H-6b), 2.093(s, 3H, OAc CH_3), 2.088(s, 3H, OAc CH_3), 2.04(s, 3H, OAc CH_3), 2.03(s, 3H, OAc CH_3). **^{13}C NMR:** (101 MHz, $CDCl_3$) ∂ = 170.6 (OAc C), 170.0 (OAc C), 169.9 (OAc C), 169.6 (OAc C), 86.7 (C-1), 72.3 (C-5), 70.7 (C-2), 70.3 (C-3), 67.3 (C-4), 61.1 (C-6 CH_2), 20.79 (OAc CH_3), 20.77 (OAc CH_3), 20.73 (OAc CH_3), 20.67 (OAc CH_3).

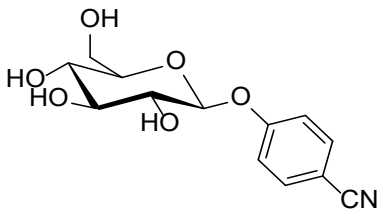
Acetobromo-α-D-glucopyranose (507):







8.2.2.3. *Nitrile-containing compounds*

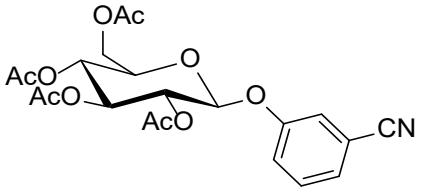


(4-cyanophenyl)-β-D-glucopyranoside (*p*CNPh-Glc, 30): The title compound was synthesized according to a modified literature procedure following **General Procedure 8-2** and **General Procedure 8-3**.[167,326,525] β-D-glucose pentaacetate (**503**, 25.5 mmol, 1.0 eq) and 4-cyanophenol (35.7 mmol, 1.4 eq) were dissolved in dry DCM (0.25 M) in a flame dried flask under argon at 0 °C with 4 Å molecular sieves. Boron trifluoride diethyl etherate (48 % solution) (64.9 mmol, 2.5 eq) was added to the solution slowly. The solution was stirred overnight (18 h), diluted with DCM, and then quenched with sat. $NaHCO_3$ upon reaction completion. The solution was filtered through Celite®, and the organic layer was washed with sat. $NaHCO_3$, H_2O, and brine. The organic layer was dried using Na_2SO_4, filtered, and concentrated *in vacuo*. The crude yellow oil was recrystallized from 99 % EtOH and the resulting white powder (**506**) was then used in the next step without further purification.

The previous recrystallized material (**506**, 1.0 eq) was dissolved in MeOH (0.2 M) and a 1 M solution of NaOMe in MeOH (0.05 eq) was added to the solution to stir for 1 hour. Upon reaction completion, Amberlite IR120 H+ resin (washed in MeOH) was added to a pH < 4. The solution was filtered, and the filtrate was concentrated *in vacuo*. The product was recrystallized in dH_2O to yield the final product as a white powder (**41 %, over two steps**).

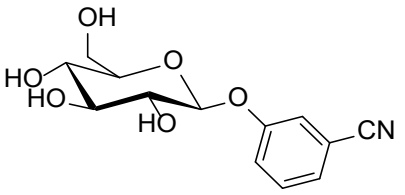
Characterization was consistent with that found in literature.[528]

^{1}H NMR: (400 MHz, CD_3OD-d_4) ∂7.69-7.65(m, 2H, *arom.*), 7.24-7.20(m, 2H, *arom.*), 5.04-4.99(m, 1H, H-1), 3.90(dd, *J* = 12.0, 2.2 Hz, 1H, H-6a), 3.69(dd, *J* = 12.1, 5.7 Hz, 1H, H-6b), 3.51-3.45(m, 3H, H-2 and H-5 and H-3/H-4), 3.43-3.37(m, 1H, H-3/H-4). **^{13}C NMR:** (101 MHz, CD_3OD-d_4) ∂ = 162.4 (C *arom.*), 135.1 (*arom.* 2xCH), 119.8 (CN), 118.4 (*arom.* 2xCH), 106.4 (C *arom.*), 101.6 (C-1), 78.3 (C-2/C-3/C-4/C-5), 77.9 (C-2/C-3/C-4/C-5), 74.7 (C-2/C-3/C-4/C-5), 71.2 (C-2/C-3/C-4/C-5), 62.4 (C-6 CH_2).



(3-cyanophenyl)-2,3,4,6-tetra-*O*-acetyl-β-D-glucopyranoside (509): The title compound was synthesized according to a modified literature procedure following **General Procedure 8-2**.[167,525] β-D-glucose pentaacetate (**503**, 0.9 mmol, 1.0 eq) and 3-cyanophenol (1.0 mmol, 1.2 eq) were dissolved in dry DCM (0.25 M) in a flame dried flask under argon at 0 °C with 4 Å molecular sieves. Boron trifluoride diethyl etherate (48 % solution) (1.9 mmol, 2.5 eq) was added to the solution slowly. The solution was stirred overnight (18 h), diluted with DCM, and then quenched with sat. $NaHCO_3$ upon reaction completion. The solution was filtered through Celite®, and the organic layer was washed with sat. $NaHCO_3$, H_2O, and brine. The organic layer was dried using Na_2SO_4, filtered, and concentrated *in vacuo*. The crude off-white foam was purified by column chromatography (1:1 Hexanes:EtOAc) to yield the final product as a white powder (**46 %**). The crude product could alternatively be recrystallized from 99 % EtOH/H_2O (**93 %**).

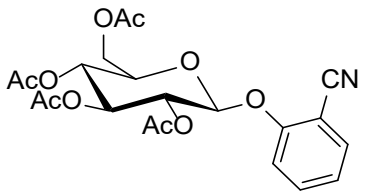
^{1}H NMR: (400 MHz, $CDCl_3$) ∂7.43-7.36(m, 2H, *arom.*), 7.29-7.27(m, 1H, *arom.*), 7.22(ddd, *J* = 7.7, 2.3, 1.8 Hz, 1H, *arom.*), 5.33-5.25(m, 2H, H-2 and H-3), 5.16-5.09(m, 2H, H-1 and H-4), 4.25(dd, *J* = 12.3, 5.9 Hz, 1H, H-6a), 4.18(dd, *J* = 12.3, 2.4 Hz, 1H, H-6b), 3.90(ddd, *J* = 10.0, 5.9, 2.5 Hz, 1H, H-5), 2.11(s, 3H, OAc CH_3), 2.06(s, 3H, OAc CH_3), 2.05(s, 3H, OAc CH_3), 2.03(s, 3H, OAc CH_3). **^{13}C NMR:** (101 MHz, $CDCl_3$) ∂ = 170.7 (OAc C), 170.3 (OAc C), 169.5 (OAc C), 169.3 (OAc C), 156.8 (C *arom.*), 130.7 (*arom.* CH), 127.2 (*arom.* CH), 122.3 (*arom.* CH), 119.9 (*arom.* CH), 118.4 (CN), 113.6 (C *arom.*), 98.8 (C-1), 72.6 (C-2/C-3), 72.5 (C-5), 71.1 (C-2/C-3), 68.3 (C-4), 62.1 (C-6 CH_2), 20.8 (OAc CH_3), 20.74 (OAc CH_3), 20.71 (2x OAc CH_3). **LRMS (ESI):** m/z calcd for $C_{21}H_{23}NO_{10}Na$ $[M+Na]^+$ 472.1, found 472.0.



(3-cyanophenyl)-β-D-glucopyranoside (*m*CNPh-Glc, 37): The title compound was synthesized according to a modified literature procedure following **General Procedure 8-3**.[167,326] (3-cyanophenyl)-2,3,4,6-tetra-*O*-acetyl-β-D-glucopyranoside (**509**, 0.4 mmol, 1.0 eq) was dissolved in MeOH (0.2 M) and a 1 M solution of NaOMe in MeOH (1.0 eq) was added to the solution to stir for 1 hour. Upon reaction completion, Amberlite IR120 H+ resin (washed in MeOH) is added to a pH < 4. The solution was filtered, and the filtrate was concentrated *in vacuo*. The product was recrystallized from dH_2O to yield the final product as a white powder (**89 %**).

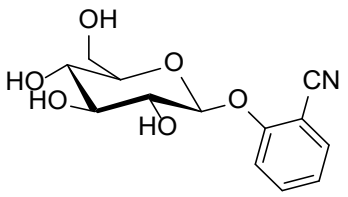
^{1}H NMR: (400 MHz, DMSO-d_6) ∂7.53-7.45(m, 3H, *arom.*), 7.37-7.34(m, 1H, *arom.*), 5.37(d, *J* = 4.7 Hz, 1H, OH-2/OH-3), 5.12(d, *J* = 4.6 Hz, 1H, OH-2/OH-3), 5.06(d, *J* = 5.3 Hz, 1H, OH-4), 4.98(d, *J* = 7.3 Hz, 1H, H-1), 4.60(t, *J* = 5.6 Hz, 1H, OH-6), 3.69(ddd, *J* = 11.6, 6.0, 1.3 Hz, 1H, H-6a), 3.48-3.38(m, 2H, H-5 and H-6b), 3.30-3.21(m, 2H, H-2 and H-3), 3.17-3.12(m, 1H, H-4). **^{13}C NMR:** (101 MHz, DMSO-d_6) ∂ = 157.4 (C *arom.*), 130.8 (*arom.* CH), 125.7 (*arom.* CH), 121.8 (*arom.* CH), 119.2 (*arom*. CH), 118.6 (CN), 112.2 (C *arom.*), 100.1 (C-1), 77.1 (C-5), 76.5 (C-2/C-3), 73.2 (C-2/C-3), 69.7 (C-4), 60.7 (C-6 CH_2). **HRMS (ESI):** m/z calcd for $C_{13}H_{15}NO_6Na$ $[M+Na]^+$ 304.0796, found 304.0797.

(2-cyanophenyl)-2,3,4,6-tetra-*O*-acetyl-β-D-glucopyranoside (510): The title compound was synthesized according to a modified literature procedure following **General Procedure 8-2**.[167,525] β-D-glucose pentaacetate (**503**, 2.7 mmol, 1.0 eq) and 2-cyanophenol (3.2 mmol, 1.1 eq) were dissolved in dry DCM (0.25 M) in a flame dried flask under argon at 0 °C with 4 Å molecular sieves (powdered). Boron trifluoride diethyl etherate (48 % solution) (7.8 mmol, 2.5 eq) was added to the solution slowly. The solution was stirred overnight (18 h), diluted with DCM, and then quenched with sat. $NaHCO_3$ upon reaction completion. The solution was filtered through Celite® and the organic layer (DCM) was washed using sat. $NaHCO_3$, H_2O, and brine. The organic layer was dried using Na_2SO_4, filtered, and concentrated *in vacuo*. The crude white solid was purified by recrystallization from ethyl acetate/hexanes to yield the final product as a white fluffy powder (**35 %**).



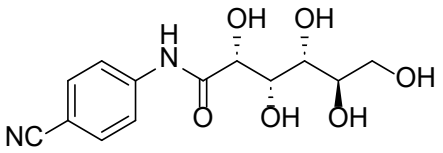
Characterization was consistent with that found in literature.[529]

^{1}H NMR: (400 MHz, $CDCl_3$) ∂7.59(dd, *J* = 7.7, 1.6 Hz, 1H, *arom.*), 7.54(ddd, *J* = 9.2, 7.6, 1.7 Hz, 1H, *arom.*), 7.27-7.25(m, 1H, *arom.*), ∂7.18(dt, *J* = 7.9, 1.2 Hz, 1H, *arom.*), 5.36(dd, *J* = 9.4, 7.7 Hz, 1H, H-2/H-3), 5.30(t, *J* = 8.9 Hz, 1H, H-2/H-3), 5.19(t, *J* = 9.8 Hz, 1H, H-4), 5.10(d, *J* = 7.5 Hz, 1H, H-1), 4.28(dd, *J* = 12.3, 5.2 Hz, 1H, H-6a), 4.22(dd, *J* = 12.3, 2.6 Hz, 1H, H-6b), 3.88(ddd, *J* = 9.9, 5.0 Hz, 2.7 Hz, 1H, H-5), 2.13(s, 3H, OAc CH_3), 2.09(s, 3H, OAc CH_3), 2.05(s, 3H, OAc CH_3), 2.04(s, 3H, OAc CH_3). **^{13}C NMR:** (101 MHz, $CDCl_3$) ∂ = 170.6 (OAc C), 170.4 (OAc C), 169.5 (OAc C), 169.4 (OAc C), 158.3 (C *arom.*), 134.4 (*arom.* CH), 133.8 (*arom.* CH), 124.1 (*arom.* CH), 117.7 (*arom.* CH), 115.4 (CN), 104.5 (C *arom.*), 100.0 (C-1), 72.5 (C-2/C-3), 72.4 (C-2/C-3/C-5), 70.6 (C-2/C-3/C-5), 68.2 (C-4), 61.9 (C-6 CH_2), 20.84 (OAc CH_3), 20.81 (OAc CH_3), 20.74 (OAc CH_3), 20.72 (OAc CH_3).



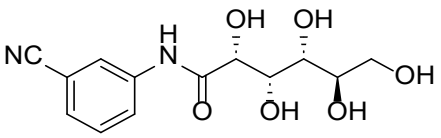
(2-cyanophenyl)-β-D-glucopyranoside (*o*CNPh-Glc, 38): The title compound was synthesized according to a modified literature procedure following **General Procedure 8-3**.[167,326] (2-cyanophenyl)-2,3,4,6-tetra-*O*-acetyl-β-D-glucopyranoside (**510**, 1.0 mmol, 1.0 eq) was dissolved in MeOH (0.15 M) and a 1 M solution of NaOMe in MeOH (0.5 eq) was added to the solution to stir for 1 hour. Upon reaction completion, Amberlite IR120 H+ resin (washed in MeOH) was added to a pH < 4. The solution was filtered, and the filtrate was concentrated *in vacuo*. The product was recrystallized in 95 % EtOH/Ether to yield the final product as a white powder (**93 %**).

^{1}H NMR: (400 MHz, DMSO-d_6) ∂7.74(dd, J = 7.7, 1.6 Hz, 1H, *arom.*), 7.68-7.63(m, 1H, *arom.*), 7.34(d, J = 8.6 Hz, 1H, *arom.*), 7.15(t, J = 7.6 Hz, 1H, *arom.*), 5.37(d, J = 5.1 Hz, 1H, OH-2/OH-3), 5.17-5.13(m, 2H, OH-2/OH-3 and H-1), 5.09(d, J = 5.3 Hz, 1H, OH-4), 4.58(t, J = 5.9 Hz, 1H, OH-6), 3.63(ddd, J = 11.8, 5.4, 1.8 Hz, 1H, H-6a), 3.49-3.43(m, 1H, H-6b), 3.41-3.38(m, 1H, H-5), 3.33-3.26(m, 2H, H-2 and H-3), ∂3.22-3.16(m, 1H, H-4). **^{13}C NMR:** (101 MHz, DMSO-d_6) ∂ = 158.6 (C *arom.*), 135.0 (*arom.* CH), 133.7 (*arom.* CH), 122.2 (*arom.* CH), 116.2 (CN), 115.1 (*arom.* CH), 101.2 (C *arom.*), 99.5 (C-1), 77.2 (C-5), 76.8 (C-2/C-3), 73.1 (C-2/C-3), 69.4 (C-4), 60.5 (C-6 CH_2). **HRMS (ESI):** m/z calcd for $C_{13}H_{15}NO_6Na$ $[M+Na]^+$ 304.0784, found 304.0797.



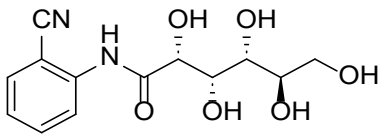
***N*-(4-cyanophenyl)-D-gluconamide (*p*CNA, 39):** The title compound was synthesized according to a modified literature procedure following **General Procedure 8-1** with the assistance of undergraduate student Abigail Kos.[166] Gluconolactone (**511**, 2.9 mmol, 1.0 eq) was dissolved in acetic acid (0.2 M) and 4-aminobenzonitrile (4.6 mmol, 1.5 eq) was added. The solution was stirred at 100 °C for 1.5 hours and then concentrated. The crude brown sludge was recrystallized from 95 % EtOH to yield the pure product as a white powder (**16 %**).

^{1}H NMR: (400 MHz, DMSO-d_6): ∂10.02(b sr, 1H, NH), 7.96-7.94(m, 2H, *arom.*), 7.78-7.76(m, 2H, *arom.*), 5.81(d, J = 5.2 Hz, 1H, OH-2), 4.62-4.57(m, 3H, OH-3 and OH-4 and OH-5), 4.38(t, J = 5.6 Hz, 1H, OH-6), 4.22-4.20(m, 1H, H-2), 4.03-3.99(m, 1H, H-3), 3.58(ddd, J = 11.2, 5.7, 2.5 Hz, 1H, H-6a), 3.53-3.47(m, 2H, H-4 and H-5), 3.41-3.39(m, 1H, H-6b). **^{13}C NMR:** (101 MHz, DMSO-d_6): ∂ = 172.6 (C *carbonyl*), 142.9 (C *arom.*), 133.1 (*arom.* 2xCH), 119.7 (*arom.* 2xCH), 119.1 (CN), 105.1 (C *arom.*), 74.3 (C-2), 72.1 (C-4/C-5), 71.5 (C-4/C-5), 70.4 (C-3), 63.3 (C-6 CH_2). **HRMS (ESI):** m/z calcd for $C_{13}H_{16}N_2O_6Na$ $[M+Na]^+$ 319.0906, found 319.0912.



***N*-(3-cyanophenyl)-D-gluconamide (*m*CNA, 40):** The title compound was synthesized according to a modified literature procedure following **General Procedure 8-1**.[166] Gluconolactone (**511**, 9.9 mmol, 1.0 eq) was dissolved in acetic acid (0.5 M) and 3-aminobenzonitrile (12.1 mmol, 1.2 eq) was added. The solution was stirred at 100 °C for 1.5 hours and then concentrated *in vacuo*. The crude brown sludge was recrystallized from 95 % EtOH to yield the pure product as a brown powder (**50 %**). The product was recrystallized from dH_2O and then lyophilized prior to use (to a white powder).

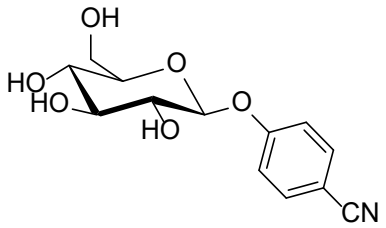
^{1}H NMR: (400 MHz, DMSO-d_6): ∂9.93(br s, 1H, NH), 8.21-8.19(m, 1H*, arom.*), 8.02-7.98(m, 1H*, arom.*), 7.54-7.49(m, 2H*, arom.*), 5.81(d, *J* = 5.1 Hz, 1H, OH-2), 4.63(d, *J* = 5.1 Hz, 1H, OH-3), 4.60-4.58(m, 2H, OH-4 and OH-5), 4.42(t, *J* = 5.6 Hz, 1H, OH-6), 4.20(dd, *J* = 4.9, 3.8 Hz, 1H, H-2), 4.02-3.99(m, 1H, H-3), 3.58(ddd, *J* = 11.0, 5.6, 2.6 Hz, 1H, H-6a), 3.53-3.49(m, 2H, H-4 and H-5), 3.41-3.36(m, 1H, H-6b). **^{13}C NMR:** (101 MHz, DMSO-d_6): ∂ = 172.6 (C *carbonyl*), 139.5 (C *arom.*), 130.2 (*arom.* CH), 127.1 (*arom.* CH), 124.5 (*arom.* CH), 122.6 (*arom.* CH), 118.9 (CN), 111.5 (C *arom.*), 74.3 (C-2), 72.2 (C-4/C-5), 71.6 (C-4/C-5), 70.5 (C-3), 63.4 (C-6 CH_2). **HRMS (ESI):** m/z calcd for $C_{13}H_{16}N_2O_6Na$ $[M+Na]^+$ 319.0906, found 319.0920.



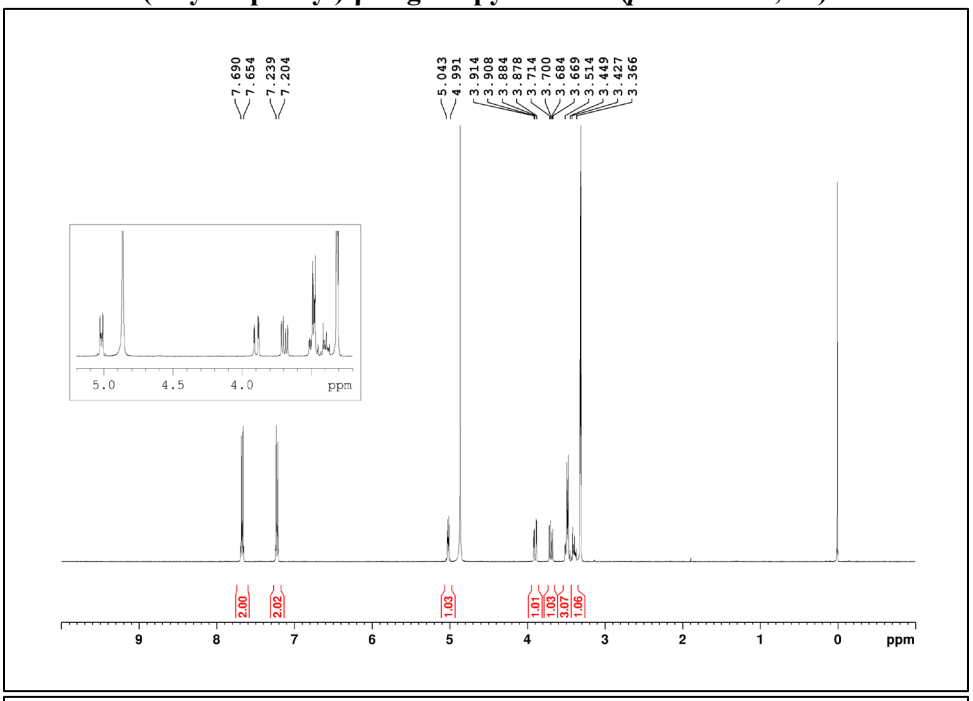
***N*-(2-cyanophenyl)-D-gluconamide (*o*CNA, 41):** The title compound was synthesized according to a modified literature procedure following **General Procedure 8-1** with the assistance of undergraduate student Abigail Kos.[166] Gluconolactone (**511**, 28.4 mmol, 1.0 eq) was dissolved in acetic acid (0.2 M) and 2-aminobenzonitrile (55.6 mmol, 2.0 eq) was added. The solution was stirred at 100 °C for 1.5 hours and then concentrated. The crude was washed with hot acetone to yield the pure product as a white solid (**8 %**). If necessary, the crude may be recrystallized first from 95 % EtOH to remove any remaining gluconolactone. The filtrate was then dried and washed with hot acetone to yield the desired product and was lyophilized prior to use.

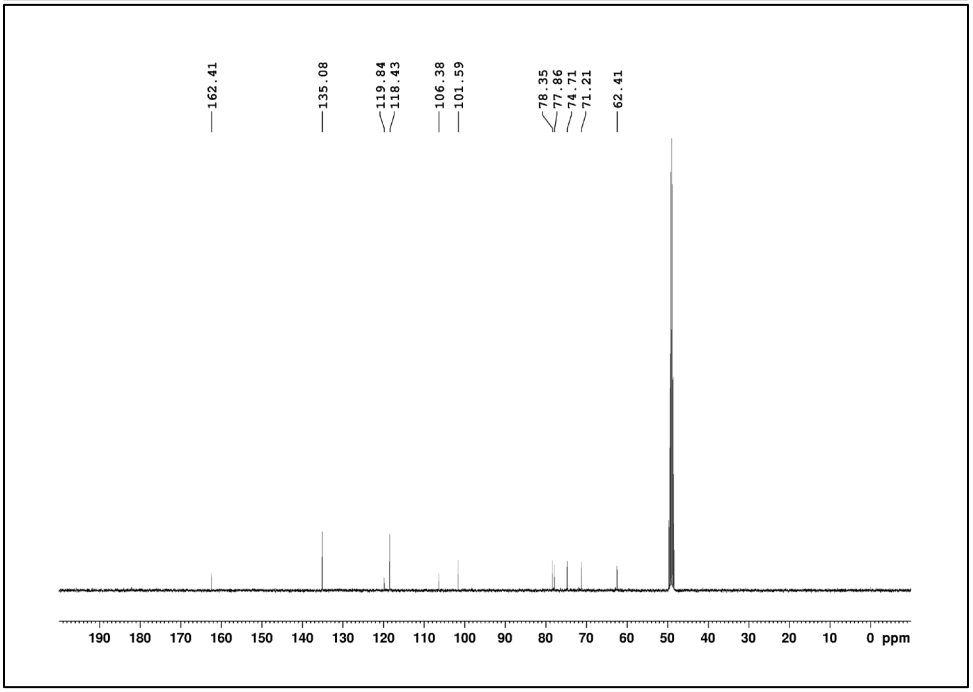
^{1}H NMR: (400 MHz, DMSO-d_6): ∂9.68(br s, 1H, NH), 8.14(d, *J* = 8.4 Hz, 1H*, arom.*), 7.83-7.81(m, 1H*, arom.*), 7.72-7.68(m, 1H*, arom.*), 7.29(t, *J* = 7.6 Hz, 1H, *arom.*), 6.12(d, *J* = 4.6 Hz, 1H, OH-2), 4.70(d, *J* = 7.1 Hz, 1H, OH-3), 4.66-4.64(m, 2H, OH-4 and OH-5), 4.40(t, *J* = 5.5 Hz, 1H, OH-6), 4.27(br t,

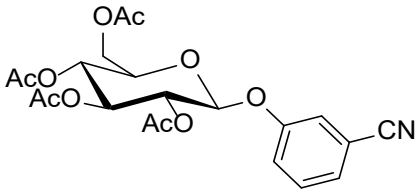
J = 3.5 Hz, 1H, H-2), 4.06-4.02(m, 1H, H-3), 3.63-3.48(m, 3H, H-4 and H-5 and H-6a), 3.42-3.37(m, 1H, H-6b). **^{13}C NMR:** (101 MHz, DMSO-d_6): ∂ = 172.1 (C *carbonyl*), 140.1 (C *arom.*), 134.2 (*arom.* CH), 132.9 (*arom.* CH), 124.6 (*arom.* CH), 121.8 (*arom.* CH), 116.4 (CN), 103.4 (C *arom.*), 73.8 (C-2), 72.0 (C-4/C-5), 71.6 (C-4/C-5), 70.3 (C-3), 63.3 (C-6 CH_2). **HRMS (ESI):** m/z calcd for $C_{13}H_{16}N_2O_6Na$ $[M+Na]^+$ 319.0906, found 319.0904.



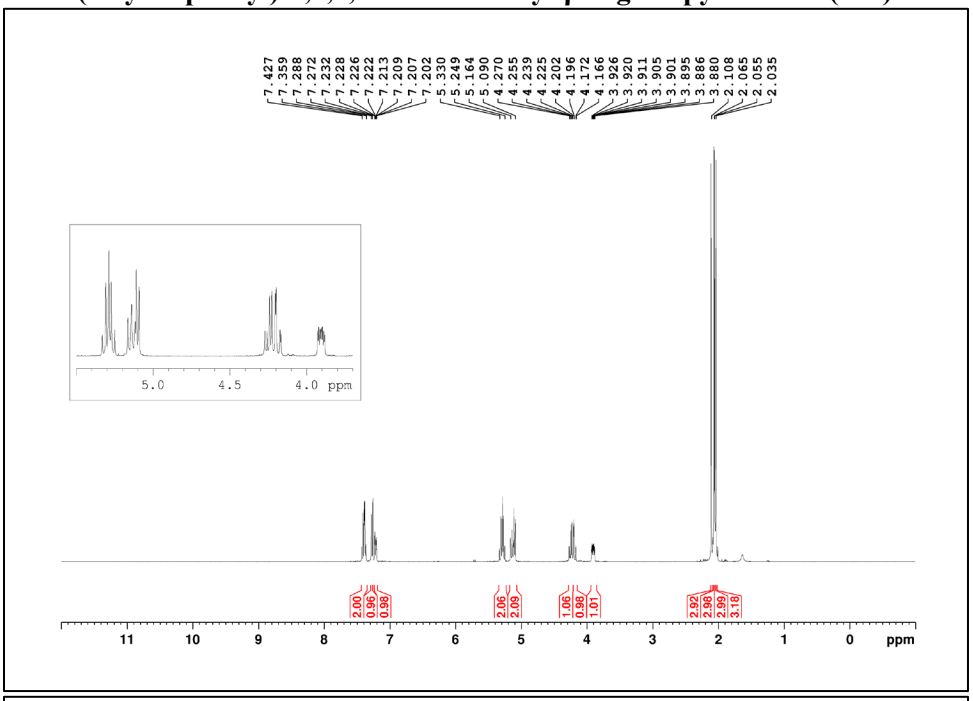
(4-cyanophenyl)-β-D-glucopyranoside (*p*CNPh-Glc, 30)

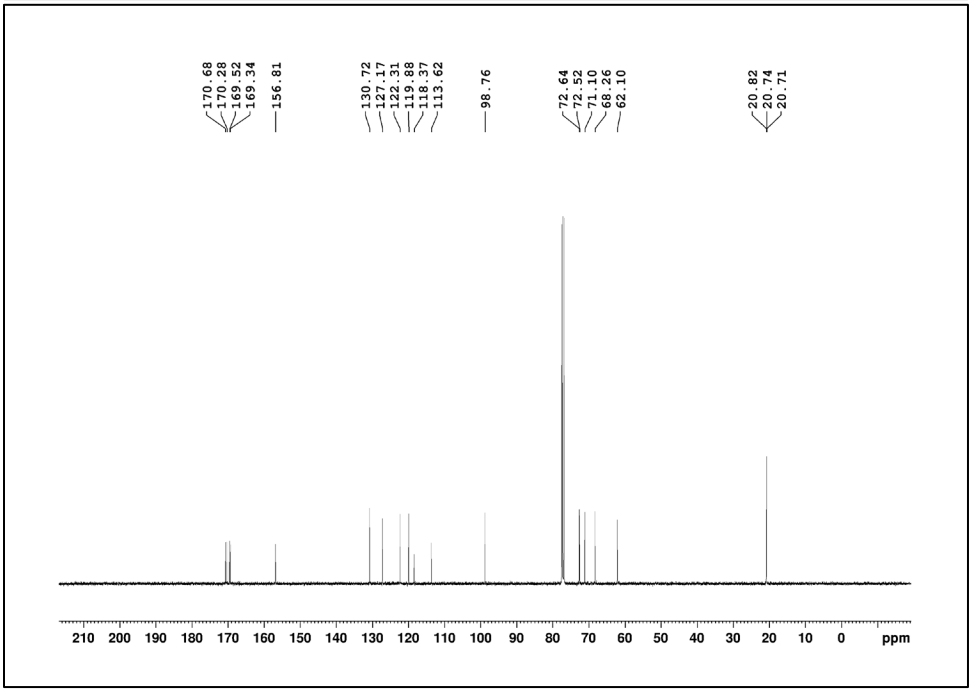


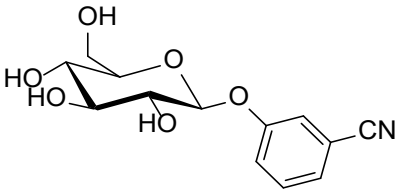




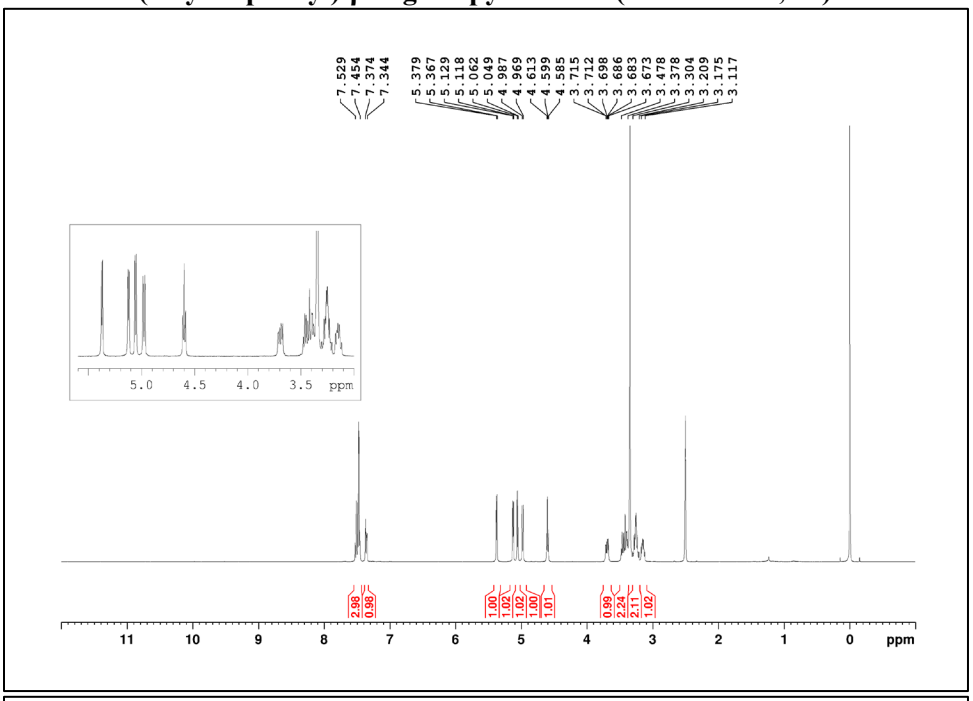
(3-cyanophenyl)-2,3,4,6-tetra-*O*-acetyl-β-D-glucopyranoside (509)

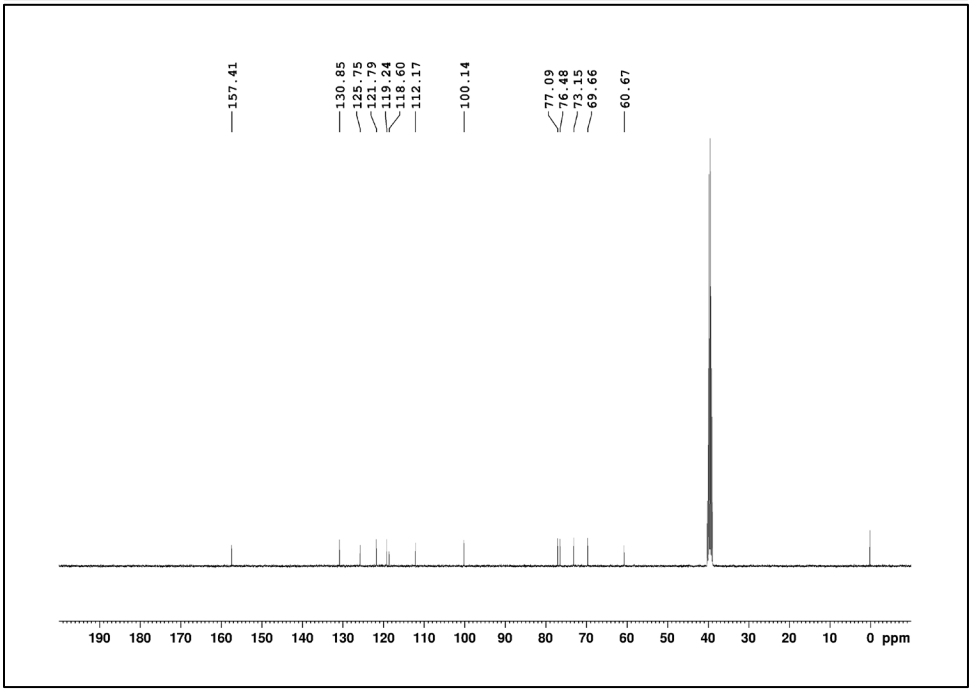


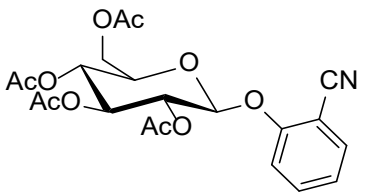




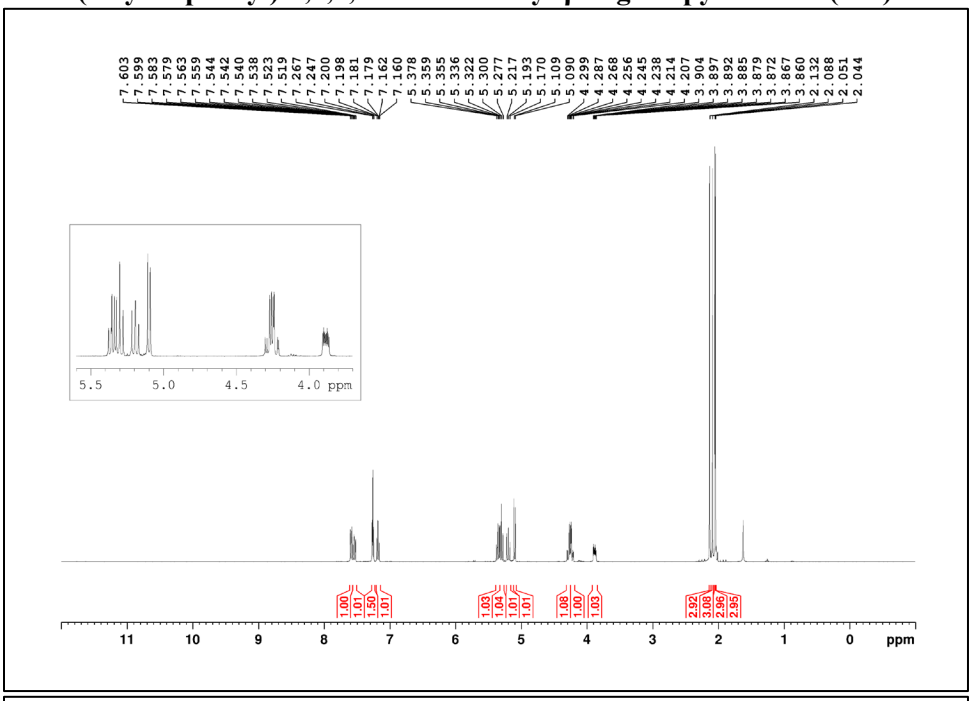
(3-cyanophenyl)-β-D-glucopyranoside (*m*CNPh-Glc, 37)

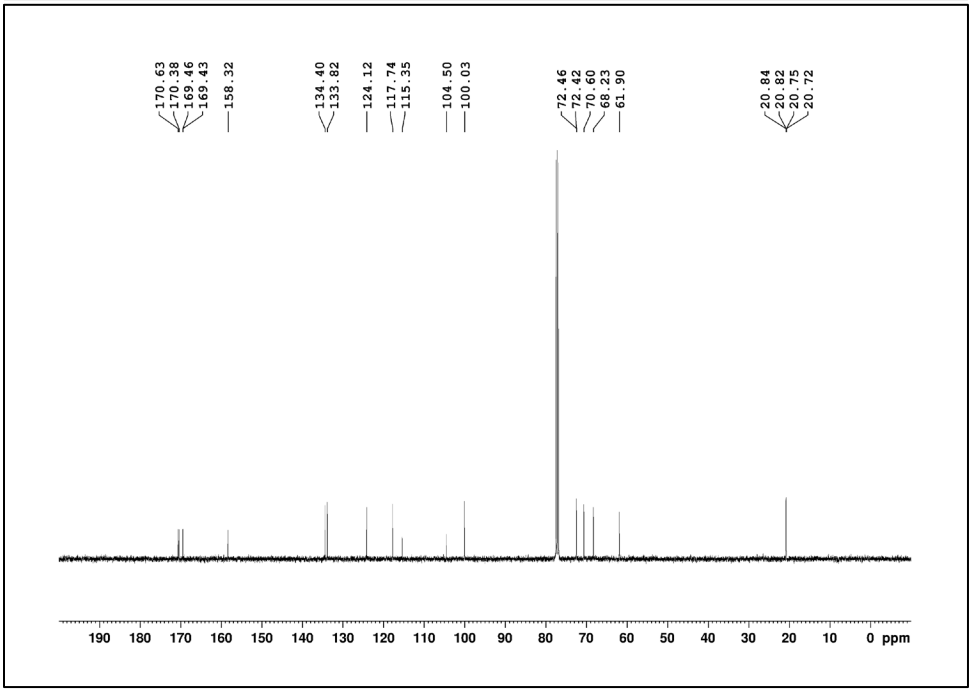


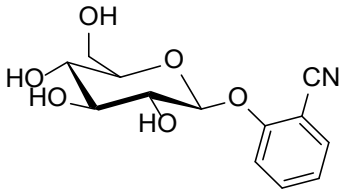




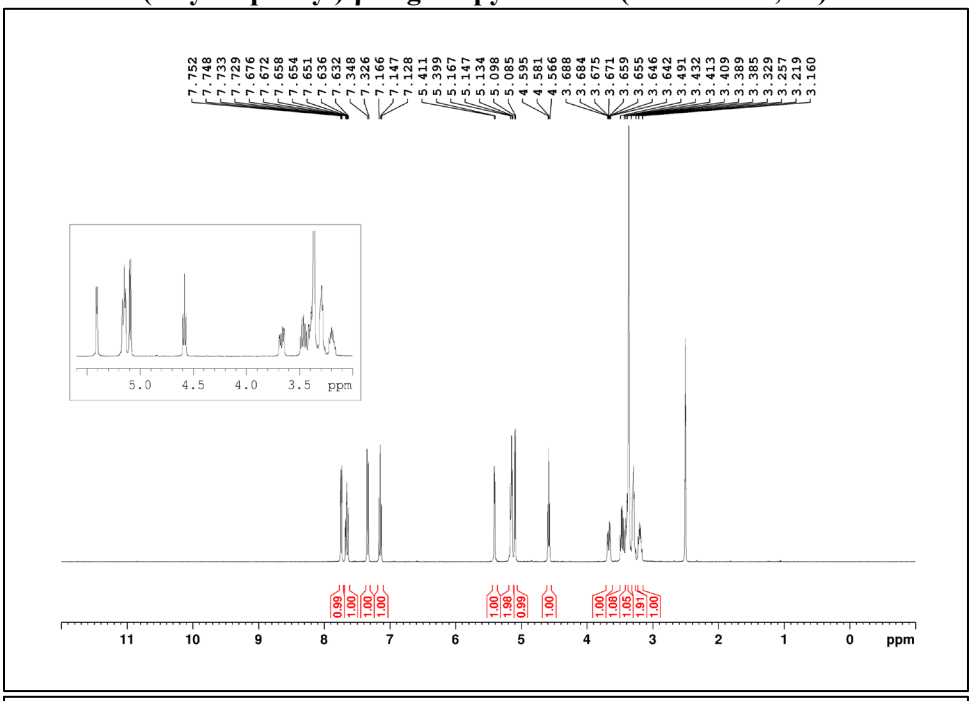
(2-cyanophenyl)-2,3,4,6-tetra-*O*-acetyl-β-D-glucopyranoside (510)

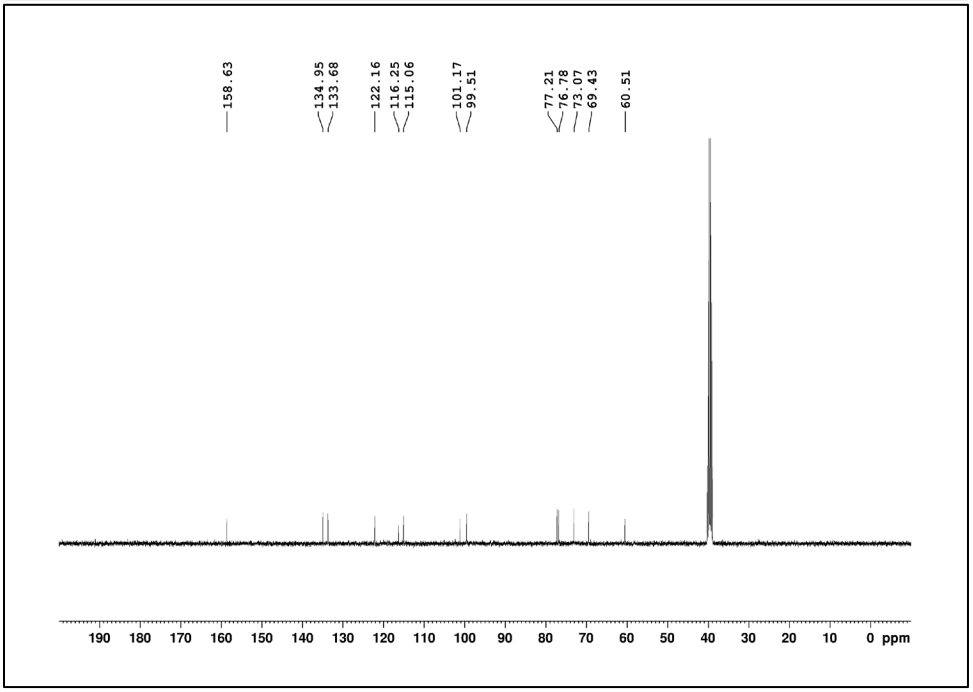


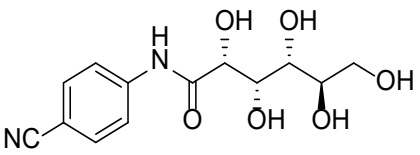




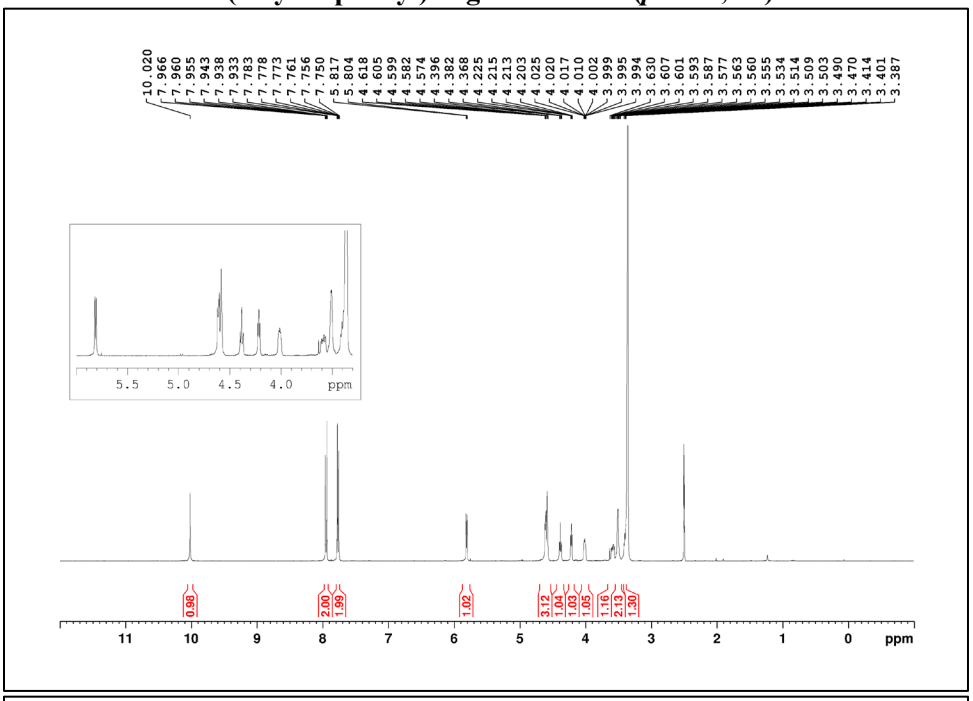
(2-cyanophenyl)-β-D-glucopyranoside (*o*CNPh-Glc, 38)

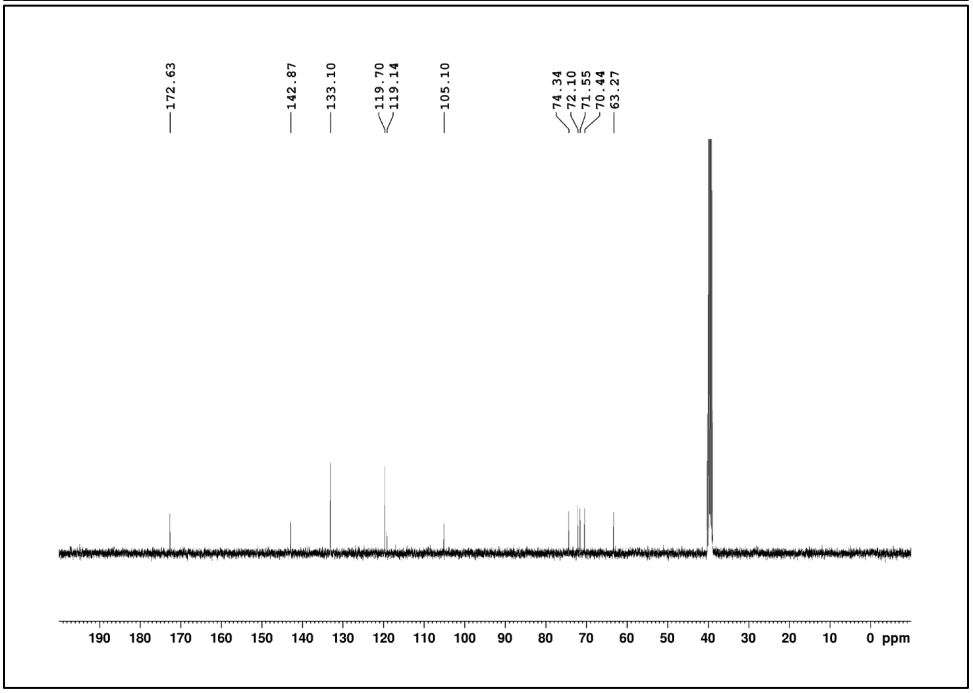


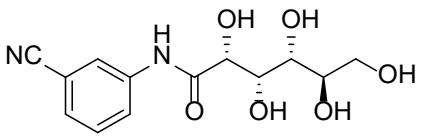




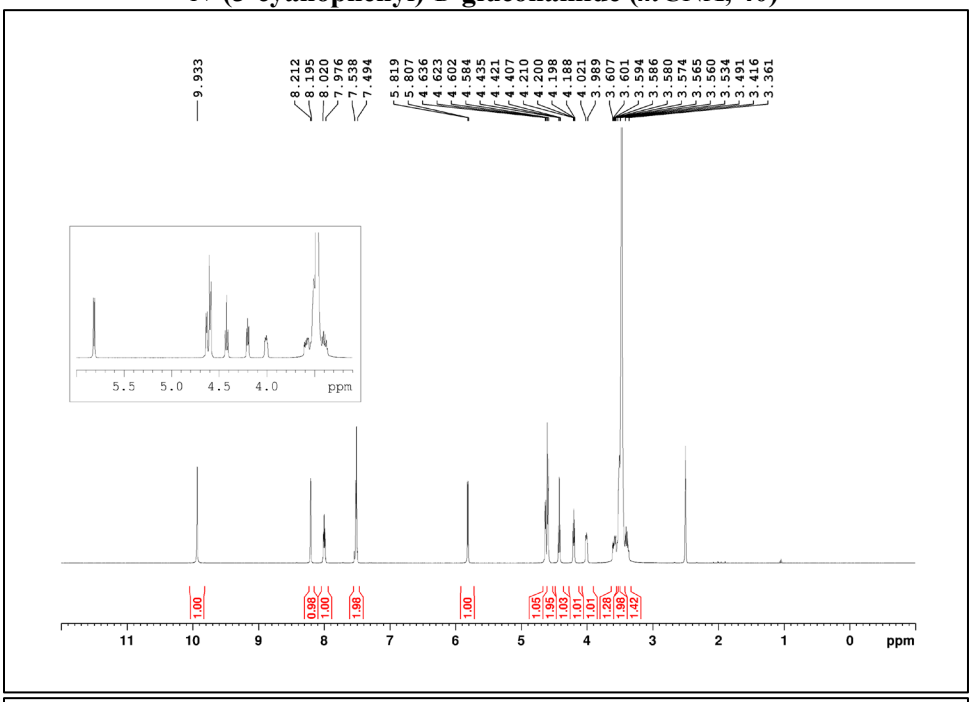
***N*-(4-cyanophenyl)-D-gluconamide (*p*CNA, 39)**

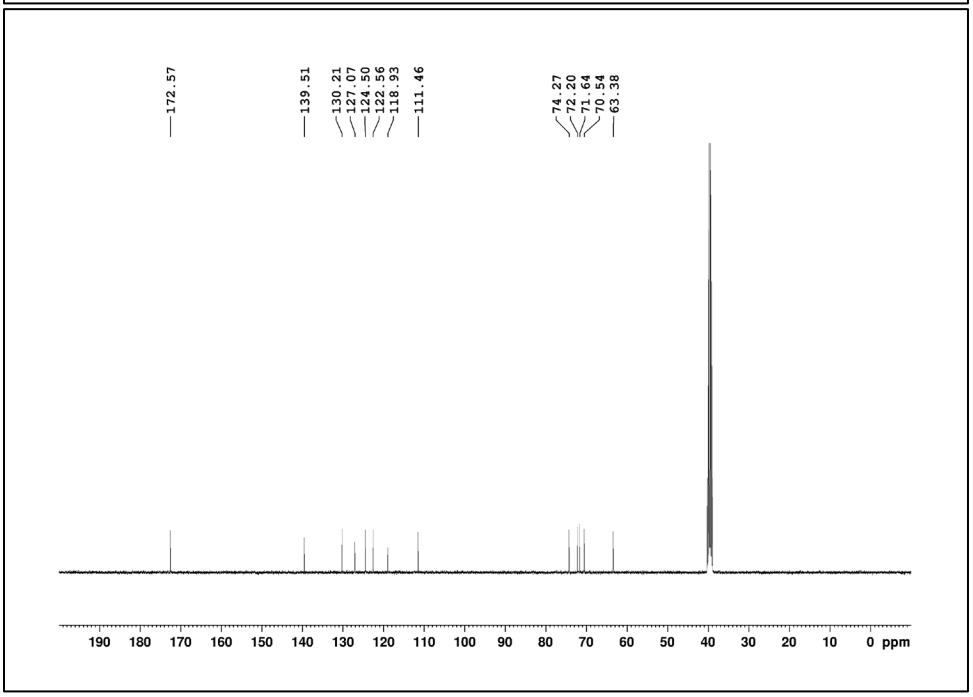


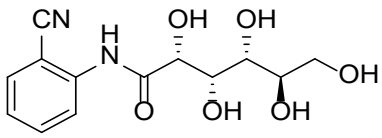




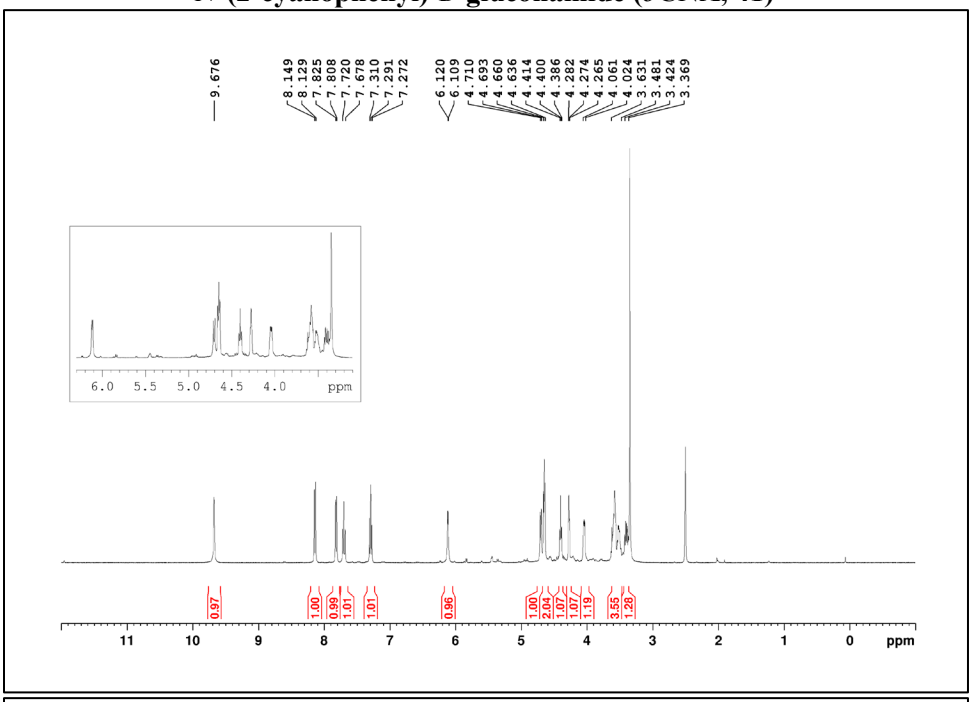
***N*-(3-cyanophenyl)-D-gluconamide (*m*CNA, 40)**

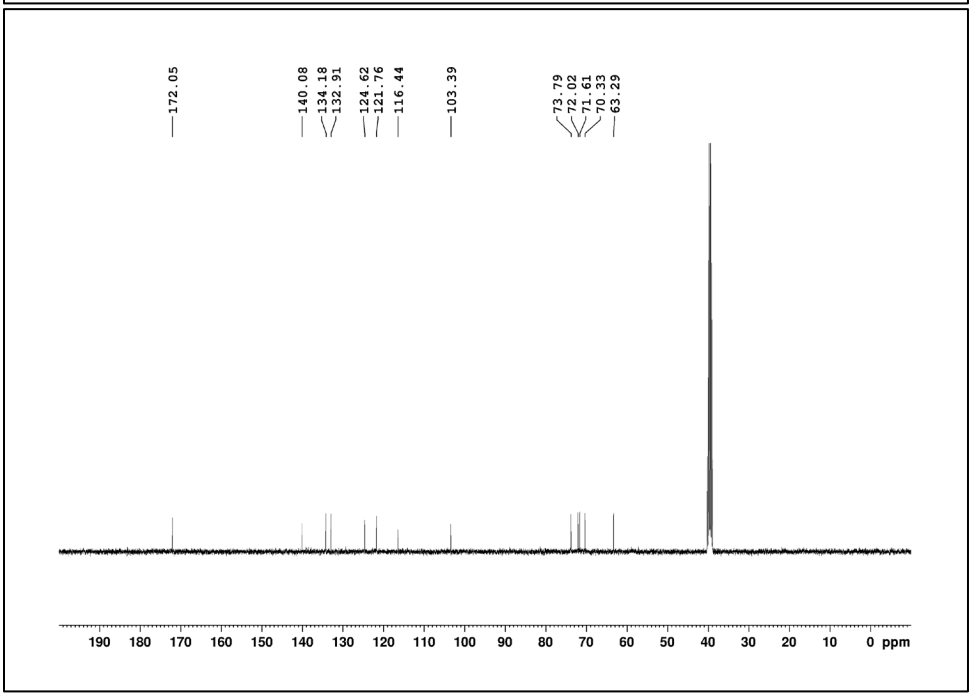




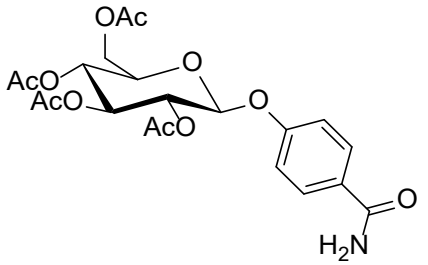


***N*-(2-cyanophenyl)-D-gluconamide (*o*CNA, 41)**



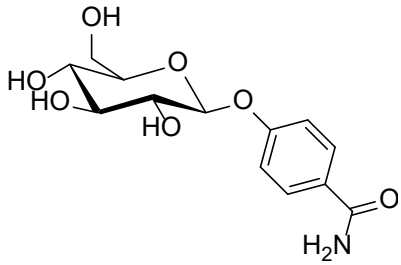


8.2.2.4. Amide-containing compounds



(4-carbamoylphenyl)-2,3,4,6-tetra-*O*-acetyl-β-D-glucopyranoside (508): Acetobromo-α-D-glucopyranose (**507**, 3.7 mmol, 1.0 eq) was dissolved in acetone (1.0 M). KOH (5.1 mmol, 1.0 eq) and 4-hydroxybenzamide (4.0 mmol, 1.0 eq) were dissolved in dH_2O (1.0 M). The two solutions were mixed and stirred at room temperature for 24 hours. The solution was then concentrated *in vacuo*, diluted in DCM, and washed with water. The organic layer was dried with Na_2SO_4, filtered, and concentrated *in vacuo*. The crude solid was recrystallized from 95 % EtOH/Ether to yield the purified product as a white solid (**19 %**).

^{1}H NMR: (400 MHz, $CDCl_3$) ∂7.79-7.77(m, 2H, *arom.*), 7.04-7.02(m, 2H, *arom.*), 5.99(br s, 1H, NH_2), 5.70(br s, 1H, NH_2), 5.34-5.27(m, 2H, H-2 and H-3), 5.20-5.15(m, 2H, H-1 and H-4), 4.28(dd, *J* = 12.3, 5.4 Hz, 1H, H-6a), 4.17(dd, J = 12.3, 2.3 Hz, 1H, H-6b), 3.90(ddd, *J* = 10.0, 5.4, 2.4Hz, 1H, H-5), 2.05(s, 3H, OAc OCH_3), 2.04(s, 3H, OAc OCH_3), 2.03(s, 3H, OAc OCH_3), 2.02(s, 3H, OAc OCH_3). **^{13}C NMR:** (101 MHz, $CDCl_3$) ∂ = 170.7 (OAc C), 170.3 (OAc C), 169.5 (OAc C), 169.4 (OAc C), 168.5 (C), 159.6 (C), 129.4 (*arom.* 2xCH), 128.2 (C), 116.6 (*arom.* 2xCH), 98.5 (C-1), 72.7 (C-2/C-3), 72.4 (C-5), 71.2 (C-2/C-3), 68.3 (C-4), 62.0 (C-6 CH_2), 20.83 (OAc CH_3), 20.76 (OAc CH_3), 20.74 (OAc CH_3), 20.72 (OAc CH_3). **HRMS (ESI):** m/z calcd for $C_{21}H_{25}NO_{11}Na$ $[M+Na]^+$ 490.1311, found 490.1325.

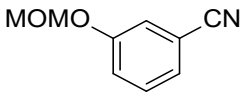


(4-carbamoylphenyl)-β-D-glucopyranoside (*p*AmPh-Glc, 31): The title compound was synthesized according to a modified literature procedure following **General Procedure 8-3**.[167,326] (4-carbamoylphenyl)-2,3,4,6-tetra-*O*-acetyl-β-D-glucopyranoside (**508**, 0.7 mmol, 1.0 eq) was dissolved in MeOH (0.2 M) and a 1 M solution of NaOMe in MeOH (0.1 eq) was added to the solution to stir for 1 hour. Upon reaction completion a white precipitate formed in solution. The solid was filtered and recrystallized from 95 % EtOH/Ether to yield the purified product as a white solid (**97 %**).

^{1}H NMR: (400 MHz, DMSO-d_6) ∂7.82(br s, 1H, NH_2), 7.79(d, *J* = 8.8 Hz, 2H, *arom.*), 7.19(br s, 1H, NH_2), 7.01(d, *J* = 8.8 Hz, 2H, *arom.*), 5.32(br s, 1H, OH-3), 5.09(br d, *J* = 3.9 Hz, 1H, OH-2), 5.02(br d, *J* = 4.5 Hz, 1H, OH-4), 4.91(d, *J* = 7.3 Hz, 1H, H-1), 4.55(br t, *J* = 5.4 Hz, 1H, OH-6), 3.65(dd, *J* = 11.6, 3.0 Hz, 1H, H-6a), 3.39-3.45(m, 1H, H-6b), 3.40-3.38(m, 1H, H-5), 3.18-3.27(m, 2H, H-2 and H-3), 3.10-3.15(m, 1H,

H-4). **^{13}C NMR:** (101 MHz, DMSO-d_6) ∂ = 167.4 (C), 159.6 (C), 129.2 (*arom.* 2xCH), 127.6 (C *arom.*), 115.5 (*arom.* 2xCH), 99.9 (C-1), 77.1 (C-5), 76.6 (C-2/C-3), 73.2 (C-2/C-3), 69.7 (C-4), 60.7 (C-6 CH_2). **HRMS (ESI):** m/z calcd for $C_{13}H_{17}NO_7Na$ $[M+Na]^+$ 322.0907, found 322.0903.

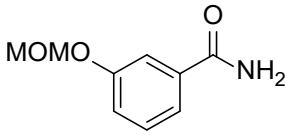
3-(methoxymethoxy)-benzonitrile (515): 3-hydroxybenzonitrile (**514**, 5.3 mmol, 1.0 eq) was dissolved in DMF (0.1 M) in a flame-dried flask under argon cooled to 0 °C. NaH (60% dispersion in mineral oil) (9.2 mmol, 1.5 eq) was added portion-wise to the flask followed by drop-wise addition of MOM-Cl (8.0 mmol, 1.5 eq). The reaction was stirred at room temperature for 1.5 hours or until complete by TLC (1:1 EtOAc:Hexanes, RF = 0.78). The solution was then diluted with EtOAc and quenched with the slow addition of water. Following extraction using EtOAc/brine (sat.) the organic phase was dried with Na_2SO_4, filtered, and concentrated *in vacuo*. The product was isolated as a clear, colourless oil (**94 %**) and was used in subsequent steps without further purification.



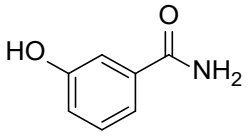
Characterization was consistent with that found in literature.[530]

^{1}H NMR: (400 MHz, $CDCl_3$) ∂7.38-7.34(m, 1H, arom.), 7.31-7.23(m, 3H, arom.), 5.17(s, 2H, OCH_2), 3.46(s, 3H, OCH_3). **^{13}C NMR:** (101 MHz, $CDCl_3$) ∂ = 157.5 (C *arom.*), 130.5 (CH *arom.*), 125.7 (CH *arom.*), 121.3 (CH *arom.*), 119.6 (CH *arom.*), 118.7 (CN), 113.4 (C *arom.*), 94.6 (CH_2), 56.3 (CH_3).

3-(methoxymethoxy)-benzamide (516): 3-(methoxymethoxy)-benzonitrile (**515**, 10.5 mmol, 1.0 eq) and potassium *tert*-butoxide (34.3 mmol, 3.0 eq) were dissolved in toluene (0.2 M) in a flame-dried flask under argon. The reaction was stirred at room temperature for 24 hours or until complete by TLC (1:1 EtOAc:Hexanes, RF = 0.2). The solution was then diluted with EtOAc and washed with water. The organic phase was dried with Na_2SO_4, filtered, and concentrated *in vacuo*. The crude product was purified by recrystallization from EtOAc/hexanes and isolated as a white solid (**22 %**).

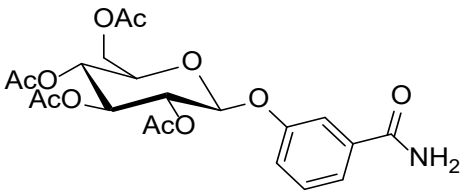


^{1}H NMR: (400 MHz, $CDCl_3$) ∂7.50-7.49(m, 1H, *arom.*), 7.43-7.41(m, 1H, *arom.*), 7.36(t, J = 7.9 Hz, 1H, *arom.*), 7.20(ddd, J = 8.1, 2.5, 1.1 Hz, 1H, *arom.*), 6.13(br s, 1H, $CONH_2$), 5.85(br s, 1H, $CONH_2$), 5.22(s, 2H, OCH_2), 3.48(s, 3H, OCH_3). **^{13}C NMR:** (101 MHz, $CDCl_3$) ∂ = 169.3 (C), 157.6 (C), 134.8 (C). 129.9 (CH *arom.*), 120.8 (CH *arom.*), 120.2 (CH *arom.*), 115.4 (CH *arom.*), 94.5 (CH_2), 56.3 (CH_3). **LRMS (ESI):** m/z calcd for $C_9H_{11}NO_3Na$ $[M+Na]^+$ 204.1, found 204.1.



3-hydroxybenzamide (517): 3-(methoxymethoxy)-benzamide (**516**, 2.3 mmol, 1.0 eq) was dissolved in a solution of 1 M HCl in MeOH (0.1 M). The reaction was stirred at 55 °C for 30 minutes. The solution was then diluted with EtOAc and washed with water. The organic phase was dried with Na_2SO_4, filtered, and concentrated *in vacuo*. The crude product was purified by recrystallization from EtOAc/hexanes and isolated as a white solid (**23 %**).

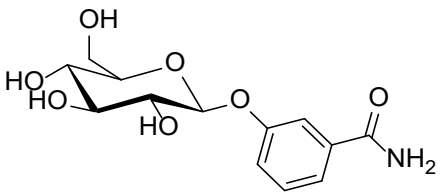
^{1}H NMR: (400 MHz, D_2O) ∂7.43-7.40(m, 1H, *arom.*), 7.38-7.35(m, 1H, *arom.*), 7.29-7.28(m, 1H, *arom.*), 7.12(ddd, *J* = 7.9, 2.6, 1.3 Hz, 1H, *arom.*). **^{13}C NMR:** (101 MHz, D_2O) ∂ = 172.8 (C), 155.7 (C), 134.3 (C *arom.*), 130.2 (CH *arom.*), 119.5 (CH *arom.*), 119.4 (CH *arom.*), 114.2 (CH *arom.*).



(3-carbamoylphenyl)-2,3,4,6-tetra-*O*-acetyl-β-D-glucopyranoside (512): Acetobromo-α-D-glucopyranose (**507**, 0.4 mmol, 1.0 eq) was dissolved in acetone (1.0 M). KOH (0.4 mmol, 1.0 eq) and 3-hydroxybenzamide (**517**, 0.4 mmol, 1.0 eq) were dissolved in dH_2O (1.0 M). The two solutions were mixed and stirred at room temperature for 24 hours. The solution was then concentrated *in vacuo*, diluted in DCM and washed with water. The organic was dried with Na_2SO_4, filtered, and concentrated *in vacuo*. The crude solid was recrystallized from MeOH/H_2O to yield the purified product as a white solid (**9 %**).

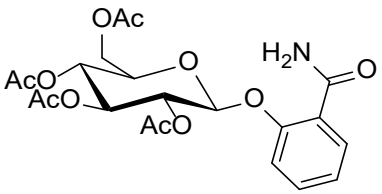
^{1}H NMR: (400 MHz, $CDCl_3$) ∂7.52-7.50(m, 2H, *arom.*), 7.40-7.36(m, 1H, *arom.*), 7.15(ddd, *J* = 8.1, 2.5, 1.0 Hz, 1H, *arom.*), 6.39(br s, 1H, NH_2), 5.87(br s, 1H, NH_2), 5.32-5.25(m, 2H, H-2 and H-3), 5.19-5.13(m, 2H, H-1 and H-4), 4.28-4.20(m, 2H, H-6), 3.88(ddd, *J* = 9.9, 5.8, 4.2 Hz, 1H, H-5), 2.08(s, 3H, OAc CH_3), 2.07(s, 3H, OAc CH_3), 2.05(s, 3H, OAc CH_3), 2.04(s, 3H, OAc CH_3). **^{13}C NMR:** (101 MHz, $CDCl_3$) ∂ = 170.9 (OAc C), 170.3 (OAc C), 169.6 (OAc C). 169.5 (OAc C), 168.7 (C), 156.9 (C), 135.0 (C), 130.0 (*arom.* CH), 122.3 (*arom.* CH), 121.3 (*arom.* CH), 116.4 (*arom.* CH), 99.0 (C-1), 72.8 (C-2/C-3/C-5), 72.3 (C-2/C-3/C-5), 71.3 (C-2/C-3/C-5), 68.4 (C-4), 61.9 (C-6 CH_2), 20.80 (OAc CH_3), 20.79 (OAc CH_3), 20.7 (2x OAc CH_3). **HRMS (ESI):** m/z calcd for $C_{21}H_{25}NO_{11}Na$ $[M+Na]^+$ 490.1325, found 490.1310.

(3-carbamoylphenyl)-β-D-glucopyranoside (*m*AmPh-Glc. 42): The title compound was synthesized according to a modified literature procedure following **General Procedure 8-3**.[167,326] (3-carbamoylphenyl)-2,3,4,6-tetra-*O*-acetyl-β-D-glucopyranoside (**512**, 0.04 mmol, 1.0 eq) was dissolved in MeOH (0.1 M) and a 1 M solution of NaOMe in MeOH (0.04 mmol, 0.1 eq) was added to the solution to stir for 1 hour. Upon reaction completion Amberlite IR120 H+ resin (washed in MeOH) was added. The solution was filtered, and the filtrate was concentrated *in vacuo*. The product was obtained as a white powder (**87 %**) without further purification.



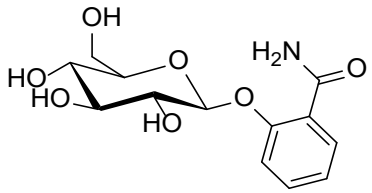
^{1}H NMR: (400 MHz, D_2O) ∂7.42-7.35(m, 3H, *arom.*), 7.22(ddd, *J* = 7.7, 2.7, 1.5 Hz, 1H, *arom.*), 5.05(d, *J* = 7.4 Hz, 1H, H-1), 3.83(dd, *J* = 12.4, 2.2 Hz, 1H, H-6a), 3.63(dd, *J* = 12.4, 5.9 Hz, 1H, H-6b), 3.55(ddd, *J* = 9.7, 5.8, 2.1 Hz, 1H, H-5), 3.53-3.45(m, 2H, H-2 and H-3), 3.41-3.36(m, 1H, H-4). **^{13}C NMR:** (101 MHz, D_2O) ∂ = 172.4 (C), 156.6 (C), 134.5 (C), 130.3 (*arom.* CH), 122.1 (*arom.* CH), 120.5 (*arom.* CH), 115.5 (*arom.* CH), 100.2 (C-1), 76.2 (C-5), 75.5 (C-2/C-3), 72.9 (C-2/C-3), 69.4 (C-4), 60.6 (C-6 CH_2). **HRMS (ESI):** m/z calcd for $C_{13}H_{17}NO_7Na$ $[M+Na]^+$ 322.0903, found 322.0912.

(2-carbamoylphenyl)-2,3,4,6-tetra-*O*-acetyl-β-D-glucopyranoside (513): Acetobromo-α-D-glucopyranose (**507**, 3.6 mmol, 1.0 eq) was dissolved in acetone (1.0 M). KOH (3.8 mmol, 1.0 eq) and salicylamide (3.7 mmol, 1.0 eq) were dissolved in dH_2O (1.0 M). The two solutions were mixed and stirred at room temperature for 24 hours. The solution was then concentrated *in vacuo*, diluted in DCM and then washed with water. The organic was dried with Na_2SO_4, filtered, and concentrated *in vacuo*. The crude oil was purified by column chromatography (1:1 EtOAc:Hexanes) to yield the product as a white solid (**19 %**).



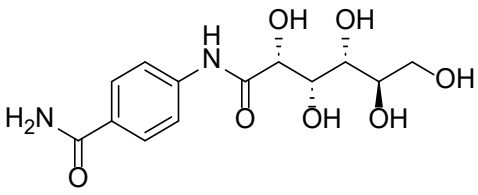
^{1}H NMR: (400 MHz, $CDCl_3$) ∂8.18(dd, *J* = 7.8, 1.9 Hz, 1H, *arom.*), 7.46(ddd, *J* = 9.1, 7.4, 1.8 Hz, 1H, *arom.*), 7.22-7.18(m, 2H, *arom.* and NH_2), 7.07-7.05(m, 1H, *arom.*), 5.75(br s, 1H, NH_2), 5.41-5.33(m, 2H, H-2 and H-3), 5.23(d, *J* = 7.6 Hz, 1H, H-1), 5.20-5.15(m, 1H, H-4), 4.32(dd, *J* = 12.4, 5.4 Hz, 1H, H-6a), 4.18(dd, *J* = 12.4, 2.4 Hz, 1H, H-6b), 3.93(ddd, *J* = 10.1, 5.4, 2.4 Hz, 1H, H-5), 2.08(s, 3H, OAc CH_3), 2.07(s, 3H, OAc CH_3), 2.06(s, 3H, OAc CH_3), 2.05(s, 3H, OAc CH_3). **^{13}C NMR:** (101 MHz, $CDCl_3$) ∂ = 170.6 (OAc C), 170.14 (OAc C), 170.12 (OAc C), 169.5 (OAc C), 166.2 (C), 154.8 (C), 133.4 (*arom.* CH), 132.9 (*arom.* CH), 123.8 (*arom.* CH), 122.5 (C), 114.9 (*arom.* CH), 98.9 (C-1), 72.5

(C-2/C-3/C-5), 72.4 (C-2/C-3/C-5), 70.9 (C-2/C-3), 68.3 (C-4), 61.8 (C-6 CH_2), 20.8 (OAc 2xCH_3), 20.7 (OAc 2xCH_3). **HRMS (ESI):** m/z calcd for $C_{21}H_{25}NO_{11}Na$ $[M+Na]^+$ 490.1325, found 490.1307.



(2-carbamoylphenyl)-β-D-glucopyranoside (*o*AmPh-Glc, 43): The title compound was synthesized according to a modified literature procedure following **General Procedure 8-3**.[167,326] (2-carbamoylphenyl)-2,3,4,6-tetra-*O*-acetyl-β-D-glucopyranoside (**513**, 0.6 mmol, 1.0 eq) was dissolved in MeOH (0.2 M) and a 1 M solution of NaOMe in MeOH (0.1 eq) was added to the solution to stir for 1 hour. Upon reaction completion, Amberlite IR120 H+ resin (washed in MeOH) was added to a pH < 4. The solution was filtered, and the filtrate was concentrated *in vacuo*. The product was recrystallized in 95 % EtOH/Ether to yield the final product as a white powder (**75 %**).

^{1}H NMR: (400 MHz, DMSO-d_6) ∂7.82(dd, *J* = 7.8, 1.8 Hz, 2H, *arom*. and NH_2), 7.58(br s, 1H, NH_2), 7.49-7.45(m, 1H, *arom.*), 7.32(d, *J* = 7.8 Hz, 1H, *arom.*), 7.14-7.10(m, 1H, *arom*.), 5.60(d, *J* = 5.0 Hz, 1H, OH-2/OH-3), 5.16(d, *J* = 4.7 Hz, 1H, OH-2/OH-3), 5.11(d, *J* = 5.4 Hz, 1H, OH-4), 4.94(d, *J* = 7.5 Hz, 1H, H-1), 4.66(t, *J* = 5.7 Hz, 1H, OH-6), 3.73(ddd, *J* = 11.9, 5.5, 1.9 Hz, 1H, H-6a), 3.52-3.46(m, 1H, H-6b), 3.39(dd, *J* = 5.9, 1.6 Hz, 1H, H-5), 3.32-3.27(m, 2H, H-2 and H-3), 3.21-3.15(m, 1H, H-4). **^{13}C NMR:** (101 MHz, DMSO-d_6) ∂ = 166.2 (C), 155.7 (C), 132.6 (*arom.* CH), 130.8 (*arom.* CH), 123.5 (C *arom.*), 122.3 (*arom.* CH), 116.5 (*arom.* CH), 102.0 (C-1), 77.5 (C-5), 76.4 (C-2/C-3), 73.4 (C-2/C-3), 69.7 (C-4), 60.7 (C-6 CH_2). **HRMS (ESI):** m/z calcd for $C_{13}H_{17}NO_7Na$ $[M+Na]^+$ 322.0903, found 322.0900.

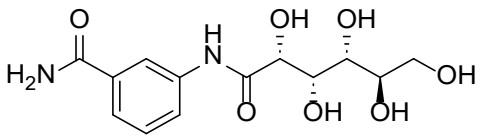


***N*-(4-carbamoylphenyl)-D-gluconamide (*p*AmA, 44):** The title compound was synthesized according to a modified literature procedure following **General Procedure 8-1** with the assistance of undergraduate student Abigail Kos.[166] Gluconolactone (**511**, 1.9 mmol, 1.0 eq) was dissolved in acetic acid (0.2 M) and 4-aminobenzamide (2.9 mmol, 1.5 eq) was added. The solution was stirred at 100 °C for 1.5 hours and then concentrated. The crude brown sludge was washed several times with hot 95 % EtOH to yield the pure product as a white powder (**11 %**).

^{1}H NMR: (400 MHz, DMSO-d_6): ∂9.74(s, 1H, NH), 7.86(br s, 1H, NH_2), 7.83-7.77(m, 4H, *arom.*), 7.25(br s, 1H, NH_2), 5.76(d, *J* = 5.2 Hz, 1H, OH-2), 4.62-4.57(m, 3H, OH-3 and OH-4 and OH-5), 4.38(br t,

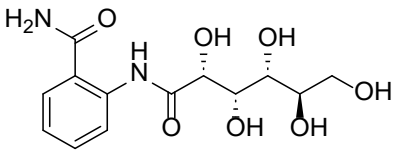
J = 5.6 Hz, 1H, OH-6), 4.20(dd, *J* = 5.1, 3.8 Hz, 1H, H-2), 4.03-4.00(m, 1H, H-3), 3.59(ddd, *J* = 11.2, 5.7, 2.6 Hz, 1H, H-6a), 3.54-3.42(m, 2H, H-4 and H-5), 3.42-3.39(m, 1H, H-6b). **^{13}C NMR:** (101 MHz, DMSO-d_6): ∂ = 172.0 (C), 167.4 (C), 141.2 (C), 128.9 (C), 128.2 (*arom.* 2xCH), 118.7 (*arom.* 2xCH), 74.3 (C-2), 72.2 (C-4/C-5), 71.6 (C-4/C-5), 70.4 (C-3), 63.3 (C-6 CH_2). **HRMS (ESI):** m/z calcd for $C_{13}H_{18}N_2O_7Na$ $[M+Na]^+$ 337.1012, found 337.1030.

***N*-(3-carbamoylphenyl)-D-gluconamide (*m*AmA, 45):** The title compound was synthesized according to a modified literature procedure following **General Procedure 8-1**.[166] Gluconolactone (**511**, 4.8 mmol, 1.0 eq) was dissolved in acetic acid (0.5 M) and 3-aminobenzamide (1.2 eq) was added. The solution was stirred at 100 °C for 1 hour and then concentrated. The crude brown sludge was recrystallized twice from 95 % EtOH to yield the pure product as an off-white (slightly brown) powder (**16 %**).



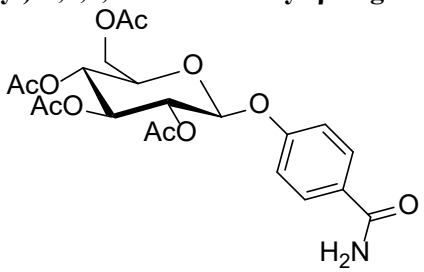
^{1}H NMR: (400 MHz, DMSO-d_6) ∂9.63(br s, 1H, NH), 8.16(br s, 1H, NH_2), 7.91(br s, 1H, NH_2), 7.86-7.82(m, 1H, *arom.*), 7.56-7.52(m, 1H, *arom.*), 7.38-7.33(m, 2H, *arom.*), 5.70(d, *J* = 5.3 Hz, 1H, OH-2), 4.61-4.56(m, 3H, OH-3 and OH-4 and OH-5), 4.37(t, *J* = 5.6 Hz, 1H, OH-6), 4.19(dd, *J* = 4.5, 4.1 Hz, 1H, H-2), 4.04-4.00(m, 1H, H-3), 3.59(ddd, *J* = 11.1, 5.5, 2.2 Hz, 1H, H-6a), 3.54-3.48(m, 2H, H-4 and H-5), 3.42-3.37(m, 1H, H-6b). **^{13}C NMR:** (101 MHz, DMSO-d_6) ∂ = 172.1 (C), 168.3 (C), 139.0 (C), 135.4 (C), 128.9 (*arom.* CH), 122.8 (*arom.* CH), 122.7 (*arom.* CH), 119.6 (*arom.* CH), 74.6 (C-2), 72.7 (C-4/C-5), 72.0 (C-4/C-5), 70.8 (C-3), 63.8 (C-6 CH_2). **HRMS (ESI):** exact m/z calcd for $C_{13}H_{18}N_2O_7Na$ $[M+Na]^+$ 337.1012, found 337.1020.

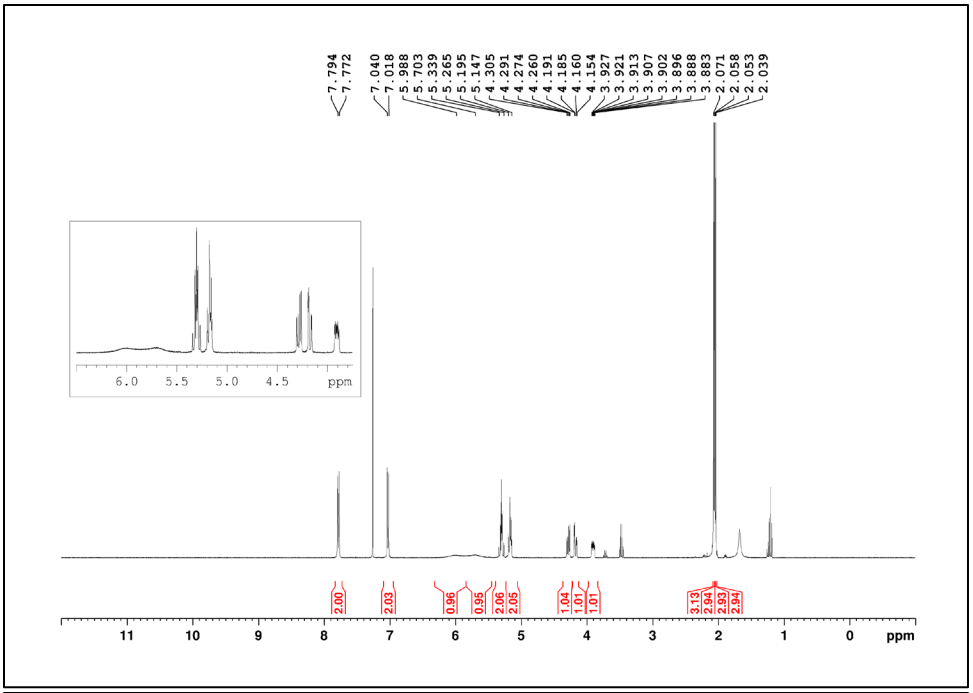
***N*-(2-carbamoylphenyl)-D-gluconamide (*o*AmA, 46):** The title compound was synthesized according to a modified literature procedure following **General Procedure 8-1** with the assistance of undergraduate student Abigail Kos.[166] Gluconolactone (**511**, 3.0 mmol, 1.0 eq) was dissolved in acetic acid (0.2 M) and 2-aminobenzamide (3.1 mmol, 1.5 eq) was added. The solution was stirred at 100 °C for 1.5 hours and then concentrated. The crude brown sludge was recrystallized from 95 % EtOH to yield the pure product as a white powder (**36 %**).

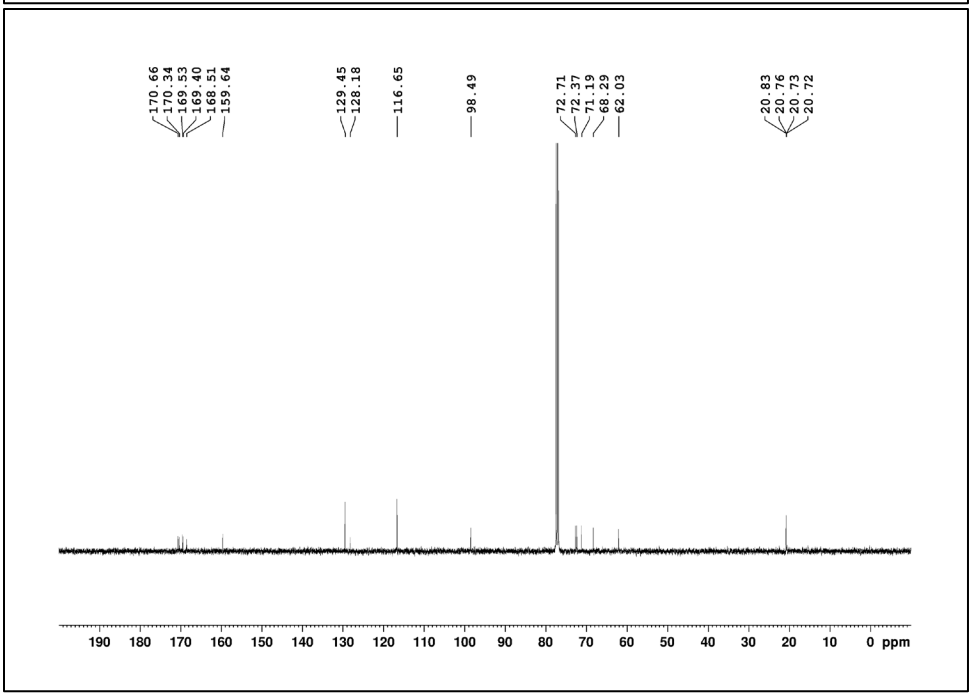


^{1}H NMR: (400 MHz, DMSO-d_6): ∂11.96(br s, 1H, NH), 8.60(dd, J = 8.4, 0.9 Hz, 1H*, arom.*), 8.15(br s, 1H*,* NH_2), 7.73(dd, J = 7.9, 1.4 Hz, 1H*, arom.*), 7.57(br s, 1H, NH_2), 7.49-7.45(m, 1H, *arom.*), 7.11(dt, J = 7.7, 1.1 Hz, 1H, *arom.*), 5.89(d, J = 4.8 Hz, 1H, OH-2), 4.60(d, J = 5.3 Hz, 1H, OH-4/OH-5), 4.56(d, J = 5.8 Hz, 1H, OH-4/OH-5), 4.50(d, J = 7.4 Hz, 1H, OH-3), 4.37(t, J = 5.7 Hz, 1H, OH-6), 4.14(dd, J = 4.6, 3.3 Hz, 1H, H-2), 4.04(dt, J = 7.3, 2.8 Hz, 1H, H-3), 3.60-3.46(m, 3H, H-4 and H-5 and H-6a), 3.41-3.37(m, 1H, H-6b). **^{13}C NMR:** (101 MHz, DMSO-d_6): ∂ = 172.2 (C), 170.2 (C), 138.7 (C), 131.8 (*arom.* CH), 128.5 (*arom.* CH), 122.3 (*arom.* CH), 120.9 (C *arom.*), 119.9 (*arom.* CH), 74.2 (C-2), 72.5 (C-4/C-5), 71.6 (C-4/C-5), 70.2 (C-3), 63.3 (C-6 CH_2). **HRMS (ESI):** exact m/z calcd for $C_{13}H_{18}N_2O_7Na$ $[M+Na]^+$ 337.1012, found 337.1002.

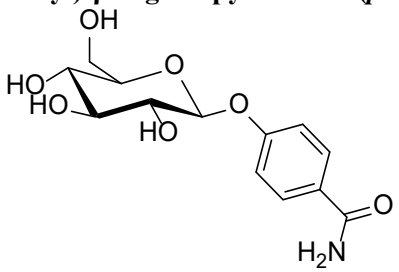
(4-carbamoylphenyl)-2,3,4,6-tetra-*O*-acetyl-β-D-glucopyranoside (508):

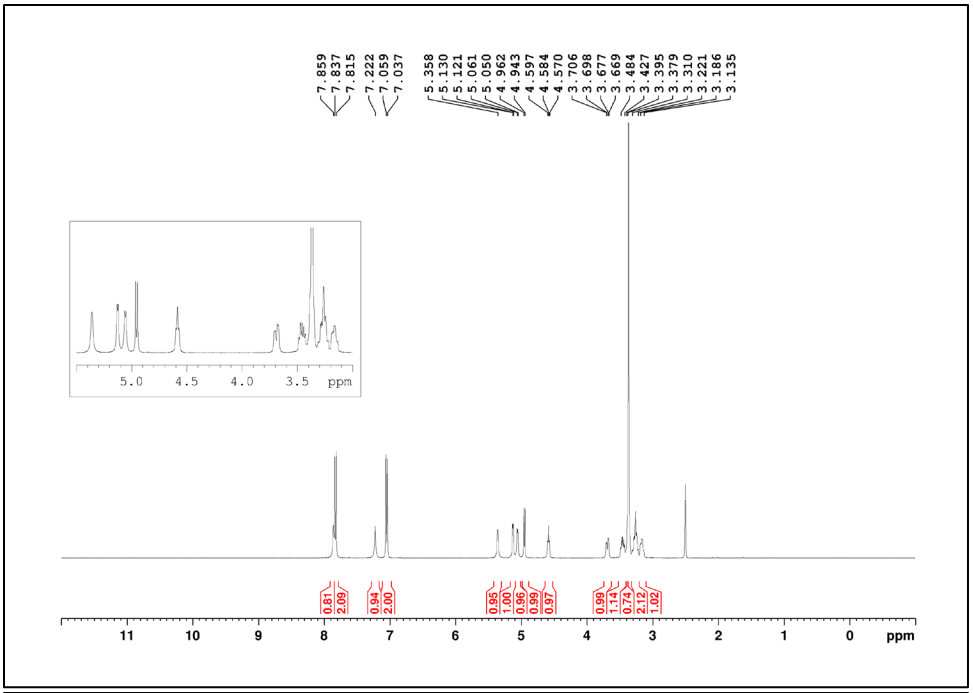


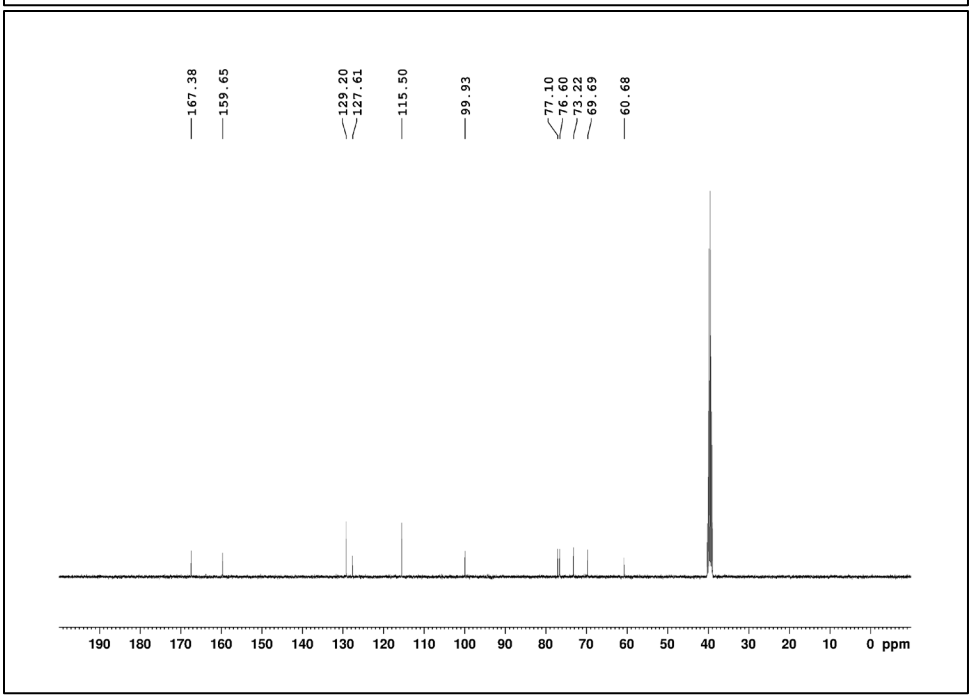




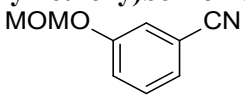
(4-carbamoylphenyl)-β-D-glucopyranoside (*p*AmPh-Glc, 31):

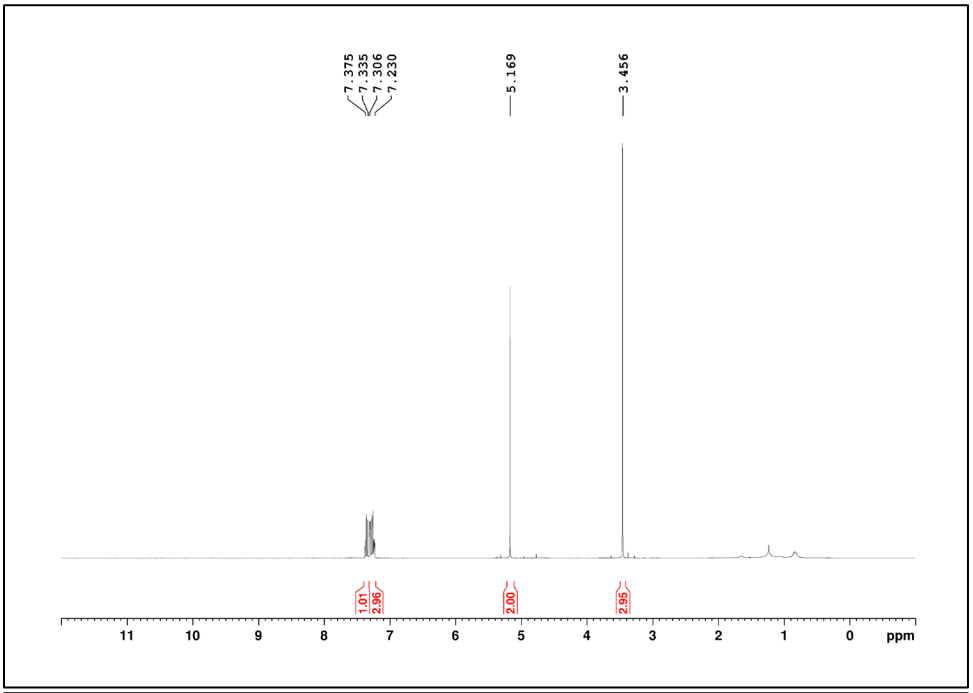


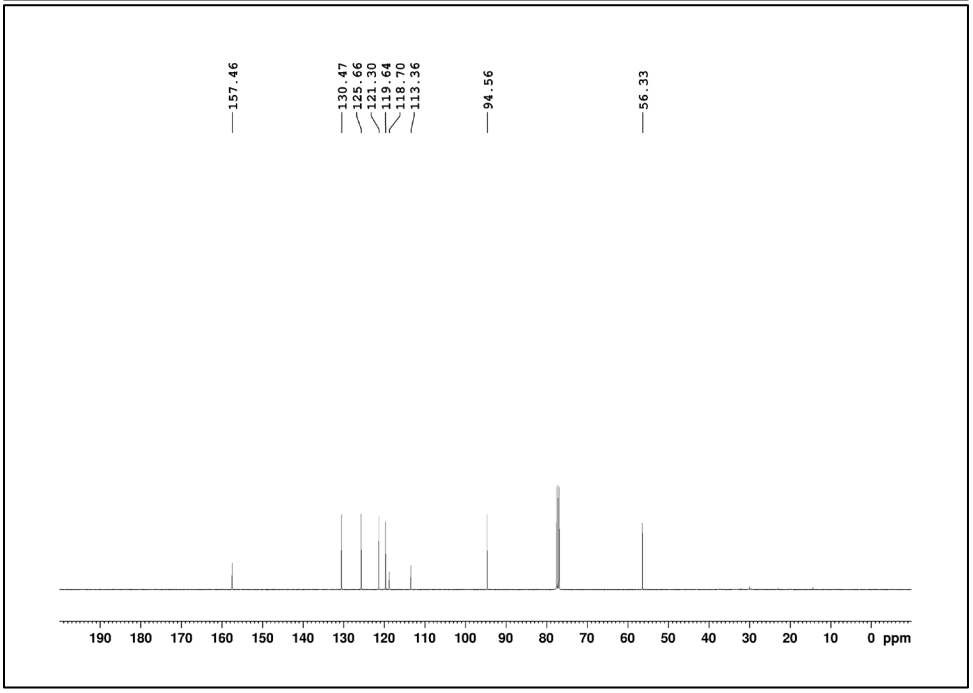




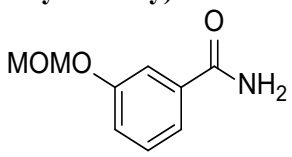
3-(methoxymethoxy)benzonitrile (515)

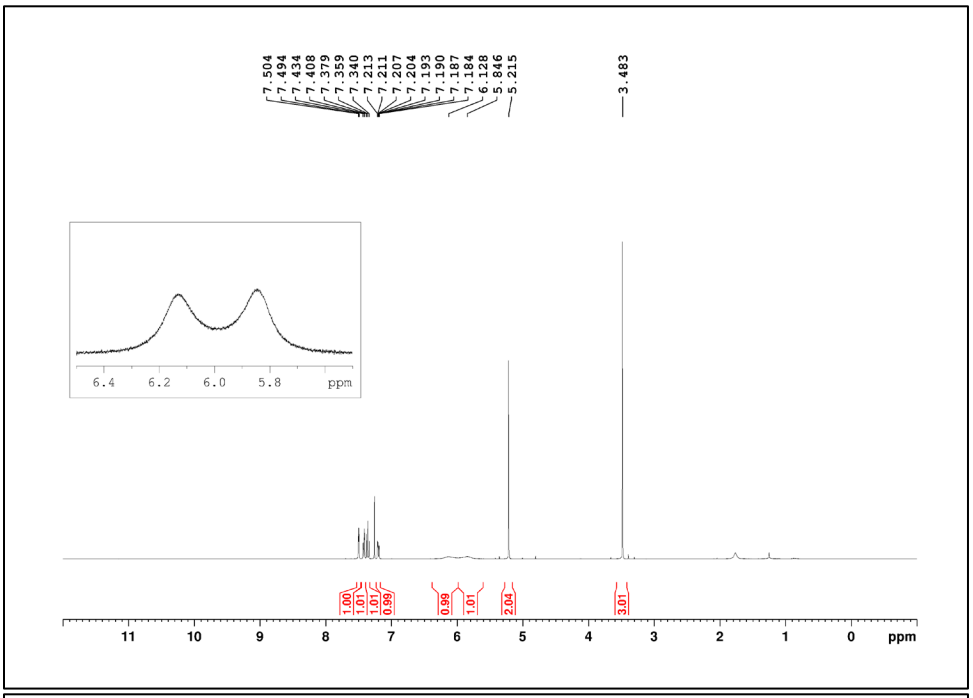


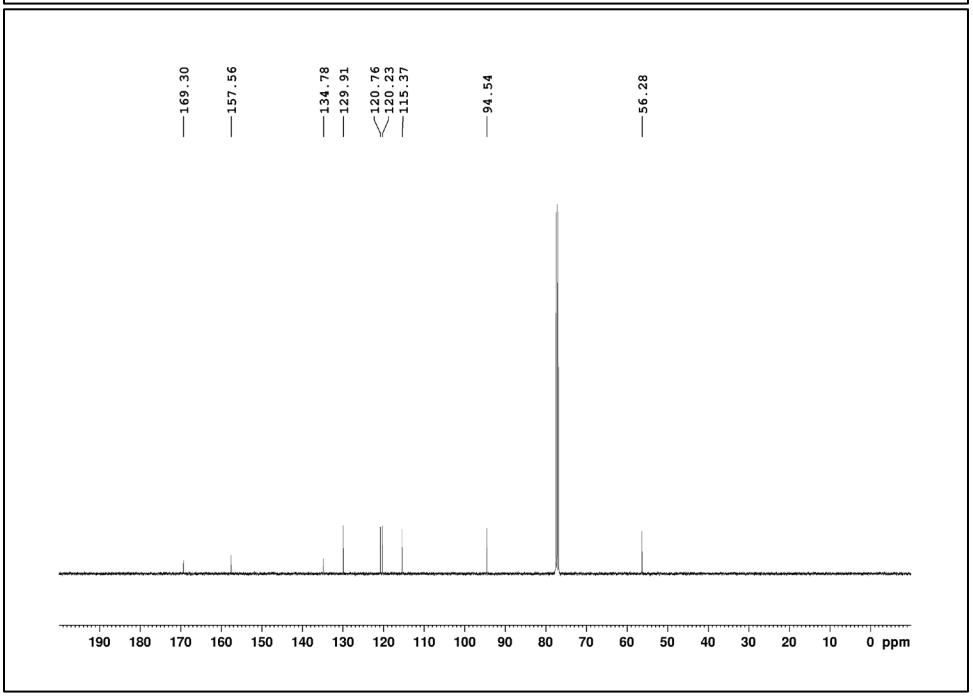




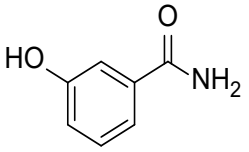
3-(methoxymethoxy)benzamide (516)

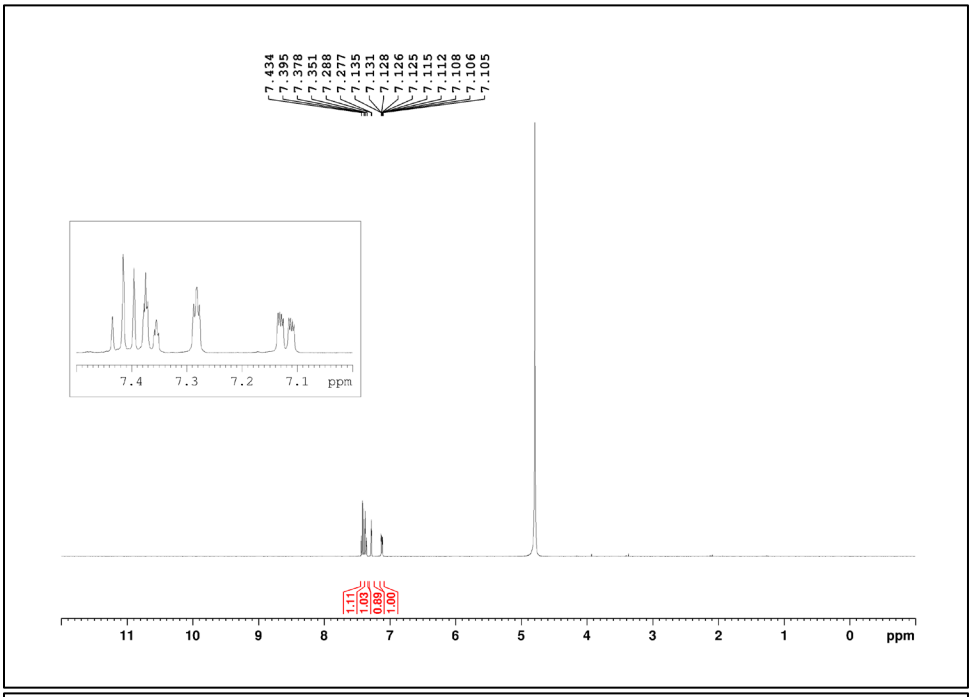


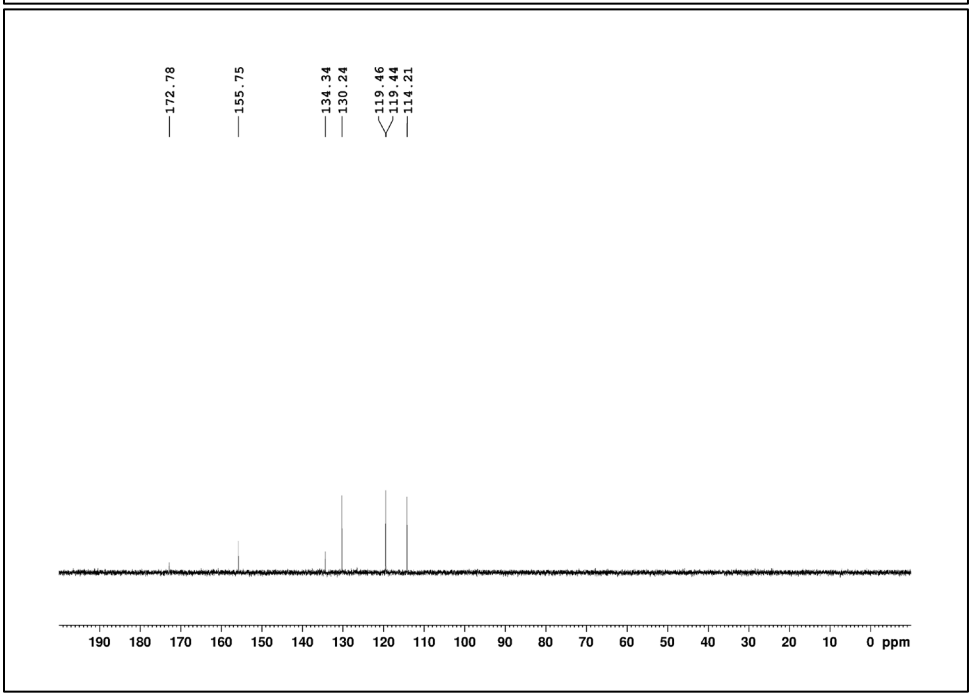




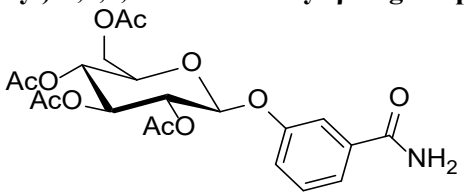
3-hydroxybenzamide (517)

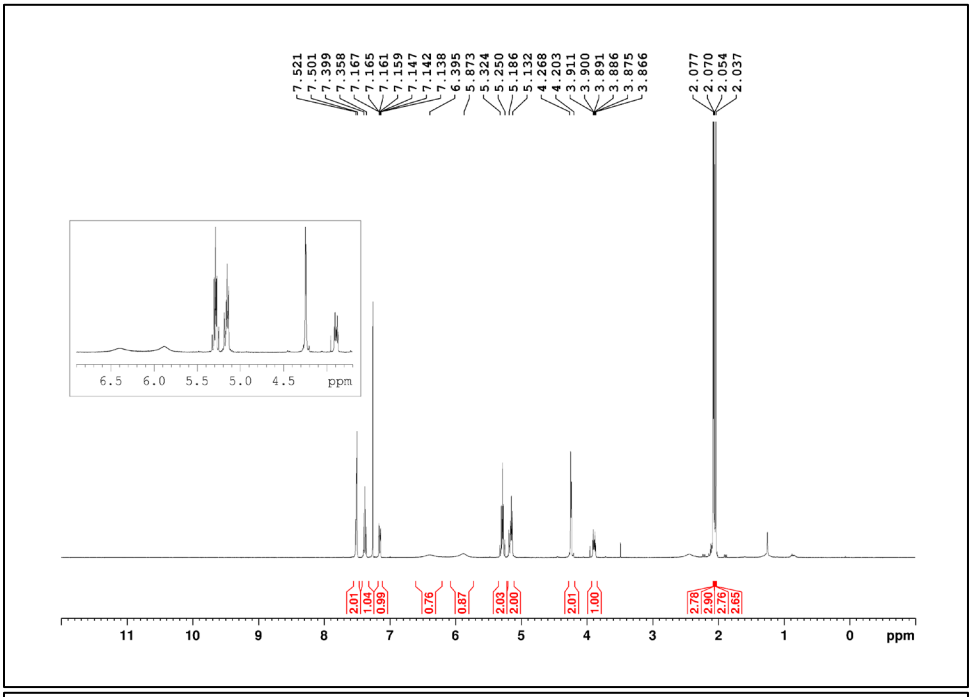


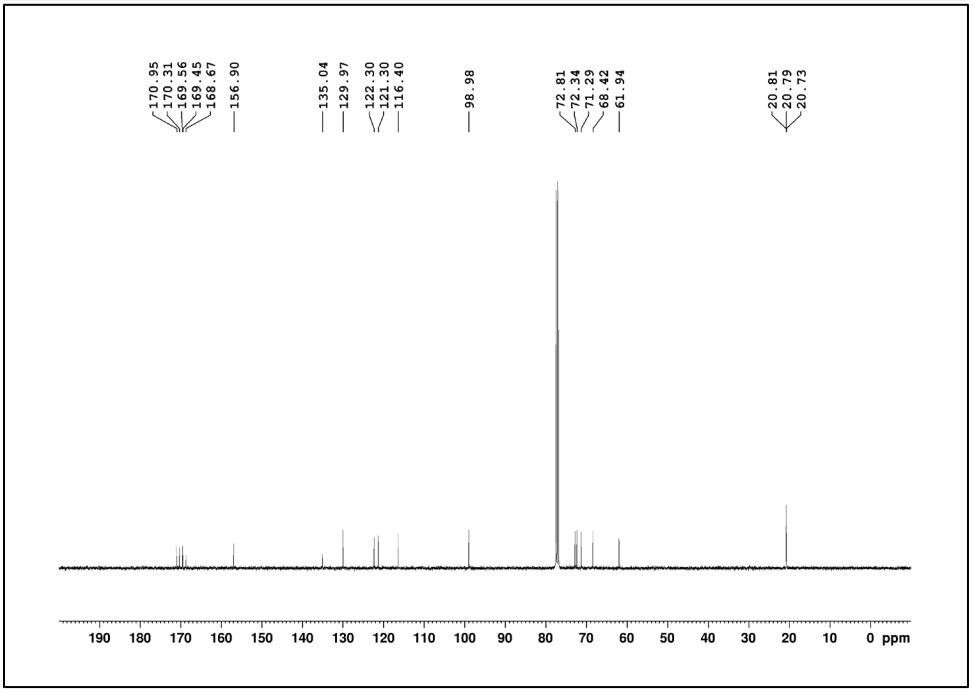




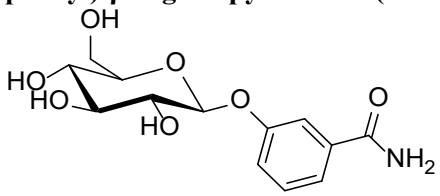
(3-carbamoylphenyl)-2,3,4,6-tetra-*O*-acetyl-β-D-glucopyranoside (512):

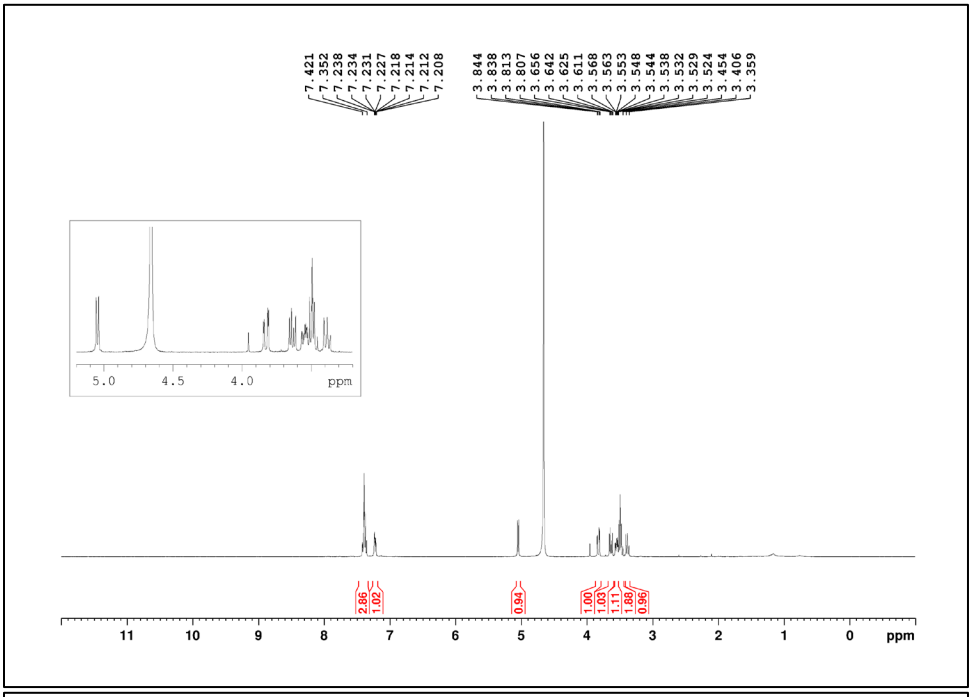


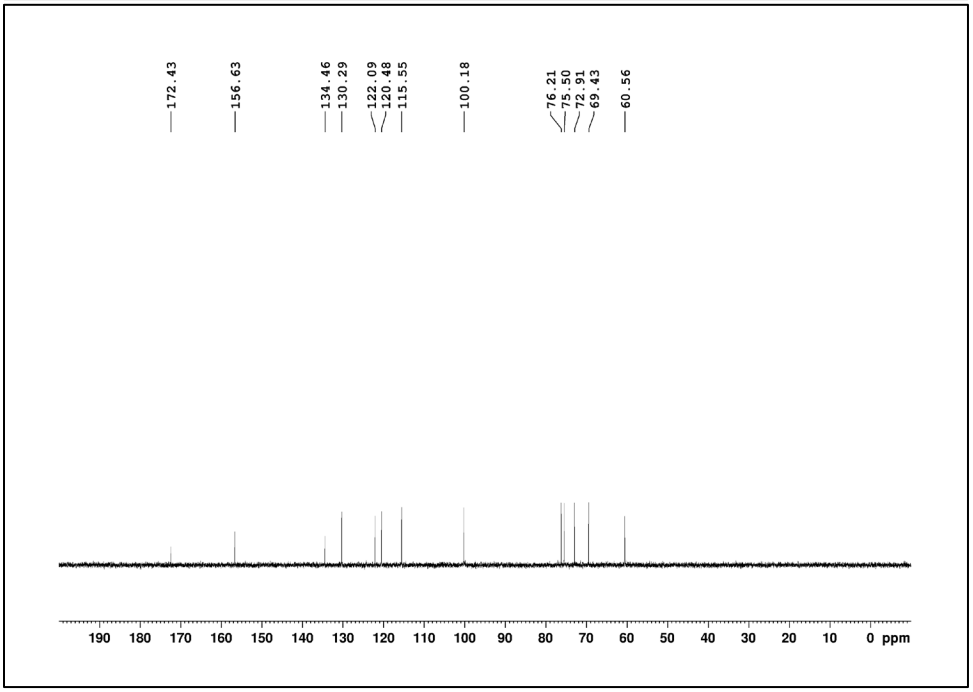




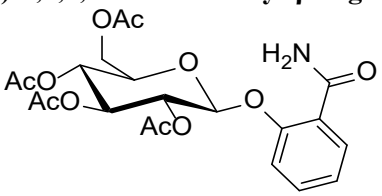
(3-carbamoylphenyl)-β-D-glucopyranoside (*m*AmPh-Glc, 42):

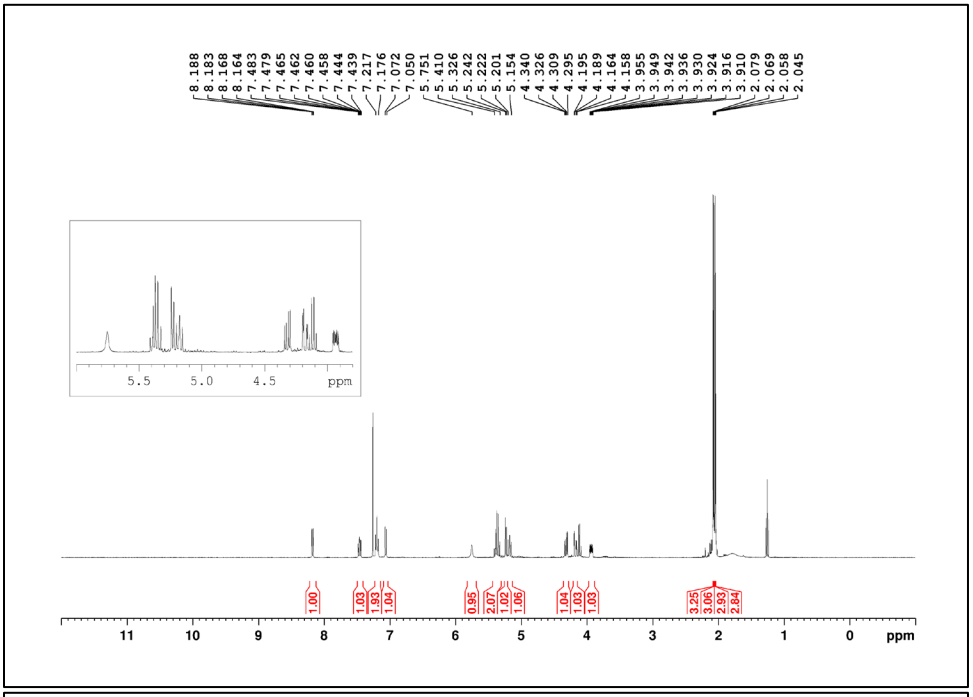


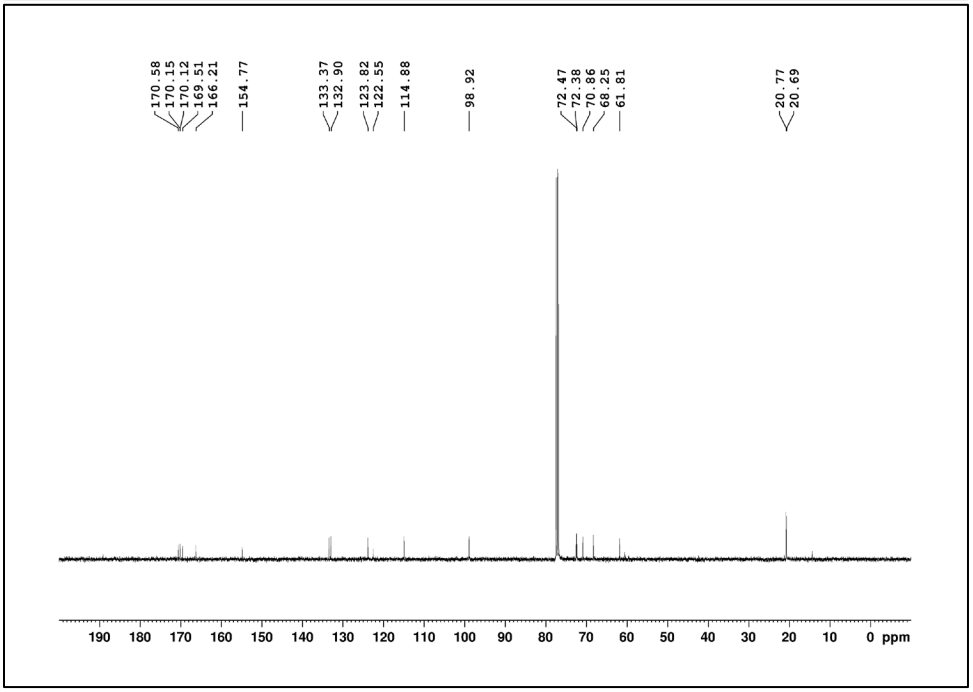




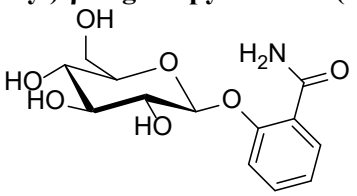
(2-carbamoylphenyl)-2,3,4,6-tetra-*O*-acetyl-β-D-glucopyranoside (513):

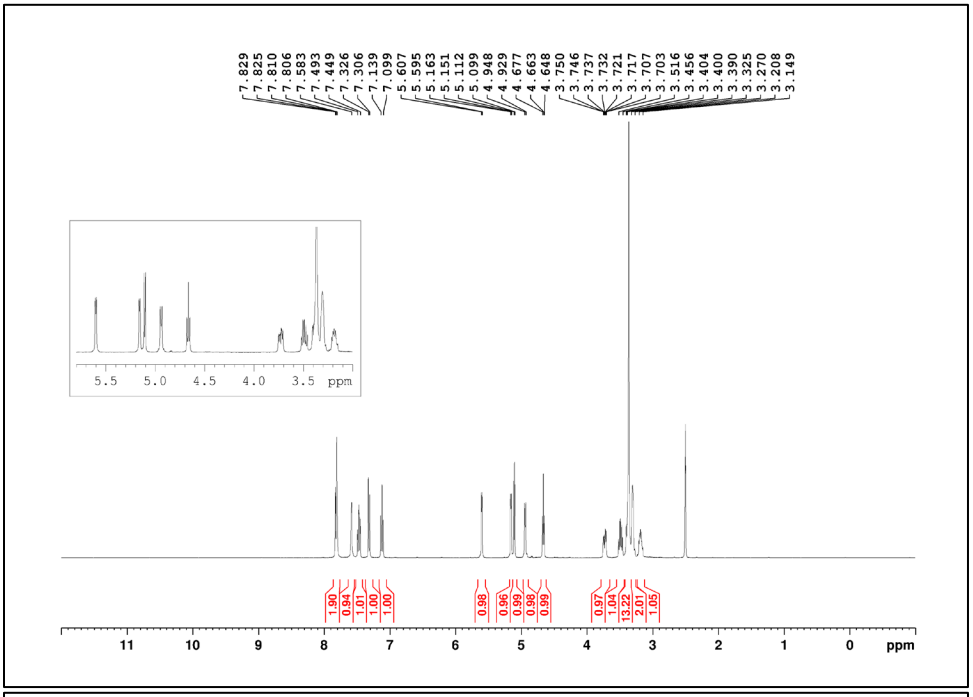


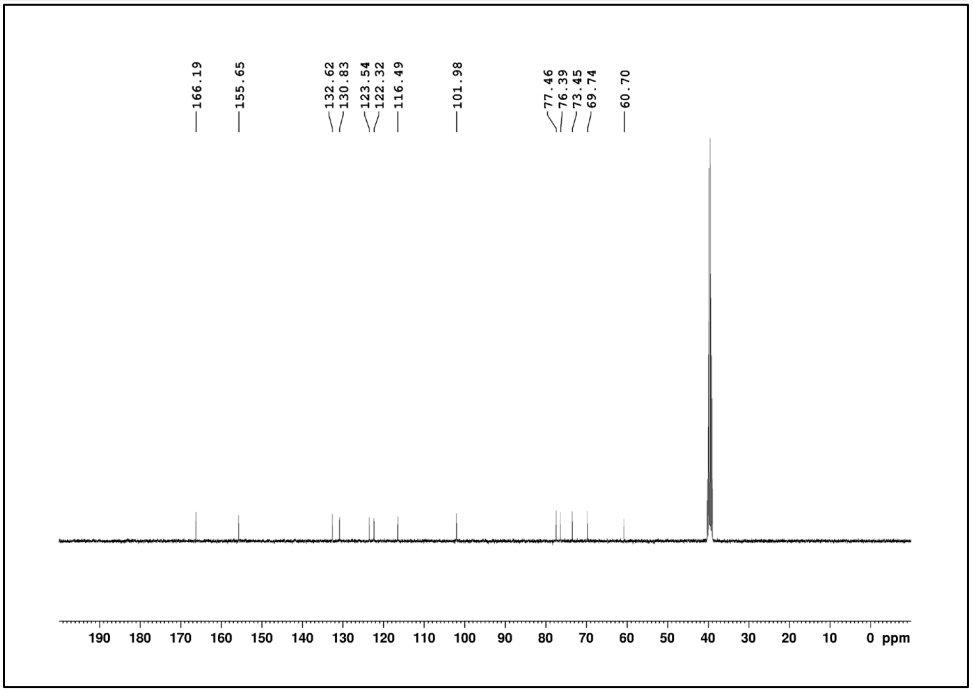




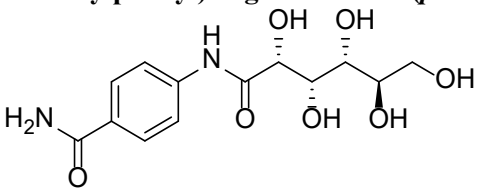
(2-carbamoylphenyl)-β-D-glucopyranoside (*o*AmPh-Glc, 43):

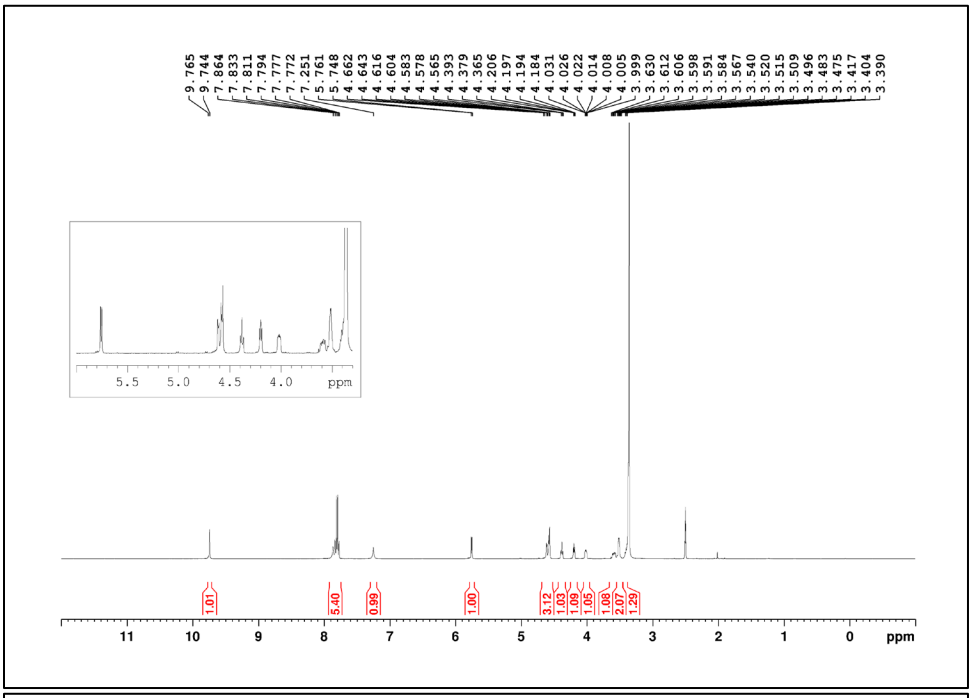


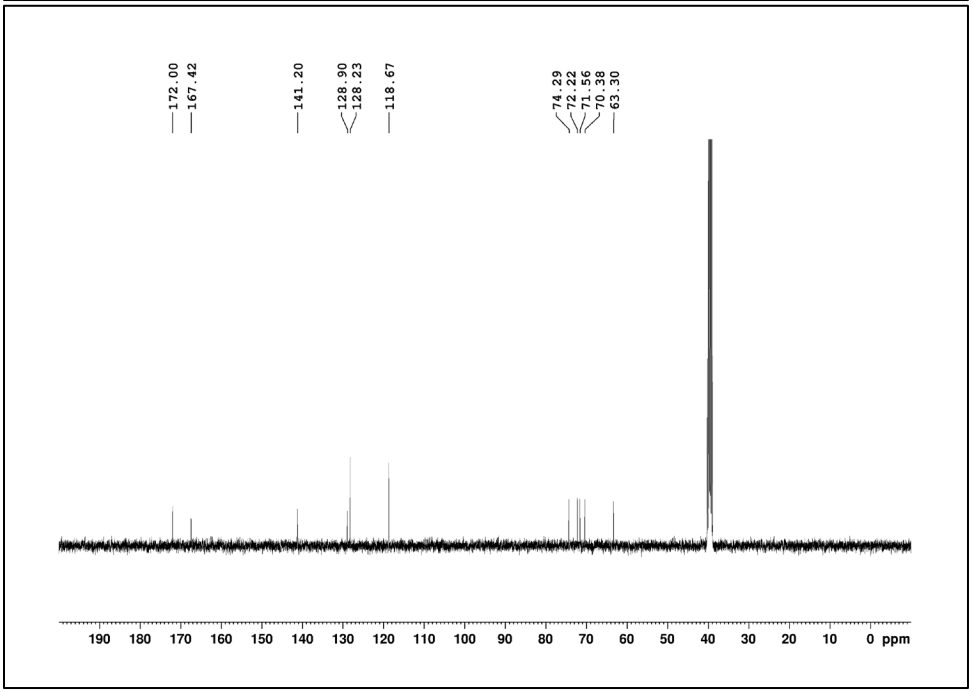




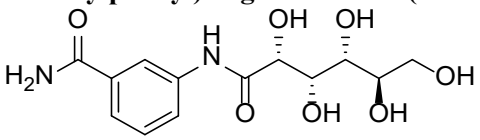
_N_-(4-carbamoylphenyl)-D-gluconamide (_p_AmA, 44):

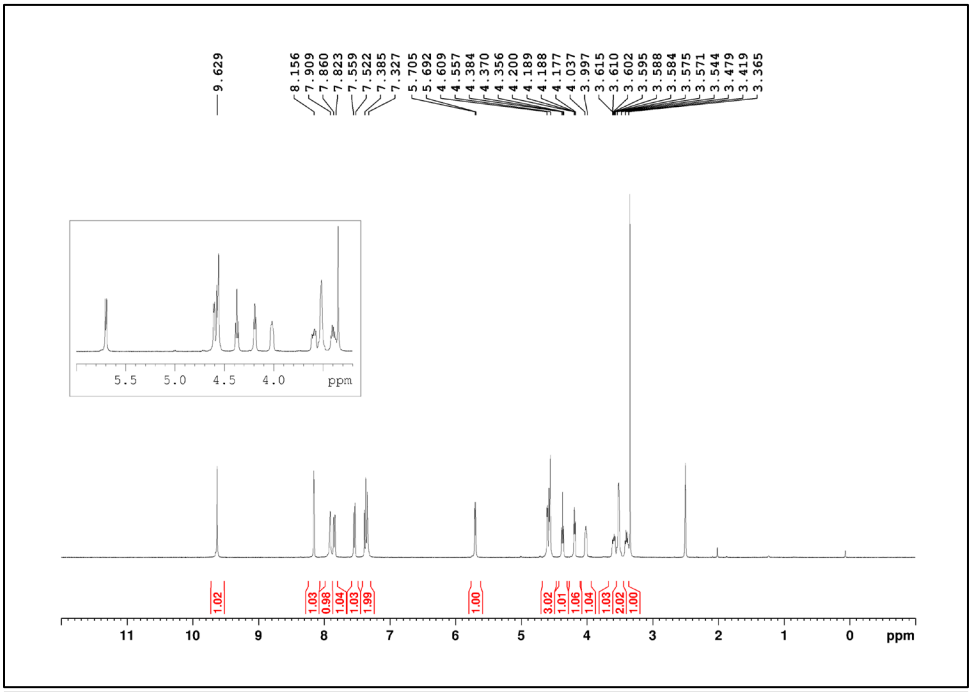


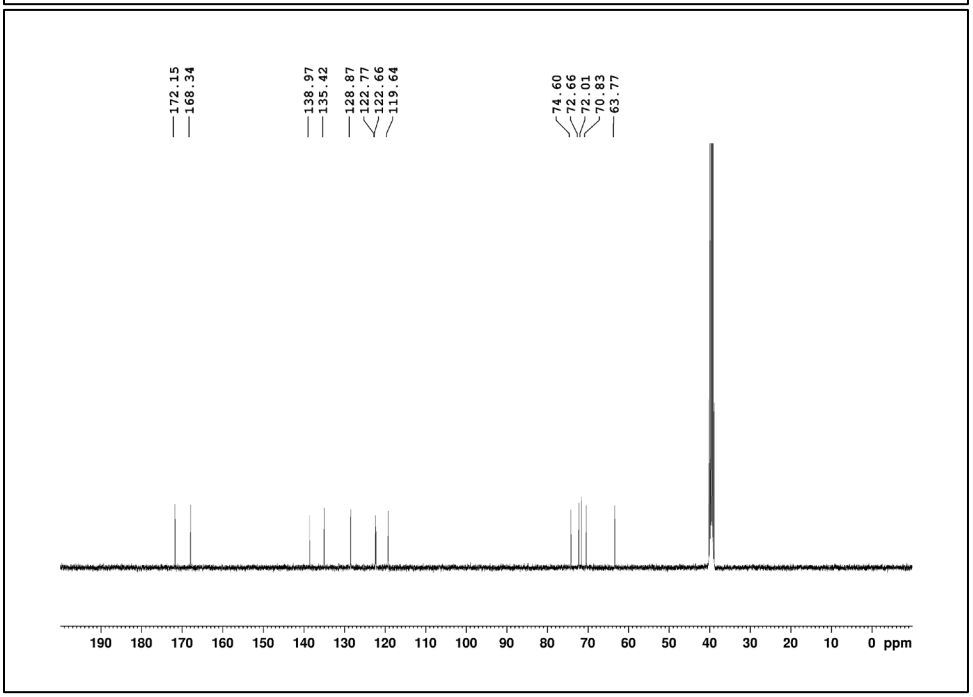




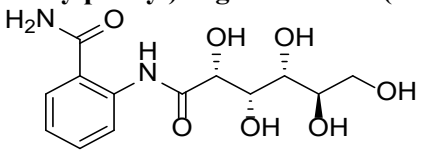
_N_-(3-carbamoylphenyl)-D-gluconamide (_m_AmA, 45):

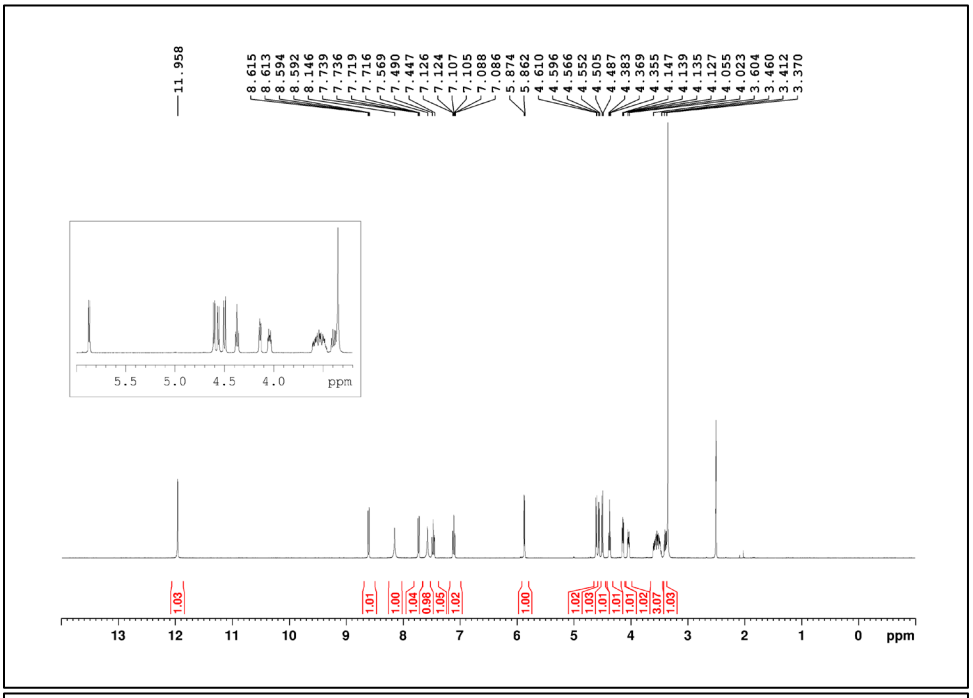


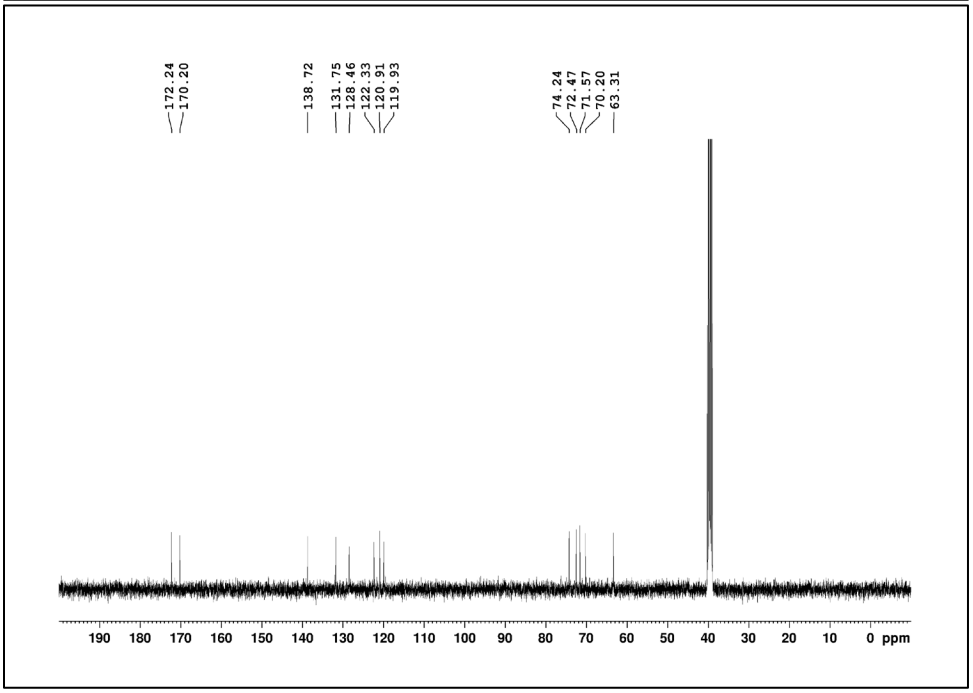




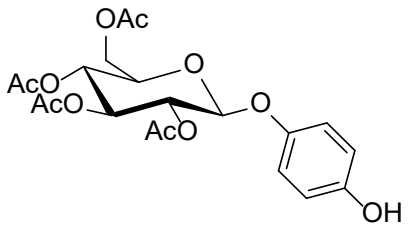
_N_-(2-carbamoylphenyl)-D-gluconamide (_o_AmA, 46):







8.2.2.5. O-aryl-β-D-glucopyranosides for structure activity relationship studies (chapter 4)



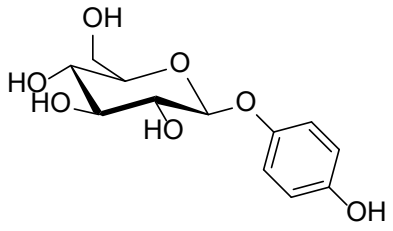
(4-hydroxyphenyl)-2,3,4,6-tetra-*O*-acetyl-β-D-glucopyranoside (518): The title compound was synthesized according to a modified literature procedure following **General Procedure 8-2**.[167,525] β-D-glucose pentaacetate (**503**, 5.0 mmol, 1.0 eq) and 4-hydroxyphenol (6.5 mmol, 1.2 eq) were dissolved in dry DCM (0.25 M) in a flame dried flask under argon at 0 ºC with 4 Å molecular sieves (powdered). Boron trifluoride diethyl etherate (48 % solution) (12.4 mmol, 2.5 eq) was added to the solution slowly. The solution was stirred overnight (18 h) and then quenched with sat. $NaHCO_3$ upon reaction completion. The solution was diluted in DCM, filtered through a Celite® pad, and the organic layer was washed with sat. $NaHCO_3$, H_2O, and brine. The organic layer was dried using Na_2SO_4, filtered, and concentrated *in vacuo*. The crude white powder was purified by column chromatography (6:4 Hexanes:EtOAc) to yield the final product as a white powder (**25 %**). The bi-product of the di-substituted phenol [1,4-bis(2,3,4,6-tetra-*O*-acetyl-β-D-glucopyranosyloxy)benzene] was also obtained as a white powder (**13 %**).

Characterization was consistent with that found in literature.[167]

518 ^{1}H NMR: (400 MHz, $CDCl_3$) ∂6.89-6.85(m, 2H, *arom.*), 6.76-6.72(m, 2H, *arom.*), 5.29-5.20(m, 2H, H-2 and H-3), 5.16(t, *J* = 9.8 Hz, 1H, H-4), 4.93(d, *J* = 7.6 Hz, 1H, H-1). 4.28(dd, *J* = 12.3, 5.1 Hz, 1H, H-6a), 4.16(dd, *J* = 12.3, 2.5 Hz, 1H, H-6b), 3.79(ddd, *J* = 9.9, 5.0, 2.5 Hz, 1H, H-5), 2.08(s, 3H, OAc OCH_3), 2.07(s, 3H, OAc OCH_3), 2.03(s, 3H, OAc OCH_3), 2.02(s, 3H, OAc OCH_3). **^{13}C NMR:** (101 MHz, $CDCl_3$) ∂ = 171.0 (OAc C), 170.5 (OAc C), 169.7 (OAc 2xC), 152.1 (C *arom.*), 150.9 (C *arom.*), 119.1 (*arom.* 2xCH), 116.1 (*arom.* 2xCH), 100.5 (C-1), 72.9 (C-2/C-3), 72.0 (C-5), 71.4 (C-2/C-3), 68.4 (C-4), 62.1(C-6 CH_2), 20.84 (OAc OCH_3), 20.80 (OAc OCH_3), 20.76 (OAc OCH_3), 20.73 (OAc OCH_3).

1,4-bis(2,3,4,6-tetra-*O*-acetyl-β-D-glucopyranosyloxy)benzene ^{1}H NMR: (400 MHz, $CDCl_3$) 6.91(s, 4H, *arom.*), 5.29-5.20(m, 4H, H-2 and H-3), 5.15(t, *J* = 9.8 Hz, 2H, H-4), 4.98(d, *J* = 7.5 Hz, 2H, H-1), 4.27(dd, *J* = 12.3, 5.1 Hz, 2H, H-6a), 4.15(dd, *J* = 12.3, 2.5 Hz, 2H, H-6b), 3.80(ddd, J = 9.9, 5.0, 2.5 Hz, 2H, H-5), 2.06(s, 6H, OAc CH_3), 2.05(s, 6H, OAc CH_3), 2.03(s, 6H, OAc CH_3), 2.02(s, 6H, OAc CH_3). **^{13}C NMR:** (101 MHz, $CDCl_3$) ∂ = 170.7 (OAc 2xC), 170.4 (OAc 2xC), 169.5 (OAc 2xC), 169.4 (OAc 2xC), 152.9 (2xC *arom.*), 118.5 (*arom* 4xCH), 99.9 (2x C-1), 72.8 (2x C-2/C-3), 72.1 (2x C-4), 71.3 (2x C-2/C-3), 68.3

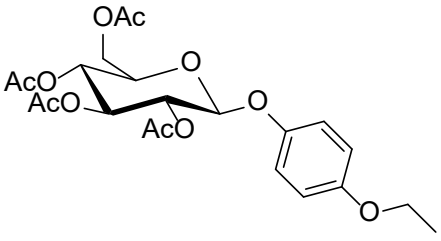
(2x C-5), 62.0 (2x C-6 CH_2), 20.81 (2x OAc CH_3), 20.76 (2x OAc CH_3), 20.72 (2x OAc CH_3), 20.70 (2x OAc CH_3)



4-hydroxyphenyl-β-D-glucopyranoside (*p*OHPh-Glc, 53): The title compound was synthesized according to a modified literature procedure following **General Procedure 8-3**.[167,326] (4-hydroxyphenyl)-2,3,4,6-tetra-*O*-acetyl-β-D-glucopyranoside (**518**, 1.2 mmol, 1.0 eq) was dissolved in MeOH (0.2 M) and a 1 M solution of NaOMe in MeOH (0.1 eq) was added to the solution to stir for 1 hour. Upon reaction completion, Amberlite IR120 H+ resin (washed in MeOH) was added to a pH < 4. The solution was filtered, and the filtrate was concentrated *in vacuo*. The product was obtained as an off-white powder without further purification (**86 %**).

Characterization was consistent with that found in literature.[531]

^{1}H NMR: (400 MHz, DMSO-d_6) 9.06(s, 1H, *arom.* OH), 6.86-6.84(m, 2H, *arom.*), 6.66-6.64(m, 2H, *arom.*), 5.27(d, J = 5.0 Hz, 1H, OH-2), 5.06(d, J = 4.7 Hz, 1H, OH-3/OH-4), 5.01(d, J = 5.3 Hz, 1H, OH-3/OH-4), 4.63(d, J = 7.5 Hz, 1H, H-1), 4.59(t, J = 5.8 Hz, 1H, OH-6), 3.67(ddd, J = 11.9, 5.3, 1.7 Hz, 1H, H-6a), 3.25-3.09(m, 4H, H-2 and H-3 and H-4 and H-5). *one proton, H-6b, is obscured by the H_2O peak at 3.45 ppm *. **^{13}C NMR:** (101 MHz, DMSO-d_6) ∂ = 152.3 (C *arom.*), 150.5 (C *arom.*), 117.8 (*arom.* 2xCH), 115.6 (*arom.* 2xCH), 101.8 (C-1), 77.0 (C-2/C-3/C-4/C-5), 76.7 (C-2/C-3/C-4/C-5), 73.4 (C-2/C-3/C-4/C-5), 69.9 (C-2/C-3/C-4/C-5), 60.9 (C-6 CH_2).



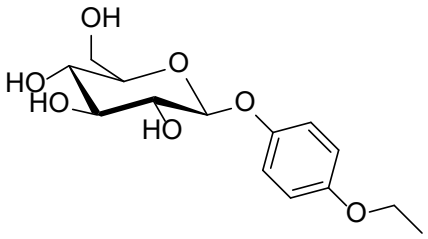
(4-ethoxyphenyl)-2,3,4,6-tetra-*O*-acetyl-β-D-glucopyranoside (520): The title compound was synthesized according to a modified literature procedure following **General Procedure 8-2**.[167,525] β-D-glucose pentaacetate (**503**, 4.3 mmol, 1.0 eq) and 4-ethoxyphenol (5.6 mmol, 1.2 eq) were dissolved in dry DCM (0.25 M) in a flame dried flask under argon at 0 ºC with 4 Å molecular sieves (powdered). Boron trifluoride diethyl etherate (48 % solution) (10.5 mmol, 2.5 eq) was added to the solution slowly. The solution was stirred overnight (18 h) and then quenched with sat. $NaHCO_3$. The solution was diluted in DCM, filtered through a Celite® pad, and the organic layer was washed with sat. $NaHCO_3$, H_2O, and brine. The organic layer was then dried using

Na_2SO_4, filtered, and concentrated *in vacuo*. The crude white powder was purified by recrystallization from EtOAc/Hexanes to yield the final product as a white powder (**66 %**).

Characterization was consistent with that found in literature.[532]

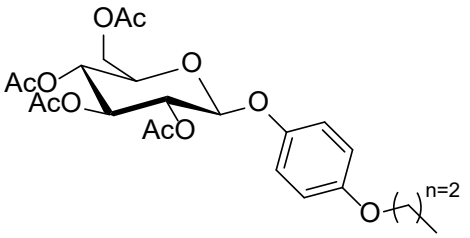
^{1}H NMR: (400 MHz, $CDCl_3$) ∂6.95-6.91(m, 2H, *arom.*), 6.83-6.79(m, 2H, *arom.*), 5.30-5.21(m, 2H, H-2 and H-3), 5.16(t, *J* = 9.7 Hz, 1H, H-4), 4.95(d, *J* = 7.6 Hz, 1H, H-1), 4.29(dd, *J* = 12.3, 5.2 Hz, 1H, H-6a), 4.16(dd, *J* = 12.3, 2.4 Hz, 1H, H-6b), 3.98(q, *J* = 6.9 Hz, 2H, O*CH*$_2$CH$_3$), 3.80(ddd, *J* = 10.0, 5.1, 2.4 Hz, 1H, H-5), 2.07(s, 3H, OAc CH_3), 2.06(s, 3H, OAc CH_3), 2.05(s, 3H, OAc CH_3), 2.03(s, 3H, OAc CH_3), 1.39(t, *J* = 7.4 Hz, 3H, OCH$_2$*CH*$_3$). **^{13}C NMR:** (101 MHz, $CDCl_3$) ∂ = 170.8 (OAc C), 170.4 (OAc C), 169.6 (OAc C), 169.5 (OAc C), 155.3 (*arom.* C), 151.0 (*arom.* C), 118.8 (2xCH *arom.*), 115.4 (2xCH *arom.*), 100.5 (C-1), 72.9 (C-2/C-3), 72.1 (C-5), 71.4 (C-2/C-3), 68.5 (C-4), 64.1 (O*CH*$_2$CH$_3$), 62.1 (C-6 CH_2), 20.9 (OAc CH_3), 20.83 (OAc CH_3), 20.79 (OAc CH_3), 20.76 (OAc CH_3), 15.0 (OCH$_2$*CH*$_3$).

(4-ethoxyphenyl)-β-D-glucopyranoside (PEP-Glc, 54): The title compound was synthesized according to a modified literature procedure following **General Procedure 8-3**.[167,326] (4-ethoxyphenyl)-2,3,4,6-tetra-*O*-acetyl-β-D-glucopyranoside (**520**, 2.8 mmol, 1.0 eq) was dissolved in MeOH (0.2 M) and a 1 M solution of NaOMe in MeOH (0.1 eq) was added to the solution to stir for 1 hour. Upon reaction completion, a white precipitate formed that was filtered and dried to yield the final product (**65 %**). If poor yields were obtained, the filtrate was acidified with Amberlite IR120 H+ resin to a pH < 4, filtered, and concentrated *in vacuo*.



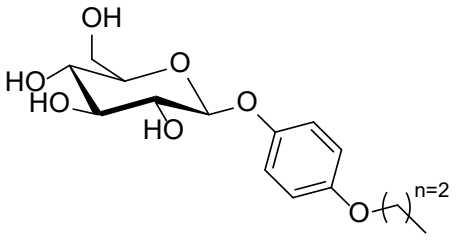
^{1}H NMR: (400 MHz, DMSO-*d*$_6$) ∂6.98-6.94(m, 2H, *arom.*), 6.84-6.80(m, 2H, *arom.*), 5.28(d, *J* = 4.6 Hz, 1H, OH-2), 5.07(d, *J* = 4.5 Hz, 1H, OH-3/OH-4), 5.00(d, *J* = 5.0 Hz, 1H, OH-3/OH-4), 4.69(d, *J* = 7.5 Hz, 1H, H-1), 4.57(t, *J* = 5.8 Hz, 1H, OH-6), 3.95(q, *J* = 7.0 Hz, 2H, O*CH*$_2$CH$_3$), 3.68(ddd, *J* = 11.6, 4.7, 1.6 Hz, 1H, H-6a), 3.48-3.43(m, 1H, H-6b), 3.28-3.10(m, 4H, H-2 and H-3 and H-4 and H-5), 1.29(t, *J* = 7.0 Hz, 3H, OCH$_2$*CH*$_3$). **^{13}C NMR:** (101 MHz, DMSO-*d*$_6$) ∂ = 153.6 (*arom.* C), 151.5 (*arom.* C), 117.7 (2xCH *arom.*), 115.1(2xCH *arom.*), 101.6 (C-1), 77.1 (C-2/C-3/C-4/C-5), 76.7 (C-2/C-3/C-4/C-5), 73.4 (C-2/C-3/C-4/C-5), 69.9 (C-2/C-3/C-4/C-5), 63.4 (O*CH*$_2$CH$_3$), 60.9 (C-6 CH_2), 14.8 (OCH$_2$*CH*$_3$). **LRMS (ESI):** m/z calcd for $C_{14}H_{20}O_7Na$ $[M+Na]^+$ 323.1, found 323.1.

(4-propoxyphenyl)-2,3,4,6-tetra-*O*-acetyl-β-D-glucopyranoside (521): The title compound was synthesized according to a modified literature procedure following **General Procedure 8-2**.[167,525] β-D-glucose pentaacetate (**503**, 4.0 mmol, 1.0 eq) and 4-propoxyphenol (5.2 mmol, 1.2 eq) were dissolved in dry DCM (0.25 M) in a flame dried flask under argon at 0 ºC with 4 Å molecular sieves (powdered). Boron trifluoride diethyl etherate (48 % solution) (10.1 mmol, 2.5 eq) was added to the solution slowly. The solution was stirred overnight (18 h) and then quenched with sat. $NaHCO_3$. The solution was diluted in DCM, filtered through a Celite® pad, and the organic layer was washed with sat. $NaHCO_3$, H_2O, and brine. The organic layer was then dried using Na_2SO_4, filtered, and concentrated *in vacuo*. The crude white powder was purified by recrystallization from EtOAc/Hexanes to yield the final product as a white powder (**72 %**).

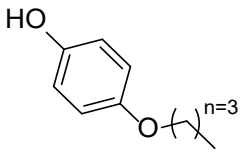


^{1}H NMR: (400 MHz, $CDCl_3$) ∂6.95-6.91(m, 2H, *arom.*), 6.83-6.79(m, 2H, *arom.*), 5.30-5.21(m, 2H, H-2 and H-3), 5.16(t, *J* = 9.6 Hz, 1H, H-4), 4.95(d, *J* = 7.6 Hz, 1H, H-1), 4.29(dd, *J* = 12.3, 5.2 Hz, 1H, H-6a), 4.16(dd, *J* = 12.2, 2.4 Hz, 1H, H-6b), 3.87(t, *J* = 6.6 Hz, 2H, O*CH*$_2$CH$_2$CH$_3$), 3.80(ddd, *J* = 10.0, 5.2, 2.4 Hz, 1H, H-5), 2.08(s, 3H, OAc CH_3), 2.07(s, 3H, OAc CH_3), 2.04(s, 3H, OAc CH_3), 2.03(s, 3H, OAc CH_3), 1.78(sxt, *J* = 6.9 Hz, 2H, OCH$_2$*CH*$_2$CH$_3$), 1.02(t, *J* = 7.4 Hz, 3H, OCH$_2$CH$_2$*CH*$_3$). **^{13}C NMR:** (101 MHz, $CDCl_3$) ∂ = 170.8 (OAc C), 170.4 (OAc C), 169.6 (OAc C), 169.5 (OAc C), 155.5 (*arom.* C), 150.9 (*arom.* C), 118.8 (2xCH *arom.*), 115.4 (2xCH *arom.*), 100.5 (C-1), 72.9 (C-2/C-3), 72.1 (C-5), 71.4 (C-2/C-3), 70.2 (O*CH*$_2$CH$_2$CH$_3$), 68.5 (C-4), 62.1 (C-6 CH_2), 22.7 (OCH$_2$*CH*$_2$CH$_3$), 20.9 (OAc CH_3), 20.82 (OAc CH_3), 20.78 (OAc CH_3), 20.75 (OAc CH_3), 10.6 (OCH$_2$CH$_2$*CH*$_3$). **LRMS (ESI):** m/z calcd for $C_{23}H_{30}O_{11}Na$ $[M+Na]^+$ 505.2, found 505.1.

(4-propoxyphenyl)-β-D-glucopyranoside (PPP-Glc, 55): The title compound was synthesized according to a modified literature procedure following **General Procedure 8-3**.[167,326] (4-propoxyphenyl)-2,3,4,6-tetra-*O*-acetyl-β-D-glucopyranoside (**521**, 2.9 mmol, 1.0 eq) was dissolved in MeOH (0.2 M) and a 1 M solution of NaOMe in MeOH (0.1 eq) was added to the solution to stir for 1 hour. Upon reaction completion, Amberlite IR120 H+ resin (washed in MeOH) was added to a pH < 4. The solution was filtered, and the filtrate was concentrated *in vacuo*. The final product was obtained as a white powder (**93 %**).



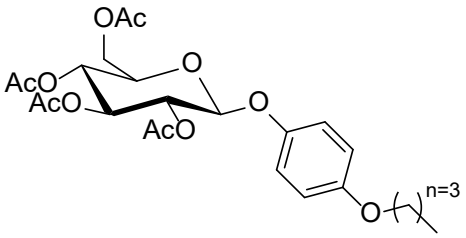
^{1}H NMR: (400 MHz, DMSO-d_6) ∂6.98-6.94(m, 2H, *arom.*), 6.85-6.81(m, 2H, *arom.*), 5.26(d, *J* = 4.9 Hz, 1H, OH-2), 5.05(d, *J* = 4.6 Hz, 1H, OH-3/OH-4), 4.99(d, *J* = 5.2 Hz, 1H, OH-3/OH-4), 4.70(d, *J* = 7.4 Hz, 1H, H-1), 4.55(t, *J* = 5.8 Hz, 1H, OH-6), 3.85(t, *J* = 6.5 Hz, 2H, O*CH*$_2$CH$_2$CH$_3$), 3.69(ddd, J = 11.8, 5.3, 1.7 Hz, 1H, H-6a), 3.49-3.43(m, 1H, H-6b), 3.28-3.11(m, 4H, H-2 and H-3 and H-4 and and H-5), 1.69(sxt, *J* = 7.2 Hz, 2H, OCH$_2$*CH*$_2$CH$_3$), 0.96(t, *J* = 7.4 Hz, 1H, OCH$_2$CH$_2$*CH*$_3$). **^{13}C NMR:** (101 MHz, DMSO-d_6) ∂ = 153.8 (*arom.* C), 151.5 (*arom.* C), 117.7 (2xCH *arom.*), 115.2(2xCH *arom.*), 101.6 (C-1), 77.1 (C-2/C-3/C-4/C-5), 76.7 (C-2/C-3/C-4/C-5), 73.4 (C-2/C-3/C-4/C-5), 69.9 (C-2/C-3/C-4/C-5), 69.4 (O*CH*$_2$CH$_2$CH$_3$), 60.9 (C-6 CH$_2$), 22.2 (OCH$_2$*CH*$_2$CH$_3$), 10.6 (OCH$_2$CH$_2$*CH*$_3$). **LRMS (ESI):** m/z calcd for $C_{15}H_{22}O_7Na$ $[M+Na]^+$ 337.1, found 337.1.



4-butoxyphenol: Hydroxyquinone (9.5 mmol, 1.0 eq) was dissolved in dry DMF (1.5 M) with NaOH (356 mg, 8.9 mmol, 1.0 eq) in a flame-dried flask under argon. 1-bromobutane (7.4 mmol, 0.8 eq) was added slowly and the reaction was stirred for 24 h at room temperature. The reaction was quenched by diluting with EtOAc and the addition of 1 M HCl. The organic EtOAc layer was then washed with and 1 M HCl, H_2O, and brine. The organic layer was dried using Na_2SO_4, filtered, and concentrated *in vacuo*. The crude brown sludge was purified by column chromatography from 1:9 EtOAc/Hexanes to yield the final product as a white powder (**34 %**).

Characterization was consistent with that found in literature.[533]

^{1}H NMR: (400 MHz, $CDCl_3$) ∂6.80-6.74(m, 4H, *arom.*), 4.48(bs, 1H, *arom.* OH), 3.90(t, *J* = 6.5 Hz 2H, O*CH*$_2$CH$_2$CH$_2$CH$_3$), 1.74(qu, *J* = 6.5 Hz, 2H, OCH$_2$*CH*$_2$CH$_2$CH$_3$), 1.48(sxt, *J* = 7.5 Hz, 2H, OCH$_2$CH$_2$*CH*$_2$CH$_3$), 0.97(t, *J* = 7.4 Hz, 3H, OCH$_2$CH$_2$CH$_2$*CH*$_3$). **^{13}C NMR:** (101 MHz, $CDCl_3$) ∂ = 153.5 (*arom.* C), 149.5 (*arom.* C), 116.1 (2xCH *arom.*), 115.8 (2xCH *arom.*), 68.6 (O*CH*$_2$CH$_2$CH$_2$CH$_3$), 31.6 (OCH$_2$*CH*$_2$CH$_2$CH$_3$), 19.4 (OCH$_2$CH$_2$*CH*$_2$CH$_3$), 14.0 (OCH$_2$CH$_2$CH$_2$*CH*$_3$).

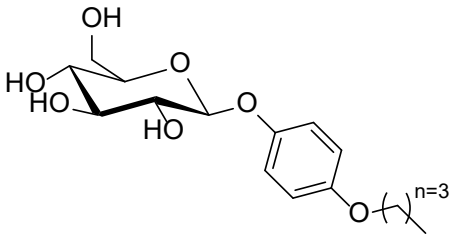


(4-butoxyphenyl)-2,3,4,6-tetra-*O*-acetyl-β-D-glucopyranoside (522): The title compound was synthesized according to a modified literature procedure following **General Procedure 8-2**.[167,525] β-D-glucose pentaacetate (**503**, 1.6 mmol, 1.0 eq) and 4-butoxyphenol (2.6 mmol, 1.5 eq) were dissolved in dry DCM (0.25 M) in a flame dried flask under

argon at 0 ºC with 4 Å molecular sieves (powdered). Boron trifluoride diethyl etherate (48 % solution) (3.9 mmol, 2.5 eq) was added to the solution slowly. The solution was stirred overnight (18 h) and then quenched with sat. $NaHCO_3$. The solution was diluted in DCM, filtered through a Celite® pad, and then washed with sat. $NaHCO_3$, H_2O, and brine. The organic layer was dried using Na_2SO_4, filtered, and concentrated *in vacuo*. The crude white powder was purified by recrystallization from EtOAc/Hexanes to yield the final product as a white powder (**65 %**).

Characterization was consistent with that found in literature.[532]

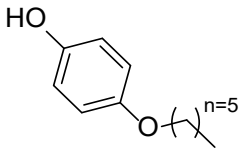
^{1}H NMR: (400 MHz, $CDCl_3$) ∂6.95-6.91(m, 2H, *arom.*), 6.83-6.78(m, 2H, *arom.*), 5.30-5.21(m, 2H, H-2 and H-3), 5.16(t, *J* = 9.7 Hz, 1H, H-4), 4.94(d, *J* = 7.5 Hz, 1H, H-1), 4.29(dd, *J* = 12.3, 5.2 Hz, 1H, H-6a), 4.16(dd, *J* = 12.2, 2.4 Hz, 1H, H-6b), 3.91(t, *J* = 6.5 Hz, 2H, O*CH*$_2$CH$_2$CH$_2$CH$_3$), 3.80(ddd, J = 9.9, 5.2, 2.4 Hz, 1H, H-5), 2.08(s, 3H, OAc CH_3), 2.07(s, 3H, OAc CH_3), 2.04(s, 3H, OAc CH_3), 2.03(s, 3H, OAc CH_3), 1.74(qu, *J* = 6.5 Hz, 2H, OCH$_2$*CH*$_2$CH$_2$CH$_3$), 1.48(sxt, *J* = 6.5 Hz, 2H, OCH$_2$CH$_2$*CH*$_2$CH$_3$), 0.97(t, *J*<= 7.4Hz, 3H, OCH$_2$CH$_2$CH$_2$*CH*$_3$). **^{13}C NMR:** (101 MHz, $CDCl_3$) ∂ = 170.7 (OAc C), 170.4 (OAc C), 169.5 (OAc C), 169.4 (OAc C). 155.6 (*arom.* C), 151.0 (*arom.* C), 118.9 (2xCH *arom.*), 115.4 (2xCH *arom.*), 100.5 (C-1), 72.9 (C-2/C-3), 72.1 (C-5), 71.4 (C-2/C-3), 68.5 (C-4), 68.4 (O*CH*$_2$CH$_2$CH$_2$CH$_3$), 62.1 (C-6 CH_2), 31.5 (OCH$_2$*CH*$_2$CH$_2$CH$_3$), 20.9 (OAc CH_3), 20.81 (OAc CH_3), 20.77 (OAc CH_3), 20.74 (OAc CH_3), 19.4 (OCH$_2$CH$_2$*CH*$_2$CH$_3$), 14.0 (OCH$_2$CH$_2$CH$_2$*CH*$_3$).



(4-butoxyphenyl)-β-D-glucopyranoside (PBP-Glc, 56): The title compound was synthesized according to a modified literature procedure following **General Procedure 8-3**.[167,326] (4-butoxyphenyl)-2,3,4,6-tetra-*O*-acetyl-β-D-glucopyranoside (**522**, 1.0 mmol, 1.0 eq) was dissolved in MeOH (0.1 M) and a 1 M solution of NaOMe in MeOH (0.1 eq) was added to the solution to stir for 1 hour. Upon reaction completion, Amberlite IR120 H+ resin (washed in MeOH) was added to a pH < 4. The solution was filtered, and the filtrate was concentrated *in vacuo*. The final product was obtained as a white powder (**99 %**).

^{1}H NMR: (400 MHz, DMSO-d_6) ∂6.97-6.93(m, 2H, *arom.*), 6.85-6.81(m, 2H, *arom.*), 5.25(d, *J* = 4.9 Hz, 1H, OH-2), 5.04(d, *J* = 4.6 Hz, 1H, OH-3/OH-4), 4.98(d, *J* = 5.2 Hz, 1H, OH-3/OH-4), 4.69(d, *J* = 7.4 Hz, 1H, H-1), 4.54(t, *J* = 5.8 Hz, 1H, OH-6), 3.89(t, *J* = 6.5 Hz, 2H, O*CH*$_2$CH$_2$CH$_2$CH$_3$), 3.68(ddd, *J* = 11.8, 5.4, 1.8 Hz, 1H, H-6a), 3.48-3.42(m, 1H, H-6b), 3.27-3.10(m, 4H, H-2 and H-3 and H-4 and H-5), 1.66(qu,

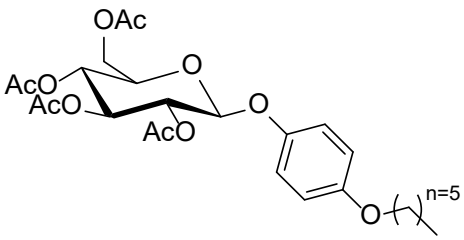
J = 6.6 Hz, 2H, $OCH_2CH_2CH_2CH_3$), 1.41(sxt, *J* = 7.4 Hz, 2H, $OCH_2CH_2CH_2CH_3$), 0.92(t, *J* = 7.4 Hz, 1H, $OCH_2CH_2CH_2CH_3$). **^{13}C NMR:** (101 MHz, DMSO-d_6) ∂ = 153.7 (*arom.* C), 151.4 (*arom.* C), 117.5 (2xCH *arom.*), 115.0 (2xCH *arom.*), 101.5 (C-1), 77.0 (C-2/C-3/C-4/C-5), 76.6 (C-2/C-3/C-4/C-5), 73.3 (C-2/C-3/C-4/C-5), 69.8 (C-2/C-3/C-4/C-5), 67.5 ($OCH_2CH_2CH_2CH_3$), 60.8 (C-6 CH_2), 30.8 ($OCH_2CH_2CH_2CH_3$), 18.7 ($OCH_2CH_2CH_2CH_3$), 13.7 ($OCH_2CH_2CH_2CH_3$). **LRMS (ESI):** m/z calcd for $C_{15}H_{22}O_7Na$ $[M+Na]^+$ 337.1, found 337.1.



4-hexyloxyphenol: Hydroxyquinone (9.6 mmol, 1.0 eq) was dissolved in dry DMF (1.5 M) with NaOH (8.7 mmol, 1.0 eq) in a flame-dried flask under argon. 1-bromohexane (7.1 mmol, 0.8 eq) was added slowly and the reaction was stirred for 24 h at room temperature. The reaction was quenched by diluting with EtOAc and the addition of 1 M HCl. The organic EtOAc layer was then washed with 1 M HCl, H_2O, and brine. The organic layer was dried using Na_2SO_4, filtered, and concentrated *in vacuo*. The crude brown sludge was purified by column chromatography from 1:9 EtOAc/Hexanes to yield the final product as a white powder (**33 %**).

Characterization was consistent with that found in literature.[534]

^{1}H NMR: (400 MHz, $CDCl_3$) ∂6.80-6.74(m, 4H, *arom.*), 4.50(bs, 1H, *arom.* OH), 3.89(t, *J* = 6.6 Hz, 2H, $OCH_2(CH_2)_4CH_3$), 1.75(qu, *J* = 8.0 Hz, 2H, $OCH_2CH_2(CH_2)_3CH_3$), 1.48-1.41(m, 2H, $O(CH_2)_2CH_2(CH_2)_2CH_3$), 1.36-1.29(m, 4H, $O(CH_2)_3CH_2CH_2CH_3$), 0.90(t, *J* = 7.0 Hz, 3H, $O(CH_2)_5CH_3$). **^{13}C NMR:** (101 MHz, $CDCl_3$) ∂ = 153.5 (*arom.* C), 149.5 (*arom.* C), 116.1 (2xCH *arom.*), 115.8 (2xCH *arom.*), 68.9 ($OCH_2(CH_2)_4CH_3$), 31.8 ($OCH_2CH_2(CH_2)_3CH_3$), 29.5 ($O(CH_2)_2CH_2(CH_2)_2CH_3$), 25.9 ($O(CH_2)_3CH_2CH_2CH_3$), 22.7 ($O(CH_2)_4CH_2CH_3$), 14.0 ($O(CH_2)_5CH_3$).



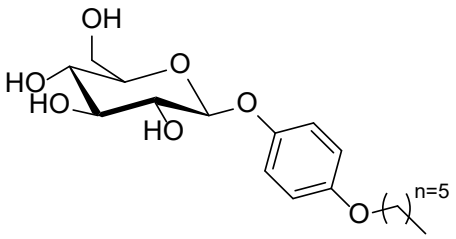
(4-hexyloxyphenyl)-2,3,4,6-tetra-*O*-acetyl-β-D-glucopyranoside (523): The title compound was synthesized according to a modified literature procedure following **General Procedure 8-2**.[167,525] β-D-glucose pentaacetate (**503**, 1.4 mmol, 1.0 eq) and 4-hexyloxyphenol (1.6 mmol, 1.2 eq) were dissolved in dry DCM (0.25 M) in a flame dried flask under argon at 0 ºC with 4 Å molecular sieves (powdered). Boron trifluoride diethyl etherate (48 % solution) (3.5 mmol, 2.5 eq) was added to the solution slowly. The solution was stirred overnight (18 h) and then

quenched with sat. $NaHCO_3$. The solution was diluted in DCM, filtered through a Celite® pad, and then the organic layer was washed using sat. $NaHCO_3$, H_2O, and brine. The organic layers were dried using Na_2SO_4, filtered, and concentrated *in vacuo*. The crude white powder was purified by recrystallization from EtOAc/Hexanes to yield the final product as a white powder (**64 %**).

Characterization was consistent with that found in literature.[532]

^{1}H NMR: (400 MHz, $CDCl_3$) 6.95-6.91(m, 2H, *arom.*), 6.82-6.78(m, 2H, *arom.*), 5.30-5.21(m, 2H, H-2 and H-3), 5.16(t, *J* = 9.7 Hz, 1H, H-4), 4.95(d, *J* = 7.5 Hz, 1H, H-1), 4.29(dd, J = 12.3, 5.3 Hz, 1H, H-6a), 4.16(dd, *J* = 12.1, 2.4 Hz, 1H, H-6b), 3.90(t, *J* = 6.6 Hz, 2H, OCH_2(CH_2)$_4$$CH_3$), 3.80(ddd, *J* = 9.9, 5.2, 2.4 Hz, 1H, H-5), 2.08(s, 3H, OAc CH_3), 2.07(s, 3H, OAc CH_3), 2.04(s, 3H, OAc CH_3), 2.03(s, 3H, OAc CH_3), 1.75(qu, *J* = 6.8 Hz, 2H, OCH_2CH_2(CH_2)$_3$$CH_3$), 1.48-1.41(m, 2H, O($CH_2$)$_2CH_2$($CH_2$)$_2$$CH_3$), 1.36-1.31(m, 4H, O($CH_2$)$_3CH_2CH_2$$CH_3$), 0.88(t, *J* = 7.2 Hz, 3H, O(CH_2)$_5CH_3$). **^{13}C NMR:** (101 MHz, $CDCl_3$) ∂ = 170.7 (OAc C), 170.4 (OAc C), 169.5 (OAc C), 169.4 (OAc C), 155.6 (*arom.* C), 150.9 (*arom.* C), 118.8 (2xCH *arom.*), 115.4 (2xCH *arom.*), 100.5 (C-1), 72.9 (C-2/C-3), 72.1 (C-5), 71.4 (C-2/C-3), 68.7 (OCH_2(CH_2)$_4$$CH_3$), 68.5 (C-4), 62.1 (C-6 CH_2), 31.7 (OCH_2CH_2(CH_2)$_3$$CH_3$), 29.4 (O($CH_2$)$_2CH_2$($CH_2$)$_2$$CH_3$), 25.9 (O($CH_2$)$_3CH_2$$CH_2CH_3$), 22.7 (O($CH_2$)$_4CH_2$$CH_3$), 20.9 (OAc CH_3), 20.8 (OAc CH_3), 20.76 (OAc CH_3), 20.7 (OAc CH_3), 14.2 (O(CH_2)$_5CH_3$).

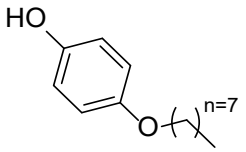
(4-hexyloxyphenyl)-β-D-glucopyranoside (PHP-Glc, 80): The title compound was synthesized according to a modified literature procedure following **General Procedure 8-3**.[167,326] (4-hexyloxyphenyl)-2,3,4,6-tetra-*O*-acetyl-β-D-glucopyranoside (**523**, 0.9 mmol, 1.0 eq) was dissolved in MeOH (0.1 M) and a 1 M solution of NaOMe in MeOH (0.1 eq) was added to the solution to stir for 1 hour. Upon reaction completion, Amberlite IR120 H+ resin (washed in MeOH) was added to a pH < 4. The solution was filtered, and the filtrate was concentrated *in vacuo*. The final product was obtained as a white powder (**91 %**).



^{1}H NMR: (400 MHz, DMSO-d_6) 6.97-6.93(m, 2H, *arom.*), 6.85-6.81(m, 2H, *arom.*), 5.25(d, *J* = 4.9 Hz, 1H, OH-2), 5.04(d, *J* = 4.4 Hz, 1H, OH-3/OH-4), 4.98(d, *J* = 5.2 Hz, 1H, OH-3/OH-4), 4.69(d, *J* = 7.4 Hz, 1H, H-1), 4.54(t, *J* = 5.6 Hz, 1H, OH-6), 3.89(t, *J* = 6.5 Hz, 2H, OCH_2(CH_2)$_4$$CH_3$), 3.68(ddd, *J* = 11.8, 5.0, 1.7 Hz, 1H, H-6a), 3.48-3.42(m, 1H, H-6b), 3.28-3.10(m, 4H, H-2 and H-3 and H-4 and H-5), 1.67(sxt, *J* = 6.8 Hz, 2H, OCH_2CH_2(CH_2)$_3$$CH_3$), 1.43-1.36(m, 2H, O($CH_2$)$_2CH_2$($CH_2$)$_2$$CH_3$), 1.34-1.26(m, 4H,

$O(CH_2)_3CH_2CH_2CH_3$), 0.87(t, *J* = 6.9 Hz, 3H, $O(CH_2)_5CH_3$). **^{13}C NMR:** (101 MHz, DMSO-d_6) ∂ = 153.7 (*arom.* C), 151.4 (*arom.* C), 117.5 (2xCH *arom.*), 115.0 (2xCH *arom.*), 101.5 (C-1), 77.0 (C-2/C-3/C-4/C-5), 76.6 (C-2/C-3/C-4/C-5), 73.3 (C-2/C-3/C-4/C-5), 69.8 (C-2/C-3/C-4/C-5), 67.8 ($OCH_2(CH_2)_4CH_3$), 60.8 (C-6 CH_2), 31.0 ($OCH_2CH_2(CH_2)_3CH_3$), 28.7 ($O(CH_2)_2CH_2(CH_2)_2CH_3$), 25.2 ($O(CH_2)_3CH_2CH_2CH_3$), 22.0 ($O(CH_2)_4CH_2CH_3$), 13.9 ($O(CH_2)_5CH_3$). **LRMS (ESI):** m/z calcd for $C_{18}H_{28}O_7Na$ $[M+Na]^+$ 379.2, found 379.2

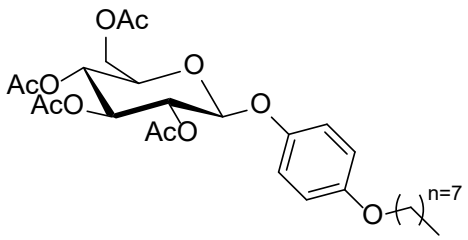
4-octyloxyphenol: Hydroxyquinone (9.1 mmol, 1.0 eq) was dissolved in dry DMF (1.5 M) with NaOH (10.5 mmol, 0.8 eq) in a flame-dried flask under argon. 1-bromooctane (6.9 mmol, 0.8 eq) was added slowly and the reaction was stirred for 24 h at room temperature. The reaction was quenched by diluting with EtOAc and the addition of 1 M HCl. The organic EtOAc layer was then washed with 1 M HCl, H_2O, and brine. The organic layer was dried using Na_2SO_4, filtered, and concentrated *in vacuo*. The crude brown sludge was purified by column chromatography from 1:9 EtOAc/Hexanes to yield the final product as a white powder (**32 %**).



Characterization was consistent with that found in literature.[535]

^{1}H NMR: (400 MHz, $CDCl_3$) ∂6.80-6.73(m, 4H, *arom.*), 4.43(bs, 1H, *arom.* OH), 3.89(t, *J* = 6.6 Hz, 2H, $OCH_2(CH_2)_6CH_3$), 1.78(qu, *J* = 6.9 Hz, 2H, $OCH_2CH_2(CH_2)_5CH_3$), 1.47-1.40(m, 2H, $O(CH_2)_2CH_2(CH_2)_4CH_3$), 1.37-1.24(m, 8H, $O(CH_2)_3(CH_2)_4CH_3$), 0.89(t, *J* = 6.5 Hz, 3H, $O(CH_2)_7CH_3$). **^{13}C NMR:** (101 MHz, $CDCl_3$) ∂ = 153.5 (*arom.* C), 149.4 (*arom.* C), 116.1 (2xCH *arom.*), 115.7 (2xCH *arom.*), 68.9 ($OCH_2(CH_2)_6CH_3$), 31.9 ($OCH_2CH_2(CH_2)_5CH_3$), 29.5 ($O(CH_2)_2CH_2(CH_2)_4CH_3$), 29.4 ($O(CH_2)_3CH_2CH_2(CH_2)_2CH_3$), 26.2 ($O(CH_2)_5CH_2CH_2CH_3$), 22.8($O(CH_2)_5CH_2CH_3$), 14.2 ($O(CH_2)_7CH_3$).

(4-octyloxyphenyl)-2,3,4,6-tetra-*O*-acetyl-β-D-glucopyranoside (524): The title compound was synthesized according to a modified literature procedure following **General Procedure 8-2**.[167,525] β-D-glucose pentaacetate (**503**, 2.3 mmol, 1.0 eq) and 4-octyloxyphenol (2.1 mmol, 0.9 eq) were dissolved in dry DCM (0.25 M) in a flame dried flask under argon at 0 ºC with 4 Å molecular sieves (powdered). Boron trifluoride diethyl etherate (48 % solution) (5.8 mmol, 2.5 eq) was added to the solution slowly. The solution was stirred overnight (18 h) and then

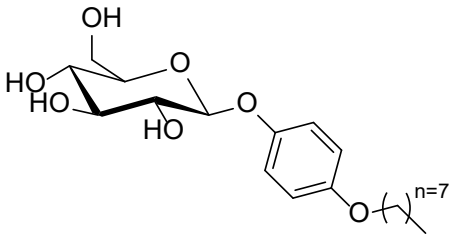


quenched with sat. $NaHCO_3$. The solution was diluted in DCM, filtered through a Celite® pad, and the organic layer was washed with sat. $NaHCO_3$, H_2O, and brine. The organic layer was dried using Na_2SO_4, filtered, and concentrated *in vacuo*. The crude white powder was purified by column chromatography in 8:2 Hexanes:EtOAc to yield the final product as a white powder (**40 %**).

Characterization was consistent with that found in literature.[532]

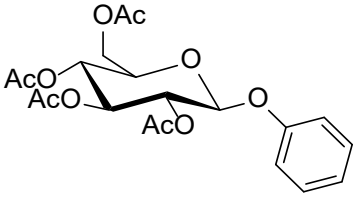
^{1}H NMR: (400 MHz, $CDCl_3$) 6.94-6.90(m, 2H, *arom.*), 6.82-6.78(m, 2H, *arom.*), 5.29-5.20(m, 2H, H-2 and H-3), 5.15(t, *J* = 9.6 Hz, 1H, H-4), 4.94(d, J = 7.3 Hz, 1H, H-1), 4.28(dd, *J* = 12.3, 5.2 Hz, 1H, H-6a), 4.16(dd, *J* = 12.2, 2.3 Hz, 1H, H-6b), 3.90(t, *J* = 6.6 Hz, 2H, O*CH*$_2$(CH_2)$_6$$CH_3$), 3.79(ddd, J = 9.8, 5.2, 2.4 Hz, 1H, H-5), 2.08(s, 3H, OAc CH_3), 2.07(s, 3H, OAc CH_3), 2.03(s, 3H, OAc CH_3), 2.02(s, 3H, OAc CH_3), 1.75(qu, *J* = 6.7 Hz, 2H, OCH_2*CH*$_2$(CH_2)$_5$$CH_3$), 1.47-1.39(m, 2H, O($CH_2$)$_2$*CH*$_2$($CH_2$)$_4$$CH_3$), 1.36-1.25(m, 8H, O($CH_2$)$_3$*(CH*$_2$*)*$_4$$CH_3$), 0.88(t, *J* = 6.5 Hz, 3H, O(CH_2)7*CH*$_3$). **^{13}C NMR:** (101 MHz, $CDCl_3$) *∂* = 170.7 (OAc C), 170.4 (OAc C), 169.5 (OAc C), 169.4 (OAc C), 155.5(*arom.* C), 150.9 (*arom.* C), 118.8 (2xCH *arom.* C), 115.3 (2xCH *arom.* C), 100.5 (C-1), 72.9 (C-2/C-3), 72.1 (C-5), 71.4 (C-2/C-3), 68.6 (O*CH*$_2$(CH_2)$_6$$CH_3$), 68.5 (C-4), 62.1 (C-6 CH_2), 31.9 (OCH_2*CH*$_2$(CH_2)$_5$$CH_3$), 29.44 (O($CH_2$)$_2$*CH*$_2$($CH_2$)$_4$$CH_3$), 29.39 (O($CH_2$)$_3$*CH*$_2$($CH_2$)$_3$$CH_3$), 29.3 (O($CH_2$)$_4$*CH*$_2$($CH_2$)$_2$$CH_3$), 26.1 (O($CH_2$)$_5$*CH*$_2$$CH_2$$CH_3$), 22.7 (O($CH_2$)$_6$*CH*$_2$$CH_3$), 20.8 (OAc CH_3), 20.75 (OAc CH_3), 20.70 (OAc CH_3), 20.67 (OAc CH_3), 14.2 (O(CH_2)$_7$*CH*$_3$).

(4-octyloxyphenyl)-β-D-glucopyranoside (POP-Glc, 81): The title compound was synthesized according to a modified literature procedure following **General Procedure 8-3**.[167,326] (4-octyloxyphenyl)-2,3,4,6-tetra-*O*-acetyl-β-D-glucopyranoside (**524**, 0.8 mmol, 1.0 eq) was dissolved in MeOH (0.1 M) and a 1 M solution of NaOMe in MeOH (0.1 eq) was added to the solution to stir for 1 hour. Upon reaction completion, Amberlite IR120 H+ resin (washed in MeOH) was added to a pH < 4. The solution was filtered, and the filtrate was concentrated *in vacuo*. The final product was obtained as a white powder (**90 %**).



^{1}H NMR: (400 MHz, DMSO-*d*$_6$*)* 7.32-7.28(m, 2H, *arom.*), 7.10-7.05(m, 2H, *arom.*), 5.25(d, *J* = 4.7 Hz, 1H, OH-2), 5.05(d, *J* = 3.3 Hz, 1H, OH-3/OH-4), 4.98(d, *J* = 5.0 Hz, 1H, OH-3/OH-4), 4.68(d, *J* = 7.4 Hz, 1H, H-1), 4.54(t, *J* = 5.7 Hz, 1H, OH-6), 3.88(t, *J* = 6.5Hz, 2H, O*CH*$_2$(CH_2)$_6$$CH_3$), 3.68(ddd, J = 11.6, 5.3, 1.7 Hz, 1H, H-6a), 3.48-3.70(m, 1H, H-6b), 3.27-3.10(m, 4H, H-2 and H-3 and H-4 and and H-5), 1.66(qu,

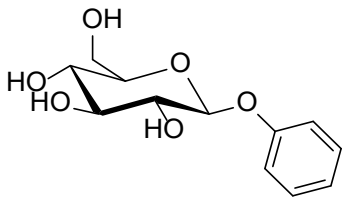
J = 6.7 Hz, 2H, $OCH_2CH_2(CH_2)_5CH_3$), 1.44-1.34(m, 2H, $O(CH_2)_2CH_2(CH_2)_4CH_3$), 1.33-1.21(m, 8H, $O(CH_2)_3(CH_2)_4CH_3$), 0.85(t, *J* = 6.7 Hz, 3H, $O(CH_2)_7CH_3$). **^{13}C NMR:** (101 MHz, DMSO-d_6) ∂ = 153.7 (*arom.* C), 151.4 (*arom.* C), 117.5 (2xCH *arom.*), 115.0 (2xCH *arom.*), 101.5 (C-1), 77.0 (C-2/C-3/C-4/C-5), 76.6 (C-2/C-3/C-4/C-5), 73.3 (C-2/C-3/C-4/C-5), 69.8 (C-2/C-3/C-4/C-5), 67.8 ($OCH_2(CH_2)_6CH_3$), 60.8 (C-6 CH_2), 31.2 ($OCH_2CH_2(CH_2)_5CH_3$), 28.7 ($O(CH_2)_2CH_2(CH_2)_4CH_3$), 28.6 ($O(CH_2)_3CH_2CH_2(CH_2)_2CH_3$), 25.5 ($O(CH_2)_5CH_2CH_2CH_3$), 22.1($O(CH_2)_5CH_2CH_3$), 13.9 ($O(CH_2)_7CH_3$). **LRMS (ESI):** m/z calcd for $C_{20}H_{32}O_7Na$ $[M+Na]^+$ 407.2, found 407.2.



phenyl-2,3,4,6-tetra-*O*-acetyl-β-D-glucopyranoside (528): The title compound was synthesized according to a modified literature procedure following **General Procedure 8-2**.[167,525] β-D-glucose pentaacetate (**503**, 5.3 mmol, 1.0 eq) and phenol (7.2 mmol, 1.3 eq) were dissolved in dry DCM (0.25 M) in a flame dried flask under argon at 0 ºC with 4 Å molecular sieves (powdered). Boron trifluoride diethyl etherate (48 % solution) (13.2 mmol, 2.5 eq) was added to the solution slowly. The solution was stirred overnight (18 h) and then quenched with sat. $NaHCO_3$. The solution was diluted in DCM, filtered through a Celite® pad, and the organic layer was washed with sat. $NaHCO_3$, H_2O, and brine. The organic layer was dried using Na_2SO_4, filtered, and concentrated *in vacuo*. The crude white powder was purified by recrystallization from EtOAc/Hexanes to yield the final product as a white powder (**60 %**).

Characterization was consistent with that found in literature.[536]

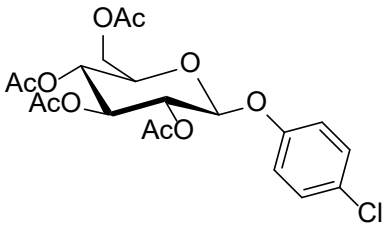
^{1}H NMR: (400 MHz, $CDCl_3$) ∂7.32-7.28(m, 2H, *arom.*), 7.09-7.05(m, 1H, *arom.*), 7.00-6.98(m, 2H, *arom.*), 5.32-5.25(m, 2H, H-2 and H-3), 5.19-5.15(m, 1H, H-4), 5.08(d, *J* = 7.7 Hz, 1H, H-1), 4.29(dd, *J* = 12.3, 5.3 Hz, 1H, H-6a), 4.16(dd, *J* = 12.3, 2.4 Hz, 1H, H-6a), 3.86(ddd, J = 10.0, 5.3, 2.5 Hz, 1H, H-5), 2.07(s, 3H, OAc CH_3), 2.06(s, 3H, OAc CH_3), 2.05(s, 3H, OAc CH_3), 2.03(s, 3H, OAc CH_3). **^{13}C NMR:** (101 MHz, $CDCl_3$) ∂ = 170.6 (OAc C), 170.3 (OAc C), 169.4 (OAc C), 169.3 (OAc C), 156.9 (C *arom.*), 129.6 (2xCH *arom.*), 123.4 (CH *arom.*), 117.0 (2xCH *arom.*), 99.1 (C-1), 72.8 (C-2/C-3), 72.0 (C-5), 71.2 (C-2/C-3), 68.3 (C-4), 62.0(CH_2), 20.7 (OAc CH_3), 20.65 (OAc CH_3), 20.64 (OAc CH_3), 20.61 (OAc CH_3).



phenyl-β-D-glucopyranoside (Ph-Glc, 82): The title compound was synthesized according to a modified literature procedure following **General Procedure 8-3**.[167,326] phenyl-2,3,4,6-tetra-*O*-acetyl-β-D-glucopyranoside (**528**, 3.2 mmol, 1.0 eq) was dissolved in MeOH (0.2 M) and a 1 M solution of NaOMe in MeOH (0.1 eq) was added to the solution to stir for 1 hour. Upon reaction completion, Amberlite IR120 H+ resin (washed in MeOH) was added to a pH < 4. The solution was filtered, and the filtrate was concentrated *in vacuo*. The crude material was recrystallized from dH_2O to obtain the final purified product as a white powder (**92 %**).

Characterization was consistent with that found in literature.[537]

^{1}H NMR: (400 MHz, DMSO-d_6) ∂7.31-7.26(m, 2H, *arom.*), 7.03-6.97(m, 3H, *arom.*), 5.31(d, *J* = 4.8 Hz, 1H, OH-2), 5.09(d, *J* = 4.6 Hz, 1H, OH-3), 5.03(d, *J* = 5.3 Hz, 1H, OH-4), 4.84(d, *J* = 7.4 Hz, 1H, H-1), 4.57(t, *J* = 5.8 Hz, 1H, OH-6), 3.69(ddd, J = 11.8, 5.2, 1.9 Hz, 1H, H-6a), 3.48-3.42(m, 1H, H-6b), 3.33-3.12(m, 4H, H-2 and H-3 and H-4 and H-5). **^{13}C NMR:** (101 MHz, DMSO-d_6) ∂ = 157.5 (C *arom.*), 129.4 (2xCH *arom.*), 121.7 (CH *arom.*), 116.2 (2xCH *arom.*), 100.4 (C-1), 77.0 (C-2/C-3/C-5), 76.6 (C-2/C-3/C-5), 73.3 (C-2/C-3/C-5), 69.7 (C-4), 60.7 (C-6 CH_2).

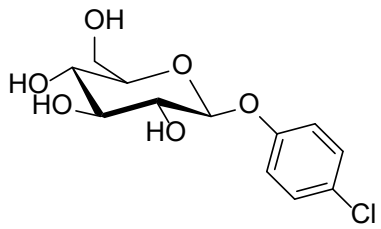


(4-chlorophenyl)-2,3,4,6-tetra-*O*-acetyl-β-D-glucopyranoside (525): The title compound was synthesized according to a modified literature procedure following **General Procedure 8-2**.[167,525] β-D-glucose pentaacetate (**503**, 5.4 mmol, 1.0 eq) and 4-chlorophenol (6.3 mmol, 1.1 eq) were dissolved in dry DCM (0.25 M) in a flame dried flask under argon at 0 ºC with 4 Å molecular sieves (powdered). Boron trifluoride diethyl etherate (48 % solution) (14.0 mmol, 2.5 eq) was added to the solution slowly. The solution was stirred overnight (18 h) and then quenched with sat. $NaHCO_3$. The solution was diluted in DCM, filtered through a Celite® pad, and the organic layer was washed with sat. $NaHCO_3$, H_2O, and brine. The organic layer was dried using Na_2SO_4, filtered, and concentrated *in vacuo*. The crude white powder was purified by recrystallization from EtOAc/Hexanes yield the final product as a white powder (**57 %**).

Characterization was consistent with that found in literature.[538]

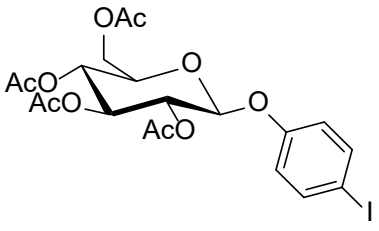
^{1}H NMR: (400 MHz, $CDCl_3$) ∂7.26-7.24(m, 2H, *arom.*), 6.94-6.92(m, 2H, *arom.*), 5.31-5.23(m, 2H, H-2 and H-3), 5.16(t, *J* = 9.9 Hz, 1H, H-4), 5.03(d, *J* = 7.6 Hz, 1H, H-1), 4.28(dd, *J* = 12.3, 5.4 Hz, 1H, H-6a), 4.16(dd, *J* = 12.3, 2.4 Hz, 1H, H-6b), 3.84(ddd, *J* = 10.0, 5.3, 2.5 Hz, 1H, H-5), 2.07(s, 3H, OAc CH_3), 2.06(s, 3H, OAc CH_3), 2.04(s, 3H, OAc CH_3), 2.03(s, 3H, OAc CH_3). **^{13}C NMR:** (101 MHz, $CDCl_3$) ∂ = 170.7 (OAc C), 170.4 (OAc C), 169.5 (OAc C), 169.4 (OAc C), 155.5 (2xCH *arom.*), 129.7 (C *arom.*), 128.7 (2xCH *arom.*), 118.6 (C *arom.*), 99.4 (C-1), 72.8 (C-2/C-3), 72.3 (C-2/C-3), 71.2 (C-5), 68.3 (C-4), 62.0 (C-6 CH_2), 20.83 (OAc CH_3), 20.77 (OAc CH_3), 20.75 (OAc CH_3), 20.73 (OAc CH_3).

(4-chlorophenyl)-β-D-glucopyranoside (*p*ClPh-Glc, 83): The title compound was synthesized according to a modified literature procedure following **General Procedure 8-3**.[167,326] (4-chlorophenyl)-2,3,4,6-tetra-*O*-acetyl-β-D-glucopyranoside (**525**, 3.1 mmol, 1.0 eq) was dissolved in MeOH (0.2 M) and a 1 M solution of NaOMe in MeOH (0.1 eq) was added to the solution to stir for 1 hour. Upon reaction completion, Amberlite IR120 H+ resin (washed in MeOH) was added to a pH < 4. The solution was filtered, and the filtrate was concentrated *in vacuo*. The crude material was precipitated from a mixture of 95 % EtOH, ether, and petroleum ether to obtain the final purified product as a white powder (**91 %**).



^{1}H NMR: (400 MHz, DMSO-d_6) ∂7.34-7.32(m, 2H, arom.), 7.05-7.03(m, 2H, arom.), 5.34(d, *J* = 4.7 Hz, 1H, OH-2), 5.11(d, *J* = 4.6 Hz, 1H, OH-3), 5.04(d, *J* = 5.3 Hz, 1H, OH-4), 4.84(d, *J* = 7.4 Hz, 1H, H-1), 4.58(t, *J* = 5.8 Hz, 1H, OH-6), 3.68(ddd, *J* = 11.9, 5.4, 1.9 Hz, 1H, H-6a), 3.48-3.42(m, 1H, H-6b), 3.35-3.29(m, 1H, H-5), 3.28-3.20(m, 2H, H-2 and H-3), 3.18-3.12(m, 1H, H-4). **^{13}C NMR:** (101 MHz, DMSO-d_6) ∂ = 156.3 (C *arom.*), 129.2 (2xCH *arom.*),125.5 (C *arom.*), 118.0 (2xCH *arom.*), 100.5 (C-1), 77.1 (C-2/C-3/C-5), 76.5 (C-2/C-3/C-5), 73.2 (C-2/C-3/C-5), 69.7 (C-4), 60.7 (C-6 CH_2). **LRMS (ESI):** m/z calcd for $C_{12}H_{15}ClO_6Na$ $[M+Na]^+$ 313.1, found 313.3.

(4-iodophenyl)-2,3,4,6-tetra-*O*-acetyl-β-D-glucopyranoside (527): The title compound was synthesized according to a modified literature procedure following **General Procedure 8-2**.[167,525] β-D-glucose pentaacetate (**503**, 4.7 mmol, 1.0 eq) and 4-iodophenol (5.6 mmol, 1.2 eq) were dissolved in dry DCM (0.25 M) in a flame dried flask under argon at 0 ºC with 4 Å molecular sieves

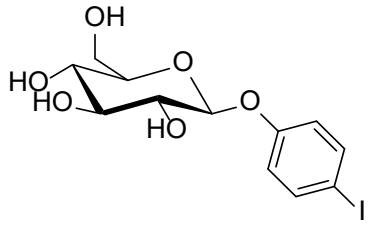


(powdered). Boron trifluoride diethyl etherate (48 % solution) (11.7 mmol, 2.5 eq) was added to the solution slowly. The solution was stirred overnight (18 h) and then quenched with sat. $NaHCO_3$. The solution was diluted in DCM, filtered through a Celite® pad, and the organic layer was washed with sat. $NaHCO_3$, H_2O, and brine. The organic layer was dried using Na_2SO_4, filtered, and concentrated *in vacuo*. The crude white powder was purified by recrystallization from EtOAc/Hexanes yield the final product as a white powder (**30 %**).

Characterization was consistent with that found in literature.[538]

^{1}H NMR: (400 MHz, $CDCl_3$) ∂7.59-7.57(m, 2H, *arom.*), 6.77-6.75(m, 2H, *arom.*), 5.31-5.22(m, 2H, H-2 and H-3), 5.15(t, *J* = 9.8 Hz 1H, H-4), 5.03(d, *J* = 7.5 Hz, 1H, H-1), 4.27(dd, *J* = 12.3, 5.4 Hz, 1H, H-6a), 4.16(dd, *J* = 12.3, 2.4 Hz, 1H, H-6b), 3.84(ddd, J = 10.0, 5.4, 2.5 Hz, 1H, H-5), 2.07(s, 3H, OAc CH_3), 2.05(s, 3H, OAc CH_3), 2.04(s, 3H, OAc CH_3), 2.03(s, 3H, OAc CH_3). **^{13}C NMR:** (101 MHz, $CDCl_3$) ∂ = 170.5 (OAc C), 170.2 (OAc C), 169.4 (OAc C), 169.2 (OAc C), 156.7 (C *arom.*), 138.5 (2xCH *arom.*), 119.3 (2xCH *arom.*), 99.0 (C-1), 86.2 (C *arom.*), 72.6 (C-2/C-3), 72.2 (C-5), 71.1 (C-2/C-3), 68.2 (C-4), 61.9 (C-6 CH_2), 20.7 (OAc CH_3), 20.61 (OAc CH_3), 20.59 (OAc CH_3), 20.58 (OAc CH_3).

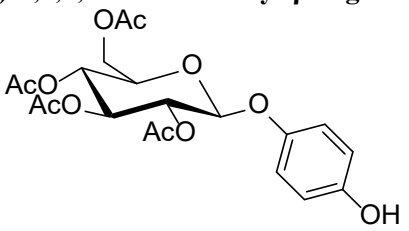
(4-iodophenyl)-β-D-glucopyranoside (*p*IPh-Glc, 84): The title compound was synthesized according to a modified literature procedure following **General Procedure 8-3**.[167,326] (4-iodophenyl)-2,3,4,6-tetra-*O*-acetyl-β-D-glucopyranoside (**527**, 1.4 mmol, 1.0 eq) was dissolved in MeOH (0.2 M) and a 1 M solution of NaOMe in MeOH (0.1 eq) was added to the solution to stir for 1 hour. Upon reaction completion, Amberlite IR120 H+ resin (washed in MeOH) was added to a pH < 4. The solution was filtered, and the filtrate was concentrated *in vacuo*. The final product was obtained as a white powder without further purification (**78 %**).

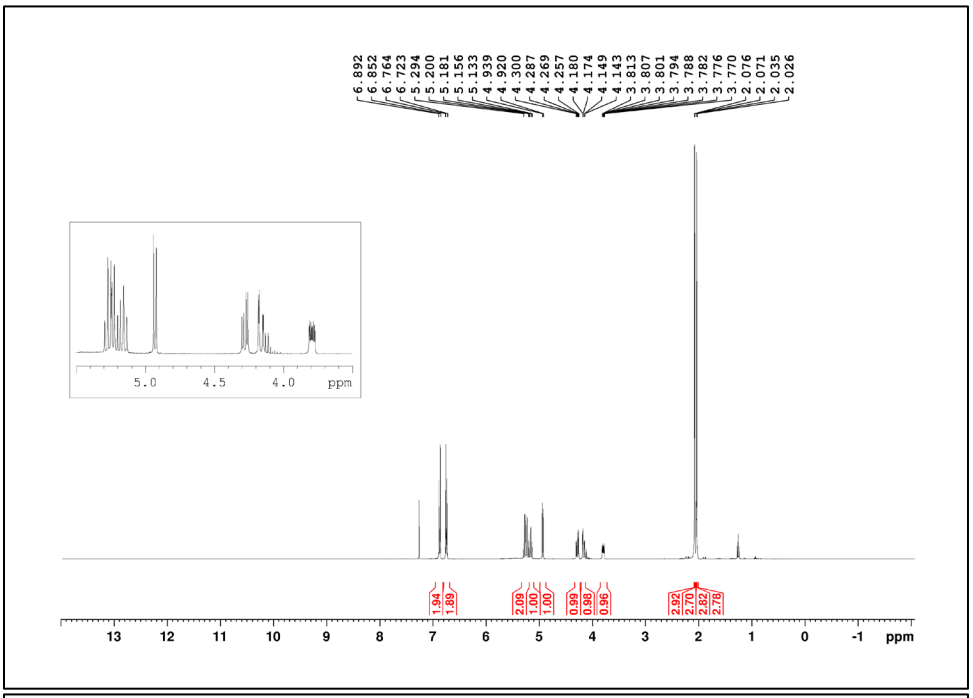


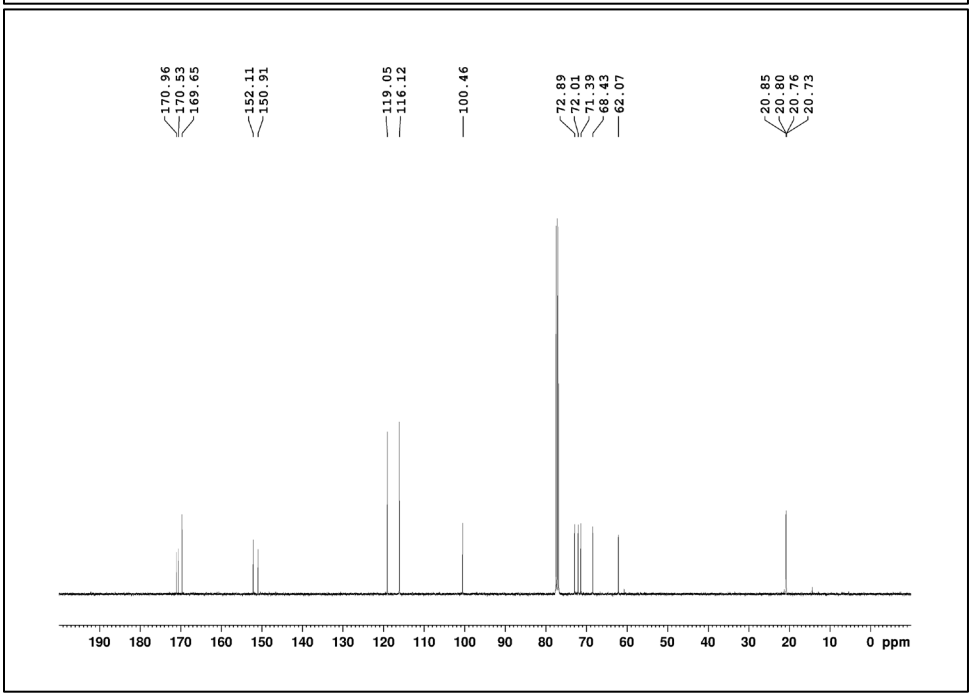
^{1}H NMR: (400 MHz, DMSO-d_6) ∂7.60-7.58(m, 2H, *arom.*), 6.87-6.85(m, 2H, *arom.*), 5.37(d, *J* = 4.9 Hz, 1H, OH-2/OH-3/OH-4), 5.12(d, *J* = 4.7 Hz, 1H, OH-2/OH-3/OH-4), 5.05(d, *J* = 5.4 Hz, 1H, OH-2/OH-3/OH-4), 4.83(d, *J* = 7.4 Hz, 1H, H-1), 4.61(t, *J* = 5.7 Hz, 1H, OH-6), 3.67(ddd, *J* = 11.9, 5.3, 1.9 Hz, 1H, H-6a), 3.47-3.41(m, 1H, H-6b), 3.33-3.11(m, 4H, H-2 and H-3 and H-4 and H-5). **^{13}C NMR:** (101 MHz, DMSO-d_6) ∂ = 157.4 (C *arom.*), 138.1 (2xCH *arom.*), 119.1 (2xCH *arom.*), 100.3 (C-1), 84.8 (C *arom.*), 77.1 (C-2/C-3/C-4/C-5), 76.6 (C-2/C-3/C-4/C-5), 73.3 (C-2/C-3/C-4/C-5), 69.8 (C-2/C-3/C-4/C-5), 60.8 (C-6 CH_2). **LRMS (ESI):** m/z calcd for $C_{12}H_{15}IO_6Na$ $[M+Na]^+$ 405.0, found 404.9.

(4-nitrophenyl)-β-D-glucopyranoside (*p*NO_2Ph-Glc, 85): The title compound was tested directly from commercially available product CAS 2492-87-7 (Sigma, 487507).

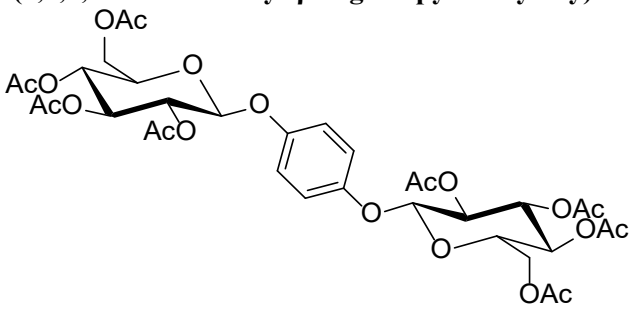
(4-hydroxyphenyl)-2,3,4,6-tetra-*O*-acetyl-β-D-glucopyranoside (518):

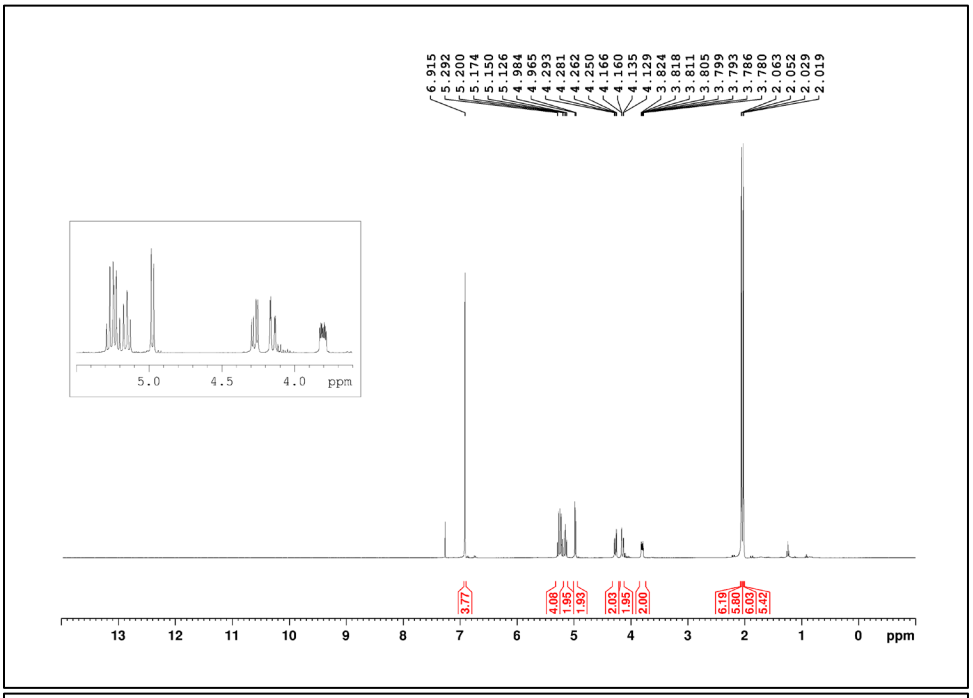


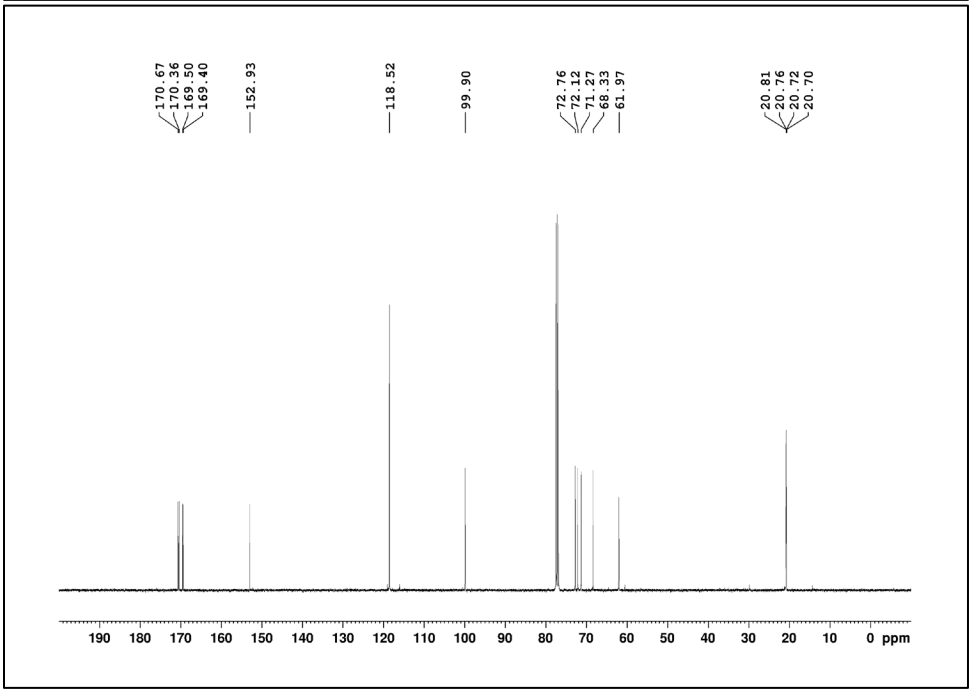




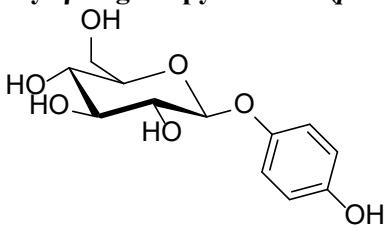
1,4-bis(2,3,4,6-tetra-*O*-acetyl-β-D-glucopyranosyloxy)benzene:

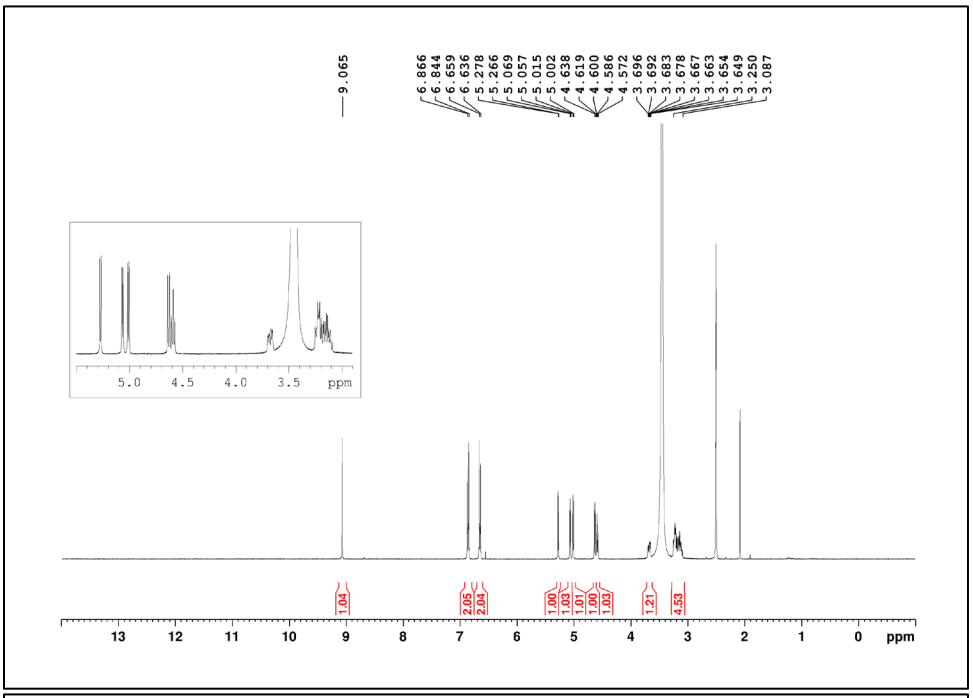


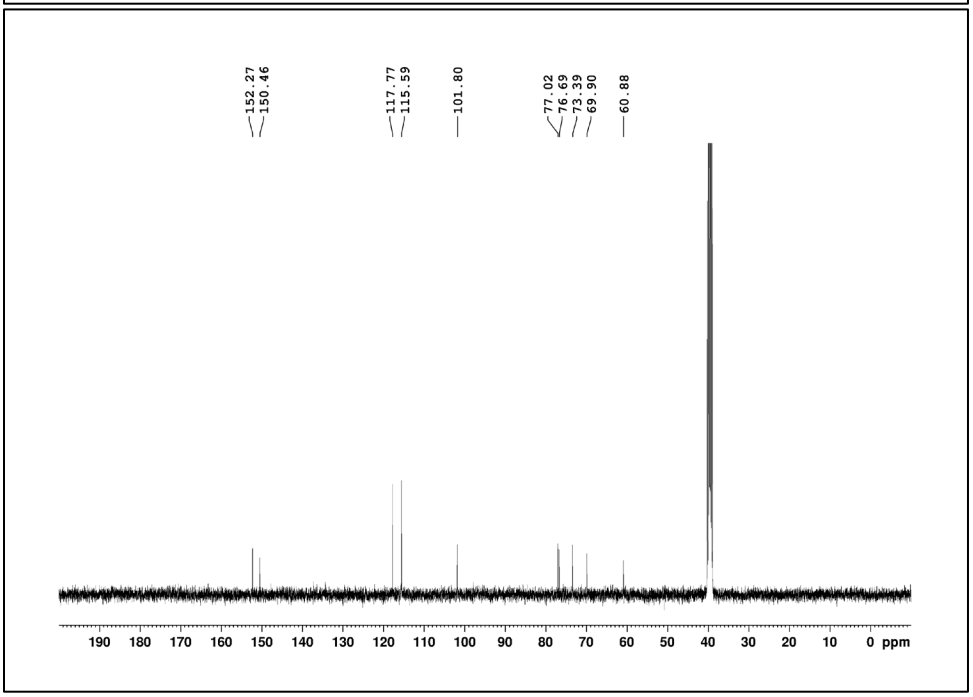




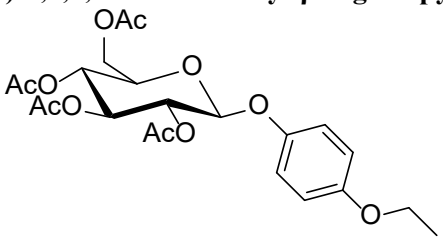
4-hydroxyphenyl-β-D-glucopyranoside (*p*OHPh-Glc, 53):

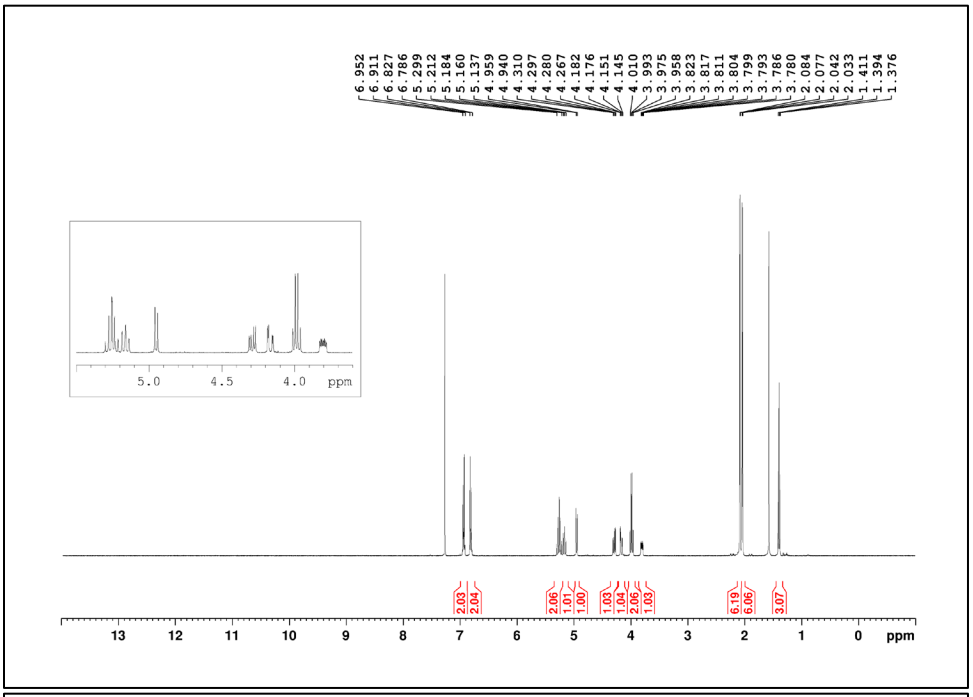


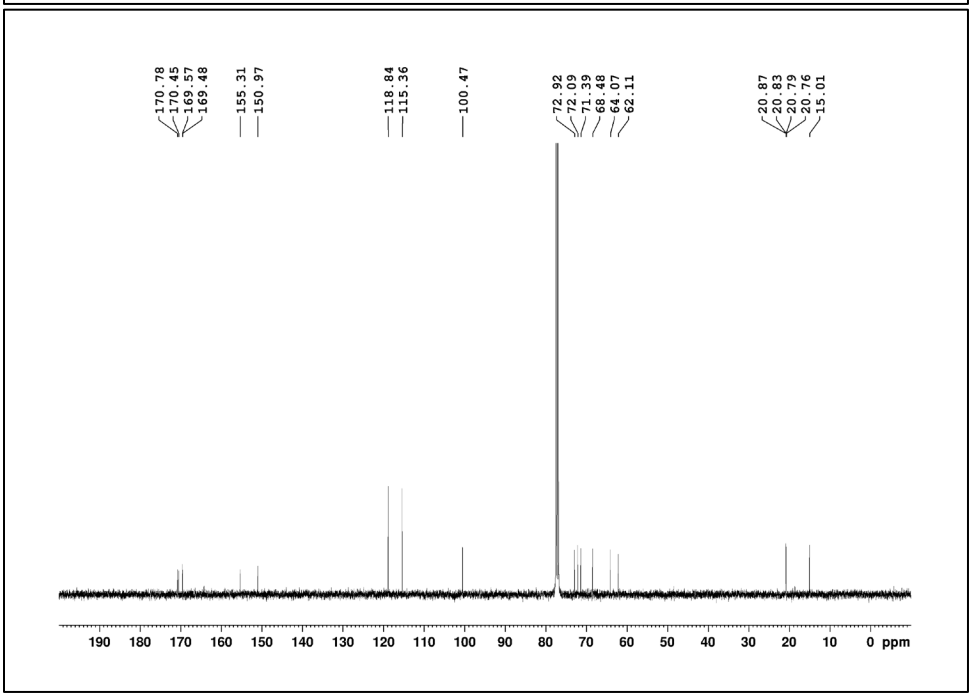




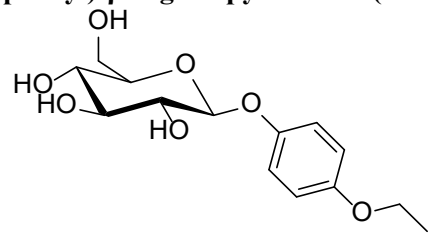
(4-ethoxyphenyl)-2,3,4,6-tetra-*O*-acetyl-β-D-glucopyranoside (520):

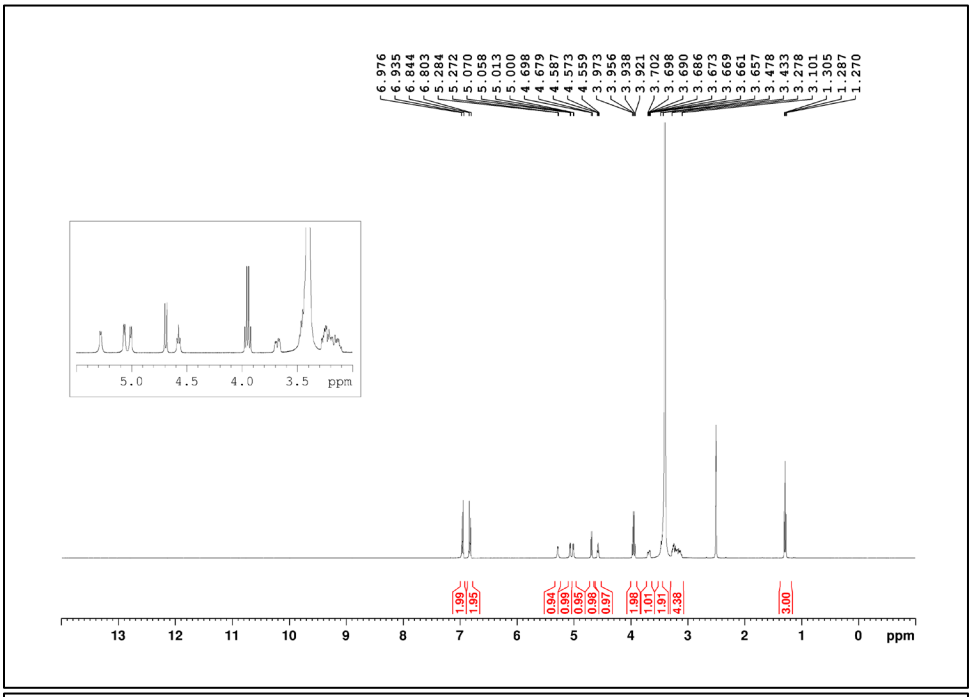


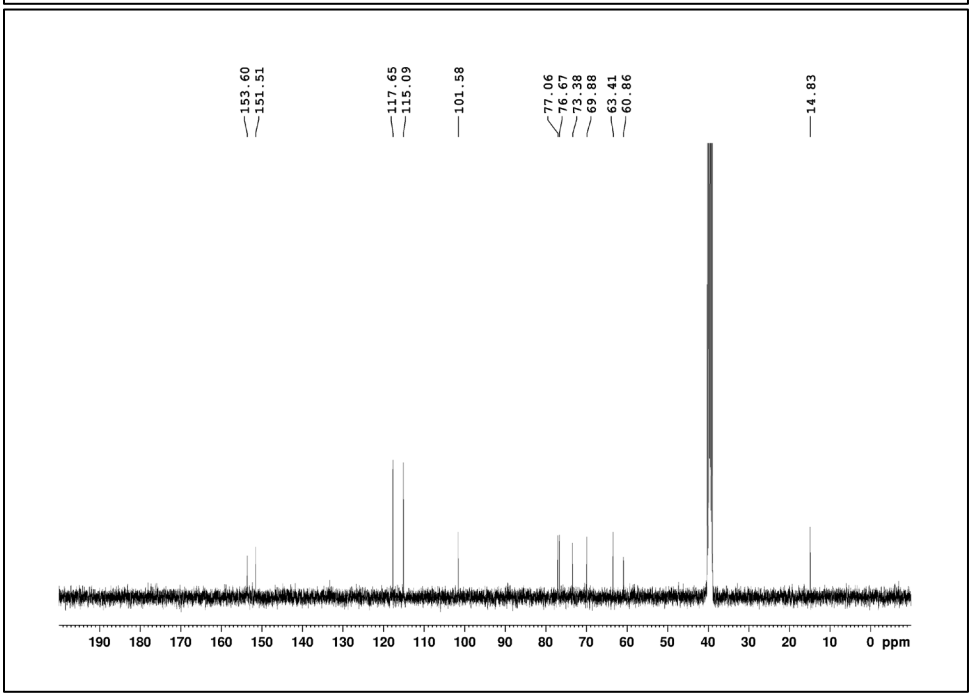




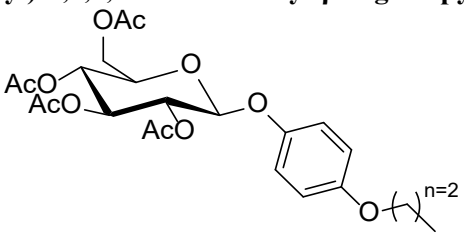
(4-ethoxyphenyl)-β-D-glucopyranoside (PEP-Glc, 54):

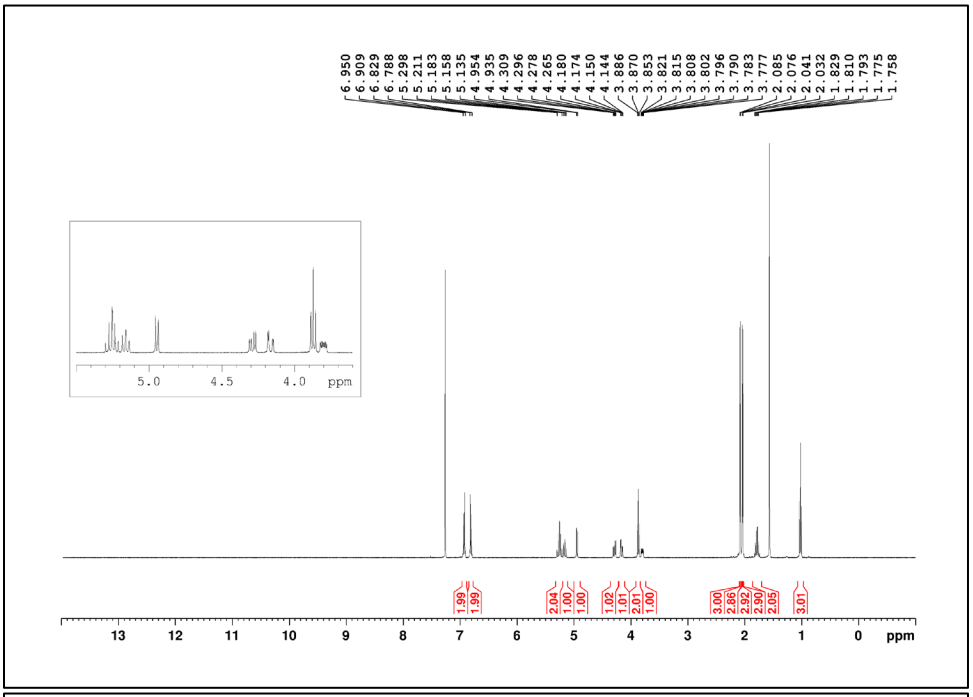


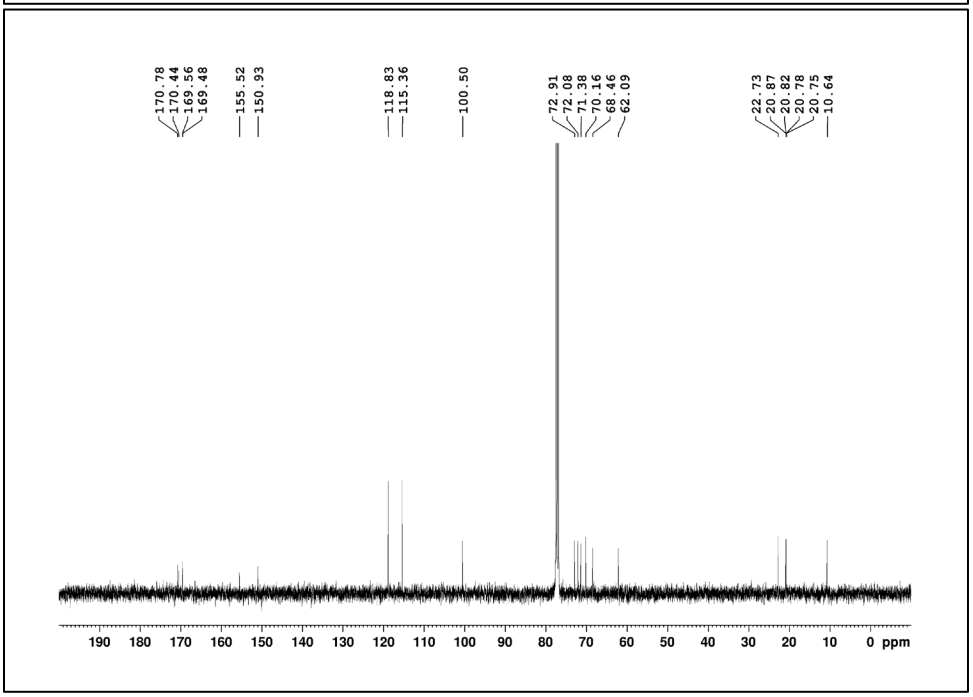




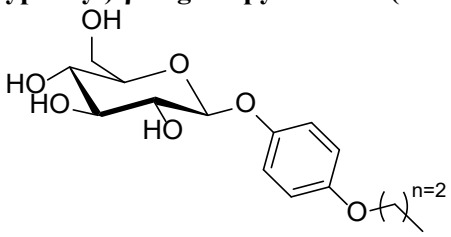
(4-propoxyphenyl)-2,3,4,6-tetra-*O*-acetyl-β-D-glucopyranoside (521):

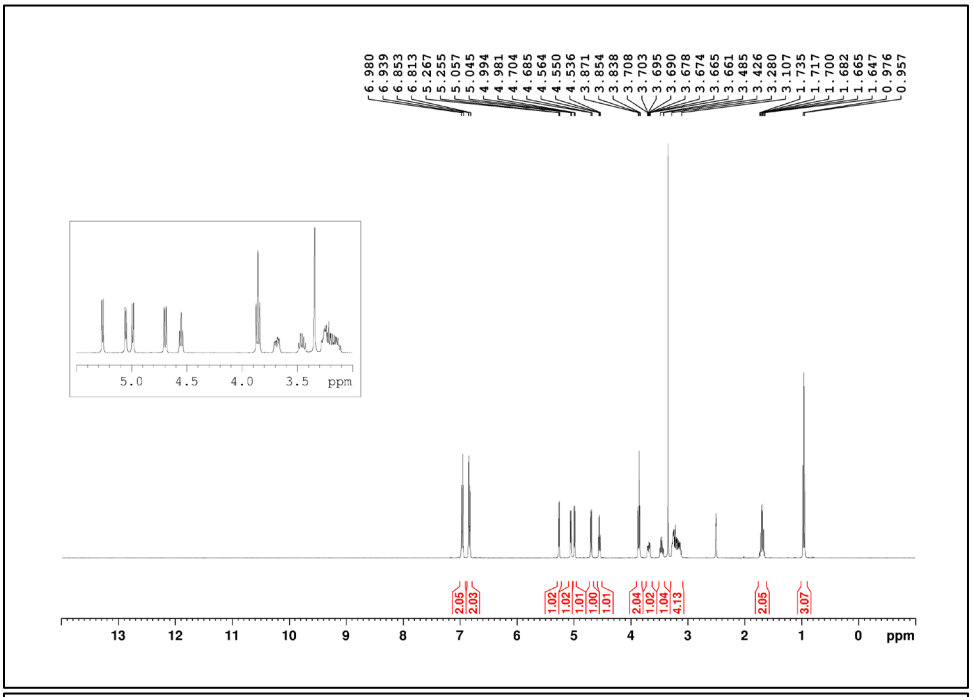


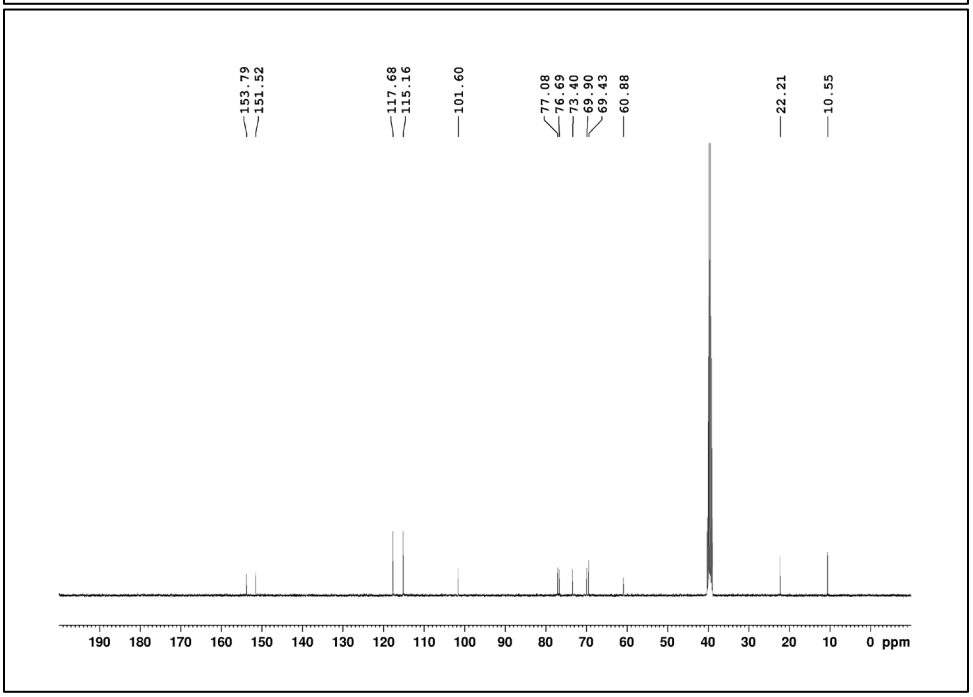




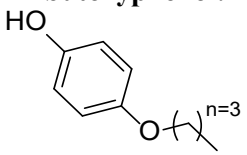
(4-propoxyphenyl)-β-D-glucopyranoside (PPP-Glc, 55):

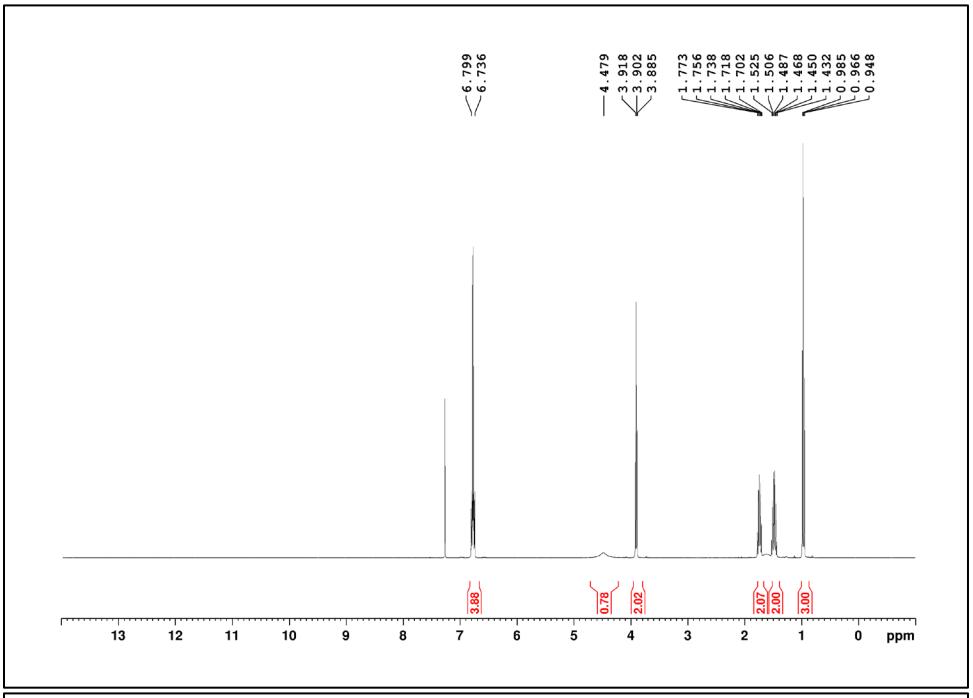


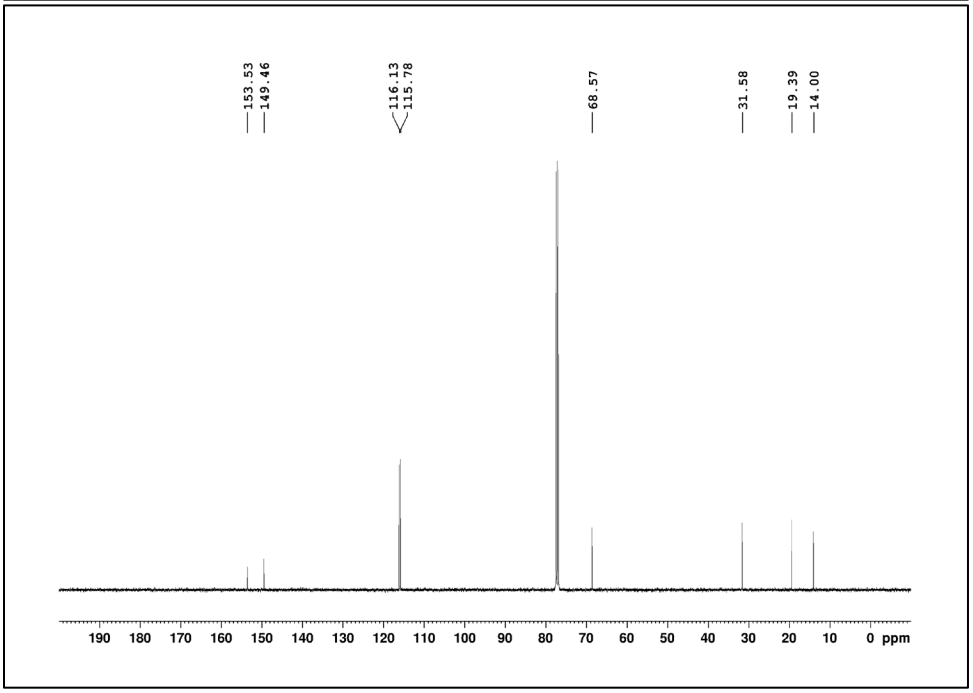




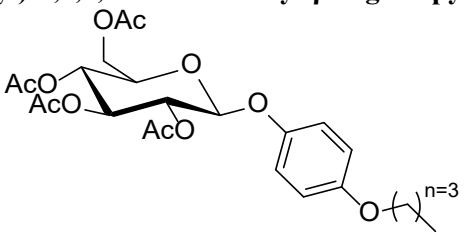
4-butoxyphenol:

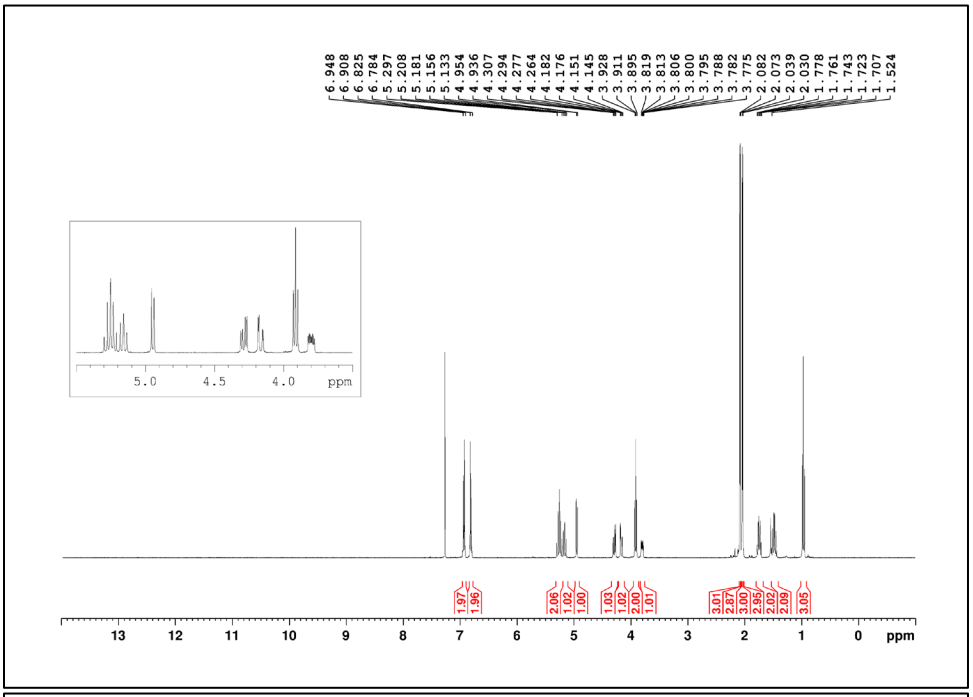


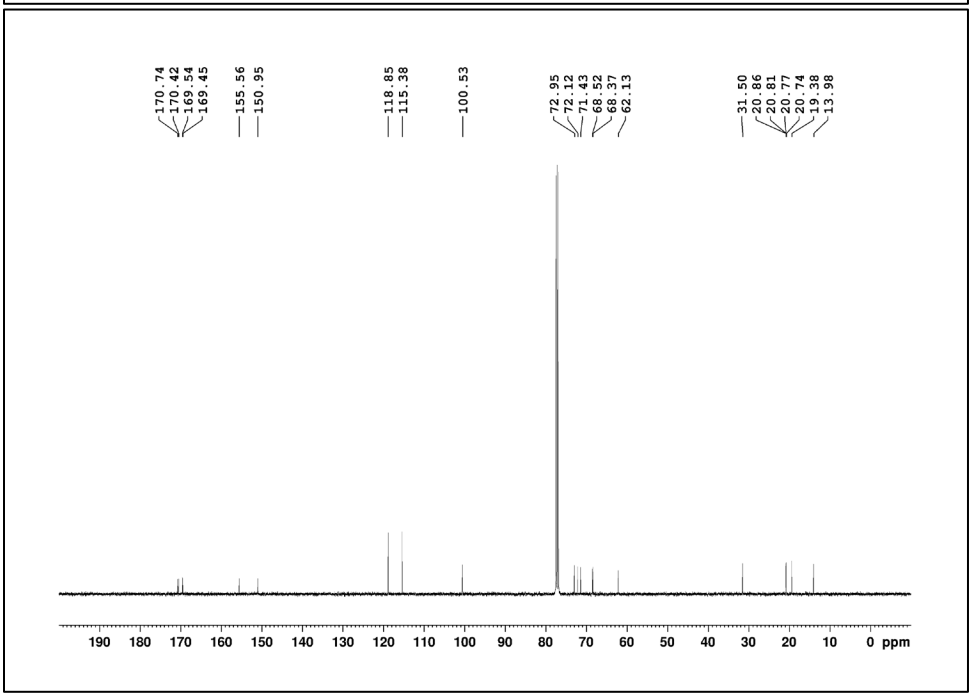




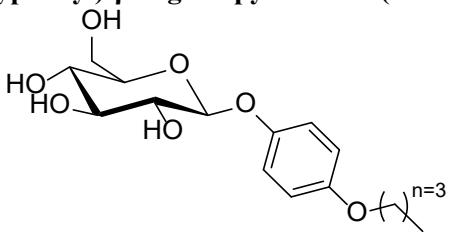
(4-butoxyphenyl)-2,3,4,6-tetra-*O*-acetyl-β-D-glucopyranoside (522):

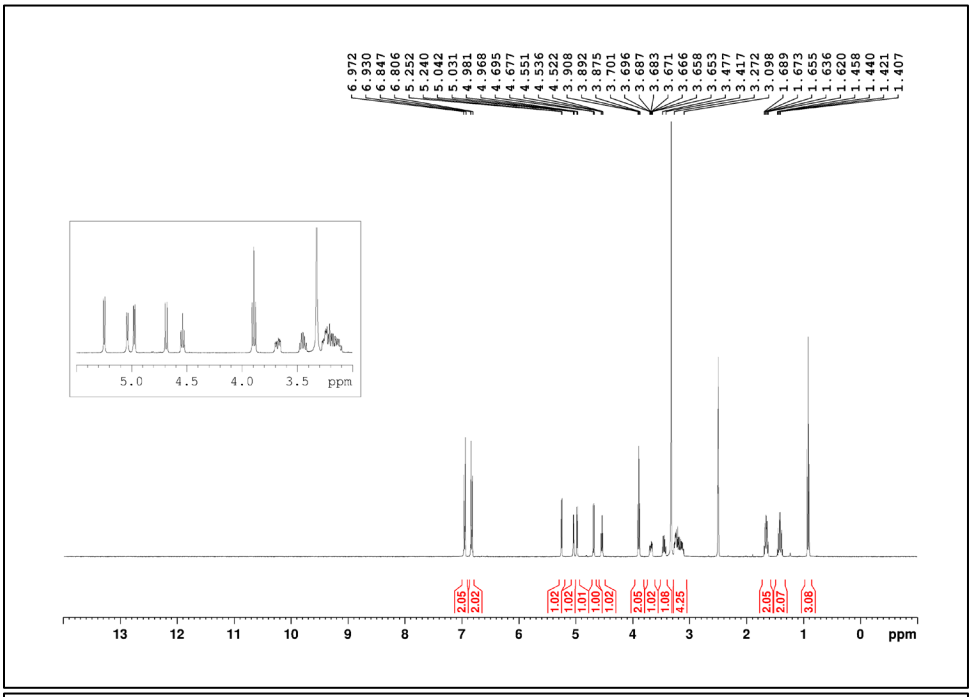


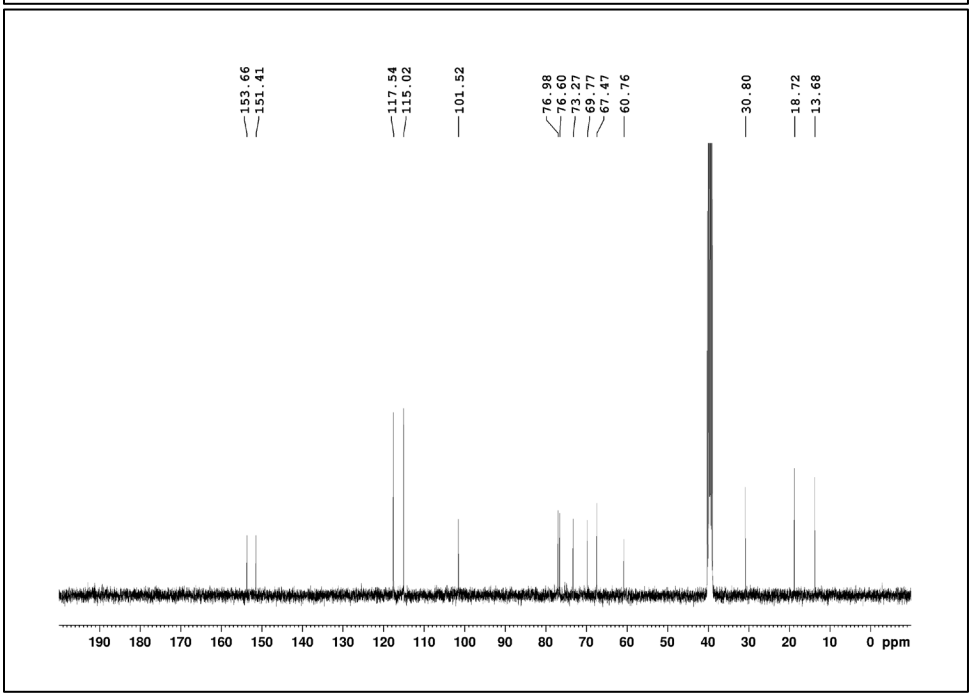




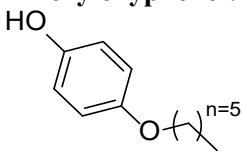
(4-butoxyphenyl)-β-D-glucopyranoside (PBP-Glc, 56):

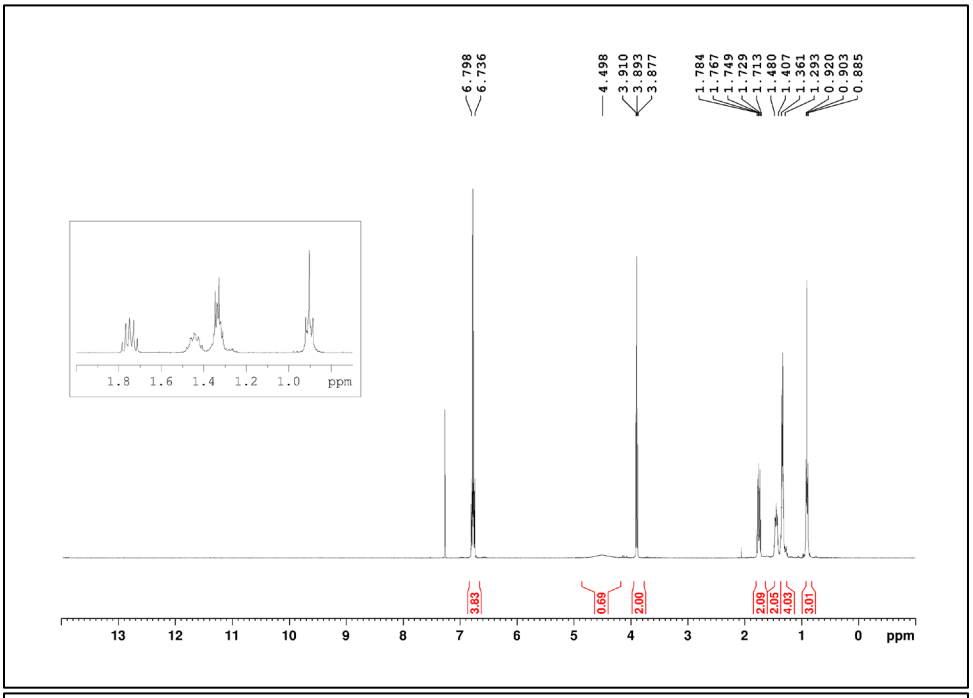


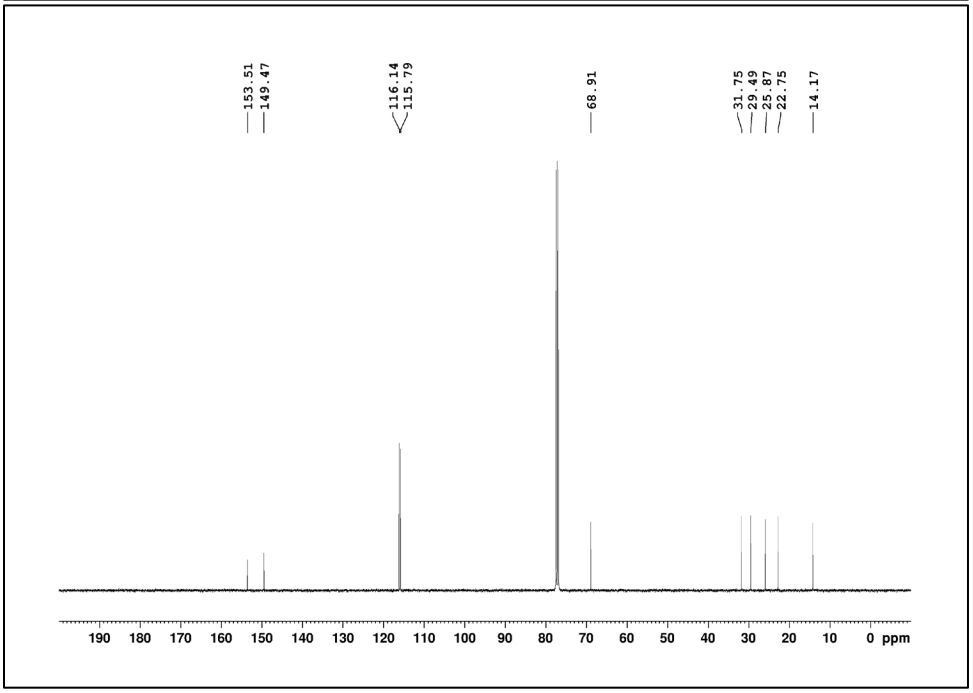




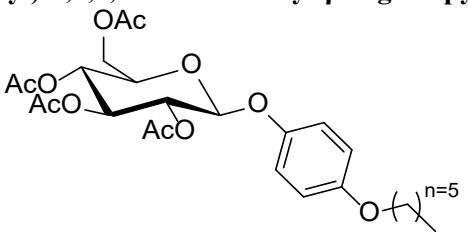
4-hexyloxyphenol:

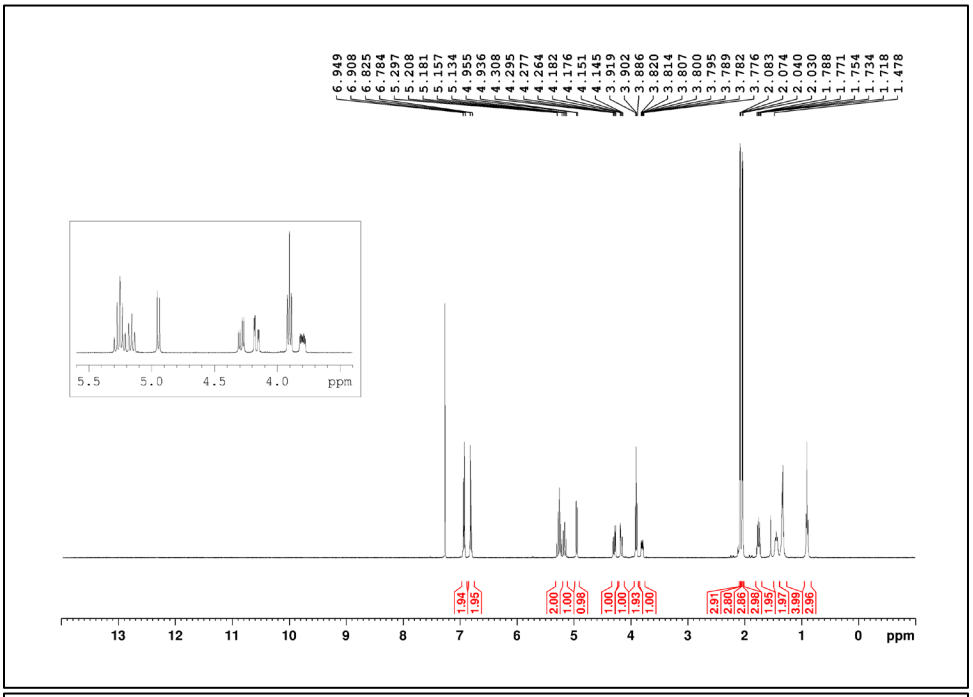


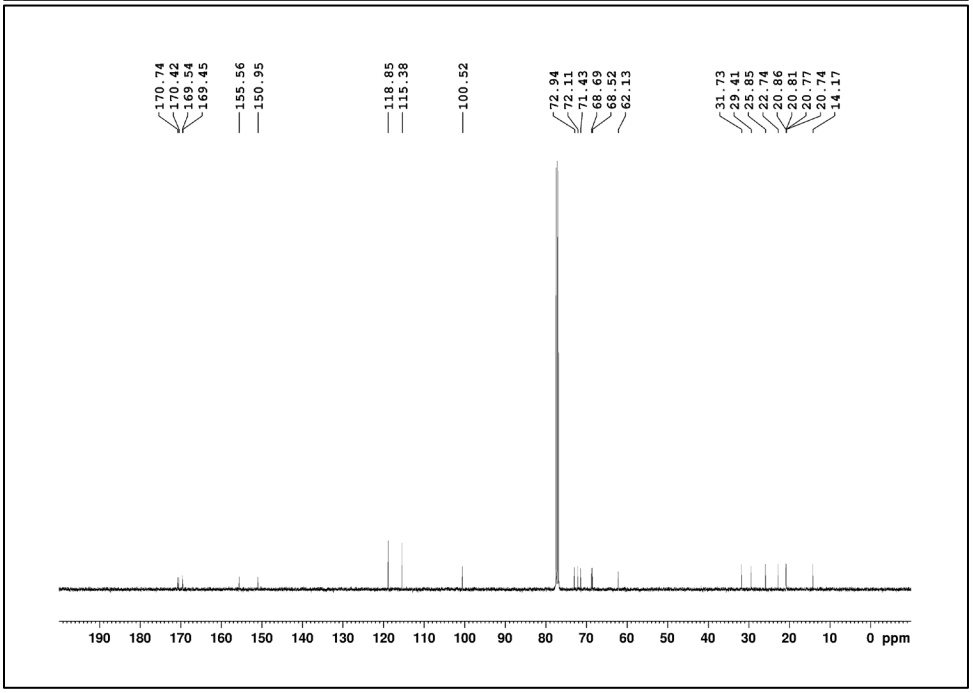




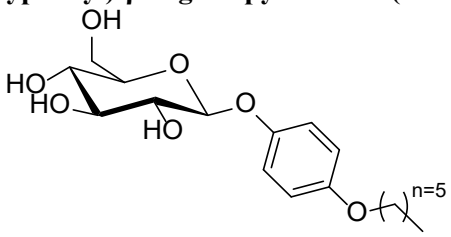
(4-hexyloxyphenyl)-2,3,4,6-tetra-*O*-acetyl-β-D-glucopyranoside (523):

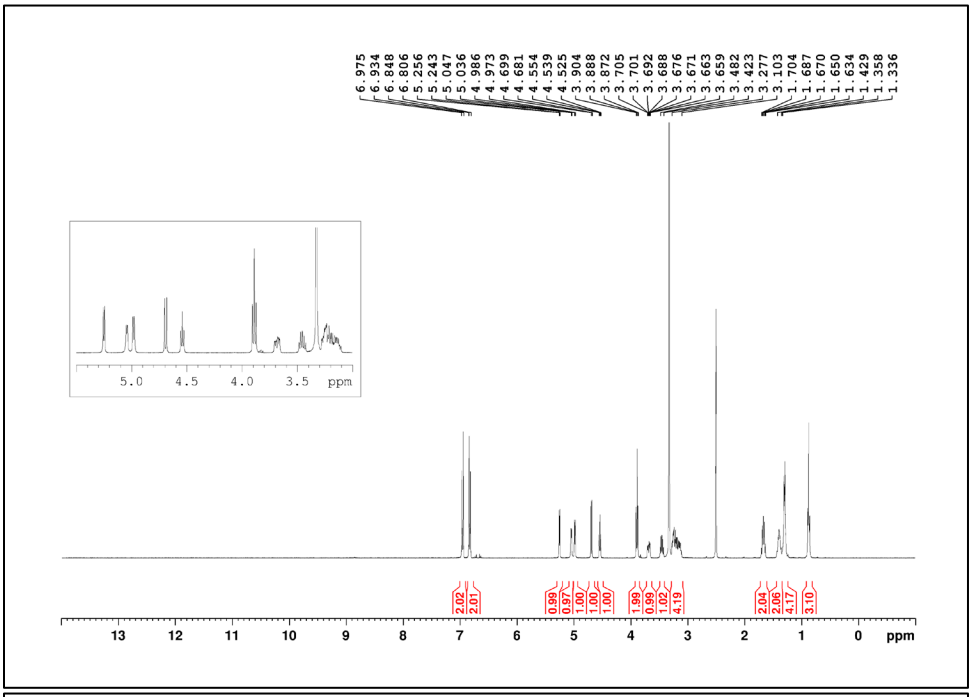


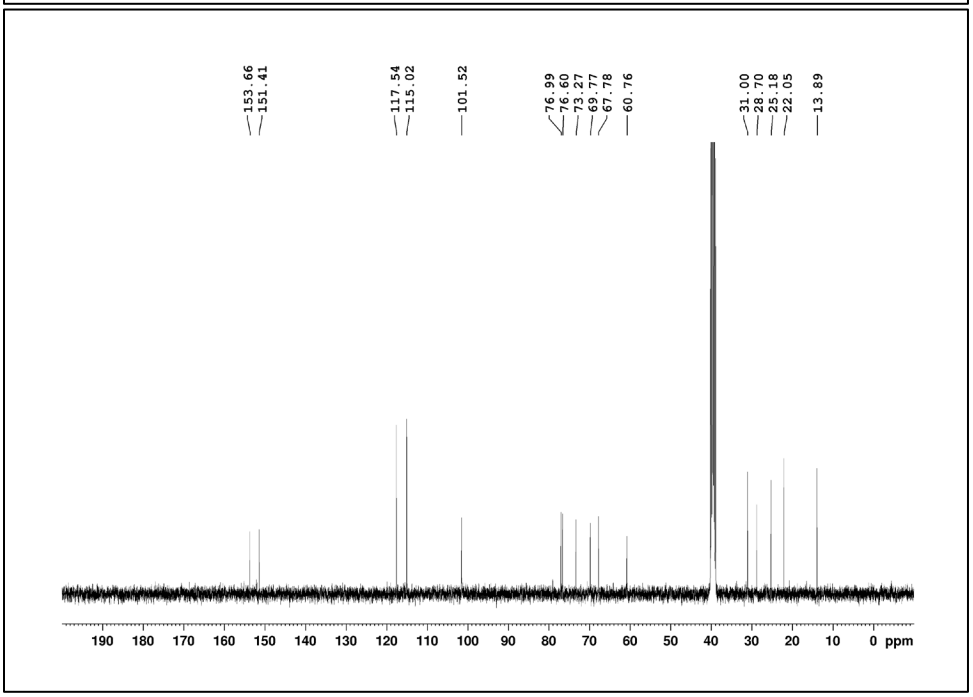




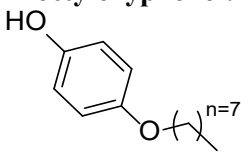
(4-hexyloxyphenyl)-β-D-glucopyranoside (PHP-Glc, 80):

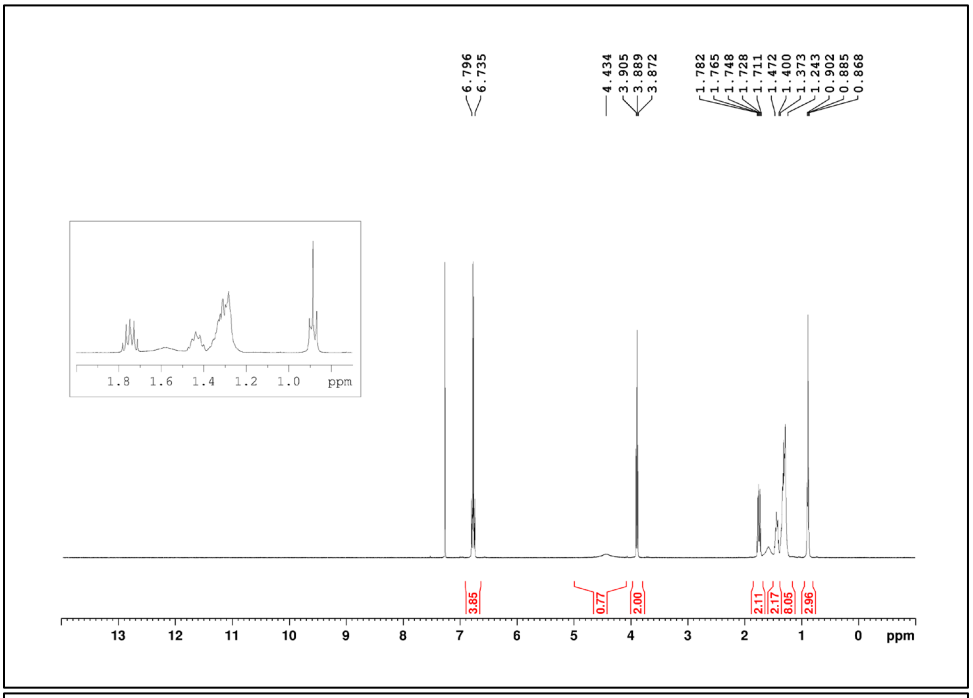


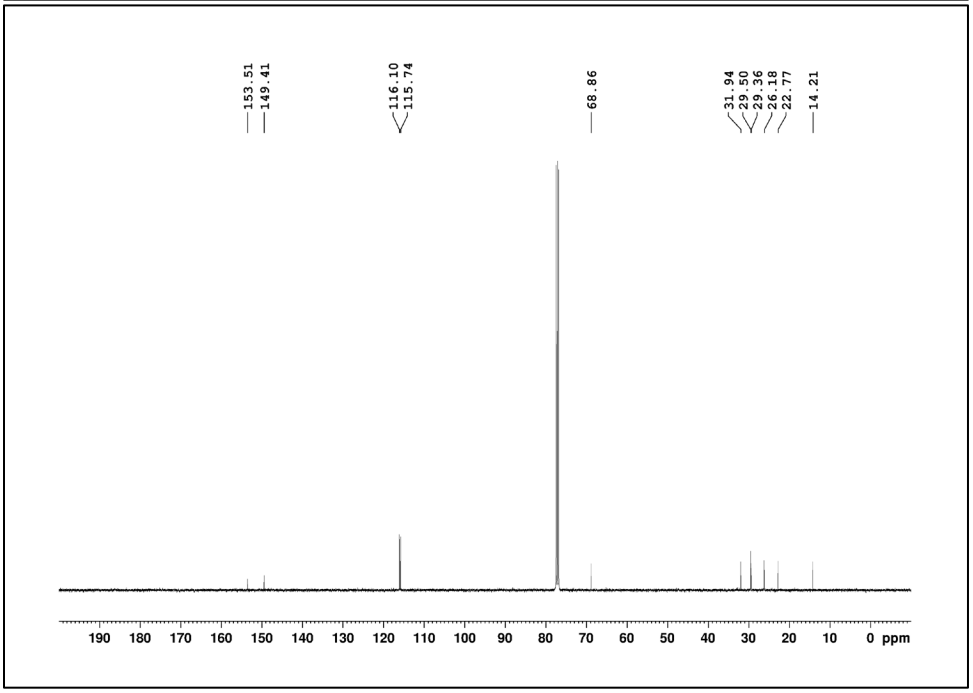




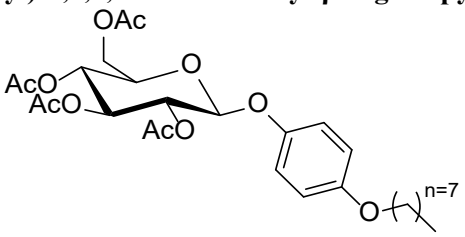
4-octyloxyphenol:

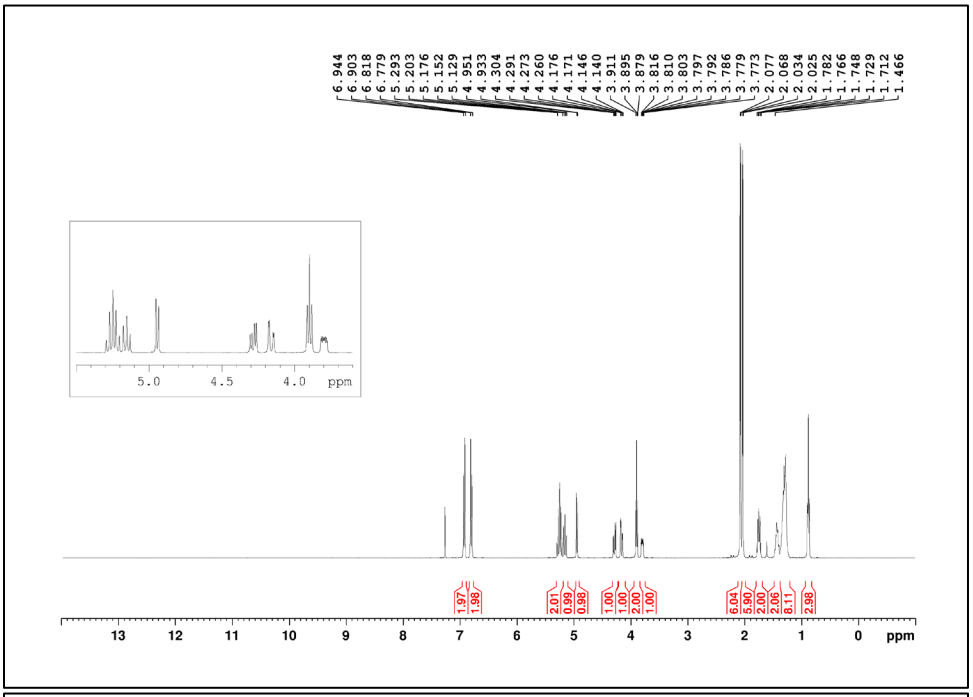


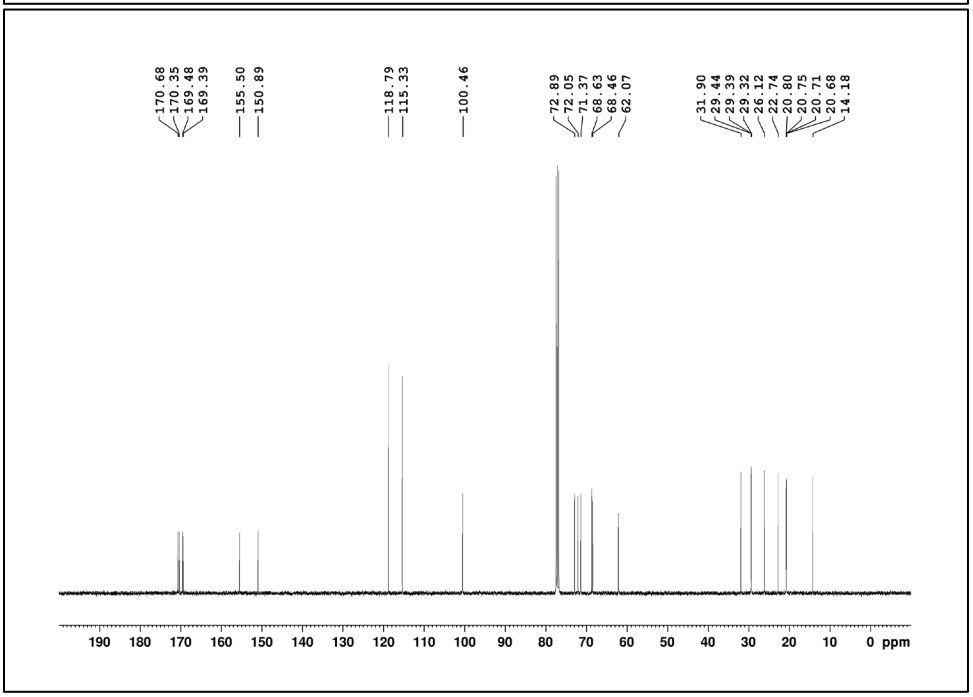




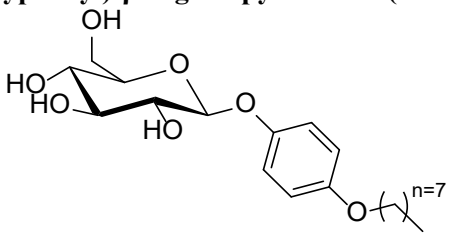
(4-octyloxyphenyl)-2,3,4,6-tetra-*O*-acetyl-β-D-glucopyranoside (524):

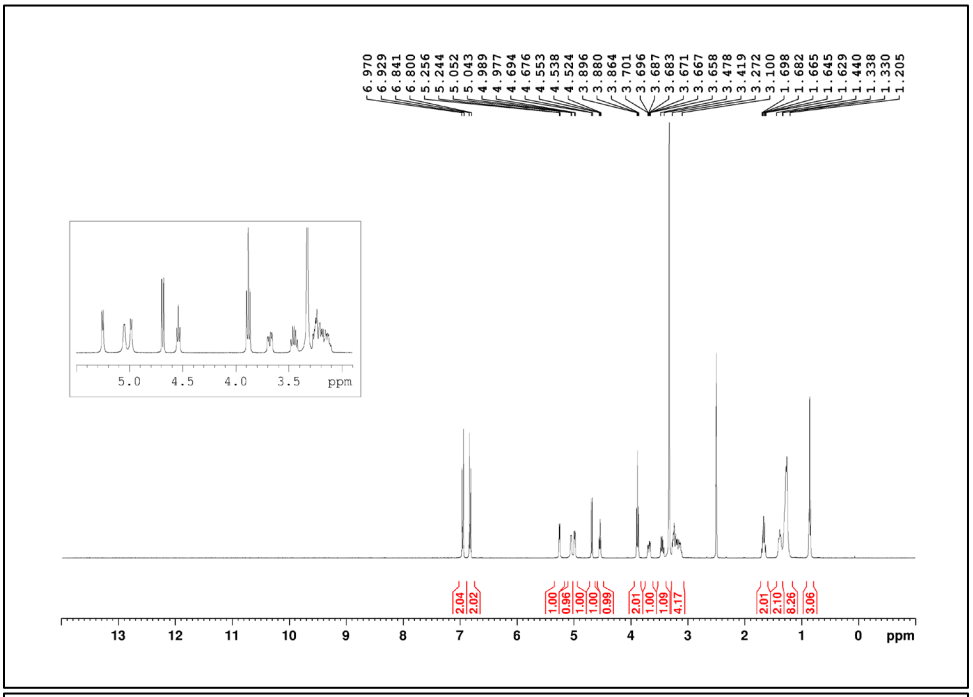


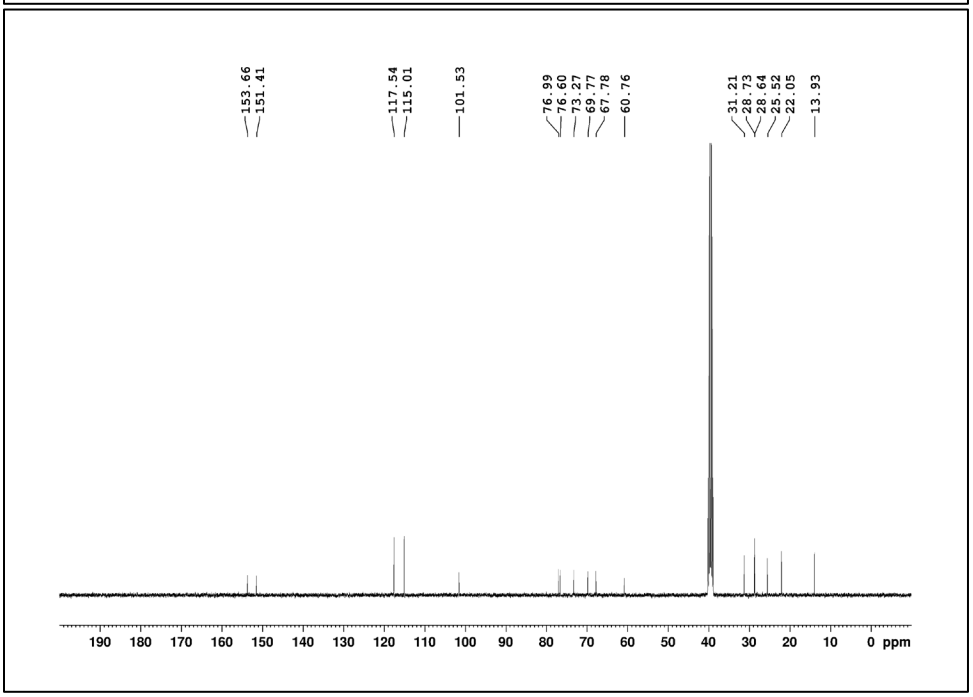




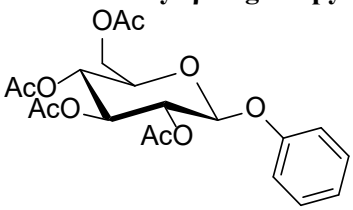
(4-octyloxyphenyl)-β-D-glucopyranoside (POP-Glc, 81):

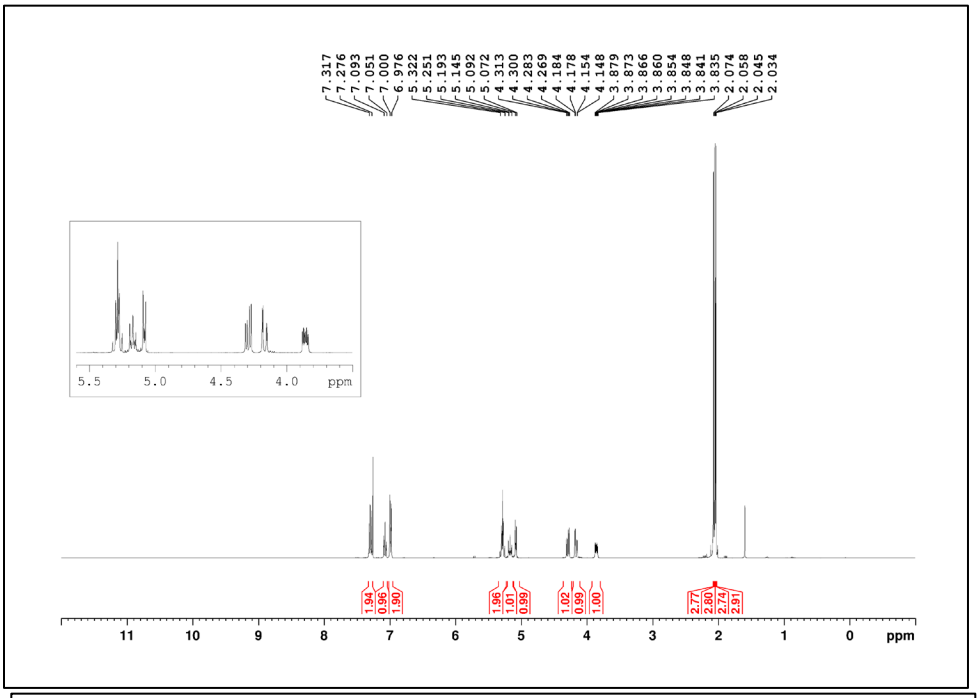


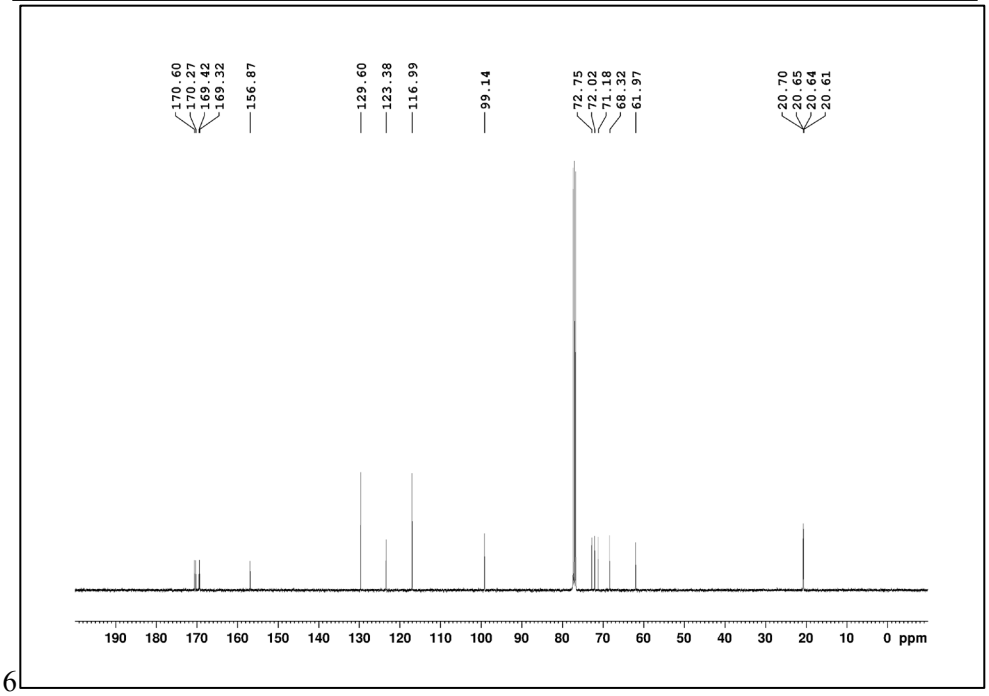




phenyl-2,3,4,6-tetra-*O*-acetyl-β-D-glucopyranoside (528):

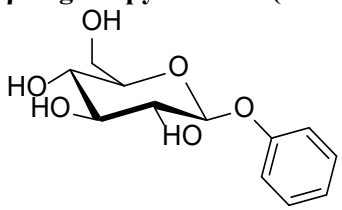


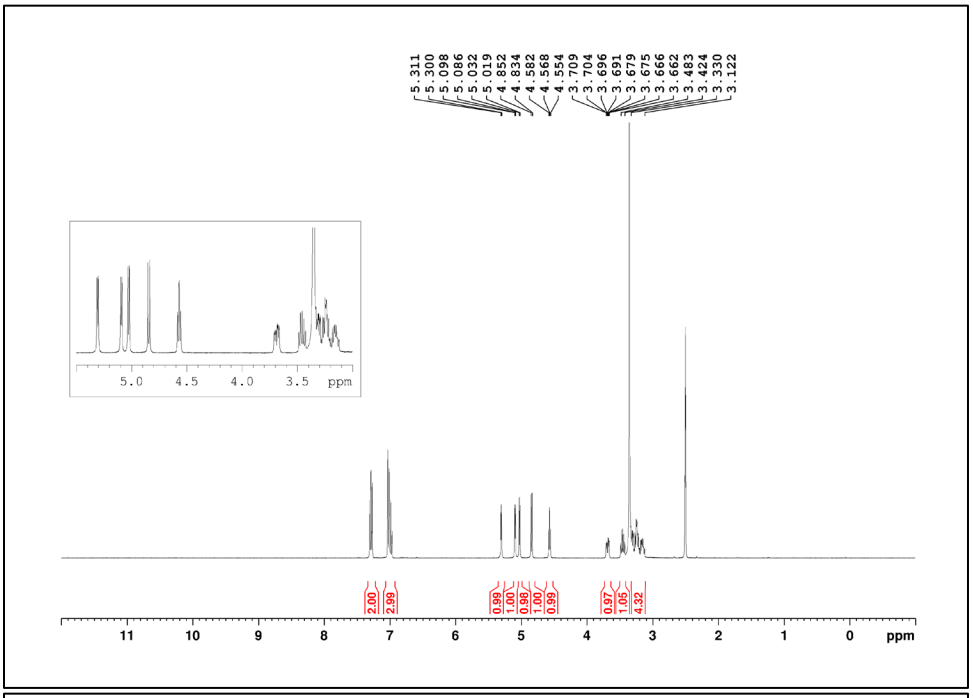


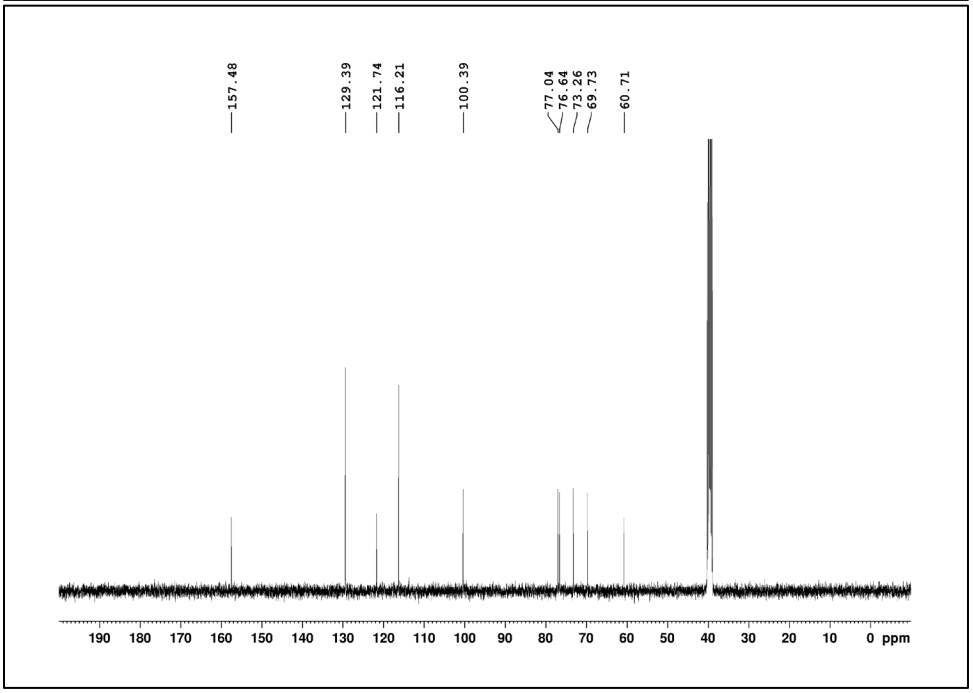


6

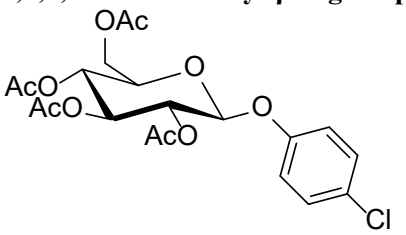
phenyl-β-D-glucopyranoside (Ph-Glc, 82):

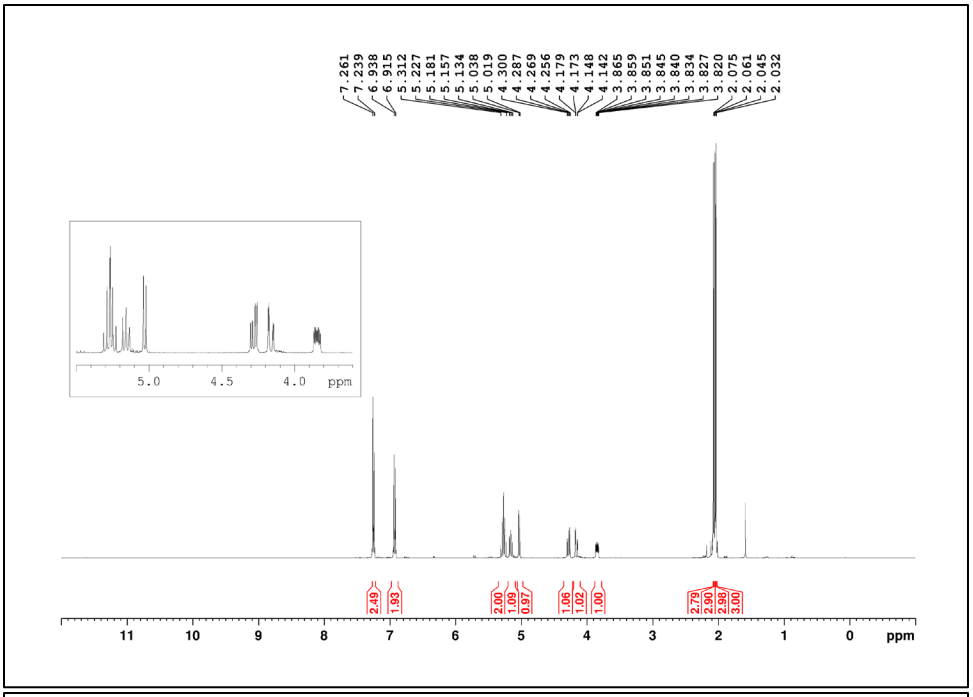


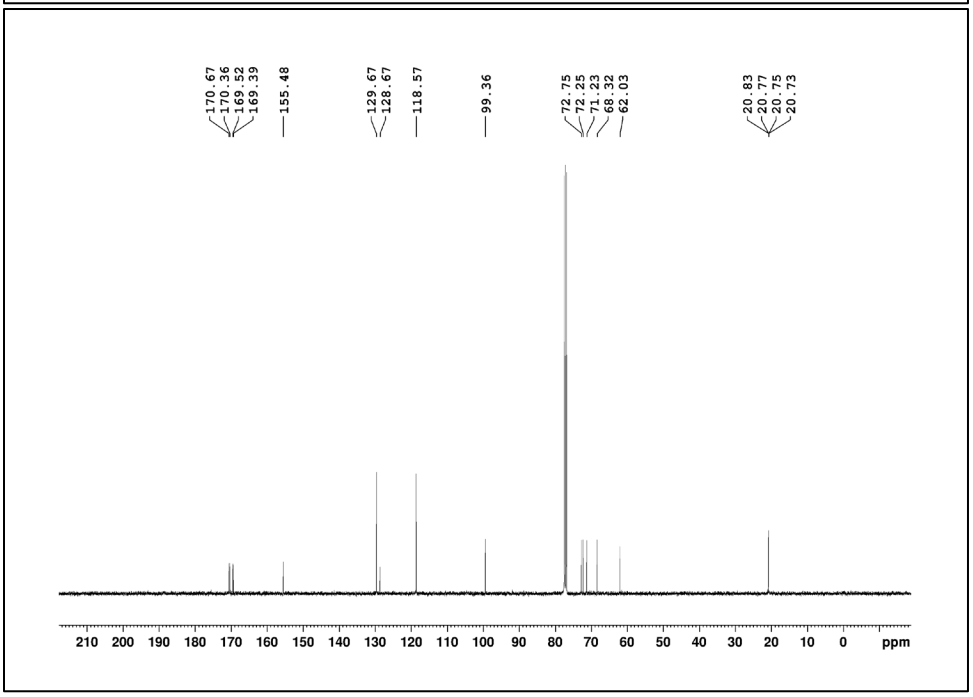




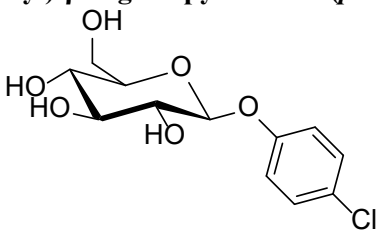
(4-chlorophenyl)-2,3,4,6-tetra-*O*-acetyl-β-D-glucopyranoside (525):

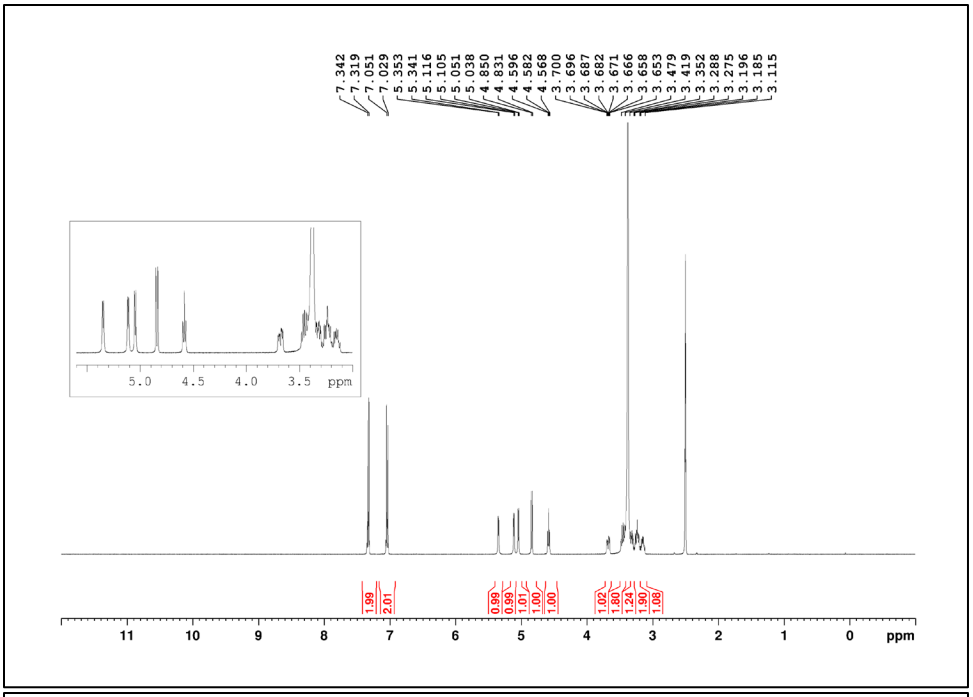


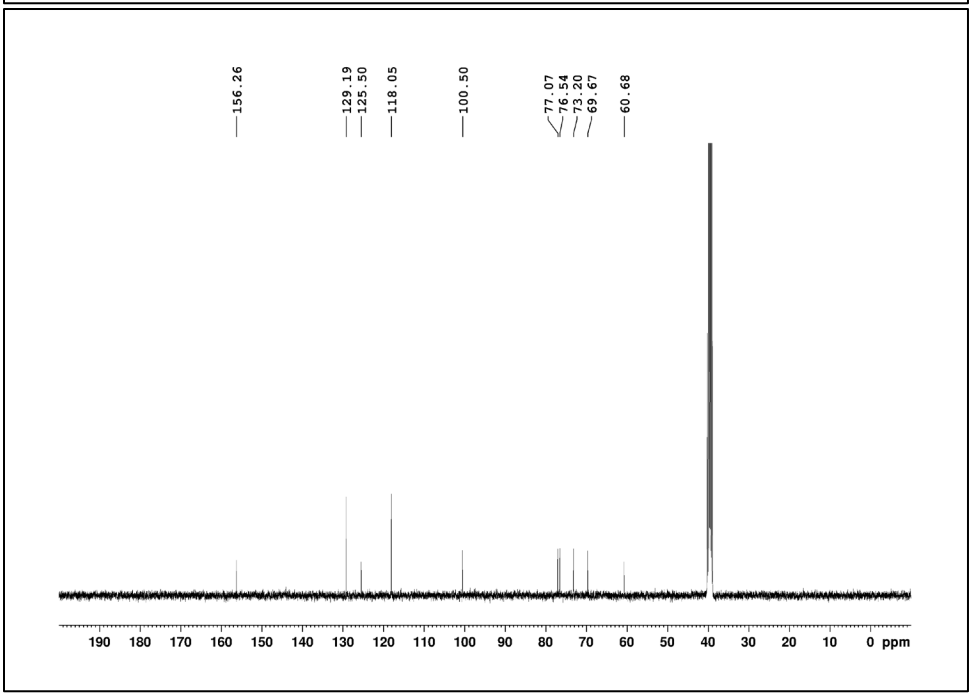




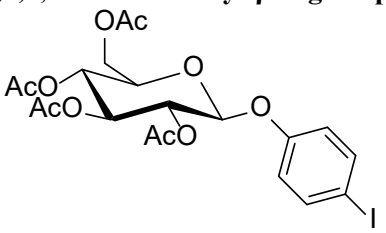
(4-chlorophenyl)-β-D-glucopyranoside (*p*ClPh-Glc, 83):

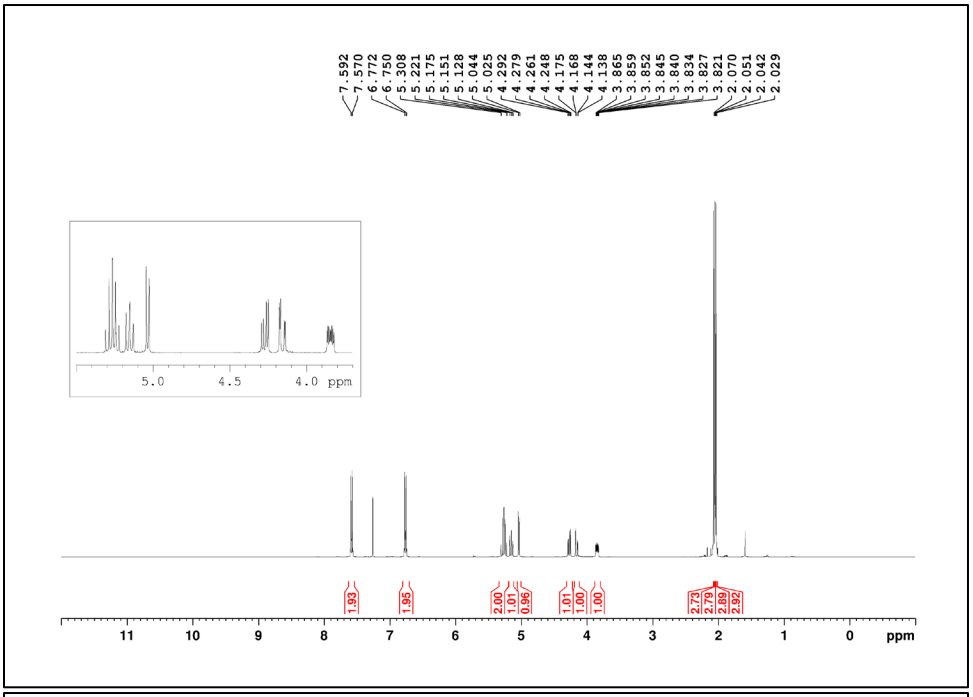


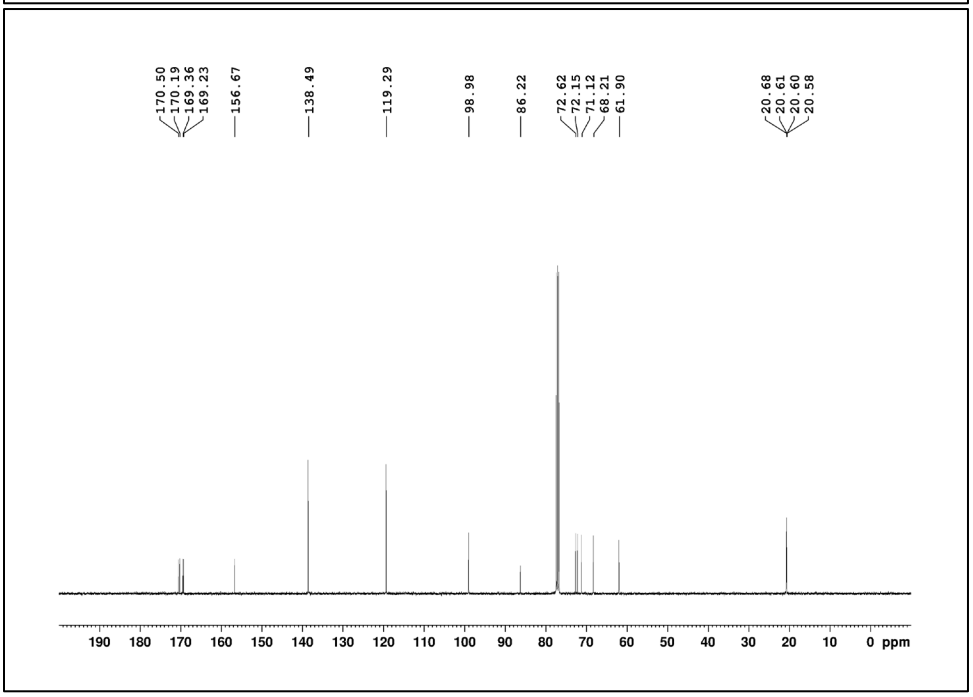




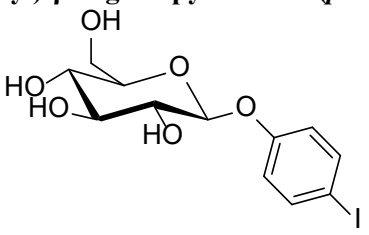
(4-iodophenyl)-2,3,4,6-tetra-*O*-acetyl-β-D-glucopyranoside (527):

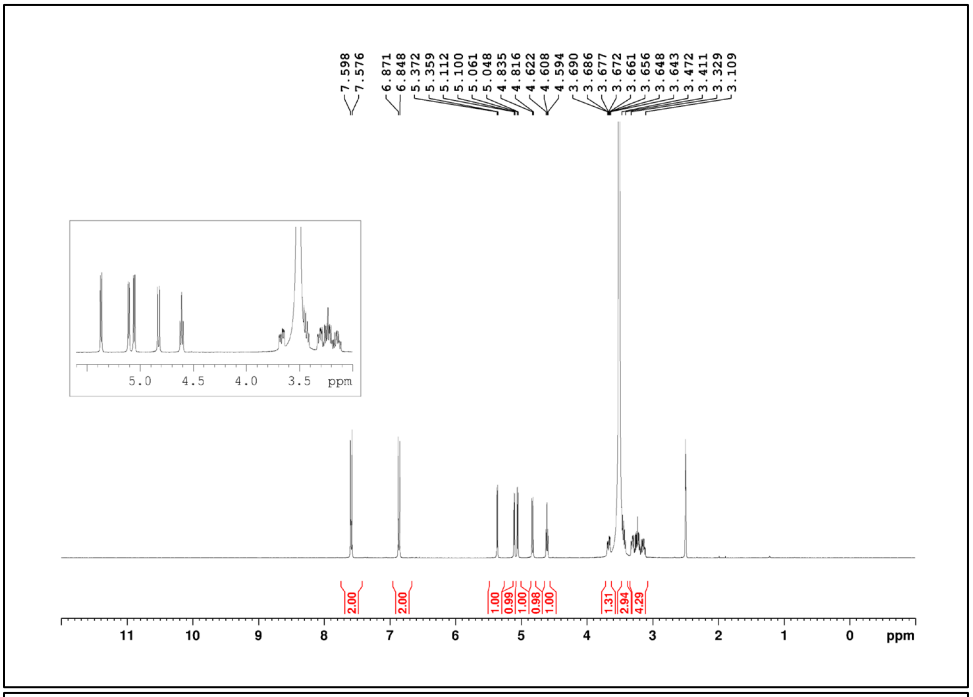


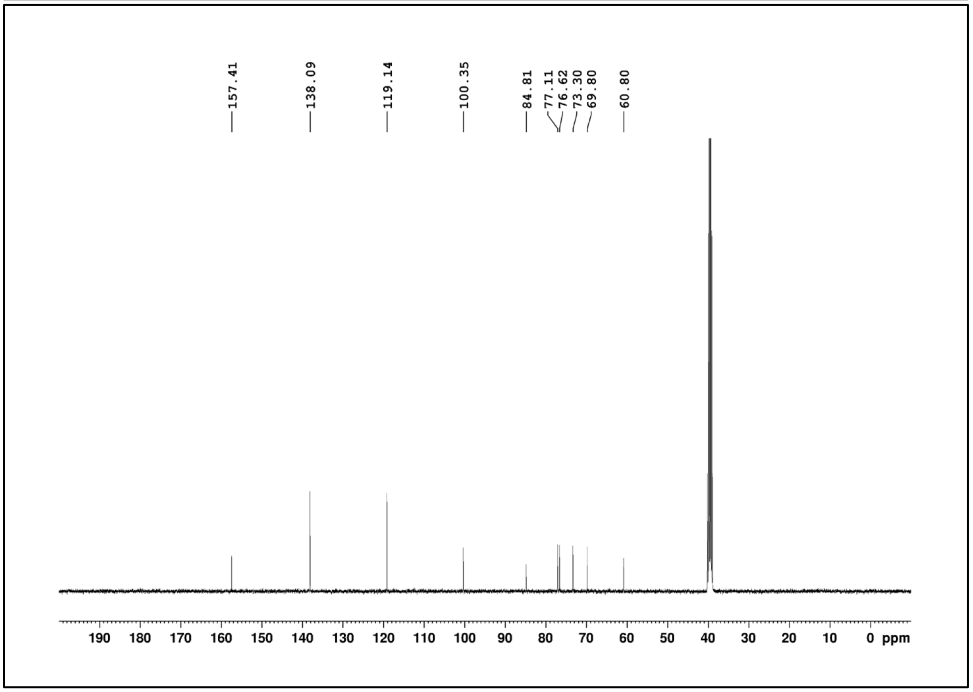




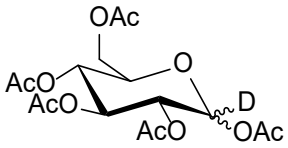
(4-iodophenyl)-β-D-glucopyranoside (*p*IPh-Glc, 84):







8.2.2.6. *Deuterated derivatives*

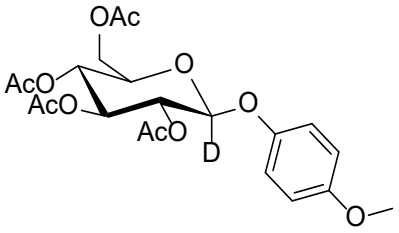


1,2,3,4,6-penta-*O*-acetyl-1-deutero-D-glucopyranose (529): The title compound was synthesized according to **General Procedure 8-4**.[214] D-glucose (1-d_1) (98%) (**94**, 0.6 mmol, 1.0 eq) was dissolved in acetic anhydride (4.2 mmol, 7.0 eq) in a flame-dried flask under argon. NaOAc (1.9 mmol, 3.0 eq) was added to the reaction mixture and it was stirred at 100 °C for two hours. Reaction progress was monitored *via* TLC, and upon completion the reaction is cooled, diluted with DCM, and washed with water. The organic phase was dried with Na_2SO_4, filtered, and concentrated *in vacuo*. The white solid was used in the next step without further purification as a mixture of alpha and beta products (**89 %**, α:β 1:2.5).

Characterization was consistent with that found in literature.[539]

^{1}H NMR (α anomer): (400 MHz, $CDCl_3$): ∂5.46(dd, *J* = 10.2, 9.5 Hz, 1H, H-3), 5.16-5.07(m, 2H, H-2 and H-4), 4.26(dd, *J* = 12.9, 4.3 Hz, 1H, H-6a), 4.12-4.06(m, 2H, H-5 and H-6b), 2.17(s, 3H, OAc CH_3), 2.08(s, 3H, OAc CH_3), 2.03(s, 3H, OAc CH_3), 2.02(s, 3H, OAc CH_3), 2.01(s, 3H, OAc CH_3). **^{1}H NMR (β anomer):** (400 MHz, $CDCl_3$): ∂5.24(dd, *J* = 9.4, 9.3 Hz, 1H, H-3), 5.16-5.07(m, 2H, H-2 and H-4), 4.28(dd, *J* = 12.3, 4.5 Hz, 1H, H-6a), 4.12-4.06(m, 1H, H-6b), 3.83(ddd, *J* = 10.0, 4.5, 2.2 Hz, 1H, H-5), 2.10(s, 3H, OAc CH_3), 2.08(s, 3H, OAc CH_3), 2.02(s, 3H, OAc CH_3), 2.02(s, 3H, OAc CH_3), 2.00(s, 3H, OAc CH_3). **^{13}C NMR:** (101 MHz, $CDCl_3$): ∂ = 170.8 (α OAc C), 170.7 (β OAc C), 170.4 (α OAc C), 170.2 (β OAc C), 169.8 (α OAc C), 169.5 (α OAc C and β OAc C), 169.4 (β OAc C), 169.1 (β OAc C), 168.9 (α OAc C), 72.9 (β C-3), 72.8 (β C-5), 70.3 (β C-2/C-4), 69.93 (α C-3/C-5), 69.91 (α C-3/C-5), 69.2 (α C-2/C-4), 68.0 (α C-2/C-4), 67.8 (β C-2/C-4), 61.6 (α C-6 CH_2 and β C-6 CH_2), 21.0 (α OAc CH_3), 20.9 (β OAc CH_3), 20.82 (α OAc CH_3 and β OAc CH_3), 20.78 (α OAc CH_3), 20.7 (3x β OAc CH_3 and 1x α OAc CH_3), 20.6 (α OAc CH_3).

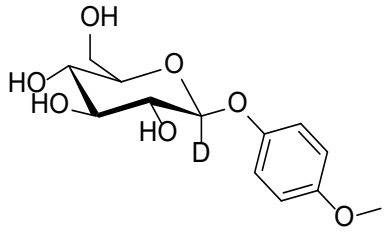
* The C-1 carbon was not observed in the ^{13}C NMR spectra due to insufficient recycle delay. Deuterium relaxation is less efficient than proton relaxation leading to slower relaxation and weaker signals therefore, to observe the C-1 carbon a longer recycle delay would have been required during acquisition.[460]



(4-methoxyphenyl)-2,3,4,6-tetra-*O*-acetyl-1-deutero-β-D-glucopyranose (532): The title compound was synthesized according a modified **General Procedure 8-2**.[167,525] 1,2,3,4,6-penta-*O*-acetyl-1-deutero-D-glucopyranose (**529,** 0.5 mmol, 1.0 eq) and 4-methoxyphenol (0.8 mmol, 1.6 eq) were dissolved in dry DCM (0.125 M) in a flame dried flask under argon at 0 °C with 4 Å molecular sieves (powdered). Boron trifluoride diethyl etherate (99 % solution) (1.6 mmol, 2.5 eq) was added to the solution slowly. The solution was stirred overnight (18 h) and then quenched with sat. $NaHCO_3$ upon reaction completion. The solution was diluted in DCM, filtered through a Celite® pad, and then washed with sat. $NaHCO_3$, H_2O, and brine. The organic layer was dried using Na_2SO_4, filtered, and concentrated *in vacuo*. The crude clear oil was purified by column chromatography (30 % EtOAc in hexanes) and then recrystallized from Et_2O/hexanes to yield the final product as a white powder (**33 %**).

^{1}H NMR: (400 MHz, $CDCl_3$) *∂*6.96-6.92(m, 2H, *arom.*), 6.83-6.79(m, 2H, *arom.*), 5.30-5.22(m, 2H, H-2/H-3), 5.16(dd, *J* = 9.9, 8.8 Hz, 1H, H-4), 4.29(dd, *J* = 12.3, 5.2 Hz, 1H, H-6a), 4.16(dd, *J* = 12.3, 2.5 Hz, 1H, H-6b), 3.80(ddd, *J* = 10.0, 5.2, 2.5 Hz, 1H, H-5), 3.77(s, 3H, OCH_3), 2.08(s, 3H, OAc CH_3), 2.07(s, 3H, OAc CH_3), 2.04(s, 3H, OAc CH_3), 2.03(s, 3H, OAc CH_3). **^{13}C NMR:** (101 MHz, $CDCl_3$) *∂* = 170.8 (OAc C), 170.4 (OAc C), 169.6 (OAc C), 169.5 (OAc C), 155.9 (*arom.* C), 151.0 (*arom.* C), 118.9 (2xCH *arom.*), 114.7 (2xCH *arom.*), 72.9 (C-2/C-3), 72.1 (C-5), 71.3 (C-2/C-3), 68.5 (C-4), 62.1 (C-6 CH_2), 55.8 (OCH_3), 20.9 (OAc CH_3), 20.81 (OAc CH_3), 20.77 (OAc CH_3), 20.7 (OAc CH_3). **LRMS (ESI):** m/z calcd for $C_{21}H_{25}DO_{11}Na$ $[M+Na]^+$ 478.1, found 478.1

***** The C-1 carbon was not observed in the ^{13}C NMR spectra due to insufficient recycle delay. Deuterium relaxation is less efficient than proton relaxation leading to slower relaxation and weaker signals therefore, to observe the C-1 carbon a longer recycle delay would have been required during acquisition.[460]



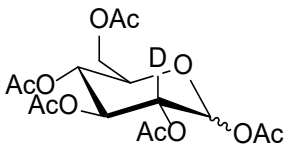
(4-methoxyphenyl)-1-deutero-β-D-glucopyranose (1D1 PMP-Glc, 90): The title compound was synthesized according to **General Procedure 8-3**.[167,326] (4-methoxyphenyl)-2,3,4,6-tetra-*O*-acetyl-1-deutero-β-D-glucopyranose (**532**, 0.1 mmol, 1.0 eq) was dissolved in MeOH (0.2 M) and a 1 M solution of NaOMe in MeOH (0.1 eq) was added to the solution to stir for 1 hour. Upon reaction completion, Amberlite IR120 H+ resin (washed in

MeOH) was added to a pH < 4. The solution was filtered, and the filtrate was concentrated *in vacuo* to yield the final product as a white powder (**79 %**).

^{1}H NMR: (400 MHz, DMSO-d_6 with 1% D_2O*)* ∂6.97-6.94(m, 2H, *arom.*), 6.83-6.81(m, 2H, *arom.*), 3.69-3.64(m, 4H, OCH_3 and H-6a), 3.44(dd, *J* = 11.9 and 5.9 Hz, 1H, H-6b), 3.28-3.10(m, 4H, H-2 and H-3 and H-4 and H-5). **^{13}C NMR:** (101 MHz, DMSO-d_6) ∂ = 154.3 (C *arom.*), 151.5 (C *arom.*), 117.6 (2xCH *arom.*), 114.4 (2xCH *arom.*), 77.0, 76.6, 73.2, 69.8, 60.8 (C-6 CH_2), 55.4 (OCH_3). **HRMS (ESI):** m/z calcd for $C_{13}H_{17}DO_7Na$ $[M+Na]^+$ 310.1013, found 310.1015.

* The C-1 carbon was not observed in the ^{13}C NMR spectra due to insufficient recycle delay. Deuterium relaxation is less efficient than proton relaxation leading to slower relaxation and weaker signals therefore, to observe the C-1 carbon a longer recycle delay would have been required during acquisition.[460]

1,2,3,4,6-penta-*O*-acetyl-2-deutero-D-glucopyranose (530): The title compound was synthesized according to **General Procedure 8-4**.[214] D-glucose (2-d_1) (98%) (**95**, 1.0 mmol, 1.0 eq) was dissolved in acetic anhydride (7.4 mmol, 7.0 eq) in a flame-dried flask under argon. NaOAc (3.2 mmol, 3.0 eq) was added to the reaction mixture and it was stirred at 100 °C for two hours. Reaction progress was monitored *via* TLC, and upon completion the reaction was cooled, diluted with DCM and washed with water. The organic phase was dried with Na_2SO_4, filtered, and concentrated *in vacuo*. The white solid was used in the next step without further purification as a mixture of alpha and beta products (**99 %**, α:β 1:3.3).

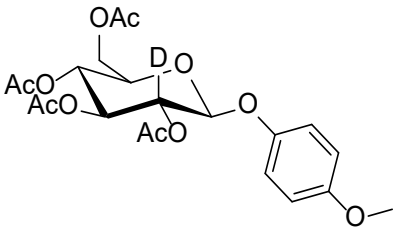


Characterization was consistent with that found in literature.[540]

^{1}H NMR (α anomer): (400 MHz, $CDCl_3$): ∂6.33(s, 1H, H-1), 5.47(d, *J* = 9.6 Hz, 1H, H-3), 5.16-5.10(m, 1H, H-4), 4.31(m, 1H, H-6a), 4.13-4.07(m, 2H, H-5 and H-6b), 2.18(s, 3H, OAc CH_3), 2.09(s, 3H, OAc CH_3), 2.04(s, 3H, OAc CH_3), 2.03(s, 3H, OAc CH_3), 2.01(s, 3H, OAc CH_3). **^{1}H NMR (β anomer):** (400 MHz, $CDCl_3$): ∂5.71(s, 1H, H-1), 5.25(d, *J* = 9.4 Hz, 1H, H-3), 5.16-5.10(m, 1H, H-4), 4.31(m, 1H, H-6a), 4.13-4.07(m, 1H, H-6b), 3.84(ddd, *J* = 10.0 and 4.4 and 2.1 Hz, 1H, H-5), 2.11(s, 3H, OAc CH_3), 2.08(s, 3H, OAc CH_3), 2.03(s, 3H, 2x OAc CH_3), 2.01(s, 3H, OAc CH_3). **^{13}C NMR:** (101 MHz, $CDCl_3$) ∂ = 170.7 (α and β OAc C), 170.4 (α OAc C), 170.2 (β OAc C), 169.8 (2x α OAc C), 169.5 (β OAc C), 169.4 (β OAc C), 169.1 (β OAc C), 168.9 (α OAc C), 91.8 (β C-1), 89.2 (α C-1), 72.9 (β C-3 and C-5), 70.0 (α C-3/C-5),

69.9 (α C-3/C-5), 68.1 (α C-4), 67.9 (β C-4), 61.6 (α and β C-6 CH_2), 21.0 (α OAc CH_3), 20.9 (β OAc CH_3), 20.8 (β OAc CH_3), 20.8 (α OAc CH_3), 20.7 (2x α OAc CH_3 and 3x β OAc CH_3), 20.6 (α OAc CH_3).

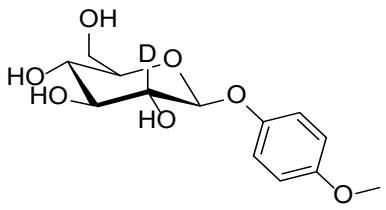
* The C-2 carbon was not observed in the ^{13}C NMR spectra due to insufficient recycle delay. Deuterium relaxation is less efficient than proton relaxation leading to slower relaxation and weaker signals therefore, to observe the C-2 carbon a longer recycle delay would have been required during acquisition.[460]



(4-methoxyphenyl)-2,3,4,6-tetra-*O*-acetyl-2-deutero-β-D-glucopyranose (533): The title compound was synthesized according a modified **General Procedure 8-2**.[167,525] 1,2,3,4,6-penta-*O*-acetyl-2-deutero-D-glucopyranose (**530**, 0.9 mmol, 1.0 eq) and 4-methoxyphenol (1.4 mmol, 1.2 eq) were dissolved in dry DCM (0.25 M) in a flame dried flask under argon at 0 °C with 4 Å molecular sieves (powdered). Boron trifluoride diethyl etherate (46.5% solution) (2.6 mmol, 2.5 eq) was added to the solution slowly. The solution was stirred overnight (18 h) and then quenched with sat. $NaHCO_3$ upon reaction completion. The solution was diluted in DCM, filtered through a Celite® pad, and then washed using sat. $NaHCO_3$, H_2O, and brine. The organic layer was dried using Na_2SO_4, filtered, and concentrated *in vacuo*. The crude white powder was purified by column chromatography (10% EtOAc in hexanes) and then recrystallized from Et_2O/hexanes to yield the final product as a white powder (**17 %**).

^{1}H NMR: (400 MHz, $CDCl_3$) *∂*6.97-6.93(m, 2H, *arom.*), 6.84-6.80(m, 2H, *arom.*), 5.27(d, *J* = 9.3 Hz, 1H, H-3), 5.20(t, *J* = 9.7 Hz, 1H, H-4), 4.96(s, 1H, H-1), 4.29(dd, *J* = 12.3, 5.2 Hz, 1H, H-6a), 4.17(dd, *J* = 12.2, 2.4 Hz, 1H, H-6b), 3.80(ddd, *J* = 9.9, 5.2, 2.2 Hz, 1H, H-5), 3.77(s, 3H, OCH_3). **^{13}C NMR:** (101 MHz, $CDCl_3$) *∂* = 170.7 (OAc C), 170.4 (OAc C), 169.5 (OAc C), 169.4 (OAc C), 156.0 (*arom.* C), 151.1 (*arom.* C), 118.9 (2x *arom*. CH), 114.7 (2x *arom*. CH), 100.5 (C-1), 72.9 (C-3), 72.1 (C-5), 68.5 (C-4), 62.1 (C-6 CH_2), 55.8 (OCH_3), 20.84 (OAc CH_3), 20.80 (OAc CH_3), 20.76 (OAc CH_3), 20.73 (OAc CH_3). **LRMS (ESI):** m/z calcd for $C_{21}H_{25}DO_{11}Na$ $[M+Na]^+$ 478.1, found 478.1.

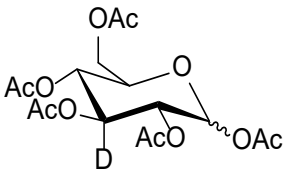
* The C-2 carbon was not observed in the ^{13}C NMR spectra due to insufficient recycle delay. Deuterium relaxation is less efficient than proton relaxation leading to slower relaxation and weaker signals therefore, to observe the C-2 carbon a longer recycle delay would have been required during acquisition.[460]



(4-methoxyphenyl)-2-deutero-β-D-glucopyranose (2D1 PMP-Glc, 91): The title compound was synthesized according to **General Procedure 8-3**.[167,326] (4-methoxyphenyl)-2,3,4,6-tetra-*O*-acetyl-2-deutero-β-D-glucopyranose (**533**, 0.1 mmol, 1.0 eq) was dissolved in MeOH (0.1 M) and a 1 M solution of NaOMe in MeOH (0.01 mmol, 0.1 eq) was added to the solution to stir for 1 hour. Upon reaction completion, Amberlite IR120 H+ resin (washed in MeOH) was added to a pH < 4. The solution was filtered, and the filtrate was concentrated *in vacuo* to yield the final product as a white powder (**99 %**).

^{1}H NMR: (400 MHz, D_2O*) ∂*7.16-7.12(m, 2H, *arom.*), 7.03-7.00(m, 2H, *arom.*), 5.00(s, 1H, H-1), 3.94(dd, *J* = 12.5, 2.2 Hz, 1H, H-6a), 3.83(s, 3H, OCH_3), 3.81-3.75(m, 1H, H-6b), 3.62-3.58(m, 2H, H-5 and H-3), 3.53-3.48(m, 1H, H-4). **^{13}C NMR:** (101 MHz, D_2O) *∂* = 154.8 (C *arom.*), 150.9 (C *arom.*), 118.2 (2x *arom*. CH), 115.1 (2x *arom*. CH), 101.2 (C-1), 76.1 (C-3/C-5), 75.5 (C-3/C-5), 69.4 (C-4), 60.6 (C-6 CH_2), 55.8 (OCH_3). **HRMS (ESI):** m/z calcd for $C_{13}H_{17}DO_7Na$ $[M+Na]^+$ 310.1013, found 310.0995.

***** The C-2 carbon was not observed in the ^{13}C NMR spectra due to insufficient recycle delay. Deuterium relaxation is less efficient than proton relaxation leading to slower relaxation and weaker signals therefore, to observe the C-2 carbon a longer recycle delay would have been required during acquisition.[460]

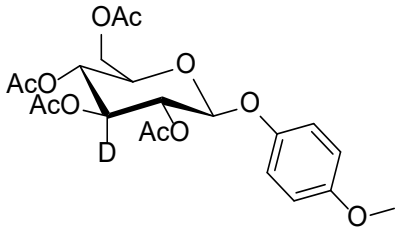


1,2,3,4,6-penta-*O*-acetyl-3-deutero-D-glucopyranose (531): The title compound was synthesized according to **General Procedure 8-4**.[214] D-glucose (3-d_1) (97-98%) (**96**, 0.2 mmol, 1.0 eq) was dissolved in acetic anhydride (2.1 mmol, 12.0 eq) in a flame-dried flask under argon. NaOAc (0.7 mmol, 4.0 eq) was added to the reaction mixture and it was stirred at 100 °C for two hours. Reaction progress was monitored *via* TLC, and upon completion the reaction was cooled, diluted with DCM and washed with water. The organic phase was dried with Na_2SO_4, filtered, and concentrated *in vacuo*. The white solid was used in the next step without further purification as a mixture of alpha and beta products (**99 %**, α:β 1:2.4).

^{1}H NMR (α anomer): (400 MHz, $CDCl_3$*)*: *∂*6.33(d, *J* = 3.7 Hz, 1H, H-1), 5.15-5.08(m, 2H, H-2 and H-4), 4.26(dd*, J* = 12.3, 4.2 Hz, 1H, H-6a), 4.13-4.07(m, 2H, H-5 and H-6b), 2.17(s, 3H, OAc CH_3), 2.10(s, 3H, OAc CH_3), 2.03(s, 3H, OAc CH_3), 2.02(s, 3H, OAc CH_3), 2.01(s, 3H, OAc CH_3). **^{1}H NMR (β anomer):** (400 MHz, $CDCl_3$): *∂*5.71(d, *J* = 8.4 Hz, 1H, H-1), 5.15-5.08(m, 2H, H-2 and H-4), 4.28(dd*, J* = 12.6,

4.5 Hz, 1H, H-6a), 4.13-4.07(m, 1H, H-6b), 3.83(ddd, *J* = 10.1, 4.5, 2.2 Hz, 1H, H-5), 2.10(s, 3H, OAc CH_3), 2.08(s, 3H, OAc CH_3), 2.03(s, 3H, 2x OAc CH_3), 2.01(s, 3H, OAc CH_3). **^{13}C NMR:** (101 MHz, $CDCl_3$) ∂ = 170.8 (OAc C), 170.7 (OAc C), 170.3 (OAc C), 170.2 (OAc C), 169.8 (OAc C), 169.5 (OAc C), 169.4 (OAc C), 169.1 (OAc C), 168.9 (OAc C), 91.8 (β C-1), 89.2 (α C-1), 72.8 (β C-5), 70.3 (β C-2/C-4), 69.9 (α C-5), 69.2 (α C-2/C-4), 67.9 (α C-2/C-4), 67.8 (β C-2/C-4), 61.5 (α and β C-6 CH_2), 21.0 (α OAc CH_3), 20.9 (β OAc CH_3), 20.92 (β OAc CH_3), 20.78 (α OAc CH_3), 20.68 (2x α OAc CH_3 and 3x β OAc CH_3), 20.56 (α OAc CH_3). **LRMS (ESI):** m/z calcd for $C_{16}H_{21}DO_{11}Na$ $[M+Na]^+$ 414.1, found 414.2.

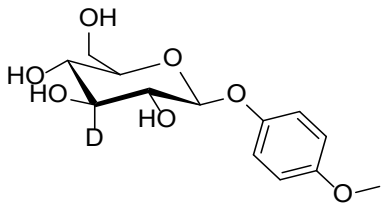
* The C-3 carbon is not observed in the ^{13}C NMR spectra due to insufficient recycle delay. Deuterium relaxation is less efficient than proton relaxation leading to slower relaxation and weaker signals therefore, to observe the C-3 carbon a longer recycle delay would have been required during acquisition.[460]



(4-methoxyphenyl)-2,3,4,6-tetra-*O*-acetyl-3-deutero-β-D-glucopyranose (534): The title compound was synthesized according a modified **General Procedure 8-2**.[167,525] 1,2,3,4,6-penta-*O*-acetyl-3-deutero-D-glucopyranose (**531**, 0.2 mmol, 1.0 eq) and 4-methoxyphenol (0.3 mmol, 1.5 eq) were dissolved in dry DCM (0.125 M) in a flame dried flask under argon at 0 °C with 4 Å molecular sieves (powdered). Boron trifluoride diethyl etherate (99% solution) (0.8 mmol, 2.5 eq) was added to the solution slowly. The solution was stirred overnight (18 h) and then quenched with sat. $NaHCO_3$ upon reaction completion. The solution was diluted in DCM, filtered through a Celite® pad, and then washed with sat. $NaHCO_3$, H_2O, and brine. The organic layer was dried using Na_2SO_4, filtered, and concentrated *in vacuo*. The crude clear oil was purified by column chromatography (a gradient of 10 to 30 % EtOAc in hexanes) to yield the final product as a white powder (**47 %**).

^{1}H NMR: (400 MHz, $CDCl_3$) ∂6.97-6.93(m, 2H, *arom.*), 6.84-6.80(m, 2H, *arom.*), 5.24(d, *J* = 8.0 Hz, 1H, H-2), 5.16(d, *J* = 10.1 Hz, 1H, H-4), 4.95(d, *J* = 8.0 Hz, 1H, H-1), 4.29(dd, *J* = 12.3, 5.2 Hz, 1H, H-6a), 4.16(dd, *J* = 12.3, 2.5 Hz, 1H, H-6b), 3.80(ddd, *J* = 10.1, 5.2, 2.5 Hz, 1H, H-5), 3.78(s, 3H, OCH_3), 2.09(s, 3H, OAc CH_3), 2.08(s, 3H, OAc CH_3), 2.04(s, 3H, OAc CH_3), 2.03(s, 3H, OAc CH_3). **^{13}C NMR:** (101 MHz, $CDCl_3$) ∂ = 170.8 (OAc C), 170.4 (OAc C), 169.54 (OAc C), 169.46 (OAc C), 155.9 (*arom.* C), 151.0 (*arom.* C), 118.9 (2x *arom*. CH), 114.7 (2x *arom*. CH), 100.5 (C-1), 72.1 (C-5), 71.3 (C-2), 68.4 (C-4), 62.1 (C-6 CH_2), 55.8 (OCH_3), 20.9 (OAc CH_3), 20.81 (OAc CH_3), 20.77 (OAc CH_3), 20.74 (OAc CH_3). **LRMS (ESI):** m/z calcd for $C_{21}H_{25}DO_{11}Na$ $[M+Na]^+$ 478.1, found 478.1.

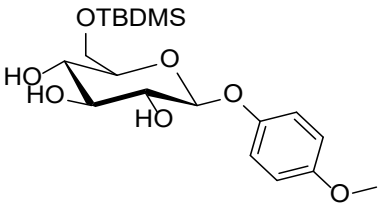
* The C-3 carbon is not observed in the ^{13}C NMR spectra due to insufficient recycle delay. It can be observed at 77.4 on the DEPT-135 spectra. Deuterium relaxation is less efficient than proton relaxation leading to slower relaxation and weaker signals therefore, to observe the C-3 carbon a longer recycle delay would have been required during acquisition.[460]



(4-methoxyphenyl)-3-deutero-β-D-glucopyranose (3D1 PMP-Glc, 92): The title compound was synthesized according to **General Procedure 8-3**.[167,326] (4-methoxyphenyl)-2,3,4,6-tetra-*O*-acetyl-3-deutero-β-D-glucopyranose (**534**, 0.07 mmol, 1.0 eq) was dissolved in MeOH (0.2 M) and a 1 M solution of NaOMe in MeOH (0.07 mmol, 1.0 eq) was added to the solution to stir for 1 hour. Upon reaction completion, Amberlite IR120 H+ resin (washed in MeOH) was added to a pH < 4. The solution was filtered, and the filtrate was concentrated *in vacuo* to yield the final product as a white powder (**99 %**).

^{1}H NMR: (400 MHz, DMSO-d_6) ∂6.99-6.97(m, 2H, *arom.*), 6.86-6.82(m, 2H, *arom.*), 5.27(br s, 1H, OH-2/OH-4), 5.04(br s, 1H, OH-3), 5.00(br s, 1H, OH-2/OH-4), 4.70(d, J = 7.8 Hz, 1H, H-1), 4.56(br s, 1H, OH-6), 3.70(s, 3H, OCH_3), 3.68(br, 1H, H-6a), 3.45(br, 1H, H-6b), 3.26(ddd, J = 9.8, 5.7, 2.0 Hz, 1H, H-5), 3.19-3.12(m, 2H, H-2 and H-4). **^{13}C NMR:** (101 MHz, DMSO-d_6) ∂ = 154.3 (C *arom.*), 151.1 (C *arom.*), 117.6 (2x *arom.* CH), 114.4 (2x *arom.* CH), 101.5 (C-1), 77.0 (C-5), 73.2 (C-2/C-4), 69.7 (C-2/C-4), 60.8 (C-6 CH_2), 55.3 (OCH_3). **HRMS (ESI):** m/z calcd for $C_{13}H_{17}DO_7Na$ $[M+Na]^+$ 310.1013, found 310.0995.

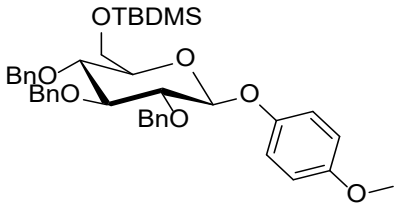
* The C-3 carbon is not observed in the ^{13}C NMR spectra due to insufficient recycle delay. Deuterium relaxation is less efficient than proton relaxation leading to slower relaxation and weaker signals therefore, to observe the C-3 carbon a longer recycle delay would have been required during acquisition.[460]



(4-methoxyphenyl)-6-*O*-*tert*-butyldimethylsilyl-β-D-glucopyranoside (535): The title compound was synthesized with the assistance of undergraduate students Hannah Mayer and Stephanie Sibbald. To a flame dried flask under argon, (4-methoxyphenyl)-β-D-glucopyranoside (PMP-Glc, **26**, 11.0 mmol, 1.0 eq) was dissolved in dry DMF (0.1 M). The reaction mixture was cooled to 0 °C and imidazole (27.4 mmol, 2.5 eq) was added to the flask, followed by *tert*-butyldimethylsilyl chloride (TBDMS-Cl,

13.2 mmol, 1.2 eq). The reaction mixture was stirred for one day (24h) and then it was diluted with ethyl acetate and washed with water and brine. The organic layers were combined, dried using Na_2SO_4, filtered, and concentrated *in vacuo* to yield the crude oil. The oil was purified by column chromatography (100 % EtOAc) to yield the purified product as a white powder (**77 %**).

^{1}H NMR: (400 MHz, $CDCl_3$) ∂7.02-6.98(m, 2H, *arom.*), 6.82-6.78(m, 2H, *arom.*), 4.77(d, *J* = 7.1 Hz, 1H, H-1), 3.88(d, *J* = 5.64 Hz, 2H, H-6), 3.76(s, 3H, OCH_3), 3.70-3.58(m, 3H, H-2 and H-3 and H-4), 3.49-3.44(m, 1H, H-5), 3.07(br s, 3H, 3xOH), 0.89(s, 9H, *tert*-butyl Si), 0.08(s, 3H, CH_3 Si), 0.06 (s, 3H, CH_3 Si). **^{13}C NMR:** (101 MHz, $CDCl_3$) ∂155.6 (C *arom.*), 151.2 (C *arom.*), 118.6 (2xCH *arom.*), 114.7 (2xCH *arom.*), 101.9 (C-1), 76.4 (C-2/C-3/C-4), 74.7 (C-5), 73.5 (C-2/C-3/C-4), 72.7 (C-2/C-3/C-4), 64.6 (C-6 CH_2), 55.8 (OCH_3), 26.0 (3xCH_3 *tert*-butyl Si), 18.3 (C *tert*-butyl Si), -5.3 (CH_3, Si), -5.4 (CH_3 Si). **LRMS (ESI):** m/z calcd. for $C_{19}H_{32}O_7Si$ $[M+Na]^+$ 423.2, found 423.2.



(4-methoxyphenyl)-2,3,4-tri-*O*-benzyl-6-*O*-*tert*-butyldimethylsilyl-β-D-glucopyranoside (536): The title compound was synthesized with the assistance of undergraduate students Hannah Mayer and Stephanie Sibbald. (4-methoxyphenyl)-6-*O*-*tert*-butyldimethylsilyl-β-D-glucopyranoside (**535**, 8.8 mmol, 1.0 eq) was dissolved in dry DMF (0.2 M) in a flame-dried flask under argon. Benzyl bromide (BnBr, 65.9 mmol, 7.5 eq) was added dropwise to the flask followed by NaH (60 % mineral oil dispersion) (52.7 mmol, 6.0 eq) portion-wise at 0 °C. The reaction was stirred overnight (18 h) at room temperature and then diluted with DCM and quenched with minimal MeOH followed by water. The organic layer was collected and washed with sat. $NaHCO_3$, water, and brine. The organic layer was dried with Na_2SO_4, filtered, and concentrated *in vacuo* to yield a crude orange oil. The crude product was purified by column chromatography (9:1 Hexanes:EtOAc) to yield the final product as white crystals (**65 %**).

Characterization was consistent with that found in literature.[541]

^{1}H NMR: (400 MHz, $CDCl_3$) ∂7.36-7.28(m, 15H, OBn *arom.*), 7.06-7.02(m, 2H, *arom.*), 6.83-6.79(m, 2H, *arom.*), 5.06(d, *J* = 10.9 Hz, 1H, OBn CH_2), 4.93(d, *J* = 10.8 Hz, 1H, OBn CH_2), 4.87(d, *J* = 10.9 Hz, 1H, OBn CH_2), 4.85-4.81(m, 3H, H-1 and 2xOBn CH_2), 4.76(d, *J* = 10.9 Hz, 1H, OBn CH_2), 3.87(dd, *J* = 11.3, 1.8 Hz, 1H, H-6a), 3.78-3.74(m, 4H, OCH_3 and H-6b), 3.65(m, 3H, H-2 and H-3 and H-4), 3.39(ddd, *J* = 9.7, 4.9, 1.8 Hz, 1H, H-5), 0.90(s, 9H, *tert*-butyl Si), 0.06(s, 3H, CH_3 Si), 0.02 (s, 3H, CH_3 Si).

(4-methoxyphenyl)-2,3,4-tri-*O*-benzyl-β-D-glucopyranoside (537): The title compound was synthesized with the assistance of undergraduate students Hannah Mayer and Stephanie Sibbald. To a flame-dried round bottom flask, (4-methoxyphenyl)-2,3,4-tri-*O*-benzyl-6-*O*-*tert*-butyldimethylsilyl-β-D-glucopyranoside (**536**, 5.8 mmol, 1.0 eq) was dissolved in a mixture of MeCN:H_2O (120 mL:12 mL). *p*-toluene sulfonic acid monohydrate (*p*TsOH•H_2O) was added to the flask until a pH of ~3 was reached (monitored using pH paper). The reaction mixture was stirred overnight (18 h) at room temperature. Following reaction completion the solution was concentrated, re-dissolved in DCM, and washed with sat. $NaHCO_3$, water, and brine. The organic layer was dried with Na_2SO_4, filtered, and concentrated *in vacuo*. The crude product was purified by recrystallization from 95% EtOH as white crystals (**79 %**).

Characterization was consistent with that found in literature.[542]

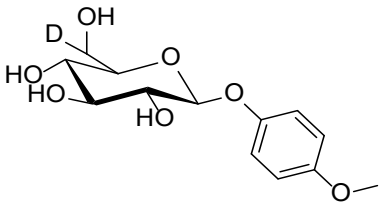
^{1}H NMR: (400 MHz, $CDCl_3$) ∂7.36-7.27(m, 15H, OBn *arom.*), 7.00-6.96(m, 2H, *arom.*), 6.86-6.82(m, 2H, *arom.*), 5.03(d, *J* = 10.8 Hz, 1H, OBn CH_2), 4.96(d, *J* = 10.8 Hz, 1H, OBn CH_2), 4.95(d, *J* = 7.7 Hz, 1H, H-1), 4.88(d, *J* = 10.9 Hz, 1H, OBn CH_2), 4.84(d, *J* = 9.7 Hz, 1H, OBn CH_2), 4.82(d, *J* = 9.8 Hz, 1H, OBn CH_2), 4.66(d, *J* = 10.9 Hz, 1H, OBn CH_2), 3.89(dd, *J* = 12.1, 2.7 Hz, 1H, H-6a), 3.78(s, 3H, OCH_3), 3.77-3.62(m, 4H, H-2 and H-3 and H-4 and H-6b), 3.47(ddd, *J* = 9.5, 4.7, 2.7 Hz, 1H, H-5). **^{13}C NMR:** (101 MHz, $CDCl_3$) ∂ = 155.6 (C *arom.*), 151.4 (C *arom.*), 138.7 (C *arom.*), 138.4 (C *arom.*), 138.1 (C *arom.*), 128.8 (2x OBn *arom.* CH), 128.7 (4x OBn *arom.* CH), 128.5 (2x OBn *arom.* CH), 128.3 (2x OBn *arom.* CH), 128.2 (OBn *arom.* CH), 128.13 (2x OBn *arom.* CH), 128.06 (OBn *arom.* CH), 127.9 (OBn *arom.* CH), 118.3 (2x PMP *arom.* CH), 114.9 (2x PMP *arom.* CH), 102.8 (C-1), 84.7 (C-2/C-3/C-4), 82.3 (C-2/C-3/C-4), 77.5 (C-2/C-3/C-4), 76.0 (OBn CH_2), 75.5 (C-5), 75.4 (OBn CH_2), 75.3 (OBn CH_2), 62.3 (C-6 CH_2), 55.9 (OCH_3).

(4-methoxyphenyl)-6-deutero-2,3,4-tri-O-benzyl-β-D-glucopyranoside (539): (4-methoxyphenyl)-2,3,4-tri-*O*-benzyl-α-D-glucopyranoside (**537**, 6.1 mmol, 1.0 eq), DMSO (dried over activated 4 Å beaded molecular sieves, 135.0 mmol, 22.0 eq), and acetic anhydride (135.0, 22.0 eq) was added to a flame dried round bottom flask under argon atmosphere. The reaction mixture was stirred overnight (18 h) at room temperature after which it was diluted with ethyl acetate and washed with water. The organic layers were combined and dried with Na_2SO_4.

Crude (4-methoxyphenyl)-6-aldehydo-2,3,4-tri-*O*-benzyl-α-D-glucopyranoside (1.0 eq) was then dissolved directly into a mixture of dry DCM (1.3 mL) and MeOH (1.3 mL) in a flame-dried flask under argon. $NaBD_4$ (1.5 mmol, 3.0 eq) was added to the reaction mixture and it was stirred at room temperature. Reaction progress was monitored by TLC and upon reaction completion (approximately 1 hour), the solution was diluted with DCM and washed with water until a neutral pH was measured (~7). The crude yellow oil was then purified by column chromatography (using a gradient of 9:1 to 7:3 Hexanes:EtOAc) to yield the final product as a white powder (**23 %, 2 steps**).

^{1}H NMR: (400 MHz, DMSO-d_6) ∂7.38-7.30(m, 15H, OBn *arom.*), 7.02-6.98(m, 2H, *arom.*), 6.87-6.83(m, 2H, *arom.*), 5.03(d, *J* = 10.9 Hz, 1H, OBn CH_2), 4.96(d, *J* = 10.6 Hz, 1H, OBn CH_2), 4.95(d, *J* = 7.7 Hz, 1H, H-1), 4.89(d, *J* = 10.9 Hz, 1H, OBn CH_2), 4.84(d, *J* = 10.7 Hz, 1H, OBn CH_2), 4.82(d, *J* = 10.8 Hz, 1H, OBn CH_2), 4.68(d, *J* = 10.9 Hz, 1H, OBn CH_2), 3.97-3.61(m, 7H), 3.48(d, *J* = 5.5 Hz, 1H). **^{13}C NMR:** (101 MHz, DMSO-d_6) ∂ = 155.5 (C *arom.*), 151.3 (C *arom.*), 138.6 (C OBn *arom.*), 138.3 (C OBn *arom.*), 138.0 (C OBn *arom.*), 128.6 (2xCH OBn *arom.*), 128.5 (4xCH OBn *arom.*), 128.3 (2xCH OBn *arom.*), 128.2 (2xCH OBn *arom.*), 128.1 (CH OBn *arom.*), 128.0 (2xCH OBn *arom.*), 127.9 (CH OBn *arom.*), 127.8 (CH OBn *arom.*), 118.2 (2xCH *arom.*), 114.8 (2xCH *arom.*), 102.7 (C-1), 84.6, 82.2, 75.9 (OBn CH_2), 75.4, 75.30, 75.25 (OBn CH_2), 75.2 (OBn CH_2), 55.8 (OCH_3).

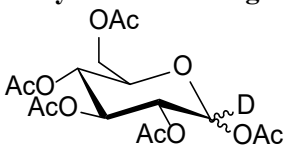
* The C-6 carbon is not observed in the ^{13}C NMR spectra due to insufficient recycle delay. Deuterium relaxation is less efficient than proton relaxation leading to slower relaxation and weaker signals therefore, to observe the C-6 carbon a longer recycle delay would have been required during acquisition.[460]

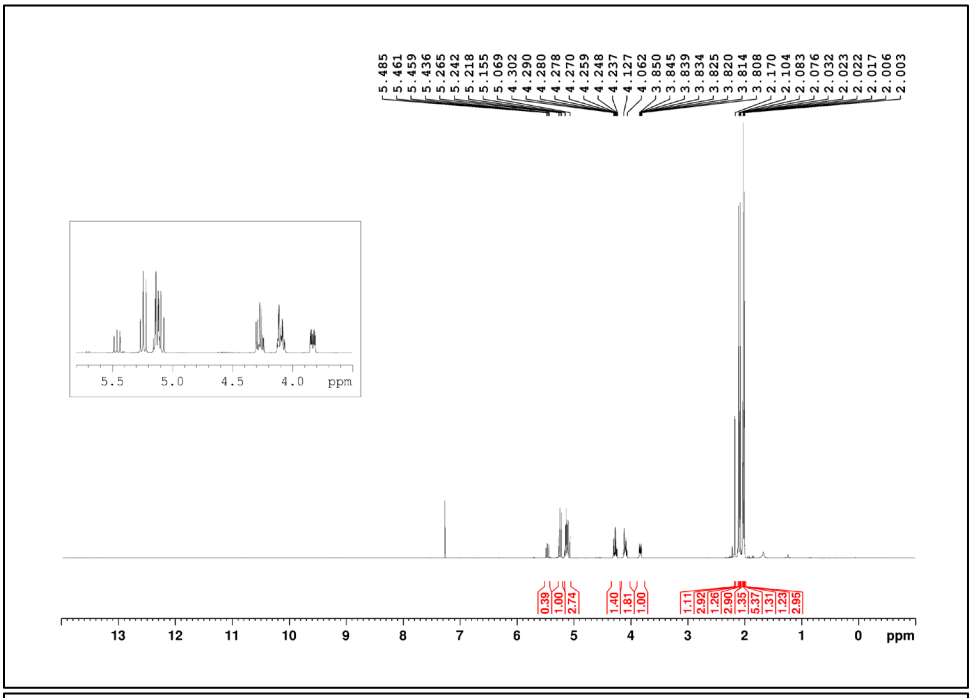


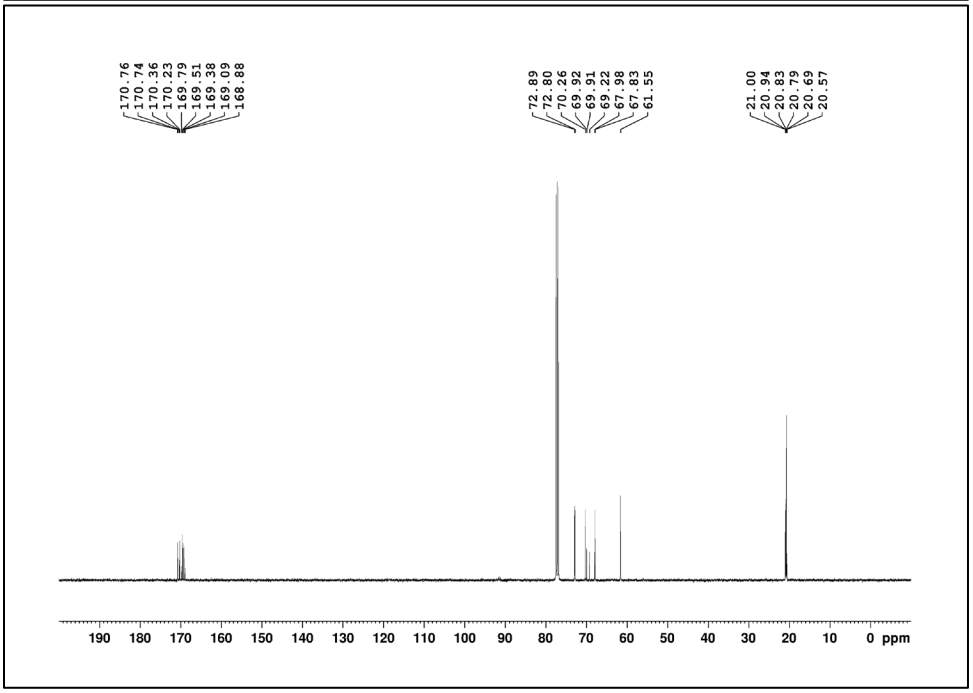
(4-methoxyphenyl)-6-deutero-β-D-glucopyranoside (93): The title compound was synthesized according to **General Procedure 8-7**. (4-methoxyphenyl)-6-deutero-2,3,4-tri-*O*-benzyl-β-D-glucopyranoside (**539**, 0.1 mmol, 1.0 eq) was dissolved in a 1:1 mixture of EtOAc and MeOH (2.0 mL each solvent). Pd/C (10 %, 0.05 mmol, 0.5 eq) was added and the reaction mixture was purged several times with H_2. The mixture was stirred under H_2 atmosphere until complete (monitored by TLC, approximately 24 hours). Upon reaction completion, the reaction was diluted with MeOH, filtered through a Celite® pad, and the volatiles were evaporated to afford the desired product as a white powder (**67 %**).

^{1}H NMR: (400 MHz, DMSO-d_6) ∂8.49(s, 1H, NH), 6.99-6.95(m, 2H, *arom.*), 6.86-6.82(m, 2H, *arom.*), 5.30(br s, 1H, OH), 5.20(br s, 1H, OH), 4.69(d, *J* = 7.6 Hz, 1H, H-1), 4.59(br s, 1H, OH), 3.70(s, 3H, OCH_3), 3.27-3.11(m, 5H, H-2 and H-3 and H-4 and H-5 and H-6). **^{13}C NMR:** (101 MHz, DMSO-d_6) ∂ = 166.1 (C *amide*) 154.2 (C *arom.*), 151.5 (C *arom.*), 117.6 (2xCH *arom.*), 114.4 (2xCH *arom.*), 101.6 (C-1), 77.0 (C-2/C-3/C-4/C-5/C-6), 76.9 (C-2/C-3/C-4/C-5/C-6), 76.6 (C-2/C-3/C-4/C-5/C-6), 73.3 (C-2/C-3/C-4/C-5/C-6), 69.8 (C-2/C-3/C-4/C-5/C-6), 55.3 (OCH_3). **LRMS (ESI):** m/z calcd for $C_{13}H_{17}DO_7Na$ $[M+Na]^+$ 310.1, found 310.2.

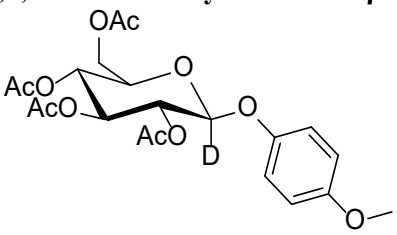
1,2,3,4,6-penta-*O*-acetyl-1-deutero-D-glucopyranose (529):

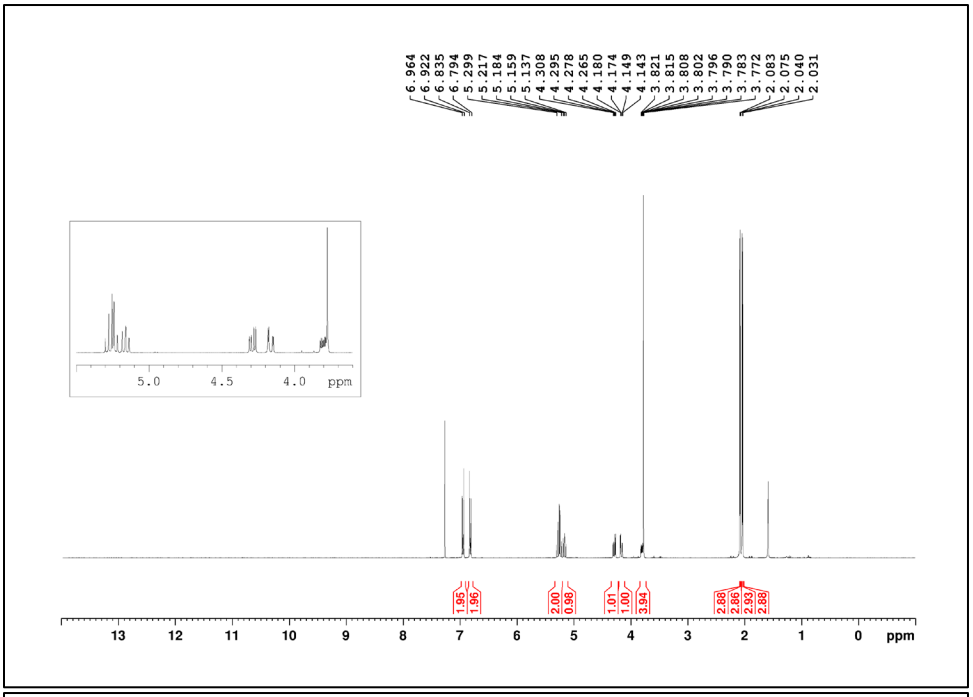


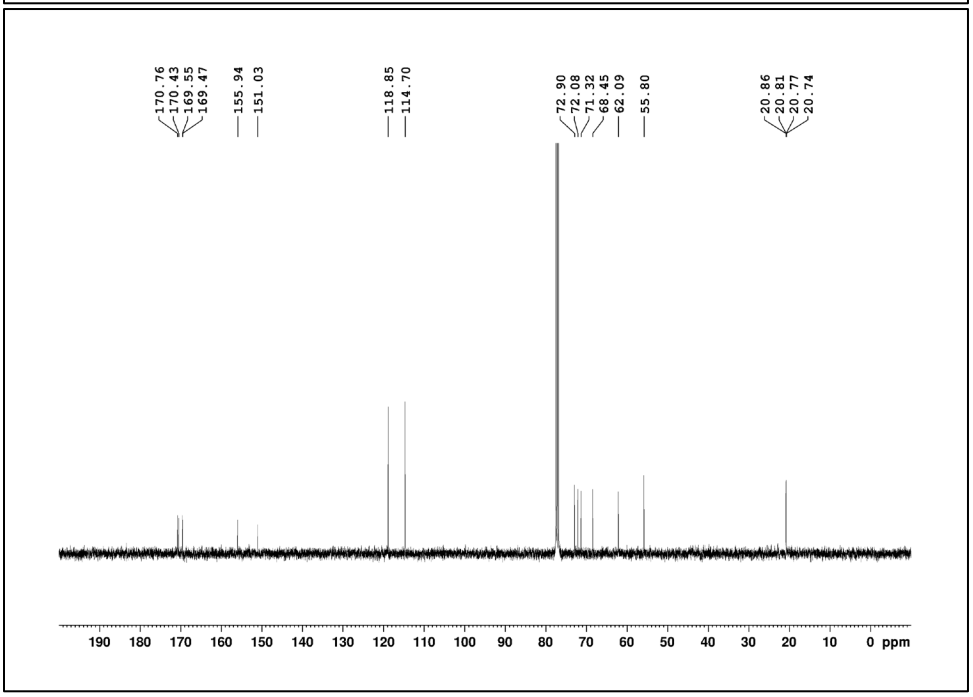




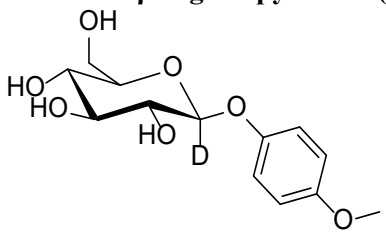
(4-methoxyphenyl)-2,3,4,6-tetra-*O*-acetyl-1-deutero-β-D-glucopyranose (532):

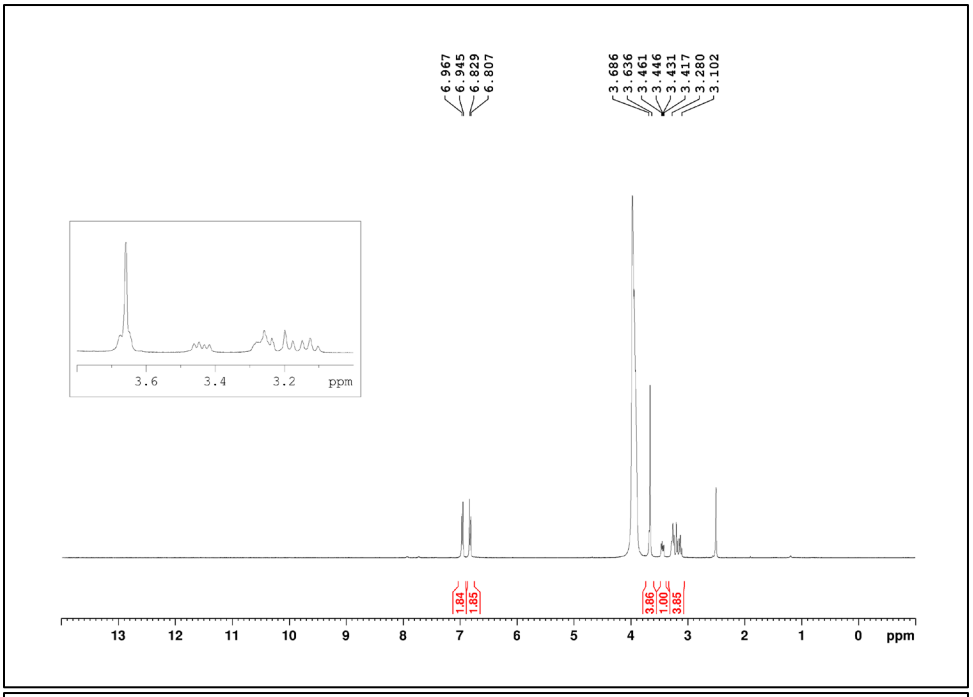


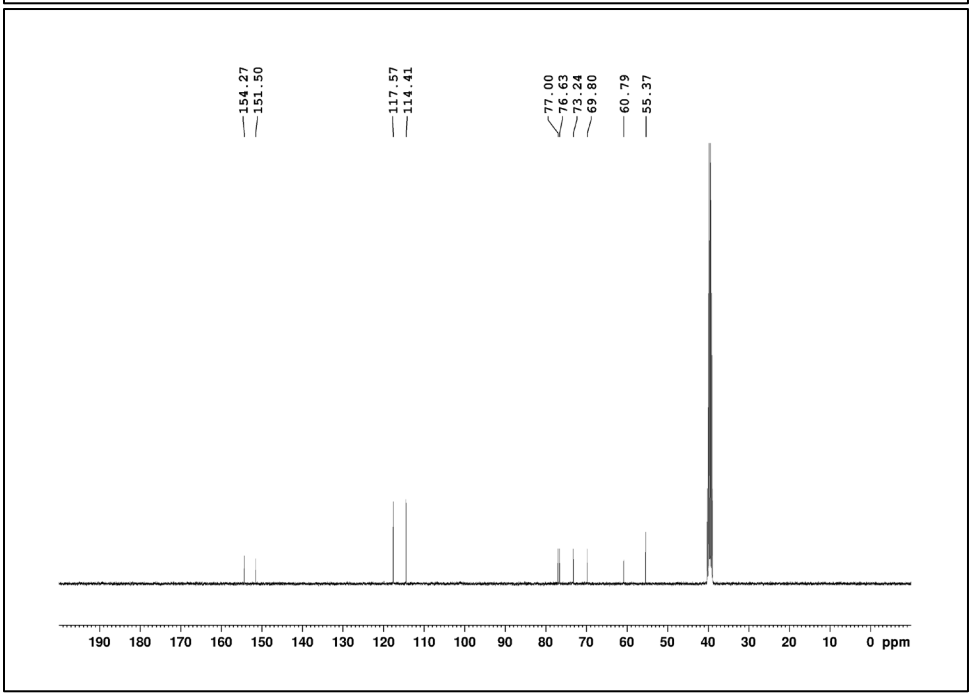




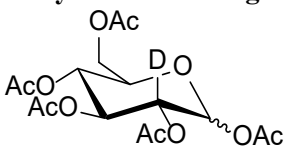
(4-methoxyphenyl)-1-deutero-β-D-glucopyranose (1D1 PMP-Glc, 90):

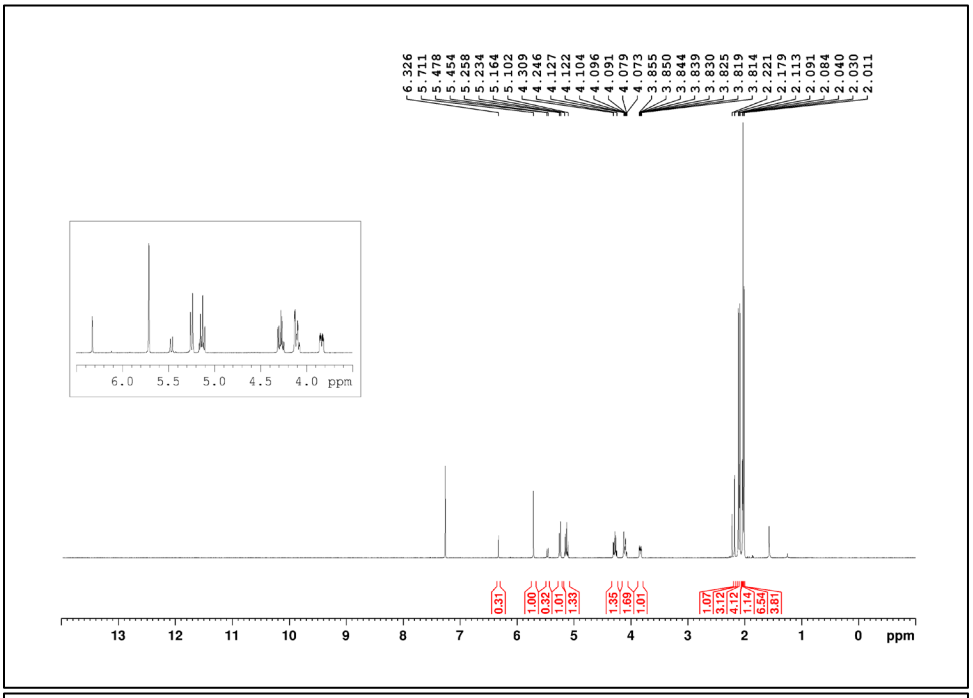


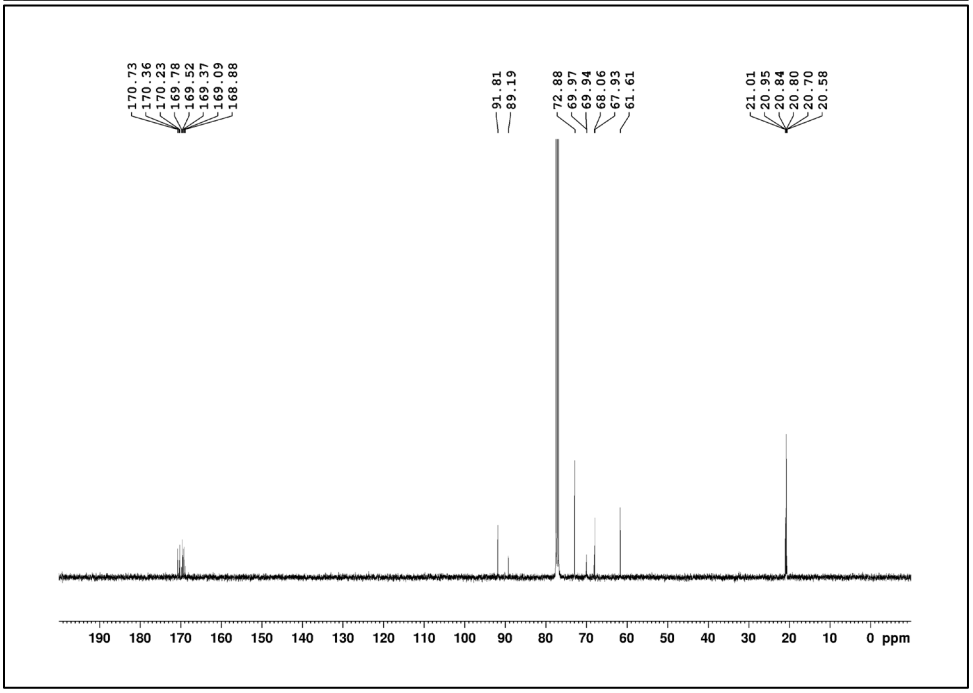




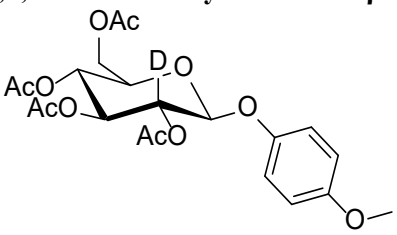
1,2,3,4,6-penta-*O*-acetyl-2-deutero-D-glucopyranose (530):

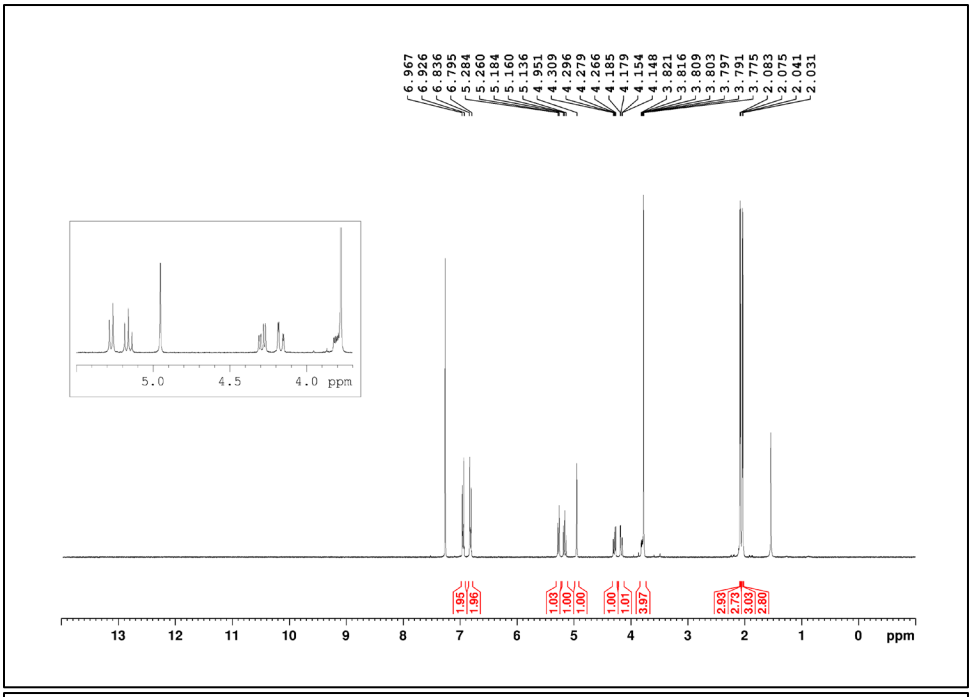


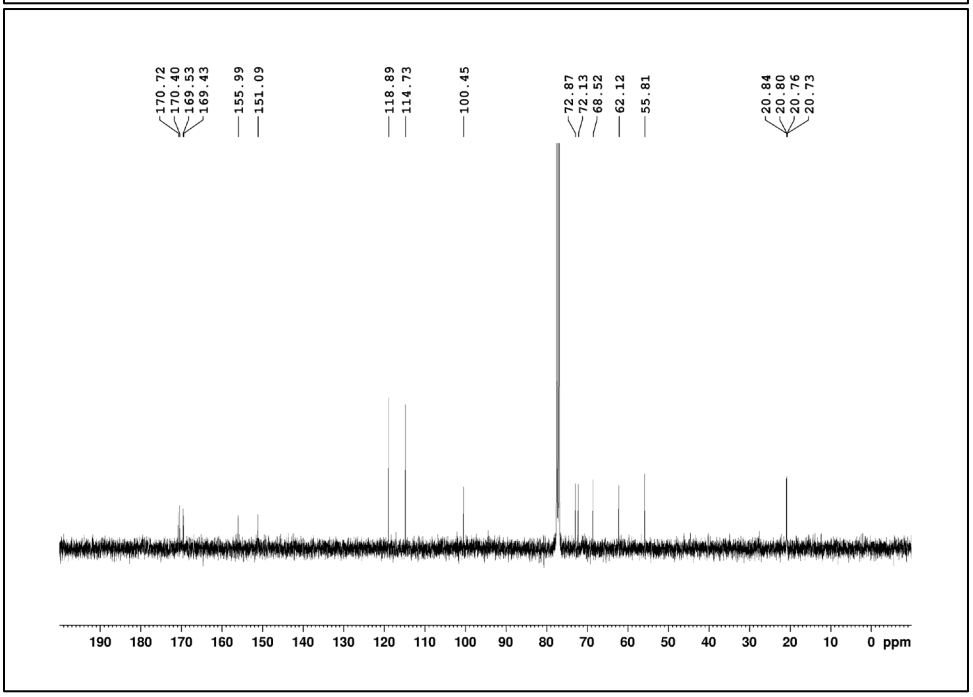




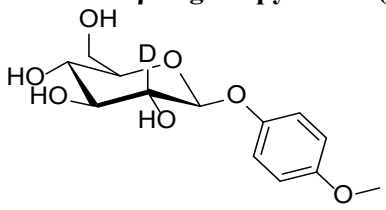
(4-methoxyphenyl)-2,3,4,6-tetra-*O*-acetyl-2-deutero-β-D-glucopyranose (533):

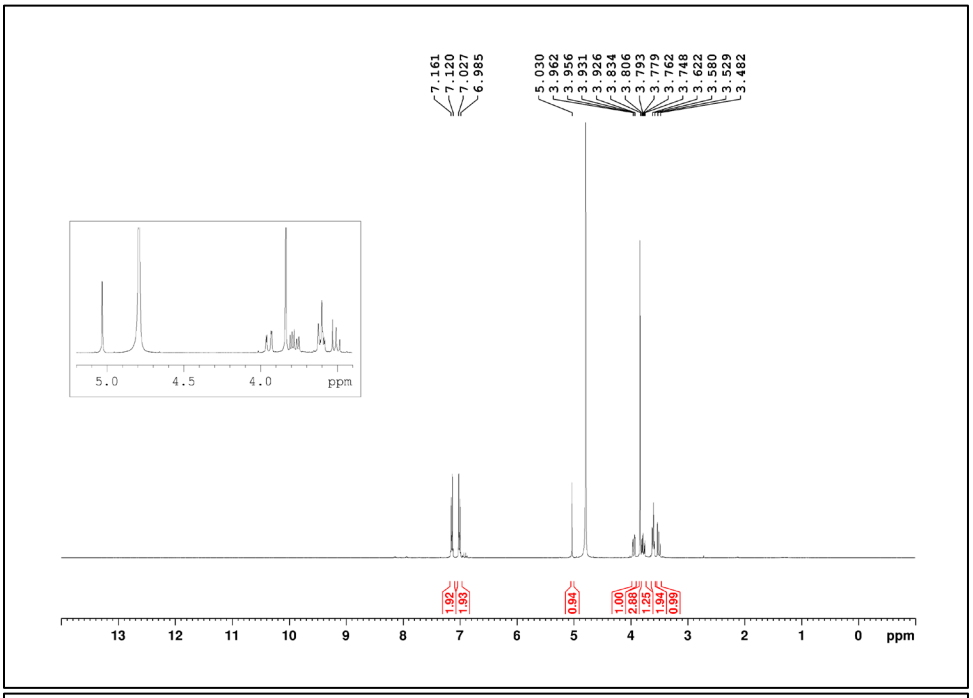


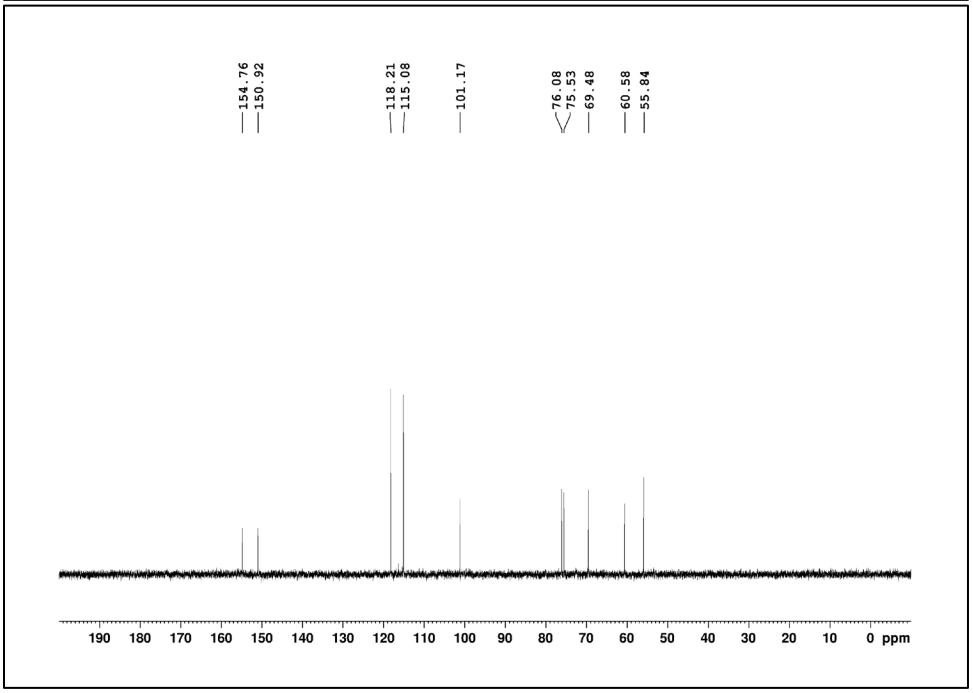




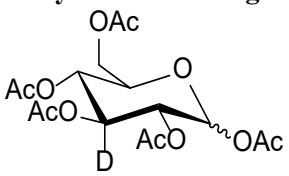
(4-methoxyphenyl)-2-deutero-β-D-glucopyranose (2D1 PMP-Glc, 91):

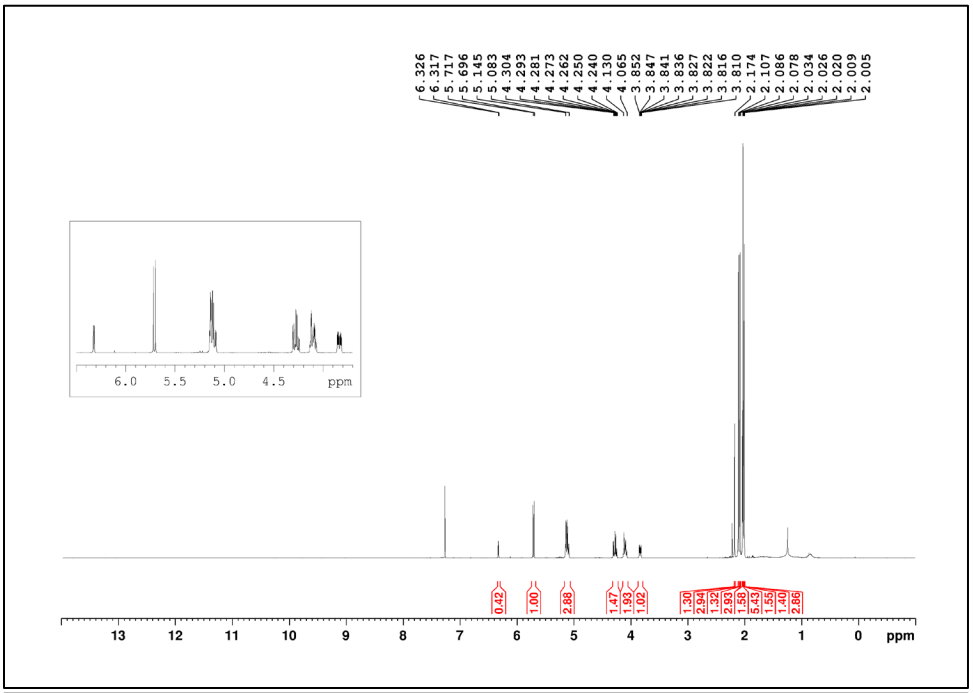


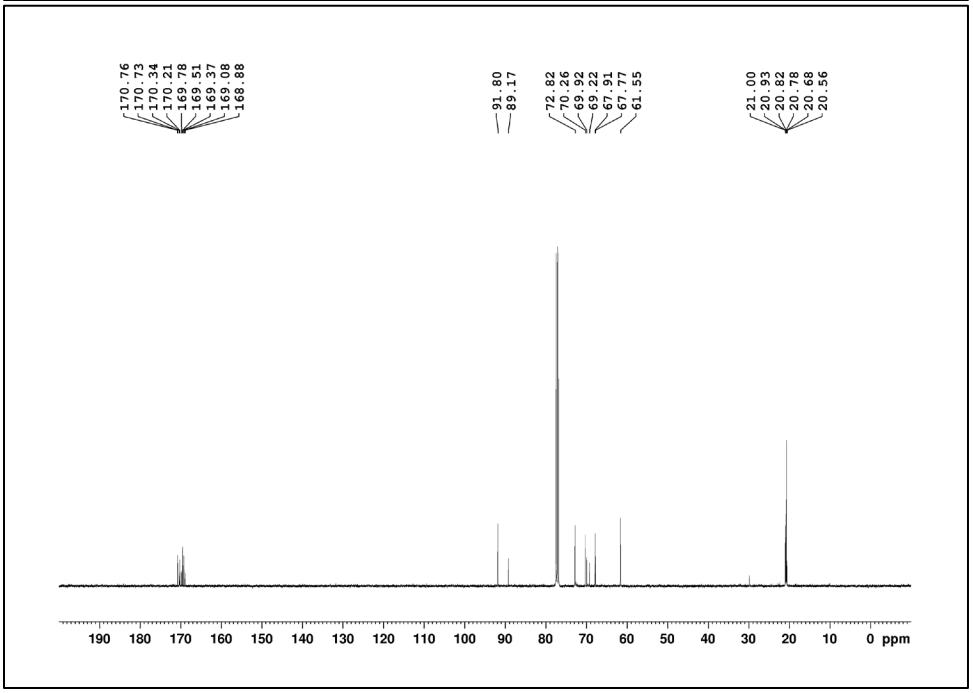




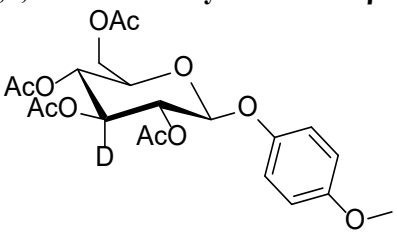
1,2,3,4,6-penta-*O*-acetyl-3-deutero-D-glucopyranose (531):

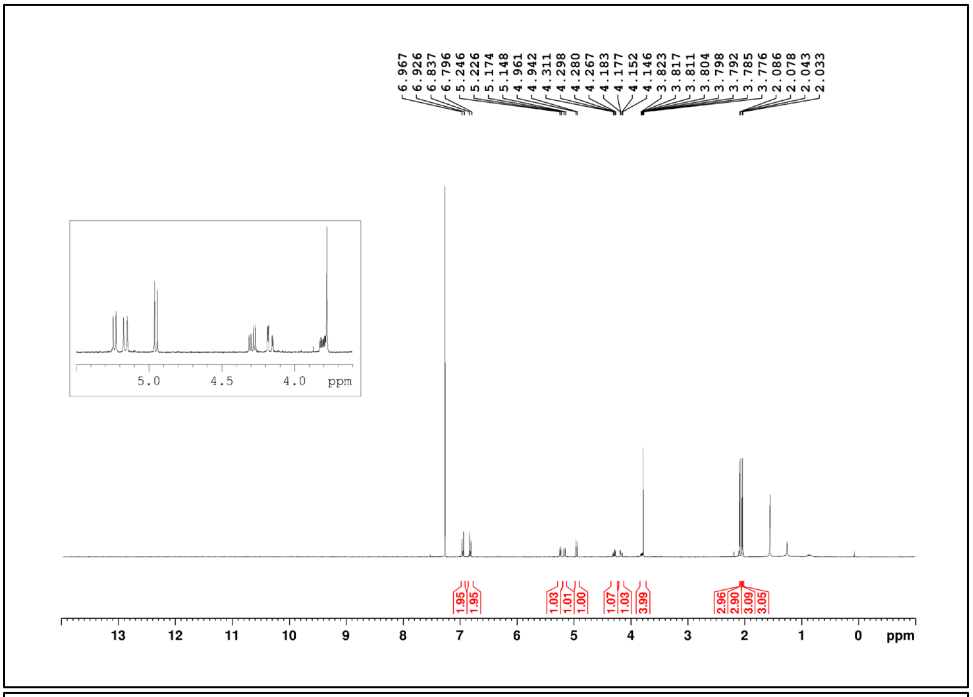


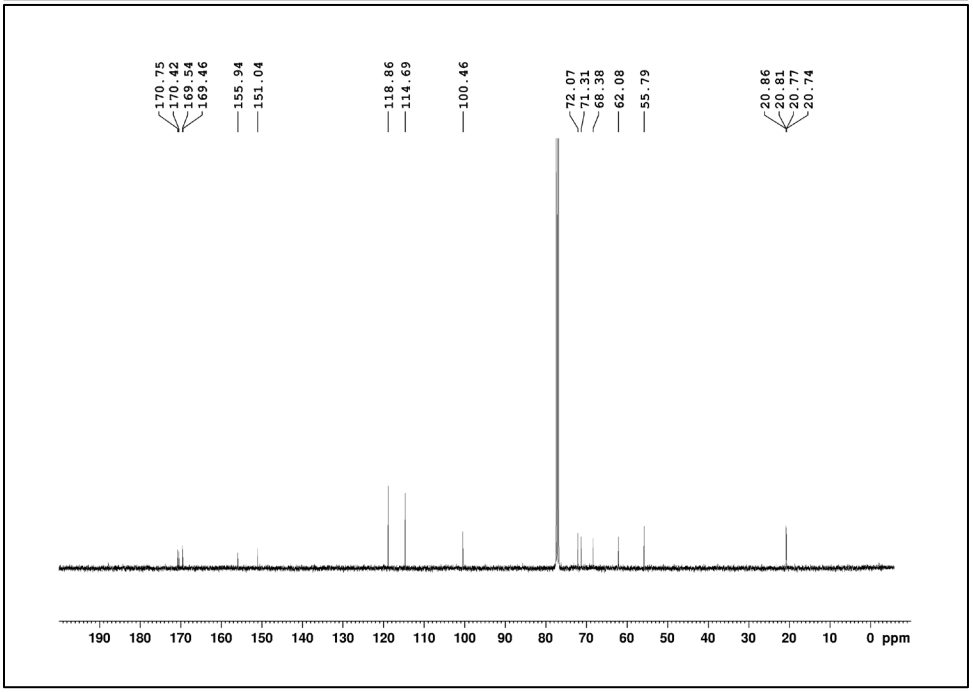


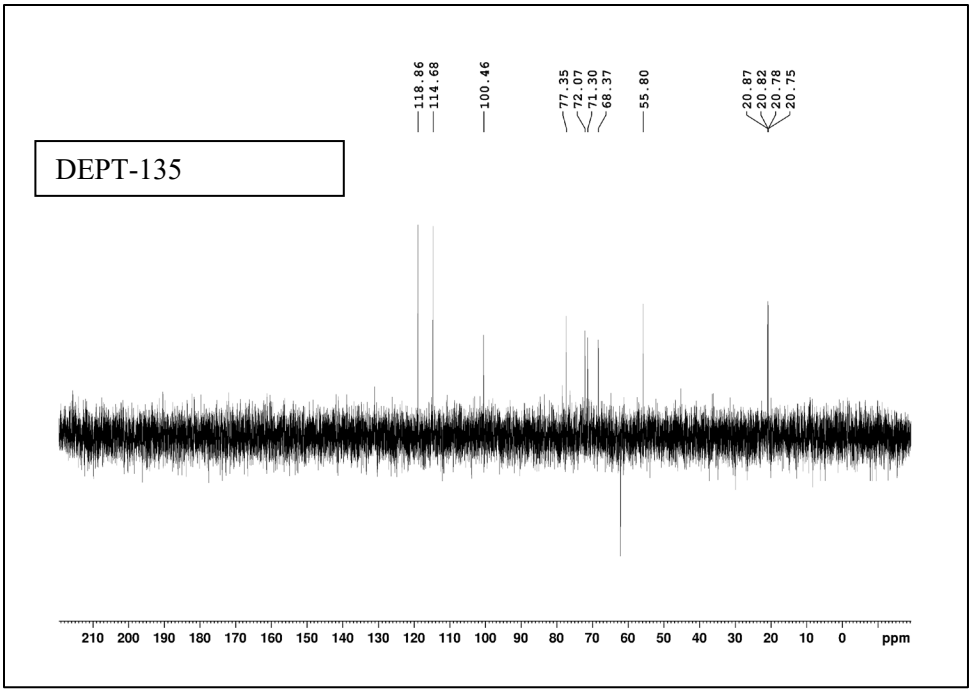


(4-methoxyphenyl)-2,3,4,6-tetra-*O*-acetyl-3-deutero-β-D-glucopyranose (534):

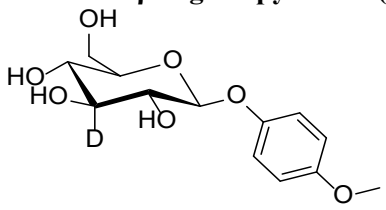


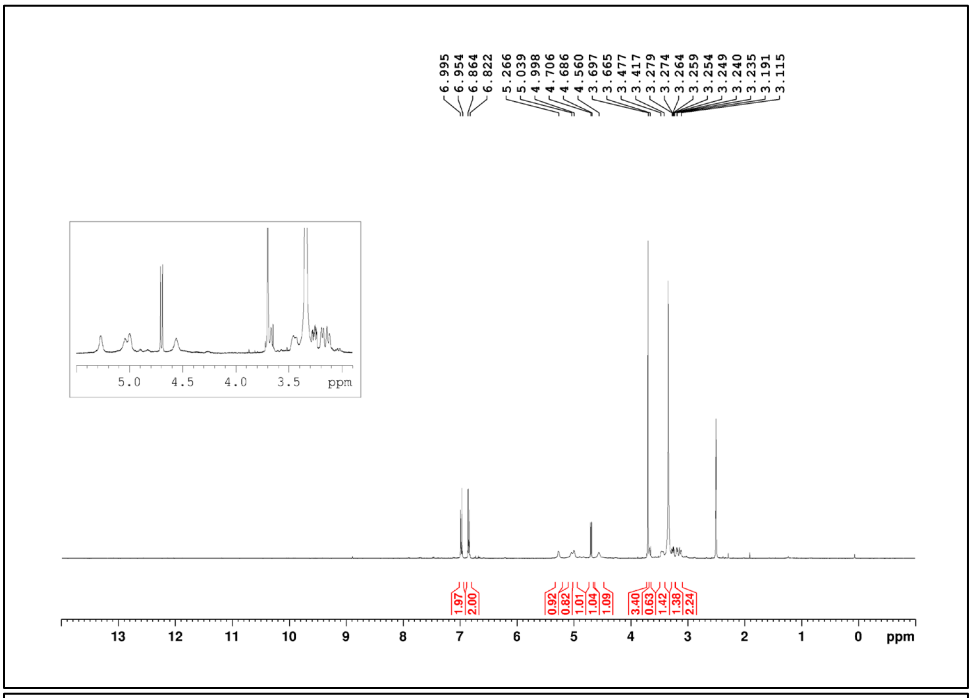


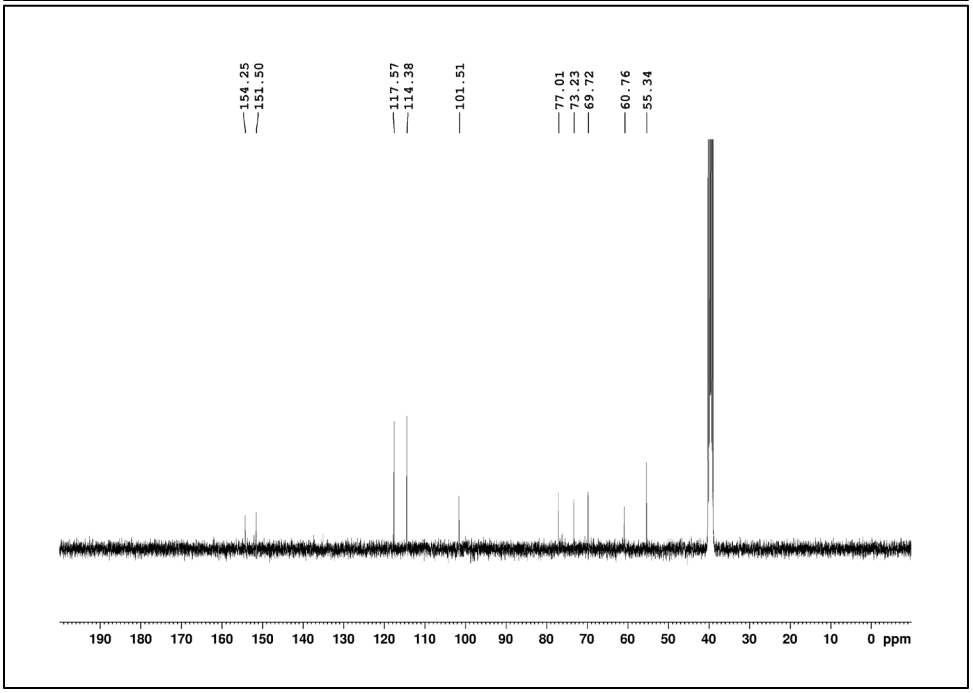



118.86
114.68
100.46
77.35
72.07
71.30
68.37
55.80
20.87
20.82
20.78
20.75
DEPT-135
210 200 190 180 170 160 150 140 130 120 110 100 90 80 70 60 50 40 30 20 10 0 ppm

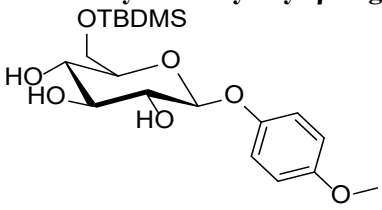
(4-methoxyphenyl)-3-deutero-β-D-glucopyranose (3D1 PMP-Glc, 92):

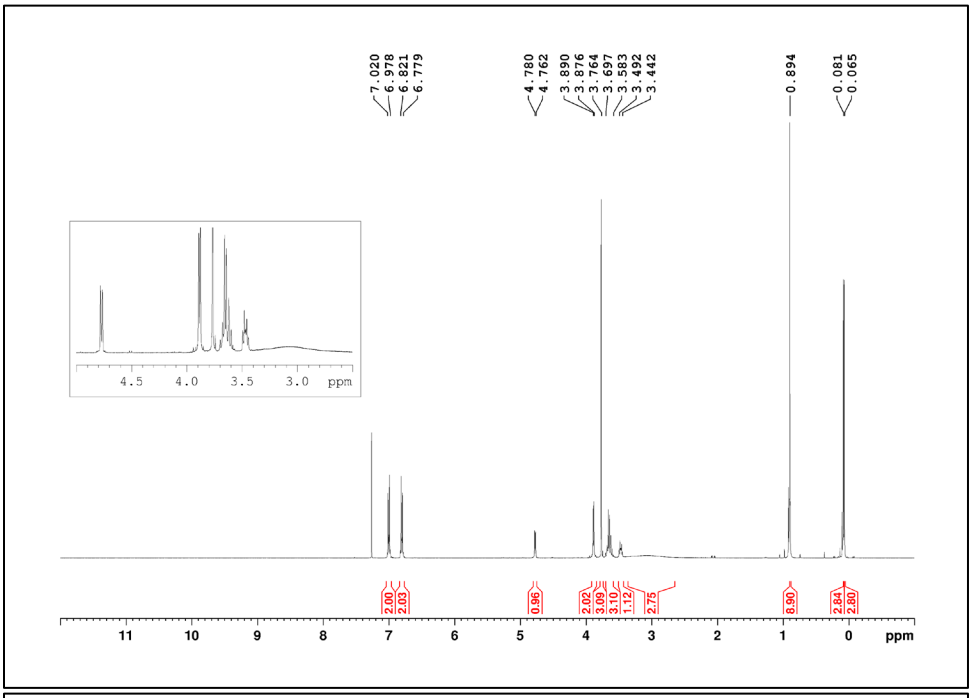


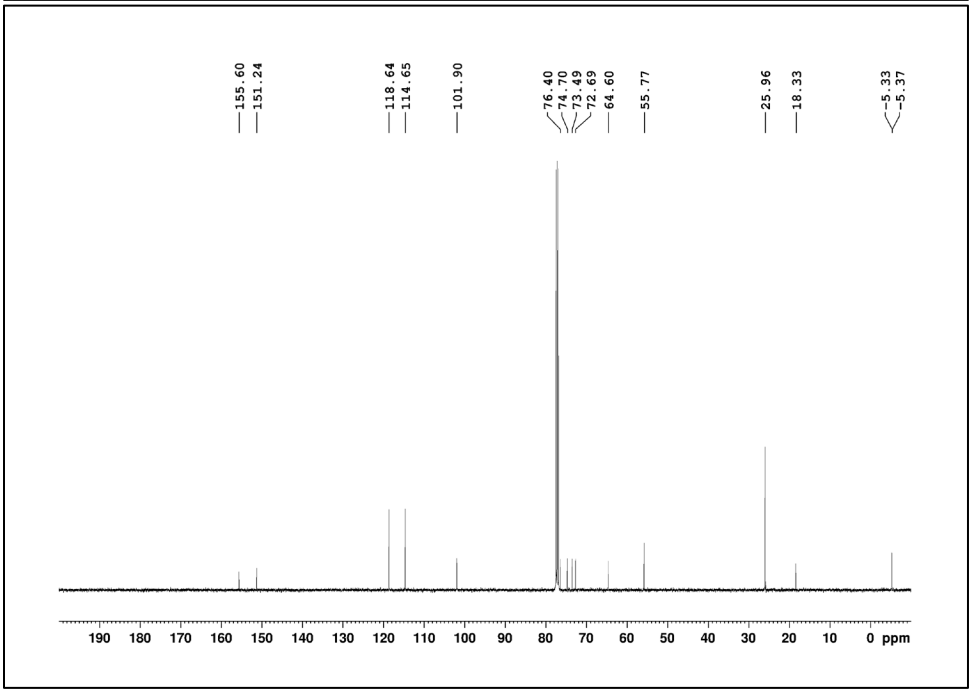




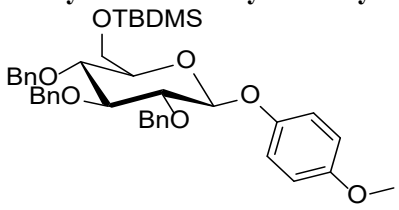
(4-methoxyphenyl)-6-*O-tert*-butyldimethylsilyl-β-D-glucopyranoside (535):

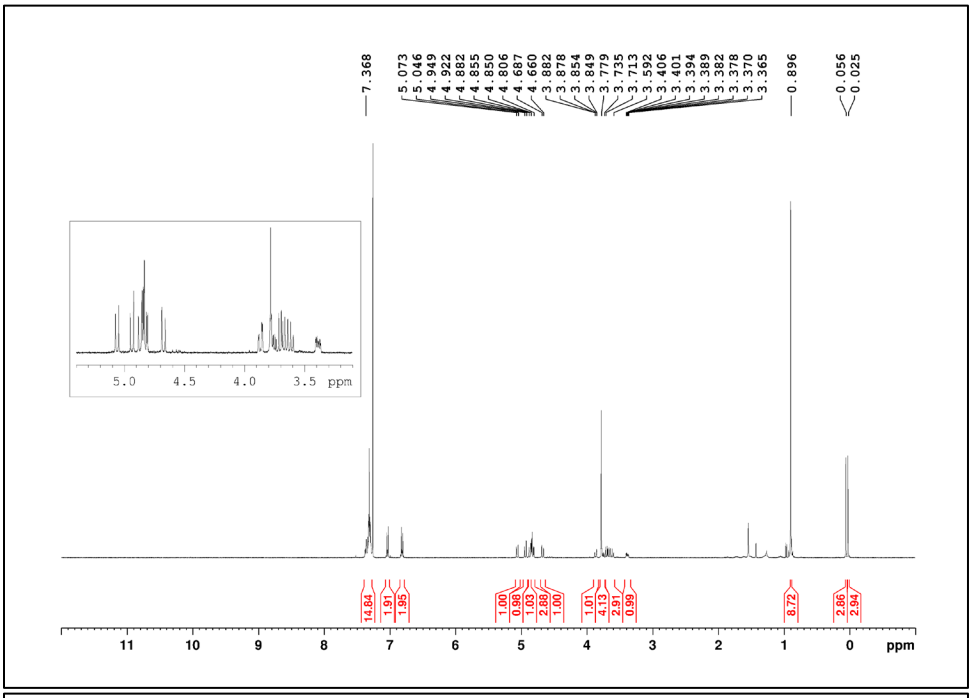


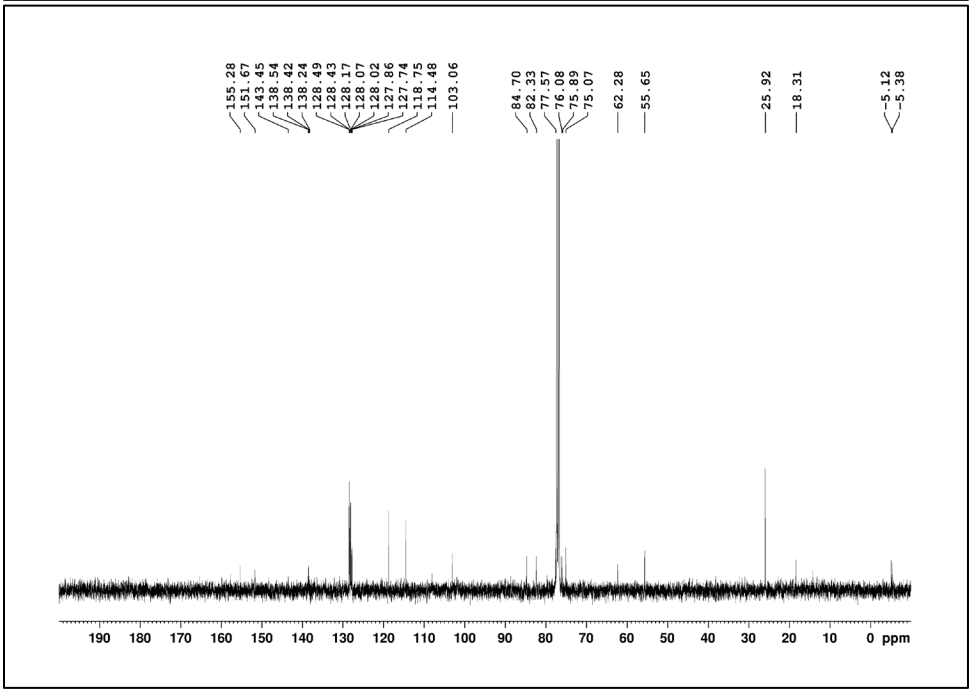




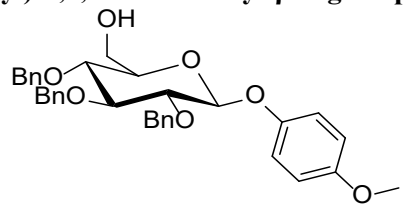
(4-methoxyphenyl)-2,3,4-tri-*O*-benzyl-6-*O*-*tert*-butyldimethylsilyl-β-D-glucopyranoside (536):

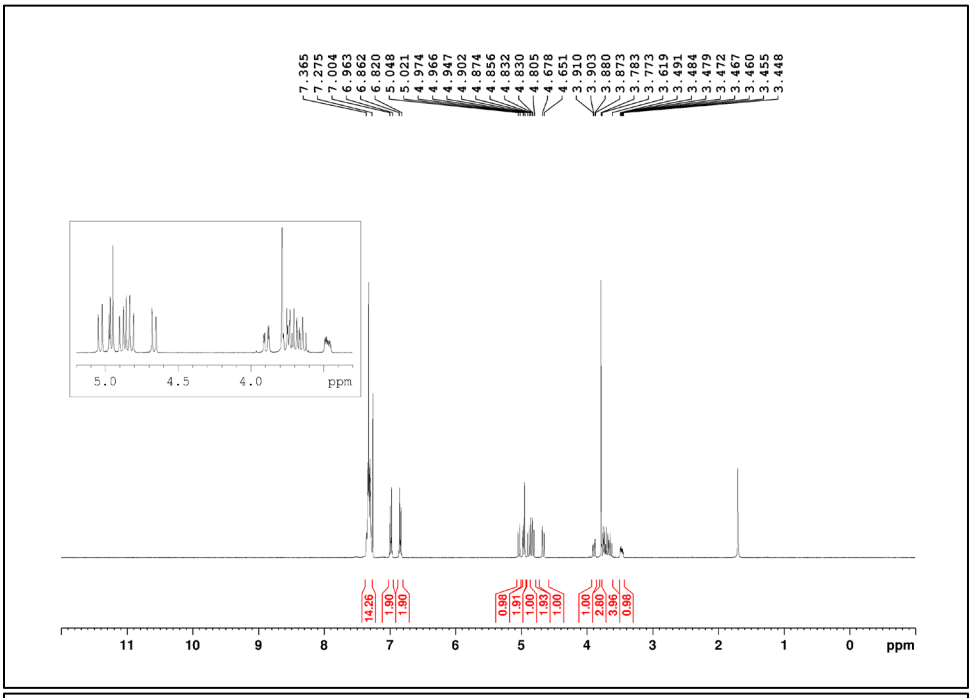


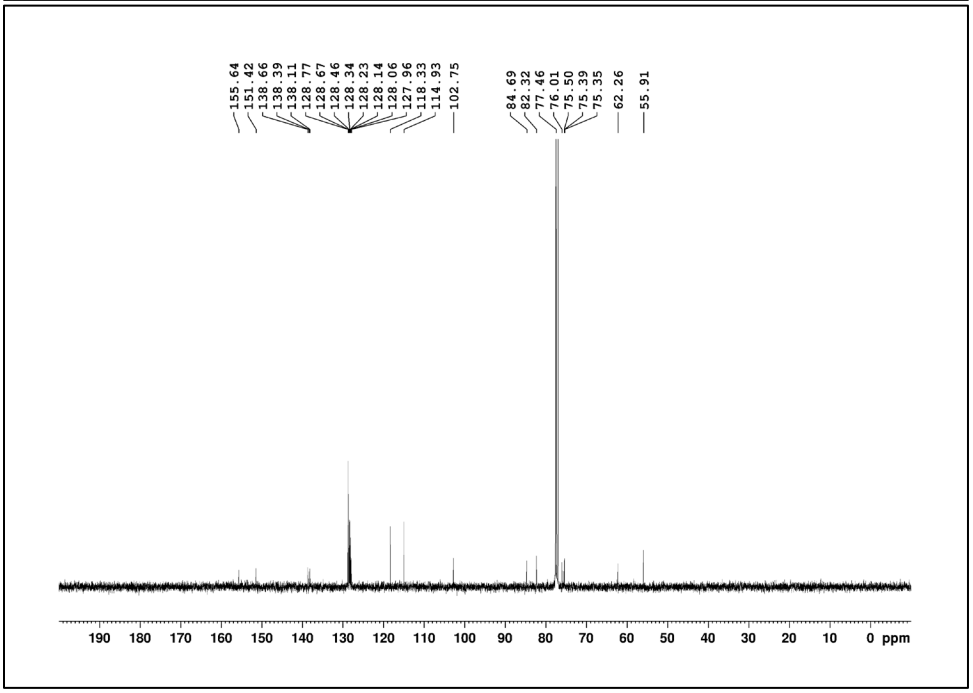




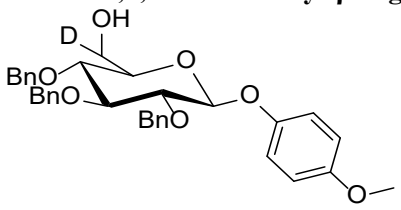
(4-methoxyphenyl)-2,3,4-tri-*O*-benzyl-β-D-glucopyranoside (537):

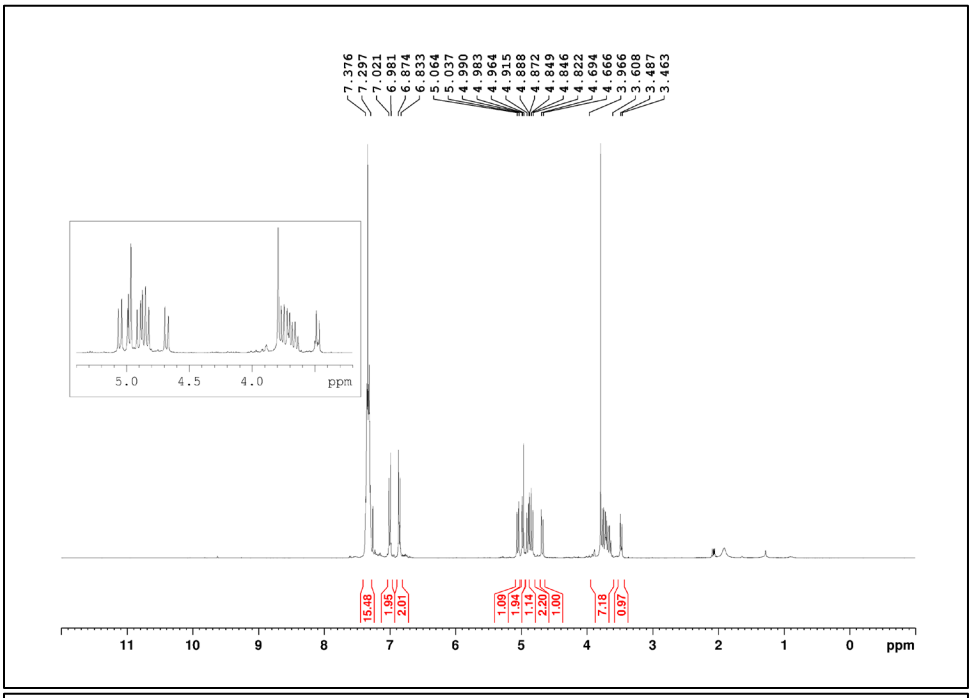


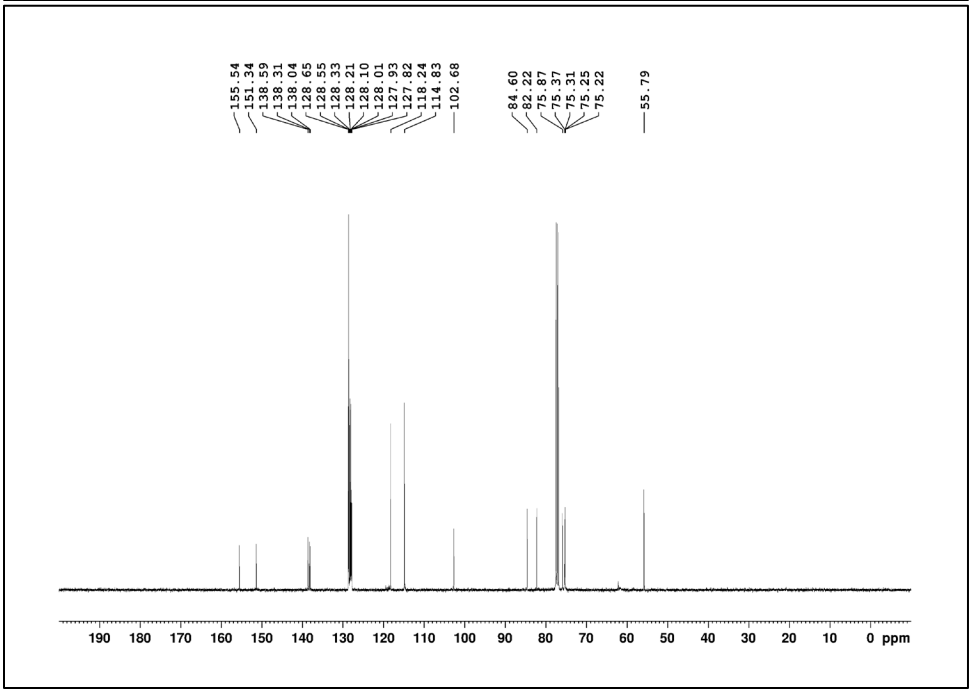




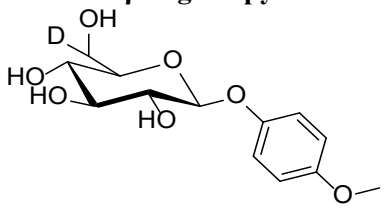
(4-methoxyphenyl)-6-deutero-2,3,4-tri-O-benzyl-β-D-glucopyranoside (539):

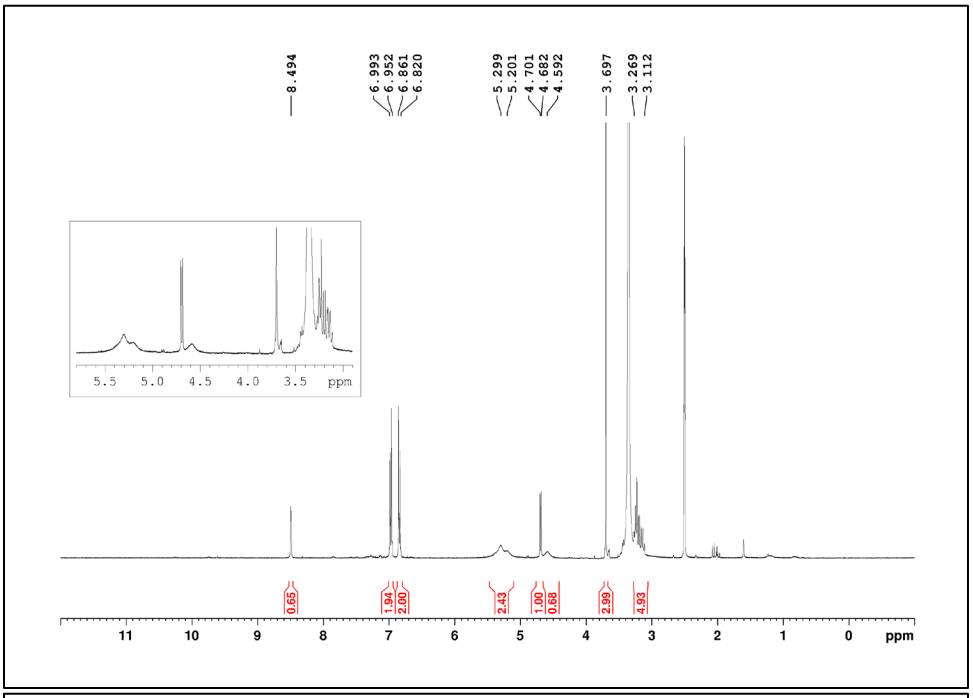


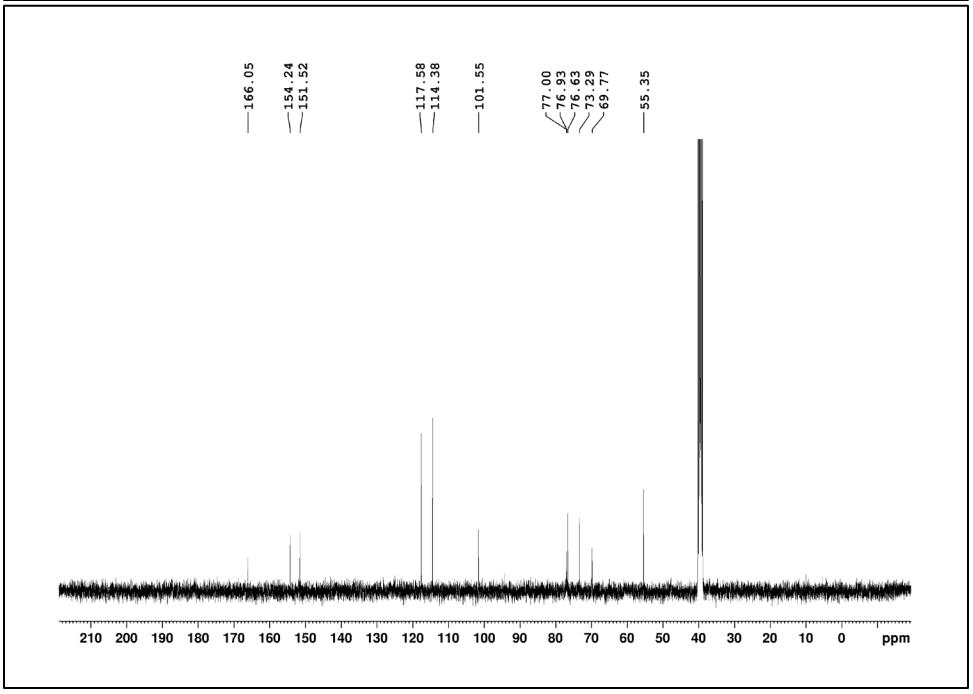




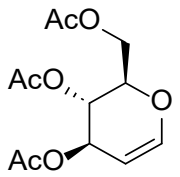
(4-methoxyphenyl)-6-deutero-β-D-glucopyranoside (6D1 PMP-Glc, 93):







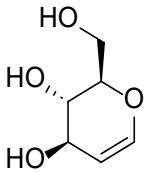
8.2.2.7. Methoxy- derivatives



3,4,6-tri-*O*-acetyl-D-glucal (540): The title compound was synthesized according to a modified literature procedure.[543] β-D-glucose pentacetate (**503**, 1.3 mmol, 1.0 eq) was dissolved in 33% HBr in AcOH (1.0 M) and stirred at room temperature for 40 minutes. The reaction was diluted with AcOH (0.25 M). Zn dust (20.0 mmol, 15.0 eq) and a solution of anhydrous $CuSO_4$ (0.6 mmol, 0.5 eq) in dH_2O (1.0 M) were added to the reaction and stirred for 1.5 hours at room temperature. Following reaction completion, the solution was diluted with EtOAc and filtered through a Celite® pad. The resulting solution was washed with sat. $NaHCO_3$, water, and brine. The organic layers were dried using Na_2SO_4, filtered, and concentrated *in vacuo* to yield a clear oil (**90 %**) that was used without further purification.

Characterization is consistent with that found in literature.[544]

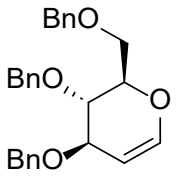
^{1}H NMR: (400 MHz, $CDCl_3$): ∂6.47(dd, *J* = 6.2, 1.1 Hz, 1H, H-1), 5.36-5.33(m, 1H, H-3), 5.23(dd, *J* = 7.5, 5.8 Hz, 1H, H-4), 4.85(dd, *J* = 6.2, 3.2 Hz, 1H, H-2), 4.40(dd, *J* = 12.0, 5.7 Hz, 1H, H-6a), 4.28-4.24(m, 1H, H-5), 4.20(dd, *J* = 12.0, 3.1 Hz, 1H, H-6b), 2.10(s, 3H, OAc CH_3), 2.08(s, 3H, OAc CH_3), 2.05(s, 3H, OAc CH_3). **^{13}C NMR:** (101 MHz, $CDCl_3$): ∂ = 170.8 (OAc C), 170.6 (OAc C), 169.7 (OAc C), 145.8 (C-1), 99.1 (C-2), 74.1 (C-5), 67.6 (C-3/C-4), 67.3 (C-3/C-4), 61.5 (C-6 CH_2), 21.2 (OAc CH_3), 21.0 (OAc CH_3), 20.9 (OAc CH_3).



D-glucal (541): 3,4,6-tri-*O*-acetyl-D-glucal (**540**, 1.1 mmol, 1.0 eq) was dissolved in MeOH (0.2 M) and a 1 M solution of NaOMe in MeOH (0.1 mmol, 0.1 eq) was added to the solution to stir for 1.5 hours. Upon reaction completion, 1 M HCl (0.09 mL) was added to obtain a neutral pH. The solution was concentrated *in vacuo* to yield the final product as a white powder that was used without further purification.

Compound characterization was consistent with that found in literature.[545]

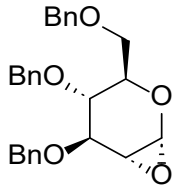
^{1}H NMR: (400 MHz, MeOD-d_4): ∂6.35(dd, *J* = 6.0, 1.6 Hz, 1H, H-1), 4.68(dd, *J* = 6.1, 2.3 Hz, 1H, H-2), 4.11(dt, *J* = 7.1, 1.9 Hz, 1H, H-3), 3.88(dd, *J* = 12.1, 2.5 Hz, 1H, H-6a), 3.78(dd, *J* = 12.0, 5.3 Hz, 1H, H-6b), 3.72(ddd, *J* = 9.6, 5.3, 2.4 Hz, 1H, H-5), 3.56(dd, *J* = 9.8, 7.1 Hz, 1H, H-4). **^{13}C NMR:** (101 MHz, MeOD-d_4): ∂ = 144.9 (C-1), 104.5 (C-2), 80.3 (C-5), 70.9 (C-3/C-4), 70.5 (C-3/C-4), 62.2 (C-6 CH_2).



3,4,6-tri-*O*-benzyl-D-glucal (542): The title compound was synthesized according to a modified **General Procedure 8-6**. To a solution of D-glucal (**541,** 1.3 mmol, 1.0 eq) in dry DMF (0.2 M) was added NaH (60 % dispersion in mineral oil) (5.5 mmol, 4.5 eq) portion-wise at 0 °C to a flame dried flask under argon. Benzyl bromide (5.9 mmol, 4.5 eq) was then added slowly and the reaction mixture was stirred overnight (18 h) at room temperature. The solution was diluted with DCM and H_2O and washed using sat. $NaHCO_3$, H_2O, and brine. The organic layer was dried using Na_2SO_4, filtered, and concentrated *in vacuo*. The crude residue was purified by column chromatography (1% EtOAc in hexanes) to afford the desired product as a clear oil (**54 %, 2 steps from 3,4,6-tri-*O*-acetyl-D-glucal**)

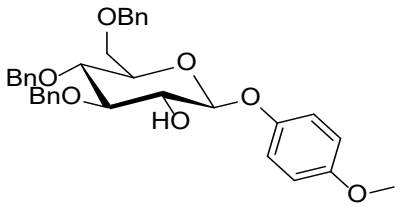
Characterization was consistent with that found in literature.[546]

^{1}H NMR: (400 MHz, $CDCl_3$): ∂7.33-7.28(m, 13H, *arom.*), 7.25-7.23(m, 2H, *arom.*), 6.43(dd, *J* = 6.1, 1.3 Hz, 1H, H-1), 4.88(dd, *J* = 6.2, 2.7 Hz, 1H, H-2), 4.84(d, *J* = 11.3 Hz, 1H, OBn CH_2), 4.64(d, *J* = 11.1 Hz, 1H, OBn CH_2), 4.63(d, *J* = 11.8 Hz, 1H, OBn CH_2), 4.60(d, *J* = 12.0 Hz, 1H, OBn CH_2), 4.56(d, *J* = 12.0 Hz, 1H, OBn CH_2), 4.56(d, *J* = 12.0 Hz, 1H, OBn CH_2), 4.21(dddd, *J* = 6.3, 4.9, 2.7, 0.6 Hz, 1H, H-3), 4.07(ddd, *J* = 8.3, 5.0, 2.8 Hz, 1H, H-5), 3.86(dd, *J* = 8.6, 6.2 Hz, 1H, H-4), 3.81(dd, *J* = 10.7, 5.0 Hz, 1H, H-6a), 3.76(dd, *J* = 10.6, 3.0 Hz, 1H, H-6b). **^{13}C NMR:** (101 MHz, $CDCl_3$): ∂ = 144.9 (C-1), 138.5 (C OBn *arom.*), 138.3 (C OBn *arom.*), 138.1 (C OBn *arom.*), 128.55 (*arom.* CH), 128.53 (*arom.* CH), 128.51 (*arom.* CH), 128.1 (*arom.* CH), 128.0 (*arom.* CH), 127.9 (*arom.* CH), 127.8 (*arom.* CH), 100.1 (C-2), 76.9 (C-5), 75.9 (C-3), 74.5 (C-4), 73.9 (OBn CH_2), 73.6 (OBn CH_2), 70.6 (OBn CH_2), 68.7 (C-6 CH_2).



3,4,6-tri-*O*-benzyl-D-glucal epoxide (543): The title compound was synthesized according to a modified two-step literature procedure.[547,548] 3,4,6-tri-*O*-benzyl-D-glucopyranose (**542**, 1.44 g, 3.5 mmol, 1.0 eq) was dissolved in a mixture of acetone (1.4 mL, 2.4 M), DCM (13.8 mL, 0.25 M), and a saturated solution of $NaHCO_3$ (24.7 mL, 0.14 M). Oxone (2.1 g, 6.8 mmol, 2.0 eq) was dissolved in dH_2O (16.9 mL, 0.4 M) and added dropwise to the stirring reaction solution at 0 °C over a period of 15 minutes. The reaction was stirred for 30 minutes at 0 °C and then allowed to warm to room temperature over a period of 2 hours. The reaction was then diluted with DCM and washed with dH_2O and brine. The organic layer was dried using Na_2SO_4, filtered, and concentrated. The crude material was used in the next step directly without further purification.

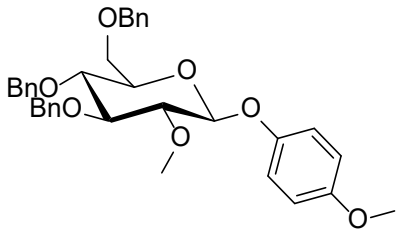
(4-methoxyphenyl)-3,4,6-tri-*O*-benzyl-β-D-glucopyranoside (544): 4-methoxyphenol (2.1 mmol, 1.1 eq) and K_2CO_3 (1.8 mmol, 1.0 eq) were added to toluene (0.5 M) in a flame-dried flask under argon and stirred until the entire mixture reached 110 °C. This solution was then added to the crude mixture of 3,4,6-tri-*O*-benzyl-D-glucal epoxide (**543**) in a new flask, which was maintained at reflux for 30 minutes. The solution was removed from heat and dried under air. The crude oil was purified by column chromatography (20% EtOAc in hexanes) to yield a pure white solid (**26 %, 2 steps from 3,4,6-tri-*O*-benzyl-D-glucal**).



Characterization was consistent with that found in literature.[549]

^{1}H NMR: (400 MHz, $CDCl_3$): ∂7.42-7.28(m, 13H, OBn *arom.*), 7.23-7.21(m, 2H, OBn *arom.*), 7.07-7.02(m, 2H, *arom.*), 6.83-6.79(m, 2H, *arom.*), 4.97(d, *J* = 11.3 Hz, 1H, OBn CH_2), 4.89(d, *J* = 11.3 Hz, 1H, OBn CH_2), 4.87(d, *J* = 10.8 Hz, 1H, OBn CH_2), 4.76(d, *J* = 7.8 Hz, 1H, H-1), 4.62(d, *J* = 11.9 Hz, 1H, OBn CH_2), 4.59(d, *J* = 10.2 Hz, 1H, OBn CH_2), 4.55(d, *J* = 12.0 Hz, 1H, OBn CH_2), 3.85-3.79(m, 2H, H-2 and H-6a), 3.77(s, 3H, OCH_3), 3.74-3.65(m, 3H, H-3 and H-4 and H-6b), 3.62-3.58(m, 1H, H-5), 2.49(bd, *J* = 2.4 Hz, 1H, OH-2). **^{13}C NMR:** (101 MHz, $CDCl_3$): ∂ = 155.5 (C PMP *arom.*), 151.4 (C PMP *arom.*), 138.6 (C OBn *arom.*), 138.2 (C OBn *arom.*), 138.1 (C OBn *arom.*), 128.63 (*arom.* CH), 128.55 (*arom.* CH), 128.46 (*arom.* CH), 128.09 (*arom.* CH), 128.08 (*arom.* CH), 127.96 (*arom.* CH), 127.92 (*arom.* CH), 127.86 (*arom.* CH), 127.7 (*arom.* CH), 118.6 (*arom.* 2xCH), 114.6 (*arom.* 2xCH), 102.1 (C-1), 84.5 (C-3/C-4), 77.6 (C-3/C-4), 75.44 (C-5), 75.37 (OBn CH_2), 75.2 (OBn CH_2), 74.6 (C-2), 73.6 (OBn CH_2), 68.9 (C-6 CH_2), 55.7 (OCH_3).

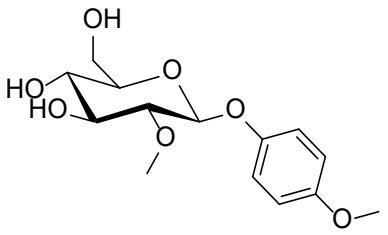
(4-methoxyphenyl)-2-*O*-methyl-3,4,6-tri-*O*-benzyl-β-D-glucopyranoside (545): The title compound was synthesized according to **General Procedure 8-5**. (4-methoxyphenyl)-3,4,6-tri-*O*-benzyl-β-D-glucopyranoside (**544**, 0.9 mmol, 1.0 eq) was dissolved in DMF (0.1 M) in a flame-dried flask under argon at 0 °C. NaH (60 % dispersion in mineral oil) (2.0 mmol, 2.0 eq) was added and the solution was stirred for 5 minutes. MeI (4.4 mmol, 5.0 eq) was added dropwise and the reaction was stirred at room temperature for 18 hours. The reaction was diluted in DCM and washed with dH_2O and brine. The organic phase was dried using Na_2SO_4, filtered, and concentrated *in vacuo*. The



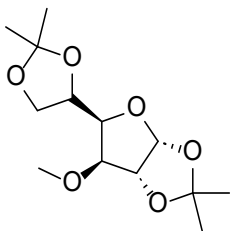
resulting crude product was purified by column chromatography (20% EtOAc in hexanes) to yield the final product as a white solid (**72 %**).

^{1}H NMR: (400 MHz, $CDCl_3$): ∂7.40-7.27(m, 13H, OBn *arom.*), 7.22-7.19(m, 2H, OBn, *arom.*), 7.06-7.02(m, 2H, *arom.*), 6.83-6.79(m, 2H, *arom.*), 4.94(d, *J* = 11.0 Hz, 1H, OBn CH_2), 4.86(d, *J* = 10.8 Hz, 1H, OBn CH_2), 4.82(d, *J* = 11.0 Hz, 1H, OBn CH_2), 4.78(d, *J* = 7.8 Hz, 1H, H-1), 4.60(d, *J* = 12.0 Hz, 1H, OBn CH_2), 4.57(d, *J* = 12.1 Hz, 1H, OBn CH_2), 4.54(d, *J* = 12.1 Hz, 1H, OBn CH_2), 3.80-3.77(m, 4H, H-6a and OCH_3), 3.71(s, 3H, OCH_3), 3.68(dd, *J* = 10.7, 5.6 Hz, 1H, H-6b), 3.65-3.61(m, 2H, H-3 and H-4), 3.55(ddd, *J* = 9.8, 5.1, 2.0 Hz, 1H, H-5), 3.46-3.39(m, 1H, H-2). **^{13}C NMR:** (101 MHz, $CDCl_3$): ∂ = 155.4 (C PMP *arom.*), 151.7 (C PMP *arom.*), 138.7 (C OBn *arom.*), 138.3 (C OBn *arom.*), 138.2 (C OBn *arom.*), 128.5 (*arom.* CH), 128.4 (*arom.* CH), 128.11 (*arom.* CH), 128.10 (*arom.* CH), 127.9 (*arom.* CH), 127.8 (*arom.* CH), 127.7 (*arom.* CH), 118.6 (*arom.* 2xCH), 114.6 (*arom.* 2xCH), 102.9 (C-1), 84.9 (C-3/C-4), 84.2 (C-2), 77.7 (C-3/C-4), 75.8 (OBn CH_2), 75.2 (OBn CH_2), 75.1 (C-5), 73.6 (OBn CH_2), 69.0 (C-6 CH_2), 60.8 (OCH_3), 55.8 (OCH_3). **HRMS (ESI):** m/z calcd for $C_{35}H_{38}O_7Na$ $[M+Na]^+$ 593.2515, found 593.2510.

(4-methoxyphenyl)-2-*O*-methyl-β-D-glucopyranoside (C_2 OMe PMP-Glc, 97): The title compound was synthesized according to a modified **General Procedure 8-7**. (4-methoxyphenyl)-3,4,6-tri-*O*-benzyl-2-*O*-methyl-β-D-glucopyranoside (**545**, 0.6 mmol, 1.0 eq) in a 2:1 mixture of EtOAc and MeOH (0.06 M), Pd/C (10 mol %) (0.06 mmol, 0.1 eq) was added and the reaction mixture was purged several times with H_2. The mixture was stirred under H_2 atmosphere for 3.5 h, filtered over Celite® and the volatiles were evaporated to afford the desired product as a white powder without further purification (**92 %**).



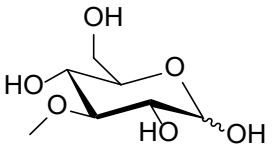
^{1}H NMR: (400 MHz, DMSO-d_6): ∂6.99-6.95(m, 2H, *arom.*), 6.87-6.83(m, 2H, *arom.*), 5.25(bs, 1H, OH-3), 5.16(bs, 1H, OH-4), 4.80(d, *J* = 7.8 Hz, 1H, H-1), 4.61(bs, 1H, OH-6), 3.70-3.67(m, 4H, H-6a and OCH_3), 3.52(s, 3H, OCH_3), 3.45(dd, *J* = 11.7, 5.7 Hz, 1H, H-6b), 3.30-3.25(m, 2H, H-5 and H-3), 3.15(t, *J* = 9.2 Hz, 1H, H-4), 2.95(dd, *J* = 9.0, 7.9 Hz, 1H, H-2). **^{13}C NMR:** (101 MHz, DMSO-d_6): ∂ = 154.4 (C *arom.*), 151.2 (C *arom.*), 117.4 (*arom.* 2xCH), 114.5 (*arom.* 2xCH), 101.1 (C-1), 83.3 (C-2), 76.9 (C-3), 75.7 (C-5), 69.9 (C-4), 60.7 (C-6 CH_2), 59.9 (OCH_3), 55.4 (OCH_3). **HRMS (ESI):** m/z calcd for $C_{14}H_{20}O_7Na$ $[M+Na]^+$ 323.1107, found 323.1117.



1,2:5,6-di-*O*-isopropylidene-3-*O*-methyl-α-D-glucofuranose (547): The title compound was synthesized according to a modified **General Procedure 8-5**. 1,2:5,6-di-*O*-isopropylidene-α-D-glucofuranose (DAG, **546**, 2.3 mmol, 1.0 eq) was dissolved in dry DMF (0.1 M) in a flame-dried flask under argon atmosphere. NaH (60 % dispersion in mineral oil) (4.8 mmol, 2.0 eq) was added portion-wise to the flask followed by drop-wise addition of MeI (11.2 mmol, 5.0 eq). The solution was stirred at room temperature for 18 h. Upon reaction completion the solution was diluted with DCM, quenched with water, and washed with brine. The organic layer was dried using Na_2SO_4, filtered, and concentrated *in vacuo*. The pure product was isolated as a light-yellow oil (**68 %**).

Characterization was consistent with that found in literature.[550]

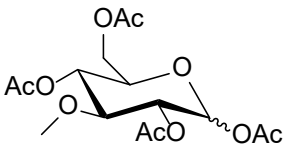
^{1}H NMR: (400 MHz, $CDCl_3$): ∂5.84(d, *J* = 3.7 Hz, 1H, H-1), 4.54(d, *J* = 3.7 Hz, 1H, H-2), 4.30-4.25(m, 1H), 4.09-4.03(m, 2H), 3.98(dd, *J* = 8.6, 5.4 Hz, 1H, H-6b), 3.75(d, *J* = 3.0 Hz, 1H), 3.43(s, 3H, OCH_3), 1.47(s, 3H, *isopropylidene* CH_3), 1.40(s, 3H, *isopropylidene* CH_3), 1.33(s, 3H, *isopropylidene* CH_3), 1.29(s, 3H, *isopropylidene* CH_3). **^{13}C NMR:** (101 MHz, $CDCl_3$): ∂ = 111.8 (C), 109.1 (C), 105.3 (C-1), 83.8, 82.0 (C-2), 81.1, 72.5, 67.3 (C-6 CH_2), 58.3 (OCH_3), 27.0 (*isopropylidene* CH_3), 26.9 (*isopropylidene* CH_3), 26.3 (*isopropylidene* CH_3), 25.5 (*isopropylidene* CH_3).



3-*O*-methyl-D-glucopyranoside (3-OMG, 548): 1,2:5,6-di-*O*-isopropylidene-3-*O*-methyl-α-D-glucofuranose (**547,** 1.6 mmol, 1.0 eq) was dissolved in dH_2O (0.25 M). Amberlite IR120 H+ resin (washed with MeOH) (3.5 g) was added and the solution was stirred at 60 °C for 8 h. Following reaction completion, the solution was filtered and concentrated *in vacuo* to yield the product as a clear oil (**95 %**, α:β 1:1).

Characterization was consistent with that found in literature.[551]

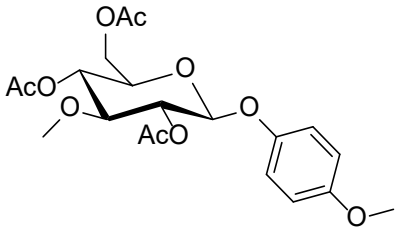
^{1}H NMR: (400 MHz, D_2O): ∂5.17(d, *J* = 3.7 Hz, 1H, H-1α), 4.61(d, *J* = 7.7 Hz, 1H, H-1β), 3.87-3.76(m, 3H), 3.74-3.65(m, 2H), 3.59(s, 6H, 2xOCH_3), 3.56-3.53(m, 1H), 3.48-3.40(m, 4H), 3.29-3.22(m, 2H). **^{13}C NMR:** (101 MHz, D_2O): ∂ = 95.8 (C-1β), 92.0 (C-1α), 85.3, 82.7, 75.8, 73.4, 71.4, 70.9, 69.0, 68.9, 60.6 (C-6 CH_2), 60.4 (C-6 CH_2), 60.0 (OCH_3), 59.8 (OCH_3).



1,2,4,6-tetra-*O*-acetyl-3-*O*-methyl-D-glucopyranoside (549): The title compound was synthesized according to **General Procedure 8-4**. 3-*O*-methyl-D-glucopyranoside (3-OMG, **548**, 1.5 mmol, 1.0 eq) and NaOAc (4.5 mmol, 3.0 eq) were suspended in Ac_2O (10.6 mmol, 7.0 eq) in a flame-dried flask under argon. The solution was stirred at 100 °C for 2 h. Upon completion the reaction was cooled, diluted with DCM and washed with water. The organic phase was dried with Na_2SO_4, filtered, and concentrated *in vacuo*. The clear oil was used in the next step without further purification as a mixture of alpha and beta products (**78 %**, α:β 1:1.9).

Characterization was consistent with that found in literature.[550]

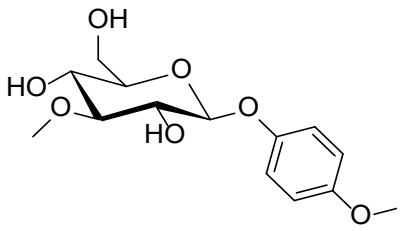
^{1}H NMR: (400 MHz, $CDCl_3$): ∂6.29(d, *J* = 3.7 Hz, 1H, H-1α), 5.64(d, *J* = 8.2 Hz, 1H, H-1β), 5.13-5.06(m, 3H, H-4α and H-2β and H-4β), 5.00(dd, *J* = 10.1, 3.7 Hz, 1H, H-2α), 4.25-4.18(m, 2H, H-6a α and β), 4.11-4.05(m, 2H, H-6b α and β), 4.00(ddd, *J* = 10.5, 4.6, 2.3 Hz, 1H, H-5α), 3.75-3.69(m, 2H, H-3α and H-5β), 3.53(t, *J* = 9.3 Hz, 1H, H-3β), 3.47(s, 3H, OCH_3 α), 3.42(s, 3H, OCH_3 β), 2.17(s, 3H, OAc CH_3 α), 2.11(s, 3H, OAc CH_3 α), 2.104(s, 3H, OAc CH_3 β), 2.100(s, 3H, OAc CH_3 β), 2.091(s, 3H, OAc CH_3 β), 2.086(s, 3H, OAc CH_3 α), 2.08(s, 3H, OAc CH_3 β), 2.07(s, 3H, OAc CH_3 α). **^{13}C NMR:** (101 MHz, $CDCl_3$): ∂ = 170.9 (OAc C), 169.8 (OAc C), 169.44 (OAc C), 169.41 (OAc C), 169.3 (OAc C), 168.9 (OAc C), 92.1 (C-1β), 89.6 (C-1α), 81.5 (C-3β), 78.3 (C-3α), 73.1 (C-5β), 71.2 (C-2α/β), 71.1 (C-2α/β), 70.3 (C-5α), 69.0 (C-4α), 68.6 (C-4β), 61.9 (C-6 CH_2 α and β), 60.3 (OCH_3 α), 59.4 (OCH_3 β), 21.0 (OAc CH_3), 20.93 (OAc CH_3), 20.89 (OAc CH_3), 20.8 (OAc CH_3).



(4-methoxyphenyl)-2,4,6-tri-*O*-acetyl-3-*O*-methyl-β-D-glucopyranoside (550): The title compound was synthesized according to a modified **General Procedure 8-2**.[167,525] 1,2,4,6-tetra-*O*-acetyl-3-*O*-methyl-β-D-glucopyranoside (**549**, 1.1 mmol, 1.0 eq) and 4-methoxyphenol (1.6 mmol, 1.4 eq) were dissolved in dry DCM (0.25 M) in a flame-dried flask under argon at 0 °C with 4 Å molecular sieves. Boron trifluoride diethyl etherate (99 % solution) (3.2 mmol, 3.0 eq) was added to the solution slowly. The solution was stirred overnight (18 h), diluted with DCM, and then quenched with sat. $NaHCO_3$ upon reaction completion. The solution was filtered through Celite®, and the organic layer was washed using sat. $NaHCO_3$, dH_2O, and brine. The organic layer was dried using Na_2SO_4, filtered, and concentrated *in vacuo*. The crude off-white foam was purified by column chromatography (7:3 Hexanes:EtOAc) and then recrystallized from EtOAc/hexanes to yield the final product as a white solid (**16 %**).

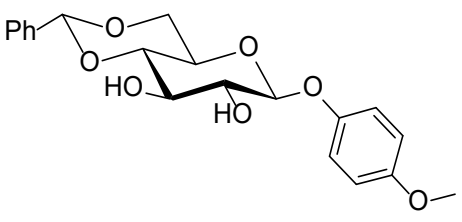
^{1}H NMR: (400 MHz, $CDCl_3$): ∂6.96-6.92(m, 2H, *arom.*), 6.83-6.79(m, 2H, *arom.*), 5.23(dd, *J* = 9.5, 7.8 Hz, 1H, H-2), 5.13(t, *J* = 9.6 Hz, 1H, H-4), 4.86(d, *J* = 7.8 Hz, 1H, H-1), 4.24(dd, *J* = 12.2, 5.6 Hz, 1H, H-6a), 4.15(dd, *J* = 12.2, 2.6 Hz, 1H, H-6b), 3.77(s, 3H, OCH_3), 3.70(ddd, *J* = 9.8, 5.7, 2.6 Hz, 1H, H-5), 3.56(t, *J* = 9.4 Hz, 1H, H-3), 3.44(s, 3H, OCH_3), 2.13(s, 3H, OAc CH_3), 2.11(s, 3H, OAc CH_3), 2.08(s, 3H, OAc CH_3). **^{13}C NMR:** (101 MHz, $CDCl_3$): ∂ = 170.8 (OAc C), 169.5 (OAc C), 169.4 (OAc C), 155.8 (C *arom.*), 151.3 (C *arom.*), 118.7 (2xCH *arom.*), 114.6 (2xCH *arom.*), 100.6 (C-1), 81.3 (C-3), 72.3 (C-5), 71.9 (C-2), 69.0 (C-4), 62.4 (C-6 CH_2), 58.8 (OCH_3), 55.8 (OCH_3), 21.03 (OAc CH_3), 20.97 (OAc CH_3), 20.9 (OAc CH_3). **HRMS (ESI):** m/z calcd for $C_{20}H_{26}O_{10}Na$ $[M+Na]^+$ 449.1424, found 449.1451.

(4-methoxyphenyl)-3-*O*-methyl-β-D-glucopyranoside (C_3 OMe PMP-Glc, 98): The title compound was synthesized according to a modified **General Procedure 8-3**.[167,326] (4-methoxyphenyl)-2,4,6-tri-*O*-acetyl-3-*O*-methyl-β-D-glucopyranoside (**550**, 0.2 mmol, 1.0 eq) was dissolved in MeOH (0.2 M) and a 1 M solution of NaOMe in MeOH (0.15 mmol, 1.0 eq) was added to the solution to stir for 1 hour. Upon reaction completion, Amberlite IR120 H+ resin (washed in MeOH) was added to a pH < 4. The solution was filtered, and the filtrate was concentrated *in vacuo* to yield the pure product a white powder (**91 %**).



^{1}H NMR: (400 MHz, DMSO-d_6): ∂7.00-6.96(m, 2H, *arom.*), 6.87-6.83(m, 2H, *arom.*), 5.44(d, *J* = 5.5 Hz, 1H, OH-2), 5.17(d, *J* = 5.6 Hz, 1H, OH-4), 4.73(d, *J* = 7.8 Hz, 1H, H-1), 4.59(t, *J* = 5.8 Hz, 1H, OH-6), 3.70(s, 3H, OCH_3), 3.67(ddd, *J* = 11.8, 5.3, 1.6 Hz, 1H, H-6a), 3.52(s, 3H, OCH_3), 3.48-3.42(m, 1H, H-6b), 3.30-3.20(m, 3H, H-2 and H-5 and H-4), 3.04(t, *J* = 8.8 Hz, 1H, H-3). **^{13}C NMR:** (101 MHz, DMSO-d_6): ∂ = 154.3 (C *arom.*), 151.4 (C *arom.*), 117.6 (2xCH *arom.*), 114.4 (2xCH *arom.*), 101.4 (C-1), 86.5 (C-3), 76.8 (C-5), 72.9 (C-4), 69.1 (C-2), 60.5 (C-6 CH_2), 60.1 (OCH_3), 55.3 (OCH_3). **HRMS (ESI):** m/z calcd for $C_{14}H_{20}O_7Na$ $[M+Na]^+$ 323.1107, found 323.1121.

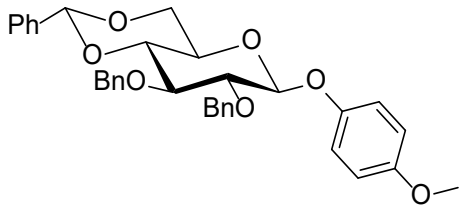
(4-methoxyphenyl)-4,6-*O*-benzylidene-β-D-glucopyranoside (551): The title compound was synthesized according to a modified literature procedure.[552,553] To a solution of (4-methoxyphenyl)-β-D-glucopyranoside (19.9 mmol, 1.0 eq) in DMF (0.5 M) was added benzaldehyde



dimethyl acetal (21.9 mmol, 1.1 eq) and *p*-toluene sulfonic acid monohydrate (pTSA•H_2O, 2.2 mmol, 0.1 eq) to a flame-dried flask under argon. The reaction mixture was warmed to 60 °C and stirred for 18 h. The reaction was then diluted with EtOAc and washed with brine. The organic layer was dried using Na_2SO_4, filtered, and concentrated *in vacuo*. The crude residue was recrystallized from DCM to afford the desired product as a white solid (**59 %**).

Characterization was consistent with that found in literature.[552]

^{1}H NMR: (400 MHz, CD_3OD-d_4): ∂7.53-7.49(m, 2H, OPh *arom.*), 7.36-7.33(m, 3H, OPh *arom.*), 7.06-7.02(m, 2H, *arom.*), 6.87-6.83(m, 2H, *arom.*), 5.61(s, 1H, benzylidene CH), 4.92(d, *J* = 7.7 Hz, 1H, H-1), 4.31(d, *J* = 10.8, 4.3 Hz, 1H, H-6a), 3.82-3.71(m, 2H, H-5 and H-6b), 3.75(s, 3H, OCH_3), 3.60-3.50(m, 3H, H-2 and H-3 and H-4).



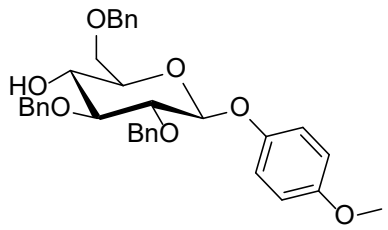
(4-methoxyphenyl)-2,3-di-*O*-benzyl-4,6-*O*-benzylidene-β-D-glucopyranoside (552): The title compound was synthesized according to a modified **General Procedure 8-6**. To a solution of (4-methoxyphenyl)-4,6-*O*-benzylidene-β-D-glucopyranoside (**551**, 2.5 mmol, 1.0 eq) in DMF (0.2 M) was added NaH (60 % dispersion in mineral oil) (11.2 mmol, 4.5 eq) portion-wise at 0 °C to a flame-dried flask under argon. Benzyl bromide (7.3 mmol, 3.0 eq) was then added slowly and the reaction mixture was stirred for 18 h at room temperature. Following reaction completion, the reaction was diluted slowly with DCM and dH_2O. The organic phase was washed with sat. $NaHCO_3$, dH_2O, and brine. The organic layer was dried using Na_2SO_4, filtered, and concentrated *in vacuo*. The crude residue was purified by column chromatography (9:1 Hexanes:EtOAc) to afford the desired product as a white solid (**64 %**).

Characterization was consistent with that found in literature.[554]

^{1}H NMR: (400 MHz, $CDCl_3$): ∂7.51-7.49(m, 2H, OBn *arom.*), 7.42-7.28(m, 13H, OBn *arom.*), 7.04-7.00(m, 2H, *arom.*), 6.87-6.83(m, 2H, *arom.*), 5.60(s, 1H, benzylidene CH), 5.01(d, *J* = 7.5 Hz, 1H, H-1), 4.99(d, *J* = 10.0 Hz, 1H, OBn CH_2), 4.95(d, *J* = 11.4 Hz, 1H, OBn CH_2), 4.87(d, *J* = 10.8 Hz, 1H, OBn CH_2), 4.83(d, *J* = 11.4 Hz, 1H, OBn CH_2), 4.38(dd, *J* = 10.5, 5.0 Hz, 1H, H-6a), 3.86-3.71(m, 7H, H-2 and H-3 and H-4 and H-6b and OCH_3), 3.51(ddd, *J* = 9.9, 9.2, 5.0 Hz, 1H, H-5). **^{13}C NMR:** (101 MHz, $CDCl_3$): ∂ = 155.7 (C *arom.*), 151.3 (C *arom.*), 138.5 (C *arom.*), 138.3 (C *arom.*), 137.4 (C *arom.*), 129.1 (*arom.* CH), 128.52 (*arom.* 2xCH), 128.46 (*arom.* 2xCH), 128.4 (*arom.* 2xCH), 128.3 (*arom.* 2xCH), 128.2

(*arom.* 2xCH), 127.9 (*arom.* CH), 127.8 (*arom.* CH), 126.1 (*arom.* 2xCH), 118.7 (*arom.* 2xCH), 114.8 (*arom.* 2xCH), 103.4 (C-1), 101.3 (benzylidene CH), 82.0 (C-2/C-3/C-4), 81.4 (C-2/C-3/C-4), 81.0 (C-2/C-3/C-4), 75.7 (OBn CH_2), 75.3 (OBn CH_2), 68.9 (C-6 CH_2), 66.3 (C-5), 55.8 (OCH_3)**.**

(4-methoxyphenyl)-2,3,6-tri-*O*-benzyl-β-D-glucopyranoside (553): Two methods for the selective opening of the 4-6-*O*-benzylidene acetal.



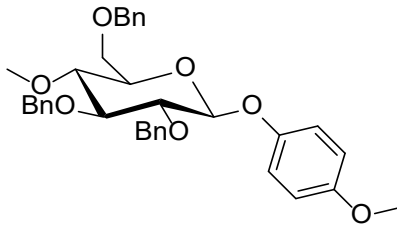
Method 1: The title compound is synthesized according to literature procedure.[448] (4-methoxyphenyl)-2,3-di-*O*-benzyl-4,6-*O*-benzylidene-β-D-glucopyranoside (**552**, 1.5 mmol, 1.0 eq) was dissolved in MeCN (0.1 M) in a flame-dried flask under argon. $NaCNBH_3$ (7.9 mmol, 5.0 eq) was added followed by the portion-wise addition of I_2 (5.1 mmol, 3.5 eq). The reaction was diluted with DCM no longer than 15 minutes past the first addition of I_2 (scale-dependent) and filtered through Celite®. The solution was washed with dH_2O and brine and the organic was collected, dried using Na_2SO_4, filtered, and concentrated *in vacuo*. The crude orange oil was purified by column chromatography (10 % EtOAc in hexanes) to yield the purified product as a white solid (**31 %**). Starting material (**552**) was also recovered as a white solid (**25 %**).

Method 2: The title compound was synthesized according to a literature procedure.[555] (4-methoxyphenyl)-2,3-di-*O*-benzyl-4,6-*O*-benzylidene-β-D-glucopyranoside (**552**, 1.7 mmol, 1.0 eq) was dissolved in DCM (0.2 M) in a flame-dried flask under argon at 0 °C. Triethylsilane (TES, 8.2 mmol, 5.0 eq) then trifluoroacetic acid (TFA, 7.8 mmol, 5.0 eq) were added and the reaction was allowed to warm to room temperature and stirred for 5 hours. The reaction was then diluted with DCM, washed with dH_2O and brine, and then the organic was collected, dried using Na_2SO_4, filtered, and concentrated *in vacuo*. The resulting white solid was used without further purification (**93 %**).

Characterization was consistent with that found in literature.[556]

^{1}H NMR: (400 MHz, $CDCl_3$): ∂7.40-7.28(m, 15H, OBn *arom.*), 7.07-7.03(m, 2H, *arom.*), 6.85-6.81(m, 2H, *arom.*), 5.08(d, *J* = 10.9 Hz, 1H, OBn CH_2), 4.98(d, *J* = 11.5 Hz, 1H, OBn CH_2), 4.93(d, *J* = 7.7 Hz, 1H, H-1), 4.84(d, *J* = 10.9 Hz, 1H, OBn CH_2), 4.77(d, *J* = 11.4 Hz, 1H, OBn CH_2), 4.61(d, *J* = 12.0 Hz, 1H, OBn CH_2), 4.57(d, *J* = 12.0 Hz, 1H, OBn CH_2), 3.84(dd, *J* = 10.5, 3.7 Hz, 1H, H-6a), 3.79(s, 3H, OCH_3), 3.75-3.66(m, 3H, H-2 and H-6b and H-3/H-4/H-5), 3.59-3.52(m, 2H, H-3/H-4/H-5), 2.57(bs, 1H, OH-4). **^{13}C NMR:** (101 MHz, $CDCl_3$): ∂ = 155.4 (C *arom.*), 151.5 (C *arom.*), 138.6 (C OBn *arom.*), 138.3

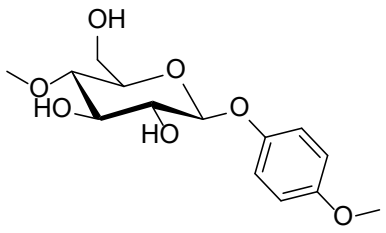
(C OBn *arom.*), 138.1 (C OBn *arom.*), 128.7 (*arom.* 2xCH), 128.54 (*arom.* 2xCH), 128.51 (*arom.* 2xCH), 128.4 (*arom.* 2xCH), 128.1 (*arom.* 2xCH), 128.0 (*arom.* CH), 127.9 (*arom.* CH), 127.8 (*arom.* CH), 127.8 (*arom.* 2xCH), 118.5 (*arom.* 2xCH), 114.7 (*arom.* 2xCH), 102.9 (C-1), 84.1 (C-2/C-3/C-4/C-5), 81.7 (C-2/C-3/C-4/C-5), 75.5 (OBn CH_2), 75.0 (OBn CH_2), 74.4 (C-2/C-3/C-4/C-5), 73.7 (OBn CH_2), 71.4 (C-2/C-3/C-4/C-5), 70.2 (C-6 CH_2), 55.7 (OCH_3).



(4-methoxyphenyl)-2,3,6-tri-*O*-benzyl-4-*O*-methyl-β-D-glucopyranoside (555): The title compound was synthesized according to a modified **General Procedure 8-5**. (4-methoxyphenyl)-2,3,6-tri-*O*-benzyl-β-D-glucopyranoside (**553**, 0.4 mmol, 1.0 eq) was dissolved in dry DMF (0.1 M) in a flame-dried flask under argon atmosphere. NaH (60 % dispersion in mineral oil) (2.4 mmol, 2.5 eq) was added portion-wise to the flask followed by drop-wise addition of MeI (2.4 mmol, 6.0 eq). The solution was stirred at room temperature for 2.5 h. Upon reaction completion the solution was diluted with DCM, quenched with water, and washed with brine. The organic layer was dried using Na_2SO_4, filtered, and concentrated *in vacuo*. The pure product was isolated as a colourless cloudy oil (**90 %**) without further purification. If necessary, the product was purified by column chromatography (10 % EtOAc in hexanes).

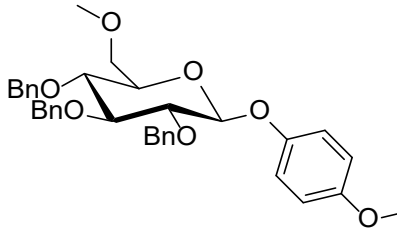
^{1}H NMR: (400 MHz, $CDCl_3$): ∂7.37-7.27(m, 15H, *arom.*), 7.07-7.03(m, 2H, *arom.*), 6.84-6.80(m, 2H, *arom.*), 5.05(d, *J* = 10.9 Hz, 1H, OBn CH_2), 4.92(d, *J* = 10.9 Hz, 1H, OBn CH_2), 4.87(d, *J* = 7.6 Hz, 1H, H-1), 4.81(d, *J* = 10.8 Hz, 2H, OBn CH_2), 4.65(d, *J* = 12.0 Hz, 1H, OBn CH_2), 4.58(d, *J* = 12.0 Hz, 1H, OBn CH_2), 3.82(dd, *J* = 10.8, 2.1 Hz, 1H, H-6a), 3.78(s, 1H, OCH_3), 3.73-3.60(m, 3H, H-2 and H-3 and H-6b), 3.53(s, 3H, OCH_3), 3.50(ddd, *J* = 9.9, 5.3, 2.0 Hz, 1H, H-5), 3.37(dd, *J* = 9.8, 8.6 Hz, 1H, H-4). **^{13}C NMR:** (101 MHz, $CDCl_3$): ∂ = 155.4 (C PMP *arom.*), 151.6 (C PMP *arom.*), 138.7 (C OBn *arom.*), 138.43 (C OBn *arom.*), 138.37 (C OBn *arom.*), 128.52 (*arom.* 2xCH), 128.49 (*arom.* 2xCH), 128.4 (*arom.* 2xCH), 128.3 (*arom.* 2xCH), 128.1 (*arom.* 2xCH), 127.9 (*arom.* CH), 127.78 (*arom.* CH), 127.77 (*arom.* 2xCH), 127.67 (*arom.* CH), 118.5 (*arom.* 2xCH), 114.6 (*arom.* 2xCH), 102.8 (C-1), 84.7 (C-2/C-3), 82.0 (C-2/C-3), 79.9 (C-4), 75.8 (OBn CH_2), 75.3 (C-5), 75.2 (OBn CH_2), 73.6 (OBn CH_2), 69.1 (C-6 CH_2), 60.9 (OCH_3), 55.8 (OCH_3). **HRMS (ESI):** m/z calcd for $C_{35}H_{38}O_7Na$ $[M+Na]^+$ 593.2515, found 593.2480.

(4-methoxyphenyl)-4-*O*-methyl-β-D-glucopyranoside (C_4 OMe PMP-Glc, 99): The title compound was synthesized according to **General Procedure 8-7**. To a solution of (**555**, 4-methoxyphenyl)-2,3,6-tri-*O*-benzyl-4-*O*-methyl-β-D-glucopyranoside (0.3 mmol, 1.0 eq) in a 1:1 mixture of EtOAc and MeOH (0.1 M), Pd/C (10 mol %) (0.1 mmol, 0.35 eq) was added and the reaction mixture was purged several times with H_2. The mixture was stirred under H_2 atmosphere for 6 h, filtered over Celite® and the volatiles were evaporated to afford the desired product as a white powder (**91 %**).



^{1}H NMR: (400 MHz, DMSO-d_6): ∂6.98-6.94(m, 2H, *arom.*), 6.86-6.82(m, 2H, *arom.*), 5.36(d, J = 5.1 Hz, 1H, OH-2), 5.24(d, J = 5.3 Hz, 1H, OH-3), 4.73-4.68(m, 2H, H-1 and OH-6), 3.70(s, 3H, OCH_3), 3.62(ddd, J = 12.0, 4.8, 1.8 Hz, 1H, H-6a), 3.52-3.46(m, 1H, H-6b), 3.44(s, 3H, OCH_3), 3.41-3.35(m, 1H, H-3), 3.31(ddd, J = 10.0, 5.0, 1.9 Hz, 1H, H-5), 3.23-3.17(m, 1H, H-2), 3.01(t, J = 9.2 Hz, 1H, H-4). **^{13}C NMR:** (101 MHz, DMSO-d_6): ∂ = 154.2 (C *arom.*), 151.4 (C *arom.*), 117.5 (*arom.* 2xCH), 114.4 (*arom.* 2xCH), 101.1 (C-1), 79.0 (C-4), 76.3 (C-3), 75.5 (C-5), 73.5 (C-2), 60.3 (C-6 CH_2), 59.7 (OCH_3), 55.3 (OCH_3). **HRMS (ESI):** m/z calcd for $C_{14}H_{20}O_7Na$ $[M+Na]^+$ 323.1119, found 323.1107.

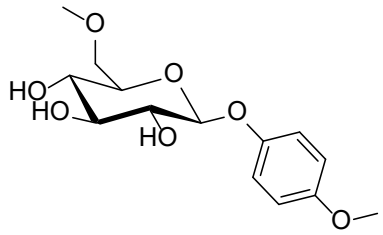
(4-methoxyphenyl)-2,3,4-tri-*O*-benzyl-6-*O*-methyl-β-D-glucopyranoside (556): The title compound was synthesized according to a modified **General Procedure 8-5** with the assistance of undergraduate student Abigail Kos. (4-methoxyphenyl)-2,3,4-tri-*O*-benzyl-β-D-glucopyranoside (**537**, 0.7 mmol, 1.0 eq) was dissolved in DMF (0.1 M) in a flame-dried flask under argon at 0 °C. NaH (60 % dispersion in mineral oil) (1.2 mmol, 2.0 eq) was added and the solution was stirred for 5 minutes. MeI (2.6 mmol, 4.0 eq) was added dropwise and the reaction was stirred at room temperature for 24 hours. The reaction was diluted in DCM and washed with brine. The organic phase was dried using Na_2SO_4, filtered, and concentrated *in vacuo*. The resulting crude product was purified by column chromatography (20% EtOAc in Hexanes) to yield the final product as a white solid (**74 %**).



^{1}H NMR: (400 MHz, $CDCl_3$): ∂7.41-7.31(m, 15H, *arom.*), 7.09-7.05(m, 2H, *arom.*), 6.90-6.85(m, 2H, *arom.*), 5.09(d, J = 10.9 Hz, 1H, OBn CH_2), 5.00(d, J = 11.0 Hz, 1H, OBn CH_2), 4.94-4.85(m, 4H, 3x OBn CH_2 and H-1), 4.68(d, J = 10.9 Hz, 1H, OBn CH_2), 3.81(s, 3H, OCH_3), 3.77-3.69(m, 4H, H-2 and H-3 and H-4 and H-6a), 3.66(dd, J = 10.7, 4.3 Hz, 1H, H-6b), 3.58-3.53(m, 1H, H-5), 3.41(s, 3H,

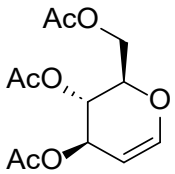
C-6 OCH_3). **^{13}C NMR:** (101 MHz, $CDCl_3$): ∂ = 155.3 (C PMP *arom.*), 151.7 (C PMP *arom.*), 138.7 (C OBn *arom.*), 138.4 (C OBn *arom.*), 138.2 (C OBn *arom.*), 128.6 (*arom.* 2xCH), 128.49 (*arom.* 4xCH), 128.48 (*arom.* 2xCH), 128.1 (*arom.* 2xCH), 127.9 (*arom.* 3xCH), 127.8 (*arom.* CH), 127.7 (*arom.* CH), 118.5 (*arom.* 2xCH), 114.6 (*arom.* 2xCH), 102.9 (C-1), 84.7 (C-2/C-3/C-4), 82.1 (C-2/C-3/C-4), 77.6 (C-2/C-3/C-4), 75.8 (OBn CH_2), 75.2 (OBn CH_2), 75.1 (OBn CH_2), 75.0 (C-5), 71.2 (C-6 CH_2), 59.5 (OCH_3), 55.7 (OCH_3). **HRMS (ESI):** m/z calcd for $C_{35}H_{38}O_7Na$ $[M+Na]^+$ 593.2515, found 593.2498.

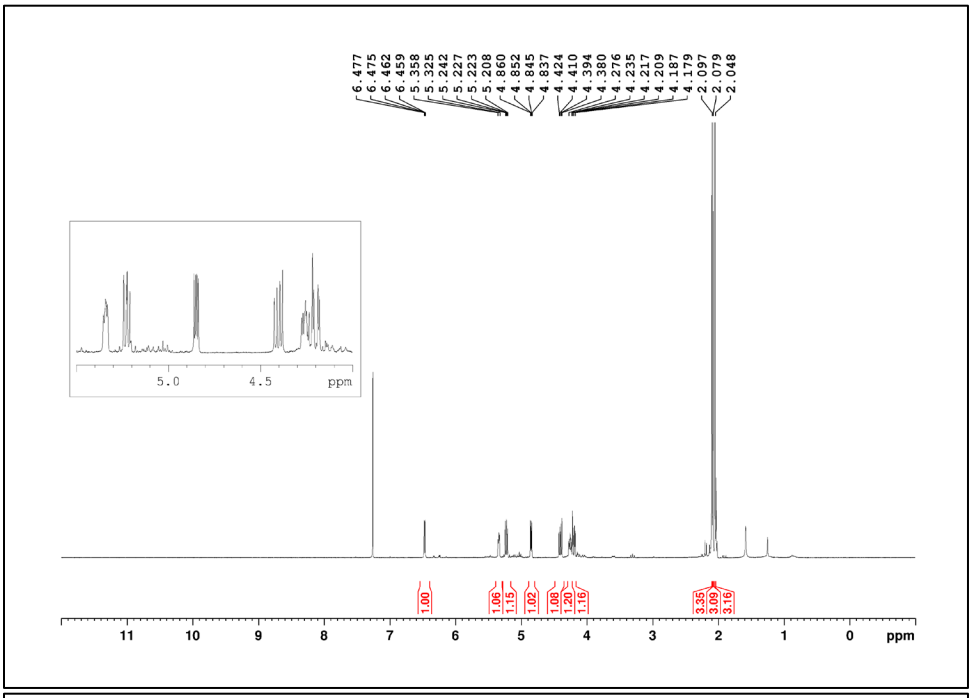
(4-methoxyphenyl)-6-*O*-methyl-β-D-glucopyranoside (C_6 OMe PMP-Glc, 89): The title compound was synthesized according to **General Procedure 8-7**. (4-methoxyphenyl)-2,3,4-tri-*O*-benzyl-6-*O*-methyl-β-D-glucopyranoside (**556**, 0.5 mmol, 1.0 eq) in a 1:1 mixture of EtOAc and MeOH (4.6 mL, 0.1 M), Pd/C (10 mol %) (0.04 mmol, 0.1 eq) was added and the reaction mixture was purged several times with H_2. The mixture was stirred under H_2 atmosphere for 6 h, filtered over Celite® and the volatiles were evaporated to afford the desired product as a white powder (**85 %**).

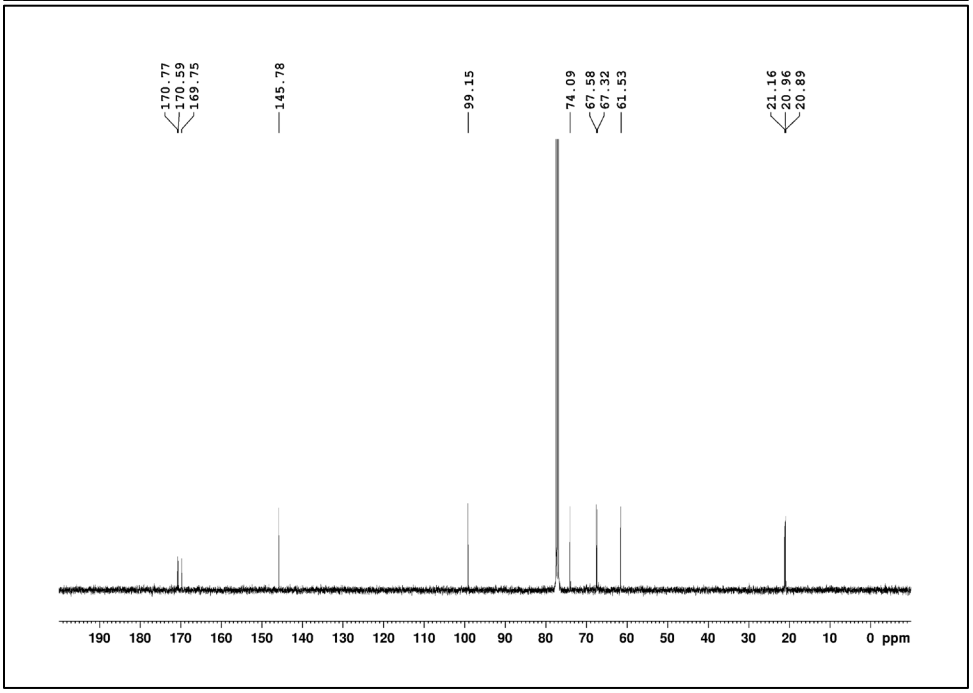


^{1}H NMR: (400 MHz, DMSO-d_6): ∂6.97-6.93(m, 2H, *arom.*), 6.87-6.93(m, 2H, *arom.*), 5.31(d, *J* = 4.9 Hz, 1H, OH-2), 5.13(d, *J* = 5.5 Hz, 1H, OH-4), 5.11(d, *J* = 4.8 Hz, 1H, OH-3), 4.73(d, *J* = 7.5 Hz, 1H, H-1), 3.70(s, 3H, *arom.* OCH_3), 3.59(d, *J* = 9.3 Hz, 1H, H-6a), 3.45-3.37(m, 2H, H-5 and H-6b), 3.27-3.15(m, 5H, OCH_3 and H-2 and H-3), 3.12-3.06(m, 1H, H-4). **^{13}C NMR:** (101 MHz, DMSO-d_6): ∂ = 154.3 (C *arom.*), 151.3 (C *arom.*), 117.5 (*arom.* 2xCH), 114.4 (*arom.* 2xCH), 101.2 (C-1), 76.5 (C-3), 75.3 (C-5), 73.2 (C-2), 71.8 (C-6 CH_2), 69.8 (C-4), 58.5 (OCH_3), 55.3 (*arom.* OCH_3). **HRMS (ESI):** m/z calcd for $C_{14}H_{20}O_7Na$ $[M+Na]^+$ 323.1107, found 323.1128.

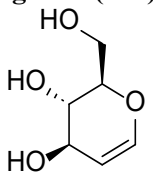
3,4,6-tri-*O*-acetyl-D-glucal (540):

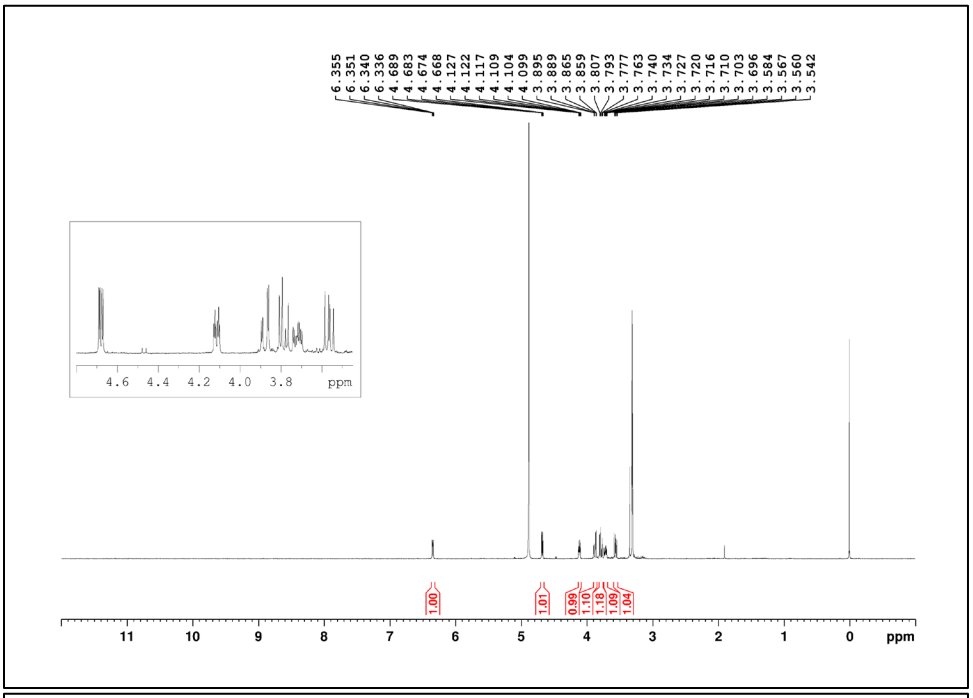


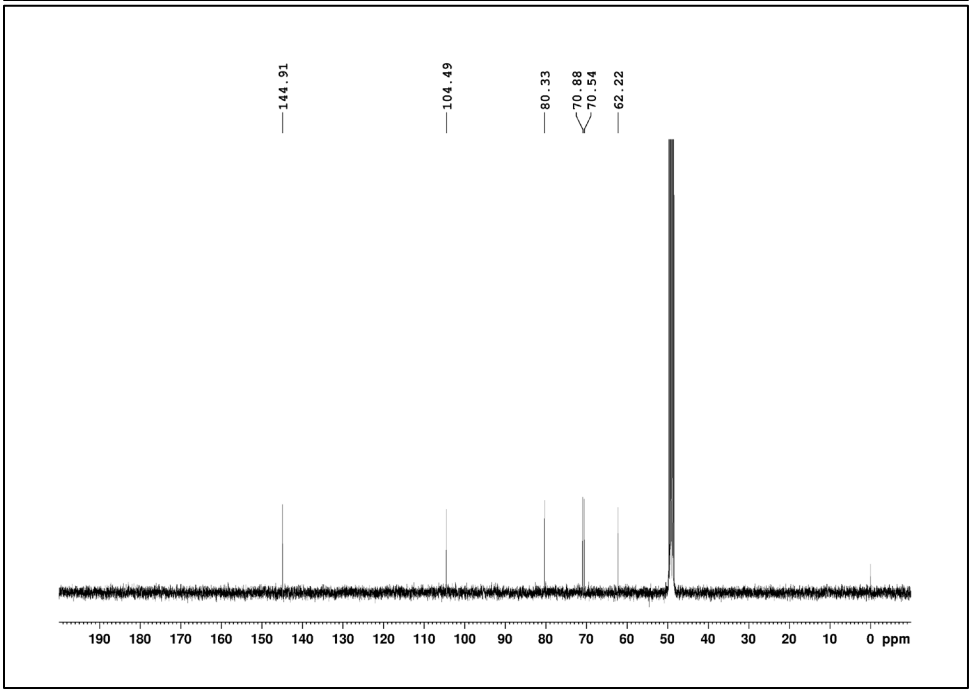




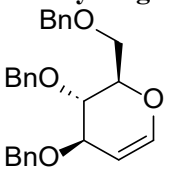
D-glucal (541):

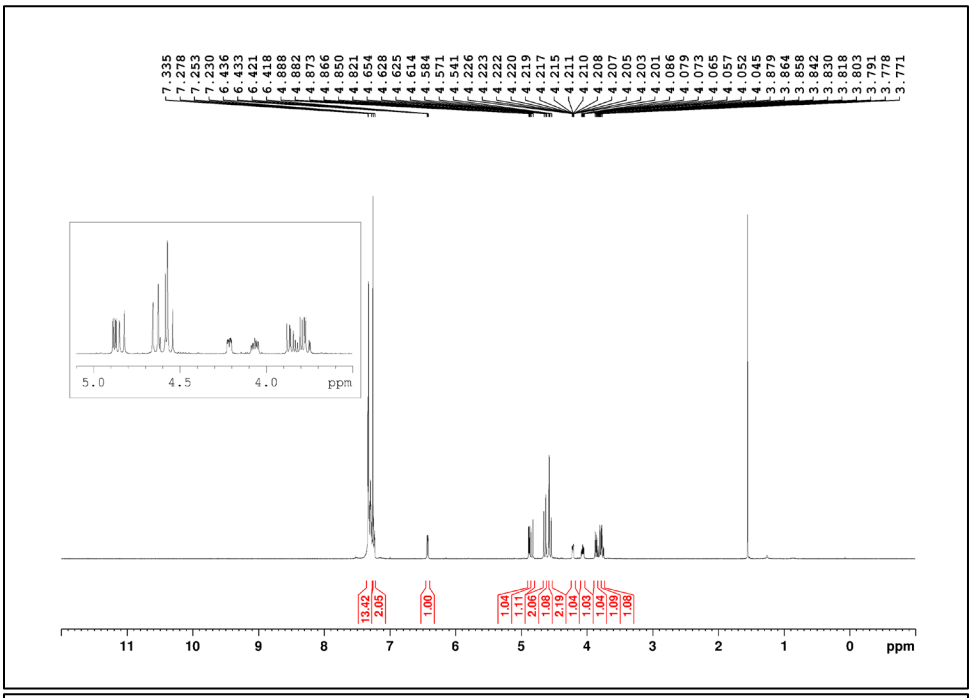

HO
HO
O
HO

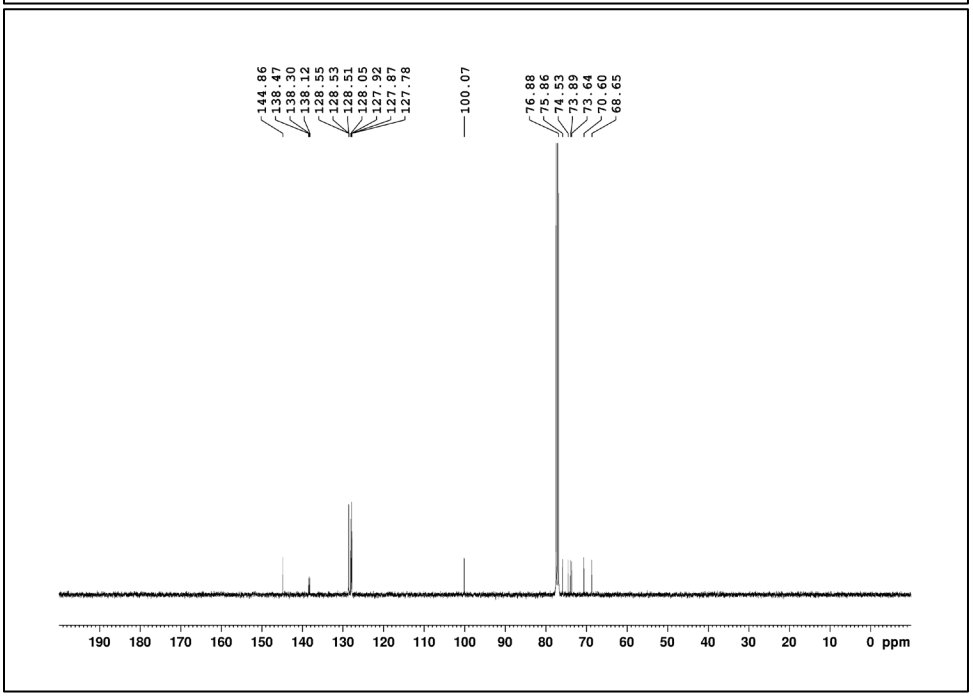

6.355
6.351
6.340
6.336
4.689
4.683
4.674
4.668
4.127
4.122
4.117
4.109
4.104
4.099
3.895
3.889
3.865
3.859
3.807
3.793
3.777
3.763
3.740
3.734
3.727
3.720
3.716
3.710
3.703
3.696
3.584
3.567
3.560
3.542
4.6 4.4 4.2 4.0 3.8 ppm
1.00
1.01
0.99
1.10
1.18
1.09
1.04
11 10 9 8 7 6 5 4 3 2 1 0 ppm


144.91
104.49
80.33
70.88
70.54
62.22
190 180 170 160 150 140 130 120 110 100 90 80 70 60 50 40 30 20 10 0 ppm

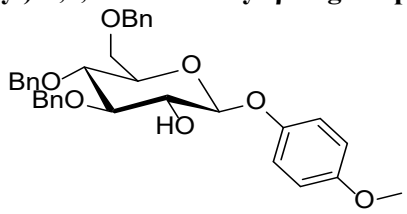
3,4,6-tri-*O*-benzyl-D-glucal (542):

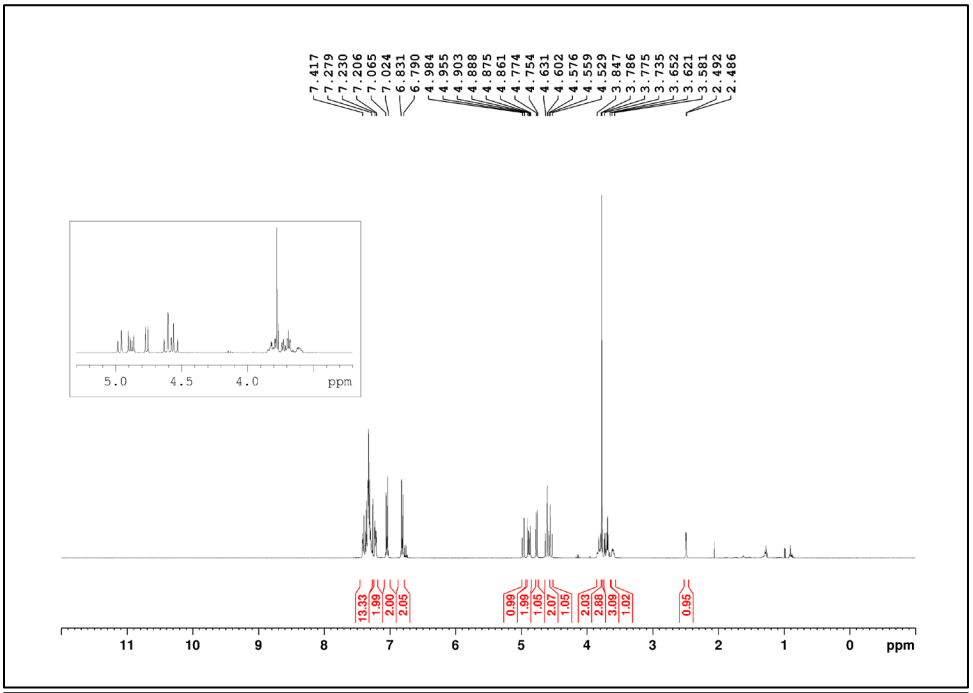


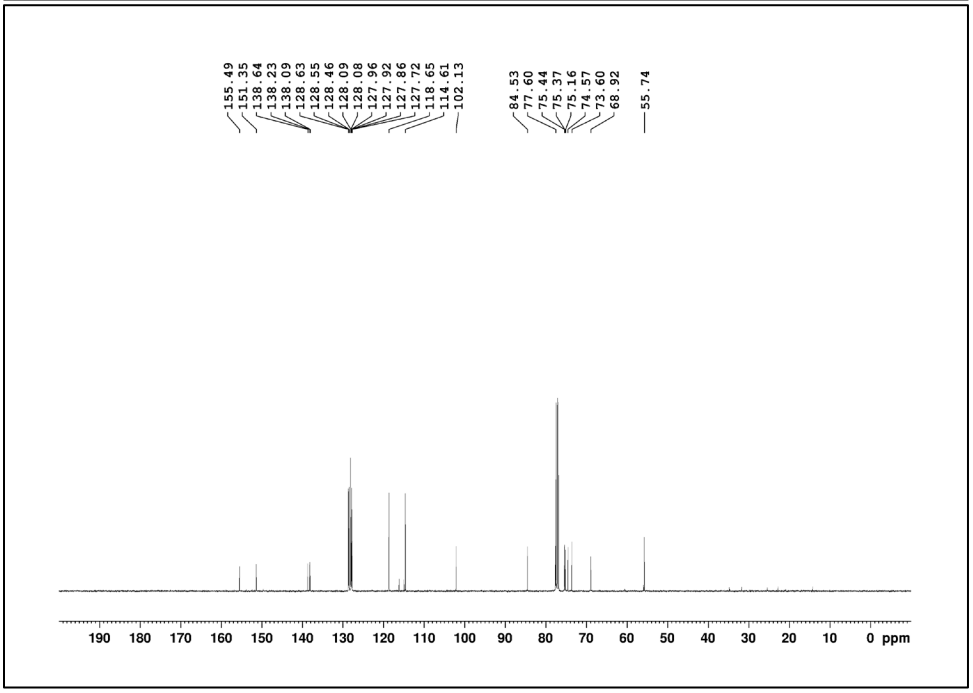




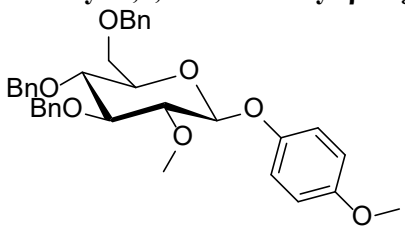
(4-methoxyphenyl)-3,4,6-tri-*O*-benzyl-β-D-glucopyranoside (544):

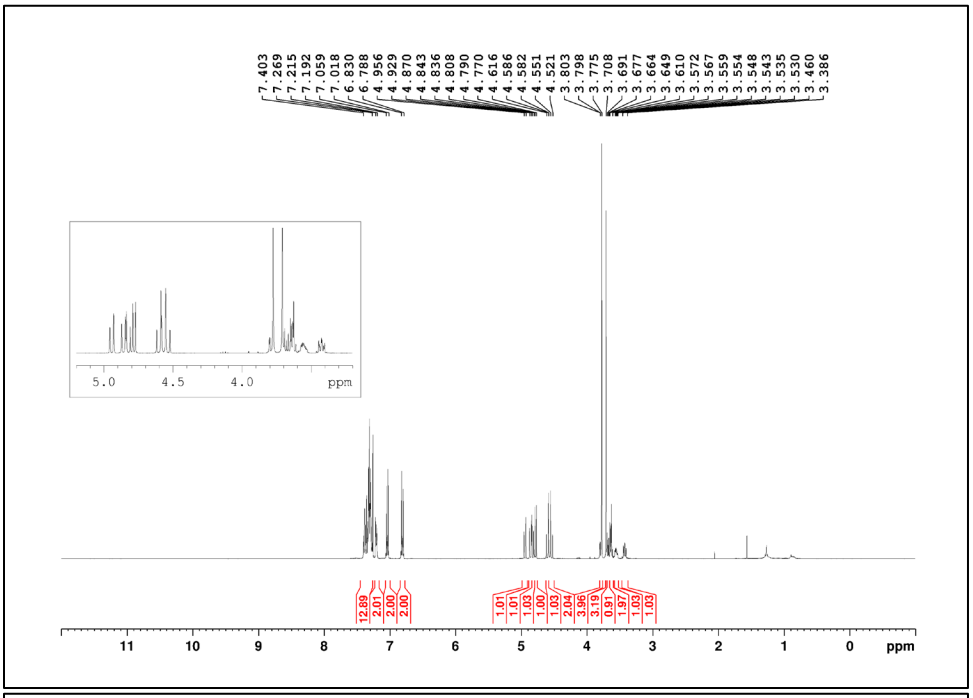


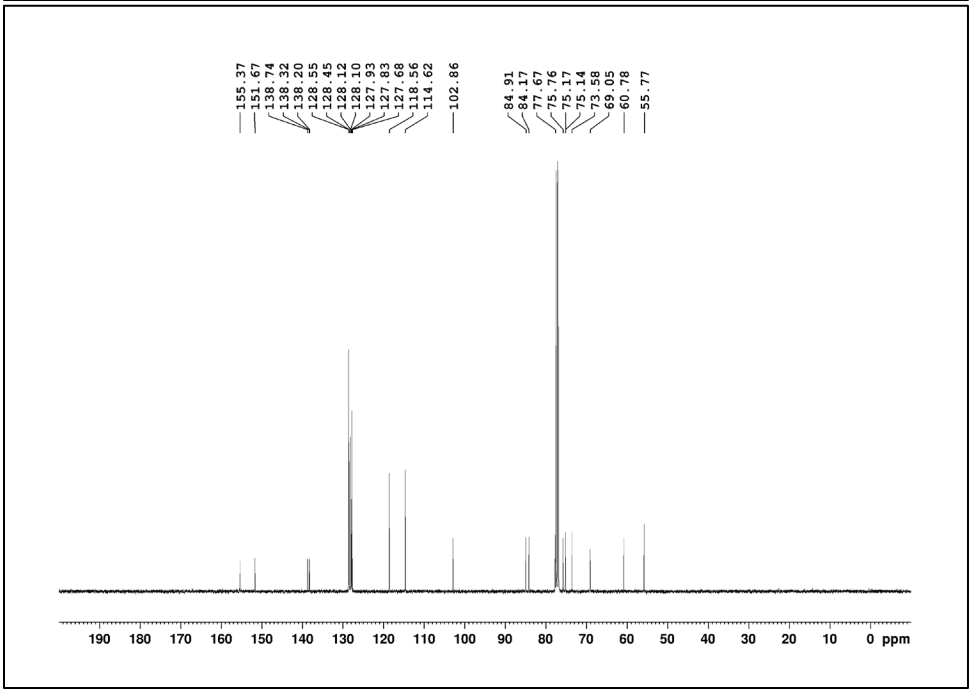




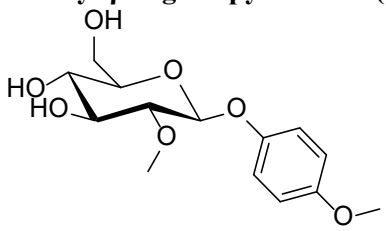
(4-methoxyphenyl)-2-*O*-methyl-3,4,6-tri-*O*-benzyl-β-D-glucopyranoside (545):

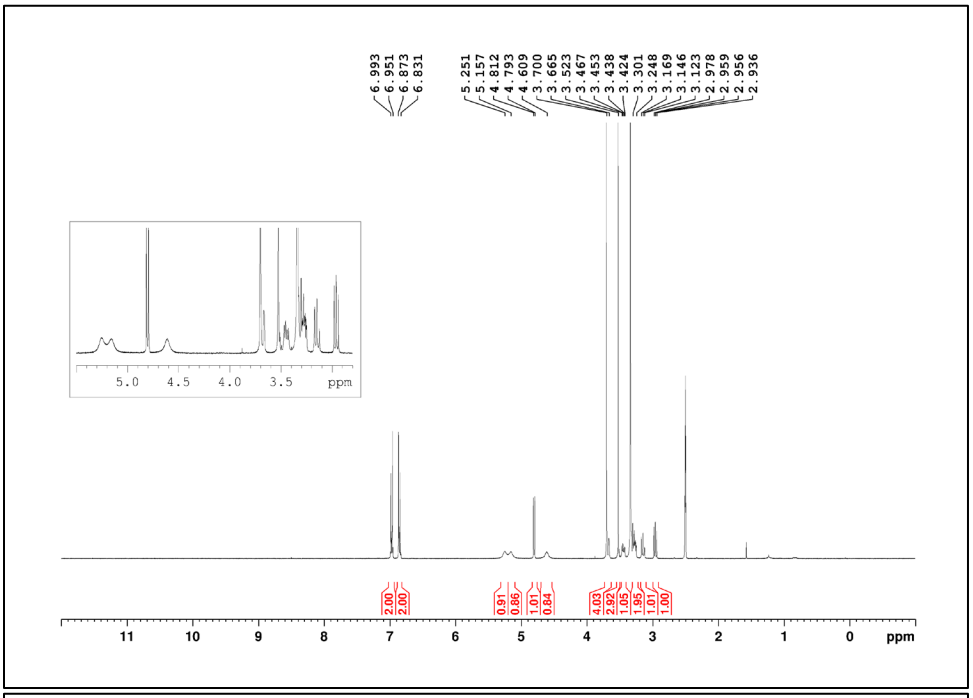


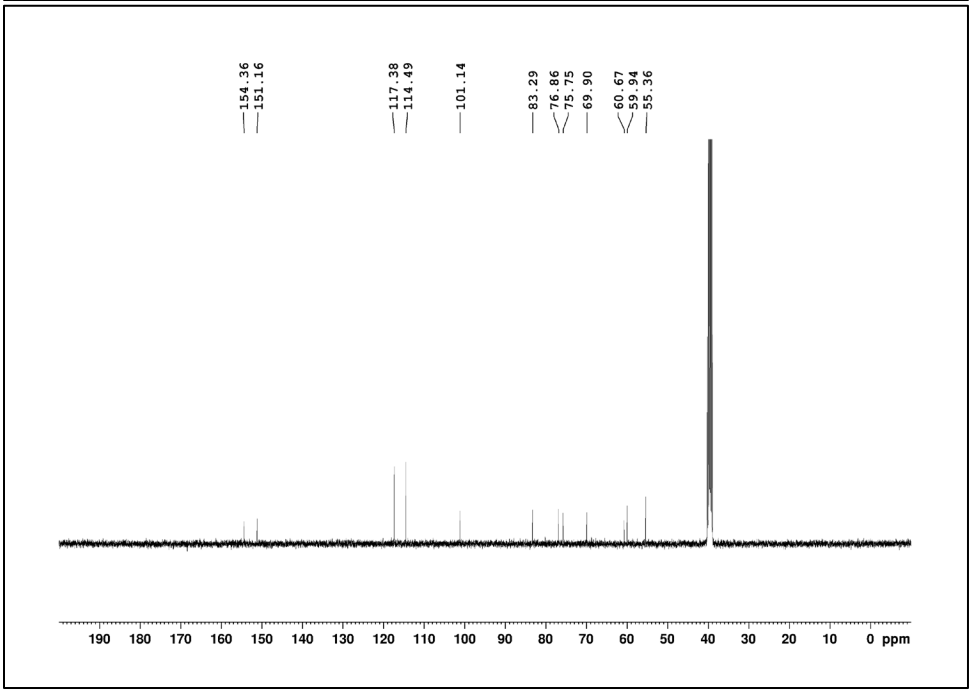




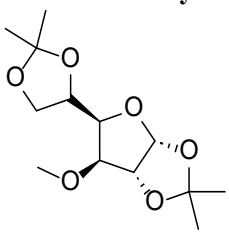
(4-methoxyphenyl)-2-*O*-methyl-β-D-glucopyranoside (C_2 OMe PMP-Glc, 97):

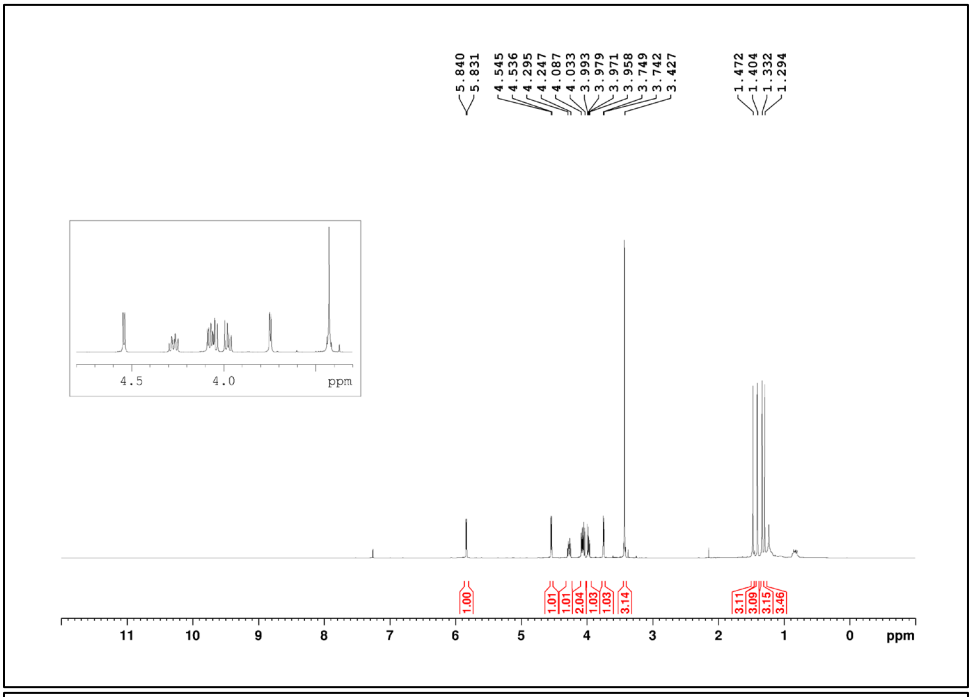


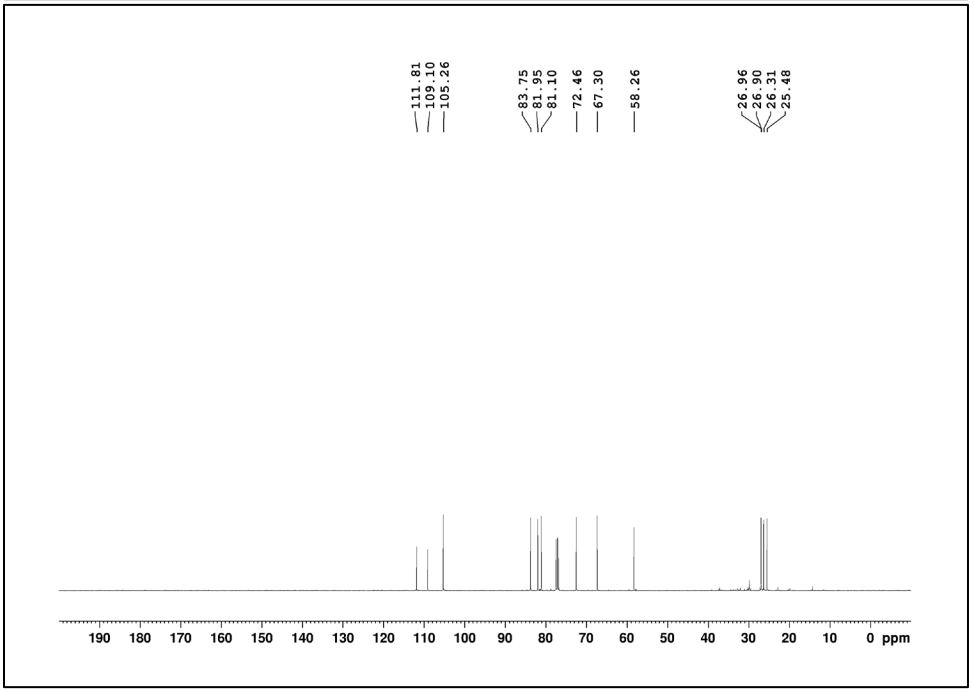




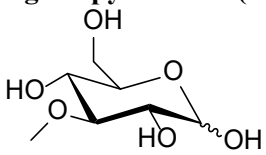
1,2:5,6-di-*O*-isopropylidene-3-*O*-methyl-α-D-glucofuranose (547):

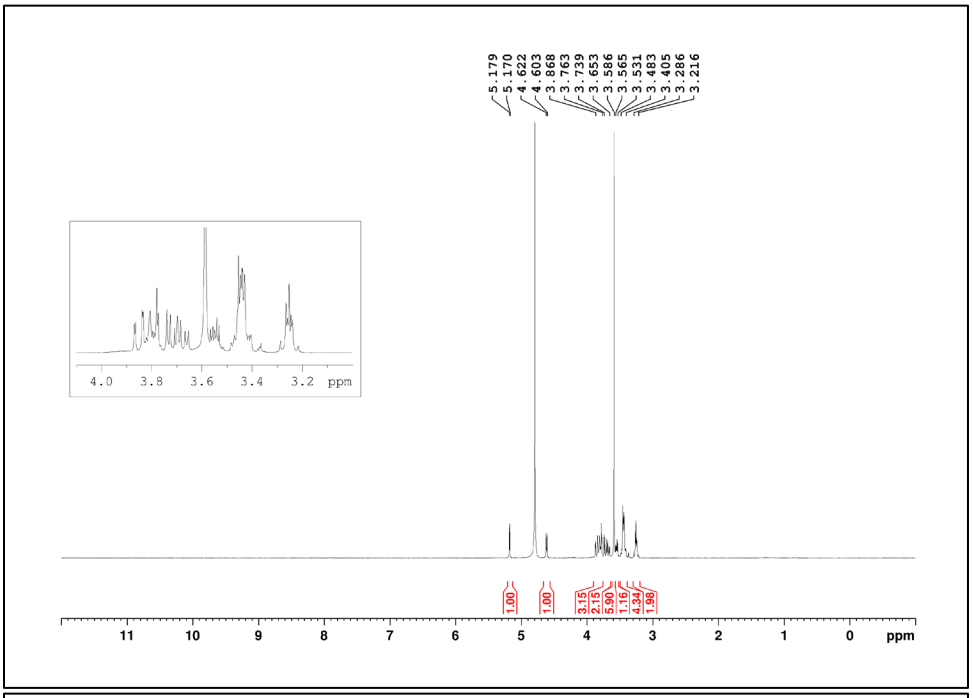


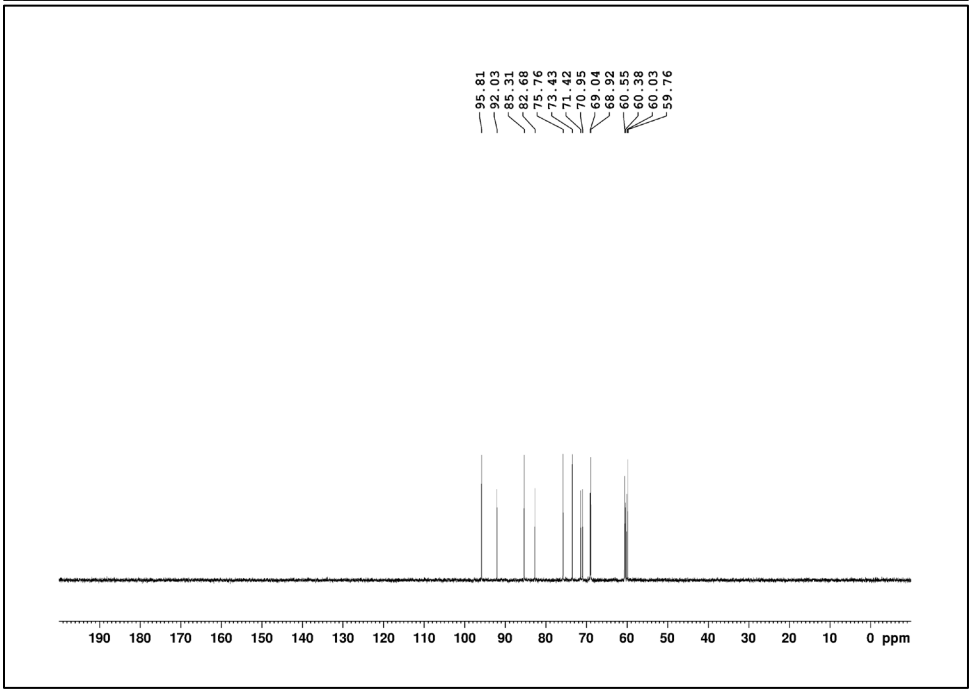




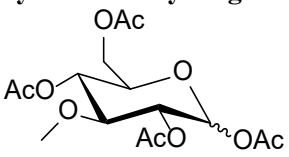
3-*O*-methyl-D-glucopyranoside (3-OMG, 548):

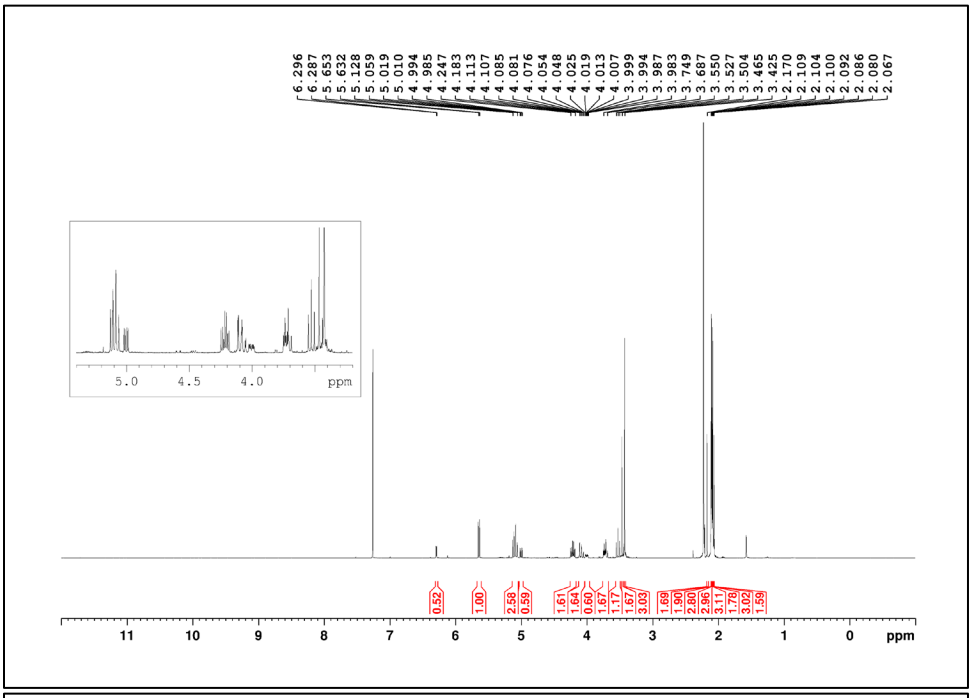


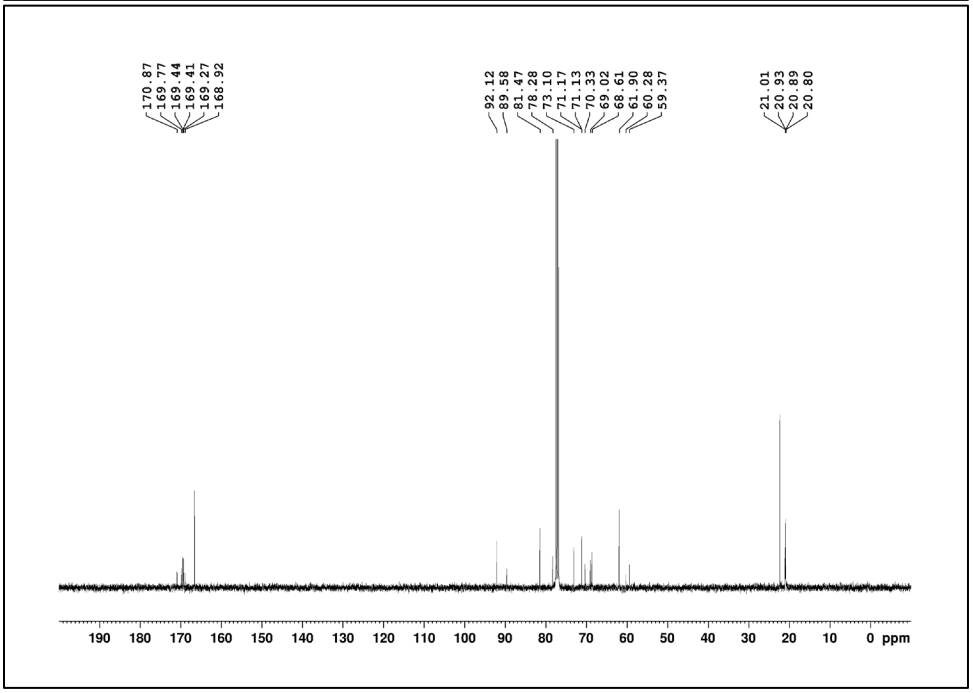




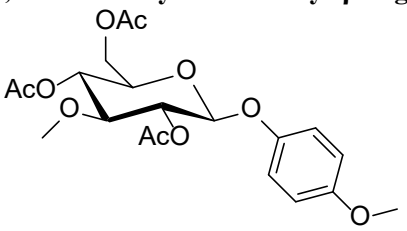
1,2,4,6-tetra-*O*-acetyl-3-*O*-methyl-D-glucopyranoside (549):

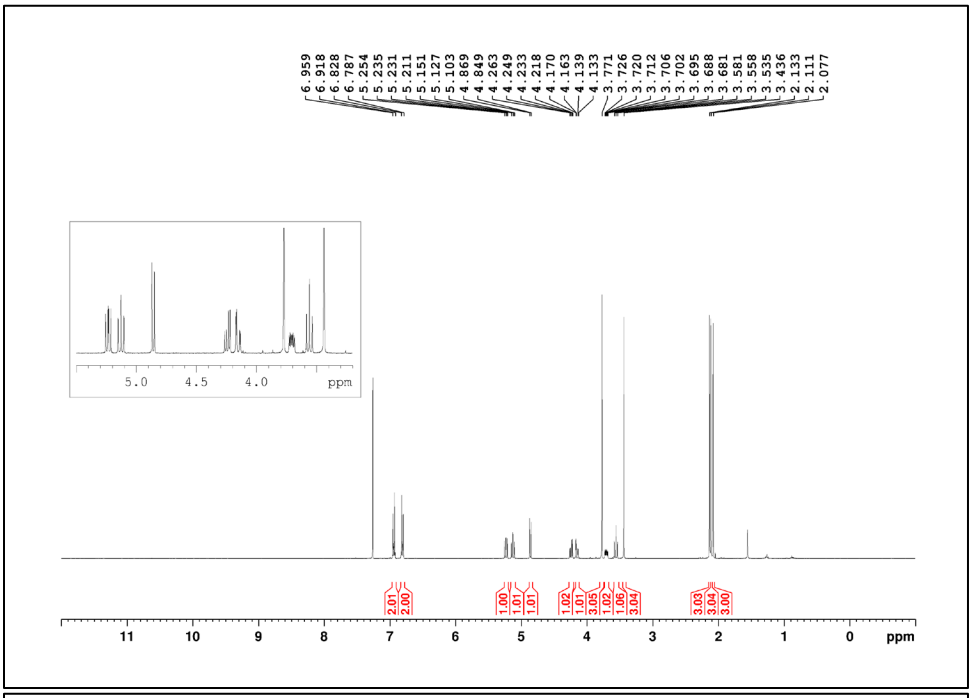


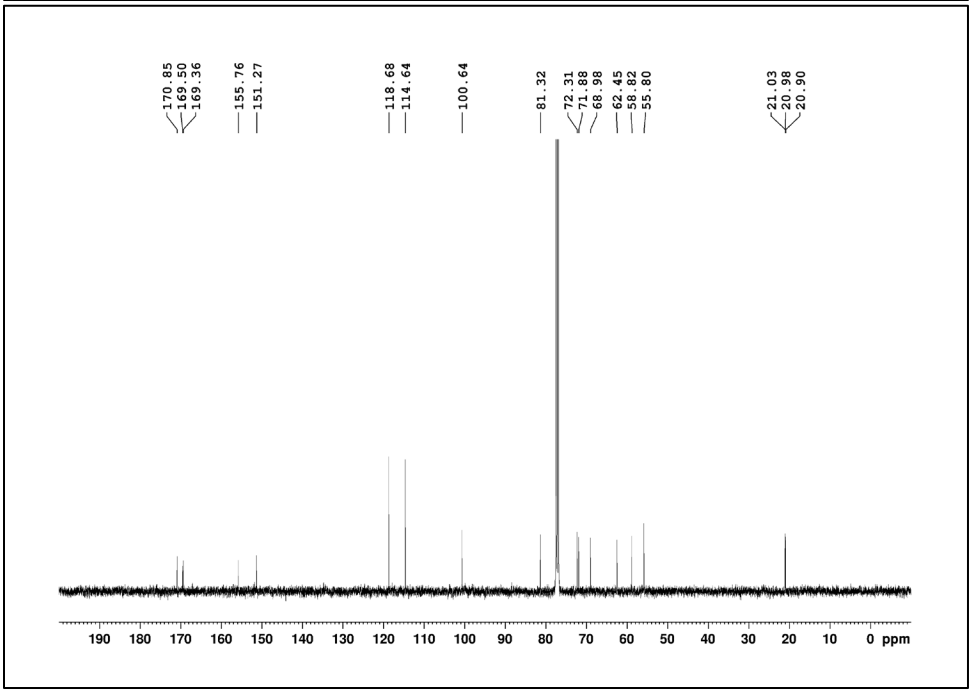




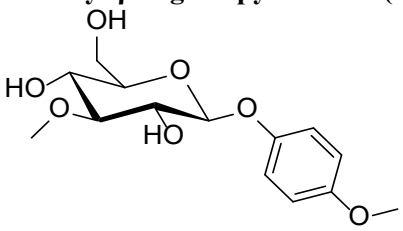
(4-methoxyphenyl)-2,4,6-tri-*O*-acetyl-3-*O*-methyl-β-D-glucopyranoside (550):

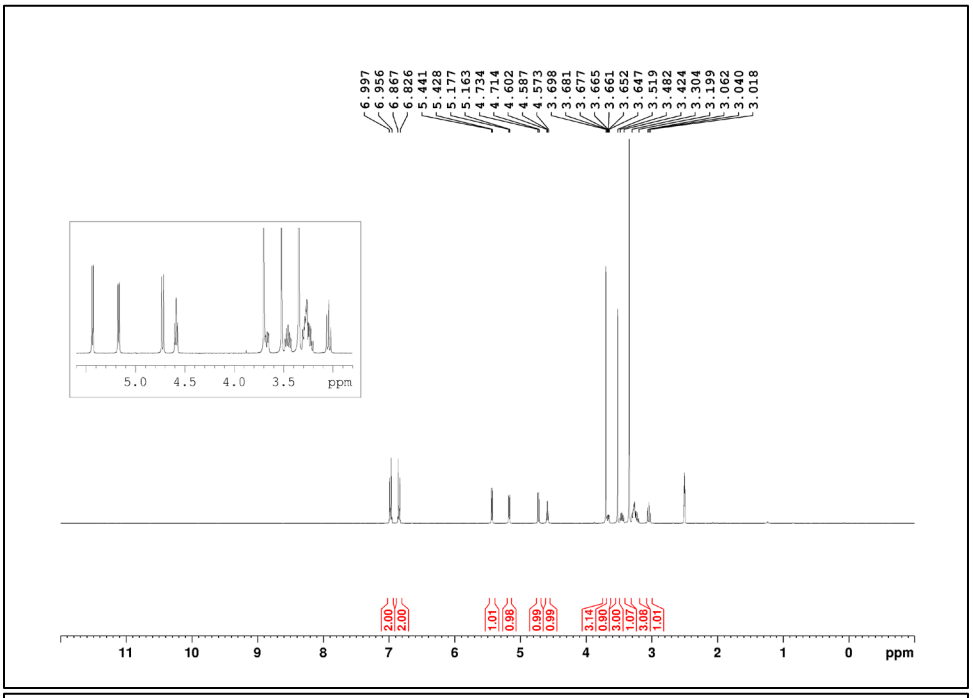


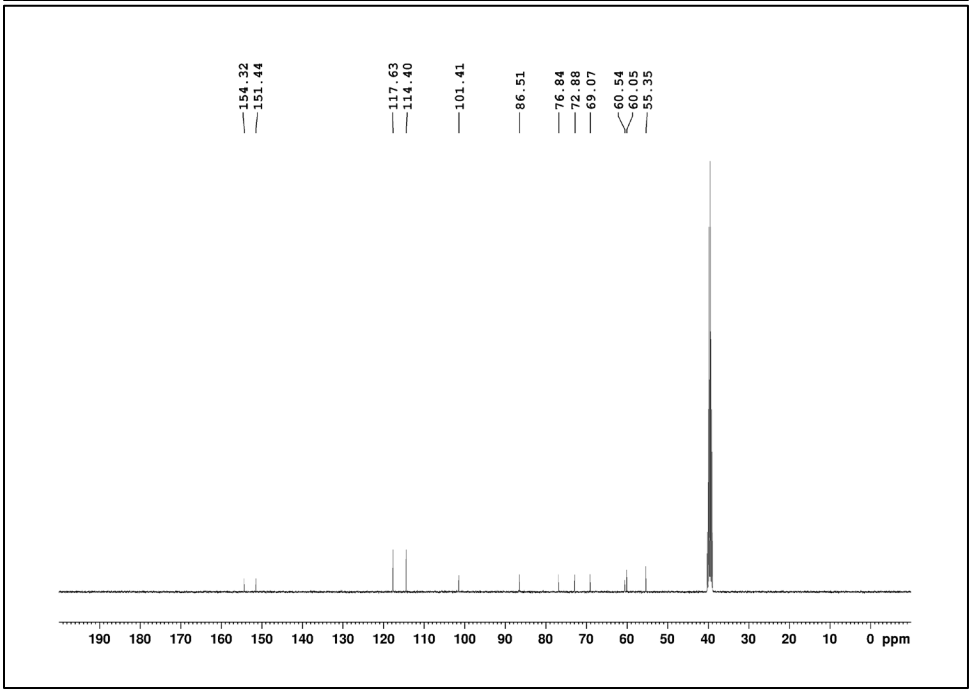




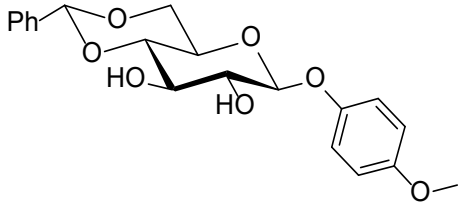
(4-methoxyphenyl)-3-*O*-methyl-β-D-glucopyranoside (C_3 OMe PMP-Glc, 98):

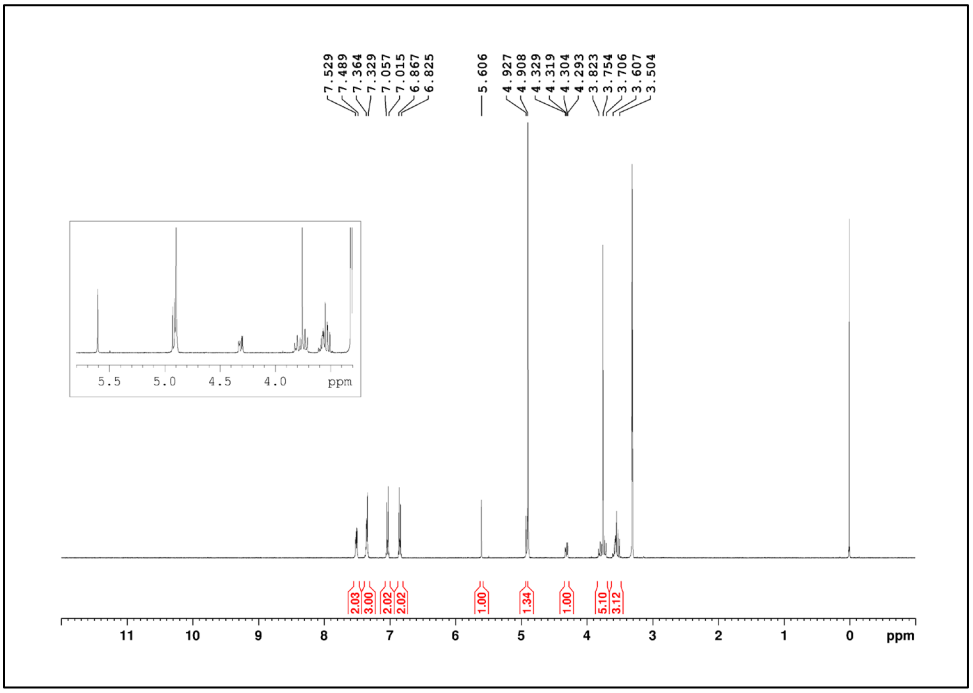




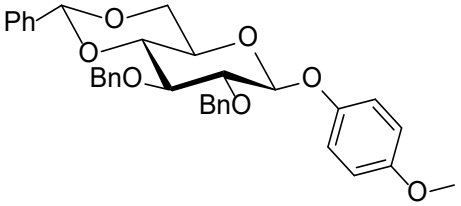


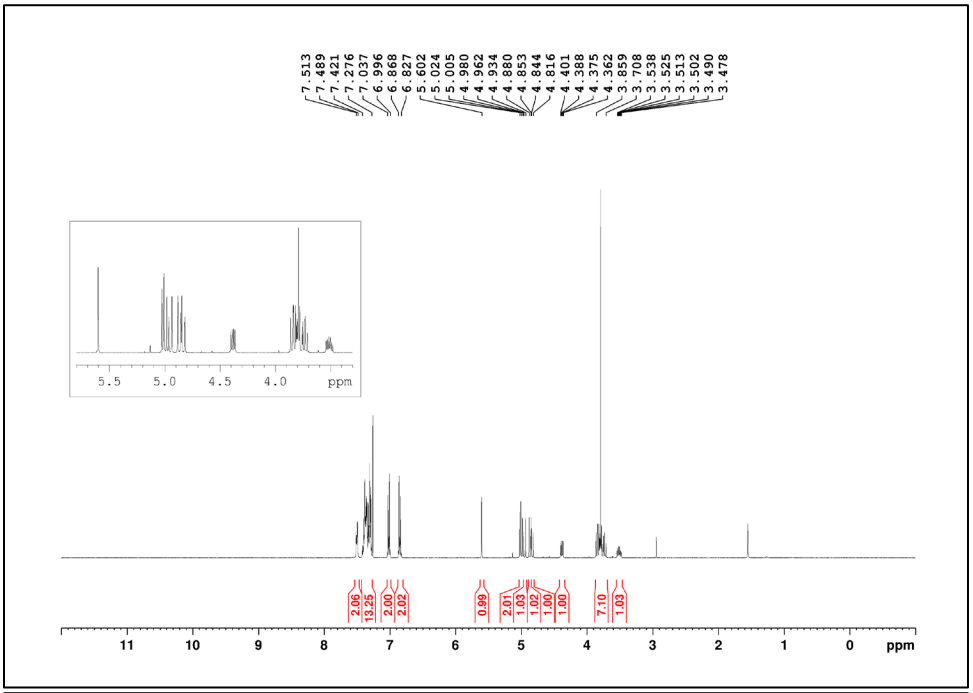
(4-methoxyphenyl)-4,6-*O*-benzylidene-β-D-glucopyranoside (551):

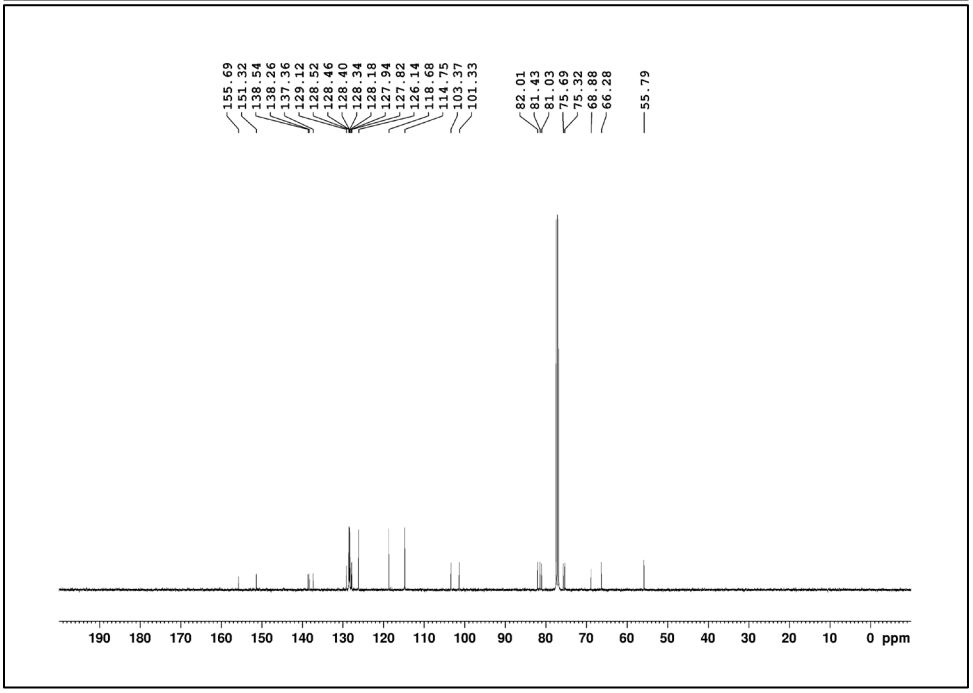




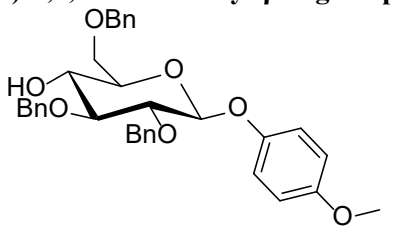
(4-methoxyphenyl)-2,3-di-*O*-benzyl-4,6-*O*-benzylidene-β-D-glucopyranoside (552):

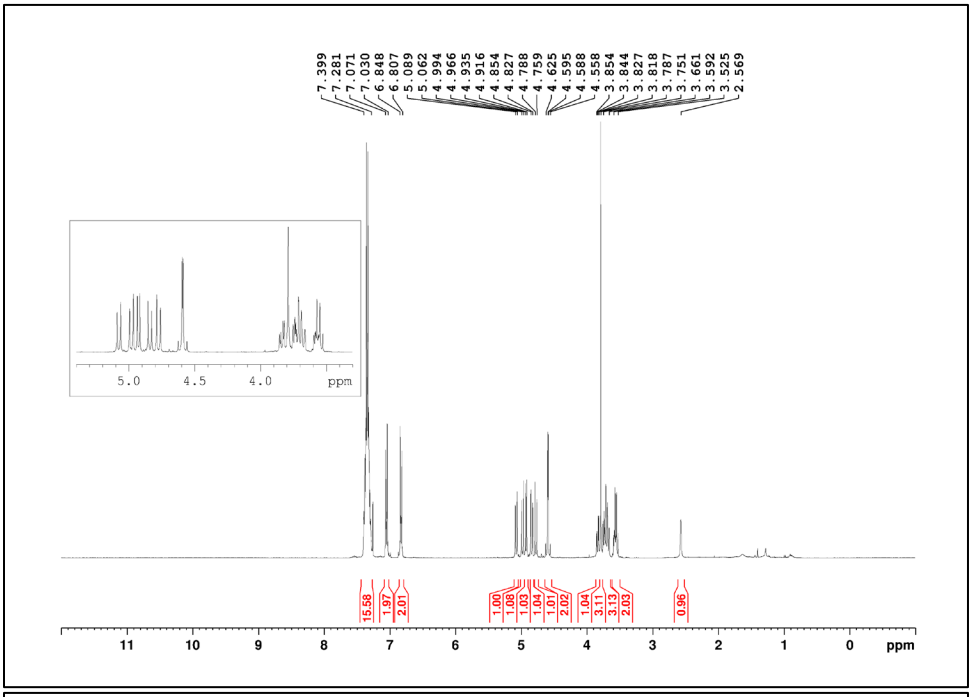


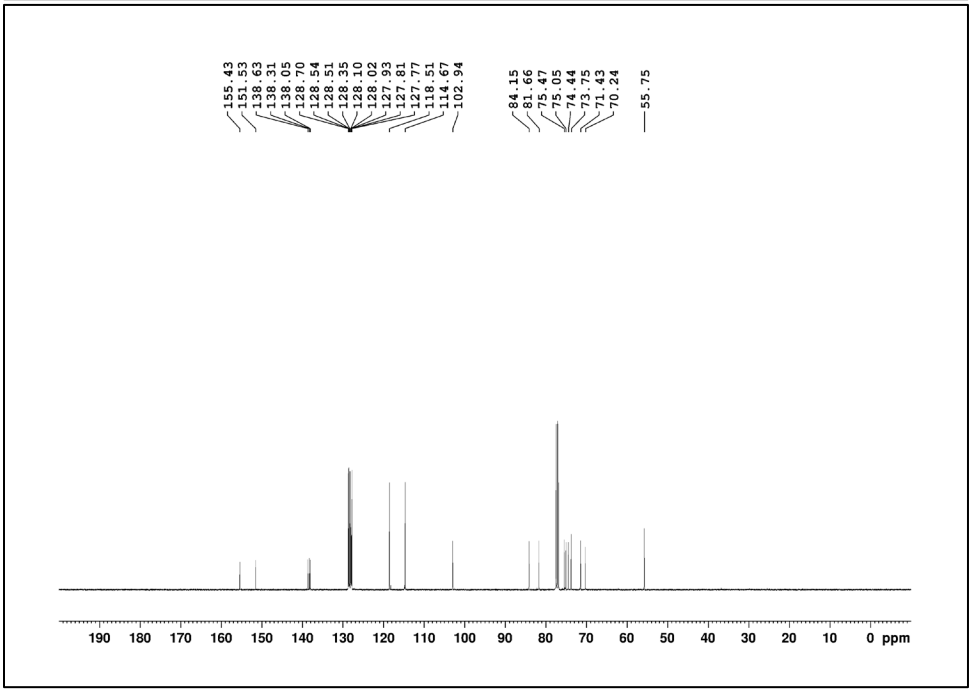




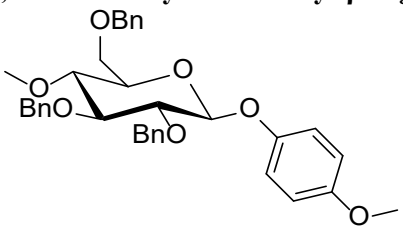
(4-methoxyphenyl)-2,3,6-tri-*O*-benzyl-β-D-glucopyranoside (553):

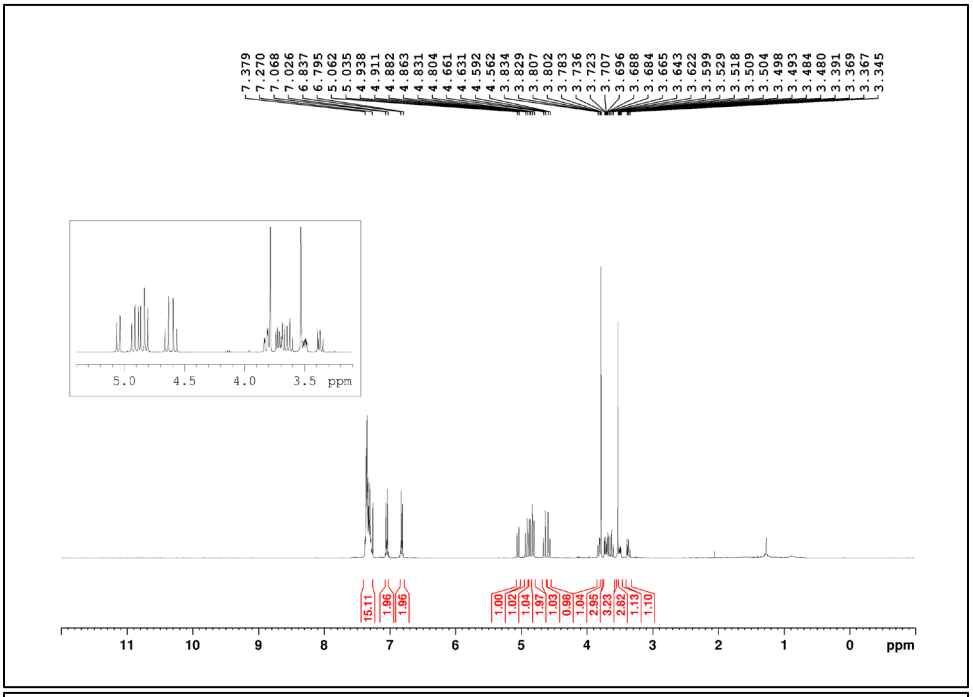


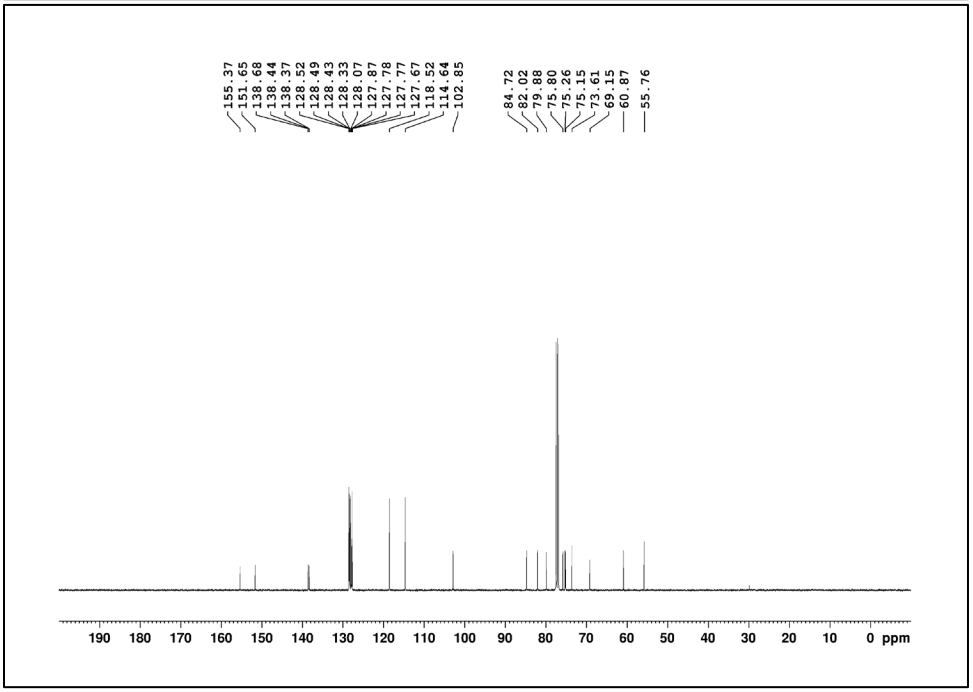




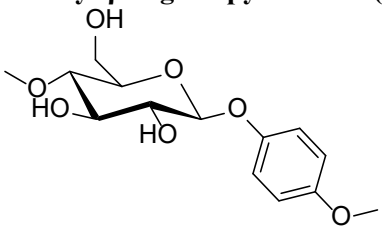
(4-methoxyphenyl)-2,3,6-tri-*O*-benzyl-4-*O*-methyl-β-D-glucopyranoside (555):

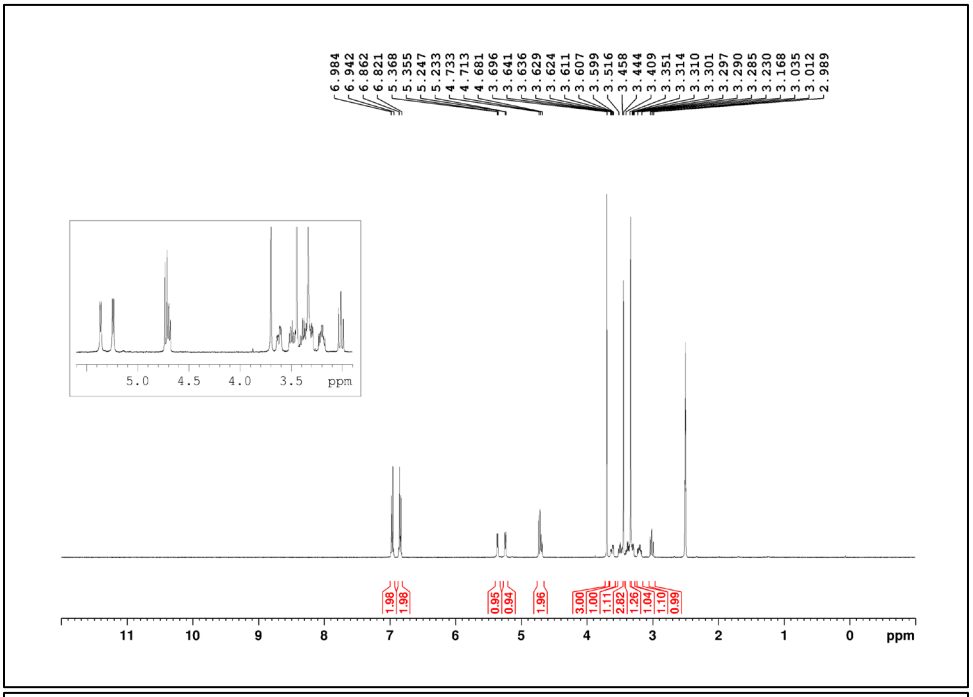


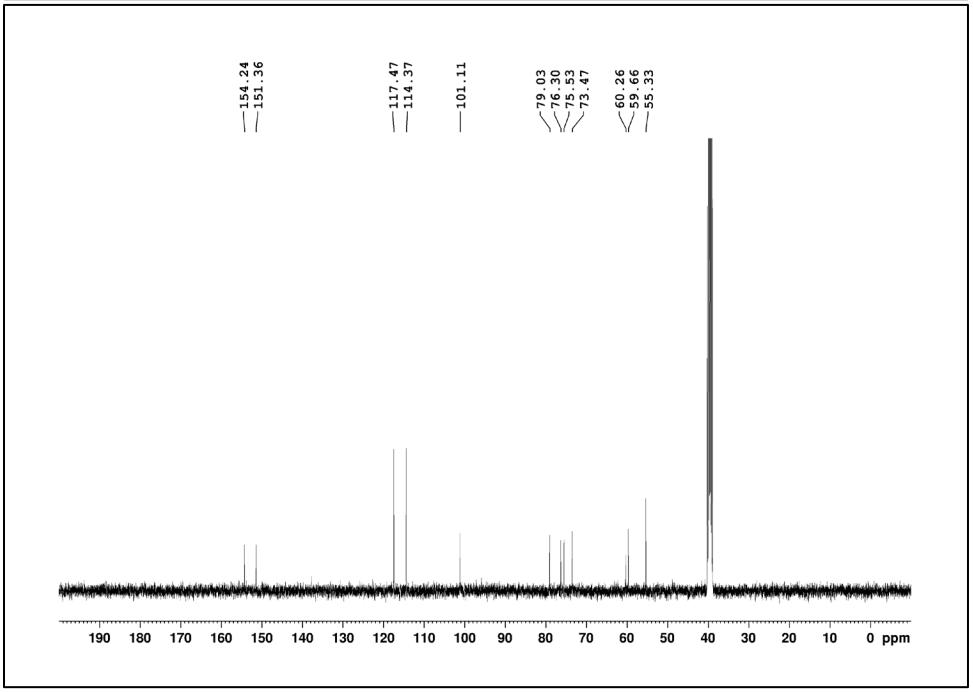




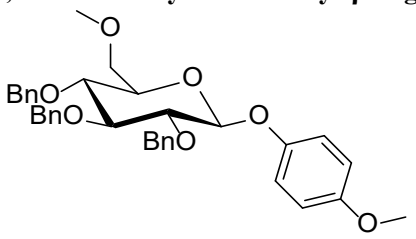
(4-methoxyphenyl)-4-*O*-methyl-β-D-glucopyranoside (C_4 OMe PMP-Glc, 99):

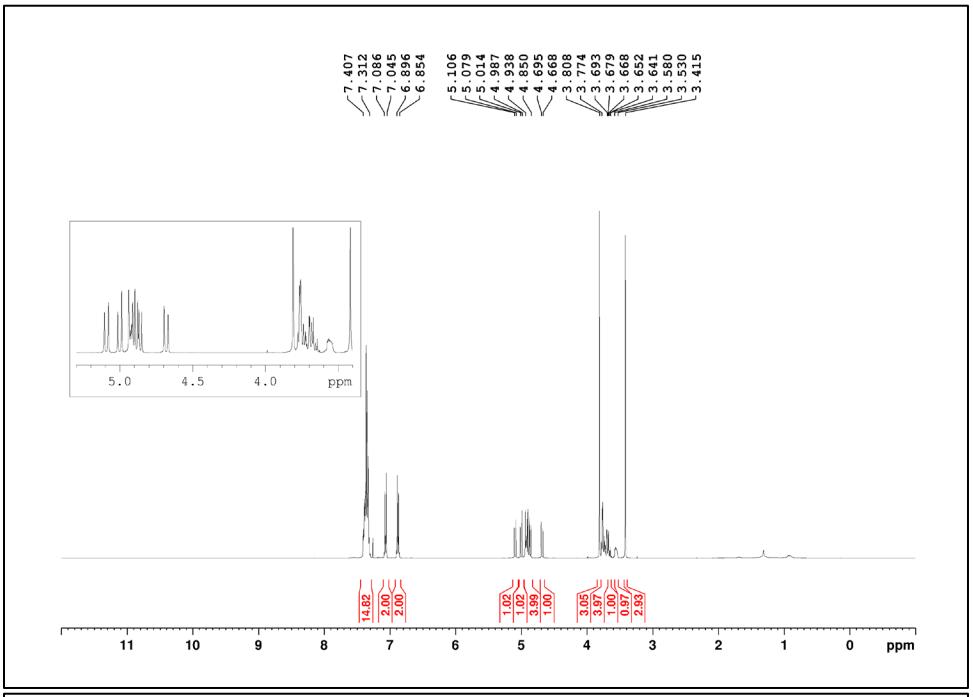


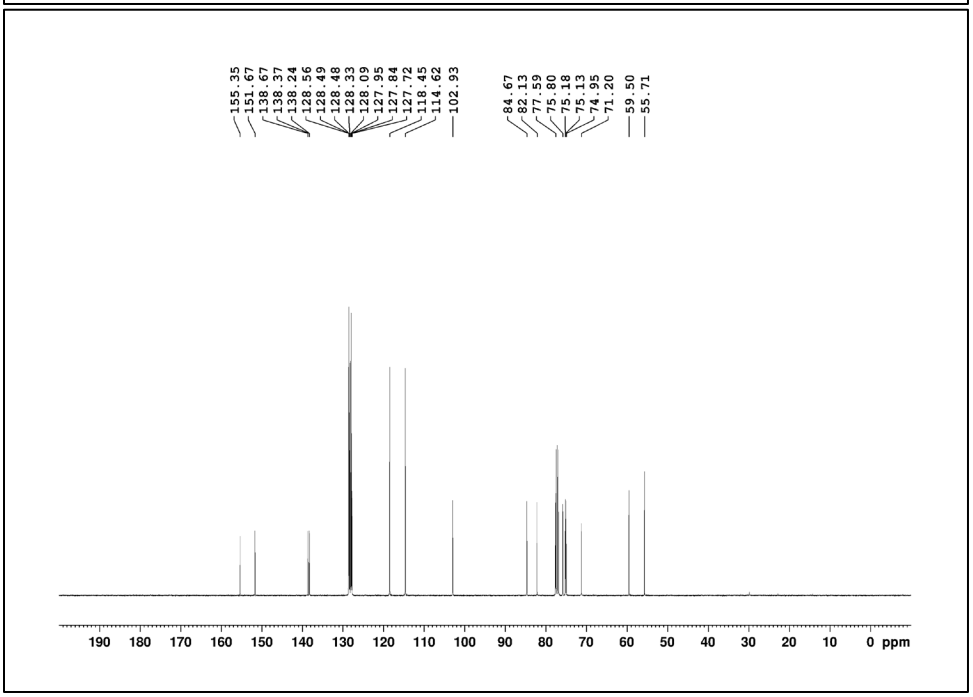




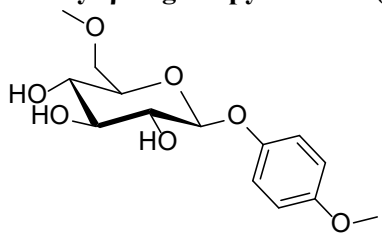
(4-methoxyphenyl)-2,3,4-tri-*O*-benzyl-6-*O*-methyl-β-D-glucopyranoside (556):

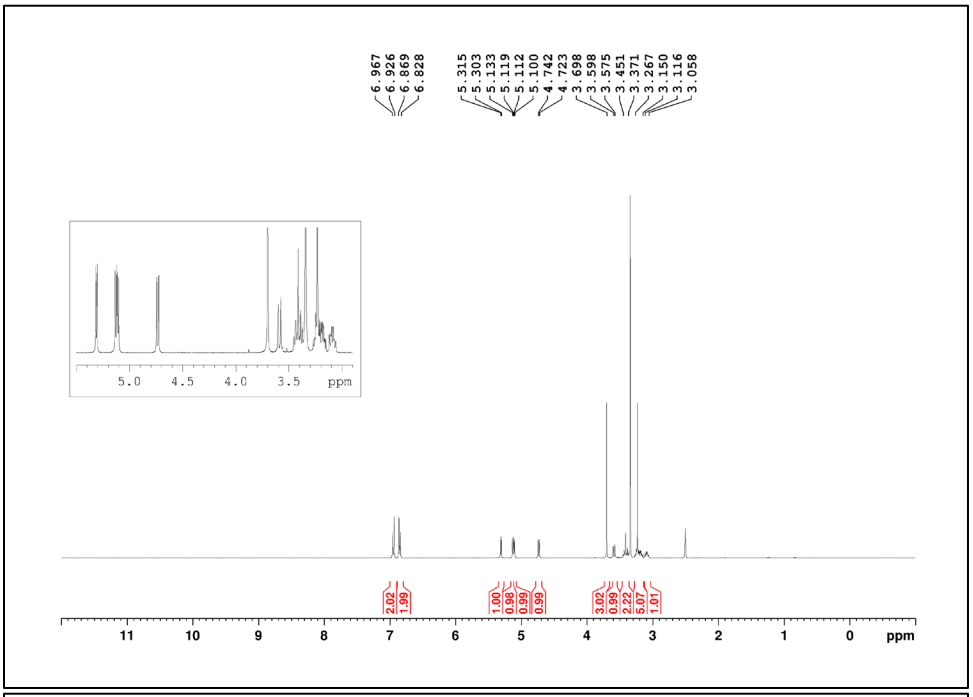


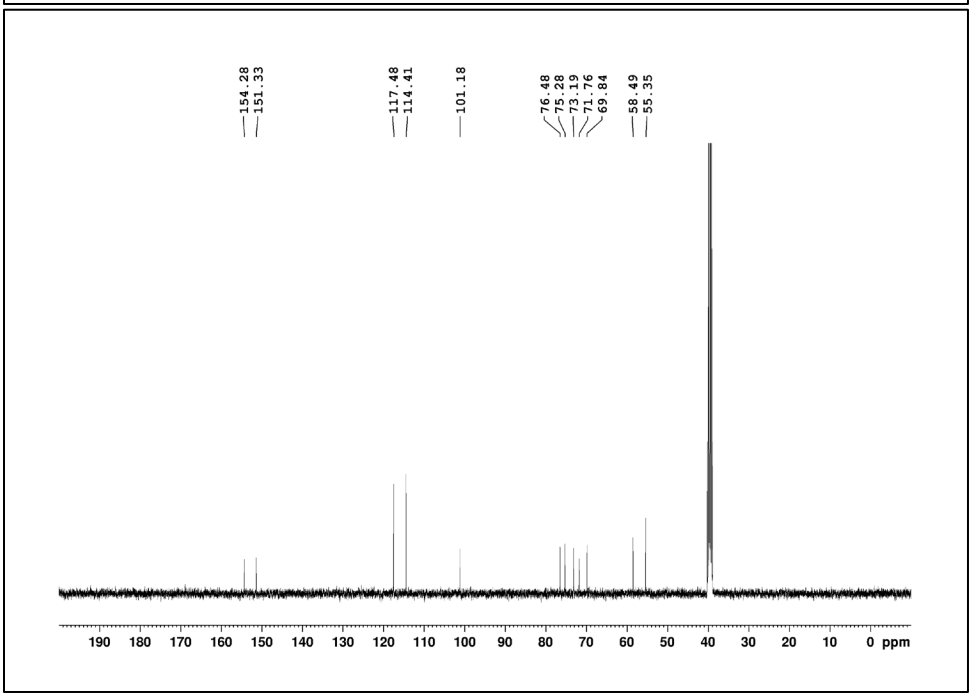




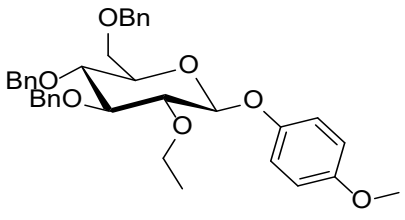
(4-methoxyphenyl)-6-*O*-methyl-β-D-glucopyranoside (C_6 OMe PMP-Glc, 89):





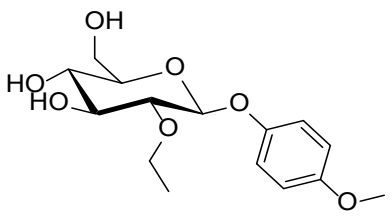


8.2.2.8. Additional alkylation compounds (chapter 5)



(4-methoxyphenyl)-3,4,6-tri-*O*-benzyl-2-*O*-ethyl-β-D-glucopyranoside (557): The title compound was synthesized according to a modified **General Procedure 8-5**. (4-methoxyphenyl)-3,4,6-tri-*O*-benzyl-β-D-glucopyranoside (**544**, 0.18 mmol, 1.0 eq) was dissolved in dry DMF (0.1 M) in a flame-dried flask under argon atmosphere. NaH (60 % dispersion in mineral oil) (0.44 mmol, 2.0 eq) was added portion-wise to the flask followed by drop-wise addition of EtI (1.2 mmol, 8.0 eq). The solution was stirred at room temperature for 18 h. Upon reaction completion the solution was diluted with DCM, quenched with water, and washed with brine. The organic layer was dried using Na_2SO_4, filtered, and concentrated *in vacuo*. The crude product was purified by column chromatography (20 % EtOAc in Hexanes) to yield a white solid (**66 %**).

^{1}H NMR: (500 MHz, $CDCl_3$): ∂7.39-7.26(m, 13H, *arom.*), 7.21-7.19(m, 2H, *arom.*), 7.05-7.01(m, 2H, *arom.*), 6.82-6.79(m, 2H, *arom.*), 4.98(d, *J* = 10.9 Hz, 1H, OBn CH_2), 4.85(d, *J* = 10.9 Hz, 1H, OBn CH_2), 4.82(d, *J* = 11.0 Hz, 1H, OBn CH_2), 4.78(d, *J* = 7.8 Hz, 1H, H-1), 4.60(d, *J* = 12.0 Hz, 1H, OBn CH_2), 4.56(d, *J* = 10.9 Hz, 1H, OBn CH_2), 4.53(d, *J* = 12.1 Hz, 1H, OBn CH_2), 4.09-4.03(m, 1H, CH_2CH_3), 3.86-3.77(m, 2H, OCH_2CH_3 and H-6a), 3.77(s, 3H, OCH_3), 3.70-3.60(m, 3H, H-4 and H-5 and H-6b), 3.57-3.50(m, *2*H, H-2 and H-3), 1.25(t, *J* = 7.0 Hz, 3H, OCH_2CH_3). **^{13}C NMR:** (125 MHz, $CDCl_3$): ∂ = 155.4 (C PMP *arom.*), 151.8 (C PMP *arom.*), 138.8 (C OBn *arom.*), 138.4 (C OBn *arom.*), 138.2 (C OBn *arom.*), 128.57 (*arom.* 2xCH), 128.55 (*arom.* 2xCH), 128.46 (*arom.* 2xCH), 128.12 (*arom.* 2xCH), 128.10 (*arom.* 2xCH), 127.9 (*arom.* CH), 127.84 (*arom.* 2xCH), 127.83 (*arom.* CH), 127.7 (*arom.* CH), 118.6 (*arom.* 2xCH), 114.6 (*arom.* 2xCH), 103.0 (C-1), 84.9 (C-4/C-5), 82.4 (C-2/C-), 77.8 (C-4/C-5), 75.9 (OBn CH_2), 75.2 (OBn CH_2 and C-2/C-3), 73.6 (OBn CH_2), 69.1 (OCH_2CH_3), 68.6 (C-6 CH_2), 55.8(OCH_3), 16.0 (OCH_2CH_3). **HRMS (ESI):** m/z calcd for $C_{36}H_{40}O_7Na$ $[M+Na]^+$ 607.2672, found 607.2651.

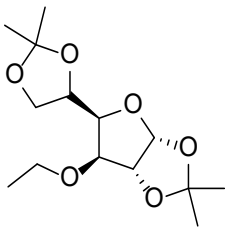


(4-methoxyphenyl)-4-*O*-ethyl-β-D-glucopyranoside (C_2 OEt PMP-Glc, 100): The title compound was synthesized according to a modified **General Procedure 8-7**. To a solution of (4-methoxyphenyl)-3,4,6-tri-*O*-benzyl-4-*O*-ethyl-β-D-glucopyranoside (**557**, 0.12 mmol, 1.0 eq) in a 1:1 mixture of EtOAc and MeOH (1.2 mL, 0.1 M), Pd/C (10 mol %) (0.01 mmol, 0.1 eq) was added and the reaction mixture was purged several times with H_2. The mixture was stirred under

H_2 atmosphere for 5 h, filtered over Celite® and the volatiles were evaporated to afford the desired product as a white powder (**99 %**).

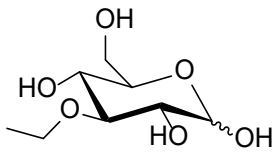
^{1}H NMR: (400 MHz, $CDCl_3$): ∂6.98-6.94(m, 2H, *arom.*), 6.87-6.83(m, 2H, *arom.*), 5.14(d, *J* = 5.2 Hz, 1H, OH-3), 5.08(d, *J* = 5.3 Hz, 1H, OH-4), 4.78(d, *J* = 7.8 Hz, 1H, H-1), 4.59(t, *J* = 5.7 Hz, 1H, OH-6), 3.88-3.78(m, 1H, O*CH*$_2$CH$_3$), 3.76-3.72(m, 1H, O*CH*$_2$CH$_3$), 3.70(s, 3H, OCH_3), 3.70-3.66(m, 1H, H-6a), 3.48-4.42(m, 1H, H-6b), 3.33-3.25(m, 2H, H-3 and H-5), 3.17-3.11(m, 1H, H-4), 3.05(t, *J* = 8.1 Hz, 1H, H-2), 1.11(t, *J* = 7.0 Hz, 1H, OCH_2*CH*$_3$). **^{13}C NMR:** (101 MHz, $CDCl_3$): ∂ = 154.4 (C *arom.*), 151.4 (C *arom.*), 117.4 (*arom.* 2xCH), 114.5 (*arom.* 2xCH), 101.4 (C-1), 81.6 (C-2), 76.9 (C-3/C-5), 75.8 (C-3/C-5), 69.9 (C-4), 67.3(O*CH*$_2$CH$_3$), 60.7 (C-6 CH_2), 55.4(OCH_3), 15.7(OCH_2*CH*$_3$). **HRMS (ESI):** m/z calcd for $C_{15}H_{22}O_7Na$ $[M+Na]^+$ 337.1263, found 337.1280.

1,2:5,6-di-*O*-isopropylidene-3-*O*-ethyl-α-D-glucofuranose (558): The title compound was synthesized according to a modified **General Procedure 8-5**. 1,2:5,6-di-*O*-isopropylidene-α-D-glucofuranose (**546**, 9.0 mmol, 1.0 eq) was dissolved in dry DMF (0.2 M) in a flame-dried flask under argon atmosphere. NaH (60 % dispersion in mineral oil) (18.3 mmol, 2.0 eq) was added portion-wise to the flask followed by drop-wise addition of ethyl iodide (27.4 mmol, 3.0 eq). The solution was stirred at room temperature for 18 h. Upon reaction completion the solution was diluted with DCM, quenched with water, and washed with brine. The organic layer was dried using Na_2SO_4, filtered, and concentrated *in vacuo*. The crude oil was purified by column chromatography (10 % EtOAc in Hexanes) and isolated as a clear oil (**82 %**).



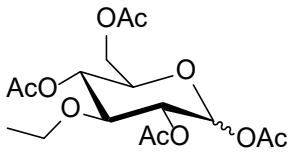
^{1}H NMR: (300 MHz, $CDCl_3$): ∂5.73(d, *J* = 3.7 Hz, 1H, H-1), 4.39(d, *J* = 3.6 Hz, 1H, H-2), 4.18-4.12(m, 1H), 3.99-3.90(m, 2H), 3.83(dd, *J* = 8.5, 5.8 Hz, 1H, H-6b), 3.72(d, *J* = 3.1 Hz, 1H), 3.59-3.35(m, 2H, O*CH*$_2$CH$_3$), 1.35(s, 3H, *isopropylidene* CH_3), 1.28(s, 3H, *isopropylidene* CH_3), 1.21(s, 3H, *isopropylidene* CH_3), 1.17(s, 3H, *isopropylidene* CH_3), 1.06(t, *J* = 7.0 Hz, 3H, OCH_2*CH*$_3$). **^{13}C NMR:** (101 MHz, $CDCl_3$): ∂ = 111.4 (C), 108.6 (C), 105.1 (C-1), 82.6, 81.8 (C-2), 80.9, 72.4, 67.0 (C-6 CH_2), 65.9 (O*CH*$_2$CH$_3$), 26.7 (*isopropylidene* CH_3), 26.6 (*isopropylidene* CH_3), 26.1 (*isopropylidene* CH_3), 25.2 (*isopropylidene* CH_3), 15.1 (OCH_2*CH*$_3$). **HRMS (ESI):** m/z calcd for $C_{14}H_{24}O_6Na$ $[M+Na]^+$ 311.1471, found 311.1445.

3-*O*-ethyl-D-glucopyranoside (560): 1,2:5,6-di-*O*-isopropylidene-3-*O*-ethyl-α-D-glucofuranose (**558**, 7.1 mmol, 1.0 eq) was dissolved in dH_2O (0.25 M). Amberlite IR120 H+ resin (washed with MeOH) (9.99 g) was added and the solution was stirred at 60 °C for 8 h. Following reaction completion, the solution was filtered and concentrated *in vacuo* to yield the product as a clear oil without further purification (**99 %**, α:β 1:1.5).

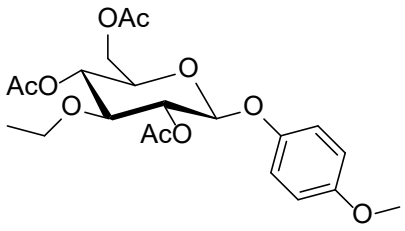


^{1}H NMR: (400 MHz, D_2O): ∂5.04(d, *J* = 2.5 Hz, 1H, H-1α), 4.47(d, *J* = 7.8 Hz, 1.5H, H-1β), 3.73-3.63(m, 8.5H), 3.60-3.51(m, 2.5H), 3.38-3.37(m, 2H), 3.31-3.24(m, 3.5H), 3.19-3.11(m, 1.5H), 3.09(dd, *J* = 9.3, 7.8 Hz, 1.5H), 1.05(t, *J* = 7.1 Hz, 8H, OCH_2CH_3 α and β). **^{13}C NMR:** (101 MHz, D_2O): ∂ = 95.8 (C-1 β), 92.1 (C-1 α), 83.9, 81.1, 75.8, 73.7, 71.5, 71.1, 69.21, 69.15, 68.8 (C-6 CH_2 α), 68.7 (C-6 CH_2 β), 60.6 (OCH_2CH_3 β), 60.4 (OCH_2CH_3 α), 14.7 (OCH_2CH_3 α and β). **HRMS (ESI):** m/z calcd for $C_8H_{16}O_6Na$ $[M+Na]^+$ 231.0845, found 230.8295.

1,2,4,6-tetra-*O*-acetyl-3-*O*-ethyl-D-glucopyranoside (562): The title compound was synthesized according to a modified **General Procedure 8-4**. 3-*O*-ethyl-D-glucopyranoside (**560**, 6.7 mmol, 1.0 eq) and NaOAc (21.2 mmol, 3.0 eq) were suspended in Ac_2O (46.5 mmol, 7.0 eq) in a flame-dried flask under argon. The solution was stirred at 100 °C for 1 h. Upon completion the reaction was cooled, diluted with DCM and washed with water. The organic phase was dried with Na_2SO_4, filtered, and concentrated *in vacuo*. The crude oil was purified by column chromatography (40 % EtOAc in Hexanes) and isolated as a white solid containing a mixture of alpha and beta products (**62 %**, α:β 1:3)

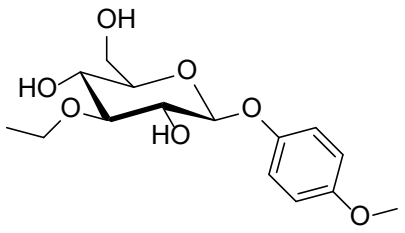


^{1}H NMR: (400 MHz, $CDCl_3$): ∂6.28(d, *J* = 3.7 Hz, 1H, H-1 α), 5.62(d, *J* = 8.3 Hz, 3H, H-1 β), 5.10-5.03(m, 7H), 4.97(dd, *J* = 10.0, 3.7 Hz, 1H, α), 4.24-4.18(m, 4H), 4.13-4.03(m, 4H), 3.99(ddd, *J* = 10.3, 4.4, 2.3 Hz, 1H, α), 3.77(d, *J* = 9.7 Hz, 1H, α), 3.75-3.65(m, 4H), 3.62-3.53(m, 10H), 2.15(s, 3H, OAc CH_3 α), 2.09(s, 12H, OAc CH_3 α and β), 2.08(s, 9H, OAc CH_3 β), 2.07(s, 12H, OAc CH_3 α and β), 2.06(s, 9H, OAc CH_3 β), 2.04(s, 3H, OAc CH_3 α), 1.09(t, *J* = 7.0 Hz, 12H, OCH_2CH_3 α and β). **^{13}C NMR:** (101 MHz, $CDCl_3$): ∂ = 170.89 (OAc C), 170.86 (OAc C), 169.7 (OAc C), 169.4 (OAc C), 169.34 (OAc C), 169.31 (OAc C), 169.2 (OAc C), 168.9 (OAc C), 92.1 (C-1 β), 89.6 (C-1 α), 80.2 (β), 73.1 (β), 71.5 (β), 71.3 (α), 70.3 (α), 69.2 (α), 69.0 (β), 68.3 (α), 67.8 (β), 61.9 (C-6 CH_2 β), 60.5 (C-6 CH_2 α), 21.01 (OAc CH_3), 20.99 (OAc CH_3), 20.87 (OAc CH_3), 20.86 (OAc CH_3), 20.85 (OAc CH_3), 20.7 (OAc CH_3), 15.8 (OCH_2CH_3 α), 15.7 (OCH_2CH_3 β). **HRMS (ESI):** m/z calcd for $C_{16}H_{24}O_{10}Na$ $[M+Na]^+$ 399.1267, found 399.1237.



(4-methoxyphenyl)-2,4,6-tri-*O*-acetyl-3-*O*-ethyl-β-D-glucopyranoside (564): The title compound was synthesized according to a modified **General Procedure 8-2**.[167,525] 1,2,4,6-tetra-*O*-acetyl-3-*O*-ethyl-β-D-glucopyranoside (**562**, 3.9 mmol, 1.0 eq) and 4-methoxyphenol (5.0 mmol, 1.2 eq) were dissolved in dry DCM (0.25 M) in a flame-dried flask under argon at 0 °C with 4 Å molecular sieves. Boron trifluoride diethyl etherate (46.5 % solution) (2.6 mL, 9.8 mmol, 2.5 eq) was added to the solution slowly. The solution was stirred overnight (18 h), diluted with DCM, and then quenched with sat. $NaHCO_3$. The solution was filtered through Celite®, and the organic layer was washed using sat. $NaHCO_3$, dH_2O, and brine. The organic layer was dried using Na_2SO_4, filtered, and concentrated *in vacuo*. The crude compound was purified by column chromatography (20 % EtOAc in Hexanes) to yield the final product as a white solid (**27 %**).

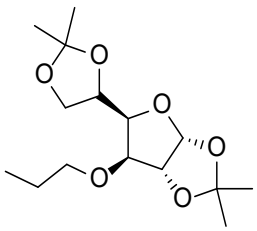
^{1}H NMR: (400 MHz, $CDCl_3$): ∂6.96-6.92(m, 2H, *arom.*), 6.82-6.78(m, 2H, *arom.*), 5.21(dd, *J* = 9.4, 8.0 Hz, 1H, H-2), 5.11(t, *J* = 9.6 Hz, 1H, H-4), 4.85(d, *J* = 7.9 Hz, 1H, H-1), 4.24(dd, *J* = 12.2, 5.6 Hz, 1H, H-6a), 4.15(dd, *J* = 12.2, 2.5 Hz, 1H, H-6b), 3.77(s, 3H, OCH_3), 3.70(ddd, *J* = 9.8, 5.6, 2.5 Hz. 1H, H-5), 3.65-3.57(m, 3H, H-3 and OCH_2CH_3), 2.12(s, 3H, OAc CH_3), 2.10(s, 3H, OAc CH_3), 2.07(s, 3H, OAc CH_3), 1.12(t, *J* = 7.0 Hz, 3H, OCH_2CH_3). **^{13}C NMR:** (101 MHz, $CDCl_3$): ∂ = 170.9 (OAc C), 169.4 (OAc C), 169.3 (OAc C), 155.7 (C *arom.*), 151.3 (C *arom.*), 118.7 (2xCH *arom.*), 114.6 (2xCH *arom.*), 100.7 (C-1), 80.2 (C-3), 72.38 (C-2/C-5), 72.36 (C-2/C-5), 69.5 (C-4), 67.4 (OCH_2CH_3), 62.5 (C-6 CH_2), 55.8 (OCH_3), 21.0 (OAc CH_3), 20.94 (OAc CH_3), 20.90 (OAc CH_3), 15.8 (OCH_2CH_3). **HRMS (ESI):** m/z calcd for $C_{21}H_{28}O_{10}Na$ $[M+Na]^+$ 463.1580, found 463.1588.



(4-methoxyphenyl)-3-*O*-ethyl-β-D-glucopyranoside (C_3 OEt, PMP-Glc, 101): The title compound was synthesized according to a modified **General Procedure 8-3**.[167,326] (4-methoxyphenyl)-2,4,6-tri-*O*-acetyl-3-*O*-ethyl-β-D-glucopyranoside (**564**, 0.9 mmol, 1.0 eq) was dissolved in MeOH (0.2 M) and a 1 M solution of NaOMe in MeOH (0.1 mmol, 0.1 eq) was added to the solution to stir for 1 hour. Upon reaction completion, Amberlite IR120 H+ resin (washed in MeOH) was added to a solution pH < 4. The solution was filtered, and the filtrate was concentrated *in vacuo* to yield the pure product a white powder (**81 %**).

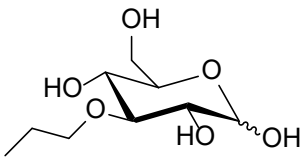
^{1}H NMR: (400 MHz, DMSO-*d*$_6$ with 1 % D_2O): ∂6.97-6.95(m, 2H, *arom.*), 6.84-6.82(m, 2H, *arom.*), 4.70(d, *J* = 7.7 Hz, 1H, H-1), 3.72-3.63(m, 3H, O*CH*$_2$CH$_3$ and H-6a + residual H_2O), 3.43(dd, *J* = 11.8, 5.7 Hz, 1H, H-6b), 3.29-3.10(m, 4H, H-2 and H-3 and H-4 and H-5), 1.10(t, *J* = 7.0 Hz, 3H, OCH$_2$*CH*$_3$). **^{13}C NMR:** (101 MHz, DMSO-*d*$_6$ with 1 % D_2O): ∂ = 154.7 (C *arom.*), 151.7 (C *arom.*), 118.1 (2xCH *arom.*), 114.8 (2xCH *arom.*), 101.8 (C-1), 84.9 (C-2/C-3/C-4/C-5), 77.1 (C-2/C-3/C-4/C-5), 73.2 (C-2/C-3/C-4/C-5), 69.6 (C-2/C-3/C-4/C-5), 67.9 (O*CH*$_2$CH$_3$), 60.9 (C-6 CH_2), 55.8 (OCH_3), 16.1 (OCH$_2$*CH*$_3$). **HRMS (ESI):** m/z calcd for $C_{15}H_{22}O_7Na$ $[M+Na]^+$ 337.1263, found 337.1277.

1,2:5,6-di-*O*-isopropylidene-3-*O*-propyl-α-D-glucofuranose (559): The title compound was synthesized according to a modified **General Procedure 8-5**. 1,2:5,6-di-*O*-isopropylidene-α-D-glucofuranose (**546**, 7.9 mmol, 1.0 eq) was dissolved in dry DMF (0.2 M) in a flame-dried flask under argon atmosphere. NaH (60 % dispersion in mineral oil) (15.5 mmol, 2.0 eq) was added portion-wise to the flask followed by drop-wise addition of propyl iodide (23.7 mmol, 3.0 eq). The solution was stirred at room temperature for 18 h. Upon reaction completion the solution was diluted with DCM, quenched with water, and washed with brine. The organic layer was dried using Na_2SO_4, filtered, and concentrated *in vacuo*. The crude oil was purified by column chromatography (10 % EtOAc in Hexanes) and isolated as a clear oil (**46 %**).



^{1}H NMR: (300 MHz, $CDCl_3$): ∂5.82(d, *J* = 3.6 Hz, 1H, H-1), 4.48(d, *J* = 3.9 Hz, 1H, H-2), 4.30-4.23(m, 1H), 4.10-4.00(m, 2H), 3.93(dd, *J* = 8.4, 6.0 Hz, 1H, H-6b), 3.80(d, *J* = 3.0 Hz, 1H), 3.56-3.39(m, 2H, O*CH*$_2$CH$_2$CH$_3$), 1.53(s, *J* = 6.4 Hz, 3H, OCH$_2$*CH*$_2$CH$_3$), 1.44(s, 3H, *isopropylidene* CH_3), 1.37(s, 3H, *isopropylidene* CH_3), 1.29(s, 3H, *isopropylidene* CH_3), 1.26(s, 3H, *isopropylidene* CH_3), 0.87(t, *J* = 7.4 Hz, 3H, OCH$_2$CH$_2$*CH*$_3$). **^{13}C NMR:** (101 MHz, $CDCl_3$): ∂ = 111.7 (C), 108.8 (C), 105.3 (C-1), 82.6, 82.1 (C-2), 81.2, 72.5, 72.3 (O*CH*$_2$CH$_2$CH$_3$), 67.2 (C-6 CH_2), 26.9 (*isopropylidene* CH_3), 26.8 (*isopropylidene* CH_3), 26.3 (*isopropylidene* CH_3), 25.4 (*isopropylidene* CH_3), 23.0 (OCH$_2$*CH*$_2$CH$_3$), 10.6 (OCH$_2$CH$_2$*CH*$_3$). **HRMS (ESI):** m/z calcd for $C_{15}H_{26}O_6Na$ $[M+Na]^+$ 325.1640, found 325.1606.

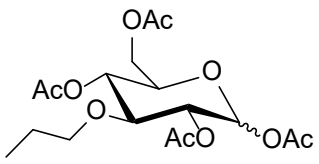
3-*O*-propyl-D-glucopyranoside (561): 1,2:5,6-di-*O*-isopropylidene-3-*O*-propyl-α-D-glucofuranose (**559**, 3.5 mmol, 1.0 eq) was dissolved in dH_2O (0.25 M). Amberlite IR120 H+ resin (washed with MeOH) (5.37 g) was added and the solution was stirred at 60 °C for 8 h. Following reaction



completion, the solution was filtered and concentrated *in vacuo* to yield the product as a clear oil (**99 %**, α:β 1:1.6).

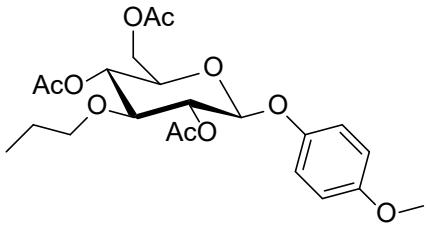
^{1}H NMR: (400 MHz, D_2O): ∂5.04(d, *J* = 2.7 Hz, 1H, H-1 α), 4.47(d, *J* = 7.7 Hz, 1H, H-1 β), 3.74-3.52(m, 8H), 3.42-3.26(m, 6H), 3.21-3.16(m, 1H, H-3 β), 3.11(dd, *J* = 9.3, 7.8 Hz, 1H, H-2 β), 1.48(sxt, *J* = 7.2 Hz, 4H, $OCH_2CH_2CH_3$ α and β), 0.77(t, *J* = 7.4 Hz, 6H, $OCH_2CH_2CH_3$ α and β). **^{13}C NMR:** (101 MHz, D_2O): ∂ = 95.9 (C-1 β), 92.1 (C-1 α), 84.0 (β), 81.3 (α), 75.9 (β), 75.1 ($OCH_2CH_2CH_3$ α), 74.9 ($OCH_2CH_2CH_3$ β), 73.7 (β), 71.5 (α), 71.1 (α), 69.2 (α), 69.1 (β), 60.6 (C-6 CH_2 β), 60.5 (C-6 CH_2 α), 22.6 ($OCH_2CH_2CH_3$ α and β), 9.7 ($OCH_2CH_2CH_3$ α and β). **HRMS (ESI):** m/z calcd for $C_9H_{18}O_6Na$ $[M+Na]^+$ 245.1101, found 245.1107.

1,2,4,6-tetra-*O*-acetyl-3-*O*-propyl-D-glucopyranoside (563): The title compound was synthesized according to a modified **General Procedure 8-4**. 3-*O*-propyl-D-glucopyranoside (**561**, 3.7 mmol, 1.0 eq) and NaOAc (11.5 mmol, 3.0 eq) were suspended in Ac_2O (25.4 mmol, 7.0 eq) in a flame-dried flask under argon. The solution was stirred at 100 °C for 1 h. Upon completion the reaction was cooled, diluted with DCM and washed with water. The organic phase was dried with Na_2SO_4, filtered, and concentrated *in vacuo*. The crude oil was purified by column chromatography (40 % EtOAc in Hexanes) and isolated as a white solid containing a mixture of alpha and beta products (**70 %**, α:β 1:4)



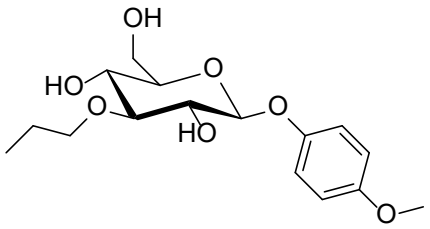
^{1}H NMR: (400 MHz, $CDCl_3$): ∂6.27(d, *J* = 3.6 Hz, 1H, H-1 α), 5.63(d, *J* = 8.3 Hz, 4H, H-1 β), 5.11-5.05(m, 9H), 4.99(dd, *J* = 10.0, 3.7 Hz, 1H, α), 4.24-4.18(m, 5H), 4.13-4.03(m, 5H), 3.99(ddd, *J* = 10.3, 4.3, 2.2 Hz, 1H, α), 3.78-3.69(m, 5H), 3.59-3.53(m, 5H), 3.51-3.47(m, 9H), 2.16(s, 3H, OAc CH_3 α), 2.09(s, 12H, OAc CH_3 β), 2.07(s, 15H, OAc CH_3 α and β), 2.06(s, 24H, OAc CH_3 2xβ), 2.04(s, 3H, 3H, OAc CH_3 α), 2.03(s, 3H, OAc CH_3 α), 1.48(sxt, *J* = 6.6 Hz, 10H, $OCH_2CH_2CH_3$ α and β), 0.85(t, *J* = 7.3 Hz, 3H, $OCH_2CH_2CH_3$ α), 0.83(t, *J* = 7.4 Hz, 12H, $OCH_2CH_2CH_3$ β). **^{13}C NMR:** (101 MHz, $CDCl_3$): ∂ = 171.3 (OAc C), 170.91 (OAc C), 170.88 (OAc C), 169.7 (OAc C), 169.41 (OAc C), 169.36 (OAc C), 169.3 (OAc C), 169.2 (OAc C), 168.9 (OAc C), 92.1 (C-1 β), 89.6 (C-1 α), 80.4 (β), 77.1 (α), 74.8 ($OCH_2CH_2CH_3$ α), 74.3 ($OCH_2CH_2CH_3$ β), 73.1 (β), 71.6 (β), 71.4 (α), 70.4 (α), 69.2 (α), 69.1 (β), 61.9 (C-6 CH_2 β), 60.5 (C-6 CH_2 α), 23.5 ($OCH_2CH_2CH_3$ α), 23.4 ($OCH_2CH_2CH_3$ β), 21.2 (OAc CH_3), 21.03 (OAc CH_3), 21.00 (OAc CH_3), 20.91 (OAc CH_3), 20.87 (OAc CH_3), 20.8 (OAc CH_3), 10.6 ($OCH_2CH_2CH_3$ α), 10.5 ($OCH_2CH_2CH_3$ β). **HRMS (ESI):** m/z calcd for $C_{17}H_{26}O_{10}Na$ $[M+Na]^+$ 413.1424, found 413.1454.

(4-methoxyphenyl)-2,4,6-tri-*O*-acetyl-3-*O*-propyl-β-D-glucopyranoside (565): The title compound was synthesized according to a modified **General Procedure 8-2**.[167,525] 1,2,4,6-tetra-*O*-acetyl-3-*O*-propyl-β-D-glucopyranoside (**563**, 2.0 mmol, 1.0 eq) and 4-methoxyphenol (3.1 mmol, 1.5 eq) were dissolved in dry DCM (0.25 M) in a flame-dried flask under argon at 0 °C with 4 Å molecular sieves. Boron trifluoride diethyl etherate (46.5 % solution) (4.9 mmol, 2.5 eq) was added to the solution slowly. The solution was stirred overnight (18 h), diluted with DCM, and then quenched with sat. $NaHCO_3$. The solution was filtered through Celite®, and the organic layer was washed using sat. $NaHCO_3$, dH_2O, and brine. The organic layer was dried using Na_2SO_4, filtered, and concentrated *in vacuo*. The crude compound was purified by column chromatography (20 % EtOAc in Hexanes) to yield the final product as a white solid (**27 %**).



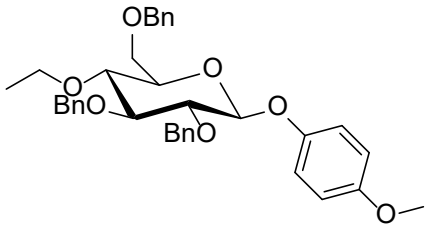
^{1}H NMR: (400 MHz, $CDCl_3$): ∂6.96-6.92(m, 2H, *arom.*), 6.82-6.78(m, 2H, *arom.*), 5.22(dd, *J* = 9.5, 7.9 Hz, 1H, H-2), 5.12(t, *J* = 9.6 Hz, 1H, H-4), 4.85(d, *J* = 7.9 Hz, 1H, H-1), 4.24(dd, *J* = 12.1, 5.6 Hz, 1H, H-6a), 4.15(dd, *J* = 12.2, 2.6 Hz, 1H, H-6b), 3.77(s, 3H, OCH_3), 3.70(ddd, *J* = 9.9, 5.6, 2.6 Hz. 1H, H-5), 3.59(t, *J* = 9.3 Hz, 1H, H-3), 3.54-3.49(m, 2H, $OCH_2CH_2CH_3$), 2.12(s, 3H, OAc CH_3), 2.10(s, 3H, OAc CH_3), 2.07(s, 3H, OAc CH_3), 1.50(sxt, *J* = 7.3 Hz, 2H, $OCH_2CH_2CH_3$), 1.12(t, *J* = 7.4 Hz, 3H, $OCH_2CH_2CH_3$). **^{13}C NMR:** (101 MHz, $CDCl_3$): ∂ = 170.9 (OAc C), 169.4 (OAc C), 169.3 (OAc C), 155.7 (C *arom.*), 151.3 (C *arom.*), 118.7 (2xCH *arom.*), 114.6 (2xCH *arom.*), 100.7 (C-1), 80.4 (C-3), 73.9 ($OCH_2CH_2CH_3$), 72.5 (C-2/C-5), 72.4 (C-2/C-5), 69.6 (C-4), 62.5 (C-6 CH_2), 55.8 (OCH_3), 23.5 ($OCH_2CH_2CH_3$), 21.03 (OAc CH_3), 20.97 (OAc CH_3), 20.91 (OAc CH_3), 10.6 ($OCH_2CH_2CH_3$). **HRMS (ESI):** m/z calcd for $C_{22}H_{30}O_{10}Na$ $[M+Na]^+$ 477.1737, found 477.1708.

(4-methoxyphenyl)-3-*O*-propyl-β-D-glucopyranoside (C_3 OPr PMP-Glc, 102): The title compound was synthesized according to a modified **General Procedure 8-3**.[167,326] (4-methoxyphenyl)-2,4,6-tri-*O*-acetyl-3-*O*-propyl-β-D-glucopyranoside (**565**, 0.6 mmol, 1.0 eq) was dissolved in MeOH (0.2 M) and a 1 M solution of NaOMe in MeOH (0.1 mmol, 0.2 eq) was added to the solution to stir for 2.5 hours. Upon reaction completion, Amberlite IR120 H+ resin (washed in MeOH) was added to a solution pH < 4. The solution was filtered, and the filtrate was concentrated *in vacuo* and then lyophilized to yield the pure product a white powder (**29 %**).



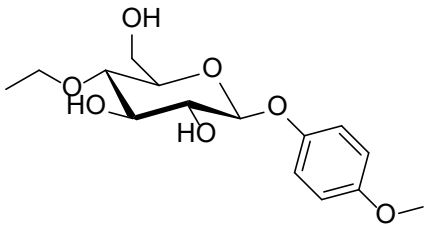
^{1}H NMR: (400 MHz, DMSO-d_6 with 1 % D_2O): ∂6.99-6.95(m, 2H, *arom.*), 6.85-6.81(m, 2H, *arom.*), 4.70(d, *J* = 7.8 Hz, 1H, H-1), 3.72-3.63(m, 3H, O*CH*$_2$CH$_2$CH$_3$ and H-6a + residual H_2O), 3.43(dd, *J* = 11.9, 5.7 Hz, 1H, H-6b), 3.28-3.10(m, 4H, H-2 and H-3 and H-4 and H-5), 1.51(sxt, *J* = 7.2 Hz, 2H, OCH$_2$*CH*$_2$CH$_3$), 0.85(t, *J* = 7.4 Hz, 3H, OCH$_2$CH$_2$*CH*$_3$). **^{13}C NMR:** (101 MHz, DMSO-d_6 with 1 % D_2O): ∂ = 154.6 (C *arom.*), 151.7 (C *arom.*), 117.9 (2xCH *arom.*), 114.7 (2xCH *arom.*), 101.7 (C-1), 85.0 (C-2/C-3/C-4/C-5), 77.0 (C-2/C-3/C-4/C-5), 74.1 (O*CH*$_2$CH$_2$CH$_3$), 73.1 (C-2/C-3/C-4/C-5), 69.5 (C-2/C-3/C-4/C-5), 60.7 (C-6 CH_2), 55.6 (OCH_3), 23.3 (OCH$_2$*CH*$_2$CH$_3$), 10.7 (OCH$_2$CH$_2$*CH*$_3$). **HRMS (ESI):** m/z calcd for $C_{16}H_{24}O_7Na$ $[M+Na]^+$ 351.1420, found 351.1392.

(4-methoxyphenyl)-2,3,6-tri-*O*-benzyl-4-*O*-ethyl-β-D-glucopyranoside (566): The title compound was synthesized according to a modified **General Procedure 8-5**. (4-methoxyphenyl)-2,3,6-tri-*O*-benzyl-β-D-glucopyranoside (**553**, 0.97 mmol, 1.0 eq) was dissolved in dry DMF (0.1 M) in a flame-dried flask under argon atmosphere. NaH (60 % dispersion in mineral oil) (3.5 mmol, 3.5 eq) was added portion-wise to the flask followed by drop-wise addition of EtI (3.7 mmol, 4.0 eq). The solution was stirred at room temperature for 18 h. Upon reaction completion the solution was diluted with DCM, quenched with water, and washed with brine. The organic layer was dried using Na_2SO_4, filtered, and concentrated *in vacuo*. The pure product was isolated as a colourless clear oil (**60 %**).



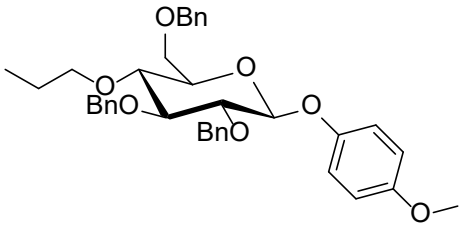
^{1}H NMR: (500 MHz, $CDCl_3$): ∂7.36-7.27(m, 15H, *arom.*), 7.05-7.01(m, 2H, *arom.*), 6.82-6.79(m, 2H, *arom.*), 5.03(d, *J* = 10.9 Hz, 1H, OBn CH_2), 4.90(d, *J* = 10.9 Hz, 1H, OBn CH_2), 4.86(d, *J* = 7.5 Hz, 1H, H-1), 4.81(d, *J* = 11.0 Hz, 2H, OBn CH_2), 4.63(d, *J* = 12.0 Hz, 1H, OBn CH_2), 4.56(d, *J* = 12.0 Hz, 1H, OBn CH_2), 3.87-3.78(m, 5H, H-3 and *CH*$_2$CH$_3$ and OCH_3), 3.71-3.55(m, 4H, H-2 and H-4 and H-6a and *CH*$_2$CH$_3$), 3.51(ddd, *J* = 9.9, 5.3, 1.9 Hz, 1H, H-5), 3.43(dd, *J* = 9.6, 8.5 Hz, 1H, H-6b), 1.13(t, *J* = 7.1 Hz, 3H, CH$_2$*CH*$_3$). **^{13}C NMR:** (125 MHz, $CDCl_3$): ∂ = 155.4 (C PMP *arom.*), 151.7 (C PMP *arom.*), 138.7 (C OBn *arom.*), 138.5 (C OBn *arom.*), 138.4 (C OBn *arom.*), 128.53 (*arom.* 2xCH), 128.52 (*arom.* 2xCH), 128.4 (*arom.* 2xCH), 128.3 (*arom.* 2xCH), 128.0 (*arom.* 2xCH), 127.9 (*arom.* CH), 127.83 (*arom.* 2xCH), 127.78 (*arom.* CH), 127.7 (*arom.* CH), 118.6 (*arom.* 2xCH), 114.7 (*arom.* 2xCH), 102.9 (C-1), 84.7 (C-2/C-3/C-4), 82.1 (C-2/C-3/C-4), 78.2 (C-2/C-3/C-4), 75.9 (OBn CH_2), 75.4 (C-5), 75.2 (OBn CH_2), 73.6

(OBn CH_2), 69.1 (C-6 CH_2/O*CH_2*CH_3), 68.6 (C-6 CH_2/O*CH_2*CH_3), 55.8(OCH_3), 15.6 (OCH_2*CH_3*). **HRMS (ESI):** m/z calcd for $C_{36}H_{40}O_7Na$ $[M+Na]^+$ 607.2672, found 607.2686.



(4-methoxyphenyl)-4-*O*-ethyl-β-D-glucopyranoside (C_4 OEt PMP-Glc, 103): The title compound was synthesized according to a modified **General Procedure 8-7**. To a solution of (4-methoxyphenyl)-2,3,6-tri-*O*-benzyl-4-*O*-ethyl-β-D-glucopyranoside (**566**, 0.5 mmol, 1.0 eq) in a 1:1 mixture of EtOAc and MeOH (5.4 mL, 0.1 M), Pd/C (10 mol %) (0.06 mmol, 0.1 eq) was added and the reaction mixture was purged several times with H_2. The mixture was stirred under H_2 atmosphere for 5.5 h, filtered over Celite® and the volatiles were evaporated to afford the desired product as a white powder (**98 %**).

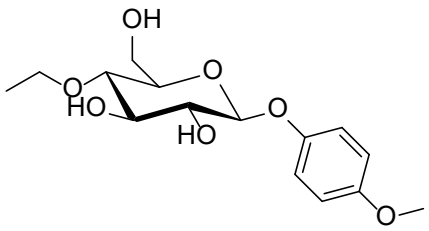
^{1}H NMR: (500 MHz, DMSO-d_6): ∂6.98-6.96(m, 2H, *arom.*), 6.85-6.84(m, 2H, *arom.*), 5.31(d, *J* = 5.1 Hz, 1H, OH-2), 5.15(d, *J* = 5.4 Hz, 1H, OH-3), 4.72(d, *J* = 7.8 Hz, 1H, H-1), 4.65(t, *J* = 6.2 Hz, 1H, OH-6), 3.83-3.77(m, 1H, O*CH_2*CH_3), 3.70(s, 3H, OCH_3), 3.63(ddd, *J* = 11.2, 4.6, 1.6 Hz, 1H, H-6a), 3.59-3.53(m, 1H, *CH_2*CH_3), 3.51-3.46(m, 1H, H-6b), 3.38-3.34(m, 1H, H-3), 3.31-3.28(m, 1H, H-5), 3.22-3.17(m, 1H, H-2), 3.09(t, *J* = 9.4 Hz, 1H, H-4), 1.09(t, *J* = 7.0 Hz, 3H, OCH_2*CH_3*). **^{13}C NMR:** (125 MHz, DMSO-d_6): ∂ = 154.3 (C *arom.*), 151.4 (C *arom.*), 117.5 (*arom.* 2xCH), 114.4 (*arom.* 2xCH), 101.2 (C-1), 77.5 (C-4), 76.4 (C-3), 75.7 (C-5), 73.5 (C-2), 67.0 (O*CH_2*CH_3), 60.2 (C-6 CH_2), 55.3 (OCH_3), 15.7 (OCH_2*CH_3*). **HRMS (ESI):** m/z calcd for $C_{15}H_{22}O_7Na$ $[M+Na]^+$ 337.1263, found 337.1259.



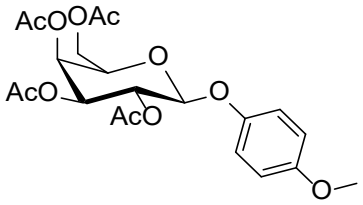
(4-methoxyphenyl)-2,3,6-tri-*O*-benzyl-4-*O*-propyl-β-D-glucopyranoside (567): The title compound was synthesized according to a modified **General Procedure 8-5**. (4-methoxyphenyl)-2,3,6-tri-*O*-benzyl-β-D-glucopyranoside (**553**, 0.8 mmol, 1.0 eq) was dissolved in dry DMF (0.1 M) in a flame-dried flask under argon atmosphere. NaH (60 % dispersion in mineral oil) (1.6 mmol, 2.0 eq) was added portion-wise to the flask followed by drop-wise addition of PrI (3.1 mmol, 4.0 eq). The solution was stirred at room temperature for 18 h. Upon reaction completion the solution was diluted with DCM, quenched with water, and extracted with brine. The organic layer was dried using Na_2SO_4, filtered, and concentrated *in vacuo*. The pure product was isolated as a colourless clear oil (**39 %**).

^{1}H NMR: (500 MHz, $CDCl_3$): ∂7.37-7.27(m, 15H, *arom.*), 7.07-7.04(m, 2H, *arom.*), 6.84-6.80(m, 2H, *arom.*), 5.05(d, *J* = 11.0 Hz, 1H, OBn CH_2), 4.92(d, *J* = 10.9 Hz, 1H, OBn CH_2), 4.89(d, *J* = 7.5 Hz, 1H, H-1), 4.82(d, *J* = 10.9 Hz, 1H, OBn CH_2), 4.81(d, *J* = 10.7 Hz, 1H, OBn CH_2), 4.64(d, *J* = 12.0 Hz, 1H, OBn CH_2), 4.58(d, *J* = 12.0 Hz, 1H, OBn CH_2), 3.82(dd, *J* = 10.8, 1.9 Hz, 1H, H-6a), 3.80-3.76(m, 4H, O*CH*$_2$$CH_2CH_3$ and OCH_3), 3.73-3.62(m, 3H, H-2 and H-3 and H-6b), 3.54(ddd, *J* = 9.9, 5.4, 1.9 Hz, 1H, H-5), 3.49-3.43(m, 2H, H-4 and O*CH*$_2$$CH_2CH_3$), 1.53(sxt, *J* = 6.9 Hz, 2H, OCH_2*CH*$_2$$CH_3$), 0.87(t, *J* = 7.4 Hz, 3H, OCH_2CH_2*CH*$_3$). **^{13}C NMR:** (125 MHz, $CDCl_3$): ∂ = 155.4 (C PMP *arom.*), 151.7 (C PMP *arom.*), 138.7 (C OBn *arom.*), 138.5 (C OBn *arom.*), 138.4 (C OBn *arom.*), 128.51 (*arom.* 2xCH), 128.49 (*arom.* 2xCH), 128.4 (*arom.* 2xCH), 128.3 (*arom.* 2xCH), 128.0 (*arom.* 2xCH), 127.84 (*arom.* CH), 127.83 (*arom.* 2xCH), 127.74 (*arom.* CH), 127.67 (*arom.* CH), 118.5 (*arom.* 2xCH), 114.7 (*arom.* 2xCH), 102.9 (C-1), 84.8 (C-2/C-3), 82.1 (C-2/C-3), 78.2 (C-4), 75.8 (OBn CH_2), 75.4 (C-5), 75.2 (OBn CH_2), 74.9 (OBn CH_2), 73.6 (O*CH*$_2$$CH_2CH_3$), 69.1 (C-6 CH_2), 55.8 (OCH_3), 23.6(OCH_2*CH*$_2$$CH_3$), 10.7 ($OCH_2CH_2$*CH*$_3$). **HRMS (ESI):** m/z calcd for $C_{37}H_{42}O_7Na$ $[M+Na]^+$ 621.2828, found 621.2802.

(4-methoxyphenyl)-4-*O*-propyl-β-D-glucopyranoside (C$_4$ OPr PMP-Glc, 104): The title compound was synthesized according to a modified **General Procedure 8-7**. To a solution of (4-methoxyphenyl)-2,3,6-tri-*O*-benzyl-4-*O*-propyl-β-D-glucopyranoside (**567**, 0.3 mmol, 1.0 eq) in a 1:1 mixture of EtOAc and MeOH (2.6 mL, 0.1 M), Pd/C (10 mol %) (0.02 mmol, 0.07 eq) was added and the reaction mixture was purged several times with H_2. The mixture was stirred under H_2 atmosphere for 3.5 h, filtered over Celite® and the volatiles were evaporated to afford the desired product as a white powder (**99 %**).



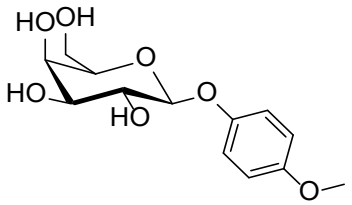
^{1}H NMR: (500 MHz, DMSO-*d*$_6$): ∂6.98-6.95(m, 2H, *arom.*), 6.86-6.83(m, 2H, *arom.*), 5.33(d, *J* = 4.9 Hz, 1H, OH-2), 5.15(d, *J* = 5.5 Hz, 1H, OH-3), 4.72(d, *J* = 7.8 Hz, 1H, H-1), 4.64(t, *J* = 6.1 Hz, 1H, OH-6), 3.77-3.73(m, 1H, O*CH*$_2$$CH_2CH_3$), 3.70(s, 3H, OCH_3), 3.64(ddd, *J* = 11.4, 4.5, 1.4 Hz, 1H, H-6a), 3.51-3.42(m, 2H, O*CH*$_2$$CH_2CH_3$ and H-6b), 3.40-3.35(m, 1H, H-5), 3.30(dd, *J* = 5.0, 1.8 Hz, 1H, H-3), 3.21-3.17(m, 1H, H-2), 3.09(t, *J* = 9.3 Hz, 1H, H-4), 1.49(sxt, *J* = 7.2 Hz, 2H, OCH_2*CH*$_2$$CH_3$), 0.85(t, *J* = 7.4 Hz, 3H, OCH_2CH_2*CH*$_3$). **^{13}C NMR:** (125 MHz, DMSO-*d*$_6$): ∂ = 154.2 (C *arom.*), 151.4 (C *arom.*), 117.5 (*arom.* 2xCH), 114.4 (*arom.* 2xCH), 101.2 (C-1), 77.6 (C-4), 76.4 (C-5), 75.7 (C-3), 73.5 (C-2), 73.4 (O*CH*$_2$$CH_2CH_3$), 60.3 (C-6 CH_2), 55.3 (OCH_3), 23.0 (OCH_2*CH*$_2$$CH_3$), 10.5 ($OCH_2CH_2$*CH*$_3$). **HRMS (ESI):** m/z calcd for $C_{16}H_{24}O_7Na$ $[M+Na]^+$ 351.1420, found 351.1398.



(4-methoxyphenyl)-2,3,4,6-tetra-*O*-acetyl-β-D-galactopyranoside (569): The title compound was synthesized according to a modified **General Procedure 8-2**.[167,525] β-D-galactose pentaacetate (**568**, 4.4 mmol, 1.0 eq) and 4-methoxyphenol (5.3 mmol, 1.2 eq) were dissolved in dry DCM (0.25 M) in a flame dried flask under argon at 0 ºC with 4 Å molecular sieves (powdered). Boron trifluoride diethyl etherate (46.5 % solution) (9.5 mmol, 2.25 eq) was added to the solution slowly. The solution was stirred overnight (18 h) and then quenched with sat. $NaHCO_3$ upon reaction completion. The solution was diluted in DCM, filtered through a Celite® pad, and then washed using sat. $NaHCO_3$, H_2O, and brine. The organic layers were dried using Na_2SO_4, filtered, and concentrated *in vacuo*. The crude yellow oil was purified by column chromatography (30 % EtOAc in hexanes) to obtain the final product as a white solid (**83 %**).

Characterization was consistent with that found in literature.[538]

^{1}H NMR: (600 MHz, $CDCl_3$) ∂6.96-6.94(m, 2H, *arom.*), 6.83-6.80(m, 2H, *arom.*), 5.47-5.43(m, 2H), 5.09(dd, *J* = 10.5, 3.5 Hz, 1H), 4.91(d, *J* = 8.0 Hz, 1H, H-1), 4.23(dd, *J* = 11.4, 6.8 Hz, 1H, H-6a), 4.15(dd, *J* = 11.4, 6.6 Hz, 1H, H-6b), 4.00(dt, *J* = 6.7, 1.0 Hz, 1H, H-5), 3.77(s, 3H, OCH_3), 2.18(s, 3H, OAc CH_3), 2.08(s, 3H, OAc CH_3), 2.05(s, 3H, OAc CH_3), 2.01(s, 3H, OAc CH_3). **^{13}C NMR** (151 MHz, $CDCl_3$): ∂ = 170.5 (OAc C), 170.4 (OAc C), 170.3 (OAc C), 169.5 (OAc C), 155.9 (C *arom.*), 151.2 (C *arom.*), 118.8 (2xCH *arom.*), 114.7 (2xCH *arom.*), 101.0 (C-1), 71.1, 71.0, 68.9, 67.0, 61.4, 55.8, 20.9 (OAc CH_3), 20.81 (OAc CH_3), 20.80 (OAc CH_3), 20.7 (OAc CH_3).



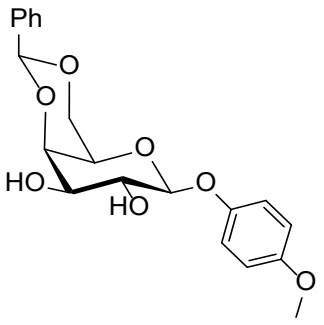
(4-methoxyphenyl)-β-D-galactopyranoside (PMP-Gal, 107): The title compound was synthesized according to **General Procedure 8-3**.[167,326] (4-methoxyphenyl)-2,3,4,6-tetra-*O*-acetyl-β-D-glucopyranoside (**569**, 10.5 mmol, 1.0 eq) was dissolved in MeOH (0.2 M) and a 1 M solution of NaOMe in MeOH (1.0 mmol, 0.1 eq) was added to the solution to stir for 2 hours. Upon reaction completion, Amberlite IR120 H+ resin (washed in MeOH) was added to a pH < 4. The solution was filtered, and the filtrate was concentrated *in vacuo*. The product was recrystallized from 99 % EtOH to yield the final product as a white powder (**87 %**).

Characterization was consistent with that found in literature.[557]

^{1}H NMR: (600 MHz, D_2O*) ∂*7.10-7.07(m, 2H, *arom.*), 6.96-6.93(m, 2H, *arom.*), 4.91 (d, *J* = 7.4 Hz, 1H, H-1), 3.95(d, *J* = 3.2 Hz, 1H), 3.80-3.67(m, 9H).

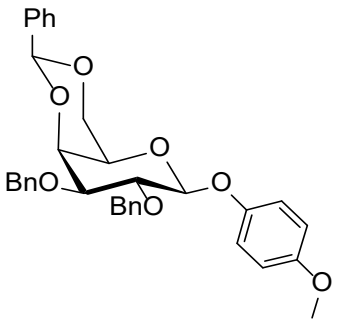
^{1}H NMR: (600 MHz, DMSO-d_6*)* ∂6.99-6.96(m, 2H, *arom.*), 6.86-6.83(m, 2H, *arom.*), 5.10(d, *J* = 5.1 Hz, 1H, OH-2), 4.80(d, *J* = 5.7 Hz, 1H, OH-3), 4.66(d, *J* = 7.7 Hz, 1H, H-1), 4.62(t, *J* = 5.4 Hz, 1H, OH-6), 4.45(d, *J* = 4.7 Hz, 1H, OH-4), 3.70(s, 3H, OCH_3), 3.69-3.67(m, 1H, H-4), 3.58-3.46(m, 4H, H-2 and H-5 and H-6), 3.39-3.36(m, 1H, H-3). **^{13}C NMR:** (101 MHz, DMSO-d_6) ∂ = 154.2 (C *arom.*), 151.6 (C *arom.*), 117.6 (2xCH *arom.*), 114.4 (2xCH *arom.*), 102.1 (C-1), 75.4 (C-2/C-5), 73.3 (C-3), 70.4 (C-2/C-5), 68.1 (C-4), 60.4 (C-6 CH_2), 55.3 (OCH_3).

(4-methoxyphenyl)-4,6-*O*-benzylidene-β-D-galactopyranoside (572): To a solution of (4-methoxyphenyl)-β-D-galactopyranoside (**107**, 20.4 mmol, 1.0 eq) in acetonitrile (0.175 M) was added benzaldehyde dimethyl acetal (40.5 mmol, 2.0 eq) and *p*-toluene sulfonic acid (1.8 mmol, 0.1 eq) to a flame-dried flask under argon. The reaction mixture was stirred at 60 °C for 30 min then was filtered. The filtrate was dried to a white solid and used in the next step without further purification. The filtrate can be dried and purified by recrystallization from EtOAc/hexanes if necessary.



Characterization was consistent with that found in literature.[558]

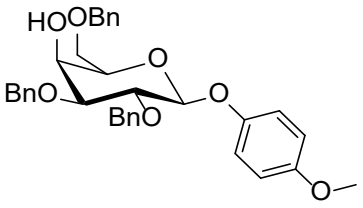
^{1}H NMR: (600 MHz, $CDCl_3$): ∂7.54-7.51(m, 2H, OPh *arom.*), 7.40-7.37(m, 3H, OPh *arom.*), 7.08-7.06(m, 2H, *arom.*), 6.84-6.81(m, 2H, *arom.*), 5.58(s, 1H, benzylidene CH), 4.79(d, *J* = 7.8 Hz, 1H, H-1), 4.37(dd, *J* = 12.5, 1.4 Hz, 1H, H-6a), 4.27(dd, *J* = 3.8, 1.0 Hz, 1H, H-6a), 4.11(dd, *J* = 12.5, 1.6 Hz, 1H, H-6a), 4.01(dd, *J* = 9.4, 7.9 Hz, 1H, H-6a), 3.78(s, 3H, OCH_3), 3.77(dd, *J* = 9.7, 3.9 Hz, 1H, H-6a), 3.59-3.57(m, 1H, H-2), 1.92(br s, 2H, OH-2 and OH-3).



(4-methoxyphenyl)-2,3-di-*O*-benzyl-4,6-*O*-benzylidene-β-D-galactopyranoside (573): The title compound was synthesized according to **General Procedure 8-6**. (4-methoxyphenyl)-4,6-*O*-benzylidene-β-D-galactopyranoside (**572**) was dissolved in DMF (0.2 M) was added NaH (60 % dispersion in mineral oil) (40.0 mmol, 2.0 eq) portion-wise at 0 °C to a flame-dried flask under argon. Benzyl bromide (61.5 mmol, 3.0 eq) was then added slowly and the reaction mixture was stirred for 2 h at room temperature. Following reaction completion, the reaction was diluted slowly with DCM and dH_2O. The organic phase was washed with dH_2O and brine. The organic layer was dried using Na_2SO_4, filtered, and concentrated *in vacuo*. The crude residue was purified over a silica pad (DCM) to afford the desired purified product as a white solid (**46 %, 2 steps**).

Characterization was consistent with that found in literature.[559]

^{1}H NMR: (600 MHz, $CDCl_3$): ∂7.60-7.57(m, 2H, OBn *arom.*), 7.41-7.27(m, 13H, OBn *arom.*), 7.08-7.05(m, 2H, *arom.*), 6.83-6.80(m, 2H, *arom.*), 5.52(s, 1H, benzylidene CH), 5.00(d, *J* = 10.8 Hz, 1H, OBn CH_2), 4.89(d, *J* = 6.8 Hz, 1H, H-1), 4.87(d, *J* = 9.7 Hz, 1H, OBn CH_2), 4.81(d, *J* = 12.4 Hz, 1H, OBn CH_2), 4.77(d, *J* = 12.3 Hz, 1H, OBn CH_2), 4.33(dd, *J* = 12.3, 1.7 Hz, 1H, H-6a), 4.16(d, *J* = 3.5 Hz, 1H, H-4), 4.11(dd, *J* = 9.7, 7.8 Hz, 1H, H-2), 4.04(dd, *J* = 12.3, 1.7 Hz, 1H, H-6b), 3.78(s, 3H, OCH_3), 3.64(dd, *J* = 9.4, 3.5 Hz, 1H, H-3), 3.42-3.41(m, 1H, H-5). **^{13}C NMR:** (151 MHz, $CDCl_3$): ∂ = 155.5 (C *arom.*), 151.8 (C *arom.*), 138.8 (C OBn *arom.*), 138.5 (C OBn *arom.*), 137.9 (C OBn *arom.*), 129.1 (*arom.* CH), 128.5 (*arom.* 2xCH), 128.4 (*arom.* 2xCH), 128.3 (*arom.* 2xCH), 128.2 (*arom.* 2xCH), 127.91 (*arom.* 2xCH), 127.87 (*arom.* CH), 127.8 (*arom.* CH), 126.7 (*arom.* 2xCH), 119.2 (*arom.* 2xCH), 114.6 (*arom.* 2xCH), 103.4 (C-1), 101.5 (benzylidene CH), 79.4 (C-3), 78.2 (C-2), 75.6 (OBn CH_2), 73.9 (C-4), 72.2 (OBn CH_2), 69.3 (C-6 CH_2), 66.7 (C-5), 55.8 (OCH_3).



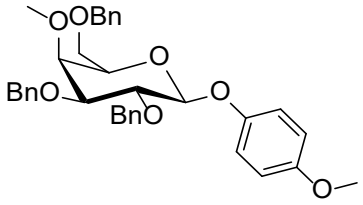
(4-methoxyphenyl)-2,3,6-tri-*O*-benzyl-β-D-galactopyranoside (574): (4-methoxyphenyl)-2,3-di-*O*-benzyl-4,6-*O*-benzylidene-β-D-galactopyranoside (**573**, 3.6 mmol, 1.0 eq) was dissolved in DCM (0.2 M) in a flame-dried flask under argon at 0 °C. Triethylsilane (18.2 mmol, 5.0 eq) then trifluoroacetic acid (18.3 mmol, 5.0 eq) were added and the reaction was allowed to warm to room temperature and stirred for 3 hours. The reaction was then diluted with DCM, washed with dH_2O and brine and then the organic was collected, dried using

Na_2SO_4, filtered, and concentrated *in vacuo*. The resulting crude solid was purified by recrystallization from EtOAc/Hexanes as a fluffy white solid (**69 %**).

Characterization was consistent with that found in literature.[560]

^{1}H NMR: (600 MHz, $CDCl_3$): ∂7.39-7.28(m, 15H, *arom.* OBn), 7.06-7.03(m, 2H, *arom.* PMP), 6.82-6.79(m, 2H, *arom.* PMP), 5.02(d, *J* = 11.0 Hz, 1H, OBn CH_2), 4.85(d, *J* = 7.8 Hz, 1H, H-1), 4.84(d, *J* = 10.9 Hz, 1H, OBn CH_2), 4.75(s, 2H, OBn CH_2), 4.58(s, 2H, OBn CH_2), 4.07(d, *J* = 3.1 Hz, 1H, H-4), 3.92(dd, *J* = 9.3, 7.9 Hz, 1H, H-2), 3.87(dd, *J* = 10.1, 5.6 Hz, 1H, H-6a), 3.79-3.76(m, 4H, H-6b and OCH_3), 3.67(t, *J* = 5.9 Hz, 1H, H-5), 3.58(dd, *J* = 9.6, 3.5 Hz, 1H, H-3). **^{13}C NMR:** (151 MHz, $CDCl_3$): ∂ = 155.4 (C PMP *arom.*), 151.6 (C PMP *arom.*), 138.5 (C OBn *arom.*), 138.1 (C OBn *arom.*), 137.9 (C OBn *arom.*), 128.64 (*arom.* 2xCH), 128.55 (*arom.* 2xCH), 128.5 (*arom.* 2xCH), 128.3 (*arom.* 2xCH), 128.1 (*arom.* CH), 128.0 (*arom.* 2xCH), 127.89 (*arom.* 2xCH), 127.88 (*arom.* CH), 127.86 (*arom.* CH), 118.7 (*arom.* 2xCH PMP), 114.6 (*arom.* 2xCH PMP), 103.1 (C-1), 80.7 (C-3), 78.8 (C-2), 75.5 (OBn CH_2), 73.9 (OBn CH_2), 73.7 (C-5), 72.7 (OBn CH_2), 69.4 (C-6 CH_2), 67.0 (C-4), 55.8(OCH_3). **HRMS (ESI):** m/z calcd for $C_{34}H_{36}O_7Na$ $[M+Na]^+$ 579.2359, found 579.2382.

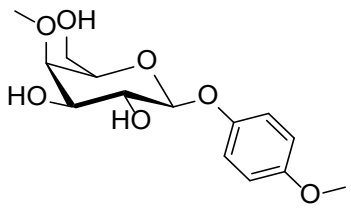
(4-methoxyphenyl)-2,3,6-tri-*O*-benzyl-4-*O*-methyl-β-D-galactopyranoside (575): The title compound was synthesized according to a modified **General Procedure 8-5**. (4-methoxyphenyl)-2,3,6-tri-*O*-benzyl-β-D-galactopyranoside (**574**, 2.5 mmol, 1.0 eq) was dissolved in dry DMF (0.1 M) in a flame-dried flask under argon atmosphere. NaH (60 % dispersion in mineral oil) (5.1 mmol, 2.0 eq) was added portion-wise to the flask followed by drop-wise addition of MeI (9.6 mmol, 4.0 eq). The solution was stirred at room temperature for 18 h. Upon reaction completion the solution was diluted with DCM, quenched with water, and washed with brine. The organic layer was dried using Na_2SO_4, filtered, and concentrated *in vacuo*. The crude material was purified by column chromatography (0-30 % gradient of EtOAc in Hexanes) and the pure product was isolated as a white solid (**81 %**).



^{1}H NMR: (600 MHz, $CDCl_3$): ∂7.39-7.26(m, 15H, *arom.* OBn), 7.04-7.01(m, 2H, *arom.* PMP), 6.81-6.78(m, 2H, *arom.* PMP), 5.00(d, *J* = 10.8 Hz, 1H, OBn CH_2), 4.84(d, *J* = 10.8 Hz, 1H, OBn CH_2), 4.83(d, *J* = 7.7 Hz, 1H, H-1), 4.78(s, 2H, OBn CH_2), 4.57(d, *J* = 11.7 Hz, 1H, OBn CH_2), 4.54(d, *J* = 11.7 Hz, 1H, OBn CH_2), 3.98(dd, *J* = 9.5, 7.7 Hz, 1H, H-2), 3.78-3.76(m, 1H, H-6a), 3.77(s, 3H, OCH_3), 3.70-3.62(m, 3H, H-4 and H-5 and H-6b), 3.61(s, 3H, OCH_3), 3.50(dd, *J* = 9.7, 2.9 Hz, 1H, H-3). **^{13}C NMR:**

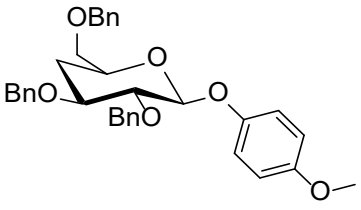
(151 MHz, $CDCl_3$): ∂ = 155.3 (C *arom.* PMP), 151.8 (C *arom.* PMP), 138.7 (C *arom.* OBn), 138.5 (C *arom.* OBn), 138.0 (C *arom.* OBn), 128.6 (*arom.* 2xCH OBn), 128.5 (*arom.* 2xCH OBn), 128.4 (*arom.* 2xCH OBn), 128.3 (*arom.* 2xCH OBn), 128.01 (*arom.* 2xCH OBn), 127.97 (*arom.* CH OBn), 127.82 (*arom.* CH OBn), 127.81 (*arom.* 2xCH OBn), 127.76 (*arom.* CH OBn), 118.8 (*arom.* 2xCH PMP), 114.5 (*arom.* 2xCH PMP), 103.2 (C-1), 81.9 (C-3), 79.5 (C-2), 76.0 (C-4), 75.6 (OBn CH_2), 73.8 (OBn CH_2), 73.7 (C-5), 73.1 (OBn CH_2), 68.6 (C-6 CH_2), 61.5 (OCH_3), 55.8 (OCH_3). **HRMS (ESI):** m/z calcd for $C_{35}H_{38}O_7Na$ $[M+Na]^+$ 593.2515, found 593.2534.

(4-methoxyphenyl)-4-*O*-methyl-β-D-galactopyranoside (C_4 OMe PMP-Gal, 108): The title compound was synthesized according to a modified **General Procedure 8-7**. To a solution of (4-methoxyphenyl)-2,3,6-tri-*O*-benzyl-4-*O*-methyl-β-D-galactopyranoside (**575**, 2.0 mmol, 1.0 eq) in a 1:1 mixture of EtOAc and MeOH (18.6 mL, 0.1 M), Pd/C (10 mol %) (313 mg, 0.2 mmol, 0.1 eq) was added and the reaction mixture was purged several times with H_2. The mixture was stirred under H_2 atmosphere for 24 h, filtered over Celite® and the volatiles were evaporated to afford the desired product as a white powder (**99 %**).



^{1}H NMR: (600 MHz, D_2O): ∂7.08-7.07(m, 2H, *arom.*), 6.95-6.94(m, 2H, *arom.*), 4.88(d, *J* = 7.8 Hz, 1H, H-1), 3.80-3.75(m, 7H, OCH_3 and H-3 and H-4 and H-6), 3.70-3.66(m, 2H, H-2 and H-5), 3.51(s, 3H, OCH_3). **^{13}C NMR:** (151 MHz, $CDCl_3$): ∂ = 154.7 (C *arom.*), 151.0 (C *arom.*), 118.2 (2xCH *arom.*), 115.0 (2xCH *arom.*), 101.7 (C-1), 78.9 (C-2/C-5), 75.5 (C-3/C-4), 73.0 (C-3/C-4), 70.9 (C-2/C-5), 61.5 (OCH_3), 60.3 (C-6 CH_2), 55.8 (OCH_3). **HRMS (ESI):** m/z calcd for $C_{14}H_{20}O_7Na$ $[M+Na]^+$ 323.1107, found 323.1124

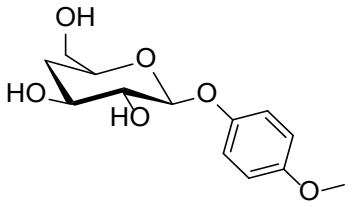
(4-methoxyphenyl)-2,3,6-tri-*O*-benzyl-4-deoxy-β-D-glucopyranoside (576): (4-methoxyphenyl)-2,3,6-tri-*O*-benzyl-β-D-glucopyranoside (**553**, 1.5 mmol, 1.0 eq) was dissolved in DCM (0.1 M) and pyridine (3.5 M) in a flame-dried flask under argon at 0 °C. Triflic anhydride (4.8 mmol, 3.0 eq) was added drop-wise and the reaction was stirred for 30 minutes on ice. The reaction was then diluted with DCM, poured over ice, and the organic layer was washed with brine. The organic phase was collected, dried using Na_2SO_4, filtered, and concentrated *in vacuo* to yield an orange-yellow oil. Once completely dry, the reaction was immediately placed under argon atmosphere and dissolved in dry



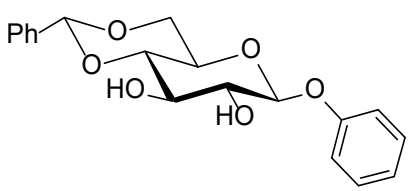
acetonitrile (0.2 M) at room temperature. $NaBH_4$ (12.1 mmol, 8.0 eq) was added portion-wise and the reaction was stirred for 18 h or until completion by TLC. Following reaction completion, the solution was diluted with DCM and washed with brine. The organic layer was dried with Na_2SO_4, filtered, and concentrated *in vacuo*. The crude product was purified by column chromatography (10 % EtOAc in Hexanes) to yield the purified product as a white solid (**2 steps, 33 %**).

^{1}H NMR: (400 MHz, $CDCl_3$): ∂7.40-7.27(m, 15H, OBn *arom.*), 7.07-7.02(m, 2H, *arom.*), 6.83-6.79(m, 2H, *arom.*), 5.02(d, *J* = 11.0 Hz, 1H, OBn CH_2), 4.86(d, *J* = 11.8 Hz, 1H, OBn CH_2), 4.85(d, *J* = 7.4 Hz, 1H, H-1), 4.71(s, 2H, OBn CH_2), 4.58(d, *J* = 11.9 Hz, 1H, OBn CH_2), 4.54(d, *J* = 11.9 Hz, 1H, OBn CH_2), 3.77(s, 3H, OCH_3), 3.74-3.53(m, 5H, H-2 and H-3 and H-5 and H-6), 2.17(ddd, *J* = 12.5, 5.0, 1.6 Hz, 1H, H-4a), 1.55(q, *J* = 11.6 Hz, 1H, H-4b). **^{13}C NMR:** (101 MHz, $CDCl_3$): 155.3 (*arom.* C), 151.8 (*arom.* C), 138.7 (C OBn *arom.*), 138.6 (C OBn *arom.*C), 138.2 (C OBn *arom.*), 128.52 (OBn *arom.* CH), 128.47 (*arom.* CH), 128.3 (*arom.* CH), 127.81 (*arom.* CH), 127.76 (*arom.* CH), 118.5 (2xCH *arom.*), 114.6 (2xCH *arom.*), 103.1 (C-1), 82.7 (C-2/C-3/C-5), 78.4 (C-2/C-3/C-5), 75.3 (OBn CH_2), 73.7 (OBn CH_2), 72.51 (OBn CH_2/C-6 CH_2), 72.48 (OBn CH_2/C-6 CH_2), 71.5 (C-2/C-3/C-5), 55.8 (OCH_3), 33.7 (C-4 CH_2). **HRMS (ESI):** m/z calcd for $C_{34}H_{36}O_6Na$ $[M+Na]^+$ 563.2410, found 563.2437.

(4-methoxyphenyl)-4-deoxy-β-D-glucopyranoside (C_4 Deoxy PMP-Glc, 109): The title compound was synthesized according to a modified **General Procedure 8-7**. To a solution of (4-methoxyphenyl)-2,3,6-tri-*O*-benzyl-6-deoxy-β-D-glucopyranoside (**576**, 0.5 mmol, 1.0 eq) in a 1:1 mixture of EtOAc and MeOH (5.0 mL, 0.1 M), Pd/C (10 mol %) (0.05 mmol, 0.1 eq) was added and the reaction mixture was purged several times with H_2. The mixture was stirred under H_2 atmosphere for 4 h, filtered over Celite® and the volatiles were evaporated to afford the desired product as a white powder (**96 %**).



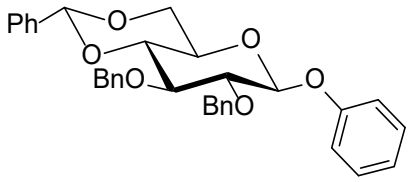
^{1}H NMR: (400 MHz, $CDCl_3$): ∂6.98-6.94(m, 2H, *arom.*), 6.86-6.82(m, 2H, *arom.*), 5.24(d, *J* = 4.8 Hz, 1H, OH-2), 4.97(d, *J* = 4.6 Hz, 1H, OH-3), 4.73(t, *J* = 5.8 Hz, 1H, OH-6), 4.66(d, *J* = 7.7 Hz, H-1), 3.70(s, 3H, OCH_3), 3.57-3.46(m, 2H, H-3 and H-5), 3.43-3.36(m, 2H, H-6), 3.10(dt, *J* = 8.7, 4.3 Hz, 1H, H-2), 1.83(ddd, *J* = 12.9, 5.2, 1.5 Hz, 1H, H-4a), 1.29-1.20(m, 1H, H-4b). **^{13}C NMR:** (101 MHz, $CDCl_3$): 154.2 (C *arom.*), 151.6 (C *arom.*), 117.6 (2xCH *arom.*), 114.4 (2xCH *arom.*), 101.9 (C-1), 75.0 (C-2), 72.5 (C-5), 70.3 (C-3), 63.6 (C-6 CH_2), 55.3 (OCH_3), 35.6 (C-4 CH_2). **HRMS (ESI):** m/z calcd for $C_{13}H_{18}O_6Na$ $[M+Na]^+$ 293.1001, found 293.1009.



phenyl-4,6-*O*-benzylidene-β-D-glucopyranoside (578): To a solution of (phenyl)-β-D-glucopyranoside (**82**, 10.7 mmol, 1.0 eq) in DMF (0.5 M) was added benzaldehyde dimethyl acetal (11.9 mmol, 1.1 eq) and *p*-toluene sulfonic acid (1.1 mmol, 0.1 eq) to a flame-dried flask under argon. The reaction mixture was warmed to 60 °C and stirred for 18 h. The reaction was then diluted with EtOAc and washed with brine. The organic layer was dried using Na_2SO_4, filtered, and concentrated *in vacuo*. The crude residue was recrystallized from DCM to afford the desired product as a white solid (**24 %**)

Characterization was consistent with that found in literature.[561]

^{1}H NMR: (400 MHz, $CDCl_3$): ∂7.52-7.49(m, 2H, *benzylidene acetal arom.*), 7.40-7.38(m, 3H, *benzylidene acetal arom.*), 7.35-7.31(m, 2H, *arom.*), 7.10-7.05(m, 3H, *arom.*), 5.57(s, 1H, benzylidene CH), 5.05(d, *J* = 7.7 Hz, 1H, H-1), 4.39(d, *J* = 10.7, 4.8 Hz, 1H, H-6a), 3.94(t, *J* = 8.9 Hz, 1H, H-3), 3.86-3.80(m, 2H, H-2 and H-6b), 3.67(t, *J* = 9.2 Hz, 1H, H-4), 3.62(dd, *J* = 9.6, 4.8 Hz, 1H, H-5), 2.81(br s, 1H, OH), 2.70(br s, 1H, OH). **^{13}C NMR:** (100 MHz, $CDCl_3$): ∂ = 156.9 (C *arom.*), 136.9 (C *arom.*), 129.8 (*arom.* CH), 129.5 (*arom.* CH), 128.5 (*arom.* CH), 126.4 (*arom.* CH), 123.4 (*arom.* CH), 117.0 (*arom.* CH), 102.2 (*benzylidene* CH), 101.3 (C-1), 80.4, 74.5, 73.3, 68.7 (C-6 CH_2), 66.7.

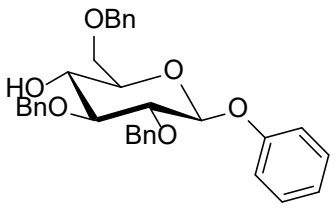


(phenyl)-2,3-di-*O*-benzyl-4,6-*O*-benzylidene-β-D-glucopyranoside (579): The title compound was synthesized according to **General Procedure 8-6**. To a solution of (phenyl)-4,6-*O*-benzylidene-β-D-glucopyranoside (**578**, 2.6 mmol, 1.0 eq) in DMF (0.2 M) was added NaH (60 % dispersion in mineral oil) (10.1 mmol, 4.0 eq) portion-wise at 0 °C to a flame-dried flask under argon. Benzyl bromide (7.6 mmol, 3.0 eq) was then added slowly and the reaction mixture was stirred for 18 h at room temperature. Following reaction completion, the reaction was diluted slowly with DCM and dH_2O. The organic phase was washed with sat. $NaHCO_3$, dH_2O, and brine. The organic layer was dried using Na_2SO_4, filtered, and concentrated *in vacuo*. The crude residue was purified by column chromatography (gradient hexanes to 8:2 Hexanes:EtOAc) to afford the desired product as a clear colourless oil (**72 %**)

Characterization was consistent with that found in literature.[561]

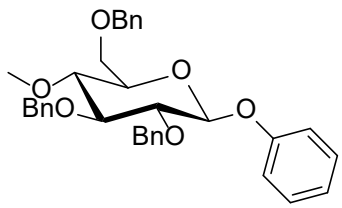
^{1}H NMR: (600 MHz, $CDCl_3$): ∂7.57-7.54(m, 2H, OBn *arom.*), 7.46-7.32(m, 15H, OBn *arom*. + OPh *arom.*), 7.04-7.00(m, 3H, OPh *arom.*), 5.64(s, 1H, benzylidene CH), 5.20(d, *J* = 7.6 Hz, 1H, H-1), 5.04(d, *J* = 10.9 Hz, 1H, OBn CH_2), 5.01(d, *J* = 11.4 Hz, 1H, OBn CH_2), 4.92(d, *J* = 10.9 Hz, 1H, OBn CH_2), 4.89(d, *J* = 11.4 Hz, 1H, OBn CH_2), 4.43(dd, *J* = 10.5, 5.0 Hz, 1H, H-6a), 3.92-3.81(m, 4H, H-2 and H-3 and H-4 and H-6b), 3.60(dt, *J* = 10.0, 5.0 Hz, 1H, H-5). **^{13}C NMR:** (151 MHz, $CDCl_3$): ∂ = 157.2 (C Ph *arom.*), 138.5 (C OBn *arom.*), 138.2 (C OBn *arom.*), 137.3 (C OBn *arom.*), 129.7 (*arom.* 2xCH), 129.1 (*arom.* CH), 128.5 (*arom.* 2xCH), 128.42 (*arom.* 2xCH), 128.35 (*arom.* 2xCH), 128.32 (*arom.* 2xCH), 128.1 (*arom.* 2xCH), 127.9 (*arom.* CH), 127.8 (*arom.* CH), 126.1 (*arom.* 2xCH), 123.1 (*arom.* CH), 117.0 (*arom.* 3xCH), 102.1 (C-1), 101.3 (benzylidene CH), 81.9 (C-2/C-3/C-4), 81.4 (C-2/C-3/C-4), 81.0 (C-2/C-3/C-4), 75.6 (OBn CH_2), 75.3 (OBn CH_2), 68.8 (C-6 CH_2), 66.3 (C-5).

(phenyl)-2,3,6-tri-*O*-benzyl-β-D-glucopyranoside (580): (phenyl)-2,3-di-*O*-benzyl-4,6-*O*-benzylidene-β-D-glucopyranoside (**579**, 1.6 mmol, 1.0 eq) was dissolved in DCM (0.2 M) in a flame-dried flask under argon at 0 °C. Triethylsilane (8.2 mmol, 5.0 eq) then trifluoroacetic acid (7.8 mmol, 5.0 eq) were added and the reaction was allowed to warm to room temperature and stirred for 5 hours. The reaction was then diluted with DCM, washed with dH_2O and brine and then the organic was collected, dried using Na_2SO_4, filtered, and concentrated *in vacuo*. The resulting white solid was used without further purification (**92 %**).



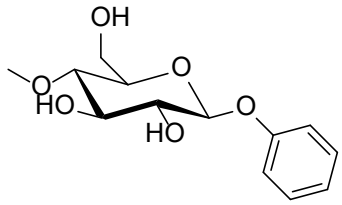
Characterization was consistent with that found in literature.[561]

^{1}H NMR: (600 MHz, $CDCl_3$): ∂7.37-7.27(m, 17H, *arom.*), 7.10-7.04(m, 3H, *arom.*), 5.07-5.04(m, 2H, OBn CH_2 and H-1), 4.98(d, *J* = 11.5 Hz, 1H, OBn CH_2), 4.84(d, *J* = 10.9 Hz, 1H, OBn CH_2), 4.77(d, *J* = 11.4 Hz, 1H, OBn CH_2), 4.60(d, *J* = 12.0 Hz, 1H, OBn CH_2), 4.57(d, *J* = 11.9 Hz, 1H, OBn CH_2), 3.84(dd, *J* = 10.4, 3.7 Hz, 1H), 3.75-3.70(m, 2H), 3.68(d, *J* = 9.2 Hz, 1H), 3.62-3.59(m, 1H), 3.56(t, *J* = 9.0 Hz, 1H), 2.53(bs, 1H, OH-4). **^{13}C NMR:** (151 MHz, $CDCl_3$): ∂ = 157.4 (C Ph *arom.*), 138.6 (C OBn *arom.*), 138.3 (C OBn *arom.*), 138.0 (C OBn *arom.*), 129.7 (*arom.* 2xCH), 128.7 (*arom.* 2xCH), 128.6 (*arom.* 2xCH), 128.5 (*arom.* 2xCH), 128.4 (*arom.* 2xCH), 128.1 (*arom.* 2xCH), 128.06 (*arom.* CH), 127.96 (*arom.* CH), 127.84 (*arom.* CH), 127.79 (*arom.* 2xCH), 122.9 (*arom.* CH), 117.0 (*arom.* 2xCH), 101.8 (C-1), 84.2, 81.6, 75.5 (OBn CH_2), 75.1 (OBn CH_2), 74.5, 73.8 (OBn CH_2), 71.4, 70.2 (C-6 CH_2).

(phenyl)-2,3,6-tri-*O*-benzyl-4-*O*-methyl-β-D-glucopyranoside (581): 

The title compound was synthesized according to a modified **General Procedure 8-5**. (phenyl)-2,3,6-tri-*O*-benzyl-β-D-glucopyranoside (**580**, 0.6 mmol, 1.0 eq) was dissolved in dry DMF (0.1 M) in a flame-dried flask under argon atmosphere. NaH (60 % dispersion in mineral oil) (2.7 mmol, 4.0 eq) was added portion-wise to the flask followed by drop-wise addition of MeI (4.8 mmol, 8.0 eq). The solution was stirred at room temperature for 18 h. Upon reaction completion the solution was diluted with DCM, quenched with water, and extracted with brine. The organic layer was dried using Na_2SO_4, filtered, and concentrated *in vacuo*. The crude product was purified by column chromatography (20 % EtOAc in hexanes) to yield the pure product as a colourless clear oil (**65 %**).

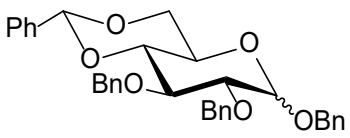
^{1}H NMR: (600 MHz, $CDCl_3$): ∂7.35-7.27(m, 17H, *arom.*), 7.09-7.04(m, 3H, *arom.*), 5.04(d, *J* = 10.9 Hz, 1H, OBn CH_2), 4.99(d, *J* = 7.7 Hz, 1H, H-1), 4.92(d, *J* = 10.9 Hz, 1H, OBn CH_2), 4.82(d, *J* = 11.0 Hz, 1H, OBn CH_2), 4.63(d, *J* = 12.0 Hz, 1H, OBn CH_2), 4.56(d, *J* = 12.0 Hz, 1H, OBn CH_2), 3.81(dd, *J* = 10.8, 1.6 Hz, 1H, H-6a), 3.73-3.70(m, 2H, H-2 and H-6b), 3.63(t, *J* = 8.8 Hz, 1H, H-3), 3.56-3.52(m, 4H, H-5 and OCH_3), 3.40-3.36(m, 1H, H-4). **^{13}C NMR:** (151 MHz, $CDCl_3$): ∂ = 157.5 (C Ph *arom.*), 138.7 (C OBn *arom.*), 138.4 (C OBn *arom.*), 138.3 (C OBn *arom.*), 129.6 (*arom.* 2xCH), 128.53 (*arom.* 2xCH), 128.51 (*arom.* 2xCH), 128.45 (*arom.* 2xCH), 128.37 (*arom.* 2xCH), 128.1 (*arom.* 2xCH), 127.9 (*arom.* CH), 127.81 (*arom.* CH), 127.78 (*arom.* 2xCH), 127.7 (*arom.* CH), 122.8 (*arom.* CH), 117.0 (*arom.* 2xCH), 101.8 (C-1), 84.7 (C-3), 82.0 (C-2), 79.9 (C-4), 75.8 (OBn CH_2), 75.4 (C-5), 75.2 (OBn CH_2), 73.6 (OBn CH_2), 69.1 (C-6 CH_2), 60.9 (OCH_3). **HRMS (ESI):** m/z calcd for $C_{34}H_{36}O_6Na$ $[M+Na]^+$ 563.2410, found 563.2388.

(phenyl)-4-*O*-methyl-β-D-glucopyranoside (C_4 OMe Ph-Glc, 110): 

The title compound was synthesized according to a modified **General Procedure 8-7**. To a solution of (phenyl)-2,3,6-tri-*O*-benzyl-4-*O*-methyl-β-D-glucopyranoside (**581**, 0.4 mmol, 1.0 eq) in a 1:1 mixture of EtOAc and MeOH (4.0 mL, 0.1 M), Pd/C (10 mol %) (0.04 mmol, 0.1 eq) was added and the reaction mixture was purged several times with H_2. The mixture was stirred under H_2 atmosphere for 6 h, filtered over Celite® and the volatiles were evaporated to afford the desired product as a white powder (**99 %**). If necessary, the material can be recrystallized from dH_2O.

^{1}H NMR: (600 MHz, D_2O): ∂7.38-7.35(m, 2H, *arom.*), 7.13-7.09(m, 3H, *arom.*), 5.06(d, *J* = 7.9 Hz, 1H, H-1), 3.89(d, *J* = 12.4 Hz, 1H, H-6a), 3.73(dd, *J* = 12.5, 5.1 Hz, 1H, H-6b), 3.66(t, *J* = 9.5 Hz, 1H, H-3),

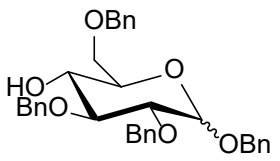
3.58(ddd, *J* = 9.3, 4.7, 2.5 Hz, 1H, H-5), 3.56-3.53(m, 4H, H-2 and OCH_3), 3.27(t, *J* = 9.7 Hz, 1H, H-4). **^{13}C NMR:** (151 MHz, D_2O): ∂ = 156.5 (C *arom.*), 130.0 (2xCH *arom.*), 123.3 (CH *arom.*), 116.6 (2xCH *arom.*), 100.1 (C-1), 79.1 (C-4), 75.3 (C-3), 75.1 (C-5), 73.0 (C-2), 60.3 (C-6 CH_2), 60.1 (OCH_3). **HRMS (ESI):** m/z calcd for $C_{13}H_{18}O_6Na$ $[M+Na]^+$ 293.1001, found 293.1004.



1,2,3-tri-*O*-benzyl-4,6-*O*-benzylidene-D-glucopyranoside (583): The title compound was synthesized according to a modified **General Procedure 8-6**. To a solution of 4,6-*O*-benzylidene-D-glucopyranoside (**582**, 7.6 mmol, 1.0 eq) in DMF (0.2 M) was added benzyl bromide (45.5 mmol, 6.0 eq) at 0 °C to a flame-dried flask under argon. NaH (60 % dispersion in mineral oil) (29.0 mmol, 4.0 eq) was then added portion wise and the reaction mixture was stirred for 18 h at room temperature. Following reaction completion, the reaction was diluted slowly with DCM and dH_2O. The organic phase was washed with sat. $NaHCO_3$, dH_2O, and brine. The organic layer was dried using Na_2SO_4, filtered, and concentrated *in vacuo*. The crude residue was purified by column chromatography (10 % EtOAc in hexanes) to afford the desired product as a white solid with a mixture of alpha and beta products (**64 %**, α:β 1:1.3)

Characterization was consistent with that found in literature.[562]

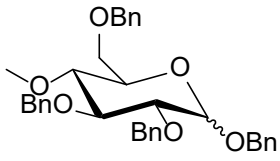
^{1}H NMR: (600 MHz, $CDCl_3$): ∂7.52-7.28(m, 40H, OBn *arom.* α and β), 5.60(s, 1H, *benzylidene* CH β), 5.57(s, 1H, *benzylidene* CH α), 5.01-4.93(m, 4H, OBn CH_2 2xα and 2xβ), 4.92(d, *J* = 3.8 Hz, 1H, H-1 α), 4.88-4.69(m, 9H, OBn CH_2 4xα and 5xβ), 4.66(d, *J* = 7.7 Hz, 1H, H-1 β), 4.62-4.53(m, 3H, OBn CH_2 2xα and 1xβ), 4.40(dd, *J* = 10.5, 5.1 Hz, 1H, H-6a β), 4.22(dd, *J* = 10.3, 5.0 Hz, 1H, H-6a α), 4.13(t, *J* = 8.9 Hz, 1H, H-3 α), 3.93(dt, *J* = 10.1, 5.0 Hz, 1H, H-5 α), 3.84(t, *J* = 10.3 Hz, 1H, H-6b β), 3.79-3.62(m, 4H, H-3 β and H-4 β and H-4 α and H-6a α), 3.59-3.54(m, 2H H-2 α and H-2 β), 3.44(dt, *J* = 9.6, 5.0 Hz, 1H, H-5 β). **^{13}C NMR:** (151 MHz, $CDCl_3$): ∂ = 138.9-137.1 (8C, 4xC *arom.* α and β), 129.1-126.2 (40C, 20xCH *arom*. α and β), 103.2 (C-1 β), 101.4 (*benzylidene* CH β), 101.3 (*benzylidene* CH α), 96.7 (C-1 α), 82.35, 82.28, 81.7, 81.1, 79.4 (C-2 α), 78.8 (C-3 α), 75.54 (OBn CH_2), 75.48 (OBn CH_2), 75.3 (OBn CH_2), 73.6 (OBn CH_2), 71.7 (OBn CH_2), 69.5 (OBn CH_2), 69.2 (C-6 CH_2 α), 68.9 (C-6 CH_2 β), 66.2 (C-5 β), 62.8 (C-5 α).



1,2,3,6-tetra-*O*-benzyl-D-glucopyranoside (584): The title compound was synthesized according to a literature procedure.[555] 1,2,3-tri-*O*-benzyl-4,6-*O*-benzylidene-D-glucopyranoside (**583**, 6.1 mmol, 1.0 eq) was dissolved in DCM (0.2 M) in a flame-dried flask under argon at 0 °C. Triethylsilane (TES, 30.8 mmol, 5.0 eq) then trifluoroacetic acid (TFA, 31.4 mmol, 5.0 eq) were added and the reaction was allowed to warm to room temperature and stirred for 5 hours. The reaction was then diluted with DCM, washed with dH_2O and brine, and then the organic was collected, dried using Na_2SO_4, filtered, and concentrated *in vacuo*. The resulting material was purified by column chromatography (20 % EtOAc in hexanes) as clear oil with a mixture of alpha and beta products (**55 %**, α:β 1:1.7).

Characterization was consistent with that found in literature.[563]

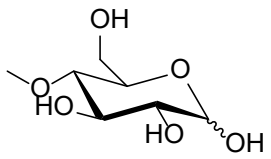
^{1}H NMR (α anomer): (600 MHz, $CDCl_3$): ∂7.42-7.28(m, 20H, *arom.*), 5.03(d, *J* = 11.4 Hz, 1H, OBn CH_2), 4.87(d, *J* = 3.6 Hz, 1H, H-1), 4.76-4.71(m, 4H, OBn CH_2), 4.67-4.53(m, 3H, OBn CH_2), 3.86(t, *J* = 9.2 Hz, 1H, H-6a), 3.81-3.77(m, 1H), 3.68-3.60(m, 3H), 3.55-3.44(m, 1H), 2.35(d, *J* = 2.4 Hz, 1H, OH-4). **^{1}H NMR (β anomer):** (600 MHz, $CDCl_3$): ∂7.42-7.28(m, 20H, *arom.*), 4.96(d, *J* = 11.0 Hz, 2H, OBn CH_2), 4.93(d, *J* = 11.4 Hz, 1H, OBn CH_2), 4.76-4.71(m, 1H, H-1), 4.67-4.53(m, 5H, OBn CH_2), 3.81-3.77(m, 1H, H-6a), 3.74(dd, *J* = 10.5, 5.4 Hz, 1H, H-6b), 3.68-3.60(m, 1H), 3.55-3.44(m, 3H), 2.48(d, *J* = 2.2 Hz, 1H, OH-4). **^{13}C NMR:** (151 MHz, $CDCl_3$): ∂ = 139.0 (C), 138.8 (C), 138.5 (C), 138.21 (C), 138.19 (C), 138.1 (C), 137.5 (C), 137.3 (C), 128.7, 128.58, 128.6, 128.5, 128.3, 128.13, 128.11, 128.08, 128.06, 128.01, 127.99, 127.94, 127.88, 127.84, 127.78, 127.77, 102.8 (C-1 β), 95.7 (C-1 α), 84.2, 81.9, 79.7, 75.6, 75.4 (OBn CH_2), 74.9 (OBn CH_2), 74.2 (OBn CH_2), 73.8, 73.7 (OBn CH_2), 72.9 (OBn CH_2), 71.7 (OBn CH_2), 71.3, 71.0 (OBn CH_2), 70.4 (OBn CH_2), 70.3, 69.6 (C-6 CH_2), 69.2 (C-6 CH_2).



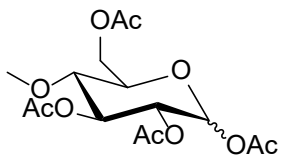
1,2,3,6-tetra-*O*-benzyl-4-*O*-methyl-D-glucopyranoside (585): The title compound was synthesized according to a modified **General Procedure 8-5**. 2,3,6-tri-*O*-benzyl-D-glucopyranoside (**584**, 0.5 mmol, 1.0 eq) was dissolved in dry DMF (0.1 M) in a flame-dried flask under argon atmosphere. NaH (60 % dispersion in mineral oil) (1.0 mmol, 2.0 eq) was added portion-wise to the flask followed by drop-wise addition of MeI (1.9 mmol, 4.0 eq). The solution was stirred at room temperature for 18 h. Upon reaction completion the solution was diluted with DCM, quenched with water, and extracted with brine. The organic layer was dried using Na_2SO_4, filtered, and concentrated *in vacuo*. The crude product was purified by column chromatography (a gradient from 0-20 % EtOAc in hexanes) to yield the pure product as a colourless clear oil with a mixture of alpha and beta products (**74 %**, α:β 1:1.5).

^{1}H NMR: (600 MHz, $CDCl_3$): ∂7.41-7.26(m, 40H, *arom.* α and β), 4.98-4.93(m, 2x OBn CH_2 β and 1x OBn CH_2 α), 4.89(d, *J* = 10.9 Hz, 1H, 1x OBn CH_2 β), 4.83(d, *J* = 3.7 Hz, 1H, H-1 α), 4.81(d, *J* = 10.8 Hz, 1H, 1x OBn CH_2 α), 4.77(d, *J* = 10.9 Hz, 1H, 1x OBn CH_2 β), 4.72-4.66(m, 2x OBn CH_2 α and 3x OBn CH_2 β), 4.64(d, *J* = 12.1 Hz, 1H, 1x OBn CH_2 α), 4.60(d, *J* = 12.2 Hz, 1H, 1x OBn CH_2 β), 4.56(d, *J* = 10.3 Hz, 1H, 1x OBn CH_2 α), 4.54(d, *J* = 10.0 Hz, 1H, 1x OBn CH_2 α), 4.52(d, *J* = 12.1 Hz, 1H, 1x OBn CH_2 α), 4.49(d, *J* = 7.6 Hz, 1H, H-1 β), 3.93(t, *J* = 9.5 Hz, 1H, H-3/H-4 α), 3.78(dd, *J* = 10.8, 1.9 Hz, 1H, H-6a β), 3.73-3.66(m, 3H, H-6a α and H-3/H-4 α and H-6b β), 3.58(dd, *J* = 10.5, 1.9 Hz, 1H, H-6b α), 3.55-3.47(m, 9H, H-2 α and OCH_3 α and H-2 β and H-3/H-4 β and OCH_3 β), 3.40-3.30(m, 3H, H-5 β and H-3/H-4 β and H-5 α). **^{13}C NMR:** (151 MHz, $CDCl_3$): ∂ = 139.1 (C *arom.*), 138.8 (C *arom.*), 138.6 (C *arom.*), 138.44 (C *arom.*), 138.37 (C *arom.*), 138.2 (C *arom.*), 137.6 (C *arom.*), 137.4 (C *arom.*), 128.6-127.7 (40C, 20x CH *arom.* OBn α and β), 102.7 (C-1 β), 95.7 (C-1 α), 84.8, 82.28, 82.26, 80.0, 79.8, 79.6, 75.8 (OBn CH_2), 75.7 (OBn CH_2), 75.2, 75.0 (OBn CH_2), 73.7 (OBn CH_2), 73.6 (OBn CH_2), 73.2 (OBn CH_2), 71.2 (OBn CH_2), 70.6, 69.2 (C-6 CH_2 β), 68.7 (C-6 CH_2 α), 60.8 (2xCH_3 OCH_3 α and OCH_3 β). **HRMS (ESI):** m/z calcd for $C_{35}H_{38}O_6Na$ $[M+Na]^+$ 577.2566, found 577.2576.

4-*O*-methyl-D-glucopyranoside (112): The title compound was synthesized according to a modified **General Procedure 8-7**. To a solution of 2,3,6-tri-*O*-benzyl-4-*O*-methyl-D-glucopyranoside (**585**, 0.4 mmol, 1.0 eq) in a 1:1 mixture of EtOAc and MeOH (3.6 mL, 0.1 M), Pd/C (10 mol %) (0.1 eq) was added and the reaction mixture was purged several times with H_2. The mixture was stirred under H_2 atmosphere for 4 h, filtered over Celite® and the volatiles were evaporated to afford the desired product as a white powder with a mixture of alpha and beta products (**80 %**, α:β 1.2:1).



^{1}H NMR: (600 MHz, MeOD-d_4): ∂5.09(d, *J* = 3.7 Hz, 1H, H-1 α), 4.44(d, *J* = 7.8 Hz, 1H, H-1 β), 3.80(dd, *J* = 11.9, 2.1 Hz, 1H, H-6a β), 3.77-3.73(m, 3H), 3.69-3.64(m, 2H), 3.56(s, 3H, OCH_3 β), 3.55(s, 3H, OCH_3 α), 3.44(t, *J* = 9.1 Hz, 1H, α), 3.37-3.35(m, 1H, H-2 α), 3.25(ddd, *J* = 9.7, 5.0, 2.1 Hz, 1H, α), 3.13(dd, *J* = 9.3, 7.8 Hz, 1H, H-2 β), 3.11-3.06(m, 2H). **^{13}C NMR:** (151 MHz, MeOD-d_4): ∂ = 98.2 (C-1 β), 93.8 (C-1 α), 81.2, 81.0, 78.1, 77.1, 76.4, 74.9, 74.0, 72.1, 62.4 (C-6 CH_2 β), 62.3 (C-6 CH_2 α), 60.83 (OCH_3 β), 60.76 (OCH_3 α).

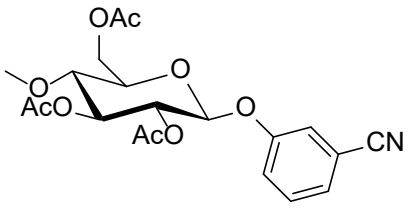


1,2,3,6-tetra-*O*-acetyl-4-*O*-methyl-D-glucopyranoside (586): The title compound was synthesized according to a modified **General Procedure 8-4**. 4-*O*-methyl-D-glucopyranoside (**112**, 1.7 mmol, 1.0 eq) and NaOAc (6.7 mmol, 4.0 eq) were suspended in Ac_2O (21.2 mmol, 12.0 eq) in a flame-dried flask under argon. The solution was stirred at 100 °C for 2.5 h. Upon completion the reaction was cooled, diluted with DCM and washed with water. The organic phase was dried with Na_2SO_4, filtered, and concentrated *in vacuo*. The desired material was obtained without further purification as a white solid containing a mixture of alpha and beta products (**64 %**, α:β 1:3)

Characterization was consistent with that found in literature.[564,565]

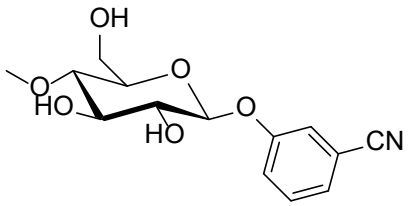
^{1}H NMR (α anomer): (600 MHz, $CDCl_3$): ∂6.25(d, *J* = 3.9 Hz, 1H, H-1), 5.45(t, *J* = 9.8 Hz, 1H, H-3), 5.03-4.99(m, 1H, H-2), 4.36-4.32(m, 1H, H-6a), 4.28-4.25(m, 1H, H-6b), 3.96(ddd, *J* = 10.1, 4.1, 2.2 Hz, 1H, H-5), 3.45(s, 3H, OCH_3), 3.43-3.39(m, 1H, H-4), 2.16(s, 3H, OAc CH_3), 2.12(s, 3H, OAc CH_3), 2.110(s, 3H, OAc CH_3), 2.01(s, 3H, OAc CH_3). **^{13}C NMR (α anomer):** (151 MHz, $CDCl_3$): ∂ = 170.8 (OAc C), 170.1 (OAc C), 170.0 (OAc C), 169.10 (OAc C), 89.4 (C-1), 71.9 (C-3), 71.1 (C-5), 69.7 (C-2), 62.46 (C-6 CH_2), 60.7 (OCH_3), 21.1 (OAc CH_3), 21.0 (OAc CH_3), 20.74 (OAc CH_3), 20.65 (OAc CH_3). *C-4 is under the chloroform solvent*

^{1}H NMR (β anomer): (600 MHz, $CDCl_3$): ∂5.68(d, *J* = 8.3 Hz, 1H, H-1), 5.21(t, *J* = 9.4 Hz, 1H, H-3), 5.03-4.99(m, 1H, H-2), 4.36-4.32(m, 1H, H-6a), 4.28-4.25(m, 1H, H-6b), 3.68(ddd, *J* = 9.7, 4.6, 2.0 Hz, 1H, H-5), 3.43(s, 3H, OCH_3), 3.43-3.39(m, 1H, H-4), 2.11(s, 3H, OAc CH_3), 2.09(s, 3H, OAc CH_3), 2.08(s, 3H, OAc CH_3), 2.02(s, 3H, OAc CH_3). **^{13}C NMR (β anomer):** (151 MHz, $CDCl_3$): ∂ = 170.8 (OAc C), 170.0 (OAc C), 169.8 (OAc C), 169.06 (OAc C), 91.8 (C-1), 74.9 (C-3), 73.9 (C-5), 70.9 (C-2), 62.55 (C-6 CH_2), 60.5 (OCH_3), 21.0 (3xOAc CH_3), 20.74 (OAc CH_3). *C-4 is under the chloroform solvent*



(3-cyanophenyl)-2,3,6-tri-*O*-acetyl-4-*O*-methyl-β-D-glucopyranoside (587): The title compound was synthesized according to a modified **General Procedure 8-2**.[167,525] 1,2,3,6-tetra-*O*-acetyl-4-*O*-methyl-D-glucopyranoside (**586**, 1.1 mmol, 1.0 eq) and 3-cyanophenol (2.4 mmol, 2.2 eq) were dissolved in dry DCM (0.25 M) in a flame dried flask under argon at 0°°C with 4 Å molecular sieves (powdered). Boron trifluoride diethyl etherate (46.5 % solution) (2.6 mmol, 2.5 eq) was added to the solution slowly. The solution was stirred overnight (18 h) and then quenched with sat. $NaHCO_3$ upon reaction completion. The solution was diluted in DCM, filtered through a Celite® pad, and then washed using sat. $NaHCO_3$, H_2O,

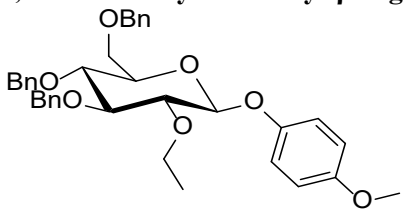
and brine. The organic layer was dried using Na_2SO_4, filtered, and concentrated *in vacuo*. The crude material was cleaned by column chromatography (10 % DCM in hexanes) and isolated as a clear oil for use directly in the next step.

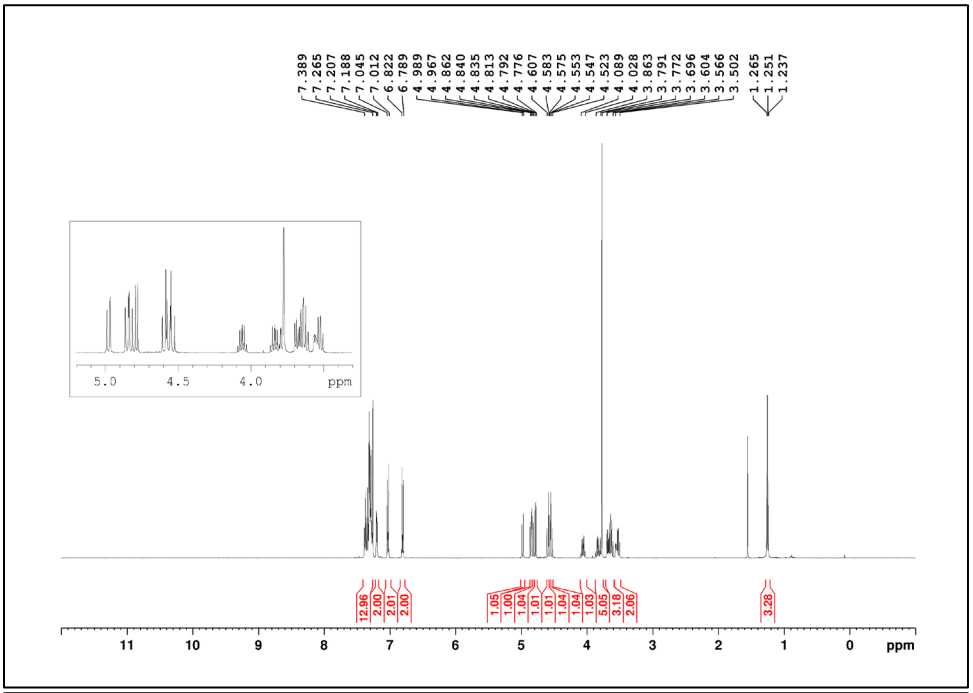


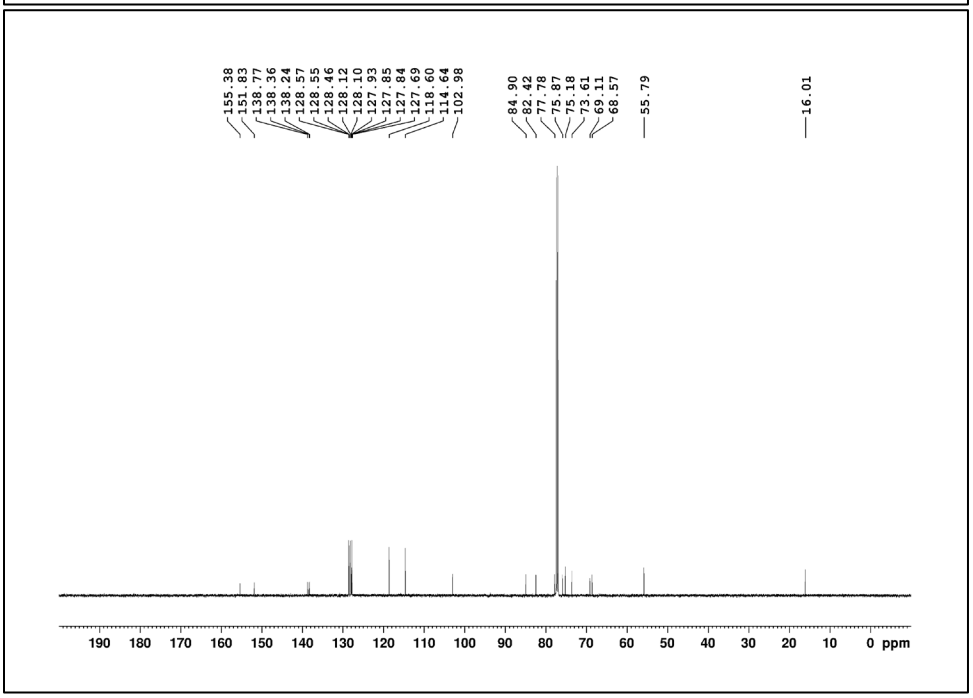
(3-cyanophenyl)-4-*O*-methyl-β-D-glucopyranoside (111): The title compound was synthesized according to a modified **General Procedure 8-3**.[167,326] (3-cyanophenyl)-2,3,6-tri-*O*-acetyl-4-*O*-methyl-D-glucopyranoside (**587**, 0.1 mmol, 1.0 eq) was dissolved in MeOH (0.2 M) and a 1 M solution of NaOMe in MeOH (0.05 mmol, 0.3 eq) was added to the solution to stir for 1 hour. Upon reaction completion, Amberlite IR120 H+ resin (washed in MeOH) was added to a pH < 4. The solution was filtered, and the filtrate was concentrated *in vacuo*. The product was obtained without further purification as a white powder (**11 %, 2 steps**).

^{1}H NMR: (600 MHz, DMSO-d_6): ∂7.52(t, *J* = 8.2 Hz, 1H, *arom.*), 7.48-7.46(m, 2H, *arom.*), 7.35(ddd, *J* = 8.3, 2.5, 1.2 Hz, 1H, *arom.*), 5.46(br s, 1H, OH-2), 5.30(br s, 1H, OH-3), 5.00(d, *J* = 7.8 Hz, 1H, H-1), 4.71(br s, 1H, OH-6), 3.63(d, *J* = 11.5 Hz, 1H, H-6a), 3.50-3.44(m, 5H, H-5 and H-6b and OCH_3), 3.41(t, *J* = 9.0 Hz, 1H, H-3), 3.25(t, *J* = 8.0 Hz, 1H, H-2), 3.03(t, *J* = 9.3 Hz, 1H, H-4). **^{13}C NMR:** (151 MHz, $CDCl_3$): ∂ = 157.3 (C *arom.*), 130.9 (CH *arom.*), 125.8 (CH *arom.*), 121.7 (CH *arom.*), 119.1 (CH *arom.*), 118.6 (CN), 112.2 (C *arom.*), 99.7 (C-1), 78.9 (C-4), 76.2 (C-3), 75.6 (C-5), 73.3 (C-2), 60.2 (C-6 CH_2), 59.7 (OCH_3). **HRMS (ESI):** m/z calcd for $C_{14}H_{17}NO_6Na$ $[M+Na]^+$ 318.0954, found 318.2329.

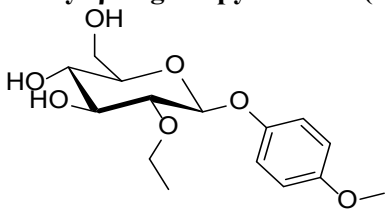
(4-methoxyphenyl)-3,4,6-tri-*O*-benzyl-2-*O*-ethyl-β-D-glucopyranoside (557):

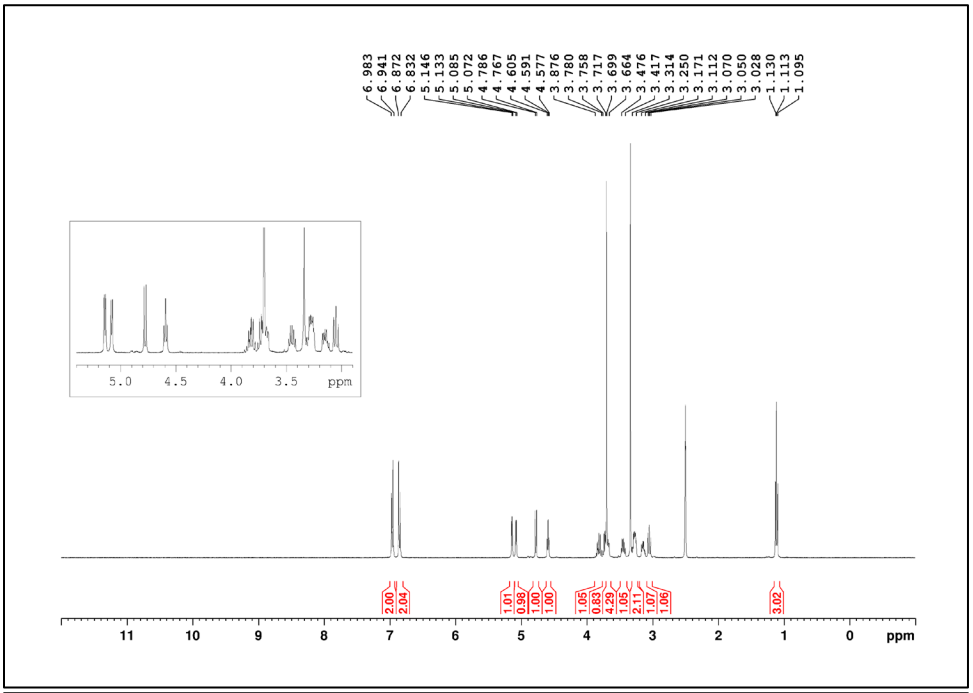


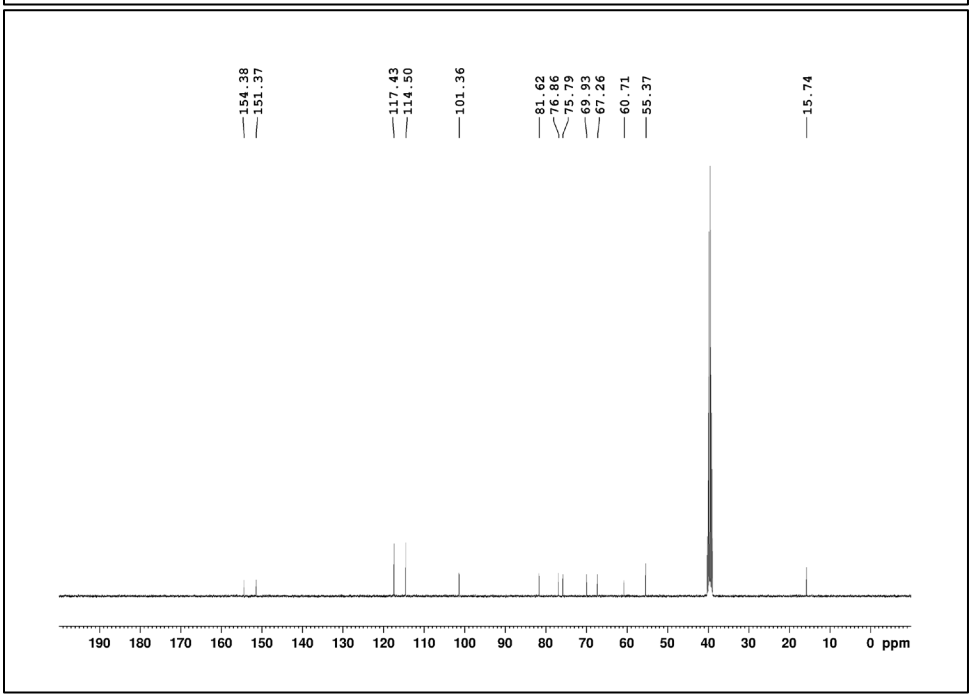




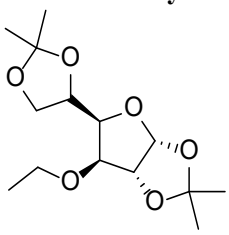
(4-methoxyphenyl)-4-*O*-ethyl-β-D-glucopyranoside (C_2 OEt PMP-Glc, 100):

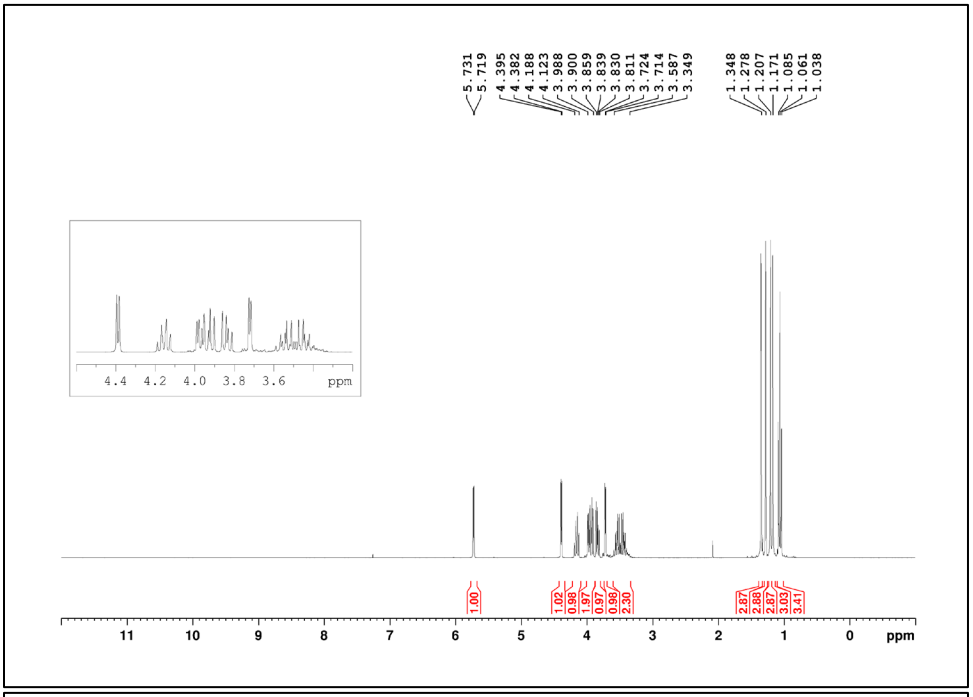


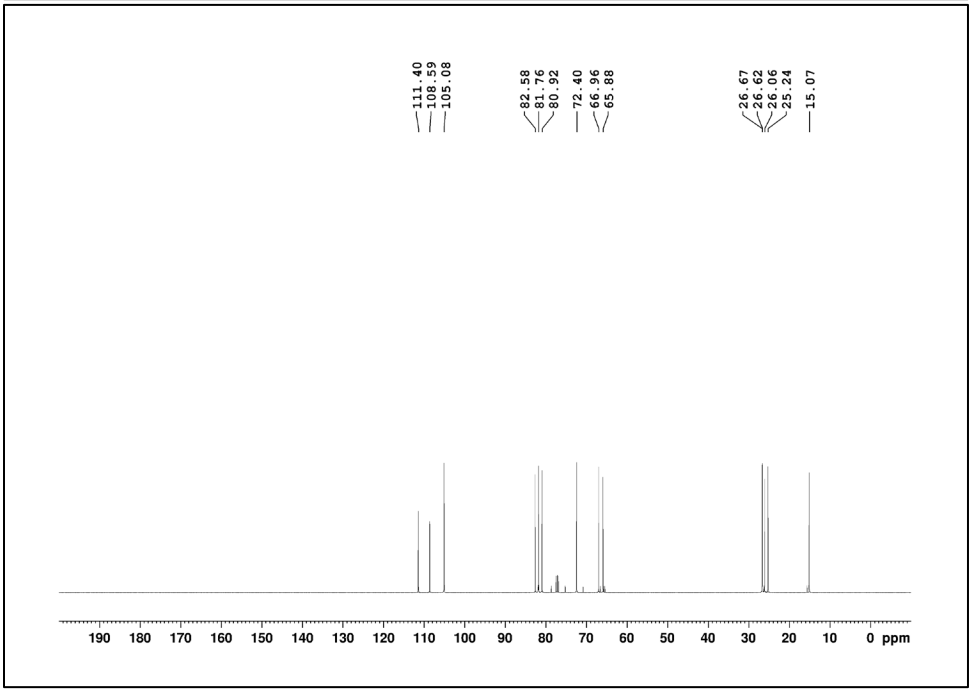




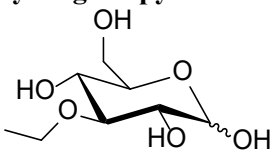
1,2:5,6-di-*O*-isopropylidene-3-*O*-ethyl-α-D-glucofuranose (558):

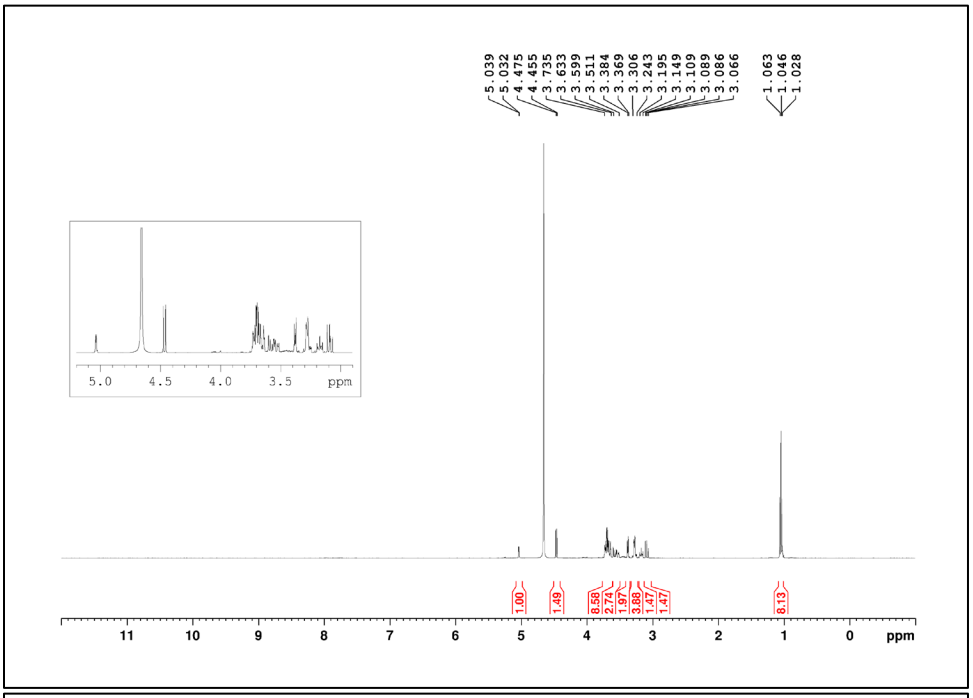


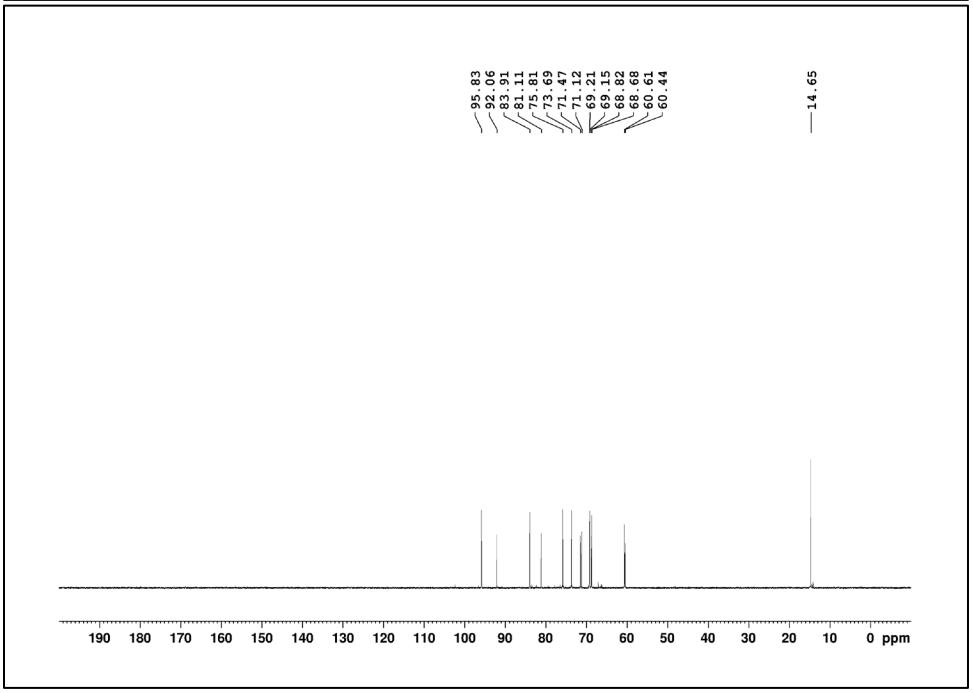




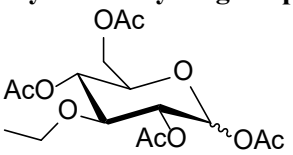
3-*O*-ethyl-D-glucopyranoside (560):

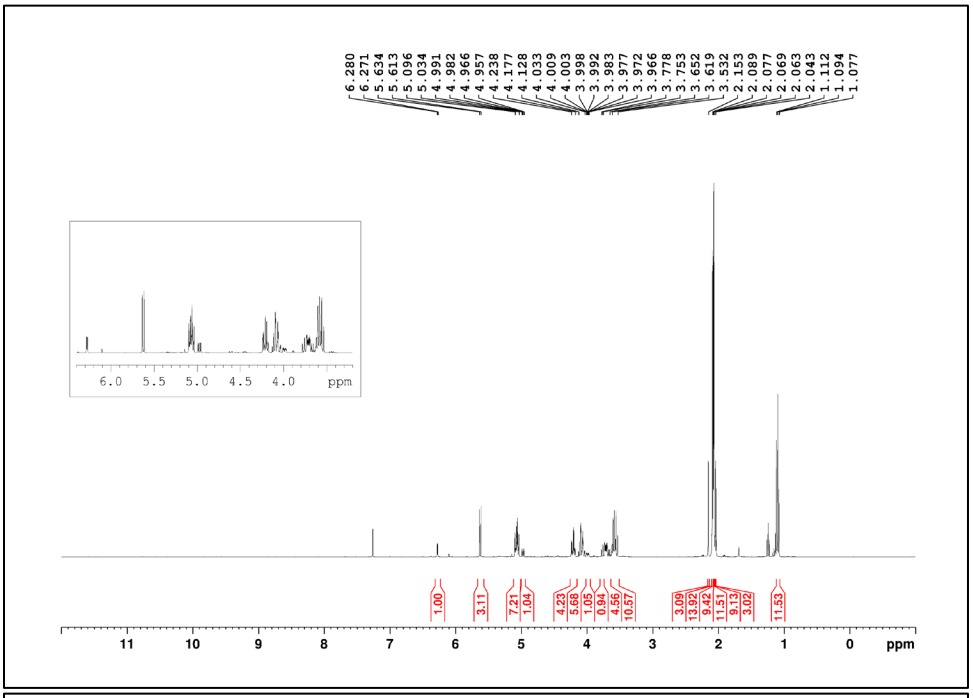


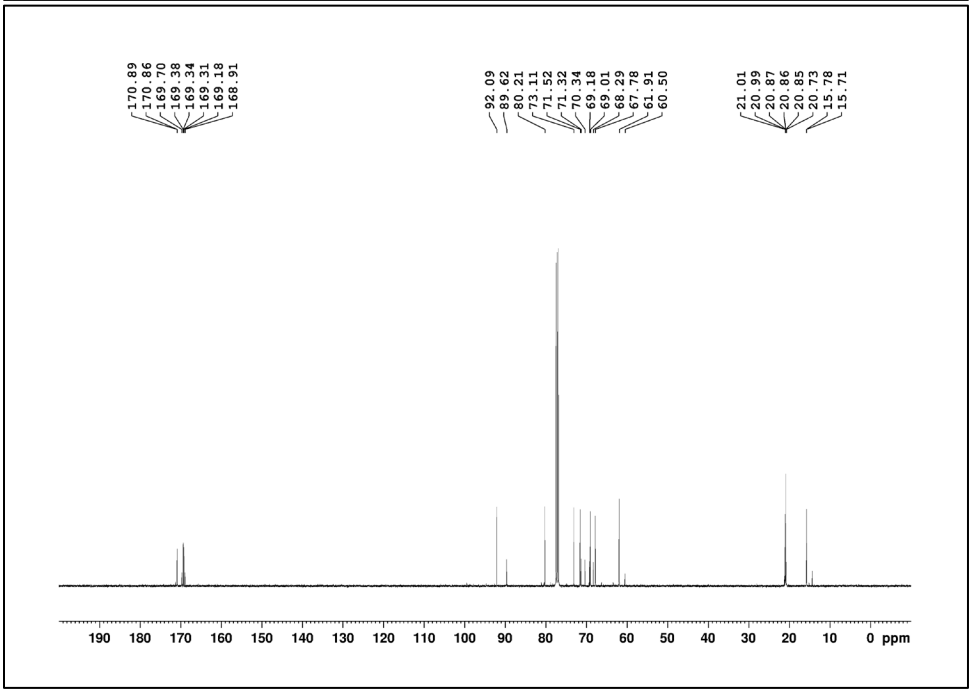




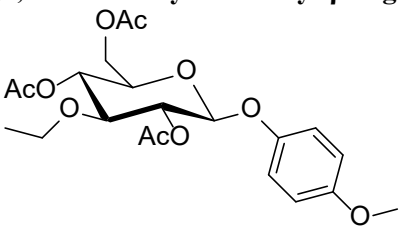
1,2,4,6-tetra-*O*-acetyl-3-*O*-ethyl-D-glucopyranoside (562):

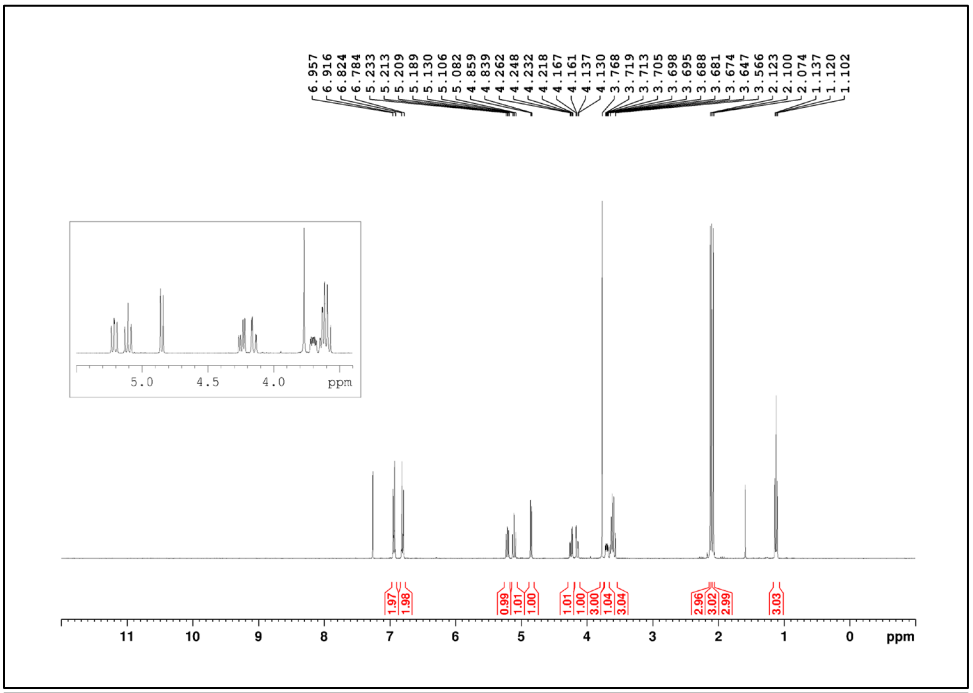


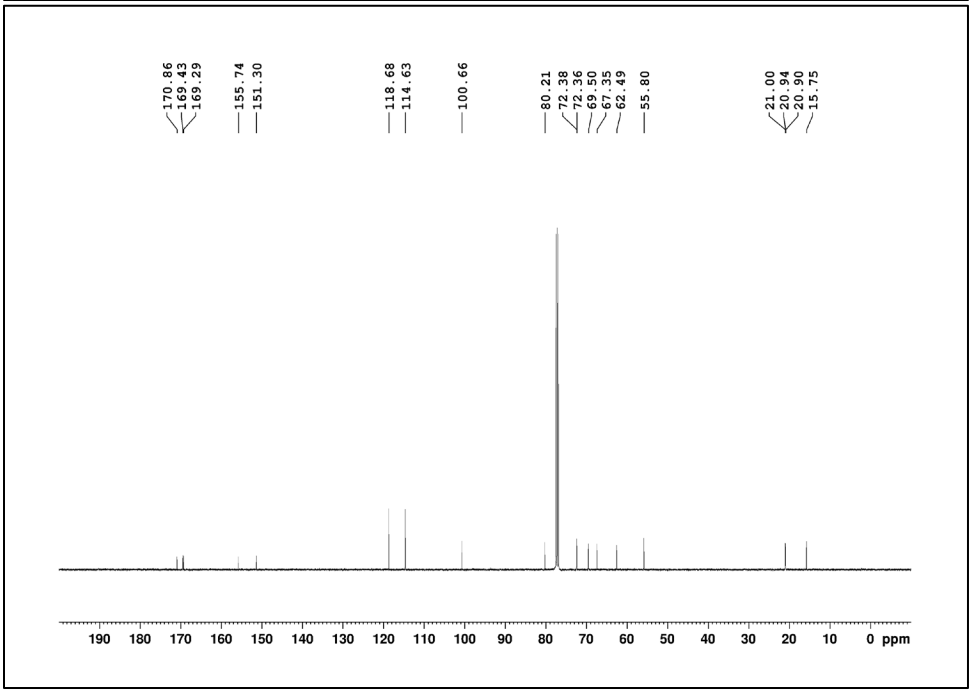




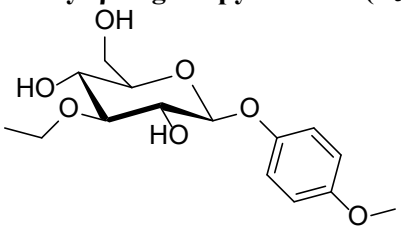
(4-methoxyphenyl)-2,4,6-tri-*O*-acetyl-3-*O*-ethyl-β-D-glucopyranoside (564):

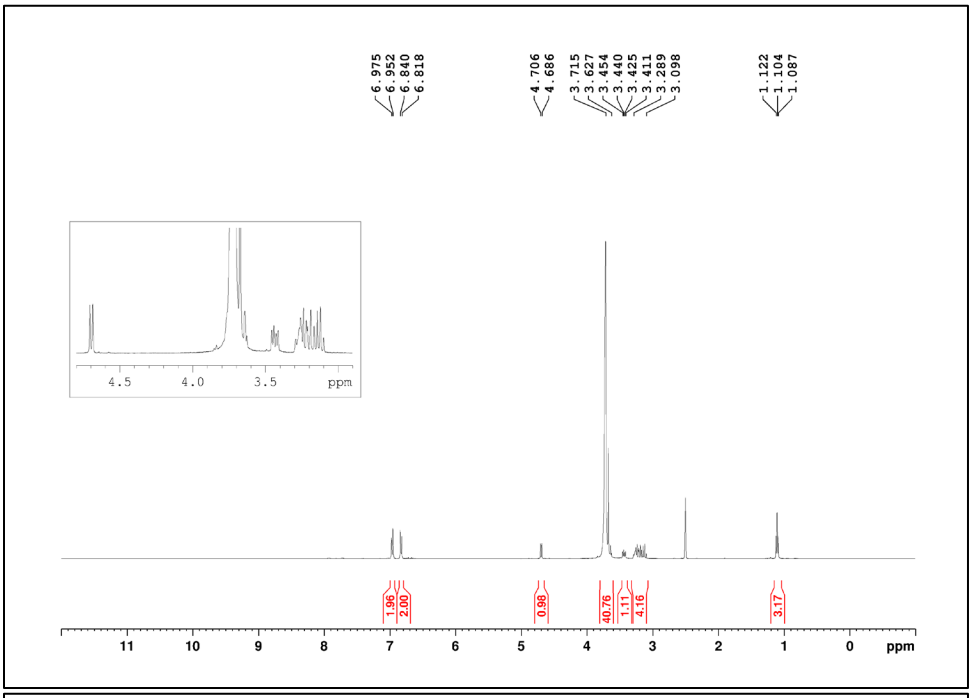


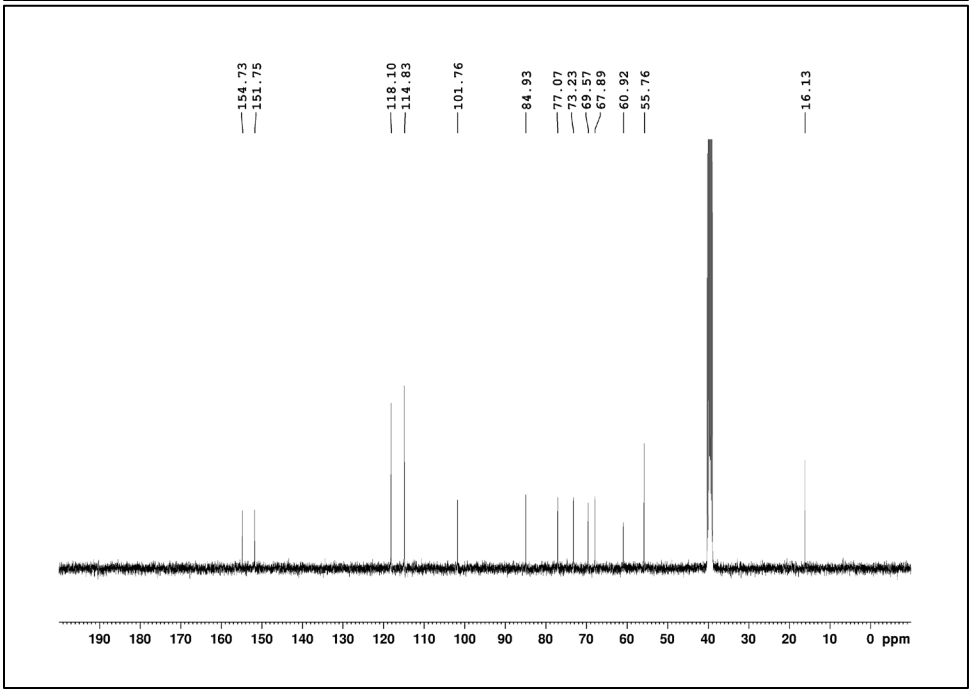




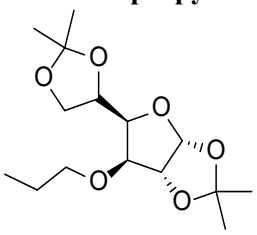
(4-methoxyphenyl)-3-*O*-ethyl-β-D-glucopyranoside (C_3 OEt, PMP-Glc, 101):

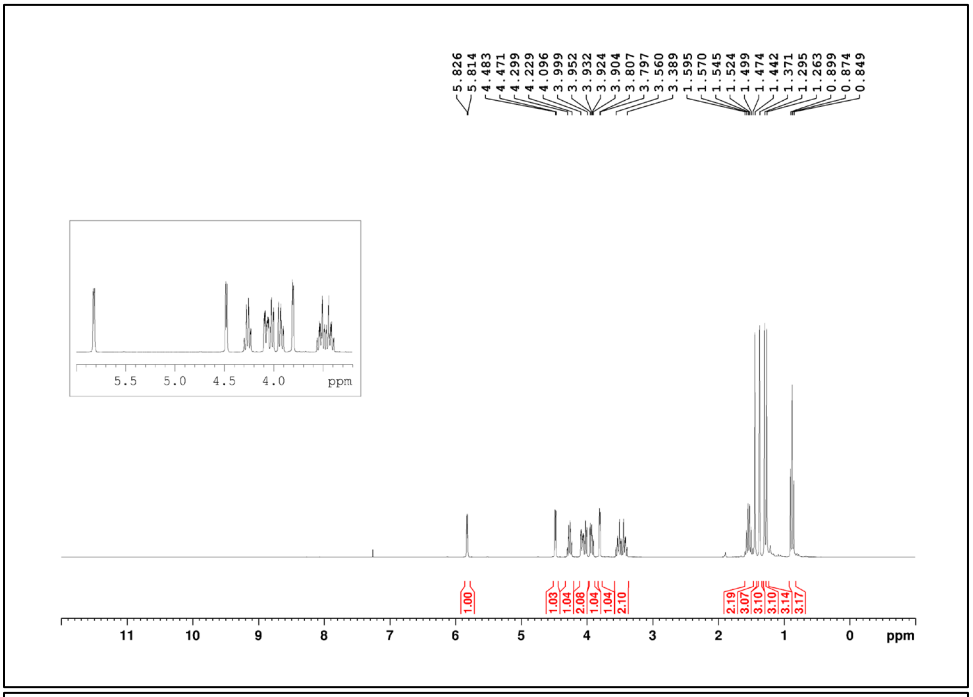


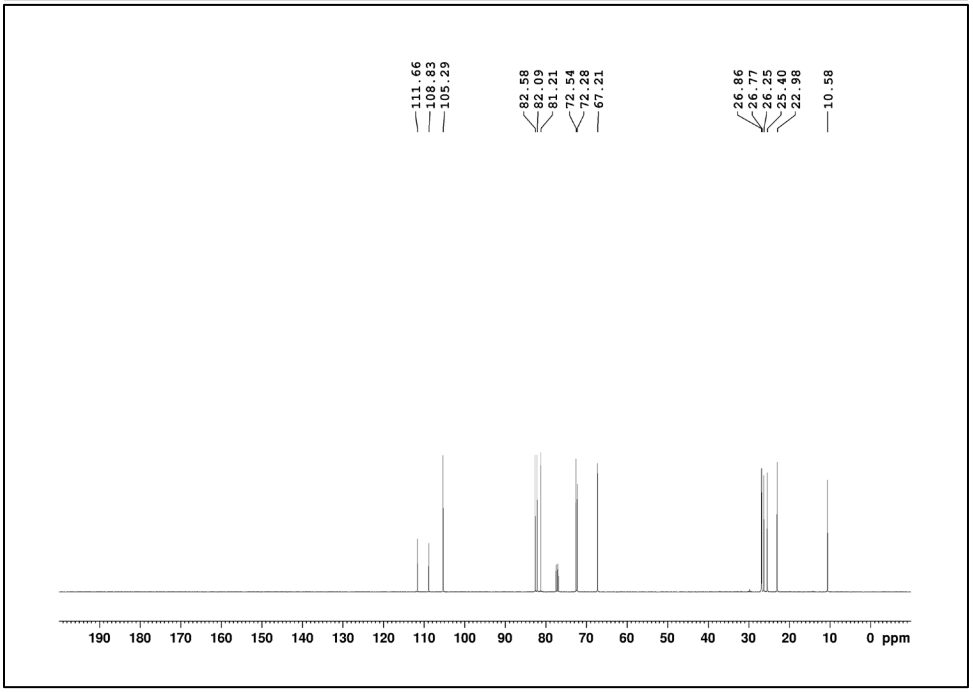




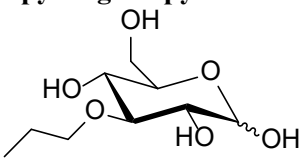
1,2:5,6-di-*O*-isopropylidene-3-*O*-propyl-α-D-glucofuranose (559):

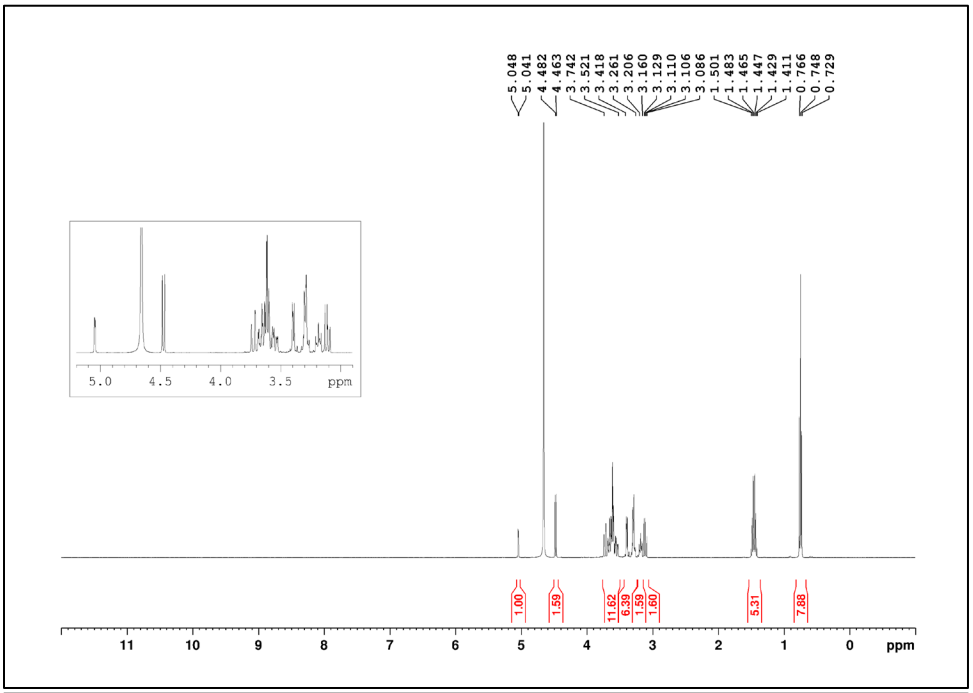


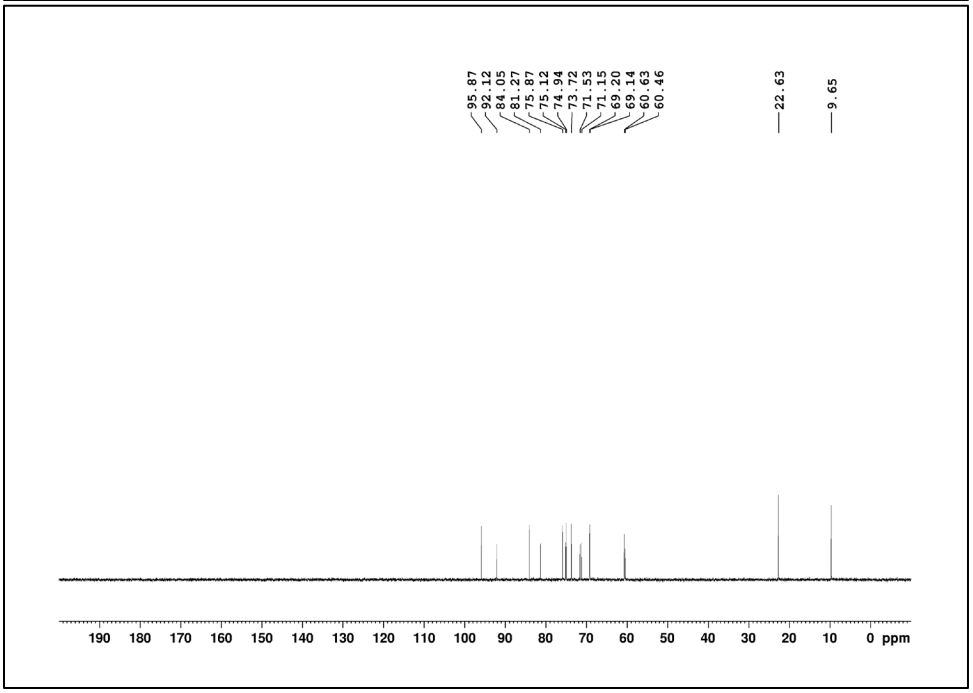




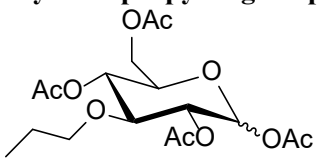
3-*O*-propyl-D-glucopyranoside (561):

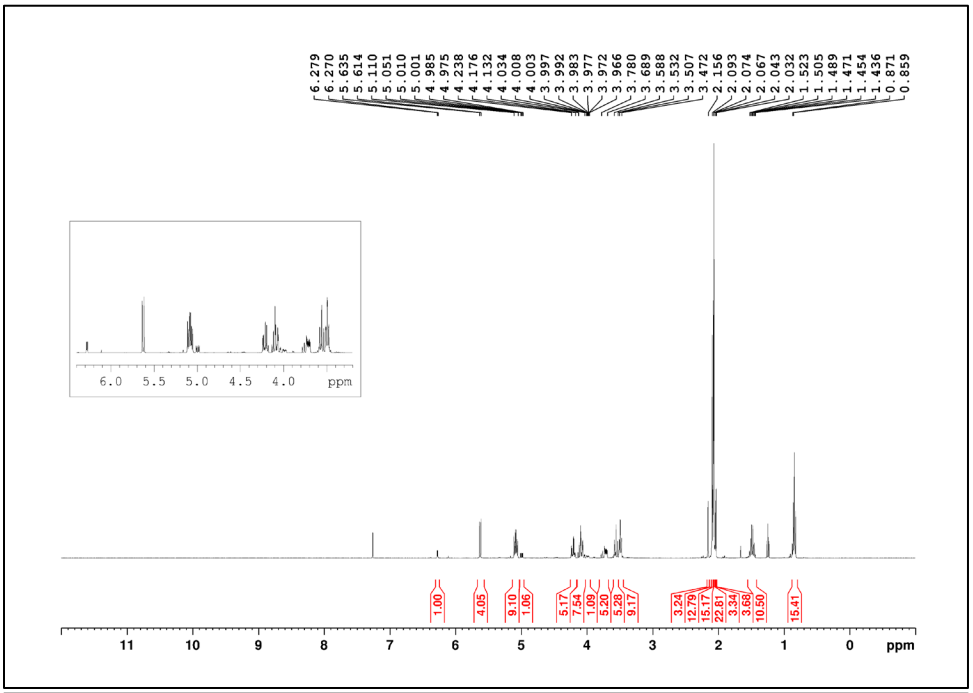


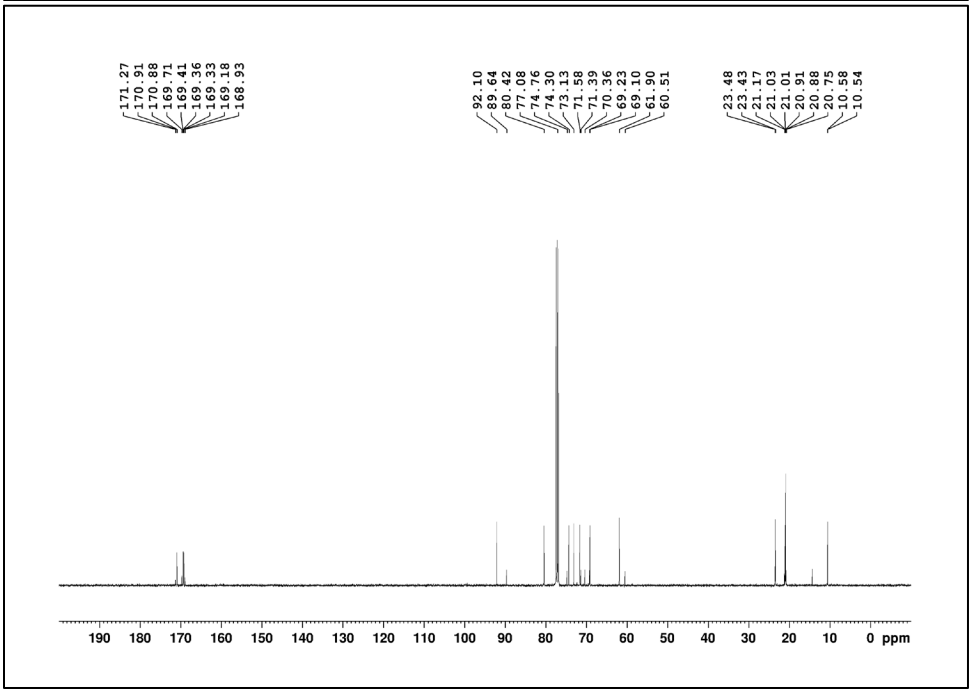




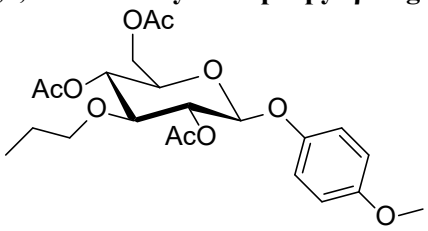
1,2,4,6-tetra-*O*-acetyl-3-*O*-propyl-D-glucopyranoside (563):

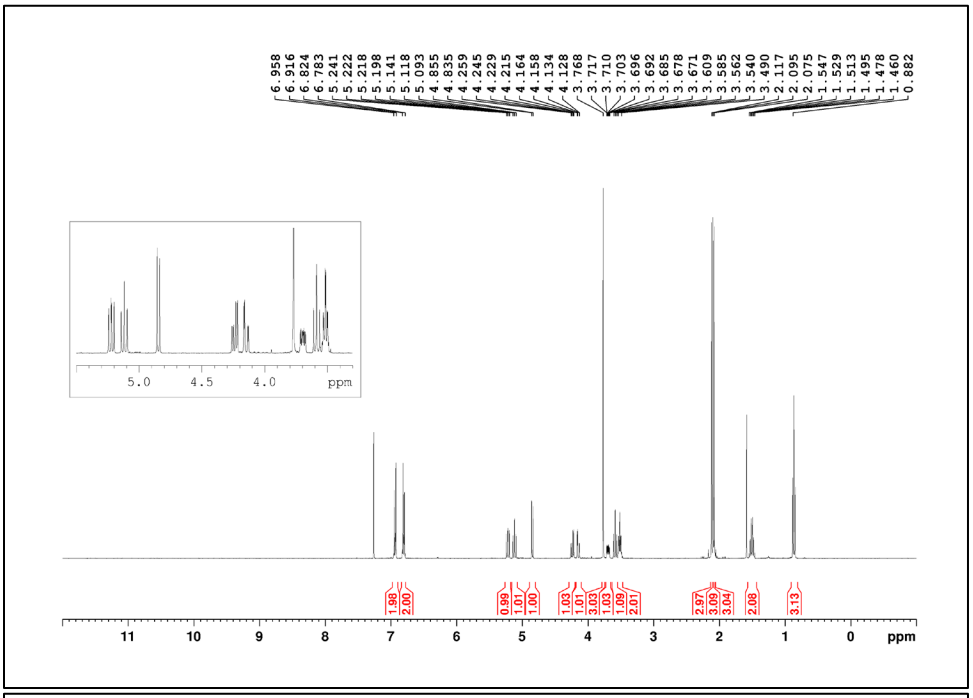


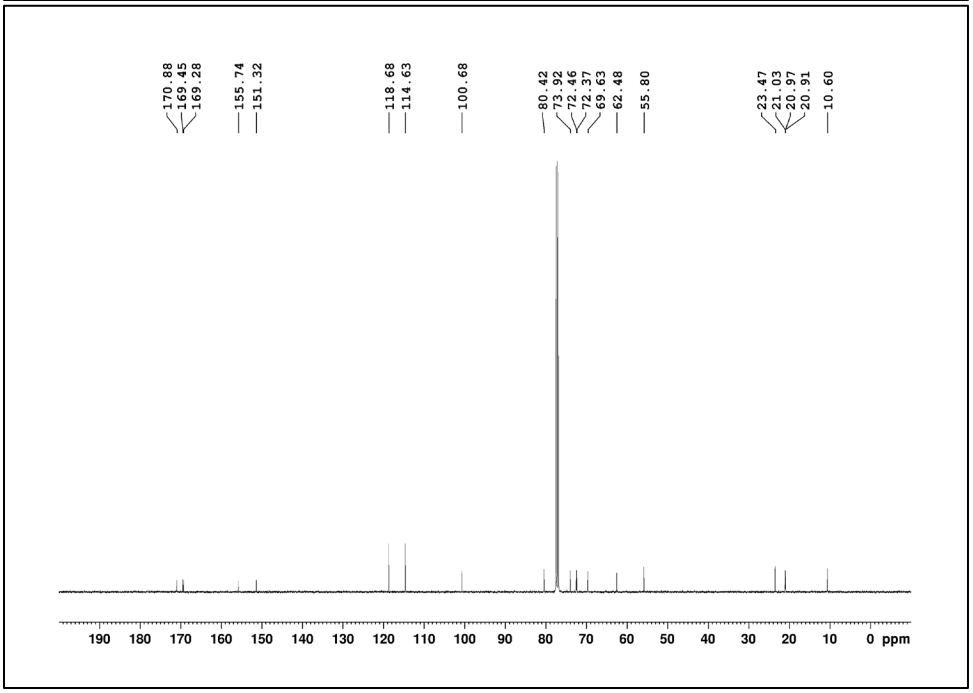




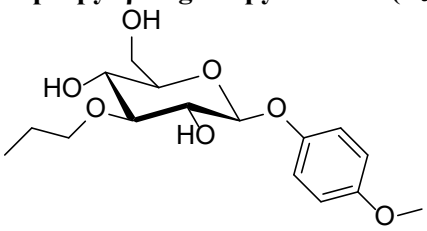
(4-methoxyphenyl)-2,4,6-tri-*O*-acetyl-3-*O*-propyl-β-D-glucopyranoside (565):

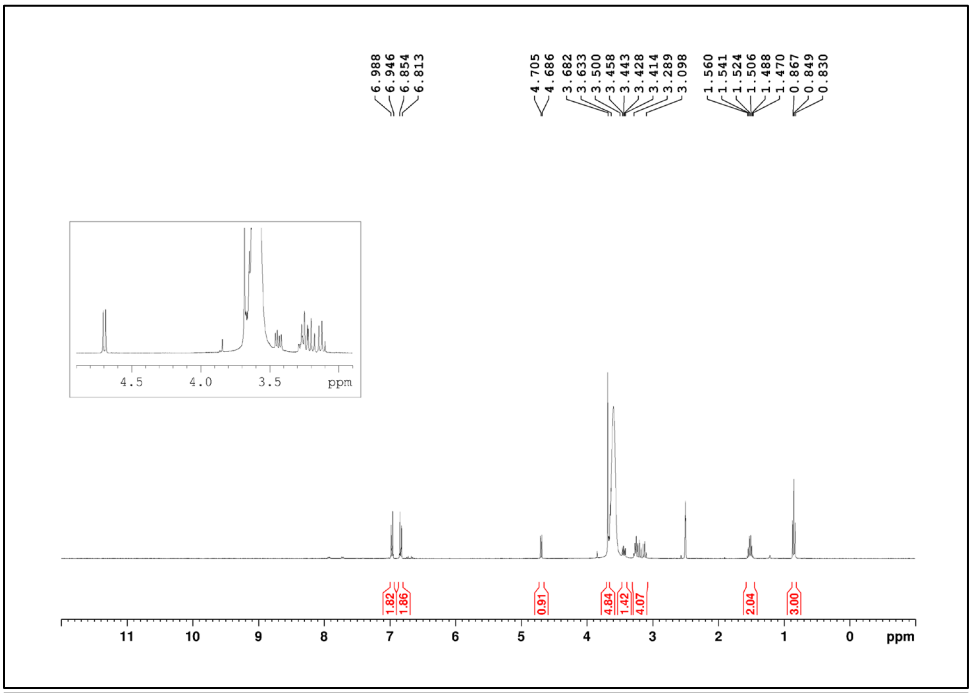


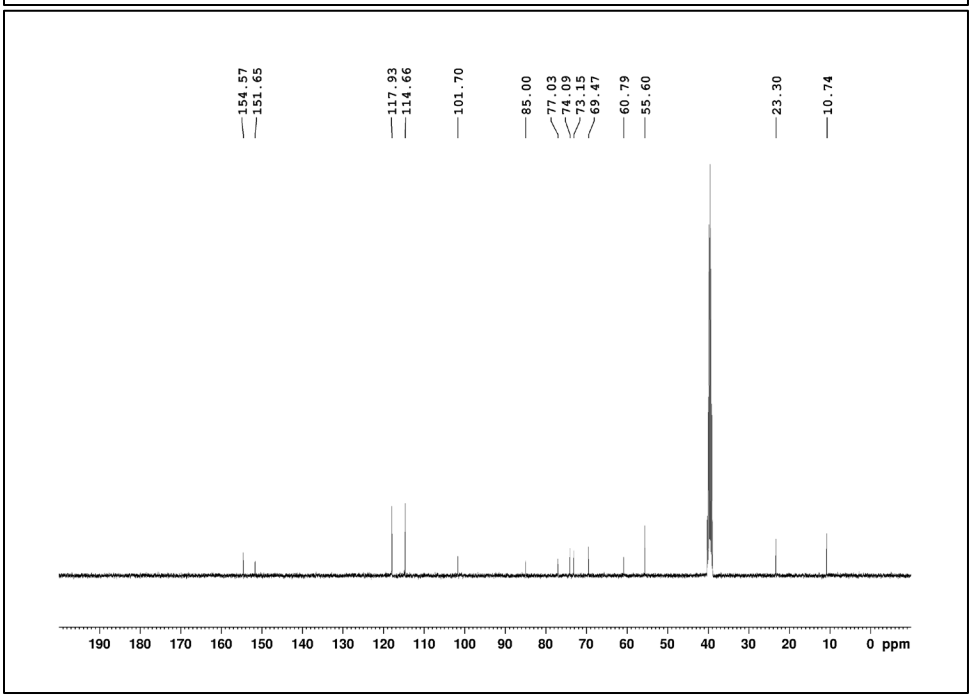




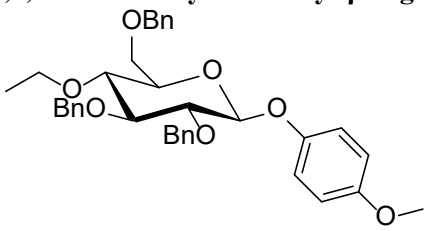
(4-methoxyphenyl)-3-*O*-propyl-β-D-glucopyranoside (C_3 OPr PMP-Glc, 102):

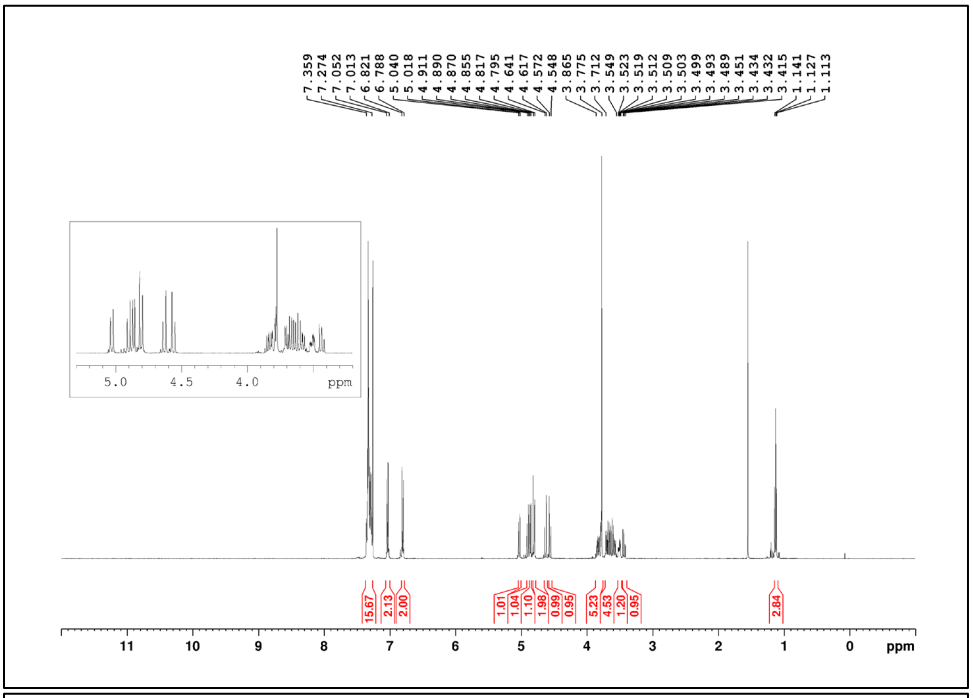


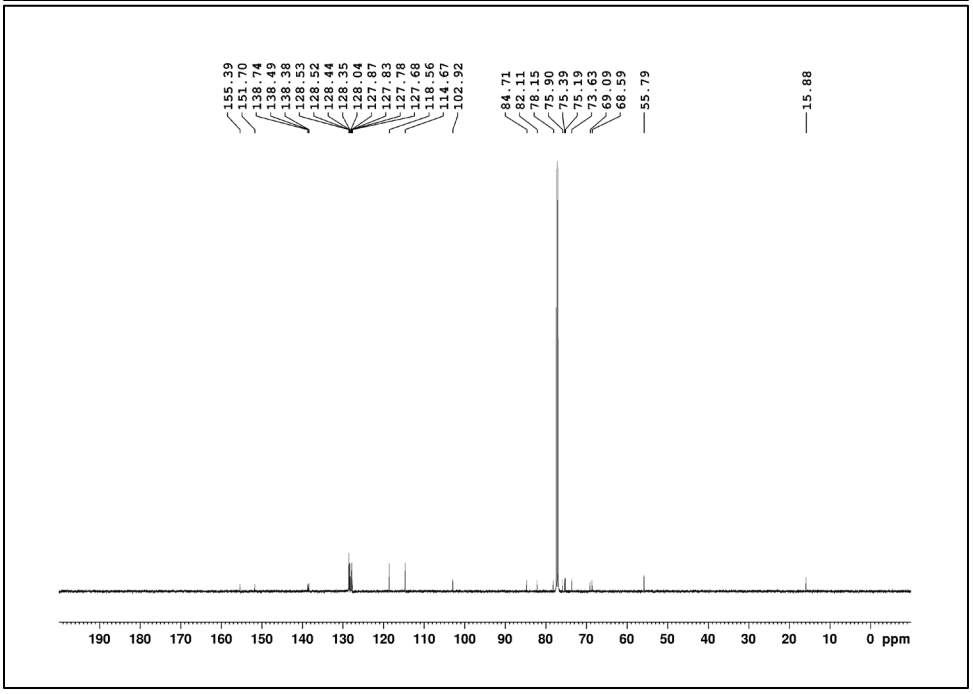




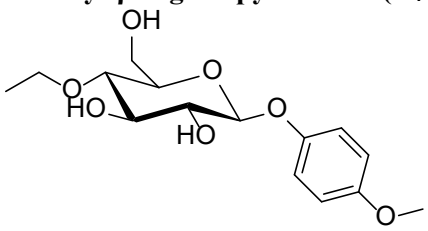
(4-methoxyphenyl)-2,3,6-tri-*O*-benzyl-4-*O*-ethyl-β-D-glucopyranoside (566):

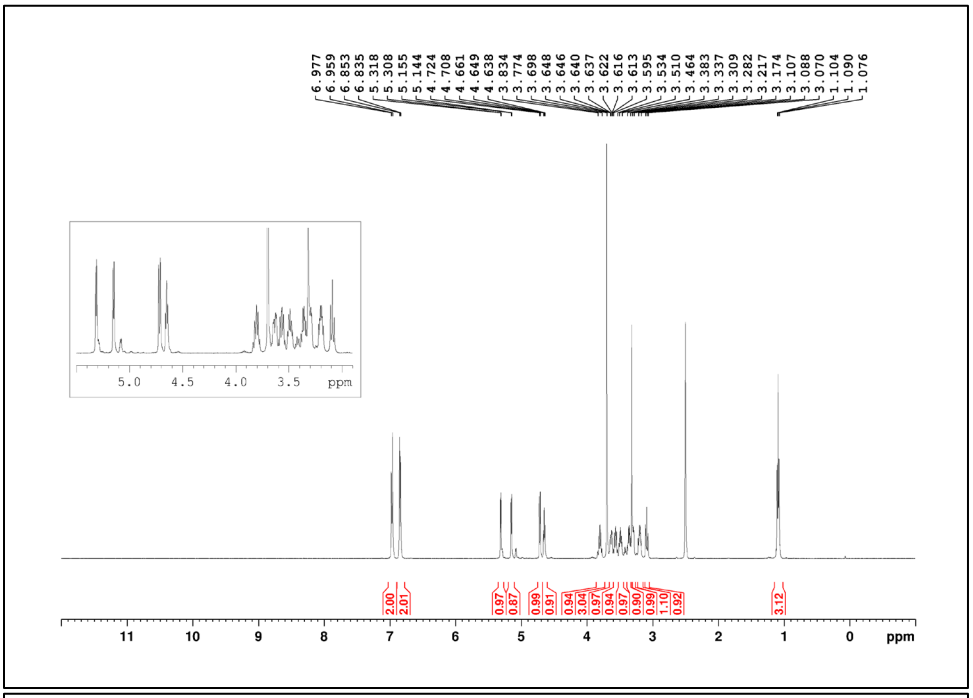


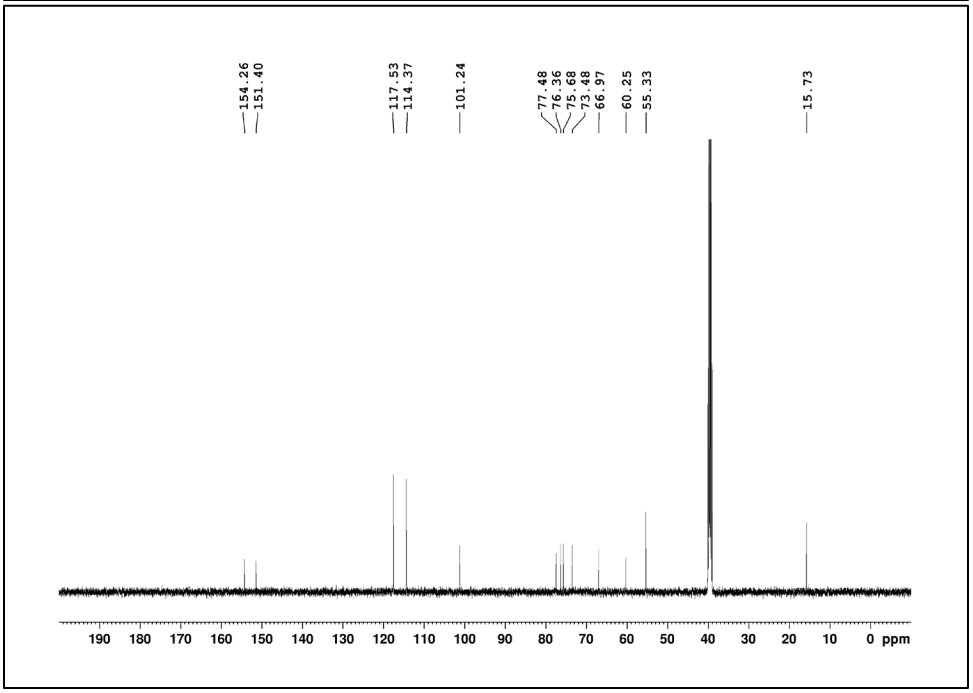




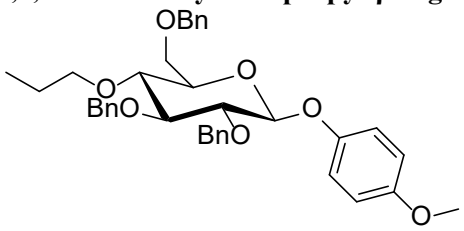
(4-methoxyphenyl)-4-*O*-ethyl-β-D-glucopyranoside (C_4 OEt PMP-Glc, 103):

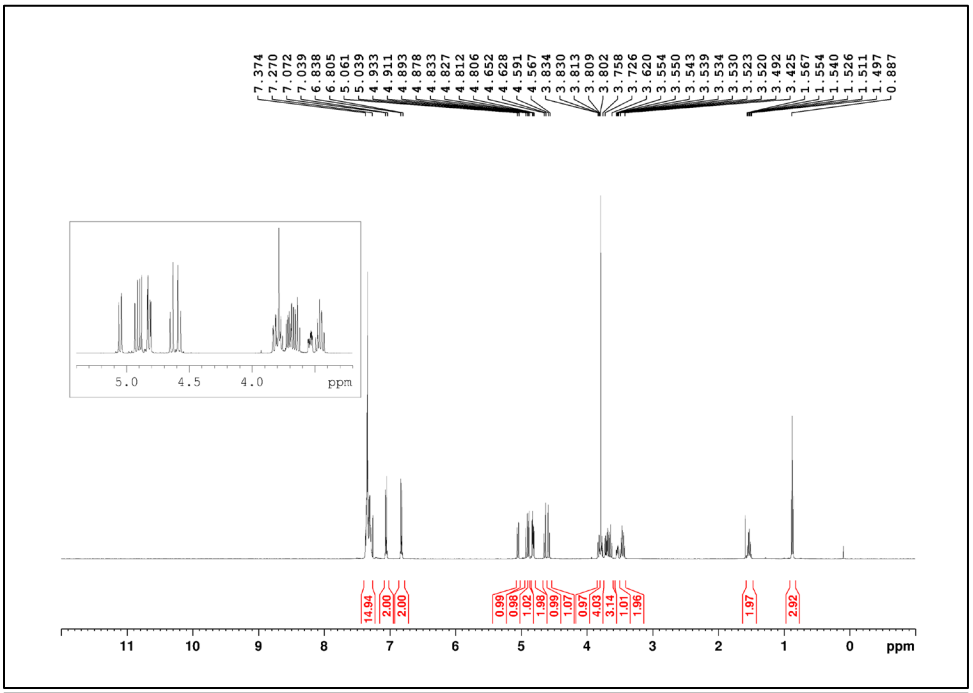


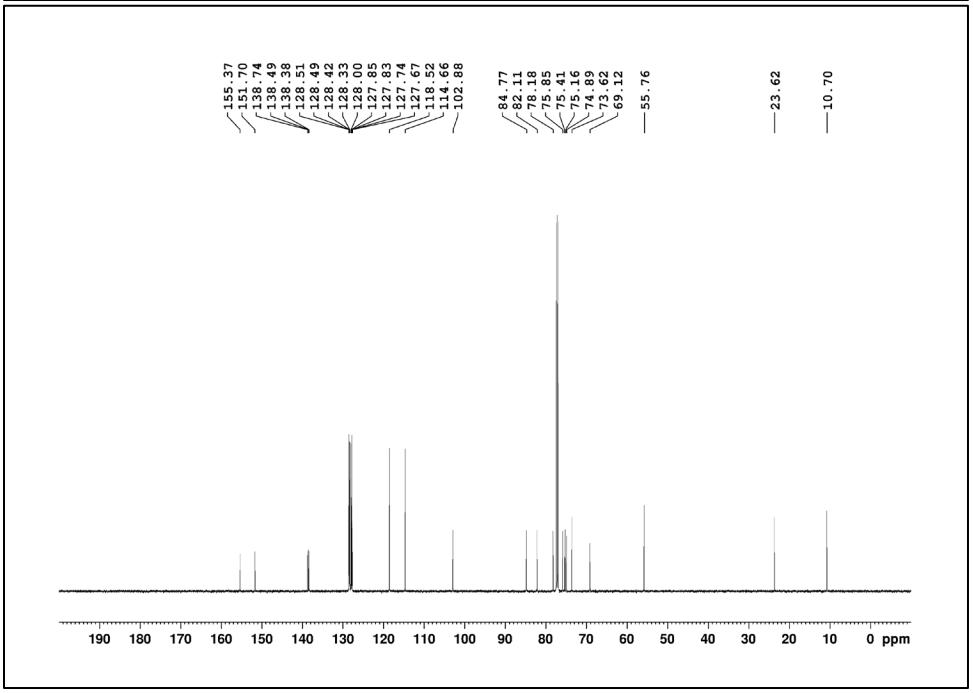




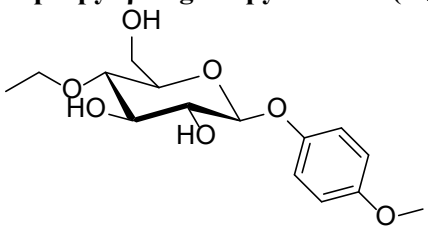
(4-methoxyphenyl)-2,3,6-tri-*O*-benzyl-4-*O*-propyl-β-D-glucopyranoside (567):

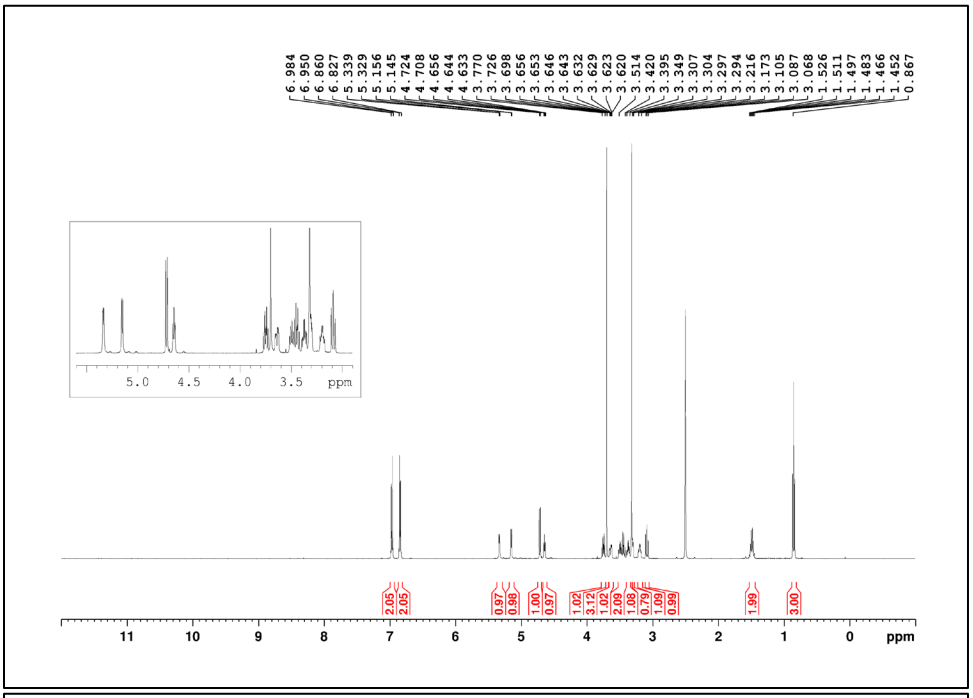


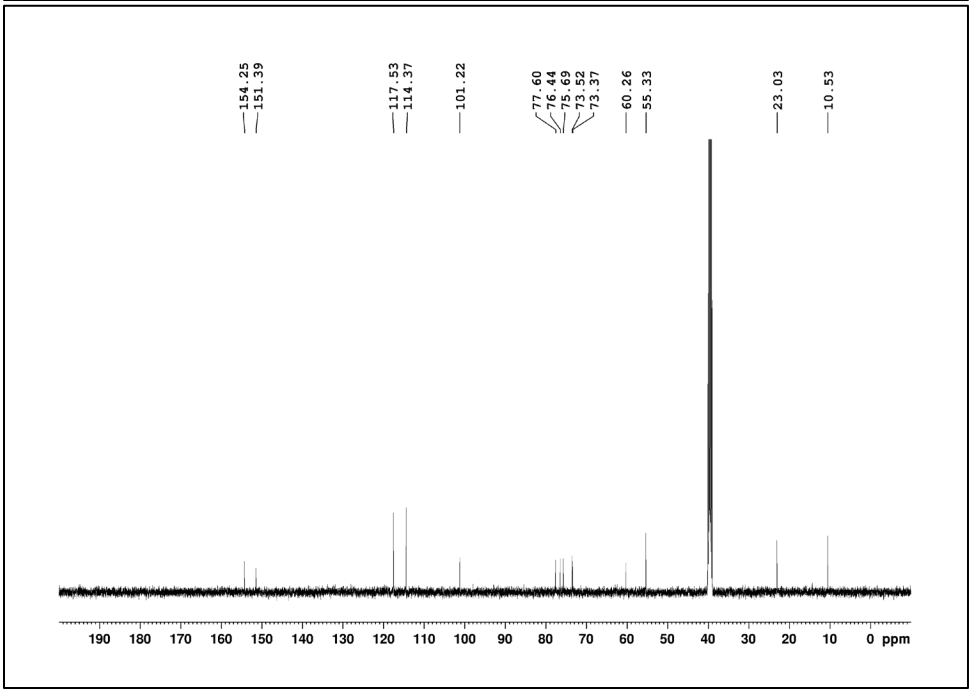




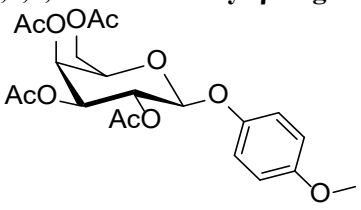
(4-methoxyphenyl)-4-*O*-propyl-β-D-glucopyranoside (C_4 OPr PMP-Glc, 104):

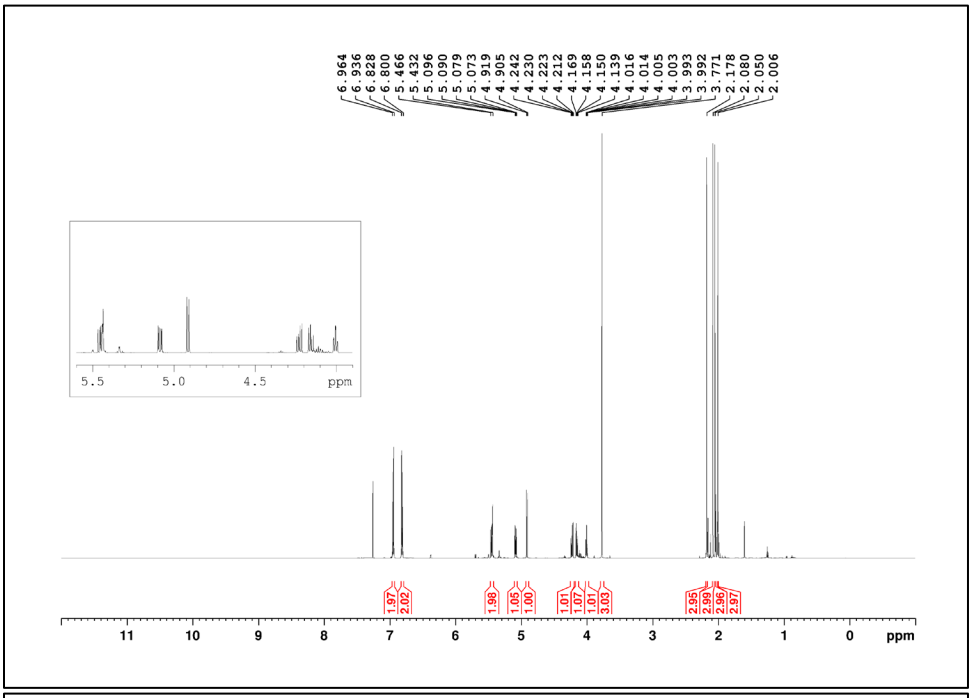


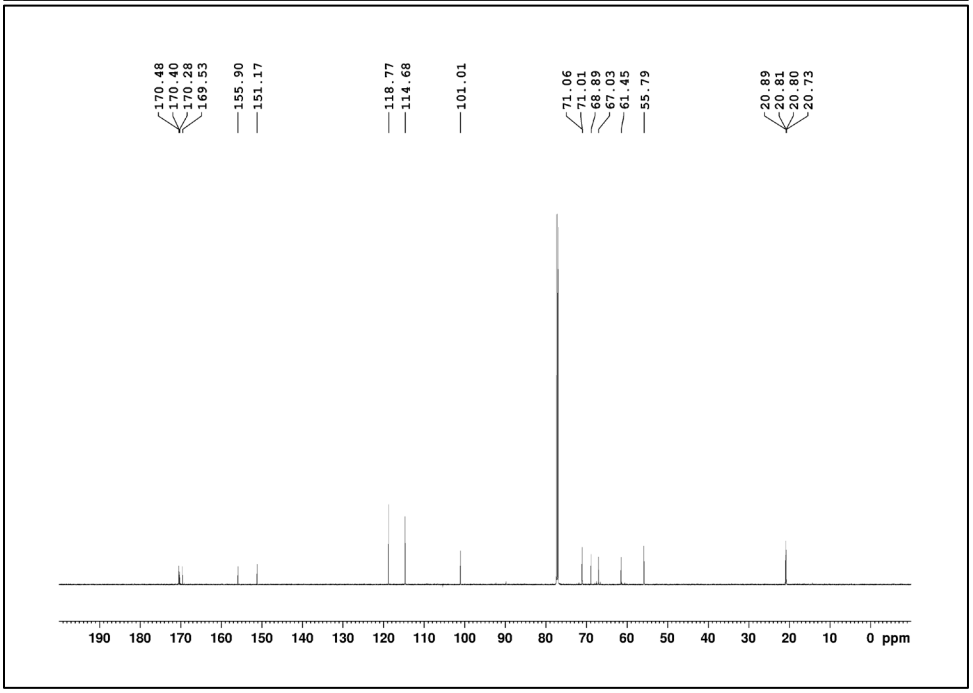




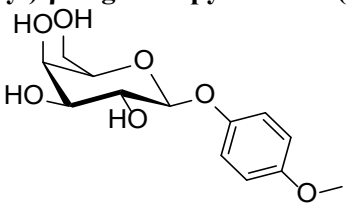
(4-methoxyphenyl)-2,3,4,6-tetra-*O*-acetyl-β-D-galactopyranoside (569):



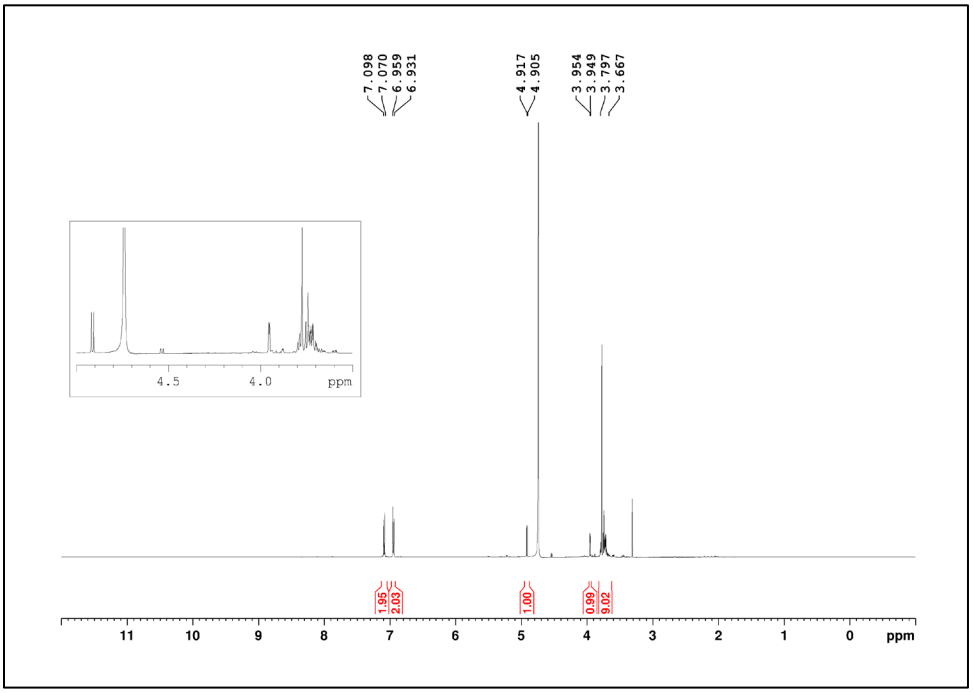




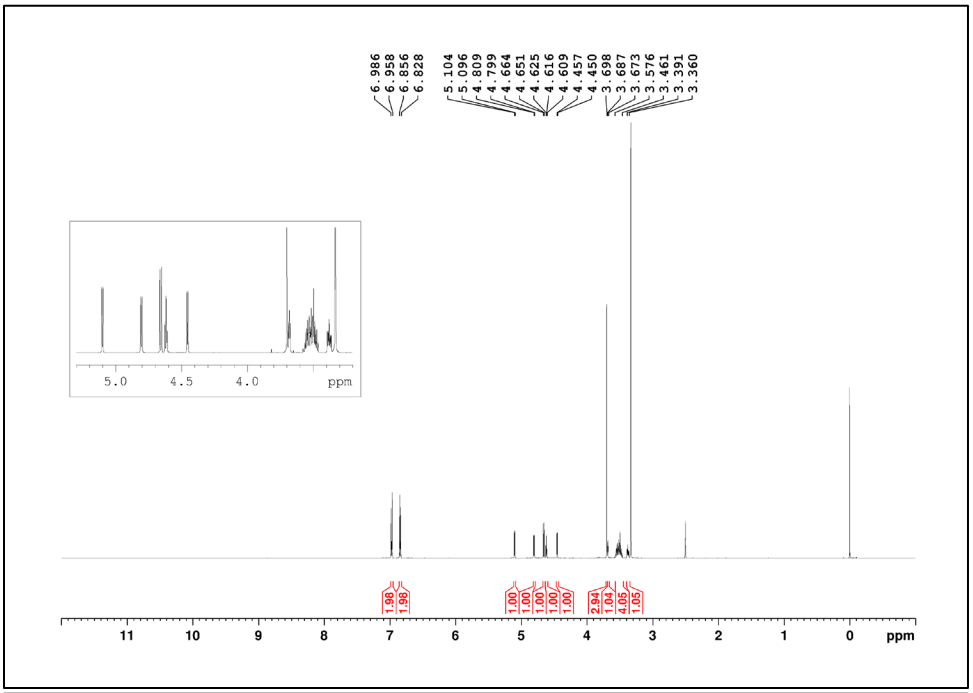
(4-methoxyphenyl)-β-D-galactopyranoside (PMP-Gal, 107):

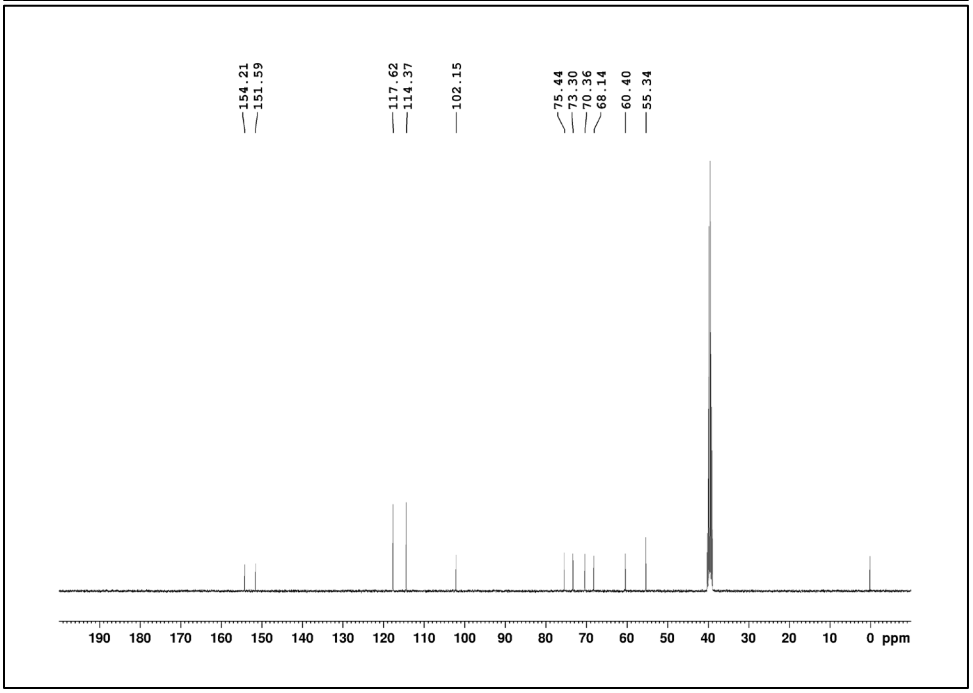


In D_2O:

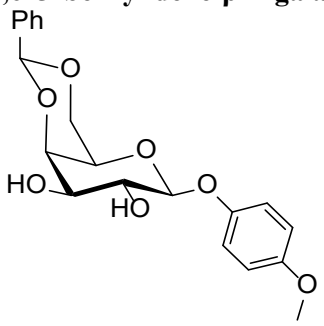


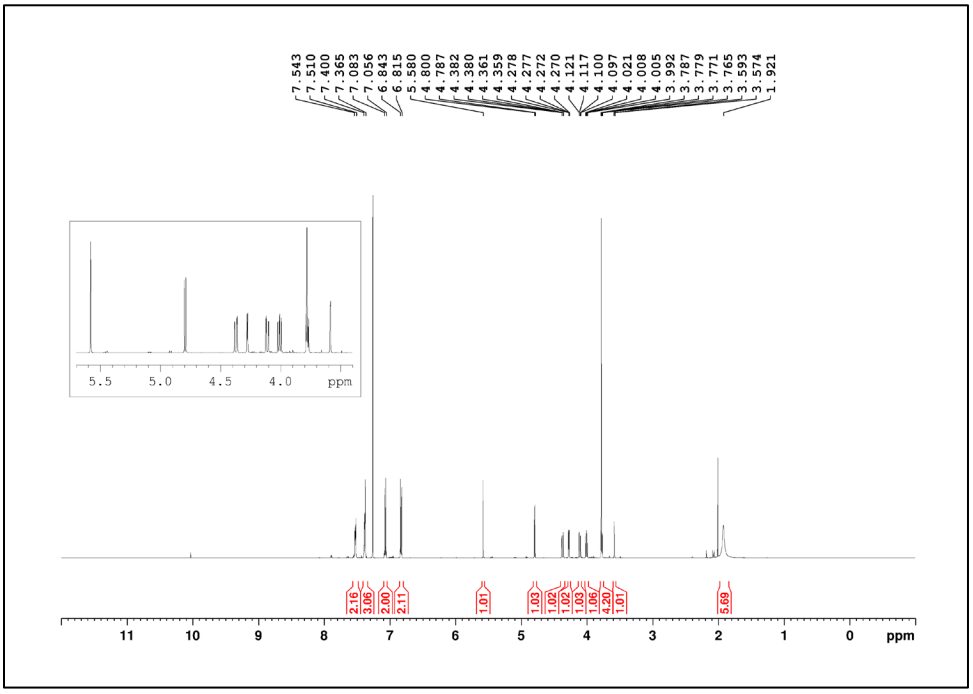
In DMSO-d_6:


6.986
6.958
6.856
6.828
5.104
5.096
4.809
4.799
4.664
4.651
4.625
4.616
4.609
4.457
4.450
3.698
3.687
3.673
3.576
3.461
3.391
3.360
5.0
4.5
4.0
ppm
1.98
1.98
1.00
1.00
1.00
1.00
1.00
2.94
1.04
4.05
1.05
11
10
9
8
7
6
5
4
3
2
1
0
ppm

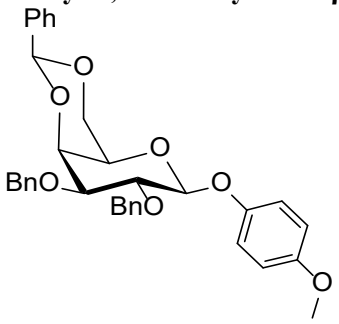

154.21
151.59
117.62
114.37
102.15
75.44
73.30
70.36
68.14
60.40
55.34
190
180
170
160
150
140
130
120
110
100
90
80
70
60
50
40
30
20
10
0 ppm

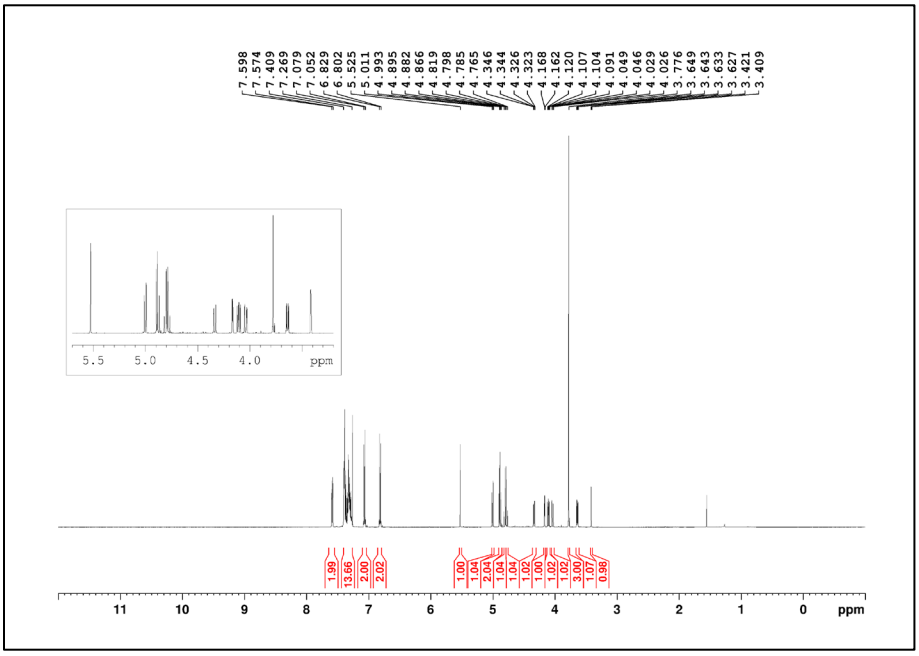
(4-methoxyphenyl)-4,6-*O*-benzylidene-β-D-galactopyranoside (572):

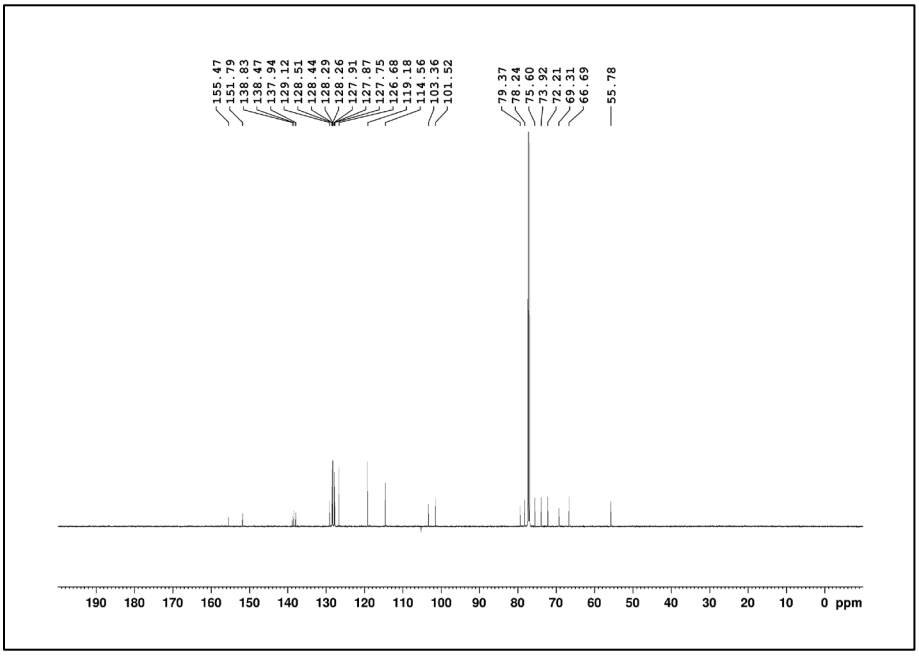




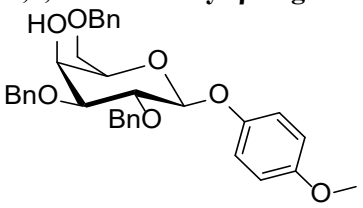
(4-methoxyphenyl)-2,3-di-*O*-benzyl-4,6-*O*-benzylidene-β-D-galactopyranoside (573):

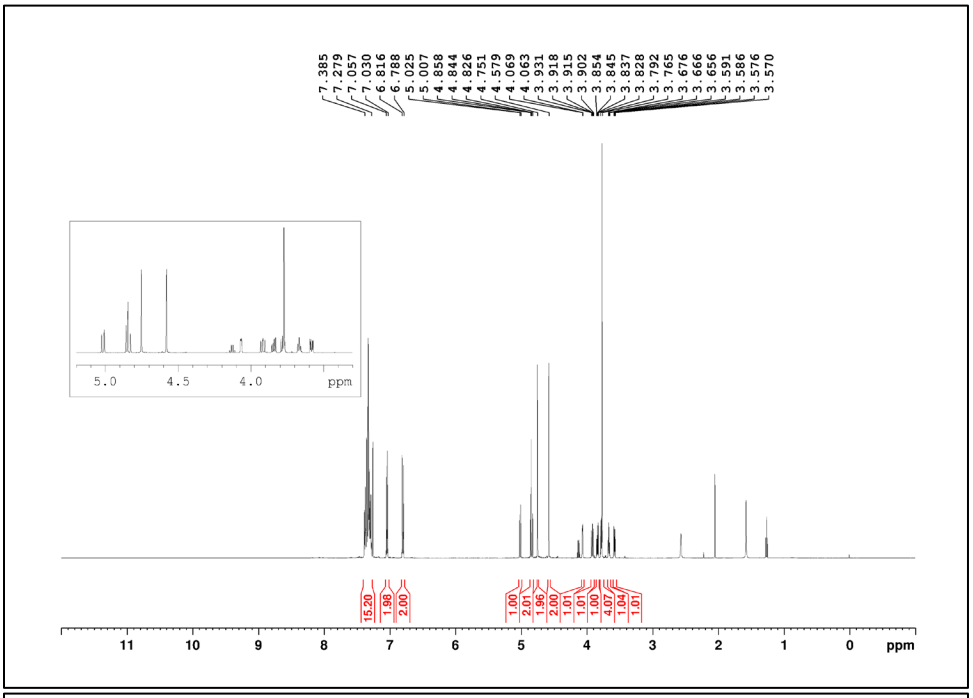


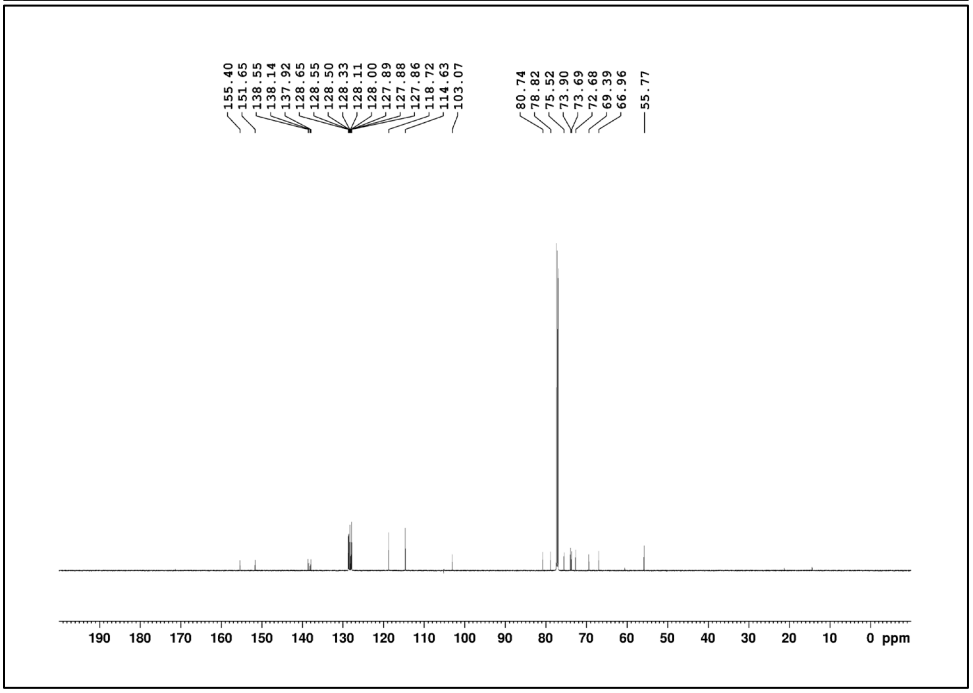




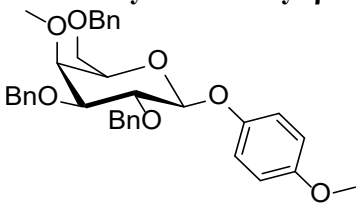
(4-methoxyphenyl)-2,3,6-tri-*O*-benzyl-β-D-galactopyranoside (574):

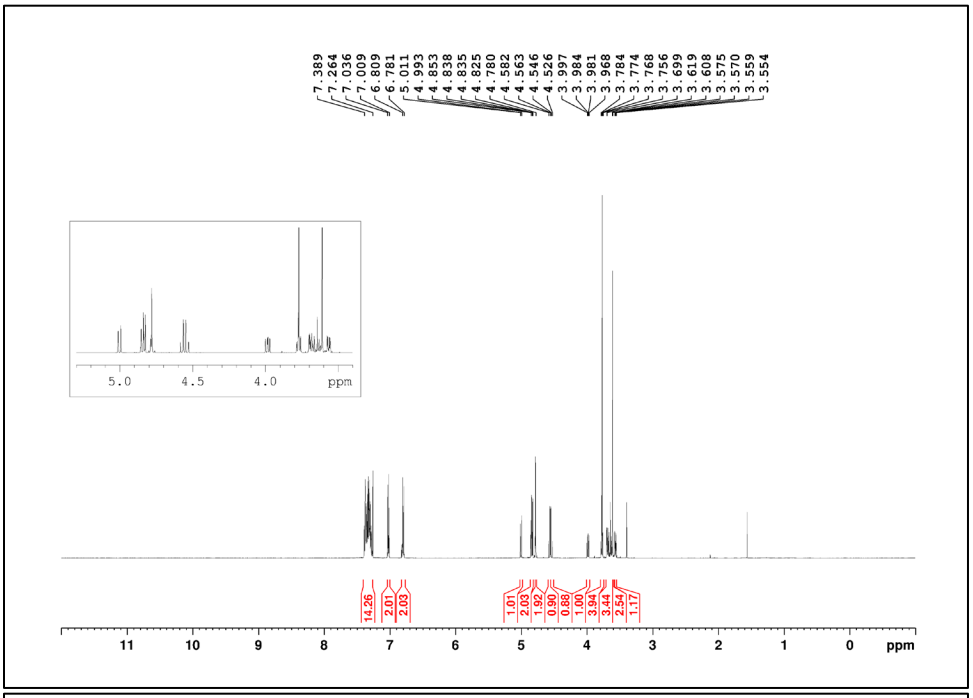


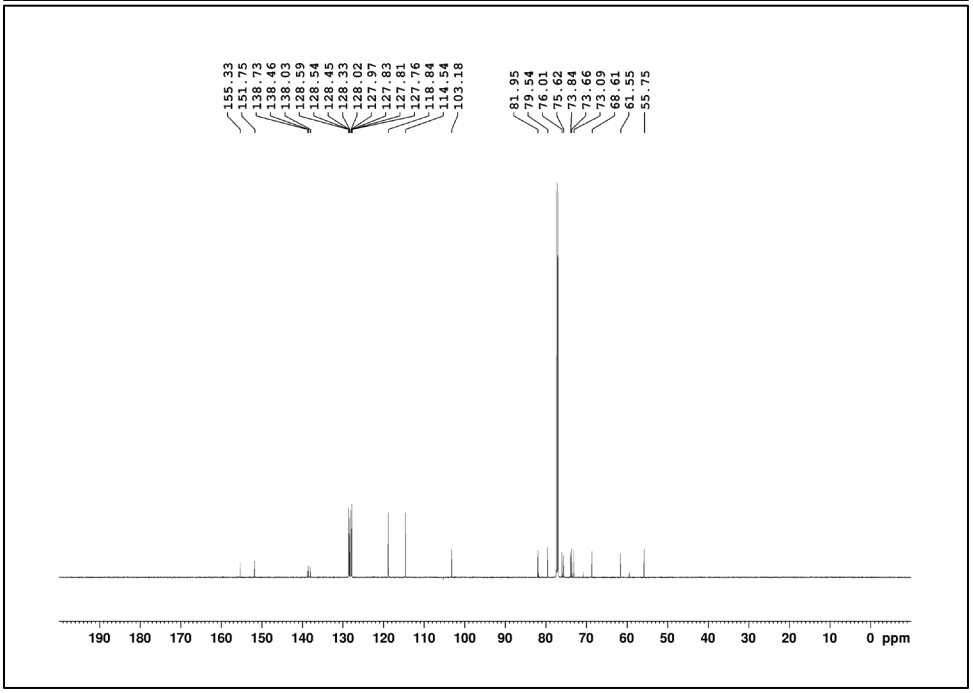




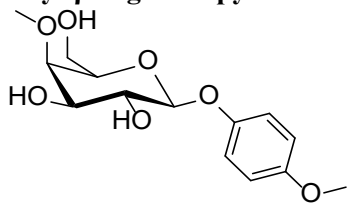
(4-methoxyphenyl)-2,3,6-tri-*O*-benzyl-4-*O*-methyl-β-D-galactopyranoside (575):

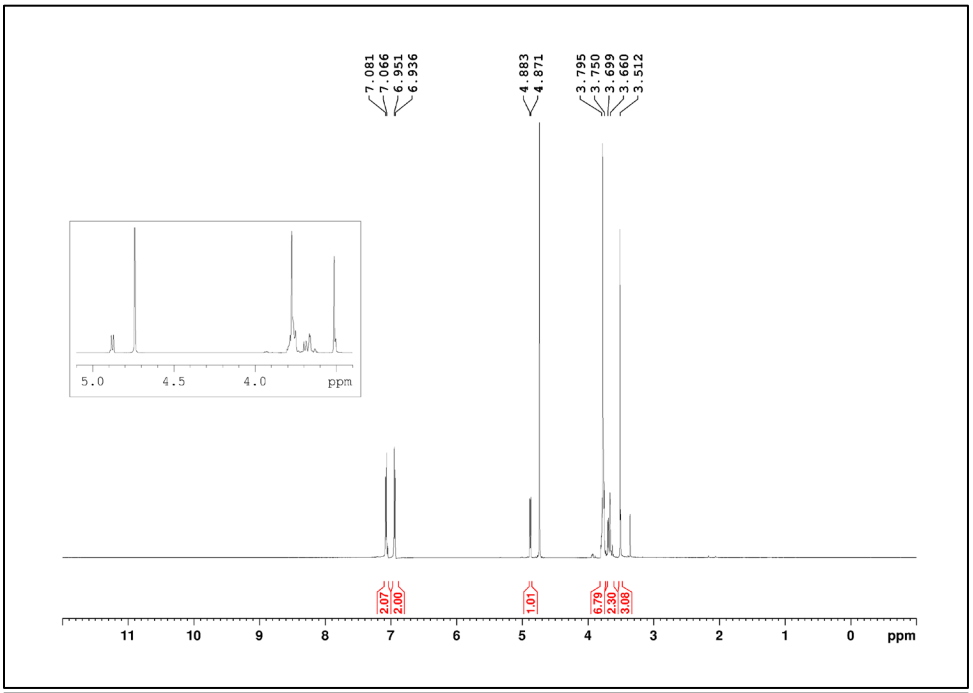


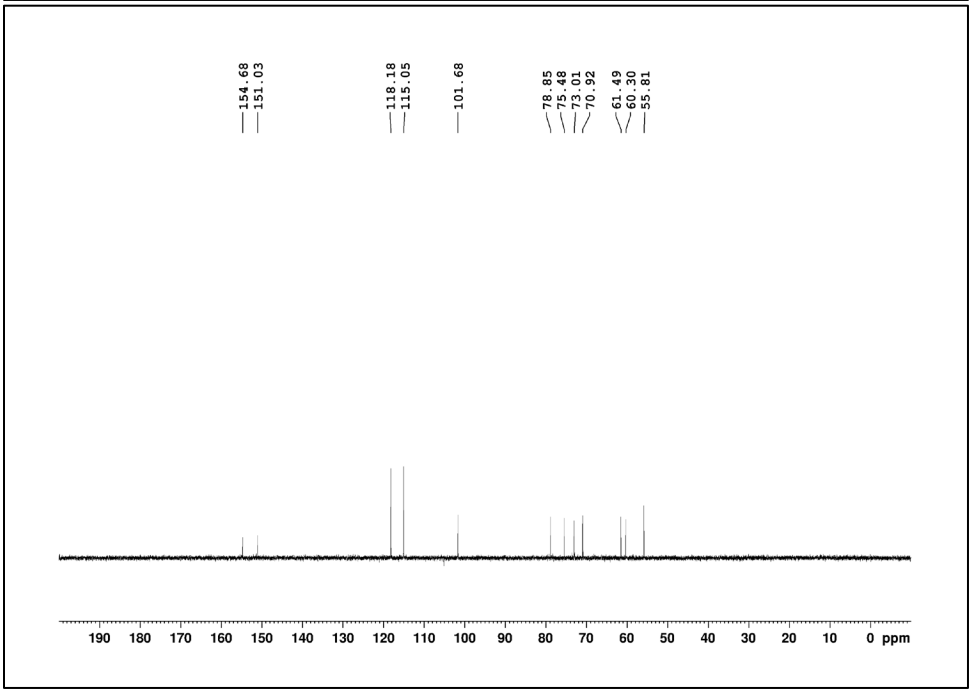




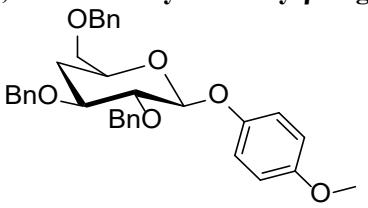
(4-methoxyphenyl)-4-*O*-methyl-β-D-galactopyranoside (C_4 OMe PMP-Gal, 108):

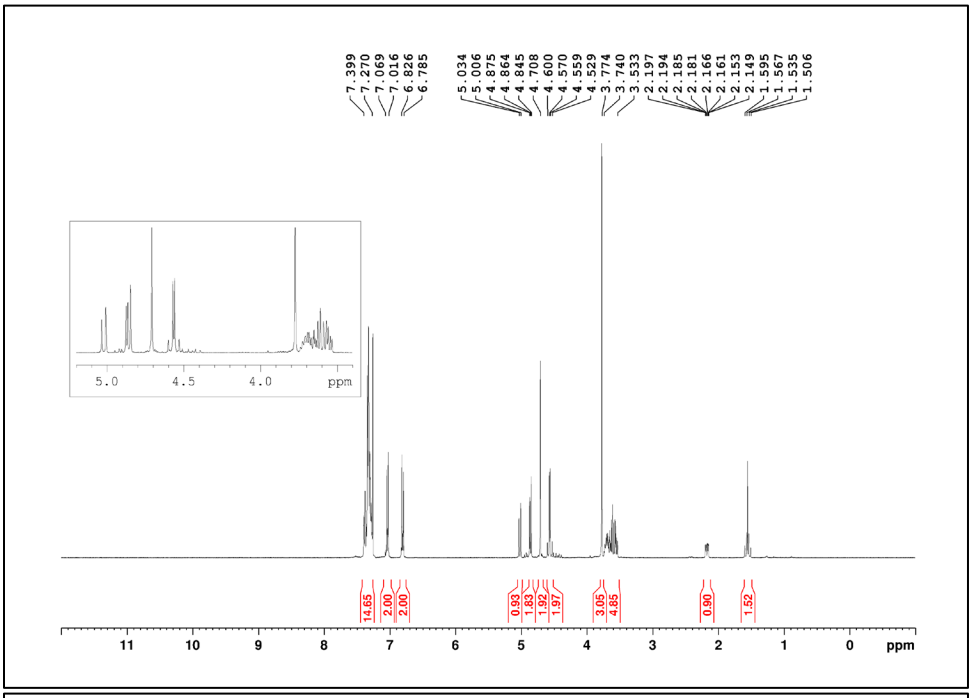


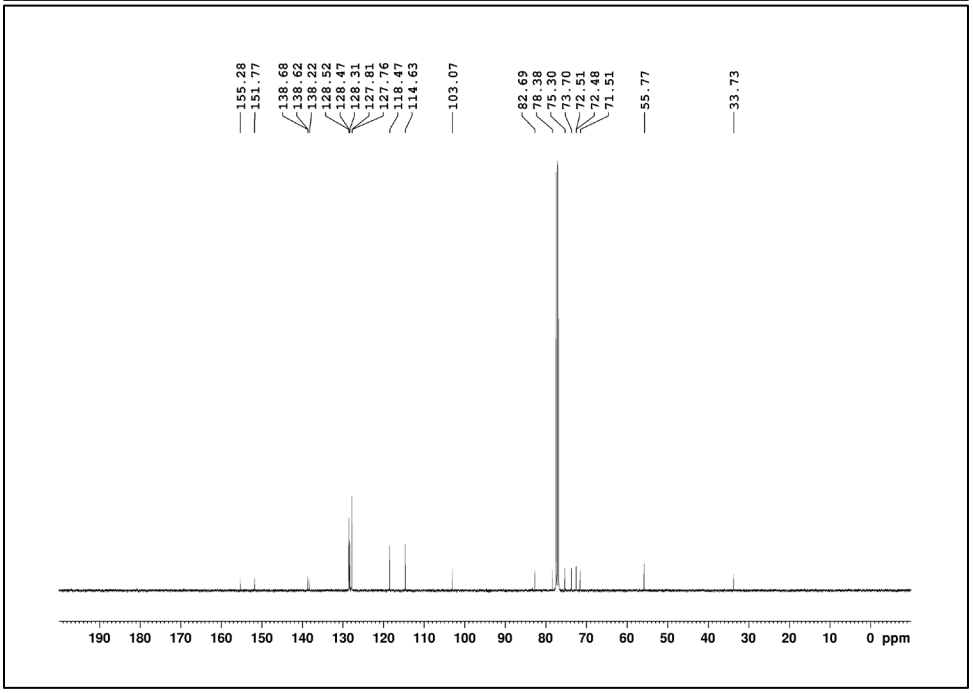




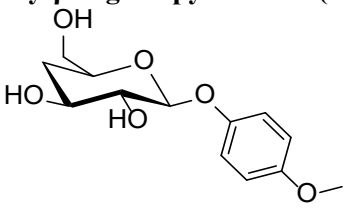
(4-methoxyphenyl)-2,3,6-tri-*O*-benzyl-4-deoxy-β-D-glucopyranoside (576):

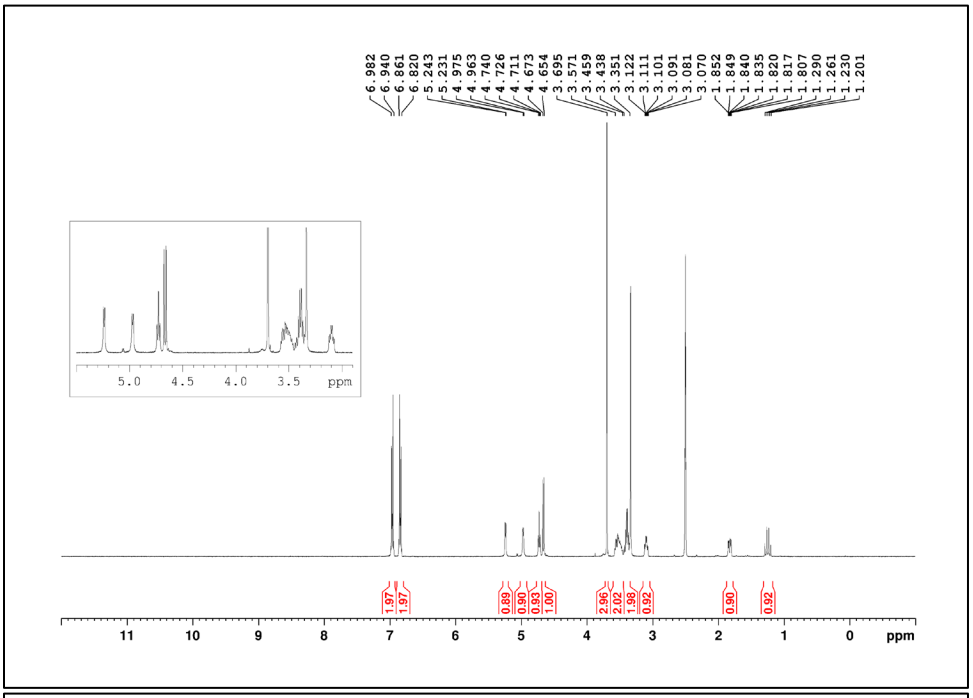


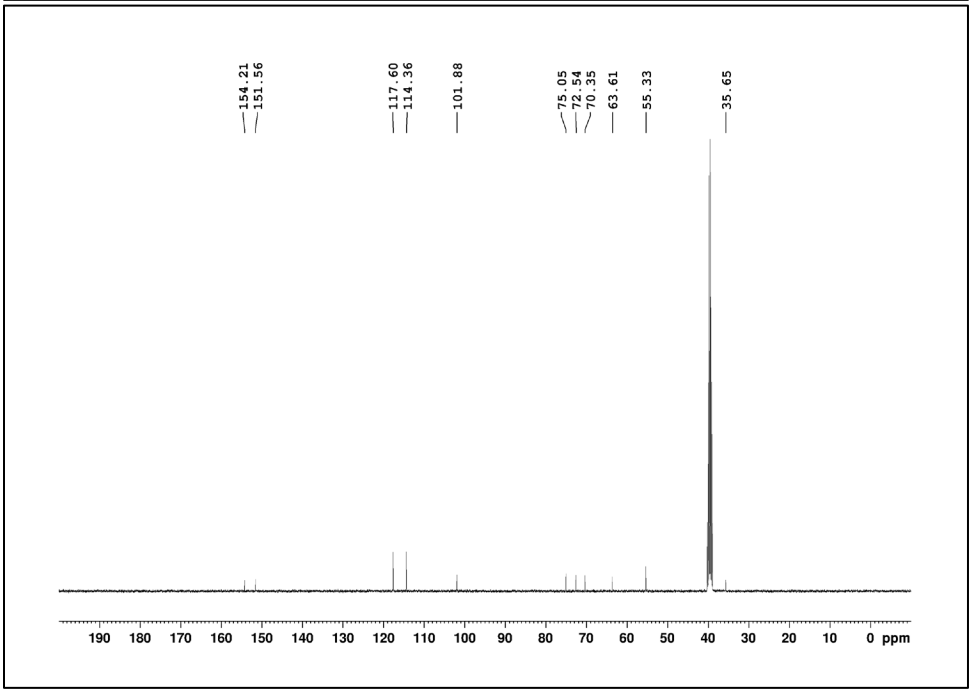




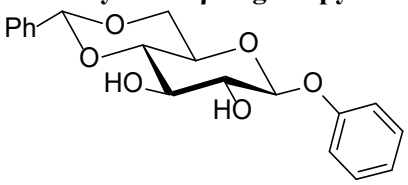
(4-methoxyphenyl)-4-deoxy-β-D-glucopyranoside (C_4 Deoxy PMP-Glc, 109):

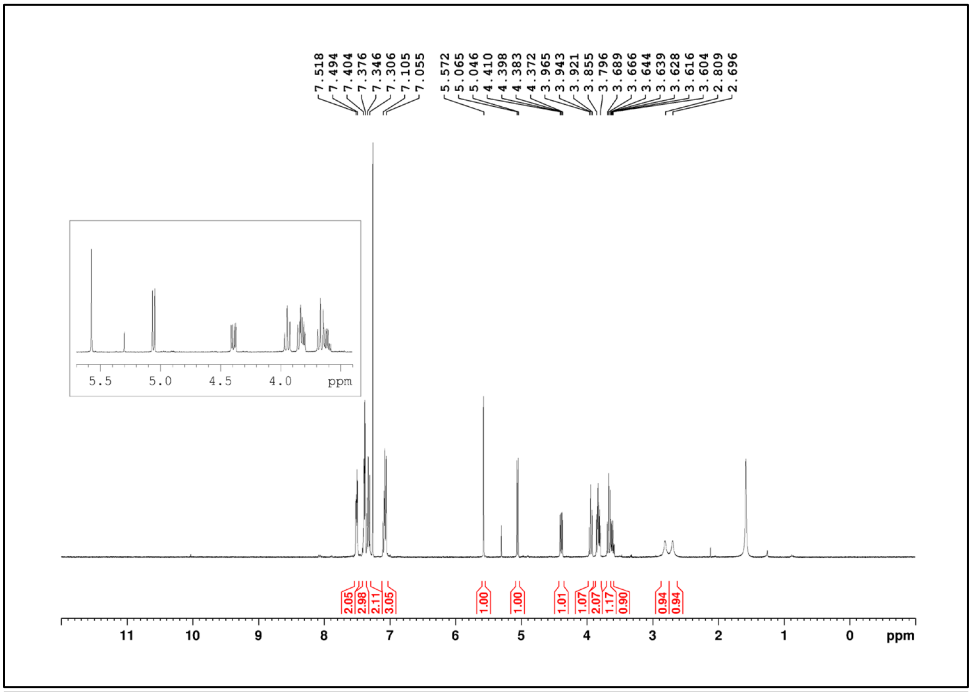


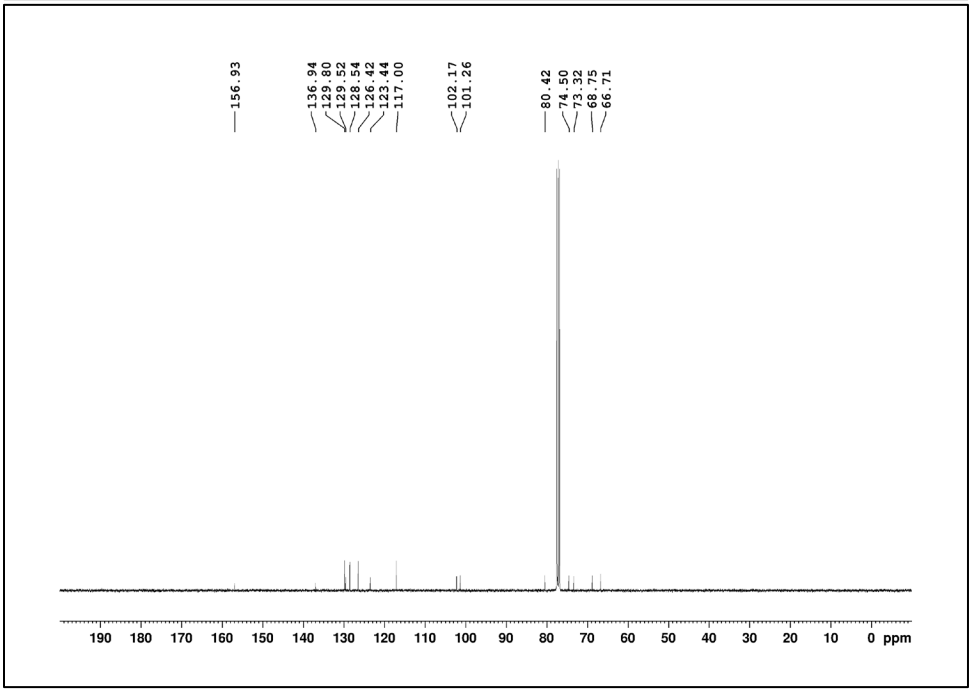




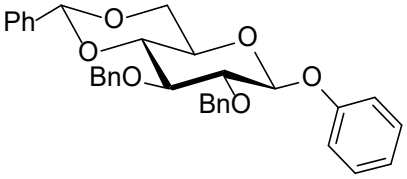
phenyl-4,6-*O*-benzylidene-β-D-glucopyranoside (578):

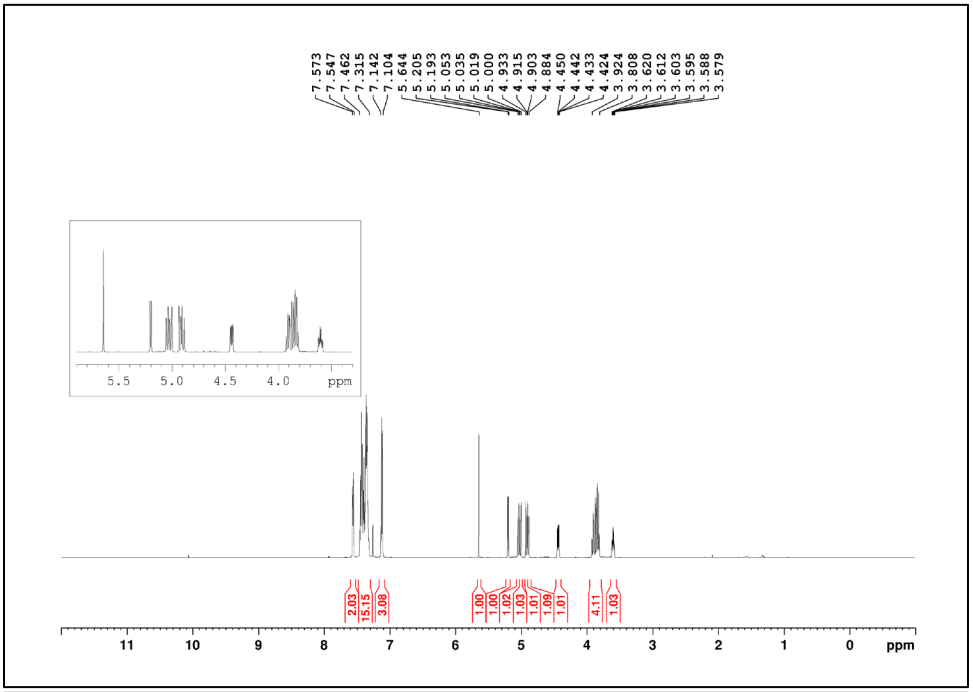


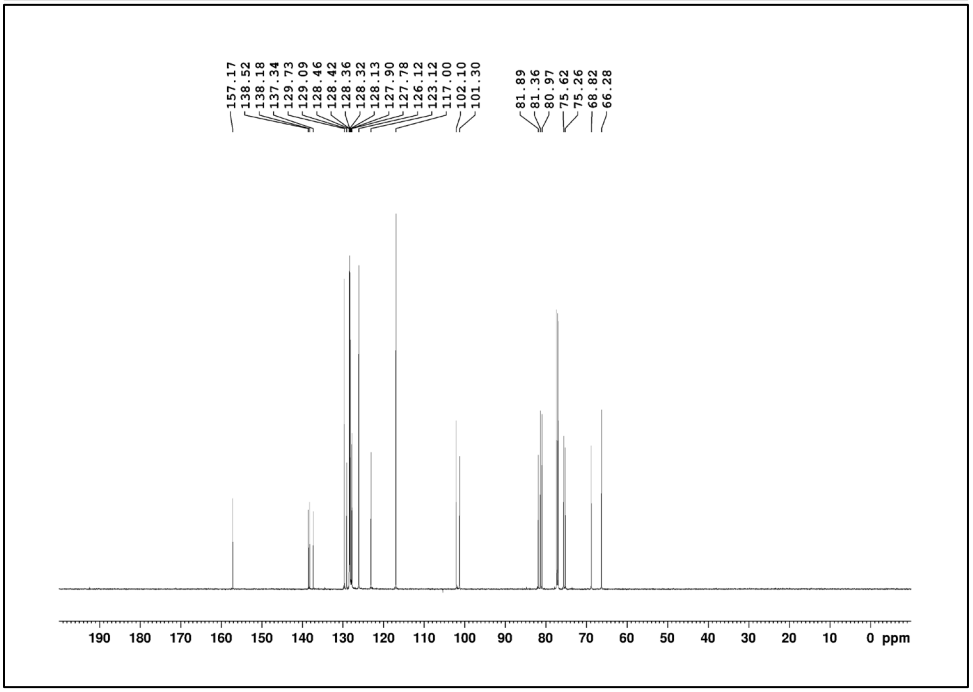




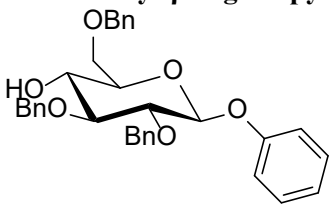
(phenyl)-2,3-di-*O*-benzyl-4,6-*O*-benzylidene-β-D-glucopyranoside (579):

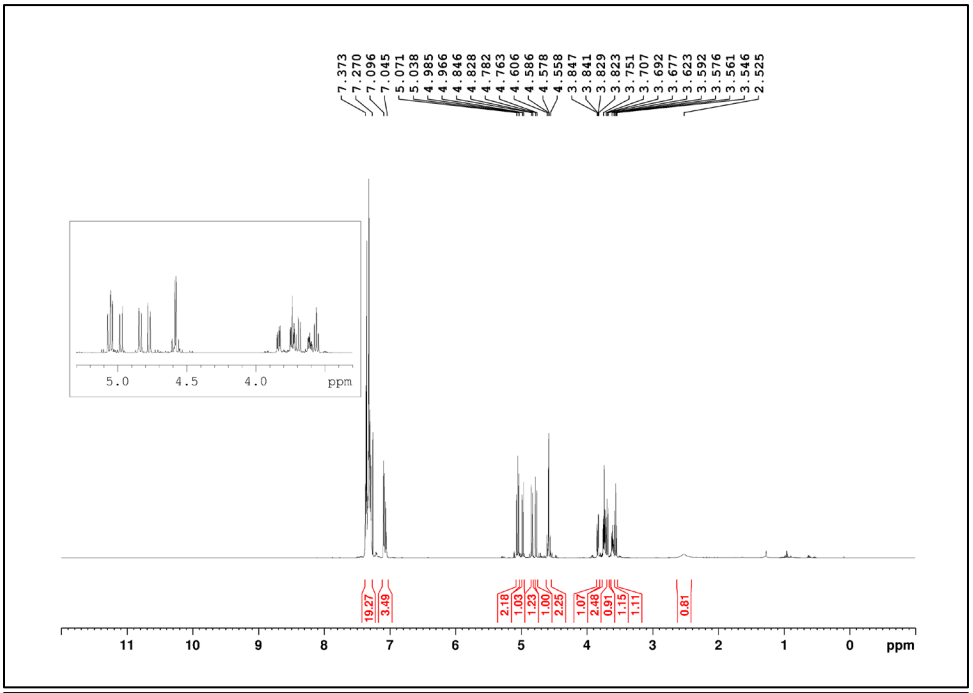


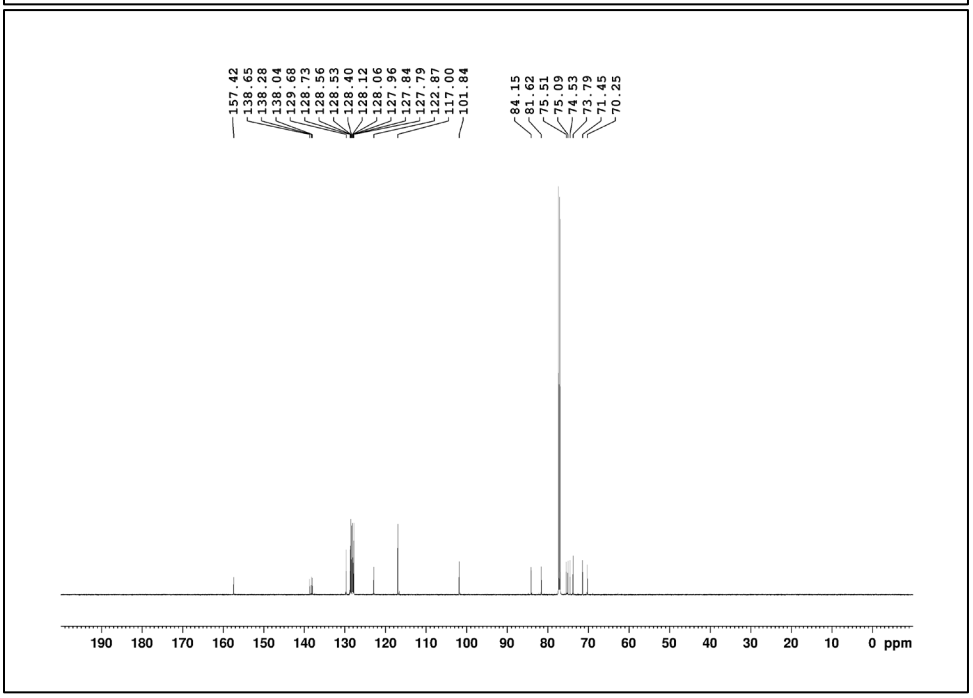




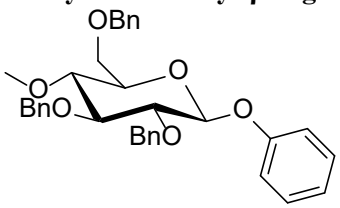
(phenyl)-2,3,6-tri-*O*-benzyl-β-D-glucopyranoside (580):

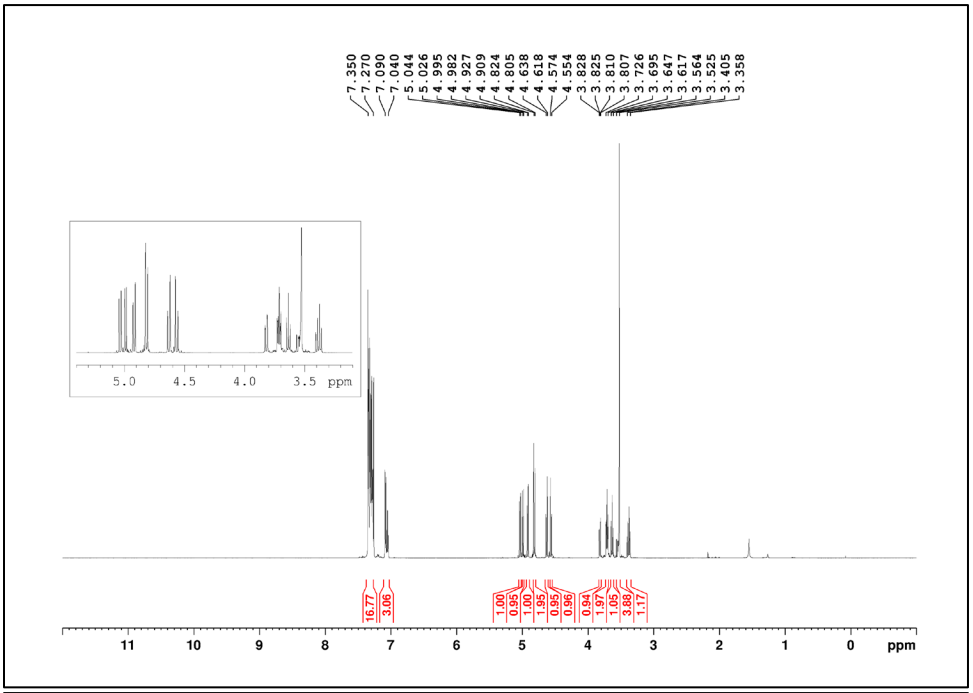


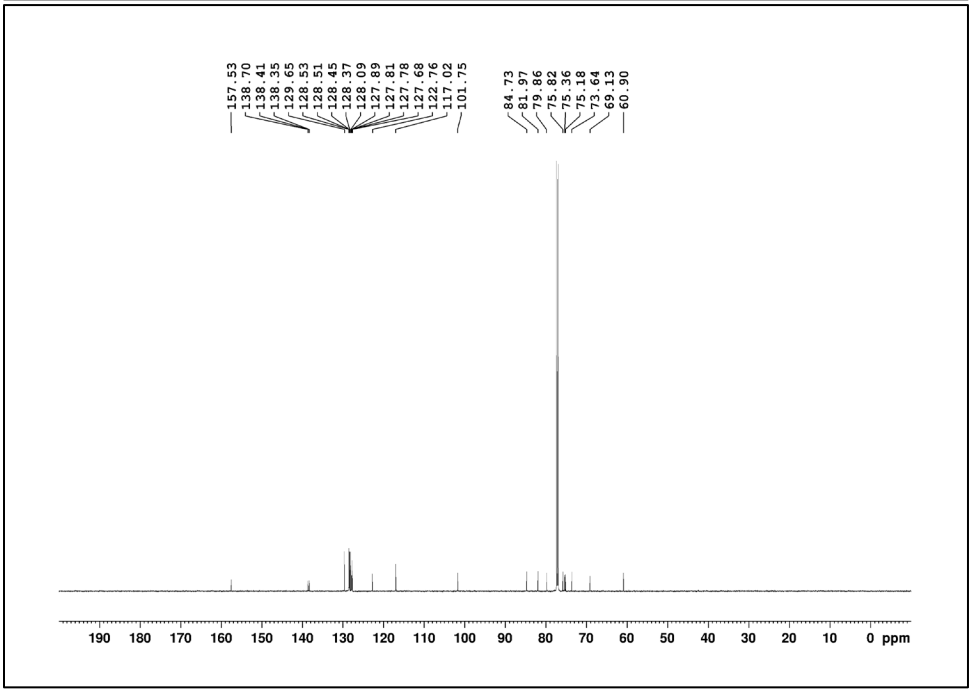




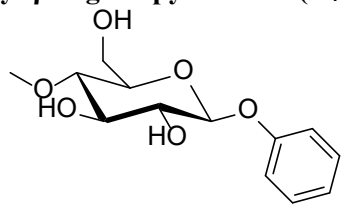
(phenyl)-2,3,6-tri-*O*-benzyl-4-*O*-methyl-β-D-glucopyranoside (581):

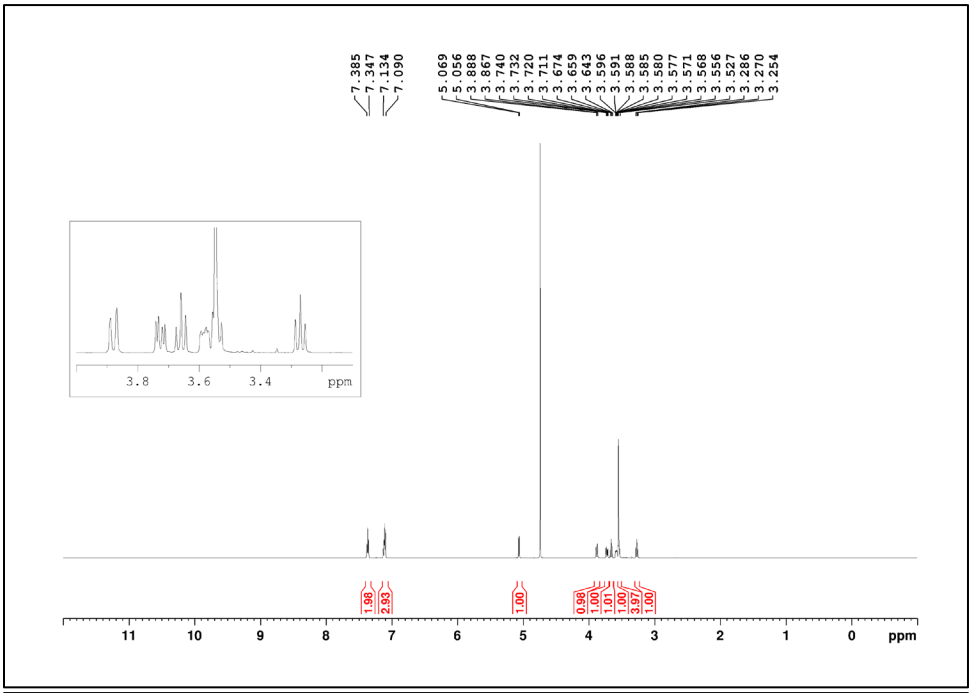


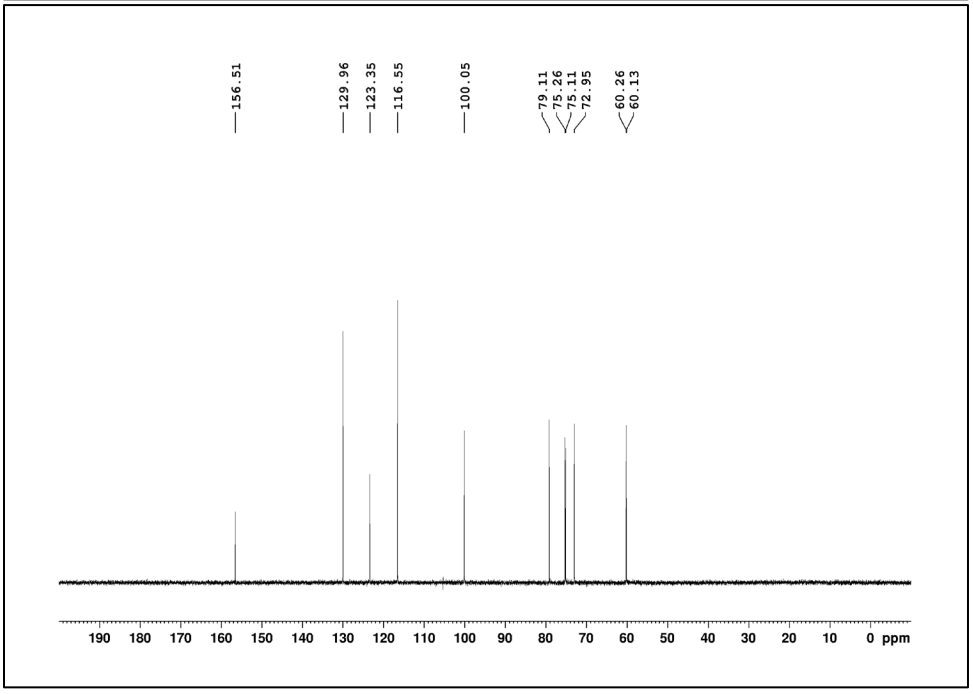




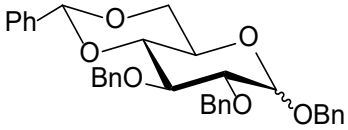
(phenyl)-4-*O*-methyl-β-D-glucopyranoside (C_4 OMe Ph-Glc, 110):

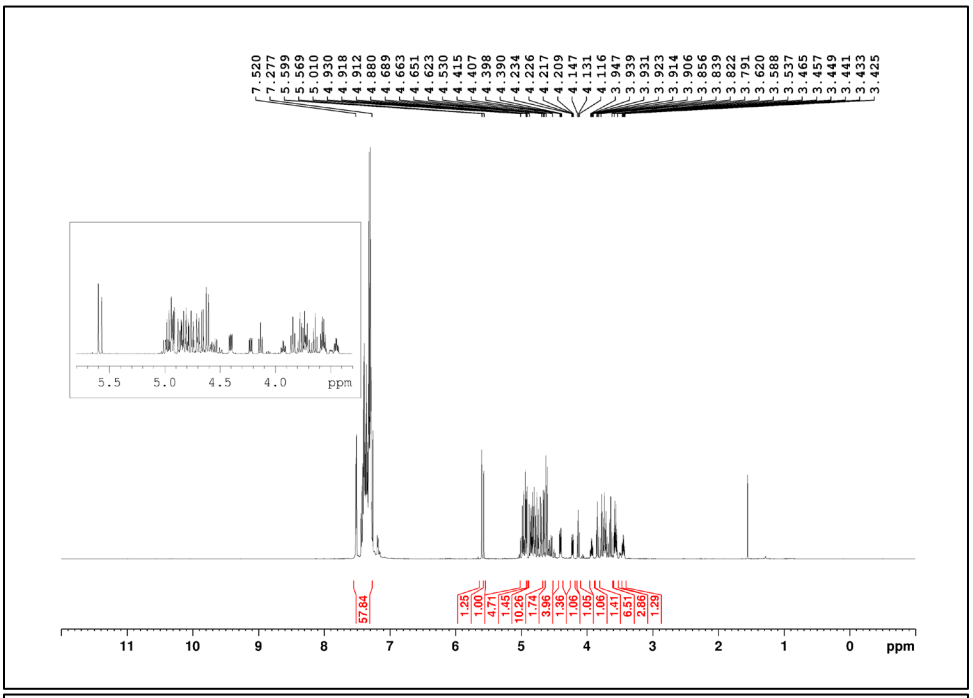


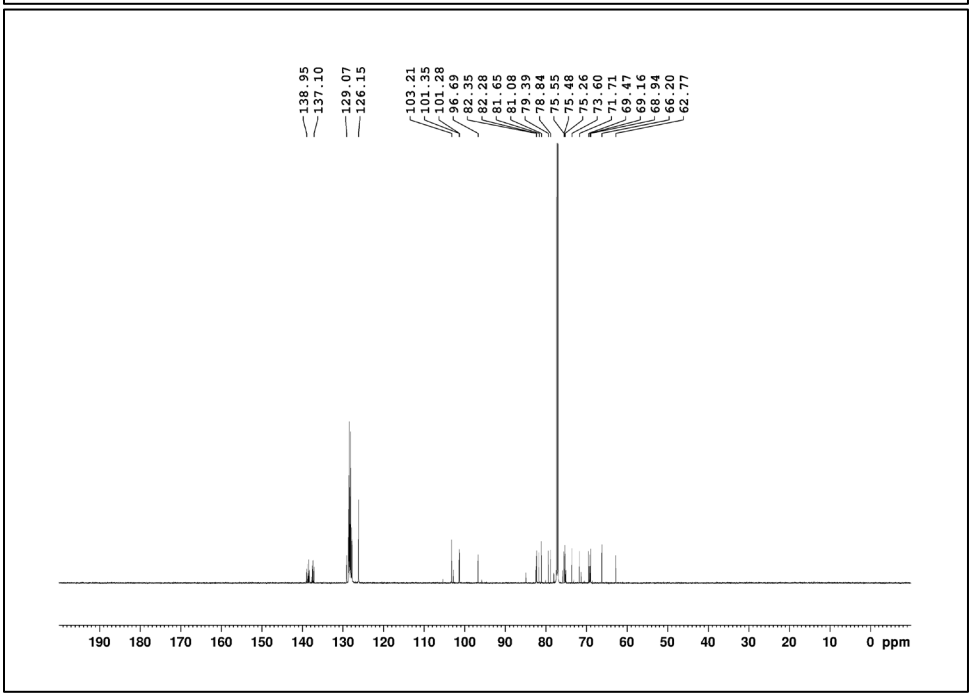




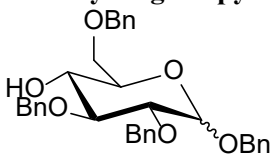
1,2,3-tri-*O*-benzyl-4,6-*O*-benzylidene-D-glucopyranoside (583):

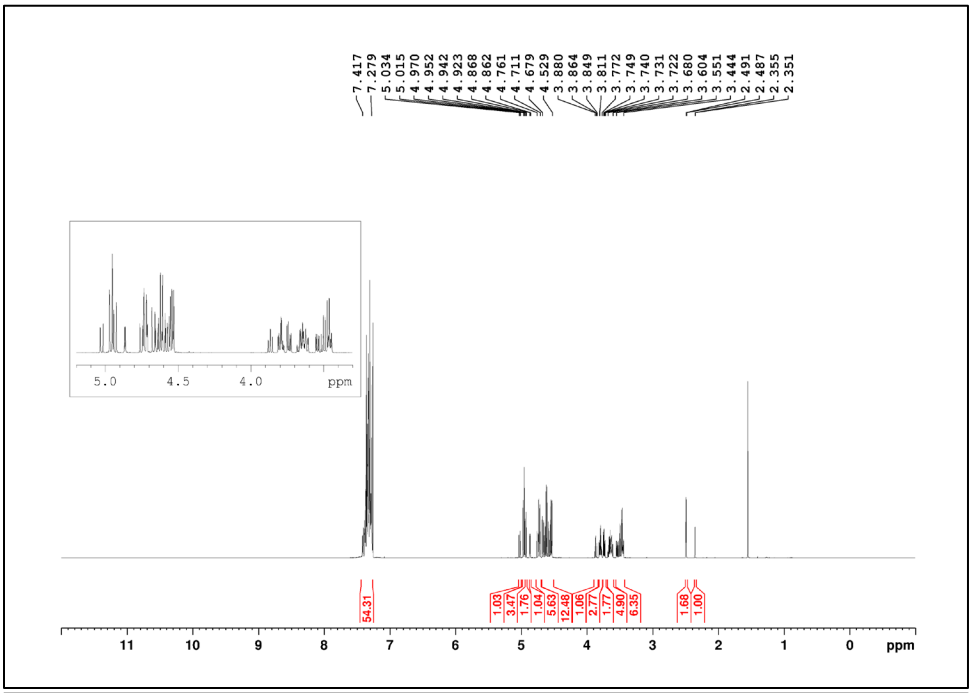


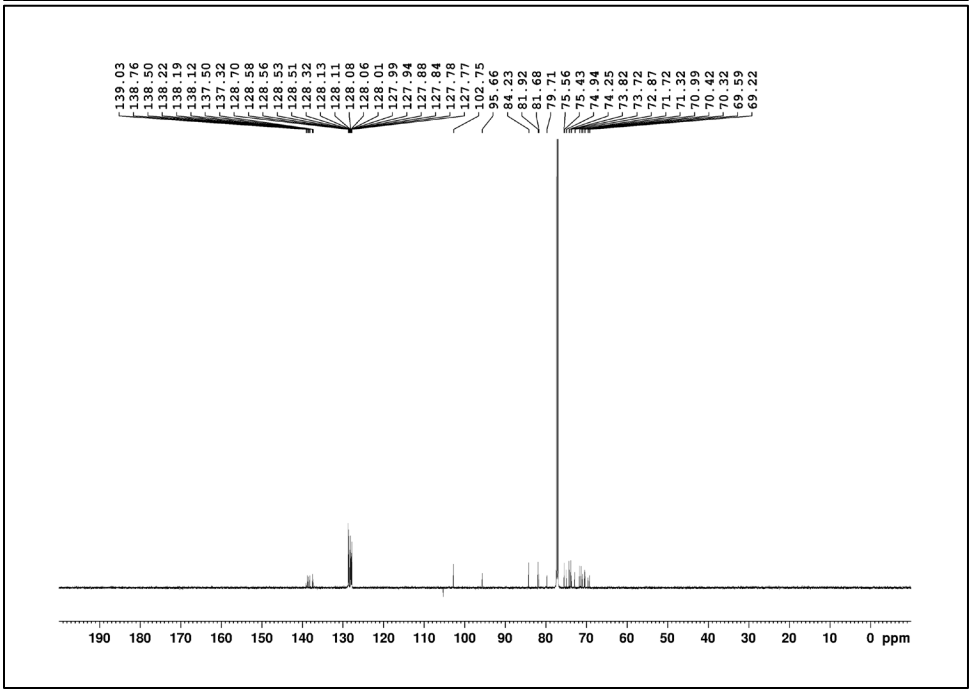




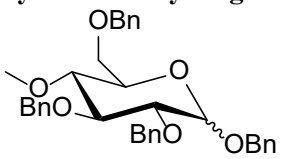
1,2,3,6-tetra-*O*-benzyl-D-glucopyranoside (584):

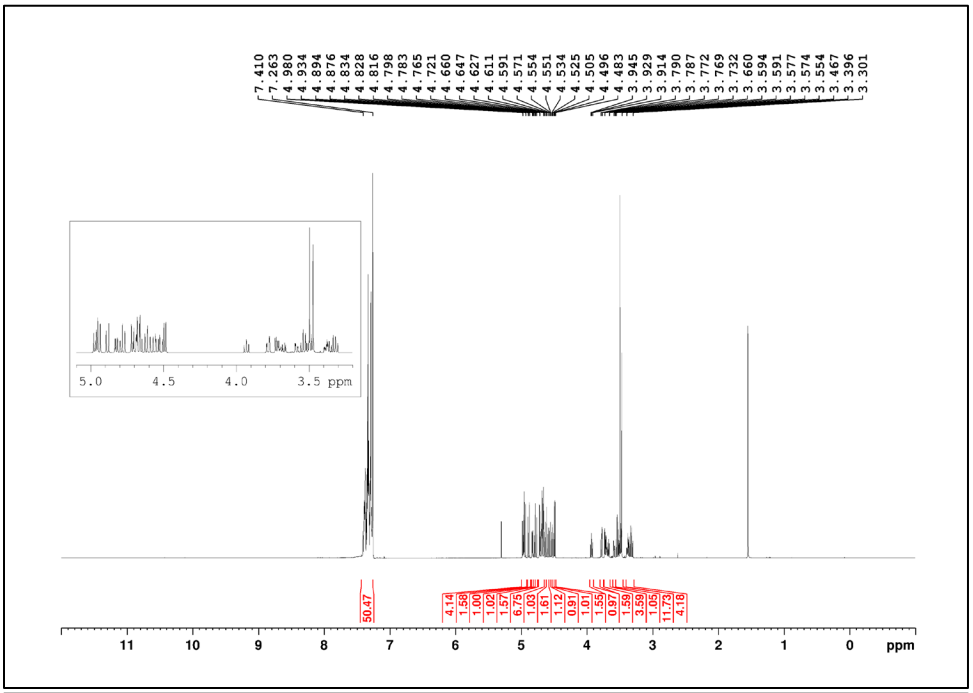


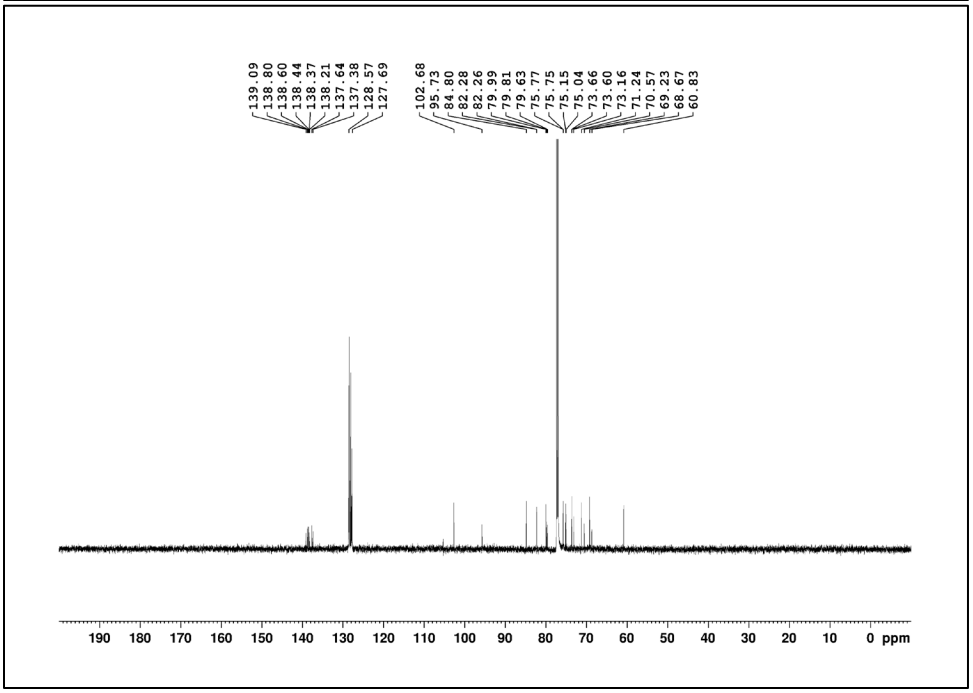




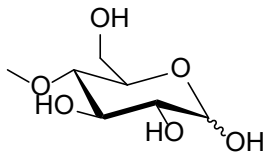
1,2,3,6-tetra-*O*-benzyl-4-*O*-methyl-D-glucopyranoside (585):

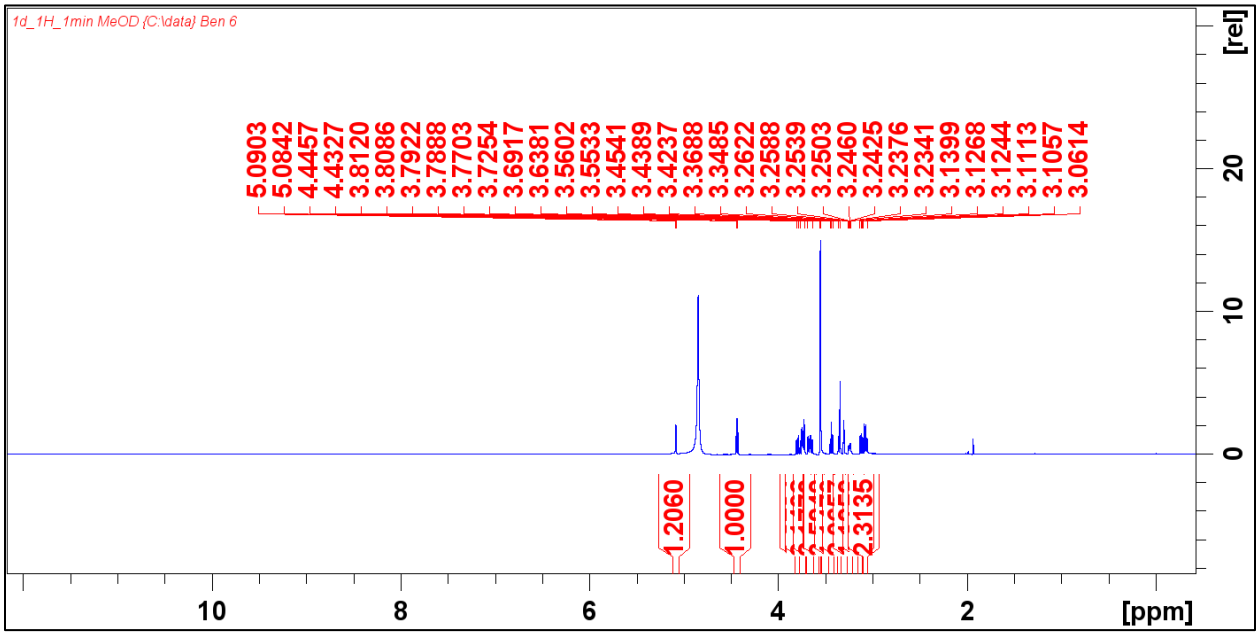


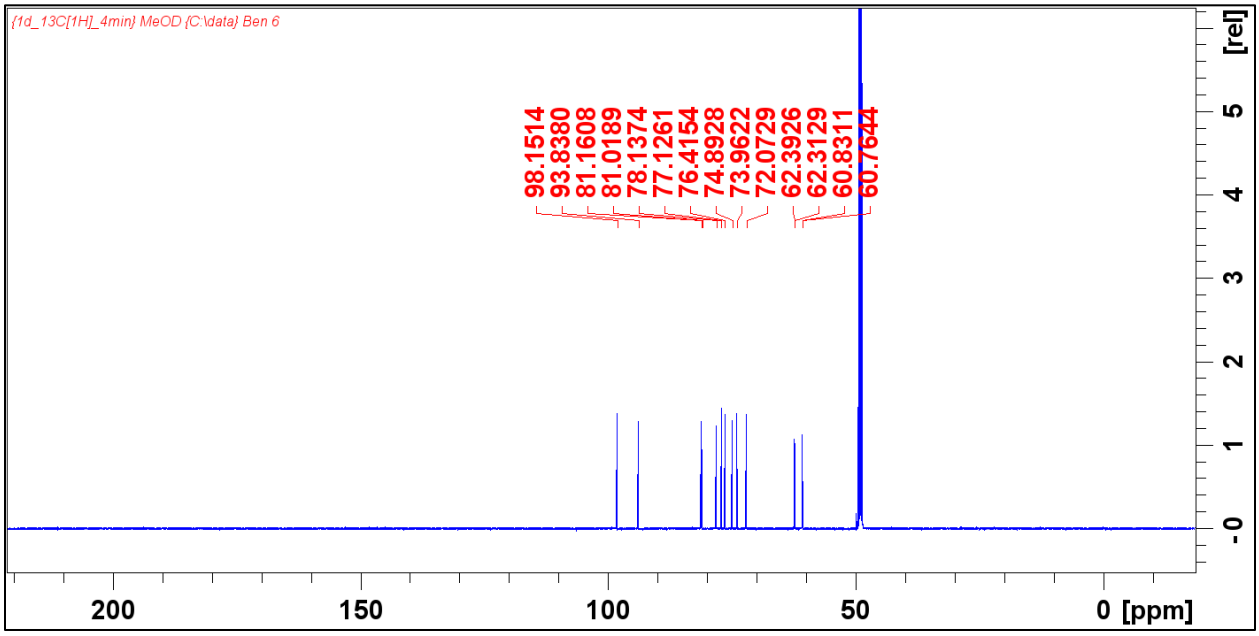




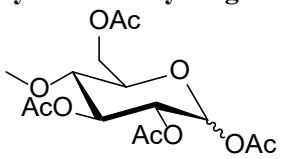
4-*O*-methyl-D-glucopyranoside (112):

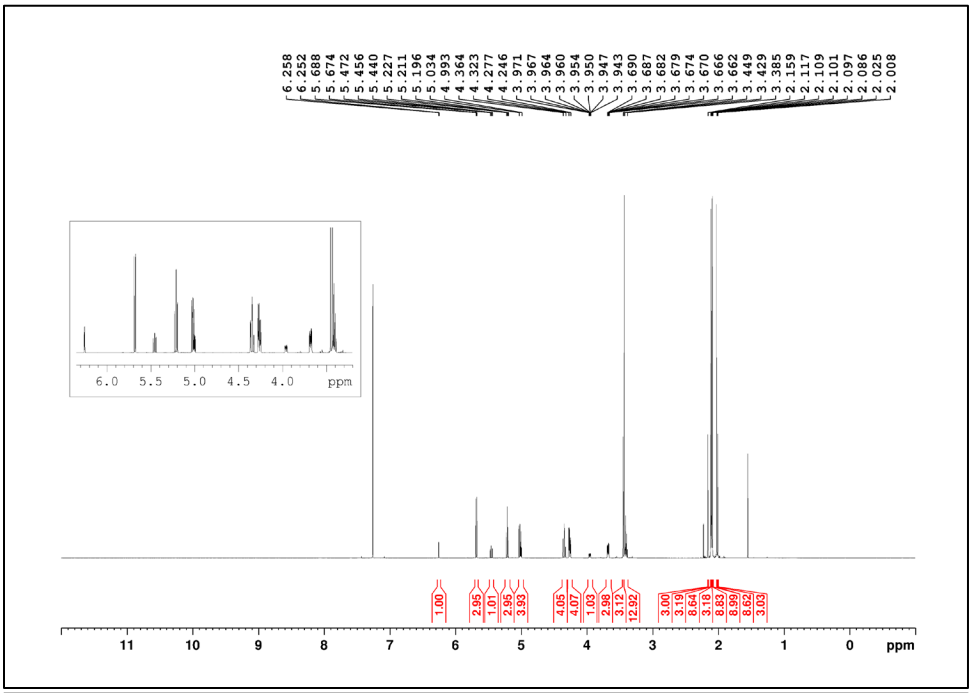


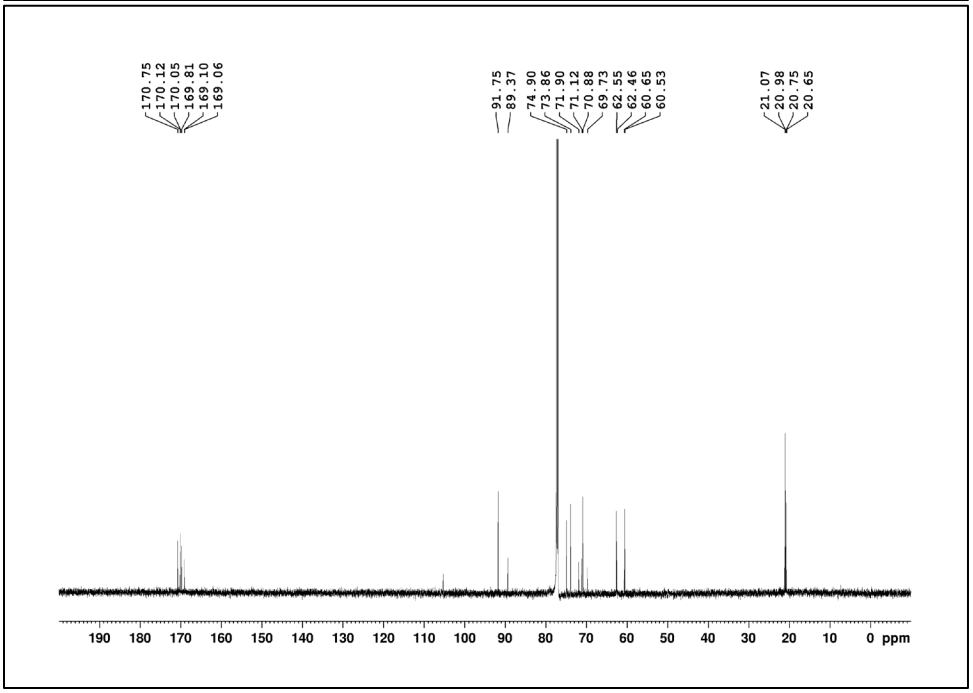


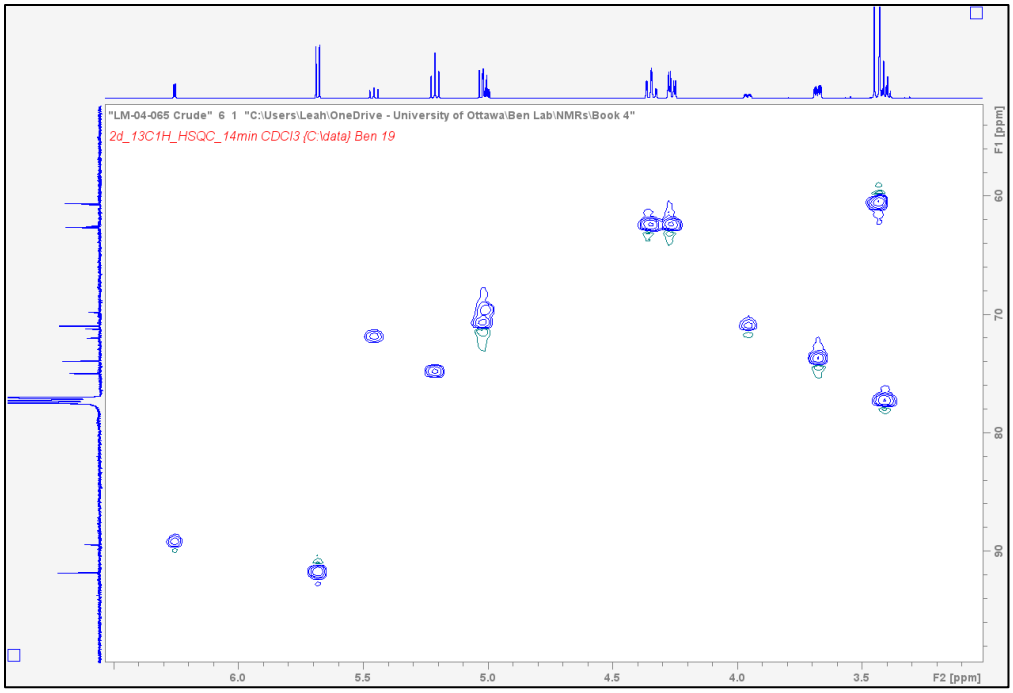


1,2,3,6-tetra-*O*-acetyl-4-*O*-methyl-D-glucopyranoside (586):

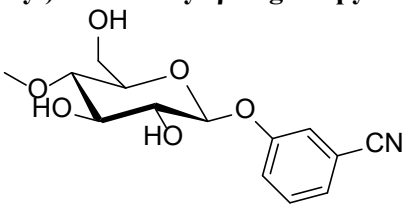


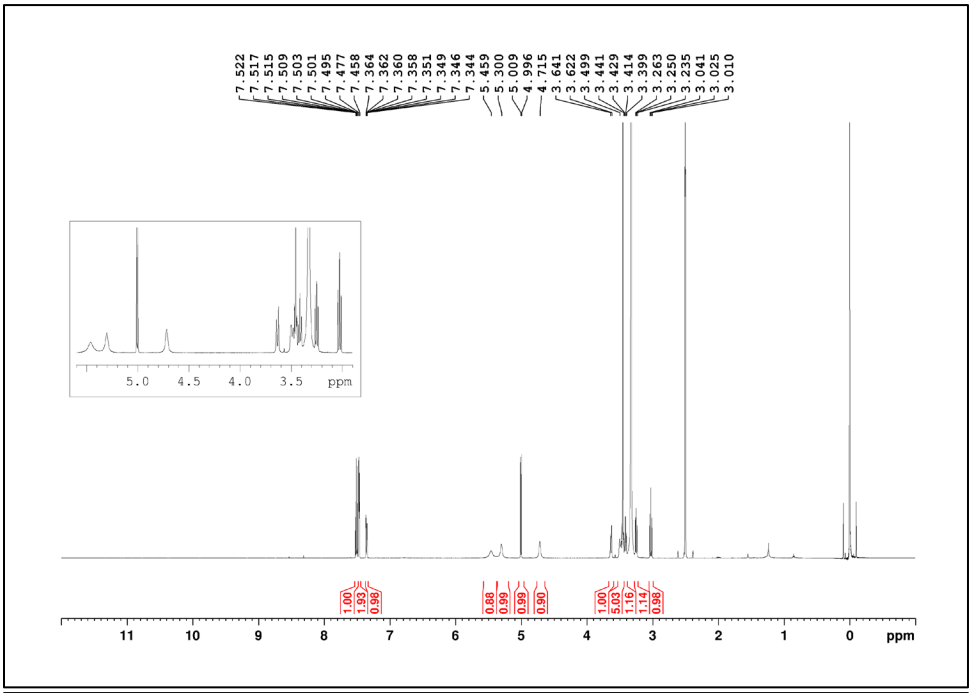


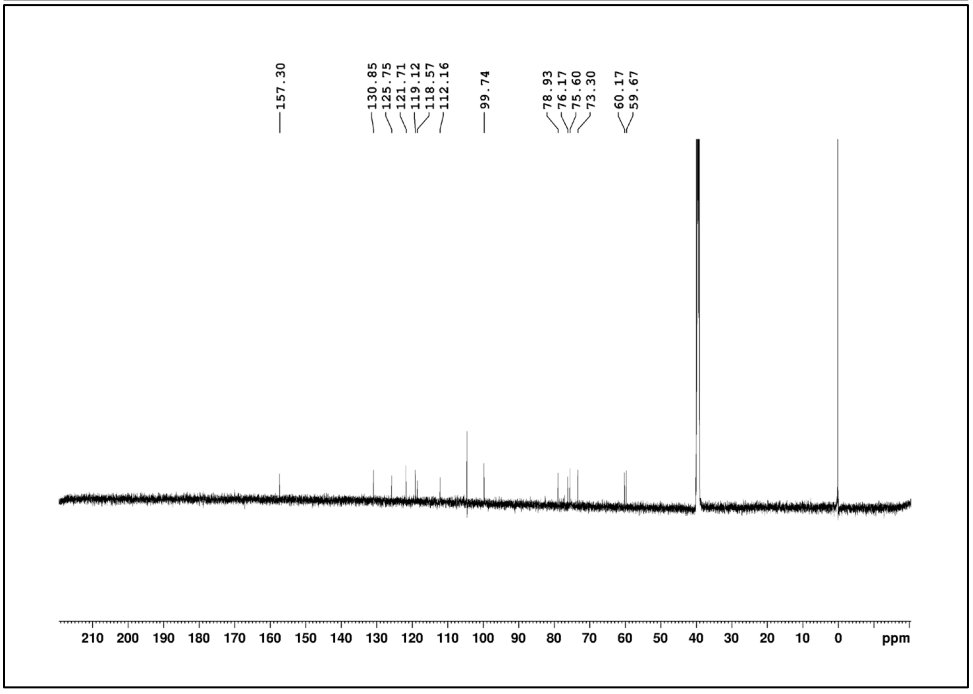



"LM-04-065 Crude" 6 1 "C:\Users\Leah\OneDrive - University of Ottawa\Ben Lab\NMRs\Book 4"
2d_13C1H_HSQC_14min CDCl3 (C:\data) Ben 19
F1 [ppm]
60
70
80
90
6.0
5.5
5.0
4.5
4.0
3.5
F2 [ppm]

(3-cyanophenyl)-4-*O*-methyl-β-D-glucopyranoside (111):







8.3. Raw data for figures and additional plots

Unless otherwise specified, all IC_{50} dose response curves throughout this section were determined by modified splat-cooling assay using a 5-minute annealing time at -6.4 °C.[169] Data fit to a two-parameter logistic regression with top and bottom plateau set to 100 and 0 respectively: $v_{norm} = \frac{100}{1+10^{[(HillSlope)(logIC_{50}-log[Compound])]}}$.

Unless otherwise specified, all LD_{50} dose response curves throughout this section were fit to a two-parameter logistic regression with top and bottom plateau set to 100 and 0 respectively: % viability $= \frac{100}{1+10^{[(HillSlope)(logLD_{50}-log[Compound])]}}$. Unless otherwise indicated all incubations were completed for 24 hours.

8.3.1. Ice recrystallization inhibition activity

8.3.1.1. % MGS and mean grain size values for previously developed IRIs as tested by the 30-minute SCA

Table 8-1. Raw data for the mean grain size (MGS) of various compounds in phosphate-buffered saline (PBS). Data reported as a mean and error of n=3 ice wafers with analysis of 12-random crystals in the wafer. Incomplete cells indicate that the data was not presented within this thesis; the data may have been reported in past but was not compiled here.

Compound Abbreviation	Compound #	Concentration	MGS (mm^2)	SEM	MGS (%)	SD (%)	Ref.
PBS	---	---	1.26E-02	3.96E-04	100.0	0	
AFGP-8	**1**	5.5 µM	1.52E-03	6.60E-05	11.9	0.24	[147,156]
OGG-Gal	**2**	5.5 µM	3.54E-03	1.32E-04	27.4	0.25	[147,156]
C-serine	**3**	5.5 µM			19.6	1.40	[148,156]
OGG-Glc	**4**	5.5 µM	9.51E-03	1.59E-03	75.4	0.28	[156]
OGG-Man	**5**	5.5 µM	1.20E-02	7.26E-04	94.7	0.13	[156]
OGG-Tal	**6**	5.5 µM	1.13E-02	5.28E-04	89.5	0.09	[156]
Galactose	**7**	0.022 mM	1.26E-02	1.17E-03	100.2	0.20	
		2.2 mM	1.26E-02	1.30E-03	100.2	0.22	
		11 mM	11.0E-02	1.17E-03	87.4	0.20	
		22 mM	8.21E-03	8.02E-04	63.6	3.25	[157]
		44 mM	8.10E-03	5.55E-04	64.2	0.10	
		220 mM	4.92E-03	4.32E-04	39.0	0.07	
Glucose	**8**	22 mM			76.5	3.60	[157]
Mannose	**9**	22 mM			83.9	3.60	[157]
Talose	**10**	22 mM			87.0	4.38	[157]

Melibiose	**11**	22 mM	64.1	2.65	[157]
Lactose	**12**	22 mM	72.2	3.64	[157]
Trehalose	**13**	22 mM	79.2	4.08	[157]
Maltose	**14**	22 mM	84.6	3.64	[157]
Sucrose	**15**	22 mM	88.0	2.87	[157]
β-octyl-Gal	**16**	22 mM	20.8	1.32	[161]
NOGlc	**17**	0.5 mM	11.9	0.78	[161]
		5.5 mM	8.14	0.74	[168]
NPrGlc	**18**	22 mM	81.8	3.44	[161]
			82.3	4.88	[168]
	19	22 mM	67.7	2.78	[165]
	20	22 mM	55.9	3.47	[165]
	21	22 mM	9.03	0.35	[165]
	22	22 mM	67.6	4.6	[160]
	23	22 mM	56.4	2.7	[160]
NHexGlc	**24**	22 mM	3.38	1.95	[160]
*p*BrPh-Glc	**25**	22 mM	9.81	0.82	[167]
PMP-Glc	**26**	22 mM	22.9	1.03	[167]
			23.8	0.73	[411]
2FA	**27**	22 mM	2.60	0.37	[166]
2,6DFB	**28**	22 mM	12.3	0.74	[166]
pNH_2Ph-Glc	**32**	22 mM	88.7	4.79	[411]
MMP-Glc	**33**	22 mM	80.7	3.11	[167]
OMP-Glc	**34**	22 mM	54.7	2.48	[167]
*p*MePh-Glc	**35**	22 mM	62.4	3.35	[167]
*m*MePh-Glc	**36**	22 mM	54.7	2.48	[167]
	49	22 mM	70.2	2.83	[411]
	50	22 mM	50.1	3.05	[411]
	51	22 mM	23.3	1.53	[411]
	52	22 mM	17.4	1.09	[411]
*p*OHPh-Glc	**53**	22 mM	61.5	2.93	[411]
PEP-Glc	**54**	22 mM	5.77	0.15	[411]
PPP-Glc	**55**	22 mM	31.7	2.05	[411]
PBP-Glc	**56**	22 mM	39.5	1.76	[411]
	57	22 mM	100.8	6.83	[168]
	58	22 mM	95.2	2.93	[168]
	59	22 mM	71.5	4.88	[168]
	60	22 mM	73.8	6.83	[168]
	61	22 mM	63.3	2.12	[168]
	62	22 mM	53.4	2.83	[168]
	63	22 mM	57.4	5.66	[168]
	64	22 mM	54.4	4.95	[168]
	65	22 mM	47.9	1.41	[168]
	66	22 mM	45.4	4.95	[168]
	67	22 mM	64.4	4.24	[168]
	68	22 mM	65.4	5.66	[168]
	69	22 mM	70.0	7.78	[168]
	70	22 mM	70.9	7.07	[168]
	71	22 mM	59.1	2.12	[168]
	72	22 mM	61.5	3.53	[168]
	73	22 mM	74.4	4.95	[168]

	74	22 mM	58.2	1.41	[168]
	75	22 mM	79.5	4.94	[168]
	76	22 mM	91.1	7.07	[168]
Ph-Glc	**82**	22 mM	64.4	2.83	[158,167]
*p*ClPh-Glc	**83**	22 mM	14.1	0.77	[158,167]
pNO_2Ph-Glc	**85**	22 mM	61.0	2.58	[158,167]
*p*FPh-Glc	**86**	22 mM	23.0	0.51	[158,167]
	87	22 mM	59.5	3.25	[158,167]
	88	22 mM	82.7	3.00	[158,167]
C_6 OMe PMP-Glc	**89**	22 mM	70.8	3.25	[158,167]
PMP-Gal	**107**	22 mM	78.8	3.14	[158,167]
pCH_3Ph-Glc	**128**	22 mM	62.4	3.35	[158,167]
*p*COOHPh-Glc	**129**	22 mM	73.2	3.61	[158,167]
pCO_2MePh-Glc	**130**	22 mM	49.0	2.96	[158,167]
pCF_3Ph-Glc	**131**	22 mM	33.0	1.80	[158,167]
pNH_2Ph-Gal	**132**	22 mM	67.1	5.00	[158,167]
*p*OHPh-Gal	**133**	22 mM	81.2	6.25	[158,167]
pCH_3Ph-Gal	**134**	22 mM	88.4	6.25	[158,167]
*p*FPh-Gal	**135**	22 mM	79.8	5.63	[158,167]
*p*ClPh-Gal	**136**	22 mM	21.3	1.25	[158,167]
*p*BrPh-Gal	**137**	22 mM	6.14	0.63	[158,167]
*p*COOHPh-Gal	**138**	22 mM	82.3	7.50	[158,167]
pCO_2MePh-Gal	**139**	22 mM	30.0	3.75	[158,167]
pCF_3Ph-Gal	**140**	22 mM	58.1	5.63	[158,167]
pNO_2Ph-Gal	**141**	22 mM	45.5	6.88	[158,167]
Ph-Gal	**142**	22 mM	79.4	5.63	[158,167]
	143	22 mM	45.6	4.83	[168]
	144	22 mM	4.65	1.61	[168]
	145	22 mM	28.8	3.22	[168]
	146	22 mM	86.5	6.44	[168]
	147	11 mM	27.0	1.61	[168]
	148	22 mM	13.9	0.07	[168]
	149	22 mM	99.5	6.44	[168]
	150	22 mM	34.4	3.22	[168]
	151	22 mM	89.3	6.44	[168]
	152	22 mM	31.6	3.22	[168]
	153	22 mM	83.7	6.44	[168]
	154	22 mM	44.7	3.22	[168]
	155	22 mM	80.0	4.83	[168]
	156	22 mM	19.5	12.9	[168]
	157	22 mM	61.4	6.44	[168]
	158	11 mM	23.3	1.61	[168]
	159	11 mM	5.58	1.61	[168]

Table 8-2. Raw data for the mean grain size (MGS) in mm^2 of D-galactose (**7**) and PMP-Glc (**26**) in phosphate-buffered saline (PBS) as a function of annealing time with analysis of *12-random ice crystals* in the wafer. Data reported as a mean ± standard deviation of n=3 ice wafers. Plotted in **Figure 1-18** and **Figure 1-19**. *Data collected by Capicciotti (2014).*[158]

	Compound			**D-Galactose (7)**			**PMP-Glc (26)**	
Time (min)	**PBS**	**22 mM**	**55 mM**	**110 mM**	**220 mM**	**5.5 mM**	**11 mM**	**22 mM**
0	3.78E-4 ± 9.36E-5	1.62E-4 ± 2.81E-4	3.24E-4 ± 5.62E-4	2.70E-4 ± 4.68E-4	1.08E-4 ± 1.87E-4	1.04E-4 ± 9.48E-5	2.69E-4 ± 9.48E-5	1.59E-4 ± 9.48E-5
5	1.51E-3 ± 2.81E-4		1.41E-3 ± 1.87E-4	8.65E-4 ± 9.36E-5	4.86E-4 ± 9.36E-5	9.25E-4 ± 9.48E-5	1.03E-3 ± 1.90E-4	4.32E-4 ± 9.48E-5
10	2.32E-3 ± 1.87E-4	2.00E-3 ± 1.87E-4	1.78E-3 ± 9.36E-5	1.41E-3 ± 9.36E-5	8.11E-4 ± 9.36E-5	2.02E-3 ± 9.48E-5	1.31E-3 ± 9.48E-5	4.87E-4 ± 9.48E-5
15	3.08E-3 ± 2.81E-4	2.11E-3 ± 1.87E-4	2.60E-3 ± 2.81E-4	1.73E-3 ± 9.36E-5	1.35E-3 ± 9.36E-5	2.78E-3 ± 1.90E-4	1.75E-3 ± 1.90E-4	7.06E-4 ± 1.90E-4
20	3.95E-3 ± 2.81E-4	3.19E-3 ± 3.74E-4 ±	3.30E-3 ± 1.87E-4	2.16E-3 ± 1.87E-4	1.46E-3 ± 1.87E-4	3.06E-3 ± 2.84E-4	2.57E-3 ± 9.48E-5	8.15E-4 ± 9.48E-5
25	4.76E-3 ± 3.74E-4	3.46E-3 ± 9.36E-5	3.68E-3 ± 2.81E-4	2.54E-3 ± 2.81E-4	1.73E-3 ± 9.36E-5	4.15E-3 ± 3.79E-4	3.17E-3 ± 1.89E-4	8.69E-4 ± 9.48E-5
30	5.73E-3 ± 4.68E-4	4.54E-3 ± 2.81E-4	4.43E-3 ± 3.74E-4	2.87E-3 ± 2.81E-4	2.05E-3 ± 2.81E-4	5.08E-3 ± 3.79E-4	3.60E-3 ± 2.84E-4	9.24E-4 ± 1.90E-4
45	7.24E-3 ± 4.68E-4	6.32E-3 ± 4.68E-4	5.30E-3 ± 3.74E-4	4.54E-3 ± 2.81E-4	3.03E-3 ± 1.87E-4	5.85E-3 ± 3.79E-4	4.37E-3 ± 2.84E-4	9.78E-4 ± 1.90E-4
60	8.11E-3 ± 7.49E-4	7.08E-3 ± 6.55E-4	6.49E-3 ± 3.74E-4	5.14E-3 ± 3.74E-4	3.57E-3 ± 2.81E-4	6.72E-3 ± 5.69E-4	5.85E-3 ± 3.79E-4	9.77E-4 ± 1.90E-4
75	9.41E-3 ± 7.49E-4	8.22E-3 ± 9.36E-4	7.08E-3 ± 5.62E-4	6.32E-3 ± 4.68E-4	3.57E-3 ± 1.87E-4	8.53E-3 ± 6.63E-4	4.31E-3 ± 4.74E-4	9.77E-4 ± 1.90E-4
90	8.97E-3 ± 8.43E-4	1.09E-2 ± 8.43E-4	7.19E-3 ± 6.55E-4	6.49E-3 ± 7.49E-4	4.22E-3 ± 2.81E-4	9.73E-3 ± 7.58E-4	4.48E-3 ± 3.79E-4	3.20E-4 ± 1.90E-4
120	9.14E-3 ± 8.43E-4	1.21E-2 ± 1.03E-3	6.70E-3 ± 4.68E-4	7.03E-3 ± 9.36E-4	5.35E-3 ± 5.62E-4	1.12E-2 ± 8.53E-4	5.57E-3 ± 5.68E-4	3.18E-4 ± 9.48E-5

Table 8-3. Raw data for the mean grain size (MGS) in mm^2 of PMP-Glc (**26**) in phosphate-buffered saline (PBS) as a function of annealing time with analysis of the *entire* ice wafer. Data reported as a mean ± standard deviation of n=3 ice wafers. Plotted in Figure 1-19.

Time (min)	PBS	22 mM	100 mM
0		2.21E-4 ± 1.0E-6	4.42E-5 ± 1.0E-6
5	8.85E-4 ± 7.66E-5	4.42E-4 ± 1.0E-6	6.64E-5 ± 1.0E-6
10	1.62E-3 ± 1.92E-4	5.97E-4 ± 1.0E-6	8.85E-5 ± 1.0E-6
15	2.04E-3 ± 1.15E-4	6.42E-4 ± 1.0E-6	8.85E-5 ± 1.0E-6
20	2.48E-3 ± 7.66E-5	7.52E-4 ± 1.0E-6	1.11E-4 ± 1.0E-6
25	2.99E-3 ± 4.98E-4	8.41E-4 ± 1.0E-6	1.11E-4 ± 1.0E-6
30	3.41E-3 ± 4.98E-4	9.29E-4 ± 1.0E-6	1.55E-4 ± 1.0E-6
45	3.89E-3 ± 6.93E-4	12.8E-3 ± 1.0E-6	1.77E-4 ± 1.0E-6
60	4.40E-3 ± 3.83E-4	14.4E-3 ± 1.0E-6	1.99E-4 ± 3.83E-5

8.3.1.2. D-Galactose (7)

Table 8-4. Raw data for the plot of normalized ice crystal growth (v_{norm}) in phosphate-buffered saline (PBS) as a function of D-galactose (**7**) concentration (in mM). Data reported as a mean and standard deviation of n=3 ice wafers.

[7] (mM)	Log[7] (mM)	v_{norm} (%)	Standard Deviation (%)
10	1.00	94.7	11.6
22	1.34	87.8	7.05
50	1.70	71.1	7.83
75	1.88	60.4	3.66
100	2.00	41.1	7.81
125	2.10	18.1	3.02
150	2.18	26.0	4.64
175	2.24	2.22	3.85

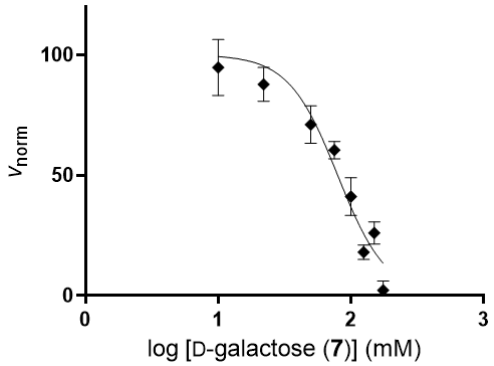


Figure 8-9. Plot of normalized ice crystal growth (v_{norm}) in phosphate-buffered saline (PBS) against D-galactose (**7**) concentration (in mM). $R^2 = 0.95$. IC_{50}: 79.6 mM, 95% CI [62.7-95.4].

*8.3.1.3. D-Glucose (**8**)*

Table 8-5. Raw data for the plot of normalized ice crystal growth (v_{norm}) in phosphate-buffered saline (PBS) as a function of D-glucose (**8**) concentration (in mM). Data reported as a mean and standard deviation of n=3 ice wafers.

[8] (mM)	Log[8] (mM)	v_{norm} (%)	Standard Deviation (%)
22	1.34	91.6	7.68
50	1.70	86.1	2.11
75	1.88	55.5	7.18
105	2.02	14.9	9.10
100	2.00	12.3	7.90
300	2.48	11.1	7.05
500	2.70	4.50	4.44

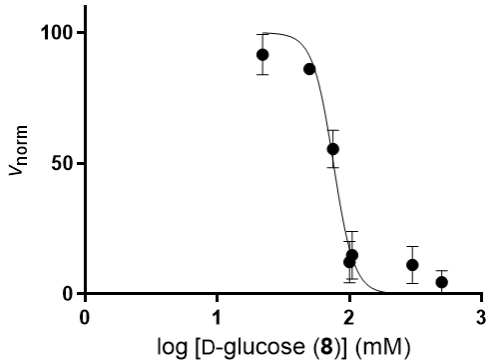


Figure 8-10. Plot of normalized ice crystal growth (v_{norm}) in phosphate-buffered saline (PBS) against D-glucose (**8**) concentration (in mM). R^2 = 0.97. IC_{50}: 75.7 mM, 95% CI [65.9-84.2].

*Previously reported data for the ice recrystallization inhibition activity of (D-glucose, **8**) by Dr. Anna Ampaw (2022)*[177]

Table 8-6. Raw data for the plot of normalized ice crystal growth (v_{norm}) in phosphate-buffered saline (PBS) as a function of D-glucose (**8**) concentration (in mM) as reported by Dr. Anna Ampaw (2022).[177] Data reported as a mean and standard deviation of n=3 ice wafers.

[8] (mM)	Log[8] (mM)	v_{norm} (%)	Standard Deviation (%)
10	1.00	97.0	13.5
20	1.30	97.0	15.2
50	1.70	87.5	19.2
100	2.00	59.5	13.0
500	2.70	0.00	0.00

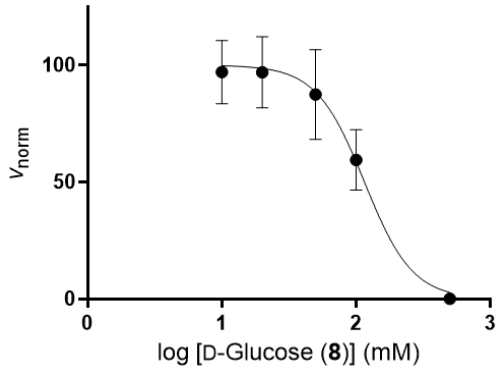


Figure 8-11. Plot of normalized ice crystal growth (v_{norm}) in phosphate-buffered saline (PBS) against D-glucose (**8**) concentration (in mM) as reported by Dr. Anna Ampaw (2022).[177] $R^2 = 0.99$. IC_{50}: 115.5 mM, 95% CI [101.4-136.2].

Previously reported data for the ice recrystallization inhibition activity of (D-glucose, **8***) by Stephanie Abraham (2015)*[170]

Table 8-7. Raw data for the plot of normalized ice crystal growth (v_{norm}) in phosphate-buffered saline (PBS) as a function of D-glucose (**8**) concentration (in mM) as reported by Stephanie Abraham (2015).[170] Data reported as a mean and standard deviation of n=3 ice wafers.

[8] (mM)	Log[8] (mM)	v_{norm} (%)	Standard Deviation (%)
1	0.00	115.3	15.7
10	1.00	114.8	27.9
22	1.34	96.6	14.8
44	1.64	81.5	12.2
100	2.00	62.9	6.10

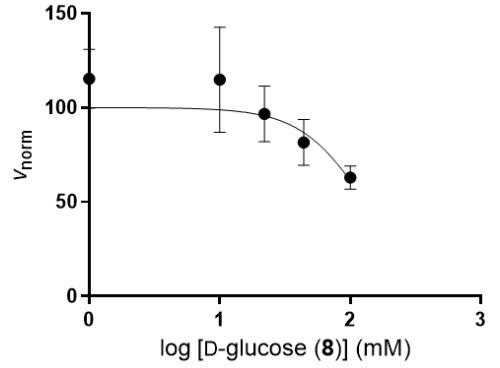


Figure 8-12. Plot of normalized ice crystal growth (v_{norm}) in phosphate-buffered saline (PBS) against D-glucose (**8**) concentration (in mM) as reported by Stephanie Abraham (2015).[170] $R^2 = 0.74$. IC_{50}: ~130.4 mM, 95% CI [59.2-∞].

Previously reported data for the ice recrystallization inhibition activity of (D-glucose, **8***) by Jatinder Singh (2022).*[178]

Table 8-8. Raw data for the plot of normalized ice crystal growth (v_{norm}) in phosphate-buffered saline (PBS) as a function of D-glucose (**8**) concentration (in mM) as reported by Jatinder Singh (2022).[178] Data reported as a mean and standard deviation of n=3 ice wafers.

[8] (mM)	Log[8] (mM)	v_{norm} (%)	Standard Deviation (%)
1	0.00	96.78	1.40
10	1.00	93.6	1.86
20	1.30	91.2	1.86
50	1.70	72.2	1.40
100	2.00	42.1	3.72
500	2.70	0.00	0.00

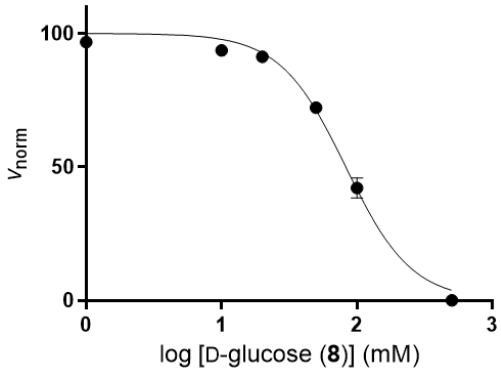


Figure 8-13. Plot of normalized ice crystal growth (v_{norm}) in phosphate-buffered saline (PBS) against D-glucose (**8**) concentration (in mM) as reported by Jatinder Singh (2022).[178] R^2 = 0.99. IC_{50}: 82.8 mM, 95% CI [70.8-98.4].

Previously unpublished data for the ice recrystallization inhibition activity of (D-glucose, **8***) by Sarah MacPhedran (undergraduate Honour's student).*

Table 8-9. Raw data for the plot of normalized ice crystal growth (v_{norm}) in phosphate-buffered saline (PBS) as a function of D-glucose (**8**) concentration (in mM) as reported by Sarah MacPhedran (undergraduate Honour's student). Data reported as a mean and standard deviation of n=3 ice wafers.

[8] (mM)	Log[8] (mM)	v_{norm} (%)	Standard Deviation (%)
1	0.00	88.2	8.11
30	1.49	98.8	2.13
50	1.70	76.5	8.99
100	2.00	56.5	3.29
150	2.17	42.9	12.5
250	2.40	25.1	5.46

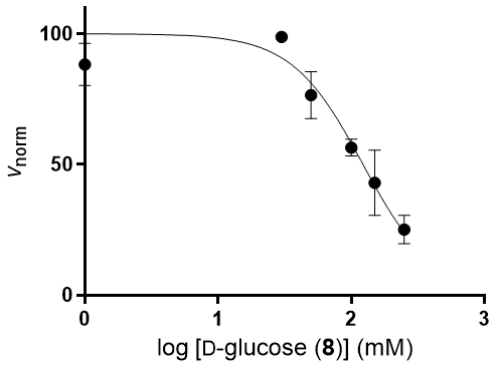


Figure 8-14. Plot of normalized ice crystal growth (v_{norm}) in phosphate-buffered saline (PBS) against D-glucose (**8**) concentration (in mM) as reported by Sarah MacPhedran (undergraduate Honour's student). $R^2 = 0.94$. IC_{50}: 122.6 mM, 95% CI [90.3-173.2].

8.3.1.4. D-Mannose (9)

Table 8-10. Raw data for the plot of normalized ice crystal growth (v_{norm}) in phosphate-buffered saline (PBS) as a function of D-mannose (**9**) concentration (in mM). Data reported as a mean and standard deviation of n=3 ice wafers.

[9] (mM)	Log[9] (mM)	v_{norm} (%)	Standard Deviation (%)
1	0.00	94.6	1.89
22	1.34	87.5	3.84
75	1.88	62.5	10.1
100	2.00	29.8	12.1
150	2.18	2.83	2.81
200	2.30	0.00	0.00

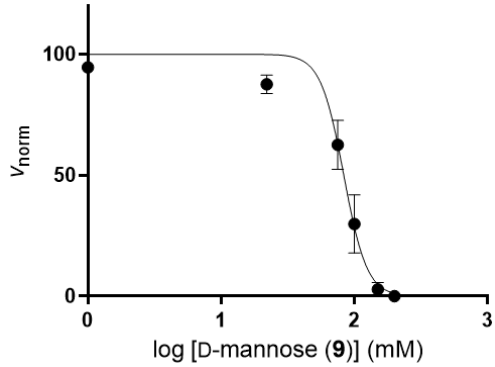


Figure 8-15. Plot of normalized ice crystal growth (v_{norm}) in phosphate-buffered saline (PBS) against D-mannose (**9**) concentration (in mM). $R^2 = 0.98$. IC_{50}: 83.4 mM, 95% CI [68.0-94.1].

*8.3.1.5. (4-bromophenyl)-β-D-glucopyranoside (pBrPh-Glc, **25**)*

Data collected with the assistance of undergraduate COOP student Abigail Kos (Summer 2021)

Table 8-11. Raw data for the plot of normalized ice crystal growth (v_{norm}) in phosphate-buffered saline (PBS) as a function of *p*BrPh-Glc (**25**) concentration (in mM). Data reported as a mean and standard deviation of n=3 ice wafers.

[25] (mM)	Log[25] (mM)	v_{norm} (%)	Standard Deviation (%)
1	0.00	104.8	3.76
5	0.70	76.2	5.73
10	1.00	17.8	6.68
20	1.30	2.16	1.70
30	1.48	0.00	0.00
40	1.60	0.00	0.00

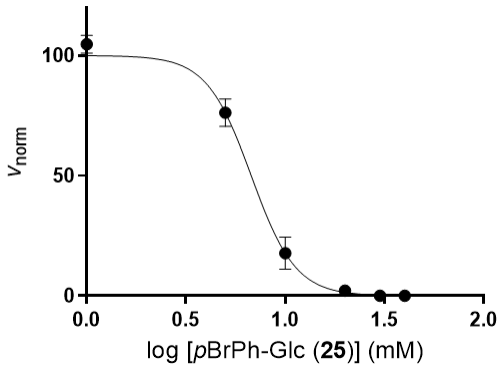


Figure 8-16. Plot of normalized ice crystal growth (v_{norm}) in phosphate-buffered saline (PBS) against *p*BrPh-Glc (**25**) concentration (in mM). $R^2 = 0.99$. IC_{50}: 6.75 mM, 95% CI [6.27-7.28].

*Previously reported data for the ice recrystallization inhibition activity of (pBrPh-Glc, **25**) by Stephanie Abraham (2015)*[170]

Table 8-12. Raw data for the proportionate area of ice crystals over time for *p*BrPh-Glc (**25**) in phosphate-buffered saline (PBS). Data reported as a mean ± standard deviation of n=3 ice wafers. Plotted in **Figure 1-20**. *Data collected by Abraham (2015).*[170]

	Concentration (mM)						
Time (min)	**PBS (0 mM)**	**1**	**5**	**10**	**15**	**22**	**40**
0	1.0	1.0	1.0	1.0	1.0	1.0	1.0
5	0.283 ± 0.036	0.329 ± 0.045	0.405 ± 0.027	0.506 ± 0.080	0.668 ± 0.095	0.807 ± 0.050	1.0
10	0.181 ± 0.020	0.158 ± 0.031	0.182 ± 0.012	0.317 ± 0.068	0.500 ± 0.104	0.681 ± 0.040	1.0
15	0.083 ± 0.037	0.074 ± 0.026	0.125 ± 0.019	0.212 ± 0.037	0.405 ± 0.093	0.614 ± 0.043	1.0
20	0.030 ± 0.017	0.034 ± 0.007	0.107 ± 0.021	0.177 ± 0.044	0.332 ± 0.065	0.562 ± 0.057	1.0
25	0.018 ± 0.004	0.029 ± 0.021	0.071 ± 0.021	0.187 ± 0.058	0.348 ± 0.071	0.535 ± 0.048	1.0
30	0.018 ± 0.007	0.010 ± 0.017	0.050 ± 0.014	0.160 ± 0.058	0.324 ± 0.075	0.490 ± 0.057	1.0
45	0.016 ± 0.013	0.018 ± 0.007	0.040 ± 0.013	0.118 ± 0.024	0.293 ± 0.095	0.376 ± 0.055	1.0
60	0.007 ± 0.002	0.007 ± 0.011	0.018 ± 0.013	0.102 ± 0.025	0.240 ± 0.091	0.276 ± 0.067	1.0

Table 8-13. Raw data for the plot of normalized ice crystal growth (v_{norm}) in phosphate-buffered saline (PBS) as a function of *p*BrPh-Glc (**25**) concentration (in mM) as reported by Stephanie Abraham (2015) with a *10-minute* annealing time.[169] Data reported as a mean and standard deviation of n=3 ice wafers. Data plotted in **Figure 1-20**.

[25] (mM)	**Log[25] (mM)**	**v_{norm} (%)**	**Standard Deviation (%)**
1	0.00	106.1	14.0
5	0.70	103.2	14.6
10	1.00	91.5	21.3
15	1.18	80.6	17.0
22	1.34	59.5	34.7
40	1.60	0.42	0.00
60	1.78	0.39	0.00

Table 8-14. Raw data for the plot of the *rate constants from the proportionate area of ice crystals over time* (k_{norm}) in phosphate-buffered saline (PBS) as a function of *p*BrPh-Glc (**25**) concentration (in mM) as reported by Stephanie Abraham (2015).[169] Data reported as a mean and standard deviation of n=3 ice wafers. Data plotted in **Figure 1-20**.

[25] (mM)	Log[25] (mM)	k_{norm} (%)	Standard Deviation (%)
1	0	94.1	21.0
5	0.70	84.8	8.07
10	1.00	77.3	21.0
15	1.18	55.0	17.8
22	1.34	17.7	8.07
40	1.60	0.00	4.84
60	1.78	0.00	3.23

Table 8-15. Raw data for the plot of normalized ice crystal growth (v_{norm}) in phosphate-buffered saline (PBS) as a function of *p*BrPh-Glc (**25**) concentration (in mM) as reported by Stephanie Abraham (2015) with a *5-minute* annealing time.[169] Data reported as a mean and standard deviation of n=3 ice wafers.

[25] (mM)	Log[25] (mM)	v_{norm} (%)	Standard Deviation (%)
1	0.00	92.2	5.23
5	0.70	82.5	3.85
10	1.00	67.6	9.91
15	1.18	46.1	13.5
22	1.34	26.2	7.26
40	1.60	0.00	0.00
60	1.78	0.00	0.00

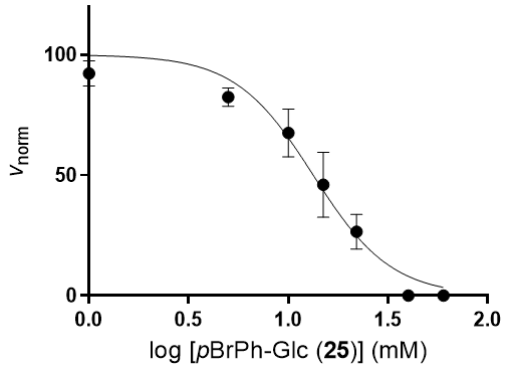


Figure 8-17. Plot of normalized ice crystal growth (v_{norm}) in phosphate-buffered saline (PBS) against *p*BrPh-Glc (**25**) concentration (in mM) as reported by Stephanie Abraham (2015) with a *5-minute* annealing time.[170] $R^2 = 0.98$. IC_{50}: 13.4 mM, 95% CI [10.8-16.0].

*8.3.1.6. (4-methoxyphenyl)-β-D-glucopyranoside (PMP-Glc, **26**)*

Table 8-16. Raw data for the plot of normalized ice crystal growth (v_{norm}) in phosphate-buffered saline (PBS) as a function of PMP-Glc (**26**) concentration (in mM). Data reported as a mean and standard deviation of n=3 ice wafers.

[26] (mM)	Log[26] (mM)	v_{norm} (%)	Standard Deviation (%)
1	0.00	101.8	5.63
10	1.00	93.9	5.05
15	1.18	87.1	1.77
25	1.40	63.4	8.21
50	1.70	12.6	2.66
100	2.00	0.00	0.00

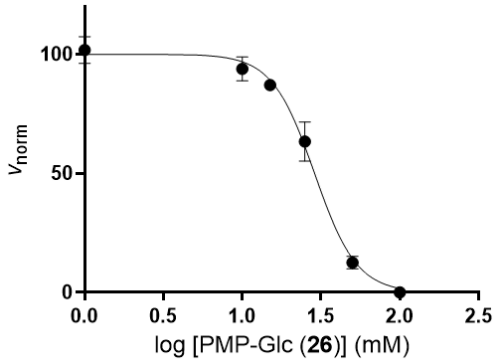


Figure 8-18. Plot of normalized ice crystal growth (v_{norm}) in phosphate-buffered saline (PBS) against PMP-Glc (**26**) concentration (in mM). $R^2 = 0.99$. IC_{50}: 28.8 mM, 95% CI [26.6-31.2].

*Previously reported data for the ice recrystallization inhibition activity of (PMP-Glc, **26**) by Stephanie Abraham (2015)*[170]

Table 8-17. Raw data for the plot of normalized ice crystal growth (v_{norm}) in phosphate-buffered saline (PBS) as a function of PMP-Glc (**26**) concentration (in mM) as reported by Stephanie Abraham (2015).[170] Data reported as a mean and standard deviation of n=3 ice wafers.

[26] (mM)	Log[26] (mM)	v_{norm} (%)	Standard Deviation (%)
1	0.00	97.3	9.67
10	1.00	100.5	6.45
15	1.18	67.6	22.1
22	1.34	38.6	12.9
40	1.61	0.00	0.00
100	2.00	0.00	0.00

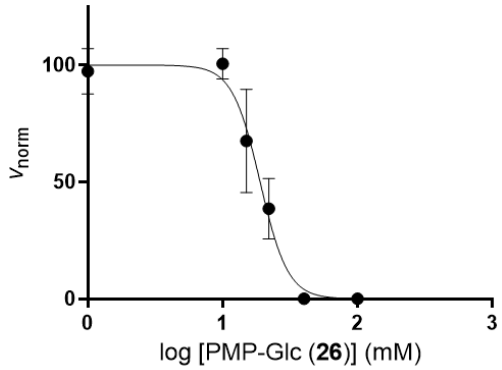


Figure 8-19. Plot of normalized ice crystal growth (v_{norm}) in phosphate-buffered saline (PBS) against PMP-Glc (**26**) concentration (in mM) as reported by Stephanie Abraham (2015).[170] R^2 = 0.99. IC_{50}: 19.0 mM, 95% CI [17.0-21.4].

*8.3.1.7. N-2-fluorophenyl-D-gluconamide (2FA, **27**)*

Data collected with the assistance of undergraduate COOP student Abigail Kos (Summer 2021)

Table 8-18. Raw data for the plot of normalized ice crystal growth (v_{norm}) in phosphate-buffered saline (PBS) as a function of 2FA (**27**) concentration (in mM). Data reported as a mean and standard deviation of n=3 ice wafers.

[27] (mM)	Log[27] (mM)	v_{norm} (%)	Standard Deviation (%)
1	0.00	96.0	13.2
2	0.30	96.9	9.77
3	0.48	87.4	8.06
3.5	0.54	48.0	15.0
4	0.60	8.8	7.45
5	0.70	0.00	0.00
10	1.00	0.00	0.00

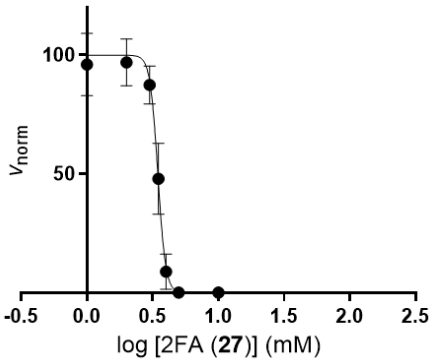


Figure 8-20. Plot of normalized ice crystal growth (v_{norm}) in phosphate-buffered saline (PBS) against 2FA (**27**) concentration (in mM). R^2 = 0.99. IC_{50}: 3.47 mM, 95% CI [3.41-3.52].

Previously reported data for the ice recrystallization inhibition activity of (2FA, ***27****) by Dr. Madeleine Adam (2020)*[176]

Table 8-19. Raw data for the plot of normalized ice crystal growth (v_{norm}) in phosphate-buffered saline (PBS) as a function of 2FA (**27**) concentration (in mM) as reported by Dr. Madeleine Adam (2020).[176] Data reported as a mean and standard deviation of n=3 ice wafers.

[27] (mM)	Log[27] (mM)	v_{norm} (%)	Standard Deviation (%)
0.5	-0.30	99.0	5.07
1	0.00	98.0	2.75
1.5	0.18	99.3	5.35
2	0.30	95.2	1.93
3	0.48	57.2	1.22
3.5	0.54	18.5	2.18
4	0.60	0.00	0.00

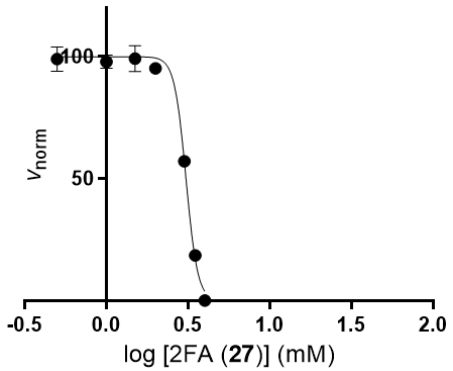


Figure 8-21. Plot of normalized ice crystal growth (v_{norm}) in phosphate-buffered saline (PBS) against 2FA (**27**) concentration (in mM) as reported by Dr. Madeleine Adam (2020).[176] $R^2 = 0.99$. IC_{50}: 3.07 mM, 95% CI [3.01-3.14].

8.3.1.8. N-(2,6-difluorobenzyl)-D-gluconamide (2,6DFB, ***28****)*

Previously reported data for the ice recrystallization inhibition activity of (2,6DFB, ***28****) by Dr. Madeleine Adam (2020)*[176]

Table 8-20. Raw data for the plot of normalized ice crystal growth (v_{norm}) in phosphate-buffered saline (PBS) as a function of 2,6DFB (**28**) concentration (in mM) as reported by Dr. Madeleine Adam (2020).[176] Data reported as a mean and standard deviation of n=3 ice wafers.

[28] (mM)	Log[28] (mM)	v_{norm} (%)	Standard Deviation (%)
1	0.00	118.6	3.43
5	0.70	90.0	6.86
10	1.00	59.7	6.17
15	1.17	12.3	6.86
20	1.30	2.74	4.11
30	1.48	0.00	0.00

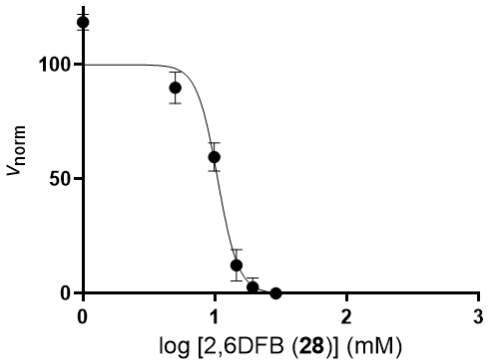


Figure 8-22. Plot of normalized ice crystal growth (v_{norm}) in phosphate-buffered saline (PBS) against 2,6DFB (**28**) concentration (in mM) as reported by Dr. Madeleine Adam (2020).[176] R^2 = 0.97. IC_{50}: 10.5 mM, 95% CI [7.74-12.7].

*8.3.1.9. (4-azidophenyl)-β-D-glucopyranoside (pN$_3$Ph-Glc, **29**)*

*Previously reported data for the ice recrystallization inhibition activity of (pN$_3$Ph-Glc, **29**) by Dr. Jessica Poisson (2019)*[214]

Table 8-21. Raw data for the plot of normalized ice crystal growth (v_{norm}) in phosphate-buffered saline (PBS) as a function of *p*N$_3$Ph-Glc (**29**) concentration (in mM) as reported by Dr. Jessica Poisson (2019).[214] Data reported as a mean and standard deviation of n=3 ice wafers.

[29] (mM)	Log[29] (mM)	v_{norm} (%)	Standard Deviation (%)
1	0.00	92.2	6.77
10	1.00	83.8	5.81
30	1.47	45.3	0.97
70	1.84	10.1	7.74
100	2.00	0.56	0.10

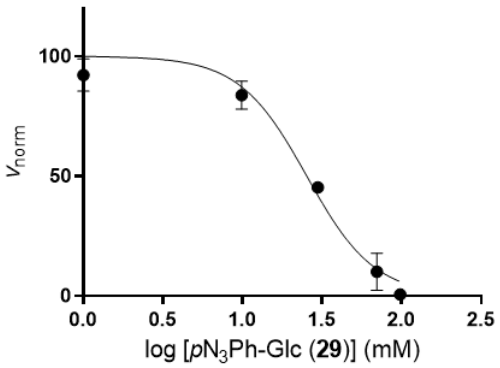


Figure 8-23. Plot of normalized ice crystal growth (v_{norm}) in phosphate-buffered saline (PBS) against *p*N$_3$Ph-Glc (**29**) concentration (in mM) as reported by Dr. Jessica Poisson (2019).[214] R^2 = 0.98. IC_{50}: 25.4 mM, 95% CI [17.3-35.1].

*8.3.1.10. (4-aminophenyl)-β-D-glucopyranoside (pNH$_2$Ph-Glc, **32**)*

*Previously reported data for the ice recrystallization inhibition activity of (pNH$_2$Ph-Glc, **32**) by Dr. Jessica Poisson (2019)*[214]

Table 8-22. Raw data for the plot of normalized ice crystal growth (v_{norm}) in phosphate-buffered saline (PBS) as a function of *p*NH$_2$Ph-Glc (**32**) concentration (in mM) as reported by Dr. Jessica Poisson (2019).[214] Data reported as a mean and standard deviation of n=3 ice wafers.

[32] (mM)	Log[32] (mM)	v_{norm} (%)	Standard Deviation (%)
1	0.00	95.9	5.04
10	1.00	88.4	9.07
30	1.47	58.7	9.06
70	1.84	36.6	5.04
100	2.00	14.5	2.01
150	2.18	1.74	1.01
200	2.30	0.00	0.00

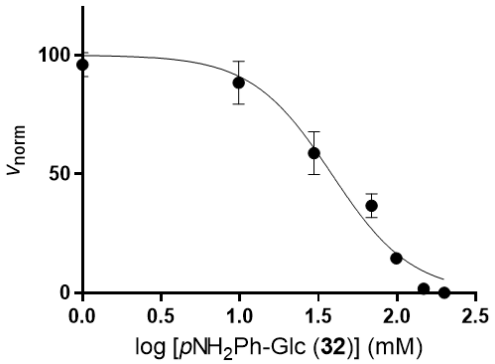


Figure 8-24. Plot of normalized ice crystal growth (v_{norm}) in phosphate-buffered saline (PBS) against *p*NH$_2$Ph-Glc (**32**) concentration (in mM) as reported by Dr. Jessica Poisson (2019).[214] R^2 = 0.98. IC_{50}: 38.4 mM, 95% CI [27.7-50.8].

8.3.1.11. (cyanophenyl)-β-D-glucopyranosides and N-cyanophenyl-D-gluconamides

Table 8-23. Raw data for the plot of normalized ice crystal growth (v_{norm}) in phosphate-buffered saline (PBS) as a function of nitrile-containing compound 4-(cyanophenyl)-β-D-glucopyranoside (*p*CNPh-Glc, **30**) concentration (in mM). Data reported as a mean and standard deviation of n=3 ice wafers.

[30] (mM)	Log[30] (mM)	v_{norm} (%)	Standard Deviation (%)
1	0.00	98.6	7.58
5	0.70	90.8	2.28
25	1.40	81.9	5.52
60	1.78	45.8	4.72
78	1.89	30.0	3.26

Table 8-24. Raw data for the plot of normalized ice crystal growth (v_{norm}) in phosphate-buffered saline (PBS) as a function of nitrile-containing compound 3-(cyanophenyl)-β-D-glucopyranoside (*m*CNPh-Glc, **37**) concentration (in mM). Data reported as a mean and standard deviation of n=3 ice wafers.

[37] (mM)	Log[37] (mM)	v_{norm} (%)	Standard Deviation (%)
1	0.00	105.9	6.83
5	0.70	91.1	7.24
15	1.18	92.9	8.53
22	1.34	81.0	4.64
30	1.48	29.9	1.64
50	1.70	8.95	9.19
65	1.81	0.00	0.00

Table 8-25. Raw data for the plot of normalized ice crystal growth (v_{norm}) in phosphate-buffered saline (PBS) as a function of nitrile-containing compound 2-(cyanophenyl)-β-D-glucopyranoside (*o*CNPh-Glc, **38**) concentration (in mM). Data reported as a mean and standard deviation of n=3 ice wafers.

[38] (mM)	Log[38] (mM)	v_{norm} (%)	Standard Deviation (%)
1	0.00	96.4	5.35
5	0.70	91.6	2.64
30	1.48	63.7	2.61
75	1.88	45.6	4.47
150	2.18	17.5	8.43
250	2.40	0.00	0.00

Table 8-26. Raw data for the plot of normalized ice crystal growth (v_{norm}) in phosphate-buffered saline (PBS) as a function of nitrile-containing compound *N*-4-(cyanophenyl)-D-gluconamide (*p*CNA, **39**) concentration (in mM). Data reported as a mean and standard deviation of n=3 ice wafers.

[39] (mM)	Log[39] (mM)	v_{norm} (%)	Standard Deviation (%)
1	0.00	101.1	4.26
10	1.00	96.5	2.01
80	1.90	72.8	1.70

Table 8-27. Raw data for the plot of normalized ice crystal growth (v_{norm}) in phosphate-buffered saline (PBS) as a function of nitrile-containing compound *N*-3-(cyanophenyl)-D-gluconamide (*m*CNA, **40**) concentration (in mM). Data reported as a mean and standard deviation of n=3 ice wafers.

[40] (mM)	Log[40] (mM)	v_{norm} (%)	Standard Deviation (%)
1	0.00	102.5	13.4
10	1.00	91.6	12.5
20	1.30	86.2	8.47
45	1.65	82.6	6.76

Table 8-28. Raw data for the plot of normalized ice crystal growth (v_{norm}) in phosphate-buffered saline (PBS) as a function of nitrile-containing compound *N*-2-(cyanophenyl)-D-gluconamide (*o*CNA, **41**) concentration (in mM). Data reported as a mean and standard deviation of n=3 ice wafers.

[41] (mM)	Log[41] (mM)	v_{norm} (%)	Standard Deviation (%)
1	0.00	102.0	4.01
10	1.00	92.2	7.62
50	1.70	74.2	5.94
100	2.00	36.8	10.3

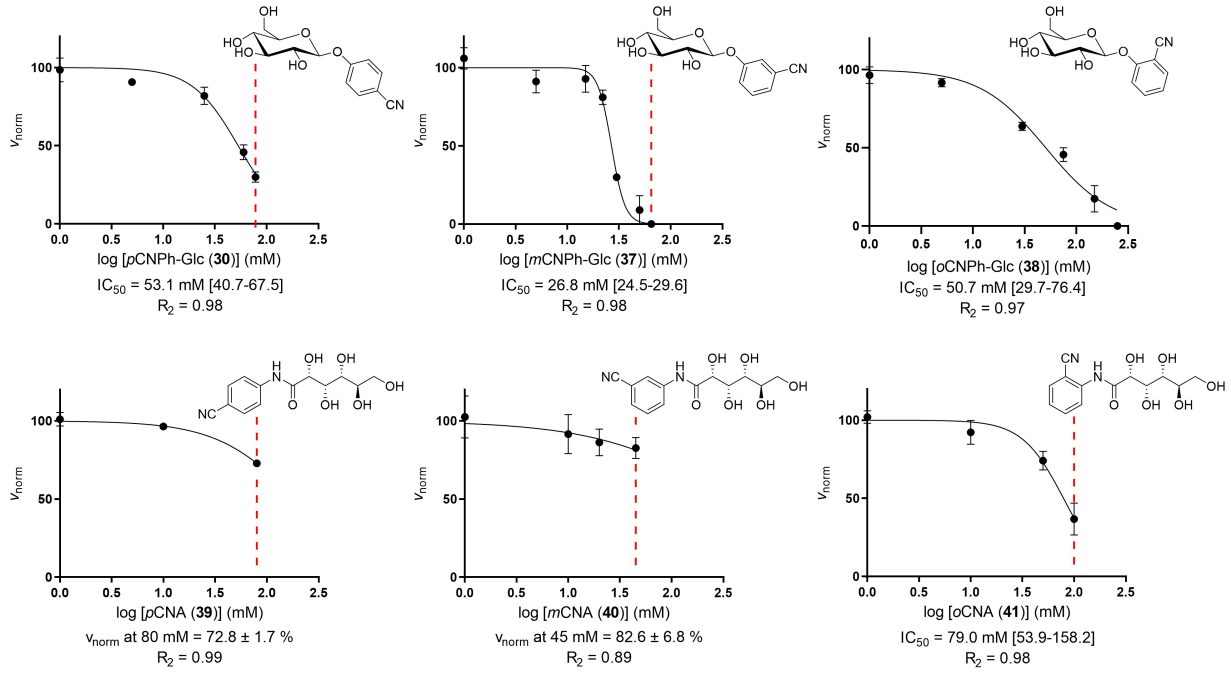


Figure 8-25. Plot of normalized ice crystal growth (v_{norm}) in phosphate-buffered saline (PBS) against nitrile-containing ice recrystallization inhibitors **30** and **37**-**41** with concentration (in mM). Red lines denote the maximum solubility of the compound in PBS (maximum heating to 100 °C).

8.3.1.12. (carbamoylphenyl)-β-D-glucopyranosides and N-carbamoylphenyl-D-gluconamides

Table 8-29. Raw data for the plot of normalized ice crystal growth (v_{norm}) in phosphate-buffered saline (PBS) as a function of amide-containing compound 4-(carbamoylphenyl)-β-D-glucopyranoside (*p*AmPh-Glc, **31**) concentration (in mM). Data reported as a mean and standard deviation of n=3 ice wafers.

[31] (mM)	Log[31] (mM)	v_{norm} (%)	Standard Deviation (%)
1	0.00	102.9	2.30
15	1.18	101.4	5.09
25	1.40	82.0	7.67
35	1.54	58.3	5.25
50	1.70	51.0	3.76
60	1.78	7.75	13.4
80	1.90	0.00	0.00
100	2.00	0.00	0.00

Table 8-30. Raw data for the plot of normalized ice crystal growth (v_{norm}) in phosphate-buffered saline (PBS) as a function of amide-containing compound 3-(carbamoylphenyl)-β-D-glucopyranoside (*m*AmPh-Glc, **42**) concentration (in mM). Data reported as a mean and standard deviation of n=3 ice wafers.

[42] (mM)	Log[42] (mM)	v_{norm} (%)	Standard Deviation (%)
1	0.00	91.4	4.78
25	1.40	89.3	8.08
75	1.88	63.6	4.53
100	2.00	50.6	6.27
130	2.11	34.8	8.48
175	2.24	15.4	8.94

Table 8-31. Raw data for the plot of normalized ice crystal growth (v_{norm}) in phosphate-buffered saline (PBS) as a function of amide-containing compound 2-(carbamoylphenyl)-β-D-glucopyranoside (*o*AmPh-Glc, **43**) concentration (in mM). Data reported as a mean and standard deviation of n=3 ice wafers.

[43] (mM)	Log[43] (mM)	v_{norm} (%)	Standard Deviation (%)
1	0.00	87.4	6.72
10	1.00	98.6	8.99
35	1.48	83.5	1.17
45	1.65	51.2	7.29
75	1.88	42.6	7.13
100	2.00	18.9	7.01
135	2.13	0.00	0.00
190	2.28	0.00	0.00

Table 8-32. Raw data for the plot of normalized ice crystal growth (v_{norm}) in phosphate-buffered saline (PBS) as a function of amide-containing compound *N*-4-(carbamoylphenyl)-D-glucoamide (*p*AmA, **44**) concentration (in mM). Data reported as a mean and standard deviation of n=3 ice wafers.

[44] (mM)	Log[44] (mM)	v_{norm} (%)	Standard Deviation (%)
10	1.00	93.0	2.13
25	1.40	83.3	7.05
50	1.70	56.1	9.07

Table 8-33. Raw data for the plot of normalized ice crystal growth (v_{norm}) in phosphate-buffered saline (PBS) as a function of amide-containing compound *N*-3-(carbamoylphenyl)-D-glucoamide (*m*AmA, **45**) concentration (in mM). Data reported as a mean and standard deviation of n=3 ice wafers.

[45] (mM)	Log[45] (mM)	v_{norm} (%)	Standard Deviation (%)
10	1.00	96.9	10.7

Table 8-34. Raw data for the plot of normalized ice crystal growth (v_{norm}) in phosphate-buffered saline (PBS) as a function of amide-containing compound *N*-2-(carbamoylphenyl)-D-glucoamide (*o*AmA, **46**) concentration (in mM). Data reported as a mean and standard deviation of n=3 ice wafers.

[46] (mM)	Log[46] (mM)	v_{norm} (%)	Standard Deviation (%)
1	0.00	96.6	0.93
10	1.00	93.1	7.38
25	1.40	86.0	7.98
30	1.48	79.2	12.1
40	1.60	35.2	12.6
50	1.70	2.23	2.48
75	1.88	0.00	0.00
150	2.18	0.00	0.00

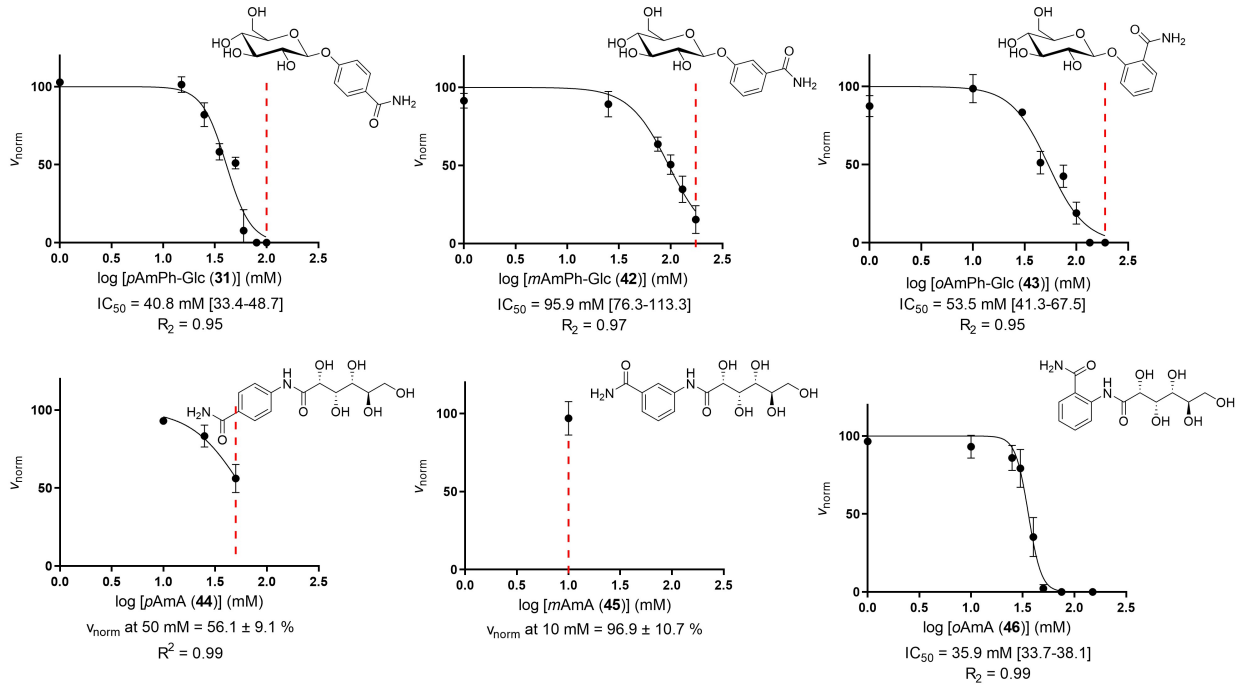


Figure 8-26. Plot of normalized ice crystal growth (v_{norm}) in phosphate-buffered saline (PBS) against nitrile-containing ice recrystallization inhibitors **31** and **42**-**46** with concentration (in mM). Red lines denote the maximum solubility of the compound in PBS (maximum heating to 100 °C).

*8.3.1.13. (4-hydroxyphenyl)-β-D-glucopyranoside (pOHPh-Glc, **53**)*

Table 8-35. Raw data for the plot of normalized ice crystal growth (v_{norm}) in phosphate-buffered saline (PBS) as a function of *p*OHPh-Glc (**53**) concentration (in mM). Data reported as a mean and standard deviation of n=3 ice wafers.

[53] (mM)	Log[53] (mM)	v_{norm} (%)	Standard Deviation (%)
1	0.00	96.9	10.3
10	1.00	107.2	4.33
25	1.40	98.0	7.23
100	2.00	92.9	3.13
125	2.10	44.8	11.3
150	2.18	36.1	14.6
200	2.30	22.5	4.12
300	2.48	0.00	0.00

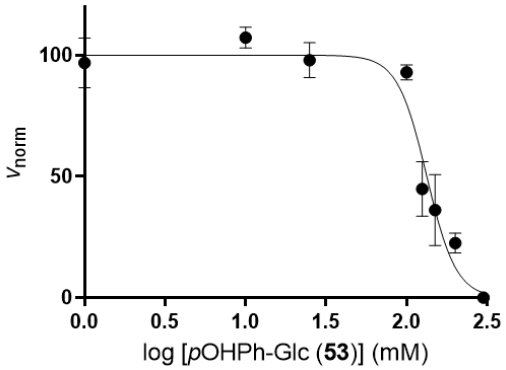


Figure 8-27. Plot of normalized ice crystal growth (v_{norm}) in phosphate-buffered saline (PBS) against *p*OHPh-Glc (**53**) concentration (in mM). $R^2 = 0.96$. IC_{50}: 133.3 mM, 95% CI [117.9-152.7].

*8.3.1.14. (4-ethoxyphenyl)-β-D-glucopyranoside (PEP-Glc, **54**)*

Table 8-36. Raw data for the plot of normalized ice crystal growth (v_{norm}) in phosphate-buffered saline (PBS) as a function of PEP-Glc (**54**) concentration (in mM). Data reported as a mean and standard deviation of n=3 ice wafers.

[54] (mM)	Log[54] (mM)	v_{norm} (%)	Standard Deviation (%)
1	0.00	99.7	9.57
2.5	0.40	83.1	4.65
4	0.60	58.3	7.47
8	0.90	14.5	2.93
10	1.00	10.3	6.44
25	1.40	0.00	0.00

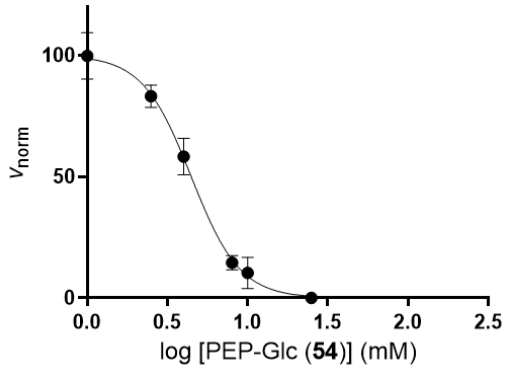


Figure 8-28. Plot of normalized ice crystal growth (v_{norm}) in phosphate-buffered saline (PBS) against PEP-Glc (**54**) concentration (in mM). $R^2 = 0.99$. IC_{50}: 4.45 mM, 95% CI [4.29-4.62].

*8.3.1.15. (4-propoxyphenyl)-β-D-glucopyranoside (PPP-Glc, **55**)*

Table 8-37. Raw data for the plot of normalized ice crystal growth (v_{norm}) in phosphate-buffered saline (PBS) as a function of PPP-Glc (**55**) concentration (in mM). Data reported as a mean and standard deviation of n=3 ice wafers.

[55] (mM)	Log[55] (mM)	v_{norm} (%)	Standard Deviation (%)
1	0.00	103.8	3.10
5	0.70	95.4	6.99
15	1.18	69.2	2.56
20	1.30	55.2	10.0
40	1.60	0.00	0.00

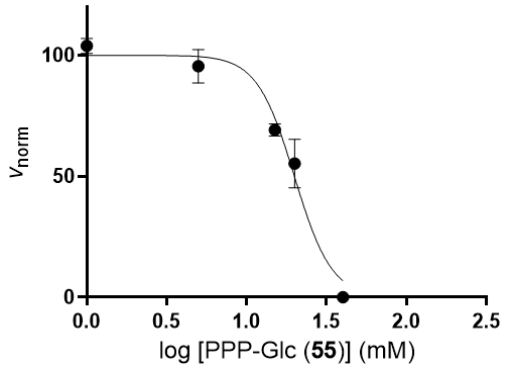


Figure 8-29. Plot of normalized ice crystal growth (v_{norm}) in phosphate-buffered saline (PBS) against PPP-Glc (**55**) concentration (in mM). $R^2 = 0.98$. IC_{50}: 19.9 mM, 95% CI [16.4-24.4].

*8.3.1.16. (4-butoxyphenyl)-β-D-glucopyranoside (PBP-Glc, **56**)*

Table 8-38. Raw data for the plot of normalized ice crystal growth (v_{norm}) in phosphate-buffered saline (PBS) as a function of PBP-Glc (**56**) concentration (in mM). Data reported as a mean and standard deviation of n=3 ice wafers.

[56] (mM)	Log[56] (mM)	v_{norm} (%)	Standard Deviation (%)
1	0.00	94.1	7.55
5	0.70	62.0	5.24
15	1.18	15.4	9.19
25	1.40	0.00	0.00

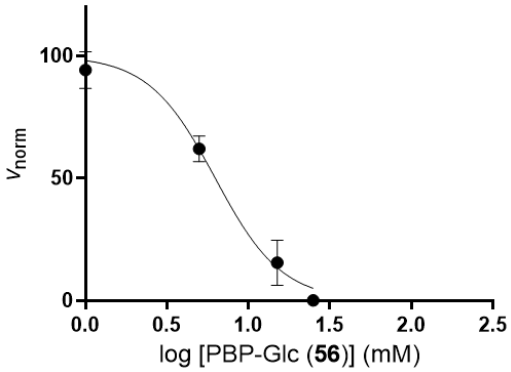


Figure 8-30. Plot of normalized ice crystal growth (v_{norm}) in phosphate-buffered saline (PBS) against PBP-Glc (**56**) concentration (in mM). $R^2 = 0.99$. IC_{50}: 6.25 mM, 95% CI [4.08-8.93].

*8.3.1.17. (4-hexyloxyphenyl)-β-D-glucopyranoside (PHP-Glc, **80**)*

Table 8-39. Raw data for the plot of normalized ice crystal growth (v_{norm}) in phosphate-buffered saline (PBS) as a function of PHP-Glc (**80**) concentration (in mM). Data reported as a mean and standard deviation of n=3 ice wafers.

[80] (mM)	Log[80] (mM)	v_{norm} (%)	Standard Deviation (%)
0.25	-0.60	95.6	9.18
1	0.00	99.2	3.53
2.5	0.40	81.4	7.14
4	0.60	69.7	6.24

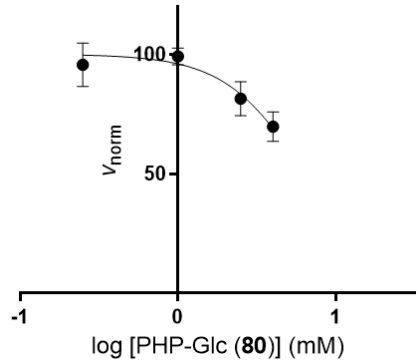


Figure 8-31. Plot of normalized ice crystal growth (v_{norm}) in phosphate-buffered saline (PBS) against PHP-Glc (**80**) concentration (in mM). $R^2 = 0.95$. LD_{50}: NA, Minimum $v_{norm} = 69.7 \pm 6.24$ %

*8.3.1.18. phenyl-β-D-glucopyranoside (Ph-Glc, **82**)*

Table 8-40. Raw data for the plot of normalized ice crystal growth (v_{norm}) in phosphate-buffered saline (PBS) as a function of Ph-Glc (**82**) concentration (in mM). Data reported as a mean and standard deviation of n=3 ice wafers.

[82] (mM)	Log[82] (mM)	v_{norm} (%)	Standard Deviation (%)
1	0.00	96.6	9.27
10	1.00	80.1	5.27
20	1.30	44.8	4.83
30	1.48	5.33	9.23
40	1.60	0.89	1.54
60	1.78	0.00	0.00

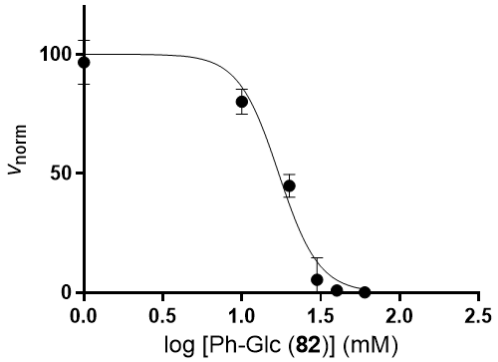


Figure 8-32. Plot of normalized ice crystal growth (v_{norm}) in phosphate-buffered saline (PBS) against Ph-Glc (**82**) concentration (in mM). $R^2 = 0.98$. IC_{50}: 17.1 mM, 95% CI [13.5-21.1].

*8.3.1.19. (4-chlorophenyl)-β-D-glucopyranoside (pClPh-Glc, **83**)*

Table 8-41. Raw data for the plot of normalized ice crystal growth (v_{norm}) in phosphate-buffered saline (PBS) as a function of *p*ClPh-Glc (**83**) concentration (in mM). Data reported as a mean and standard deviation of n=3 ice wafers.

[83] (mM)	Log[83] (mM)	v_{norm} (%)	Standard Deviation (%)
1	0.00	105.4	1.30
5	0.70	90.9	9.29
12.5	1.10	40.8	2.48
25	1.40	2.57	2.25
50	1.70	0.00	0.00

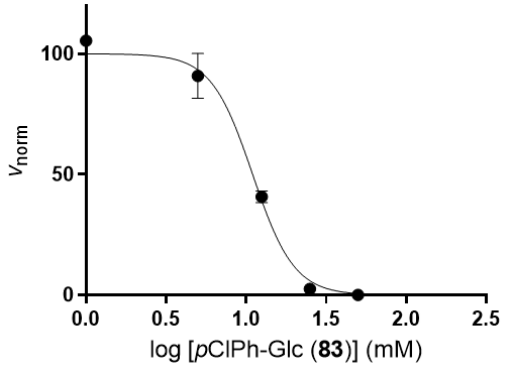


Figure 8-33. Plot of normalized ice crystal growth (v_{norm}) in phosphate-buffered saline (PBS) against *p*ClPh-Glc (**83**) concentration (in mM). $R^2 = 0.99$. IC_{50}: 11.0 mM, 95% CI [9.11-12.8].

*8.3.1.20. (4-iodophenyl)-β-D-glucopyranoside (pIPh-Glc, **84**)*

Table 8-42. Raw data for the plot of normalized ice crystal growth (v_{norm}) in phosphate-buffered saline (PBS) as a function of *p*IPh-Glc (**84**) concentration (in mM). Data reported as a mean and standard deviation of n=3 ice wafers.

[84] (mM)	Log[84] (mM)	v_{norm} (%)	Standard Deviation (%)
1	0.00	86.2	3.86
5	0.70	80.6	14.2
7	0.85	81.9	5.08
10	1.00	58.5	6.68

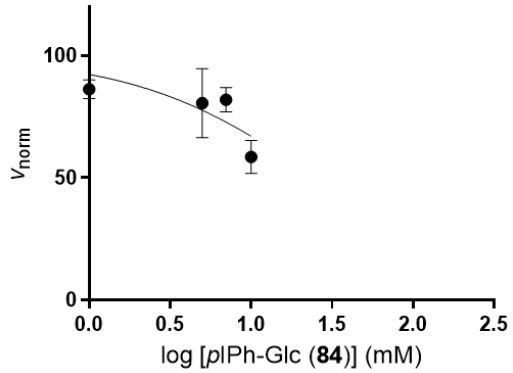


Figure 8-34. Plot of normalized ice crystal growth (v_{norm}) in phosphate-buffered saline (PBS) against *p*IPh-Glc (**84**) concentration (in mM). $R^2 = 0.57$. IC_{50}: NA, Minimum $v_{norm} = 58.5 \pm 6.68$ %

*8.3.1.21. (4-nitrophenyl)-β-D-glucopyranoside (pNO$_2$Ph-Glc, **85**)*

Table 8-43. Raw data for the plot of normalized ice crystal growth (v_{norm}) in phosphate-buffered saline (PBS) as a function of *p*NO_2Ph-Glc (**85**) concentration (in mM). Data reported as a mean and standard deviation of n=3 ice wafers.

[85] (mM)	Log[85] (mM)	v_{norm} (%)	Standard Deviation (%)
1	0.00	101.1	4.93
15	1.18	85.6	4.76
25	1.40	78.2	5.78
50	1.70	13.0	4.93
100	2.00	0.00	0.00

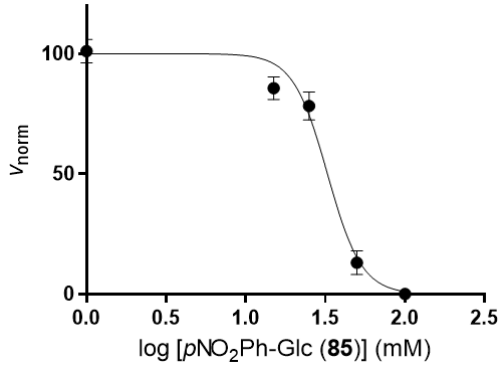


Figure 8-35. Plot of normalized ice crystal growth (v_{norm}) in phosphate-buffered saline (PBS) against pNO$_2$Ph-Glc (**85**) concentration (in mM). R^2 = 0.99. IC_{50}: 32.6 mM, 95% CI [26.6-40.6].

*8.3.1.22. (4-fluorophenyl)-β-D-glucopyranoside (pFPh-Glc, **86**)*

Previously reported data for the ice recrystallization inhibition activity of (pFPh-Glc, **86***) by Dr. Jessica Poisson (2019)*[214]

Table 8-44. Raw data for the plot of the normalized ice crystal growth rate constants (k_{norm}) in phosphate-buffered saline (PBS) as a function of pFPh-Glc (**86**) concentration (in mM) as reported by Dr. Jessica Poisson (2019).[214] Data reported as a mean and standard deviation of n=3 ice wafers.

[86] (mM)	Log[86] (mM)	k_{norm} (%)	Standard Deviation (%)
10	1.00	94.2	8.51
30	1.47	73.7	0.01
60	1.77	54.0	5.41
80	1.90	9.82	4.64
100	2.00	0.00	0.00

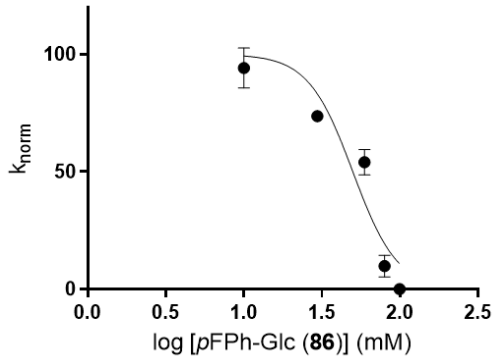


Figure 8-36. Plot of normalized ice crystal growth rate constants (k_{norm}) in phosphate-buffered saline (PBS) against pFPh-Glc (**86**) concentration (in mM) as reported by Dr. Jessica Poisson (2019).[214] R^2 = 0.91. IC_{50}: 49.9 mM, 95% CI [22.5-75.1].

*8.3.1.23. (4-methoxyphenyl)-1-deutero-β-D-glucopyranoside (1D1 PMP-Glc, **90**)*

Table 8-45. Raw data for the plot of normalized ice crystal growth (v_{norm}) in phosphate-buffered saline (PBS) as a function of 1D1 PMP-Glc (**90**) concentration (in mM). Data reported as a mean and standard deviation of n=3 ice wafers.

[90] (mM)	Log[90] (mM)	v_{norm} (%)	Standard Deviation (%)
1	0.00	102.5	1.94
10	1.00	100.7	2.19
20	1.30	97.9	2.62
50	1.70	83.5	7.17
75	1.88	69.6	10.2
110	2.04	26.0	4.99

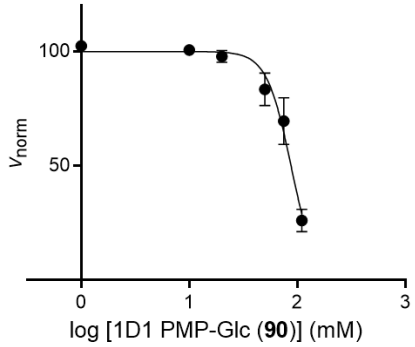


Figure 8-37. Plot of normalized ice crystal growth (v_{norm}) in phosphate-buffered saline (PBS) against 1D1 PMP-Glc (**90**) concentration (in mM). $R^2 = 0.98$. IC_{50}: 87.3 mM, 95% CI [78.8-97.3].

*8.3.1.24. (4-methoxyphenyl)-2-deutero-β-D-glucopyranoside (2D1 PMP-Glc, **91**)*

Table 8-46. Raw data for the plot of normalized ice crystal growth (v_{norm}) in phosphate-buffered saline (PBS) as a function of 2D1 PMP-Glc (**91**) concentration (in mM). Data reported as a mean and standard deviation of n=3 ice wafers.

[91] (mM)	Log[91] (mM)	v_{norm} (%)	Standard Deviation (%)
1	0.00	107.1	6.37
10	1.00	93.8	4.90
25	1.40	90.5	4.94
50	1.70	65.7	4.45

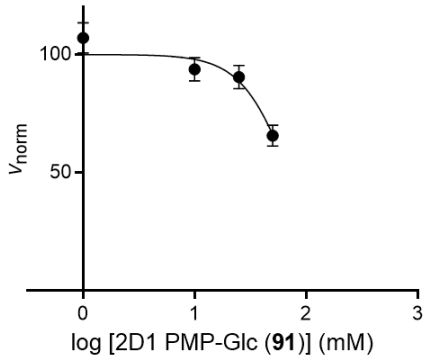


Figure 8-38. Plot of normalized ice crystal growth (v_{norm}) in phosphate-buffered saline (PBS) against 2D1 PMP-Glc (**91**) concentration (in mM). $R^2 = 0.92$. IC_{50}: NA, Minimum $v_{norm} = 65.7 \pm 4.45$ %.

*8.3.1.25. (4-methoxyphenyl)-3-deutero-β-D-glucopyranoside (3D1 PMP-Glc, **92**)*

Table 8-47. Raw data for the plot of normalized ice crystal growth (v_{norm}) in phosphate-buffered saline (PBS) as a function of 3D1 PMP-Glc (**92**) concentration (in mM). Data reported as a mean and standard deviation of n=3 ice wafers.

[92] (mM)	Log[92] (mM)	v_{norm} (%)	Standard Deviation (%)
	1.70	82.9	7.26
	2.00	75.3	2.80
	2.18	48.6	2.10
	2.30	18.0	3.33

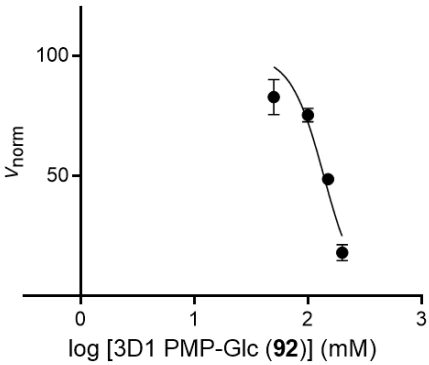


Figure 8-39. Plot of normalized ice crystal growth (v_{norm}) in phosphate-buffered saline (PBS) against 3D1 PMP-Glc (**92**) concentration (in mM). $R^2 = 0.91$. IC_{50}: 137.9 mM, 95% CI [56.3-6360].

*8.3.1.26. D-glucose (1-d_1) (D1 D-glucose, **94**)*

Table 8-48. Raw data for the plot of normalized ice crystal growth (v_{norm}) in phosphate-buffered saline (PBS) as a function of D1 D-glucose (**94**) concentration (in mM). Data reported as a mean and standard deviation of n=3 ice wafers.

[94] (mM)	Log[94] (mM)	v_{norm} (%)	Standard Deviation (%)
10	1.00	96.0	6.66
50	1.70	79.2	8.25
100	2.00	56.7	5.40
200	2.30	31.6	10.3
300	2.48	18.0	6.87
500	2.70	0.00	0.00

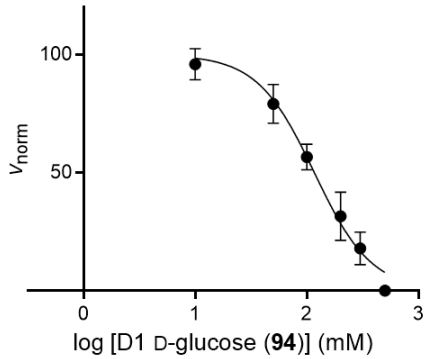


Figure 8-40. Plot of normalized ice crystal growth (v_{norm}) in phosphate-buffered saline (PBS) against D1 D-glucose (**94**) concentration (in mM). $R^2 = 0.99$. IC_{50}: 116.6 mM, 95% CI [95.0-140.8].

*8.3.1.27. D-glucose (2-d_1) (D2 D-glucose, **95**)*

Table 8-49. Raw data for the plot of normalized ice crystal growth (v_{norm}) in phosphate-buffered saline (PBS) as a function of D2 D-glucose (**95**) concentration (in mM). Data reported as a mean and standard deviation of n=3 ice wafers.

[95] (mM)	Log[95] (mM)	v_{norm} (%)	Standard Deviation (%)
10	1.00	99.0	4.87
50	1.70	77.1	5.54
100	2.00	58.4	7.82
200	2.30	44.3	11.3
300	2.48	13.4	10.1
500	2.70	0.00	0.00

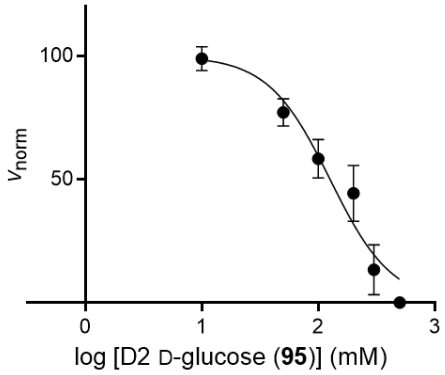


Figure 8-41. Plot of normalized ice crystal growth (v_{norm}) in phosphate-buffered saline (PBS) against D2 D-glucose (**95**) concentration (in mM). $R^2 = 0.96$. IC_{50}: 126.0 mM, 95% CI [81.4-181.8].

*8.3.1.28. D-glucose (3-d_1) (D3 D-glucose, **96**)*

Table 8-50. Raw data for the plot of normalized ice crystal growth (v_{norm}) in phosphate-buffered saline (PBS) as a function of D3 D-glucose (**96**) concentration (in mM). Data reported as a mean and standard deviation of n=3 ice wafers.

[96] (mM)	Log[96] (mM)	v_{norm} (%)	Standard Deviation (%)
10	1.00	96.4	5.97
50	1.70	78.5	4.36
100	2.00	60.9	2.36
200	2.30	29.4	8.50
300	2.48	14.6	10.5
500	2.70	2.30	3.98

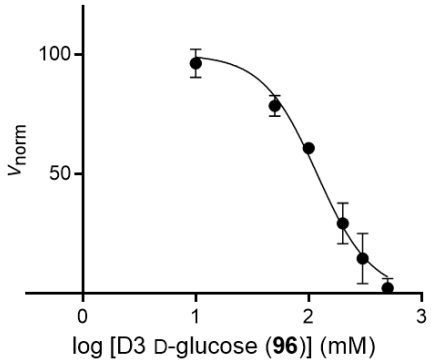


Figure 8-42. Plot of normalized ice crystal growth (v_{norm}) in phosphate-buffered saline (PBS) against D3 D-glucose (**96**) concentration (in mM). $R^2 = 0.99$. IC_{50}: 118.6 mM, 95% CI [100.3-138.6].

*8.3.1.29. (4-methoxyphenyl)-2-O-methyl-β-D-glucopyranoside (C_2 OMe PMP-Glc, **97**)*

Table 8-51. Raw data for the plot of normalized ice crystal growth (v_{norm}) in phosphate-buffered saline (PBS) as a function of C_2 OMe PMP-Glc (**97**) concentration (in mM). Data reported as a mean and standard deviation of n=3 ice wafers.

[97] (mM)	Log[97] (mM)	v_{norm} (%)	Standard Deviation (%)
1	0.00	99.7	7.79
10	1.00	88.5	3.15
20	1.30	63.9	3.91
40	1.60	33.1	5.83
50	1.70	0.00	0.00
80	1.90	0.00	0.00

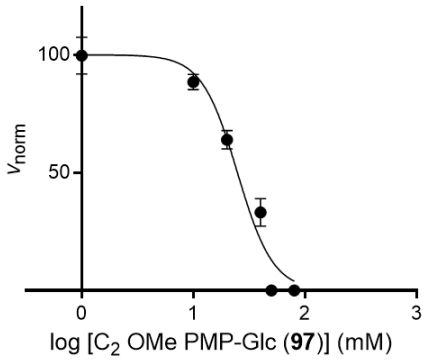


Figure 8-43. Plot of normalized ice crystal growth (v_{norm}) in phosphate-buffered saline (PBS) against C_2 OMe PMP-Glc (**97**) concentration (in mM). $R^2 = 0.96$. IC_{50}: 24.8 mM, 95% CI [17.7-33.4].

*8.3.1.30. (4-methoxyphenyl)-3-O-methyl-β-D-glucopyranoside (C_3 OMe PMP-Glc, **98**)*

Table 8-52. Raw data for the plot of normalized ice crystal growth (v_{norm}) in phosphate-buffered saline (PBS) as a function of C_3 OMe PMP-Glc (**98**) concentration (in mM). Data reported as a mean and standard deviation of n=3 ice wafers.

[98] (mM)	Log[98] (mM)	v_{norm} (%)	Standard Deviation (%)
1	0.00	100.0	4.03
10	1.00	90.3	0.51
30	1.48	82.1	6.21
50	1.70	61.7	2.84
100	2.00	25.4	1.74
250	2.40	0.00	0.00

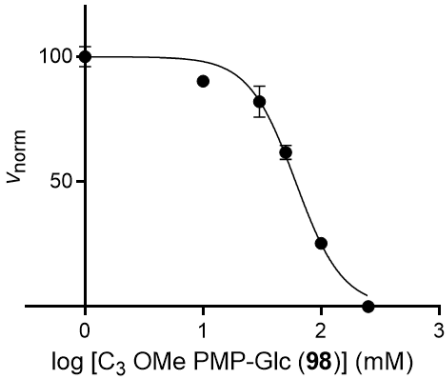


Figure 8-44. Plot of normalized ice crystal growth (v_{norm}) in phosphate-buffered saline (PBS) against C_3 OMe PMP-Glc (**98**) concentration (in mM). $R^2 = 0.99$. IC_{50}: 60.7 mM, 95% CI [51.3-72.0].

*8.3.1.31. (4-methoxyphenyl)-4-O-methyl-β-D-glucopyranoside (C_4 OMe PMP-Glc, **99**)*

Table 8-53. Raw data for the plot of normalized ice crystal growth (v_{norm}) in phosphate-buffered saline (PBS) as a function of C_4 OMe PMP-Glc (**99**) concentration (in mM). Data reported as a mean and standard deviation of n=3 ice wafers.

[99] (mM)	Log[99] (mM)	v_{norm} (%)	Standard Deviation (%)
0.5	-0.30	99.2	7.68
2.5	0.40	70.5	9.43
6	0.78	9.39	5.41
8	0.90	4.93	4.39
10	1.00	0.00	0.00

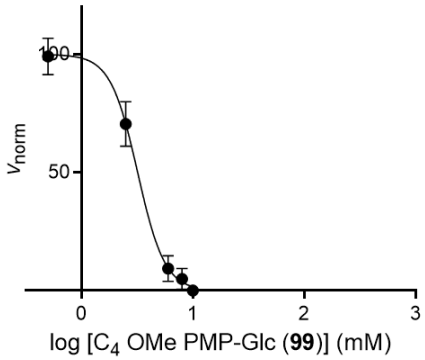


Figure 8-45. Plot of normalized ice crystal growth (v_{norm}) in phosphate-buffered saline (PBS) against C_4 OMe PMP-Glc (**99**) concentration (in mM). $R^2 = 0.99$. IC_{50}: 3.19 mM, 95% CI [3.04-3.37].

*8.3.1.32. (4-methoxyphenyl)-6-O-methyl-β-D-glucopyranoside (C_6 OMe PMP-Glc, **89**)*

Table 8-54. Raw data for the plot of normalized ice crystal growth (v_{norm}) in phosphate-buffered saline (PBS) as a function of C_6 OMe PMP-Glc (**89**) concentration (in mM). Data reported as a mean and standard deviation of n=3 ice wafers.

[89] (mM)	Log[89] (mM)	v_{norm} (%)	Standard Deviation (%)
30	1.48	90.7	5.85

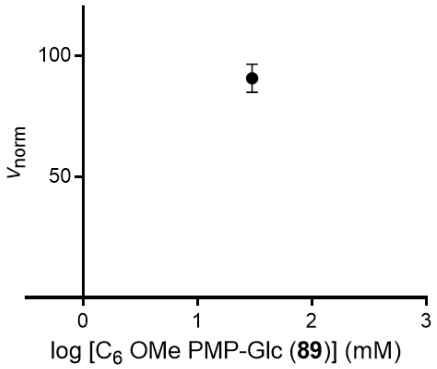


Figure 8-46. Plot of normalized ice crystal growth (v_{norm}) in phosphate-buffered saline (PBS) against C_6 OMe PMP-Glc (**89**) concentration (in mM). IC_{50}: NA, Minimum v_{norm} = 90.7 ± 5.9 %.

*8.3.1.33. (4-methoxyphenyl)-2-O-ethyl-β-D-glucopyranoside (C_2 OEt PMP-Glc, **100**)*

Table 8-55. Raw data for the plot of normalized ice crystal growth (v_{norm}) in phosphate-buffered saline (PBS) as a function of C_2 OEt PMP-Glc (**100**) concentration (in mM). Data reported as a mean and standard deviation of n=3 ice wafers.

[100] (mM)	Log[100] (mM)	v_{norm} (%)	Standard Deviation (%)
1	0.00	95.8	10.1
3	0.48	91.4	12.8
6	0.78	57.4	14.7
10	1.00	8.13	3.77
20	1.30	0.00	0.00

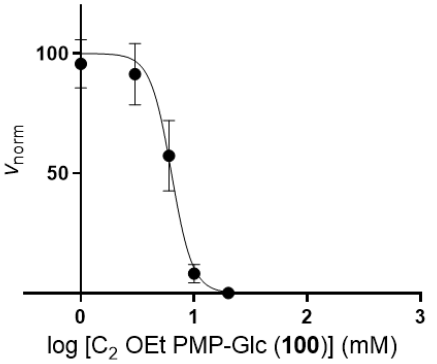


Figure 8-47. Plot of normalized ice crystal growth (v_{norm}) in phosphate-buffered saline (PBS) against C_2 OEt PMP-Glc (**100**) concentration (in mM). R^2 = 0.99. IC_{50}: 6.31 mM, 95% CI [5.51-7.06].

*8.3.1.34. (4-methoxyphenyl)-3-O-ethyl-β-D-glucopyranoside (C_3 OEt PMP-Glc, **101**)*

Table 8-56. Raw data for the plot of normalized ice crystal growth (v_{norm}) in phosphate-buffered saline (PBS) as a function of C_3 OEt PMP-Glc (**101**) concentration (in mM). Data reported as a mean and standard deviation of n=3 ice wafers.

[101] (mM)	Log[101] (mM)	v_{norm} (%)	Standard Deviation (%)
1	0.00	97.8	6.63
10	1.00	81.7	14.9
25	1.40	64.6	13.0
50	1.70	48.9	2.44
100	2.00	19.8	9.87

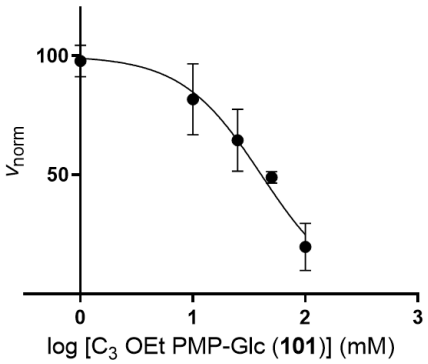


Figure 8-48. Plot of normalized ice crystal growth (v_{norm}) in phosphate-buffered saline (PBS) against C_3 OEt PMP-Glc (**101**) concentration (in mM). $R^2 = 0.98$. IC_{50}: 40.5 mM, 95% CI [29.8-55.1].

*8.3.1.35. (4-methoxyphenyl)-3-O-propyl-β-D-glucopyranoside (C_3 OPr PMP-Glc, **102**)*

Table 8-57. Raw data for the plot of normalized ice crystal growth (v_{norm}) in phosphate-buffered saline (PBS) as a function of C_3 OPr PMP-Glc (**102**) concentration (in mM). Data reported as a mean and standard deviation of n=3 ice wafers.

[102] (mM)	Log[102] (mM)	v_{norm} (%)	Standard Deviation (%)
1	0.00	92.8	8.68
10	1.00	88.8	3.24
20	1.30	74.9	10.0
40	1.60	63.2	7.00

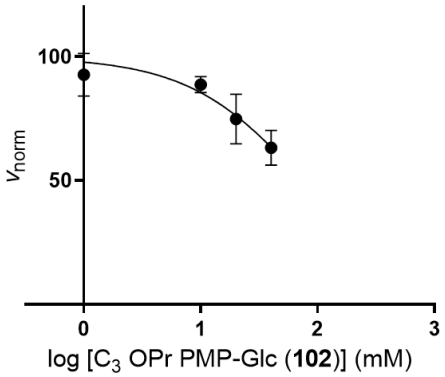


Figure 8-49. Plot of normalized ice crystal growth (v_{norm}) in phosphate-buffered saline (PBS) against C_3 OPr PMP-Glc (**102**) concentration (in mM). $R^2 = 0.93$. IC_{50}: NA, Minimum $v_{norm} = 63.2 \pm 7.0$ %.

*8.3.1.36. (4-methoxyphenyl)-4-O-ethyl-β-D-glucopyranoside (C_4 OEt PMP-Glc, **103**)*

Table 8-58. Raw data for the plot of normalized ice crystal growth (v_{norm}) in phosphate-buffered saline (PBS) as a function of C_4 OEt PMP-Glc (**103**) concentration (in mM). Data reported as a mean and standard deviation of n=3 ice wafers.

[103] (mM)	Log[103] (mM)	v_{norm} (%)	Standard Deviation (%)
1	0.00	100.4	6.08
3	0.48	42.5	10.3
6	0.78	21.9	10.9
10	1.00	0.00	0.00
35	1.54	0.00	0.00

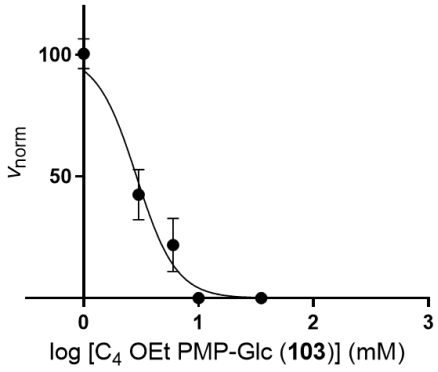


Figure 8-50. Plot of normalized ice crystal growth (v_{norm}) in phosphate-buffered saline (PBS) against C_4 OEt PMP-Glc (**103**) concentration (in mM). $R^2 = 0.98$. IC_{50}: 2.88 mM, 95% CI [2.01-3.96].

*8.3.1.37. (4-methoxyphenyl)-4-O-propyl-β-D-glucopyranoside (C_4 OPr PMP-Glc, **104**)*

Table 8-59. Raw data for the plot of normalized ice crystal growth (v_{norm}) in phosphate-buffered saline (PBS) as a function of C_4 OPr PMP-Glc (**104**) concentration (in mM). Data reported as a mean and standard deviation of n=3 ice wafers.

[104] (mM)	Log[104] (mM)	v_{norm} (%)	Standard Deviation (%)
0.5	-0.30	100.0	2.66
2	0.30	57.0	5.59
3	0.48	45.7	2.71
4	0.60	29.3	8.84
6	0.78	26.1	4.08

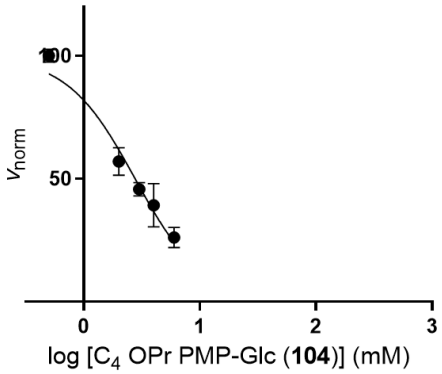


Figure 8-51. Plot of normalized ice crystal growth (v_{norm}) in phosphate-buffered saline (PBS) against C_4 OPr PMP-Glc (**104**) concentration (in mM). $R^2 = 0.97$. IC_{50}: 2.77 mM, 95% CI [2.08-3.60].

*8.3.1.38. (4-methoxyphenyl)-β-D-galactopyranoside (PMP-Gal, **107**)*

Table 8-60. Raw data for the plot of normalized ice crystal growth (v_{norm}) in phosphate-buffered saline (PBS) as a function of PMP-Gal (**107**) concentration (in mM). Data reported as a mean and standard deviation of n=3 ice wafers.

[107] (mM)	Log[107] (mM)	v_{norm} (%)	Standard Deviation (%)
1	0.00	97.3	5.68
5	0.70	89.6	9.24
35	1.54	75.0	5.90
65	1.81	38.5	8.93
145	2.16	15.1	1.04
250	2.40	0.00	0.00

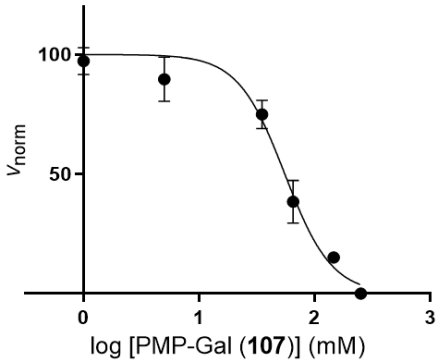


Figure 8-52. Plot of normalized ice crystal growth (v_{norm}) in phosphate-buffered saline (PBS) against PMP-Gal (**107**) concentration (in mM). $R^2 = 0.98$. IC_{50}: 55.2 mM, 95% CI [42.2-70.2].

*8.3.1.39. (4-methoxyphenyl)-4-O-methyl-β-D-galactopyranoside (C_4 OMe PMP-Gal, **108**)*

Table 8-61. Raw data for the plot of normalized ice crystal growth (v_{norm}) in phosphate-buffered saline (PBS) as a function of C_4 OMe PMP-Gal (**108**) concentration (in mM). Data reported as a mean and standard deviation of n=3 ice wafers.

[108] (mM)	Log[108] (mM)	v_{norm} (%)	Standard Deviation (%)
1	0.00	98.1	5.26
3	0.48	73.3	7.55
6	0.78	40.5	3.44
10	1.00	0.00	0.00
50	1.70	0.00	0.00
100	2.00	0.00	0.00

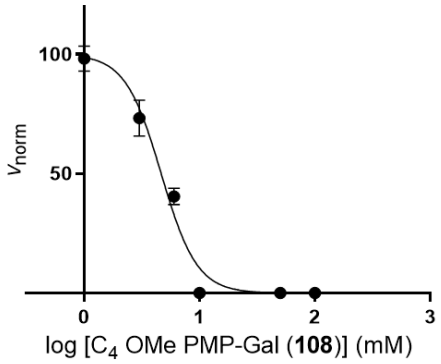


Figure 8-53. Plot of normalized ice crystal growth (v_{norm}) in phosphate-buffered saline (PBS) against C_4 OMe PMP-Gal (**108**) concentration (in mM). $R^2 = 0.98$. IC_{50}: 4.65 mM, 95% CI [3.60-5.83].

*8.3.1.40. (4-methoxyphenyl)-4-deoxy-β-D-galactopyranoside (C_4 Deoxy PMP-Gal, **109**)*

Table 8-62. Raw data for the plot of normalized ice crystal growth (v_{norm}) in phosphate-buffered saline (PBS) as a function of C_4 Deoxy PMP-Gal (**109**) concentration (in mM). Data reported as a mean and standard deviation of n=3 ice wafers.

[109] (mM)	Log[109] (mM)	v_{norm} (%)	Standard Deviation (%)
1	0.00	96.1	2.50
5	0.70	93.8	2.90
15	1.18	85.7	3.14
35	1.48	80.4	6.10
50	1.70	51.7	5.62
60	1.78	67.8	6.36
90	1.95	39.8	4.21

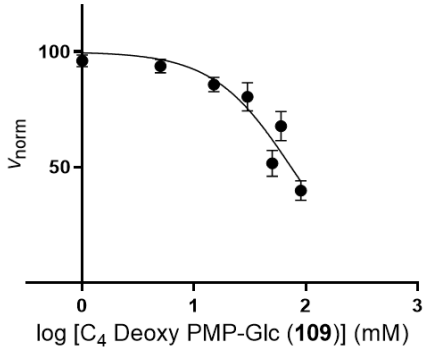


Figure 8-54. Plot of normalized ice crystal growth (v_{norm}) in phosphate-buffered saline (PBS) against C_4 Deoxy PMP-Gal (**109**) concentration (in mM). R^2 = 0.89. IC_{50}: 73.7 mM, 95% CI [53.0-160.3].

*8.3.1.41. phenyl-4-O-methyl-β-D-glucopyranoside (C_4 OMe Ph-Glc, **110**)*

Table 8-63. Raw data for the plot of normalized ice crystal growth (v_{norm}) in phosphate-buffered saline (PBS) as a function of C_4 OMe Ph-Glc (**110**) concentration (in mM). Data presented as a mean and standard deviation of n=3 ice wafers.

[110] (mM)	Log[110] (mM)	v_{norm} (%)	Standard Deviation (%)
0.50	-0.30	87.0	5.16
1	0.00	94.2	10.0
2.5	0.40	29.6	11.4
5	0.70	0.00	0.00
20	1.30	0.00	0.00

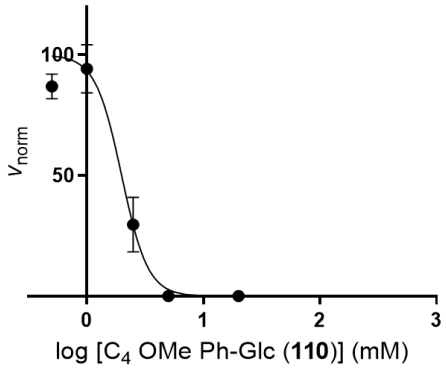


Figure 8-55. Plot of normalized ice crystal growth (v_{norm}) in phosphate-buffered saline (PBS) against C_4 OMe Ph-Glc (**110**) concentration (in mM). $R^2 = 0.98$. IC_{50}: 1.99 mM, 95% CI [1.40-2.56].

*8.3.1.42. (3-cyanophenyl)-4-O-methyl-β-D-glucopyranoside (C_4 OMe mCNPh-Glc, **111**)*

Table 8-64. Raw data for the plot of normalized ice crystal growth (v_{norm}) in phosphate-buffered saline (PBS) as a function of C_4 OMe *m*CNPh-Glc (**111**) concentration (in mM). Data presented as a mean and standard deviation of n=3 ice wafers.

[111] (mM)	Log[111] (mM)	v_{norm} (%)	Standard Deviation (%)
0.1	-1.00	101.4	6.03
0.5	-0.30	103.1	7.29
0.75	-0.12	80.2	8.35
1	0.00	2.96	2.84
2.5	0.40	0.00	0.00
5	0.70	0.00	0.00

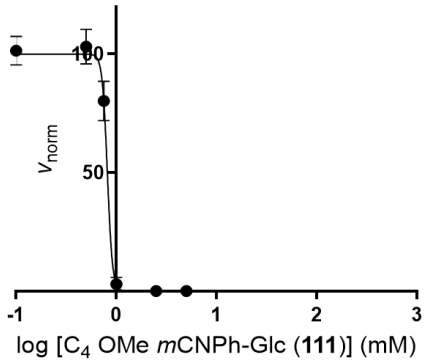


Figure 8-56. Plot of normalized ice crystal growth (v_{norm}) in phosphate-buffered saline (PBS) against C_4 OMe *m*CNPh-Glc (**111**) concentration (in mM). $R^2 = 0.99$. IC_{50}: 0.81 mM, 95% CI [0.78-0.84].

*8.3.1.43. 4-O-methyl-D-glucose (C_4 OMe Glc, **112**)*

Table 8-65. Raw data for the plot of normalized ice crystal growth (v_{norm}) in phosphate-buffered saline (PBS) as a function of C_4 OMe Glc (**112**) concentration (in mM). Data reported as a mean and standard deviation of n=3 ice wafers.

[112] (mM)	Log[112] (mM)	v_{norm} (%)	Standard Deviation (%)
1	0.00	99.7	13.4
7.5	0.88	97.8	13.6
15	1.18	100.6	2.21
50	1.70	77.9	12.6
75	1.88	49.5	9.69
100	2.00	32.7	11.8

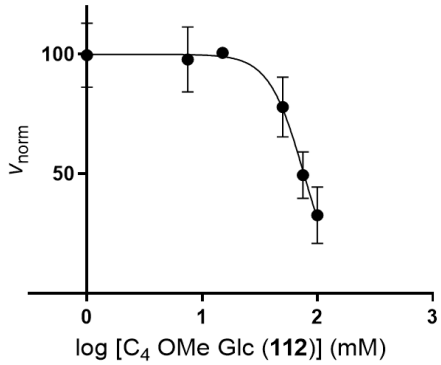


Figure 8-57. Plot of normalized ice crystal growth (v_{norm}) in phosphate-buffered saline (PBS) against C_4 OMe Glc (**112**) concentration (in mM). $R^2 = 0.99$. IC_{50}: 76.2 mM, 95% CI [72.9-79.7].

*8.3.1.44. N-3-fluorophenyl-D-gluconamide (3FA, **113**)*

Table 8-66. Raw data for the plot of normalized ice crystal growth (v_{norm}) in phosphate-buffered saline (PBS) as a function of 3FA (**113**) concentration (in mM). Data reported as a mean and standard deviation of n=3 ice wafers.

[113] (mM)	Log[113] (mM)	v_{norm} (%)	Standard Deviation (%)
5	0.70	95.6	6.05
10	1.00	59.7	12.7
15	1.18	0.18	0.31

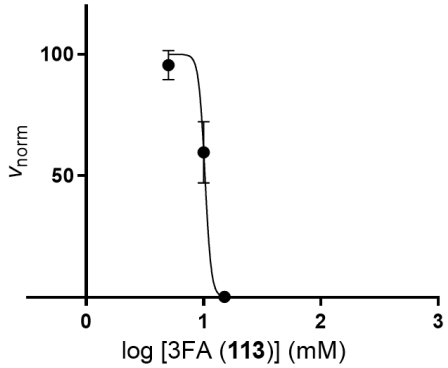


Figure 8-58. Plot of normalized ice crystal growth (v_{norm}) in phosphate-buffered saline (PBS) against 3FA (**113**) concentration (in mM). $R^2 = 0.99$. IC_{50}: 10.3 mM, 95% CI [5.26-14.5].

*8.3.1.45. N-4-chlorophenyl-D-gluconamide (4ClA, **114**)*

Table 8-67. Raw data for the plot of normalized ice crystal growth (v_{norm}) in phosphate-buffered saline (PBS) as a function of 4ClA (**114**) concentration (in mM). Data reported as a mean and standard deviation of n=3 ice wafers.

[114] (mM)	Log[114] (mM)	v_{norm} (%)	Standard Deviation (%)
1	0.00	104.8	8.56
8.5	0.93	94.5	1.31
10	1.00	54.7	10.3
12	1.08	42.1	5.05

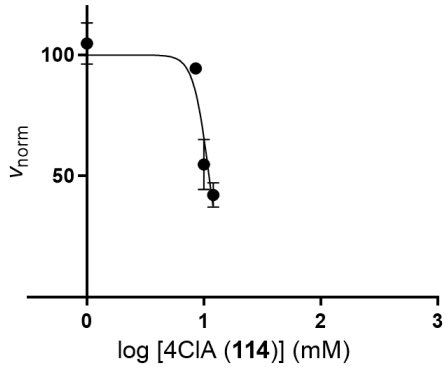


Figure 8-59. Plot of normalized ice crystal growth (v_{norm}) in phosphate-buffered saline (PBS) against 4ClA (**114**) concentration (in mM). $R^2 = 0.90$. IC_{50}: 11.1 mM, 95% CI [9.40-∞].

8.3.1.46. Ammonium C-(1-deoxy-β-D-glucopyranosyl) methanephosphonate (G1CP-NH_4, ***115****)*

Previously reported data for the ice recrystallization inhibition activity of (G1CP-NH_4, **115***) by Dr. Anna Ampaw (2019)*[177]

Table 8-68. Raw data for the plot of normalized ice crystal growth (v_{norm}) in phosphate-buffered saline (PBS) as a function of G1CP-NH_4 (**115**) concentration (in mM) as reported by Dr. Anna Ampaw (2022).[177] Data reported as a mean and standard deviation of n=3 ice wafers.

[115] (mM)	Log[115] (mM)	v_{norm} (%)	Standard Deviation (%)
0.5	-0.30	102.3	3.90
1	0.00	82.9	11.4
2	0.30	73.0	6.92
5	0.70	14.9	10.6
7	0.85	3.64	3.95
10	1.00	1.04	1.80
14	1.15	0.00	0.00

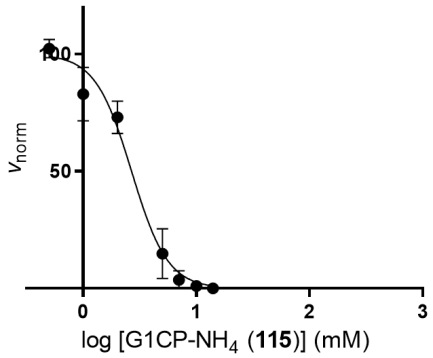


Figure 8-60. Plot of normalized ice crystal growth (v_{norm}) in phosphate-buffered saline (PBS) against G1CP-NH_4 (**115**) concentration (in mM) as reported by Dr. Anna Ampaw (2022).[177] R^2 = 0.99. IC_{50}: 2.67 mM, 95% CI [2.19-3.26].

8.3.2. Cytotoxicity Curves (LD_{50})

*8.3.2.1. (4-bromophenyl)-β-D-glucopyranoside (pBrPh-Glc, **25**) and 4-bromophenol*

Table 8-69. Raw data for the plot of cytotoxicity (resazurin-based assay) as a function of *p*BrPh-Glc (**25**) concentration (in mM). Data reported as a mean and standard deviation.

Incubation Time (hours)	+ 10 % DMSO	[25] (mM)	Log[25] (mM)	Cell Viability (%)	Standard Deviation (%)	Number of Biological Replicates
1	Yes	0		93.4	9.21	8
		0.9	-0.05	76.4	16.5	3
		4.5	0.65	74.3	16.3	2
		9	0.95	74.2	26.6	2
		10.8	1.03	72.7	22.6	2
		13.5	1.13	68.8	25.7	2
		16.2	1.21	67.3	22.6	2
		19.8	1.30	56.0	16.8	3
		27	1.43	39.0	15.0	3
		30	1.48	50.6	10.6	2
		36	1.56	13.8	14.4	2
		40.5	1.61	1.40	0.00	1
24	Yes	0		38.3	15.9	7
		0.9	-0.05	26.6	11.8	3
		4.5	0.65	6.29	6.65	2
		9	0.95	11.9	12.0	2
		10.8	1.03	-0.34	0.93	2
		13.5	1.13	0.66	2.08	2
		16.2	1.21	-0.86	0.35	2
		19.8	1.30	-1.11	0.34	3
		27	1.43	-1.09	0.23	3
		30	1.48	-1.33	0.68	2
		36	1.56	-1.03	0.21	2
		40.5	1.61	-1.22	0.00	1

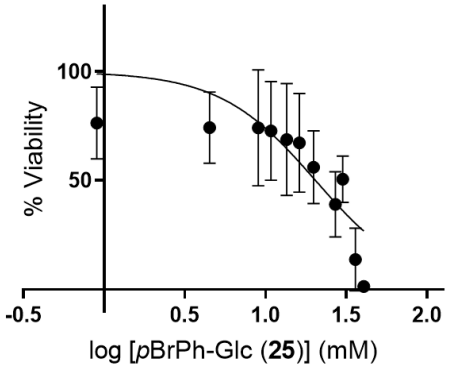


Figure 8-61. Plot of percent cell viability as measured by resazurin-based cytotoxicity assay in phosphate-buffered saline (PBS) against *p*BrPh-Glc (**25**) concentration (in mM) following a 1-hour incubation. Determined by resazurin-based cytotoxicity assay. $R^2 = 0.46$. LD_{50}: 20.4 mM, 95% CI [14.1-29.9].

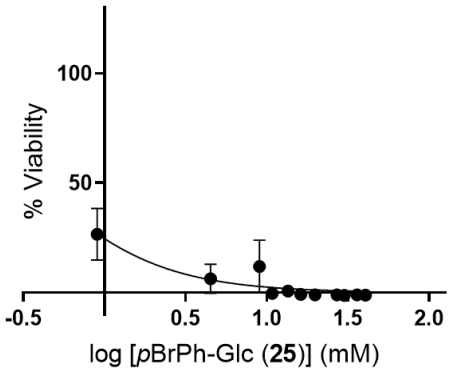


Figure 8-62. Plot of percent cell viability as measured by resazurin-based cytotoxicity assay in phosphate-buffered saline (PBS) against *p*BrPh-Glc (**25**) concentration (in mM) following a 24-hour incubation. Determined by resazurin-based cytotoxicity assay. $R^2 = 0.72$. LD_{50}: NA, Maximum % Viability = 26.6 ± 11.8 %.

Table 8-70. Raw data for the plot of cytotoxicity (resazurin-based assay) as a function of *p*BrPh-Glc (**25**) concentration (in mM). Data reported as a mean and standard deviation.

Incubation Time (hours)	+ 10 % DMSO	[25] (mM)	Log[25] (mM)	Cell Viability (%)	Standard Deviation (%)	Number of Biological Replicates
1	No	1	0.00	97.5	6.15	3
		5	0.70	88.5	8.37	2
		10	1.00	79.3	7.71	2
		12	1.08	74.7	0.47	3
		15	1.18	71.2	8.13	3
		18	1.26	59.2	3.58	2
		22	1.34	19.2	10.9	2
		30	1.48	-2.31	1.31	2
		33.3	1.52	-1.55	0.73	2
		40	1.60	-2.10	1.22	2
24	No	1	0.00	108.5	14.6	3
		5	0.70	61.6	11.8	2
		10	1.00	33.5	21.0	2
		12	1.08	4.90	7.39	2
		15	1.18	-1.32	1.19	2
		18	1.26	-1.47	0.15	2
		22	1.34	-1.89	0.62	3
		30	1.48	-1.76	0.41	3
		33.3	1.52	-1.61	0.43	2
		40	1.60	-1.49	0.23	2

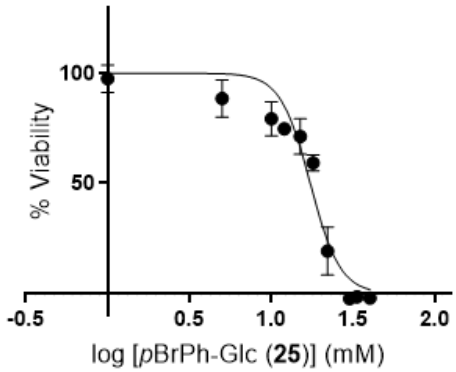


Figure 8-63. Plot of percent cell viability as measured by resazurin-based cytotoxicity assay in phosphate-buffered saline (PBS) against *p*BrPh-Glc (**25**) concentration (in mM) following a 1-hour incubation. Determined by resazurin-based cytotoxicity assay. $R^2 = 0.94$. LD_{50}: 17.3 mM, 95% CI [15.8-18.6].

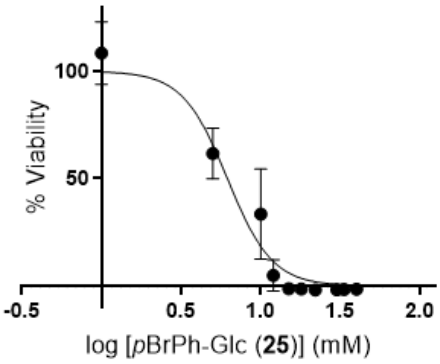


Figure 8-64. Plot of percent cell viability as measured by resazurin-based cytotoxicity assay in phosphate-buffered saline (PBS) against *p*BrPh-Glc (**25**) concentration (in mM) following a 24-hour incubation. Determined by resazurin-based cytotoxicity assay. $R^2 = 0.94$. LD_{50}: 6.17 mM, 95% CI [5.12-7.32].

Table 8-71. Raw data for the plot of cytotoxicity (resazurin-based assay) as a function of 4-bromophenol concentration (in mM). Data reported as a mean and standard deviation.

Incubation Time (hours)	+ 10 % DMSO	[4-bromophenol] (mM)	Log[4-bromophenol] (mM)	Cell Viability (%)	Standard Deviation (%)	Number of Biological Replicates
		0		93.4	9.21	8
		0.5	-0.30	97.0	0.00	1
		0.9	-0.05	95.9	0.00	1
		2	0.30	100.1	0.00	1
		4	0.60	77.3	0.00	1
		4.5	0.65	71.8	0.00	1
		6	0.78	11.0	0.00	1
		7	0.85	-0.51	0.00	1
1	Yes	8	0.90	-1.48	0.00	1
		10	1.00	-1.79	0.00	1
		10.8	1.03	-2.39	0.00	1
		15	1.18	-2.16	0.00	1
		16.2	1.21	-3.06	0.00	1
		19.8	1.30	-3.44	0.00	1
		27	1.43	-4.04	0.00	1
		30	1.48	-4.25	0.00	1
		36	1.56	-4.73	0.00	1
		0		38.3	15.9	7
		0.5	-0.30	97.8	0.00	1
		2	0.30	14.7	0.00	1
		4	0.60	-1.29	0.00	1
24	Yes	6	0.78	-1.33	0.00	1
		7	0.85	-1.52	0.00	1
		8	0.90	-1.69	0.00	1
		10	1.00	-2.04	0.00	1
		15	1.18	-2.74	0.00	1

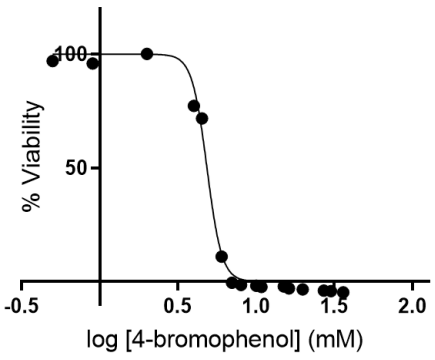


Figure 8-65. Plot of percent cell viability as measured by resazurin-based cytotoxicity assay in phosphate-buffered saline (PBS) against 4-bromophenol concentration (in mM) following a 1-hour incubation. Determined by resazurin-based cytotoxicity assay. $R^2 = 0.99$. LD_{50}: 4.84 mM, 95% CI [4.68-5.02].

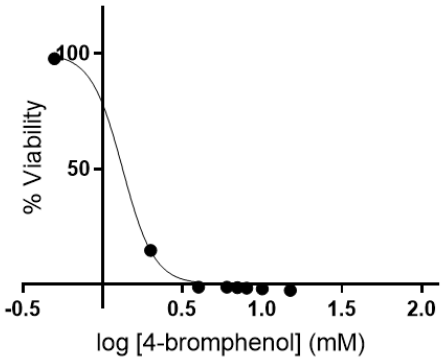


Figure 8-66. Plot of percent cell viability as measured by resazurin-based cytotoxicity assay in phosphate-buffered saline (PBS) against 4-bromophenol concentration (in mM) following a 24-hour incubation. Determined by resazurin-based cytotoxicity assay. $R^2 = 0.99$. LD_{50}: 1.34 mM, 95% CI [1.12-∞].

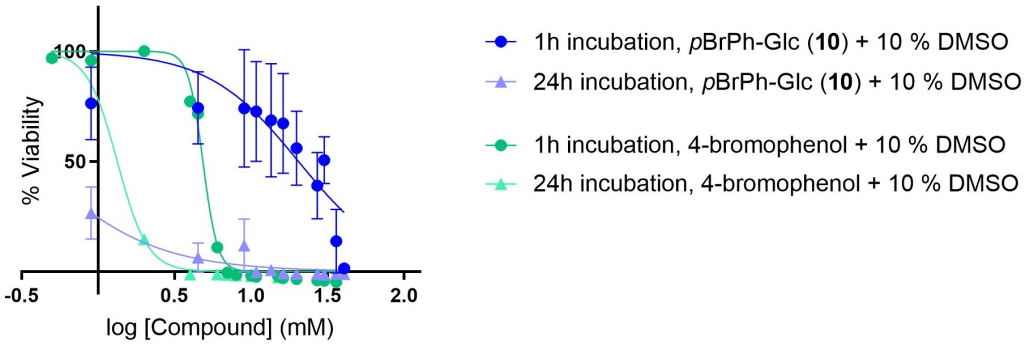


Figure 8-67. Plot of percent cell viability as measured by resazurin-based cytotoxicity assay in phosphate-buffered saline (PBS) with 10 % DMSO against *p*BrPh-Glc (**25**) and 4-bromophenol concentration (in mM). Determined by resazurin-based cytotoxicity assay.

*8.3.2.2. N-2-fluorophenyl-D-gluconamide (2FA, **27**)*

Table 8-72. Raw data for the plot of cytotoxicity (resazurin-based assay) as a function of 2FA (**27**) concentration (in mM). Data reported as a mean and standard deviation.

Incubation Time (hours)	+ 10 % DMSO	[27] (mM)	Log[27] (mM)	Cell Viability (%)	Standard Deviation (%)	Number of Biological Replicates
		0		93.4	9.21	8
		0.9	-0.05	85.6	9.44	3
		2.25	0.35	90.6	7.38	3
		4.5	0.65	89.0	8.76	3
1	Yes	6.75	0.83	92.5	5.35	3
		9	0.95	80.6	9.00	3
		11.25	1.05	82.2	7.17	2
		13.5	1.13	72.2	10.0	2
		15	1.18	79.8	1.52	2
		0		38.3	15.9	7
		0.9	-0.05	31.7	12.2	3
		2.25	0.35	38.3	13.7	3
		4.5	0.65	35.7	12.9	3
24	Yes	6.75	0.83	26.5	29.3	2
		9	0.95	33.1	19.4	3
		11.25	1.05	26.2	27.7	2
		13.5	1.13	31.4	20.9	3
		15	1.18	33.3	5.27	2

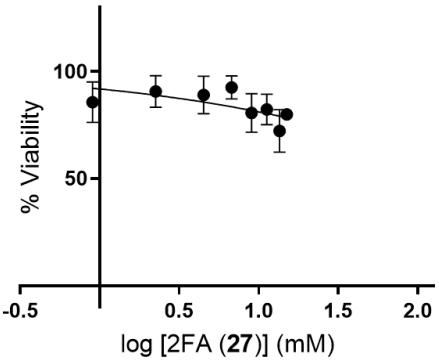


Figure 8-68. Plot of percent cell viability as measured by resazurin-based cytotoxicity assay in phosphate-buffered saline (PBS) against 2FA (**27**) concentration (in mM) following a 1-hour incubation. Determined by resazurin-based cytotoxicity assay. $R^2 = 0.21$. LD_{50}: NA, Minimum % Viability = 72.2 ± 10.0 %.

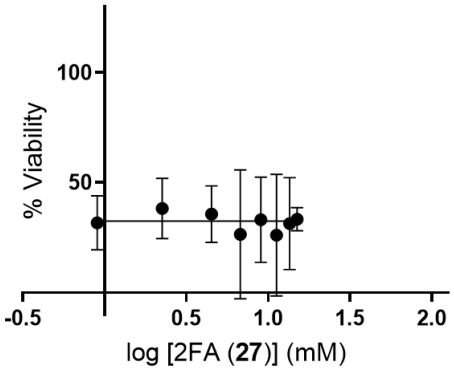


Figure 8-69. Plot of percent cell viability as measured by resazurin-based cytotoxicity assay in phosphate-buffered saline (PBS) against 2FA (**27**) concentration (in mM) following a 24-hour incubation. Determined by resazurin-based cytotoxicity assay.

Table 8-73. Raw data for the plot of cytotoxicity (resazurin-based assay) as a function of 2FA (**27**) concentration (in mM). Data reported as a mean and standard deviation.

Incubation Time (hours)	+ 10 % DMSO	[27] (mM)	Log[27] (mM)	Cell Viability (%)	Standard Deviation (%)	Number of Biological Replicates
1	No	1	0.00	99.8	4.59	3
		2.5	0.40	91.3	5.07	3
		5	0.70	84.3	5.00	3
		7.5	0.88	78.3	4.45	3
		10	1.00	71.8	6.05	3
		12.5	1.10	71.9	3.36	2
		15	1.18	73.5	5.95	3
24	No	0.5	-0.30	94.3	6.36	2
		1	0.00	95. 7	2.02	3
		2.5	0.40	88.3	6.08	3
		5	0.70	80.5	7.81	3
		7.5	0.88	72.8	9.14	3
		10	1.00	62.2	12.2	3
		12.5	1.10	61.0	15.1	2
		15	1.18	72.5	6.70	2

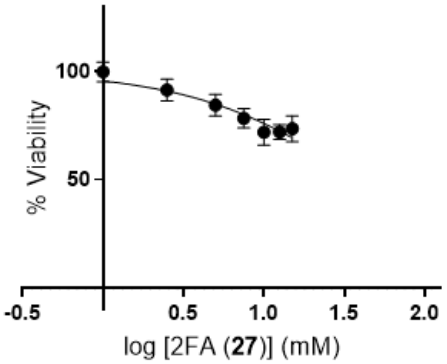


Figure 8-70. Plot of percent cell viability as measured by resazurin-based cytotoxicity assay in phosphate-buffered saline (PBS) against 2FA (**27**) concentration (in mM) following a 1-hour incubation. Determined by resazurin-based cytotoxicity assay. $R^2 = 0.78$. LD_{50}: NA, Minimum % Viability = 73.5 ± 5.9 %.

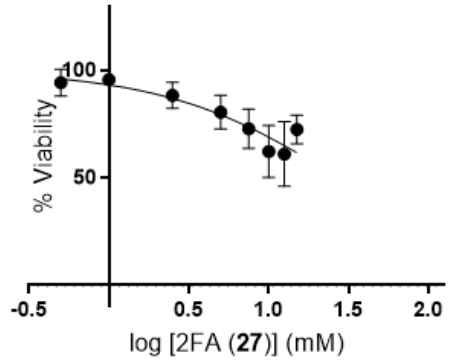


Figure 8-71. Plot of percent cell viability as measured by resazurin-based cytotoxicity assay in phosphate-buffered saline (PBS) against 2FA (**27**) concentration (in mM) following a 24-hour incubation. Determined by resazurin-based cytotoxicity assay. $R^2 = 0.94$. LD_{50}: NA, Minimum % Viability = 72.5 ± 6.7 %.

8.3.2.3. (cyanophenyl)-β-D-glucopyranosides and N-cyanophenyl-D-gluconamides

Table 8-74. Raw data for the plot of cytotoxicity (resazurin-based assay) as a function of *p*CNPh-Glc (**30**) concentration (in mM) following a 24-hour incubation. Data reported as a mean and standard deviation of N=1 biological replicates.

[30] (mM)	Log[30] (mM)	Viability (%)	Standard Deviation (%)
5	0.70	101.6	6.26
15	1.18	74.6	5.24
30	1.48	48.6	4.85
60	1.78	8.74	2.92

Table 8-75. Raw data for the plot of cytotoxicity (resazurin-based assay) as a function of *m*CNPh-Glc (**37**) concentration (in mM) following a 24-hour incubation. Data reported as a mean and standard deviation of N=4 biological replicates.

[37] (mM)	Log[37] (mM)	Viability (%)	Standard Deviation (%)
5	0.70	105.5	9.17
15	1.18	86.2	8.76
30	1.48	60.9	13.1
60	1.78	12.3	1.11

Table 8-76. Raw data for the plot of cytotoxicity (resazurin-based assay) as a function of *o*CNPh-Glc (**38**) concentration (in mM) following a 24-hour incubation. Data reported as a mean and standard deviation of N=1 biological replicates.

[38] (mM)	Log[38] (mM)	Viability (%)	Standard Deviation (%)
5	0.70	102.1	5.52
15	1.18	81.1	6.05
40	1.60	40.9	4.36
75	1.88	5.54	1.67

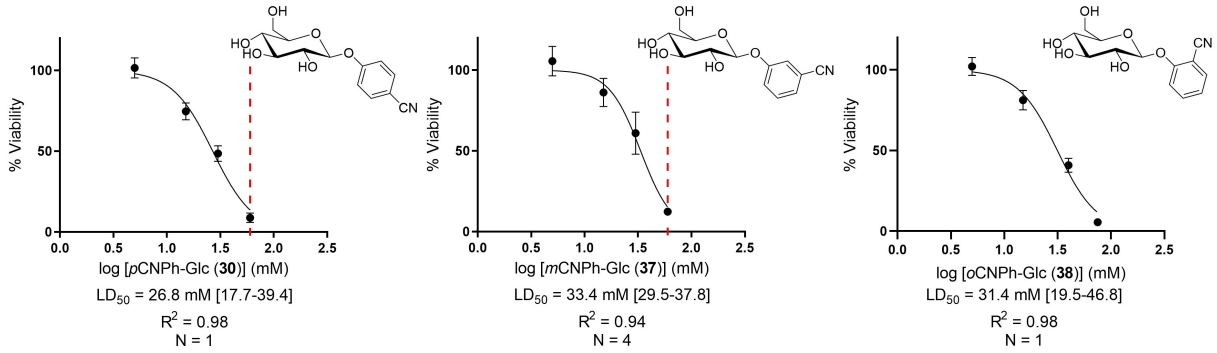


Figure 8-72. Plot of percent cell viability as measured by resazurin-based cytotoxicity assay in phosphate-buffered saline (PBS) against compound (**30**, **37**-**38**) concentration (in mM) following a 24-hour incubation. Red lines denote the maximum solubility of the compound in the appropriate cell culture media (maximum heating to 37 °C).

Table 8-77. Raw data for the plot of cytotoxicity (resazurin-based assay) as a function of *m*CNA (**40**) concentration (in mM) following a 24-hour incubation. Data reported as a mean and standard deviation of N=1 biological replicates.

[40] (mM)	Log[40] (mM)	Viability (%)	Standard Deviation (%)
5	0.70	80.7	8.10
15	1.18	52.7	7.26
22	1.34	44.0	6.20
30	1.48	37.1	3.99
40	1.60	23.8	2.15

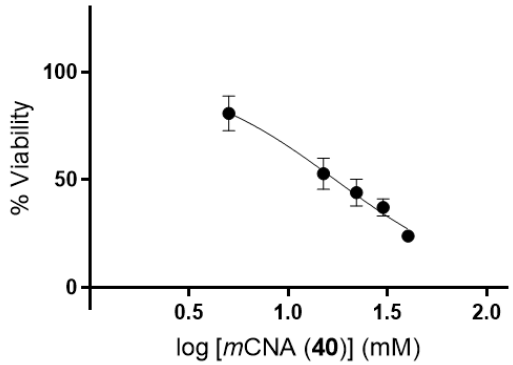


Figure 8-73. Plot of percent cell viability as measured by resazurin-based cytotoxicity assay in phosphate-buffered saline (PBS) against *m*CNA (**40**) concentration (in mM) following a 24-hour incubation. Determined by resazurin-based cytotoxicity assay. $R^2 = 0.99$. LD_{50}: 17.1 mM, 95% CI [14.5-20.0].

mCNPh Time dependent data Resazurin

Table 8-78. Raw data for the plot of cytotoxicity (resazurin-based assay) as a function of *m*CNPh-Glc (**37**) concentration (in mM) following different incubation times. Data reported as a mean and standard deviation.

Incubation Time (h)	[37] (mM)	Log[37] (mM)	Viability (%)	Standard Deviation (%)	Biological Replicates (N=)
1	5	0.70	95.3	4.39	1
	15	1.18	75.2	5.16	1
	22	1.34	63.8	10.1	1
	30	1.48	59.3	2.93	1
	45	1.65	46.2	5.77	1
	60	1.78	48.3	6.20	1
3	5	0.70	95.3	14.8	1
	15	1.18	79.3	6.22	1
	22	1.34	61.4	10.5	1
	30	1.48	55.0	11.0	1
	45	1.65	49.1	8.50	1
	60	1.78	42.2	7.22	1
5.5	5	0.70	89.8	2.46	2
	15	1.18	79.1	5.75	2
	22	1.34	65.6	21.8	2
	30	1.48	63.6	16.8	3
	45	1.65	57.9	20.1	2
	60	1.78	46.5	25.0	2

mCNPh Time dependent data LDH

Table 8-79. Raw data for the plot of cytotoxicity (lactate dehydrogenase assay) as a function of *m*CNPh-Glc (**37**) concentration (in mM) following different incubation times. Data reported as a mean and standard deviation.

Incubation Time (h)	[37] (mM)	Log[37] (mM)	Viability (%)	Standard Deviation (%)	Biological Replicates (N=)
1	5	0.70	99.4	0.21	2
	15	1.18	96.0	6.55	2
	22	1.34	91.7	10.1	2
	30	1.48	95.7	6.87	2
	45	1.65	96.8	4.35	2
	60	1.78	90.3	11.3	2
3	5	0.70	100.8		1
	15	1.18	90.3		1
	22	1.34	86.8		1
	30	1.48	70.5		1
	45	1.65	98.4		1
	60	1.78	83.6		1
5.5	5	0.70	92.0	14.5	2
	15	1.18	93.5	7.88	2
	22	1.34	94.5	7.49	2
	30	1.48	92.6	14.5	3
	45	1.65	98.9	0.96	2
	60	1.78	95.2	1.39	2
24	5	0.70	94.1	11.7	2
	15	1.18	94.0	1.73	2
	22	1.34	90.3	19.7	2
	30	1.48	110.5		1
	45	1.65	90.1	2.53	2
	60	1.78	59.3	1.86	2

*8.3.2.4. (2-carbamoylphenyl)-β-D-glucopyranoside (oAmPh-Glc, **43**) and N-2-(carbamoylphenyl-D-gluconamide) (oAmA, **46**)*

Table 8-80. Raw data for the plot of cytotoxicity (resazurin-based assay) as a function of *o*AmPh-Glc (**43**) concentration (in mM) following a 24-hour incubation. Data reported as a mean and standard deviation of N=1 biological replicates.

[43] (mM)	Log[43] (mM)	Viability (%)	Standard Deviation (%)
1	0.00	94.5	9.40
10	1.00	85.7	12.2
25	1.40	78.5	14.2
50	1.70	55.2	9.58
70	1.85	39.0	5.48
90	1.95	69.4	4.53

Table 8-81. Raw data for the plot of cytotoxicity (resazurin-based assay) as a function of *o*AmA (**46**) concentration (in mM) following a 24-hour incubation. Data reported as a mean and standard deviation of N=1 biological replicates.

[46] (mM)	Log[46] (mM)	Viability (%)	Standard Deviation (%)
1	0.00	97.2	12.4
10	1.00	69.9	6.56
25	1.40	57.7	7.87
50	1.70	34.4	5.63
75	1.87	27.9	3.55
100	2.00	22.5	6.15

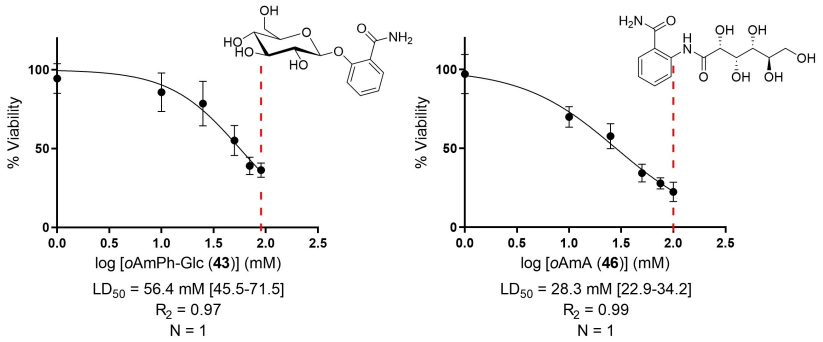


Figure 8-74. Plot of percent cell viability as measured by resazurin-based cytotoxicity assay in phosphate-buffered saline (PBS) against *o*AmPh-Glc (**43**) and *o*AmA (**46**) concentration (in mM) following a 24-hour incubation. Red lines denote the maximum solubility of the compound in the appropriate cell culture media (maximum heating to 37 °C).

8.3.3. MSC Cell Data

8.3.3.1. BM-MSC Donor Information

All MSC studies were performed on cells at passage 3 and none of the cells had gone through more than 20 doublings at the time of analysis.

Table 8-82. Donor information from the ENACT-AMI clinical trial (NCT00936819) at the Ottawa Hospital Research Institute. Infectious disease panel included Hep B, Hep C, HIV, CMV, EBV, and HTLV1/2.

Donor	Sex	Age	Ethnicity	Health Status	Infectious Disease Testing *
1	Male	27	Caucasian	Healthy	Negative
2	Male	23	Caucasian	Healthy	Negative
3	Male	23	Caucasian	Healthy	Negative

8.3.3.2. BM-MSC Donor 1

All data for donor 1 collected, analyzed, and reported by Dr. Jessica Poisson (PhD, 2019) and our collaborators at the Ottawa Hospital Research Institute under the supervision of Dr. David Courtman.[214]

Table 8-83. Numerical data for **Figure 2-5**, **Figure 2-6**, and **Figure 2-7**. Standard freezing medium (SFM) 10 % DMSO + 5 % HA in PLA. Results mean ± standard error of the mean (SEM), n=1 SFM, n=3 *p*BrPh-Glc (**25**) and 2FA (**27**).

		SFM	**SFM + 30 mM *p*BrPh-Glc (25)**	**SFM + 15 mM 2FA (27)**
Immediately Post-Thaw	Cell Viability, Trypan Blue (%)	92.5	87.6 ± 0.8	90.9 ± 0.9
	Cell Viability, (AV-/PI-) (%)	82.3	82.0 ± 4.2	91.7 ± 0.6
	Cell Recovery (%)	80.0	73.3 ± 6.7	91.3 ± 0.7
	Proliferation (% in S-phase) [a]	6.9	5.6 ± 0.5	23.6 ± 1.9
Three-Days Post-Thaw	Cell Viability, Trypan Blue (%)	92.8	89.1 ± 1.6	95.3 ± 0.6
	Cell Viability, (AV-/PI-) (%)	91.5	94.5 ± 0.07	93.2 ± 1.2
	Cell Yield (% change from seeding)	260.0	233.0 ± 32.0	654.0 ± 134.0
	Population Doubling	1.4	1.2 ± 0.1	2.7 ± 0.3
	Doubling Time (h)	52.2	59.7 ± 5.3	27.4 ± 3.6

[a] Proliferation measured two-days post-thaw

[b] Data collected, analyzed, and reported by Dr. Jessica Poisson (PhD, 2019) and our collaborators at the Ottawa Hospital Research Institute under the supervision of Dr. David Courtman.[214]

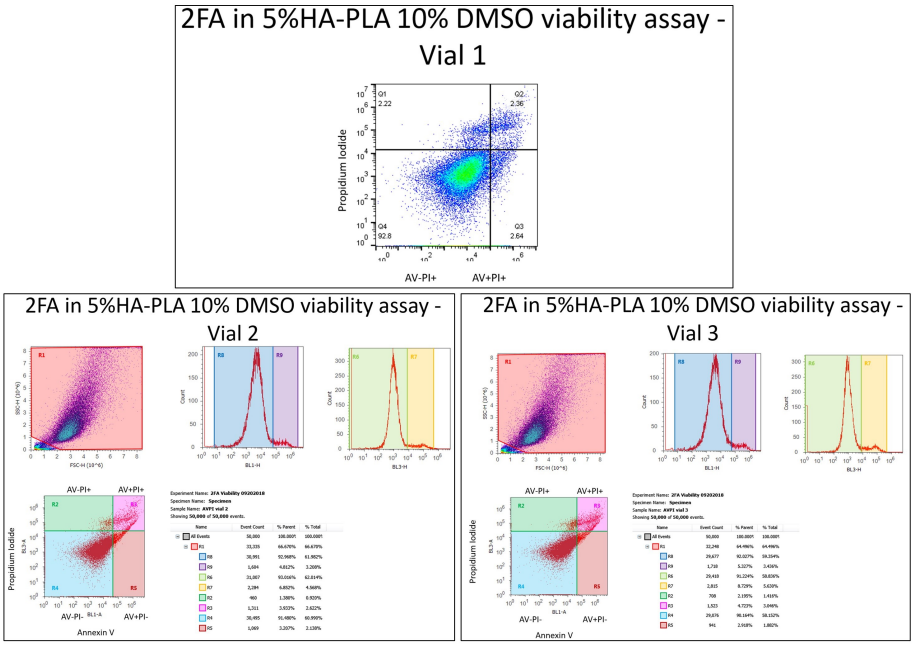


Figure 8-75. Representative density plots and histograms for the AV/PI viability assay immediately post thaw of cells isolated from donor 1 cryopreserved in standard freezing medium (SFM) 10 % DMSO + 5 % HA in PLA with the addition of 2FA (**27**, 15 mM).

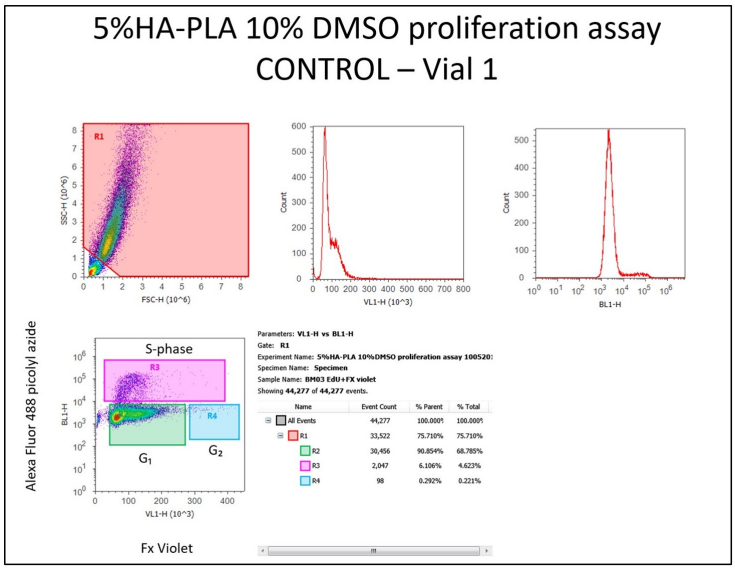


Figure 8-76. Representative density plots and histograms for the EdU proliferation assay of cells isolated from donor 1 cryopreserved in standard freezing medium (SFM) 10 % DMSO + 5 % HA in PLA (control solution).

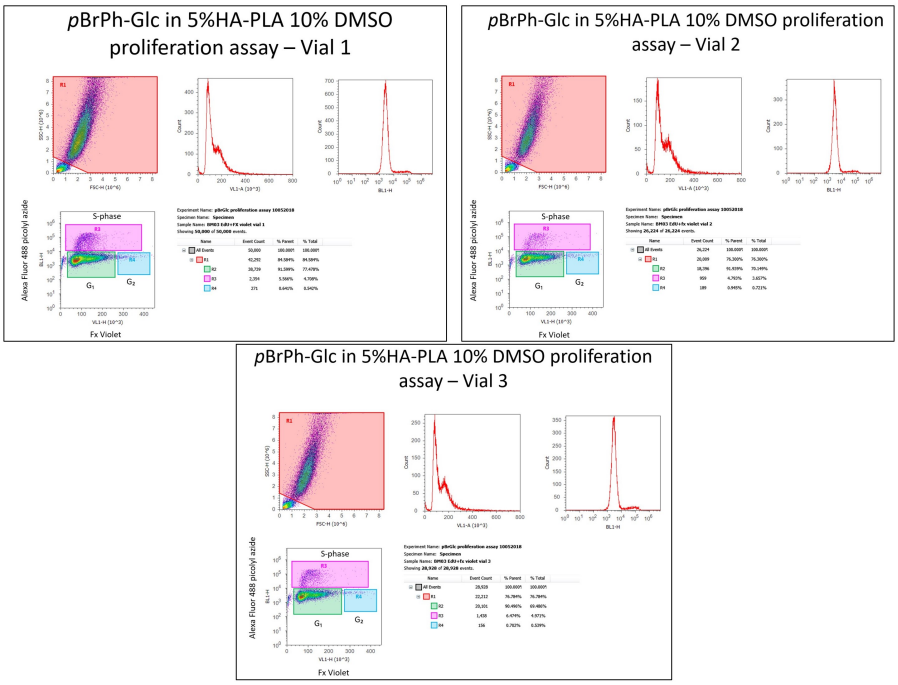


Figure 8-77. Representative density plots and histograms for the EdU proliferation assay of cells isolated from donor 1 cryopreserved in standard freezing medium (SFM) 10 % DMSO + 5 % HA in PLA with the addition of *p*BrPh-Glc (**25**, 30 mM).

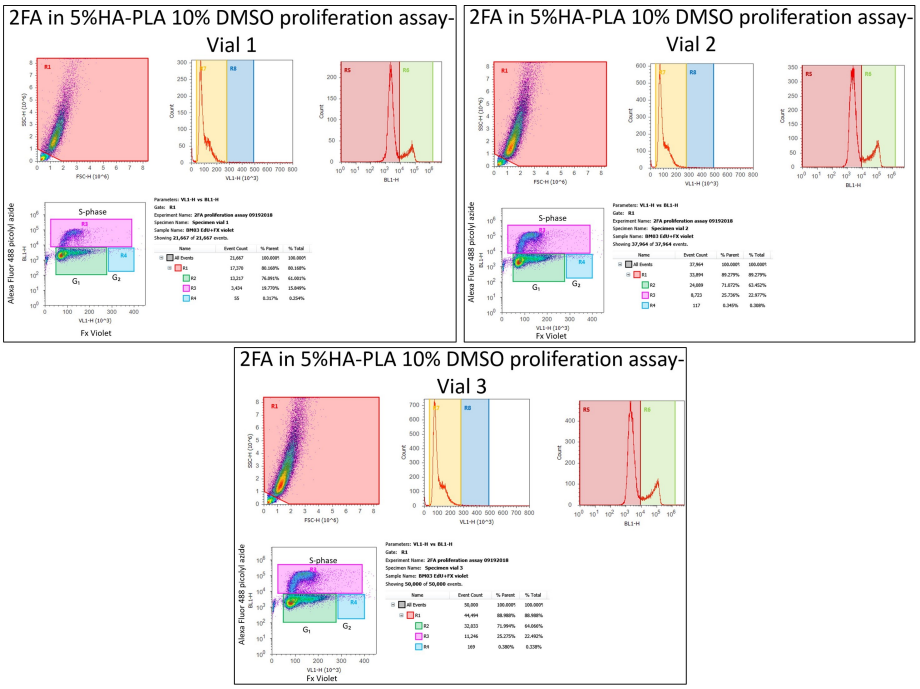


Figure 8-78. Representative density plots and histograms for the EdU proliferation assay of cells isolated from donor 1 cryopreserved in standard freezing medium (SFM) 10 % DMSO + 5 % HA in PLA with the addition of 2FA (**27**, 15 mM).

8.3.3.3. BM-MSC Donor 2 and 3

Table 8-84. Results for donor 2 immediately post-thaw. Standard freezing medium (SFM) 10 % DMSO + 5 % HA in PLA. Results mean ± standard deviation (SD), n≥3 for all conditions.

	Standard Freezing Medium (SFM)	**SFM + 30 mM *p*BrPh-Glc (25)**	**SFM + 15 mM 2FA (27)**
Cell Viability, Trypan Blue (%)	94.6 ± 2.8	77.7 ± 10.7	95.9 ± 1.7
Cell Viability, (AV-/PI-) (%)	86.0 ± 6.7	7.9 ± 7.2	91.3 ± 5.9
Cell Recovery (%)	84.4 ± 13.4	80.1 ± 10.3	96.0 ± 19.5
Proliferation (% in S-phase) [a]	16.9 ± 9.0	n.d. [b]	46.1 ± 12.1

[a] Proliferation measured two days post-thaw

[b] n.d. no data as an insufficient quantity of cells was recovered after two days in culture

[c] Data collected, analyzed, and reported by our collaborators at the Ottawa Hospital Research Institute under the supervision of Dr. David Courtman.

Table 8-85. Results for donor 2 three-days post-thaw. Standard freezing medium (SFM) 10 % DMSO + 5 % HA in PLA. Results mean ± standard deviation (SD), n≥3, for samples that did not double in population, a doubling time was not calculated. Data for cells cryopreserved with **25** (30 mM) was omitted due to an insufficient quantity of viable cells.

Seeding Density		**Standard Freezing Medium (SFM)**	**SFM + 15 mM 2FA (27)**
0.25×10^6 cells/mL	Cell Viability, Trypan Blue (%)	91.7 ± 3.7	80.5 ± 25.9
	Cell Yield (% change from seeding)	109.3 ± 56.2	297.33 ± 72.6
	Population Doublings	-0.010 ± 0.797	1.547 ± 0.338
	Doubling Time (h)	96.2 (n=1)	48.0 ± 9.5 (n=3)
0.10×10^6 cells/mL	Cell Viability, Trypan Blue (%)	77.9 ± 8.9	88.5 ± 4.5
	Cell Yield (% change from seeding)	69.3 ± 8.1	190.0 ± 55.7
	Population Doublings	-0.537 ± 0.166	0.887 ± 0.416
	Doubling Time (h)	NA	54.5 (n=1)
0.05×10^6 cells/mL	Cell Viability, Trypan Blue (%)	82.7 ± 11.7	81.6 ± 15.9
	Cell Yield (% change from seeding)	70.0 ± 36.7	172.0 ± 101.0
	Population Doublings	-0.637 ± 0.705	0.520 ± 1.179
	Doubling Time (h)	NA	60.0 ± 4.2 (n=2)

[a] NA indicates population did not double, a sample size less than three indicates that a proportion of the replicates did not achieve a population doubling

[b] Data collected, analyzed, and reported by our collaborators at the Ottawa Hospital Research Institute under the supervision of Dr. David Courtman.

Table 8-86. Results for donor 3 immediately post-thaw. Standard freezing medium (SFM) 10 % DMSO + 5 % HA in PLA. Results mean ± standard deviation (SD), n=4 for all conditions for cell viability as measured by Trypan Blue exclusion assay and cell recovery, n=1 for cell viability as measured by AV/PI.

	Standard Freezing Medium (SFM)	**SFM + 30 mM *p*BrPh-Glc (25)**	**SFM + 15 mM 2FA (27)**
Cell Viability, Trypan Blue (%)	93.9 ± 3.2	79.5 ± 11.5	94.4 ± 2.4
Cell Viability, (AV-/PI-) (%)	81.1 [a]	2.84 [a]	79.7 [a]
Cell Recovery (%)	76.0 ± 16.9	112.0 ± 15.6	116.3 ± 26.0

[a] Only one replicate obtained for this assay due to laboratory shutdowns caused by the COVID-19 pandemic
[b] Data collected, analyzed, and reported by our collaborators at the Ottawa Hospital Research Institute under the supervision of Dr. David Courtman.

Table 8-87. Results for donor 3 three-days post-thaw. Standard freezing me medium dia (SFM) 10 % DMSO + 5 % HA in PLA. Results mean ± standard deviation (SD), n=1. Data for cells cryopreserved with **25** (30 mM) was omitted due to an insufficient quantity of viable cells.

	Standard Freezing Medium (SFM)	**SFM + 15 mM 2FA (27)**
Cell Viability, Trypan Blue (%)	97.8	93.2
Cell Yield (% change from seeding)	112	152
Population Doublings	0.16	0.60
Doubling Time (h)	NA	NA

[a] Only one replicate obtained for this assay due to laboratory shutdowns caused by the COVID-19 pandemic
[b] Data collected, analyzed, and reported by our collaborators at the Ottawa Hospital Research Institute under the supervision of Dr. David Courtman.
[c] NA indicates population did not double

8.3.3.4. BM-MSC Pooled Data

Table 8-88. Pooled BM-MSC results immediately post-thaw. Standard freezing medium (SFM) 10 % DMSO + 5 % HA in PLA. Results mean ± standard deviation (SD). N=3 unless otherwise indicated.

	Standard Freezing Medium (SFM)	**SFM + 30 mM *p*BrPh-Glc (25)**	**SFM + 15 mM 2FA (27)**
Cell Viability, Trypan Blue (%)	93.7 ± 1.08	81.6 ± 5.27	93.7 ± 2.57
Cell Viability, (AV-/PI-) (%)	83.1 ± 2.54	30.9 ± 44.3	87.6 ± 6.82
Cell Recovery (%)	80.1 ± 4.22	88.5 ± 20.7	101.2 ± 13.3
Proliferation (% in S-phase) [a]	11.9 ± 7.10 (N=2)	5.60 (N=1)	34.9 ± 15.9 (N=2)

[a] Proliferation measured two days post-thaw
[b] Data collected, analyzed, and reported by our collaborators at the Ottawa Hospital Research Institute under the supervision of Dr. David Courtman.

Table 8-89. Pooled BM-MSC results three-days post-thaw. Standard freezing medium (SFM) 10 % DMSO + 5 % HA in PLA. Results mean ± standard deviation (SD), n≥3, for samples that did not double in population, a doubling time was not calculated. N=3 unless otherwise indicated.

	Standard Freezing Medium (SFM)	**SFM + 30 mM *p*BrPh-Glc (25)**	**SFM + 15 mM 2FA (27)**
Cell Viability, Trypan Blue (%)	94.1 ± 3.26	89.1 (N=1)	89.7 ± 7.99
Cell Yield (% change from seeding)	160.4 ± 86.2	233.0 (N=1)	367.8 ± 258.3
Population Doublings	0.52 ± 0.77	1.20 (N=1)	1.62 ± 1.05
Doubling Time (h)	74.2 ± 31.1 (N=2)	59.7 (N=1)	37.7 ± 14.5 (N=2)

[a] Proliferation measured two days post-thaw

[b] Data collected, analyzed, and reported by our collaborators at the Ottawa Hospital Research Institute under the supervision of Dr. David Courtman.

8.3.3.5. IDO expression

Table 8-90. Numerical data for **Figure 2-27**. Average cycle number to quantification (Cq) measured by RT-qPCR for control and 2FA (**27**) treated samples after 24-hour incubation. Results presented at the mean ± standard deviation for n=3 wells.

Sample/treatment	**24h control +IFN**		**24h control -IFN**	
Primers	**IDO**	**GAPDH**	**IDO**	**GAPDH**
Average Cq value	22.00 ± 0.51	18.43 ± 0.38	34.30 ± 0.65	17.50 ± 0.40
ΔΔCt	13.24			
Fold Change	9652.4			

Sample/treatment	**24h 2FA (27) +IFN**		**24h 2FA (27) -IFN**	
Primers	**IDO**	**GAPDH**	**IDO**	**GAPDH**
Average Cq value	20.68 ± 0.21	17.79 ± 0.21	33.71 ± 0.41	17.79 ± 0.21
ΔΔCt	13.46			
Fold Change	11268.4			

8.3.3.6. UC-MSCs

Table 8-91. Numerical data for **Figure 2-28.** Results for UC-MSCs seeded at 1.0 x 10^4 cells/cm^2. Standard freezing medium (SFM) 10 % DMSO + 5 % HA in PLA. Results mean ± standard deviation (SD), n=3 for viability measurements, n=1 for proliferation measurements, n=3 for cell yield measurements.

Assay	Time (h)	Standard Freezing Medium (SFM)	SFM + 15 mM 2FA (27)
Cell Viability, Trypan Blue (%)	0	96.1 ± 2.67	95.5 ± 2.62
	24	98.5 ± 0.20	99.4 ± 1.10
	48	99.5 ± 0.42	99.4 ± 0.42
	72	99.2 ± 0.12	98.8 ± 0.66
Proliferation (% in S-phase)	8	17.7	14.2
	16	18.1	30.5
	24	44.6	48.4
	36	47.9	48.1
Cell Yield (%)	0	73.7 ± 1.53	76.3 ± 5.86
	24	72.0 ± 6.56	75.3 ± 7.57
	48	164.0 ± 74.7	187.7 ± 33.3
	72	489.0 ± 242.0	607.3 ± 260.5

[a] Data collected, analyzed, and reported by our collaborators at the Ottawa Hospital Research Institute under the supervision of Dr. David Courtman.

Table 8-92. Numerical data for **Figure 2-28.** Results for UC-MSCs seeded at 2.0 x 10^4 cells/cm^2. Standard freezing medium (SFM) 10 % DMSO + 5 % HA in PLA. Results mean ± standard deviation (SD), n=3 for viability measurements, n=1 for proliferation measurements, n=3 for cell yield measurements.

Assay	Time (h)	Standard Freezing Medium (SFM)	SFM + 15 mM 2FA (27)
Cell Viability, Trypan Blue (%)	0	96.1 ± 2.67	95.5 ± 2.62
	24	98.9 ± 0.25	99.5 ± 0.40
	48	99.3 ± 0.06	99.1 ± 0.38
	72	98.7 ± 0.57	98.8 ± 0.62
Proliferation (% in S-phase)	8	18.0	16.2
	16	33.3	45.6
	24	47.6	48.3
	36	45.8	47.1
Cell Yield (%)	0	73.5 ± 1.50	76.4 ± 6.05
	24	73.8 ± 6.01	73.5 ± 10.4
	48	187.3 ± 50.9	212.8 ± 18.9
	72	462.3 ± 91.8	482.0 ± 75.1

[a] Data collected, analyzed, and reported by our collaborators at the Ottawa Hospital Research Institute under the supervision of Dr. David Courtman.

8.3.4. RBC Cryopreservation Data

Table 8-93. Numerical data for **Figure 3-2**. Measurement of the percentage of intact red blood cells post-thaw in the presence of *p*BrPh-Glc (**25**, 30 mM) and PMP-Glc (**26**, 110 mM) at reduced glycerol concentrations. RBCs were slow cooled (1 °C/min) to -40 °C and then rapidly cooled to the storage temperature of -80 °C prior to thawing (rapid) to 37 °C and measurement of hemolysis. Results presented as mean ± standard error of the mean (SEM). n=2 frozen RBC samples for each condition.

	Glycerol Alone	Glycerol + *p*BrPh-Glc (**25**) (30 mM)	Glycerol + PMP-Glc (**26**) (110 mM)
40 % Glycerol	98.3 ± 0.33	n.d.	n.d.
20 % Glycerol	82.9 ± 1.67	87.6 ± 1.34	n.d.
15 % Glycerol	25.7 ± 1.00	49.1 ± 1.67	69.6 ± 2.08
10 % Glycerol	9.95 ± 1.67	15.3 ± 1.00	22.9 ± 1.66
5 % Glycerol	3.57 ± 2.01	8.60 ± 0.67	n.d.

[a] n.d. indicates that a measurement was not made for this condition

Table 8-94. Numerical data for **Figure 3-5**. Percentage of intact red blood cells (RBCs) post-thaw using 15 % glycerol in combination with compound **30** (12.5 mM, 25 mM, or 40 mM) or compound **31** (2.5 mM, 20 mM, or 50 mM). Data reported as mean ± standard error of the mean (SEM), n=2 cryovials frozen from units pooled from three blood-type and sex-matched donors provided by NetCAD.

		% RBCs intact	
Compound	Concentration (mM)	Rate controlled (slow) freeze to -40 °C	Dump freeze (rapid) to -80 °C
Glycerol Alone	15 %	35.3 ± 1.51	90.2 ± 3.07
*p*CNPh-Glc (**30**)	+ 12.5 mM	31.1 ± 0.04	93.2 ± 2.26
	+ 25 mM	26.8 ± 3.96	93.5 ±1.56
	+ 40 mM	33.3 ± 1.99	81.4 ± 7.29
*p*AmPh-Glc (**31**)	+ 2.5 mM	40.6 ± 4.06	92.2 ± 2.40
	+ 20 mM	36.4 ± 2.00	94.5 ± 2.24
	+ 50 mM	35.3 ± 1.53	79.7 ± 0.85

8.3.5. Raman internalization intensity

Table 8-95. Numerical data for **Figure 3-29**. Internalization of *m*CNPh-Glc (**37**) (30 mM) into HepG2 cells over time as monitored by Raman spectroscopy techniques and reported as a ratio of the signal intensity following imaging at the nitrile wavelength (2230 cm^{-1}) relative to the lipid wavelength (2900 cm^{-1}). Data reported as the mean and standard deviation of three different locations in the cell cluster at each time point.

Time (h)	**Signal Intensity (CN/CH)**
0.00	0.00 ± 0.00
1.00	0.0244 ± 0.0141
2.25	0.0921 ± 0.0209
4.00	0.1083 ± 0.0176
5.25	0.1233 ± 0.0255

8.3.6. Chapter 4

Table 8-96. % Mean grain size (MGS) of various monosaccharides and disaccharides (**7**-**15**) at 22 mM and their corresponding hydration number (n_h) and hydration index (HI).[157]

Compound	Compound #	MGS (%)	SD (%)	n_h	HI (mol•cm^{-3})
Galactose	**7**	63.6	3.25	8.7 ± 0.2	0.078947
Glucose	**8**	76.5	3.60	8.4 ± 0.2	0.075201
Mannose	**9**	83.9	3.60	8.1 ± 0.2	0.072776
Talose	**10**	87.0	4.38	7.7 ± 0.2	0.068444
Melibiose	**11**	64.0	2.65	15.5 ± 0.3	0.075980
Lactose	**12**	72.1	3.64	15.3 ± 0.3	0.073171
Trehalose	**13**	78.9	4.08	15.3 ± 0.3	0.073949
Maltose	**14**	84.3	3.64	14.5 ± 0.3	0.069444
Sucrose	**15**	87.7	2.87	13.9 ± 0.3	0.065690

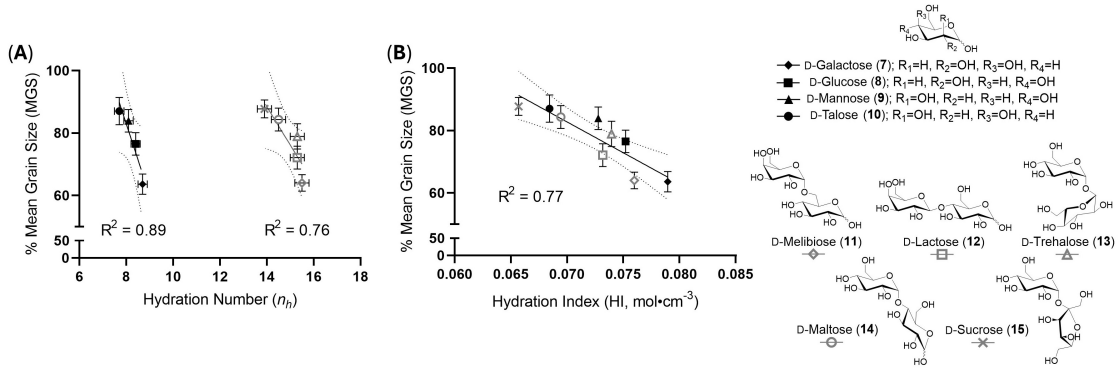


Figure 8-79. Plot of the hydration number (n_h) of monosaccharides (**7-10**) and disaccharides (**11-15**) relative to their % MGS fit to a linear regression ($R^2 = 0.89$ and $R^2 = 0.76$ respectively with 95 % confidence bands of the linear regression shown).[157] (**B**) Plot of the hydration index (HI) of all carbohydrates relative to their % MGS combined into a single linear regression ($R^2 = 0.77$ with 95 % confidence bands of the linear regression shown and significant deviation of the slope from zero, ** $p \leq 0.01$).[157] Ice recrystallization inhibition activity presented as mean ± standard deviation (SD) of the percent mean grain size (% MGS) normalized to phosphate-buffered saline (PBS) of n=3 ice wafers assessed at 22 mM using a splat-cooling assay with a 30-minute annealing time at -6.4 °C. *Figure adapted from Tam et. al. (2008).*[157]

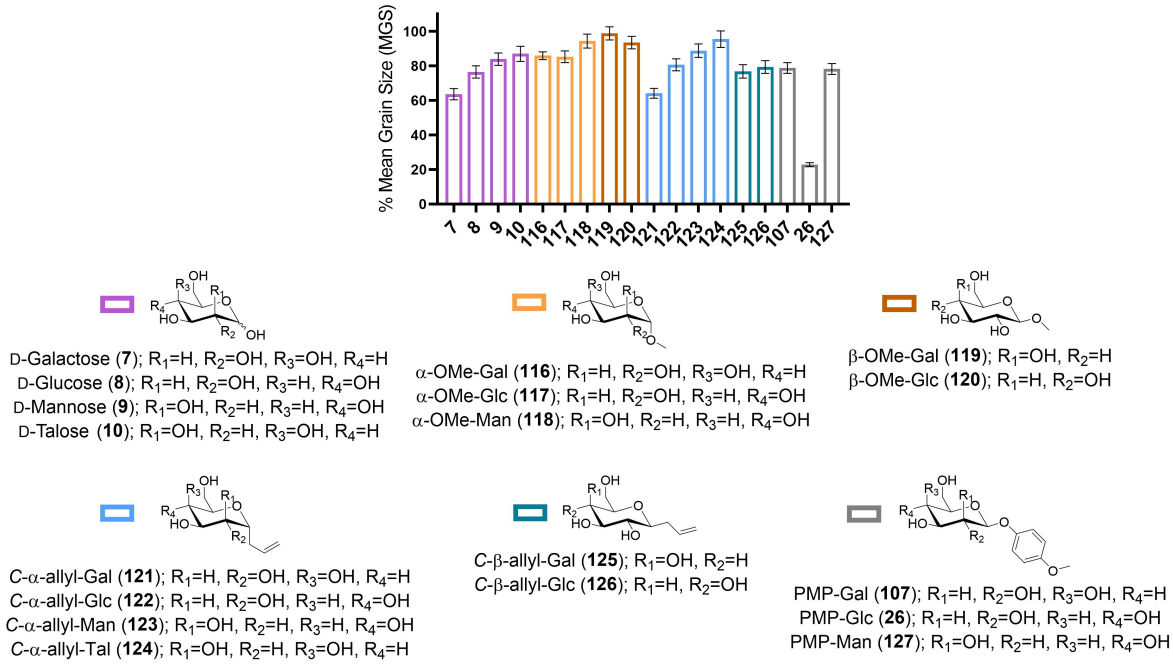
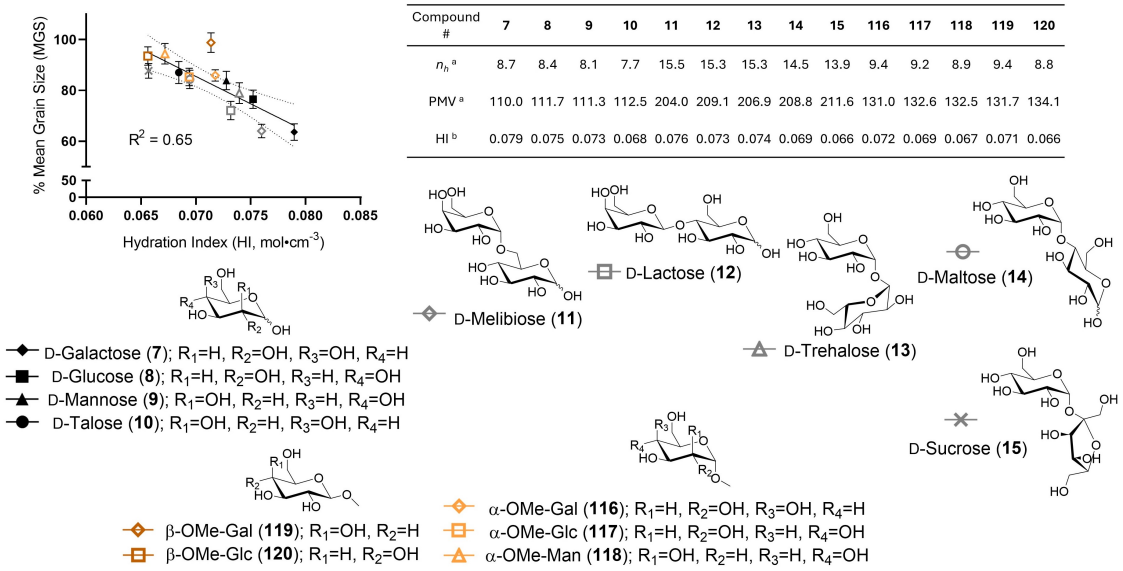


Figure 8-80. Ice recrystallization inhibition activity of various monosaccharides including reducing sugars (**7-10**),[158] *O*-methyl derivatives (**116-120**),[158] allyl derivatives (**121-126**)[566], and *O*-aryl derivatives (**26**, **107**, **127**)[167]. Activity presented as mean ± standard deviation of the percent mean grain size (% MGS) normalized to phosphate-buffered saline of n=3 ice wafers assessed at 22 mM using a splat-cooling assay with a 30-minute annealing time at -6.4 °C. *Figure recreated using data from Czechura et. al. (2008), Tam (2011) and Capicciotti (2014)*.[156–158,167,566]



Compound #	7	8	9	10	11	12	13	14	15	116	117	118	119	120
n_h [a]	8.7	8.4	8.1	7.7	15.5	15.3	15.3	14.5	13.9	9.4	9.2	8.9	9.4	8.8
PMV [a]	110.0	111.7	111.3	112.5	204.0	209.1	206.9	208.8	211.6	131.0	132.6	132.5	131.7	134.1
HI [b]	0.079	0.075	0.073	0.068	0.076	0.073	0.074	0.069	0.066	0.072	0.069	0.067	0.071	0.066

Figure 8-81. Plot of the hydration index (HI) of compounds **7-15** and **116-120** relative to their ice recrystallization inhibition activity fit to a linear regression (R^2 = 0.69 with 95 % confidence bands of the linear regression shown).[157,158] Activity presented as mean ± standard deviation of the percent mean grain size (% MGS) normalized to phosphate-buffered saline of n=3 ice wafers assessed at 22 mM using a splat-cooling assay with a 30-minute annealing time at -6.4 °C. [a] Hydration number (n_h) and partial molar volume (PMV, cm^3•mol^{-1}) values obtained from literature.[401,406] [b] Hydration index (HI, mol•cm^{-3}) HI = n_h/PMV. *Figure adapted from Capicciotti (2014).*[158]

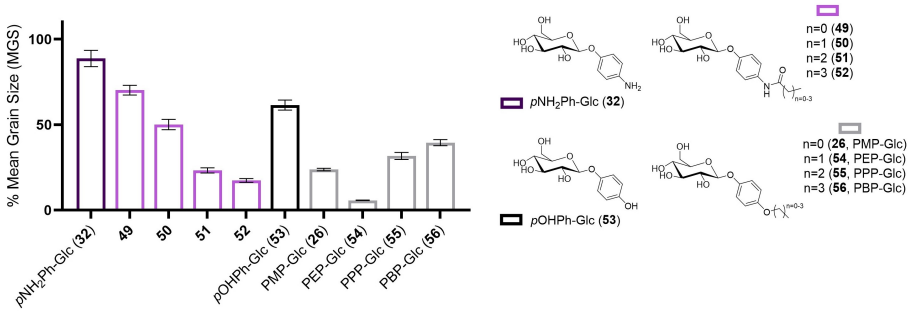


Figure 8-82. Plot of the ice recrystallization inhibition activity of *O*-alkoxyphenyl- (**26**, **53-56**) and *O*-alkamidophenyl- (**32**, **49-52**) β-D-glucopyranosides as measured by the 30-minute SCA and reported as a percent mean grain size (% MGS).

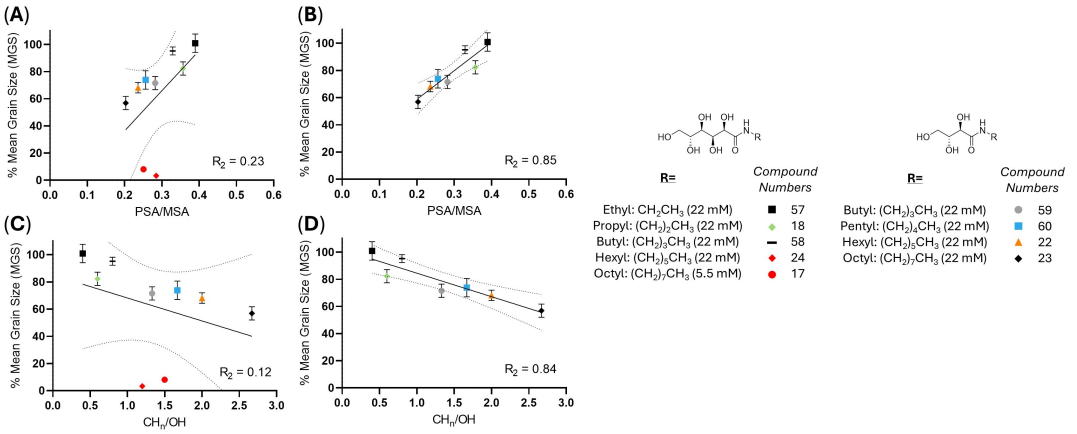


Figure 8-83. Plot of the ratio of a compound's polar surface area (PSA) to its molecular surface area (MSA) as calculated by MarvinSketch® (**A** and **B**) or its ratio of the number of alkyl chain tcarbons (CH_n) to hydroxyls (OH) (**C** and **D**) for *N*-alkyl-D-gluconamides (**17-18**, **24**, **57-58**) and *N*-alkyl-D-erythronamides (**22-23**, **59-60**) relative to their ice recrystallization inhibition activity.[160,168] Data fit to a linear regression (A: $R^2 = 0.69$, B: $R^2 = 0.85$, C: $R^2 = 0.12$, D: $R^2 = 0.84$) with 95 % confidence bands of the linear regression shown. Significant deviation of the slope from zero, $p \leq 0.01$, for panels A and C, not significant, $p > 0.05$ for panels B and D. Ice recrystallization inhibition activity presented as mean ± standard deviation (SD) of the percent mean grain size (% MGS) normalized to phosphate-buffered saline (PBS) of n=3 ice wafers assessed at 22 mM (except **17** assessed at 5.5 mM) using a splat-cooling assay with a 30-minute annealing time at -6.4 °C. *Figure adapted from Briard (2016).*[168]

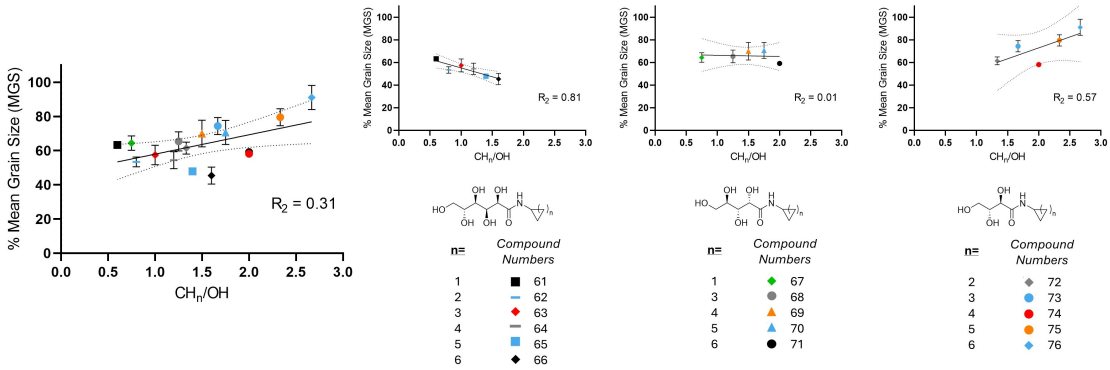


Figure 8-84. Plot of the ratio of a compound's ratio of the number of alkyl chain carbons (CH_n) to hydroxyls (OH) (**C** and **D**) for *N*-cycloalkyl-D-gluconamides (**61-66**), *N*-cycloalkyl-D-arabonamides (**67-71**), and *N*-alkyl-D-erythronamides (**72-76**) relative to their ice recrystallization inhibition activity.[168] Data of all three compound classes fit to a linear regression and presented as pooled ($R^2 = 0.31$) or individually ($R^2 =$ 0.81, 0.01, and 0.57 respectively) with 95 % confidence bands of the linear regression shown. Ice recrystallization inhibition activity presented as mean ± standard deviation (SD) of the percent mean grain size (% MGS) normalized to phosphate-buffered saline (PBS) of n=3 ice wafers assessed at 22 mM using a splat-cooling assay with a 30-minute annealing time at -6.4 °C. *Figure adapted from Briard (2016).*[168]

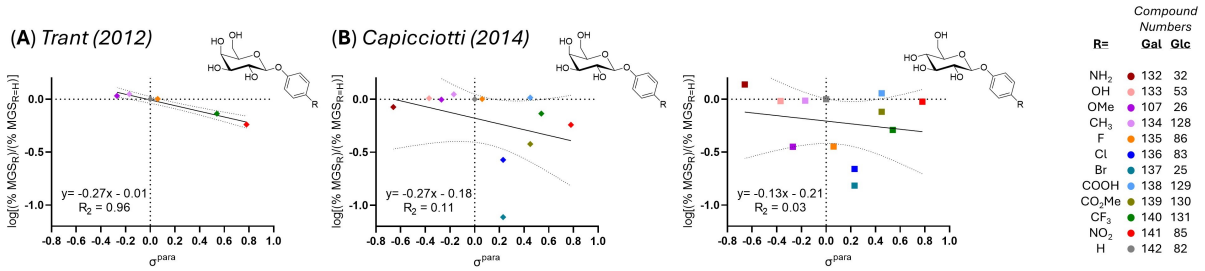


Figure 8-85. Hammett plots of the relationship between % MGS and the electronic effect of the *para*-substituent for *O*-aryl-β-D-galactopyranosides and *O*-aryl-β-D-glucopyranosides as measured by (**A**) Dr. Trant (2012) and (**B**) Dr. Capicciotti (2014). The log[(% MGS_R)/(% $MGS_{R=H}$)] for each derivative is plotted against the σ^{para} value for each substituent.[158,412,419]

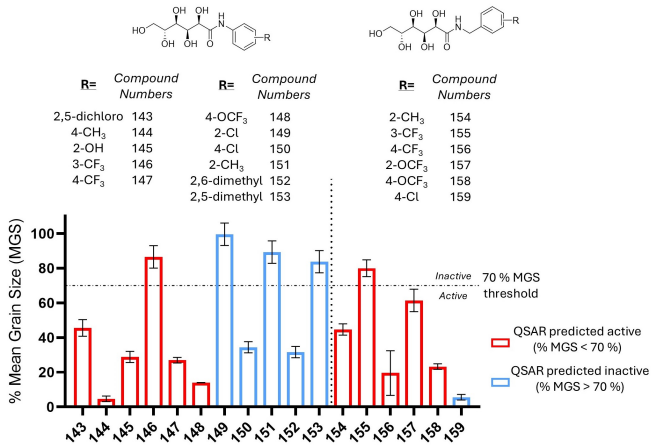
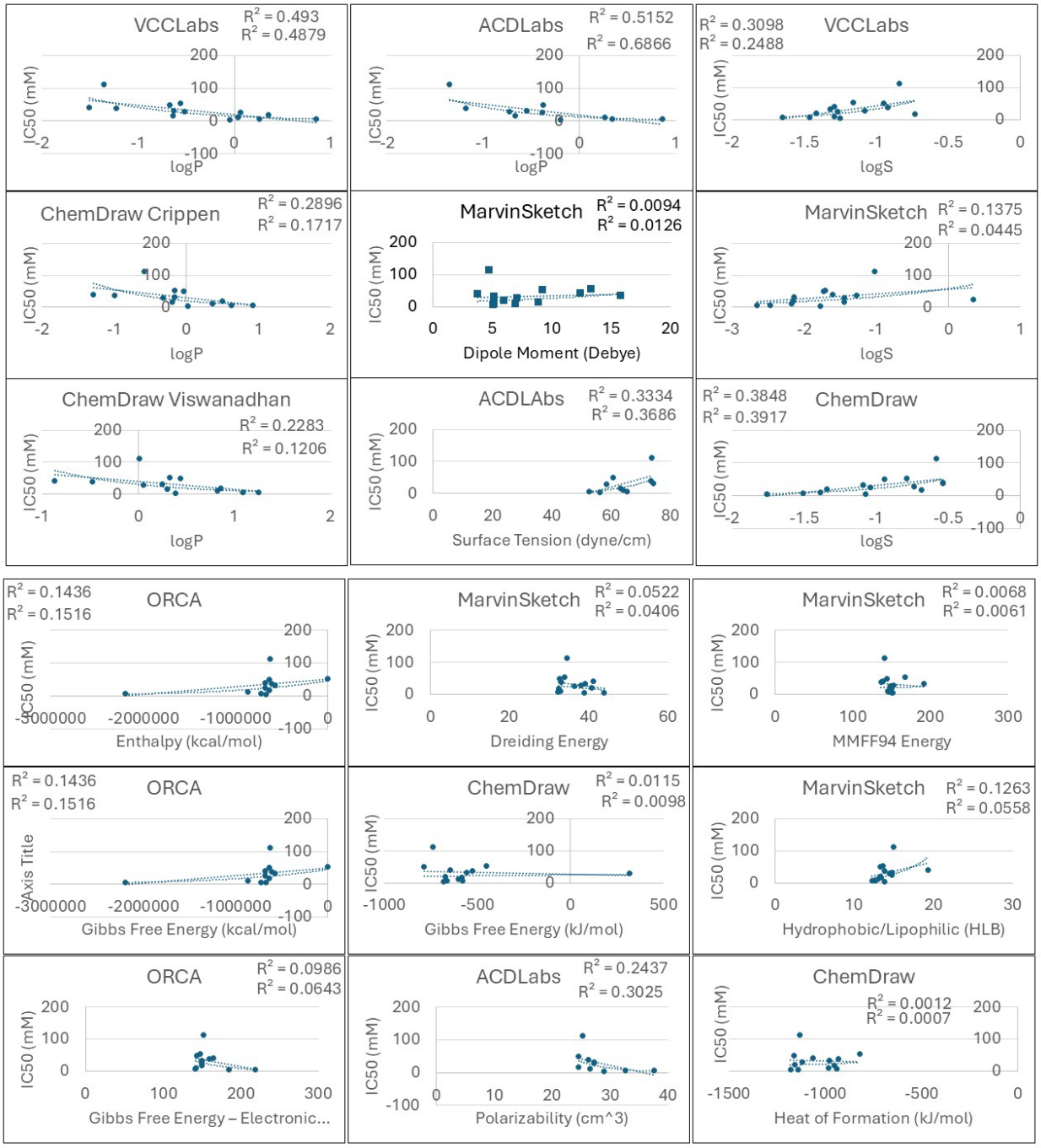
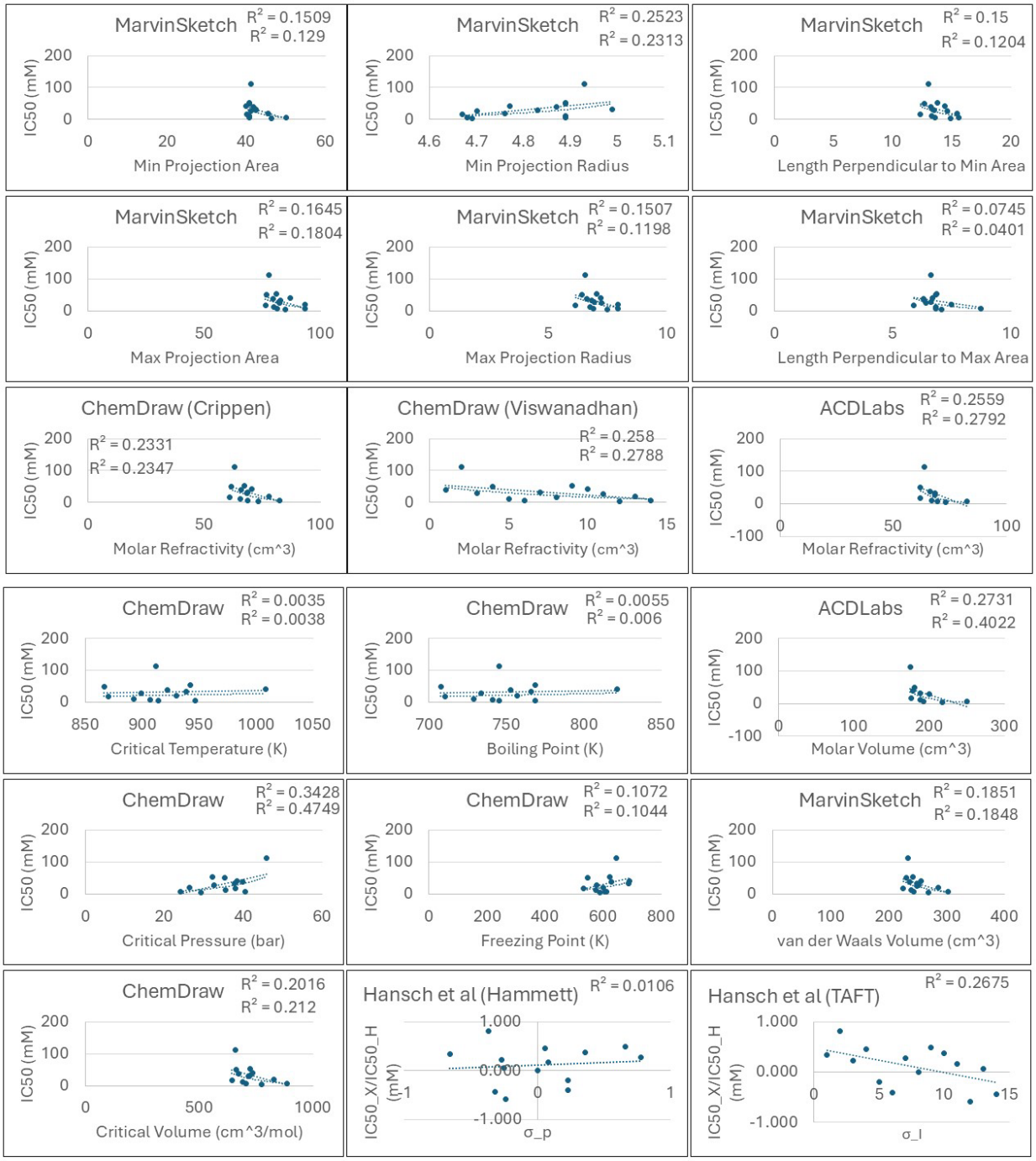


Figure 8-86. Ice recrystallization inhibition activity of compounds **143-159** assessed at 22 mM (except **147** and **158-159** that were tested at 11 mM) Presented as mean ± standard deviation (SD) of the percent mean grain size (% MGS) normalized to phosphate-buffered saline (PBS) of n=3 ice wafers using a splat-cooling assay with a 30-minute annealing time at -6.4 °C. Bars in red are compounds that were predicted to be active (% MGS > 70 %) by the QSAR model, bars in blue were predicted to be inactive (% MGS > 70 %). *Figure adapted from Briard et. al. (2016).*[217]


VCCLabs
R² = 0.493
R² = 0.4879
IC50 (mM)
logP
ACDLabs
R² = 0.5152
R² = 0.6866
IC50 (mM)
logP
R² = 0.3098
R² = 0.2488
VCCLabs
IC50 (mM)
logS
ChemDraw Crippen
R² = 0.2896
R² = 0.1717
IC50 (mM)
logP
MarvinSketch
R² = 0.0094
R² = 0.0126
IC50 (mM)
Dipole Moment (Debye)
MarvinSketch
R² = 0.1375
R² = 0.0445
IC50 (mM)
logS
ChemDraw Viswanadhan
R² = 0.2283
R² = 0.1206
IC50 (mM)
logP
ACDLAbs
R² = 0.3334
R² = 0.3686
IC50 (mM)
Surface Tension (dyne/cm)
R² = 0.3848
R² = 0.3917
ChemDraw
IC50 (mM)
logS
R² = 0.1436
R² = 0.1516
ORCA
IC50 (mM)
Enthalpy (kcal/mol)
MarvinSketch
R² = 0.0522
R² = 0.0406
IC50 (mM)
Dreiding Energy
MarvinSketch
R² = 0.0068
R² = 0.0061
IC50 (mM)
MMFF94 Energy
R² = 0.1436
R² = 0.1516
ORCA
Axis Title
Gibbs Free Energy (kcal/mol)
ChemDraw
R² = 0.0115
R² = 0.0098
IC50 (mM)
Gibbs Free Energy (kJ/mol)
MarvinSketch
R² = 0.1263
R² = 0.0558
IC50 (mM)
Hydrophobic/Lipophilic (HLB)
ORCA
R² = 0.0986
R² = 0.0643
IC50 (mM)
Gibbs Free Energy – Electronic...
ACDLabs
R² = 0.2437
R² = 0.3025
IC50 (mM)
Polarizability (cm^3)
ChemDraw
R² = 0.0012
R² = 0.0007
IC50 (mM)
Heat of Formation (kJ/mol)


MarvinSketch
R² = 0.1509
R² = 0.129
IC50 (mM)
Min Projection Area
MarvinSketch
R² = 0.2523
R² = 0.2313
IC50 (mM)
Min Projection Radius
MarvinSketch
R² = 0.15
R² = 0.1204
IC50 (mM)
Length Perpendicular to Min Area
MarvinSketch
R² = 0.1645
R² = 0.1804
IC50 (mM)
Max Projection Area
MarvinSketch
R² = 0.1507
R² = 0.1198
IC50 (mM)
Max Projection Radius
MarvinSketch
R² = 0.0745
R² = 0.0401
IC50 (mM)
Length Perpendicular to Max Area
ChemDraw (Crippen)
R² = 0.2331
R² = 0.2347
IC50 (mM)
Molar Refractivity (cm^3)
ChemDraw (Viswanadhan)
R² = 0.258
R² = 0.2788
IC50 (mM)
Molar Refractivity (cm^3)
ACDLabs
R² = 0.2559
R² = 0.2792
IC50 (mM)
Molar Refractivity (cm^3)
ChemDraw
R² = 0.0035
R² = 0.0038
IC50 (mM)
Critical Temperature (K)
ChemDraw
R² = 0.0055
R² = 0.006
IC50 (mM)
Boiling Point (K)
ACDLabs
R² = 0.2731
R² = 0.4022
IC50 (mM)
Molar Volume (cm^3)
ChemDraw
R² = 0.3428
R² = 0.4749
IC50 (mM)
Critical Pressure (bar)
ChemDraw
R² = 0.1072
R² = 0.1044
IC50 (mM)
Freezing Point (K)
MarvinSketch
R² = 0.1851
R² = 0.1848
IC50 (mM)
van der Waals Volume (cm^3)
ChemDraw
R² = 0.2016
R² = 0.212
IC50 (mM)
Critical Volume (cm^3/mol)
Hansch et al (Hammett)
R² = 0.0106
IC50_X/IC50_H (mM)
σ_p
Hansch et al (TAFT)
R² = 0.2675
IC50_X/IC50_H (mM)
σ_I

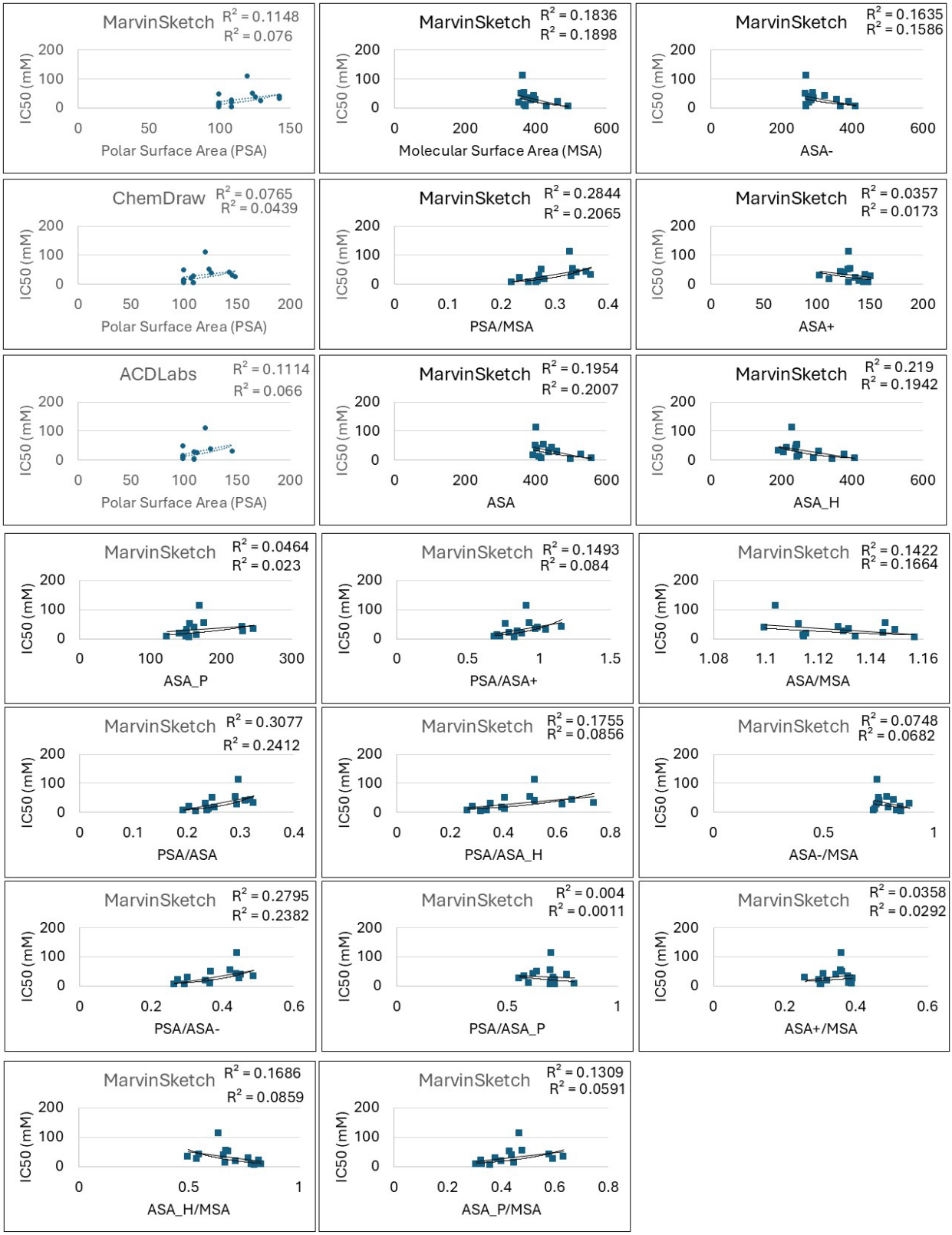


Figure 8-87. Plot for all correlations as calculated using Microsoft Excel® See Table 4-1 for a summary of correlation coefficients.

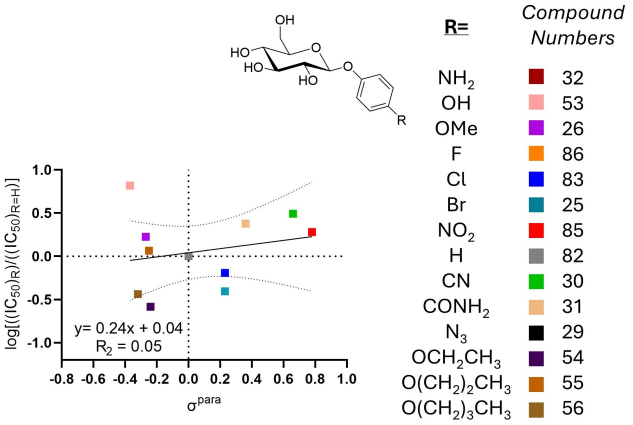


Figure 8-88. Hammett plot of the relationship between IC_{50} and the electronic effect of the *para*- substituent for *O*-aryl-β-D-glucopyranosides as measured only by the author of this thesis. Data points from **Figure 4-13** that were collected by other researchers were removed to create this plot. The $\log[(IC50_R)/(IC50_{R=H})]$ for each derivative is plotted against the σ^{para} value for each substituent.[158,412,419]

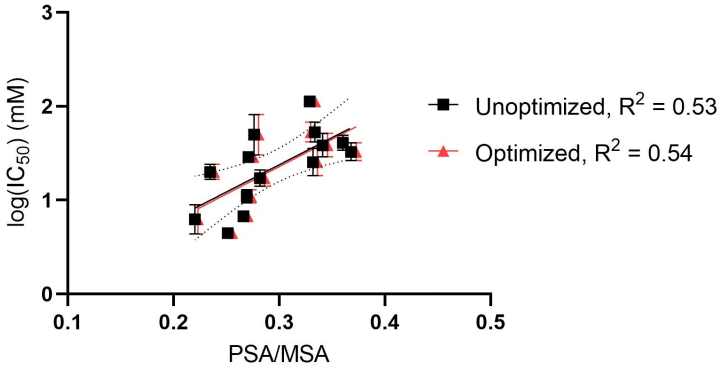


Figure 8-89. Ratio of PSA/MSA relative to their log transformed IC_{50} value (mM) as measured by the 5-minute SCA for *O*-aryl-β-D-glucopyranosides using unoptimized structures (drawn in three dimensions in ChemDraw) or optimized structures (geometry optimized using ORCA 5.0.1). 95 % confidence of the linear regression shown.

8.3.7. Chapter 5

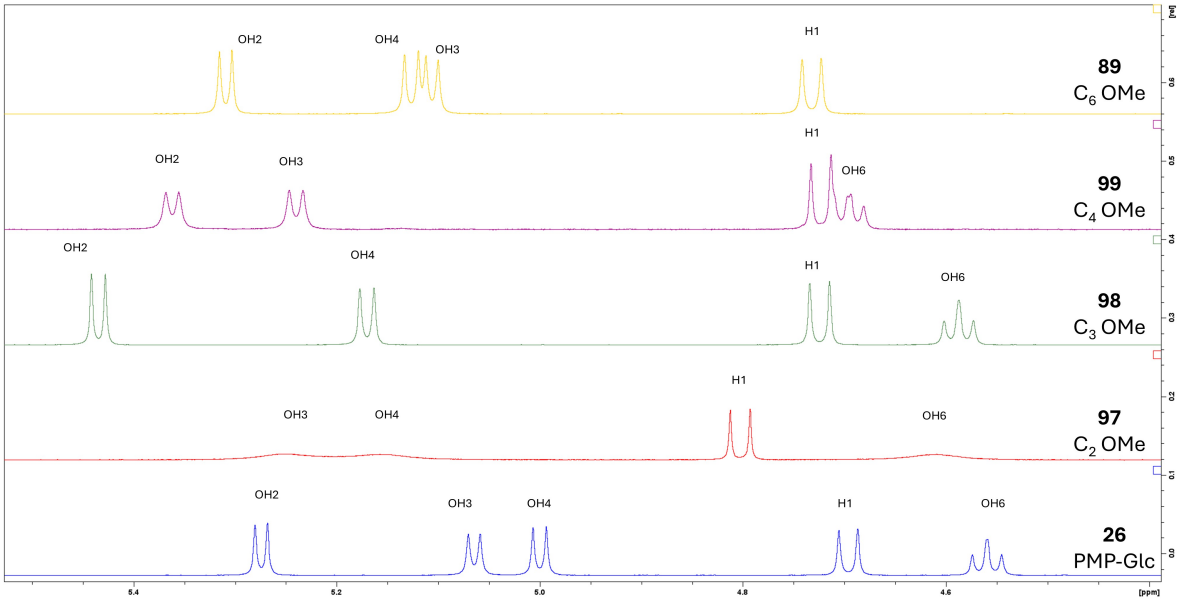


Figure 8-90. Proton (^{1}H) NMR spectra of *O*-methylated derivatives (**89**, **97-99**) compared to PMP-Glc (**26**) zoomed in to show the 4.4-5.5 ppm region. All relevant protons on each spectrum are labelled accordingly.

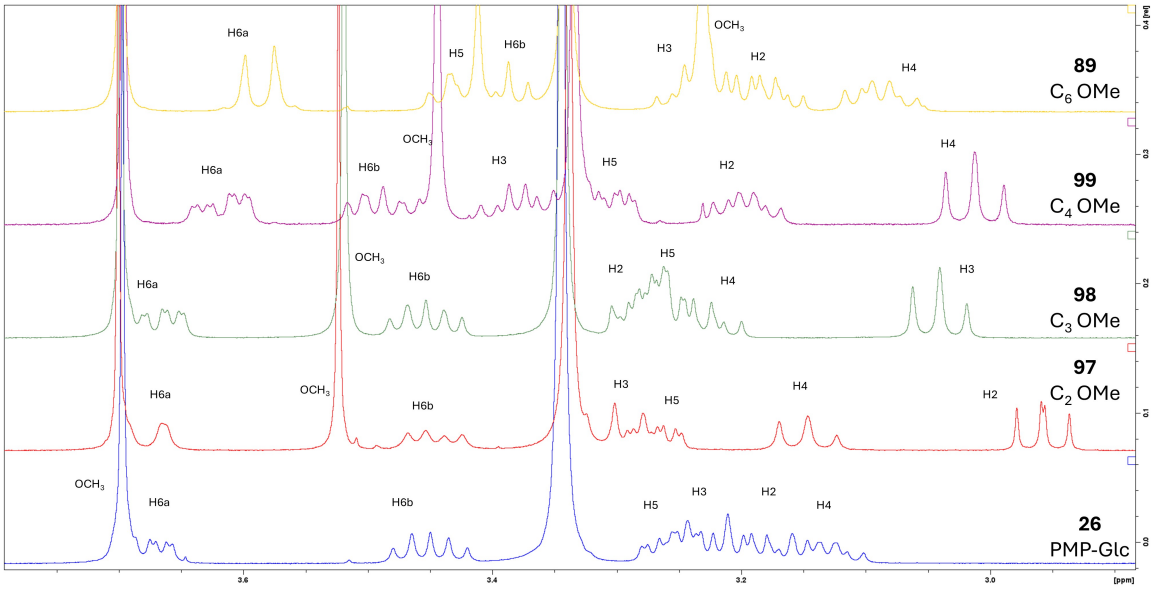


Figure 8-91. Proton (^{1}H) NMR spectra of *O*-methylated derivatives (**89**, **97-99**) compared to PMP-Glc (**26**) zoomed in to show the 3.75-2.8 ppm region. All relevant protons on each spetrum are labelled accordingly.

	^{1}H Chemical Shift														^{13}C Chemical Shift							
Compound	H_1	H_2	H_3	H_4	H_5	H_{6a}	H_{6b}	OCH_3 arom.	OCH_3	H_2O	OH_2	OH_3	OH_4	OH_6	C_1	C_2	C_3	C_4	C_5	C_6	OCH_3 arom.	OCH_3
26	4.70	3.21	3.24	3.14	3.24	3.68	3.45	3.70	NA	3.34	5.28	5.06	5.00	4.56	101.5	73.3	76.6	69.8	77.0	60.8	55.4	NA
97	4.80	2.95	3.29	3.15	3.27	3.68	3.45	3.70	3.52	3.34	NA	5.25	5.16	4.61	101.1	83.3	75.7	69.9	76.9	60.7	55.4	59.9
98	4.73	3.27	3.04	3.22	3.25	3.67	3.45	3.70	3.52	3.34	5.44	NA	5.17	4.59	101.4	72.9	86.5	69.1	76.8	60.5	55.3	60.1
99	4.72	3.20	3.38	3.01	3.31	3.62	3.48	3.70	3.44	3.33	5.36	5.24	NA	4.70	101.1	73.5	76.3	79.0	75.5	60.3	55.3	59.7
89	4.73	3.17	3.22	3.09	3.42	3.59	3.39	3.70	3.23	3.34	5.31	5.11	5.13	NA	101.2	73.2	76.5	69.8	75.3	71.8	55.3	58.5

Figure 8-92. Chemical shift (ppm) of all protons and carbons from the NMR spectra of *O*-methylated derivatives (**89**, **97**-**99**) compared to PMP-Glc (**26**).

8.3.8. Chapter 6

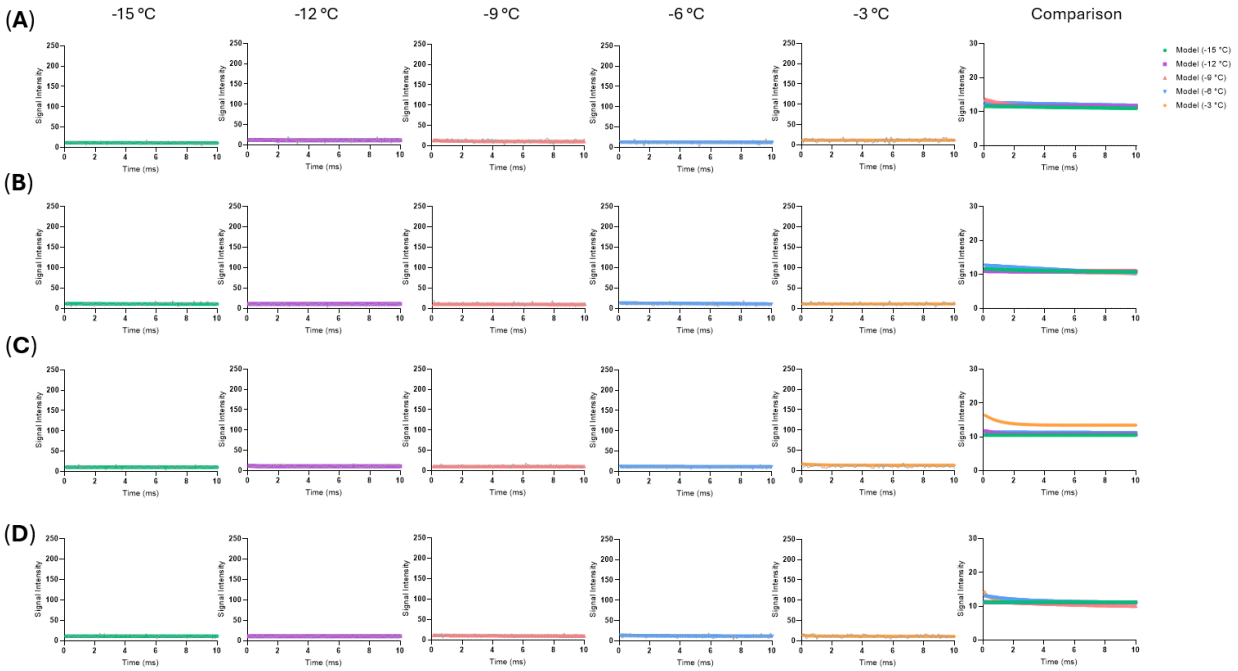


Figure 8-93. Exemplar CPMG relaxation of 2FA (A) 1 mM (B) 3 mM (C) 5 mM (D) 10 mM. Data shown from one trial that is representative of the mean (from n=3 replicates). Comparison between -15 °C and -3 °C.

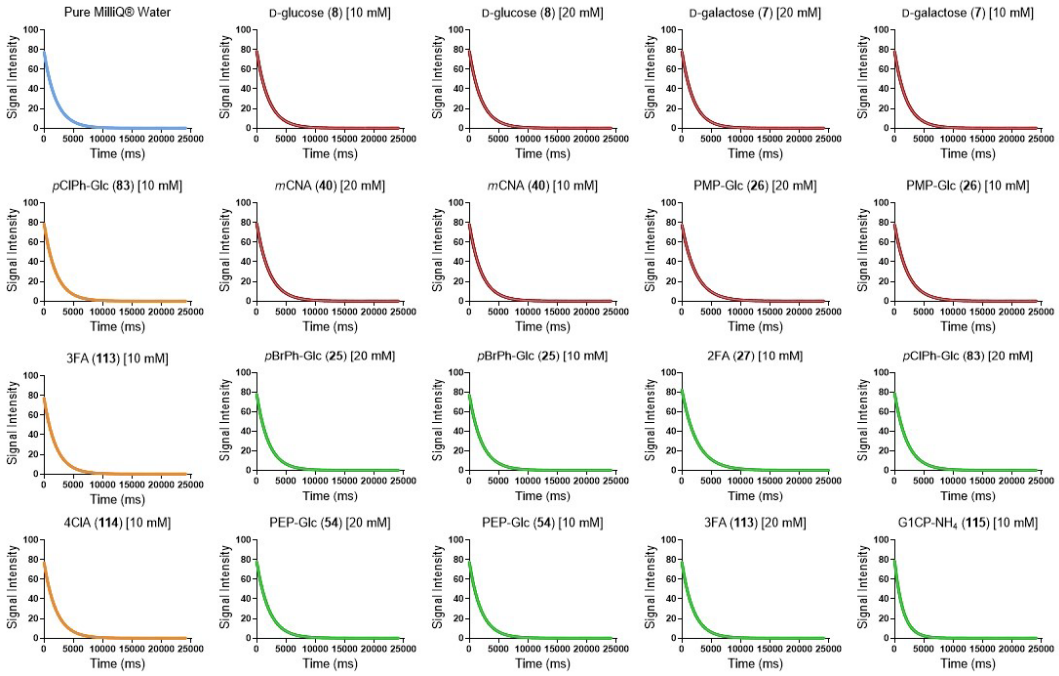


Figure 8-94. Exemplar of compound supplemented water solutions (concentrations of 10 mM or 20 mM) $T_{2\text{-CPMG}}$ relaxation at +25 °C. Red = v_{norm} > 90 % at the tested concentration; orange = v_{norm} between 10 and 90 %; green = v_{norm} < 10 %. Grey = raw data, coloured = fitted model to **Equation 6-3**.

9. Appendices

9.1. Appendix 1: Statement of Contributions

Chapter 1: This section reviewed the development of small-molecule ice recrystallization inhibitors and important factors to consider throughout their development, including discussion of relevant literature in the context of the cryopreservation of biological materials and the mechanism of ice recrystallization inhibition by small-molecules. A review pertaining to much of this content was published in CryoLetters in 2024 (DOI: 10.54680/fr24210110112) and was co-authored by myself and Elly Walsh (PhD Candidate in the Ben Lab at the time of writing).[188]

Chapter 2: This chapter discussed the application of small-molecule ice recrystallization inhibitors for the cryopreservation of mesenchymal stromal cells (MSCs) and related primary cells. Work on this project was initially started by Dr. Jessica Poisson (Ben Lab, PhD 2019) in collaboration with researchers under the supervision of Dr. David Courtman at the Ottawa Hospital Research Institute (OHRI). Synthesis of compounds **25** and **27** was completed by the author of this thesis. Cytotoxicity studies of *p*BrPh-Glc (**25**) were completed by the author of this thesis. All *in vitro* assessment of MSCs and related primary cells as reported in this thesis was completed by research associates Charlotte Mitz, Liliana Davila, and Dr. Angus

Macaulay as part of a team of researchers at the cell manufacturing facility at the OHRI including Dr. Saad Khan and Dr. David Courtman with assistance from the author of this thesis. Interpretation of data and the impact of ice recrystallization inhibitors on MSCs and related primary cells was completed by the author of this thesis and the research team at OHRI. This project began in the summer of 2019 and was heavily interrupted by the COVID shutdowns during the spring and summer of 2020.

Chapter 3: This chapter discussed the development of Raman-active probes for investigating the internalization of small-molecule ice recrystallization inhibitors. This project was in collaboration with Dr. Albert Stolow (Department of Physics & Department of Chemistry and Biomolecular Sciences, University of Ottawa, Ottawa, ON) and Dr. Adrian Pegoraro [National Research Council (NRC), Ottawa, ON]. All microscopy imaging was completed by Dr. Pegoraro at the Sussex site NRC facilities and the methods used for much of these experiments were published in Optics Express in 2024 (DOI: 10.1364/OE.531274).[519] All cell culture, including preparation of relevant compound containing cell culture media, was completed by the author of this thesis. Compound synthesis and cytotoxicity testing of compounds **30**-**31**, and **37**-**46** was completed by the author of this thesis with synthetic assistance from summer CO-OP student Abigail Kos (Summer 2021) for compounds **39**, **41**, **44**, and **46**. Compound **29** was synthesized and tested for ice recrystallization inhibition activity by Dr. Jessica Poisson (Ben Lab, PhD 2019) and was generously provided for testing by Raman microscopy imaging in this thesis. This project began in the fall of 2019 and was heavily interrupted by the COVID shutdowns during the spring and summer of 2020.

Chapter 4: This chapter discussed the structure activity relationships of *O*-aryl-β-D-glucopyranosides with the aim of developing new and improved ice recrystallization inhibitors with activity measured by the 5-minute SCA. The synthesis and activity testing of all compounds discussed in this chapter was completed by the author of this thesis with the exception of compounds **29**, **32**, and **86** which were synthesized and tested by Dr. Jessica Poisson (Ben Lab, PhD 2019). All data analysis and graphical comparisons were completed by the author of this thesis.

Chapter 5: This chapter discussed the iterative investigation of deuteration and methylation of PMP-Glc (**26**) towards understanding the hydrogen bonding interactions of *O*-aryl-β-D-glucopyranosides as they relate to ice recrystallization inhibition activity. The synthesis and activity testing of all compounds discussed in this chapter was completed by the author of this thesis. Undergraduate students Hannah Mayer and Stephanie Sibbald assisted with the synthesis of intermediates towards the C-6 modified compounds **89** and **93**. All data and computational analysis were completed by the author of this thesis. Dr. Patrick Szell, NMR Core Facility Manager at uOttawa, assisted with setup of many NMR pulse sequences used for

experiments not explicitly discussed in this thesis, but were instrumental in the final results obtained throughout this chapter.

Chapter 6: This chapter discussed critical studies to elucidate the mechanism of action of small-molecule ice recrystallization inhibitors, including discussion of relevant external literature. Portions of this work were published in The Journal of Physical Chemistry Letters in 2023 (DOI: 10.1021/acs.jpclett.3c00845) in collaboration with Dr. Nicolas Bordenave and his doctoral student Adrian S. D'Costa (PhD 2024, Department of Chemistry and Biomolecular Sciences, University of Ottawa, Ottawa, ON);[567] Adrian collected all T_1 measurements presented in this chapter. This work also acknowledges Prof. Francois Mariette (INRAE UR OPAALE, Rennes, France) who provided advice regarding the initial experimental design and setup of the methods described in this chapter based on his expertise in the field. Compound **115** was synthesized and tested for ice recrystallization inhibition activity by Dr. Anna Ampaw (Ben Lab, PhD 2022) and was generously provided for relaxation time testing in this thesis.

Synthesis of Compounds: The synthesis and/or ice recrystallization inhibition activity testing of the following compounds was aided by undergraduate students during Honour's project, CO-OP, or other student placements.

- Abigail Kos (Summer 2021 CO-OP student)
    - *p*BrPh-Glc (**25**)
    - *p*CNA (**39**)
    - *o*CNA (**41**)
    - *p*AmA (**44**)
    - *o*AmA (**46**)
    - 3FA (**113**)
    - 4ClA (**114**)
    - (4-methoxyphenyl)-2,3,4-tri-*O*-benzyl-6-*O*-methyl-β-D-glucopyranoside (**556**)
- Hannah Mayer (2019-2020 Honour's Project) and Stephanie Sibbald (2021-2022 Honour's Project)
    - (4-methoxyphenyl)-6-*O*-*tert*-butyldimethylsilyl-β-D-glucopyranoside (**535**)
    - (4-methoxyphenyl)-2,3,4-tri-*O*-benzyl-6-*O*-*tert*-butyldimethylsilyl-β-D-glucopyranoside (**536**)
    - (4-methoxyphenyl)-2,3,4-tri-*O*-benzyl-β-D-glucopyranoside (**537**)

9.2. Appendix 2: Thesis Related Publications and Presentations

†: indicates equal contribution by the authors

9.2.1. Publications

- **McMunn, L. E.** †; Walsh, E. M. †; Ben, R. N. Targeted Development and Optimization of Small-Molecule Ice Recrystallization Inhibitors (IRIs) for the Cryopreservation of Biological Systems. *Cryoletters*. **2024**, 45 (2), 69–87. https://doi.org/10.54680/fr24210110112.
- **McMunn, L. E.**; D'Costa, A. S; Bordenave, N.; Ben, R. N. Probing the Mechanism of Action of Small-Molecule Ice Recrystallization Inhibitors Using Proton Nuclear Magnetic Resonance Relaxation. *J. Phys. Chem. Lett.* **2023**, 14 (26), 6043–6050. https://doi.org/10.1021/acs.jpclett.3c00845

9.2.2. Presentations

The presenting author is indicated with an asterisk (*).

9.2.2.1. Oral presentations

- **McMunn, L. E.** *; Ben, R. N.; A deeper understanding of the structure activity relationship of *O*-aryl-glucopyranoside ice recrystallization inhibitors; **Cryobiology 2023**; Minneapolis, MN, USA; July 24th-28th, 2023. https://doi.org/10.1016/j.cryobiol.2023.104647
- **McMunn, L. E.** *; Pegoraro, A.; Stolow, A.; Ben, R. N.; Development of nitrile containing ice recrystallization inhibitors for use in live-cell imaging; **Canadian Blood Services Research Day**; Montreal, QC, Canada; May 25th, 2023
- **McMunn, L. E.** *; Improving cryopreservation outcomes using small-molecule ice recrystallization inhibitors; **EWOC 2022 Symposia Series**; Online; October 21st, 2022
- **McMunn, L. E.** *; D'Costa, A. S; Bordenave, N.; Ben, R. N.; Probing interactions between small-molecule ice recrystallization inhibitors (IRIs) and water molecules using ^{1}H NMR; **Cryobiology 2022**; Dublin, Ireland; July 18th – 22nd, 2022. https://doi.org/10.1016/j.cryobiol.2022.11.049
- **McMunn, L. E.** *; Pegoraro, A.; Stolow, A.; Ben, R. N.; Development of nitrile containing ice recrystallization inhibitors for use in live-cell imaging; **CSC 2021**; Online; August 13th – 20th, 2021
- **McMunn, L. E.** *; Ben, R. N.; Development of nitrile containing ice recrystallization inhibitors for use in live-cell imaging; **Extreme Cryo 2021**; Online; March 27th, 2021

- **McMunn, L. E.** *; Khan, S.; Poisson, J.; Davila, L.; Mitz, C.; Courtman, D. W.; Ben, R. N.; Improving the post-thaw outcome of cryopreserved mesenchymal stem cells and peripheral blood mononuclear cells using ice recrystallization inhibitors; **Extreme Cryo 2020**; Edmonton, ON, Canada; January 31st – February 1st, 2020
- **McMunn, L. E.** *; Ben, R. N.; The use of novel aryl nitrile and aryl amide glucopyranosides as ice recrystallization inhibitors for human red blood cells; **QOMSBOC 2019**; Ottawa, ON, Canada; November 8th – 10th, 2019

9.2.2.2. Poster presentations

- **McMunn, L. E.** *; D'Costa, A. S; Bordenave, N.; Ben, R. N.; Probing interactions between small-molecule ice recrystallization inhibitors (IRIs) and water molecules using ^{1}H NMR; **CSC 2022**; Calgary, AB, Canada; June 13th – 17th, 2022
- Khan, S. *; Macaulay, M.; **McMunn, L. E.**; Ben, R. N.; Courtman, D. W.; Ice recrystallization inhibitor increases post-thaw functional capacity of bone marrow and umbilical cord derived mesenchymal stromal cells; **Cytotherapy 2022**; San Francisco, CA, USA; May 4th – 7th, 2022; https://doi.org/10.1016/S1465-3249(22)00210-9
- **McMunn, L. E.***; Ben, R. N.; The use of novel aryl nitrile and aryl amide glucopyranosides as ice recrystallization inhibitors for human red blood cells; **QOMSBOC 2019**; Ottawa, ON, Canada; November 8th – 10th, 2019
- **McMunn, L. E.** *; Pegoraro, A.; Stolow, A.; Ben, R. N.; Live Cell Observation of Novel Nitrile Containing Carbohydrate-Based Ice Recrystallization Inhibitors Using Coherent Anti-Stokes Raman Spectroscopy; **CSC 2019**; Quebec City, QC, Canada; June 3rd – 7th 2019

9.3. Appendix 3: Non-Thesis Related Publications and Presentations

9.3.1. Publications

- Leclerc, Z.; **McMunn, L. E.**; Nastic, A.; Ben, R. N.; Jodoin, B. Manufacturing and Icephobic Performance Evaluation of Cold Sprayed Adhesive Perfluoroalkoxy Alkane Coatings. *J. Therm. Spray Tech.* **2023**, 32 (4), 851-876. https://doi.org/10.1007/s11666-023-01551-z
    - **Abstract:** "There is an increasing need for ice protection systems that do not require complex manufacturing considerations or are energy intensive. Fluorinated polymer coatings are potential candidates for such systems although conventional manufacturing processes can be costly, limited in the achievable coating thickness or can degrade the

coating's material mechanical properties during deposition. The current work aims to offer an alternative approach by using cold spray as the mean of coating production. Computational and experimental approaches are used to design a new cold spray nozzle for the efficient deposition of adhesive perfluoroalkoxy alkane. The icephobicity of as-sprayed coatings are evaluated using three-fold characterization, one for each stage of the icing process. First, the surface's wetting behaviour is established using single droplet analysis, followed by a time-lapse study of the water droplets to observe their freezing process, and finally ice adhesion is evaluated with both macro and micro ice adhesion tests. While the as-sprayed coatings exhibited superhydrophobic properties that should be sought in icephobic coatings, their behavior changed when exposed to frost formation. Ice adhesion testing revealed that surface frosting leads to degraded wetting behaviors resulting in much higher ice adhesion, which demonstrates the importance of this phenomena when studying icephobic coatings."[568]

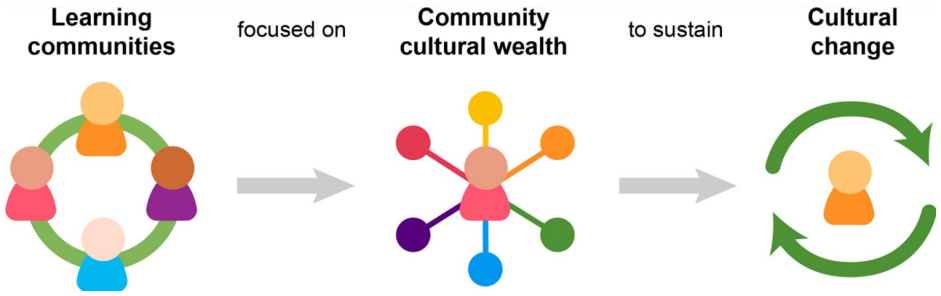
- **Keywords:** cold spray, PFA, superhydrophobic, CFD
- Awarded the JTST volume 32 best paper award (2024) by ""a panel of 39 international thermal spray scientists, who commented [that the] paper [is] "an extremely thorough and well explained paper, covering nozzle development, modelling, and ice adhesion testing. The work is a fabulous example of combining detailed fundamental analysis and modelling to develop a practical, real-world solution." Another judge commented on [the] paper that "the prepared coatings are thoroughly tested and compared to other possible protective layers. All the results are systematically presented, experimental data are supported by numerical modelling, and even fundamental physical explanations of coating functional properties are drawn. To me, it is very complex paper targeted to real world application."".
- **Contribution:** Co-development and operation of the micro-shear testing apparatus in collaboration with Z. Leclerc (who developed the load cell apparatus) to obtain "wetting behaviour", "droplet freezing", "ice growth time", and "ice growth type" results. Interpretation of micro-shear testing and droplet freezing results in the context of ice growth dynamics.

- Deng, J. M.; **McMunn, L. E.** †; Oakley, M. S. †; Dang, H. T. †; Rodriguez, R. S. † Toward Sustained Cultural Change through Chemistry Graduate Student Diversity, Equity, and Inclusion

Communities. *J. Chem. Educ.* **2022**, 99 (1), 373–382. https://doi.org/10.1021/acs.jchemed.1c00485

- **Abstract:** "Evidence from the past several decades has repeatedly found that the chemical enterprise presents systemic barriers for people with marginalized identities. Initiatives and actions that remove systemic barriers and support the success of all students, especially those from equity-deserving groups, are essential. However, fostering a culture of inclusion requires actions that focus on not only immediate outcomes but also sustained and lasting impacts. Chemistry graduate student communities focused on diversity, equity, inclusion, and respect (DEIR) can contribute to the transformation of our share chemistry community into one where DEIR principles are foundational. Chemistry graduate student DEIR communities (CGDEIRCs) are learning communities in which students from equity-deserving groups in chemistry gain various forms of cultural wealth that support their attainment of cultural capital. By supporting students' development of skills, networks, and resources to attain success, over time, CGDEIRCs may contribute to both short- and long-term DEIR cultural shifts in the broader chemistry community."[569]

- **Keywords:** Graduate education/research, minorities in chemistry, professional development, women in chemistry, collaborative/cooperative learning, public understanding/outreach, interdisciplinary/multidisciplinary



9.3.2. Presentations

The presenting author is indicated with an asterisk (*).

- **McMunn, L. E.** *; Carle, M.; Meyer, J. E.; Building a community to improve equity, diversity, and inclusion at the University of Ottawa; **CSC 2021**; Online; August 13th – 20th, 2021

9.4. Appendix 4: Community Work

In addition to my direct contributions to scientific research, I also had the privileged opportunity to work on various initiatives aimed at improving equity, inclusion, and student well-being within the

scientific community both locally and globally. During my time at the University of Ottawa I co-founded a campus chapter of Canadian's Working for Inclusivity in Chemistry alongside Julia Meyer establishing a platform to promote dialogue around equity, diversity, and inclusion (EDI) in STEM through events, speaker series, and resource sharing events such as book clubs and an EDI-focused community library. Recognizing the need for better support structures for students within our department, I also co-created a peer-mentorship program for incoming graduate students in the Department of Chemistry and Biomolecular Sciences with Dr. Meredith Allen, which connected new students with senior graduate mentors to ease the academic and social transition into graduate studies.

Beyond these initiatives, I served on the Chemistry and Biomolecular Graduate Student Association (CBGSA) as treasurer for three years, contributing to advocacy and event planning to enhance the graduate student experience. During my time with the CBGSA I co-organized the annual Ottawa Carleton Chemistry Institute (OCCI) conference, providing graduate students across the region with opportunities to share their research and build professional networks. I also co-led an initiative with CBGSA President Dr. Connor Bourgonje to advocate for increased graduate student stipends, conducting a nationwide analysis of chemistry graduate student stipends that was used to support our case for improved financial support at the institutional level and resulted in a minimum annual stipend increase of ~$3,000 CAD.

Finally, I also volunteered with Cam's Kids, promoting mental health awareness and support, and with Let's Talk Science, where I facilitated hands-on STEM outreach activities for youth in the community. These combined experiences reflect my ongoing commitment to creating a more inclusive, supportive, and engaging environment in both academic and public science spaces.

9.5. Awards and Recognition

- JTST Volume 32 Best Paper Award for doi: 10.1007/s11666-023-01551-z (2024) – No Financial Value
- Society of Cryobiology Student Travel Award (2023) – Value $700 CAD
- Canadian Blood Services Travel Award (2023) – Value $700 CAD
- The J. C. (Tito) Scaiano Graduate Student of the Year Award (2022) – No Financial Value
- Society of Cryobiology Student Travel Award (2022) – Value $1,000 CAD
- Canadian Blood Services Travel Award (2019-2024) – Value $4,000 CAD
- Canadian Blood Services Graduate Fellowship (2019 – 2024) – Value $100,000 CAD
- General Chemistry Lecture Teaching Assistant Award (2018 – 2019) – Value $100 CAD
- uOttawa Graduate Admission Scholarship (2018 – Present) – Value $9,000 CAD Annually

10. References

(1) Scott, K. L.; Lecak, J.; Acker, J. P. Biopreservation of Red Blood Cells: Past, Present, and Future. *Transfus. Med. Rev.* **2005**, *19* (2), 127–142. https://doi.org/10.1016/j.tmrv.2004.11.004.

(2) Meneghel, J.; Kilbride, P.; Morris, G. J. Cryopreservation as a Key Element in the Successful Delivery of Cell-Based Therapies—A Review. *Front. Med.* **2020**, *7* (592242). https://doi.org/10.3389/fmed.2020.592242.

(3) Whaley, D.; Damyar, K.; Witek, R. P.; Mendoza, A.; Alexander, M.; Lakey, J. R. Cryopreservation: An Overview of Principles and Cell-Specific Considerations. *Cell Transplant.* **2021**, *30* (963689721999617). https://doi.org/10.1177/0963689721999617.

(4) Taylor, M. J.; Weegman, B. P.; Baicu, S. C.; Giwa, S. E. New Approaches to Cryopreservation of Cells, Tissues, and Organs. *Transfus. Med. Hemotherapy* **2019**, *46* (3), 197–215. https://doi.org/10.1159/000499453.

(5) Ma, Y.; Gao, L.; Tian, Y.; Chen, P.; Yang, J.; Zhang, L. Advanced Biomaterials in Cell Preservation: Hypothermic Preservation and Cryopreservation. *Acta Biomater.* **2021**, *131*, 97–116. https://doi.org/10.1016/j.actbio.2021.07.001.

(6) Rubinsky, B. Principles of Low Temperature Cell Preservation. *Heart Fail. Rev.* **2003**, *8* (3), 277–284. https://doi.org/10.1023/A:1024734003814.

(7) Van Buskirk, R. G.; Baust, J. M.; Snyder, K. K.; Mathew, A. J.; Baust, J. G. Hypothermic Storage and Cryopreservation: Successful Short- and Long-Term Preservation of Cells and Tissues. *Bioprocess Tech.* **2004**.

(8) *The Effects of Low Temperatures on Biological Systems*; Grout, B. W. W., Morris, G. J., Eds.; E. Arnold: London, 1987.

(9) *Effects of Low Temperatures on Biological Membranes*; Morris, G. J., Clarke, A., Eds.; Academic Press: London; New York, 1981.

(10) Brinkkoetter, P.-T.; Song, H.; Lösel, R.; Schnetzke, U.; Gottmann, U.; Feng, Y.; Hanusch, C.; Beck, G.; Schnuelle, P.; Wehling, M.; Van Der Woude, F.; Yard, B. Hypothermic Injury: The Mitochondrial Calcium, ATP and ROS Love-Hate Triangle out of Balance. *Cell. Physiol. Biochem.* **2008**, *22* (1–4), 195–204. https://doi.org/10.1159/000149797.

(11) Fuller, B. J.; Lee, C. Y. Hypothermic Perfusion Preservation: The Future of Organ Preservation Revisited? *Cryobiology* **2007**, *54* (2), 129–145. https://doi.org/10.1016/j.cryobiol.2007.01.003.

(12) Taylor, M. J.; Baicu, S. C. Current State of Hypothermic Machine Perfusion Preservation of Organs: The Clinical Perspective. *Cryobiology* **2010**, *60* (3), S20–S35. https://doi.org/10.1016/j.cryobiol.2009.10.006.

(13) Pegg, D. E. Principles of Cryopreservation. In *Cryopreservation and Freeze-Drying Protocols*; Day, J. G., Stacey, G. N., Eds.; Walker, J. M., Series Ed.; Methods in Molecular Biology; Humana Press: Totowa, NJ, 2007; Vol. 368, pp 39–57. https://doi.org/10.1007/978-1-59745-362-2_3.

(14) Taylor, M. J.; Song, Y. C.; Brockbank, K. G. Vitrification in Tissue Preservation: New Developments. In *Life in the frozen state*; Fuller, B. J., Lane, N., Benson, E. E., Eds.; CRC Press: Boca Raton, Fla, 2004; pp 604–641.

(15) Fahy, G. M.; MacFarlane, D. R.; Angell, C. A.; Meryman, H. T. Vitrification as an Approach to Cryopreservation. *Cryobiology* **1984**, *21* (4), 407–426. https://doi.org/10.1016/0011-2240(84)90079-8.

(16) Elliott, G. D.; Wang, S.; Fuller, B. J. Cryoprotectants: A Review of the Actions and Applications of Cryoprotective Solutes That Modulate Cell Recovery from Ultra-Low Temperatures. *Cryobiology* **2017**, *76*, 74–91. https://doi.org/10.1016/j.cryobiol.2017.04.004.

(17) Bojic, S.; Murray, A.; Bentley, B. L.; Spindler, R.; Pawlik, P.; Cordeiro, J. L.; Bauer, R.; De Magalhães, J. P. Winter Is Coming: The Future of Cryopreservation. *BMC Biol.* **2021**, *19* (1), 56. https://doi.org/10.1186/s12915-021-00976-8.

(18) *Life in the Frozen State*; Fuller, B. J., Lane, N., Benson, E. E., Eds.; CRC Press: Boca Raton, Fla, 2004.
(19) Fahy, G. M.; Levy, D. I.; Ali, S. E. Some Emerging Principles Underlying the Physical Properties, Biological Actions, and Utility of Vitrification Solutions. *Cryobiology* **1987**, *24* (3), 196–213. https://doi.org/10.1016/0011-2240(87)90023-X.
(20) Mukaida, T.; Oka, C. Vitrification of Oocytes, Embryos and Blastocysts. *Best Pract. Res. Clin. Obstet. Gynaecol.* **2012**, *26* (6), 789–803. https://doi.org/10.1016/j.bpobgyn.2012.07.001.
(21) Gao, D.; Critser, J. K. Mechanisms of Cryoinjury in Living Cells. *ILAR J.* **2000**, *41* (4), 187–196. https://doi.org/10.1093/ilar.41.4.187.
(22) Fowler, A.; Toner, M. Cryo-Injury and Biopreservation. *Ann. N. Y. Acad. Sci.* **2005**, *1066* (1), 119–135. https://doi.org/10.1196/annals.1363.010.
(23) Gage, A. A.; Baust, J. Mechanisms of Tissue Injury in Cryosurgery. *Cryobiology* **1998**, *37* (3), 171–186. https://doi.org/10.1006/cryo.1998.2115.
(24) Baust, J. M. Molecular Mechanisms of Cellular Demise Associated with Cryopreservation Failure. *Cell Preserv. Technol.* **2002**, *1* (1), 17–31. https://doi.org/10.1089/15383440260073266.
(25) Hubel, A. Advancing the Preservation of Cellular Therapy Products. *Transfusion (Paris)* **2011**, *51*, 82S-86S. https://doi.org/10.1111/j.1537-2995.2011.03370.x.
(26) Mazur, P. Freezing of Living Cells: Mechanisms and Implications. *Am. J. Physiol.-Cell Physiol.* **1984**, *247* (3), C125–C142. https://doi.org/10.1152/ajpcell.1984.247.3.C125.
(27) Mazur, P.; Leibo, S. P.; Chu, E. H. Y. A Two-Factor Hypothesis of Freezing Injury. *Exp. Cell Res.* **1972**, *71* (2), 345–355. https://doi.org/10.1016/0014-4827(72)90303-5.
(28) Mazur, P. Physical Factors Implicated in the Death of Microorganisms at Subzero Temperatures. *Ann. N. Y. Acad. Sci.* **1960**, *85* (2), 610–629. https://doi.org/10.1111/j.1749-6632.1960.tb49986.x.
(29) Mazur, P. Limits to Life at Low Temperatures and at Reduced Water Contents and Water Activities. *Orig. Life* **1980**, *10* (2), 137–159. https://doi.org/10.1007/BF00928665.
(30) Law, P.; Sprott, D.; Lepock, J.; Kruuv, J. Post-Thaw Lysing and Osmotic Reactivation of Frozen-Thawed Cells. *Cryoletters* **1980**, *1*, 173–180.
(31) McGrath, J. J.; Cravalho, E. G.; Huggins, C. E. An Experimental Comparison of Intracellular Ice Formation and Freeze-Thaw Survival of Hela S-3 Cells. *Cryobiology* **1975**, *12* (6), 540–550. https://doi.org/10.1016/0011-2240(75)90048-6.
(32) Wesley-Smith, J.; Walters, C.; Pammenter, N. W.; Berjak, P. Why Is Intracellular Ice Lethal? A Microscopical Study Showing Evidence of Programmed Cell Death in Cryo-Exposed Embryonic Axes of Recalcitrant Seeds of *Acer Saccharinum*. *Ann. Bot.* **2015**, *115* (6), 991–1000. https://doi.org/10.1093/aob/mcv009.
(33) Acker, J. P.; McGann, L. E. Innocuous Intracellular Ice Improves Survival of Frozen Cells. *Cell Transplant.* **2002**, *11* (6), 563–571.
(34) Muldrew, K.; McGann, L. E. Mechanisms of Intracellular Ice Formation. *Biophys. J.* **1990**, *57* (3), 525–532. https://doi.org/10.1016/S0006-3495(90)82568-6.
(35) McGann, L. E. Differing Actions of Penetrating and Nonpenetrating Cryoprotective Agents. *Cryobiology* **1978**, *15* (4), 382–390. https://doi.org/10.1016/0011-2240(78)90056-1.
(36) Lovelock, J. E. The Protective Action of Neutral Solutes against Haemolysis by Freezing and Thawing. *Biochem. J.* **1954**, *56* (2), 265–270. https://doi.org/10.1042/bj0560265.
(37) Lovelock, J. E. Het Mechanism of the Protective Action of Glycerol against Haemolysis by Freezing and Thawing. *Biochim. Biophys. Acta* **1953**, *11*, 28–36. https://doi.org/10.1016/0006-3002(53)90005-5.
(38) Meryman, H. T. Cryoprotective Agents. *Cryobiology* **1971**, *8* (2), 173–183. https://doi.org/10.1016/0011-2240(71)90024-1.
(39) Anchordoguy, T. J.; Rudolph, A. S.; Carpenter, J. F.; Crowe, J. H. Modes of Interaction of Cryoprotectants with Membrane Phospholipids during Freezing. *Cryobiology* **1987**, *24* (4), 324–331. https://doi.org/10.1016/0011-2240(87)90036-8.

(40) Crowe, J. H.; Crowe, L. M.; Carpenter, J. F.; Rudolph, A. S.; Wistrom, C. A.; Spargo, B. J.; Anchordoguy, T. J. Interactions of Sugars with Membranes. *Biochim. Biophys. Acta BBA - Rev. Biomembr.* **1988**, *947* (2), 367–384. https://doi.org/10.1016/0304-4157(88)90015-9.
(41) Awan, M.; Buriak, I.; Fleck, R.; Fuller, B.; Goltsev, A.; Kerby, J.; Lowdell, M.; Mericka, P.; Petrenko, A.; Petrenko, Y.; Rogulska, O.; Stolzing, A.; Stacey, G. N. Dimethyl Sulfoxide: A Central Player since the Dawn of Cryobiology, Is Efficacy Balanced by Toxicity? *Regen. Med.* **2020**, *15* (3), 1463–1491. https://doi.org/10.2217/rme-2019-0145.
(42) Fahy, G. M. The Relevance of Cryoprotectant "Toxicity" to Cryobiology. *Cryobiology* **1986**, *23* (1), 1–13. https://doi.org/10.1016/0011-2240(86)90013-1.
(43) Best, B. P. Cryoprotectant Toxicity: Facts, Issues, and Questions. *Rejuvenation Res.* **2015**, *18* (5), 422–436. https://doi.org/10.1089/rej.2014.1656.
(44) Meryman, H. T.; Hornblower, M. A Method for Freezing and Washing Red Blood Cells Using a High Glycerol Concentration. *Transfusion (Paris)* **1972**, *12* (3), 145–156. https://doi.org/10.1111/j.1537-2995.1972.tb00001.x.
(45) Cabrita, E.; Robles, V.; Chereguini, O.; Wallace, J. C.; Herráez, M. P. Effect of Different Cryoprotectants and Vitrificant Solutions on the Hatching Rate of Turbot Embryos (Scophthalmus Maximus). *Cryobiology* **2003**, *47* (3), 204–213. https://doi.org/10.1016/j.cryobiol.2003.10.001.
(46) Raju, R.; Bryant, S. J.; Wilkinson, B. L.; Bryant, G. The Need for Novel Cryoprotectants and Cryopreservation Protocols: Insights into the Importance of Biophysical Investigation and Cell Permeability. *Biochim. Biophys. Acta BBA - Gen. Subj.* **2021**, *1865* (1), 129749. https://doi.org/10.1016/j.bbagen.2020.129749.
(47) Lovelock, J. E.; Bishop, M. W. H. Prevention of Freezing Damage to Living Cells by Dimethyl Sulphoxide. *Nature* **1959**, *183* (4672), 1394–1395. https://doi.org/10.1038/1831394a0.
(48) Brayton, C. F. Dimethyl Sulfoxide (DMSO): A Review. *Cornell Vet.* **1986**, *76* (1), 61–90.
(49) David, N. A. The Pharmacology of Dimethyl Sulfoxide. *Annu. Rev. Pharmacol.* **1972**, *12* (1), 353–374. https://doi.org/10.1146/annurev.pa.12.040172.002033.
(50) Shu, Z.; Heimfeld, S.; Gao, D. Hematopoietic SCT with Cryopreserved Grafts: Adverse Reactions after Transplantation and Cryoprotectant Removal before Infusion. *Bone Marrow Transplant.* **2014**, *49* (4), 469–476. https://doi.org/10.1038/bmt.2013.152.
(51) Ruiz-Delgado, G. J.; Mancías-Guerra, C.; Tamez-Gómez, E. L.; Rodríguez-Romo, L. N.; López-Otero, A.; Hernández-Arizpe, A.; Gómez-Almaguer, D.; Ruiz-Argüelles, G. J. Dimethyl Sulfoxide-Induced Toxicity in Cord Blood Stem Cell Transplantation: Report of Three Cases and Review of the Literature. *Acta Haematol.* **2009**, *122* (1), 1–5. https://doi.org/10.1159/000227267.
(52) Petzold, G.; Aguilera, J. M. Ice Morphology: Fundamentals and Technological Applications in Foods. *Food Biophys.* **2009**, *4* (4), 378–396. https://doi.org/10.1007/s11483-009-9136-5.
(53) Alley, R. B.; Perepezko, J. H.; Bentley, C. R. Grain Growth in Polar Ice: I. Theory. *J. Glaciol.* **1986**, *32* (112), 415–424. https://doi.org/10.3189/S0022143000012120.
(54) Knight, C. A. Grain Boundary Migration and Other Processes in the Formation of Ice Sheets on Water. *J. Appl. Phys.* **1966**, *37* (2), 568–574. https://doi.org/10.1063/1.1708217.
(55) Gleiter, H. The Mechanism of Grain Boundary Migration. *Acta Metall.* **1969**, *17* (5), 565–573. https://doi.org/10.1016/0001-6160(69)90115-1.
(56) Budke, C.; Heggemann, C.; Koch, M.; Sewald, N.; Koop, T. Ice Recrystallization Kinetics in the Presence of Synthetic Antifreeze Glycoprotein Analogues Using the Framework of LSW Theory. *J. Phys. Chem. B* **2009**, *113* (9), 2865–2873. https://doi.org/10.1021/jp805726e.
(57) Sutton, R. L.; Lips, A.; Piccirillo, G.; Sztehlo, A. Kinetics of Ice Recrystallization in Aqueous Fructose Solutions. *J. Food Sci.* **1996**, *61* (4), 741–745. https://doi.org/10.1111/j.1365-2621.1996.tb12194.x.
(58) Hagiwara, T.; Hartel, R. W.; Matsukawa, S. Relationship between Recrystallization Rate of Ice Crystals in Sugar Solutions and Water Mobility in Freeze-Concentrated Matrix. *Food Biophys.* **2006**, *1* (2), 74–82. https://doi.org/10.1007/s11483-006-9009-0.

(59) Rios, P. R.; Siciliano Jr, F.; Sandim, H. R. Z.; Plaut, R. L.; Padilha, A. F. Nucleation and Growth during Recrystallization. *Mater. Res.* **2005**, *8* (3), 225–238. https://doi.org/10.1590/S1516-14392005000300002.
(60) Doherty, R. D.; Hughes, D. A.; Humphreys, F. J.; Jonas, J. J.; Jensen, D. J.; Kassner, M. E.; King, W. E.; McNelley, T. R.; McQueen, H. J.; Rollett, A. D. Current Issues in Recrystallization: A Review. *Mater. Sci. Eng. A* **1997**, *238* (2), 219–274. https://doi.org/10.1016/S0921-5093(97)00424-3.
(61) Hayward, J. A.; Haymet, A. D. J. The Ice/Water Interface: Molecular Dynamics Simulations of the Basal, Prism, {20$\bar{2}$1}, and {21$\bar{1}$0} Interfaces of Ice Ih. *J. Chem. Phys.* **2001**, *114* (8), 3713–3726. https://doi.org/10.1063/1.1333680.
(62) Fletcher, N. H. *The Chemical Physics of Ice*, Digitally printed version.; Cambridge monographs on physics; Cambridge Univ. Press: Cambridge, 2009.
(63) Karim, O. A.; Haymet, A. D. J. The Ice/Water Interface. *Chem. Phys. Lett.* **1987**, *138* (6), 531–534. https://doi.org/10.1016/0009-2614(87)80118-5.
(64) Beaglehole, D.; Nason, D. Transition Layer on the Surface on Ice. *Surf. Sci.* **1980**, *96* (1–3), 357–363. https://doi.org/10.1016/0039-6028(80)90313-1.
(65) Shi, J.; Fulford, M.; Li, H.; Marzook, M.; Reisjalali, M.; Salvalaglio, M.; Molteni, C. Investigating the Quasi-Liquid Layer on Ice Surfaces: A Comparison of Order Parameters. *Phys. Chem. Chem. Phys.* **2022**, *24* (20), 12476–12487. https://doi.org/10.1039/D2CP00752E.
(66) Kahan, T. F.; Reid, J. P.; Donaldson, D. J. Spectroscopic Probes of the Quasi-Liquid Layer on Ice. *J. Phys. Chem. A* **2007**, *111* (43), 11006–11012. https://doi.org/10.1021/jp074551o.
(67) Nenow, D.; Trayanov, A. Thermodynamics of Crystal Surfaces with Quasi-Liquid Layer. *J. Cryst. Growth* **1986**, *79* (1–3), 801–805. https://doi.org/10.1016/0022-0248(86)90557-9.
(68) Döppenschmidt, A.; Kappl, M.; Butt, H.-J. Surface Properties of Ice Studied by Atomic Force Microscopy. *J. Phys. Chem. B* **1998**, *102* (40), 7813–7819. https://doi.org/10.1021/jp981396s.
(69) Döppenschmidt, A.; Butt, H.-J. Measuring the Thickness of the Liquid-like Layer on Ice Surfaces with Atomic Force Microscopy. *Langmuir* **2000**, *16* (16), 6709–6714. https://doi.org/10.1021/la990799w.
(70) Sazaki, G.; Zepeda, S.; Nakatsubo, S.; Yokomine, M.; Furukawa, Y. Quasi-Liquid Layers on Ice Crystal Surfaces Are Made up of Two Different Phases. *Proc. Natl. Acad. Sci.* **2012**, *109* (4), 1052–1055. https://doi.org/10.1073/pnas.1116685109.
(71) Nagata, Y.; Hama, T.; Backus, E. H. G.; Mezger, M.; Bonn, D.; Bonn, M.; Sazaki, G. The Surface of Ice under Equilibrium and Nonequilibrium Conditions. *Acc. Chem. Res.* **2019**, *52* (4), 1006–1015. https://doi.org/10.1021/acs.accounts.8b00615.
(72) Asakawa, H.; Sazaki, G.; Nagashima, K.; Nakatsubo, S.; Furukawa, Y. Two Types of Quasi-Liquid Layers on Ice Crystals Are Formed Kinetically. *Proc. Natl. Acad. Sci.* **2016**, *113* (7), 1749–1753. https://doi.org/10.1073/pnas.1521607113.
(73) Yasuda, I.; Endo, K.; Arai, N.; Yasuoka, K. In-Layer Inhomogeneity of Molecular Dynamics in Quasi-Liquid Layers of Ice. *Commun. Chem.* **2024**, *7* (1), 117. https://doi.org/10.1038/s42004-024-01197-0.
(74) Huang, Z.; Su, M.; Yang, Q.; Li, Z.; Chen, S.; Li, Y.; Zhou, X.; Li, F.; Song, Y. A General Patterning Approach by Manipulating the Evolution of Two-Dimensional Liquid Foams. *Nat. Commun.* **2017**, *8* (1), 14110. https://doi.org/10.1038/ncomms14110.
(75) Taylor, P. Ostwald Ripening in Emulsions. *Colloids Surf. Physicochem. Eng. Asp.* **1995**, *99* (2–3), 175–185. https://doi.org/10.1016/0927-7757(95)03161-6.
(76) Pronk, P.; Infante Ferreira, C. A.; Witkamp, G. J. A Dynamic Model of Ostwald Ripening in Ice Suspensions. *J. Cryst. Growth* **2005**, *275* (1–2), e1355–e1361. https://doi.org/10.1016/j.jcrysgro.2004.11.173.
(77) Van Westen, T.; Groot, R. D. Predicting the Kinetics of Ice Recrystallization in Aqueous Sugar Solutions. *Cryst. Growth Des.* **2018**, *18* (4), 2405–2416. https://doi.org/10.1021/acs.cgd.8b00038.

(78) Scholander, P. F.; van Dam, L.; Kanwisher, J. W.; Hammel, H. T.; Gordon, M. S. Supercooling and Osmoregulation in Arctic Fish. *J. Cell. Comp. Physiol.* **1957**, *49* (1), 5–24. https://doi.org/10.1002/jcp.1030490103.
(79) DeVries, A. L.; Wohlschlag, D. E. Freezing Resistance in Some Antarctic Fishes. *Science* **1969**, *163* (3871), 1073–1075. https://doi.org/10.1126/science.163.3871.1073.
(80) Gordon, M. S.; Amdur, B. H.; Scholander, P. F. Freezing Resistance in Some Northern Fishes. *Biol. Bull.* **1962**, *122* (1), 52–62. https://doi.org/10.2307/1539321.
(81) Devries, A. L. Biological Antifreeze Agents in Coldwater Fishes. *Comp. Biochem. Physiol. A Physiol.* **1982**, *73* (4), 627–640. https://doi.org/10.1016/0300-9629(82)90270-5.
(82) Capicciotti, C. J.; Doshi, M.; Ben, R. N. Ice Recrystallization Inhibitors: From Biological Antifreezes to Small Molecules. In *Recent Developments in the Study of Recrystallization*; Wilson, P., Ed.; InTech, 2013; pp 177–224. https://doi.org/10.5772/54992.
(83) Duman, J. G.; Devries, A. L. Freezing Resistance in Winter Flounder Pseudopleuronectes Americanus. *Nature* **1974**, *247* (5438), 237–238. https://doi.org/10.1038/247237a0.
(84) Davies, P. L.; Baardsnes, J.; Kuiper, M. J.; Walker, V. K. Structure and Function of Antifreeze Proteins. *Philos. Trans. R. Soc. Lond. B. Biol. Sci.* **2002**, *357* (1423), 927–935. https://doi.org/10.1098/rstb.2002.1081.
(85) Venketesh, S.; Dayananda, C. Properties, Potentials, and Prospects of Antifreeze Proteins. *Crit. Rev. Biotechnol.* **2008**, *28* (1), 57–82. https://doi.org/10.1080/07388550801891152.
(86) Bang, J.; Lee, J.; Murugan, R.; Lee, S.; Do, H.; Koh, H.; Shim, H.-E.; Kim, H.-C.; Kim, H. Antifreeze Peptides and Glycopeptides, and Their Derivatives: Potential Uses in Biotechnology. *Mar. Drugs* **2013**, *11* (6), 2013–2041. https://doi.org/10.3390/md11062013.
(87) Devries, A. L. Glycoproteins as Biological Antifreeze Agents in Antarctic Fishes. *Science* **1971**, *172* (3988), 1152–1155. https://doi.org/10.1126/science.172.3988.1152.
(88) Wilson, P. W. Explaining Thermal Hysteresis by the Kelvin Effect. *Cryoletters* **1993**, *14*, 31–36.
(89) Knight, C. A.; DeVries, A. L. Effects of a Polymeric, Nonequilibrium "Antifreeze" upon Ice Growth from Water. *J. Cryst. Growth* **1994**, *143* (3–4), 301–310. https://doi.org/10.1016/0022-0248(94)90071-X.
(90) Raymond, J. A.; DeVries, A. L. Adsorption Inhibition as a Mechanism of Freezing Resistance in Polar Fishes. *Proc. Natl. Acad. Sci.* **1977**, *74* (6), 2589–2593. https://doi.org/10.1073/pnas.74.6.2589.
(91) Knight, C. A.; De Vries, A. L.; Oolman, L. D. Fish Antifreeze Protein and the Freezing and Recrystallization of Ice. *Nature* **1984**, *308* (5956), 295–296. https://doi.org/10.1038/308295a0.
(92) Knight, C. A.; Driggers, E.; DeVries, A. L. Adsorption to Ice of Fish Antifreeze Glycopeptides 7 and 8. *Biophys. J.* **1993**, *64* (1), 252–259. https://doi.org/10.1016/S0006-3495(93)81361-4.
(93) Knight, C. A.; Cheng, C. C.; DeVries, A. L. Adsorption of Alpha-Helical Antifreeze Peptides on Specific Ice Crystal Surface Planes. *Biophys. J.* **1991**, *59* (2), 409–418. https://doi.org/10.1016/S0006-3495(91)82234-2.
(94) Kristiansen, E.; Zachariassen, K. E. The Mechanism by Which Fish Antifreeze Proteins Cause Thermal Hysteresis. *Cryobiology* **2005**, *51* (3), 262–280. https://doi.org/10.1016/j.cryobiol.2005.07.007.
(95) Budke, C.; Koop, T. Ice Recrystallization Inhibition and Molecular Recognition of Ice Faces by Poly(Vinyl Alcohol). *ChemPhysChem* **2006**, *7* (12), 2601–2606. https://doi.org/10.1002/cphc.200600533.
(96) Chakrabartty, A.; Hew, C. L. The Effect of Enhanced Alpha-Helicity on the Activity of a Winter Flounder Antifreeze Polypeptide. *Eur. J. Biochem.* **1991**, *202* (3), 1057–1063. https://doi.org/10.1111/j.1432-1033.1991.tb16470.x.
(97) Buckley, S. L.; Lillford, P. J. Antifreeze Proteins. In *Modern Biopolymer Science*; Elsevier, 2009; pp 93–128. https://doi.org/10.1016/B978-0-12-374195-0.00003-3.
(98) Chao, H.; Davies, P. L.; Carpenter, J. F. Effects of Antifreeze Proteins on Red Blood Cell Survival during Cryopreservation. *J. Exp. Biol.* **1996**, *199* (9), 2071–2076. https://doi.org/10.1242/jeb.199.9.2071.

(99) Rubinsky, B.; Arav, A.; Devries, A. L. The Cryoprotective Effect of Antifreeze Glycopeptides from Antarctic Fishes. *Cryobiology* **1992**, *29* (1), 69–79. https://doi.org/10.1016/0011-2240(92)90006-N.
(100) Carpenter, J. F.; Hansen, T. N. Antifreeze Protein Modulates Cell Survival during Cryopreservation: Mediation through Influence on Ice Crystal Growth. *Proc. Natl. Acad. Sci.* **1992**, *89* (19), 8953–8957. https://doi.org/10.1073/pnas.89.19.8953.
(101) Kuhs, W. F.; Lehmann, M. S. The Structure of the Ice Ih by Neutron Diffraction. *J. Phys. Chem.* **1983**, *87* (21), 4312–4313. https://doi.org/10.1021/j100244a063.
(102) Harding, M. M.; Ward, L. G.; Haymet, A. D. J. Type I "antifreeze" Proteins. Structure-Activity Studies and Mechanisms of Ice Growth Inhibition. *Eur. J. Biochem.* **1999**, *264* (3), 653–665. https://doi.org/10.1046/j.1432-1327.1999.00617.x.
(103) Kontogiorgos, V. Water. In *Introduction to Food Chemistry*; Springer International Publishing: Cham, 2021; pp 1–17. https://doi.org/10.1007/978-3-030-85642-7_1.
(104) Graether, S. P.; Kuiper, M. J.; Gagné, S. M.; Walker, V. K.; Jia, Z.; Sykes, B. D.; Davies, P. L. β-Helix Structure and Ice-Binding Properties of a Hyperactive Antifreeze Protein from an Insect. *Nature* **2000**, *406* (6793), 325–328. https://doi.org/10.1038/35018610.
(105) Scotter, A. J.; Marshall, C. B.; Graham, L. A.; Gilbert, J. A.; Garnham, C. P.; Davies, P. L. The Basis for Hyperactivity of Antifreeze Proteins. *Cryobiology* **2006**, *53* (2), 229–239. https://doi.org/10.1016/j.cryobiol.2006.06.006.
(106) Liou, Y.-C.; Tocilj, A.; Davies, P. L.; Jia, Z. Mimicry of Ice Structure by Surface Hydroxyls and Water of a β-Helix Antifreeze Protein. *Nature* **2000**, *406* (6793), 322–324. https://doi.org/10.1038/35018604.
(107) Halwani, D. O.; Brockbank, K. G. M.; Duman, J. G.; Campbell, L. H. Recombinant Dendroides Canadensis Antifreeze Proteins as Potential Ingredients in Cryopreservation Solutions. *Cryobiology* **2014**, *68* (3), 411–418. https://doi.org/10.1016/j.cryobiol.2014.03.006.
(108) Hew, C. L.; Yang, D. S. C. Protein Interaction with Ice. *Eur. J. Biochem.* **1992**, *203* (1–2), 33–42. https://doi.org/10.1111/j.1432-1033.1992.tb19824.x.
(109) Hall, D. G.; Lips, A. Phenomenology and Mechanism of Antifreeze Peptide Activity. *Langmuir* **1999**, *15* (6), 1905–1912. https://doi.org/10.1021/la980657m.
(110) Osuga, D. T.; Feeney, R. E.; Yeh, Y.; Hew, C.-L. Co-Functional Activities of Two Different Antifreeze Proteins: The Antifreeze Glycoprotein from Polar Fish and the Nonglycoprotein from a Newfoundland Fish. *Comp. Biochem. Physiol. Part B Comp. Biochem.* **1980**, *65* (2), 403–406. https://doi.org/10.1016/0305-0491(80)90036-X.
(111) Osuga, D. T.; Ward, F. C.; Yeh, Y.; Feeney, R. E. Cooperative Functioning between Antifreeze Glycoproteins. *J. Biol. Chem.* **1978**, *253* (19), 6669–6672.
(112) Wen, D.; Laursen, R. A. A Model for Binding of an Antifreeze Polypeptide to Ice. *Biophys. J.* **1992**, *63* (6), 1659–1662. https://doi.org/10.1016/S0006-3495(92)81750-2.
(113) Yeh, Y.; Feeney, R. E. Antifreeze Proteins: Structures and Mechanisms of Function. *Chem. Rev.* **1996**, *96* (2), 601–618. https://doi.org/10.1021/cr950260c.
(114) Gharib, G.; Saeidiharzand, S.; Sadaghiani, A. K.; Koşar, A. Antifreeze Proteins: A Tale of Evolution From Origin to Energy Applications. *Front. Bioeng. Biotechnol.* **2022**, *9*, 770588. https://doi.org/10.3389/fbioe.2021.770588.
(115) Tachibana, Y.; Fletcher, G. L.; Fujitani, N.; Tsuda, S.; Monde, K.; Nishimura, S.-I. Antifreeze Glycoproteins: Elucidation of the Structural Motifs That Are Essential for Antifreeze Activity. *Angew. Chem. Int. Ed.* **2004**, *43* (7), 856–862. https://doi.org/10.1002/anie.200353110.
(116) Haymet, A. D. J.; Ward, L. G.; Harding, M. M.; Knight, C. A. Valine Substituted Winter Flounder `antifreeze': Preservation of Ice Growth Hysteresis. *FEBS Lett.* **1998**, *430* (3), 301–306. https://doi.org/10.1016/S0014-5793(98)00652-8.
(117) Chao, H.; Houston, M. E.; Hodges, R. S.; Kay, C. M.; Sykes, B. D.; Loewen, M. C.; Davies, P. L.; Sönnichsen, F. D. A Diminished Role for Hydrogen Bonds in Antifreeze Protein Binding to Ice. *Biochemistry* **1997**, *36* (48), 14652–14660. https://doi.org/10.1021/bi970817d.

(118) Komatsu, S.; DeVries, A. L.; Feeney, R. E. Studies of the Structure of Freezing Point-Depressing Glycoproteins from an Antarctic Fish. *J. Biol. Chem.* **1970**, *245* (11), 2909–2913.
(119) Urbańczyk, M.; Góra, J.; Latajka, R.; Sewald, N. Antifreeze Glycopeptides: From Structure and Activity Studies to Current Approaches in Chemical Synthesis. *Amino Acids* **2017**, *49* (2), 209–222. https://doi.org/10.1007/s00726-016-2368-z.
(120) Madura, J. D.; Baran, K.; Wierzbicki, A. Molecular Recognition and Binding of Thermal Hysteresis Proteins to Ice. *J. Mol. Recognit.* **2000**, *13* (2), 101–113. https://doi.org/10.1002/(SICI)1099-1352(200003/04)13:2<101::AID-JMR493>3.0.CO;2-9.
(121) McDonald, S. M.; Brady, J. W.; Clancy, P. Molecular Dynamics Simulations of a Winter Flounder "Antifreeze" Polypeptide in Aqueous Solution. *Biopolymers* **1993**, *33* (10), 1481–1503. https://doi.org/10.1002/bip.360331002.
(122) Sicheri, F.; Yang, D. S. C. Ice-Binding Structure and Mechanism of an Antifreeze Protein from Winter Flounder. *Nature* **1995**, *375* (6530), 427–431. https://doi.org/10.1038/375427a0.
(123) Madura, J. D.; Taylor, M. S.; Wierzbicki, A.; Harrington, J. P.; Sikes, C. S.; Sönnichsen, F. The Dynamics and Binding of a Type III Antifreeze Protein in Water and on Ice. *J. Mol. Struct. THEOCHEM* **1996**, *388*, 65–77. https://doi.org/10.1016/S0166-1280(96)80020-0.
(124) Cheng, A.; Merz, K. M. Ice-Binding Mechanism of Winter Flounder Antifreeze Proteins. *Biophys. J.* **1997**, *73* (6), 2851–2873. https://doi.org/10.1016/S0006-3495(97)78315-2.
(125) Jorgensen, H.; Mori, M.; Matsui, H.; Kanaoka, M.; Yanagi, H.; Yabusaki, Y.; Kikuzono, Y. Molecular Dynamics Simulation of Winter Flounder Antifreeze Protein Variants in Solution: Correlation between Side Chain Spacing and Ice Lattice. *Protein Eng. Des. Sel.* **1993**, *6* (1), 19–27. https://doi.org/10.1093/protein/6.1.19.
(126) Zhang, W.; Laursen, R. A. Structure-Function Relationships in a Type I Antifreeze Polypeptide. *J. Biol. Chem.* **1998**, *273* (52), 34806–34812. https://doi.org/10.1074/jbc.273.52.34806.
(127) Inada, T.; Lu, S.-S. Thermal Hysteresis Caused by Non-Equilibrium Antifreeze Activity of Poly(Vinyl Alcohol). *Chem. Phys. Lett.* **2004**, *394* (4–6), 361–365. https://doi.org/10.1016/j.cplett.2004.07.021.
(128) Weng, L.; Stott, S. L.; Toner, M. Molecular Dynamics at the Interface between Ice and Poly(Vinyl Alcohol) and Ice Recrystallization Inhibition. *Langmuir* **2018**, *34* (17), 5116–5123. https://doi.org/10.1021/acs.langmuir.7b03243.
(129) Inada, T.; Lu, S.-S. Inhibition of Recrystallization of Ice Grains by Adsorption of Poly(Vinyl Alcohol) onto Ice Surfaces. *Cryst. Growth Des.* **2003**, *3* (5), 747–752. https://doi.org/10.1021/cg0340300.
(130) Knight, C. A.; Wen, D.; Laursen, R. A. Nonequilibrium Antifreeze Peptides and the Recrystallization of Ice. *Cryobiology* **1995**, *32* (1), 23–34. https://doi.org/10.1006/cryo.1995.1002.
(131) Bachtiger, F.; Congdon, T. R.; Stubbs, C.; Gibson, M. I.; Sosso, G. C. The Atomistic Details of the Ice Recrystallisation Inhibition Activity of PVA. *Nat. Commun.* **2021**, *12* (1), 1323. https://doi.org/10.1038/s41467-021-21717-z.
(132) Su, C.; Wang, H.; Cai, W.; Shao, X. Ice Growth Inhibition by Poly(Vinyl Alcohol): Insights from near-Infrared Spectroscopy and Molecular Dynamics Simulation. *J. Mol. Liq.* **2024**, *402*, 124795. https://doi.org/10.1016/j.molliq.2024.124795.
(133) Ahmed, A. I.; Osuga, D. T.; Feeney, R. E. Antifreeze Glycoprotein from an Antarctic Fish. *J. Biol. Chem.* **1973**, *248* (24), 8524–8527. https://doi.org/10.1016/S0021-9258(19)43164-5.
(134) Schrag, J. D.; Devries, A. L. The Effect of Freezing Rate on the Cooperativity of Antifreeze Glycopeptides. *Comp. Biochem. Physiol. A Physiol.* **1983**, *74* (2), 381–385. https://doi.org/10.1016/0300-9629(83)90619-9.
(135) Peltier, R.; Brimble, M. A.; Wojnar, J. M.; Williams, D. E.; Evans, C. W.; DeVries, A. L. Synthesis and Antifreeze Activity of Fish Antifreeze Glycoproteins and Their Analogues. *Chem. Sci.* **2010**, *1* (5), 538. https://doi.org/10.1039/c0sc00194e.
(136) William, N.; Mangan, S.; Ben, R. N.; Acker, J. P. Engineered Compounds to Control Ice Nucleation and Recrystallization. *Annu. Rev. Biomed. Eng.* **2023**, *25* (1), 333–362. https://doi.org/10.1146/annurev-bioeng-082222-015243.

(137) Christner, B. C. Bioprospecting for Microbial Products That Affect Ice Crystal Formation and Growth. *Appl. Microbiol. Biotechnol.* **2010**, *85* (3), 481–489. https://doi.org/10.1007/s00253-009-2291-2.
(138) Meldolesi, A. GM Fish Ice Cream. *Nat. Biotechnol.* **2009**, *27* (8), 682–682. https://doi.org/10.1038/nbt0809-682b.
(139) Tab, M. M.; Hashim, N. H. F.; Najimudin, N.; Mahadi, N. M.; Bakar, F. D. A.; Murad, A. M. A. Large-Scale Production of Glaciozyma Antarctica Antifreeze Protein 1 (Afp1) by Fed-Batch Fermentation of Pichia Pastoris. *Arab. J. Sci. Eng.* **2018**, *43* (1), 133–141. https://doi.org/10.1007/s13369-017-2738-1.
(140) Solomon, R. G.; Appels, R. Stable, High-Level Expression of a Type I Antifreeze Protein in Escherichia Coli. *Protein Expr. Purif.* **1999**, *16* (1), 53–62. https://doi.org/10.1006/prep.1999.1040.
(141) Robles, V.; G. Valcarce, D.; F. Riesco, M. The Use of Antifreeze Proteins in the Cryopreservation of Gametes and Embryos. *Biomolecules* **2019**, *9* (5), 181. https://doi.org/10.3390/biom9050181.
(142) Koshimoto, C.; Mazur, P. Effects of Warming Rate, Temperature, and Antifreeze Proteins on the Survival of Mouse Spermatozoa Frozen at an Optimal Rate. *Cryobiology* **2002**, *45* (1), 49–59. https://doi.org/10.1016/S0011-2240(02)00105-0.
(143) Ishiguro, H.; Rubinsky, B. Mechanical Interactions between Ice Crystals and Red Blood Cells during Directional Solidification. *Cryobiology* **1994**, *31* (5), 483–500. https://doi.org/10.1006/cryo.1994.1059.
(144) Riesco, M. F.; Martínez-Pastor, F.; Chereguini, O.; Robles, V. Evaluation of Zebrafish (Danio Rerio) PGCs Viability and DNA Damage Using Different Cryopreservation Protocols. *Theriogenology* **2012**, *77* (1), 122-130.e2. https://doi.org/10.1016/j.theriogenology.2011.07.024.
(145) Correia, L. F. L.; Alves, B. R. C.; Batista, R. I. T. P.; Mermillod, P.; Souza-Fabjan, J. M. G. Antifreeze Proteins for Low-Temperature Preservation in Reproductive Medicine: A Systematic Review over the Last Three Decades. *Theriogenology* **2021**, *176*, 94–103. https://doi.org/10.1016/j.theriogenology.2021.09.025.
(146) Mehdipour, M.; Daghigh-Kia, H.; Najafi, A.; Martínez-Pastor, F. Type III Antifreeze Protein (AFP) Improves the Post-Thaw Quality and in Vivo Fertility of Rooster Spermatozoa. *Poult. Sci.* **2021**, *100* (8), 101291. https://doi.org/10.1016/j.psj.2021.101291.
(147) Eniade, A.; Purushotham, M.; Ben, R. N.; Wang, J. B.; Horwath, K. A Serendipitous Discovery of Antifreeze Protein-Specific Activity in C-Linked Antifreeze Glycoprotein Analogs. *Cell Biochem. Biophys.* **2003**, *38* (2), 115–124. https://doi.org/10.1385/CBB:38:2:115.
(148) Liu, S.; Ben, R. N. *C*-Linked Galactosyl Serine AFGP Analogues as Potent Recrystallization Inhibitors. *Org. Lett.* **2005**, *7* (12), 2385–2388. https://doi.org/10.1021/ol050677x.
(149) Horwath, K. L.; Easton, C. M.; Poggioli, G. J.; Myers, K.; Schnorr, I. L. Tracking the Profile of a Specific Antifreeze Protein and Its Contribution to the Thermal Hysteresis Activity in Cold Hardy Insects. *Eur J Entomol* **1996**, *93* (3), 419–433.
(150) Jackman, J.; Noestheden, M.; Moffat, D.; Pezacki, J. P.; Findlay, S.; Ben, R. N. Assessing Antifreeze Activity of AFGP 8 Using Domain Recognition Software. *Biochem. Biophys. Res. Commun.* **2007**, *354* (2), 340–344. https://doi.org/10.1016/j.bbrc.2006.12.225.
(151) Knight, C. A.; Hallett, J.; DeVries, A. L. Solute Effects on Ice Recrystallization: An Assessment Technique. *Cryobiology* **1988**, *25* (1), 55–60. https://doi.org/10.1016/0011-2240(88)90020-X.
(152) Leclère, M.; Kwok, B. K.; Wu, L. K.; Allan, D. S.; Ben, R. N. *C*-Linked Antifreeze Glycoprotein (*C*-AFGP) Analogues as Novel Cryoprotectants. *Bioconjug. Chem.* **2011**, *22* (9), 1804–1810. https://doi.org/10.1021/bc2001837.
(153) Li, T.; Zhao, Y.; Zhong, Q.; Wu, T. Inhibiting Ice Recrystallization by Nanocelluloses. *Biomacromolecules* **2019**, *20* (4), 1667–1674. https://doi.org/10.1021/acs.biomac.9b00027.
(154) Biggs, C. I.; Stubbs, C.; Graham, B.; Fayter, A. E. R.; Hasan, M.; Gibson, M. I. Mimicking the Ice Recrystallization Activity of Biological Antifreezes. When Is a New Polymer "Active"? *Macromol. Biosci.* **2019**, 1900082. https://doi.org/10.1002/mabi.201900082.

(155) Tachibana, Y.; Matsubara, N.; Nakajima, F.; Tsuda, T.; Tsuda, S.; Monde, K.; Nishimura, S.-I. Efficient and Versatile Synthesis of Mucin-like Glycoprotein Mimics. *Tetrahedron* **2002**, *58* (51), 10213–10224. https://doi.org/10.1016/S0040-4020(02)01359-5.

(156) Czechura, P.; Tam, R. Y.; Dimitrijevic, E.; Murphy, A. V.; Ben, R. N. The Importance of Hydration for Inhibiting Ice Recrystallization with C-Linked Antifreeze Glycoproteins. *J. Am. Chem. Soc.* **2008**, *130* (10), 2928–2929. https://doi.org/10.1021/ja7103262.

(157) Tam, R. Y.; Ferreira, S. S.; Czechura, P.; Chaytor, J. L.; Ben, R. N. Hydration Index - A Better Parameter for Explaining Small Molecule Hydration in Inhibition of Ice Recrystallization. *J. Am. Chem. Soc.* **2008**, *130* (51), 17494–17501. https://doi.org/10.1021/ja806284x.

(158) Capicciotti, C. The Rational Design of Potent Ice Recrystallization Inhibitors for Use as Novel Cryoprotectants. PhD Thesis, University of Ottawa, Ottawa, ON, 2014. http://ruor.uottawa.ca/handle/10393/30634 (accessed 2022-09-22).

(159) Balcerzak, A. K.; Capicciotti, C. J.; Briard, J. G.; Ben, R. N. Designing Ice Recrystallization Inhibitors: From Antifreeze (Glyco)Proteins to Small Molecules. *RSC Adv* **2014**, *4* (80), 42682–42696. https://doi.org/10.1039/C4RA06893A.

(160) Ampaw, A.; Charlton, T. A.; Briard, J. G.; Ben, R. N. Designing the next Generation of Cryoprotectants - From Proteins to Small Molecules. *Pept. Sci.* **2019**, *111* (1), e24086. https://doi.org/10.1002/pep2.24086.

(161) Capicciotti, C. J.; Leclère, M.; Perras, F. A.; Bryce, D. L.; Paulin, H.; Harden, J.; Liu, Y.; Ben, R. N. Potent Inhibition of Ice Recrystallization by Low Molecular Weight Carbohydrate-Based Surfactants and Hydrogelators. *Chem. Sci.* **2012**, *3* (5), 1408. https://doi.org/10.1039/c2sc00885h.

(162) Capicciotti, C. J.; Kurach, J. D. R.; Turner, T. R.; Mancini, R. S.; Acker, J. P.; Ben, R. N. Small Molecule Ice Recrystallization Inhibitors Enable Freezing of Human Red Blood Cells with Reduced Glycerol Concentrations. *Sci. Rep.* **2015**, *5* (1), 9692. https://doi.org/10.1038/srep09692.

(163) Baron, C.; Thompson, T. E. Solubilization of Bacterial Membrane Proteins Using Alkyl Glucosides and Dioctanoyl Phosphatidylcholine. *Biochim. Biophys. Acta BBA - Biomembr.* **1975**, *382* (3), 276–285. https://doi.org/10.1016/0005-2736(75)90270-9.

(164) Hildreth, J. E. K. *N*-D-Gluco-*N*-Methylalkanamide Compounds, a New Class of Non-Ionic Detergents for Membrane Biochemistry. *Biochem. J.* **1982**, *207* (2), 363–366. https://doi.org/10.1042/bj2070363.

(165) Trant, J. F.; Biggs, R. A.; Capicciotti, C. J.; Ben, R. N. Developing Highly Active Small Molecule Ice Recrystallization Inhibitors Based upon C-Linked Antifreeze Glycoprotein Analogues. *RSC Adv.* **2013**, *3* (48), 26005. https://doi.org/10.1039/c3ra43835j.

(166) Briard, J. G.; Jahan, S.; Chandran, P.; Allan, D.; Pineault, N.; Ben, R. N. Small-Molecule Ice Recrystallization Inhibitors Improve the Post-Thaw Function of Hematopoietic Stem and Progenitor Cells. *ACS Omega* **2016**, *1* (5), 1010–1018. https://doi.org/10.1021/acsomega.6b00178.

(167) Capicciotti, C. J.; Mancini, R. S.; Turner, T. R.; Koyama, T.; Alteen, M. G.; Doshi, M.; Inada, T.; Acker, J. P.; Ben, R. N. *O*-Aryl-Glycoside Ice Recrystallization Inhibitors as Novel Cryoprotectants: A Structure–Function Study. *ACS Omega* **2016**, *1* (4), 656–662. https://doi.org/10.1021/acsomega.6b00163.

(168) Briard, J. G. The Rational Design and Use of Novel Small-Molecule Ice Recrystallization Inhibitors for the Cryopreservation of Hematopoietic Stem Cells and Red Blood Cells. PhD Thesis, University of Ottawa, Ottawa, ON, 2016. http://ruor.uottawa.ca/handle/10393/35005 (accessed 2022-09-22).

(169) Abraham, S.; Keillor, K.; Capicciotti, C. J.; Perley-Robertson, G. E.; Keillor, J. W.; Ben, R. N. Quantitative Analysis of the Efficacy and Potency of Novel Small Molecule Ice Recrystallization Inhibitors. *Cryst. Growth Des.* **2015**, *15* (10), 5034–5039. https://doi.org/10.1021/acs.cgd.5b00995.

(170) Abraham, S. Development and Implementation of a Kinetic Quantitative Analysis of Novel Small Molecule Ice Recrystallization Inhibitors. MSc Thesis, University of Ottawa, Ottawa, ON, 2015. http://ruor.uottawa.ca/handle/10393/33189 (accessed 2022-09-22).

(171) Tomczak, M. M.; Marshall, C. B.; Gilbert, J. A.; Davies, P. L. A Facile Method for Determining Ice Recrystallization Inhibition by Antifreeze Proteins. *Biochem. Biophys. Res. Commun.* **2003**, *311* (4), 1041–1046. https://doi.org/10.1016/j.bbrc.2003.10.106.

(172) Smallwood, M.; Worrall, D.; Byass, L.; Elias, L.; Ashford, D.; Doucet, C. J.; Holt, C.; Telford, J.; Lillford, P.; Bowles, D. J. Isolation and Characterization of a Novel Antifreeze Protein from Carrot (Daucus Carota). *Biochem. J.* **1999**, *340* (2), 385–391.
(173) Mitchell, D. E.; Congdon, T.; Rodger, A.; Gibson, M. I. Gold Nanoparticle Aggregation as a Probe of Antifreeze (Glyco) Protein-Inspired Ice Recrystallization Inhibition and Identification of New IRI Active Macromolecules. *Sci. Rep.* **2015**, *5* (1), 15716. https://doi.org/10.1038/srep15716.
(174) Graham, L. A.; Agrawal, P.; Oleschuk, R. D.; Davies, P. L. High-Capacity Ice-Recrystallization Endpoint Assay Employing Superhydrophobic Coatings That Is Equivalent to the 'Splat' Assay. *Cryobiology* **2018**, *81*, 138–144. https://doi.org/10.1016/j.cryobiol.2018.01.011.
(175) Ampaw, A. A.; Sibthorpe, A.; Ben, R. N. Use of Ice Recrystallization Inhibition Assays to Screen for Compounds That Inhibit Ice Recrystallization. In *Cryopreservation and Freeze-Drying Protocols*; Wolkers, W. F., Oldenhof, H., Eds.; Methods in Molecular Biology; Springer US: New York, NY, 2021; Vol. 2180, pp 271–283. https://doi.org/10.1007/978-1-0716-0783-1_9.
(176) Adam, M. K. Improving the Engraftment Activities of Cryopreserved Human Umbilical Cord Blood Through the Development of Novel Glyco(Peptide)-Based Aryl Ice Recrystallization Inhibitors. PhD Thesis, University of Ottawa, Ottawa, ON, 2020. http://ruor.uottawa.ca/handle/10393/40808 (accessed 2022-09-22).
(177) Ampaw, A. A. Addressing Solubility Limitations in Small-Molecule Ice Recrystallization Inhibitors and Evaluating Their Use in Hematopoietic Stem Cell and Red Blood Cell Cryopreservation. PhD Thesis, University of Ottawa, Ottawa, ON, 2022. http://ruor.uottawa.ca/handle/10393/43271 (accessed 2022-09-22).
(178) Singh, J. S. Correlation of Ice Recrystallization Inhibition Activity to Hydration Parameters and Effect of the C-3 Hydroxyl Group. MSc Thesis, University of Ottawa, 2022. http://ruor.uottawa.ca/handle/10393/43628 (accessed 2022-09-22).
(179) Smith, A. Prevention of Hemolysis during Freezing and Thawing of Red Blood Cells. *The Lancet* **1950**, *256* (6644), 910–911. https://doi.org/10.1016/S0140-6736(50)91861-7.
(180) Yong, K. W.; Wan Safwani, W. K. Z.; Xu, F.; Wan Abas, W. A. B.; Choi, J. R.; Pingguan-Murphy, B. Cryopreservation of Human Mesenchymal Stem Cells for Clinical Applications: Current Methods and Challenges. *Biopreservation Biobanking* **2015**, *13* (4), 231–239. https://doi.org/10.1089/bio.2014.0104.
(181) Pollock, K.; Sumstad, D.; Kadidlo, D.; McKenna, D. H.; Hubel, A. Clinical Mesenchymal Stromal Cell Products Undergo Functional Changes in Response to Freezing. *Cytotherapy* **2015**, *17* (1), 38–45. https://doi.org/10.1016/j.jcyt.2014.06.008.
(182) Marquez-Curtis, L. A.; Janowska-Wieczorek, A.; McGann, L. E.; Elliott, J. A. W. Mesenchymal Stromal Cells Derived from Various Tissues: Biological, Clinical and Cryopreservation Aspects. *Cryobiology* **2015**, *71* (2), 181–197. https://doi.org/10.1016/j.cryobiol.2015.07.003.
(183) François, M.; Copland, I. B.; Yuan, S.; Romieu-Mourez, R.; Waller, E. K.; Galipeau, J. Cryopreserved Mesenchymal Stromal Cells Display Impaired Immunosuppressive Properties as a Result of Heat-Shock Response and Impaired Interferon-γ Licensing. *Cytotherapy* **2012**, *14* (2), 147–152. https://doi.org/10.3109/14653249.2011.623691.
(184) Moll, G.; Alm, J. J.; Davies, L. C.; Von Bahr, L.; Heldring, N.; Stenbeck-Funke, L.; Hamad, O. A.; Hinsch, R.; Ignatowicz, L.; Locke, M.; Lönnies, H.; Lambris, J. D.; Teramura, Y.; Nilsson-Ekdahl, K.; Nilsson, B.; Blanc, K. Do Cryopreserved Mesenchymal Stromal Cells Display Impaired Immunomodulatory and Therapeutic Properties? *Stem Cells* **2014**, *32* (9), 2430–2442. https://doi.org/10.1002/stem.1729.
(185) Baust, J. G.; Gao, D.; Baust, J. M. Cryopreservation: An Emerging Paradigm Change. *Organogenesis* **2009**, *5* (3), 90–96. https://doi.org/10.4161/org.5.3.10021.
(186) Baust, J. M.; Vogel, M. J.; Van Buskirk, R.; Baust, J. G. A Molecular Basis of Cryopreservation Failure and Its Modulation to Improve Cell Survival. *Cell Transplant.* **2001**, *10* (7), 561–571.
(187) Hess, J. R. Red Cell Freezing and Its Impact on the Supply Chain. *Transfus. Med.* **2004**, *14* (1), 1–8. https://doi.org/10.1111/j.0958-7578.2004.00472.x.

(188) McMunn, L. E.; Walsh, E. M.; Ben, R. N. Targeted Development and Optimization of Small-Molecule Ice Recrystallization Inhibitors (IRIs) for the Cryopreservation of Biological Systems. *Cryoletters* **2024**, *45* (2), 69–87. https://doi.org/10.54680/fr24210110112.
(189) Hunt, C. J. Cryopreservation of Human Stem Cells for Clinical Application: A Review. *Transfus. Med. Hemotherapy* **2011**, *38* (2), 107–123. https://doi.org/10.1159/000326623.
(190) Iafolla, M. A. J.; Tay, J.; Allan, D. S. Transplantation of Umbilical Cord Blood–Derived Cells for Novel Indications in Regenerative Therapy or Immune Modulation: A Scoping Review of Clinical Studies. *Biol. Blood Marrow Transplant.* **2014**, *20* (1), 20–25. https://doi.org/10.1016/j.bbmt.2013.09.010.
(191) Harris, D. T. Non-Haematological Uses of Cord Blood Stem Cells. *Br. J. Haematol.* **2009**, *147* (2), 177–184. https://doi.org/10.1111/j.1365-2141.2009.07767.x.
(192) Ullah, I.; Subbarao, R. B.; Rho, G. J. Human Mesenchymal Stem Cells - Current Trends and Future Prospective. *Biosci. Rep.* **2015**, *35* (2), e00191. https://doi.org/10.1042/BSR20150025.
(193) Bashir, J.; Sherman, A.; Lee, H.; Kaplan, L.; Hare, J. M. Mesenchymal Stem Cell Therapies in the Treatment of Musculoskeletal Diseases. *PM&R* **2014**, *6* (1), 61–69. https://doi.org/10.1016/j.pmrj.2013.05.007.
(194) Freitag, J.; Bates, D.; Boyd, R.; Shah, K.; Barnard, A.; Huguenin, L.; Tenen, A. Mesenchymal Stem Cell Therapy in the Treatment of Osteoarthritis: Reparative Pathways, Safety and Efficacy – a Review. *BMC Musculoskelet. Disord.* **2016**, *17* (1), 230. https://doi.org/10.1186/s12891-016-1085-9.
(195) Thakker, R.; Yang, P. Mesenchymal Stem Cell Therapy for Cardiac Repair. *Curr. Treat. Options Cardiovasc. Med.* **2014**, *16* (7), 323. https://doi.org/10.1007/s11936-014-0323-4.
(196) Kalinina, N. I.; Sysoeva, V. Y.; Rubina, K. A.; Parfenova, Y. V.; Tkachuk, V. A. Mesenchymal Stem Cells in Tissue Growth and Repair. *Acta Naturae* **2011**, *3* (4), 30–37. https://doi.org/10.3389/fimmu.2013.00201.
(197) Lavorato, A.; Raimondo, S.; Boido, M.; Muratori, L.; Durante, G.; Cofano, F.; Vincitorio, F.; Petrone, S.; Titolo, P.; Tartara, F.; Vercelli, A.; Garbossa, D. Mesenchymal Stem Cell Treatment Perspectives in Peripheral Nerve Regeneration: Systematic Review. *Int. J. Mol. Sci.* **2021**, *22* (2), 572. https://doi.org/10.3390/ijms22020572.
(198) Margiana, R.; Markov, A.; Zekiy, A. O.; Hamza, M. U.; Al-Dabbagh, K. A.; Al-Zubaidi, S. H.; Hameed, N. M.; Ahmad, I.; Sivaraman, R.; Kzar, H. H.; Al-Gazally, M. E.; Mustafa, Y. F.; Siahmansouri, H. Clinical Application of Mesenchymal Stem Cell in Regenerative Medicine: A Narrative Review. *Stem Cell Res. Ther.* **2022**, *13* (1), 366. https://doi.org/10.1186/s13287-022-03054-0.
(199) Singh, V. K.; Kalsan, M.; Kumar, N.; Saini, A.; Chandra, R. Induced Pluripotent Stem Cells: Applications in Regenerative Medicine, Disease Modeling, and Drug Discovery. *Front. Cell Dev. Biol.* **2015**, *3* (2). https://doi.org/10.3389/fcell.2015.00002.
(200) Wu, S. M.; Hochedlinger, K. Harnessing the Potential of Induced Pluripotent Stem Cells for Regenerative Medicine. *Nat. Cell Biol.* **2011**, *13* (5), 497–505. https://doi.org/10.1038/ncb0511-497.
(201) Rubinstein, P.; Dobrila, L.; Rosenfield, R. E.; Adamson, J. W.; Migliaccio, G.; Migliaccio, A. R.; Taylor, P. E.; Stevens, C. E. Processing and Cryopreservation of Placental/Umbilical Cord Blood for Unrelated Bone Marrow Reconstitution. *Proc. Natl. Acad. Sci.* **1995**, *92* (22), 10119–10122. https://doi.org/10.1073/pnas.92.22.10119.
(202) Hornberger, K.; Yu, G.; McKenna, D.; Hubel, A. Cryopreservation of Hematopoietic Stem Cells: Emerging Assays, Cryoprotectant Agents, and Technology to Improve Outcomes. *Transfus. Med. Hemotherapy* **2019**, *46* (3), 188–196. https://doi.org/10.1159/000496068.
(203) Nishiyama, Y.; Iwanami, A.; Kohyama, J.; Itakura, G.; Kawabata, S.; Sugai, K.; Nishimura, S.; Kashiwagi, R.; Yasutake, K.; Isoda, M.; Matsumoto, M.; Nakamura, M.; Okano, H. Safe and Efficient Method for Cryopreservation of Human Induced Pluripotent Stem Cell-Derived Neural Stem and Progenitor Cells by a Programmed Freezer with a Magnetic Field. *Neurosci. Res.* **2016**, *107*, 20–29. https://doi.org/10.1016/j.neures.2015.11.011.

(204) Imaizumi, K.; Nishishita, N.; Muramatsu, M.; Yamamoto, T.; Takenaka, C.; Kawamata, S.; Kobayashi, K.; Nishikawa, S.; Akuta, T. A Simple and Highly Effective Method for Slow-Freezing Human Pluripotent Stem Cells Using Dimethyl Sulfoxide, Hydroxyethyl Starch and Ethylene Glycol. *PLoS ONE* **2014**, *9* (2), e88696. https://doi.org/10.1371/journal.pone.0088696.

(205) Allan, D.; Keeney, M.; Howson-Jan, K.; Popma, J.; Weir, K.; Bhatia, M.; Sutherland, D.; Chin-Yee, I. Number of Viable CD34+ Cells Reinfused Predicts Engraftment in Autologous Hematopoietic Stem Cell Transplantation. *Bone Marrow Transplant.* **2002**, *29* (12), 967–972. https://doi.org/10.1038/sj.bmt.1703575.

(206) Abrahamsen, J. F.; Wentzel-Larsen, T.; Bruserud, Ø. Autologous Transplantation: The Viable Transplanted CD34+ Cell Dose Measured Post-Thaw Does Not Predict Engraftment Kinetics Better than the Total CD34+ Cell Dose Measured Pre-Freeze in Patients That Receive More than 2×106 CD34+ Cells/Kg. *Cytotherapy* **2004**, *6* (4), 356–362. https://doi.org/10.1080/14653240410004925.

(207) Yang, H.; Acker, J. P.; Cabuhat, M.; Letcher, B.; Larratt, L.; McGann, L. E. Association of Post-Thaw Viable CD34+ Cells and CFU-GM with Time to Hematopoietic Engraftment. *Bone Marrow Transplant.* **2005**, *35* (9), 881–887. https://doi.org/10.1038/sj.bmt.1704926.

(208) Donaldson, C.; Armitage, W. J.; Denning-Kendall, P. A.; Nicol, A. J.; Bradley, B. A.; Hows, J. M. Optimal Cryopreservation of Human Umbilical Cord Blood. *Bone Marrow Transplant.* **1996**, *18* (4), 725–731.

(209) Gao, D. Y.; Chang, Q.; Liu, C.; Farris, K.; Harvey, K.; McGann, L. E.; English, D.; Jansen, J.; Critser, J. K. Fundamental Cryobiology of Human Hematopoietic Progenitor Cells I: Osmotic Characteristics and Volume Distribution. *Cryobiology* **1998**, *36* (1), 40–48. https://doi.org/10.1006/cryo.1997.2060.

(210) Wu, L.; Al-Hejazi, A.; Filion, L.; Ben, R.; Halpenny, M.; Yang, L.; Giulivi, A.; Allan, D. S. Increased Apoptosis in Cryopreserved Autologous Hematopoietic Progenitor Cells Collected by Apheresis and Delayed Neutrophil Recovery after Transplantation: A Nested Case-Control Study. *Cytotherapy* **2012**, *14* (2), 205–214. https://doi.org/10.3109/14653249.2011.610302.

(211) Sasnoor, L. M.; Kale, V. P.; Limaye, L. S. Prevention of Apoptosis as a Possible Mechanism behind Improved Cryoprotection of Hematopoietic Cells by Catalase and Trehalose: *Transplantation* **2005**, *80* (9), 1251–1260. https://doi.org/10.1097/01.tp.0000169028.01327.90.

(212) Jahan, S.; Adam, M. K.; Manesia, J. K.; Doxtator, E.; Ben, R. N.; Pineault, N. Inhibition of Ice Recrystallization during Cryopreservation of Cord Blood Grafts Improves Platelet Engraftment. *Transfusion (Paris)* **2020**, *60* (4), 769–778. https://doi.org/10.1111/trf.15759.

(213) Khan, S.; Poisson, J.; Davila, L.; Ben, R. N.; Courtman, D. W. Small-Molecule Ice Recrystallization Inhibitors Improve Post-Thaw Recovery of Mesenchymal Stromal Cells. *Cytotherapy* **2019**, *21* (5), S76. https://doi.org/10.1016/j.jcyt.2019.03.477.

(214) Poisson, J. Synthesis and In Vitro Applications of Ice Recrystallization Inhibitors. PhD Thesis, University of Ottawa, Ottawa, ON, 2019. https://ruor.uottawa.ca/handle/10393/39466.

(215) Alasmar, S.; Huang, J.; Chopra, K.; Baumann, E.; Aylsworth, A.; Hewitt, M.; Sandhu, J. K.; Tauskela, J. S.; Ben, R. N.; Jezierski, A. Improved Cryopreservation of Human Induced Pluripotent Stem Cell (iPSC) and iPSC Derived Neurons Using Ice-Recrystallization Inhibitors. *Stem Cells* **2023**, sxad059. https://doi.org/10.1093/stmcls/sxad059.

(216) Alasmar, S. Cryopreservation of Induced Pluripotent Stem Cell Derived Neurons and Primary T-Cells and Natural Killer Cells Using Ice Recrystallization Inhibitor Technology. PhD Thesis, University of Ottawa, Ottawa, ON, 2022. http://ruor.uottawa.ca/handle/10393/44260 (accessed 2023-04-18).

(217) Briard, J. G.; Fernandez, M.; De Luna, P.; Woo, Tom. K.; Ben, R. N. QSAR Accelerated Discovery of Potent Ice Recrystallization Inhibitors. *Sci. Rep.* **2016**, *6* (1), 26403. https://doi.org/10.1038/srep26403.

(218) Poisson, J. S.; Acker, J. P.; Briard, J. G.; Meyer, J. E.; Ben, R. N. Modulating Intracellular Ice Growth with Cell-Permeating Small-Molecule Ice Recrystallization Inhibitors. *Langmuir* **2019**, *35* (23), 7452–7458. https://doi.org/10.1021/acs.langmuir.8b02126.

(219) Chopra, K. Improved Cryopreservation of Induced Pluripotent Stem Cells Using N-Aryl Glycosidic Small Molecule Ice Recrystallization Inhibitors. MSc Thesis, University of Ottawa, Ottawa, ON, 2021. http://ruor.uottawa.ca/handle/10393/42323 (accessed 2022-09-22).
(220) Chopra, K.; Alasmar, S.; Zafer, A.; Huang, J.; Jezierski, A.; Mccomb, S.; Bauman, E.; Ben, R. N. Improving The Cryopreservation Of Human Induced Pluripotent Stem Cells (Ipscs) And Human T-Cells With Ice Recrystallization Inhibitors (Iris). *Cryobiology* **2019**, *91*, 162. https://doi.org/10.1016/j.cryobiol.2019.10.070.
(221) Pittenger, M. F.; Mackay, A. M.; Beck, S. C.; Jaiswal, R. K.; Douglas, R.; Mosca, J. D.; Moorman, M. A.; Simonetti, D. W.; Craig, S.; Marshak, D. R. Multilineage Potential of Adult Human Mesenchymal Stem Cells. *Science* **1999**, *284* (5411), 143–147. https://doi.org/10.1126/science.284.5411.143.
(222) Crisan, M.; Yap, S.; Casteilla, L.; Chen, C.-W.; Corselli, M.; Park, T. S.; Andriolo, G.; Sun, B.; Zheng, B.; Zhang, L.; Norotte, C.; Teng, P.-N.; Traas, J.; Schugar, R.; Deasy, B. M.; Badylak, S.; Bűhring, H.-J.; Giacobino, J.-P.; Lazzari, L.; Huard, J.; Péault, B. A Perivascular Origin for Mesenchymal Stem Cells in Multiple Human Organs. *Cell Stem Cell* **2008**, *3* (3), 301–313. https://doi.org/10.1016/j.stem.2008.07.003.
(223) Wagner, W.; Wein, F.; Seckinger, A.; Frankhauser, M.; Wirkner, U.; Krause, U.; Blake, J.; Schwager, C.; Eckstein, V.; Ansorge, W.; Ho, A. D. Comparative Characteristics of Mesenchymal Stem Cells from Human Bone Marrow, Adipose Tissue, and Umbilical Cord Blood. *Exp. Hematol.* **2005**, *33* (11), 1402–1416. https://doi.org/10.1016/j.exphem.2005.07.003.
(224) Si, Z.; Wang, X.; Sun, C.; Kang, Y.; Xu, J.; Wang, X.; Hui, Y. Adipose-Derived Stem Cells: Sources, Potency, and Implications for Regenerative Therapies. *Biomed. Pharmacother.* **2019**, *114*, 108765. https://doi.org/10.1016/j.biopha.2019.108765.
(225) Krawczenko, A.; Klimczak, A. Adipose Tissue-Derived Mesenchymal Stem/Stromal Cells and Their Contribution to Angiogenic Processes in Tissue Regeneration. *Int. J. Mol. Sci.* **2022**, *23* (5), 2425. https://doi.org/10.3390/ijms23052425.
(226) In `T Anker, P. S.; Scherjon, S. A.; Kleijburg-van Der Keur, C.; Noort, W. A.; Claas, F. H. J.; Willemze, R.; Fibbe, W. E.; Kanhai, H. H. H. Amniotic Fluid as a Novel Source of Mesenchymal Stem Cells for Therapeutic Transplantation. *Blood* **2003**, *102* (4), 1548–1549. https://doi.org/10.1182/blood-2003-04-1291.
(227) Harrell, C. R.; Gazdic, M.; Fellabaum, C.; Jovicic, N.; Djonov, V.; Arsenijevic, N.; Volarevic, V. Therapeutic Potential of Amniotic Fluid Derived Mesenchymal Stem Cells Based on Their Differentiation Capacity and Immunomodulatory Properties. *Curr. Stem Cell Res. Ther.* **2019**, *14* (4), 327–336. https://doi.org/10.2174/1574888X14666190222201749.
(228) Semenova, E.; Grudniak, M. P.; Machaj, E. K.; Bocian, K.; Chroscinska-Krawczyk, M.; Trochonowicz, M.; Stepaniec, I. M.; Murzyn, M.; Zagorska, K. E.; Boruczkowski, D.; Kolanowski, T. J.; Oldak, T.; Rozwadowska, N. Mesenchymal Stromal Cells from Different Parts of Umbilical Cord: Approach to Comparison & Characteristics. *Stem Cell Rev. Rep.* **2021**, *17* (5), 1780–1795. https://doi.org/10.1007/s12015-021-10157-3.
(229) Schüring, A. N.; Schulte, N.; Kelsch, R.; Röpke, A.; Kiesel, L.; Götte, M. Characterization of Endometrial Mesenchymal Stem-like Cells Obtained by Endometrial Biopsy during Routine Diagnostics. *Fertil. Steril.* **2011**, *95* (1), 423–426. https://doi.org/10.1016/j.fertnstert.2010.08.035.
(230) Mutlu, L.; Hufnagel, D.; Taylor, H. S. The Endometrium as a Source of Mesenchymal Stem Cells for Regenerative Medicine1. *Biol. Reprod.* **2015**, *92* (6). https://doi.org/10.1095/biolreprod.114.126771.
(231) Huang, G. T.-J.; Gronthos, S.; Shi, S. Mesenchymal Stem Cells Derived from Dental Tissues *vs* . Those from Other Sources: Their Biology and Role in Regenerative Medicine. *J. Dent. Res.* **2009**, *88* (9), 792–806. https://doi.org/10.1177/0022034509340867.
(232) Gan, L.; Liu, Y.; Cui, D.; Pan, Y.; Zheng, L.; Wan, M. Dental Tissue-Derived Human Mesenchymal Stem Cells and Their Potential in Therapeutic Application. *Stem Cells Int.* **2020**, *2020*, 1–17. https://doi.org/10.1155/2020/8864572.

(233) Maldonado, V. V.; Patel, N. H.; Smith, E. E.; Barnes, C. L.; Gustafson, M. P.; Rao, R. R.; Samsonraj, R. M. Clinical Utility of Mesenchymal Stem/Stromal Cells in Regenerative Medicine and Cellular Therapy. *J. Biol. Eng.* **2023**, *17* (1), 44. https://doi.org/10.1186/s13036-023-00361-9.

(234) Hass, R.; Kasper, C.; Böhm, S.; Jacobs, R. Different Populations and Sources of Human Mesenchymal Stem Cells (MSC): A Comparison of Adult and Neonatal Tissue-Derived MSC. *Cell Commun. Signal.* **2011**, *9* (1), 12. https://doi.org/10.1186/1478-811X-9-12.

(235) Galipeau, J.; Sensébé, L. Mesenchymal Stromal Cells: Clinical Challenges and Therapeutic Opportunities. *Cell Stem Cell* **2018**, *22* (6), 824–833. https://doi.org/10.1016/j.stem.2018.05.004.

(236) Parekkadan, B.; Milwid, J. M. Mesenchymal Stem Cells as Therapeutics. *Annu. Rev. Biomed. Eng.* **2010**, *12* (1), 87–117. https://doi.org/10.1146/annurev-bioeng-070909-105309.

(237) Kannan, S.; Gokul Krishna, S.; Gupta, P. K.; Kolkundkar, U. K. Advantages of Pooling of Human Bone Marrow-Derived Mesenchymal Stromal Cells from Different Donors versus Single-Donor MSCs. *Sci. Rep.* **2024**, *14* (1), 12654. https://doi.org/10.1038/s41598-024-62544-8.

(238) Widholz, B.; Tsitlakidis, S.; Reible, B.; Moghaddam, A.; Westhauser, F. Pooling of Patient-Derived Mesenchymal Stromal Cells Reduces Inter-Individual Confounder-Associated Variation without Negative Impact on Cell Viability, Proliferation and Osteogenic Differentiation. *Cells* **2019**, *8* (6), 633. https://doi.org/10.3390/cells8060633.

(239) Vacanti, V.; Kong, E.; Suzuki, G.; Sato, K.; Canty, J. M.; Lee, T. Phenotypic Changes of Adult Porcine Mesenchymal Stem Cells Induced by Prolonged Passaging in Culture. *J. Cell. Physiol.* **2005**, *205* (2), 194–201. https://doi.org/10.1002/jcp.20376.

(240) Rombouts, W. J. C.; Ploemacher, R. E. Primary Murine MSC Show Highly Efficient Homing to the Bone Marrow but Lose Homing Ability Following Culture. *Leukemia* **2003**, *17* (1), 160–170. https://doi.org/10.1038/sj.leu.2402763.

(241) Chen, G.; Yue, A.; Ruan, Z.; Yin, Y.; Wang, R.; Ren, Y.; Zhu, L. Monitoring the Biology Stability of Human Umbilical Cord-Derived Mesenchymal Stem Cells during Long-Term Culture in Serum-Free Medium. *Cell Tissue Bank.* **2014**, *15* (4), 513–521. https://doi.org/10.1007/s10561-014-9420-6.

(242) Ben-David, U.; Mayshar, Y.; Benvenisty, N. Large-Scale Analysis Reveals Acquisition of Lineage-Specific Chromosomal Aberrations in Human Adult Stem Cells. *Cell Stem Cell* **2011**, *9* (2), 97–102. https://doi.org/10.1016/j.stem.2011.06.013.

(243) Cooper, K.; Viswanathan, C. Establishment of a Mesenchymal Stem Cell Bank. *Stem Cells Int.* **2011**, *2011*, 1–8. https://doi.org/10.4061/2011/905621.

(244) Pal, R.; Hanwate, M.; Totey, S. M. Effect of Holding Time, Temperature and Different Parenteral Solutions on Viability and Functionality of Adult Bone Marrow-Derived Mesenchymal Stem Cells before Transplantation. *J. Tissue Eng. Regen. Med.* **2008**, *2* (7), 436–444. https://doi.org/10.1002/term.109.

(245) Haack-Sørensen, M.; Kastrup, J. Cryopreservation and Revival of Mesenchymal Stromal Cells. In *Mesenchymal Stem Cell Assays and Applications*; Vemuri, M., Chase, L. G., Rao, M. S., Eds.; Methods in Molecular Biology; Humana Press: Totowa, NJ, 2011; Vol. 698, pp 161–174. https://doi.org/10.1007/978-1-60761-999-4_13.

(246) Galipeau, J. Concerns Arising from MSC Retrieval from Cryostorage and Effect on Immune Suppressive Function and Pharmaceutical Usage in Clinical Trials. *ISBT Sci. Ser.* **2013**, *8* (1), 100–101. https://doi.org/10.1111/voxs.12022.

(247) Neuhuber, B.; Swanger, S. A.; Howard, L.; Mackay, A.; Fischer, I. Effects of Plating Density and Culture Time on Bone Marrow Stromal Cell Characteristics. *Exp. Hematol.* **2008**, *36* (9), 1176–1185. https://doi.org/10.1016/j.exphem.2008.03.019.

(248) Briard, J. G.; Poisson, J. S.; Turner, T. R.; Capicciotti, C. J.; Acker, J. P.; Ben, R. N. Small Molecule Ice Recrystallization Inhibitors Mitigate Red Blood Cell Lysis during Freezing, Transient Warming and Thawing. *Sci. Rep.* **2016**, *6* (1), 23619. https://doi.org/10.1038/srep23619.

(249) Waters, L.; Ben, R.; Acker, J. P.; Padula, M. P.; Marks, D. C.; Johnson, L. Characterizing the Ability of an Ice Recrystallization Inhibitor to Improve Platelet Cryopreservation. *Cryobiology* **2020**, *96*, 152–158. https://doi.org/10.1016/j.cryobiol.2020.07.003.

(250) Stewart, D. J. The Enhanced Angiogenic Cell Therapy in Acute Myocardial Infarction (ENACT-AMI) Trial. https://doi.org/10.1186/ISRCTN47943321.
(251) Taljaard, M.; Ward, M. R.; Kutryk, M. J. B.; Courtman, D. W.; Camack, N. J.; Goodman, S. G.; Parker, T. G.; Dick, A. J.; Galipeau, J.; Stewart, D. J. Rationale and Design of Enhanced Angiogenic Cell Therapy in Acute Myocardial Infarction (ENACT-AMI): The First Randomized Placebo-Controlled Trial of Enhanced Progenitor Cell Therapy for Acute Myocardial Infarction. *Am. Heart J.* **2010**, *159* (3), 354–360. https://doi.org/10.1016/j.ahj.2009.12.021.
(252) Brockbank, K. G. M.; Covault, J. C.; Taylor, M. J. *A Guide to Cryopreservation Techniques*; 2004.
(253) Kurach, J.; Brandon-Coatham, M.; Olafson, C.; Turner, T. R.; Phan, C.; Yazdanbakhsh, M.; Osmani, R.; Ehsani-Moghaddam, B.; Clarke, G.; Acker, J. P. Exposure of Cryopreserved Red Cell Concentrates to Real-world Transient Warming Events Has a Negligible Impact on Quality. *Transfusion (Paris)* **2024**, *64* (12), 2353–2363. https://doi.org/10.1111/trf.18054.
(254) Chabot, D.; Tremblay, T.; Paré, I.; Bazin, R.; Loubaki, L. Transient Warming Events Occurring after Freezing Impairs Umbilical Cord–Derived Mesenchymal Stromal Cells Functionality. *Cytotherapy* **2017**, *19* (8), 978–989. https://doi.org/10.1016/j.jcyt.2017.04.005.
(255) Pasha, R.; Howell, A.; Turner, T. R.; Halpenny, M.; Elmoazzen, H.; Acker, J. P.; Pineault, N. Transient Warming Affects Potency of Cryopreserved Cord Blood Units. *Cytotherapy* **2020**, *22* (11), 690–697. https://doi.org/10.1016/j.jcyt.2020.04.039.
(256) Strober, W. Trypan Blue Exclusion Test of Cell Viability. *Curr. Protoc. Immunol.* **2015**, *111* (1). https://doi.org/10.1002/0471142735.ima03bs111.
(257) Rieger, A. M.; Nelson, K. L.; Konowalchuk, J. D.; Barreda, D. R. Modified Annexin V/Propidium Iodide Apoptosis Assay For Accurate Assessment of Cell Death. *J. Vis. Exp.* **2011**, No. 50, 2597. https://doi.org/10.3791/2597.
(258) Krishan, A.; Hamelik, R. M. Click-iT Proliferation Assay with Improved DNA Histograms. *Curr. Protoc. Cytom.* **2010**, *52* (1). https://doi.org/10.1002/0471142956.cy0736s52.
(259) Salic, A.; Mitchison, T. J. A Chemical Method for Fast and Sensitive Detection of DNA Synthesis *in Vivo*. *Proc. Natl. Acad. Sci.* **2008**, *105* (7), 2415–2420. https://doi.org/10.1073/pnas.0712168105.
(260) Fossett, E.; Khan, W. S. Optimising Human Mesenchymal Stem Cell Numbers for Clinical Application: A Literature Review. *Stem Cells Int.* **2012**, *2012*, 1–5. https://doi.org/10.1155/2012/465259.
(261) Colter, D. C.; Class, R.; DiGirolamo, C. M.; Prockop, D. J. Rapid Expansion of Recycling Stem Cells in Cultures of Plastic-Adherent Cells from Human Bone Marrow. *Proc. Natl. Acad. Sci.* **2000**, *97* (7), 3213–3218. https://doi.org/10.1073/pnas.97.7.3213.
(262) Abo-Aziza, F. A. M.; A A, Z. The Impact of Confluence on Bone Marrow Mesenchymal Stem (BMMSC) Proliferation and Osteogenic Differentiation. *Int. J. Hematol.-Oncol. Stem Cell Res.* **2017**, *11* (2), 121–132.
(263) Bartmann, C.; Rohde, E.; Schallmoser, K.; Pürstner, P.; Lanzer, G.; Linkesch, W.; Strunk, D. Two Steps to Functional Mesenchymal Stromal Cells for Clinical Application. *Transfusion (Paris)* **2007**, *47* (8), 1426–1435. https://doi.org/10.1111/j.1537-2995.2007.01219.x.
(264) Sigma Millipore. *Mesenchymal Stem Cell Culture Protocols*. https://www.sigmaaldrich.com/CA/en/technical-documents/protocol/cell-culture-and-cell-culture-analysis/stem-cell-culture/mesenchymal-stem-cell-culture-protocols (accessed 2024-08-22).
(265) Kolliopoulos, V.; Tiffany, A.; Polanek, M.; Harley, B. A. C. DONOR VARIABILITY IN HUMAN MESENCHYMAL STEM CELL OSTEOGENIC RESPONSE AS A FUNCTION OF PASSAGE CONDITIONS AND DONOR SEX. *BioRxiv Prepr. Serv. Biol.* **2023**, 2023.11.12.566781. https://doi.org/10.1101/2023.11.12.566781.
(266) Maged, G.; Abdelsamed, M. A.; Wang, H.; Lotfy, A. The Potency of Mesenchymal Stem/Stromal Cells: Does Donor Sex Matter? *Stem Cell Res. Ther.* **2024**, *15* (1), 112. https://doi.org/10.1186/s13287-024-03722-3.

(267) Siegel, G.; Kluba, T.; Hermanutz-Klein, U.; Bieback, K.; Northoff, H.; Schäfer, R. Phenotype, Donor Age and Gender Affect Function of Human Bone Marrow-Derived Mesenchymal Stromal Cells. *BMC Med.* **2013**, *11* (1), 146. https://doi.org/10.1186/1741-7015-11-146.

(268) Zaim, M.; Karaman, S.; Cetin, G.; Isik, S. Donor Age and Long-Term Culture Affect Differentiation and Proliferation of Human Bone Marrow Mesenchymal Stem Cells. *Ann. Hematol.* **2012**, *91* (8), 1175–1186. https://doi.org/10.1007/s00277-012-1438-x.

(269) Dunn, S. E.; Perry, W. A.; Klein, S. L. Mechanisms and Consequences of Sex Differences in Immune Responses. *Nat. Rev. Nephrol.* **2024**, *20* (1), 37–55. https://doi.org/10.1038/s41581-023-00787-w.

(270) Klein, S. L.; Morgan, R. The Impact of Sex and Gender on Immunotherapy Outcomes. *Biol. Sex Differ.* **2020**, *11* (1), 24. https://doi.org/10.1186/s13293-020-00301-y.

(271) Bangasser, D. A.; Valentino, R. J. Sex Differences in Molecular and Cellular Substrates of Stress. *Cell. Mol. Neurobiol.* **2012**, *32* (5), 709–723. https://doi.org/10.1007/s10571-012-9824-4.

(272) Riss, T. L.; Moravec, R. A.; Niles, A. L.; Duellman, S.; Benink, H. A.; Worzella, T. J.; Minor, L. Cell Viability Assays. In *Assay Guidance Manual*; Markossian, S., Grossman, A., Arkin, M., Auld, D., Austin, C., Baell, J., Brimacombe, K., Chung, T. D. Y., Coussens, N. P., Dahlin, J. L., Devanarayan, V., Foley, T. L., Glicksman, M., Gorshkov, K., Haas, J. V., Hall, M. D., Hoare, S., Inglese, J., Iversen, P. W., Lal-Nag, M., Li, Z., Manro, J. R., McGee, J., McManus, O., Pearson, M., Riss, T., Saradjian, P., Sittampalam, G. S., Tarselli, M., Trask, O. J., Weidner, J. R., Wildey, M. J., Wilson, K., Xia, M., Xu, X., Eds.; Eli Lilly & Company and the National Centre for Advancing Translational Sciences: Bethesda (MD), 2004.

(273) Arzumanian, V. A.; Kiseleva, O. I.; Poverennaya, E. V. The Curious Case of the HepG2 Cell Line: 40 Years of Expertise. *Int. J. Mol. Sci.* **2021**, *22* (23), 13135. https://doi.org/10.3390/ijms222313135.

(274) de Abreu Costa, L.; Henrique Fernandes Ottoni, M.; Dos Santos, M. G.; Meireles, A. B.; Gomes de Almeida, V.; de Fátima Pereira, W.; Alves de Avelar-Freitas, B.; Eustáquio Alvim Brito-Melo, G. Dimethyl Sulfoxide (DMSO) Decreases Cell Proliferation and TNF-α, IFN-γ, and IL-2 Cytokines Production in Cultures of Peripheral Blood Lymphocytes. *Mol. Basel Switz.* **2017**, *22* (11), 1789. https://doi.org/10.3390/molecules22111789.

(275) Dludla, P. V.; Nkambule, B. B.; Mazibuko-Mbeje, S. E.; Nyambuya, T. M.; Silvestri, S.; Orlando, P.; Mxinwa, V.; Louw, J.; Tiano, L. The Impact of Dimethyl Sulfoxide on Oxidative Stress and Cytotoxicity in Various Experimental Models. In *Toxicology*; Elsevier, 2021; pp 243–261. https://doi.org/10.1016/B978-0-12-819092-0.00025-X.

(276) Verheijen, M.; Lienhard, M.; Schrooders, Y.; Clayton, O.; Nudischer, R.; Boerno, S.; Timmermann, B.; Selevsek, N.; Schlapbach, R.; Gmuender, H.; Gotta, S.; Geraedts, J.; Herwig, R.; Kleinjans, J.; Caiment, F. DMSO Induces Drastic Changes in Human Cellular Processes and Epigenetic Landscape in Vitro. *Sci. Rep.* **2019**, *9* (1), 4641. https://doi.org/10.1038/s41598-019-40660-0.

(277) Hristova, S. H.; Zhivkov, A. M. Cytotoxicity of Dimethyl Sulfoxide on Human Hematopoietic Stem Cells at Different Temperatures. *J. Appl. Hematol.* **2023**, *14* (4), 263–267. https://doi.org/10.4103/joah.joah_96_23.

(278) Henrissat, B.; Davies, G. Structural and Sequence-Based Classification of Glycoside Hydrolases. *Curr. Opin. Struct. Biol.* **1997**, *7* (5), 637–644. https://doi.org/10.1016/S0959-440X(97)80072-3.

(279) Passi, S.; Picardo, M.; Nazzaro-Porro, M. Comparative Cytotoxicity of Phenols *in Vitro*. *Biochem. J.* **1987**, *245* (2), 537–542. https://doi.org/10.1042/bj2450537.

(280) Fernandes, C.; Videira, A. J. C.; Veloso, C. D.; Benfeito, S.; Soares, P.; Martins, J. D.; Gonçalves, B.; Duarte, J. F. S.; Santos, A. M. S.; Oliveira, P. J.; Borges, F.; Teixeira, J.; Silva, F. S. G. Cytotoxicity and Mitochondrial Effects of Phenolic and Quinone-Based Mitochondria-Targeted and Untargeted Antioxidants on Human Neuronal and Hepatic Cell Lines: A Comparative Analysis. *Biomolecules* **2021**, *11* (11), 1605. https://doi.org/10.3390/biom11111605.

(281) Chang, Y.; Tai, K.; Huang, F.; Huang, M. Cytotoxic and Nongenotoxic Effects of Phenolic Compounds in Human Pulp Cell Cultures. *J. Endod.* **2000**, *26* (8), 440–443. https://doi.org/10.1097/00004770-200008000-00002.

(282) Selassie, C. D.; Kapur, S.; Verma, R. P.; Rosario, M. Cellular Apoptosis and Cytotoxicity of Phenolic Compounds: A Quantitative Structure−Activity Relationship Study. *J. Med. Chem.* **2005**, *48* (23), 7234–7242. https://doi.org/10.1021/jm050567w.

(283) Merck KGaA. *Glucose in Cell Culture*. https://www.sigmaaldrich.com/CA/en/technical-documents/technical-article/cell-culture-and-cell-culture-analysis/mammalian-cell-culture/glucose (accessed 2024-10-11).

(284) Satchwell, T. J. Generation of Red Blood Cells from Stem Cells: Achievements, Opportunities and Perspectives for Malaria Research. *Front. Cell. Infect. Microbiol.* **2022**, *12*, 1039520. https://doi.org/10.3389/fcimb.2022.1039520.

(285) Nakamura, T.; Fahmi, M.; Tanaka, J.; Seki, K.; Kubota, Y.; Ito, M. Genome-Wide Analysis of Whole Human Glycoside Hydrolases by Data-Driven Analysis in Silico. *Int. J. Mol. Sci.* **2019**, *20* (24), 6290. https://doi.org/10.3390/ijms20246290.

(286) Ling, W.; Zhang, J.; Yuan, Z.; Ren, G.; Zhang, L.; Chen, X.; Rabson, A. B.; Roberts, A. I.; Wang, Y.; Shi, Y. Mesenchymal Stem Cells Use IDO to Regulate Immunity in Tumor Microenvironment. *Cancer Res.* **2014**, *74* (5), 1576–1587. https://doi.org/10.1158/0008-5472.CAN-13-1656.

(287) Gu, T.; Rowswell-Turner, R. B.; Kilinc, M. O.; Egilmez, N. K. Central Role of IFNγ–Indoleamine 2,3-Dioxygenase Axis in Regulation of Interleukin-12–Mediated Antitumor Immunity. *Cancer Res.* **2010**, *70* (1), 129–138. https://doi.org/10.1158/0008-5472.CAN-09-3170.

(288) DelaRosa, O.; Lombardo, E.; Beraza, A.; Mancheño-Corvo, P.; Ramirez, C.; Menta, R.; Rico, L.; Camarillo, E.; García, L.; Abad, J. L.; Trigueros, C.; Delgado, M.; Büscher, D. Requirement of IFN-γ–Mediated Indoleamine 2,3-Dioxygenase Expression in the Modulation of Lymphocyte Proliferation by Human Adipose–Derived Stem Cells. *Tissue Eng. Part A* **2009**, *15* (10), 2795–2806. https://doi.org/10.1089/ten.tea.2008.0630.

(289) Krampera, M.; Cosmi, L.; Angeli, R.; Pasini, A.; Liotta, F.; Andreini, A.; Santarlasci, V.; Mazzinghi, B.; Pizzolo, G.; Vinante, F.; Romagnani, P.; Maggi, E.; Romagnani, S.; Annunziato, F. Role for Interferon-γ in the Immunomodulatory Activity of Human Bone Marrow Mesenchymal Stem Cells. *Stem Cells* **2006**, *24* (2), 386–398. https://doi.org/10.1634/stemcells.2005-0008.

(290) Kern, S.; Eichler, H.; Stoeve, J.; Klüter, H.; Bieback, K. Comparative Analysis of Mesenchymal Stem Cells from Bone Marrow, Umbilical Cord Blood, or Adipose Tissue. *STEM CELLS* **2006**, *24* (5), 1294–1301. https://doi.org/10.1634/stemcells.2005-0342.

(291) Huang, Y.; Dong, Y.; Gao, B.; Ma, R.; Gao, F. L.; Shen, L. Transmembrane Water Transport and Intracellular Ice Formation of Human Umbilical Vein Endothelial Cells During Freezing. *Biopreservation Biobanking* **2022**, *20* (4), 311–316. https://doi.org/10.1089/bio.2022.0111.

(292) Yea, J.-H.; Kim, Y.; Jo, C. H. Comparison of Mesenchymal Stem Cells from Bone Marrow, Umbilical Cord Blood, and Umbilical Cord Tissue in Regeneration of a Full-Thickness Tendon Defect in Vitro and in Vivo. *Biochem. Biophys. Rep.* **2023**, *34*, 101486. https://doi.org/10.1016/j.bbrep.2023.101486.

(293) Jin, H.; Bae, Y.; Kim, M.; Kwon, S.-J.; Jeon, H.; Choi, S.; Kim, S.; Yang, Y.; Oh, W.; Chang, J. Comparative Analysis of Human Mesenchymal Stem Cells from Bone Marrow, Adipose Tissue, and Umbilical Cord Blood as Sources of Cell Therapy. *Int. J. Mol. Sci.* **2013**, *14* (9), 17986–18001. https://doi.org/10.3390/ijms140917986.

(294) American Red Cross. *What Happens to Donated Blood*. https://www.redcrossblood.org/donate-blood/blood-donation-process/what-happens-to-donated-blood.html#:~:text=Red%20cells%20are%20stored%20in,for%20up%20to%20one%20year.

(295) Tinmouth, A.; Fergusson, D.; Yee, I. C.; Hébert, P. C.; ABLE Investigators and the Canadian Critical Care Trials Group. Clinical Consequences of Red Cell Storage in the Critically Ill. *Transfusion (Paris)* **2006**, *46* (11), 2014–2027. https://doi.org/10.1111/j.1537-2995.2006.01026.x.

(296) Högman, C. F.; Meryman, H. T. Storage Parameters Affecting Red Blood Cell Survival and Function after Transfusion. *Transfus. Med. Rev.* **1999**, *13* (4), 275–296. https://doi.org/10.1016/S0887-7963(99)80058-3.

(297) Min, J. J.; Bae, J.-Y.; Kim, T. K.; Hong, D. M.; Hwang, H. Y.; Kim, K.-B.; Han, K.-S.; Jeon, Y. Association between Red Blood Cell Storage Duration and Clinical Outcome in Patients Undergoing

Off-Pump Coronary Artery Bypass Surgery: A Retrospective Study. *BMC Anesthesiol.* **2014**, *14* (1), 95. https://doi.org/10.1186/1471-2253-14-95.

(298) Cholette, J. M.; Pietropaoli, A. P.; Henrichs, K. F.; Alfieris, G. M.; Powers, K. S.; Phipps, R.; Spinelli, S. L.; Swartz, M.; Gensini, F.; Daugherty, L. E.; Nazarian, E.; Rubenstein, J. S.; Sweeney, D.; Eaton, M.; Blumberg, N. Longer RBC Storage Duration Is Associated With Increased Postoperative Infections in Pediatric Cardiac Surgery: *Pediatr. Crit. Care Med.* **2015**, *16* (3), 227–235. https://doi.org/10.1097/PCC.0000000000000320.

(299) Weinberg, J. A.; McGwin, G.; Vandromme, M. J.; Marques, M. B.; Melton, S. M.; Reiff, D. A.; Kerby, J. D.; Rue, L. W. Duration of Red Cell Storage Influences Mortality After Trauma. *J. Trauma Inj. Infect. Crit. Care* **2010**, *69* (6), 1427–1432. https://doi.org/10.1097/TA.0b013e3181fa0019.

(300) Bruun-Rasmussen, P.; Kragh Andersen, P.; Banasik, K.; Brunak, S.; Johansson, P. I. Intervening on the Storage Time of RBC Units and Its Effects on Adverse Recipient Outcomes Using Real-World Data. *Blood* **2022**, *139* (25), 3647–3654. https://doi.org/10.1182/blood.2022015892.

(301) Shinde, S.; Bhor, P.; Kale, S.; Vatkar, A.; Kale, S.; Doshi, S.; Dey, J.; Mandal, S.; Simha, K. Causes of Blood Product Discard in the Blood Bank of Tertiary Health Centre over 5 Years: A Retrospective Study. *MGM J. Med. Sci.* **2023**, *10* (2), 252. https://doi.org/10.4103/mgmj.mgmj_77_23.

(302) Saillant, N. N.; Kornblith, L. Z.; Moore, H.; Barrett, C.; Schreiber, M. A.; Cotton, B. A.; Neal, M. D.; Makar, R.; Cap, A. P. The National Blood Shortage—An Impetus for Change. *Ann. Surg.* **2022**, *275* (4), 641–643. https://doi.org/10.1097/SLA.0000000000005393.

(303) Lecak, J.; Scott, K.; Young, C.; Hannon, J.; Acker, J. P. Evaluation of Red Blood Cells Stored at −80°C in Excess of 10 Years. *Transfusion (Paris)* **2004**, *44* (9), 1306–1313. https://doi.org/10.1111/j.1537-2995.2004.03271.x.

(304) Umlas, J.; Jacobson, M.; Kkevy, S. V. Suitable Survival and Half-life of Red Cells after Frozen Storage in Excess of 10 Years. *Transfusion (Paris)* **1991**, *31* (7), 648–649. https://doi.org/10.1046/j.1537-2995.1991.31791368344.x.

(305) Valeri, C. R.; Pivacek, L. E.; Gray, A. D.; Cassidy, G. P.; Leavy, M. E.; Dennis, R. C.; Melaragno, A. J.; Niehoff, J.; Yeston, N.; Emerson, C. P.; Altschule, M. D. The Safety and Therapeutic Effectiveness of Human Red Cells Stored at — 80°C for as Long as 21 Years. *Transfusion (Paris)* **1989**, *29* (5), 429–437. https://doi.org/10.1046/j.1537-2995.1989.29589284145.x.

(306) Valeri, C. R.; Ragno, G.; Pivacek, L. E.; Cassidy, G. P.; Srey, R.; Hansson-Wicher, M.; Leavy, M. E. An Experiment with Glycerol-Frozen Red Blood Cells Stored at -80°C for up to 37 Years. *Vox Sang.* **2000**, *79* (3), 168–174. https://doi.org/10.1046/j.1423-0410.2000.7930168.x.

(307) Rowe, A. W.; Eyster, E.; Kellner, A. Liquid Nitrogen Preservation of Red Blood Cells for Transfusion. *Cryobiology* **1968**, *5* (2), 119–128. https://doi.org/10.1016/S0011-2240(68)80154-3.

(308) Cryopreservation of Red Blood Cells. In *Preservation of Cells*; John Wiley & Sons, Inc.: Hoboken, NJ, USA, 2017; pp 141–146. https://doi.org/10.1002/9781118989883.oth5.

(309) Henkelman, S.; Noorman, F.; Badloe, J. F.; Lagerberg, J. W. M. Utilization and Quality of Cryopreserved Red Blood Cells in Transfusion Medicine. *Vox Sang.* **2015**, *108* (2), 103–112. https://doi.org/10.1111/vox.12218.

(310) Cregan, P.; Donegan, E.; Gotelli, G. Hemolytic Transfusion Reaction Following Transfusion of Frozen and Washed Autologous Red Cells. *Transfusion (Paris)* **1991**, *31* (2), 172–175. https://doi.org/10.1046/j.1537-2995.1991.31291142950.x.

(311) Bechdolt, S.; Schroeder, L. K.; Samia, C.; Schmidt, P. J. In Vivo Hemolysis of Deglycerolized Red Blood Cells. *Arch. Pathol. Lab. Med.* **1986**, *110* (4), 344–345.

(312) Sputtek, A.; Kühnl, P.; Rowe, A. W. Cryopreservation of Erythrocytes, Thrombocytes, and Lymphocytes. *Transfus. Med. Hemotherapy* **2007**, *34* (4), 262–267. https://doi.org/10.1159/000104136.

(313) Valeri, C. R.; Ragno, G.; Van Houten, P.; Rose, L.; Rose, M.; Egozy, Y.; Popovsky, M. A. Automation of the Glycerolization of Red Blood Cells with the High-separation Bowl in the Haemonetics ACP 215 Instrument. *Transfusion (Paris)* **2005**, *45* (10), 1621–1627. https://doi.org/10.1111/j.1537-2995.2005.00588.x.

(314) Bohonek, M.; Seghatchian, J. Emergency Supply Policy of Cryopreserved RBC and PLT: The Czech Republic Concept. *Transfus. Apher. Sci.* **2020**, *59* (3), 102788. https://doi.org/10.1016/j.transci.2020.102788.
(315) Moss, G. S.; Valeri, C. R.; Brodine, C. E. Clinical Experience with the Use of Frozen Blood in Combat Casualties. *N. Engl. J. Med.* **1968**, *278* (14), 747–752. https://doi.org/10.1056/NEJM196804042781401.
(316) Hess, J. R.; Thomas, M. J. G. Blood Use in War and Disaster: Lessons from the Past Century. *Transfusion (Paris)* **2003**, *43* (11), 1622–1633. https://doi.org/10.1046/j.1537-2995.2003.00576.x.
(317) Sen, A.; Khetarpal, A. Comparative Study of Automated Cryopreservation of Red Blood Cells. *Med. J. Armed Forces India* **2013**, *69* (4), 345–350. https://doi.org/10.1016/j.mjafi.2013.06.005.
(318) Bandarenko, N.; Hay, S. N.; Holmberg, J.; Whitley, P.; Taylor, H. L.; Moroff, G.; Rose, L.; Kowalsky, R.; Brumit, M.; Rose, M.; Sawyer, S.; Johnson, A.; McNeil, D.; Popovsky, M. A. Extended Storage of AS-1 and AS-3 Leukoreduced Red Blood Cells for 15 Days after Deglycerolization and Resuspension in AS-3 Using an Automated Closed System. *Transfusion (Paris)* **2004**, *44* (11), 1656–1662. https://doi.org/10.1111/j.1537-2995.2004.04101.x.
(319) Bohoněk, M.; Petráš, M.; Turek, I.; Urbanová, J.; Hrádek, T.; Chmátal, P.; Staropražská, V.; Koštířová, J.; Horčičková, D.; Duchková, S.; Svobodová, J.; Tejčková, E. Quality Evaluation of Frozen Apheresis Red Blood Cell Storage with 21-day Postthaw Storage in Additive Solution 3 and Saline-adenine-glucose-mannitol: Biochemical and Chromium-51 Recovery Measures. *Transfusion (Paris)* **2010**, *50* (5), 1007–1013. https://doi.org/10.1111/j.1537-2995.2009.02532.x.
(320) Lagerberg, J. W. M.; Truijens-de Lange, R.; De Korte, D.; Verhoeven, A. J. Altered Processing of Thawed Red Cells to Improve the in Vitro Quality during Postthaw Storage at 4°C. *Transfusion (Paris)* **2007**, *47* (12), 2242–2249. https://doi.org/10.1111/j.1537-2995.2007.01453.x.
(321) Khan, S.; Macaulay, A.; McMunn, L. E.; Ben, R. N.; Courtman, D. W. Mesenchymal Stem/Stromal Cells: ICE RECRYSTALLIZATION INHIBITOR INCREASES POST-THAW FUNCTIONAL CAPACITY OF BONE MARROW AND UMBILICAL CORD DERIVED MESENCHYMAL STROMAL CELLS. *Cytotherapy* **2022**, *24* (5), S67–S68. https://doi.org/10.1016/S1465-3249(22)00210-9.
(322) Pallotta, V.; D'Amici, G. M.; D'Alessandro, A.; Rossetti, R.; Zolla, L. Red Blood Cell Processing for Cryopreservation: From Fresh Blood to Deglycerolization. *Blood Cells. Mol. Dis.* **2012**, *48* (4), 226–232. https://doi.org/10.1016/j.bcmd.2012.02.004.
(323) Brecher, M. E. *Technical Manual*, 15th ed.; AABB: Bethesda (MD), 2005.
(324) *Azides and Nitrenes: Reactivity and Utility*; Scriven, E. F. V., Ed.; Academic Press: Orlando, Fla, 1984.
(325) Sumranjit, J.; Chung, S. Recent Advances in Target Characterization and Identification by Photoaffinity Probes. *Molecules* **2013**, *18* (9), 10425–10451. https://doi.org/10.3390/molecules180910425.
(326) Zemplén, G.; Kunz, A. Studien Über Amygdalin, IV: Synthese Des Natürlichen *l* -Amygdalins. *Berichte Dtsch. Chem. Ges. B Ser.* **1924**, *57* (8), 1357–1359. https://doi.org/10.1002/cber.19240570825.
(327) Zeller, M. P.; Rochwerg, B.; Jamula, E.; Li, N.; Hillis, C.; Acker, J. P.; Runciman, R. J. R.; Lane, S. J.; Ahmed, N.; Arnold, D. M.; Heddle, N. M. Sex-mismatched Red Blood Cell Transfusions and Mortality: A Systematic Review and Meta-analysis. *Vox Sang.* **2019**, *114* (5), 505–516. https://doi.org/10.1111/vox.12783.
(328) Dean, L. Blood Transfusions and the Immnue System. In *Blood Groups and Red Cell Antigens*; National Center for Biotechnology Information: Bethesda (MD), 2005.
(329) Drabkin, D. L. The Standardization of Hemoglobin Measurement: *Am. J. Med. Sci.* **1948**, *215* (1), 110. https://doi.org/10.1097/00000441-194801000-00017.
(330) Acker, J. P.; Hansen, A. L.; Kurach, J. D. R.; Turner, T. R.; Croteau, I.; Jenkins, C. A Quality Monitoring Program for Red Blood Cell Components: In Vitro Quality Indicators before and after

Implementation of Semiautomated Processing. *Transfusion (Paris)* **2014**, *54* (10), 2534–2543. https://doi.org/10.1111/trf.12679.
(331) Diamante, M., F. Unpublished at the Time of Writing. PhD Thesis, University of Ottawa, Ottawa, ON, 2025.
(332) Levitt, J.; Scarth, G. W. Frost-Hardening Studies with Living Cells: I. Osmotic and Bound Water Changes in Relation to Frost Resistance and the Seasonal Cycle. *Can. J. Res.* **1936**, *14c* (7), 267–284. https://doi.org/10.1139/cjr36c-022.
(333) Mazur, P. Manifestations of Injury in Yeast Cells Exposed to Subzero Temperatures I: Morphological Changes in Freeze-Substituted and in "Frozen-Thawed" Cells. *J. Bacteriol.* **1961**, *82* (5), 662–672. https://doi.org/10.1128/jb.82.5.662-672.1961.
(334) Workman, E. J.; Reynolds, S. E. Electrical Phenomena Occurring during the Freezing of Dilute Aqueous Solutions and Their Possible Relationship to Thunderstorm Electricity. *Phys. Rev.* **1950**, *78* (3), 254–259. https://doi.org/10.1103/PhysRev.78.254.
(335) Dowgert, M. F.; Steponkus, P. L. Effect of Cold Acclimation on Intracellular Ice Formation in Isolated Protoplasts. *Plant Physiol.* **1983**, *72* (4), 978–988. https://doi.org/10.1104/pp.72.4.978.
(336) Zhurova, M.; Woods, E. J.; Acker, J. P. Intracellular Ice Formation in Confluent Monolayers of Human Dental Stem Cells and Membrane Damage. *Cryobiology* **2010**, *61* (1), 133–141. https://doi.org/10.1016/j.cryobiol.2010.06.007.
(337) McGann, L. E.; Yang, H.; Walterson, M. Manifestations of Cell Damage after Freezing and Thawing. *Cryobiology* **1988**, *25* (3), 178–185. https://doi.org/10.1016/0011-2240(88)90024-7.
(338) Ross-Rodriguez, L. U.; Elliott, J. A. W.; McGann, L. E. Characterization of Cryobiological Responses in TF-1 Cells Using Interrupted Freezing Procedures. *Cryobiology* **2010**, *60* (2), 106–116. https://doi.org/10.1016/j.cryobiol.2009.09.007.
(339) Yang, G.; Zhang, A.; Xu, L. X. Experimental Study of Intracellular Ice Growth in Human Umbilical Vein Endothelial Cells. *Cryobiology* **2009**, *58* (1), 96–102. https://doi.org/10.1016/j.cryobiol.2008.10.123.
(340) Prickett, R. C.; Marquez-Curtis, L. A.; Elliott, J. A. W.; McGann, L. E. Effect of Supercooling and Cell Volume on Intracellular Ice Formation. *Cryobiology* **2015**, *70* (2), 156–163. https://doi.org/10.1016/j.cryobiol.2015.02.002.
(341) Acker, J. P.; Croteau, I. M. Pre- and Post-thaw Assessment of Intracellular Ice Formation. *J. Microsc.* **2004**, *215* (2), 131–138. https://doi.org/10.1111/j.0022-2720.2004.01375.x.
(342) Cuny, A. P.; Schlottmann, F. P.; Ewald, J. C.; Pelet, S.; Schmoller, K. M. Live Cell Microscopy: From Image to Insight. *Biophys. Rev.* **2022**, *3* (2), 021302. https://doi.org/10.1063/5.0082799.
(343) Balasubramanian, H.; Hobson, C. M.; Chew, T.-L.; Aaron, J. S. Imagining the Future of Optical Microscopy: Everything, Everywhere, All at Once. *Commun. Biol.* **2023**, *6* (1), 1096. https://doi.org/10.1038/s42003-023-05468-9.
(344) Huang, Q.; Garrett, A.; Bose, S.; Blocker, S.; Rios, A. C.; Clevers, H.; Shen, X. The Frontier of Live Tissue Imaging across Space and Time. *Cell Stem Cell* **2021**, *28* (4), 603–622. https://doi.org/10.1016/j.stem.2021.02.010.
(345) Sawyer, L. C.; Grubb, D. T. Fundamentals of Microscopy. In *Polymer Microscopy*; Springer Netherlands: Dordrecht, 1996; pp 17–47. https://doi.org/10.1007/978-94-015-8595-8_2.
(346) Girkin, J. *A Practical Guide to Optical Microscopy*; Taylor & Francis Group: Milton, 2019.
(347) *Staining Procedures*, 4. ed.; Clark, G., Ed.; Williams and Wilkins: Baltimore, 1981.
(348) Zernike, F. How I Discovered Phase Contrast. *Science* **1955**, *121* (3141), 345–349. https://doi.org/10.1126/science.121.3141.345.
(349) Masters, B. R. History of the Optical Microscope in Cell Biology and Medicine. In *Encyclopedia of Life Sciences*; Wiley, 2008. https://doi.org/10.1002/9780470015902.a0003082.
(350) Hosaka, N.; Saiki, T. Near-field Fluorescence Imaging of Single Molecules with a Resolution in the Range of 10 Nm. *J. Microsc.* **2001**, *202* (2), 362–364. https://doi.org/10.1046/j.1365-2818.2001.00815.x.

(351) Saffarian, S.; Kirchhausen, T. Differential Evanescence Nanometry: Live-Cell Fluorescence Measurements with 10-Nm Axial Resolution on the Plasma Membrane. *Biophys. J.* **2008**, *94* (6), 2333–2342. https://doi.org/10.1529/biophysj.107.117234.
(352) Sanderson, M. J.; Smith, I.; Parker, I.; Bootman, M. D. Fluorescence Microscopy. *Cold Spring Harb. Protoc.* **2014**, *2014* (10), pdb.top071795. https://doi.org/10.1101/pdb.top071795.
(353) Palonpon, A. F.; Sodeoka, M.; Fujita, K. Molecular Imaging of Live Cells by Raman Microscopy. *Curr. Opin. Chem. Biol.* **2013**, *17* (4), 708–715. https://doi.org/10.1016/j.cbpa.2013.05.021.
(354) Li, Y.; Wang, Z.; Mu, X.; Ma, A.; Guo, S. Raman Tags: Novel Optical Probes for Intracellular Sensing and Imaging. *Biotechnol. Adv.* **2017**, *35* (2), 168–177. https://doi.org/10.1016/j.biotechadv.2016.12.004.
(355) Iuliano, J. N.; French, J. B.; Tonge, P. J. Vibrational Spectroscopy of Flavoproteins. In *Methods in Enzymology*; Elsevier, 2019; Vol. 620, pp 189–214. https://doi.org/10.1016/bs.mie.2019.03.011.
(356) Rodriguez, L. G.; Lockett, S. J.; Holtom, G. R. Coherent Anti-stokes Raman Scattering Microscopy: A Biological Review. *Cytometry A* **2006**, *69A* (8), 779–791. https://doi.org/10.1002/cyto.a.20299.
(357) Tonge, P. J.; Pusztai, M.; White, A. J.; Wharton, C. W.; Carey, P. R. Resonance Raman and Fourier Transform Infrared Spectroscopic Studies of the Acyl Carbonyl Group in [3-(5-Methyl-2-Thienyl)Acryloyl]Chymotrypsin: Evidence for Artifacts in the Spectra Obtained by Both Techniques. *Biochemistry* **1991**, *30* (19), 4790–4795. https://doi.org/10.1021/bi00233a021.
(358) Zumbusch, A.; Holtom, G. R.; Xie, X. S. Three-Dimensional Vibrational Imaging by Coherent Anti-Stokes Raman Scattering. *Phys. Rev. Lett.* **1999**, *82* (20), 4142–4145. https://doi.org/10.1103/PhysRevLett.82.4142.
(359) Harada, Y.; Dai, P.; Yamaoka, Y.; Ogawa, M.; Tanaka, H.; Nosaka, K.; Akaji, K.; Takamatsu, T. Intracellular Dynamics of Topoisomerase I Inhibitor, CPT-11, by Slit-Scanning Confocal Raman Microscopy. *Histochem. Cell Biol.* **2009**, *132* (1), 39–46. https://doi.org/10.1007/s00418-009-0594-0.
(360) Van Manen, H.-J.; Kraan, Y. M.; Roos, D.; Otto, C. Intracellular Chemical Imaging of Heme-Containing Enzymes Involved in Innate Immunity Using Resonance Raman Microscopy. *J. Phys. Chem. B* **2004**, *108* (48), 18762–18771. https://doi.org/10.1021/jp046955b.
(361) Ling, J.; Weitman, S. D.; Miller, M. A.; Moore, R. V.; Bovik, A. C. Direct Raman Imaging Techniques for Study of the Subcellular Distribution of a Drug. *Appl. Opt.* **2002**, *41* (28), 6006. https://doi.org/10.1364/AO.41.006006.
(362) Huang, Y.; Karashima, T.; Yamamoto, M.; Ogura, T.; Hamaguchi, H. Raman Spectroscopic Signature of Life in a Living Yeast Cell. *J. Raman Spectrosc.* **2004**, *35* (7), 525–526. https://doi.org/10.1002/jrs.1219.
(363) Zoladek, A.; Pascut, F. C.; Patel, P.; Notingher, I. Non-invasive Time-course Imaging of Apoptotic Cells by Confocal Raman Micro-spectroscopy. *J. Raman Spectrosc.* **2011**, *42* (3), 251–258. https://doi.org/10.1002/jrs.2707.
(364) Jones, R. R.; Hooper, D. C.; Zhang, L.; Wolverson, D.; Valev, V. K. Raman Techniques: Fundamentals and Frontiers. *Nanoscale Res. Lett.* **2019**, *14* (1), 231. https://doi.org/10.1186/s11671-019-3039-2.
(365) Smith, R.; Wright, K. L.; Ashton, L. Raman Spectroscopy: An Evolving Technique for Live Cell Studies. *The Analyst* **2016**, *141* (12), 3590–3600. https://doi.org/10.1039/C6AN00152A.
(366) Puppels, G. J.; De Mul, F. F. M.; Otto, C.; Greve, J.; Robert-Nicoud, M.; Arndt-Jovin, D. J.; Jovin, T. M. Studying Single Living Cells and Chromosomes by Confocal Raman Microspectroscopy. *Nature* **1990**, *347* (6290), 301–303. https://doi.org/10.1038/347301a0.
(367) Okada, M.; Smith, N. I.; Palonpon, A. F.; Endo, H.; Kawata, S.; Sodeoka, M.; Fujita, K. Label-Free Raman Observation of Cytochrome c Dynamics during Apoptosis. *Proc. Natl. Acad. Sci.* **2012**, *109* (1), 28–32. https://doi.org/10.1073/pnas.1107524108.
(368) Walrafen, G. E.; Hokmabadi, M. S.; Yang, W.-H. Raman Isosbestic Points from Liquid Water. *J. Chem. Phys.* **1986**, *85* (12), 6964–6969. https://doi.org/10.1063/1.451383.

(369) Walrafen, G. E. Raman Spectral Studies of the Effects of Temperature on Water Structure. *J. Chem. Phys.* **1967**, *47* (1), 114–126. https://doi.org/10.1063/1.1711834.
(370) D'Arrigo, G.; Maisano, G.; Mallamace, F.; Migliardo, P.; Wanderlingh, F. Raman Scattering and Structure of Normal and Supercooled Water. *J. Chem. Phys.* **1981**, *75* (9), 4264–4270. https://doi.org/10.1063/1.442629.
(371) Green, J. L.; Lacey, A. R.; Sceats, M. G. Spectroscopic Evidence for Spatial Correlations of Hydrogen Bonds in Liquid Water. *J. Phys. Chem.* **1986**, *90* (17), 3958–3964. https://doi.org/10.1021/j100408a027.
(372) Carey, D. M.; Korenowski, G. M. Measurement of the Raman Spectrum of Liquid Water. *J. Chem. Phys.* **1998**, *108* (7), 2669–2675. https://doi.org/10.1063/1.475659.
(373) Krishnamurthy, S.; Bansil, R.; Wiafe-Akenten, J. Low-Frequency Raman Spectrum of Supercooled Water. *J. Chem. Phys.* **1983**, *79* (12), 5863–5870. https://doi.org/10.1063/1.445756.
(374) Hare, D. E.; Sorensen, C. M. Raman Spectroscopic Study of Bulk Water Supercooled to −33 °C. *J. Chem. Phys.* **1990**, *93* (1), 25–33. https://doi.org/10.1063/1.459599.
(375) Aliotta, F.; Vasi, C.; Maisano, G.; Majolino, D.; Mallamace, F.; Migliardo, P. Role of the H Bond and Cooperative Effects in Normal and Supercooled Water Studied by Anisotropic Low Frequency Light Scattering. *J. Chem. Phys.* **1986**, *84* (9), 4731–4738. https://doi.org/10.1063/1.450007.
(376) Whalley, E. A Detailed Assignment of the O–H Stretching Bands of Ice I. *Can. J. Chem.* **1977**, *55* (19), 3429–3441. https://doi.org/10.1139/v77-481.
(377) Sivakumar, T. C.; Schuh, D.; Sceats, M. G.; Rice, S. A. The 2500–4000 Cm−1 Raman and Infrared Spectra of Low Density Amorphous Solid Water and of Polycrystalline Ice I. *Chem. Phys. Lett.* **1977**, *48* (2), 212–218. https://doi.org/10.1016/0009-2614(77)80302-3.
(378) Saito, S.; Ohmine, I. Fifth-Order Two-Dimensional Raman Spectroscopy of Liquid Water, Crystalline Ice Ih and Amorphous Ices: Sensitivity to Anharmonic Dynamics and Local Hydrogen Bond Network Structure. *J. Chem. Phys.* **2006**, *125* (8), 084506. https://doi.org/10.1063/1.2232254.
(379) Halter, P. U.; Bilgram, J. H.; Känzig, W. Properties of the Solid–Liquid Interface Layer of Growing Ice Crystals: A Raman and Rayleigh Scattering Study. *J. Chem. Phys.* **1988**, *89* (5), 2622–2629. https://doi.org/10.1063/1.455011.
(380) Tomimatsu, Y.; Scherer, J. R.; Yeh, Y.; Feeney, R. E. Raman Spectra of a Solid Antifreeze Glycoprotein and Its Liquid and Frozen Aqueous Solutions. *J. Biol. Chem.* **1976**, *251* (8), 2290–2298. https://doi.org/10.1016/S0021-9258(17)33585-8.
(381) Chaytor, J. L. Examining the Role of Carbohydrate Hydration and Structure in Preventing Ice-Recrystallization. PhD Thesis, University of Ottawa, Ottawa, ON, 2010. http://ruor.uottawa.ca/handle/10393/29967 (accessed 2024-02-15).
(382) Tipping, W. J.; Merchant, A. S.; Fearon, R.; Tomkinson, N. C. O.; Faulds, K.; Graham, D. Temporal Imaging of Drug Dynamics in Live Cells Using Stimulated Raman Scattering Microscopy and a Perfusion Cell Culture System. *RSC Chem. Biol.* **2022**, *3* (9), 1154–1164. https://doi.org/10.1039/D2CB00160H.
(383) Yamakoshi, H.; Dodo, K.; Okada, M.; Ando, J.; Palonpon, A.; Fujita, K.; Kawata, S.; Sodeoka, M. Imaging of EdU, an Alkyne-Tagged Cell Proliferation Probe, by Raman Microscopy. *J. Am. Chem. Soc.* **2011**, *133* (16), 6102–6105. https://doi.org/10.1021/ja108404p.
(384) Xu, J.; Yu, T.; Zois, C. E.; Cheng, J.-X.; Tang, Y.; Harris, A. L.; Huang, W. E. Unveiling Cancer Metabolism through Spontaneous and Coherent Raman Spectroscopy and Stable Isotope Probing. *Cancers* **2021**, *13* (7), 1718. https://doi.org/10.3390/cancers13071718.
(385) Vardaki, M. Z.; Gregoriou, V. G.; Chochos, C. L. Biomedical Applications, Perspectives and Tag Design Concepts in the Cell – Silent Raman Window. *RSC Chem. Biol.* **2024**, *5* (4), 273–292. https://doi.org/10.1039/D3CB00217A.
(386) Yamakoshi, H.; Dodo, K.; Palonpon, A.; Ando, J.; Fujita, K.; Kawata, S.; Sodeoka, M. Alkyne-Tag Raman Imaging for Visualization of Mobile Small Molecules in Live Cells. *J. Am. Chem. Soc.* **2012**, *134* (51), 20681–20689. https://doi.org/10.1021/ja308529n.

(387) Cebeci-Maltaş, D.; Ben-Amotz, D.; Anik Alam, M.; Wang, P.; Pinal, R. *Photobleaching profile of Raman peaks and fluorescence background*. https://www.europeanpharmaceuticalreview.com/article/70503/raman-peaks-fluorescence-background/ (accessed 2024-08-13).
(388) Wei, D.; Chen, S.; Liu, Q. Review of Fluorescence Suppression Techniques in Raman Spectroscopy. *Appl. Spectrosc. Rev.* **2015**, *50* (5), 387–406. https://doi.org/10.1080/05704928.2014.999936.
(389) Kumar, P.; Nagarajan, A.; Uchil, P. D. Analysis of Cell Viability by the Lactate Dehydrogenase Assay. *Cold Spring Harb. Protoc.* **2018**, *2018* (6), pdb.prot095497. https://doi.org/10.1101/pdb.prot095497.
(390) Shen, S.; Shao, Y.; Li, C. Different Types of Cell Death and Their Shift in Shaping Disease. *Cell Death Discov.* **2023**, *9* (1), 284. https://doi.org/10.1038/s41420-023-01581-0.
(391) Galluzzi, L.; Vitale, I.; Abrams, J. M.; Alnemri, E. S.; Baehrecke, E. H.; Blagosklonny, M. V.; Dawson, T. M.; Dawson, V. L.; El-Deiry, W. S.; Fulda, S.; Gottlieb, E.; Green, D. R.; Hengartner, M. O.; Kepp, O.; Knight, R. A.; Kumar, S.; Lipton, S. A.; Lu, X.; Madeo, F.; Malorni, W.; Mehlen, P.; Nuñez, G.; Peter, M. E.; Piacentini, M.; Rubinsztein, D. C.; Shi, Y.; Simon, H.-U.; Vandenabeele, P.; White, E.; Yuan, J.; Zhivotovsky, B.; Melino, G.; Kroemer, G. Molecular Definitions of Cell Death Subroutines: Recommendations of the Nomenclature Committee on Cell Death 2012. *Cell Death Differ.* **2012**, *19* (1), 107–120. https://doi.org/10.1038/cdd.2011.96.
(392) Elmore, S. Apoptosis: A Review of Programmed Cell Death. *Toxicol. Pathol.* **2007**, *35* (4), 495–516. https://doi.org/10.1080/01926230701320337.
(393) Zhang, X. D.; Gillespie, S. K.; Hersey, P. Staurosporine Induces Apoptosis of Melanoma by Both Caspase-Dependent and -Independent Apoptotic Pathways. *Mol. Cancer Ther.* **2004**, *3* (2), 187–197.
(394) Hanson, K. M.; Finkelstein, J. N. An Accessible and High-Throughput Strategy of Continuously Monitoring Apoptosis by Fluorescent Detection of Caspase Activation. *Anal. Biochem.* **2019**, *564–565*, 96–101. https://doi.org/10.1016/j.ab.2018.10.022.
(395) McCall, A. L. Glucose Transport. In *Stress: Physiology, Biochemistry, and Pathology*; Elsevier, 2019; pp 293–307. https://doi.org/10.1016/B978-0-12-813146-6.00022-9.
(396) Carruthers, A.; DeZutter, J.; Ganguly, A.; Devaskar, S. U. Will the Original Glucose Transporter Isoform Please Stand Up! *Am. J. Physiol.-Endocrinol. Metab.* **2009**, *297* (4), E836–E848. https://doi.org/10.1152/ajpendo.00496.2009.
(397) Barnett, J. E.; Holman, G. D.; Chalkley, R. A.; Munday, K. A. Evidence for Two Asymmetric Conformational States in the Human Erythrocyte Sugar-Transport System. *Biochem. J.* **1975**, *145* (3), 417–429. https://doi.org/10.1042/bj1450417a.
(398) García-Álvarez, I.; Garrido, L.; Fernández-Mayoralas, A. Studies on the Uptake of Glucose Derivatives by Red Blood Cells. *ChemMedChem* **2007**, *2* (4), 496–504. https://doi.org/10.1002/cmdc.200600282.
(399) Guha, R. On Exploring Structure–Activity Relationships. In *In Silico Models for Drug Discovery*; Kortagere, S., Ed.; Methods in Molecular Biology; Humana Press: Totowa, NJ, 2013; Vol. 993, pp 81–94. https://doi.org/10.1007/978-1-62703-342-8_6.
(400) Balaban, A. T. Drug Design, Molecular Descriptors In. In *Encyclopedia of Complexity and Systems Science*; Meyers, R. A., Ed.; Springer New York: New York, NY, 2009; pp 2196–2215. https://doi.org/10.1007/978-0-387-30440-3_136.
(401) Galema, S. A.; Hoeiland, H. Stereochemical Aspects of Hydration of Carbohydrates in Aqueous Solutions. 3. Density and Ultrasound Measurements. *J. Phys. Chem.* **1991**, *95* (13), 5321–5326. https://doi.org/10.1021/j100166a073.
(402) Galema, S. A.; Howard, E.; Engberts, J. B. F. N.; Grigera, J. R. The Effect of Stereochemistry upon Carbohydrate Hydration. A Molecular Dynamics Simulation of β-d-Galactopyranose and (α,β)-d-Talopyranose. *Carbohydr. Res.* **1994**, *265* (2), 215–225. https://doi.org/10.1016/0008-6215(94)00241-X.

(403) Penkov, N. V. Relationships between Molecular Structure of Carbohydrates and Their Dynamic Hydration Shells Revealed by Terahertz Time-Domain Spectroscopy. *Int. J. Mol. Sci.* **2021**, *22* (21), 11969. https://doi.org/10.3390/ijms222111969.
(404) Andersson, C.; Balling Engelsen, S. The Mean Hydration of Carbohydrates as Studied by Normalized Two-Dimensional Radial Pair Distributions. *J. Mol. Graph. Model.* **1999**, *17* (2), 101–105. https://doi.org/10.1016/S1093-3263(99)00022-4.
(405) Lee, S. L.; Debenedetti, P. G.; Errington, J. R. A Computational Study of Hydration, Solution Structure, and Dynamics in Dilute Carbohydrate Solutions. *J. Chem. Phys.* **2005**, *122* (20), 204511. https://doi.org/10.1063/1.1917745.
(406) Hoiland, H.; Holvik, H. Partial Molal Volumes and Compressibilities of Carbohydrates in Water. *J. Solut. Chem.* **1978**, *7* (8), 587–596. https://doi.org/10.1007/BF00646036.
(407) Shahidi, F.; Farrell, P. G.; Edward, J. T. Partial Molar Volumes of Organic Compounds in Water. III. Carbohydrates. *J. Solut. Chem.* **1976**, *5* (12), 807–816. https://doi.org/10.1007/BF01167236.
(408) Lipinski, C. A. Lead- and Drug-like Compounds: The Rule-of-Five Revolution. *Drug Discov. Today Technol.* **2004**, *1* (4), 337–341. https://doi.org/10.1016/j.ddtec.2004.11.007.
(409) Lipinski, C. A.; Lombardo, F.; Dominy, B. W.; Feeney, P. J. Experimental and Computational Approaches to Estimate Solubility and Permeability in Drug Discovery and Development Settings 1PII of Original Article: S0169-409X(96)00423-1. The Article Was Originally Published in Advanced Drug Delivery Reviews 23 (1997) 3–25. 1. *Adv. Drug Deliv. Rev.* **2001**, *46* (1–3), 3–26. https://doi.org/10.1016/S0169-409X(00)00129-0.
(410) Balcerzak, A. K.; Febbraro, M.; Ben, R. N. The Importance of Hydrophobic Moieties in Ice Recrystallization Inhibitors. *RSC Adv.* **2013**, *3* (10), 3232. https://doi.org/10.1039/c3ra23220d.
(411) Alteen, M. Investigating the Importance of Electronic and Hydrophobic Effects for Ice Recrystallization Inhibition Using 'Beta'-'O'-Aryl Glycosides. MSc Thesis, University of Ottawa, Ottawa, ON, 2013. http://ruor.uottawa.ca/handle/10393/30335 (accessed 2022-09-22).
(412) Trant, J. F. Importance of the Structural Components of C-Linked Glycopeptides to Specific-Antifreeze Activity: From Glycopeptides to Small Molecule Inhibitors of Ice Recrystallization. PhD Thesis, Unviversity of Ottawa, Ottawa, ON, 2012. http://ruor.uottawa.ca/handle/10393/20710 (accessed 2024-11-20).
(413) Warren, M. T.; Biggs, C. I.; Bissoyi, A.; Gibson, M. I.; Sosso, G. C. Data-Driven Discovery of Potent Small Molecule Ice Recrystallisation Inhibitors. *Nat. Commun.* **2024**, *15* (1), 8082. https://doi.org/10.1038/s41467-024-52266-w.
(414) ChemDraw, 2019. https://chem.beloit.edu/classes/programs/ChemDraw_18_manual.pdf.
(415) MarvinSketch, 2024. https://docs.chemaxon.com/display/docs/calculators_index.md.
(416) Tetko, I. V.; Gasteiger, J.; Todeschini, R.; Mauri, A.; Livingstone, D.; Ertl, P.; Palyulin, V. A.; Radchenko, E. V.; Zefirov, N. S.; Makarenko, A. S.; Tanchuk, V. Yu.; Prokopenko, V. V. Virtual Computational Chemistry Laboratory – Design and Description. *J. Comput. Aided Mol. Des.* **2005**, *19* (6), 453–463. https://doi.org/10.1007/s10822-005-8694-y.
(417) VCCLAB, 2005. https://vcclab.org/lab/alogps/.
(418) ACD Labs PhysChem Suite.
(419) Hansch, Corwin.; Leo, A.; Taft, R. W. A Survey of Hammett Substituent Constants and Resonance and Field Parameters. *Chem. Rev.* **1991**, *91* (2), 165–195. https://doi.org/10.1021/cr00002a004.
(420) Hammett, L. P. Some Relations between Reaction Rates and Equilibrium Constants. *Chem. Rev.* **1935**, *17* (1), 125–136. https://doi.org/10.1021/cr60056a010.
(421) Hammett, L. P. The Effect of Structure upon the Reactions of Organic Compounds. Benzene Derivatives. *J. Am. Chem. Soc.* **1937**, *59* (1), 96–103. https://doi.org/10.1021/ja01280a022.
(422) Taft, R. W. Linear Free Energy Relationships from Rates of Esterification and Hydrolysis of Aliphatic and Ortho-Substituted Benzoate Esters. *J. Am. Chem. Soc.* **1952**, *74* (11), 2729–2732. https://doi.org/10.1021/ja01131a010.
(423) Taft, R. W. Linear Steric Energy Relationships. *J. Am. Chem. Soc.* **1953**, *75* (18), 4538–4539. https://doi.org/10.1021/ja01114a044.

(424) Toews, M. L. Pharmacologic Principles for Combination Therapy. *Proc. Am. Thorac. Soc.* **2005**, *2* (4), 282–289. https://doi.org/10.1513/pats.200504-037SR.
(425) Mazzobre, M. F.; Román, M. V.; Mourelle, A. F.; Corti, H. R. Octanol–Water Partition Coefficient of Glucose, Sucrose, and Trehalose. *Carbohydr. Res.* **2005**, *340* (6), 1207–1211. https://doi.org/10.1016/j.carres.2004.12.038.
(426) Sun, Y.; Hou, T.; He, X.; Man, V. H.; Wang, J. Development and Test of Highly Accurate Endpoint Free Energy Methods. 2: Prediction of Logarithm of *n* -octanol–Water Partition Coefficient (LOGP) for Druglike Molecules Using MM-PBSA Method. *J. Comput. Chem.* **2023**, *44* (13), 1300–1311. https://doi.org/10.1002/jcc.27086.
(427) Hasel, W.; Hendrickson, T. F.; Still, W. C. A Rapid Approximation to the Solvent Accessible Surface Areas of Atoms. *Tetrahedron Comput. Methodol.* **1988**, *1* (2), 103–116. https://doi.org/10.1016/0898-5529(88)90015-2.
(428) Ferrara, P.; Apostolakis, J.; Caflisch, A. Evaluation of a Fast Implicit Solvent Model for Molecular Dynamics Simulations. *Proteins Struct. Funct. Bioinforma.* **2002**, *46* (1), 24–33. https://doi.org/10.1002/prot.10001.
(429) Ertl, P.; Rohde, B.; Selzer, P. Fast Calculation of Molecular Polar Surface Area as a Sum of Fragment-Based Contributions and Its Application to the Prediction of Drug Transport Properties. *J. Med. Chem.* **2000**, *43* (20), 3714–3717. https://doi.org/10.1021/jm000942e.
(430) Pracht, P.; Grimme, S.; Bannwarth, C.; Bohle, F.; Ehlert, S.; Feldmann, G.; Gorges, J.; Müller, M.; Neudecker, T.; Plett, C.; Spicher, S.; Steinbach, P.; Wesołowski, P. A.; Zeller, F. CREST—A Program for the Exploration of Low-Energy Molecular Chemical Space. *J. Chem. Phys.* **2024**, *160* (11), 114110. https://doi.org/10.1063/5.0197592.
(431) Chai, J.-D.; Head-Gordon, M. Long-Range Corrected Hybrid Density Functionals with Damped Atom–Atom Dispersion Corrections. *Phys. Chem. Chem. Phys.* **2008**, *10* (44), 6615. https://doi.org/10.1039/b810189b.
(432) Rappoport, D.; Furche, F. Property-Optimized Gaussian Basis Sets for Molecular Response Calculations. *J. Chem. Phys.* **2010**, *133* (13), 134105. https://doi.org/10.1063/1.3484283.
(433) Barone, V.; Cossi, M. Quantum Calculation of Molecular Energies and Energy Gradients in Solution by a Conductor Solvent Model. *J. Phys. Chem. A* **1998**, *102* (11), 1995–2001. https://doi.org/10.1021/jp9716997.
(434) Meyer, J. E. Unpublished at the Time of Writing. PhD Thesis, University of Ottawa, Ottawa, ON, 2025.
(435) Cheetham, N. W. H.; Lam, K. Molecular Dynamics Simulations of Glycosides in Aqueous Solution. *Carbohydr. Res.* **1996**, *282* (1), 13–23. https://doi.org/10.1016/0008-6215(95)00363-0.
(436) Dashnau, J. L.; Sharp, K. A.; Vanderkooi, J. M. Carbohydrate Intramolecular Hydrogen Bonding Cooperativity and Its Effect on Water Structure. *J. Phys. Chem. B* **2005**, *109* (50), 24152–24159. https://doi.org/10.1021/jp0543072.
(437) Edelman, R.; Kusner, I.; Kisiliak, R.; Srebnik, S.; Livney, Y. D. Sugar Stereochemistry Effects on Water Structure and on Protein Stability: The Templating Concept. *Food Hydrocoll.* **2015**, *48*, 27–37. https://doi.org/10.1016/j.foodhyd.2015.01.028.
(438) Laidler, K. J. *Chemical Kinetics*, 3. ed., [Nachdr.].; HarperCollins: New York, NY, 1998.
(439) Isaacs, N. S. *Physical Organic Chemistry*, 2nd ed.; Longman Scientific & Technical ; Wiley & Sons: Burnt Mill, Harlow, Essex, England : New York, N.Y, 1995.
(440) Bechalany, A.; El Tayar, N.; Carrupt, P.; Testa, B.; Falconnet, J.; Cherrah, Y.; Benchekroun, Y.; Brazier, J. Isotope Effects on the Lipophilicity of Deuterated Caffeines. *Helv. Chim. Acta* **1989**, *72* (3), 472–476. https://doi.org/10.1002/hlca.19890720308.
(441) Wade, D. Deuterium Isotope Effects on Noncovalent Interactions between Molecules. *Chem. Biol. Interact.* **1999**, *117* (3), 191–217. https://doi.org/10.1016/S0009-2797(98)00097-0.
(442) Buchachenko, A. L.; Breslavskaya, N. N. Noncovalent Hydrogen Isotope Effects. *Russ. J. Phys. Chem. A* **2018**, *92* (2), 315–320. https://doi.org/10.1134/S003602441802005X.

(443) Garegg, P. J.; Hultberg, H. A Novel, Reductive Ring-Opening of Carbohydrate Benzylidene Acetals, with Unusual Regioselectivity. *Carbohydr. Res.* **1981**, *93* (1), C10–C11. https://doi.org/10.1016/S0008-6215(00)80766-1.

(444) Eliel, E.; Rerick, M. Communications Reduction of Acetals to Ethers by Means of Lithium Aluminum Hydride-Aluminum Chloride. *J. Org. Chem.* **1958**, *23* (7), 1088–1088. https://doi.org/10.1021/jo01101a029.

(445) Eliel, E. L.; Badding, V. G.; Rerick, M. N. **Reduction with Metal Hydrides. XII. Reduction of Acetals and Ketals with Lithium Aluminum Hydride-Aluminum Chloride**. *J. Am. Chem. Soc.* **1962**, *84* (12), 2371–2377. https://doi.org/10.1021/ja00871a020.

(446) Bhattacharjee, S. S.; Gorin, P. A. J. Hydrogenolysis of Carbohydrate Acetals, Ketals, and Cyclic Orthoesters with Lithium Aluminium Hydride – Aluminium Trichloride. *Can. J. Chem.* **1969**, *47* (7), 1195–1206. https://doi.org/10.1139/v69-194.

(447) Ohlin, M.; Johnsson, R.; Ellervik, U. Regioselective Reductive Openings of 4,6-Benzylidene Acetals: Synthetic and Mechanistic Aspects. *Carbohydr. Res.* **2011**, *346* (12), 1358–1370. https://doi.org/10.1016/j.carres.2011.03.032.

(448) Rao, K. V.; Patil, P. R.; Atmakuri, S.; Kartha, K. P. R. Iodine–Sodium Cyanoborohydride-Mediated Reductive Ring Opening of 4,6-O-Benzylidene Acetals of Hexopyranosides. *Carbohydr. Res.* **2010**, *345* (18), 2709–2713. https://doi.org/10.1016/j.carres.2010.10.013.

(449) Song, Yong Chen. Hydrogen Bonding Analysis of Hydroxyl Groups in Glucose Aqueous Solutions by a Molecular Dynamics Simulation Study. *Bull. Korean Chem. Soc.* **2012**, *33* (7), 2238–2246. https://doi.org/10.5012/BKCS.2012.33.7.2238.

(450) Charlton, T. A. Synthesis of Novel Charged Ice Recrystallization Inhibitors. PhD Thesis, University of Ottawa, Ottawa, ON, 2021. http://ruor.uottawa.ca/handle/10393/42333 (accessed 2022-09-22).

(451) Koffi Teki, D. S.-E.; Coulibaly, B.; Bil, A.; Vallin, A.; Lesur, D.; Fanté, B.; Chagnault, V.; Kovensky, J. Synthesis of Novel *S* - and *O* -Disaccharide Analogs of Heparan Sulfate for Heparanase Inhibition. *Org. Biomol. Chem.* **2022**, *20* (17), 3528–3534. https://doi.org/10.1039/D2OB00250G.

(452) Mehta, S.; Andrews, J. S.; Svensson, B.; Pinto, B. M. Synthesis and Enzymic Activity of Novel Glycosidase Inhibitors Containing Sulfur and Selenium. *J. Am. Chem. Soc.* **1995**, *117* (39), 9783–9790. https://doi.org/10.1021/ja00144a001.

(453) Battistelli, C. L.; De Castro, C.; Iadonisi, A.; Lanzetta, R.; Mangoni, L.; Parrilli, M. Synthesis and NMR Characterisation of Methyl Mono- and Di- *O* -α-L-Rhamnopyranosyl-α-D-Glucopyranosiduronic Acids. *J. Carbohydr. Chem.* **1999**, *18* (1), 69–86. https://doi.org/10.1080/07328309908543980.

(454) Magaud, D.; Dolmazon, R.; Anker, D.; Doutheau, A.; Dory, Y. L.; Deslongchamps, P. Differential Reactivity of α- and β-Anomers of Glycosyl Acceptors in Glycosylations. A Remote Consequence of the *Endo* -Anomeric Effect? *Org. Lett.* **2000**, *2* (15), 2275–2277. https://doi.org/10.1021/ol006039q.

(455) Çarçabal, P.; Jockusch, R. A.; Hünig, I.; Snoek, L. C.; Kroemer, R. T.; Davis, B. G.; Gamblin, D. P.; Compagnon, I.; Oomens, J.; Simons, J. P. Hydrogen Bonding and Cooperativity in Isolated and Hydrated Sugars: Mannose, Galactose, Glucose, and Lactose. *J. Am. Chem. Soc.* **2005**, *127* (32), 11414–11425. https://doi.org/10.1021/ja0518575.

(456) Mayorkas, N.; Rudić, S.; Cocinero, E. J.; Davis, B. G.; Simons, J. P. Carbohydrate Hydration: Heavy Water Complexes of α and β Anomers of Glucose, Galactose, Fucose and Xylose. *Phys. Chem. Chem. Phys.* **2011**, *13* (41), 18671. https://doi.org/10.1039/c1cp22348h.

(457) Gunther, H. *NMR Spectroscopy: Basic Principles, Concepts and Applications in Chemistry*; Wiley-VCH: Place of publication not identified, 2014.

(458) Babij, N. R.; McCusker, E. O.; Whiteker, G. T.; Canturk, B.; Choy, N.; Creemer, L. C.; Amicis, C. V. D.; Hewlett, N. M.; Johnson, P. L.; Knobelsdorf, J. A.; Li, F.; Lorsbach, B. A.; Nugent, B. M.; Ryan, S. J.; Smith, M. R.; Yang, Q. NMR Chemical Shifts of Trace Impurities: Industrially Preferred Solvents Used in Process and Green Chemistry. *Org. Process Res. Dev.* **2016**, *20* (3), 661–667. https://doi.org/10.1021/acs.oprd.5b00417.

(459) Gottlieb, H. E.; Kotlyar, V.; Nudelman, A. NMR Chemical Shifts of Common Laboratory Solvents as Trace Impurities. *J. Org. Chem.* **1997**, *62* (21), 7512–7515. https://doi.org/10.1021/jo971176v.
(460) Keeler, J. *Understanding NMR Spectroscopy*, 2nd ed.; John Wiley and Sons: Chichester, U.K, 2010.
(461) Richards, S. A.; Hollerton, J. C. *Essential Practical NMR for Organic Chemistry*, 1st ed.; Wiley, 2010. https://doi.org/10.1002/9780470976401.
(462) Bekiroglu, S.; Sandström, C.; Norberg, T.; Kenne, L. Hydroxy Protons in Conformational Study of a Lewis b Tetrasaccharide Derivative in Aqueous Solution by NMR Spectroscopy. *Carbohydr. Res.* **2000**, *328* (3), 409–418. https://doi.org/10.1016/S0008-6215(00)00104-X.
(463) Sandström, C.; Baumann, H.; Kenne, L. The Use of Chemical Shifts of Hydroxy Protons of Oligosaccharides as Conformational Probes for NMR Studies in Aqueous Solution. Evidence for Persistent Hydrogen Bond Interaction in Branched Trisaccharides. *J. Chem. Soc. Perkin Trans. 2* **1998**, No. 11, 2385–2394. https://doi.org/10.1039/a805678a.
(464) Sandström, C.; Baumann, H.; Kenne, L. NMR Spectroscopy of Hydroxy Protons of 3,4-Disubstituted Methyl α-D-Galactopyranosides in Aqueous Solution. *J. Chem. Soc. Perkin Trans. 2* **1998**, No. 4, 809–816. https://doi.org/10.1039/a708550h.
(465) Sandström, C.; Magnusson, G.; Nilsson, U.; Kenne, L. Comparative 1H NMR Study of Hydroxy Protons in Galabioside and Its S-Linked 4-Thiodisaccharide Analogue in Aqueous Solution. *Carbohydr. Res.* **1999**, *322* (1–2), 46–56. https://doi.org/10.1016/S0008-6215(99)00215-3.
(466) Kindahl, L.; Sandström, C.; Norberg, T.; Kenne, L. ^{1}H NMR Studies of Hydroxy Protons of ASN- and Ser-Linked Disaccharides in Aqueous Solution. *J. Carbohydr. Chem.* **2000**, *19* (9), 1291–1303. https://doi.org/10.1080/07328300008544152.
(467) Ivarsson, I.; Sandström, C.; Sandström, A.; Kenne, L. 1H NMR Chemical Shifts of Hydroxy Protons in Conformational Analysis of Disaccharides in Aqueous Solution. *J. Chem. Soc. Perkin Trans. 2* **2000**, No. 10, 2147–2152. https://doi.org/10.1039/b002401p.
(468) Asakawa, N.; Kuroki, S.; Kurosu, H.; Ando, I.; Shoji, A.; Ozaki, T. Hydrogen-Bonding Effect on Carbon-13 NMR Chemical Shifts of L-Alanine Residue Carbonyl Carbons of Peptides in the Solid State. *J. Am. Chem. Soc.* **1992**, *114* (9), 3261–3265. https://doi.org/10.1021/ja00035a016.
(469) Onche, E. U.; Tukura, B. W.; Bako, S. S. Nuclear Magnetic Resonance (NMR) Analysis of D - (+) - Glucose: A Guide to Spectrometric Structural Elucidation of Sugars. *IOSR J. Appl. Chem.* **2013**, *6* (1), 45–51. https://doi.org/10.9790/5736-0614551.
(470) Casu, B.; Reggiani, M.; Gallo, G. G.; Vigevani, A. Hydrogen Bonding and Conformation of Glucose and Polyglucoses in Dimethyl-Sulphoxide Solution. *Tetrahedron* **1966**, *22* (9), 3061–3083. https://doi.org/10.1016/S0040-4020(01)82286-9.
(471) Poppe, L.; Halbeek, H. V. NMR Spectroscopy of Hydroxyl Protons in Supercooled Carbohydrates. *Nat. Struct. Mol. Biol.* **1994**, *1* (4), 215–216. https://doi.org/10.1038/nsb0494-215.
(472) Chemcraft - Graphical Software for Visualization of Quantum Chemistry Computations. https://www.chemcraftprog.com.
(473) Neese, F. The ORCA Program System. *WIREs Comput. Mol. Sci.* **2012**, *2* (1), 73–78. https://doi.org/10.1002/wcms.81.
(474) Neese, F. Software Update: The ORCA Program System—Version 5.0. *WIREs Comput. Mol. Sci.* **2022**, *12* (5), e1606. https://doi.org/10.1002/wcms.1606.
(475) Hellweg, A.; Rappoport, D. Development of New Auxiliary Basis Functions of the Karlsruhe Segmented Contracted Basis Sets Including Diffuse Basis Functions (Def2-SVPD, Def2-TZVPPD, and Def2-QVPPD) for RI-MP2 and RI-CC Calculations. *Phys. Chem. Chem. Phys.* **2015**, *17* (2), 1010–1017. https://doi.org/10.1039/C4CP04286G.
(476) Squillacote, M.; Sheridan, R. S.; Chapman, O. L.; Anet, F. A. L. Spectroscopic Detection of the Twist-Boat Conformation of Cyclohexane. Direct Measurement of the Free Energy Difference between the Chair and the Twist-Boat. *J. Am. Chem. Soc.* **1975**, *97* (11), 3244–3246. https://doi.org/10.1021/ja00844a068.
(477) Correia, L. F. L.; Espírito-Santo, C. G.; Braga, R. F.; Carvalho-de-Paula, C. J.; da Silva, A. A.; Brandão, F. Z.; Freitas, V. J. F.; Ungerfeld, R.; Souza-Fabjan, J. M. G. Addition of Antifreeze Protein

Type I or III to Extenders for Ram Sperm Cryopreservation. *Cryobiology* **2021**, *98*, 194–200. https://doi.org/10.1016/j.cryobiol.2020.11.001.

(478) Murray, K. A.; Gibson, M. I. Chemical Approaches to Cryopreservation. *Nat. Rev. Chem.* **2022**, *6* (8), 579–593. https://doi.org/10.1038/s41570-022-00407-4.

(479) Gran, H. C.; Hansen, E. W.; Pedersen, B.; Fondo, M.; Gómez-Fórneas, E.; McAuliffe, C. A.; Styring, S.; Tommos, C.; Warncke, K.; Wood, B. R. Defect Structure and Molecular Dynamics of Doped Ice and Natural Snow. *Acta Chem. Scand.* **1997**, *51*, 24–30. https://doi.org/10.3891/acta.chem.scand.51-0024.

(480) Conde, M. M.; Rovere, M.; Gallo, P. Spontaneous NaCl-Doped Ice at Seawater Conditions: Focus on the Mechanisms of Ion Inclusion. *Phys. Chem. Chem. Phys.* **2017**, *19* (14), 9566–9574. https://doi.org/10.1039/C7CP00665A.

(481) Vrbka, L.; Jungwirth, P. Brine Rejection from Freezing Salt Solutions: A Molecular Dynamics Study. *Phys. Rev. Lett.* **2005**, *95* (14), 148501. https://doi.org/10.1103/PhysRevLett.95.148501.

(482) Zhao, W.-H.; Wang, L.; Bai, J.; Yuan, L.-F.; Yang, J.; Zeng, X. C. Highly Confined Water: Two-Dimensional Ice, Amorphous Ice, and Clathrate Hydrates. *Acc. Chem. Res.* **2014**, *47* (8), 2505–2513. https://doi.org/10.1021/ar5001549.

(483) Heyden, M.; Bründermann, E.; Heugen, U.; Niehues, G.; Leitner, D. M.; Havenith, M. Long-Range Influence of Carbohydrates on the Solvation Dynamics of Water—Answers from Terahertz Absorption Measurements and Molecular Modeling Simulations. *J. Am. Chem. Soc.* **2008**, *130* (17), 5773–5779. https://doi.org/10.1021/ja0781083.

(484) Feng, T.; Li, M.; Zhou, J.; Zhuang, H.; Chen, F.; Ye, R.; Campanella, O.; Fang, Z. Application of Molecular Dynamics Simulation in Food Carbohydrate Research—a Review. *Innov. Food Sci. Emerg. Technol.* **2015**, *31*, 1–13. https://doi.org/10.1016/j.ifset.2015.06.015.

(485) Bakó, I.; Pusztai, L.; Pothoczki, S. Outstanding Properties of the Hydration Shell around β- D -Glucose: A Computational Study. *ACS Omega* **2024**, *9* (18), 20331–20337. https://doi.org/10.1021/acsomega.4c00798.

(486) Roozen, M. J. G. W.; Hemminga, M. A. Molecular Motion in Carbohydrate + Water Mixtures in the Liquid and Glassy States as Studied by Spin-Probe ESR. In *Food Polymers, Gels and Colloids*; Elsevier, 1991; pp 531–536. https://doi.org/10.1533/9781845698331.1.531.

(487) Hosur, R. V.; Kakita, V. M. R. Fourier Transform NMR. In *A Graduate Course in NMR Spectroscopy*; Springer International Publishing: Cham, 2022; pp 89–142. https://doi.org/10.1007/978-3-030-88769-8_3.

(488) Rodríguez-Alonso, E.; Vergeldt, F. J.; Van Der Goot, A. J. TD-NMR to Understand Water-binding Food Properties. *Magn. Reson. Chem.* **2019**, *57* (9), 603–606. https://doi.org/10.1002/mrc.4815.

(489) Belton, P. Spectroscopic Approaches to the Understanding of Water in Foods. *Food Rev. Int.* **2011**, *27* (2), 170–191. https://doi.org/10.1080/87559129.2010.535234.

(490) Chen, P. L.; Long, Z.; Ruan, R.; Labuza, T. P. Nuclear Magnetic Resonance Studies of Water Mobility in Bread during Storage. *LWT - Food Sci. Technol.* **1997**, *30* (2), 178–183. https://doi.org/10.1006/fstl.1996.0163.

(491) Schmidt, S. J.; Lai, H.-M. Use of NMR and MRI to Study Water Relations in Foods. In *Water Relationships in Foods*; Levine, H., Slade, L., Eds.; Advances in Experimental Medicine and Biology; Springer US: Boston, MA, 1991; Vol. 302, pp 405–452. https://doi.org/10.1007/978-1-4899-0664-9_23.

(492) Cao, R.; Liu, X.; Liu, Y.; Zhai, X.; Cao, T.; Wang, A.; Qiu, J. Applications of Nuclear Magnetic Resonance Spectroscopy to the Evaluation of Complex Food Constituents. *Food Chem.* **2021**, *342*, 128258. https://doi.org/10.1016/j.foodchem.2020.128258.

(493) Louro, R. O. Introduction to Biomolecular NMR and Metals. In *Practical Approaches to Biological Inorganic Chemistry*; Elsevier, 2013; pp 77–107. https://doi.org/10.1016/B978-0-444-56351-4.00004-X.

(494) Cowan, B. *Nuclear Magnetic Resonance and Relaxation*, 1st ed.; Cambridge University Press, 1997. https://doi.org/10.1017/CBO9780511524226.

(495) Tudorache, M.; Bordenave, N. Phenolic Compounds Mediate Aggregation of Water-Soluble Polysaccharides and Change Their Rheological Properties: Effect of Different Phenolic Compounds. *Food Hydrocoll.* **2019**, *97*, 105193. https://doi.org/10.1016/j.foodhyd.2019.105193.
(496) McConville, P.; Whittaker, M. K.; Pope, J. M. Water and Polymer Mobility in Hydrogel Biomaterials Quantified by ^{1}H NMR: A Simple Model Describing Both T_1 and T_2 Relaxation. *Macromolecules* **2002**, *35* (18), 6961–6969. https://doi.org/10.1021/ma020539c.
(497) Mehta, M.; Kothari, K.; Ragoonanan, V.; Suryanarayanan, R. Effect of Water on Molecular Mobility and Physical Stability of Amorphous Pharmaceuticals. *Mol. Pharm.* **2016**, *13* (4), 1339–1346. https://doi.org/10.1021/acs.molpharmaceut.5b00950.
(498) Zhou, D.; Zhang, G. G. Z.; Law, D.; Grant, D. J. W.; Schmitt, E. A. Physical Stability of Amorphous Pharmaceuticals: Importance of Configurational Thermodynamic Quantities and Molecular Mobility. *J. Pharm. Sci.* **2002**, *91* (8), 1863–1872. https://doi.org/10.1002/jps.10169.
(499) Mariette, F.; Lucas, T. NMR Signal Analysis To Attribute the Components to the Solid/Liquid Phases Present in Mixes and Ice Creams. *J. Agric. Food Chem.* **2005**, *53* (5), 1317–1327. https://doi.org/10.1021/jf049294o.
(500) Lucas, T.; Mariette, F.; Dominiawsyk, S.; Le Ray, D. Water, Ice and Sucrose Behavior in Frozen Sucrose–Protein Solutions as Studied by 1H NMR. *Food Chem.* **2004**, *84* (1), 77–89. https://doi.org/10.1016/S0308-8146(03)00177-8.
(501) Eisenberg, D. S.; Kauzmann, W. *The Structure and Properties of Water*; Oxford classic texts in the physical sciences; OUP Oxford: Oxford, 2005.
(502) Millard, M. M.; Veisz, O. B.; Krizek, D. T.; Line, M. Thermodynamic Analysis of the Physical State of Water during Freezing in Plant Tissue, Based on the Temperature Dependence of Proton Spin-Spin Relaxation. *Plant Cell Environ.* **1996**, *19* (1), 33–42. https://doi.org/10.1111/j.1365-3040.1996.tb00224.x.
(503) Smith, K. E.; Bradley, R. L. Effects on Freezing Point of Carbohydrates Commonly Used in Frozen Desserts. *J. Dairy Sci.* **1983**, *66* (12), 2464–2467. https://doi.org/10.3168/jds.S0022-0302(83)82112-2.
(504) Barnaal, D. E.; Lowe, I. J. Proton Spin–Lattice Relaxation in Hexagonal Ice. *J. Chem. Phys.* **1968**, *48* (10), 4614–4618. https://doi.org/10.1063/1.1668036.
(505) Mills, R. Self-Diffusion in Normal and Heavy Water in the Range 1-45.Deg. *J. Phys. Chem.* **1973**, *77* (5), 685–688. https://doi.org/10.1021/j100624a025.
(506) Boyd, G. E.; Soldano, B. A. Self-Diffusion of Water Molecules and Mobile Anions in Cation Exchangers. *J. Am. Chem. Soc.* **1953**, *75* (24), 6105–6107. https://doi.org/10.1021/ja01120a003.
(507) Tanaka, K. Measurements of Self-Diffusion Coefficients of Water in Pure Water and in Aqueous Electrolyte Solutions. *J. Chem. Soc. Faraday Trans. 1 Phys. Chem. Condens. Phases* **1975**, *71* (0), 1127. https://doi.org/10.1039/f19757101127.
(508) Tsukiashi, A.; Min, K. S.; Kitayama, H.; Terasawa, H.; Yoshinaga, S.; Takeda, M.; Lindoy, L. F.; Hayami, S. Application of Spin-Crossover Water Soluble Nanoparticles for Use as MRI Contrast Agents. *Sci. Rep.* **2018**, *8* (1), 14911. https://doi.org/10.1038/s41598-018-33362-6.
(509) Groot, C. C. M.; Meister, K.; DeVries, A. L.; Bakker, H. J. Dynamics of the Hydration Water of Antifreeze Glycoproteins. *J. Phys. Chem. Lett.* **2016**, *7* (23), 4836–4840. https://doi.org/10.1021/acs.jpclett.6b02483.
(510) Keita, D.; Léger, G.; Bordenave, N. Rheological and Water Binding Properties of Xanthan, Guar and Ultra-Finely Milled Oatmeal in White Birch Sap: Influence of Sap Minor Constituents. *Food Res. Int.* **2021**, *147*, 110478. https://doi.org/10.1016/j.foodres.2021.110478.
(511) Dridi, W.; Bordenave, N. Influence of Polysaccharide Concentration on Polyphenol-Polysaccharide Interactions. *Carbohydr. Polym.* **2021**, *274*, 118670. https://doi.org/10.1016/j.carbpol.2021.118670.
(512) Robalo, J. R.; Streacker, L. M.; Mendes de Oliveira, D.; Imhof, P.; Ben-Amotz, D.; Verde, A. V. Hydrophobic but Water-Friendly: Favorable Water–Perfluoromethyl Interactions Promote Hydration Shell Defects. *J. Am. Chem. Soc.* **2019**, *141* (40), 15856–15868. https://doi.org/10.1021/jacs.9b06862.

(513) Kilbride, P.; Meneghel, J.; Fonseca, F.; Morris, J. The Transfer Temperature from Slow Cooling to Cryogenic Storage Is Critical for Optimal Recovery of Cryopreserved Mammalian Cells. *PLOS ONE* **2021**, *16* (11), e0259571. https://doi.org/10.1371/journal.pone.0259571.
(514) Gran, H. C.; Hansen, E. W.; Pedersen, B. Defect Structure and Molecular Dynamics of Doped Ice and Natural Snow. *Acta Chem. Scand.* **1997**, *51* (1), 24–30. https://doi.org/10.3891/acta.chem.scand.51-0024.
(515) Benmore, C.; Gallington, L. C.; Soignard, E. Intermediate Range Order in Supercooled Water. *Mol. Phys.* **2019**, *117* (18), 2470–2476. https://doi.org/10.1080/00268976.2019.1567853.
(516) Mokshin, A. V.; Vlasov, R. V. Liquid–Liquid Crossover in Water Model: Local Structure vs Kinetics of Hydrogen Bonds. *J. Phys. Chem. B* **2024**, *128* (10), 2337–2346. https://doi.org/10.1021/acs.jpcb.3c07650.
(517) Kim, K. H.; Amann-Winkel, K.; Giovambattista, N.; Späh, A.; Perakis, F.; Pathak, H.; Parada, M. L.; Yang, C.; Mariedahl, D.; Eklund, T.; Lane, Thomas. J.; You, S.; Jeong, S.; Weston, M.; Lee, J. H.; Eom, I.; Kim, M.; Park, J.; Chun, S. H.; Poole, P. H.; Nilsson, A. Experimental Observation of the Liquid-Liquid Transition in Bulk Supercooled Water under Pressure. *Science* **2020**, *370* (6519), 978–982. https://doi.org/10.1126/science.abb9385.
(518) Nucci, N. V.; Vanderkooi, J. M. Effects of Salts of the Hofmeister Series on the Hydrogen Bond Network of Water. *J. Mol. Liq.* **2008**, *143* (2–3), 160–170. https://doi.org/10.1016/j.molliq.2008.07.010.
(519) Pegoraro, A. F.; Stolow, A. Chirp Modulation Stimulated Raman Scattering Microscopy. *Opt. Express* **2024**, *32* (18), 31297. https://doi.org/10.1364/OE.531274.
(520) Abdolghader, P.; Ridsdale, A.; Grammatikopoulos, T.; Resch, G.; Légaré, F.; Stolow, A.; Pegoraro, A. F.; Tamblyn, I. Unsupervised Hyperspectral Stimulated Raman Microscopy Image Enhancement: Denoising and Segmentation via One-Shot Deep Learning. *Opt. Express* **2021**, *29* (21), 34205. https://doi.org/10.1364/OE.439662.
(521) Bannwarth, C.; Ehlert, S.; Grimme, S. GFN2-xTB—An Accurate and Broadly Parametrized Self-Consistent Tight-Binding Quantum Chemical Method with Multipole Electrostatics and Density-Dependent Dispersion Contributions. *J. Chem. Theory Comput.* **2019**, *15* (3), 1652–1671. https://doi.org/10.1021/acs.jctc.8b01176.
(522) Schneider, C. A.; Rasband, W. S.; Eliceiri, K. W. NIH Image to ImageJ: 25 Years of Image Analysis. *Nat. Methods* **2012**, *9* (7), 671–675. https://doi.org/10.1038/nmeth.2089.
(523) GraphPad Prism, 2020.
(524) Burfield, D. R.; Smithers, R. H. Desiccant Efficiency in Solvent Drying. 3. Dipolar Aprotic Solvents. *J. Org. Chem.* **1978**, *43* (20), 3966–3968. https://doi.org/10.1021/jo00414a038.
(525) Smits, E.; Engberts, J. B. F. N.; Kellogg, R. M.; van Doren, H. A. Reliable Method for the Synthesis of Aryl β-D-Glucopyranosides, Using Boron Trifluoride–Diethyl Ether as Catalyst. *J Chem Soc Perkin Trans 1* **1996**, No. 24, 2873–2877. https://doi.org/10.1039/P19960002873.
(526) Kartha, K. P. R.; Jennings, H. J. A Simplified, One-Pot Preparation of Acetobromosugars from Reducing Sugars. *J. Carbohydr. Chem.* **1990**, *9* (5), 777–781. https://doi.org/10.1080/07328309008543873.
(527) Nie, X.; Wang, G. Synthesis of a Ring-Oxygenated Variant of the 2-Carboxy-6-Hydroxyoctahydroindole Core of Aeruginosin 298-A from Glucose. *J. Org. Chem.* **2005**, *70* (22), 8687–8692. https://doi.org/10.1021/jo0507901.
(528) Wadzinski, T. J.; Steinauer, A.; Hie, L.; Pelletier, G.; Schepartz, A.; Miller, S. J. Rapid Phenolic O-Glycosylation of Small Molecules and Complex Unprotected Peptides in Aqueous Solvent. *Nat. Chem.* **2018**, *10* (6), 644–652. https://doi.org/10.1038/s41557-018-0041-8.
(529) Kumar, V.; Talisman, I. J.; Malhotra, S. V. Application of Halide Molten Salts as Novel Reaction Media for O-Glycosidic Bond Formation. *Eur. J. Org. Chem.* **2010**, *2010* (18), 3377–3381. https://doi.org/10.1002/ejoc.201000188.

(530) He, D.; Wang, B.; Duan, K.; Zhou, Y.; Li, M.; Jiang, H.; Wu, W. Synthesis of Densely Substituted Pyridine Derivatives from 1-Methyl-1,3-(Ar)Enynes and Nitriles by a Formal [4+2] Cycloaddition Reaction. *Org. Lett.* **2022**, *24* (6), 1292–1297. https://doi.org/10.1021/acs.orglett.1c04192.
(531) Jafarova, S.; Aydin, T.; Isayev, J.; Saglamtas, R.; Ozgokce, F.; Kazaz, C.; Cakir, A. Anti-Alzheimer, Antiglaucoma, and Antidiabetic Activities of Sainfoin (*Onobrychis Buhseana* Boiss.). *Chem. Biodivers.* **2025**, e202402013. https://doi.org/10.1002/cbdv.202402013.
(532) Wang, T. C.; Furukawa, H.; Nihro, Y.; Kakegawa, H.; Matsumoto, H.; Satoh, T. Synthesis of 4-Alkoxyaryl-Beta-D-Glucopyranosides and Their Inhibitory Effects on Histamine Release from Rat Peritoneal Mast Cells Induced by Concanavalin A. *Chem. Pharm. Bull. (Tokyo)* **1994**, *42* (3), 570–575. https://doi.org/10.1248/cpb.42.570.
(533) Wagh, R. B.; Nagarkar, J. M. Silica Chloride: An Efficient Promoter for Oxidation of Arylboronic Acids to Phenols. *Tetrahedron Lett.* **2017**, *58* (33), 3323–3326. https://doi.org/10.1016/j.tetlet.2017.07.041.
(534) Chatterjee, I.; Porwal, D.; Oestreich, M. $B(C_6F_5)_3$-Catalyzed Chemoselective Defunctionalization of Ether-Containing Primary Alkyl Tosylates with Hydrosilanes. *Angew. Chem. Int. Ed.* **2017**, *56* (12), 3389–3391. https://doi.org/10.1002/anie.201611813.
(535) Trân, H. Q.; Kawano, S.; Thielemann, R. E.; Tanaka, K.; Ravoo, B. J. Calamitic Liquid Crystals for Reversible Light-Modulated Phase Regulation Based on Arylazopyrazole Photoswitches. *Chem. – Eur. J.* **2024**, *30* (2), e202302958. https://doi.org/10.1002/chem.202302958.
(536) Dimakos, V.; Liu, J. J. W.; Ge, Z.; Taylor, M. S. Copper-Mediated Anomeric *O*-Arylation with Organoboron Reagents. *Org. Biomol. Chem.* **2019**, *17* (23), 5671–5674. https://doi.org/10.1039/C9OB01022J.
(537) Okamoto, K.; Akiyama, R.; Kobayashi, S. Recoverable, Reusable, Highly Active, and Sulfur-Tolerant Polymer Incarcerated Palladium for Hydrogenation. *J. Org. Chem.* **2004**, *69* (8), 2871–2873. https://doi.org/10.1021/jo0358527.
(538) Sui, J.-J.; Xiong, D.-C.; Ye, X.-S. Copper-Mediated O-Arylation of Lactols with Aryl Boronic Acids. *Chin. Chem. Lett.* **2019**, *30* (8), 1533–1537. https://doi.org/10.1016/j.cclet.2019.06.014.
(539) Indurugalla, D.; Bennet, A. J. A Kinetic Isotope Effect Study on the Hydrolysis Reactions of Methyl Xylopyranosides and Methyl 5-Thioxylopyranosides: Oxygen versus Sulfur Stabilization of Carbenium Ions. *J. Am. Chem. Soc.* **2001**, *123* (44), 10889–10898. https://doi.org/10.1021/ja011232g.
(540) Balmond, E. I.; Benito-Alifonso, D.; Coe, D. M.; Alder, R. W.; McGarrigle, E. M.; Galan, M. C. A 3,4- *Trans* -Fused Cyclic Protecting Group Facilitates α-Selective Catalytic Synthesis of 2-Deoxyglycosides. *Angew. Chem. Int. Ed.* **2014**, *53* (31), 8190–8194. https://doi.org/10.1002/anie.201403543.
(541) ZHANG, Z.; HUANG, S.; ZHANG, Z.; SU, Y.; REN, Y. SGLT-2 INHIBITORS. WO2015CN89492.
(542) Li, J.; Li, W.; Yu, B. A Divergent Approach to the Synthesis of Simplexides and Congeners via a Late-Stage Olefin Cross-Metathesis Reaction. *Org. Biomol. Chem.* **2013**, *11* (30), 4971. https://doi.org/10.1039/c3ob40552d.
(543) Shull, B. K.; Wu, Z.; Koreeda†, M. A Convenient, Highly Efficient One-Pot Preparation of Peracetylated Glycals From Reducing Sugars. *J. Carbohydr. Chem.* **1996**, *15* (8), 955–964. https://doi.org/10.1080/07328309608005701.
(544) Mora Flores, E. W.; Suarez, D.; Uhrig, M. L.; Postigo, A. Photocatalyzed Perfluoroalkylation of Endoglycals. *J. Org. Chem.* **2023**, *88* (24), 16803–16816. https://doi.org/10.1021/acs.joc.3c01488.
(545) Van Der Kaaden, M.; Breukink, E.; Pieters, R. J. Synthesis and Antifungal Properties of Papulacandin Derivatives. *Beilstein J. Org. Chem.* **2012**, *8*, 732–737. https://doi.org/10.3762/bjoc.8.82.
(546) Singh, A. K.; Kandasamy, J. Palladium Catalyzed Stereocontrolled Synthesis of *C* -Aryl Glycosides Using Glycals and Arenediazonium Salts at Room Temperature. *Org. Biomol. Chem.* **2018**, *16* (28), 5107–5112. https://doi.org/10.1039/C8OB01393D.
(547) Cheshev, P.; Marra, A.; Dondoni, A. Direct Epoxidation of D-Glucal and d-Galactal Derivatives with in Situ Generated DMDO. *Carbohydr. Res.* **2006**, *341* (16), 2714–2716. https://doi.org/10.1016/j.carres.2006.09.003.

(548) Somasundaram, D.; Balasubramanian, K. K.; Bhagavathy, S. Tunable Stereoselectivity in the Synthesis of α- and β-Aryl Glycosides Using 1,2-α-Anhydrosugars as Glycosyl Donors. *Carbohydr. Res.* **2017**, *449*, 95–102. https://doi.org/10.1016/j.carres.2017.07.007.

(549) Liu, C.-F.; Xiong, D.-C.; Ye, X.-S. KOtBu-Mediated Aromatic O-Glycosylation of 1,2-Anhydrosugar and Aryl Boronic Acid. *Tetrahedron Lett.* **2016**, *57* (12), 1372–1374. https://doi.org/10.1016/j.tetlet.2016.02.059.

(550) Henderson, A. S.; Bower, J. F.; Galan, M. C. Carbohydrate-Based N-Heterocyclic Carbenes for Enantioselective Catalysis. *Org Biomol Chem* **2014**, *12* (45), 9180–9183. https://doi.org/10.1039/C4OB02056A.

(551) Yu, Y.; Tyrikos-Ergas, T.; Zhu, Y.; Fittolani, G.; Bordoni, V.; Singhal, A.; Fair, R. J.; Grafmüller, A.; Seeberger, P. H.; Delbianco, M. Systematic Hydrogen-Bond Manipulations To Establish Polysaccharide Structure–Property Correlations. *Angew. Chem. Int. Ed.* **2019**, *58* (37), 13127–13132. https://doi.org/10.1002/anie.201906577.

(552) Cox, D. J.; Singh, G. P.; Watson, A. J. A.; Fairbanks, A. J. Neighbouring Group Participation During Glycosylation: Do 2-Substituted Ethyl Ethers Participate? *Eur. J. Org. Chem.* **2014**, *2014* (21), 4624–4642. https://doi.org/10.1002/ejoc.201402260.

(553) Demchenko, A. V.; Pornsuriyasak, P.; De Meo, C. Acetal Protecting Groups in the Organic Laboratory: Synthesis of Methyl 4,6-O-Benzylidene-α-D-Glucopyranoside. *J. Chem. Educ.* **2006**, *83* (5), 782. https://doi.org/10.1021/ed083p782.

(554) Puri, K.; Kulkarni, S. S. Total Synthesis of the Phosphorylated Zwitterionic Trisaccharide Repeating Unit of *Photorhabdus Temperata Cinerea* 3240. *Org. Lett.* **2021**, *23* (18), 7083–7087. https://doi.org/10.1021/acs.orglett.1c02487.

(555) DeNinno, M. P.; Etienne, J. B.; Duplantier, K. C. A Method for the Selective Reduction of Carbohydrate 4,6-O-Benzylidene Acetals. *Tetrahedron Lett.* **1995**, *36* (5), 669–672. https://doi.org/10.1016/0040-4039(94)02348-F.

(556) Ochiai, H.; Niwa, T.; Hosoya, T. Stereoinversion of Stereocongested Carbocyclic Alcohols via Triflylation and Subsequent Treatment with Aqueous *N* , *N* -Dimethylformamide. *Org. Lett.* **2016**, *18* (23), 5982–5985. https://doi.org/10.1021/acs.orglett.6b02675.

(557) Traboni, S.; Bedini, E.; Silipo, A.; Vessella, G.; Iadonisi, A. Solvent-Free Glycosylation from Per- *O* -Acylated Donors Catalyzed by Methanesulfonic Acid. *Eur. J. Org. Chem.* **2021**, *2021* (41), 5669–5676. https://doi.org/10.1002/ejoc.202101121.

(558) Inuki, S.; Kishi, J.; Kashiwabara, E.; Aiba, T.; Fujimoto, Y. Convergent Synthesis of Digalactosyl Diacylglycerols. *Org. Lett.* **2017**, *19* (24), 6482–6485. https://doi.org/10.1021/acs.orglett.7b03043.

(559) Dorokhova, V. S.; Gerbst, A. G.; Komarova, B. S.; Previato, J. O.; Previato, L. M.; Dmitrenok, A. S.; Shashkov, A. S.; Krylov, V. B.; Nifantiev, N. E. Synthesis and Conformational Analysis of Vicinally Branched Trisaccharide β-D-Gal*f*-(1→2)-[β-D-Gal*f*-(1→3)-]-α-Gal*p* from *Cryptococcus Neoformans* Galactoxylomannan. *Org. Biomol. Chem.* **2021**, *19* (13), 2923–2931. https://doi.org/10.1039/D0OB02071K.

(560) Huang, J.; Huang, W.; Meng, X.; Wang, X.; Gao, P.; Yang, J. Stereoselective Synthesis of α-3-Deoxy-D-*Manno*-oct-2-ulosonic Acid (α-Kdo) Glycosides Using 5,7-*O*-Di-*Tert*-butylsilylene-Protected Kdo Ethyl Thioglycoside Donors. *Angew. Chem. Int. Ed.* **2015**, *54* (37), 10894–10898. https://doi.org/10.1002/anie.201505176.

(561) Cocinero, E. J.; Gamblin, D. P.; Davis, B. G.; Simons, J. P. The Building Blocks of Cellulose: The Intrinsic Conformational Structures of Cellobiose, Its Epimer, Lactose, and Their Singly Hydrated Complexes. *J. Am. Chem. Soc.* **2009**, *131* (31), 11117–11123. https://doi.org/10.1021/ja903322w.

(562) Jalsa, N. K. Regioselective Removal of the Anomeric O-Benzyl from Differentially Protected Carbohydrates. *Tetrahedron Lett.* **2011**, *52* (49), 6587–6590. https://doi.org/10.1016/j.tetlet.2011.09.130.

(563) David, S.; Thieffry, A.; Veyrières, A. A Mild Procedure for the Regiospecific Benzylation and Allylation of Polyhydroxy-Compounds via Their Stannylene Derivatives in Non-Polar Solvents. *J Chem Soc Perkin Trans 1* **1981**, No. 0, 1796–1801. https://doi.org/10.1039/P19810001796.

(564) Berry, J. M.; Dutton, G. G. S. Synthesis of 6-*O*-(4-*O*-Methyl-β-D-Galactose. *Can. J. Chem.* **1972**, *50* (9), 1424–1426. https://doi.org/10.1139/v72-222.
(565) Bochkov, A. F.; Voznyi, Y. V. Sugar Ortho Esters. *Carbohydr. Res.* **1974**, *32* (1), 1–8. https://doi.org/10.1016/S0008-6215(00)82456-8.
(566) Tam, R. Y. Studies Into the Structural Features of C-Linked Antifreeze Glycoprotein Analogues Responsible for Ice-Recrystallization Inhibition Activity. PhD Thesis, University of Ottawa, Ottawa, ON, 2011. http://ruor.uottawa.ca/handle/10393/19739 (accessed 2024-11-13).
(567) McMunn, L. E.; D'Costa, A. S.; Bordenave, N.; Ben, R. N. Probing the Mechanism of Action of Small-Molecule Ice Recrystallization Inhibitors Using Proton Nuclear Magnetic Resonance Relaxation. *J. Phys. Chem. Lett.* **2023**, *14* (26), 6043–6050. https://doi.org/10.1021/acs.jpclett.3c00845.
(568) Leclerc, Z.; McMunn, L. E.; Nastic, A.; Ben, R. N.; Jodoin, B. Manufacturing and Icephobic Performance Evaluation of Cold-Sprayed Adhesive Perfluoroalkoxy Alkane Coatings. *J. Therm. Spray Technol.* **2023**, *32* (4), 851–876. https://doi.org/10.1007/s11666-023-01551-z.
(569) Deng, J. M.; McMunn, L. E.; Oakley, M. S.; Dang, H. T.; Rodriguez, R. S. Toward Sustained Cultural Change through Chemistry Graduate Student Diversity, Equity, and Inclusion Communities. *J. Chem. Educ.* **2022**, *99* (1), 373–382. https://doi.org/10.1021/acs.jchemed.1c00485.